Lecture Notes in Electrical Engineering 243

Jiadong Sun · Wenhai Jiao
Haitao Wu · Chuang Shi
Editors

China Satellite Navigation Conference (CSNC) 2013 Proceedings

BeiDou/GNSS Navigation Applications • Test & Assessment Technology • User Terminal Technology

Springer

Lecture Notes in Electrical Engineering

Volume 243

For further volumes:
http://www.springer.com/series/7818

Jiadong Sun · Wenhai Jiao
Haitao Wu · Chuang Shi
Editors

China Satellite Navigation Conference (CSNC) 2013 Proceedings

BeiDou/GNSS Navigation Applications •
Test & Assessment Technology •
User Terminal Technology

Springer

Editors
Jiadong Sun
China Aerospace Science and Technology Corporation
Chinese Academy of Sciences
Beijing
People's Republic of China

Wenhai Jiao
China Satellite Navigation Office
Beijing
People's Republic of China

Haitao Wu
Navigation Headquarters
Chinese Academy of Sciences
Beijing
People's Republic of China

Chuang Shi
Wuhan University
Wuhan
People's Republic of China

ISSN 1876-1100 ISSN 1876-1119 (electronic)
ISBN 978-3-642-37397-8 ISBN 978-3-642-37398-5 (eBook)
DOI 10.1007/978-3-642-37398-5
Springer Heidelberg New York Dordrecht London

Library of Congress Control Number: 2013938171

Printed on acid-free paper

Springer is part of Springer Science+Business Media (www.springer.com)

Preface

China's BeiDou Navigation Satellite System (BDS) has been independently developed, which is similar in principle to global positioning system (GPS) and compatible with other global satellite navigation systems (GNSS). The BeiDou will provide highly reliable and precise positioning, navigation, and timing (PNT) services as well as short-message communication for all users under all-weather, all-time, and worldwide conditions.

Since BeiDou Navigation Satellite System provided the test run services on December 27, 2011, more than 6 satellites have been successfully launched in 4 times with large improvements in system coverage, constellation robustness and positioning accuracy. Currently, all in-orbit satellites and ground systems run well, which meet the design requirements through the testing and evaluation of various user terminals. After the news conference announced the Full Operational Capability (FOC) of BeiDou Navigation Satellite System for China and surrounding area on December 27, 2012, the BeiDou Navigation Satellite System officially starts to provide continuous passive positioning, navigation and timing services as well as active positioning, two-way timing and short message communication services.

China Satellite Navigation Conference (CSNC) is an open platform for academic exchanges in the field of satellite navigation. It aims to encourage technological innovation, accelerate GNSS engineering and boost the development of the satellite navigation industry in China and in the world.

The 4th China Satellite Navigation Conference (CSNC 2013) is held on May 13–17, 2013, Wuhan, China. The theme of CSNC 2013 is BeiDou Application—Opportunities and Challenges, which covers a wide range of activities, including technical seminars, academic exchange, forum, exhibition, lectures as well as ION panel. The main topics are as:

1. BeiDou/GNSS Navigation Applications
2. Satellite Navigation Signal System, Compatibility and Interoperability
3. Precise Orbit Determination and Positioning
4. Atomic Clock Technique and Time–Frequency System

5. Satellite Navigation Augmentation and Integrity Monitoring
6. BeiDou/GNSS Test and Assessment Technology
7. BeiDou/GNSS User Terminal Technology
8. Satellite Navigation Models and Methods
9. Integrated Navigation and New Methods

The proceedings have 181 papers in nine topics of the conference, which were selected through a strict peer-review process from 627 papers presented at CSNC 2013.

We thank the contribution of each author and extend our gratitude to over 100 referees and 36 session chairmen who are listed as members of editorial board. The assistance of CSNC 2013's organizing committees and the Springer editorial office is highly appreciated.

Jiadong Sun
Chair of CSNC 2013

Editorial Board

The 4th China Satellite Navigation Conference (CSNC 2013)

Scientific Committee

Chairman:
Jiadong Sun, China Aerospace Science and Technology Corporation

Vice-Chairman:
Rongjun Shen, China
Jisheng Li, China
Qisheng Sui, China
Zuhong Li, China Academy of Space Technology
Shusen Tan, Beijing Satellite Navigation Center, China

Executive Chairman:
Jingnan Liu, Wuhan University
Yuanxi Yang, China National Administration of GNSS and Applications
Shiwei Fan, China

Committee Members (By Surnames Stroke Order):
Xiancheng Ding, China Electronics Technology Group Corporation
Qingjun Bu, China
Liheng Wang, China Aerospace Science and Technology Corporation
Yuzhu Wang, Shanghai Institute of Optics and Fine Mechanics, Chinese Academy of Sciences
Guoxiang Ai, National Astronomical Observatories, Chinese Academy of Sciences
Shuhua Ye, Shanghai Astronomical Observatories, Chinese Academy of Sciences
Zhaowen Zhuang, National University of Defense Technology
Qifeng Xu, PLA Information Engineering University
Houze Xu, Institute of Geodesy and Geophysics, Chinese Academy of Sciences
Guirong Min, China Academy of Space Technology
Xixiang Zhang, China Electronics Technology Group Corporation
Lvqian Zhang, China Aerospace Science and Technology Corporation

Junyong Chen, National Administration of Surveying, Mapping and Geoinformation
Benyao Fan, China Academy of Space Technology
Dongjin Luo, China
Guohong Xia, China Aerospace Science and Industry Corporation
Chong Cao, China Research Institute of Radio Wave Propagation (CETC 22)
Faren Qi, China Academy of Space Technology
Sili Liang, China Aerospace Science and Technology Corporation
Shancheng Tu, China Academy of Space Technology
Rongsheng Su, China
Zhipeng Tong, China Electronics Technology Group Corporation
Ziqing Wei, Xi′an Institute of Surveying and Mapping

Organizing Committee

Secretary General:
Haitao Wu, Navigation Headquarters, Chinese Academy of Sciences

Vice-Secretary General:
Wenhai Jiao, China Satellite Navigation Office
Tao Peng, Academy of Satellite Application, China Aerospace Science and Technology Corporation
Wenjun Zhao, Beijing Satellite Navigation Center
Chuang Shi, Wuhan University
Weina Hao, Navigation Headquarters, Chinese Academy of Sciences

Committee Members (By Surnames Stroke Order):
Qun Ding, Xi'an Institute of Navigation Technology
Miao Yu, Beijing Institute of Space Science and Technology Information
Yinhu Ma, Navigation Satellite Systems Engineering Center, China Academy of Aerospace Electronics Technology
Xiuwan Chen, Institute of Digital China, Peking University
Mingquan Lu, Tsinghua University
Guangzhou Ouyang, Academy of Opto-Electronics, Chinese Academy of Sciences
Shuanggen Jin, Shanghai Astronomical Observatory, Chinese Academy of Sciences
Xiang'an Zhao, China Defense Science and Technology Information Center
Hong Yuan, Navigation Headquarters, Chinese Academy of Sciences
Yamin Dang, Chinese Academy of Surveying and Mapping
Zhong Dou, National Time Service Center, Chinese Academy of Sciences

Contents

Part I
BeiDou/GNSS Navigation Applications

Chapter 1
Research on the Short-Time Time Series of CORS Reference Stations

Qianming Wang, Hui Liu, Huchun Ye and Chuang Qian

Abstract CORS system, an very important terrestrial geographic information collection infrastructure, provides not only services in the field of surveying and mapping, but also plays an important role in the aspects of earthquake monitoring, traffic navigation, planning and construction, disaster prevention. After completion of CORS system, with the inference of the stability of antenna substrate, the real position of CORS reference station antennas will change tiny in real time. If the variation trend of the reference station antennas can be grasped, then appropriate measures can be taken to eliminate or weaken the impact of the reference station movement, correspondingly, the positioning accuracy will be improved. Especially in the field of earthquake monitoring and disaster prevention, it is more essential to monitor the movement of CORS reference stations in short-term or real-time at high-precision, because the state of CORS reference station are of great importance to monitoring points. The data in JXCORS net and BERNESE5.0 software were adopted to probe the stability of CORS reference stations with short-time and long-distance. The results showed that the variation of plane coordinates in the adjacent periods was less than 1 cm, and the variation of elevation coordinates was less than 2.5 cm which are in accordance with the theory; also the variation of stations had the similarity trend. The data strategies proposed in this paper is reasonable.

Keywords CORS station · Stability · BERNESE5.0 software · Variation

Q. Wang · H. Liu (✉) · H. Ye · C. Qian
GNSS Center, Wuhan University, Wuhan, Hubei Province, China
e-mail: loweliu@hotmail.com

J. Sun et al. (eds.), *China Satellite Navigation Conference (CSNC) 2013 Proceedings*, Lecture Notes in Electrical Engineering 243,
DOI: 10.1007/978-3-642-37398-5_1,

1.1 Introduction

After completion of CORS system, with the inference of the stability of antenna substrate, the real position of CORS reference station antennas will change tiny in real time. If the variation is rather large which is showed that the stability of the station is bad, then the station cannot be used to provide service for the user. Especially in the field of earthquake monitoring and disaster prevention, it is more essential to monitor the movement of CORS reference stations in short-term or real-time at high-precision, because the state of CORS reference station are of great importance to monitoring points. And now many researches concentrate on study the long-term stability of stations [1–4], while the research of short-term stability of stations need to be studied further.

Three consecutive days' data of 9 stations (ANYU FUZH JIAN JIUJ QNAN QXXX SHIC SRAO WANZ) in JXCORS were used, from 19th April 2012 to 21st April 2012. The interval of data is 1 s, the receiver is TRIMBLE NETR3 and the type of antenna is TRM55971.00, also the mean distant between stations is 200 km. The distribution is shown in Fig. 1.1.

RNX2SNX module in high precision data processing software BRNESE5.0 was applied to process three consecutive days' observation data of 9 stations in JXCORS, those data were cut into pieces of two hours. And the initial coordinates

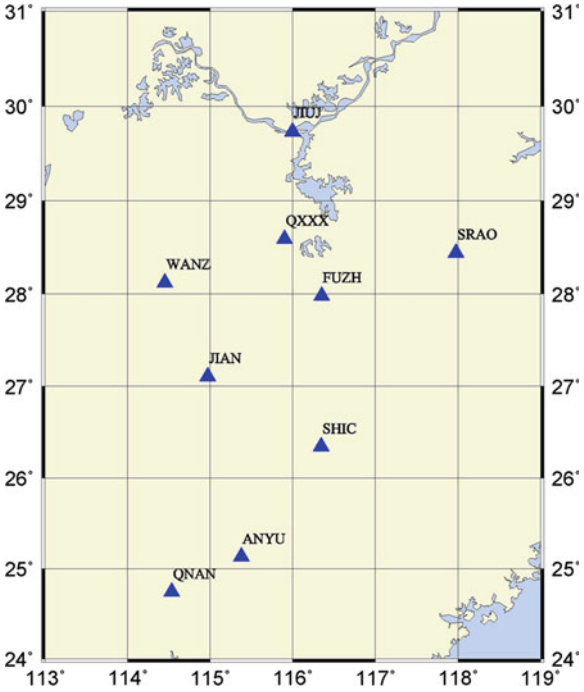

Fig. 1.1 Distribution of 9 stations

of those stations were very precise. The coordinates of those stations in every session were obtained in the end.

1.2 Data Processing Method

High precision data processing software BERNESE5.0 was utilized to process data. It is developed by the Astronomical Institute, University of Bern, and it can be used to process data of GPS, GLONASS, the mixed data of GPS and GLONASS, and data of SLR. The version 5.0 is consisted of PPP module, RNX2SNX module, CLKDET module and BASTST module, in which the coordinate results acquired in PPP module are acted as the initial coordinates in RNX2SNX module, CLKDET module and BASTST module [5].

1.2.1 Analysis of Data Quality

Data conversion, edit and quality analysis software TEQC was used to analyze the quality of observation data. The most important information of data quality are multipath effect index Mp1, Mp2 in $L1$, $L2$ carrier and ratio value o/slps of observation and cycle slips in S file. Usually the CSR value is used to describe the number of cycle slips and it is described as follows:

$$\mathrm{CSR} = 1,000/(\mathrm{o/slps}) \tag{1.1}$$

Test results of IGS data quality shows that Mp1, Mp2 and *CSR* of 2/3 of IGS stations are less than 0.5, 0.75, 10 respectively.

The statistical results of data analysis are as follows:

What Table 1.1 shows are: data utilization of QNNA and SRAO are less than 90 %; the MP1 of 9 stations are less than 0.5, but the MP1 of WANZ and SRAO are larger relatively; the MP2 of 9 stations are less than 0.75, but the MP2 of QNAN, WANZ and SRAO are larger relatively; the CSR of 9 stations are less than 10, but the CSR of WANZ and SRAO are larger relatively, and it shows that cycle slips of QNAN station are larger.

We can know from the above analysis that data quality of QNAN SRAO and WANZ stations are poor relatively. When data of one day are cut into pieces with two hours, data utilization of some sessions of some stations will lower and multipath effect will be serious, also cycle slips will large, resulting poor result of data processing.

Table 1.1 The statistics results of station quality analysis

Station	DOY	Data utilization (%)	MP1 (m)	MP2 (m)	CSR
ANYU	110	97	0.28	0.29	0.23
	111	97	0.28	0.28	0.23
	112	97	0.29	0.29	0.27
FUZH	110	95	0.27	0.27	0.37
	111	95	0.28	0.27	0.05
	112	95	0.28	0.27	0.09
JIAN	110	95	0.3	0.28	0.63
	111	95	0.29	0.26	0.03
	112	95	0.34	0.32	0.65
JIUJ	110	99	0.28	0.28	0.1
	111	99	0.28	0.28	0.01
	112	99	0.28	0.28	0.2
QNAN	110	87	0.29	0.34	2.1
	111	86	0.29	0.33	2.06
	112	86	0.3	0.34	2.14
QXXX	110	99	0.32	0.32	0.59
	111	99	0.31	0.31	0.02
	112	99	0.31	0.31	0.23
SHIC	110	99	0.28	0.27	0.21
	111	99	0.28	0.26	0.13
	112	99	0.28	0.27	0.76
SRAO	110	88	0.35	0.36	0.48
	111	78	0.37	0.35	0.27
	112	85	0.37	0.36	0.56
WANZ	110	95	0.44	0.49	0.83
	111	94	0.39	0.36	0.18
	112	95	0.38	0.35	0.58

1.2.2 Strategy of Data Processing

1. initial benchmark: ANYU, FUZH and SHIC stations are used as fixed stations because of their better data quality.

BERNESE5.0 software was utilized to process three consecutive days' data from 21st April 2011 to 24th April 2011 of above 9 stations. And we can obtain the coordinates of those stations in the epoch first January 2005 in frame IGS08, and then we set those coordinates as prior coordinates.

2. the other strategies are listed in the following Table 1.2, [6, 7].

1.2.3 Quality Analysis of Data Processing Results

The main indexes of BERNESE data processing results are [5]:

Table 1.2 Calculation strategy of 9 stations

Strategy	Illustration
Linear combination of observations	Ionosphere-free combination L3
Baseline resolving type	BASELINE
Baseline selection strategy	OBS-MAX
Ambiguity resolving strategy	QIF
Satellite orbit	IGS precise ephemeris
Reference frame	IGS08
Reference epoch	12:00 clock everyday
Troposphere parameter estimation	Piecewise linearity, interval 30 min
Troposphere modified model	Saastamoinen
Antenna phase position center	Absolute

1. the value of Normalized Root Mean Square (NRMS): It is described as the degree of the baseline values deviate from the weighted average in single session. Generally, the larger of NRMS value, the lower precision of baseline and cycle slips may be repaired uncompleted.

Table 1.3 shows that variation of NRMS is slight, the maximum is 2.06 mm, and the minimum is 1.67 mm and the average value is 1.84 mm. It indicates that the overall stability of BERNESE results is good and it is in accordance with quality requirements of highly data processing.

2. repeatability of coordinates

It is an assessment index of coordinate calculation results. The repeatability results are originated from the coordinates which calculated by the ADDNEQ2 module.

Table 1.4 describes that the repeatability value of ANYU, FUZH, JIAN, JIUJ, QXXX and SHIC stations are in millimeter level, and the repeatability value of other three stations are larger relatively because of their poor data quality.

Table 1.3 NRMS value of every session (unit: mm)

	DOY	0–2	2–4	4–6	6–8	8–10	10–12	12–14	14–16	16–18	18–20	20–22	22–24
NRMS	110	1.73	1.78	1.78	1.81	1.94	1.97	1.72	1.82	1.72	1.81	1.76	1.86
	111	1.92	1.93	1.89	1.88	2.06	1.93	1.93	1.9	1.81	1.92	1.83	1.85
	112	1.86	1.79	1.86	1.86	2.04	1.95	1.8	1.88	1.67	1.78	1.67	1.72

Table 1.4 Repeatability results of stations (unit: m)

Station	Coordinate	DOY = 110	DOY = 111	DOY = 112
ANYU	X	0.0038	0.0046	0.0044
	Y	0.0045	0.0041	0.0052
	Z	0.005	0.0062	0.0051
FUZH	X	0.0047	0.0076	0.0067
	Y	0.0085	0.0088	0.0089
	Z	0.0076	0.0061	0.0064
JIAN	X	0.0072	0.0067	0.0058
	Y	0.0096	0.0085	0.0089
	Z	0.0072	0.0073	0.0074
JIUJ	X	0.0083	0.005	0.0058
	Y	0.0085	0.0088	0.0083
	Z	0.0077	0.0074	0.0054
QNAN	X	0.0136	0.0174	0.0133
	Y	0.0125	0.0181	0.0169
	Z	0.0116	0.0065	0.0129
QXXX	X	0.0065	0.007	0.005
	Y	0.0074	0.0054	0.0083
	Z	0.0072	0.0053	0.0072
SHIC	X	0.049	0.0067	0.0036
	Y	0.053	0.0058	0.0042
	Z	0.035	0.007	0.0034
SRAO	X	0.0311	0.031	0.0225
	Y	0.0382	0.0275	0.0324
	Z	0.0188	0.0133	0.012
WANZ	X	0.0313	0.0392	0.0368
	Y	0.0335	0.0315	0.0323
	Z	0.0365	0.0409	0.0389

1.3 Analysis of Results

1.3.1 Comparison Results of Coordinate Variation

The Cartesian coordinates of stations in frame IGS08 were obtained according to the strategies above, and then we converted those coordinates to the plane coordinates. The coordinates variation of those stations in the adjacent sessions are described in Figs. 1.2, 1.3 and 1.4.

Figures 1.2, 1.3 and 1.4 reveal that x and y coordinate variation of stations in the adjacent sessions are mostly less than 1 cm and h coordinate variation of stations are less than 2.5 cm except QNAN SRAO and WANZ stations. The variation in the adjacent sessions is small which complies with the changing nature of stations, and it may be caused by temperature, environment, data quality and other factors. We know from the above analysis of data quality that data utilization of WANZ SRAO and QNAN stations are lower and the multipath effect of those

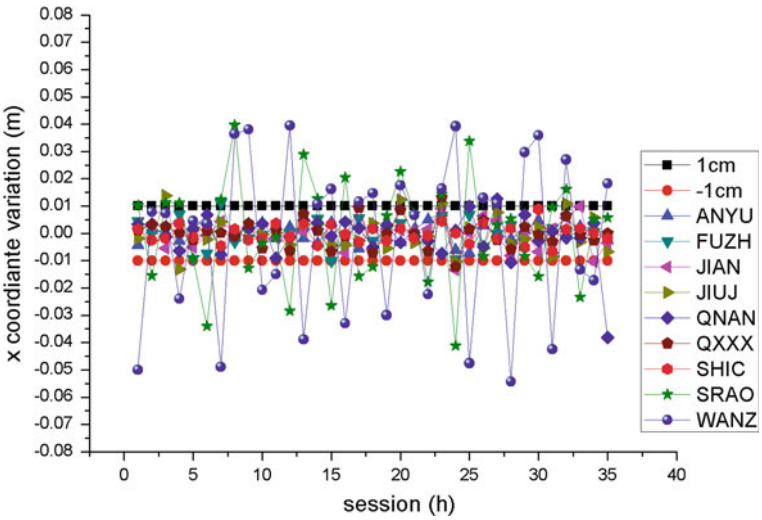

Fig. 1.2 x coordinate variation of stations in the adjacent sessions

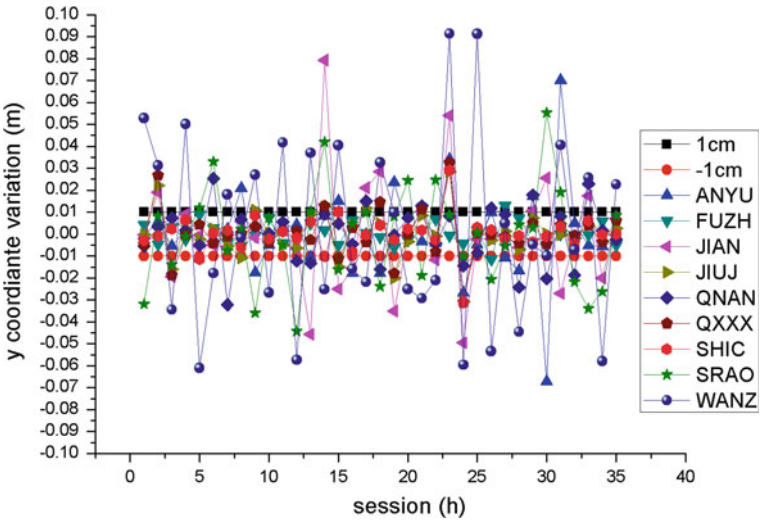

Fig. 1.3 y coordinate variation of stations in the adjacent sessions

three stations are serious, and also cycle slips are larger which can lead to get the poor results of those stations and larger coordinate variation in the adjacent sessions.

From the above figures we also know that changing amplitude in elevation is larger than that in plane, and it indicates that measuring precision in elevation is lower than that in plane.

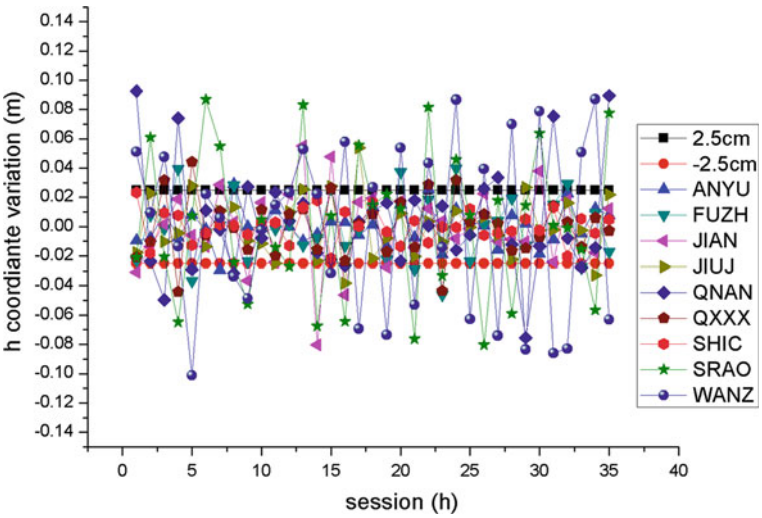

Fig. 1.4 h coordinate variation of stations in the adjacent sessions

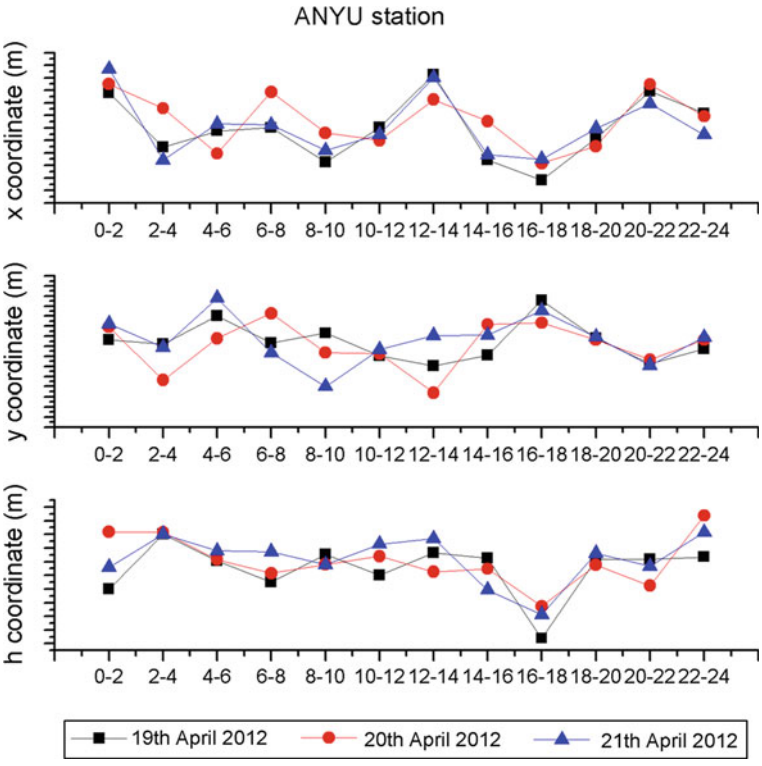

Fig. 1.5 Coordinate variation of ANYU station in consecutive days

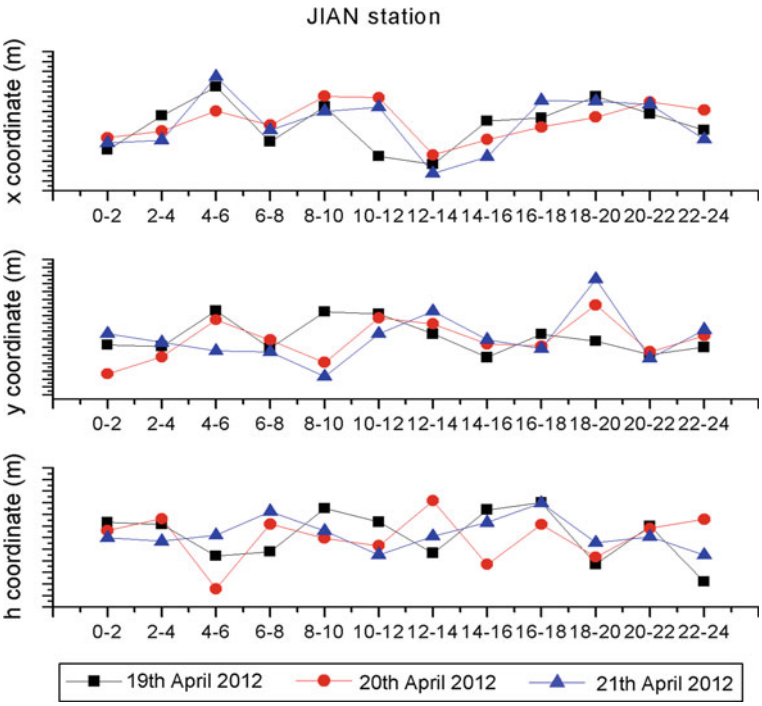

Fig. 1.6 Coordinate variation of JIAN station in consecutive days

1.3.2 Analysis of Coordinate Variation Consistency of Stations

We select the coordinates of ANYU, JIAN and WANZ stations to analyze. The following figures are the coordinate trends of these stations in consecutive days.

From Figs. 1.5, 1.6 and 1.7 we know that coordinate variation of ANYU JIAN and WANZ stations everyday has similar trends. For WANZ station, the trend is similar even though the date quality is poor and the variation value is larger relatively. The variation trends everyday of stations are not exactly the same due to the different environment around the station.

the location of CORS system,an very important terrestrial geographic information collection infrastructure, should be abided by the following principals [8]: (1) the distant between stations and features which is easy to produce multipath effect should be over 200 m; (2) there should have satellites of which the elevation angle is over 10 degrees; (3) the distant away from electromagnetic interference area and lighting area should be over 200 m; (4) the stations should be away from the shock area; (5) stations should be away from unstable area. From these conditions, we can conclude that the factors which affect the stability of CORS stations is mainly the variation of temperature. However, the trend of temperature

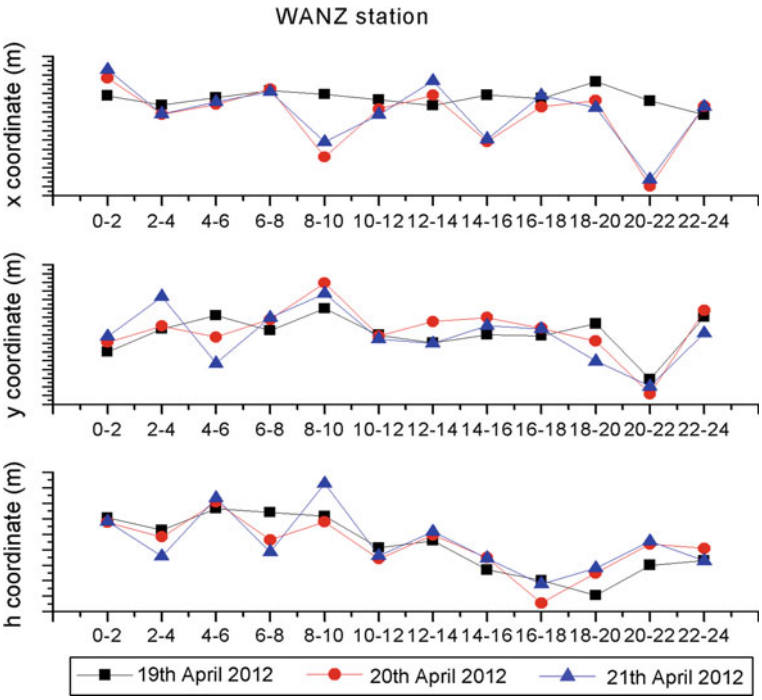

Fig. 1.7 Coordinate variation of WANZ station in consecutive days

variation in the same area is similarly normally (especially in the case of weather change suddenly), that is the temperature in the morning and evening is rather lower while the temperature in the noon is rather higher. So the fact that the variation of CORS stations everyday is conformity is abided by the theory.

1.4 Conclusions

Through the analysis of three days' data of 9 stations in JXCORS net, the following conclusions are drawn:

1. precise coordinates of stations can be obtained in case fixing stations in the net instead of IGS stations, using precise initial coordinates and processing observation data of short time through RNX2SNX module in BEERNESE5.0 software. What's more, the variation in the adjacent sessions is in accordance with the theoretical.
2. the trends of stations everyday are similar. Even though the data quality is poor and the variation value is significant.

This article has some points for improvement:

1. Some additional circumstantial information, such as whether the effect of multipath and receiver regularly identified should be considered.
2. On studying CORS stations coordinate time series regularity, it is recommended to increase the analysis for antenna piers' change with the local time and information about pier foundation materials analysis.

Acknowledgments This paper was funded by the National high technology research and development plan (863 Program), 2007AA12Z309; The National Basic Research Program of China (973 Program) (2007CB310805); Surveying and Mapping Basic Research Fund of Earth Space Environment and Geodesic Measurement Laboratory in Wuhan University (100110).

References

1. Agnew DC, Bock Y, Wyatt F (2001) Comments on NGS proposed CORS monumentation. Institute of Geophysics and Planetary Physics, Scripps Institution of Oceanography, University of California
2. Nikolaidis R (2002) Observation of geodetic and seismic deformation with the global positioning system. University of California, San Digeo
3. Dong D, Fang P, Bock Y, et al (2002) Anatomy of apparent seasonal variations from GPS-derived site position time series. J Geophys Res 107(B4):2075
4. Fu Y (2002) Present-day crustal deformation in China and GPS-derived coordinate time series analysis. Shanghai Astronomical Observatory, Chinese Academy of Sciences
5. Hugentobler U, Dach R, Fridez P, et al (2007) Bernese GPS software version 5.0
6. Haasdyk J (2009) Automatic Bernese Processing of CORSnet-NSW GPS data for deformation monitoring. The University of New South Wales, New South Wales
7. Xu Y (2011) Research on the stability of GPS reference stations in Tianjin CORS. Wuhan University, Wuhan
8. Huang J, Chen W (2009) Construction and application of continuous operation reference system (CORS). Science Press, China

Chapter 2
Study on the Earth's Volume Change by Using Space Observed Technology

Xinhui Zhu, Fuping Sun and Ren Wang

Abstract Although plate tectonics already being the studying basis and mainstream of global tectonics nowadays, theories of expanding or compressing about the Earth have not been ceased in deed, which were still the main objects of investigating and searching proofs for many geoscientists. In the research of plate tectonics, a basic hypothesis which has been used until now is that the solid Earth's volume (or radius) keeps unchanging because the lithosphere's expanding and compressing could be compensated mutually. Whether and in which time scale these hypothesizes is correct or not, that has not been proved rigorously. Along with the development of space techniques and improvement of geodetic precision, it is possible to detect and resolve above problems in the help of more and higher precision observations and stations distributing globally. The earth's unsymmetrical phenomenon and the doctrine of its expansion and compression was discussed and expounded. After a detailed analysis of the status of global change phenomena research, one data processing method by unifying the global vertical velocity to the optimal global crustal vertical motion reference datum was put forward. Then the solid earth's volume and radius change were detected by using Delaunay arithmetic and plate motion model interpolation method. The result shows that the earth volume's change rate is $(-0.0379 \pm 0.0902) \times 10^3 km^3/a$, which is similar to (-0.1 ± 0.2) mm/a after being converted to the change of the earth's radius, and is close to the result (near to -0.24 mm/a) by using global observed station's radial velocity. The conclusion is that the radius of the earth cannot be considered changed in the range of one time mean error, which is corresponded to the results of others by using space observed data and physical geography information.

Keywords Space-geodetic data · Earth · Asymmetrical deformation · Delaunay triangle gridding · Reference datum of global vertical crustal motion

X. Zhu (✉) · F. Sun · R. Wang
Navigation and Aerospace Engineering Institute, Information and Engineering University, Longhai Middle Road No 66, Zhengzhou 450052, China
e-mail: 13673360571@126.com

J. Sun et al. (eds.), *China Satellite Navigation Conference (CSNC) 2013 Proceedings*, Lecture Notes in Electrical Engineering 243,
DOI: 10.1007/978-3-642-37398-5_2,

2.1 Introduction

The shape of the Earth and its changes are still ancient pending scientific issues, not only lively discussion by many domestic and foreign scholars and Earth science enthusiasts, but also good for geophysical mechanism for analysis and detection, use of space observation technology experimental verification, given different results and conclusions.

As early as in the mid-90s of the last century, domestic scholars in China have carried out the first research based on space geodetic measured global tectonic changes, Sun [1, 2] qualitatively validated unsymmetrical global detection of north hemisphere expending and south hemisphere shortening by using North and South mid-latitude belts changing rate observed by VLBI and SLR respectively; while its quantitive results were also gotten by those of the integration of GPS, VLBI and SLR stations geodesic variation rate and station speed measurement in Sun et al. [3], which pointed out that the northern hemisphere latitudes compressed change in magnitude of around 8–10 mm/a, the southern hemisphere middle-latitude belt expansion change about 12–14 mm/a. Subsequently, Ma [4, 5], Huang [6], Jin [7], Sun [8] equality using tectonics and space geodetic data confirms the earth exists south up north shrinkage asymmetric global tectonic change. Sun et al. [9, 10] used the geodetic data updated to 2003 from more than 700 stations all over the world to detect the changing of the solid earth's volume and radius, pointed out that the earth may be in a state of compression which means a 3–4 mm decrease of radius per year, while Shen et al. [11–13] showed that the earth may be expanding at the same time. There is nothing strange about this; a study made by some overseas researchers in 2007 came up the different result either. Russian scientists' study based on SLR [14] showed that the radius of earth is increasing in 1 mm per year; while German scientists [15] used VLBI find out that the radius of earth is decreasing in 0.5 mm/a. Wu et al. [16] made full use of the accurate station position and velocity fields under ITRF2008 frame, combined with gravity data from Gravity Recovery and Climate Experiment (GRACE) and Linear changing data from two Ocean Bottom Pressure (OBP) models, researched the movement of the origin of ITRF2008 frame and the changing of the earth radius, the result shown that the earth radius is changing in 0.1 ± 0.2 mm/a, which means the radius of the earth cannot be considered changed in the range of one time mean error.

Why could this situation happen? According to our analysis, there maybe have several aspects of reasons, as the followings: (1) Precision of geodetic data. As everybody knows, the precision of crustal movement that space geodesy techniques surveyed is closely related to terms that stations survey continuously, the longer the surveying time, the higher the accuracy of data. Generally speaking, data used of above research results were almost surveyed to 2003 or 2004, the precision of crustal movement is superior to 1–2 mm/a barely. (2) Numbers and distribution of stations. In early days, the high-quality stations were less, the stations of VLBI and SLR only has a few, and is distributed unevenly; In southern hemisphere, there has a few stations, in northern hemisphere, there has none. Taking a consideration of influence

of ocean, the problem of stations of the numbers and distribution, there could have great influence on test result. (3) Data preprocessing. Between different technologies, different batches of solving velocity field of crustal movement, there usually have systemic bias as a result of the different of vertical crustal movement reference; these deviations would usually be ignored. Specifically, vertical crustal movement reference datum's bias will have an influence on the estimation result of the earth volume change directly. (4) Detection method. Because different researchers adopt different detection method, there will have biased estimate. (5) The earth volume almost doesn't change, theoretical result is near zero, and then, estimation result will have positive and negative.

To sum up, We believe that (1) the earth's south up north shrinkage asymmetric global geodetic changes have been confirmed by tectonics and space geodetic results; (2) the earth volume is compressed, expansion, or unchanged, has not yet been confirmed, the causes has been analyzed at the head, this problem is still necessary to further study; (3) To determine the earth's shape, size and its change is the basic task of geodesy, with stations increases and the improvement of observation precision, Global tectonic change research which is based on the spatial geodetic data is becoming research frontier and hot point in the field of domestic and international. Consequently, a high accuracy of geocentric coordinates global crustal motion velocity field would be built by using the data of the latest global ITRF2008 international terrestrial reference frame, whose station accuracy is better than 0.3 mm/a, datum reference is completely unified, and which was used to study on global tectonic change phenomenon, such as the compression or expansion of the solid earth, asymmetry between the southern and northern hemispheres structure change and so on and give quantitative estimation, according to global data to discuss the possible mechanisms about these global tectonic change.

2.2 Data-Processing

The data comes from ITRF2008. Because most DORIS stations of geocentric coordinate velocity precision is under 0.3 mm/a, we only use GPS, VLBI and SLR data sequence in ITRF2008. In order to build a global relatively uniform distribution, precision is better than 0.3 mm/a, a completely unified global reference of high accuracy of geocentric coordinates global crustal motion velocity field, we need to do some data processing work.

First of all, some stations that geocentric coordinate velocity error more than 0.3 mm per year should be eliminated in order to ensure the accuracy of data calculation.

Secondly, systematic bias solved by using different techniques between the co-location station and the common station velocity field, should be using to unify those three kinematics technique data reference. Among them, the vertical direction reference datum, presented by Zhu [17] determined global vertical crust

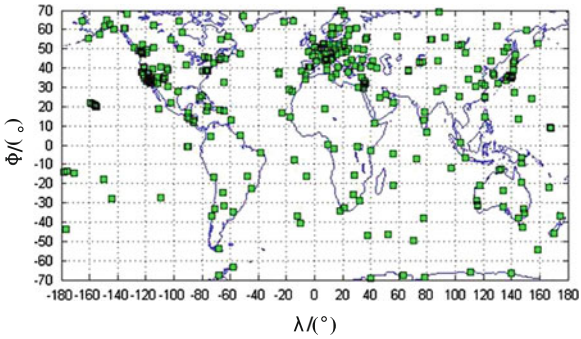

Fig. 2.1 Distribution of sites in ITRF2008 after pre-processing

movement reference, the geocentric coordinate velocity field is converted to a site-centric coordinate velocity field, and GPS and VLBI vertical velocity are converted to a unified global vertical crustal movement reference.

Finally, these 3 kinds' data would be used synthetically. To the different technology between the co-location stations, you can choose the station coordinate and velocity which keep the highest accuracy.

After above three steps of data pretreatment, 337 effective stations were choose whose precision is better than 0.3 mm/a, and reference datum completely unified of global crustal motion velocity field of geocentric coordinates, the distribution of stations such as shown in Fig. 2.1.

2.3 Detection Method

Inscribed polyhedron can always be formed with N (number) points for vertex that distributed in a sphere. As long as these vertex coordinates are defined, the polyhedron volume can be calculated. If the vertex coordinates changed, the polyhedral volume has always been changed. Based on this idea, we adopt three stations (assuming called A and B, C station) on the earth's surface with the Earth's core to constitute a tetrahedron O-ABC, as shown in Fig. 2.2, with a series sum of tetrahedral volume to approximate the total volume of the earth. Then the earth's surface shall surrounded by a series of triangle mesh, the triangular grid should be satisfied with neither overlap nor no crack condition [9, 10].

Every tetrahedron's volume can be obtained as sixth of mix product of those three independent vectors by using analytic geometry knowledge [6, 7, 12]. The tetrahedron is shown in Fig. 2.2, where point A, B and C are three peaks of spherical triangle, namely three stations distributed in the earth's surface. Supposed r_A, r_B, r_C as three station's position vector respectively, so tetrahedron O-ABC volume can be obtained by formula (2.1):

$$V = \frac{1}{6} r_A \cdot (r_B \times r_C) \tag{2.1}$$

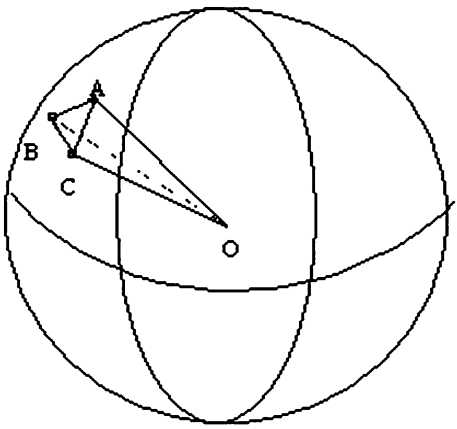

Fig. 2.2 Sketch map of tetrahedron from 3-sites and the earth's core

The change of volume can also be gotten by differential of time t as both sides of above formula. Polyhedron volume changes can be quite well reflecting part of the earth's volume change of different area [6].

Based on the coordinates, velocities and their error estimations of GPS and VLBI stations in 2003, using Delaunay arithmetic forming series of triangles to approach the surface of the Earth, the Earth's area, volume and their changes were studied [9, 10]. That's to say, the solid Earth's volume change can be acquired from Delaunay algorithm to make all global station form a continuous Delaunay triangulation grids, where all triangles of the grid with the earth's core constitute a geometric polyhedron, whose change of all geometry polyhedral can be calculated by all station's geocentric coordinate velocity. And the accumulation is the solid earth volume change which can be regarded as the change of solid earth's radius change. The idiographic methods are shown in reference [9, 10].

For the quantitative estimation of earth's radius change, this paper proposes the following method. First we are going to build High precision geocentric coordinates and speed fields, and convert it into topocentric coordinate velocity field, then make all station's radial velocity unified to the global vertical crustal motion's reference datum [17], finally make all the station's vertical velocity after unified to a weighted average, the earth radius change rate can be obtained.

In order to be able to use Delaunay algorithm to realize triangular mesh change, it is necessary to project all stations into one plane. If the equator as the boundary, then the earth is divided into north and south hemisphere; if the longitude line of 0–180° is taken as the boundary, the earth is divided into East and West hemisphere; if the longitude line of 90–270° as the boundary, the earth is divided into Pacific and Atlantic hemisphere (which include the Pacific Ocean and Atlantic Ocean respectively) [9, 10]. Here we only take the most representative of the north and south hemispheres as an example, to analyze the solid earth's asymmetrical detected change. Then the volume change of north and south hemisphere would be calculated respectively, and which characteristics of asymmetrical change could also be analyzed.

By measuring technique, measurement instrument and other objective factors limit, and few observed stations in some parts of the region, global stations were distributed unevenly, which can also be seen from Fig. 2.1. According to the vertical projection way, if hemisphere is regular, the graphics that projected to one plane should be close to an ellipse. That is to say, if station's distributed density around the equator are enough, the graphics that projection to the equatorial plane also ought to be an elliptic [6], while the actual observed station can't meet this condition, so the calculation on the area that there is few station should be for interpolation processing, increase of virtual stations, and calculates the movement rate of these new stations.

For the interpolation principle of interpolation points, scholars have done some research, summarizes several interpolation methods. A kind of method is: if in a Delaunay triangle meet any two vertex to sphere core have open angle is greater than 5°, then it can be taken its geometric center of this Delaunay triangle as the interpolation point. After interpolation, the original Delaunay triangle will be divided into three Delaunay triangles, and so on, until every Delaunay triangle to sphere core of opening angle is no more than 5° [12]. After inspection by a lot of data, this method had been detected that the interpolation effect of parts of the southern hemisphere is not ideal, its effect is bad is likely to be due to the influence of long and narrow triangles. Now improve the method further, and made some adjustments to the restrictions, that's to make the original angle to be greater than 5° to exchange the three angles that greater than 30°. This restriction conditions may be too strict to lead to the interpolation effect is not very ideal. If taking each Delaunay triangular surface area as a basis for judgment, we arrange the existing Delaunay triangular surface area by area values in descending order, and choose a standard area values as needing to interpolation control range. Thereby controlling the insertion point in the number and approximate position, such adjustments can make the global distribution of stations seem relatively uniform, and here we adopt this method. After interpolation, the stations distributions are shown in Fig. 2.3.

The interpolation theory has been explained in reference [9, 10] more detail, which applying interpolation to the stable plates, it doesn't affect the plate's motion trend after interpolations. Thus, according to stable plates Euler vector of plate motion model ITRF2008VEL in reference Zhu [17] and formula (2.2), we can solve the interpolation points movement rate, thereby solving the whole earth volume and its change.

$$\begin{bmatrix} V_i^x \\ V_i^y \\ V_i^z \end{bmatrix} = \begin{bmatrix} 0 & R\sin\phi_i & -R\cos\phi_i\sin\lambda_i \\ -R\sin\phi_i & 0 & R\cos\phi_i\cos\lambda_i \\ R\cos\phi_i\sin\lambda_i & -R\cos\phi\cos\lambda_i & 0 \end{bmatrix} \begin{bmatrix} \Omega_k^x \\ \Omega_k^y \\ \Omega_k^z \end{bmatrix} \tag{2.2}$$

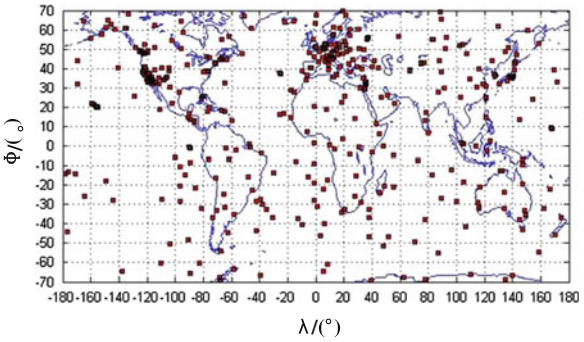

Fig. 2.3 Distribution of global sites after interpolation

2.4 Results and Discussions

After interpolations of the original 337 stations, a total of 450 groups of station data were received, which includes 155 of southern hemisphere and 295 of northern hemisphere respectively. There were formed 812 Delaunay triangles by using after interpolated data, wherein 257 of southern hemisphere and 555 of Northern Hemisphere respectively. The interpolation effects are shown as below (Figs. 2.4, 2.5, 2.6).

The results of two methods in reference [9, 10] and [6, 12] respectively were similar, which showing those two methods have no big difference theoretically. The results are shown in Table 2.1.

From the results in Table 2.1, we can include that the Earth is in asymmetrical change detected by ITRF2008 data, the north hemisphere is compressing and the south expending, which is in consistent with reference [2, 3, 6, 8–10] and Shen [12], that's to say, the Earth is still in south up north shrinkage asymmetrical change, this point has been verified by space observed data.

If the earth is taken as a regular sphere, the earth radius is 6366.740 km, the earth's total volume is $V0 = 4\pi R^3/3 = 1.01 \times 10^{12}\text{km}^3$, if the radius of the earth changes in 1 mm, earth volume change rate is $dV = 0.510 \times 10^3\text{km}^3/\text{a}$. The calculation results detected by observed data show the earth volume change rate was $(-0.0379 \pm 0.0902) \times 10^3\text{km}^3/\text{a}$, converted to the Earth radius change approximate to (-0.1 ± 0.2) mm/a, the conclusion is similar to reference [16], i.e., the radius of the earth cannot be considered changed in the range of one time mean error.

For the quantitative estimation of the Earth radius change, here we take observed site's velocity as base. Viz. building high accuracy geocentric coordinates and speed fields, converting into topocentric coordinate velocity field, and then make all station's radial velocity unified to the global vertical crustal motion's reference datum [17], finally make all the station's vertical velocity after unified to a weighted average, the earth radius change rate could be approximate to -0.24 mm/a, which was corresponding to above results.

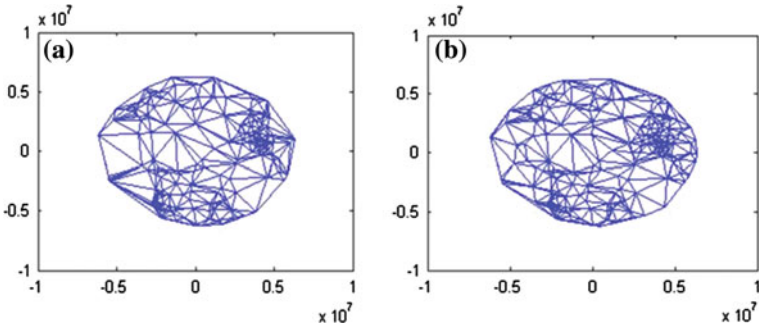

Fig. 2.4 Distribution of delaunay triangle in north-hemisphere before (**a**) and after (**b**) interpolation

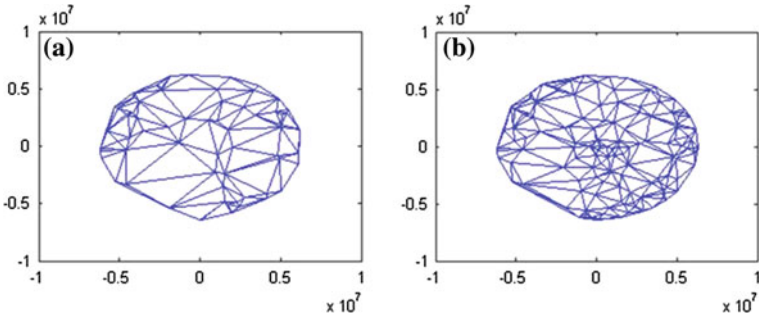

Fig. 2.5 Distribution of delaunay triangle in south-hemisphere before (**a**) and after (**b**) interpolation

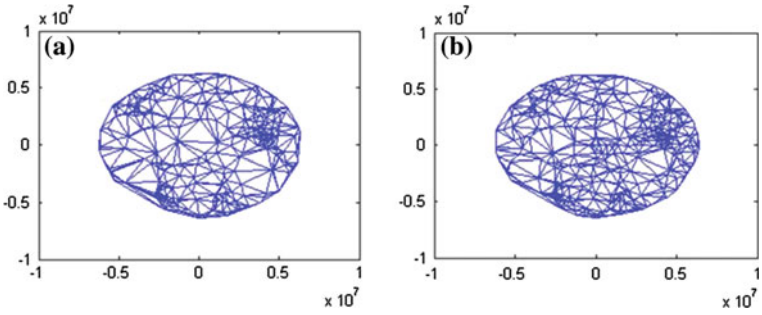

Fig. 2.6 Distribution of delaunay triangle in the earth before (**a**) and after (**b**) interpolation

Table 2.1 The Earth volume and its changing rates

Title	Volume [10^{12}km^3]	Changing rate [km^3·a^{-1}]	Error [km^3·a^{-1}]	Stations number	Delaunay triangles number
North	0.4206	−1.3724	0.0851	295	555
South	0.4147	1.3345	0.0299	155	257
Global (NS)	0.8353	−0.0379	0.0902	450	812

2.5 Conclusions

Compared above results detected by space observed techniques with such reference [6, 9, 10] and Shen [12], there were three points cannot but put forward.

Firstly, it is the problem of data precision. Here, we all chose the observed data that its geocentric coordinate is excelled 0.3 mm/a, while in reference [9, 10], which is under 5 mm/a, obviously higher quality data is better to reflect the results reliability.

Secondly, in data preprocessing, we unified all stations vertical velocity to the global vertical crustal motion reference datum, which is not appeared or discussed in current kindred references. For the necessary of unifying the vertical datum, Zhu [17] had been discussed and explained, so we have reason to believe that unifying vertical velocity is necessary, as well as providing the reliable basis of the main results of this paper. At the same time, the results here are similar to Wu et al. [16] which both using space observation data and geophysical information, which shown that it's reliability and dependability to estimate the Earth's change trend here.

Thirdly, this paper used ITRF2008 data to detect that the earth is still in south up north shrinkage asymmetric change, which is corresponding to the author's before work and the related literature, that's shown that the earth changes have been confirmed by space observations. In addition, because of emphasizing data's high precision and high quality, it is inevitable to delete more stations in the data pretreatment; while the distribution of global station is essentially uneven, some marine station is few and quality is not high, so we adopted reference Zhu [9], proposed the method of plate motion model interpolation The stable plate were interpolated, and the interpolation principle and conditions also made some modified and improved, the interpolation effect could even more improve global station distribution, and interpolated station does not affect the whole plate motion trend, and then the Earth change would not be affected.

In short, for the precise estimation of global change phenomena, it will depend on the higher quality data, more uniform distribution of stations and more reliable estimated method. With the rapid development of space technology and the progress of science, we have the reason to believe that those can be achieved.

Acknowledgments This work is supported by project of National Natural Science Foundation of China (41074011).

References

1. Sun F (1994) Study on present-day crustal motion based on space technologies. Shanghai Astronomical Observatory, Chinese Academy of Sciences
2. Sun F (1998) Application of space geodetic data in geodynamic. Wuhan Technical University of Surveying and Mapping
3. Sun F, Zhao M, Ning J et al (1999) Detection of unsymmetrical global tectonic change by using space geodetic data. Sci Report 20:2225–2229
4. Ma Z, Song X, Du P et al (2002) Asymmetry between the southern and northern hemispheres of the earth. Chin J Geophys 45(1):26–33
5. Ma Z, Zhang P, Ren J et al (2003) New cognitions on the global and Chinese continental crustal movements from GPS horizontal vector fields. Adv Earth Sci 18(1):4–11
6. Huang L, Ma Z, Zhu J (2002) The newest observational evidence on asymmetrical deformation of the earth. J Seismic 2:196–199
7. Jin S, Zhu W (2003) Quantitative analysis of the slowing expansion in the southern hemisphere. Chin J Geophys 46(6):760–766
8. Sun F (2004) Study on space geodynamics. Surveying and Mapping Institute, Information and Engineering University
9. Zhu X (2005) Study on space geodynamics. Surveying and Mapping Institute, Information and Engineering University
10. Sun FP, Zhu XH, Wang R et al (2006) Detection of changes of the earth's volume and geometry by using GPS and VLBI data. Chin J Geophys 49(4):1015–1021
11. Shen WB, Chen W, Li J (2007) Proving the Earth expansion by time-variable gravity field. Chineses geophysics, Ocean University Press, Qingdao
12. Shen WB, Zhang ZG (2008) Detecting the Earth expansion effect based on space-geodetic data. Sci Surv Map 33(3):5–6
13. Shen WB, Chen W, Han JC et al (2009) Temporal influence of the inner core wobble on the Earth's principle moments of inertia. Sci Surv Map 4(3):7–10
14. http://it.sohu.com/20070227/n24 (2007a)
15. http://news.sohu.com/20070709 (2007b)
16. Wu X, Collilieux X, Altamimi Z, et al (2011) Accuracy of the international terrestrial reference frame origin and earth expansion. Geophys Res Lett 38:L13304. doi:10.1029/2011GL047450
17. Zhu X (2012) Study on datum of modern crustal motion. Information and Engineering University

Chapter 3
Satellite Clock Bias Estimation Based on Backward Filtering

Li Li, Sichun Long, Haojun Li and Liya Zhang

Abstract A new method was presented for estimating GPS satellite clock biases (SCB) based on a backward filter. It can improve the estimated SCBs precision, when the initial phase ambiguity is not converged. This method overcomes the disadvantage that the ambiguity parameters of conventional Kalman filter does not converge. It is simple and easy to be implemented. The experimental results show that the same positioning accuracy as using the final IGS SCBs can be obtained, when the estimated SCBs are used.

Keywords Satellite clock biases (SCB) · Kalman filter · Backward filter · Precise point positioning

3.1 Introduction

Presently, the main estimation methods for the GPS undifferenced data include least square [1–4], Kalman filtering [5] and square-root information filtering [6]. In Post-processing of satellite clock biases (SCB), the least squares and Kalman filtering can be used [7]. In real-time processing, the Kalman filtering and square-root information filtering can be used [8].

L. Li (✉) · S. Long · L. Zhang
Hunan Key Laboratory of Coal Resources Clean-utilization and Mine Environment Protection, Hunan University of Science and Technology, Xiangtan, Hunan, China
e-mail: gszl.lili@gmail.com

S. Long
e-mail: lsc2002@126.com

L. Zhang
e-mail: lyzhang47@163.com

H. Li
Shanghai Astronomical Observatory, Chinese Academy of Sciences, Shanghai, China
e-mail: yanlhjch@126.com

J. Sun et al. (eds.), *China Satellite Navigation Conference (CSNC) 2013 Proceedings*, Lecture Notes in Electrical Engineering 243,
DOI: 10.1007/978-3-642-37398-5_3,

Kalman filtering is a recursive parameter estimation method, the principle is simple, and easy to implement. But, it requires a certain amount of time to converge, when the phase observation is used processed [9]. Before ambiguity convergence, the accuracy of estimated SCBs is not high. When the estimated SCBs are used in PPP, the positioning accuracy and the convergence time will be affected. In this contribution, a new approach based backward filtering is presented. It can smooth the forward estimated SCBs. To evaluate the new method, the PPP is performed using the estimated SCBS. The positioning accuracy and convergence time Of PPP was studied and analyzed.

3.2 Forward and Backward Filtering and Its Smooth Process

3.2.1 Conventional Kalman Filtering

Kalman filtering is a recursive parameter estimation method [10, 11], its state and measurement equations are:

$$\begin{cases} x_k = Ax_{k-1} + w_{k-1}, \quad w_{k-1} \sim N(0, Q_{k-1}) \\ z_k = Hx_k + v_k, \quad v_k \sim N(0, R_k) \end{cases} \tag{3.1}$$

where, x_k is the state vector at t_k; A is the state transition matrix; w_{k-1} is the process error vector with Gaussian white noise, Q_{k-1} is the process noise covariance; z_k is observation vector at t_k; H is design matrix (also known as observation matrix); v_k is observation error vector with Gaussian white, R_k is the observation noise covariance. The Fig. 3.1 is the kalman filtering recursive process.

In Fig. 3.1, $\hat{x}_{k-1}$, P_{k-1} are the state estimated value and its covariance matrix at t_{k-1} respectively; $\hat{x}_k^-$, P_k^- are the predicted state vector and its covariance matrix respectively; K_k is the gain matrix; $\hat{x}_k$, P_k are the state estimated value and its covariance matrix at t_k respectively.

3.2.2 Backward/Smoother

Kalman filter is a recursive procedure. When the undifferenced observation is used to estimate the SCBs based on Kalman filter, the presence of the carrier ambiguity is bound to require a certain time to converge so that the estimated accuracy of initial SCBs is not high. Given this, the paper will use backward filtering to smooth SCB. Its estimation process will filter with opposite direction. After forward filtering has finished, its final result was the initial information of the backward filtering and it is the precise priori information. After the end of backward filtering,

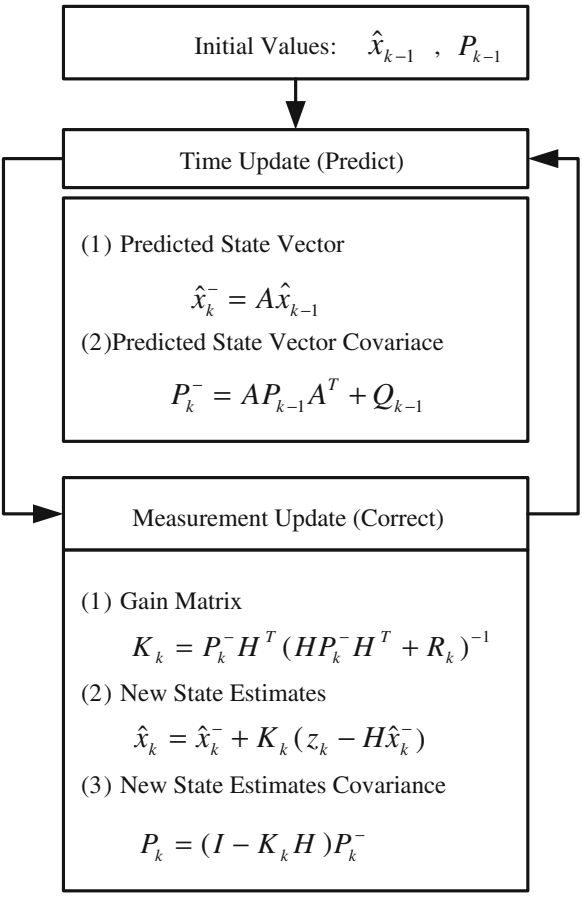

Fig. 3.1 Flow chart of Kalman filter estimator

the smoothing value can be obtained based on the values of forward and backward filtering, the smoothing formula is [12, 13]:

$$\bar{x}_k = \left(\mathbf{P}_k + \mathbf{P}_k^b\right)^{-1}\left(\mathbf{P}_k\hat{\mathbf{x}}_k + \mathbf{P}_k^b\hat{\mathbf{x}}_k^b\right) \tag{3.2}$$

where, $\bar{x}_k$ is the smoothing value at t_k; $\hat{\mathbf{x}}_k$ is the forward value; $\hat{\mathbf{x}}_k^b$ is the backward value; $\mathbf{P}_k$ and $\mathbf{P}_k^b$ are the covariance of forward and backward filtering value, respectively. There are three steps to obtain smoothing estimated SCBs. Firstly, filtering from the first observation epoch until the end of the last epoch, which can be called forward filtering; Secondly, making the last updated parameter estimates and their variance of forward filter as the initial information of the backward filtering, filtering from the last epoch to the first epoch, which is called as backward filtering; Lastly, the smoothing values can be gotten based on the formula (3.2).

3.3 SCB Estimation with Backward Filtering

3.3.1 SCB Estimation Theory

Generally, the undifferenced ionosphere-free combination observation is used to estimated SCBs. The ionosphere-free combination observation equation is written as following [3, 14].

$$P_{IF} = c(dt - dT) + \Delta T + d_{mult/P(L1+L2)} + \varepsilon(P(L1 + L2)) \tag{3.3}$$

$$\Phi_{IF} = c(dt - dT) + \Delta T + \lambda N^{'} + d_{mult/\Phi(L1+L2)} + \varepsilon(\Phi(L1 + L2)) \tag{3.4}$$

where, P_{IF}, Φ_{IF} are the pseudorange and phase combination observation(m); c is light speed(m/s); dt is SCB(s); dT is receiver clock biases(s); ΔT is the tropospheric delay with horizontal gradients(m); λ is the wave length of ionosphere-free combination observation(m); $N^{'}$ is the float ambiguities of ionosphere-free combination observation(circle); $d_{mult/P(L1+L2)}$ is the multipath effect of pseudorange observation(m); $d_{mult/\Phi(L1+L2)}$ is the multipath effect of carrier phase observation(m); $\varepsilon(\cdot)$ is measurement noise(m).

Figure 3.2 is the flow chart of SCB estimation. It includes observation data preprocessing, SCB estimation based on the reference stations data and IGU orbit data, and provide SCBs to the users. In data processing, corrections include relativistic effects, phase wind-up, the phase center biases and variations of the the satellite and the receiver, earth tides, ocean tides, polar motion and nutation [3]. Epoch-by-epoch Kalman filter was used to estimate the unknown parameters satellites clock parameters (clock biases dt and clock drifts $\dot{dt}$), the receiver clock biases (dT), zenith total delay (ZTD), tropospheric gradient (G_N, G_E) and ionosphere-free combination float ambiguities ($N^{'}$). The phase observation noise was set to 0.01 m, the estimation method of filter state vector, priori standard deviation and process noise was set as Table 3.1.

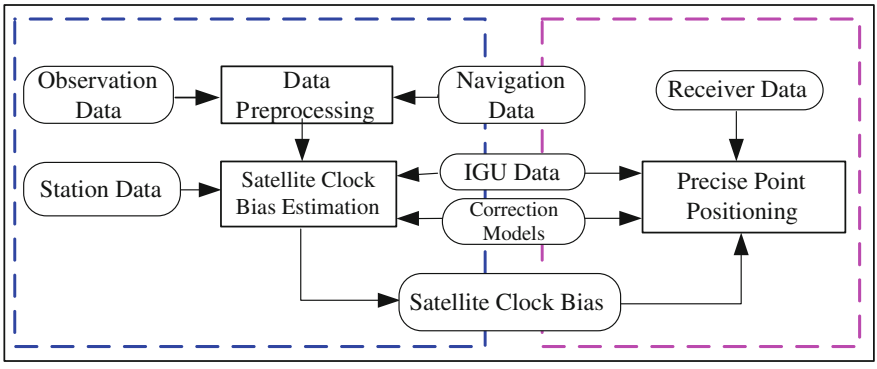

Fig. 3.2 Flow chart of satellite clock bias estimation

Table 3.1 Settings for a priori standard deviation and process noise

Estimated parameters	Priori standard deviation	Process noise	Estimation strategy
Satellite clock bias	1e+1 m	1e−1 m	White noise
Satellite clock drift	1e−2 m/s	1e−5 m/s	White noise
Receiver clock bias	1e+1 m	1e−1 m	White noise
Tropospheric delay	5e−1 m	1e−5 m	Random walk
Horizontal gradients	1e−3 m	1e−5 m	Random walk
Phase ambiguity	1e−1 m	1e−5 m	–

In applications, all the relative SCBs should be precise determined in advance, rather than to determine the absolute SCBs. Although the relative SCBs have some biases, their affects to the positioning accurancy is negligible as long as they are a certain constants in time series. Therefore, the satellite and receiver clock biases mentioned below are relative SCBs relative to a reference station clock.

3.3.2 Smooth Processing Method Based on Backward Filtering

Figure 3.3 is the flow chart of smoothing SCBs with backward filter. 1-pass, 2-pass and 3-pass are the forward, backward and smoothed SCBs, respectively. Firstly, the forward filter start from the first epoch until the last epoch, and the state values and their variances of each epoch are saved. The 1-pass precise SCBs are obtained. Secondly, we let the state value and its variance of last epoch of forward filtering as the initial information of backward filtering, and begin to rollback processing until the first epoch. The state values and their variances of each epoch are saved too. The 2-pass precise SCBs are obtained. Finally, the 3-pass smoothed SCBs are obtained based on the each epoch state values and their variances of forward and

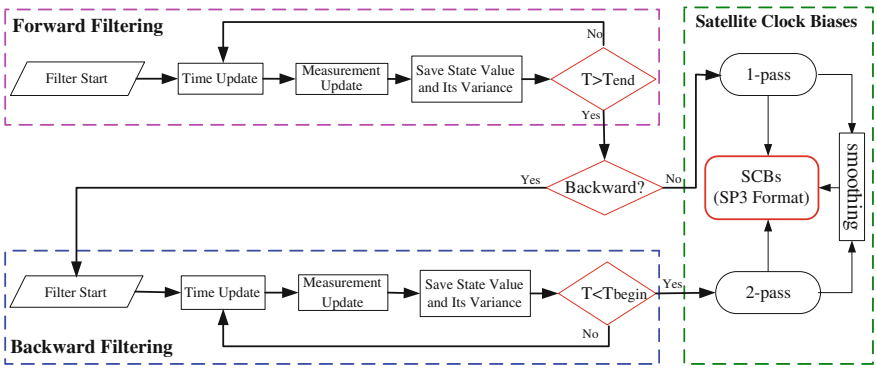

Fig. 3.3 Flow chart of smoothing SCBs with backward filter

backward filtering. According to the actual needs, the 1-pass, 2-pass and 3-pass SCBs can be outputted. For instance, real PPP can use 1-pass real-time SCBs, and post-PPP (or quasi real-time) can use 2-pass or 3-pass smoothed SCBs.

3.4 SCB Estimation and Its Application in PPP

3.4.1 SCB Estimation

The 24-h data from 22 IGS stations is used to estimate the SCBs based on a Matlab routine (see Fig. 3.4). The data sample interval is 30 s. The clock of AMC2 is select as reference clock. Cutting angle is 10°.

Table 3.2 is the experimental statistical result about estimated pricision (ns) and costing time (m/s). The RMS of the difference between estimated SCBs and IGS final product is computed. The costing time includes the times of data preprocessing and SCB's estimation. The precisions of 2-pas and 3-pass SCBs are all better than 1-pass SCBs. Its precision improved about 10 % from 24 h observation data. As to costing time, 2-pass and 3-pass are almost double and triple to 1-pass.

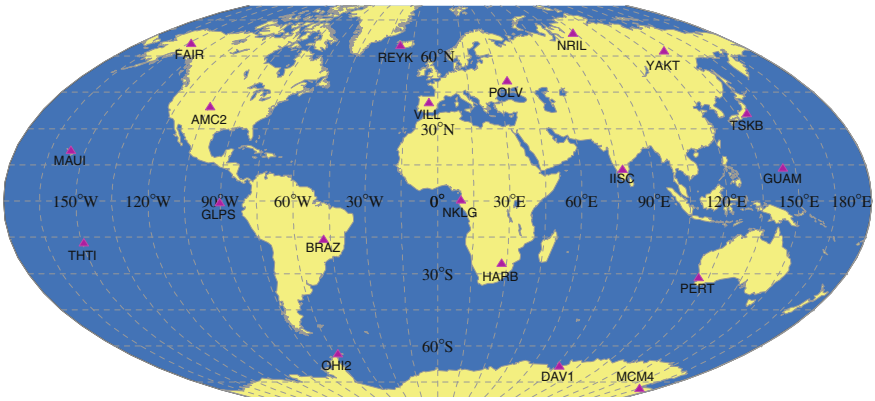

Fig. 3.4 Distribution map of selected IGS reference stations

Table 3.2 Costing time and precision statistical table

Process method	Precision(ns)	Costing Time (m/s)
1-pass	0.29	12 m 31 s
2-pass	0.26	22 m 37 s
3-pass	0.25	34 m 06 s

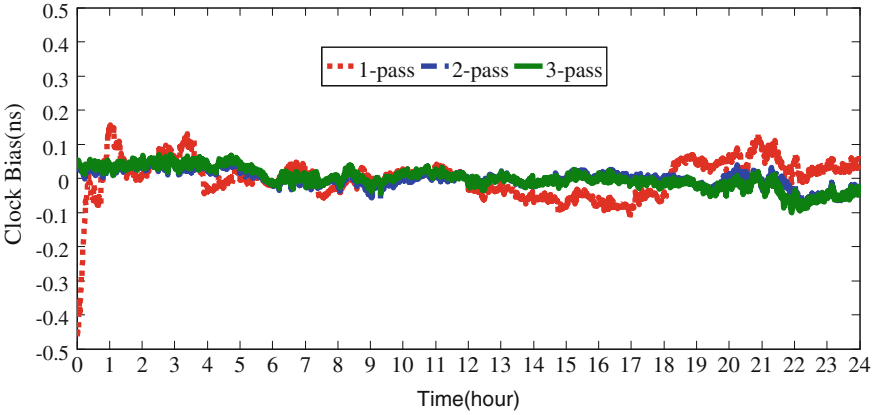

Fig. 3.5 Biases comparison of 1-pass, 2-pass and 3-pass SCBs (PRN14)

Therefore, considering the precision and costing time, 2-pass is the best and can be used preferentially.

Figure 3.5 is the biases of SCBs of 1-pass, 2-pass and 3-pass compared to the IGS final product (PRN14). In the 10 min of initial forward filter, the estimated precision of 1-pass SCBs is poor, but its precision increases and converges to 0.2 ns along with the observation data gradually. The variation trend of 2-pass and 3-pass estimated SCBs are almost same and stable.

3.4.2 The PPP Positioning with Estimated SCBs

Based on the 1-pass, 2-pass and 3-pass SCBs, the static PPP is performance. The estimated results are compared with the known coordinates. The positioning precision and converge time were analyzed.

Figure 3.6 show the convergence procedure in up direction, when the estimated SCBs are used. It can be seen that the 2-pass and 3-pass SCBs are almost same to the IGS final product. All results can reach to 0.1 m, when less than an hour data is processed. However, the convergence time based on the 1-pass SCBs is significantly greater than the IGS SCBs. This is because the precision of 1-pass SCBs in its initial phase is poor, resulting in the poor PPP accuracy in this phase. It will need longer time to converge to 0.1 m. But, with the accurate determination of ambiguity and better SCBs subsequently, the PPP positioning results will gradually converge at last. It is thus clear that the smoothed SCBs with backward filter are better than the 1-pass SCBs, which is more conducive to improve the PPP convergence rate.

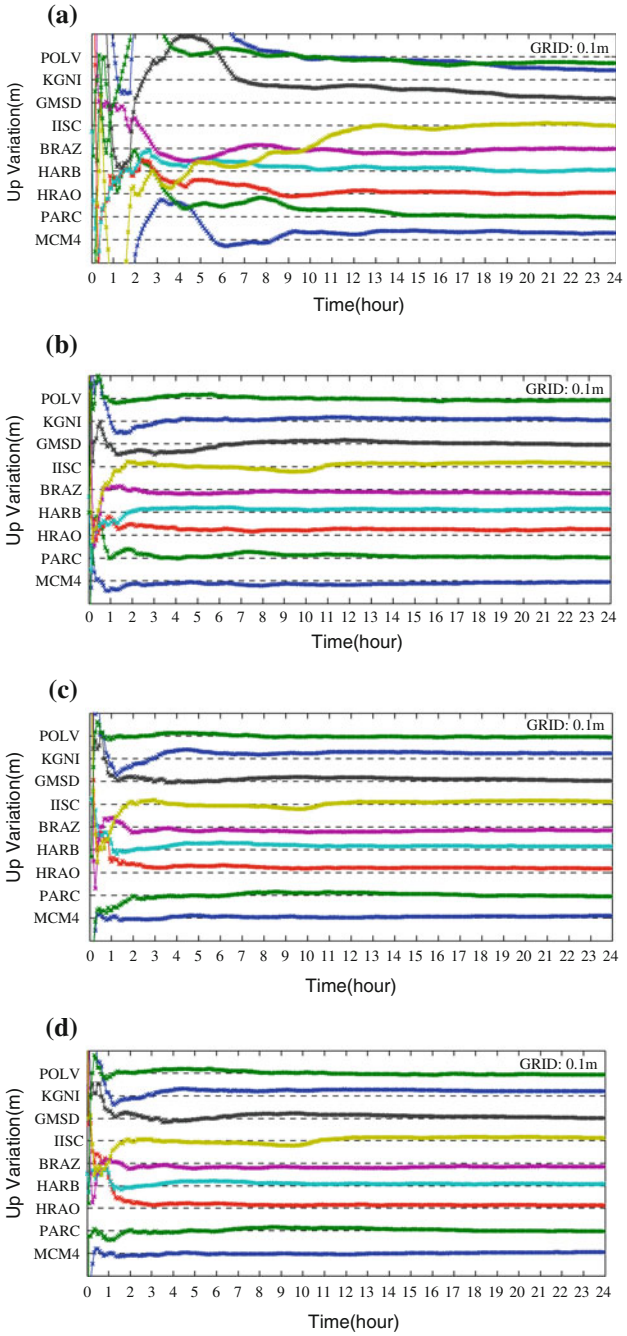

Fig. 3.6 Convergent process of PPP (*Up Direction*). **a** 1-Pass satellite clock biases. **b** 2-Pass satellite clock biases. **c** 3-Pass satellite clock biases. **d** Final IGS satellite clock biases

3.5 Conclusions

A new method for estimating SCBs smoothed with backward filter was proposed in the paper. The test shows that the backward filter is simple and effective, which overcome the drawback of poor precision of estimated SCBs before ambiguity convergence. The 2-pass and 3-pass SCBs are all better than 1-pass, their estimated precision increased about 10 % than 1-pass. The performance of PPP shows that the PPP precision and convergence time are almost same, when the 2-pass and 3-pass SCBs are used. Their results are better than 1-pass. The poor estimated precision of 1-pass SCBs in its initial phase is one of the main reasons of poor PPP and slow convergence.

Backward filter not only can be used to estimate SCBs, but also to PPP. In static PPP, the high precision positioning results can be obtained with ordinary filter. But, as to post dynamic PPP, the backward filter can smooth and get more accurate positioning results in its initial phase where the ambiguity has not converged yet.

Acknowledgments This research is supported by the Scientific Research Project of Hunan Provincial Education Department (No: 12C0105), the National Natural Science Foundation of China (NSFC) (No: 41004002; 41204034) and the Opening Project of Shanghai Key Laboratory of Space Navigation and Position Techniques (No: Y224353002).

References

1. Chen W, Hu C, Li Z, Chen Y, Ding X, Gao S, Ji S (2004) Kinematic GPS precise point positioning for sea level monitoring with GPS buoy. J Global Positioning Syst 3(1–2):302–307
2. Zhang X, Dongchen E (2005) Dynamic parameters determination of amery ice shelf using PPP. Geomatics Info Sci Wuhan Univ 30(10):909–913
3. Kouba J (2003) A guide to using International GNSS service (IGS) products. http://acc.igs.org/UsingIGSProductsVer21.pdf
4. Dach R, Hugentobler U, Fridez P, Meindl M (2007) User manual of the bernese GPS software version 5.0. Astronomical Institute, University of Berne, Berne
5. Abdel-salam MA-T(2005) Precise point positioning using un-differenced code and carrier phase observations. University of Calgary, Calgary
6. Zumberge JF (1999) Automated GPS data analysis service. GPS solutions 2(3):76–78
7. Li X, Xu Y, Wang L (2010) Undifferenced precise satellite clock error estimation and precision analysis. Geomatics Info Sci Wuhan Univ 35(6):662–665
8. Zhang X, Li X, Guo F, Li P, Wang L (2010) Server-based real-time precise point positioning and its application. Chin J Geophys 53(6):1308–1314
9. Lou Y, Shi C, Zhou X, Ye S (2009) Realization and analysis of GPS precise clock products. Geomatics Info Sci Wuhan Univ 34(1):88–91
10. Kalman RE (1960) A new approach to linear filtering and prediction problems. Trans ASME-J Basic Eng 82(Series D):35–45
11. Yang Y (2006) Adaptive dynamic navigation positioning. Survey and Mapping Press, Beijing
12. Fraser D, Potter J (1969) The optimum linear smoother as a combination of two optimum linear filters. Automatic control, IEEE transactions on Massachusetts Institute of Technology, Cambridge, MA, USA

13. Gelb A, Joseph F, Kasper J, Raymond A, Nash J, Price CF, Arthur A, Sutherland J (1974) Applied optimal estimation. Massachusetts Institute of Technology Press, Carnbride
14. Zumberge JF, Heflin MB, Jefferson DC, Watkins MM, Webb FH (1997) Precise point positioning for the efficient and robust analysis of GPS data from large networks. J Geophys Res 102(B3):5005–5017

Chapter 4
Performance Analysis of Interference Localization Based on Doppler Frequency Shift of a Single Satellite

Anfei Liu, Liang Yuan, Jun Wang and Ting Zhang

Abstract Two interference localization methods for a single satellite based on Doppler frequency are introduced in this paper, with the relationship between the localization error, frequency measurement accuracy and ephemeris accuracy derived. By using ephemeris data of synchronous orbit satellites, the interference localization performance is analyzed in detail, resulting in the quantitative estimation about the influence on positioning of each factor. According to the results, the target references of all factors are presented to achieve hundred-kilometer-level positioning error, as well as some considerations in implementation.

Keywords Doppler frequency · GEO satellite · IGEO satellite · Interference localization

4.1 Introduction

With the rapid development of satellite communication, the interference on ground becomes a threat to the normal operation of the satellite communication system, which makes the interference source localization necessary. Although the most effective method used commonly is the geolocation method using TDOA & FDOA, the requirements in the localization operation limits its application. If the interference can be detected only in the signal transmitted by the interfered satellite, and there is no partner satellite with the same polarization mode, it is difficult to use this method for interference source localization. At present, the synchronous orbit satellite is the most commonly type used in satellite communication system, whose larger height (about 36,000 km) and severe running

A. Liu (✉) · L. Yuan · J. Wang · T. Zhang
Beijing Satellite Navigation Center, Beijing 100094, China
e-mail: liu_anfei@163.com

J. Sun et al. (eds.), *China Satellite Navigation Conference (CSNC) 2013 Proceedings*, Lecture Notes in Electrical Engineering 243,
DOI: 10.1007/978-3-642-37398-5_4,

environment make the study on the corresponding interference localization technology very necessary.

Interference localization technology based on the Doppler frequency shift [1, 2] is an effective solution for interference localization aiming to a single satellite. Two localization methods based on Doppler frequency shift of a single satellite are presented in this paper, as well as in-depth study on interference localization performance of GEO satellites and IGEO satellites [3]. Through the positioning precision formula derivation and data processing, quantitative analysis on the relationship between the positioning error and each factor of the positioning accuracy is presented, resulting in some related conclusion on interference localization based on Doppler shift of a single synchronous orbit satellite.

4.2 The Interference Localization Principle Based on Doppler Frequency Shift of a Single Satellite

Due to gravity, the moon's gravity and atmospheric drag effect, a standard signal received in ground via a synchronous orbit satellite transmission will have a Doppler offset [4], which is just the frequency deviation of the signal received in ground from that emitted by the satellite:

$$f_d = f_r - f_0 = \frac{f_0}{C} \cdot \frac{\vec{v} \cdot \vec{r}}{\|r\|} \tag{4.1}$$

where f_0 is the emitting frequency, f_r is the frequency received, C is the velocity of light, $\vec{v}$ is the relative velocity of the satellite to the stationary satellite orbit, $\frac{\vec{r}}{\|r\|}$ is the unit vector in the connection direction between the receiving ground station and the satellite.

Therefore, in a certain coordinate system and a certain moment, assuming that the coordinate of the interference source is $\vec{x}_I = (x, y, z)$, the coordinate of the satellite is $\vec{x}_S = (x_s, y_s, z_s)$, the frequency of interference source is f_I, the local oscillator frequency of the satellite transponder is f_{T0}, the frequency received in ground is defined as:

$$f_{Er} = (f_I \cdot (1 + \frac{\vec{v} \cdot (\vec{x}_I - \vec{x}_S)}{\|\vec{x}_I - \vec{x}_S\|}) + f_{T0}) \cdot (1 + \frac{\vec{v} \cdot (\vec{x}_E - \vec{x}_S)}{\|\vec{x}_E - \vec{x}_S\|}) \tag{4.2}$$

while the corresponding Doppler frequency is defined as:

$$f_d = f_{Er} - f_I \tag{4.3}$$

So, it is possible to achieve the position of interference source from the relationship equation between interference source coordinate and Doppler frequency.

4.2.1 Positioning Model Based on Doppler Frequency Offset

When a motionless jammer in ground transmits a signal with stable frequency continuously, aiming at a satellite, it is possible to accomplish the interference localization using the frequencies of signals received in ground at 4 moments. Positioning model based on received frequencies at multiple moments is as follows:

$$\begin{cases} f_{Er}^{i} = \left(f_I \cdot \left(1 + \vec{v}_i \cdot \dfrac{\vec{r}_i}{\|\vec{r}_i\|}\right) + f_{T0}\right) \cdot \left(1 + \vec{v}_i \cdot \dfrac{\vec{r}_{Ei}}{\|\vec{r}_{Ei}\|}\right) \\ \vec{r}_i = \vec{x}_I - \vec{x}_{Si}, \quad \vec{r}_{Ei} = \vec{x}_E - \vec{x}_{Si} \ (i = 1, 2, 3, 4\ldots) \end{cases} \tag{4.4}$$

For a synchronous orbit satellite, position variation of the satellite is so small that makes the assumption possible that position and velocity of the satellite are constants during the signal transmission from a jammer to the satellite, then to the earth station. Then, a solution for the position and frequency of the jammer is presented in Eq. (4.4), as long as frequencies of more than 4 moments are acquired.

4.2.2 Positioning Model Based on Doppler Frequency Difference

To decrease the effect of interference signal frequency error and satellite transponder local oscillator frequency error, Doppler frequency difference between two moments can be used to interference localization and the corresponding model is as follows:

$$\begin{cases} \Delta f_d^i = f_{Er}^i - f_{Er}^{i+1} \\ f_{Er}^i = (f_I \cdot (1 + \vec{v}_i \cdot \dfrac{\vec{r}_i}{\|\vec{r}_i\|}) + f_{T0}) \cdot (1 + \vec{v}_i \cdot \dfrac{\vec{r}_{Ei}}{\|\vec{r}_{Ei}\|}) \\ \vec{r}_i = \vec{x}_I - \vec{x}_{Si}, \quad \vec{r}_{Ei} = \vec{x}_E - \vec{x}_{Si} \ (i = 1, 2, 3, 4\ldots) \end{cases} \tag{4.5}$$

From Eq. (4.5) above, if the Doppler frequency difference used for interference localization, then frequencies received in ground at more than 4 moments are needed.

4.3 Analysis of Positioning Error

Interference localization method based on the Doppler frequency shift achieved the positioning solution, by establishing the relationship between the observation vector and target position. Make Z for the observation vector, which is expressed

as $Z = [f_{Er}^1, f_{Er}^2, \ldots, f_{Er}^Q]^T$ or $Z = [\Delta f_d^1, \Delta f_d^2, \ldots, \Delta f_d^Q]^T$, where Q is the number of observing moments. Then the left of the localization equation is the function of the measurements, as the right the function of satellite positions and velocities at different moments, the local oscillator frequency of satellite transponder, frequency and position of the jammer, which is supposed as $F(X, X_1, \ldots X_M, V_1, \ldots V_M, f_I, f_{T0})$, where M is the number of all satellite moments used. So, Eqs. (4.4, 4.5) can be expressed as follows:

$$G(Z) = F(X, X_1, X_M, V_1, \ldots V_M, f_I, f_{T0}) \tag{4.6}$$

To calculate the differential of Eq. (4.6), make the error instead of the differential [5, 6], when the error is small, then there is

$$H_Z d_Z = HdX + \sum_{i=1}^{M} H_i dX_i + \sum_{i=1}^{M} H_{V_i} dV_i + H_{f_I} df_I + H_{f_{T_0}} df_{T0} \tag{4.7}$$

where $dX = [dx\ dy\ dz]^T$ representing the interference source localization error vector, $dX_i = [dx_i\ dy_i\ dz_i]^T$, $VdV_i = [dv_{xi}\ dv_{yi}\ dv_{zi}]^T$ $(i = 1, \ldots M)$ representing satellite position and velocity error vector at different moments, df_I representing the jammer frequency precision with df_{T0} the local oscillator frequency precision of satellite transponder and dZ the observation error vector, i.e. frequency measurement error (frequency or frequency difference measurement error).

$$H_Z = \frac{\partial G}{\partial Z} \quad H_X = \frac{\partial F}{\partial X} \quad H_{X_i} = \frac{\partial F}{\partial X_i}$$
$$H_{V_i} = \frac{\partial F}{\partial V_i} \quad H_{f_I} = \frac{\partial F}{\partial f_I} \quad H_{f_{T0}} = \frac{\partial F}{\partial f_{T0}}$$

Then, interference localization error of the can be expressed as follows:

$$\begin{aligned} dX = (H^T H)^{-1} H^T (H_Z dZ - \sum_{i=1}^{M} H_i dX_i \\ - \sum_{i=1}^{M} H_{V_i} dV_i - H_{f_I} df_I - H_{f_{T0}} df_{T0}) \end{aligned} \tag{4.8}$$

Assuming that the random measurement errors of all parameters are independent and conform to Gauss distribution with zero mean, as well as the satellite position and velocity measurement error component has the same standard difference, i.e., $df_{Er} \sim N(0, \sigma_f^2)$, $d\Delta f_d \sim N(0, \sigma_{\Delta f_d}^2)$, $dv_{xi}, dv_{yi}, dv_{zi} \sim N(0, \sigma_v^2)$, dx_i, dy_i, $dz_i \sim N(0, \sigma_s^2)$, $df_I \sim N(0, \sigma_{f_I}^2)$, $df_{T0} \sim N(0, \sigma_{f_{T0}}^2)$, the localization error covariance matrix P_X can be expressed as follows:

$$\begin{aligned} P_X &= E(dX \cdot dX^T) = (H^T H)^{-1} H^T \cdot \left[H_Z \sigma_Z^2 H_Z^T \right. \\ &+ \sum_{i=1}^{M} H_{X_i} \sigma_S^2 H_{X_i}^T + \sum_{i=1}^{M} H_{V_i} \sigma_v^2 H_{V_i}^T + H_{f_I} \sigma_{f_I}^2 H_{f_I}^T \\ &\left. + H_{f_{T_0}} \sigma_{f_{T_0}}^2 H_{f_{T_0}}^T \right] \cdot H (H^T H)^{-1} \end{aligned} \tag{4.9}$$

where, $\sigma_Z = \sigma_f$ or $\sigma_Z = \sigma_{\Delta f_d}$.

Then the root-mean-square error of Interference source position is expressed as:

$$\sigma_x = \sqrt{trace(P_X)} \tag{4.10}$$

where $trace(P_X)$ is the trace of covariance matrix P_X. Usually, Positioning accuracy is expressed by circular error probability (CEP), and the relationships between equivalent error radius R and root mean square error in 50 % probability condition are as follows [7]:

$$\text{3D: } R = 1.5381\sigma_x \tag{4.11}$$

$$\text{2D: } R = 1.1774\sigma_x \tag{4.12}$$

4.4 Performance Analysis and Conclusion

4.4.1 Experiments

The localization performance of two methods in this paper is tested by experiments, using ephemeris data of synchronous orbit satellites in a satellite system. According to the satellite simulation data, variation of Doppler frequency shift in a running cycle of a synchronous orbit satellite is shown in Fig. 4.1. For the effective analysis of the influence on localization performance of various factors, information of satellite positions and velocities at five moments marked by diamond in Fig. 4.1 is selected to establish the localization equations, when the Doppler frequency shifts are of the peak value or zero. According to the analysis result mentioned in segment 3, the corresponding positioning error formula is derived with the algorithm programmed based on the localization equations, achieving the positioning error results under various factors of different value.

4.4.2 Test Results and Error Analysis

In order to analyze the effect of various factors on localization exclusively, errors of other factors are supposed to be zero, when analyzing the effects of non-frequency measurement error, and the frequency measurement error is selected to

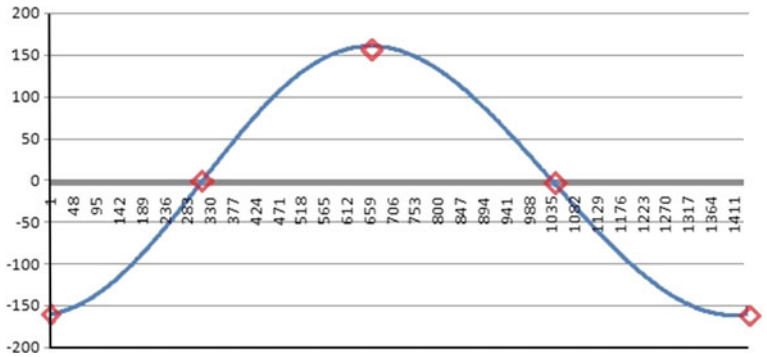

Fig. 4.1 *Curve* variation of Doppler frequency shift

ensure a 100 km-level positioning error. Specific data are presented in Tables 4.1 and 4.2.

Results of error analysis are as follows:

(1) To achieve the same level of positioning error, frequency measurement accuracy demand of GEO is different from IGEO. Positioning error increases in almost the same quantitative level as the frequency measurement error increasing. In condition of the same frequency measurement accuracy, positioning performance difference between two methods for GEO is more distinct than that for IGEO. According to data in Table 4.1, the frequency measurement accuracy demand of GEO and IGEO are respectively 10^{-9} Hz and 10^{-5} Hz for a hundred-kilometer-level positioning error.

(2) The effect of satellite position error is small when that is less than 50 m for GEO, but for IGEO, satellite position error has almost no effect on the final positioning. So, in these two cases, influence of satellite position can be ignored. Compared with satellite position, effect of satellite velocity on the positioning is more obvious. It is seen that from data in Table 4.2, satellite velocity accuracy demand of GEO is different from IGEO with the positioning

Table 4.1 Variation of positioning error along with frequency measurement accuracy ($\sigma_S = \sigma_v = \sigma_{fl} = \sigma_{ft_0} = 0$)

Frequency measurement accuracy (Hz)	Method based on Doppler frequency offset (km)		Method based on Doppler frequency difference (km)	
	GEO	IGEO	GEO	IGEO
10^{-9}	*37.0157*	0.0088	*61.5080*	0.0083
10^{-5}	3.7016×10^5	*88.1309*	6.1508×10^5	*82.9095*
10^{-3}	3.7016×10^7	8.8131×10^3	6.1508×10^7	8.2909×10^3
10^{-2}	3.7016×10^8	8.8131×10^4	6.1508×10^8	8.2909×10^4
0.1	3.7016×10^9	8.8131×10^5	6.1508×10^9	8.2909×10^5
1	3.7016×10^{10}	8.8131×10^6	6.1508×10^{10}	8.2909×10^6

Table 4.2 Variation of positioning error along with other factors except for frequency measurement accuracy (GEO: $\sigma_Z = 10^{-9}$, IGEO: $\sigma_Z = 10^{-5}$)

Factor/unit	Factor error (accuracy/precision)	Method based on Doppler frequency offset (km)		Method based on Doppler frequency difference (km)	
		GEO	IGEO	GEO	IGEO
Satellite position (m)	20	43.6000	88.1312	63.6541	82.9123
	50	68.4664	88.1327	73.9056	82.9166
	100	120.9963	88.1597	102.4619	82.9541
	500	577.1643	88.3105	414.3225	83.1880
	1,000	1,152.5468	88.8472	821.7682	84.0181
Satellite velocity (m/s)	10^{-6}	37.0221	88.1309	61.5182	82.9095
	10^{-2}	6.8678×10^3	88.1461	1.1217×10^4	82.9374
	10^{-1}	6.8678×10^4	89.6350	1.1217×10^5	85.6516
	1	6.8678×10^5	185.7528	1.1217×10^6	230.4232
	10	6.8678×10^6	1637.5196	1.1217×10^7	2,151.5025
Interference frequency (Hz)	10^{-8}	417.2249	88.6435	61.5080	82.9095
	10^{-5}	4.1558×10^5	129.7245	61.5080	82.9095
	10^{-3}	4.1558×10^7	9.5195×10^3	61.5082	82.9095
	0.1	4.1558×10^9	9.5195×10^5	63.2231	82.9525
	1	4.1558×10^{10}	9.5195×10^6	158.6669	87.1103
Oscillator frequency (Hz)	10^{-9}	55.6527	88.1309	61.5080	82.9095
	10^{-5}	4.1558×10^5	129.7245	61.5080	82.9095
	10^{-3}	4.1558×10^7	9.5195×10^3	61.5081	82.9095
	0.1	4.1558×10^9	9.5195×10^5	61.9412	82.9203
	1	4.1558×10^{10}	9.5195×10^6	95.5575	83.9794

error change trend similar, which is that positioning error increases suddenly when the satellite velocity error reaches a certain level.

(3) Demand on frequency precision of interference source is very high in localization method based on Doppler frequency shift, almost equaling to that of frequency measurement accuracy. In the method based on Doppler frequency difference, interference source emission frequency precision requirements are relatively several orders of magnitude lower. However, there is a great degree of deterioration in positioning accuracy for both two methods, when the emission frequency error reaches a certain magnitude. Fluctuations of local oscillator frequency of satellite transponder have an effect on the frequency received in ground, whose influence is similar to that of interference source emission frequency.

4.4.3 Performance Aanalysis Conclusions

As mentioned above all, in the interference localization methods based on Doppler frequency shift of a single satellite, main factors effecting the final positioning include frequency received in ground, satellite position, satellite velocity,

interference emission frequency and local oscillator frequency of satellite transponder. Precision requirements of each factor for a 100 km-level of localization accuracy are shown in Table 4.3. Usually, crystal oscillator frequency stability and accuracy of the satellite transponder is better than 10^{-9}, so effect of local oscillator frequency can be ignored, and effect of the satellite velocity may be reduced by ephemeris correction algorithm mentioned in paper [8, 9]. Therefore, more attention should be paid to the receiving frequency measurement accuracy in ground and inference emission frequency precision for the performance analysis interference localization based on Doppler frequency shift of a single satellite.

From the above analysis, conclusions can be drawn: In condition of the same frequency measurement accuracy, positioning error of the method based on Doppler frequency difference is slightly higher than method based on frequency offset, whose requirement of interference source emission frequency precision is much lower. In fact, frequency accuracy of removable interference equipment is usually below the level of 10^{-8} Hz, in which case the method based on Doppler frequency difference is obviously easier for realization. In practical application, effect of interference frequency stability should be considered, for its result frequency deviation will be added to the frequency received in ground directly, and be regarded as a part of Doppler frequency shift in positioning solution, which results in positioning error. Therefore, it is suggested that time domain transient measurement mode should be used in the measurement of frequency received in ground and the frequency measurement accuracy be lower than stability of interference emission frequency.

Targets of factors presented in Table 4.3 are estimated using satellite data of a whole running cycle, and some adjustment should be done in practical application based on targets in Table 4.3 according to the actual duration of disturbance, with an enhancement under the duration less than 24 h.

Table 4.3 Target references of each factor for 100 km-level positioning error

Target	Frequency measurement error (m)	Satellite position error (m)	Satellite velocity error (m/s)	Interference frequency error (Hz)	Interference frequency error (Hz)
GEO: method based on frequency offset	$\leq 10^{-9}$	≤ 50	$\leq 10^{-4}$	$\leq 10^{-9}$	$\leq 10^{-9}$
IGEO: method based on frequency offset	$\leq 10^{-5}$	None	≤ 0.1	$\leq 10^{-5}$	$\leq 10^{-5}$
GEO: method based on frequency difference	$\leq 10^{-9}$	≤ 100	$\leq 10^{-4}$	≤ 0.1	≤ 1
IGEO: method based on frequency difference	$\leq 10^{-5}$	None	≤ 0.1	≤ 1	≤ 1

4.5 Ending

Aiming at the interference localization problem of a single synchronous-orbit satellite, theoretical and data analysis on positioning performance of two methods based on Doppler frequency shift are discussed in this paper. Based on the particular analysis on influences of all the affecting factors, reference target of each factor is given for a 100 km-level positioning accuracy, which provides important reference data for the studies on interference localization of a single synchronous-orbit satellite in communication systems.

References

1. Yu Z (2007) Passive localization with Doppler frequency. Xi'an Electron Sci 2007(01):9–14
2. Lu X, Zhu W, Zheng T (2008) The study of passive orientation method with Doppler frequency difference. Aerospace Electron Warfare 24(3):40-43
3. Lv H, Cai J, Gan Z (1999) Satellite communication system. People's Post and Telecommunication Press, Beijing, pp 124–125
4. Ma L (2007) The study of interference orientation. The JiLin University 6:8–10
5. Zhu W, Huang P, Ma Q, Lu X (2010) High precision positioning technology with TDOA-FDOA among multi stations. Data Acquisition Process 25(3):307–312
6. Guo F, Fan Y (2008) A method of dual-satellites geolocation using TDOA and FDOA and its precision analysis. J Astronaut 29(4):1381–1386
7. Hu L (2005) Passive localization. National Defense Industry Press, Beijing, pp 25–30
8. Wang H, Liu L, Cheng H (2010) Ephemeris correction technology for interference location in satellite systems. Chin J Radio Sci 25(5):905–912
9. Qu W, Ye S, Sun Z (2005) Position correction algorithm for interference location in satellite systems. Chin J Radio Sci 3:342–346

Chapter 5
The 1st August 2010 Solar Storm Effects on the Ionosphere in the Yangtze River Delta Region Based on Ground and Space GPS Technology

Hu Wang, Qian-xin Wang and Ying-yan Cheng

Abstract On 1st August 2010, the entire side of the sun facing earth erupted in a frenzy of solar activity. This solar storm just like a solar tsunami, the massive multiple filaments of magnetism were released from the solar surface during the solar storm. Then these high energy particles, protons and electrons from coronal mass ejections hit against the earth's magnetic field. These hits caused intensively geomagnetic storms and ionospheric variations. Now well established ground and space based GPS instruments can offer a unique chance for a real time monitoring of ionosphere variations and characteristics. So in this paper we investigate ionospheric behavior responded to the solar storm using Ground and Space based GPS measurements. Firstly this paper describes a method of real-time solving TEC and GPS instrumental biases using Kalman filtering, so this can be used to provide absolute amount of ionospheric TEC for real-time monitoring of ionosphere changes during the solar storm. The Yangtze River Delta regional ground based GPS network measurements are used and a real-time regional ionosphere model is created, then real-time VTEC and TEC rate are also calculated. Furthermore, in order to analyze electron density structure changes during the solar storm, electron density profiles derived from GPS measurements onboard the LEO satellite COSMIC (Constellation Observing System for Meteorology, Ionosphere, and Climate) are used. Whereas the ground based GPS measurements show horizontal distribution during the solar storm, the space based GPS measurements show a vertical distribution. Meanwhile, with consideration of the solar and geomagnetic parameter, the ionospheric anomallies with phenomenon of TEC and electron density profiles changes in the special region during the sun storm are analyzed in detail and discussed by adopting the numerical computions.

Keywords Ionosphere · GPS · COSMIC · TEC · VTEC · Kalman filter · GPS instrumental biases

H. Wang (✉) · Q. Wang · Y. Cheng
Chinese Academy of Surveying and Mapping, Beijing 10083, China
e-mail: whxxf82@126.com; wanghutongji@qq.com

J. Sun et al. (eds.), *China Satellite Navigation Conference (CSNC) 2013 Proceedings*, Lecture Notes in Electrical Engineering 243,
DOI: 10.1007/978-3-642-37398-5_5, © Springer-Verlag Berlin Heidelberg 2013

5.1 Introduction

A fierce solar flare erupted and triggered a coronal mass ejection on 1st August 2010, then just like large clouds of charged particles from the Sun hit against the Earth on 3 and 4th August 2010. As the particles zoomed along the magnetic field, they collided with and energized oxygen and nitrogen in the atmosphere. When the energized atoms relaxed, they emitted light, providing a brilliant show. Due to the solar flare occur, the Sun also sent a coronal mass ejection, a stream of charged particles towards the Earth about at the same time. It was reported that these clouds of particles had moved away toward the Earth at more than 1,600 km per second, and moved more quickly than any other coronal mass ejection in recently years. The Sun, interplanetary and the Earth were shown in the Fig. 5.1. As usual a flare is defined as a sudden, rapid, and intense variation in brightness. When magnetic energy that has built up in the solar atmosphere is suddenly released, a solar flare will occur. Radiation is emitted across nearly the entire electromagnetic spectrum, from radio waves at the long wavelength end, through optical emission to x-rays and gamma rays at the short wavelength end. The amount of energy released is the equivalent of millions of 100 megaton hydrogen bombs exploding at the same time. These particles will cause geomagnetic storm, ionospheric anomaly, radio communications loss and so on.

This solar storm also caused geomagnetic storm and sudden, unusual ionospheric variations. So this Solar storm provided a good opportunity for studying sun storm, geomagnetic storm, the ionospheric variations associated with the

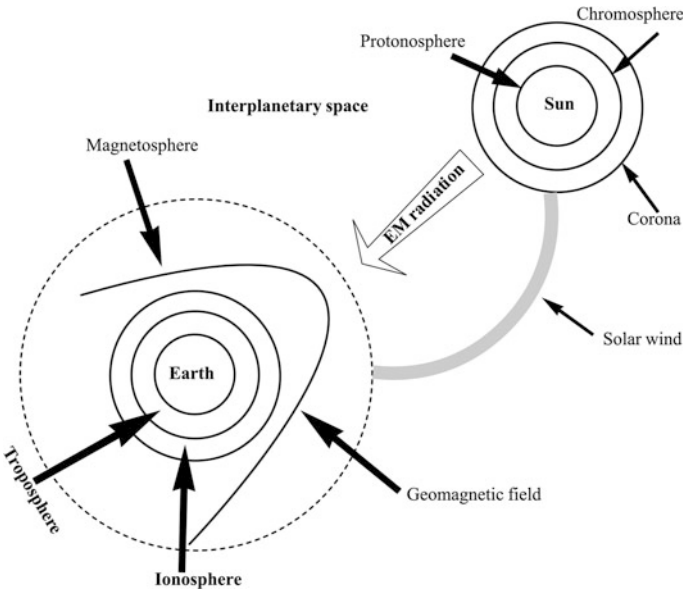

Fig. 5.1 Sun–Earth weather environment

photochemistry process and transportation process in the ionosphere and relationships to one another. It is well known that the solar storm may profoundly affect geomagnetic activity and the global ionosphere, inducing greater variations in geomagnetic parameters such as Kp index, Dst index, TEC (the total electron content), electron density distribution. Meanwhile these changes intensity will vary with latitude, longitude, local time and solar activity. So it is valuable and significant to study ionospheric variations during storm. The ionospheric changes can be monitoring by various techniques, such as ionosondes [1], incoherent scatter (ISR) [2], HF doppler, satellite beacon. On the one hand, these instruments are expensive and limited at a little area, secondly these instruments can't permanent and real-time monitor ionosphere without interval. Real-time monitoring of ionosphere changes using ground based GPS have been proven to be a powerful tool for investigating ionosphereic structure, mainly during suddenly ionosphere changes limited periods, when dynamics and energy dissipation process become extremely complex, such as geomagnetic storm [3], solar eclipse [4], earthquake [3], and so on. Meanwhile innovative space based GPS techniques have been developed in recent years. Due to occultation rise and set, COSMIC (Constellation Observing System for Meteorology, Ionosphere, and Climate) radio occultation technique can provide approximately 2,500 soundings of the ionosphere data per day which evenly distributed over the global regions. COSMIC has been demonstrated as a sounding the global ionosphere instrument more economically and effectively. Previous investigation by Lei et al. [5] verified that inversion algorithm of electron density profiles using COSMIC measurements is reliable, and their results are consistent with measurements from the ionosondes, ISR (incoherent scatter radars) and ionosphere forecast model (IRI). So electron density profiles retrieved from COSMIC measurements can be used for analyzing ionospheric variations.

The objective of this paper is to extend previous studies that ionospheric behavior during the solar storm was analyzed by combining with ground and space based GPS measurements. The organization of this paper is as follows: In Sect. 5.2, firstly, the algorithm based on the Kalman filter is proposed to obtain real-time estimation of TEC and GPS instrumental biases, due to a recursive estimator, the current measurements and the previous measurements can get the optimal estimator. Real-time and accurate TEC estimator can be calculated and the method can avoid influencing from the GPS instrumental biases. Secondly, ionospheric TEC rate were also proposed. In Sect. 5.3, we summarize the analytical about computation of ionosphere refraction error for GPS signals and also introduce the principle of inversion of electron density profiles from COSMIC occultation data. In Sect. 5.4, geomagnetic parameters are also discussed during the solar storm. Then the responses of the ground based GPS derived VTEC and TEC Rate over the Yangtze River Delta region are analyzed using the data from the Yangtze River Delta regional ground based GPS network. Following we show that during the solar storm electron density profiles from COSMIC measurements were compared with the quite days in the Yangtze River Delta region. Finally, conclusions of this paper are presented in Sect. 5.5.

5.2 Methodology of TEC Rate and TEC Derived from Ground Based GPS

5.2.1 TEC Rate Derived from Carrier Phase Data

TEC computed from the carrier phase is given as [6]:

$$TEC_{\Phi} = \frac{f_1^2 f_2^2[(\lambda_1\varphi_1 - \lambda_2\varphi_2) - (\lambda_1 N_1 - \lambda_2 N_2) - B]}{40.3(f_1^2 - f_2^2)} \tag{5.1}$$

where TEC_{Φ} is the TEC derived from carrier phase measurements; f is the carrier frequency; λ is the wave length; φ is the carrier phase; N is the integer ambiguity number; B is same as above. So the changes of TEC rate is as follow:

$$TECR_{\Phi}(t_{i+1}) = (TEC_{\Phi}(t_{i+1}) - TEC_{\Phi}(t_i))/(t_{i+1} - t_i) \tag{5.2}$$

where $TECR_{\Phi}(t_{i+1})$ is the TEC rate at epoch t_{i+1}.

5.2.2 TEC Derived from GPS

It is well known that TEC can be calculated using the differential pseudo range and carrier phase. However, the pseudo range derived TEC is corrupted by noise factors, such as multipath effects, measurement noise and GPS instrumental biases, et al. So the pseudo range derived TEC precision is lower than 5TECU. The carrier phase derived TEC is also corrupted by these factors. Due to the integer ambiguity number, the carrier phase derived TEC is not an absolute value. In order to deal with above drawbacks in TEC derived, we use a carrier phase-smoothed pseudo range technique where a new TEC estimates is derived from combining these measurements. In Hatch filter formula [7], Observation weight Q_i was established based on satellite elevation α_i, $Q_i = \sin\alpha_i$, $i = 1, 2, 3, \ldots$.

$$W_i = q_i / \sum_{k=1}^{i} q_k \tag{5.3}$$

The formula of a phase leveling technique is as follow:

$$\Delta\overline{P_i} = W_i \Delta P_i + (1 - W_i)[\Delta\overline{P_{i-1}} + (\Delta\Phi_i - \Delta\Phi_{i-1})] \tag{5.4}$$

In the above formula, we can only get TEC along the satellite transmission path. In order to get TEC over the GPS station region, we must build a ionospheric model to calculate. Commonly ionospheric models include curve polynomial fitting model, spherical harmonic model, generalized triangle model [8, 9]. In the paper, we employed curve polynomial fitting model. In the model, the ionosphere is approximated as a thin spherical shell located at a fixed height above the Earth's

surface. So each receiver-satellite link intersects the ionosphere exactly at one location, called ionospheric pierce point (IPP). The expression is as follow:

$$VTEC = TEC \cos Z^{'} \tag{5.5}$$

$$VTEC = \sum_{i=0}^{n} \sum_{j=0}^{m} E_{ij} (\varphi - \varphi_0)^i (S - S_0)^j + 9.52437 B \cos Z^{'} = 9.52437 \Delta \overline{P} \cos Z^{'} \tag{5.6}$$

where $(\varphi - \varphi_0)$ is the difference between the geomagnetic latitude of the IPP and the geomagnetic latitude of the receiver; $(S - S_0)$ is the difference the longitude of the IPP and the longitude of mean sun. B is GPS instruments biases; E_{ij} is coefficient; $\cos Z^{'}$ is the mapping function; $VTEC$ is the vertical total electron content.

In contrast with traditional least squares, the sequential Kalman filter provides a more accurate results as both the current and previous measurements is involved in the estimation process. Its process formula is as follow [10]:

$$\left.\begin{array}{cc} X_{k/k-1} = \Phi_{k/k-1} X_{k-1/k-1} & P_{k/k-1} = \Phi_{k/k-1} P_{k-1/k-1} \Phi_{k/k-1}^T + Q_k \\ X_{k/k} = X_{k/k-1} + K_k (Z_k - B_k X_{k.k-1}) & K_k = P_{k/k-1} B_k^T (B_k P_{k/k-1} B_k^T + R_k)^{-1} \\ P_{k/k} = (\mathrm{I} - K_k B_k) P_{k/k-1} & \end{array}\right\} \tag{5.7}$$

where X_k is the state vector; $\Phi_{k,k-1}$ is the state transition matrix; $P_{k/k-1}$ is the covariance matrix of state vector; Z_k is the observation vector; B_k is the observation matrix; K_k is the gain matrix; I is the identity matrix; R_k is the covariance matrix of measurement noises.

The unknown coefficients can be assumed to vary stochastically in time and approximated with a first order Gauss-Markov process. So the process noise of the white noise is given as:

$$q = \sigma^2 (1 - e^{-\frac{2\Delta t}{\tau}}) \tag{5.8}$$

where τ is correlation time; Δt is $t_{k+1} - t_k$; σ^2 is spectral density divided by $\frac{2}{\tau}$.

The expression of the transition matrix and the covariance matrix of the process noise are given as respectively:

$$\Phi = \begin{bmatrix} e^{-\frac{\Delta t}{\tau}} & & O \\ & \ddots & \\ & & e^{-\frac{\Delta t}{\tau}} \\ O & & \mathrm{I}_{nsat} \end{bmatrix}; \; Q = \begin{bmatrix} \sigma^2 (1 - e^{-\frac{2\Delta t}{\tau}}) & & & O \\ & \ddots & & \\ & & \sigma^2 (1 - e^{-\frac{2\Delta t}{\tau}}) & \\ O & & & O_{nsat} \end{bmatrix} \tag{5.9}$$

In the above equations, the satellite and receiver biases are assumed to remain constant with an identity transition matrix and zero process noise.

5.3 The Principle of Electron Density Retrieved from COSMIC Occultation Measurements

COSMIC is joint scientific mission between Taiwan and the USA, launched on 14 April 2006 with the goal of demonstrating the use of GPS radio occultation data in operational weather prediction, climate analysis, and space weather forecasting. The mission placed six small micro-satellites into six different orbits constellation at 700–800 km altitude and 30° separation in longitude between each satellite. Each COSMIC satellite is equipped with four antennas, so these satellites can receive signals from the USA GPS satellites. With the ability of performing both rising and setting occultation, COSMIC has been providing approximately 2,500 soundings of the ionosphere and atmosphere data per day, uniformly distributed around the globe since 2007. Especially, COSMIC data make a positive impact on particularly over region void of data such as oceans and polar region. Under the assumptions of spherical symmetry, straight-line propagation and electron density varies linearly with radius in between each level, electron density $N_e(r)$ was inverted by Lei et al. [5] as follows:

$$N_e(p_i) = c_{i,0}^{-1}\left[\frac{\bar{T}(p_i)}{p_i} - \sum_{k=1}^{m} c_{i,k} N_e(p_{i+k})\right] \tag{5.10}$$

where $c_{i,k}$ is a dimensionless coefficients, p_i is the distance from the Earth's center to the tangent point of a given straight line, $\bar{T}(p_i)$ is the calibrated TEC.

5.4 Results and Discussions

5.4.1 Geomagnetic Conditions

The Solar storm erupted and expelled large amount of energy and charged particles towards the Earth on 1st August 2010. Then these particles hit against the Earth and caused geomagnetic disturbance on 3rd and 4th August 2010. This disturbance was immediately identified by geomagnetic activity monitoring indices as seen in Figs. 5.2 and 5.3. The Dst index was obtained from the WDC for Geomagnetism, Kyoto. The Kp index was obtained from NOAA, USA. In the two figures show that the geomagnetic disturbance index Kp and Dst indicate twice major disturbances after the solar storm. The first geomagnetic disturbance started with the arrival of the shock at about 21:00UT on 3rd August 2010 and reached a minimum Dst value of −65nT at 24:00UT, accompanied with a maximum Kp index up to 6. Then the Dst index began to recover up to −23nT at 9:00UT, accompanied with a Kp index dropped to 3. However, second geomagnetic storm began, and subsequently the Dst index reached again −64nT at 20:00UT on

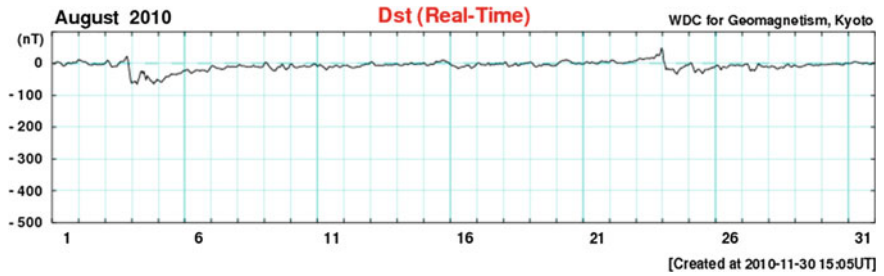

Fig. 5.2 The variation curve of DST 1st to 31th August 2010

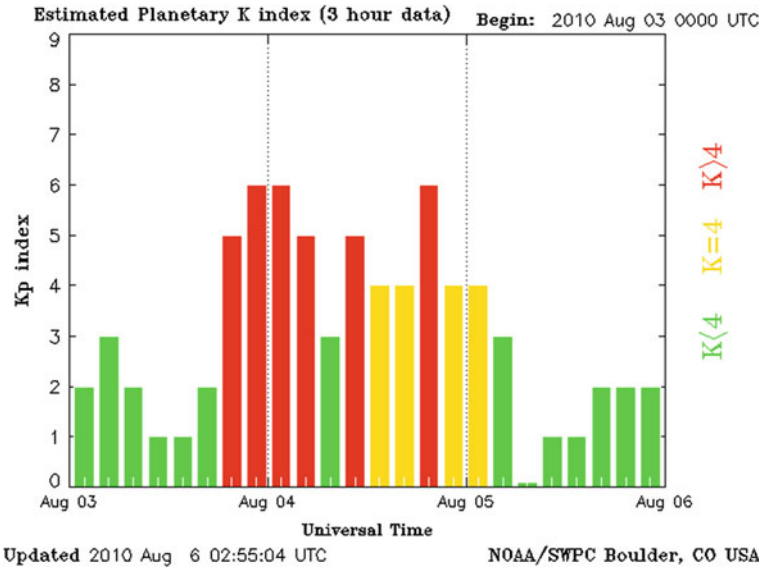

Fig. 5.3 The variation curve of KP index During 3rd 5th August 2010

4th August 2010, the Kp index also reached 6 at the same time. As can be seen from these indices, the geomagnetic activity returned to normal level on 7th August 2010.

5.4.2 Real-Time Monitoring of Ionosphere Changes Using Ground Based GPS Region Network

For this study, the ground based GPS region network measurements of the Yangtze River Delta regional GPS region network in China were used to produce real-time monitoring of *VTEC* changes and TEC rate (29th July to 7th August 2010).

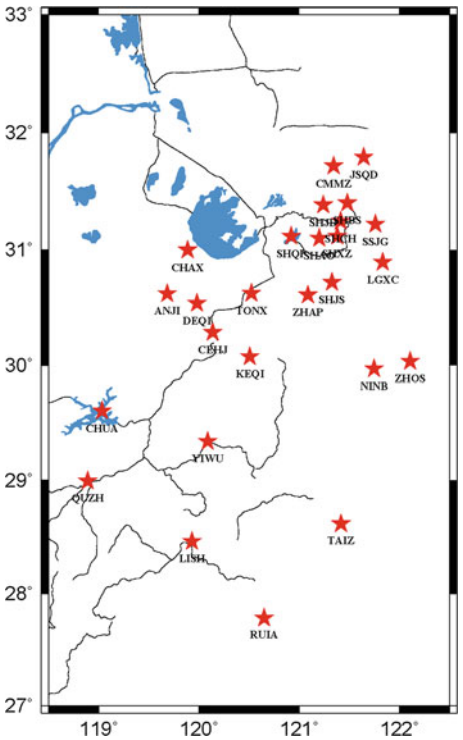

Fig. 5.4 Distribution of Shanghai regional GPS network, China

The regional GPS network consists of 26 permanent GPS sites (Fig. 5.4). In this solutions, we defined n and m value considering small region ($n = 3$; $m = 2$); in order to eliminate the multipath effects on GPS measurements, the minimum off elevation angle is selected at 15°; the ionospheric coefficients in (5.6) that describe the any point of *VTEC* above the monitoring region, and the GPS instruments biases. This solutions was proven to be robust with filter stabilizing after about one day [1, 4].

Using curve polynomial fitting model, we obtained the ionospheric coefficients, then calculated *VTEC* for GPS L1 signals above SHAO (IGS) site for a typical example. Figure 5.5 shows the diurnal variation of *VTEC* during 29th July to 7th August 2010. Before the solar storm erupted, the maximum of *VTEC* is about 22TECU in the daytime. Due to the solar storm began to erupted, more and more large amount of energy and charged particles hit against the Earth's atmosphere, the *VTEC* gradually increased, and reached the maximum value 42TECU at noon on 3rd August 2010. After this event, energetic particles receded, the maximum of *VTEC* recovered about 28TECU in the daytime. The minimum of *VTEC* on 3rd August 2010 was also bigger than other day. In a word, above the diurnal variation of *VTEC* can be due to the energy and charged particle precipitation induced by the solar wind collision with the Earth's atmosphere.

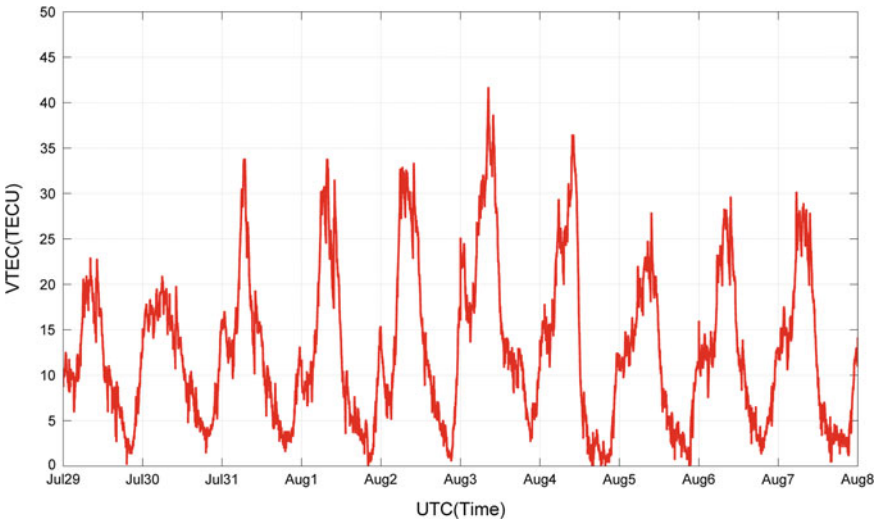

Fig. 5.5 The diurnal of *VTEC* variation during on 29th July to 7th August 2010 over SHAO (IGS) site

For the same typical example, Figs. 5.6 and 5.7 show the diurnal TEC rate changes on the two different days (29th July and 7th August, 2010) for all satellites observed (in different colors) at SHAO (IGS) site. Before the solar storm erupted, the TEC rates observed by all the satellites are below 0.02TECU/s using the 24-h data set on 29th July 2010. The TEC rate values changed relatively smoothly over the whole day period. When the energy and charged particles from the sun hit against the Earth's atmosphere, the TEC rate values changed very quickly, particularly between 4:00 and 16:00UT, showing strong variations of TEC. The maximum of TEC rate values is close to 0.05 TECU/s.

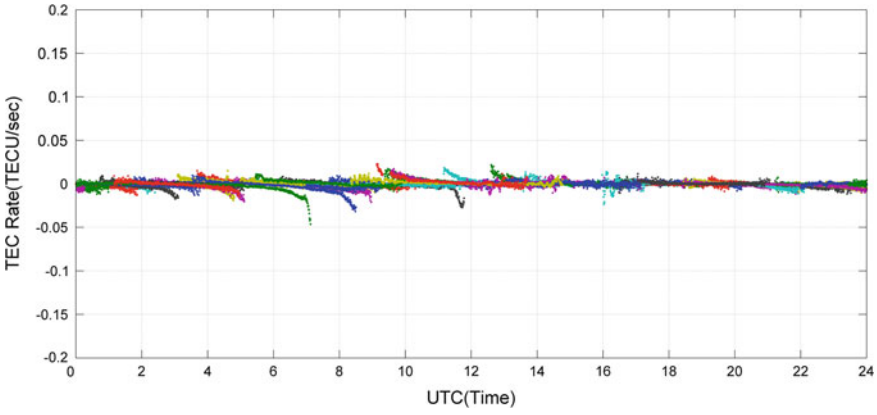

Fig. 5.6 TEC rate observed at SHAO (IGS) site on 29th July 2010

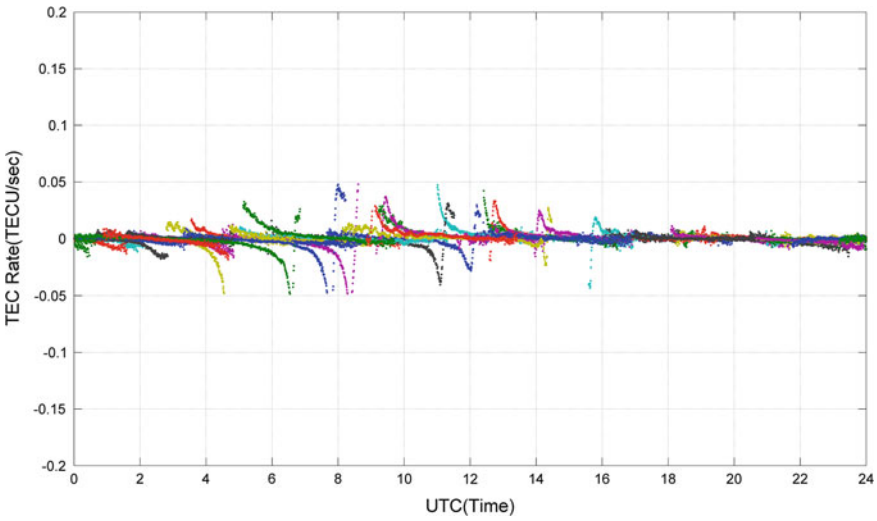

Fig. 5.7 TEC rate observed at SHAO (IGS) site on 3rd August 2010

5.4.3 Monitoring of Electron Density Profiles Changes Using Space Based GPS (COSMIC)

In this study we used electron density profiles from the COSMIC measurements. We selected coordinate of SHAO (IGS) site (31.01E, 121.20N) for examination and analysis in this study, because SHAO (IGS) site is located in the center of the Yangtze River Delta region. Positions of SHAO (IGS) site is shown in Figures with red pentacles (shown in Fig. 5.4). It is worth mentioning here that it is very difficult to find a radio occultation event that happens near any geographic location on the earth. So it should be noted that COSMIC measurements with tangent point at the at the F_2 peak height within 1 h, 5° latitude and 5° longitude at SHAO (IGS) site was selected [5, 11]. Electron density profiles of the quiet day on 29th to 30th July 2010 (according to day of 2010 year, from day 210 to 211) were compared with that of the solar storm day on 3rd to 4th August 2010 (according to day of 2010 year, from day 215 to 216).

Figure 5.8 indicates compared results at the similar time nearby SHAO (IGS) site. Since the solar storm expelled large amount of energy and charged particles towards the Earth, following happening the photochemistry process and transportation process in the ionosphere, and causing geomagnetic storm. It can be markedly seen that the electron density profiles at solar storm time featured considerably larger NmF2 and hmF2 than that at quiet time. It can be deduced that the influence from the solar storm is bigger than that from any other. It is noted that below 200 km the retrieved electron density in Fig. 5.8 become slightly inaccuracy, which is presumably a result of the horizontal gradients and the assumption of spherical symmetry in the retrieval [5].

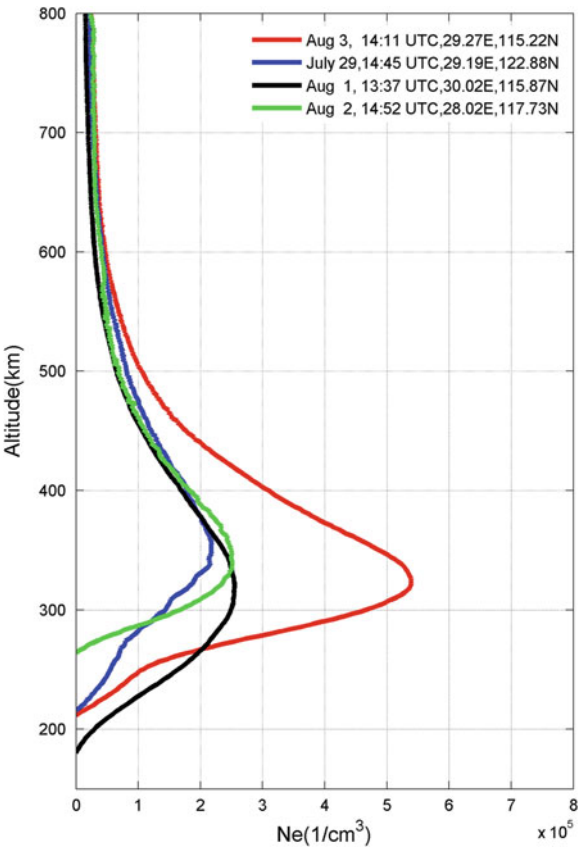

Fig. 5.8 Comparison of the COSMIC electron density profiles near IGS SHAO site

5.5 Conclusions

In this paper, we present the results of the solar storm, following the twice geomagnetic storms on 29th July 7th August 2010. Firstly, using ground based GPS measurements, the topside ionoshperic thin shell is determined, Kalman filter is also employed in order to obtain accuracy ionospheric coefficients and successfully eliminate GPS instruments biases. The real-time variations of the ionosphere are analyzed as a time series of TEC and TEC rate maps. TEC and TEC rate during the solar storm are compared and discussed with the quiet days. Secondly, using space based GPS measurements (COSMIC), electron density profiles during the solar storm are also compared and analyzed with the quiet days. The results indicate that due to the solar storm expelled large amount of energy and charged particles towards the Earth, the complicated variations of photochemistry process and transportation process happened in the ionosphere, the magnitude of TEC, TEC rate, NmF2 and HmF2 ionospheric parameters value during the solar storm become significantly higher than the quiet days.

It is worth noted that Ground based GPS measurements provide the horizontal TEC information, Space based GPS measurements (COSMIC) provide the vertical electron density distribution information. So the combined use of Ground based GPS and Space based GPS measurements provide a unique opportunity to comprehensive monitor ionospheric changes on regional or global scale. Furthermore, with more and more ground based GPS and space based GPS instruments built, the global real-time ionosphereic changes will be monitored. It will make a great contribution to studying ionosphere configuration and characteristics under any specific environment.

Acknowledgments This research was supported by National Natural Science Foundation of China (grants 41174023 and 40974018) and Scientific Research Foundation of the state Human Ministry for returned overseas Chinese Scholars (1208). The authors would like to thank Data center of Shanghai regional GPS network of China for providing the ground-based GPS tracking station data and COSMIC Data Analysis and Archiving Center (CDAAC) for providing the COSMIC occultation measurements.

References

1. Anghel A, Astilean A (2008) Near real-time monitoring of Ionosphere using Dual Frequency GPS data in a Kalman filter approach. Control Eng Appl Inform 10(2):33–38
2. Lei J, Liu L, Wan W, Zhang S (2004) Modeling the behavior of ionosphere above Millstone Hill during the September 21–27, 1998 storm. J Atmos Solar Terr Phys 66:1093–1102
3. Karia SP, Pathak KN (2011) Change in refractivity of the atmosphere and large variation in TEC associated with some earthquakes observed from GPS receiver. Adv Space Res 47:867–876. doi:10.1016/j.asr.2010.09.019
4. Wang H, Jie-Xian W (2010) Real-time monitoring of ionosphere changes in the Yangtze River Delta region based on GPS technology during the total solar eclipse of 22 July 2009. Chinese J Geophy V54(7):1718–1726. doi:10.3969/j.issn.0001-5733.2011.07.004
5. Lei J et al (2007) Comparison of COSMIC ionospheric measurements with ground-based observations and model predictions: preliminary results. J Geophys Res 112:A07308. doi:10.1029/2006JA012240
6. Liu Z, Wu C (2009) Study of the ionospheric TEC rate in Hong Kong region and its GPS/GNSS application. CGPS Meeting, pp 12–129
7. Hatch R (1982) The synergism of GPS code and carrier measurements. In: Proceedings of the 3rd international geodetic symposium on satellite doppler positioning, vol 2, New Mexico, pp 1213–1232
8. Komjathy A, Langley RB (1996) An assessment of predicated and measured ionospheric total electron content using a regional GPS net work. In: Proceedings of the national technical meeting of the Institute Of Navigation, Santa Monica, CA, 22–24 Jan 22-24 1996,pp 615–624
9. Schaer S (1999) Mapping and predicting the earth's ionosphere using the global positioning system. Ph.D dissertation, Astronomical Institute, University of Berne, Switzerland, 25 March 1999
10. Gelb A (1974) Applied optima estimation. MIT Press, Cambridge
11. Jakowski N, Wehrenpfennig A, Heise S, Reigber C, Luhr H, Grunwaldt L, Meehan TK (2002) GPS radio occultation measurements of the ionosphere from CHAMP: early results. Geophys Res Lett 29(10):1457. doi:10.1029/2001GL014364

Chapter 6
Passive Location of Emitter Source in Low Orbit Dual-Satellites System

Siqi Yu, Chenglin Cai, Xiaohui Li, Simin Li and Kequn Deng

Abstract A kind of emitter TDOA (time difference of arrival, TDOA) and FDOA (frequency difference of arrival, FDOA) differential correction method based on GNSS signal was presented against the problem that the GNSS signal and the emitter source have same bias of TDOA and FDOA such as transponder delay and relative clock error. The TDOA correction and FDOA correction can be calculated in low orbit satellites through the information of GNSS direct signal and transponder signal and location information and velocity information of the navigation signal and low orbit satellites. Using the differential correction of TDOA and FDOA, the fixed bias of TDOA and FDOA can be best eliminated and then improved the position accuracy remarkably. This kind of method not only greatly reduced the dependence of the low orbit dual-satellites platform on the ground monitoring stations, but also increased the reliability, stability and precision. The simulation results show that this kind of method can easily achieve positioning accuracy better than 1 km in the entire coverage area.

Keywords Dual-satellites position · Emitter source · Differential · GNSS signal · Space-based

S. Yu (✉) · C. Cai · S. Li · K. Deng
Institute of Information and Communication, GUET, Guilin, Guangxi Province 541004, China
e-mail: rainingsunshine@126.com

X. Li
National Time Service Center, Chinese Academy of Sciences, Taiyuan, Shanxi Province 710600, China

J. Sun et al. (eds.), *China Satellite Navigation Conference (CSNC) 2013 Proceedings*, Lecture Notes in Electrical Engineering 243,
DOI: 10.1007/978-3-642-37398-5_6,

6.1 Introduction

The precise positioning for emitter source has a special significance in the field of space information confrontation and satellite communication. Low orbit dual-satellites passive location received widespread attention with its characteristics of easy to be realized, less receive platforms and less resource occupation. Recently, the method of joint TDOA and FDOA is always used in low orbit passive position system. However, because of the influence of factors such as clock bias, transponder delay and fixed error of frequency, etc. the position error of which often reaches 3–10 km. As parameter measuring accuracy of time and frequency are huge factors which determined the location accuracy of emitter positioning, many scholars have researched and analyzed the dual-satellites passive location system and its location accuracy. Tim Pattison presented the linearized estimation problem arising from the dual-satellites geolocation of the source of a narrowband signal using TDOA and FDOA observations and an altitude constraint [1]. Wu Shilong analyzed and calculated the relationship between the positioning accuracy and dual-satellites positioning accuracy, and gave the dual-satellites system positioning accuracy performance and CEP curve in the conditions of different TDOA and FDOA [2, 3]. A kind of method using TDOA and FDOA was studied and presented which locates ground emitter from space satellites, the relationship between GDOP and TDOA error and FDOA error was also analyzed [4]. Recently, the studies on how to improve the position accuracy by eliminating the parameter measurement error were temporarily less in the literature at home and abroad.

The parameters of observation can be modified in GNSS differential location system and using the corrected measurement to position the source of emitter, high accuracy can be achieved. In view of differential position thought of satellite navigation system, by the mean time of using GNSS satellite signal to position the low orbit satellites, the system error of TDOA measuring and FDOA measuring can be greatly eliminated and the positioning accuracy can be remarkably improved by the use of low orbit dual-satellites differential positioning method. Direct against the situation of that the parameter measurement error influenced the positioning accuracy remarkably, low orbit dual-satellites emitter differential positioning system based on GNSS signal was proposed in this paper and by the use of differential technology, the measurement of TDOA and FDOA can be corrected with good effect. Simulation results show that the location accuracy can be improved remarkably using low orbit dual-satellites emitter differential positioning system based on GNSS signal auxiliary.

6.2 Low Orbit Dual-Satellites Differential Passive Location System

Through the measuring parameter arrived different observation platform, TDOA location technology format time difference Hyperboloid. Similarly, FDOA location technology format frequency difference Hyperboloid. If FDOA and TDOA are measured at the same time, we can get the intersection of time difference Hyperboloid and frequency difference Hyperboloid, and the target emitter's position can be calculated after fuzzy point removed. In the process of emitter dual-satellites location, the position accuracy was influenced by the aspects as follows:

1. Low orbit satellite determination error. The position and velocity of low orbit satellite was calculated through GNSS system instantly. While the two low orbit satellites was not far away from each other and the distance of which often reaches about 100 km, the GDOP of the two satellites in the GNSS navigation system can be considered equal and the low orbit satellite determination errors of two satellites are very close. The real sites of the low orbit satellites in the geocentric coordinate system is $\mathbf{S_i} = (x_i,\ y_i,\ z_i),\ i = 1,\ 2$, and the relative error of which is $\mathbf{dS_i} = (dx_i,\ dy_i,\ dz_i),\ i = 1,\ 2$, and the relationship between the broadcast satellite coordinate $\hat{\mathbf{S}}_\mathbf{i}$ and the real coordinate $\mathbf{S_i}$ is

$$\hat{\mathbf{S}}_\mathbf{i} = \mathbf{S_i} + \mathbf{dS_i} \tag{6.1}$$

   Where $i = 1,\ 2$.

   Supposed that the broadcast velocity is $\hat{\mathbf{v}}_\mathbf{i} = (\hat{v}_{xi},\ \hat{v}_{yi},\ \hat{v}_{zi}),\ i = 1,\ 2$, the relative velocity error is $\mathbf{dv_i}$, and the relationship between broadcast satellite velocity $\hat{\mathbf{v}}_\mathbf{i}$ and the true satellite velocity $\mathbf{v_i}$ is

$$\hat{\mathbf{v}}_\mathbf{i} = \mathbf{v_i} + \mathbf{dv_i} \tag{6.2}$$

   Where $i = 1,\ 2$.

2. The position deviation of the navigation satellites. The position deviation of the navigation satellites would affect the position accuracy of the dual-satellites system when the low orbit satellites was positioned through the parameter of the navigation satellites, in one way, it influenced the position accuracy of the low orbit satellites, and in another way, the position parameter of GEO satellites was used in low orbit dual-satellites emitter differential position system mentioned in this passage and the position error of the GEO satellites will bring some deviation to the system. The real site of the GEO satellite is $\mathbf{S_g} = (x_g,\ y_g,\ z_g)$, the broadcast site of the GEO satellite is $\hat{\mathbf{S}}_\mathbf{g} = (\hat{x}_g,\ \hat{y}_g,\ \hat{z}_g)$, the relative error of which is $\mathbf{dS_g} = (dx_g,\ dy_g,\ dz_g)$, and the relationship between $\hat{\mathbf{S}}_\mathbf{g}$ and $\mathbf{S_g}$ is

$$\hat{\mathbf{S}}_{\mathbf{g}} = \mathbf{S}_{\mathbf{g}} + \mathbf{dS}_{\mathbf{g}} \tag{6.3}$$

3. Relative clock error. In relative to the reference time, the satellites clock typically have a certain deviation which often reaches to 20 ns, with the relative clock error of the two low orbit satellites being reached up to 40 ns.
4. Transponder delay. The information communication between two low orbit satellites was implemented through the transponder and the delay of which maximum to 30 ns may caused by it.

Thus, we can draw to the conclusion that the main deviation source in the process of parameter measurement of low orbit dual-satellites emitter position system can be showed as follows

1. TDOA bias. The main TDOA bias source of the low orbit dual-satellites emitter position system include relative clock error, the transponder delay and the fixed bias caused by the ephemeris error. The random bias also makes an effect on the TDOA bias. So we can achieve

$$\Delta t = t_{TranD} + t_{Rclock} + t_{EPH} + \varepsilon_t \tag{6.4}$$

where Δt stands for the TDOA bias, t_{TranD} stands for transponder delay, t_{Rclock} is relative clock error, t_{EPH} is the fixed bias caused by the ephemeris error, and ε_t stand for the random TDOA bias.

2. FDOA bias. Because of the influence of the satellite velocity and the ephemeris error, fixed frequency bias was caused. The FDOA bias concludes the fixed frequency bias and the random FDOA bias. So

$$\Delta f = f_p + \varepsilon_f \tag{6.5}$$

Δf is FDOA bias, f_p is the fixed FDOA bias caused by satellite velocity and the ephemeris error. ε_f is the random FDOA bias.

In low orbit dual-satellites emitter position system, the positioning accuracy of which was influenced by satellite relative clock error, ephemeris error and ionosphere error etc. No matter where the locations of the users are, the influence of pseudo-range and carrier phase caused by satellite time difference error was similar. In a local radius, ephemeris error and ionosphere error have strong relevance, so we consider the bias caused by these errors to be equal. Thus, in the process of low orbit positioning, we can conclude that the position error of two low orbit satellites can be considered approximately equal in a uniform direction. A kind of low orbit dual-satellites emitter differential position system model was presented in this paper. This system consists of two low orbit satellites and the navigation satellites corresponded to them which include a GEO satellite. By the clever use of the navigation signal of GEO satellite, the fixed bias in the measurement of TDOA and FDOA can be eliminated effectively, then the position

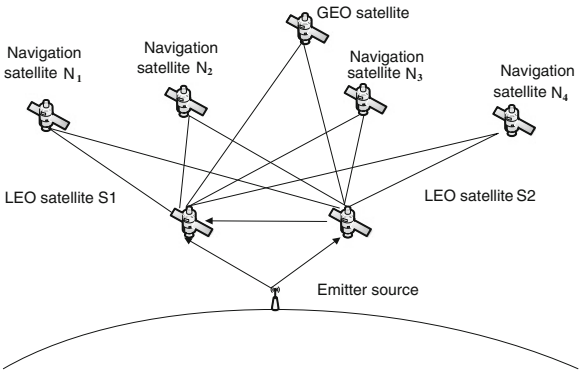

Fig. 6.1 Low orbit dual-satellites emitter differential position model

accuracy of which can be improved remarkably. This model based on space-based platform, and the low orbit satellite received GNSS signals and calculated the location and velocity of the low orbit satellites in the satellite instantly and the TDOA and FDOA of emitter signals can be corrected by the use of the parameter of the signal from the GEO satellite. The positioning model can be showed as follows (Fig. 6.1).

As the figure above shows, the GEO satellite signals can be transmitted to low orbit satellite $\mathbf{S_1}$ through two ways, the first one is from GEO satellite to low orbit satellite $\mathbf{S_1}$ directly, and the second one is from GEO satellite to low orbit satellite $\mathbf{S_2}$ firstly and then transmit it to the low orbit satellite $\mathbf{S_1}$. The total pseudo-range of the first way is

$$L_g^1 = d_g^1 + c^*(t_{Rclock1} + \varepsilon_{tg1}) \tag{6.6}$$

where $d_g^1 = \left\|\mathbf{S_g} - \mathbf{S_1}\right\|$, $t_{Rclock1}$ stands for the relative clock bias between satellite clock $\mathbf{S_1}$ and the reference time. ε_{tg1} stands for the random bias.

And the pseudo-range of the second way is

$$L_g^2 = d_g^2 + R + c^*(t_{TranD} + t_{Rclock2} + \varepsilon_{tg2}) \tag{6.7}$$

where $d_g^2 = \left\|\mathbf{S_g} - \mathbf{S}_2\right\|$, $R = \|\mathbf{S}_1 - \mathbf{S}_2\|$, $t_{Rclock2}$ stands for the relative clock bias between satellite clock $\mathbf{S_1}$ and the reference time. ε_{tg2} stands for the random bias.

The time difference of GEO satellite in the low orbit positioning platform is

$$\begin{aligned} dt_g &= (L_g^2 - L_g^1)/c \\ &= (d_g^2 + R - d_g^1)/c + t_{TranD} + t_{Rclock} + \varepsilon_{tg} \end{aligned} \tag{6.8}$$

Where $t_{Rclock} = t_{Rclock2} - t_{Rclock1}$ is the relative clock bias between two low orbit satellites. ε_{tg} is the comprehensive random time difference bias of GEO satellite.

We can get the TDOA correction by subtracting the distance calculated by the navigation information, and the main components of which includes the dual-

satellites clock bias and the transponder delay, and they belong to the fixed deviation of the satellites positioning system, the time difference correction is

$$\begin{aligned} cdt &= \left(d_g^2 + R - d_g^1\right)/c - \left(\hat{d}_g^2 + \hat{R} - \hat{d}_g^1\right)/c \\ &\quad + t_{TranD} + t_{Rclock} + \varepsilon_{tt} \\ &\approx t_{TranD} + t_{Rclock} + \varepsilon_{tt} \end{aligned} \tag{6.9}$$

Where $\hat{d}_g^1 = \left\|\hat{\mathbf{S}}_\mathbf{g} - \hat{\mathbf{S}}_\mathbf{1}\right\|$, $\hat{d}_g^2 = \left\|\hat{\mathbf{S}}_\mathbf{g} - \hat{\mathbf{S}}_2\right\|$, $\hat{R} = \left\|\hat{\mathbf{S}}_1 - \hat{\mathbf{S}}_2\right\|$ The influence caused by the ephemeris error is very small when compared to the transponder delay and relative clock error.

The time difference of emitter source $\mathbf{u} = (x, y, z)$ in the low orbit satellites platform is

$$\begin{aligned} dt_f &= (L_f^2 - L_f^1)/c \\ &= (d_f^2 + R - d_f^1)/c + t_{TranD} + t_{Rclock} + \varepsilon_{tf} \end{aligned} \tag{6.10}$$

More precise TDOA can be obtained by subtracting the time difference correction and the distance between two satellites

$$\begin{aligned} \Delta t &= dt_f - cdt \\ &\approx \left(dt_f^2 - dt_f^1\right)/c + \varepsilon_t \end{aligned} \tag{6.11}$$

Similarly, the satellite signals will appear a Doppler shift in the process of space signal transmission, and because of the influence caused by the positioning error and the velocity error of the low orbit satellites etc., fixed deviation was formed which caused by the Doppler shift, so the Doppler shift frequency of GEO satellites signals can be shown as

$$f_g = f_{gt} + f_p + \varepsilon_{fg} \tag{6.12}$$

f_{gt} is the real FDOA of GEO satellites, f_p stands for the fixed frequency difference of GEO satellites caused by positioning error and the velocity error of the low orbit satellites.etc. ε_{fg} is the random frequency difference error.

We can calculated the frequency difference bias by the information of location and velocity of the satellites

$$\hat{f}_{gt} = -\frac{f_0}{c}\left[\frac{\left(\mathbf{S_g} - \mathbf{S}_2\right)^{\mathrm{T}}\mathrm{v}_2}{\left\|\mathbf{S_g} - \mathbf{S}_2\right\|} - \frac{\left(\mathbf{S_g} - \mathbf{S}_1\right)^{\mathrm{T}}\mathrm{v}_1}{\left\|\mathbf{S_g} - \mathbf{S}_1\right\|}\right] \tag{6.13}$$

The FDOA correction can be calculated by subtracting the calculated frequency difference bias

$$\begin{aligned} df &= f_{gt} - \hat{f}_{gt} + f_p + \varepsilon_{fg} \\ &\approx f_p + \varepsilon_{fg} \end{aligned} \tag{6.14}$$

And the FDOA of the emitter source in the low orbit dual-satellites differential platform can be shown as

$$f_f = f_{ft} + f_p + \varepsilon_{ff} \tag{6.15}$$

The more precise FDOA can be obtained by subtracting the frequency difference correction

$$\Delta f = f_{ft} + \varepsilon_f \tag{6.16}$$

According to the TDOA and FDOA after correction, simultaneous equations as follows

$$\Delta t = \frac{1}{c}(\|\mathbf{S_2} - \mathbf{u}\| - \|\mathbf{S_1} - \mathbf{u}\|) \tag{6.17}$$

$$\Delta f = -\frac{f_0}{c}\left(\frac{(\mathbf{S_2} - \mathbf{u})^{\mathbf{T}}\mathbf{v_2}}{\|\mathbf{S_2} - \mathbf{u}\|} - \frac{(\mathbf{S_1} - \mathbf{u})^{\mathbf{T}}\mathbf{v_1}}{\|\mathbf{S_1} - \mathbf{u}\|}\right) \tag{6.18}$$

Assumed that the earth was ellipsoid model,

$$\mathbf{u}' = \left[\frac{x}{a_e}, \frac{y}{a_e}, \frac{z}{b}\right]^{\mathbf{T}} \tag{6.19}$$

Based on the equation of ellipsoid we can get

$$\mathbf{u}'^{\mathrm{T}}\mathbf{u}' = 1 \tag{6.20}$$

Where $a_e = 6378137$, $b = 6356752.314$, simultaneous Eqs. (6.17, 6.18 and 6.20), then we can get the emitter coordinates after calculating.

6.3 Performance Evaluation of Model

To seek partial differential to x, y, z respectively, we can get

$$\mathbf{H}\Delta\mathbf{u} = [\Delta t, \Lambda f, 0]^{\mathbf{T}} \tag{6.21}$$

Where $\mathbf{H} = [\mathbf{H_1}, \mathbf{H_2}, \mathbf{H_3}]^{\mathbf{T}}$, $\Delta\mathbf{u} = (dx, dy, dz)^{\mathbf{T}}$

$$\mathbf{H_1} = \frac{1}{c}\left(\frac{(\mathbf{u} - \mathbf{S_2})^{\mathbf{T}}}{\|\mathbf{S_2} - \mathbf{u}\|} - \frac{(\mathbf{u} - \mathbf{S_1})^{\mathbf{T}}}{\|\mathbf{S_2} - \mathbf{u}\|}\right) \tag{6.22}$$

$$\mathbf{H_2} = \frac{f_0}{c}\left(-\frac{(\mathbf{u} - \mathbf{S_2})^{\mathbf{T}}\mathbf{V_2}(\mathbf{u} - \mathbf{S_2})}{\|\mathbf{u} - \mathbf{S_2}\|^2} + \frac{\mathbf{V_2^T}}{\|\mathbf{u} - \mathbf{S_2}\|} + \frac{(\mathbf{u} - \mathbf{S_1})^{\mathbf{T}}\mathbf{V_1}(\mathbf{u} - \mathbf{S_1})}{\|\mathbf{u} - \mathbf{S_1}\|^2} - \frac{\mathbf{V_1^T}}{\|\mathbf{u} - \mathbf{S_1}\|}\right) \tag{6.23}$$

$$\mathbf{H_3} = \left[\frac{2x}{a_e^2}, \frac{2y}{a_e^2}, \frac{2z}{b^2}\right] \tag{6.24}$$

Thus, the covariance matrix of positioning error is

$$\psi = E\{\Delta \mathbf{u}^T \Delta \mathbf{u}\} = \mathbf{H}^{-1} diag\left\{\sigma_t^2, \sigma_f^2, 0\right\} \mathbf{H}^{-\mathbf{T}} \tag{6.25}$$

The GDOP of the positioning error is

$$GDOP\ (x, y, z) = \sqrt{\psi\ (1, 1) + \psi\ (2, 2) + \psi\ (3, 3)} \tag{6.26}$$

Generally, the blind zone will be formed in the link line of the two low orbit satellites in low orbit dual-satellites passive location system. In the blind zone, the GDOP will tend towards infinity. Thus, we need to avoid the blind zone or use other ways to improve the position accuracy in this kind of area. In this paper, the improvement of low orbit dual-satellites passive location accuracy emphasize on that taking method to eliminate the fixed bias of TDOA and FDOA, and issue of principle, properties of low orbit dual-satellites passive location and blind zone, interested readers can consult relative literature for detail.

6.4 Analysis of Simulation Result

6.4.1 Analysis of Position Accuracy in the Middle Line of Sub-satellite Points

Supposed that the longitude and latitude of the two satellites are (125, 29.4), (125, 30.5), and 1100 km above the earth. The velocities of the two low orbit satellites are approximately equal to (743.8, 3228.6, 6503.2), and the distance between two satellites are 143 km, the relative clock error of dual-satellites are $t_{Rclock} = 40$ ns and the transponder delay $t_{TranD} = 30$ ns. Considered the random error and skipped the blind zone, the comparison of position error distribution in the middle line of sub-satellite point can be shown as follows (Figs. 6.2, 6.3).

The result of the simulation shows that the position accuracy of low orbit dual-satellites emitter differential system is improved largely when compared to the formal dual-satellites location system. In the blind zone which in the middle line of sub-satellite point, the position errors of which are very largely and tend towards infinity. And in the two sides of the blind zone, the performance of position error is good. With the rapid growth of the distance in the two sides, the position errors turn to be bigger. Form the figure we can get that the position error before differential in the middle line of sub-satellite point turned to be 1–3 km, and after differential, the position error of which down to less than 100 m. This can reflects the position error influenced by the distance in some extent.

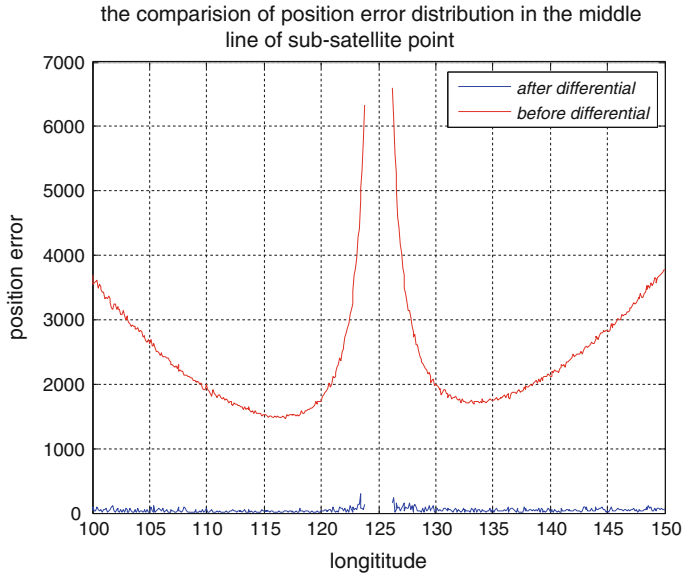

Fig. 6.2 Position error comparison in the *middle line* of sub-satellite point before differential and after differential

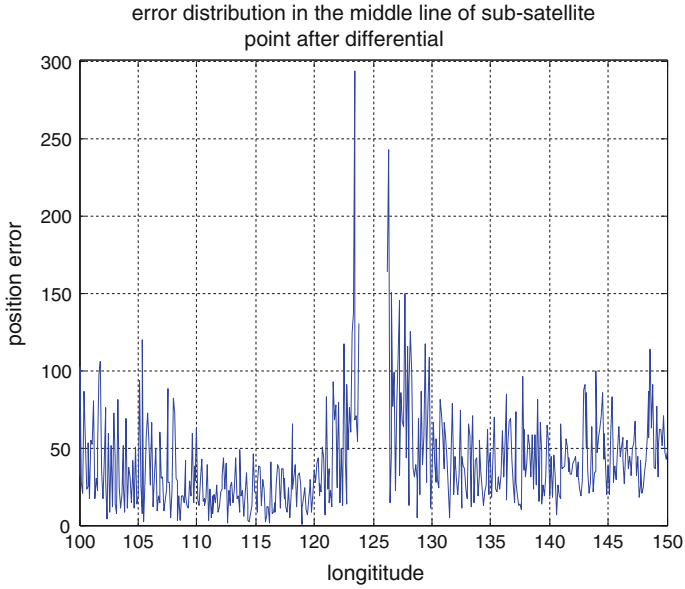

Fig. 6.3 Position error in the *middle line* of sub-satellite point after differential

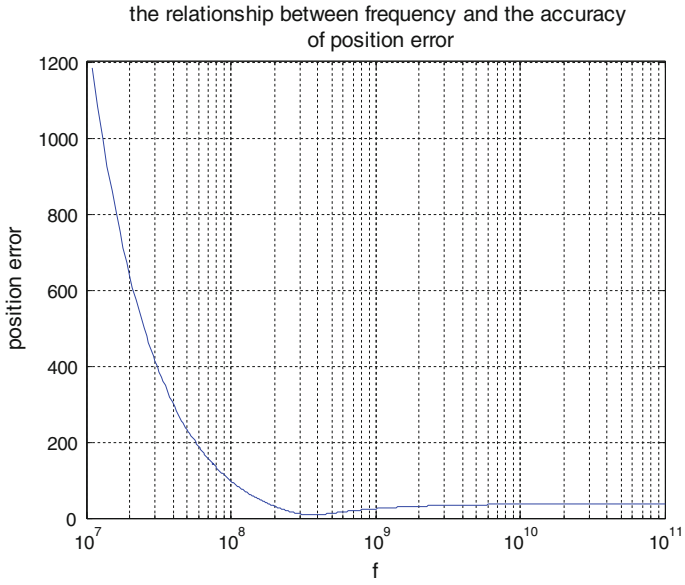

Fig. 6.4 The relationship between frequency and the position error

6.4.2 Position Error Influenced by the Frequency

In low orbit dual-satellites emitter differential position system, the frequency of GEO satellite signals $f_g = 1.5 * 10^9$ constantly, while the frequencies of ground emitter are uncertain. The simulation results of the position accuracy of different emitter frequency in the same condition can be shown as follows (Fig. 6.4).

We can learn that position errors are rather big when the frequency magnitude is in 10^7, which is greater than 1 km. When the frequency magnitude is in 10^8, the position error turn to be smaller, but in some band of frequencies, the position error is still great and cannot be neglected. When the frequencies magnitudes are in 10^9 and 10^{10}, the position errors are small and steadily, with a slight increase. When the frequency of the emitter is lower, the influence of fixed frequency bias is rather big and it will bring big influence to the position accuracy. But when the frequency of emitter source turned to reach a certain level, the influence caused by the emitter source in the calculated GEO frequency bias will increase, so it will influence the FDOA correction and make the position error a little bigger. We can get the best position accuracy in the magnitude of 10^9 and 10^{10}.

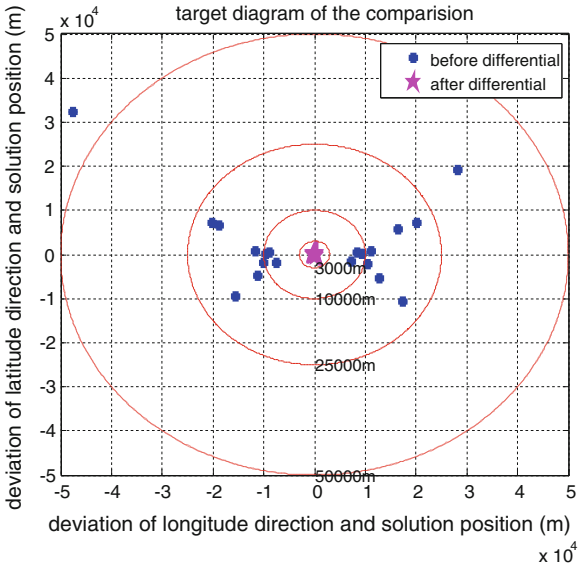

Fig. 6.5 The target diagram of the comparison

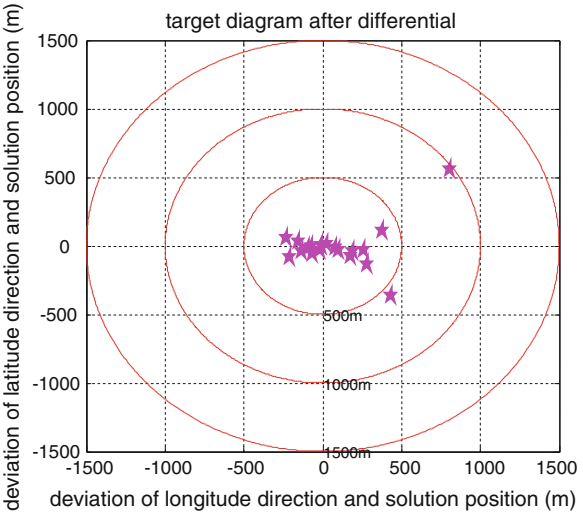

Fig. 6.6 The target diagram after differential

6.4.3 Simulation Effect of Position Error

Take 20 groups of coordinates in the position area, and we can get the target diagram of the correction as follows (Figs. 6.5, 6.6).

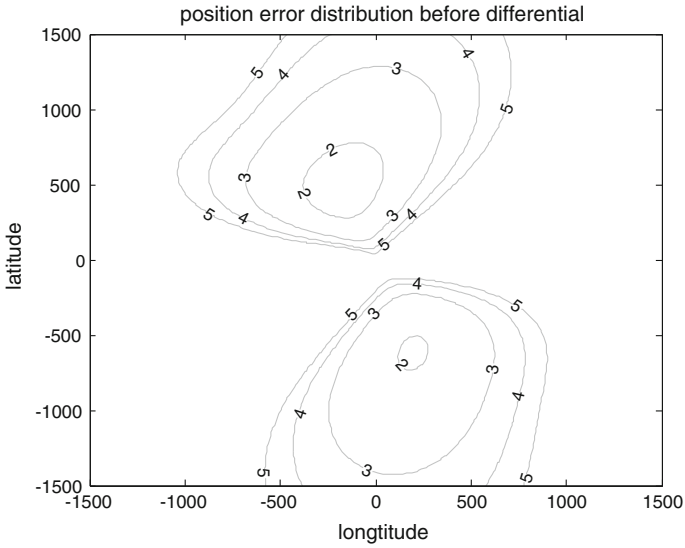

Fig. 6.7 Position error distribution before differential

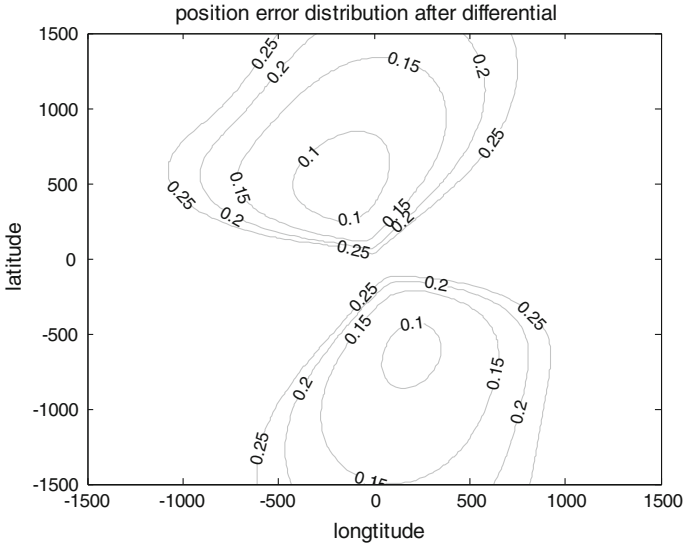

Fig. 6.8 Position error distribution before differential

From the target diagram we can come to conclusion that the position accuracy of the low orbit dual-satellites emitter position system is low, which ranges 3–10 km, and in some area the position error even surpass 10 km. But after

differential, the position error of which control to 500 m. From the simulation result we can get that the position accuracy of which can be improved remarkably with differential, and the position area turn to be larger when limiting the range of position error.

6.4.4 The Comparison of Position Error Distribution Before Differential and After Differential

We compared the GDOP of low orbit dual-satellites emitter position before differential and after differential as follows (Figs. 6.7, 6.8).

From the simulation results above we draw a conclusion that the position accuracy after differential are better than the one before differential and in the same position area the position error after differential can depress to under 1 km while the traditional system came to 3–10 km. The position accuracy can be improved remarkably using the low orbit dual-satellites emitter differential position system based on GNSS signal auxiliary, and possess applicable value.

6.5 Conclusions

In this paper, the source of position error in the low orbit dual-satellites location system was comprehensive analyzed and a kind of low orbit dual-satellites location algorithm based on GNSS differential principle was proposed. This method based on space-based platform and the dependence of the low orbit dual-satellites platform on the ground monitoring stations was reduced through the orbit determination and TDOA and FDOA correction in the low orbit satellites, and with the less dependence on the ground station, the reliability and the stability when the ground station get disturbed turned to be improved. In view of differential position thought of satellite navigation system, the fixed bias of TDOA and FDOA can be best eliminated, thus improved the passive location accuracy. Simulation results show that by the use of this kind of method, position accuracy can be easily achieved better than 1 km when compared to 3–10 km in traditional way.

Acknowledgments This paper is supported by: National Natural Science Foundation (60263028); Guangxi Natural Science Foundation (2012GXNSFDA053027); Open Fund of Key Laboratory of Precision Navigation and Technology, National Time Service Center, CAS (2012PNTT04); Innovation Project of GUET Graduate Education (XJYC2012010).

References

1. Pattison T, Chou SI (2000) Sensitivity analysis of dual-satellite geolocation. IEEE Trans Aerosp Electron Syst 36(1):56–71
2. Shilong W, Jingqing L (2009) Influence of position error on TDOA and FDOA measuring of dual-satellite passive location system. IEEE. 978-1-4244-4076-4/09
3. Shilong W, Jingqing L, Liangliang G (2010) Joint FDOA and TDOA location algorithm and performance analysis of dual-satellite formations. IEEE. 978-1-4244-6893-5
4. Zhang Y, Sheng W, Fucheng G (2007) Low orbit dual-satellites passive location algorithm and its precision analysis. J Chin Inertial Technol 15(2)
5. Schmidt RO (1980) An algorithm for two-receiver TDOA/FDOA emitter-location. Tech Memo TM-1229, ESL, May 21
6. Yan H, Cao JK, Chen L (2010) Study on location accuracy of dual-satellite geolocation system. IEEE Proceedings, 107–110
7. Kaplan ED, Hegarty CJ (1996) Understanding GPS principles and applications. Artech House, INC
8. Jiyu L (2008) GPS satellite navigation positioning principle and method
9. Ho KC, Chan YT (1997) Geolocation of a known altitude object from TDOA and FDOA measurements. IEEE transactions on aerospace and electronic systems, 33(3)
10. Hofmann-Wellenhof B, Lichtenegger H, Wasle E (2007) GNSS-global navigation satellite systems

Chapter 7
The First PPP-Based GPS Water Vapor Real-Time Monitoring System in Pearl-River-Delta Region, China

Zhizhao Liu and Min Li

Abstract The first Precipitable Water Vapor Real-Time Monitoring System (PWVRMS) based on Global Positioning System Precise Point Positioning (PPP) technique has been developed for the Pearl-River-Delta region. This PWVRMS system estimates GPS satellite clock error data in real-time while using International GNSS Service (IGS) predicted precise satellite orbit directly. Currently it processes GPS data every 10 min on a daily basis from three networks in Pearl-River-Delta region: Hong Kong SatRef GPS network, Macao MoSRef GPS network and Guangdong CORS network. Compared to traditional double-differencing technique, the advantage of using PPP technique is that (1) the PWV estimation at each station is completely independent and is not affected by data quality at other stations; (2) the computation is much faster and simpler. This PWVRMS system is evaluated using radiosonde water vapor data. The GPS PWV accuracy is about 2.20 mm though the GPS station is 4.1 km away from the radiosonde. It is expected the actual GPS PWV accuracy should be higher if the GPS station is collocated with the radiosonde station. The real-time PWV products can be widely used in weather forecasts, climate researches, and water vapor correction for remote sensing images such as SAR applications. Currently the PWVRMS supplies real-time water vapor data to several meteorological agencies in Pearl-River-Delta region including Hong Kong Observatory, Macao Meteorological and Geophysical Bureau, Shenzhen Meteorological Bureau and Guangdong Meteorological Bureau for their weather forecasting service and research.

Z. Liu (✉) · M. Li
Department of Surveying and Geo-Informatics, The Hong Kong Polytechnic University, 11 Yuk Choi Road, Hung Hom, Kowloon, Hong Kong, China
e-mail: lszzliu@polyu.edu.hk

M. Li
e-mail: lim@whu.edu.cn

M. Li
GNSS Research Center, Wuhan University, Wuhan, Hubei, China

J. Sun et al. (eds.), *China Satellite Navigation Conference (CSNC) 2013 Proceedings*, Lecture Notes in Electrical Engineering 243,
DOI: 10.1007/978-3-642-37398-5_7,

Keywords Global positioning system (GPS) · Precipitable water vapor (PWV) · Precise point positioning (PPP) · Real-time monitoring

7.1 Introduction

Precipitable water vapor (PWV) is a highly variable atmospheric composition and is one of key parameters in weather forecasting and climatological research. It is one of the most important greenhouse gases and plays a key role in radiative balance, cloud formation, precipitation processes, hydrological cycle, surface fluxes and soil moisture [1–3]. Water vapor is also shown to directly participate in atmospheric chemistry altering the composition of condensing species and increasing total organic aerosol formation [4]. The aerosol has a significant impact on human being's morbidity, mortality and visibility [5–7].

The most traditional water vapor observation technique might be the radiosonde [8, 9]. It has a long observation history and it is still widely used. It is estimated there are globally $\sim$850 radiosonde stations in operation [10]. Radiosonde has a good vertical resolution and can achieve an accuracy as high as 0.1 gcm^{-2} [11, 12]. The algorithm of retrieving water vapor from radiosonde data is relatively straightforward. However radiosonde observation is very costly and the geographic density of radiosonde stations is low as well largely because of high operational costs. For instance, there is only one operational radiosonde station in Hong Kong for an area of over 1104 km^2 [13]. Globally standard operational weather stations normally launch radiosonde twice a day and produce only two water vapor measurements daily. The 12 h temporal resolution is insufficient for short-term weather forecasting. The low temporal and spatial resolutions of radiosonde data significantly limit the use of water vapor measurements in weather forecasting modeling.

Another widely used water vapor measurement method is using remote sensing satellite. Water vapor retrieval from remote sensing satellites has been studied for decades [14, 15]. Satellite-based remote sensing can produce water vapor for a large area at very low cost. However, the water vapor accuracy is relatively low. For instance the widely used MODIS water vapor products MOD05 and MOD07 have been estimated using radiosonde data in Hong Kong and their RMS errors are 1.309 and 1.353 cm, respectively [13]. Similar to radiosonde, the temporal resolution of satellite-based water vapor is also poor. Taking the MODIS satellite as an example, the MODIS TERRA satellite passes over Hong Kong only once daily at 10:30 am. Thus the water vapor information from remote sensing satellite is not temporally dense enough to support short-term weather forecasting or nowcasting.

To overcome the drawbacks of the above water vapor observation techniques, a technique of retrieving water vapor from Global Positioning System (GPS) has been developed over the past two decades [16–19]. The GPS-derived water vapor can complement the radiosonde and satellite remote sensing water vapor observation

techniques in several aspects. First, its geographic density is much higher than radiosonde. Now many regional and national GPS networks have been deployed worldwide. For instance, International GNSS Service (IGS) routinely operates and analyze GPS data from a network of $\sim$350 stations [20]. Second, the temporal resolution of GPS water vapor is much higher. Normally one water vapor parameter is estimated every 1–2 h in GPS data analysis. Third, the GPS water vapor has a good accuracy. The integrated water vapor (IWV) can be estimated to an accuracy of 1–2 mm [21, 22]. Thus in the past decades GPS-based water vapor observation systems have been rapidly developed in many countries [11, 18, 19, 23]. In Mainland China, many provincial and municipal GPS networks have been deployed for water vapor monitoring and weather forecasting services such as [24–26].

However in the past, the GPS-based water vapor retrieval algorithm is mainly based on the double-differencing (DD) operator. In the DD operator, at least one reference GPS station is needed to form a differencing algorithm between the reference and GPS water vapor station. If the GPS network is relatively small (e.g. $<$500 km), only relative water vapor between stations can be obtained due to the fact that tropospheric delays are highly correlated in space [27]. To recover the absolute water vapor from relative one, one water vapor radiometer is collocated with one GPS station to recover the absolute water vapor for all the GPS stations [27]. In [17], an algorithm is developed by setting one reference GPS station separated from user station by at least 500 km in order to get the absolute water vapor. This requirement poses a number of inconveniences or even potential threats to GPS water vapor retrieval when highly reliable, accurate, real-time retrieval of water vapor is required. First, in real-time water vapor retrieval, the GPS data from reference station need to be real-time transmitted to the GPS data processing center for computation. This requires a very reliable communication method that might be costly to operate and maintain. Data transmission via internet is feasible but data loss is not uncommon. Second, because double-differencing algorithm is used, the GPS data quality problem at the reference station directly affects the formation of DD algorithm and water vapor retrieval. This issue will become more problematic when it is coupled with the data loss during transmission. Third, the reference station is usually not managed by operator who manages a GPS water vapor network. It is completely out of the operator's control if there are outages at the reference station or the configuration of the references needs to be adjusted.

Different from the traditional double-differencing approach, this paper proposes using Precise Point Positioning (PPP) technique to estimate absolute water vapor from a network of GPS stations. Through this PPP technique, the absolute water vapor estimation is performed independently without the introduction of any reference station. Thus it wholly eliminates the possible side effects caused by reference stations.

In the Sect. 7.2, the PPP-based water vapor retrieval algorithm is presented in details. In Sect. 7.3, the GPS networks in the Pearl-River-Delta (PRD) region of China, including Hong Kong, Macao and Guangzhou province are described. In Sect. 7.4, the GPS Water Vapor Real-Time Monitoring System in PRD Region

based on this PPP retrieval algorithm is described. The results from six months of monitoring system operation are presented. The conclusion is given in Sect. 7.5.

7.2 Principle of Retrieving Water Vapor from GPS Tropospheric Delay

GPS signals experience atmospheric range delays when they pass through ionosphere and troposphere. The ionosphere produces a dispersive delay at an order of several to tens of meters. But it can be almost completely eliminated by using an ionosphere-free combination of GPS signals at two frequencies. The troposphere however is a non-dispersive medium and the tropospheric range delay cannot be corrected like the one in ionosphere. Instead it is usually corrected using empirical models. Generally the tropospheric range delay can be decomposed into two components: dry component and wet component. The total tropospheric delay along the ray path can hence be written as [16, 17, 28, 29]:

$$\Delta L(e) = \Delta L_z^d \cdot M_d(e) + \Delta L_z^w \cdot M_w(e) \tag{7.1}$$

where ΔL is the total tropospheric delay along the ray path, e is the satellite elevation, ΔL_z^d and ΔL_z^w are Zenith Hydrostatic Delay (ZHD) and Zenith Wet Delay (ZWD), respectively; $M_d(e)$ and $M_w(e)$ are the hydrostatic and wet mapping functions, respectively, which map the zenith delay to the slant ray path direction. At satellite elevation 90°, the Zenith Tropospheric Delay (ZTD) ΔL_z can be expressed as:

$$\Delta L_z = \Delta L_z^d + \Delta L_z^w \tag{7.2}$$

Compared with the wet delay, the hydrostatic delay is much stable and it contributes $\sim$80 % to the total tropospheric delay. The ZHD thus is usually estimated using empirical models. The wet delay however has a much rapid variation, though it accounts for only $\sim$20 % of the total tropospheric delay. Due to it large variability, the modeling of wet component of tropospheric delay is thus less accurate than that of hydrostatic delay. Therefore the zenith wet delay is commonly estimated as an unknown parameter along with other geodetic parameters in GPS data analysis. Once the ZWD is obtained, this delay can be readily converted into integrated precipitable water vapor (PWV) using a formula shown below [16, 25, 28]:

$$PWV = F \cdot \Delta L_z^w \tag{7.3}$$

where the conversion factor F is a function of the weighted mean temperature of the troposphere and is related to the atmospheric temperature.

In the Precise Point Positioning data analysis, the zenith tropospheric delay ΔL_z of each station is parameterized and estimated along with other parameters such as

GPS station coordinates. The zenith hydrostatic component ΔL_z^d can be removed using an empirical model thus the zenith wet delay ΔL_z^w is obtained using Eq. (7.2). PWV is then yielded using Eq. (7.3).

7.3 PPP-Based Water Vapor Estimation Model and Strategy

PPP technique uses undifferenced GPS carrier phase observations. To eliminate the ionospheric delay in GPS signals, ionosphere-free combination observation are usually used, which can be described as:

$$\begin{aligned}\Phi_{IF} &= \frac{f_1^2 \cdot \Phi_1 - f_2^2 \cdot \Phi_2}{f_1^2 - f_2^2} + \varepsilon \\ &= \rho + c \cdot (dt - dT^s) + \Delta L_z \cdot M + \frac{c \cdot f_1 \cdot N_1 - c \cdot f_2 \cdot N_2}{f_1^2 - f_2^2} + \delta m_{IF} + \varepsilon\end{aligned} \tag{7.4}$$

where f_1 and f_2 are the GPS L1 and L2 carrier phase frequencies, respectively; Φ_1 and Φ_2 are GPS carrier phase observations at L1 and L2 frequencies, respectively; dt and dT^s are receiver clock error and satellite clock error, respectively; N_1 and N_2 are the integer phase ambiguities at L1 and L2 frequencies, respectively; ΔL_z is the zenith tropospheric delay; M is the mapping function; δm_{IF} is the multipath effect; ε is the noise term of ionosphere-free observation.

The implementation of PPP technique requires high-precision orbit and satellite clock corrections for the GPS satellites. In our study, we estimate precise satellite clock corrections based on the real-time GPS data streams from 80 worldwide GPS stations. The 80 GPS stations have an observation rate of 1 Hz. The precise GPS satellite orbits are obtained from the IGS ultra-rapid satellite orbit data, which are updated every 6 h with 24 h prediction. Meanwhile, the GPS stations' coordinates are constrained tightly to their weekly positioning solutions.

7.3.1 Mapping Functions

Mapping function is needed to transform the ZTD to the slant delay along the ray path and it is a function of satellite elevation, annual or seasonal variations of atmosphere and meteorological parameters of surface stations. The most commonly used mapping functions include Hopfield, Saastamoinen, Chao, NMF, VMF1, and Global Mapping Function (GMF). In this study, the GMF is used. It is obtained from spherical harmonic expansion of the parameters of VMF1 model at $15^\circ \times 15^\circ$ grids globally. The coefficient's calculation is only related to site coordinates and the observation day of year [29, 30].

7.3.2 Zenith Hydrostatic Delay Model

After removing the zenith hydrostatic delay from the zenith tropospheric delay using empirical model, the zenith wet delay remains. In this study, the Saastamoinen model is used to calculate the zenith hydrostatic delay [31]:

$$\begin{cases} \Delta L_z^d = 0.2277 \cdot \frac{P}{F(\varphi, h_0)} \\ F(\varphi, h_0) = 1 - 0.0026 \cdot \cos(2\varphi) - 0.00028 \cdot h_0 \end{cases} \tag{7.5}$$

where φ is the latitude of the station in radians; h_0 is the station height above mean sea level in km; P is the surface air pressure in hPa; ΔL_z^d is ZHD component in cm.

7.3.3 Converting ZWD into PWV

In Eq. (7.3), the zenith wet delay can be converted to precipitable water vapor using conversion factor F that is a function of the weighted "mean temperature" of the atmosphere and can be calculated as [16, 32]:

$$F = F(T_m) = \frac{10^6}{\rho_1 \cdot \frac{R}{m_w} \cdot \left[\frac{k_3}{T_m} + k_2 - \frac{m_w}{m_d} \cdot k_1\right]} \tag{7.6}$$

where all the quantities are constants except that T_m is a variable. Bevis et al. [16] considered that there is a linear correlation between T_m and T_0 after extensive studies of the north American region data. Chen et al. [32] employed the local radiosonde data of Hong Kong to linearly fit the T_m and T_0, and yielded the correlation between T_m and T_0 of Hong Kong region as:

$$T_m = 106.7 + 0.605T_0 \tag{7.7}$$

Thus we can compute the conversion factor using T_m and the ZWD can further be converted into PWV.

7.4 Water Vapor Observation in Hong Kong

Large variability in water vapor has been observed in the tropical atmosphere [3]. Hong Kong, a typical coastal city located in the tropical region and closely surrounded by the South China Sea, has a year-round high level of humidity and experiences remarkable water vapor variation. In summer each year, Hong Kong routinely experiences a number of strong tropical typhoons. The statistics over the past decades showed that an average of three typhoons land on South China Sea within a distance of 300 km from Hong Kong [33] and this frequency is tended to

increase. It is believed that Hong Kong is affected by the Asian Summer Monsoon (ASM) from both tropical and mid-latitudes [34].

Currently there is only one radiosonde station in service at Hong Kong, a region over 1104 km^2. Only two water vapor observations per day from the ground radiosonde station are a constraint in Hong Kong's weather forecasting services. The lack of high temporal resolution water vapor is particularly a concern for the weather prediction in the summer season when more rains and typhoons occur. This situation is basically true for other coastal cities like Macao, Guangzhou and other cities in the Pearl-River-Delta (PRD) region, one of the regions that are most frequently affected by typhoons. More accurate water vapor observations with higher temporal resolution are thus an important factor for improved weather prediction in Hong Kong and PRD region.

The Hong Kong Polytechnic University (HKPolyU) has been intensively involved with GPS research and development for many years. Considering the limited water vapor observation data available in Hong Kong, we initiated the GPS-based water vapor real-time monitoring system. Initially, the real-time GPS data are supplied by the Survey and Mapping Office of Lands Department, the Hong Kong Special Administrative Region (HKSAR). Later on, more GPS data from the Pearl-River-Delta region are included to the monitoring system. In collaboration with Wuhan University, this water vapor monitoring system is developed using Precise Point Positioning (PPP) technique on the platform of PANDA (Position and Navigation Data Analyst) software package developed at Wuhan University.

This PPP-based Precipitable Water Vapor Real-Time Monitoring System started to continuously operate (at a 24/7 mode) in full automation since 19 April 2012. Since 15 July 2012, the PPP-based Precipitable Water Vapor Real-Time Monitoring System for Pearl-River-Delta region has been fully established. This is the first such a system in Pearl-River-Delta region and it is the first water vapor monitoring system developed on the platform of PANDA software [35]. Since then, this system has been supplying a significant amount of accurate, reliable and high tempo-spatial resolution water vapor observations to the meteorological agencies in the Pearl-River-Delta region. These PWV products are currently shared in real-time mode with Hong Kong Observatory, Macao Meteorological and Geophysical Bureau, Guangdong Meteorological Bureau and Shenzhen Meteorological Bureau. The accurate real-time PWV data are expected to contribute to short-term weather forecasting and climate change monitoring in this PRD region.

7.5 PPP-Based GPS Precipitable Water Vapor Real-Time Monitoring System

The structure of the GPS PWV real-time monitoring system is shown in Fig. 7.1. The PPP-based Precipitable Water Vapor Real-Time Monitoring System in PRD region consists of three segments: real-time estimation of satellite clock errors, parameter evaluation of zenith troposphere, and real-time retrieval of PWV.

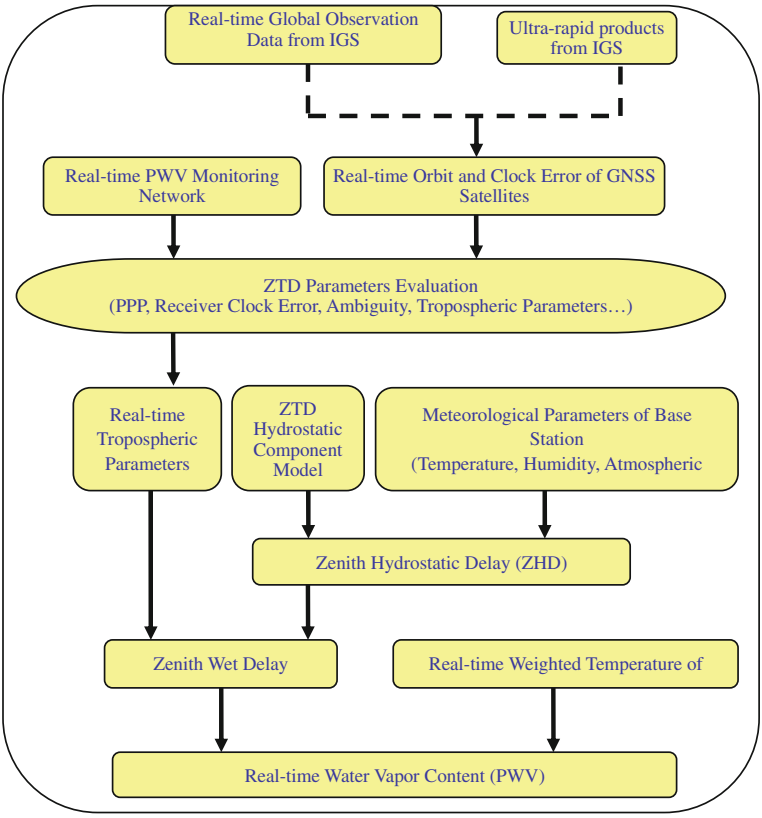

Fig. 7.1 PPP-based precipitable water vapor real-time monitoring system in Pearl-River-Delta region

7.6 Real-Time Estimation of Satellite Clock Errors

The high precision orbits and clock error corrections for navigation satellites are critical for PPP-based water vapor retrieval. GPS satellite precise orbits can be obtained from the ultra-rapid orbit released by the IGS. IGS ultra-rapid satellite orbit data are updated every 6 h and with 24-hour prediction data. The predicted orbit precision can achieve a level of 5 cm [36] and it can meet the precision demand of PPP water vapor retrieval. The IGS ultra-rapid satellite clock error correction data have a data interval of 15.0 min and have an accuracy of only 3.0 ns (RMS), equivalent to $\sim$90 cm in distance. Considering the magnitude of IGS ultra-rapid satellite clock error and the nature of rapid variation of clock errors, this type of clock correction data is not suitable for real-time PPP computation. We propose the approach of estimating GPS satellite clock correction data in real-time using the PANDA software.

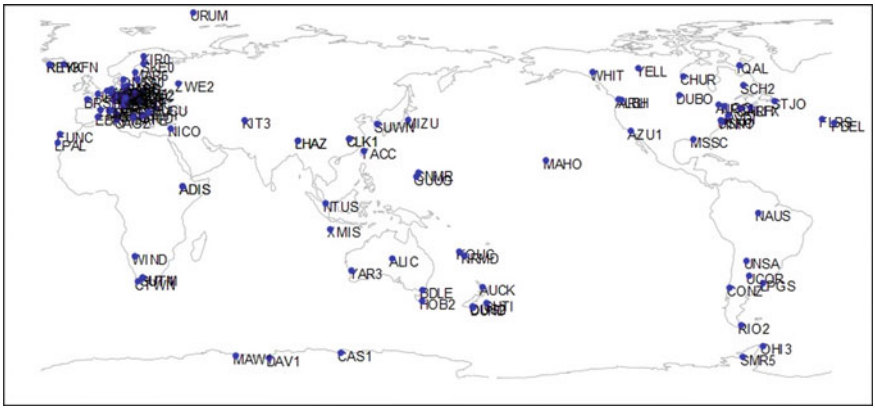

Fig. 7.2 Distribution of 80 IGS real-time tracking stations

In the estimation of precise satellite clock error correction data, the real-time data streams from 80 IGS tracking stations are received and stored [37]. The geographic distribution of the 80 global stations is shown in Fig. 7.2. The undifferenced ionosphere-free combination phase and pseudorange observations are formed, followed by fixing satellite orbits and station positions. The phase and pseudorange observations are corrected with phase center offset, solid tide, phase rotation and relativistic effect. The satellite clock error is modeled as a random process. The Gaussian elimination is used in the clock parameter estimation. This method can reduce the dimension of normal equation significantly, allowing the estimation of a large number of satellite clock parameters simultaneously. In order to evaluate the performance of real-time GPS water vapor based on the ultra-rapid orbit and real-time estimated satellite clock correction data, one test was conducted to estimate post-mission GPS water vapor using IGS final satellite orbit and final satellite clock correction data. The final satellite clock correction data have an interval of 30 s and an RMS accuracy of $\sim$75 ps, which is a significant improvement over the IGS ultra-rapid clock data. We compared the real-time and post-mission water vapor data at 18 stations and found that the RMS error of the two sets of water vapor data is 1.6 mm. This verified the good accuracy of real-time estimated satellite clock data.

7.7 GPS Data Sources and Description

The GPS data for this precipitable water vapor real-time monitoring system come from four sources: Hong Kong GPS SatRef CORS (Continuous Operational Reference System) network, Hong Kong Polytechnic University (HKPolyU), Macao GPS MoSRef CORS network and Guangdong GPS CORS network, as shown in Fig. 7.3.

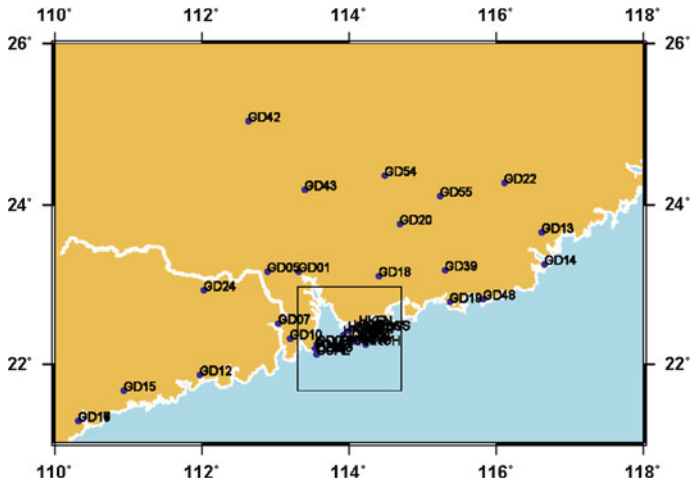

Fig. 7.3 GPS network in Pearl-River-Delta region for water vapor real-time monitoring

The Hong Kong GPS SatRef CORS is a permanent, continuously operating network established by the GPS network established by the Lands Department, Hong Kong Special Administrative Region Government. It has a network of 12 GPS stations. The SatRef GPS data are recorded at an interval of 5 s and every 10 min one GPS data file is generated at each station and then downloaded via ftp to the water vapor computation center at Hong Kong Polytechnic University (HKPolyU). Since 26 March 2012, the SatRef GPS data are continuously supplied to HKPolyU for water vapor monitoring in Hong Kong. The Hong Kong SatRef CORS stations are shown as red dots in the Fig. 7.4. In addition to the 12 SatRef stations, one GPS/Compass receiver installed on the campus of HKPolyU also provides the GPS data for water vapor estimation. This station is indicated in green dot in Fig. 7.4. The data are logged at a rate of 1 Hz and every 60 min one data file is created and downloaded for water vapor estimation. Currently only the GPS data are processed and the Compass data are not used.

The Macao MoSRef GPS CORS network is very similar to the SatRef in Hong Kong. This three-station GPS network is built and managed by the Macao Cartography and Cadastre Bureau (DSCC) of Macao Special Administrative Region Government. The GPS data are sampled every 10 s and one data file is generated every 60 min at each station. Then the GPS data files are immediately transferred to the water vapor computation center at HKPolyU. The three GPS tracking stations in Macao are shown as blue dots in Fig. 7.4. The MoSRef GPS data started to transfer to HKPolyU for water vapor computation since 14 June 2012.

The fourth data source for the Pearl-River-Delta region water vapor monitoring system is the Guangdong GPS CORS network, which is comprised of 25 GPS stations distributed across Guangdong province, Mainland China, as shown in Fig. 7.3. The GPS data are sampled at a 1-Hz rate and are received in real-time data streams by the GNSS Research Center, Wuhan University, Mainland China.

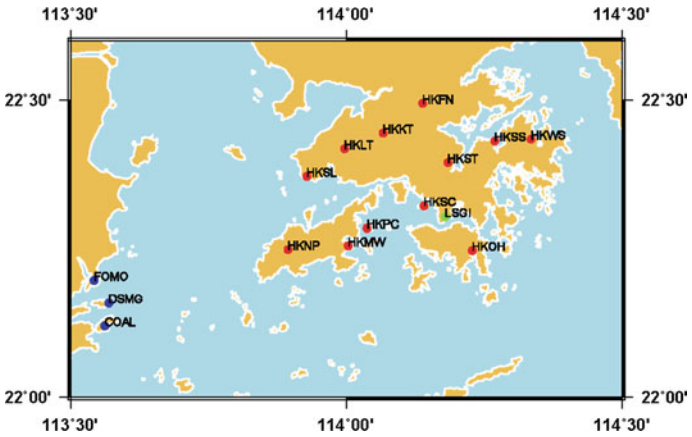

Fig. 7.4 GPS stations in Hong Kong and Macao

The GPS data are processed at Wuhan University and the computed water vapor results are transmitted to HKPolyU. Since 15 July 2012, the GPS data from Guangdong CORS network started to transmit in real-time stream to Wuhan University.

7.8 Water Vapor Estimating Models and Strategies

The real-time estimation of zenith tropospheric delay can be performed once precise predicted orbits and real-time satellite clock error data are ready. In the real-time estimation, only the tropospheric parameters of each station, receiver clock error parameters, ambiguities and tightly constrained stations' coordinates are estimated using undifferenced phase and pseudorange derived from ionosphere-free combination observations. The models and strategies used in the PPP estimation are listed in Table 7.1.

7.9 Water Vapor Accuracy Analysis and Evaluation

This PPP-based Precipitable Water Vapor Real-Time Monitoring System started to operate in full automation since 19 April 2012. The major products include precipitable water vapor (PWV), zenith wet delay (ZWD) and zenith tropospheric delay (ZTD). The relative humidity, temperature and atmospheric pressure data recorded at each Hong Kong SatRef CORS station are also stored. Those meteorological data are recorded by meteorological sensor installed at each SatRef GPS station. Figure 7.5 shows the real-time variations of PWV observed 2 August 2012

Table 7.1 Models and strategies used in the PPP estimation

Observations	Observations from ionosphere-free combination
Sampling rate	1 s
Cut-off elevation	7°
Orbits and clock errors of satellites	IGS ultra-rapid orbit, real-time estimated clock error
Relativistic effect	IERS 2003
Correction of solid tide	IERS 2003
Correction of ocean tide	IERS 2003
Correction of pole shift tide	IERS 2003
Receiver phase center	IGS08.atx
Stations' coordinates	Static, tightly constrained IGS08
Receiver clock error	Random walk model
Troposphere	SAASTAMOIN model correction of hydrostatic component and wet component + GMF mapping function + random walk estimation
Ionosphere	Influence of first order term is eliminated by ionosphere-free combination
Integer ambiguity	Constant

at HKSC, one Hong Kong SatRef station. The top panel of Fig. 7.5 shows the relative humidity (green line) and estimated PWV (red line). It clearly shows that the PWV and relative humidity are strongly correlated with each other. The bottom panel of Fig. 7.5 shows the atmospheric pressure (red line) and temperature (green line), both of which are recorded by the meteorological sensor installed at the GPS station. The atmospheric pressure and temperature are used as input data of empirical models to estimate the zenith hydrostatic delay.

We used water vapor derived from radiosonde to evaluate the GPS-derived precipitable water vapor data. This is because radiosonde is considered as one of the most accurate methods to measure water vapor and is often used as a reference to evaluate retrievals of water vapor from GPS sensing [38]. There is only one radiosonde station available in Hong Kong and it is operated by the Hong Kong Observatory, Hong Kong Special Administrative Region Government. The Hong Kong Observatory launches radiosonde balloons twice daily, at 00:00 UTC and 12:00 UTC, respectively. Hong Kong SatRef GPS stations that are within 10 km from the radiosonde station are HKSC (4.1 km from radiosonde) and HKST (9.6 km). The GPS/Compass receiver installed at HKPolyU is much closer to the radiosonde station, with a distance about 1.0 km. This station is not chosen for water vapor comparison because (1) there is no meteorological sensor at the HKPolyU station and standard meteorological parameters have to be used in the water vapor estimation. Considering the large variation of these parameters, shown in Fig. 7.5, the actual relative humidity, pressure and temperature may differ from the standard parameters significantly. Thus the accuracy of estimated precipitable water vapor is affected; (2) the HKPolyU GPS/Compass station is affected by

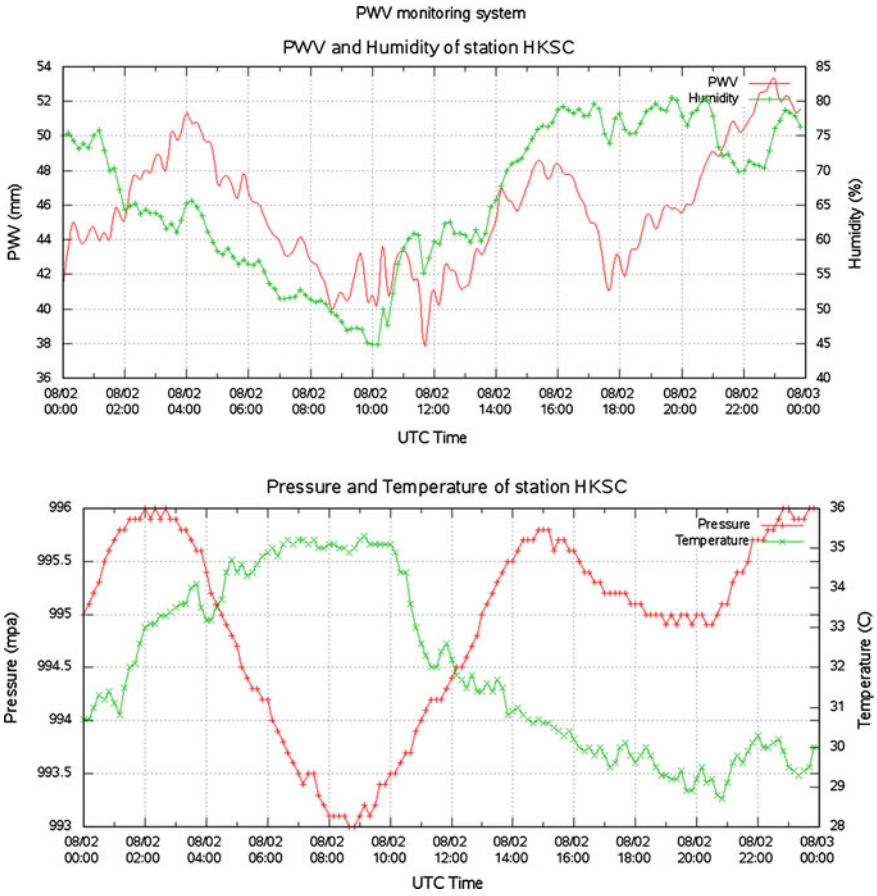

Fig. 7.5 Real-time variation of PWV observed 2 August 2012 at Hong Kong SatRef station HKSC

serious multipath and sometimes signal blockage. This station is installed on a rooftop of one building on the HKPolyU campus. A number of much higher buildings are in the vicinity of GPS installation building. Thus the HKPolyU GPS station is affected by signal blockage and multipath effect of the nearby buildings. It has been noticed that this station tracks less satellites than other Hong Kong SatRef GPS stations. Therefore, the HKPolyU GPS station is not chosen for PWV accuracy evaluation.

Figure 7.6 shows the comparison of PWV data derived from GPS with radiosonde. This comparison was made using 402 days' of GPS and radiosonde data during the period from 1 November 2010 to 7 December 2011. It is shown that the differences between HKSC station and radiosonde are smaller than those between HKST and radiosonde. This can be explained as that the distance between HKSC

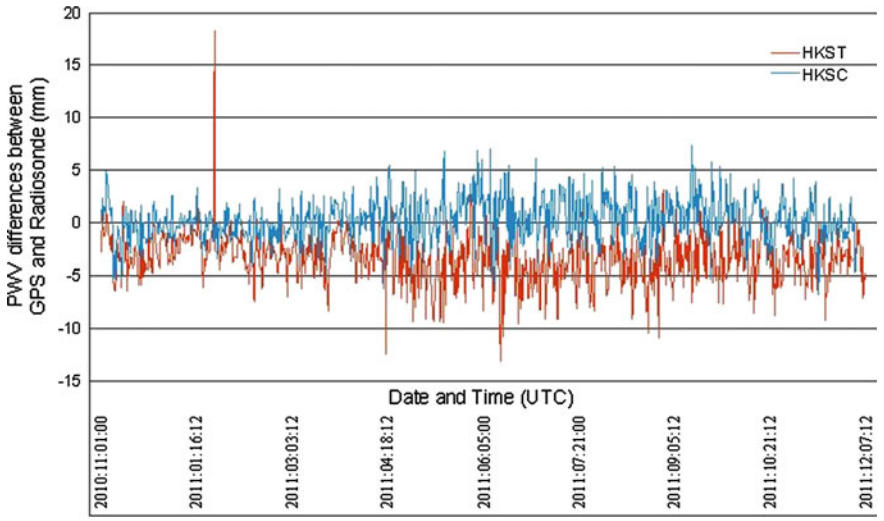

Fig. 7.6 Comparison of precipitable water vapor derived from GPS and radiosonde

Table 7.2 Statistical summary of real-time GPS PWV accuracies for HKSC and HKST stations (mm)

	HKSC (4.1 km from radiosonde)	HKST (9.6 km from radiosonde)
Min.	0.01	−0.01
Max.	7.27	18.3
Mean	0.21	−3.36
Std.	2.19	2.47
RMS	2.20	4.17

and radiosonde is only 4.1 km, much shorter than 9.6 km between HKST and radiosonde station. It is expected that if the GPS station is closer to the radiosonde, their PWV agreement will be even better. Figure 7.6 also implies that the PWV in Hong Kong has a significant variation even over a short spatial distance.

Table 7.2 shows the statistical results of the PWV differences between radiosonde and GPS stations HKSC and HKST. Table 7.2 shows that the systematic biases between the two tracking stations and radiosonde are 0.21 mm and −3.36 mm for HKSC and HKST, respectively. These biases mainly attribute to the spatial separation of the radiosonde and GPS stations. The RMS of the HKSC station is 2.20 mm and the RMS of the HKST station reaches 4.17 mm.

7.10 Conclusion

The first Precipitable Water Vapor Real-Time Monitoring System (PWVRMS) based on GPS Precise Point Positioning (PPP) technique for the Pearl-River-Delta region has been developed. This PWVRMS is developed on the platform of PANDA software package developed at Wuhan University. This PWVRMS system estimates GPS satellite clock error data in real-time while adopting the IGS precise satellite orbit directly. Currently it processes GPS CORS data from three networks in Pearl-River-Delta region (Hong Kong, Macao and Guangdong) every 10 min on a daily basis. The advantage of using PPP technique is that (1) the PWV estimation at each station is completely independent and is not affected by data quality at other stations; (2) the computation is much faster and simpler. This PWVRMS system is evaluated using radiosonde water vapor data. The PWV accuracy is about 2.20 mm though the GPS station is 4.1 km away from the radiosonde. It is expected the actual GPS PWV accuracy should be higher if the GPS station is collocated with the radiosonde station.

The real-time PWV products can be widely used in weather forecasts, water vapor researches, and water vapor correction for remote sensing images such as Synthetic Aperture Radar (SAR) applications. The PWVRMS system provides a significantly large amount of accurate, real-time water vapor data to the governmental meteorological agencies in Pearl-River-Delta region. Currently, several governmental agencies in the Pearl-River-Delta region, including Hong Kong Observatory, Macau Meteorological and Geophysical Bureau, Shenzhen Meteorological Bureau and Guangdong Meteorological Bureau, are using the PWVRMS real-time water vapor data for their weather forecasting service and research.

Acknowledgments This work is supported by the Hong Kong Research Grants Council (RGC) General Research Fund (GRF) project B-Q28F. The first author also thanks the Program of Introducing Talents of Discipline to Universities (Wuhan University, GNSS Research Center), China. The Hong Kong Observatory is appreciated for providing the radiosonde data. The authors would like to acknowledge the Survey and Mapping Office of the Lands Department, Hong Kong Special Administrative Region; Macao Cartography and Cadastre Bureau of Macao Special Administrative Region; and Guangdong GPS network for providing GPS data for this project. We would like to thank the Hong Kong Observatory, Macao Meteorological and Geophysical Bureau, Guangdong Meteorological Bureau and Shenzhen Meteorological Bureau for testing the GPS-derived PWV data in their work. We also thank the IGS for providing GPS real-time observation data streams and predicted orbit data.

References

1. Telford JW, Wagner PB (1980) The dynamical and liquid water structure of the small cumulus as determined from its environment. Pure Appl Geophys 118:935–952
2. Sun D, Yu Y, Zhang T (2009) Tropical water vapor and cloud feedbacks in climate models: a further assessment using coupled simulations. J. Climate 22:1287–1304

3. Zhang W, Xue H, Chen G (2012) The three-dimensional structure of precipitating shallow cumuli. Part two: The effect of precipitation on water vapor distribution. Atmos Res 107:171–177. doi:10.1016/j.atmosres.2012.01.008
4. Warren B, Malloy QGJ, Yee LD, Cocker DR (2009) Secondary organic aerosol formation from cyclohexene ozonolysis in the presence of water vapor and dissolved salts. Atmos Environ 43(10):1789–1795. doi:10.1016/j.atmosenv.2008.12.026
5. Pilinis C, Pandis SN, Seinfeld JH (1995) Sensitivity of direct climate forcing by atmospheric aerosols to aerosol-size and composition. J Geophys Res Atmos 100:18739–18754
6. Eldering A, Cass GR (1996) Source-oriented model for air pollutant effects on visibility. J Geophys Res Atmos 101:19343–19369
7. Schwartz J, Dockery DW, Neas LM (1996) Is daily mortality associated specifically with fine particles? J Air Waste Manag Assoc 46:927–939
8. Idrac P, Bureau I (1927) ExpeÂ riences sur la propagation des sondes radioteÂ leÁ graphique en altitude. Comptes Rendus. Paris Acad Sci 184:691
9. Brettle MJ, Galvin JFP (2003) Back to basics: radiosondes: Part 1–the instrument. Weather 58:336–341
10. Kuo YH, Schreiner WS, Wang J, Rossiter DL, Zhang Y (2005) Comparison of GPS Radio occultation soundings with radiosondes. Geophys Res Lett 32:L05817
11. Wolfe DE, Gutman SI (2000) Developing an operational, surface-based, GPS, water vapor observing system for NOAA: network design and results. J Atmos Oceanic Technol 17:426–440
12. Bokoye AI, Royer A, O'Neill NT, Cliche P, McArthur LJB, Teillet PM, Fedosejevs G, Theriault JM (2003) Multisensor analysis of integrated atmospheric water vapor over Canada and Alaska. J Geophys Res 108(D15): 4480, doi:10.1029/2002JD002721
13. Liu Z, Wong MS, Nichol J, Chan PW (2011) A multi-sensor study of water vapour from radiosonde MODIS and AERONET: a case study of Hong Kong. Int J Climatol. doi:10.1002/joc.3412
14. King MD, Kaufman YJ, Menzel WP, Tanre D (1992) Remote sensing of cloud, aerosol, and water vapor properties from the moderate resolution imaging spectrometer (MODIS). IEEE Trans Geosci Remote Sens 30:1–27
15. Parkinson CL (2003) Aqua: An earth-observing satellite mission to examine water and other climate variables. IEEE Trans Geosci Remote Sens 41:173–183
16. Bevis M, Businger S, Herring T, Rocken C, Anthes R, and Ware R (1992) GPS meteorology–Remote sensing of atmospheric water vapor using the global positioning system. J Geophys Res 97(D14): 15787–15801
17. Duan J, Bevis M, Fang P, Bock Y, Chiswell S, Businger S, Rocken C, Solheim F, van Hove T, Ware R, McClusky S, Herring TA, King RW (1996) GPS meteorology: direct estimation of the absolute value of precipitable water. J Appl Meteorol 35(6):830–838. doi:10.1175/1520-0450
18. Dick G, Gendt G, Reigber C (2001) First experience with near real-time water vapor estimation in a German GPS network. J Atmos Solar Terr Phys 63(12):1295–1304. doi:10.1016/S1364-6826(00)00248-0
19. Perler D, Geiger A, Hurter F (2011) 4D GPS water vapor tomography: new parameterized approaches. J Geodesy 85(8):539–550
20. Ferland R, Piraszewski M (2009) The IGS-combined station coordinates, earth rotation parameters and apparent geocenter. J Geodesy 83(3):385–392
21. Coster A, Niell A, Solheim F, Mendes V, Toor P, Buchmann K, Upham C (1996) Measurements of precipitable water vapor by GPS, radiosondes, and a microwave water vapor radiometer. Inst Navig 1:625–634
22. Rama Varma Raja MK, Gutman SI, Yoe JG, McMillin LM, Zhao J (2008) The validation of AIRS retrievals of integrated precipitable water vapor using measurements from a network of ground based GPS receivers over the contiguous United States. J Atmos Oceanic Technol 25:416–428

23. Nilsson T, Elgered G (2008) Long-term trends in the atmospheric water vapor content estimated from ground-based GPS data. J Geophys Res, 113(D19). doi:10.1029/2008JD010110
24. Yan H, Zhu W, Huang C (2000) The progress of GPS meteorology in Shanghai astronomical observatory. Annals of Shanghai Observatory Academia Sinica, China 21
25. Bi Y, Mao J, Li C (2006) Preliminary results of 4-D water vapor tomography in the troposphere using GPS. Advances in atmospheric sciences No 4
26. Li Z, Xu X, Luo J, Zhu Z (2003) Inversion of the distribution and variation of ZWD over the three gorge area with GPS observation. Geomatics Inf Sci Wuhan Univ 28(4):393–396
27. Rocken C, Ware R, Van Hove T, Solheim F, Alber C, Johnson J, Bevis M, Businger S (1993) Sensing atmospheric water vapor with the global positioning system. Geophys Res Lett 20(23):2631–2634. doi:10.1029/93GL02935
28. Chen J, Wang J, Lu C (2005) Study on comparison between water vapor value calculated by GPS and observed by WVR. J Geodesy Geodyn 259(3)
29. Li Z, Zhang X (2009) New techniques and precise data processing methods of satellite navigation and positioning. Wuhan University Press, Wuhan
30. Boehm J, Niell A, Tregoning P, Schuh H (2006) Global mapping function (GMF): a new empirical mapping function based on numerical weather model data. Geophys Res Lett 33:L07304. doi:10.1029/2005GL025546
31. Saastamoinen J (1972) Contributions to the theory of atmospheric refraction. Bulletin Geodesique 106:279–298
32. Chen Y, Liu Y, Wang X, Li P (2007) GPS real-time estimation of precipitable water vapor–Hong Kong experiences. Acta Geodaetica et Cartographica Sinica (AGCS), 36(1)
33. Zhou W, Yin K, Harrison PJ, Lee JHW (2012) The influence of late summer typhoons and high river discharge on water quality in Hong Kong waters. Estuar Coast Shelf Sci 111:35–47. doi:10.1016/j.ecss.2012.06.004
34. Zhao P, Zhou ZJ, Liu JP (2007) Variability of Tibetan spring snow and its associations with the hemispheric extra-tropical circulation and East Asian summer monsoon rainfall: an observational investigation. J Clim 20:3942–3955
35. Liu J, Ge M (2003) PANDA Software and its preliminary result of positioning and orbit determination. Wuhan Univ J Nat Sci 8(2B):603–609
36. Kačmařík M, Skřivánková P (2011) Comparison of satellite orbit ephemerides for use in GPS meteorology. Adv Space Res 48(2):264–269
37. Weber G, Gebhard H, Dettmering D (2003) Networked transport of RTCM via internet protocol (Ntrip). IAG, Sapporo
38. Zhang S (2009) Studies on the techniques for the remote sensing of water vapor spatial distribution by ground-based GPS and their applications. Wuhan University, Hubei

Chapter 8
Experiments and Analysis of Soil Moisture Monitoring Based on GPS Signal-to-Noise Ratio Observables

Minsi Ao, Jianjun Zhu, Youjian Hu and Yun Zeng

Abstract Effective monitoring of soil moisture is the basis of meteorological, agricultural and environmental scientific researches. Using the SNR observables to monitor the fluctuation of soil moisture is a new approach which does not suffer from destruction of environments, difficult data assimilation, limits of temporal-spatial resolutions and so on. However, it also has many issues need to be discussed deeper such as too less examples, the effective areas, the parameter setting and even how to describe and model the relationship between the SNR results and soil moisture from other measurement ways. In this paper, with measured GPS SNR observables and simulated soil water content data, the comparative experiment is carried out to discuss them. As is shown from the experiment process and results, this approach can effectively retrieve the soil water content. The effective area is within about 45 m around the antenna phase center. The exponential function can be used to described the correlation between the relative delay phase of SNR reflected signal and soil water content well. Meanwhile, selection of the advanced satellites and recording of the L2C observables would be prone to obtain the high quality SNR observables that lead to the more robust and accurate monitoring results.

Keywords Global positioning system · Signal-to-noise ratio · Soil moisture · Multipath reflection

M. Ao (✉) · J. Zhu (✉)
School of Geosciences and Info-Physics, Central South University, Changsha, Hunan, China
e-mail: aominsi@csu.edu.cn

J. Zhu
e-mail: zjj@csu.edu.cn

Y. Hu · Y. Zeng
Faculty of Information and Engineering, China University of Geosciences, Wuhan, Hubei, China

J. Sun et al. (eds.), *China Satellite Navigation Conference (CSNC) 2013 Proceedings*, Lecture Notes in Electrical Engineering 243,
DOI: 10.1007/978-3-642-37398-5_8,

8.1 Introduction

The accurate measurements and long-term monitoring of soil moisture are the basis of meteorological, agricultural and environmental quantitative scientific researches [1]. The traditional approach to monitoring the fluctuation of soil moisture can be divided into two types: active and passive monitoring. The typical active approaches include baking, probes measurement and so on. The later are usually based on remote sensing technologies. The active approaches are intuitive and precise, but also unavoidable to destroy the observed object and environments. At the same time, the results from different networks and types of equipments are difficult to be assimilated, which limits their large-area applications. Due to the limits of temporal and spatial resolution, the passive monitoring of soil moisture is often used in large-area and long-term cases. In fact, using the GPS reflected signals for soil moisture monitoring have been studied for several years. The basic thought of these approaches is to organize a pair of GPS antennas respectively upward and downward, which are used to receive the direct and reflected signal from GPS satellites. With the power differences between the two types of signals, the inversion model is constructed and the soil moisture can be retrieved. Many experiments [2] have been conducted by National Aeronautics and Space Administration (NASA) in test bases which locate in Iowa, Georgia, etc. From experiments conducted by Guan et al. [3] and Yan et al. [4], the correlation between the GPS results and measured soil moisture were also proved. This approach successfully introduced the power characteristics into retrieve the soil moisture, but the high costs limit its applications and popularization.

Larson et al. [5, 6] proposed an approach to retrieve the soil moisture based on the Signal-to-noise ratio observables from conventional geodetic GPS receivers. Bilich and Larson [7] discussed how to separate the direct and multipath reflected signal from SNR observables, and the relationship between the reflected components and environments earlier. Further, Larson demonstrated how to retrieve the soil moisture using the amplitude, frequency and relative delay phase characteristics from the SNR reflected component signals within certain elevation angle interval. In the references [5, 6] and [8], with observations of stations TASH and P484 from International GNSS Service (IGS) and Plate Boundary Observatory (PBO), the possibility that using the amplitudes characteristics to retrieve soil moisture fluctuation was discussed. The test results showed that the correlation does exit, but the accuracy and stability is vulnerable to fluctuation of temperature, pressure or other weather factors. From results from [9] and [10], the relative delay phase characteristics are more stable to retrieve soil water content compared to amplitudes. Because this approach is based on SNR observables which could be easily obtained from the Continuous Operating GPS Reference Station (CORS), it can effectively reduce the costs and extend the applications of CORS. At the same time, it does not suffer from issues as data assimilation between soil moisture networks. However, there are many problems about this approach still have to be considered deeper. More references and experiments are necessary to be proposed

and conducted to demonstrate the validity. Some important features of this approach and parameters during the data process such as effective area, selection of satellites and wavelength, are still need to be investigated. And even how to describe and model the relationships between the relative delay phase and measured soil moisture are still have to be considered. In this paper, with combination of the measured GPS observables and simulated soil moisture data, the problems mentioned above are to be discussed and analyzed.

8.2 Methodology

The signal-to-noise ratio of GPS is one of the most important indicators to describe the quality of signal from satellites. It is mainly decided by the antenna gain pattern, multipath effect and random noises. In order to mitigate the multipath effect, the designs of GPS antenna are principally that the large the elevation angle of satellite is, the more the gain is, otherwise the opposite. Furthermore, because the power of random noises is so small, the multipath effect becomes the primary factor when the elevation angle of satellite is low. According to Larson et al. [9] and Zavorotny et al. [10], the SNR observables can be expressed as,

$$SNR^2 = {A_c}^2 = {A_d}^2 + {A_m}^2 + 2A_dA_m \cos\phi \tag{8.1}$$

In Eq. (8.1), $A_c$is the raw SNR observables, A_d and A_m are respectively the amplitude of direct and multipath reflected signals, ϕ is the relative delay phase between reflected and direct signals. If there is only once reflection case, the relationship between the relative delay phase and elevation angle of satellite can be presented as,

$$\frac{d\phi}{dt} = 4\pi\frac{h}{\lambda}\cos\frac{d\theta}{dt} \tag{8.2}$$

In Eq. (8.2), h is the vertical distance from the antenna phase center to the ground. θ is the elevation angle of satellite, λ is the wavelength of carrier phase. If $x = \sin\theta$, the (8.2) can be simplified as

$$\frac{d\phi}{dx} = 4\pi\frac{h}{\lambda} \tag{8.3}$$

As is shown in Eq. (8.3), the linear correlation does exist between the relative delay phase ϕ and $\sin\theta$. Taking into account the Eq. (8.1), if the elevation angle is low, the SNR reflected signal can be expressed by $\sin\theta$ as,

$$SNR = \dot{A}_m(\dot{f}\sin\theta + \dot{\phi}) \tag{8.4}$$

In Eq. (8.4), $\dot{A}_m$ and $\dot{\phi}$ are respectively the amplitude and delay phase of the multipath reflected signals. $\dot{f}$ is the frequency, which is ideally equal to Eq. (8.3).

Generally speaking, the water in the soil can be supposed to be an equivalent reflection surface because the reflection coefficient of water is much more than soil. When the soil moisture increases, can be deemed as the antenna height from equivalent reflection surface decreases. The decreased antenna height will make the propagation path be shorter which would represents as increasing of $\dot{A}_m$ and decreasing of $\dot{\phi}$. Contrarily, the decreased antenna height will make the propagation path be longer which would represents as decreasing of $\dot{A}_m$ and increasing of $\dot{\phi}$.

There are three steps during the process of SNR observables. The first step is to separate the reflected signals from raw SNR observable series. During the separation, the signal which is caused by the antenna gain pattern can be treated as direct components signal, its amplitude is much larger than the reflected one, namely, $A_d \gg A_m$. Due to the design of antenna mentioned above, the second-order polynomial is introduced for realize the separation. The second step is to resample the reflected signal. The reflected signal from separation represents the relationship between the SNR and time, the resampling step is to achieve the relationship between the reflected signal and sin of satellite elevation angle. The cubic spline interpolation algorithm is used to fitting and sampling in this step. The third step is to calculate the characteristic parameters (amplitude, frequency and relative delay phase) in Eq. (8.4) by fitting in sin style. With the characteristic parameters, the further comparative study according to soil moisture data can be carried out.

In order to discuss the effective area of this approach, the Higgins-Fresnel principle which is usually used in electromagnetic theory is introduced. The effective area is composed by a series of ellipse regions correlated with satellite elevation angle, azimuth and antenna height. Considering that most of the GPS receivers in CORS network do not record when satellite elevation angle is below five or ten degrees, we simulate the effective areas nearly five degrees. The simulated effective areas are shown in Fig. 8.1.

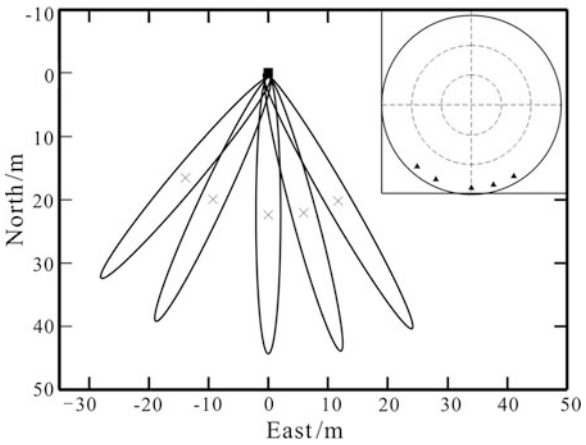

Fig. 8.1 The simulated Fresnel region of soil moisture monitoring using SNR observables. The sub-figure in *upper right corner* is the simulated trajectory of satellites which is nearly five degrees. The five elliptical regions are the reference area according to trajectory, the points centered in elliptical regions are the reflected points on ground. The original coordinate is the simulated GPS antenna phase center

As is shown in Fig. 8.1, the Fresnel region can reach as far as about 45 m. It indicates that the effective area is about 45 m around the antenna phase center on one hand. And on another hand, within this area we should avoid the reflection source and keep the homogenous soil type as much as possible to ensure the stable and precise monitoring.

8.3 Experiments and Analysis

In order to discuss the validity and core parameters selection during the process of SNR observables, comparative experiments based on the measured GPS observations and simulated soil moisture are conducted. The GPS observations are collected by station P041 from PBO, which locates in Boulder in United States. With supports of PBO, P041 started carrying out the research for GPS soil moisture study. It is continuously recording not only the conventional GPS observations but also the meteorological data such as humidity, temperature, precipitation, pressure, wind speed, etc. Meanwhile, it firstly started to record the L2C codes for high quality SNR observables. The simulated soil moisture data are calculated from the Noah_LSM model [11] which is often used to retrieve the earth surface parameters from the meteorological observations above the ground. During the simulation with Noah_LSM model, at least seven meteorological observations have to be collected to retrieve the soil water content. Due to the missing of precipitation records of station P041, the nearby data from NOAA/NWS was introduced for simulation. The short and long wave radiation data were collected from the Global Land Data Assimilation System (GLDAS) [12]. The other meteorological observations such as pressure, humidity, etc., were from the meteorology observation of GPS station P041. Excerpt the precipitation records were interpolated into 30 min interval by summation or average algorithm, the others were interpolated or resampled by cubic spline algorithm. For GPS SNR observations, the session from day of year (doy) 101–220 were selected. Furthermore, we used the SNR observables on L2 carrier phase of satellite PRN12. The elevation angle intervals were set to [7°–30°]. Two-order polynomial was adopted to separate the direct and reflected signals. The Non-linear Least Square Regression Algorithm was used to fit and get the relative delay phase of reflected signal. The relative delay phase, precipitation and simulated soil water content is shown as Fig. 8.2.

It is shown in Fig. 8.2, there are six significant precipitation events respectively on 9 doy 114, 131, 138–139, 171, 187–193, and nearly 208. According to each precipitation event, the soil water content (swc) significantly increases, which indicates that the reasons for fluctuation of swc are mainly the precipitations. Together with the relative delay phase of reflected signal, it is obvious that it changes corresponding to the swc. For example, for event on doy 114, the swc increases from 0.115 to 0.304 (by 0.189), the corresponding negative ϕ increases from -3.569 to -3.304 (by 0.265 rad). For event on doy 131, the swc increases

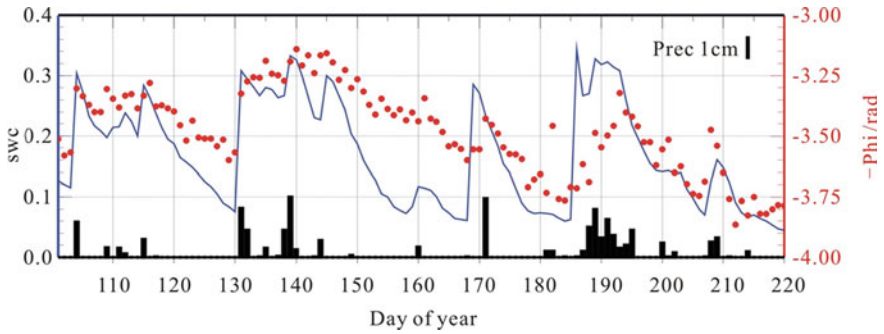

Fig. 8.2 Relationship among the soil water content, precipitation and relative delay phase at P041. The *solid line*, *point* and *bar* are respectively the swc, negative relative delay phase and precipitation. The unit of relative delay phase is rad

from 0.075 to 0.308 (by 0.233), the corresponding negative ϕ increases from -3.57 to -3.324 (by 0.244 rad). For event on doy 138–139, the swc increases from 0.263 to 0.333 (by 0.07), the corresponding negative ϕ increases from -3.249 to -3.191 (by 0.058 rad). Similarly, during the later three precipitation process, the significant correlations can be easily found between the relative delay phase and swc. It is worth noting that during the event on nearly doy 170 and 189 the delay phase does not correlated the swc well. With carefully analysis on the corresponding meteorological records such as temperature, wind states, etc., from GPS station, it may be caused by two reasons. The first reason could be the rapid weather changes which are clearly from the daily GPS meteorological records on these days. Another reason could be that the measurement time inconsistency between the GPS and simulated swc. Apparently, the effective time of GPS results are according to the satellite trajectory, but the simulated swc are according to the whole day. Both of the two reasons may lead to the differences between the relative delay phase and swc on these days. Overall, it is obvious that the relative delay phase of reflected signal changes oppositely with the swc. When the precipitation event comes, the swc arises and the relative delay phase decreases; when the precipitation finishes, the swc decreases and the delay phase arises oppositely. The scatters map of swc and relative delay phase is shown as Fig. 8.3.

The relative delay phase and swc scatters of station P041 are shown in Fig. 8.3. The correlation coefficient of the relative delay phase and swc is 0.6033, which is strongly correlated statistically. It is necessary to note that this correlation coefficient includes the error from measurement time inconsistency (e.g. doy 169–170, 186–192). The real correlation should be stronger. The exponential function used to fitting the scatters is shown in the low right corner of Fig. 8.3. During the fitting of scatters, some of the scatters which corrupted by measurement time inconsistency problem are eliminated. The R^2 index of fitting is 0.6848 which indicates that the correlation between the relative delay phase and swc can be well described with the exponential function.

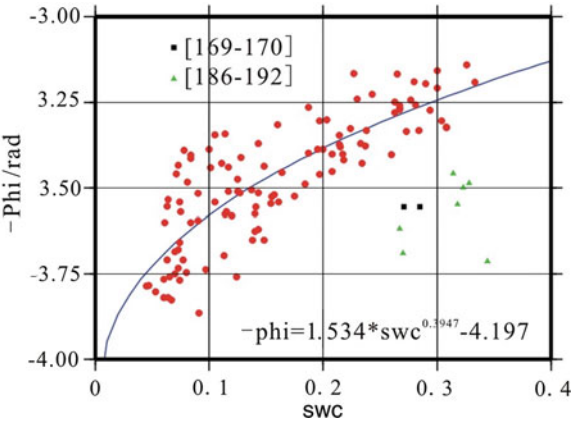

Fig. 8.3 Scatter and fitting relationship between the soil water content and relative delay phase. The *points* represent the normal scatters in session. The *square* and *triangle points* respectively represent the doy 169–170 and 186–192. The fitting result is shown in the low *right corner* in this figure

From the comparison and analysis, besides the measurement time inconsistencies there are still more factors to be noted further. The impact of the quality of SNR observables to monitoring results cannot be neglected. The high quality SNR observable is more likely to separate for reflected signal and fit it with function sin style successfully. From the aspect of GPS receivers, recording the L2C code can effectively improve the quality and amplitude of SNR observables. From the aspect of antennas, whether deploy the choke-ring and radome is also influential to the SNR observables. But their influences can be mitigated through adjustment the elevation angle of satellite. From the aspect of satellites, the SNR signals from advanced satellites (BLOCK IIR M satellites in this case) are more powerful and stable. These types of observables are more close to the SNR description model and lead to more reliable results. In summary, if the L2C is recorded, it is priori to select the advanced satellite and SNR observables on L2 wavelength; else, the observable from advanced satellites on L1 wavelength is the better choice. Despites the quality of observables, it is interesting that as if the decreasing speed of the negative relative delay phase is slower than the swc, for example, the doy 116–103, 140–168. Considering the fact that the deeper below earth surface, the slower the water evaporates, whether a more effective depth of soil layer exists is worth the further attentions.

8.4 Conclusions

Soil moisture and its fluctuation is one of the most important indicators to measure the water cycle statues. Its accurate measurement and long-term monitoring plays the significant role for meteorological, agricultural and environmental scientific research. With the introduction of methodology and principle of retrieval soil moisture based on GPS SNR observables, the effective area is discussed in this paper. Through the comparative experiments based on measured GPS observations

and simulated soil moisture, the validity and selection of parameters during the data process is discussed and analyzed. The process and results from experiments show that this approach can effectively retrieve the soil moisture and its fluctuation. The correlation between the relative delay phase and swc can be described and modelled by exponential function well. Meanwhile, selection of the advanced satellites and recording the L2C code is prone to obtain the high quality observables and reliable monitoring results. With combination of different types and depth of soil moisture data, introduction of more meteorological observations, and even applications of this approach into other fields (such as ice depth, tide gauge, etc.) are the future work need to be paid more attentions.

Acknowledgments This work is funded by open project of Engineer Research Center for GIS Software & Application (No. 20111110) and National Science Foundation of China (No. 41204001). Thanks for the advices during the data process from Professor K. M. Larson, University of Colorado and Doctor Xubo Gao, China University of Geosciences.

References

1. Liu J, Shao L, Zhang X et al (2007) Advanced in GNSS-R studies and key technology. Geomat Inf Wuhan Univ 32:955–960
2. Masters D, Katzberg S, Axelrad P et al (2003) Airbone GPS bistatic radar soil moisture measurements during SMEX02. Proc Int IEEE Geosci Remote Sens Symp 2:896–898
3. Guan Z, Zhao K, Song D et al (2006) Measuring soil moisture using reflected GPS signals. Adv Earth Sci 21:747–750
4. Yan S, Gong J, Zhang X et al (2011) Ground based GNSS-R observations for soil moisture. Chinese J Geophys 54:2735–2744
5. Larson K, Small E, Gutmann E et al (2008) Using existing GPS receivers as a soil moisture network for water cycle studies. Geophy Res Lett 35:L24405
6. Larson K, Small E, Gutmann E et al (2008) Using GPS multipath to measure soil moisture fluctuations: initial results. GPS Solut 12:173–177
7. Bilich A, Larson K (2007) Mapping the GPS multipath environment using the signal to noise ratio (SNR). Radio Sci 42:(6)
8. Ao M, Hu Y, Liu Y et al (2011) Inversion of soil moisture fluctuation based on signal-to-noise ratio of global positioning system. J Geomat Sci Tech 29:66–69
9. Larson K, Braun J, Small E et al (2010) GPS multipath and its relation to near-surface soil moisture content. IEEE J Sel Top Appl Earth Obs Remote Sens 3:91–99
10. Zavorotny V, Larson K, Braun J et al (2010) A physical model for GPS multipath caused by land reflections: toward bare soil moisture retrievals. IEEE J Sel Top Appl Earth Obs Remote Sens 3:100–110
11. Chen F, Dudhia J (2001) Coupling an advanced land-surface/hydrology model with the Penn State/NCAR MM5 modelling system Part I: model implementation and sensitivity. Mon Wea Rev 129:569–585
12. Rodell M, House P, Jambor U et al (2004) The global land data assimilation system. Bull Am Meteor Soc 85:381–394

Chapter 9
The Design and Implementation of GNSS Data Services Based on SOA

Zheng-sheng Chen, Zhi-ping Lu, Yang Cui and Yu-pu Wang

Abstract The development of network software technology makes data services towards the directions of diversification, real-time, integration and individuation etc. Currently, most GNSS data service centers use file-based data method to distribute, share and transfer data, which is good for storage but not good for data sharing and data using. It is not the direct data waned by GNSS software. The software based on Service Oriented Architecture (SOA) interact with each other by interface, which is independent from hardware platforms, operating systems and programming languages, achieved low coupling sharing of data and functions (services) of the different applications on the network. If the basic GNSS data service center is using SOA architecture to achieve GNSS data and functional services, the current GNSS applications will be greatly expanded. This paper design and briefly achieve the GNSS data services based on SOA architecture, and implement the application of data and functions sharing between different network applications. Practice has proved that the GNSS data services based on SOA conducive to the integration of multi-program, realization of personalized program, and its real-time ability is much better.

Keywords SOA · GNSS · IGS · Service · Data sharing · Function integration

1. National Science Foundation of China "Research on the distributed computing technology of large-scale survey adjustment" (41274015).
2. National 863 Project of China "Critical technology for maintaining the global dynamic geocentric reference frame"(2013AA122501).

Z. Chen (✉) · Z. Lu · Y. Cui · Y. Wang
Institute of Surveying and Mapping, Information Engineering
University, Zhengzhou 450052, China
e-mail: czsgeo@126.com

J. Sun et al. (eds.), *China Satellite Navigation Conference (CSNC) 2013 Proceedings*, Lecture Notes in Electrical Engineering 243,
DOI: 10.1007/978-3-642-37398-5_9, © Springer-Verlag Berlin Heidelberg 2013

9.1 Introductions

As the development of GNSS and networks, the precision and stability of GNSS navigation and positioning are growing better, and the applications based on GNSS are spreading everywhere, popularly and in large scale. Meanwhile, the users of GNSS are requiring a more precise, real-time and individual service [1–4]. The International GNSS Service (IGS) is an authoritative institute in providing precise positioning data service, which include observing data of tacking station or reference station, high level ephemeris data, clock offset, earth rotation parameters, ionosphere and troposphere data, etc., and uses ftp to release its products. In addition, many countries or regions built local area augmentation system, to provide difference of signal and other data service of GNSS. However, these data is mainly for professional users or terminals. It is too difficult for ordinary people and developers in other field to understand. They have to face many complicated algorithm before use it. What's more, all the users wanted are just a service, not the semi-finished GNSS data. Take ephemeris data for example, the navigation satellite provides orbital elements data, and the IGS ftp provides discrete orbit position, but the all the user wanted is just the position of satellite in a specified moment, which is a service, not a static data file. Service-Oriented Architecture (SOA) is a set of principles and methodologies for designing and developing software in the form of interoperable services [5]. It encapsulates user's requirements as services. Both the service provider and user have are only the opening service operation list and its parameter structure. The following discusses how to design and implement GNSS data service based on SOA technology.

9.2 GNSS Data Service

In the navigation and positioning of GNSS, the navigation data of satellite and observation data of receiver include kinds of errors, thus cannot meet the needs of high precise applications. In order to improve the accuracy of navigation and positioning, we must correct the errors of these data using interrelated correct models [6, 7], which include ephemeris of navigation data, clock offset, earth rotation parameters, ionosphere data, troposphere data and tide data, etc. Some organization and institute, like IGS, local CORS, provide these data for precise navigation and positioning. They do a lot to improve the precision of navigation and positioning, such as the implement and improvement of ITRF, solid Earth deformation detection, detection of Earth rotation, orbit determination, and so on. But for a non-professional user, these applications are too professional. The GNSS data offered by IGS is not the data they want, and the IGS cannot satisfy these users' needs by using ftp, because user' demands are always variable, and data in ftp server are always static; data in RTK are pushed, not wanted. These dynastic demands are services, which users really want.

9.3 Service-Oriented Architecture

The service-oriented architecture (SOA) is a component model and architectural style of software, which try to make full use of Internet technology, to meet the growing demand for business operations mode. SOA uses the concept of "service" for the same viewpoint to organize computing resources [8], which is a flexible, secure and seamless way to deal with the inner and outer resources [9] SOA have two significant characteristics: loosely coupled and indirect addressing. It link different functional units of the application (services) with well-defined interfaces and contracts. Interface is defined in a neutral manner; it should be independent of the services of hardware platforms, operating systems and programming languages. This makes the service, built in a variety of different systems, have a unified and common way to interact. Services in SOA is the core of the abstract means, it includes two parts: service interface and service implementation. Service interface is a collection of methods and the desired operation of the service requester, which describes the contract between the requester and the service that both of them must follow; service implementation is the encapsulation of specific functions and data. Separation of the service interface and implementation makes SOA loosely coupled.

The three basic elements of the SOA is service description, service discovery, and service calls, as shown in Fig. 9.1. Also SOA has three roles: service provider, service registry center and service requestor. Service providers are responsible for service implementation, and publish the interface, access address of service description to the service registry. The service requester consuming services is a process of indirect addressing. Firstly they find the description of the related services from the service registry, and then use the information provided by the service description to call services. In addition, the service requester does not have to be through the registration center to lookup service. In a closer environment, for example, can be directly obtained it from the service provider. Due to SOA has broad application prospects, some IT leader such as IBM, Microsoft, Gartner has proposed its own solution [10–12]. The following article is to introduce how to design and implementation the GNSS data service system based on the SOA model.

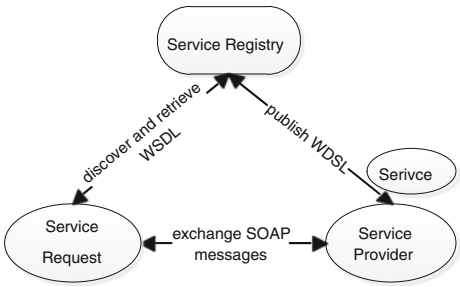

Fig. 9.1 SOA model

9.4 Design of Architecture and Interfaces of GNSS Data Service

The general idea of design GNSS data service system is to capsulate the GNSS data and its algorithm into different services, such as clock service and ephemeris service. According to user's request, the GNSS data service system response the calculation result. To accomplish this task and get a better result, the server has to connect to other online GNSS data server, usually the IGS ftp, to integration GNSS resources, as shown in Fig. 9.2.

The whole progress is transparent to users, and users cannot see what the server does, they get they want is just like to retrieve data in local database. As the following picture shows, this procedure is very simple; the server receives the user's requirement, which include with service to be called, and the service parameters with values. The server parses the parameters and return calculation result. Unlike ftp technology, this is an interactive process. Users can get they want. And with SOA, low coupling makes the progress much convenient, as shown in Fig. 9.3.

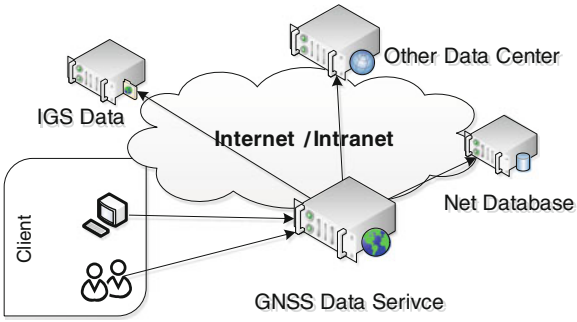

Fig. 9.2 The relationship between systems

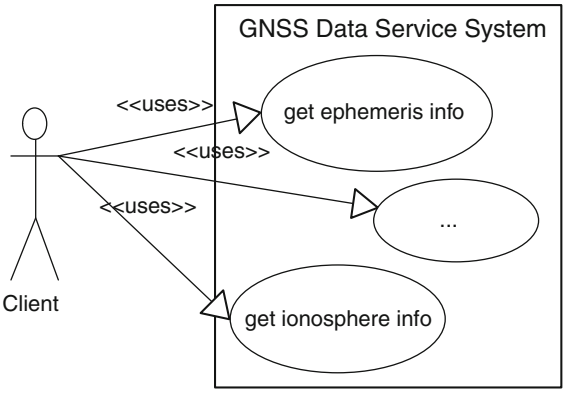

Fig. 9.3 Use case of system

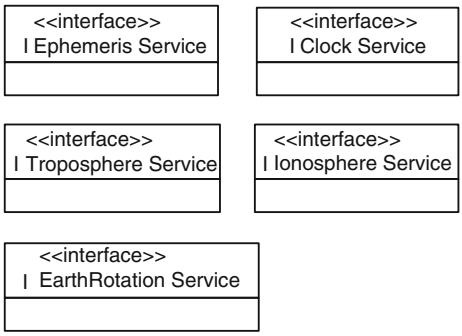

Fig. 9.4 The design of interfaces

In order to facilitate the description, we design the GNSS data service interface with Unified Modeling Language (UML), as shown in Fig. 9.4, which include five service contracts: IEphemerisService, IClockSrevice, ITroposphereService, IIonosphereService and IEarthRotaionService.

9.5 Implementation

We build this system with Visual Studio 2012 as development environment, C# as develop language, IIS 7.0 as web container, SQL Server 2008 as database and Windows Communication Foundation (WCF) to implement SOA. The whole system is divided into two layers: application layer and data layer. According the system design, we implement the interfaces in the application layer with several algorithm and models of GNSS data; the data layer composed with GNSS files and database, which can monitor the change of IGS ftp server, and fetch new IGS products.

Finally, the GNSS service system installs and runs on IIS 7.0 web container. To input its web site address in the browser, we can get the WSDL. The following is a WSDL file of ephemeris service (Fig. 9.5).

WSDL is expressed with XML which is platform-independent, and it describes how to communicate with and use the web services, which is usually parsed by tools automatically.

9.6 Cases

After the service broadcasted, users can call the service according to the WSDL. Because Web service exchanges information with XML, users can get the service in any platform, no matter in mobile phone or notebook computer, whether in

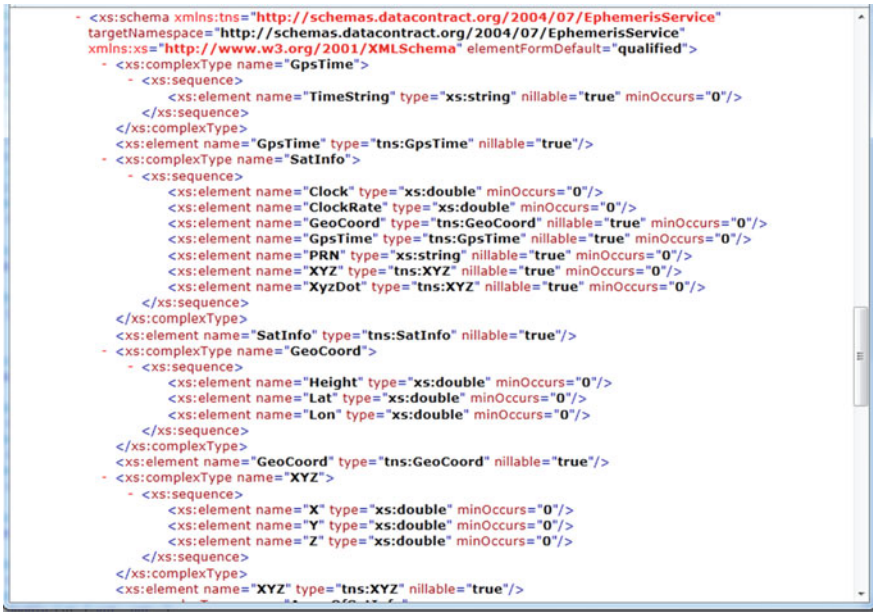

Fig. 9.5 Part of WSDL

Windows operating system or in Unix operating system, as long as the client software follows the standard of Web service.

Figure 9.6 shows in other web program call the GNSS Service. User input the PRN of navigation satellite and the specified GPS time, click request button, after several seconds, the answer is show on the page.

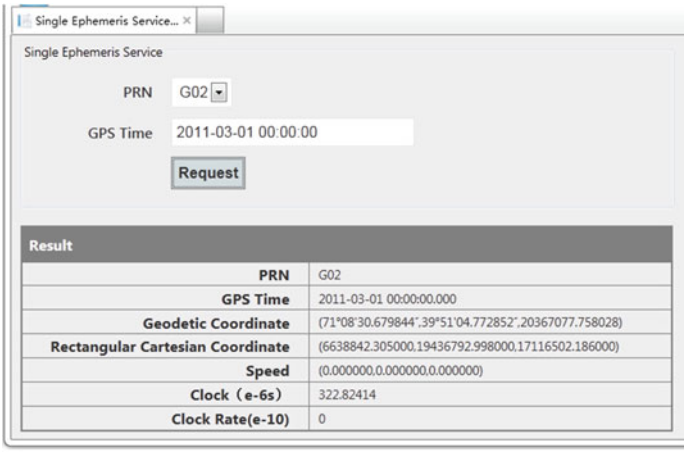

Fig. 9.6 Single ephemeris service

All the process is transparent to users. Users can use the service to build higher GNSS application, while do not worry how to realize the complicated algorithm. The GNSS data service based on SOA focus on service itself, thus can fulfill the user's versatile demands, and increase the degree of automation and timeliness.

9.7 Conclusions

With the development of network infrastructure and network technology, applications based on the network will be more extensive and in-depth. More complicated applications will build on low coupling services. SOA is the fruits of software development, and is being succeed used in many fields, and surely will contribute to GNSS application.

References

1. Xu C, Shi J, Guo J, Xu X (2011) Analysis of combining ground-based GPS network and space-based COSMIC occultation observation for precipitable water vapor application. Geomatics Inf Sci Wuhan Univ 36(4):467–470 (Ch)
2. Xu X-C, Xu A-G, Su L-J (2011) Design and implementation of terminal location LBS system. Sci Survey Mapp 36(3):193–194,189 (Ch)
3. Li S, Wu W (2012) Application of GPS in establishing control network of high-speed railway. J Liaoning Tech Univ (Natural Science Edition) (5):783–785 (Ch)
4. Zhang X-H, Li X-X, Guo F, Li P, Wang L (2010) Server-based real-time precise point positioning and its application. Chin J Geophy 53(6):1308–1314 (Ch)
5. Cibraro P, Claeys K, Cozzolino F, Grabner J (2010) Professional WCF 4: windows communication foundation with NET 4. Wiley, London
6. Ji C-D, Li H, Xu A-G, Feng L (2012) Research of single-station GPS positioning error correction mode. Sci Survey Mapp 37(3):56–58, 107 (Ch)
7. Luo F, Dai W, Tang C (2012) EMD-ICA with reference signal method and its application in GPS multipath. Acta Geodaetica et Cartographica Sinica 41(3):366–371 (Ch)
8. Zhao H-Q, Sun J (2010) A methodological study of evaluating the dependability of SOA software system. Chin J Comput 33(11):2202–2210 (Ch)
9. Seemueller WH, Kaniuth K, Drewes H (2001) Horizontal and vertical movements of the IGS regional reference network for South America. IAG 2001 Scientific Assembly, pp 14–15
10. Sprott D, Wilkes L (2004) Understanding service oriented architecture, CBDI. http://www.microsoft.com/china/MSDN/library/architecture/, Jan 2004
11. Microsoft Whitepaper (2007) Enabling real world SOA through the microsoft platform. http://msdn2.microsoft.com/en-us/architecture/aa948857.aspx, Sep 2007
12. Natis YV (2003) Service-oriented architecture scenario. Gartner Group. http://www.gartner.com/resources/114300/114358/114358.pdf, Jun 2003

Chapter 10
Research on Inverse RTD Positioning Algorithm and System Implementation

Mengqi Wu, Jiming Guo, Lili Shen and Xu Ding

Abstract Due to high cost and difficult to achieve real-time monitoring of receivers with the existing RTD technology, this paper proposes the inverse real-time pseudo-range differential technology (IRTD) based on CORS, which adds data center server between receiver and CORS system, transferring differential calculating from receiver to data center server. Data center server receives raw pseudo-range sent back by the receiver and RTCM data broadcast by CORS system, gets positioning result through parallel algorithms and returns location information to the receiver for displaying. Experiments show that without increasing data traffic, IRTD can solve the work area control problem, maintain secrecy of local coordinate parameters, realize real-time monitoring of multi-terminal, which can hardly be solved by the traditional RTD technology. And with a better accuracy, IRTD has a wide application prospect in rapidly obtaining and updating urban spatial information.

Keywords IRTD · CORS · Data center server

10.1 Introduction

Real-time differential technology (RTD) can provide positioning result with sub-meter accuracy and is widely used in urban land inspections, traffic supervision, underwater topographic survey and other industries [3]. But this technology cannot send back location information to the data center server, monitor the working condition of the rover station, and is difficult to realize data sharing. With the increasing maturity of China's urban construction, quick access of geographic

M. Wu (✉) · J. Guo · L. Shen · X. Ding
School of Geodesy and Geomatics, Wuhan University, Luoyu Road 129,
Wuhan 430079 Hubei, People's Republic of China
e-mail: 845776955@qq.com

J. Sun et al. (eds.), *China Satellite Navigation Conference (CSNC) 2013 Proceedings*, Lecture Notes in Electrical Engineering 243,
DOI: 10.1007/978-3-642-37398-5_10,

information, real-time monitoring and information sharing is becoming more and more important. The inverse RTD technology proposed in this paper transferred the differential calculating from receiver to data center server, which can monitor the location of the rover station, realize data collection and data processing simultaneously and improve the production efficiency.

10.2 Introduction to Inverse RTD Technology

For the traditional RTD technology, differential calculation is directly on the rover station. So each rover station work independently and positioning result is displayed only in the rover station. The core idea of inverse RTD technology is to add data center server between receiver and CORS system, transferring differential calculating from receiver to data center server. With powerful computing capability, data center can obtain more accurate and reliable positioning results. Since all the rover stations' positioning results are processed in the data center, the rover station's operation area can be easily controlled. With parallel algorithms, data center can simultaneously handle a couple of rover stations. And if local coordinate parameters are saved on the data center, rover station can obtain local coordinate directly. Since IRTD can solve many difficulties which stumped traditional RTD technology, the technology has a practical application in urban mapping, traffic management, planning, supervision and etc. Meanwhile, IRTD is easy to implement, does not need to upgrade the hardware of data collection terminal and can be applied both to single base station RTD and the network RTD.

10.3 Data Processing Flow

After connecting to the data center, rover station sends NMEA data (which includes coordinates information) and raw pseudo-range to data center, data center forward NMEA data to CORS center and then receives RTCM data (which includes atmospheric delay, satellite clock error and etc.) fed back by CORS. After correcting pseudo-range with the corresponding RTCM data and combining the ultra rapid ephemeris downloaded from the internet, we can easily get the coordinates of rover stations. Figure 10.1 exhibits the flow of data processing in the data center.

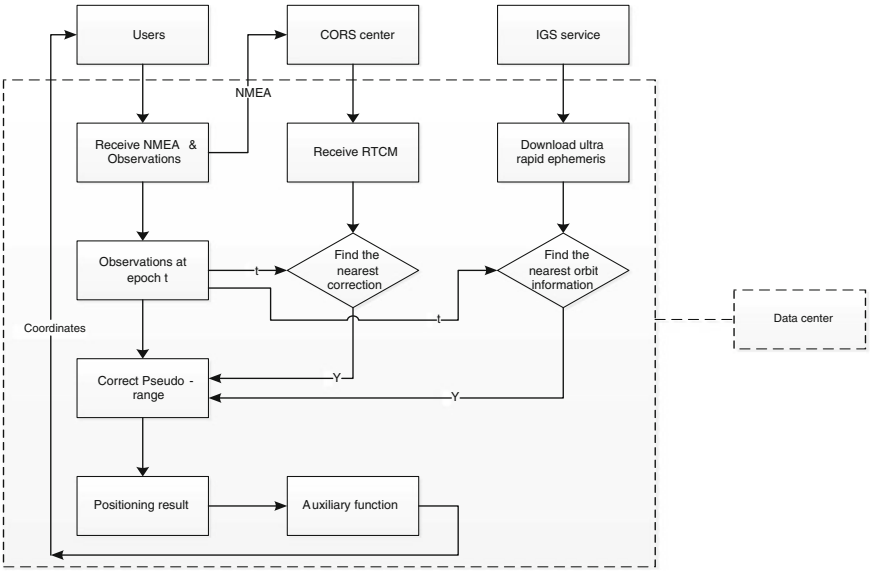

Fig. 10.1 Data flow in the data center

10.4 Key Technologies in the Algorithm

10.4.1 Decode RTCM2.3

The protocol of RTCM SC-104 is a kind of DGPS message developed by the special committees of Section 104 (SC-104) of the Maritime Radio Technical Commission (RTCM), which Include differential correction information. With the method of Byte scan, Byte scroll, Byte get complement, Message synchronization and Parity implementation [1], this paper decode type 1 message of RTCM2.3 and extract pseudo-range corrections and range rate corrections for all the available satellites.

10.4.2 Algorithm Design

The algorithm of the IRTD is similar with the traditional RTD. After single point positioning calculation with the corrected pseudo-range observations, we can get rover stations' location information. The specific process is as follows:

1. The interval of Z count in RTCM message is 0.6 s, generally not the same with GPS time of the receiver. After finding the nearest pseudo-range corrections

and range rate corrections, combining with the extrapolation method, we can get the pseudo-range correction for the current epoch. The formula is as follows:

$$PRC(t) = PRC(t_0) + RRC \cdot [t - t_0] \tag{10.1}$$

where PRC(t_0) is the pseudo-range correction, RRC is the range rate correction, and t_0 is the modified Z-count [2]. These parameters are all associated with the satellite.

2. The pseudo-range measured by the user, PRM(t), is then corrected as follows:

$$PR(t) = PRM(t) + PRC(t) \tag{10.2}$$

3. The corrected pseudo-range simplifies the observation equation significantly. Combined with ultra rapid ephemeris, we can get the rover station's coordinates.

The original observation equation is:

$$\begin{aligned} \mathrm{R}_{\mathrm{A}}^{\mathrm{j}} = \rho_{\mathrm{A}}^{\mathrm{j}} + \mathrm{c}\delta_{\mathrm{t}}^{\mathrm{j}} - c\delta_{t_A} + \delta\rho_{\mathrm{A,ion}}^{j} \\ + \delta\rho_{\mathrm{A,trop}}^{\mathrm{j}} + \delta\rho_{other} \end{aligned} \tag{10.3}$$

Since the pseudo-range correction contains ionospheric delay, tropospheric delay, satellite clock error, the corrected observation equation is:

$$\mathrm{R}_{\mathrm{A}}^{\mathrm{j}} + \mathrm{PRC(t)} = \rho_{\mathrm{A}}^{\mathrm{j}} - c\delta_{t_A} \tag{10.4}$$

10.5 Analysis of Experimental Data

Connecting data center with three rover stations for experiment. With parallel algorithms, data center can handle these rover stations and obtain positions simultaneously. Then rover stations can be monitored easily. And if local coordinate parameters are saved on the data center, rover station can obtain local coordinate directly. Then local coordinate parameters can achieve confidentiality. And since data center records the rover stations' coordinates, the operating area of different authorized users can be effectively controlled. Once exceed the operating area, data center immediately stop its provision of services for the illegal user.

Theoretically, when 12 satellites are visible each epoch, with traditional RTD technology, rover station receives 110 bytes RTCM data per second at least, while with IRTD technology, rover station sends 118 bytes pseudo-range observations per second to the data center. Experiment shows that after an hour, RTD consume

566 KB data traffic while IRTD consume 484 KB data traffic, which fully illustrates that IRTD doesnot increase data traffic.

Settle the rover station in a good environment to collect data with the interval of 1 s. The rover station sends NMEA data and raw pseudo-range to the data center in real time and records raw observations and the positioning results returned by the data center simultaneously. Afterward, combine the raw pseudo-range of the rover station and CORS reference station to solve baseline to get the high precision coordinates of the rover. Project the coordinates to Gaussian plane and make analysis of residuals, we can obtain Figs. 10.2, 10.3, 10.4, 10.5. And the accuracy comparison of RTD and IRTD is exhibited in Table 10.1.

Compared with traditional RTD technology, IRTD technology applies precise ephemeris and transfers differential calculating from receiver to data center, while core algorithms and calculation process is basically the same. As can be seen from the data in Table 10.1, the plan coordinates accuracy of IRTD is slightly better than the traditional RTD technology, both can achieve sub-meter.

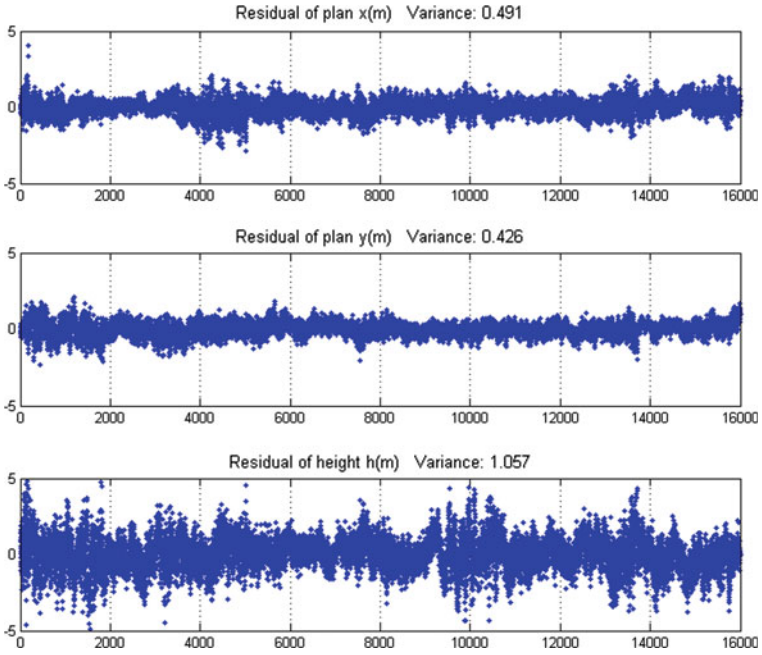

Fig. 10.2 Residuals charts of RTD (the first experiment)

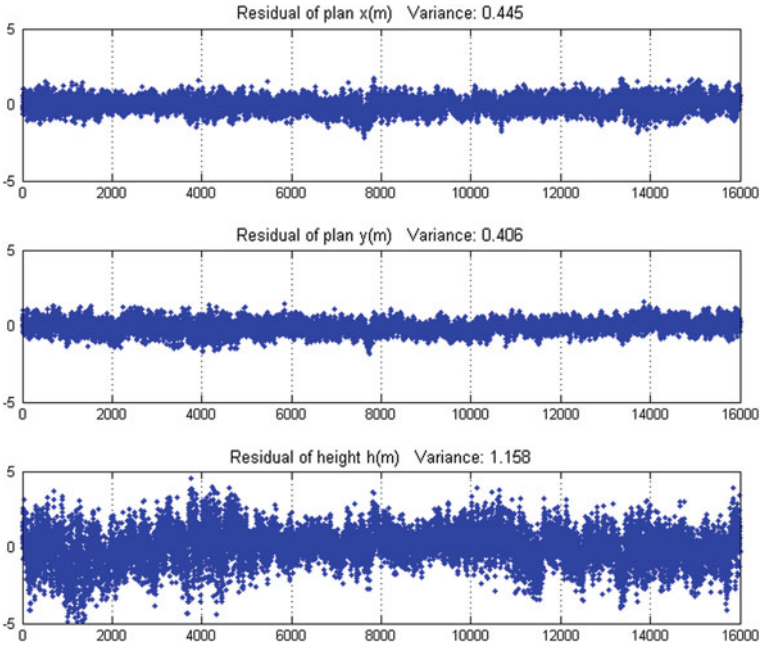

Fig. 10.3 Residuals charts of IRTD (the first experiment)

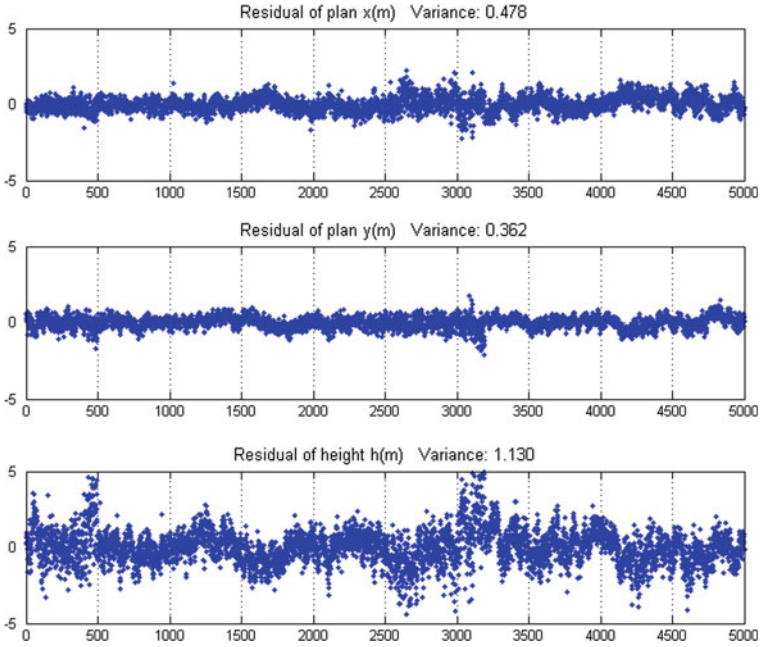

Fig. 10.4 Residuals charts of RTD (the second experiment)

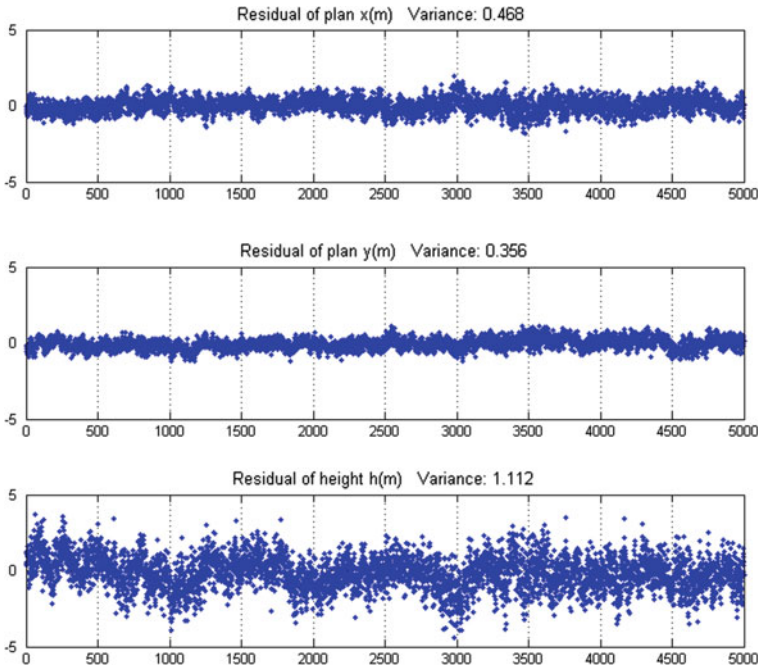

Fig. 10.5 Residuals charts of IRTD (the second experiment)

Table 10.1 Residuals tables

Experiment	RTD			IRTD		
	Var(x)	Var(y)	Var(h)	Var(x)	Var(y)	Var(h)
1	0.491	0.426	1.057	0.445	0.406	1.158
2	0.478	0.362	1.130	0.468	0.356	1.112

10.6 Conclusion

Inverse RTD technology transfer differential calculation from rover station to data center, which make it possible to monitor the working condition of rover station and realize data collection and data processing simultaneously. Experimental data show that positioning accuracy of IRTD can achieve sub-meter, which is slightly better than traditional RTD and has a broad application prospects in urban mapping, traffic management.

References

1. Li S, Ye T, Xu J (2008) Introduction and decoding arithmetic & realization of RTCM data format of DGPS. Electron Measur Technol 32(12):11–14
2. Special Committee 104. RTCM Recommended standards for differential GNSS (Global Navigation Satellite Systems) service. Radio technical commission for maritime services, 2004
3. Zhou J, Zhang Y, Zhang H (2008) Algorithms for differential GPS positioning with Code pseudo-range. Sci Technol Eng 8(4):1034–1037

Chapter 11
Real-Time Regional Ionospheric Total Electron Content Modeling Using Spherical Harmonic Function

Shoujian Zhang, Xin Chang and Wei Zhang

Abstract The Ionospheric Total Electron Content (TEC) model is very important for navigation, precise positioning and some other applications. In recent years, with the fast development of the local Continuously Operating Reference Stations (CORS) in China, determining precise local Ionospheric TEC model is very attractive for local precise positioning. Ionosphere delay is one of the most error sources. At present, the establishment of large-scale CORS system in china provided the conditions for establish real-time regional Ionospheric model using spherical harmonic function. In this paper, we will model the ionospheric TEC using the GPS geometry-free combination observable with the low order spherical harmonic function, meanwhile, the DCBs will also be solved with the Vertical TEC (VTEC). In the experiment, about 20 IGS stations from Europe are chosen to simulate a CORS network, a set of ionosphere coefficients is assumed every 2 h. By comparisons with the IGS Analysis Centre's model, it shows that the mean difference of the DCBs is less than 0.35 ns with the RMS about 0.2 ns, and the difference of the VTEC is less than 3 TECU.

Keywords CORS · Ionosphere · Regional · Modeling · TEC · DCB

11.1 Introduction

Ionosphere total electron content (TEC) and its change are not only the important materials of the morphological study of the ionosphere but also the important parameters of the ionosphere corrections for precise positioning, navigation and radio science. After the revoking of SA policy, ionospheric delay has become the

S. Zhang (✉) · X. Chang · W. Zhang
School of Geodesy and Geomatics, Wuhan University, Wuhan, China
e-mail: shjzhang@sgg.whu.edu.cn

J. Sun et al. (eds.), *China Satellite Navigation Conference (CSNC) 2013 Proceedings*, Lecture Notes in Electrical Engineering 243,
DOI: 10.1007/978-3-642-37398-5_11,

largest error source for positioning and navigation. In precision positioning, the precise estimation of ionosphere not only helps to improve the quality of GNSS observation, but also exerts significant meaning in the research of atmosphere and earth observation [1, 2]. In the recent ten years, International GNSS Service has adopted the formatted file of IONEX proposed by Schaer [3], and has launch some ionosphere products like the global ionosphere map (GIM), the hardware delay of GPS etc. An intensive study on building the model of ionosphere delay through the GPS observation data has been made by Zhang Xiaohong et al. [4]. Some experts, including Yuan [5] and Jikun Ou, have put forward the law about the delay of ionosphere and the variation of electron density based on the GPS. Zhang [6] has made a comparison between different ionosphere models.

The Continuously Operating Reference Station (CORS) can provide not only the real-time precise positioning results, but also the atmosphere and ionosphere information of the coverage area. The high precision real-time ionosphere model, based on the regional CORS network, has important implications for improving the positioning results of the single-frequency receivers, network RTK and other precise positioning. This paper advances the regional model using the fourth-order spherical harmonics. The estimation of the total electron content (TEC) was seriously affected by the DCBs, when conducting the ionosphere modelling in the use of combination observations. At present only part of the IGS tracking station DCBs products of the global model can be taken into account, so the P1 to P2 DCBs can be accurately estimated in the this paper. Considering the DCBs do not change within a day, the authors can separate the VTEC and establish the real-time regional spherical harmonic model. After comparison and analysis, the estimates

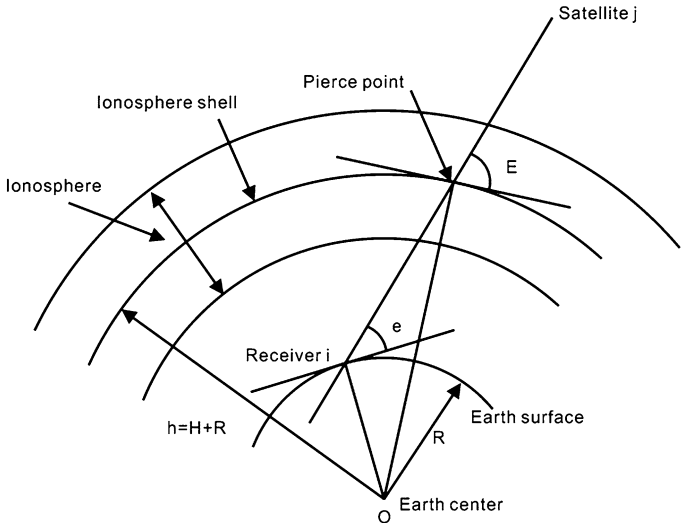

Fig. 11.1 Ionosphere shell

from this paper show good agreement with the IGS Analysis Centres with a mean difference of less than 0.35 ns and an RMS of less than 0.2 ns, a VTEC of less than 3 TECU, and it can much more perfectly reflect the TEC distribution in regional area.

11.2 GPS Ionosphere Measurements

Ionosphere is a region which is composed of ionized plasma and extends from roughly 50 to 2,000 km above the surface of the earth. Generally, the ionosphere can be divided into several layers according to electron density, which reaches its peak value at about 350 km in altitude. For 2D ionosphere modeling, ionosphere shell model is usually applied, as shown in Fig. 11.1 [7]. The ionosphere is assumed to be concentrated on a spherical shell of infinitesimal thickness located at the altitude of H above the earth's surface which is described by total electron content (TEC). TEC is a total number of free electrons in a cylinder with a bottom area of 1 m^2, which is usually represented by TECU (1TECU = 10^{16} Ne/m^2).

A dual-frequency GPS receiver has both code and carrier phase observations on L_1 (1,575.42 MHz) and L_2 (1,227.60 MHz) frequencies. Mathematically the corresponding observations can be described as [8]

$$P^i_{k,j} = \rho^i_{0,j} + d^i_{ion,k,j} + d^i_{trop,j} + c(\tau^i - \tau_j) + d^i_k + d_{k,j} + \varepsilon^i_{P,k,j} \tag{11.1}$$

$$\begin{aligned} L^i_{k,j} =& \rho^i_{0,j} + d^i_{ion,k,j} + d^i_{trop,j} + c(\tau^i - \tau_j) - \lambda\left(b^i_{k,j} + N^i_{k,j}\right) \\ &+ \varepsilon^i_{L,k,j} \end{aligned} \tag{11.2}$$

where P is the pseudorange observation, L is the carrier phase observation, ρ is the true geometric range between receiver and satellite (m), d_{ion} is the ionosphere delay (m), d_{trop} is the troposphere delay (m), c is the speed of light (m/s), τ^i is the satellite clock error with respect to GPS time (s), τ_j is the receiver clock error with respect to GPS time (s), d is the code delays for satellite and receiver instrument bias (m), b is the phase advance of the satellite and receiver instrument bias, N is the ambiguity of the carrier phase, ε is the residual in the GPS measurements, the subscript k (= 1, 2) stands for the frequency, the superscript i stands for the sequence number of the GPS satellite, and the subscript j stands for the sequence number of the GPS receiver.

Through difference with dual-frequency observations, the ionosphere delays can be obtained through the following equations:

$$P_4 = P^i_{1,j} - P^i_{2,j} = \left(d^i_{ion,1,j} - d^i_{ion,2,j}\right) + DCB^i + DCB_j \tag{11.3}$$

$$\begin{aligned} L_4 &= L^i_{1,j} - L^i_{2,j} \\ &= -(d^i_{ion,\,1,j} - d^i_{ion,\,2,j}) - \lambda(b^i_{1,j} - b^i_{2,j}) - \lambda(N^i_{1,j} - N^i_{2,j}) \end{aligned} \tag{11.4}$$

where $DCB^i = d^i_1 - d^i_2$, and $DCB_j = d_{1,j} - d_{2,j}$ stand for differential code bias of the satellite and receiver which is the delay of P_1 relative to P_2. As P_4 has larger noise, L_4 is used to smooth the P_4. Cycle slips and gross errors in the carrier phase observations should be removed before smoothing the P_4, both Melbourne-Wübbena combination (MW) and ionosphere residual observations are used to detect cycle slips and gross errors. The following equations are utilized in the smoothing of the P_4:

$$\begin{aligned} P_{4,\,s} = &\frac{(\omega_1)_t}{(\omega_1)_t + (\omega_2)_t}(P_4)_t + \frac{(\omega_2)_t}{(\omega_1)_t + (\omega_2)_t} \\ &[(P_{4,\,s})_{t-1} + \delta(L_4)_{t,\,t-1}] \end{aligned} \tag{11.5}$$

$$(\omega_1)_t = \frac{1}{\sigma^2_{(P_4)_t}} \tag{11.6}$$

$$(\omega_2)_t = \frac{1}{\sigma^2_{(P_4)_t} + \sigma^2_{\delta(L_4)_t}} \tag{11.7}$$

$$\delta(L_4)_{t,t-1} = (L_4)_t - (L_4)_{t-1} \tag{11.8}$$

where t stands for the epoch number, ω is the weight factor related with epoch t. Note that the smoothed ionosphere measurements in Eq. (11.5) are still corrupted by the DCB^i and DCB_j, which therefore should be estimated along with the ionosphere delay parameters.

Regardless of the second and third order of ionosphere refraction, the ionosphere delay can be expressed as follows [9]:

$$d_{ion} = \frac{40.28}{f^2} STEC \tag{11.9}$$

where f stands for the carrier frequency, and $STEC$ stands for the slant total electron content along the signal path. Through substituting (11.9) into (11.3), and smoothing the P_4:

$$P_{4,s} = 40.28\left(\frac{1}{f_1^2} - \frac{1}{f_2^2}\right) STEC + DCB^i + DCB_j \tag{11.10}$$

The DCBs extracted from smoothed P_4 is more reliable.

11.3 Method to Model the Real-Time Spherical Harmonic Function and to Determine the DCBs

From (11.10), it is easy to get STEC, then VTEC:

$$STEC = -\frac{f_1^2 f_2^2}{40.28\left(f_1^2 - f_2^2\right)}\left(P_{4,s} - cDCB^i - cDCB_j\right) \tag{11.11}$$

$$VTEC = MF(z)STEC \tag{11.12}$$

$$MF = \cos\left(\arcsin\left(\frac{R}{R+H}\sin\left(\alpha z\right)\right)\right) \tag{11.13}$$

where z is the satellite elevation angle, R is the earth's radius, and H is the altitude of the ionosphere thin shell. In order to accurately be compared with the results of CODE, the H and α in this paper are references to CODE. This projection function is the best agreement with the projection of JPL Extended Slab Model [10].

CODE uses 15 order of spherical harmonic function to model the globe ionosphere products. Since for the regional area, the low order spherical harmonic function is much better, the spherical harmonic function model is shown as follows [11]:

$$E(\beta, s) = \sum_{n=0}^{\max\_n}\sum_{m=0}^{n}\tilde{P}_{nm}(\sin\beta)(a_{nm}\cos ms + b_{nm}\sin ms) \tag{11.14}$$

$$\tilde{P}_{nm} = \Lambda(n,m)P_{nm} = \sqrt{2\frac{2n+1}{1+\delta_{0m}}\frac{(n-m)!}{(n+m)!}}P_{nm} \tag{11.15}$$

where β is the geocentric latitude of the ionosphere pierce point (IPP), $s = \lambda - \lambda_0$ is the sun-fixed longitude of the IPP, $\tilde{P}$ is normalized Legendre polynomial, a_{nm}, b_{nm} are the spherical harmonic function model coefficients, max_n is the maximum order, and δ is the Kronecker Delta. Substituting (11.11) and (11.12) into (11.14), the ionosphere spherical harmonic function model can be obtained:

$$\begin{aligned}&\sum_{n=0}^{\max\_n}\sum_{m=0}^{n}\tilde{P}_{nm}(\sin\beta)(a_{nm}\cos ms + b_{nm}\sin ms)\\ &= \cos\left(\arcsin\left(\tfrac{R}{R+H}\sin(\alpha z)\right)\right)\\ &-\left[\tfrac{f_1^2 f_2^2}{4028\left(f_1^2 - f_2^2\right)}\left(P_{4,s} - cDCB^i - cDCB_j\right)\right]\end{aligned} \tag{11.16}$$

where a_{nm}, b_{nm}, DCB^i, DCB_j are unknown parameters to be estimated. During the estimating, with interval of two hours, the DCBs is considered as the same. In each period of time, a group of 25 coefficients in 4 order spherical harmonic function

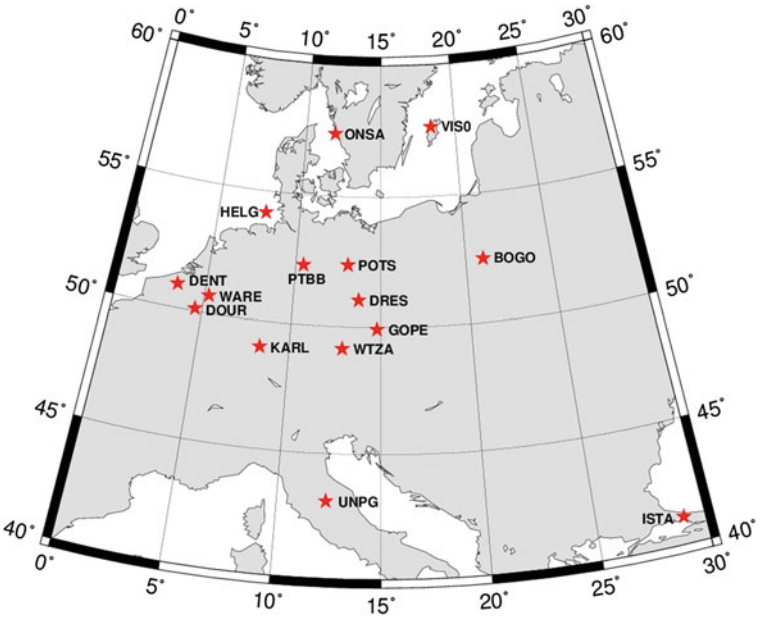

Fig. 11.2 Distributions of IGS stations chosen

model coefficients as well as the DCBs of all the satellites and receivers participated in the estimation can be obtained. According to the Least Mean Square (LMS), it still needs a constraint condition as (11.17) to separate the satellites DCB:

$$\sum_{i=1}^{\max\_i} DCB^i = 0 \tag{11.17}$$

The weight matrix of adjustment stochastic model is unit weight which implies that the observations are of mutual independence.

11.4 Experiments and Results

11.4.1 Experiments Data

15 evenly distributed IGS stations from Germany and its surrounding areas of April 9–18, 2012 (Day of Year: 100–109) are selected. A total of 10 days observations as the real time simulation data, the average distance among stations in the distribution intensive regions are about 200–300 km. With the real-time simulated data of the network, calculation once every 2 h in 10 continuous days is

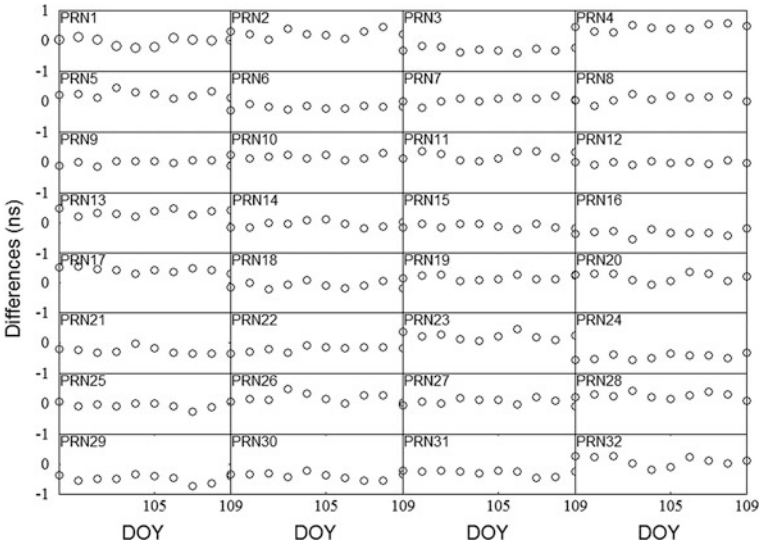

Fig. 11.3 Differences in the satellites DCB value from this paper and CODE

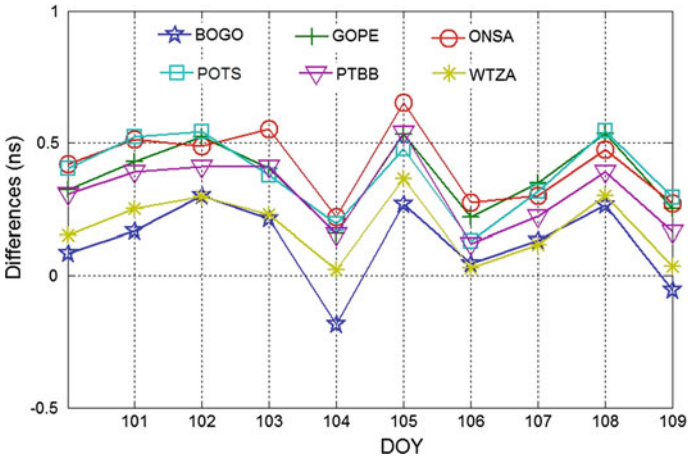

Fig. 11.4 Differences in the receivers DCB value from this paper and CODE

conducted. Finally, the ionosphere spherical-harmonic model of the estimated area and the DCB of P1 to P2 are obtained and the results are compared with the results issued by CODE (Fig. 11.2).

Table 11.1 The RMS and mean differences between satellite and receiver DCB estimates from April 9–18, 2012

Satellite	RMS	Differences	Mean DCB of test	Satellite/ station	RMS	Differences	Mean DCB of test
PRN1	0.122	−0.030	−10.804	PRN20	0.137	0.181	0.007
PRN2	0.122	0.228	6.163	PRN21	0.097	−0.274	1.606
PRN3	0.071	−0.298	−2.749	PRN22	0.081	−0.191	5.562
PRN4	0.095	0.331	−0.825	PRN23	0.116	0.220	7.884
PRN5	0.108	0.228	1.634	PRN24	0.086	−0.360	−3.479
PRN6	0.060	−0.203	−2.317	PRN25	0.091	−0.052	−8.818
PRN7	0.103	0.039	1.777	PRN26	0.144	0.186	−1.274
PRN8	0.105	0.087	−2.713	PRN27	0.098	0.057	−2.501
PRN9	0.075	−0.025	−1.676	PRN28	0.094	0.257	1.713
PRN10	0.072	0.173	−3.529	PRN29	0.120	−0.298	0.380
PRN11	0.127	0.215	2.377	PRN30	0.106	−0.203	−3.001
PRN12	0.047	−0.018	2.477	PRN31	0.085	0.291	3.019
PRN13	0.099	0.349	2.189	PRN32	0.151	0.090	−3.366
PRN14	0.098	−0.040	0.449	BOGO	0.147	0.124	−3.567
PRN15	0.067	−0.105	1.133	GOPE	0.129	0.303	7.121
PRN16	0.099	−0.322	0.824	ONSA	0.137	0.408	−5.411
PRN17	0.079	0.309	1.952	POTS	0.140	0.428	6.433
PRN18	0.101	−0.094	1.703	PTBB	0.132	0.361	−9.290
PRN19	0.075	0.154	4.203	WTZA	0.120	0.180	−8.960

11.4.2 DCBs Analysis

As one of the analysis centers of IGS, CODE applies 15 orders Spherical Harmonic Function to model the globe TEC model, and has launched DCB of part of the IGS globe distributed stations and satellites (GPS & GLONASS). In this report, the CODE results are taken as reference. DCB values estimated by the authors and those released by CODE are compared, as shown in Figs. 11.3 and 11.4. The DCBs in the figures are the mean of 10 days. The vertical axis stands for biases, or differences (in nanoseconds) and the horizontal axis stands for the days of year in 2012. More details are displayed in Table 11.1.

Receiver DCB biases are basically less than 0.4 ns and those of the ONSA and POTS are 0.408 ns and 0.428 ns respectively. Since observations of them are found out that the number of valid observations for them is less than others each day from April 9–18, the larger bias in them are probably caused by fewer observations. Satellites DCB biases show good results which are all less than 0.35 ns. The RMS of all differences is lower than 0.2 ns. Considering that the order of Spherical Harmonic Function is 4 for regional area ionosphere, it turns out to be more sensitive which will also be approved in the next section.

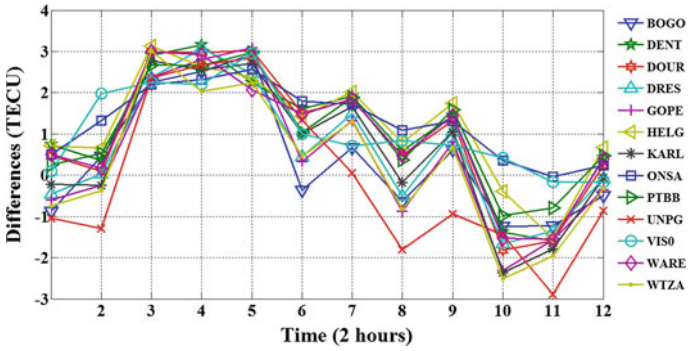

Fig. 11.5 Differences in the stations VTEC value from this paper and CODE (100th day)

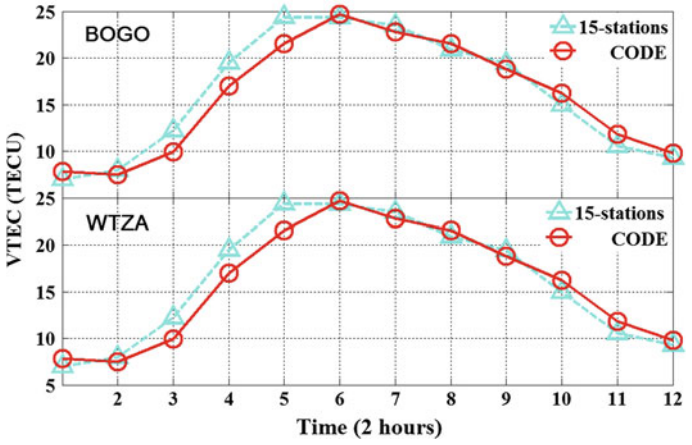

Fig. 11.6 The VTEC of BOGO&WTZA in 100th day

11.4.3 DCBs Analysis

During the estimation of real-time simulation, with interval of 2 h, VTEC data of 12 periods a day are obtained. Figure 11.5 shows the differences in all the stations VTEC per period in 100th day expect the ISTA for data anomalies. The single station VTEC per period is showed in Fig. 11.6. Due to space limitations, only BOGO and WTZA are in the figure. It shows that the differences of VTEC reach their peak value of 2–3 TECU at period 3–5, 10–11, and the rest are lower than 2TECU, especially the beginning and ending periods of which the differences reach less than 1TECU. The results show good agreement with CODE. From Fig. 11.6, the test values rise faster than CODE, and also decline faster. So it can conclude that the regional model can reflect better than globe model in which the differences are less than 3TECU. The distribution of stations net determines

effective number, density and geometric position of IPP and exercises a great influence on the accuracy of the ionosphere model. The average distance among stations in this paper is about 200–300 km and these stations are among the 30 degrees of latitude and 20 degrees of longitude, which is equivalent to the area from Beijing to Hong Kong in north-south direction and from Shanghai to Chengdu in east-west in China. However, the station distribution in CORS is more intensive in general. Therefore, the ionosphere model with higher accuracy can be achieved.

11.5 Summaries

The use of pseudorange and refined pseudorange to obtain the absolute electron content of the ionosphere, and then established regional ionosphere model is a common method. However, the determination of ionospheric delay by this method generally can not be used for precise positioning due to the precision problem. This paper use the part of global continuous tracking station to simulate aera CORS system. The effect of DCB is considered while estimating real-time regional Ionospheric modeling using spherical harmonic function, thereby the ionospheric model accuracy is improved. The comparative analytic results show that the method taken in this paper can effectively solve and exclude DCBs, and establish more accurate and sensitive real-time regional ionosphere model. It has important research significance of providing better ionosphere corrections information for single frequency receiver users by CORS network real-time monitoring of the CORS network changes of ionosphere.

References

1. Gao Y, Liu ZZ (2002) Precise ionosphere modelling using regional GPS network data. J Glob Positioning Syst 1(1):18–24
2. Xiaoya Wang, Wenyao Zhu. Method and progress on monitoring ionospheric activity by GPS. Prog Astron 21(1):33–40
3. Schaer S (1995) Global and regional ionosphere models using the GPS double difference phase observable. IGS workshop. Potsdam
4. Xiaohong Z, Zhenghang L, Changsheng C (2001) Study on regional ionospheric model using dual-frequency GPS measurements. Geomat Inf Sci Wuhan Univ 26(2):140–143, 159
5. Yunbin Y (2002) Study on theories and methods of correcting ionosphere delay and monitoring ionosphere based on GPS. Institute of geodesy and geophysics. Chinese Academy of Science, China
6. Hongping Zhang (2006) Research on China area ionosphere monitoring and delay correction based on ground-based GPS. Shanghai astronomical observatory. Chinese Academy of Science, China
7. Gao Y, Heroux P, Kouba J (1994) Estimation of GPS receiver and satellite L1/L2 signal delay biases using data from CACS. In: Proceedings of KIS-94, Banff, Canada

8. Gao Y, Liao X, Liu ZZ (2002) Ionosphere modeling using carrier smoothed ionosphere observations from a regional GPS network. Geomatica 56(2):P97–P106
9. Zhenghang L, Jinsong H (2005) GPS surveying and data processing. Wuhan University Press, Wuhan
10. Zhenghang Li, Xiaohong Zhang (2009) New techniques and precise data processing methods of satellite navigation and positioning. Wuhan University Press, Wuhan
11. Jin R, Jin S, Feng G (2012) M_DCB: Matlab code for estimating GNSS satellite and receiver differential code biases. GPS solutions. Springer, China

Chapter 12
Single-Epoch Integer Ambiguity Resolution for Long-Baseline RTK with Ionosphere and Troposphere Estimation

Denghui Wang, Chengfa Gao and Shuguo Pan

Abstract A new single-epoch ambiguity resolution for long baseline RTK, on the basis of the ionosphere-weighted model, is proposed in this paper, which is applicable to several hundred km baselines by using linear combination of the measurements, including the double-differential wide-lane combination and ionosphere-free combination carrier-phase observation equations and UofC model. By the correct ambiguity and double-differential atmosphere delay, the real-time atmosphere model was established to provide predicted value for a new risen satellite. The establishment of real-time atmosphere predicted model, estimating the relative tropospheric zenith delay and the regional ionospheric parameters, is proved to reach an acceptable accuracy. Test data from the multiple reference station GPS networks in Chongqing, consisting of 36 baselines from 40 to 350 km, were used to evaluate the performance of the proposed approach. It is showed that the proposed algorithm can reduce the effect of the ionosphere and troposphere on the network AR and the true integer ambiguity could be achieved in a short time after the establishment of the predicted atmosphere model.

Keywords Ambiguity resolution · Network RTK · UofC · Real-time atmosphere model

D. Wang (✉) · C. Gao
School of Transportation, Southeast University, Sipailou No.2,
210096 Nanjing, China
e-mail: owenxun@gmail.com

C. Gao
e-mail: gaochfa@163.com

S. Pan
School of Instrument Science and Engineering, Southeast University,
Sipailou No.2 210096 Nanjing, China
e-mail: panshuguo@gmail.com

J. Sun et al. (eds.), *China Satellite Navigation Conference (CSNC) 2013 Proceedings*, Lecture Notes in Electrical Engineering 243,
DOI: 10.1007/978-3-642-37398-5_12,

12.1 Introduction

In the larger scale multiple reference station (MRS) network, the performance of the long baseline over 100 km is greatly degraded due to the spatial correlation error, such as the atmosphere model error and the satellite orbit error. The correct ambiguity of the baseline can not only be used in simulating the regional atmosphere error, but also in providing the condition for generating the no-differential ambiguity of the reference stations. The authors have developed a new single-epoch ambiguity resolution for long baseline RTK, on the basis of the ionosphere-weighted model [1] applicable several hundred km baselines by using double-differential observations. The strategy estimates the ionosphere and the troposphere error by generating several kinds of linear combination of the measurements; including the double-differential wide-lane combination and ionosphere-free combination carrier-phase observation equations and University of Calgary Model (UofC model). What is more, the establishment of real-time atmosphere predicted model, estimating the relative tropospheric zenith delay and the regional ionospheric parameters, and integer ambiguity criterion method, using the residual atmosphere delay and residual measurements, is described in the paper.

However, the method mentioned above is focused only on single baseline ambiguity resolution and ambiguity quality control for kinematic positioning. The adjustment of the network could be done in generating the higher-accuracy regional real-time atmosphere model. The performances of the test come from Chongqing using the receivers made by Trimble, the other from Jiangsu equipped with the receivers made by Leica. It is showed that the proposed algorithm can reduce the effect of the ionosphere and troposphere on the network ambiguity resolution (AR) and the true integer ambiguity could be achieved in a single epoch after the establishment of the predicted atmosphere model. On the other hand, due to its epoch-by-epoch nature, the proposed approach is insensitive to cycle-slips, rising or setting satellites, or loss-of-lock.

In this paper, Firstly, the observation equations and the predicted atmosphere modeling methods are analyzed in Sect. 12.2. Secondly, the AR strategy and ambiguity verification condition are introduced in Sect. 12.3, and the algorithm is investigated and tested in Sect. 12.4, including the comparison between the predicted model and the empirical one, the effect of this approach on the ambiguity estimating, and especially the single-epoch ambiguity success rate in network. Finally, the concluding remarks are described in the last section.

12.2 The Observation Equations

In this section we will introduce the single-baseline model that forms the basis of our study.

$$\begin{aligned}\nabla\Delta P_{k,l}^{i,j} =& \nabla\Delta\rho_{k,l}^{i,j} + \nabla\Delta\frac{\eta}{f^2} + \nabla\Delta T_{k,l}^{i,j} + \nabla\Delta O_{k,l}^{i,j} + \nabla\Delta m_{k,l,P}^{i,j} + \nabla\Delta\varepsilon_{k,l,P}^{i,j} \\ \nabla\Delta\Phi =& \nabla\Delta\lambda\phi = \nabla\Delta\rho_{k,l}^{i,j} + \lambda^j\nabla\Delta N_{k,l}^{i,j} + (\lambda^i - \lambda^j)\Delta N_{k,l}^{i} - \nabla\Delta\frac{\eta}{f^2} \\ &+ \nabla\Delta T_{k,l}^{i,j} + \nabla\Delta O_{k,l}^{i,j} + \nabla\Delta m_{k,l,\phi}^{i,j} + \nabla\Delta\varepsilon_{k,l,\phi}^{i,j}\end{aligned} \tag{12.1}$$

where ∇ is single-difference between satellite i and j; Δ is single-difference between receiver k and l; Φ is carrier-phase measurement (m); ϕ is carrier-phase measurement (cycle);P is pseudorange measurement (m); ρ is geometric range between satellite and receiver antenna phase center (m); η is Total Electron Content in transmission path $\eta = 40.28\,TEC$; T is troposphere delay in transmission path (m); λ is carrier wave length of the satellite (m); $N$is carrier-phase ambiguity (cycle); $O$is satellite orbital error (m); $m$is multipath delay; $\varepsilon_\phi\varepsilon_P$ is measurement errors of carrier-phase and pseudorange including receiver and satellite hardware delay, plate motions error and Tidal error.

For the single-baseline over 100 km, the atmosphere, satellite orbit and multipath effects are the main error sources that influence the success rate of integer ambiguity. The empirical atmosphere model is used in this study, providing a predicted value for the atmosphere delay at the initialization period. The orbital error could be reduced or eliminated by using the International GPS Service (IGS) ultra-rapid ephemeris, which have twenty-four hours' prediction orbit, instead of broadcast orbits, especially for distances exceeding 100 km. Also the multipath effect could be avoided by using daily repeated property of GNSS multipath signal in the software and antenna fairing in the hardware to improve the quality of the measurement.

12.2.1 The Empirical Atmosphere Model

12.2.1.1 The Troposphere

A predicted correction value could be obtained from the empirical troposphere models, for example, Hopfield, Saastamoinen [2] and UNB3 [3]. These models give the similar value when the satellite's elevation angle is upon 20 degree. Due to the different environmental conditions, the temperature, air pressure and water vapour content are quite different around the world. Hopfield and Saastamoinen models rely on the real meteorological inputted parameters and UNB3 model has a good performance only in North America compared with the other empirical models.

In this study, the meteorological inputted parameters are composed of temperature and pressure from global pressure and temperature model (GPT) (Boehm et al. 2007) and the partial pressure of water vapour from Unb3 model. Global mapping function (GMF) is used to be the mapping function of the priori

troposphere model, which the zenith troposphere delay is computed by Saastamoinen model.

After the ambiguity is fixed, the un-model terms are applied to remain the residual tropospheric zenith delay. The relative tropospheric zenith delay would be estimated for the purposed of compensating the empirical model for a setting, or a new-risen GPS satellite.

12.2.1.2 The Ionosphere

The Klobuchar model and global ionosphere maps model (GIM) are mentioned in the paper. The Klobuchar model is relatively easy to obtain a 50 percent rms ionospheric error reduction [4] and GIM model could not provide real-time ionosphere parameters. The accuracy of these two empirical ionosphere models is not good enough, which influences the long-range ambiguity estimated without using ionosphere-free combination.

In the paper, for the purpose of reducing the ionospheric delay, previous GIM model parameters are used to provide a predicted value and the ionosphere-weighted model is used to give a reasonable weight of the ionospheric delay. Once the ambiguity is fixed, the regional ionospheric parameter model would be established, by using polynomial fitting method. It would provide a higher accuracy of the ionspheric delay to a new-risen satellite, instead of the empirical model.

12.2.2 The Observation Model

To the GNSS dual frequency receiver, four measurements could be obtained. According to the observation equation, reasonable combination observation is of benefit to understand and solve problems in GNSS application. The linear combination can be formed as

$$\nabla\Delta R = i\nabla\Delta\lambda\phi_1 + j\nabla\Delta\lambda\phi_2 + m\nabla\Delta P_1 + n\nabla\Delta P_2 \tag{12.2}$$

where R is the combination measurement; i, j, m, n is the combination factors.

In the paper, four kinds of combination measurements are applied in the proposed ambiguity resolution algorithm. In order to decrease the influence of the atmosphere delay and weaken the correlation of the unknown parameter, various kinds of LCs are used in estimating ambiguity and atmospheric delay. However, any linear combinations would amplify the measurement noise to the original measurement. Due to the different combinations with different measurement noise value [5], the chosen of the combinations should provide the optimum performance.

12.2.3 The Observation Weighting Schemes

In this study, we assume that the four double-differential original measurements are not correlated [6], and that the predicted DD-atmosphere delay is correlated. With these assumptions the observation vector of observations and the covariance matrix could be written as:

$$L = \begin{bmatrix} \Phi_1 \\ \Phi_2 \\ P_1 \\ P_2 \end{bmatrix}, \quad Q_L = 4\sigma_{\Phi_1}^2 \begin{bmatrix} 1 & 0 & 0 & 0 \\ 0 & \frac{f_1^2}{f_2^2} & 0 & 0 \\ 0 & 0 & k^2 & 0 \\ 0 & 0 & 0 & \frac{f_1^2}{f_2^2} \cdot k^2 \end{bmatrix} \tag{12.3}$$

In the covariance matrix, k is the ratio of the standard errors of the pseudorange and the carrier phase. We consider the standard error of L1 term is $\sigma_{\Phi_1} = 6$ mm and $k = 100$. In order to get the linear combinations of the original equations, we use transformation matrix notation, so that we can rewrite Eq. (12.2) generally for any linear combinations LCs as follows:

$$L_c = TL = \begin{bmatrix} \Phi_{i,j} \\ \Phi_{k,l} \\ R_{i,m} \\ R_{j,n} \end{bmatrix}, \quad T = \begin{bmatrix} \frac{i\lambda_{i,j}}{\lambda_1} & \frac{j\lambda_{i,j}}{\lambda_2} & 0 & 0 \\ \frac{l\lambda_{l,k}}{\lambda_1} & \frac{k\lambda_{l,k}}{\lambda_2} & 0 & 0 \\ i & 0 & m & 0 \\ 0 & j & 0 & n \end{bmatrix} \tag{12.4}$$

And the covariance matrix of the transformed observation vector LC becomes:

$$Q_{Lc} = TQ_L T^T \tag{12.5}$$

The elevation-dependent weighting scheme [7] is also used in this study by changing the variance of the original observation. With the assumptions that the predicted DD-atmosphere delay is correlated and the no-differential atmosphere delay is uncorrelated.

12.3 The AR Strategy for Long Baseline

In this section, we introduce the AR strategy for the long baseline RTK with estimation of ionosphere and troposphere terms in three steps. With the help of ambiguity criterion method, the true integer ambiguity and previous epochs are used to establish the real-time predicted atmosphere model.

12.3.1 Ambiguity Resolution

In general, most articles have used either wide-lane LC of carrier-phase measurement or the Melbourne-Wübbena (MW) wide-line LC [8]. In despite of wide-lane LC of carrier-phase measurement has a low DD noise, the ionospheric delay cannot be eliminated and influences the accuracy of the wide-lane ambiguity. On the other hand, MW wide-lane LC cancels out not only the ionosphere term but also geometry and troposphere terms. Due to the noise of the MW, the MW LC can not provide the optimum performance in a short period. To improve the conventional way, UofC model is used in the ambiguity resolution to increase redundant observation thereby the observation equation is not rank deficient. And for estimating the tropospheric delay and L1 ambiguity, ionosphere-free LCs is utilized.

With the ambiguity fixed, the least square estimation of the real-time relative tropospheric zenith delay is used to provide a predicted tropospheric delay to a new-risen satellite, instead of the empirical atmosphere model. For the ionospheric delay, the regional maps are produced as well and are also used to support AR of the new-risen satellite on the average 90 % of the initial carrier phase ambiguities can be resolved reliably [9].

Step 1. *Wide-lane Ambiguity Estimated*

Compared with the ionosphere-weighted model, UofC model $(i = 0.5, m = 0.5 \text{ or } j = 0.5, n = 0.5)$ is used in estimating the ambiguity. The observation matrix notation can be written as:

$$V = L - BX \tag{12.6}$$

Where [10]:

$$L = \begin{bmatrix} \Delta\nabla\Phi_{1,-1} - \Delta\nabla\rho - \Delta\nabla T \\ \Delta\nabla\Phi_{1,0} - \Delta\nabla\rho - \Delta\nabla T \\ \Delta\nabla UofC_1 - \Delta\nabla\rho - \Delta\nabla T \\ \Delta\nabla UofC_2 - \Delta\nabla\rho - \Delta\nabla T \\ \Delta\nabla B \end{bmatrix}, \quad X = \begin{bmatrix} \Delta_{1,-1} \\ \Delta\nabla N_{1,0} \\ \Delta\nabla I \end{bmatrix}$$
$$B = \begin{bmatrix} \lambda_{1,-1} & 0 & -\lambda_{1,-1}\frac{f_2-f_1}{f_2\lambda_1} \\ 0 & \lambda_1 & -1 \\ 0 & \lambda_1/2 & 0 \\ -\lambda_2/2 & \lambda_2/2 & 0 \\ 0 & 0 & 1 \end{bmatrix} \tag{12.7}$$

It is noted that the ionospheric delays are modeled as unknown variables and the tropospheric delay is modified by the empirical troposphere model. The use of the priori weighted ionosphere has been discussed as sated.

If the real-time regional ionospheric model is not obtained, the sample values of the ionosphere delays can be taken from the empirical ionosphere model. And the models have a different accuracy as shown in Sect. 12.4.With the assumptions that the predicted DD-atmosphere delay is correlated and the DD-LCs is no-correlated for the different pairs of satellites, it indicated the covariance matrix should be written as:

$$Q_{\varepsilon} = \begin{bmatrix} Q_{Lc}^{1} & 0 & \cdots & \cdots & 0 \\ 0 & Q_{Lc}^{2} & & & \vdots \\ \vdots & & \ddots & & \vdots \\ \vdots & & & Q_{Lc}^{n-1} & 0 \\ 0 & \cdots & \cdots & 0 & Q_{\Delta\nabla\varepsilon} \end{bmatrix} \tag{12.8}$$

After the regional maps are produced with making use of carrier-phase measurement and the correct integer ambiguity, the ionospheric delay de-correlates with the pairs of the satellites, and the effect of the ionospheric delay on DD observables varying with time and location in the ionosphere [11]. So the variance of the ionosphere can be given as [12]:

$$\sigma_B^2 = \sigma_\infty^2 \left(1 - e^{-2(|\tau|/T + |\delta|/D)}\right) \tag{12.9}$$

Where: τ, Receiver sampling interval; T, Correlation time for the DD ionosphere set as 64 min; δ, Baseline length; D: Correlation distance set as 1,500 km; $\sigma_\infty^2 = 2\ \mathrm{m}^2$.

According to the accuracy of the ionosphere model, the true wide-lane ambiguities can be obtained by the kalman-filter with ionosphere estimation in the initial stage. When the regional real-time ionosphere model could be obtained, the correct value of the wide-lane ambiguity can be resolved immediately.

Step 2. *L1 Ambiguity Estimated by Kalman filter*

After the wide-lane ambiguity fixed, the ionosphere-free LC and the correct wide-lane ambiguity can be used to estimate the L1 ambiguity, the observation matrix notation is:

$$L = \begin{bmatrix} \Delta\nabla N_{1,-1} \\ \Delta\nabla\Phi_{ion-free} - \Delta\nabla\rho - \Delta\nabla T \\ \Delta\nabla UofC_1 - \Delta\nabla\rho - \Delta\nabla T \\ \Delta\nabla UofC_2 - \Delta\nabla\rho - \Delta\nabla T \\ \Delta\nabla B \end{bmatrix}, \quad X = \begin{bmatrix} \Delta\nabla N_1 \\ \Delta\nabla N_2 \\ \Delta\nabla T_{slant} \end{bmatrix} \tag{12.10}$$

We can see that the ionosphere delay has no effect on the observation measurement, and the true wide-lane ambiguity would control the DD-observation noise so that we can get the true L1 and L2 ambiguity in a short period. In the strategy, the estimated states by kalman filter include the ambiguity of L1 and L2, double-differenced slant tropospheric delay.

In the initial stage, the relative tropospheric zenith delay could not be obtained thereby we have to improve the limit of elevation to 15(in degree).And the correlations between the different pairs of satellite should be considered, too. After initialling process, the relative tropospheric zenith delay could be used to replace the empirical model. The variance $\sigma^2_{\Delta\nabla T}$ and process noise $D_{\Delta\nabla T}$ of the troposphere can be given as [13]:

$$\begin{aligned} \sigma^2_{\Delta\nabla T} &= [MF(E^i) - MF(E^j)]^2 \times E[(RTZD)^2] \\ E[(RTZD)^2] &= 0.4844^2 \times \left(0.0012 + 1.485 \times 10^{-5} \times D\right)(\mathrm{m}^2) \\ D_{\Delta\nabla T} &= [MF(E^i) - MF(E^j)]^2 \times D[(RTZD)^2] \\ D[(RTZD)^2] &= \frac{0.0004}{3600} \times \tau(\mathrm{m}^2) \end{aligned} \tag{12.11}$$

The LAMBDA method is used to get the integer ambiguity of L1 and L2 terms on an epoch-by-epoch basis or single-epoch. In general, the ratio threshold (which is set as 3) can be easily gotten in 10 epochs, and the fixed ambiguity of L1 and L2 can also be checked by the wide-lane ambiguity directly.

Step 3. *Real-time Atmosphere model*

With the known coordinates of the reference stations and the true integer ambiguities, the geometric-free LC and ionosphere-free LC are used to generate the DD- ionospheric delay and tropospheric delay respectively. The ionospheric gradient parameters could be used to represent this character of the regional ionospheric delays. The ionospheric gradient parameters can be expressed as [14]:

$$\begin{aligned} \Delta\nabla I^{i,j}_{k,l} &= vI^j_l \cdot f^j_{l,IPP} - vI^i_l \cdot f^i_{l,IPP} + vI^i_k \cdot f^i_{k,IPP} - vI^j_k \cdot f^j_{k,IPP} \\ vI^j_k &= a_0 + a_1 dL + a_2 dB \end{aligned} \tag{12.12}$$

IPP is the ionospheric pierce point. And the kalman filter should be used to estimate the ionospheric gradient parameters. For the DD-measurements, the difference code biases for satellites and receivers have been eliminated.

To the tropospheric delay, the relative tropospheric zenith delay is real-time achieved by least squares adjustment. The equation is shown as [13]:

$$\begin{aligned} \Delta\nabla T^{i,j}_{k,l} &= ZTD_l \times [MF(E^j_l) - MF(E^i_l)] - ZTD_k \times [MF(E^j_k) - MF(E^i_k)] \\ &\cong [MF(E^j_l) - MF(E^i_k)] \times RTZD_{k,l} \end{aligned} \tag{12.13}$$

12.3.2 Ambiguity Criterion Method

Incorrect ambiguity can influence the generation of real-time atmospheric error badly, so it is necessary to maintains controls of quality strictly on the ambiguity. For the baseline, the residuals from DD measurements should be statistically acceptable by comparing the ratios of the covariance matrix. And the difference between the known coordinates and the coordinates, which is obtained by the integer ambiguity, could be considered as a detection threshold. The test shown in Sect. 12.4 proves the ambiguity criterion method which is mentioned here.

For each DD ambiguity in the network, the sum of the integer ambiguities around any baseline triangle in an MRS network should equal zero. Therefore, after all of the ambiguities of the closed loop resolved, the constraint condition should be used to verify that the fixed ambiguities are correct. If all the network ambiguities satisfy the constraint conditions for the entire network, then this verification can be used to check the correctness of the network ambiguities and generate the real-time regional atmosphere model of the entire network.

Finally, for single-epoch observations of the satellite pair, a new ambiguity solution was proposed, using the linear combination of the four measurements, with the estimation of ionosphere and troposphere.

12.4 Test Results and Analysis

A 24 h DD data set observed in Chongqing, China in November 2010 was used to test the performance of the proposed strategy for network AR. The test network consisted of 9 reference stations as shown in Fig. 12.1. The receivers at these stations were Trimble dual-frequency receivers equipped with TRM55791

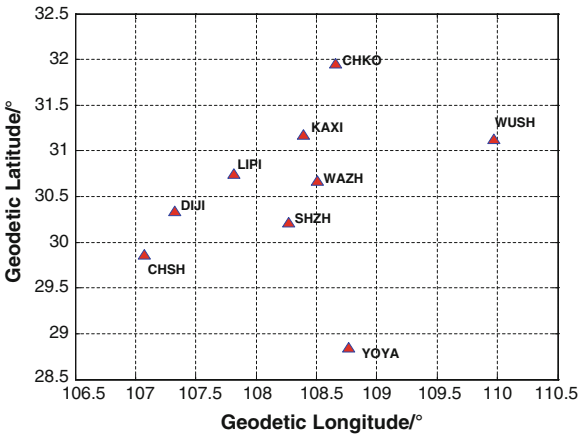

Fig. 12.1 Chongqing GPS reference network

antennas and the epoch interval is 15s. Nine reference stations formed 36 baselines, whose length were 40 to 350 km.

The effect of ionosphere and troposphere is a major inhibitor to long-range single-epoch AR among reference stations. In the study, we choose the high-elevation satellite to estimate the relative tropospheric zenith delay and the regional ionosphere model.

The comparison has been done among the true atmospheric delay, the empirical model and the predicted real-time model.

Figure 12.2 shows the comparison on the effect of ionosphere(two satellites, one was a risen one and the other was a fall one), which indicates that the regional predicted model has an acceptable accuracy within twenty centimeters of error and it is no direct relation between the accuracy of the predicted model and the satellite elevation. By the predicted ionosphere model, the wide-lane ambiguity could be estimated in one or two epochs. Figure 12.3 shows an example of the low-elevation satellite result with 133 km baseline by simple implementation of the strategy. The upper plots indicate the predicted real-time troposphere model have a good performance. Two satellites, a risen-one elevation from 11° to 17°and a setting-one elevation from 14° to 10°, are used. The model standard deviation was 9.6, 17.9 mm for the predicted model, and 28.3, 41.9 mm for the empirical model.

At the initialization period, the predicted atmospheric delay was obtained by the empirical atmosphere model and the wide-lane ambiguity of the high-elevation satellite could be achieved immediately. After the real-time atmosphere model was established, the single-epoch integer ambiguity of the low-elevation satellite is easy to go through the ambiguity criterion method by the proposed ambiguity solution. Compared to conventional method, the proposed strategy has very good effect on the wide-lane ambiguity resolution.

As shown in the Fig. 12.4, the proposed strategy for long baseline RTK seems to work well on the wide-lane ambiguity. The fluctuation of the wide-lane ambiguity could be limited within 0.2 cycles. Two satellites were shown in the figure, one has great ionosphere influence when the satellite's elevation is low and the other data was collected on the solar noon. Compared with the double-frequency LC and the MW LC, the proposed could achieve a true wide-lane ambiguity in a short period and is not sensitive to cycle-slips, rising or setting satellites. However, the performance of the wide-lane ambiguity relies on the accuracy of the

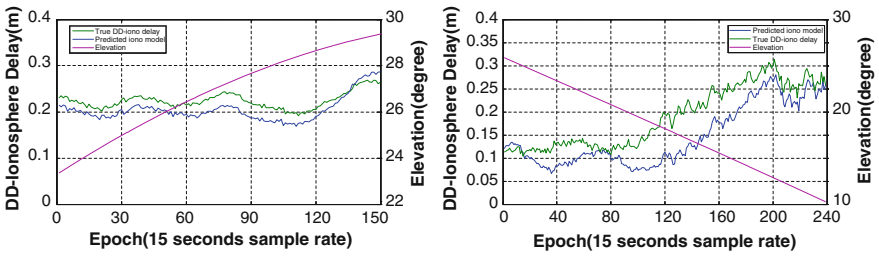

Fig. 12.2 The comparison on the effect of ionosphere

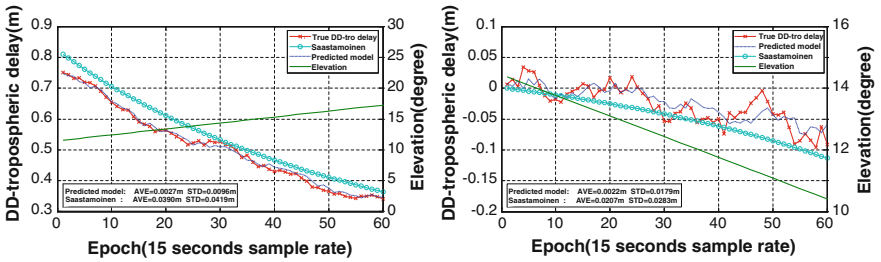

Fig. 12.3 The comparison on the effect of troposphere

predicted ionosphere model. The proposed real-time ionosphere predicted model need a long initialization time and the salient point error of the ionospheric is not considered. And it is worth further improvement to ensure the real-time ionospheric model work well to support AR of the satellite.

In the Fig. 12.5, the proposed method on L1 ambiguity resolution with slant troposphere estimated by kalman filter was shown. The example of the result with 150 km baseline, used 6 satellites and the epoch interval was 15 s. Compared with the conventional method with tropospheric zenith delay estimated by kalman filter, the new method could get the higher accuracy of the float ambiguity and the shorter convergence time. The ratio of the LAMBDA method also indicated the new method could get a reliable result of the L1 and L2 ambiguity in a short time.

12.5 Concluding Remarks

This study focuses on medium- to long-range AR among the base lines of a MRS network and the establishment of real-time atmosphere predicted model. A new single-epoch ambiguity resolution for long baseline RTK, on the basis of the ionosphere-weighted model, is proposed in this paper. The method is applicable to several hundred km baselines by using linear combination of the measurements,

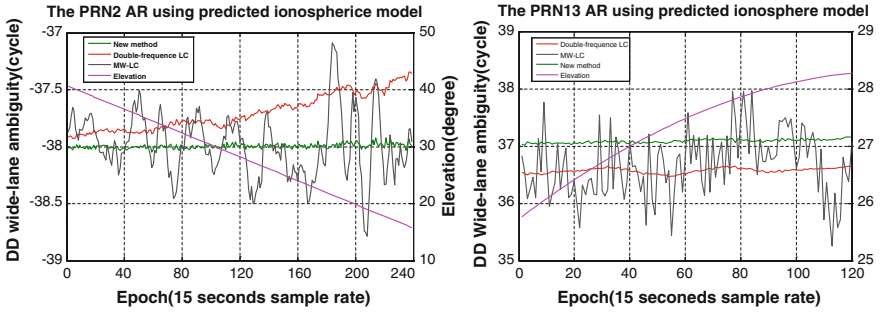

Fig. 12.4 The AR effect on the wide-lane ambiguity

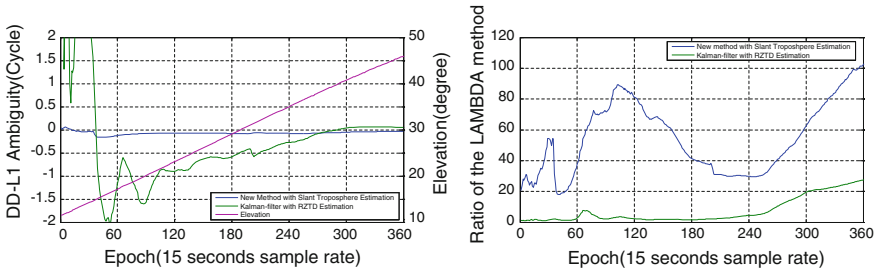

Fig. 12.5 The comparison on the effect of troposphere

including the double-differential wide-lane combination and ionosphere-free combination carrier-phase observation equations and U of C model. The establishment of real-time atmosphere predicted model, estimating the relative tropospheric zenith delay and the regional ionospheric parameters, is proved to have an acceptable accuracy. What is more, with the help of the real-time atmosphere model the ambiguity could be achieved immediately. Test data from the MRS GPS networks in Chongqing, consisting of 36 baselines from 40 to 350 km, were used to evaluate the performance of the proposed approach. However, the method mentioned above is focused only on single baseline ambiguity resolution and ambiguity quality control for kinematic positioning. The adjustment of the network will be done in generating the higher-accuracy regional real-time atmosphere model.

Acknowledgments This work is supported by the Jiangsu Province Surveying and Mapping Scientific Research Fund under grant No. JSCHKY201205.

References

1. Teunissen PJG, Kleusberg A, Teunissen PJG (1998) GPS for geodesy. Springer, Berlin
2. Spilker JJ (1996) Tropospheric effects on GPS. In: Proceedings of Global Positioning System. Theory and Applications 1:517–546
3. Collins P, Langley R, LaMance J (1996) Limiting factors in tropospheric propagation delay error modelling for GPS airborne navigation. In: Proceedings of ION 52nd Annual Meeting
4. Klobuchar JA (1987) Ionospheric time-delay algorithm for single-frequency GPS users. IEEE Transactions on Aerospace and Electronic Systems 23(3):325–331
5. Takasu T, Yasuda A (2001) Kalman-filter-based integer ambiguity resolution strategy for long-baseline RTK with ionosphere and troposphere estimation. In: Proceedings of the 23rd international technical meeting of the satellite division of the institute of navigation (ION GNSS 2010), pp 161–171
6. Horemuz M, Sjoberg LE (2002) Rapid GPS ambiguity resolution for short and long baselines. J Geodesy 76:P381–P391
7. Han S (1997) Quality-control issues relating to instantaneous ambiguity resolution for real-time GPS kinematic positioning. J Geodesy 71:P351–P361
8. Letao Z, Dingfa H, Chenggang L et al (2006) A strategy of double difference ambiguity resolution in reference station network. J Geod Geodyn 26(4):P34–P40

9. Schaer S, Beutler G, Rothacher M (1998) Mapping and predicting the ionosphere. In: Proceedings of the 1998 IGS Analysis Center Workshop, Darmstadt, Germany
10. Hu G, Abbey DA, Castleden N et al (2005) An approach for instantaneous ambiguity resolution for medium- to long-range multiple reference station networks. GPS Solution 9:1–11
11. Klobuchar J (1996) Ionospheric effects on GPS. Global Positioning System. Theory and Applications 1:485–515
12. Goad CC, Yang M (1997) A new approach to precision airborne GPS positioning for photogrammetry. Photogrammetric Eng Remote Sens 63(9):P1067–P1077
13. Zhang J, Lachapelle G (2001) Precise estimation of residual tropospheric delays using a regional GPS network for real-time kinematic applications. J Geodesy 75:P255–P266
14. X Li (2012) Improving real-time PPP ambiguity resolution with ionospheric characteristic consideration. In: Proceedings of the 25rd international technical meeting of the satellite division of the institute of navigation (ION GNSS 2012)

Chapter 13
Improving GPS Positioning Accuracy Based on Particle Filter Algorithm

Ershen Wang, Ming Cai and Tao Pang

Abstract To solve the error of GPS positioning based on traditional Kalman filter (KF) in dealing with nonlinear system and non-Gaussian noise. A novel filtering algorithm based on particle filter is proposed to improve the positioning accuracy of GPS receiver. The important density function by observing pseudorange non-Gaussian error distribution is set up. It is combined particle filter with system nonlinear dynamic state-space model. To solve the degeneracy phenomenon of particle filter (PF), Markov Chain and Monte Carlo (MCMC) method is adapted. The experimental results show that particle filter algorithm can effectively deal with non-linear and non-Gaussian state estimation. Compared with positioning optimization algorithm based on extended Kalman filter (EKF), the particle filter algorithm reduces the error of both positioning and speed estimation, attains higher positioning accuracy. The root mean square error (RMSE) parameter of particle filter is less. It is an effective method for GPS positioning to nonlinear and non-Gaussian state estimation problem. Moreover, the particle filter based on MCMC can work as an aided plan to provide higher accurate position when the quality of GPS signal is poor and useless.

Keywords GPS · Particle filter · EKF · Positioning accuracy

13.1 Introduction

At present, GPS has been used in various fields including military affairs, navigation, aviation, measurement, transportation and surveying, which involves all human activities associated with position, velocity and time. With the development of GPS,

E. Wang (✉) · M. Cai · T. Pang
School of Electronic and Information Engineering,
Shenyang Aerospace University, Shenyang, China
e-mail: wes2016@sau.edu.cn; wes2016@126.com

J. Sun et al. (eds.), *China Satellite Navigation Conference (CSNC) 2013 Proceedings*, Lecture Notes in Electrical Engineering 243,
DOI: 10.1007/978-3-642-37398-5_13,

it will be more widely used in the areas of aviation, marine and land vehicle navigation. In order to better service various application fields, improving the accuracy of GPS positioning, the technology of GPS receiver has always been the focus of GPS receiver.

In general, Kalman filtering algorithm can be used to process the positioning information of GPS receiver [1]. However, Kalman filtering generally require that the system observation model and dynamic model should be linear, and the measurement noise and dynamic model noise should be white gaussian noise. Due to the propagation characteristics of GPS signal, under some conditions, such as tall buildings and big trees, which might block GPS signal and reduce the number of satellite in view, and the effect of ground reflected multipath signals on GPS signal and the system error caused by receiver and antenna, the observational error distribution is not strictly the gaussian distribution [2]. Kalman filtering results will not have optimal filtering and prediction error will be worse. In recent years, particle filter based on sequential importance sampling and Monte Carlo is often used in non-linear and non-Gaussian system filtering. Because particle filter has not any restrictions of system process noise and measurement noise and completely overcomes the deficiencies of Kalman filter, it has been given abroad attention [3–5], and also used in GPS positioning filtering process [6].

In order to improve the accuracy of GPS positioning, the particle filter method is presented for the positioning data process of GPS receiver. The system dynamic state space model and observation model is established and the algorithm is described in detail. In order to better illustrate the effect of the particle filter algorithm, compared it with extended Kalman filter algorithm. The experimental results show that compared with the extended Kalman filter, particle filter algorithm can effectively reduce the error of position and speed of GPS positioning, and improve positioning accuracy, so its performance is better than extended Kalman filter algorithm.

13.2 Standard Particle Filter Algorithm

The standard principle of particle filter algorithm is that: First, based on the priori conditional distribution of system state vector the state space a group of random samples are generated, these samples called particles; then the particle weight and position of the particle distribution based on the measurement value are constantly adjusted, and initial priori conditional distribution are modified [7]. The algorithm is a recursive filtering algorithm, commonly used to handle non-Gaussian and nonlinear systems' state and parameter estimation. The huge computational burden is the bottleneck of particle filter algorithm.

The principal steps in the particle filter algorithm include:

(1) Initialization

Draw a set of particles for the priori $p(x_0)$ to obta$\{x_0^i\}_{i=1}^{N_s}$, the weight value of which is $\mathbf{1}/\mathbf{N_S}$.

(2) For k = 1,2,… performing the following steps:

- State prediction Priori particles from the proposal distribution $\{\mathbf{X}_{k|k-1}(i) : i = 1, 2, \ldots, N\} \sim p(\mathbf{X}_k|\mathbf{X}_{k-1})$.
- Update

Update the new weights at time k:

$$w_k^i = w_{k-1}^i p(z_k|x_k^i) = w_{k-1}^i p_{e_k}(z_k - h(x_k^i))$$

where, i = 1, 2, 3… N_s.
Normalize the weights:

$$\tilde{w}_k^i = w_k^i \Big/ \sum_{i=1}^{N_S} w_k^i, \sum_{i=1}^{N_S} \tilde{w}_k^i = 1$$

(3) Resampling

From a set of particles $\left(X_{k|k-1}^i, \tilde{w}_k^i\right)$, according to the value of the importance resampling, get a new set of particles $\left(\hat{X}_{k|k-1}^i, i = 1, \ldots, N\right)$

(4) Output

Output a set of particles that can be used to approximate the posterior distribution and the estimate as $\hat{x}_k \approx \sum_{i=1}^{N_s} \tilde{w}_k^i \hat{X}_{k|k-1}^i$

Then, k = k + 1, go to step (2).

13.3 Improving GPS Positioning Accuracy Based on Particle Filter

For GPS signal is in sight, it is easily to be blocked by objects such as tall buildings and big trees. In this case, GPS receiver positioning error will become larger or even GPS receiver will become useless, reducing the availability of positioning data. Moreover, the effect of ground reflected multipath signals on GPS signal and the system error caused by receiver and antenna will also lead to larger positioning error. Therefore, in its application, the biggest problem is the positioning error from the true position. The positioning accuracy of GPS is generally within 10 m, but sometimes positioning error can be more than 50 m [8]. For this reason, the particle filtering algorithm is used to improve the accuracy of GPS positioning.

13.3.1 Description of the Movement State

In practical applications, the output parameters of GPS receiver including latitude, longitude, speed, direction angle and so on. The system state equation and the system observation equation are set up according to the relation among the distance, speed and acceleration. Without any auxiliary equipment, the parameters of the algorithm only relies on GPS receiver output data, so the algorithm can be used for data processing such as cars, ships, aviation and other transport fields. Select the state variables

$$X = [x_e, v_e, a_e, x_n, v_n, a_n]^T$$

where x_e and x_n represent the location component of the east and north, v_e and v_n are eastward and northward velocity component, a_e and a_n are the acceleration component of east and north. The state equation of the continuous system is as follows.

$$\dot{X}(t) = AX(t) + U + W(t) \tag{13.1}$$

In Eq. (13.1),

$$A = \begin{bmatrix} 0 & 1 & 0 & 0 & 0 & 0 \\ 0 & 0 & 1 & 0 & 0 & 0 \\ 0 & 0 & -1/\tau_e & 0 & 0 & 0 \\ 0 & 0 & 0 & 0 & 1 & 0 \\ 0 & 0 & 0 & 0 & 0 & 1 \\ 0 & 0 & 0 & 0 & 0 & -1/\tau_n \end{bmatrix}$$

$$U = \begin{bmatrix} 0 \\ 0 \\ \frac{1}{\tau_e}\bar{a}_e \\ 0 \\ 0 \\ \frac{1}{\tau_n}\bar{a}_n \end{bmatrix}, \quad W(t) = \begin{bmatrix} 0 \\ 0 \\ \omega_e \\ 0 \\ 0 \\ \omega_n \end{bmatrix}$$

where ω_e, ω_n, $(0, \sigma_{a_e}^2)$ and $(0, \sigma_{a_n}^2)$ obey gaussian white noise distribution. τ_e and τ_n are the related time constant of eastward and northward acceleration change. $\bar{a}_e$ and $\bar{a}_n$ are the current average of acceleration component of east and north.

Set the sampling period T, discretize the continuous equation of system, and get the system discrete state equation:

$$X_k = \phi_{k,k-1}X_{k-1} + U_k + W_k \tag{13.2}$$

In Eq. (13.2),

$$X_k = [x_\varepsilon(k)\, v_\varepsilon(k)\, a_\varepsilon(k)\, x_n(k)\, v_n(k)\, a_n(k)]^T$$

$$\phi_{k,k-1} = diag\left\{\phi_{e(k,k-1)}, \phi_{n(k,k-1)}\right\}$$

Assume, $\alpha_e = \frac{1}{\tau_e}, \alpha_n = \frac{1}{\tau_n}$ then, $\phi_{e(k,k-1)}$ and $\phi_{n(k,k-1)}$ are respectively:

$$\phi_{e(k,k-1)} = \begin{bmatrix} 1 & T & \alpha_e^{-2}(-1+\alpha_e T + e^{-\alpha_e T}) \\ 0 & 1 & (1-e^{-\alpha_e T})\alpha_e^{-1} \\ 0 & 0 & e^{-\alpha_e T} \end{bmatrix}$$

$$\phi_{n(k,k-1)} = \begin{bmatrix} 1 & T & \alpha_n^{-2}(-1+\alpha_n T + e^{-\alpha_n T}) \\ 0 & 1 & (1-e^{-\alpha_n T})\alpha_n^{-1} \\ 0 & 0 & e^{-\alpha_n T} \end{bmatrix}$$

$$U_k = \begin{bmatrix} u_1 & u_2 & u_3 & u_4 & u_5 & u_6 \end{bmatrix}^T \tag{13.3}$$

In the Eq. (13.3),

$$u_1 = [-T + 0.5\alpha_e T^2 + (1-e^{-\alpha_e T})\alpha_e^{-1}]\alpha_e^{-1}\bar{a}_e$$

obey the gaussian white noise distribution

$$u_2 = \left[T - (1-e^{-\alpha_e T})\alpha_e^{-1}\right]\bar{a}_e$$

$$u_3 = (1-e^{-\alpha_e T})\bar{a}_e$$

$$u_4 = [-T + 0.5\alpha_n T^2 + (1-e^{-\alpha_n T})\alpha_n^{-1}]\alpha_n^{-1}\bar{a}_n$$

$$u_5 = \left[T - (1-e^{-\alpha_n T})\alpha_n^{-1}\right]\bar{a}_n$$

$$u_6 = (1-e^{-\alpha_n T})\bar{a}_n$$

$$W_k = [0\,0\,\omega_\varepsilon(k)\,0\,0\,\omega_n(k)]$$

where $\boldsymbol{\omega}_\varepsilon(k)$ and $\boldsymbol{\omega}_n(k)$ obey the gaussian white noise distribution, that is $\left(0, \sigma^2_{X_\varepsilon}\right)$, $\left(0, \sigma^2_{X_n}\right)$, $\left(0, \sigma^2_{a_e}\right)$ and $\left(0, \sigma^2_{a_n}\right)$. α_ε and α_n are the reciprocal of the related time constant of the eastward and northward acceleration rate of change. $\bar{a}_e$ and $\bar{a}_n$ are the current average of acceleration component of east and north.

13.4 Establishment of the Observation Equation

East location information z_e, north position information z_n, speed v and direction angle θ output by the GPS receiver are used as the measurement parameters. The vector described by.

$$Z = \begin{bmatrix} z_e & z_n & v & \theta \end{bmatrix}^T$$

Assume sampling period T = 1 s. Then, the relations between the measurement value and state parameters are described as follows:

$$z_e = x_e + \varepsilon_e$$

$$z_n = x_n + \varepsilon_n$$

$$v = \sqrt{v_e^2 + v_n^2} + \varepsilon_v$$

$$\theta = \arctan\frac{v_e}{v_n} + \varepsilon_\theta$$

Thus, the continuous observation equation is:

$$Z = \begin{bmatrix} z_e \\ z_n \\ v \\ \theta \end{bmatrix} = \begin{bmatrix} x_e \\ x_n \\ \sqrt{v_e^2 + v_n^2} \\ \arctan\frac{v_e}{v_n} \end{bmatrix} + \begin{bmatrix} \varepsilon_e \\ \varepsilon_n \\ \varepsilon_v \\ \varepsilon_\theta \end{bmatrix} \tag{13.4}$$

where ε_e and ε_n are the observation noise of east and north output by GPS receiver, which can be approximately used as $(0, \sigma_e^2), (0, \sigma_{\mathrm{n}}^2)$ gaussian white noise. ε_v and ε_θ are the observation noise of the speed and direction angle, which can be approximately used as $(0, \sigma_v^2), (0, \sigma_\theta^2)$ gaussian white noise distribution.

From the above equation, it is clear that the observation equation is non-linear, Linearize it by extended Kalman filter linearization, expand by Taylor series at the predictive value and ignore the second-order more items.

$$Z_k = h(\overset{\Lambda}{X}_{k,k-1}) + H_k(X_k - \overset{\Lambda}{X}_{k,k-1}) + V_k \tag{13.5}$$

To be simplified,

$$Z_k = H_k X_k + V_k + h(\overset{\Lambda}{X}_{k,k-1}) - H_k \,{}^{\Lambda}_{k,k-1} \tag{13.6}$$

where,

$$H_k = \left.\frac{\partial h(X_k)}{\partial X_k}\right|_{X_k = \overset{\Lambda}{X}_{k,k-1}} = \begin{bmatrix} 1 & 0 & 0 & 0 & 0 & 0 \\ 0 & 0 & 0 & 1 & 0 & 0 \\ 0 & h_1 & 0 & 0 & h_2 & 0 \\ 0 & h_3 & 0 & 0 & h_4 & 0 \end{bmatrix}$$

$$h_1 = \frac{v_e}{\sqrt{v_e^2 + v_n^2}},\ h_2 = \frac{v_n}{\sqrt{v_e^2 + v_n^2}},\ h_3 = \frac{v_n}{v_e^2 + v_n^2},\ h_4 = \frac{-v_e}{v_e^2 + v_n^2}$$

13.5 Experiments Test and Results Analysis

In order to verify the effect of particle filter algorithm, the u-blox RCB-4H GPS receiver is used as the experimental data acquisition equipment around the Shenyang Aerospace University playground oval track lap to collect data. The sampling frequency is set to 4 Hz, and the initial position of the GPS receiver is longitude 123°24.15436′, latitude 41°55.53523′, the initial speed is 0, the direction angle is 164.22°, and the data collection time is 5 min. The positioning accuracy of RCB-4H receiver is 2.5 m (CEP).

13.5.1 Experimental Data Process

First pretreat all the longitude and latitude data collected. Due to the relatively small movement range of GPS data acquisition system in the experiment, the longitude and latitude data gathered only changed in the decimal part, while its degree and integer part are the same. In order to make the results of the experiment more intuitive, and make it easy to calculate the procedure, the longitude and latitude data collected are processed as follows. Specifically, remove the data in front of the decimal point of latitude and longitude data, then expand the data after the decimal point 1,000 times. The velocity is converted to m/s unit. For example, a set of data is longitude 123°24.15436′, latitude 41°55.53523′, speed 1.046/s and direction angle 164.22°. The pretreatment data is longitude 154.36×10^{-3}, latitude 535.23×10^{-3}, speed 0.5381 m/s and direction angle 164.22°. The other data do as similar pretreatment.

13.5.2 Experimental Results and Analysis

The experimental data are processed using extended Kalman filter and particle filter. And particle filter algorithm selects 100 particles. The results are shown in Fig. 13.1.

In the Fig. 13.1, in the case of no measurement data available, the corresponding point A of EKF filter estimation is interrupted, but particle filter estimation is continuous. So the particle filter can make a correct state estimation based on previous experience, while EKF's effect is poor. Figures 13.2 and 13.3 demonstrate the estimate error curves in positioning latitude, longitude and speed between particle filter and extended Kalman filter.

Figures 13.2 and 13.3 show GPS positioning and speed estimation error of particle filtering algorithm is less than that of extended Kalman filter. Therefore, the performance of particle filter algorithm is better than extended Kalman filter.

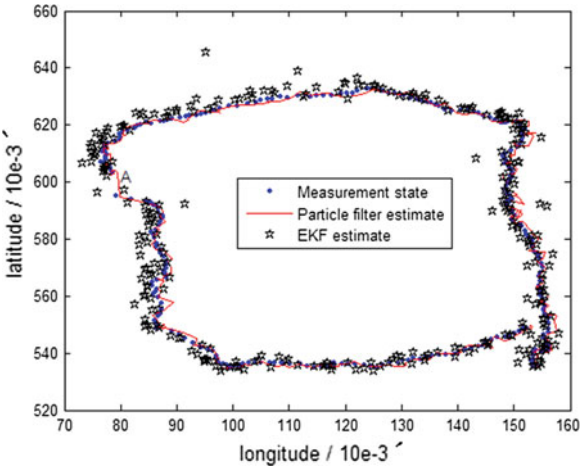

Fig. 13.1 Comparison of particle filter and EKF filter

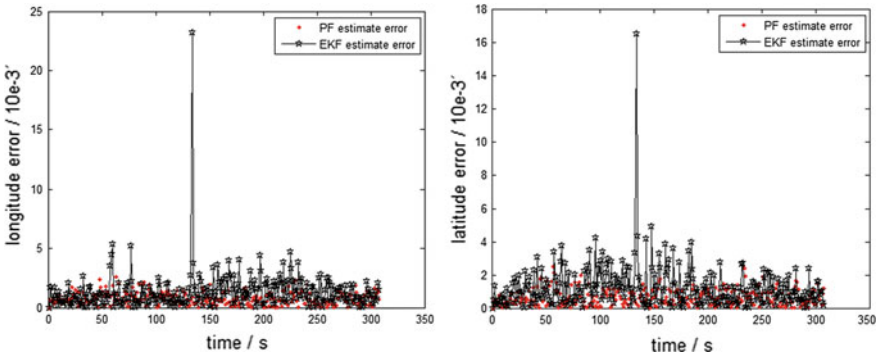

Fig. 13.2 Longitude and latitude estimation error of PF and EKF algorithm

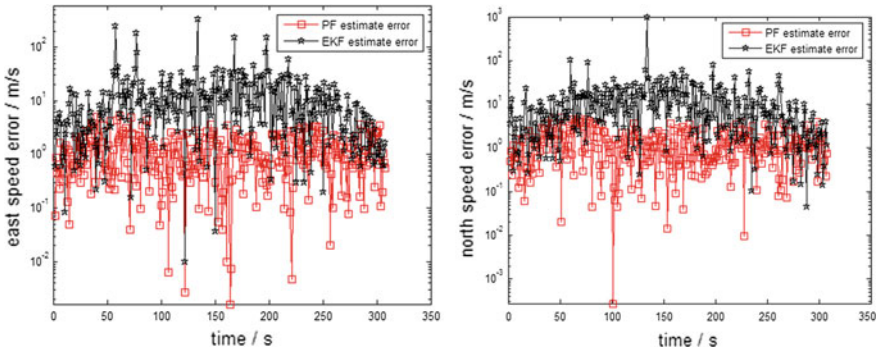

Fig. 13.3 East and north speed estimation error of PF and EKF algorithm

Table 13.1 Parameter comparison between particle filter and EKF algorithm

Algorithm	Particle number	Effective particle number	RMSE
PF	100	13.5815	2.79575
	200	15.1423	2.56044
EKF	–	–	8.9061

The accuracy of GPS positioning can be improved. The RMSE parameter comparison of experimental result between particle filter and EKF algorithm is given as shown in Table 13.1. From the table, it can be seen that the estimation accuracy of particle filter is better than that of EKF.

13.6 Conclusions

The particle filter algorithm is used to improve the accuracy of GPS positioning. The MCMC method is adapted for restraining particle degradation phenomenon. By establishing the dynamic state space model and using the real GPS data collected by GPS equipment. Compared to traditional Kalman filter algorithm, the algorithm handles nonlinear and non-Gaussian models more efficiently. The experimental results show that the effect of particle filter is better than that of extended Kalman filter, improving the accuracy of GPS positioning. Moreover, when the quality of GPS signal is poor or useless in a short time, the particle filtering algorithm can be an aided method to provide continual GPS positioning message. As a result, the particle filter algorithm is feasible and effective in improving the accuracy and increasing the availability of GPS positioning.

Acknowledgments This study is funded by National Natural Science Foundation of China (No.61101161), The Aeronautical Science Foundation of China (No. 2011ZC54010) and The Startup Foundation for Doctors of Liaoning Province (No.20101081).

References

1. Bahrami M, Ziebart M (2011) A Kalman filter based dopper-smoothing of code pseudoranges in GNSS challenged environments. In: Proceedings of the ION GNSS, Portland, pp 1–11
2. Sayim I, Pervan B, Pullen S, Enge P (2002) Experimental and theoretical results on the LAAS sigma overbound. In: Proceedings of the ION GPS, Portland, Oregon, pp 29–38
3. Zhou J, Yang Y, Zhang J, Edwan E (2011) Applying quaternion-based unscented particle filter on INS/GPS with field experiments. In: Proceedings of the ION GNSS, Portland, pp 1–14
4. Duong T-T, Chiang K-W (2011) Non-linear, non-Gaussian estimation for INS/GPS integration. In: Proceedings of the ION GNSS, Portland, pp 1–8
5. Pan P, Schonfeld D (2011) Video tracking based on sequential particle filtering on graphs. IEEE Trans Image Process 20(6):1641–1651

6. Gustafsson F, Gunnarsson F et al (2002) Particle filters for positioning, navigation, and tracking. IEEE Trans Signal Process 50(2)
7. Arulampalam MS, Maskell S, Gordon N, Clapp T (2002) A tutorial on particle filters for online nonlinear/non-Gaussian Bayesian tracking. IEEE Trans Signal Process 50(2):174–188
8. Kaplan E, Hegarty C (2006) Understanding GPS: principles and applications, 2nd edn. Artech House Inc, MA, pp 239–264

Chapter 14
The Design and Realization of Online Land Patrol System Based on CORS

Lili Shen, Lei Wang, Mengqi Wu and Xu Ding

Abstract Land patrol is very crucial to land resource management, land resource management not only face to huge amount of data, but also requires a concurrent and high accuracy data. The most popular technology for land resource management is remote sensing, but it constrained by the spatial and temporal resolution, lacking the ability to detect the illegal incidences occurred in particular, dispersed region, which is go against the land planning, utilizing, protection and management. GNSS based patrol technology can make up the shortage of remote sensing land monitoring technology. On another hand, continuous operational reference system (CORS) are widely used in many provinces and cities as urban infrastructure. Low-cost receiver can meet the requirement of land patrol with CORS aided. This paper presented the design and realization methods of a land patrol and monitoring service platform. In this system, low-cost GIS data collectors are applied to collect the spatial information, properties and even multi-media information of a land parcel, all these data are sent back to data centre according to the mobile network. Data centre can monitoring the status of data collectors, acquiring data. These data are processed, edited and checked, and then stored in the database or used to provide information service to the public. The system combined CORS positioning technology, GIS data management and wireless communication technology, allocated different authority to different role. This design makes managers can monitoring the fieldwork progress, fieldworkers can acquire the information of land parcel, and the public can access the information of their concern. The whole land patrol and data collecting, data processing procedures are paper-free, real-time, intelligence. The efficiency of fieldwork is improved, and the work strength is cut down and less professional skills are required for surveyors with this system.

L. Shen (✉) · L. Wang · M. Wu · X. Ding
School of Geodesy and Geomatics, Wuhan University, Wuhan, China
e-mail: llshen@sgg.whu.edu.cn

J. Sun et al. (eds.), *China Satellite Navigation Conference (CSNC) 2013 Proceedings*, Lecture Notes in Electrical Engineering 243,
DOI: 10.1007/978-3-642-37398-5_14,

Keywords Land patrol · CORS · Land management · Management system · System design

14.1 Introduction

Land patrol is very critical to land management. Land management need to deal with huge amount of data and have a high demand of uptodate situation and accuracy. Land management involves managing cultivated land, state owned land storage, sold land and other types of monitored land, preventing spare land and illegal land, achieving the aim of rational land utilization. Land patrol is the most directive and effective way to manage land for base land management departments and its efficiency may influence the management and utilization of land. Currently, remote sense (RS) is the most popular technique for land management, however, it restrict to its spatial resolution and temporal resolution. Especially remote sense is insensitive to sparse distributed and small scale illegal land utilization events, which is not good enough for land planning, utilization, protection and management. Global navigation satellite system (GNSS) positioning technique can make up the shortage of RS and provide precise coordinates and shape of interested land parcel. Hence, GNSS positioning technique play an important role in land patrol as well.

Wu et al. investigated vehicle-based land patrol system and proposed vehicle based 'moving-platform' relative positioning scheme to solve patrolling vehicle positioning problem [1]. The advantage of this method is that it applicable for large scale and multi-vehicle cooperative mission without base station. However, the coordinate of moving-platform is very difficult to precisely determine in real-time. Coordinate of vehicles subject to different moving-platform may existing systematic bias. Xi et al. studied PDA based land patrol technique [2], but the study focused on processing properties information and multi-media display. As developing of GNSS technique, RS technique geo-information system (GIS) technique and communication technique, the land patrol technique changed dramatically as well. This paper presents a multi-propose land patrol service system with continuous operation reference system (CORS) [3] aided positioning technique, which assembles RS, GIS and communication technique. The system utilize inverse network real-time differential (RTD) technique for positioning, utilize remote sense image for land utilization change analysis, and utilize GIS technique for land information management. The system provides evidence for decision making and enforcing the land law, which improves land management efficiency.

14.2 System Design and Implement

The land patrol system is an enhancement of GPSNet software. The basic idea of the system is adding a patrol server between field user and GPSNet server. The patrol server acts as a middle server who connects field user, Web browser and

GPSNet server. Field users can upload raw GNSS observations to the patrol server, the patrol server processes these observations and output inverse RTD solution, after transform field user coordinate to local coordinate system, the final solution was broadcast to user via wireless network. The scheme encrypts local coordinate system transformation parameters, and simplifies field user devices. Meanwhile, administrator of the system can assign new patrol mission to field users via browser, monitor field user status and analyze field data. Field worker can connect to patrol server to download new mission via field terminal. The whole system ensures the land patrol process efficient.

The system makes up by three modules.

The first module is an extension of CORS server. This module is a client/server scheme, each field user own a unique connection to the server for GNSS observation and multimedia data delivery. This CORS extension server can decode received data. Extracted GNSS observation was combined with information from CORS system to generate final positioning solution and Extracted multimedia information was saved in the database. Then, the module broadcast the final positioning solution to field users again via wireless network.

The second module is the major part of the system, which is a web server called patrol server. The patrol server supports all web services including administrator's interface and field user's interface. Meanwhile, the patrol server shares database with CORS extension module, which enables administrators monitor field work status.

The third module is embedded into handheld devices. The function of embedded module is fourfold: the first function is that the module can setup a wireless connection to CORS extension server to deliver GNSS observation and multimedia data. Furthermore, the module can receive the final positioning results and display them on the map. The third function of the module is updating land parcel information and synchronizing information with the database. Finally, the handheld device can browse webpage and download new mission from patrol server.

The structure of the system can be shown as Fig. 14.1.

14.2.1 The System Layer Scheme

In order to make the system stable, extendable and efficient, the system is divided into three layers: display layer, logical layer and data layer. The triple layer scheme is demonstrated in Fig. 14.2. Function of each layer can be described as follows:

Presentation layer: the presentation layer includes administrator's interface and field user's interface. This layer supported by web server and embedded module. The function of this layer includes system configuration, coordinate display, mission distribution et al.

Logical layer: the logical layer responds requests from both administrators and field users. Function of logical layer includes wireless communication with field

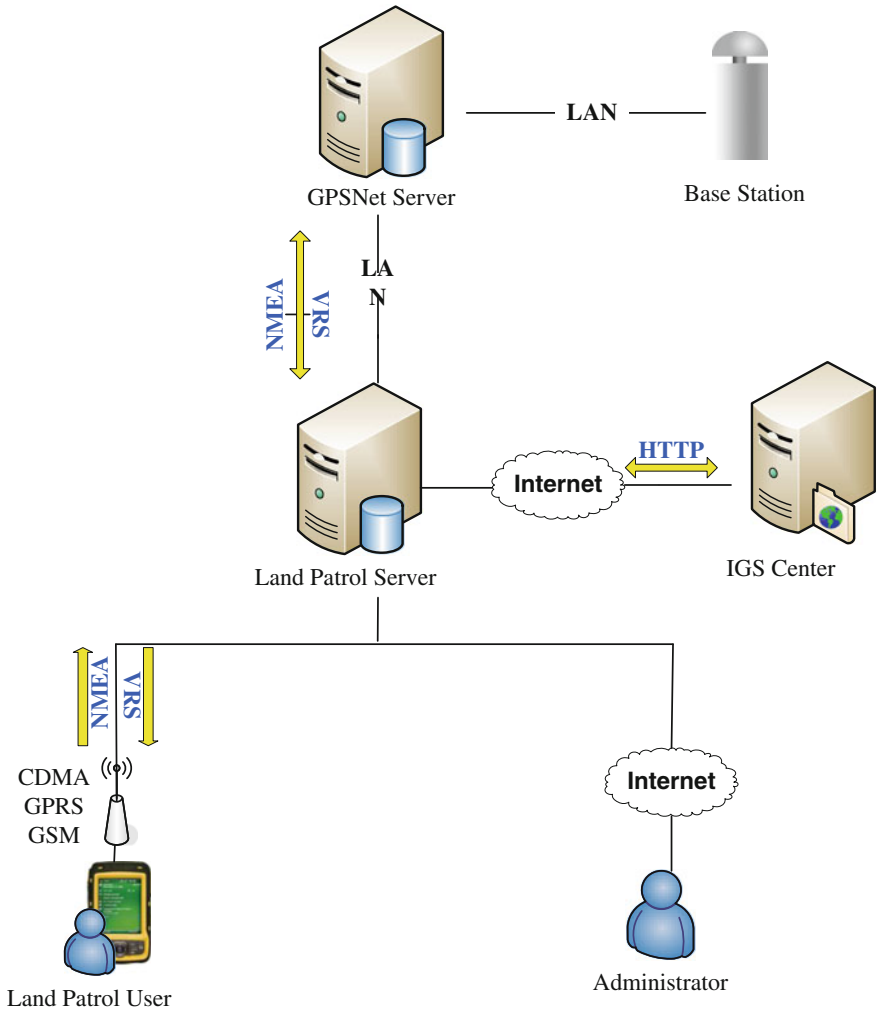

Fig. 14.1 The logic structure of the online land patrol system

users, inverse RTD data process, database manipulation, system event logging and web requests responding.

Data layer: the data layer is used to define, maintain, access and update database to support logical layer and display layer. As patrol server and CORS extension server share the database, the data layer become extremely important to make system stable.

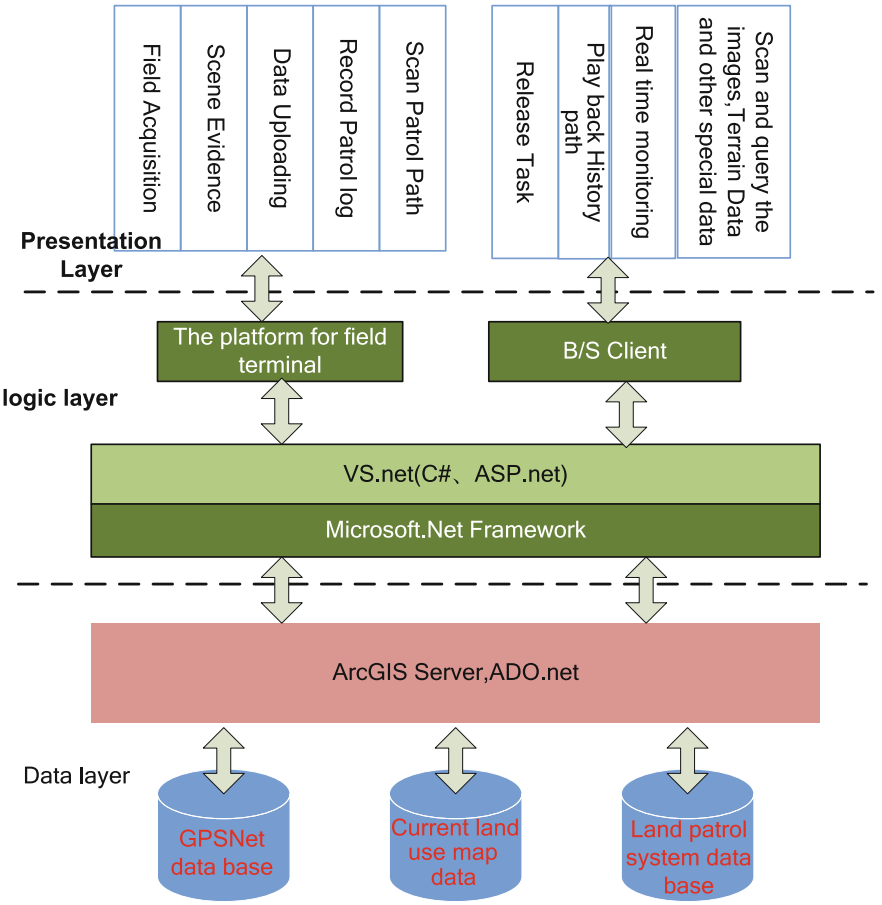

Fig. 14.2 The layer scheme of the online land patrol system

14.2.2 Role Definition and Access Control

According to user's mission type, two different role are designed in the system.

Field users use handheld devices, their tasks are collecting spatial data and property data. They can download patrol mission from embedded web browser, and communicate with CORS extension server. Field user interest in their mission-related information, such as new patrol mission, mission related land parcel information and their own patrol trace et al. Administrator can configure the system, monitor field user [4], assign mission and analysis spatial data. Most administrative work can be finished via web server, and field users only access module embedded in handheld device. Different roles have different permission to access the system, which makes the system safe and extendable.

14.2.3 Technical Routine

Download patrol mission: Land usage change can identified by various ways, such as enforcement department investigation, checking remote sense image, public report, transferred law case, leader specify et al. Administrators will publish the newest mission information on the website and assign these missions to field patroller. Each patrol can check the missions like checking email.

Investigation and taking evidence: patroller holds handheld devices to crime scene and record shape of land parcel and collecting multimedia information as evidence. Handheld devices can send back the spatial information and property information of certain land parcel to server, additional evidences such as photo, videos et al. will be send back as well [9].

Upload data and Monitoring: all GNSS position result, patrol trace and investigation data will be uploaded to the server and displayed on the handheld devices. Hence, administrator can monitor patrollers via the system, and the patrollers can enquire the current position, patrol trace, uploaded investigation data as well.

Data post-processing: After patrolling, collected spatial information, property information, multimedia information as well as other evidence will be organized and analyzed, the collected data will be compared with land usage planning, latest remote sensing image and relative policies to undertake qualitative and quantitative analyze. The final patrol report will be formed based on analyze results (Fig. 14.3).

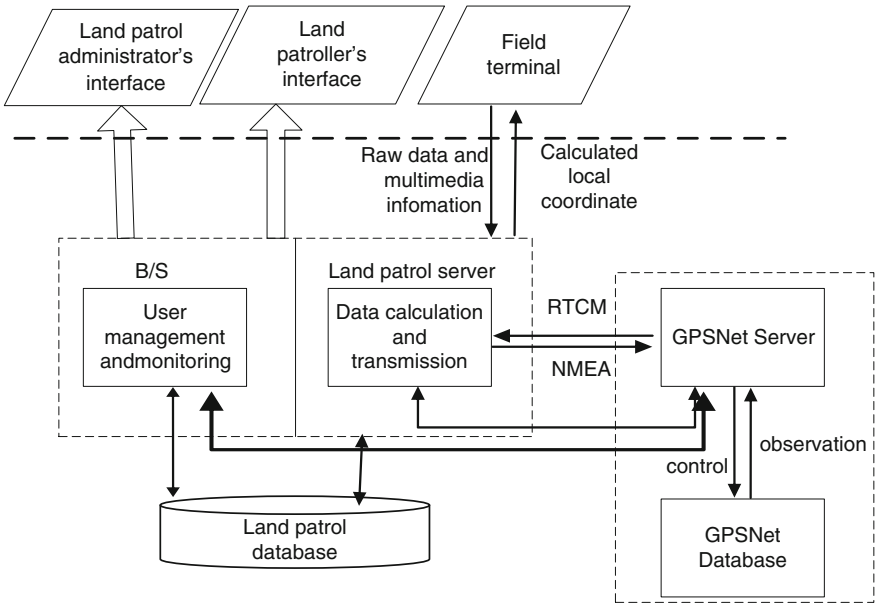

Fig. 14.3 The dataflow diagram of the online land patrol system

14.2.4 System Implementation

The system including three modules and it adopt a hybrid of B/S scheme and C/S scheme. All spatial data and property data are stored in SQL2008 database, and ArcSDE is adopted as spatial analysis engine. All geometry-related modification, analysis and enquiry are handled by the spatial analysis engine. As the system involves communication, web services and database manipulation, dot net framework is chosen, and C# is chosen as the developing language. Embedded module was a secondary development based on ArcPad package. ArcPad package can smoothly interactive with ArcSDE and help patrollers update land parcel informations. Zhonghaida Q5 GIS data collector was chosen as the handheld device, the GNSS observations was delivered back to server in raw OEM format, and the CORS extension module can decode the binary format and extract valid observations for coordinate calculation.

14.3 Key Technique

Developing a multi-propose platform requires multi-discipline knowledge. The system integrated GNSS positioning technique, GIS data management, Web service, wireless communication technique et al. The key techniques of implying the system are summarized in this section.

14.3.1 Inverse RTD Technique Based on CORS

Land patrol is sparse distributed field measurement work. However, it doesn't require centimetre accuracy. In order to acquire decimetre positioning accuracy and encrypt local coordinate system parameter, the system adopts inverse network RTD technique. Single base RTD technique broadcasts code corrections to rover receiver, the longest distance between rover and base station can be several kilometres, which is too small for land patrol. Network based RTD technique is very similar to network RTK technique, but only code observation are transferred to rover station. Double differenced observations are formed with rover station code observation and virtual reference station (VRS) code observation, corresponding ultra rapid IGS precise ephemeris are downloaded to calculate rover coordinates. Another advantage of inverse network RTD technique is easily encrypt local coordinate parameters, as user coordinates will be transformed to local coordinate system in CORS extension module, the field users don't care the local coordinate system transformation parameters, they acquires local coordinates from server and display the coordinates in corresponding electronic map.

Comparing to single station RTD technique, Network RTD technique can share the coordinate easily, moreover, it suitable for low cost devices. Inverse network RTD technique enables server monitor multi rover users. Multi rovers cooperate more efficient under server's supervision. Network RTD technique require the same data flow as single station RTD technique, but network based RTD technique is suitable for lower cost hardware and cooperative field work. Inverse RTD handheld devices don't require high performance CPU to real-time GPS positioning calculation, which can cut off handheld device cost.

14.3.2 GIS Land Information Management Technique

Land patrol data including vector geometry data, remote sense image from various sensors, hence, these spatial data need a unified spatial database engine to manage them. In order to support web application and spatial data management, ArcGIS server was chosen as the foundation of patrol server. ArcGIS server enables administrators analyzing spatial data via web browser and multi source spatial data management. Secondary development based on ArcGIS server makes patrol more suitable for land patrol application. Land utilization map, Land utilization planning map, remote sense images as well as vector geometries collected by GNSS positioning technique are transformed into a unified platform, which makes the system more efficient and extendable [5, 6].

14.3.3 Communication Technique

Communication is extremely important in the land patrol system, especially with inverse RTD technique. Communication between handheld devices and CORS extension server are realized by mobile wireless network. Currently, code division multiple access (CDMA) [7] or general packet radio service (GPRS) [8] are available for long distance wireless communication. Handheld devices connect to server by specifying IP address and port of the CORS extension server. Handheld devices communication includes sending back GNSS observation to CORS extension server and hypertext transfer protocol (HTTP) request to the patrol server. The formal one was realized by TCP connection, handheld devices sending data to the specified port, server listening and decoding. The later one includes patrol mission download, and realized by standard browser/server communication. Communication between CORS extension server and patrol server was realized by sharing database. CORS extension server write new coordinate into database and patrol server read latest coordinates to monitor field users. AJAX technique was used to real-time update latest field user coordinate on the browser.

14.4 Concluding Remarks

The system integrated mobile devices developing, GIS developing, Web application developing and GNSS positioning. Three modules cooperate each other to make the whole process more efficient, the system can satisfy both administrators and field users demands in land patrol. Field user's work was cut off by handheld devices and wireless communication. Administrators can monitor fieldwork, encrypt coordinate system parameters and finish all work on the web application. Hopefully, the system can improve land patrol efficient, make effort on protect land resources and monitoring illegal land use. With the system, the quality of land enforcement services can be greatly improved.

References

1. Wu X, Wang Q, Li C, Liang H (2009) Study and implementation of the key techniques of land inspection vehicle. Bull Surveying Mapp 3:P56–P58
2. Zhou X, Ju J, Liu G (2010) The design and dynamic implementation of land law enforcement dynamic inspection system based on PDA. Urban Geotech Inv Surveying 6:P71–P73
3. Liu J, Liu H (2003) Continuous operational reference system infrastructure of urban spatial data. Geomatics Inf Sci Wuhan Univ 28(3):P259–P264
4. Jiang Y, He T, Ming T, Li C (2010) The overall design of the land and resources mobile patrol system based on GPS, GIS and mobile communication technologies. Bull Surveying Mapp 6:P65–P68
5. Yang Y, Wang J, Jia H (2009) Research and realization of land law enforcement and monitoring geographic information system. Sci Technol Inf 17:P438–P439
6. Han J (2007) On the key technology of land monitoring and management information system based on GIS. Bull Surveying Mapp 6:P58–P60
7. Su A (2006) Study on RTK differential data transmitting technic based on CDMA. J Northeast Agric Univ 37(4):P516–P520
8. Su A, Li H, Liu X (2006) Applied research on GPRS wireless data transmitting technic used in VrsRTK system. Eng Surveying Mapp 15(4):20–23
9. Sheng R, Liu Y, Wang Q, Li C (2009) Research on land use visitation system based on GPS/RS/GIS. Sci Surveying Mapp 34(2):P103–P105

Chapter 15
Multipath Delay Weaken in Complex Situation

Xiang Lin, Zhiyun Han, Feng Zhou and Siyuan Guo

Abstract In order to decrease code and carrier phase error influence on distance measurement efficiently, it is used to applied multipath reduction techniques such as narrow correlator to eliminate estimation error when signal propagation in indoor space. However, these techniques depends heavily on the delayed value of autocorrelation peak. In this paper, an improved Projection Onto Convex Set algorithm (POCS) is discussed that estimate the effect the elimination of spurious noise peaks by using adaptive threshold in the Channel Impulse Response (CIR). Finally, a test was taken for pseudo-range estimation reduction in urban environment.

Keywords Projection Onto Convex Set algorithm · Adaptive threshold · Channel Impulse Response

15.1 Introduction

Accurately estimation between the locally PRN codes and the signals arriving from different satellites is much important for distance computation in global navigation satellite system. However, various signals superimposed in waveforms

X. Lin (✉) · F. Zhou · S. Guo
Beijing Satellite Navigation Center, Beijing 5128, China
e-mail: stationeffie@yahoo.cn

F. Zhou
e-mail: zhoufeng@163.com

S. Guo
e-mail: guosiyuan0714@yahoo.com.cn

Z. Han
China Space Technology Institute, Beijing, China
e-mail: stationeffie@yahoo.cn

J. Sun et al. (eds.), *China Satellite Navigation Conference (CSNC) 2013 Proceedings*, Lecture Notes in Electrical Engineering 243,
DOI: 10.1007/978-3-642-37398-5_15,

because of the multipath effect, produce a variety of different code delay and random phase. Although much relative error of the global navigation satellite system can be calculated using the differential correction technology, the multipath phenomenon depends on the local environmental factors, not through the differential treatment. Therefore multipath effect is a much important element for pseudo-range calculation error [1].

In this paper, a improved POCS algorithm is introduced which evaluated the channel impulse using the method of adaptive threshold to remove spurious peaks in each iteration time. After calculating the channel impulse response, the arrival time of multipath signal is starting from the first signal passing threshold, whenever the signal is blocked, the first road of multipath signal arrived can be used to calculate the pseudo-range delay. Similarly, the phase shift can be calculated by correlation phase discrimination function.

15.2 Mathematical Model

The channel impulse response model in a specular multipath situation can be expressed as [2]

$$h(t) = \sum_{k=1}^{N} a_k \delta(t - t_k). \tag{15.1}$$

where $h(t)$ is the function of CIR, N is the number of signal paths, a_k $(a_k < 1)$ is the complex attenuation factor of the k-th path. Because the received signal is the output of the multipath channel in response to the transmitted signal $s(t)$, it can be expressed as:

$$r(t) = h(t) \otimes s(t) + n(t) = \sum_{k=1}^{N} a_k s(t - t_k) + n(t). \tag{15.2}$$

$r(t)$ is the multipath error affected signal function, $n(t)$ is the channel additive white Gaussian noise and $\otimes$ denotes the convolution operation.

15.3 Error Estimation

Prior to dispreading, received GPS signal power is smaller than the noise. Compositing the received baseband signal into Eq. (15.2), the output signal $C(\tau)$ can be represented as followed ($b(\tau)$ means the channel impulse response):

$$C(\tau) = b(\tau) \otimes h(\tau) = \sum_{k-1}^{N} b(\tau - t_k)h_k + u(\tau) \tag{15.3}$$

$$b(\tau) = \frac{1}{T}\int_T s(t)s(t-\tau)dt \tag{15.4}$$

T means the code period, and $u(\tau)$ means the noise element in the output of the integration process. Equation (15.3) can be written as:

$$C = Bh + u \tag{15.5}$$

where $C = C[C_1 \ldots C_M]^T$ is the vector of samples of the matched filter output and B is

$$B = \begin{bmatrix} b(\tau_1 - t_1) & \cdots & b(\tau_1 - t_N) \\ \vdots & \ddots & \vdots \\ b(\tau_M - t_1) & \cdots & b(\tau_M - t_N) \end{bmatrix} \tag{15.6}$$

where $h = [h_1, \ldots h_N]$ is the true channel vector while t_1 means the true path delays. The vector u contains the samples of the complex noise in harsh environment.

15.4 Multipath Analyze

The least square method (L) is the most common method of channel vector calculation now, minimizing the square error $\left(\|C - Bh\|^2\right)$ as

$$\hat{h}_L = \left(B^T B\right)^{-1} B^T C. \tag{15.7}$$

where the superscript T means a matrix transpose. $\hat{h}_{\min}$ means the minimized squared error as ($\hat{\sigma}^2$ denotes the estimated noise variance):

$$\hat{h}_{\min} = \left(\hat{\sigma}^2 I + B^T B\right)^{-1} B^T C \tag{15.8}$$

The POCS approach is an iterative constraint-based deconvolution approach which evaluated the CIR by iterating Eq. (15.8) as [3]

$$\hat{h}_P^{(i)} = \hat{h}_P^{(i-1)} + \left(\hat{\sigma}^2 I + B^T B\right)^{-1} B^T C\left(C - B\hat{h}_P^{(i-1)}\right) \tag{15.9}$$

Here, $\hat{h}_P^{(i)}$ is the i-th estimated CIR. Equation (15.8) is used for initialization. The required number of iterations relies on the SNR level. Lower SNRs needs

larger number of iterations. Therefore, interference components of the signal is the key to solve the problem. The interference components in each signal can be applied to the related, POCS while find the relevant factors in each projection. Supposed Q is a parameter in modeling equation, then the projection onto convex sets with respect to the formula (15.10) can be expressed as:

$$\hat{h}_P = Q\{\hat{h}\} \tag{15.10}$$

If the interference factor can be effectively suppressed by computing the limited error variance or narrow value interval, Fig. 15.1 shows a diagram of the receiver implementing the POCS method. it should be noted that as the sampling rate is limited, the estimated CIR may not be ideal as Eq. (15.10). In order to perform a limited bandwidth, the estimated CIR can be expressed as follows [4]:

$$\hat{h}(t) = \sum_{k=1}^{N} \hat{a}(k) f_s \left[\frac{\sin(\pi(t - \hat{t}_k) f_s)}{\pi(t - \hat{t}_k) f_s} \right] \tag{15.11}$$

a_k is the complex attenuation factor of the k-th path. f is the sampling rate. Figure 15.2 show the magnitude of the estimated CIR in POCS algorithm respectively.

The LOS code delay can be used as a channel impulse response vector which reflects the maximum amplitude value. It can be expressed as:

$$\hat{\tau}_P = \arg\max_{\tau} \left| \hat{h}_P \right| \tag{15.12}$$

Here, $\hat{\tau}_P$ means the amplitude of CIR. When the LOS delay has been determined, the LOS phase offset is computed from the corresponding complex channel coefficient by applying a proper phase discriminator.

$$f = \left(\sum_{i=k/2}^{k/2} \hat{h}_P^i \left(\hat{h}_P^i \right)^{\lambda} + \frac{\sigma_n^s}{\omega} I \right) \hat{h}_P \tag{15.13}$$

where $\hat{h}_P^i$ is $\hat{h}_P$ shifted by i steps, K is the number of filter taps and s is a constant (Fig. 15.3).

15.5 Improved POCS

The Improved POCS algorithms with the conventional differs in the following aspects:

1. In the novel projection algorithm, author estimate the effect of CIR by adaptive threshold to eliminate the false peaks of signal. Supposed the threshold was $x\overline{z}$:

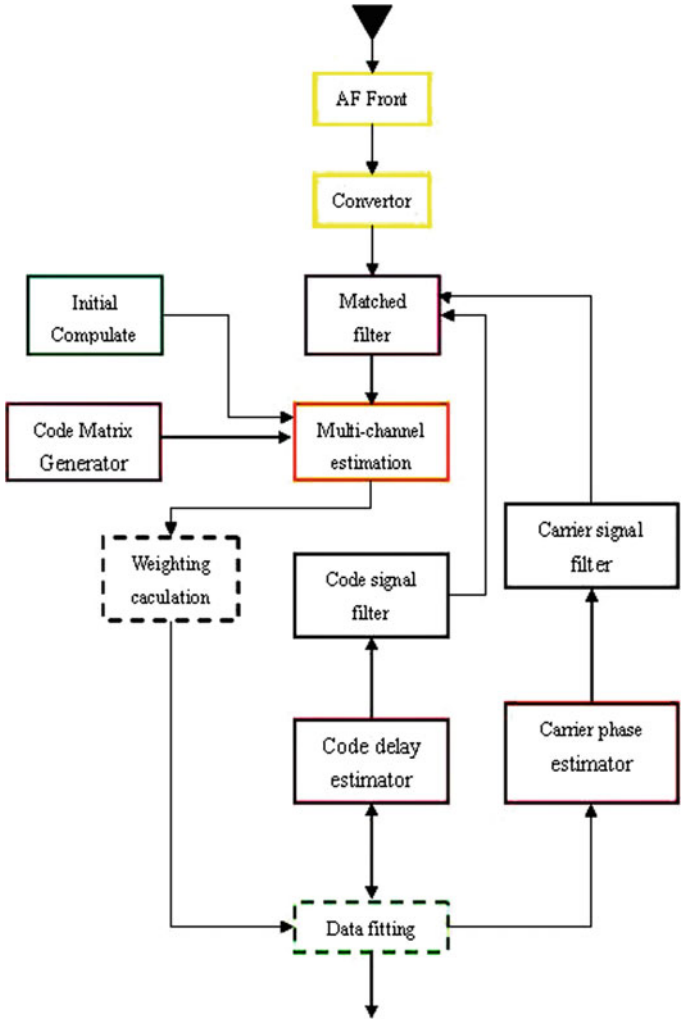

Fig. 15.1 POCS method computation diagram

$$\overline{z} = \frac{1}{N}\sum_{k=1}^{N} \hat{h}_P(x) \Big/ \max\left\{\hat{h}_P(x)\right\} \tag{15.14}$$

Here, the threshold is set as $s = \min\{x_z\overline{z}, 1\}$. In all the simulations presented in this paper, x_z was set to 2.5.

2. In preview, estimation accuracy of POCS depend on the rate of signal sampling. However, the rates of signal sampling is limited in experiment. That is to say, Some real channel impulse signal is not included. In case, the larger value

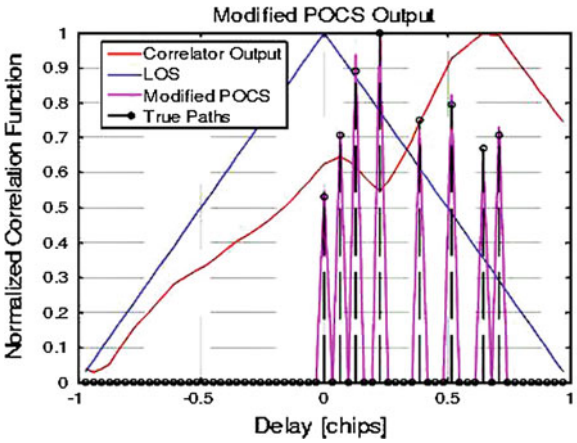

Fig. 15.2 Estimated CIR magnitude in multipath environment

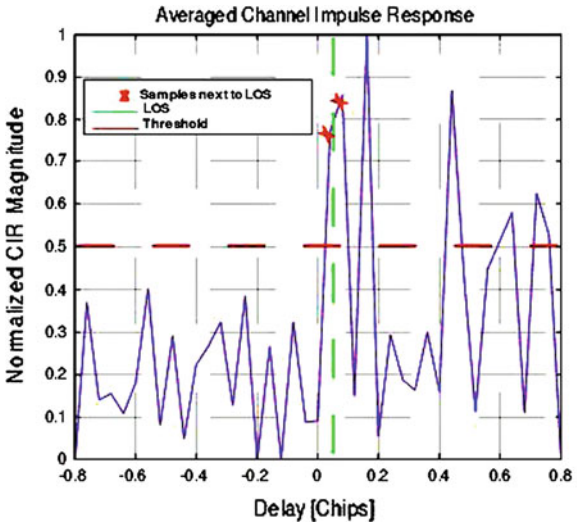

Fig. 15.3 Accuracy of TOA estimation variation tendency

of both sides' sampling-single can be indicated the true channel component. Figure 15.4 depicts such a method.

In order to increase the accuracy of the new algorithms, we do the linear combination of sample signal and LOS:

$$\begin{aligned} &\text{If } |r_{ae}(m_i-1)| > |r_{ae}(m_i+1)| \\ &\varepsilon = (m_i-1) + \frac{|r_{ae}(m_i)|}{|r_{ae}(m_i-1)|+|r_{ae}(m_i)|} samp - signal \end{aligned} \tag{15.15}$$

$$\begin{aligned} &\text{If } |r_{ae}(m_i-1)| < |r_{ae}(m_i+1)| \\ &\varepsilon = (m_i) + \frac{|r_{ae}(m_i)|}{|r_{ae}(m_i-1)|+|r_{ae}(m_i)|} samp - signal \end{aligned} \tag{15.16}$$

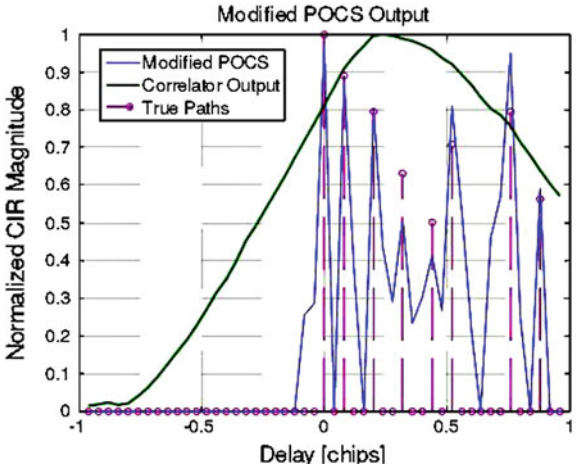

Fig. 15.4 Hardware simulator data CIR estimated diagram

Here, r_{ae} the channel impulse response average random time; m_i show the corresponds indicator with code signal.

15.6 Simulation Result

In this paper, author verify the performance of algorithms using the GSS7700 simulator for several simulations. The RF signal from simulator via Low-noise Amplifier to Signal acquisition unit that sampling signal in 25 MHZ. The estimated channel impulse response for the GSS7700 hardware simulator is depicted in Fig. 15.4. In this figure, the path attenuation factors can be optional selected from a range of 0–6 dB. It can be known that the estimated channel parameters by the improved POCS is consistent with the reality.

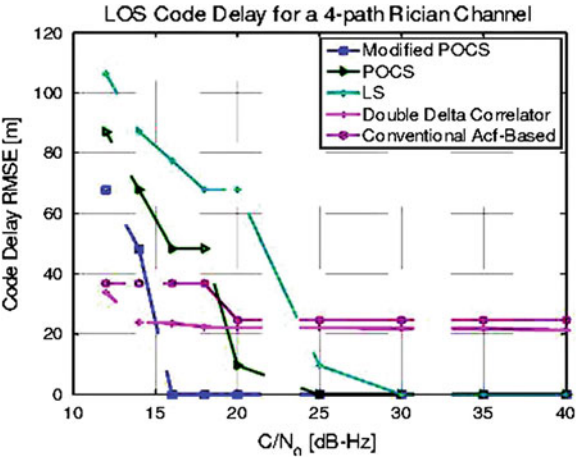

Fig. 15.5 Code phase estimation errors in different algorithms

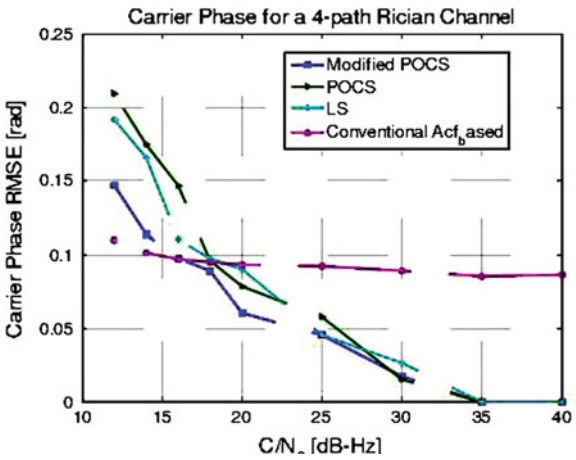

Fig. 15.6 Carrier phase estimation errors in different algorithms

In Figs. 15.5 and 15.6, properties of some different estimation is showed in the 4-path channel allocation. The correlators space 0.07 chip triangle each other.

It is observed from these figures that at low values of C/N0 (<20 dB), the improved POCS algorithm perform much better than the conventional POCS estimator. In the case of this simulation, the maximum magnitude of the auto-correlation function was close to the true LOS.

15.7 Conclusions

In this paper, author introduce a improved POCS algorithm for code and carrier phase delay estimation. It can be known apparently that the improved POCS algorithm outperforms the conventional POCS at low SNR from the figure. The simulation results illustrate that compared to the conventional error-eliminate techniques, the improved POCS algorithm can decreases the error in the position-fixed obviously also.

References

1. Pahlavan K, Krishnamurthy P (1998) Wideband radio propagation modeling for indoor geolocation applications. IEEE Commun Mag 36:60–65
2. Dragunas K (2010) Indoor multipath mitigation. International Conference on Indoor Positioning and Indoor Navigation, IPIN 2010, IEEE Press, Zürich, pp 578–584, 15–17 Sep 2010
3. Kostic Z, Pavlovic G (1993) Resolving subchip spaced multipath components in CDMA communication systems. Vehicular Technology Conference, 1993 IEEE 43rd, May, pp 469–472
4. Yang C, Porter A (2005) Frequency-domain characterization of GPS multipath for estimation thand mitigation. ION GNSS 18 International Technical Meeting of the Satellite Division, Long, Beach, California, pp 2104–2118, Sep 13–16 2005

Chapter 16
Performance of Triple-Frequency High-Precision RTK Positioning with Compass

Hairong Guo, Jinlong Li, Junyi Xu, Haibo He and Aibing Wang

Abstract Compass is the first satellite navigation system providing the triple-frequency service in the world, and its triple-frequency carrier phase observations have obvious advantages on high-precision RTK positioning. In order to verify the success rate and reliability of Beidou triple frequency ambiguity resolution, the high-precision RTK positioning has been performed for Beidou/GPS observations by using geometry mode and geometry-free ambiguity resolutions. The results showed that, (1) By using geometry ambiguity resolutions, the success rate and reliability of ambiguity resolution for Beidou single-frequency, dual-frequency and triple-frequency RTK positioning is much better than that of GPS. (2) The accuracy of triple-frequency RTK positioning can reached centimeter level by using geometry-free ambiguity resolutions, and the method is not limited to baseline length. (3) When Beidou/GPS are combined, the position accuracy, success rate and reliability will be improved obviously, especially when the elevation angle is high or the signal is shielded.

Keywords Beidou · RTK · Triple-frequency carrier phase · Ambiguity resolution · Geometry mode · Geometry-free mode

H. Guo (✉) · H. He · A. Wang
Beijing Satellite Navigation Center, Beijing 100094, China
e-mail: hairongguo@263.net

J. Li · J. Xu
Institute of Surveying and Mapping, Information Engeering University, Zhengzhou 450052, China

J. Sun et al. (eds.), *China Satellite Navigation Conference (CSNC) 2013 Proceedings*, Lecture Notes in Electrical Engineering 243,
DOI: 10.1007/978-3-642-37398-5_16,

16.1 Introduction

The constellation of Compass satellite navigation system (first phase) consists of 14 satellites, including 5 GEO satellites, 5 IGSO satellites and 4 MEO satellites. The open service and authorized service will be provided at B1(1561.098 MHz), B2(1207.14 MHz) and B3(1268.52 MHz). The system will be full operated in 2012, and it shall be the first system which provides triple-frequency signals.

Centimeter-level RTK results can be achieved by using GNSS RTK technology which has already been widely applied in reference surveying, terrain surveying, cadastral surveying, GIS mapping and so on. One of the key problems for RTK positioning is the resolution of integer carrier ambiguity. Six or more satellites are needed for dual-frequency ambiguity resolution. In city areas, the number of visible satellites is fewer due to the shielding of high building. And then the applications of dual-frequency RTK positioning will be limited. However, fewer satellites are needed for triple-frequency ambiguity resolution. The integer ambiguity can be resolved successfully even when there are only four satellites. So the application scope of high-precision surveying will be extended with the triple-frequency RTK positioning technique.

The methods for the triple-frequency ambiguity resolution can generally be categorized in two kinds. The first kind is based on the geometry-free mode, such as TCAR and CIR. The other kind is based on geometry mode, such as the LAMBDA method. The successful rate of the two kinds is close for the short baselines [1–11]. The comparison of the dual-frequency and triple-frequency ambiguity resolution with the LAMBDA method shows that the triple-frequency carrier phase of Compass will have the big advantage in precision surveying.

16.2 Compass Triple-Frequency Ambiguity Resolution

16.2.1 Geometry Mode Based Ambiguity Resolution

For short baselines, the effect of satellite position errors, the ionosphere delay errors and troposphere delay errors is pretty small after the double-difference operation, the multi-path effect and the measurement errors, which is amplified by the difference operation, become the main error sources [1]. The triple-frequency double-difference observation equation can be expressed as,

$$\begin{aligned} \nabla\Delta P_i^j &= \nabla\Delta\rho + \nabla\Delta\varepsilon_{P_j^i} \\ \nabla\Delta\Phi^i{}_j &= \nabla\Delta\rho + \nabla\Delta N^i{}_j\lambda_j + \nabla\Delta\varepsilon_{\Phi_j^i} \end{aligned} \tag{16.1}$$

where,

The superscript i	Means the index of the satellite,
The subscript $j = 1, 2, 3$	Refers to the related carrier B_i,

P_j	Is the pseudo-range measurement of the carrier B_i (m),
Φ_j	Is the carrier phase measurement of the carrier B_i (m),
λ_j	Is the wavelength of the carrier of the carrier B_i (m),
N_j	Is the integer ambiguity of the carrier B_i (cycle),
ε_{P_j} and ε_{Φ_j}	Are the measurement noise of pseudo-range and carrier phase of the carrier B_i respectively (m)

After the linearization of the double-difference observation equation, the error equation can be written as,

$$v = (A_1\, A_2) \cdot \begin{pmatrix} X \\ a \end{pmatrix} - (\underbrace{L - f(X^0, a^0)}_{l}) \tag{16.2}$$

where,

v	Refers to the $(n-1)$ residual vector of the six kinds of double-difference measurements, n is the number of the satellites
X and X^0	Are the correction value and approximate value of position vector respectively
a and a^0	Are the correction value and approximate value of integer ambiguity vector respectively
A_1 and A_2	Are the sub-matrix of design matrix A with respect to the position parameters X and the integer ambiguity parameters a respectively
L	Is the observation vector
$f(\cdot)$	Means the function model of the observation L $l = L - f(X^0, a^0)$.

The target function is

$$\Omega = (l - A_1X - A_2a)^T P(l - A_1X - A_2a) = \min\, a \in Z^m\, X \in R^n \tag{16.3}$$

The normal equation can be written as

$$\begin{pmatrix} A_1^T PA_1 & A_1^T PA_2 \\ A_2^T PA_1 & A_2^T PA_2 \end{pmatrix} \cdot \begin{pmatrix} \widehat{X} \\ \widehat{a} \end{pmatrix} = \begin{pmatrix} A_1^T Pl \\ A_2^T Pl \end{pmatrix} \tag{16.4}$$

The above formula can be simplified as

$$\begin{pmatrix} N_{11} & N_{12} \\ N_{21} & N_{22} \end{pmatrix} \cdot \begin{pmatrix} \widehat{X} \\ \widehat{a} \end{pmatrix} = \begin{pmatrix} U_1 \\ U_2 \end{pmatrix} \tag{16.5}$$

where, P refers to the weight of the observations.

The value of X, a and their covariance matrix can be get,

$$\begin{aligned}
\widehat{a} &= (N_{22} - N_{21}N_{11}^{-1}N_{12})^{-1} \cdot (U_2 - N_{21}N_{11}^{-1}U_1) \\
\Sigma_{\widehat{a}} &= (N_{22} - N_{21}N_{11}^{-1}N_{12})^{-1} \\
\widehat{X} &= N_{11}^{-1}(U_1 - N_{12}\widehat{a}) \\
\Sigma_{\widehat{X}} &= N_{11}^{-1} + N_{11}^{-1}N_{12}\Sigma_{\widehat{a}}N_{21}N_{11}^{-1} \\
\Sigma_{\widehat{X}\widehat{a}} &= -N_{11}^{-1}N_{12}\Sigma_{\widehat{a}}
\end{aligned} \tag{16.6}$$

By using of the LAMBDA method [2, 4, 6, 10], the float point solution of the integer ambiguity $\widehat{a}$ is fixed as the integer $\breve{a}$

$$\Omega'' = (\widehat{a} - a)^T \Sigma_{\widehat{a}}^{-1}(\widehat{a} - a) = \min a \in Z^m \tag{16.7}$$

Substitute the integer ambiguity $\breve{a}$ back to (16.4) or (16.5), the ambiguity fixed solution of the position parameters $\breve{X}$ and their covariance can thus be calculated,

$$\breve{X} = N_{11}^{-1}(U_1 - N_{12}\breve{a}) = \widehat{X} + N_{11}^{-1}N_{12}(\widehat{a} - \breve{a}) = \widehat{X} - \Sigma_{\widehat{x}\widehat{a}}\Sigma_{\widehat{a}}(\widehat{a} - \breve{a}) \tag{16.8}$$

$$\Sigma_{\breve{X}} = N_{11}^{-1} = \Sigma_{\breve{X}} - \Sigma_{\breve{X}\hat{a}}\Sigma_{\widehat{a}}^{-1}\Sigma_{\widehat{a}\breve{X}} \tag{16.9}$$

16.2.2 Geometry-Free Mode Based Ambiguity Resolution

The geometry-free mode only uses the one way double difference measurement (including carrier phase and code phase measurement), and it's independent from the information of other satellite. This method is not influenced by the position of satellite, satellite clock error, ionosphere delay, troposphere delay and so on. It can resolve the ambiguity of medium and long baseline in a short time [5, 8, 12].

Step one: Calculate the ultra wide lane ambiguity directly by pseudorange.

The following equation is used to calculate the ambiguity:

$$\nabla\Delta N_{i,j,k} = \text{int}\left[\frac{\nabla\Delta\Phi_{i,j,k} - \nabla\Delta P_{l,m,n}}{\lambda_{i,j,k}} + \frac{\beta_{i,j,k} + \beta_{l,m,n}}{\lambda_{i,j,k}} \cdot \frac{\nabla\Delta K}{f_1^2} - \frac{\nabla\Delta\varepsilon_{\Phi_{i,j,k}} - \nabla\Delta\varepsilon_{P_{l,m,n}}}{\lambda_{i,j,k}}\right] \tag{16.10}$$

where, (i, j, k) and (l, m, n) are integer sets, int[•] means rounding, $\nabla\Delta$ refers to the double difference operator. To get reliable ambiguity, the influence of ionosphere delay and noise should be as small as possible. The following pseudo-range combination $P_{0,1,1}$ is used to resolve the ultrawide lane ambiguity

$$\nabla\Delta N_{0,-1,1} = \text{int}\left[\frac{\nabla\Delta\Phi_{0,-1,1} - \nabla\Delta P_{0,1,1}}{\lambda_{0,-1,1}} - \frac{\nabla\Delta\varepsilon_{\Phi_{0,-1,1}} - \nabla\Delta\varepsilon_{P_{0,1,1}}}{\lambda_{0,-1,1}}\right] \tag{16.11}$$

The above equation cancels the ionosphere delay. According to the error broadcast law, its variance can be expressed as

$$\sigma_{\left[\nabla\Delta N_{0,-1,1}\right]} = \sqrt{\frac{\sigma^2_{\nabla\Delta\Phi_{0,-1,1}} + \sigma^2_{\nabla\Delta P_{0,1,1}}}{\lambda^2_{0,-1,1}}} \tag{16.12}$$

Step two: Calculate the wide lane ambiguity $\nabla\Delta N_{1,0,-1}$ and $\nabla\Delta N_{1,-1,0}$ directly by pseudorange.

The principle is the same as step one, the wide lane ambiguity is calculated as:

$$\begin{aligned}\nabla\Delta N_{1,0,-1} &= \text{int}\left[\frac{\nabla\Delta\Phi_{1,0,-1} - \nabla\Delta P_{1,0,1}}{\lambda_{1,0,-1}} - \frac{\nabla\Delta\varepsilon_{\Phi_{1,0,-1}} - \nabla\Delta\varepsilon_{P_{1,0,1}}}{\lambda_{1,0,-1}}\right] \\ \nabla\Delta N_{1,-1,0} &= \text{int}\left[\frac{\nabla\Delta\Phi_{1,-1,0} - \nabla\Delta P_{1,1,0}}{\lambda_{1,-1,0}} - \frac{\nabla\Delta\varepsilon_{\Phi_{1,-1,0}} - \nabla\Delta\varepsilon_{P_{1,1,0}}}{\lambda_{1,-1,0}}\right]\end{aligned} \tag{16.13}$$

Step three: Calculate the ionosphere-free pseudorange and ionosphere delay by using two wide lane carrier phase measurement.

The ionosphere-free pseudorange is calculated as:

$$\begin{aligned}\nabla\Delta\Phi_{IFP} = &\frac{f_2}{f_2 - f_3}\left(\nabla\Delta\Phi_{1,-1,0} - \nabla\Delta N_{1,-1,0}\cdot\lambda_{1,-1,0}\right) \\ &- \frac{f_3}{f_2 - f_3}\left(\nabla\Delta\Phi_{1,0,-1} - \nabla\Delta N_{1,0,-1}\cdot\lambda_{1,0,-1}\right)\end{aligned} \tag{16.14}$$

The ionosphere delay is mitigated by Eq. (16.14), while the carrier noise is amplified, its variance is:

$$\sigma_{[\nabla\Delta\Phi_{IFP}]} \approx 27.3\sigma_{\Delta\nabla\varphi}(m) \tag{16.15}$$

The ionosphere delay is calculated as:

$$\frac{\nabla\Delta K}{f_1^2} = \frac{f_2 f_3}{f_1(f_2 - f_3)}\left[\left(\nabla\Delta\Phi_{1,0,-1} - \nabla\Delta N_{1,0,-1}\cdot\lambda_{1,0,-1}\right) - \left(\nabla\Delta\Phi_{1,-1,0} - \nabla\Delta N_{1,-1,0}\cdot\lambda_{1,-1,0}\right)\right] \tag{16.16}$$

its variance is:

$$\sigma_{\left[\frac{\nabla\Delta K}{f_1^2}\right]} \approx 21.4\sigma_{\Delta\nabla\varphi}(m) \tag{16.17}$$

Step four: Calculate the third linear independent ambiguity $\nabla\Delta N_1$ by using two wide lane carrier phase measurement.

Assume that the carrier phase measurement equation of the third linear independent ambiguity is:

$$\nabla\Delta\Phi_1 = \nabla\Delta\rho - \beta_1\cdot\frac{\nabla\Delta K}{f_1^2} + \nabla\Delta N_1\lambda_1 + \nabla\Delta\varepsilon_{\Phi,1} \tag{16.18}$$

Substituting the ionosphere-free pseudorange and ionosphere delay into Eq. (16.18), then

$$\nabla\Delta N_1 = \frac{\nabla\Delta\Phi_1 - \nabla\Delta\Phi_{IF}}{\lambda_1} + \frac{\beta_1}{\lambda_1}\cdot\frac{\nabla\Delta K}{f_1^2} + \varepsilon_{\nabla\Delta N_1} \tag{16.19}$$

It can be seen from Eq. (16.19) that $\nabla\Delta N_1$ is mainly influenced by the noise of carrier phase, and by averaging for a while, the reliable ambiguity can be acquired.

Step five: Calculate ambiguity $\nabla\Delta N_2$, $\nabla\Delta N_3$

16.3 Calculation and Analysis

16.3.1 Data

A test was performed in Beijing on December 19, 2012 by using two Beidou/GPS dual system receiver that produced by Sinan company. The receiver was located at two test stations whose accuracy position were already known. The baseline is about 4.2 m. The signal of Beidou B1/B2/B3 and GPS L1/L2 can be received by the receiver. The sampling interval is 1 s, the elevation is 10°, and the test lasted 1 day (Fig. 16.1).

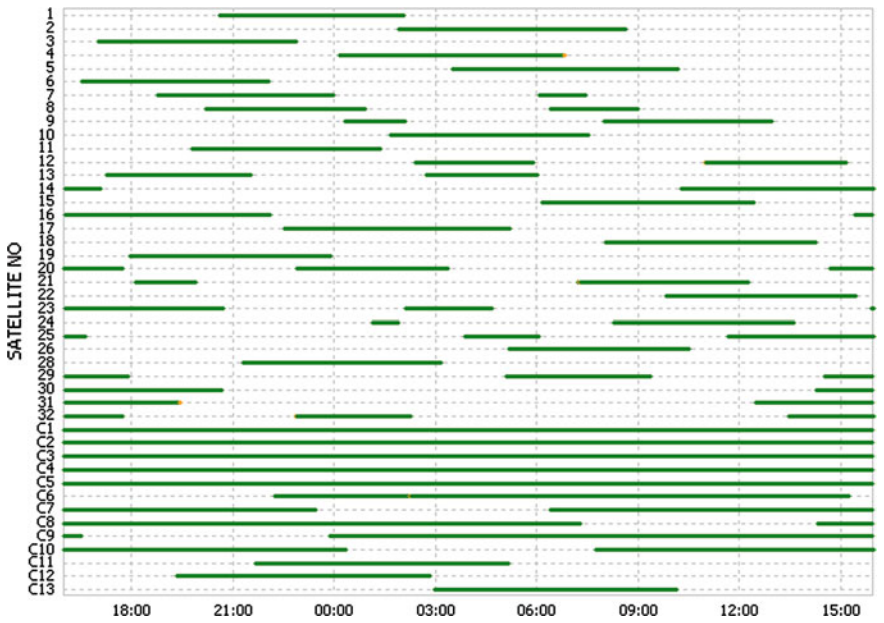

Fig. 16.1 BDS/GPS Satellite Visibility (elevation, 10)

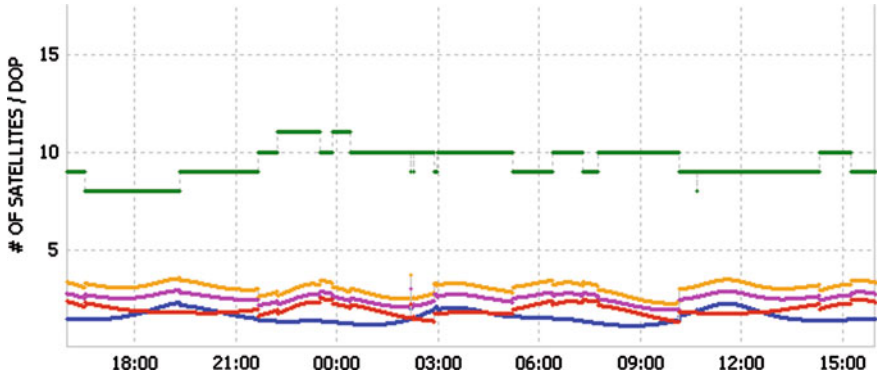

Fig. 16.2 DOP value and No. of BDS satellites (elevation, 10)

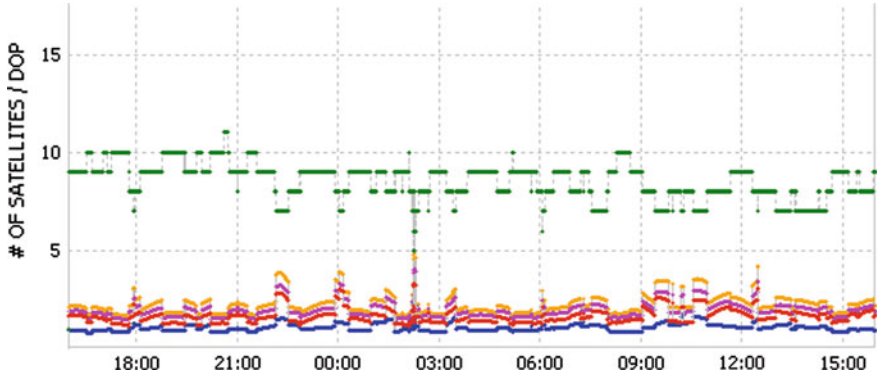

Fig. 16.3 DOP value and No. of GPS satellites (elevation, 10)

In Figs. 16.2 and 16.3, the top part of the figure depicts the number of the visible satellite, the bottom part of the figure depicts the value of DOP, from top to bottom they respectively represent GDOP, PDOP, VDOP and HDOP.

It can be seen from the above result that: (1) In Beijing area, the five GEO can be seen for all the day, the five IGSO can be seen for about 18 h, the four MEO can be seen for about 7 h. While for GPS, the average visible time of the satellite is about 6 h. (2) For Beidou, at least 8 satellite are visible, the number of visible satellite is about 9–10. While for GPS, the number of visible satellite is about 7–9, and sometimes only 5 satellite can be seen. (3) The DOP of GPS is a little better than that of Beidou, however, the DOP of Beidou varies more smoothly than that of GPS, and the DOP of GPS change frequently with the variation of the number of visible satellite.

16.3.2 Calculation and Analysis

The geometry mode and geometry-free mode are used for ambiguity resolution. The elevation is 10°. For geometry mode, the ration test is used for validation, and the threshold is 2.0. For geometry free mode, the threshold for rounding is 0.4. The epochs that pass the test is used for Fixed rate statistics, and the epochs that the three dimension error between fixed solution and the coordinate is smaller than 10 cm is used for success rate statistics.

It can be seen from Table 16.1 that, (1) The fix rate of Beidou single frequency ambiguity resolution is 97.9 % based on geometry mode; while for GPS, it is only 70.3 %. The success rate of Beidou is close to 100 % and only 98.66 for GPS. The main reason is that the variation of the DOP of Beidou is more smoothly than that of GPS, while for GPS, only a few satellites are useable in single epoch because the rapid variation of the satellite. (2) The ambiguity fix rate of Beidou dual frequency, triple frequency and GPS dual frequency is about the same based on geometry mode, they are all above 99 %. The success rate of Beidou dual frequency and triple frequency is 100 %, while for GPS, the ambiguity is wrongly fixed for some epochs. (3) The fix rate of ambiguity for dual system single frequency is 99.7, and the success rate is 100 %. That is much better than that of single system single frequency. (4) The fix rate of Beidou triple frequency is close to 100, but its success rate is only 95.7 % (Table 16.2).

It can be seen from the results of RTK that (1) the RMS of Beidou single frequency RTK in E, N, and U direction is about 1–3 cm, and 10 cm for that of GPS. (2) The RMS of Beidou dual frequency, triple frequency and Beidou/GPS RTK in E, N, and U are all smaller than 1 cm, and it is about 1 cm for GPS dual

Table 16.1 Statistics of ambiguity resolution for single epoch

		Fix rate	Success rate
Geometry mode	Beidou B1	97.9 %	99.99 %
		(84,610)	(84,600)
	Beidou B1/B2	99.4 %	100 %
		(85,875)	(85,875)
	Beidou B1/B2/B3	99.4 %	100 %
		(85,868)	(85,868)
	GPS L1	70.3 %	98.66 %
		(60,740)	(59,929)
	GPS L1/L2	99.8 %	~ 100 %
		(86,191)	(86,188)
	B1/L1	99.7 %	100 %
		(86157)	(86157)
	B1/B2/L1/L2	99.4 %	100 %
		(85,860)	(85,860)
Geometry-free mode	Beidou B1/B2/B3	~ 100 %	95.7 %
		(86,390)	(82,712)

Table 16.2 Results of RTK positioning for different modes (RMS, Unit: cm)

		E	N	G
Geometry mode	B1	0.97	1.65	2.75
	B1/B2	0.13	0.21	0.4
	B1/B2/B3	0.13	0.2	0.42
	GPS L1	7.42	10.9	21.5
	GPS L1/L2	0.95	0.79	1.15
	B1/L1	0.12	0.15	0.35
	B1/B2/L1/L2	0.1	0.13	0.28
Geometry-free mode	B1/B2/B3	4.03	2.64	6.31

frequency RTK; (3) The RMS of Beidou triple frequency based on geometry free mode is about 2–7 cm (Table 16.2).

All in all, the accuracy of Beidou, GPS RTK is about cm level. The success rate and reliability is related to the quality of the data, espically related to the anti-jamming ability of Beidou receiver.

16.4 Conclusions

The advantage of Beidou triple frequency signal in RTK is verified by using real data for the first time. Both the geometry and geometry-free mode are used for ambiguity resolution. The following conclusions can be get:

1. The success rate and reliability of Beidou single, dual and triple frequency ambiguity resolution is superior to that of GPS. This is because of the DOP OF GEO and IGSO varies slowly, while the ascending and descending of GPS satellite is much frequently than GPS, and this means that the ambiguity should be recalculated. At the beginning of the ascending, the elevation is low, so the quality is poor.
2. Cm level position accuracy can be achieved by geometry free based Beidou triple frequency RTK. The geometry free method is unrelated to the baseline length, and this will be useful for the application of Beidou.
3. When Beidou/GPS are combined, the position accuracy, success rateand reliability will be improved obviously, especially when the elevation angle is high or the signal is shielded.
4. The combined strategy should be developed to resolve the low reliability problem of Beidou triple frequency geometry free ambiguity resolution.
5. The measurement of GEO is seriously influenced by multi-path, the anti-jamming measures should be considered for the design of antenna and the receiver. The variation of multi-path shows systematic pattern in the long run, however, it is random in short time, its influence cannot be mitigated by RTK.

It should be noted that, only a very short baseline in Beijing are used for test and verification, more research by using mid-long baseline needs to be done in the future.

Acknowledgments This work is supported by the National Natural Science Funds of China (Grant Nos. 41020144004; 41104022), the National ''863 Program'' of China (Grant No: 2013AA122501) and the 2nd and 3rd China Satellite Navigation Conference (Grant Nos. CSNC2011-QY-13; CSNC2012-QY-3).

References

1. Guo HR, He HB, Li JL, Wang AB (2011) Estimation and mitigation of the main errors for centimetre-level compass RTK solutions over medium-long baselines. J Navig 64:S113–S126
2. Guo HR, He HB, Li JL, Wang AB (2012) Performance of triple-frequency high-precise RTK positioning with COMPASS. In: China satellite navigation conference (CSNC) 2012 proceedings, Lecture notes in electrical engineering 161, pp 371–378 doi:10.1007/978-3-642-29193-7_36
3. Yang YX, Li JL, Xu JY, Tang J, Guo HR, He HB (2011) Contribution of the compass satellite navigation system to global PNT users. Chin Sci Bull 56(26):2813–2819
4. He H (2002) Precise kinematic GPS positioning and quality control. Information Engineering University
5. Teunissen P et al (2002) A comparison of TCAR, CIR and LAMBDA GNSS ambiguity resolution. In: 15th international technical meeting of the satellite division of the institute of navigation ION GPS 2002, Portland, Oregon, USA, pp 2799–2808
6. Teunissen PJG (1995) The least-squares ambiguity decorrelation adjustment: a method for fast GPS integer ambiguity estimation. J Geodesy 70:65–82
7. Feng YM, Rizos C, Higgins M (2007) Multiple carrier ambiguity resolution and performance benefits for RTK and PPP positioning services in regional areas. In: Proceedings of ION GNSS 20th international technical meeting of the satellite division, Fort Worth, TX, USA, pp 668–678, 25–28 Sept 2007
8. Feng YM (2008) GNSS three carrier ambiguity resolution using ionosphere-reduced virtual signals. J Geodesy 82(12):847–862
9. Li BF (2008) Generation of third code and phase signals based on dual-frequency GPS measurements. In: ION GNSS 2008, Savannah, GA, USA, pp 282–283, 16–19 Sept 2008
10. Han SW (1997) Ambiguity recovery for long-range kinematic positioning. Navigation 44(2):257–290
11. Han SW, Rizos C (1999) The impact of two additional civilian GPS frequencies on ambiguity resolutions strategies. In: Proceedings of ION annual technical meeting, Cambridge, MA, pp 315–321, 28–30 June
12. Teunissen PJG, Joosten P, Tiberius CCJM (1999) Geometry-free ambiguity success rates in case of partial fixing. In: Proceedings of ION-NTM 1999, San Diego, CA, pp 201–207, 25–27 January

Chapter 17
Design and Implementation of Blocking Shared Memory for Satellite Navigation Application Processing System

Weijie Sun, Enqiang Dong, Jidong Cao and Xiaoping Liu

Abstract Being the computing center of satellite navigation system, application processing system is charged with lots of high-precision computing tasks including orbit determining, time synchronizing, ionosphere model calculating, difference and integrity parameters processing, and it has a large number of features, such as mass and multi-sort data, heavy computing tasks, high precision of calculation, so there are much rapid mass-data transmissions between different processes. As the primary means of communication between processes, shared memory has the characteristic of rapid mass-data transmission. Therefore there are lots of shared memories to transfer data among different processes in application processing system. This paper describes the realization principle of shared memory, focuses on parsing the blocking shared memory design principle, achieves the blocking shared memory template class based on the principle, and through the test verifies the reliability of the template class.

Keywords Blocking shared memory · Satellite navigation · Application processing system

17.1 Introduction

With the continuing development of the satellite navigation technology, the satellite navigation system has been used in every aspect of our society. As the data processing center of the satellite navigation system, the application processing system undertakes the high-accuracy computation of the satellite orbit determining, time synchronizing, ionosphere model, difference and integrity parameters

W. Sun (✉) · E. Dong · J. Cao · X. Liu
Beijing Satellite Navigation Center, Beijing, China
e-mail: sun_weijie@sina.com.cn

J. Sun et al. (eds.), *China Satellite Navigation Conference (CSNC) 2013 Proceedings*, Lecture Notes in Electrical Engineering 243,
DOI: 10.1007/978-3-642-37398-5_17,

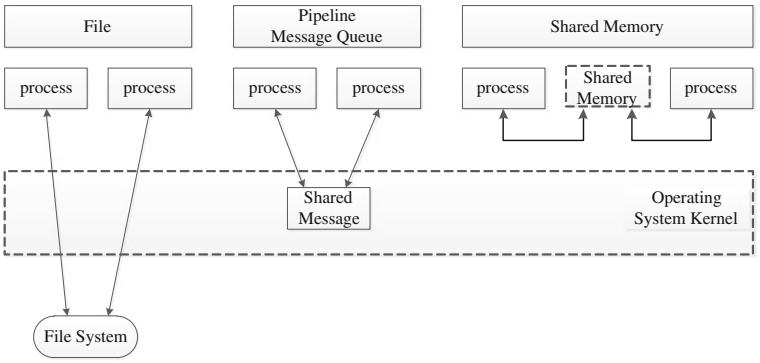

Fig. 17.1 Interprocess communication modes

processing and so on. Consequently, the application processing system has the characteristics like the high-level receiving data, the multi-types data, high-accuracy computation requirement and the heavy computation task. To ensure the real-time ability, the parallel computation technology is used to realize the high-speed processing of information by using multi- process and multi-thread technology. At the same time, the reliable communication between different processes to is required.

The most common used communication methods between processes include file, pipeline, message queue and shared memory, which theories are illustrated in Fig. 17.1.

- File

The communication between two processes is realized by shared files saved in the file system. Each process needs to traverse kernels like read, write, lseek functions etc. The synchronization mechanism is needed to realize the read and write protection between processes.

- Pipeline and message queue

The communication between two processes is realized by accessing shared messages maintained by operating system. The accessing operation by each process involves a system calling to kernels.

- Shared memory

The two different processes map their virtual addresses into the same shared memory addresses, regarding as their own virtual memories to realize communication between processes. Once the address mapping is established, the kernel is never needed on the data transfer between processes. The synchronization mechanism is needed to ensure the safety between processes.

The shared memory is common used in the application processing system of the satellite navigation because of the characteristic of rapid mass-data transmission. The System V mechanism of shared memories is illustrated in the paper.

17.2 The implementation Principles of Shared Memory

The shared memory is the most fast intercross communication type [1]. The virtual address of process can be mapped into any physical address. If the virtual addresses of two processes are mapped into the same physical address, the communication between processes can be realized by using their own virtual addresses [2]. As explained above, the kernel is never involved in the data transfer process Fig. 17.2.

The shared data needed by different processes are saved into the shared memory of IPC. The application process can get or establish a shared memory of IPC by using system function *shmget()* with corresponding identifier returned. For every established shared memory, a *shmid_ds* structure is maintained by kernel to describe the shared memory. The *shmid_ds* structure of every shared memory is saved into the *shm_segs* array. The access privilege, capability and physical address of shared memory are described by the *shmid_ds* structure.

```
struct shmid_ds
{
    struct ipc_perm shm_perm;          /*IPC access permission*/
    size_t shm_segsz;                  /* shared memory size*/
    struct vas* shm_vas;               /* virtual address entry list*/
    pid_t shm_lpid;                    /* current process pid*/
    pid_t shm_cpid;                    /*creating process pid*/
    time_t shm_atime;                  /*last shmat() time*/
    time_t shm_dtime;                  /*current shmdt() time*/
    time_t shm_ctime;                  /*last shmctl() time*/
    shmatt_t shm_nattch;               /*Number of processes connection*/
    unsigned long int shm_npages;      /*number of shared memory pages*/
    unsigned long int* shm_pages;      /*shared memory pages list*/
        …
}
```

Every process which use shared memory map its virtual memory into shared memory using system function *shmat()*. The mapping relation is described by the newly established *vm_area_struct*. When the process visit the shared memory at the first time, the system will distribute a physical page and establish the page table (pointed by *shm_pages*) and its entrance. This entrance is saved into the *vm_area_struct* corresponding to the process. When the next process uses the shared memory in the first time, the dealing function can be used directly to direct into the pages of the physical memory. Consequently, the first visiting process establishes the physical memory page and the succeeding processes can use the physical memory pages directly.

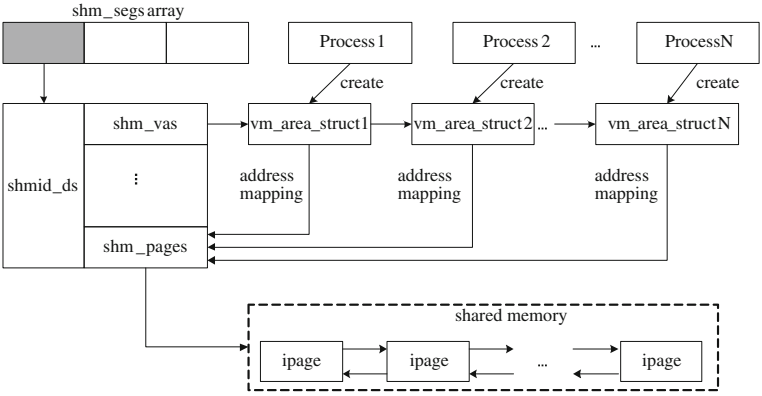

Fig. 17.2 Schematic diagram of shared memory

When the shared memory is not used by the process, the process call the *shmdt()* function to cancel the mapping of the shared memory. The corresponding *vm_area_struct* will be deleted from the *shmid_ds* structure. After the last process released its virtual address space, the system release the distributed physical page and delete the *shmid_ds* structure.

The *shmctl()* function realize the control operation of the shared memory.

17.3 Design and Implementation of Blocking Shared Memory

17.3.1 Design Principle

The two model of the shared memory can be summarized by analyzing the using method of share memory in the application processing system of the satellite navigation. One model is that one process writes and several processes read. For example, the pre-processed data received by the data receiving process is need to send to several calculation process, such as the satellite orbit determining, time synchronizing, ionosphere model etc. The second is that one process writes and only one process reads, such as the data receiving process only send its data to the pre-processing process.

At the same time, the synchronization mechanism is needed to ensure the communication safety between processes otherwise the condition that several processes read or write the shared memory simultaneously can be generated. The following errors may be generated [3]: the saved data in disorders, the taken data incomplete and the read process executes before the end of the write process. Consequently, the synchronization mechanism between different processes is needed to ensure the read or write safety of shared memory. In the paper, the value of signal is used as the synchronization mechanism between different processes.

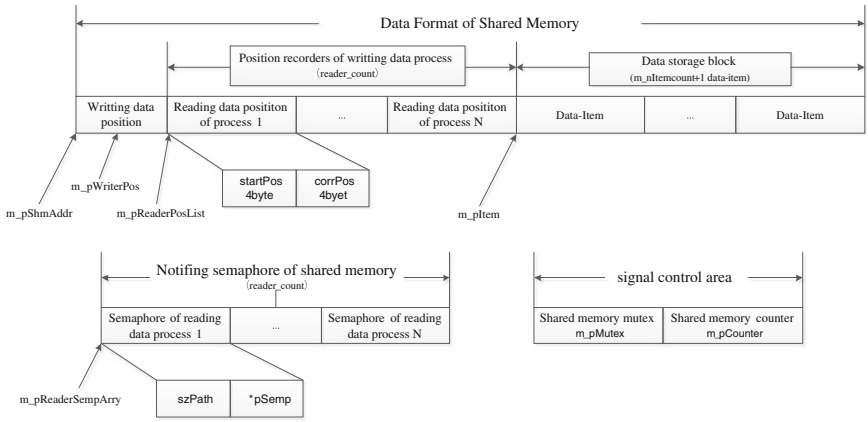

Fig. 17.3 Design diagram of shared memory

The blocking shared memory is designed in the application processing system of the satellite navigation based on the general principle. The one to many or one to one communication type can be set flexibly by the configuration file. The design structure of the blocking shared memory is illustrated in Fig. 17.3. The shared memory includes three parts: the area of the shared memory, the data notice semaphore of the shared memory and the area of the signal control.

The shared memory includes the location of writing, the record of the location of the read process and the data protection area. The location of the data writing *m_pWritePos* is used to indicate the index of the written data in the data protection area. As the processing times are different among different applications, the un-synchronization of reading is generated. The indicator of the location of the reading processes is used to show the particular location of several reading processes. The data protection area is used to save the written data in the shared memory. The written process writes the data into the record item one by one. When the last item is written, the first item is written again for the next circulation. As a result, the whole data protection area is used as a circulation queue.

In the process of using the shared memory, if the shared memory is established firstly, the data written location is directed into the first data item and the read locations are set to zero. If the shared memory exists already, the pointer of the shared memory, *m_pShmAddr*, is got by using the function *shmat()*. Then the particular data written location and the information of the reading process can be got through the *m_pShmAddr* pointer.

The semaphore of every read process is set by the semaphore of the shared memory. Every semaphore includes the indication of the signal lamp *szPath* and the pointer *pSem*. When the data is written into the shared memory, the data notice signal of the shared memory is used to inform every reading process that the written process is over. The function *acquire()* is used to block and wait the coming of the data until the function *release()* inform the write can be done.

To avoid the read/write conflicts of the shared memory, the read/write operation synchronization is realized by the signal control area. The signal control area includes the mutex and the counter of the shared memory. The mutex *m_pMutex* is mainly used to realize the data read and write synchronization. The shared memory can be accessed only when the visiting control of *m_pMutex* is got. The counter *m_pCounter* of shared memory is a group of semaphore. For every process which uses the shared memory, the counter is added one using *m_pCounter->op(1, 0, SEM_UNDO)* to record the number of the processes that use the shared memory (the record *SEM_UNDO* is set and the counter is subbed one when the process quit). When other processed quit and only the current process use the shared memory, the current process call the system function *shmdt()* to delete the shared memory.

17.3.2 Design Implementation

Using C++ language, this paper implements a template class blockSHM of blocking shared memory based on ACE middleware (Table 17.1).

template<typename TYPE>class blockSHM

There, *TYPE* is the abstract data structure of shared memory data item. The main parameters and functions of blockSHM class as follow:

```
typedef struct READER_POS
{
    int startPos;        /* last position of reading process getting the data*/
    int currPos;         /*current position of reading process getting the data*/
}READER_POS;
typedef struct READER_SEMP
{
    char szPath[NAME_LENGTH];          /*semaphores flag*/
    ACE_Process_Semaphore *pSemp;      /* semaphore pointer*/
}
```

Table 17.1 Main parameters of the blockSHM shared memory template class

Parameter declaration	Parameter description
*char *m_pShmAddr*	*Starting address of shared memory*
*ACE_SV_Semaphore_Complex *m_pCounter*	*Counter pointer of shared memory*
*ACE_Shared_Memory_SV *m_pShmObj*	*Object pointer of shared memory*
*ACE_Process_Mutex *m_pMutex;*	*Mutex pointer of shared memory*
*int *m_pWriterPos*	*Writing data location, index of the data storage block*
*TYPE*m_pItem*	*Data item pointer*
int m_nItemCount	*The number of storage data*
*READER_POS *m_pReaderPosList*	*Starting address of location array for reading process*
*ACE_Process_Semaphore *m_pReaderSemp*	*Starting address of semaphore array for reading process*

blockSHM shared memory template class has four main functions:

init_writer () function is used to complete shared memory initialization by writing process.

```
int init_writer(const char* name, const int count, const int reader_count, bool replace)
{
    Judge the variables rationality;
    Create shared memory counter(if created, open), counter is incremented by 1;
    Create the shared memory mutex between processes;
    Loop to create shared memory semaphores base on the number of reading processes;
    create shared memory, if created, open and get the writing position in shared memory;
}
```

init_reader() function is used to complete shared memory initialization by reading process.

```
int init_reader(const char* name, const int count, const int reader_count, const short reader_sn)
{
    Judge the variables rationality;
    Create shared memory counter (if created, open), counter is incremented by 1;
    Create the shared memory mutex between processes;
    Loop to create shared memory semaphores base on the number of reading processes;
    Create shared memory, if created, open and get the reading position of the current process;
}
```

put() function is used to write data into shared memory. It will write a data-item at every calling and send signals to notify all processes that are blocked and waiting to read the shared memory.

```
int put(const TYPE &Item)
{
    Lock shared memory mutex;
    Write data;
    Loop to signal shared memory semaphores by calling release() function based on the number of
    writing process;
    Unlock shared memory mutex;
}
```

get() function get only one data-item from shared memory at every calling

```
int get(TYPE &outItem)
{
    Reading process call acquire() of shared memory semaphore to block and wait ultil the release
    signal of writing process;
    Lock shared memory mutex;
    Read data;
    Unlock shared memory mutex;
}
```

17.4 Experiment and Result Analysis

With the blockSHM template class of shared memory, this article constructs Server.cpp and Client.cpp program to test the transmission delay and functionality of shared memory. The structure of test programs is shown in Fig. 17.4.

In the test, Server program put data-item into shared memory, Client program is blocking and waiting to get data-item from shared memory when it receives the signal of the shared memory semaphore. Each data packet contains the Server program's sending data time, after receiving the sending data packet, Client program calls system function to get local time and obtain the shared memory data transmission delay by calculating the difference value between local time and sending time. Server program loop to send 3000 data packets and set 1K and 100K data packets size respectively in the test.

The test work selects a HP rx4640 server, 4 × 1.6G CPU, 8G memory.

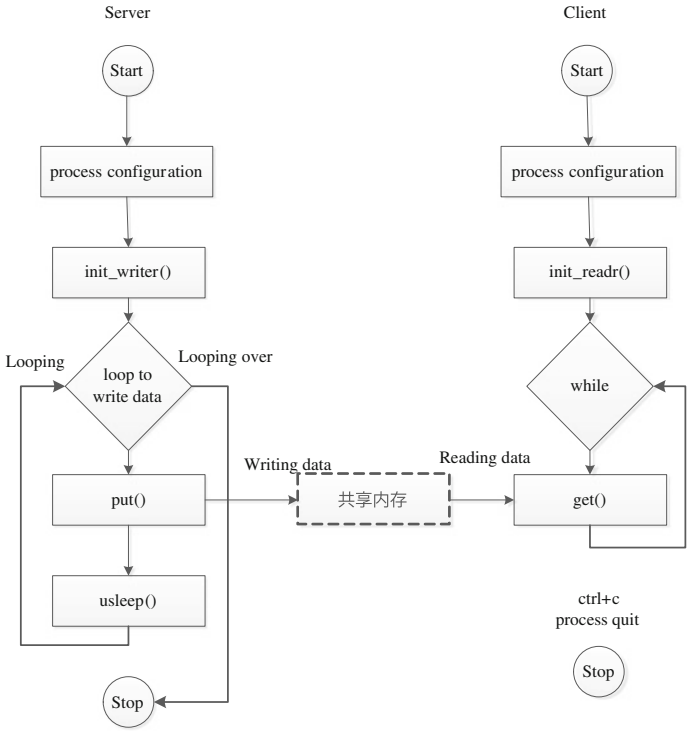

Fig. 17.4 Structure diagram of test programs

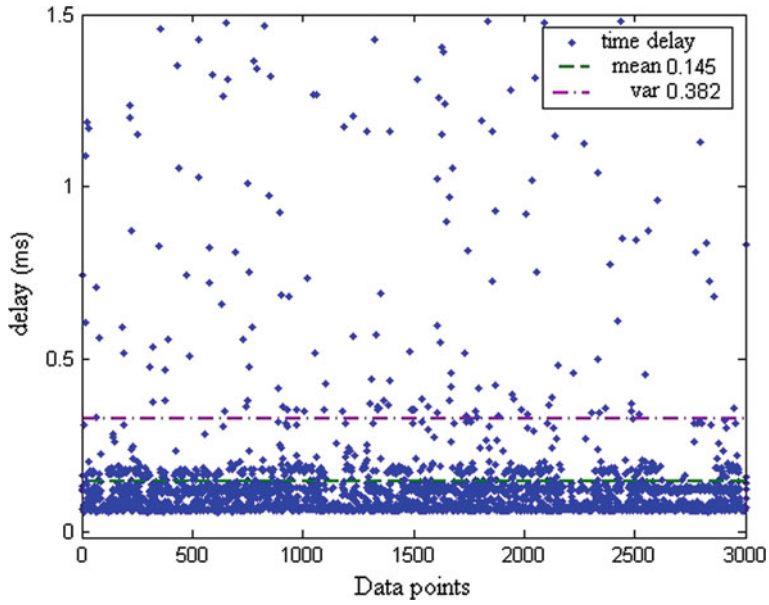

Fig. 17.5 Shared memory transmission delay: 1K data packet

17.4.1 Capability Analysis

1K data packet, shared memory transmission delay results are show in Fig. 17.5.

100K data packet, shared memory transmission delay results are shown in Fig. 17.6.

Test results of shared memory data transmission delay are shown in Table 17.2.

From the results, 1k data packet transmission delay is consistent with 100k data packet transmission delay, so shared memory transmission delay is not directly related to the size of data packet size. Analysing the reason, shared memory directly operate the memory and use *memcpy()* system function to copy block data for putting or getting data, the size of the data is basically no effect on the operation delay of *memcpy()* function, And thus the transmission delay is basically the same.

There are more discrete points of large transmission delay in Figs. 17.5 and 17.6. Analysing the reason, there are other processes working in the server, the processes will be phased share system resources to run, and the running of Server

Table 17.2 Transmission delay of shared memory

Data packet size	Mean (ms)	Variance (ms)
1K	0.145	0.382
100K	0.175	0.423

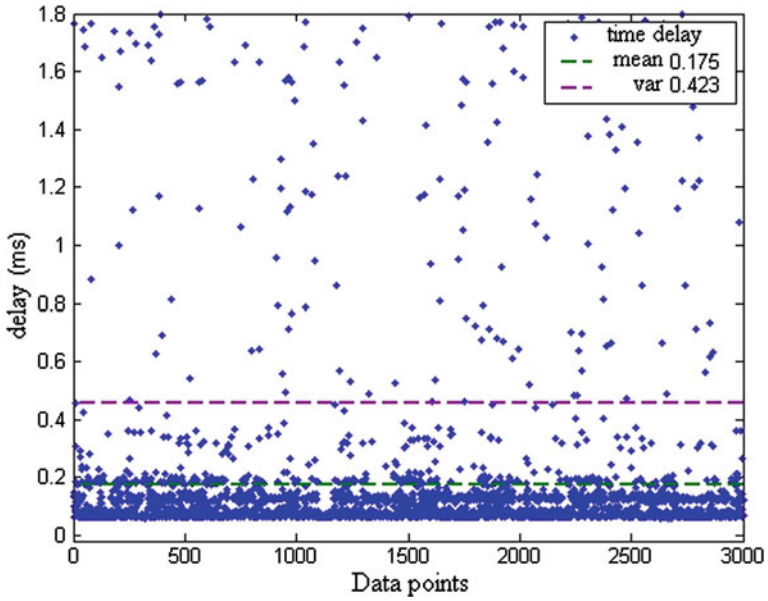

Fig. 17.6 Shared memory transmission delay: 100K data packet

and Client process need to compete for resources with other processes, therefore, the reasons for more discrete points of large transmission delay can be attributed to the waiting time of the Server process and Client process competing for resources.

17.4.2 Functionality Analysis

This paper first constructs shared memory test environment which is characterized by Server process for writing data and multiple Client process for reading data that are derived by Server.cpp and Client.cpp separately. Then, a data packet transmission experiment using different transmission frequency and size for packet is conducted to test the blockSHM obstructive shared memory. The test procedure does not demonstrate abnormal phenomenon. Moreover, the phenomenons of packet loss and data transfer that are delay too long are absence in blockSHM obstructive shared memory. The experiment indicates that template class for blockSHM shared memory shows promising robustness and stability.

17.5 Conclusion

This paper first discusses the basic principle of shared memory. Based on the analysis of inter-process communication requirement of satellite navigation business processing system, the paper focuses on principle of design and realization for obstructive shared memory, then successfully constructed template class for blocking shared memory. After that, an experimental analysis is conducted to test shared memory. The experiment verifies the effectiveness and stability of template class for the blocking shared memory, which provides basic platform components for the development of the navigation system in the future.

References

1. Stevens WR (2003) UNIX network programming, interprocess communications (vol 2, 2nd edn). Tsinghua University Press, Beijing, pp 261–262
2. Guo X, Gao S (2001) The analysis of unix system V IPC and share memory audit. Appl Res Comput 18(4):39–40
3. Zhang H, Sun C, Li J (2004) Research and implementation of synchronized shared memory in Linux. J HUNAN Indus Polytech 4(4):19–20

Chapter 18
Application of Carrier Phase Differential Relative Navigation for Shipboard Landing of Aircraft

Bao Li, Kejin Cao, Jiangning Xu and Yinbing Zhu

Abstract Shipboard landing of aircraft needs to acquire the real-time and precise relative position between shipboard and aircraft. If the technique of relative navigation based on differential carrier phase is used to solve the problem, the key point is fixing the ambiguity real-time and reliably. In general, wide lane carrier is used to solve the problem. At single epoch, the observable equations of double frequency wide lane carrier are ill-condition, so the code observable equations are needed to add in. Since the poor precision of the code pseudorange information, the ambiguity solved by it can't reach the performance requirements in shipboard landing. A fitting method by selection of parameter weights is researched based on wide lane algorithm. The method estimates the two kinds of wide lane float ambiguities at first; then solves the individual ambiguity separately. It avoids the problems of poor precision from code equations. The calculation of experiment data shows that the algorithm can solve ambiguity reliably at single epoch and improve accuracy of relative position to centimeter level, which satisfies the requirements for shipboard landing of aircraft.

Keywords GNSS · Shipboard landing of aircraft · Wide lane · Integer ambiguity · Fitting method by selection of parameter weights

18.1 Introduction

When a pilot drives aircraft to land on the shipboard, he faces more pressure compared with driving it to land on earth since the disadvantage factors such as shipboard moving, short runway and airstreams on the sea. For a long time,

B. Li (✉) · K. Cao · J. Xu · Y. Zhu
Department of Navigation Engineering, Naval University of Engineering, Jiefang Road, No.717, Wuhan 430033, China
e-mail: oabeel@yahoo.com.cn

J. Sun et al. (eds.), *China Satellite Navigation Conference (CSNC) 2013 Proceedings*, Lecture Notes in Electrical Engineering 243,
DOI: 10.1007/978-3-642-37398-5_18,

countries spare no effort on developing advanced, precise and reliable shipboard landing system [1]. The shipboard landing system of aircraft has been experienced from Landing Signals Officer, Optical Landing System, Instrument Landing System to Automatic Carrier Landing System. As the development of GNSS, their capabilities of all-weather, all-place and precise three dimensional positioning attract researchers' attentions [2].

In May 1996, the American Department of Defence proposed JPALS (Joint Precision Approach and Landing System) plan officially. JPALS consists of sea based and land Based (SB-JPALS and LB-JPALS) system. It is an all-weather, all-mission, all-user landing system based on differential Global Positioning System and supports fixed-base, tactical, and shipboard applications [3]. At present, JPALS is still being developed, and the public information is few [4–6].

As the precise and dynamic navigation performance requirements in shipboard landing of aircraft, the differential carrier phase technology is needed. The key point is fixing the integer ambiguity reliably at single epoch. From relative papers [7–9], the double frequency wide lane carrier can solve the ambiguity quickly, but the carrier phase equations are ill-condition at single epoch. A general method is adding the code observable equations in, whereas the code observable equations can't apply to fix ambiguity for its poor precision. Some researches proposed methods such as carrier phase smoothed pseudorange and dividing wide lane ambiguity based on variance to solve wide lane ambiguity [7, 8], however, they can't reach the performance requirements in shipboard landing of aircraft either. The paper [9] puts forward an algorithm. It estimates the two kinds of wide lane float ambiguities at first; then solves the individual ambiguity separately. It avoids the problems of poor precision from code equations and satisfies the requirements in shipboard landing of aircraft. This paper discusses the application of the algorithm in shipboard landing of aircraft.

18.2 The Structure and Performance Parameters of SB-JPALS

SB-JPALS is made up of three parts, which are shipboard equipments, aircraft equipments and data transmission equipments. They are showed in Fig. 18.1. The shipboard receives the GPS signal to acquire its position, and transmits its position to aircraft by data transmission equipments. The aircraft can also acquire its position by GPS signal, which is calculated with the shipboard position to work out the relative position vector form the shipboard to aircraft. There is an UHF data link between the shipboard and aircraft.

According to paper [4], the performance parameters of SB-JPALS are showed in Table 18.1. From the table, SB-JPALS applies the high precise P code for double frequency wide lane algorithm. As a result that the P code is special for American army, how to use C/A code to fix the ambiguity reliably at single epoch becomes a serious problem. A new method is proposed as below.

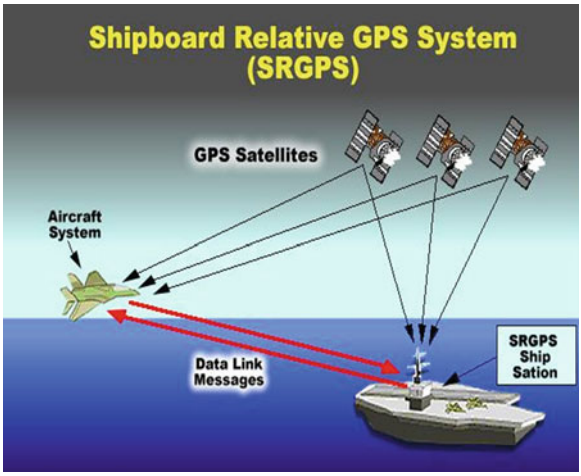

Fig. 18.1 Structure of SB-JPALS

Table 18.1 Performance parameters of SB-JPALS

Accuracy (95 %)	0.4 m
Integrity	10^{-6}
VAL	1.1 m
TTA	2 s
Continuity	1×10^{-6}/15 s
Availability	99.7 %
Basic algorithm	Wide lane fixed ambiguity, L1/L2 fixed ambiguity, shipboard and aircraft equipments are both double frequency P code

18.3 Differential Carrier Phase Algorithm for Shipboard Landing of Aircraft

18.3.1 Double Frequency Wide Lane Ambiguity Resolution

Ambiguity is easier to fix when the carrier wave length is longer. If two carriers are combined as a long wave carrier, the ambiguity is easier to fix. It's basic principle for double frequency wide lane algorithm.

In the process of aircraft landing on shipboard, if there are m satellites in view for both observable station 1 and station 2. For two satellites i, j, the L1 and L2 wide lane observable equation at some epoch is described as

$$\lambda_W \varphi_{12,W}^{ij} = \rho_{12,W}^{ij} + \lambda_W N_{12,W}^{ij} + \varepsilon_{12,W}^{ij} \tag{18.1}$$

where λ is the carrier wave length, φ is observable value of carrier phase, ρ is the distance form satellite and station, N is integer ambiguity, ε is the observable noise of carrier phase, W means wide lane. At single epoch, there are m−1 carrier observable equations but m+2 unknown variables, so the carrier observable equations are ill-condition. Combined with code observable equations can solve the problem, and paper [10] proposed the double P code pseudorange algorithm. However, the P code pseudorange is special for army. If C/A code pseudorange is used for ambiguity fixing, it can't satisfy the performance requirements of ship-board landing.

18.3.2 A New Algorithm for Wide Lane Ambiguity Resolution at Single Epoch

If we can't get precise code observables, the algorithm for ambiguity resolution at single epoch is how to solve ill-condition equations [11]. After wide lane combined, the wave length is longer. In this case, the wide lane float ambiguity can be solved with fitting method by selection of parameter weights.

The least squared equation of wide lane float ambiguity can be written as

$$\begin{bmatrix} A^T C^{-1} A & A^T C^{-1} B \\ B^T C^{-1} A & B^T C^{-1} B \end{bmatrix} \begin{bmatrix} X \\ N \end{bmatrix} = \begin{bmatrix} A^T C^{-1} L \\ B^T C^{-1} L \end{bmatrix} \tag{18.2}$$

where X is the baseline vector, N is vector of double differential ambiguity, A, B are coefficient matrix. C^{-1} is the weight matrix and the calculation method how to get it is described in paper [12]. According to the solving principle of ill-condition equation, the weight fitting matrix R can be written as

$$R = \begin{pmatrix} E_{3\times 3} & 0_{3\times(m-1)} \\ 0_{(m-1)\times 3} & 0_{(m-1)\times(m-1)} \end{pmatrix} \tag{18.3}$$

Form Eq. (18.3), the improved normal matrix can be described as

$$M_R = M + \mu R = \begin{bmatrix} A^T C^{-1} A + \mu E & A^T C^{-1} B \\ B^T C^{-1} A & B^T C^{-1} B \end{bmatrix} \tag{18.4}$$

where M is the old normal matrix, μ is regularization parameter, E is the fitting matrix, the setting method for E can be resulted from paper [11].

The covariance matrix is acquired from the improved normal matrix. The wide lane fixed ambiguity can be solved by searching with new covariance matrix. Here the part ambiguity searching method is suggested for efficiency. The method above needs an initial precise position, which can be provided from differential code pseudorange equations.

18.3.3 Resolution for Individual Carrier Phase Ambiguity

Since the noise is amplified by wide lane, the position solved by wide lane ambiguity is not precise enough. So the individual ambiguity of L1 and L2 are required for high precision. Two carriers can make up of different linear combination. If the linear coefficients are α and β, the combined carrier phase can be written as

$$\varphi_{\alpha\beta} = \alpha\varphi_{L1} + \beta\varphi_{L2} \tag{18.5}$$

The wide lane ambiguity $N_{\alpha\beta}$ can be solved by the algorithm in Sect. 18.3.2. If another wide lane ambiguity $N_{\eta\gamma}$ is solved by the same method. So ambiguity N_1 and N_2 can be solved by the equation below

$$\begin{bmatrix} N_{\alpha\beta} \\ N_{\eta\gamma} \end{bmatrix} = \begin{bmatrix} \alpha & \beta \\ \eta & \gamma \end{bmatrix} \begin{bmatrix} N_1 \\ N_2 \end{bmatrix} \tag{18.6}$$

If $\alpha\gamma - \beta\eta \neq 0$, the N_1 and N_2 will be solved out on condition that the $N_{\alpha\beta}$ and $N_{\eta\gamma}$ are solved correctly. Therefore, the high precise baseline vector can be calculated.

18.4 Algorithm Test

18.4.1 Single Epoch Data Processing in Static Test

In static situation the ambiguity solved by long time can be regarded as the true ambiguity. If the ambiguity can be solved at single epoch in static situation, we consider the algorithm satisfies the application in dynamic situation in a way.

At 10 am, Jul 26, 2012, we used two FlexPak-G2 receivers of Novatel Corporation acquire data on the roof of Electrical Engineering College building. The sampling period is 1 s, and the lowest requirement of satellite altitude angle is 15°. We acquired 3775 s data in all. The GPS satellites which can be seen for both two receivers are [20 16 6 31 29 23 30 32]. The satellite 16 is taken as reference, so 7 ambiguities are produced. The ambiguities solved by all data are taken as true ambiguities.

The combined coefficients are selected as $\alpha = 1$, $\beta = -1$, $\eta = 4$, $\gamma = -5$, so the wide lane wave $\lambda_{\alpha\beta} = 86.2\,\text{cm}$ $\lambda_{\eta\gamma} = 183.2\,\text{cm}$ which are far longer than individual wave of L1 and L2. The two kinds of wide lane ambiguities calculated by each epoch are showed in Table 18.2. From the table we can seen, the success ratio of two wide lane ambiguities resolution are 100 %; according to the Eq. (18.6), the success ratio of N_1 and N_2 resolution are 100 %, too. Therefore, it can be concluded that the new algorithm can fix the ambiguity reliably at single epoch.

Table 18.2 The results of two wide lane ambiguities resolution

Satellites team	Epoch number	Wide lane ambiguity $N_{\alpha\beta}$			Wide lane ambiguity $N_{\eta\gamma}$		
		Ambiguity	Success number	Success ratio (%)	Ambiguity	Success number	Success ratio (%)
16–20	3,032	−5	3,032	100	−15	3,032	100
16–06	3,775	4	3,775	100	25	3,775	100
16–31	3,775	2	3,775	100	13	3,775	100
16–29	2,068	−5	2,068	100	−12	2,068	100
16–23	3,775	1	3,775	100	5	3,775	100
16–30	3,775	−5	3,775	100	−15	3,775	100
16–32	2,564	−2	2,564	100	−7	2,564	100

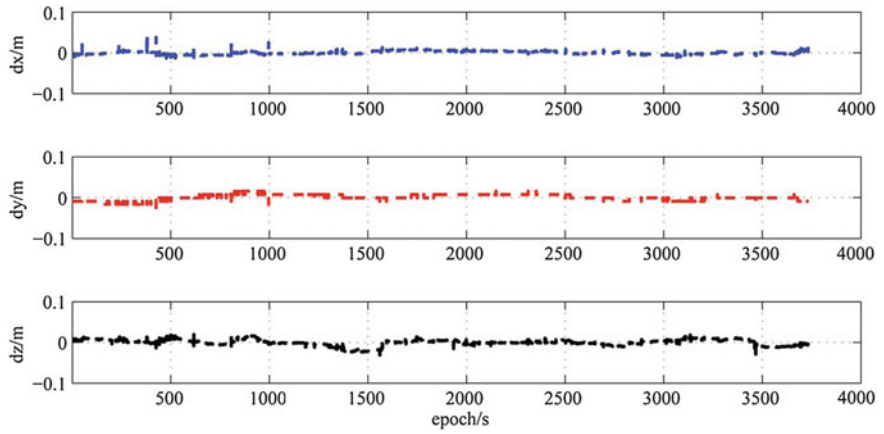

Fig. 18.2 Baseline vector biases of single epoch resolution in static test

The baseline biases of each epoch resolution are shown in Fig. 18.2. From the figure it can be seen that the new algorithm can solve the baseline with centimeter level after fixing the ambiguity successfully.

18.4.2 Dynamic Test

In dynamic situation, we can't acquire the true integer ambiguity because the calculation is not allowed to accumulate on time. So we adjust the truth of solving ambiguity by calculating the baseline vector between two carriers. The experiment system consists of three FlexPak-G2 receivers, two of which are fixed on the top of two cars respectively, and the rest one is fixed as based station. The general carrier phase RTK is processed between based station and two moving station respectively. The absolute position accuracy of general carrier phase RTK can reach

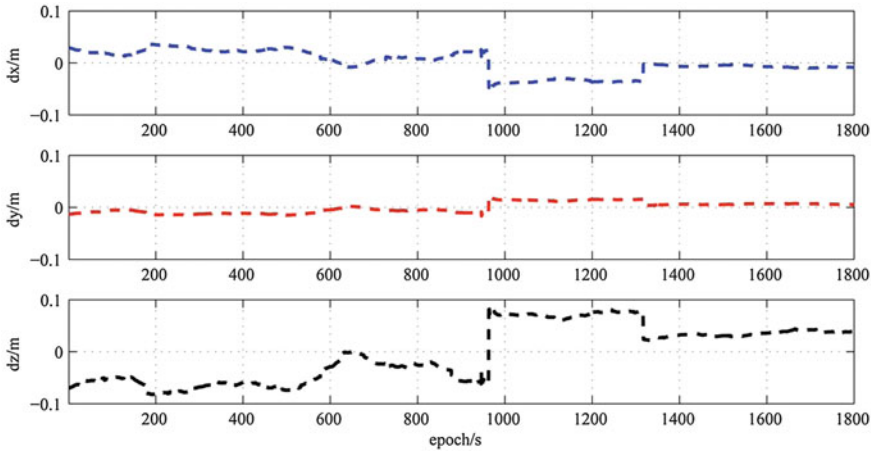

Fig. 18.3 Baseline vector biases of single epoch resolution in dynamic test

1 cm + 1 ppm, therefore the relative position vector calculated from absolute position of the two RTK is regarded as the reference value. The base line get form algorithm above is compared with this reference value, and the performance of the algorithm is adjusted in dynamic situation.

At 11 am, Dec 28, 2012, the dynamic test was carried out on the playground. The sampling period is 1 s, and the lowest requirement of satellite altitude angle is 15°. We acquired 1937 s data in all. The satellites which can be seen for three receivers are [2 4 5 10 12 13 17].

The baseline biases of each epoch resolution are shown in Fig. 18.3. From the figure it can be seen that the new algorithm can also solve the baseline with cm level in dynamic situation.

18.5 Conclusions

The double frequency wide lane carrier increases the wave length, so it's convenient for fixing ambiguity. If the ambiguity is required to solve reliably at single epoch, in general the code observable equations are added in. On the condition without P code, the precision of C/A code can't satisfy the requirements of ambiguity solving. The paper discusses a method which estimates the two kinds of wide lane ambiguities with fitting method by selection of parameter weights, then solves the each ambiguity separately. The method has advantages such as without initialization, simple process and solving the ambiguity reliably at single epoch. It can solve the baseline vector with centimeter level, which satisfies the requirements of application for aircraft landing on shipboard.

References

1. Li Y, Qiu Z (2008) Navigation and positioning, vol 537, 2nd edn. National Defence Industry Press, Beijing, pp 582–583
2. Tang D, Bi B, Wang X et al (2010) Summary on technology of automatic landing/carrier landing. J Chin Inertial Technol 18(5):550–555
3. Heo M, Pervan B, Gautier J et al (2004) Robust Airborne navigation algorithms for SRGPS. In: Proceedings of the IEEE
4. Niu F, Zhao J, Zhang Y et al (2010) Key principle and algorithms of JPALS. The 1st China satellite navigation conference, Bei Jing May 15–19
5. Pervan B, Chan F (2003) Performance analysis of carrier phase DGPS navigation for shipboard landing of aircraft. J Inst Navig 50(3):181–191
6. Rife J, Khanafseh S, Pullen S et al (2008) Navigation, interference suppression, and fault monitoring in the sea-based joint precision approach and landing system. Proc IEEE 96(12):1958–1975
7. Wang W, Gao C, Pan S (2012) Wide-lane ambiguity resolution of network RTK based on improved carrier phase smoothed pseudorange. Bull Surveying Mapp 4:41–46
8. Zhu H, Gao X, Bei J et al (2011) An algorithm of GPS ambiguity resolution on single-epoch. Sci Surveying Mapp 36(4):9–11
9. Yang R, Yuan Y, Ou J (2010) Real-time GNSS carrier phase differential technique for spacecraft rendezvous and docking. Scientia Sinica: Phys Mech Astron 40(5):651–657
10. Liu L (2005) The Research on the precise KINRTK theory and its applications. Wuhan University, Wuhan
11. Yang R, Ou J, Yuan Y et al (2006) Solving single-frequency phase ambiguity using parameter weights fitting and constrained equation ambiguity resolution methods. Cent South Univ Technol 13(1):93–98
12. Zhou Z, Yi J (1997) Principles and applications of GPS satellites surveying. Surveying and Mapping Press, Beijing, pp 123–124

Chapter 19
Research on Technical Development of BeiDou Navigation Satellite System

Jun Xie and Tianxiong Liu

Abstract The development characteristics of BeiDou satellite system have been analyzed based on the construction experiences of BeiDou Navigation Satellite regional System. The mission requirement, platform characteristics and payload technology of BeiDou Navigation Satellite have been researched in this paper. The project propositions which are required to reinforce have been suggested for next BeiDou Navigation satellite system.

Keywords BeiDou · Navigation satellite · Satellite · Bus satellite · Payload

19.1 Introduction

Satellite navigation systems can provide all time, all weather and high accuracy positioning, navigation and timing services to users on the earth surface or in the near-earth space. It is an important space infrastructure, which extends people's range of activities and promotes social development. BeiDou satellite navigation system can meet the demands of China's national security, economic development, technological advances and social progress, safeguard national interests and enhance the comprehensive national strength.

J. Xie (✉)
China Academy of Space Technology, Beijing 100081,
People's Republic of China
e-mail: heromeethero@yahoo.com

T. Liu
Institute of Satellite System Engineering, China Academy
of Space Technology, Beijing 100081, People's Republic of China
e-mail: liutianxiong@sina.com

J. Sun et al. (eds.), *China Satellite Navigation Conference (CSNC) 2013 Proceedings*, Lecture Notes in Electrical Engineering 243,
DOI: 10.1007/978-3-642-37398-5_19,

According to the development concept of starting with regional services first and expanding to global services later, BeiDou satellite navigation system is steadily accelerating the construction based on a 'three-step' development strategy.

Phase I: BeiDou Navigation Satellite Demonstration System. In 1994, China started the construction of BeiDou navigation satellite demonstration System. In 2000, two BeiDou navigation experiment satellites were launched, and the BeiDou navigation satellite demonstration system was basically established, which made China the third nation in the world in possession of an independent navigation and position satellite system. The space constellation includes two geostationary orbit (GEO) satellites, positioned at longitude of 80° east and 140° east respectively above the equator. Ground control segment consists of the ground control center and a number of calibration stations. BeiDou Navigation Satellite Demonstration System can provide the service of positioning, timing and short message communications based on the radio determining of satellite service [1].

Phase II: BeiDou Navigation Satellite (regional) System. In 2004, China started construction of BeiDou Navigation Satellite System. In 2007, the first satellite, a round medium earth orbit satellite (COMPASS-M1) was launched. In 2012, BeiDou Navigation Satellite (regional) System has provided service of positioning, timing and short message communications based on the radio determining of satellite service and the radio navigation of satellite service for the users of China and part of Asia-Pacific region. Space hybrid constellation includes five GEO satellites, five IGSO satellites, and four MEO satellites.

Phase III: BeiDou Navigation Satellite System with global coverage will completely be established by 2020.

During the course of building the BeiDou Navigation Satellite Demonstration System and the regional system, the Chinese Academy of Space Technology accumulated a lot of experience and lessons in satellite system design, production, testing and on-orbit applications. Satellite system design,space atomic clocks, large FPGA resistance space environment design, uplink injection of anti-jamming design, as well as satellite platform supply security have formed a series of achievements and experience, especially in the construction process of the regional system.

By combing, analyzing and summarizing, we can provide technical support for the next 2020 comprehensive construction BeiDou satellite navigation system.

19.2 The Characteristics and Functions of BeiDou Regional Navigation Satellite System

The space segment of BeiDou navigation satellite regional system includes 5 GEO satellites, 5 IGSO satellites, and 4 MEO satellites. The 5 GEO satellites point in 58.75° east, 80° east, 110.5° east, 140° east, 160° east respectively above the equator. To the 5 IGSO satellites, three of them are distributed in three inclined

geosynchronous orbit, orbit altitude of which is 36,000 km approximately, orbit inclination being 55°, sub-satellite track keeping coincide, intersection of longitude being 118°E, and phase position difference being 120°. The remaining two IGSO satellites also point in inclined geosynchronous orbit, the longitude of ascending node being 95°. The 4 MEO satellites distribute in two different orbits on average, orbit altitude of which is 21,500 km approximately, orbit inclination being 55°.

The three types of satellites were designed uniformly under the demand of batch production, intensive launching, and rapid make up constellation. The IGSO satellites and MEO satellites use DFH-3 satellite platform. GEO satellites use DFH-3A new satellite platform.

The satellite bus includes structure subsystem, thermal control subsystem, tracking-telemetry and command subsystem, electrical power subsystem, attitude and orbit control subsystem, propulsion subsystem, and data management subsystem. The satellite payload includes navigation subsystem and antenna subsystem. The navigation subsystem of GEO satellite are composed of RDSS, time synchronization and data repeating, uplink receiving and precision ranging, RNSS load. The navigation subsystem of IGSO and MEO satellite are composed of uplink receiving and precision ranging, RNSS load.

The basic mission and requirement of BeiDou satellite regional system as following.

1. Choosing mature satellite bus to meet the demand of effective load. The working life span of satellite is 8 years in orbit.
2. Keeping the functions of RDSS, time synchronization and data repeating of BeiDou Navigation Satellite Demonstration System, which is electromagnetic compatibility with newly added RNSS.
3. Using two-way satellite-ground time comparison technique, which can calculate accurate difference between satellite clock and ground station clock, to solve the problem that limited number of navigation satellite and ground observe and ground control station which are distributed in narrow territory.
4. Receiving the uplink receiving navigation message from ground control system, storing handling and generating downlink multichannel navigation signal. The satellite working state information is transmitted to ground operation control and user system.
5. Adapting three orbital hybrid constellation multi-satellite TT and C service, using new S band spread spectrum TT and C system and traditional mature USB TT and C system at the same time, to accomplish TT and C task independently, to ensure the reliability and safety of TT and C channel.

In the area of coverage, ensuring the G/T and EIRP values of receiving and transmitting signals, the broadcast navigation signal of satellite must be stable and continuous. Besides, scheduled interruption and unplanned interruption times and duration meet the project requirement.

19.3 The Technical Developments of BeiDou Regional Satellite Navigation System

According to the project general requirements, the conceptual design and prototype design for BeiDou regional navigation satellite system has been completed, and an experiment satellite was launched in April 14, 2007, which validated the RNSS load design, two-way satellite-ground time comparison technique, three-axis wheel control technique, yaw attitude control technique, on-board atomic clocks design. It marks China's entry into a new stage in independently development of navigation satellite system. At the same time, further measures were taken to solve the problem of anti-interference for satellite product and the complicated space environment. As a result, the technical state of satellite system, each subsystem and the product was determined, assuring the improvement of technical level and the quality of the project.

19.3.1 Satellite Bus

BeiDou regional navigation satellite system requires the satellite bus must inherit the mature technology, and the new technology also need to be applied at the same time.

Accord to the analyzing results of the missions and functions requirements of the satellite system, BeiDou regional navigation satellite system must adopt new technology based on DFH-3 satellite bus in electrical power capability, satellite attitude control requirements, thermal control requirements, self-management, TT and C. The key technology above mentioned must be breakthrough and experimental verification.

Characteristics and achievements of satellite bus are summarized as following.

1. The mixed solar array technology

The GEO satellites have RDSS and RNSS payload, which increased 900 W satellite power requirement compared with GEO satellite of BeiDou Navigation Satellite Demonstration System. Under the constraint of adopt the same DFH-3 the bus Solar Array structure and solar cell substrate, Si and GaAs/Ge mixed solar array technology were adopted firstly. The harmonizing problems of thermal characteristic, electrical characteristics and radiation characteristics were solved based on the technologies of circuit independent, sub-board layout, isolation diode and bypass diodes. The 2,500 W power requirement of GEO satellites was realized.

2. Wheel control in three axis and yaw control technology

In order to avoid or reduce the harmful effects to the system-level user positioning accuracy caused by thruster uninstalling the saturated momentum of

reaction wheel, GEO satellite control subsystem adopts the new program of wheel control in three axis. The adjustment of unloading reaction wheel momentum and station keeping are carried out at the same time especially.

The orbit inclination of IGSO and the MEO satellites are 55°. The incidence angle of the sun's rays changes with the right ascension of ascending node changing. Satellites cannot direct the sun and the Earth at the same time for DFH-3 satellite bus. Ascending node and inclination will directly affect the power output of the solar panels, according to the DFH-3 satellite bus design. Sunlight and the earth's shadow are larger than GEO satellite of the DFH-3 satellite platform, particularly the distribution of the length and number of changes to the earth's shadow. The design conditions of electrical power subsystem are different compared with the traditional DFH-3 satellite platform. In order to ensure the normal of solar array direct the sun with the accuracy better than 5°, The IGSO and the MEO orbit satellites adopted yaw control firstly.

3. Spread Spectrum structure and TT and C Technology for multi-satellite TT and C service

The new S band spread spectrum TT and C system was utilized to solve TT and C mission and frequency interference problems of multi-satellite hybrid constellation. The key technologies of low threshold, high dynamic dispreading, rapid acquisition of spreading code and Fine tracking digital baseband processor have been solved. The new S band spread spectrum TT and C system have many merits, such as strong anti-interference ability, high positioning accuracy, and low-density signal power spectrum.

4. Energy self-management techniques

In order to control the IGSO and MEO orbit satellite in invisible orbit, the new data handling system are designed to control battery power and satellite cabin temperature automatically.

5. RNSS power enhancement technology

In order to fulfill the requirements of RNSS power enhancement and the capability of anti-jamming in wartime, the data composed of satellite ephemeris, satellite attitude and antenna beam pointing come from payload, attitude and orbit control, antenna and data handling subsystems are fused.

6. High-precision thermal environment control technology

Navigation satellite atomic clocks are sensitive to ambient temperature. Their operating range is $-5\ ^{\circ}\mathrm{C} \sim +10\ ^{\circ}\mathrm{C}$ in-orbit. The rate of temperature change ratio is $\pm 0.5\ ^{\circ}\mathrm{C}/24$ h. The thermal control subsystem designs the atomic clock independent temperature control small cabin. The high-precision closed-loop automatic temperature control algorithm is designed.

19.3.2 Satellite Payload

Navigation satellite payload is the main instrument for satellite's navigation function and service performance, its technical level and reliability directly influence the function and performance of the system.

For BeiDou regional satellite navigation system, two kinds of navigation and positioning system coexistence, RNSS and RDSS. RDSS payload inherits the function of BeiDou satellite navigation experiment system. RNSS payload is a whole new payload, including uplink receiving and precision ranging subsystem, time and frequency synthesis subsystem, navigation signal generation subsystem, signal amplification link.

Satellite payload characteristics and main achievements are summed as follows:

1. High precision and stability in-board atomic clock technology

The energy level transition frequency of rubidium atomic is very stable. In use of this feature, rubidium signal with low frequency drift is generated and locked in high stability crystal oscillator through the effective power incentive of microwave cavity, spectrum signal detection and filtering, control of magnetic field and temperature field. By this way the functions of the atomic clock is realized. The domestic on-board rubidium clock in BeiDou navigation satellites is developed through advance research, prototype development and identification products development. After three manufacturer respectively developed two identification products, products for space tasks was eventually generated. During the development of rubidium atomic clock, lots of engineering problem were solved, such as life assessment, burn-in test method, high precision measurement, temperature sensitivity characteristics, performance difference between vacuum and atmospheric environment, long term stability test method, which ensured the development of on-board atomic clocks products.

At the same time, small quantity production was realized through means such as design verification and process control. The on-board rubidium atomic clock products have good consistency and compatibility.

2. Precision management technology for satellite's time and frequency standards

In order to ensure the synchronization of time and frequency between uplink and downlink, the reference frequency synthesizer was designed. The reference frequency synthesizer ensure the correlation between multiple frequency signals, including satellite's time signal, frequency signal, baseband signal and the receiver clock signals. So it can provide reliable, stable and continuous satellite clock signal to navigation payload.

By precision adjustment and control, Satellite clock has good short-term and long-term frequency stability characteristics. The precision control and management on satellite time and frequency standards, such as frequency transfer accuracy, frequency adjustment resolution, frequency adjustment and signal spectrum monitoring between main and backup atomic clock, meets the demands of

engineering construction. In using the reference frequency synthesizer, the satellite equipment integration was improved, and the volume and weight of the satellite equipment was reduced.

3. Two-way satellite-ground time comparison technique

For BeiDou satellite navigation system, range between satellite and ground station was ranged through microwave channel respectively by satellite and ground station at the same time. In this way clock bias between satellite clock and ground station clock standard is calculated and the two-way satellite-ground time comparison and synchronization are realized. High precision timing synchronization is achieved by establishing high precision ranging link and two-way satellite-ground time comparison and synchronization. Some key technology are broken through such as the long code tracking capture, multichannel receiving, on-orbit zero range monitoring and calibration.

4. Time–frequency anti-jamming technology

High density and intensity electromagnetic interference is a serious problem in the construction of BeiDou regional satellite navigation system. This problem have to solve. It directly affects the communication between the satellite and ground, including ground station and all kinds of terminal, result in reducing the system performance. The uplink data receiving directly decide whether the navigation satellite payload can work normally, therefore the anti-jamming and security design for uplink channel is particularly important. This problem was solved by precision fast acquisition and tracking algorithm, and low signal amplification technology with wide linear range and low time delay effect. The technical requirements that bit error rate is better than 10^{-8} and the ranging accuracy is better than 1 ns are satisfied.

5. Navigation signal design technology for anti complicated space environment

On-orbit satellite will inevitably be influenced by space charged particle radiation from the radiation belt of the earth, cosmic rays, solar cosmic ray, etc. Due to satellite's internal components, such as DSP, CPU, SRAM and FPGA, contains a large number of triggers and memory, there is a risk of SEU events in the effects of space environment. In order to minimize the risk and provide continuous, stable, reliable navigation signal for the user, BeiDou navigation satellite's SEU protection strategy was designed in three aspects, which is device selection, circuit design and instrument design. The satellite's surface charging and cabin deep dielectric charging protection are also designed. Through means such as hardware protection design, software fault tolerance, three modular redundancy, timing refresh and replacing FPGA with ASIC, the design and verification for the space borne products against environment are realized.

6. Continuation and stability technology for multi-channel high power signal

BeiDou navigation satellite payload include uplink receiving and precision ranging subsystem, time and frequency synthesis subsystem, navigation signal

generation subsystem and signal amplifying link. It has many signals with different frequency. In order to ensure the ground users can receive the signal from satellites more effectively, satellites are designed with high power amplifiers to ensure the signal transmitted has enough power.

In order to ensure the satellite's internal instruments working normally, EMC analysis and verification of system level is required. In accordance with the requirements of new design, many key problems were solved, such as electromagnetic isolation between RNSS and RDSS payload, intermediation suppression between uplink received signal and downlink transmitting signal, multipaction and power resistance, passive intermediation suppression for microwave high power devices, enhancing product protection and determine the product working state etc.

19.4 The Development Experience of BeiDou Navigation Satellite

BeiDou satellite navigation regional system reserved BeiDou satellite navigation experimental system of active positioning and short message communication service. It has begun to provide the continuously positioning, navigation, timing and message communication and other services in China and some areas around. BeiDou satellite navigation resolves the problem of having the RNSS positioning system in China, which is an integral part of China's economic and social development of spatial information services.

The main experiences of the BeiDou navigation satellite system as followed:

1. Combination of inheritance and innovation, and strengthen the ground test validation

According the requirements and characteristics of the BeiDou navigation satellite, CAST completed the structure model, the thermal control model, electrical model. However, we must adopt mature product inherited DFH-3 satellite platform technology. The key technical in concept phase must solve to ensure little risk in the preliminary design phase [2].

The BeiDou satellite reliability for special project has been arranged, which carry out the weaknesses of SADA, power controller, battery pack, earth sensor, and the reference frequency synthesizer etc., including the analysis, improvement and validation work.

2. To ensure the reliability and quality of the product batch approved

Based on self-research, innovation and development, the key technologies are solved, such as the space borne rubidium clock, precision ranging, two-way time range, the inhibition of the multipation and passive intermediation, large scale ASIC chip alternative FPGA devices, yaw control, rubidium, cabin small precision temperature control;

3. RNSS, and RDSS two positioning navigation system coexist, provide multi-function services

Besides high-precision, and reliable positioning, navigation and timing services, BeiDou Navigation Satellite System can provide the service of short message communications, integrity and difference service also. A differential service and integrity services, compared with the GPS system, the advantage of the BeiDou satellite navigation system is service area within diversification and the interaction between the users. It will continue to play a special role in the command and dispatch, disaster relief, and environmental data monitoring.

4. Compatible design, product interchange

The three orbiting satellite requirements in accordance with the "one-design, group batch manufacture, serial testing, intensive launching, rapid make up constellation" to carry out stand-alone product design, to ensure that most of the three types of satellite products have interchangeability; does not with interchangeable products, mechanical, electrical, thermal interface also give full consideration to compatibility. Rapid make up constellation of BeiDou satellite launch process giving top priority to the work carried out for the product quality problems is of great significance and has played a special role.

5. The coordinated integrated 3D design for satellite configuration and layout

BeiDou satellite has a coordinated integrated 3D design digital system, which has the development process and configuration and layout for satellite structure with thermal control cooling surface of thermal control subsystems, cable networks of power distribution subsystems, pipeline layout of propulsion subsystem. Using AVIDM system, integrated data interface for Unit, product layout, mechanical interface, thermal interface to improve the overall configuration and layout design. It also promotes the piping design correctness and efficiency.

6. Establish a test data comparing system.

BeiDou satellite products have batch manufacture features. We establish the test data comparing system based on the test data of different batch satellite and different phase of the same satellite. It is convenient for us to obtain the varying trends and fluctuating scopes of key technical index. So, we can carry out risk reviewing based on such critical data characteristics.

19.5 The Suggestions for BeiDou Next Navigation Satellite

The satellite navigation system is an space-based time and space infrastructure which based on the service range, accuracy, availability, continuity and integrity. In order to improve the performance of the next generation system in the process of construction BeiDou satellite navigation system, some work need to be

systematically summarized and analyzed. The works include the characteristics and results of the BeiDou satellite navigation system, the working status of satellites in orbit. The project propositions and suggestions are required to be reinforced, the works are as follows.

1. To strengthen the system top-level design analysis, to improve the system reliability

In order to ensure the continuity and stability of whole satellite navigation systems, some efforts need to be strengthened which including of the constellation configuration design and analysis, satellite and ground station integrated collaborative design, the constellation of running state satellite backup strategy and the strategy of mending their nets research, etc.

Availability, affordability and accuracy are the three key features of the satellite navigation system, in order to achieve the availability of the system, the first requirement is that the number of satellites in orbit.

Effects-based studies have shown that a constellation of 30 MEO satellites plus three backup satellites distribution will increase the availability of users for PNT in the space environment effects [3].

2. Long life, miniaturization and high reliability of space borne products

In order to improve the reliability and security of the satellite platform, reduce weight, size and power consumption of satellite products, the long life of the space borne product and miniaturization and high-reliability design work needed to be reinforced.

Through the component selection, the circuit redundancy design, system-level backup and fine coordination and management, as well as a large number of ground reliability and life testing, the working life of the satellite can be enhanced from 8 years to 12 years.

3. To strengthen the state management and selection of components

BeiDou navigation satellite system products must formulate batch production target in the design phase, identify and complete experimental verification of its products, process assessment and establish of process control file, etc. Through the analysis of the product's characteristics, the selection of components and raw materials, attention to the quantitative design for key characteristics parameters, we can obtain the best system qualify.

4. Reduction interrupt operation within plan

According to the actual situation of the our ground operation system (For limited by the area and the number of injection station, the monitoring stations, the track measurement and prediction accuracy still need to be further improved), interrupting operation of the position keeping and orbit control the need to be further reduced for satellites.

5. Strengthen crosslink and autonomous navigation technology research

The GPS system crosslink positioning changes with the system targets. Transmission of information from the support nuclear explosion detection, to support autonomous navigation of inter-satellite ranging and information transmission, to the full support of the space integrated information network communications.

BeiDou's satellite navigation constellation design, especially for management strategies in a variety of track between the link failure mode, comprehensive and in-depth analysis need to be developed on the rate of data transfer, the number of crosslink, measurement cycles, inter-satellite link frequency and autonomous navigation time and so forth. System simulation and experimental verification need to be carried out, simulation and verification work of crosslink signal system and autonomous navigation algorithm must be deep studied.

6. To improve the integrity monitoring capabilities of satellite navigation signals

As the integrity is a key performance of the satellite navigation services, design of reasonable integrity of signal system need to be further developed. The navigation signal integrity monitoring capabilities is a basic requirement, including of the system working condition, the receiving of uplink navigation message and the generation of downlink navigation signal, the health status of the satellite platform, satellite attitude and etc. Base on the autonomous integrity monitoring and diagnosis, alarming and correction of the imperfect state in time.

7. Enhance the onboard atomic clock performance

The stability of atomic clock of navigation satellite is the key factors to determine the performance of real-time user location. The stability of the atomic clock is the basis for establishing a high-precision time reference and time comparison technology with two–way ranging of satellite and ground. The performance of BeiDou system satellite-borne atomic clocks has not yet reached an excellent level of GPS BLOCK IIF satellite clock [4].

While the construction of the next generation BeiDou satellite system, the onboard atomic clock performance need to be matched with system construction, the day stability performance must be further improved, the manufacturing process and the debugger needs to be fitted the group batch production requirements. Particularly, atomic frequency discriminator signal enhancement, the light frequency shift, loop noise and temperature sensitivity suppression technology are further studied, while also further resolve the long life and reliability of space borne atomic clocks. At the same time of enhancing the onboard atomic clock performance, ground testing and assessment of methods of space borne atomic clocks need to be improved further.

8. To improve the delay stability of navigation signal

To broadcasting continuous, stable and reliable navigation signals is the basic task of the navigation satellite, the quality of the navigation signal determines the

merits of the navigation satellite. Building BeiDou next-generation system, the stability of the navigation satellite signal delay need to be improved, in order to facilitate operation and control systems and users, the navigation signal path delay value should to be strictly control to achieve the consistency of the delay of multiple frequency navigation signals for each work state.

9. Strengthen the new navigation signal system design to achieve the interoperability of GNSS systems compatible.

GPS, GALILEO, GLONASS and BeiDou systems coexist. The four systems are to provide free services to users worldwide. In order to be not interfering with each other, the compatibility must be considered to realize the joint PNT services to provide continuous, stable and reliable services for civilian and commercial users. GPS system occupied the global PNT market have a strong attraction to users, the survive possibility of the next generation BeiDou system must be compatible with the GPS system but not rely entirely on the GPS system. To this end, the design of the navigation signal system need to be further improved, including the parameters of the signal frequency, signal modulation mode, encoding format of information, the spectral characteristics, the output signal power, etc. BeiDou satellite navigation systems have to maintain continuous and stable service, but also fully compatible and interoperable with other GNSS systems.

19.6 Conclusions

BeiDou regional satellite navigation system has been established in 2012, and the satellites are working in good condition. It began to provide navigation service, including RNSS services, RDSS services and short message communications services for PRC and Asia–Pacific region.

During the navigation satellite development, CAST realized the coordination of the succession of innovation in satellite system design, adhered to the unity of the user requirements and technology, broke through several key technologies, and made a series of achievements. Moreover, a lot of valuable experience was also accumulated.

It is necessary for us to summary the BeiDou satellite development achievements. There is still need for intensive study for some subjects and items in next stage. To solve the key technical from above mentioned suggestions, establish and improve projects methods, will be beneficial to complete the construction of the BeiDou global satellite navigation system.

References

1. Navigation Satellite System(V1.0) China Satellite Navigation Office (2012) Report on the development of BeiDou(COMPASS)
2. Fuxiang X (2002) Satellite Engineering, China aeronautics press, China
3. Parkinson J (2010) ITT Exelis Completes GNSS Navigation Panel Milestone for GPS 3 Program. Satell Today, 5 Oct 2012
4. Jiao W, Wen L, Xiaorui H (translation) (2012) The preliminary review of BeiDou navigation satellite regional system, GPS Solution Online First

Chapter 20
Research of Precise Timing in Single Receiver Pseudorange Positioning Based on GPS System

Hehuan Zhu, Xiangyang Wu, Weirong Chen and Shuguo Pan

Abstract Timing service is one of the significant basic services in GPS system. Principles and mathematical models of the precise timing in single station pseudorange positioning were provided in this paper. And the automatic batch of timing procedures was developed through the C++ language. The experimental results show that, the precision of timing in single station pseudorange positioning based on GPS system can reach nanosecond level. In addition, the precision can be higher when using carrier smoothing pseudorange method. The precise timing services in GPS system has broad prospect in communications, electric power and other industries.

Keywords Precise timing · GPS system · Single station pseudorange positioning · Precision

20.1 Introduction

High-precision timing is significant to the operation of military, communication, power and transportation system, etc. It has universal application in national defense building and economic construction. With the rapid development of modern society, the requirements of timing precision are increasing. The research of precise timing based on GPS system is increasingly important, because GPS system has developed relatively more perfectly, and its precision is relatively higher.

H. Zhu (✉) · X. Wu · W. Chen
School of Transportation, Southeast University, No. 2 Sipailou,
Nanjing 210096, China
e-mail: zhuhehuan328@163.com

S. Pan
School of Instrument Science and Engineering, Southeast University,
No. 2 Sipailou, Nanjing 210096, China

J. Sun et al. (eds.), *China Satellite Navigation Conference (CSNC) 2013 Proceedings*, Lecture Notes in Electrical Engineering 243,
DOI: 10.1007/978-3-642-37398-5_20,

The precision of pseudorange observations is not high, while the determination of ambiguity is a major problem when using carrier phase observations. However, using carrier phase smoothed pseudorange method can not only improve the accuracy of positioning and timing, but also avoid the determination of ambiguity.

The precision of timing in single station pseudorange positioning based on GPS system can reach nanosecond level. By demonstrated, the precision can be higher when using carrier smoothing pseudorange method.

20.2 The Principles of Precise Timing by Pseudorange Positioning Based on GPS System

20.2.1 Observation Equations in Pseudorange Positioning

After calculating the satellite coordinates with broadcast ephemeris data, Eq. (20.1) [1] is used as fundamental model of pseudorange positioning.

$$\rho' = \sqrt{[X^j(t^j) - X_k(t_k)]^2 + [Y^j(t^j) - Y_k(t_k)]^2 + [Z^j(t^j) - Z_k(t_k)]^2} + c\delta t_k - c\delta t^j \tag{20.1}$$

According to approximate coordinates and Eq. (20.1), mark that

$$l_p^i = -\frac{X^i - X_p^0}{\rho_{p,0}^i}, m_p^i = -\frac{Y^i - Y_p^0}{\rho_{p,0}^i}, n_p^i = -\frac{Z^i - Z_p^0}{\rho_{p,0}^i} \tag{20.2}$$

The result of linearization can be written as Eq. (20.3) [1],

$$l_p^i \delta X_p + m_p^i \delta Y_p + n_p^i \delta Z_p - c\delta t_p - R_{p,0}^i + (\rho_p^i + c\delta t^i - \delta\rho_{trop}^i - \delta\rho_{ion}^i - \delta\rho_{others}^i) = 0 \tag{20.3}$$

where $\delta\rho_{ion}^i$ is ionospheric delay error (m); $\delta\rho_{trop}^i$ is tropospheric delay error (m); $\delta\rho_{others}^i$ is other errors, such as some effects of earth rotation, tidal, relativistic effects, etc.

Matrix form can be written as Eq. (20.4) [1],

$$\underbrace{\begin{bmatrix} v_p^1 \\ v_p^2 \\ v_p^3 \\ v_p^4 \end{bmatrix}}_{v} = \underbrace{\begin{bmatrix} l_p^1 & m_p^1 & n_p^1 \\ l_p^2 & m_p^2 & n_p^2 \\ l_p^3 & m_p^3 & n_p^3 \\ l_p^4 & m_p^4 & n_p^4 \end{bmatrix}}_{a} \underbrace{\begin{bmatrix} \delta X_p \\ \delta Y_p \\ \delta Z_p \end{bmatrix}}_{\delta x} + \underbrace{\begin{bmatrix} -1 \\ -1 \\ -1 \\ -1 \end{bmatrix}}_{b} \underbrace{\delta\rho_p}_{C\delta tk} - \underbrace{\begin{bmatrix} L_p^1 \\ L_p^2 \\ \cdots \\ L_p^m \end{bmatrix}}_{l} \tag{20.4}$$

If the number of simultaneous observation satellite is equal to 4, it has a unique solution, that is to say $\delta_x = A^{-1}L$. When the number is more than 4, we can use the least square method to calculate, that is to say $\delta_x = (A^TA)^{-1}A^TL$.

20.2.2 Carrier Phase Smoothed Pseudorange

Carrier phase smoothed pseudorange method is optimizing pseudorange value on the basis of pseudorange positioning. In this paper, we optimize P1 and P2 [1, 2] simultaneously. Equations are as follows:

$$\begin{aligned}\overline{p^j(t_i)} &= \frac{1}{i}p^j(t_i) + \frac{i-1}{i}[(\overline{p^j(t_{i-1})} + \delta p^j(t_{i-1}, t_i)] \\ \overline{p^j(t_i)} &= \frac{1}{i}p^j(t_i) + \frac{i-1}{i}[(\overline{p^j(t_{i-1})} + \lambda(\varphi^j(t_i) - \varphi^j(t_{i-1})]\end{aligned} \tag{20.5}$$

where

$\overline{p^j(t_i)}$	is smoothed pseudorange value on the ith epoch;
$p^j(t_i)$	is pseudorange value on the ith epoch;
$\overline{p^j(t_{i-1})}$	is smoothed pseudorange value on the $(i-1)$th epoch;
$\lambda\varphi^j(t_i)$	is carrier phase value on the ith epoch;
$\lambda\varphi^j(t_{i-1})$	is carrier phase value on the $(i-1)$th epoch.

The timing accuracy is greatly improved when using carrier phase smoothed pseudorange method.

20.2.3 Error Models

In this paper, we use broadcast ephemeris data to calculate coordinates and velocity of satellites, then compare calculated clock error, which by pseudorange positioning, with precise ephemeris clock error. Errors take ionospheric delay, tropospheric delay, error by earth rotation and relativistic effects into account.

We use ionosphere-free combination to correct ionospheric delay error. It is demonstrated in Eq. (20.6) [3]:

$$p = \frac{f_1^2 p_1 - f_2^2 p_2}{f_1^2 - f_2^2} \tag{20.6}$$

where

p_1	means pseudorange value of L1 signal;
p_2	means pseudorange value of L2 signal.

Then use Hopfield model to correct tropospheric delay error. It can be written as Eq. (20.7) [3, 4]:

$$\begin{aligned}\Delta^{trop}(E) &= \Delta d^{trop}(E) + \Delta w^{trop}(E)\\ \Delta w^{trop}(E) &= \frac{10^{-6}}{5}\frac{(-12.96T + 3.718\times 10^5)}{\sin\sqrt{E^2+6.25}}\frac{e}{T^2}11000\\ \Delta d^{trop}(E) &= \frac{10^{-6}}{5}\frac{77.64}{\sin\sqrt{E^2+6.25}}\frac{p}{T}[40{,}136 + 148.72(T-273.16)]\end{aligned} \tag{20.7}$$

where

$\Delta^{trop}(E)$ is tropospheric delay error (m);
$\Delta d^{trop}(E)$ is dry delay error (m);
$\Delta w^{trop}(E)$ is wet delay error (m).

Residual error of wet delay error is only several centimeters.

Equation of earth rotation is shown as Eq. (20.8) [4]:

$$\begin{pmatrix} X^{S'} \\ Y^{S'} \\ Z^{s'} \end{pmatrix} = \begin{bmatrix} \cos\alpha & \sin\alpha & 0 \\ -\sin\alpha & \cos\alpha & 0 \\ 0 & 0 & 1 \end{bmatrix} \begin{pmatrix} X^s \\ Y^s \\ Z^s \end{pmatrix} \tag{20.8}$$

where (X^s, Y^s, Z^s) is satellite coordinates; $\left(X^{s'}, Y^{s'}, Z^{s'}\right)$ is corrected horizontal coordinates. $\alpha = \omega \cdot \tau$, α is angles of earth when rotate. ω is earth rotation velocity, τ is time of satellite signal propagation.

According to satellite coordinates vector and velocity vector, error equation of relativistic effects is established. As shown in Eq. (20.9) [3, 4]:

$$\Delta rela = -\frac{2}{C}X^s \cdot \dot{X}^s \tag{20.9}$$

where X^s is coordinate vector of satellite; $\dot{X}^s$ is velocity vector of satellite.

20.3 Experiments and Analysis

In order to analyze and verify method of single receiver pseudorange positioning, this paper adopt the daily observation data of USNO station, which is obtained from IGS website. The receiver of USNO station has atomic clock, which is relatively stable [5, 6]. Timing standard is provided by clock error data of precise ephemeris.

Figure 20.1 shows precise clock error value of USNO by IGS, the interval is 5 min. There are 288 epochs, the average value is 6.241687×10^{-7} s.

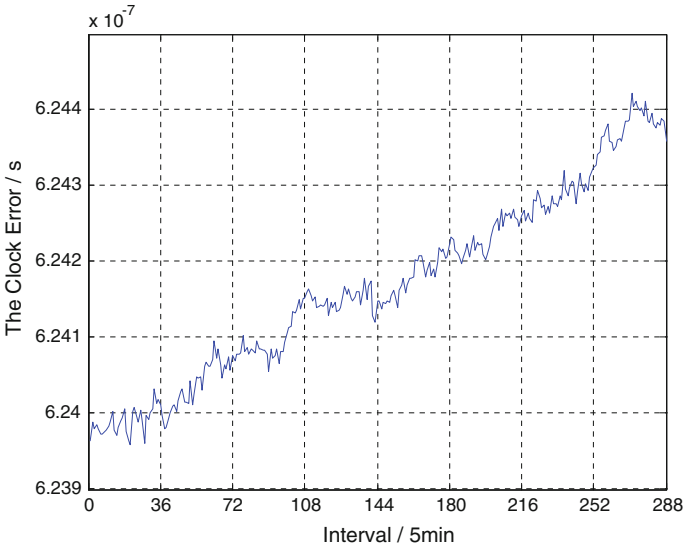

Fig. 20.1 The clock bias of USNO by IGS

20.3.1 Experimental Scheme

Firstly, we use pseudorange positioning to compute clock error (use the least square method), the average clock error of these 2,880 epochs is 6.268539×10^{-7} s, which differs 2.68518 ns with the average value of precision clock error.

Then, compare the clock error with precise clock error by IGS. In addition, interval of pseudorange positioning is 30 s, interval of precise ephemeris file is 5 min, so interval of clock contrast is 5 min. The result is shown in Fig. 20.2, the average error is 3.19 ns. We can discover that the errors are mostly nanosecond level.

On the basis of pseudorange positioning, use carrier phase smooth P1 and P2, then use the least square method to compute, the average clock error is 6.251205×10^{-7} s, which differs 0.95168 ns with the average value of precision clock error.

Figure 20.3 demonstrates that after carrier phase smoothed pseudorange, the difference between calculated clock error and precise clock error, the average difference is 2.61 ns.

The contrast of clock error between pseudorange and carrier phase smoothed pseudorange is reflected in Fig. 20.4. By comparison, the latter's accuracy is higher.

20.3.2 Precision Assessment

In the analysis of pseudorange positioning and carrier phase smoothed pseudorange, we should consider not only the clock error of two methods, but also assess

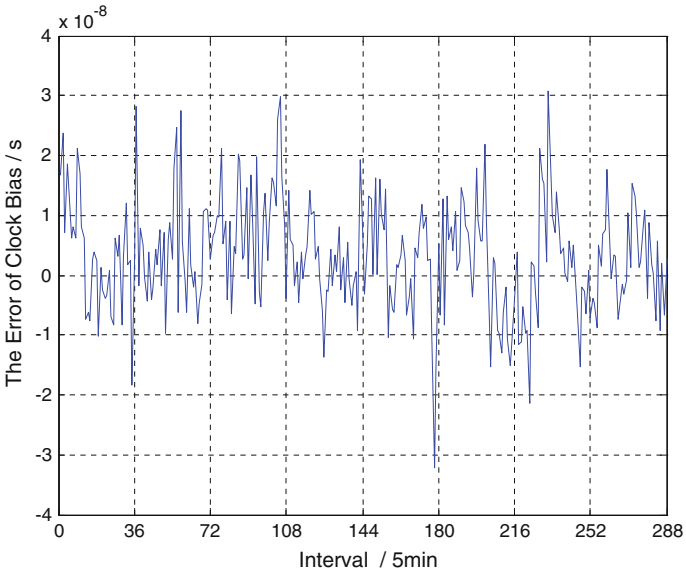

Fig. 20.2 The error of clock bias by pseudorange positioning

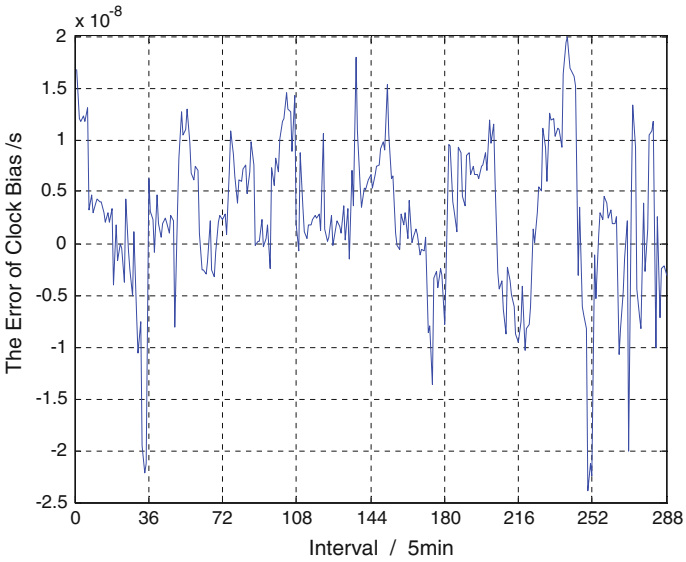

Fig. 20.3 The error of clock bias by carrier phase smoothed pseudorange

their stability respectively. In this paper, because we only evaluate timing accuracy and clock stability, we can regard internal accord RMS and external accord RMS as assessment standard [2, 7, 8]. Because the receiver of USNO station is atomic

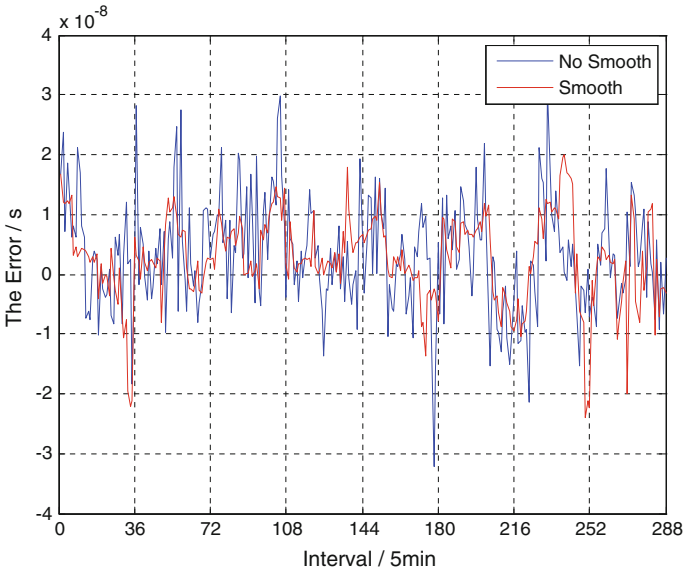

Fig. 20.4 The difference of error between pseudorange positioning and carrier phase smoothed pseudorange

clock, which clock error is very stable, we can regard the average clock error as reference value. As a result, internal accord RMS can be obtained by difference between calculated clock error and the average value of them. On the other hand, external accord RMS can be obtained by difference between computed clock error and clock error of atomic clock by IGS [8, 5].

$$\text{RMS} = \sqrt{\frac{\Delta^T P \Delta}{n}} \tag{20.10}$$

Where Δ is difference, n is the total number of samples, P is the weight matrix.

By comparison of two methods, external accord RMS of pseudorange is 9.27 ns, internal accord RMS is 10.22 ns. After carrier phase smoothed pseudorange, external accord RMS is 7.32 ns, internal accord RMS is 7.64 ns.

Detailed precision contrast is illustrated in Table 20.1.

Table 20.1 The precision index

Error	Maximum (s)	Minimum (s)	Average (s)	External accord RMS (s)	Internal accord RMS (s)
Pseudorange positioning	3.07×10^{-8}	3.21×10^{-8}	3.19×10^{-9}	9.27×10^{-9}	1.02×10^{-8}
Smoothed pseudorange	2.01×10^{-8}	2.39×10^{-8}	2.61×10^{-9}	7.32×10^{-9}	7.64×10^{-9}

By comparison, we think that the result of carrier phase smoothed pseudorange is better, the accuracy is higher. The best precision can reach milli nanosecond level.

20.4 Conclusions

In this paper, we compared RMS of pseudorange positioning with carrier phase smoothed pseudorange, it illustrates that using carrier phase smoothed paeudorange method can improve the precision of timing effectively, guarantee the stability of clock.

Experimental result indicates that, the precision of timing in single station pseudorange positioning based on GPS system can reach nanosecond level. In addition, the accuracy can be higher when using carrier smoothing pseudorange method.

In this paper, we use broadcast ephemeris data to calculate satellite coordinates and to pseudorange positioning, the precision may be higher if using precise ephemeris data to compute.

Acknowledgments This work was carried out through China "Twelfth Five-Year" Plan for National Key Technology R&D Program (contract No.2012BAJ23B01).

References

1. Hu W, Gao C (2001) GPS principles and applications. China Communications Press, China, pp 60–83
2. Liu R, Yang Z, Zhan X (2012) Research on carrier phase smoothed pseudo-range of compass. J Civil Aviat Univ China 30(3):28–31 (Ch)
3. Holfmann-Wellenhof B, Lichtenegger H, Wasle E (2008) GNSS-global navigation satellite systems—GPS, GLONASS, Galileo & more. Surveying and Mapping Press, Beijing, pp 98–102
4. Xu G (2007) GPS theory, algorithms and applications, 2nd edn. Tsinghua University Press, Beijing, pp P47–P50
5. Plumb JF (2003) Carrier phase time transfer using the global positioning system. University of Colorado, Colorado
6. Larson K (1999) Carrier-phase time transfer. IEEE Trans Ultrason Ferroelectr Freq Control 46(4):1002–1010(Ch)
7. Zhang X, Cheng S, Li X, Guo F (2009) Precise timing using carrier phase smoothed pseudorange from single receiver, J Wuhan Univ 34(4): 463–465 (Ch)
8. Highsmith DE (1988) Precise satellite-to-satellite GPS time transfer in near real-time. Virginia Commonwealth University, Virginia

Chapter 21
The Beidou2 Navigation Signal Multipath Fading Applied Research in Satellite Tracking Ship

Zhong Lin, Gu Bing-jun and Xu Rong

Abstract Around two Beidou2 generation networking success, application of Beidou2 satellite navigation system in aerospace survey ships is an inevitable trend, but the Beidou2 satellite navigation system and other satellite navigation system as there is a multipath interference problem. This paper focuses on signal processing and engineering application perspective using the method of anti multipath interference and new processing, That is the use of narrow technology and high resolution processing technology at the receiving end, and then by a suitable choice of the receiver bandwidth and receiver antenna architecture suitable deck. Through the test in space survey ship, played a good resistance to multipath effect.

Keywords Global navigation satellite system · Beidou2 · Satellite tracking Ship · Multipath error

Background: In the process of performance evaluation of navigation signals, multipath performance is an important performance index. Pseudo code and carrier phase offset caused by multipath environment depends on the receiver, Measurement of ship radar antenna is numerous, ship building block, the sea, sea clutter interference and other environmental factors, the multipath interference problem. Because of the correlation between the multipath effect in the space is very small, the receiving end by difference method to eliminate. With the receiver hardware index rising, the effects of narrow correlator technology and the increase of the high resolution processing receiver bandwidth signals to reduce multipath effect has received extensive attention both at home and abroad. In this paper, signal system based on Beidou2 open on two generation receiver adopting the technology, considering the anti-multipath performance and antenna installation engineering factors were tested in the survey ship platform, from different angles

Z. Lin (✉) · G. Bing-jun · X. Rong
China Satellite Maritime Tracking and Controlling Department,
Jiangyin 214431 Jiangsu, China
e-mail: 435735013@qq.com

J. Sun et al. (eds.), *China Satellite Navigation Conference (CSNC) 2013 Proceedings*, Lecture Notes in Electrical Engineering 243,
DOI: 10.1007/978-3-642-37398-5_21,

and GPS, inertial navigation system for performance evaluation, in order to promote the north fights navigation signal in the two generation application performance of Navigation Engineering provides reference.

21.1 Questions

The multipath phenomenon refers to the addition of receiver receives a signal by the electromagnetic wave travels in straight lines emitted from the satellite, also may receive one or more by the electromagnetic wave signal reflected by surrounding objects, and each reflection signal may be after one or multiple reflection after the arrival of the antenna. As with the principle of light reflection, metal and water are good reflectors. Measurement of ship metal deck, the sea environment will cause the multipath phenomenon, Beidou2 signals received prone to multipath interference. In addition, many measurement ship antenna, working in the bad sea condition, the reflectivity of clouds, ionospheric emission will be caused by multipath effect. Multipath causes the error code and carrier phase depends on the receiver environment, The correlation in space is very small, The traditional differential treatment to eliminate the effect of co.. With the success of the two generation network of Beidou navigation system, the Beidou navigation system in the measurement ship and civil navigation application has become the inevitable trend, However, with the maritime navigation satellite Beidou receiving signal compared to low transmission power, receiver environment is complex, the signal is susceptible to multipath interference problem.

21.2 Beidou2 Navigation Satellite Signal System

Service signal China open two Beidou2 generation signal system open (OS) and authorized signal (AS) [1] as follows in Table 21.1.

Table 21.1 Beidou2 navigation signal structure and parameters

Navigation signal	Carrier wave/MHz	Bit rit/MHz	Modulation	Type of service
B1cx data (I)	1,575.42	1.023	MBOC (6,1,1/11)	OS
B1cy Navigation frequency (Q)		1.023		
B1cz		2.046	BOC (14,2)	AS

21.3 The Navigation Signal Multipath Processing Technology

Multiple paths by using digital signal processing technology and the inhibition can be divided into two types of elimination method:

A class of estimation of component parameters of each multipath signal, and the multipath signal components and the reduction of the direct wave signal is subtracted from the received signal in the total; Parameter estimation of another kind does not involve the multi-channel signal, usually followed by related settings and code loop discriminator improved and more direct route is to restrain and eliminate the results. With the continuous improvement of the performance of receiver, narrow related new technologies and high resolution technique was gradually known by people.

21.3.1 Narrow Correlator Technology

Narrow-related technology is a digital signal processing technology multipath suppression and elimination technology, Mainly refers to the receiver using samples collected from near the left and right sides of the main peak of the correlation function to the plurality of correlators, and then analyze the autocorrelation function curve distortion, both detected whether the reception signal is destroyed, and the derivation of a multi-path and direct the method of the wave phase amount of the signal component.

Narrow correlation of noise has good inhibiting effect, when the correlation distance decreases, lead-lag increases channel noise correlation, thus noise tracking effect on PLL smaller. New narrow correlation processor and chip correlators with respect to the standard ratio, narrow correlation can be improved the accuracy of measurement of 3–4 times [2]. At the same time, narrow correlator technology also have the ability to inhibit the code phase multipath.

21.3.2 High Resolution Correlation Technique

Although the application of narrow correlator technique can make the accuracy is high, but in the actual application process, due to the impact of local multipath signals and atmospheric multipath signal is very difficult to guarantee the measurement data with high precision, so the application of another special multipath mitigation technology in circuit design, high resolution correlation (HRC) technique. HRC technical realization for each satellite configuration 5 complex correlator, 3 more than the general receiver, will completely eliminate the error average delay and delay multipath signal of carrier phase and code phase measurement, and the HRC method is compatible with narrow correlator technique [3].

21.4 The Navigation Signal Multipath Assessment Theory

21.4.1 The Multipath Effect Classification

Due to the multipath signal phase changes and different delay, multipath interference and divided into two types: if the direct signal and multipath signal with the same phase, the synthetic signal amplitude is greater than any one component amplitudes, called constructive multipath (Fig. 21.1 left); on the contrary, if the direct signal and multipath signal phase, amplitude will the synthetic signal decreases, called destructive multipath (Fig. 21.1 right). The auto correlation peak of two kinds of multipath signal shown in Fig. 21.1.

The signal receiver is composed of direct signal and multipath signal, the existence of time delay, phase shift and multipath fading signal than the direct signal, this will lead to the PN code tracking error to produce multipath effect [4]. The presence of multipath effect, the received signal $r(t)$ model:

$$r(t) = a_0 e^{j\varphi_0} x(t - \tau_0) + \sum_{n=1}^{N} a_n e^{j\varphi_n} x(t - \tau_n) \tag{21.1}$$

In the formula, the envelope signal is emitted $x(t)$, a_0, φ_0, τ_0 respectively, the direct signal amplitude, phase and propagation delay; a_n, φ_n, τ_n as the n road multipath signal amplitude, phase and propagation delay, N as the number of multipath signal. In this paper, to simplify the discussion, consider a single multipath situations, i.e.. N = 1.

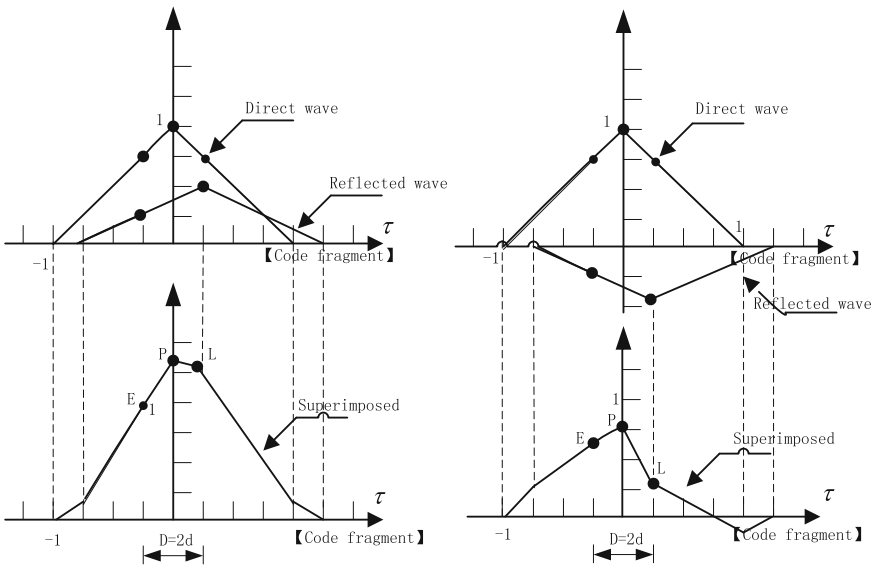

Fig. 21.1 The auto correlation peak of two kinds of multipath signal

21.4.2 Multipath Signal Model

The process of receiving the actual signals, multipath signal wave is relatively direct signal wave relative phase and amplitude changes, causes the code loop discriminator deviate from the equilibrium track points, resulting in PN code tracking error. Therefore, usually uses the output signal ring authentication code is to deviate from the true information to evaluate the multipath error. To simplify the analysis, the general choice of code loop coherent advance reduced delay locked loop delay, multipath error envelope outputs the code loop discriminator for:

$$D(\varepsilon_\tau) = a_0\left[R\left(\varepsilon_\tau - \frac{d}{2}\right) - R\left(\varepsilon_\tau + \frac{d}{2}\right)\right] \pm a_1\left[R\left(\varepsilon_\tau - \tau - \frac{d}{2}\right) - R\left(\varepsilon_\tau - \tau + \frac{d}{2}\right)\right] \tag{21.2}$$

In the formula, $R(\tau)$ for the correlation function of PN, ε_τ estimated the direct signal time delay error, τ for the multipath effect, d as the leading and lagging correlation distance (ε_τ, τ, d the unit symbol).

Multipath error performance for code loop discriminator curve of zero offset, so the discriminator output is zero ε_τ values for the multipath error, which is the solution

$$D(\varepsilon_\tau) = 0 \tag{21.3}$$

Coherent early-late delay lock loop discriminator output in code offset zero near linear relationship meet, so can be expanded to a first-order Taylor in the vicinity of zero:

$$D(\varepsilon_\tau) = D(0) + D \cdot (0) \times \varepsilon \tag{21.4}$$

Combined type (21.3) (21.4) expression to the multi-path error:

$$\overline{\varepsilon_\tau} = -D(0)/D \cdot (0) \tag{21.5}$$

Considering the signal bandwidth, code correlation function and power spectral density of the relationship:

$$R(\tau) = \int_{-\beta_r/2}^{\beta_r/2} S(f)e^{j2\pi f\tau}df \tag{21.6}$$

Type: β_r for the signal bandwidth, $S(f)$as the signal power spectral density.

By formula (21.2) (21.5) (21.6) the final output can be obtained for the multipath error:

$$\overline{\varepsilon_\tau} = \frac{\pm a\int_{-\beta_r/2}^{\beta_r/2} S(f)\sin(2\pi f\tau)\sin(\pi fd)df}{2\pi\int_{-\beta_r/2}^{\beta_r/2} fS(f)\sin(\pi fd)[1 \pm a\cos(\pi fd)]df} \tag{21.7}$$

In the formula, $a = a_1/a_0$ is MDR. When multipath signals relative phase direct signal difference is 0 , ± take ±; is 180± take−, respectively corresponding limit construction of multipath and destructive multipath, the type (21.7) are given for the envelope of the multi-path error, multipath error all actual are located in the envelope.

In addition to multipath envelope, can usually be to assess the anti-multipath performance [1] signal with average multipath error, average multipath error by definition:

$$\varepsilon_d(\tau) = \frac{1}{\tau}\int_0^{\tau}\left[\frac{abs(\varepsilon_\tau(\tau)|\varphi = 0) + abs(\varepsilon_\tau(\tau)|\varphi = 180)}{2}\right]d\tau \tag{21.8}$$

In the formula, φ as the relative phase of the multipath signals, molecule two is type (21.7) ± take +, −, two cases of the corresponding. According to the signal structure and parameters are given in Table 21.1, the power of different satellite navigation signal spectrum density function into type (21.7) (21.8), then to evaluate the two Beidou navigation signal multipath error generation.

21.4.3 The Receiver Parameters

Analysis from the angle of signal processing, navigation signal performance and multipath multipath error to the signal amplitude ratio (MDR), relative spacing of d, the signal bandwidth β, the antenna design and data processing after will reduce the effect of multipath error (Fig 21.2).

By using the evaluation model, the use of simulation theory for simulation of multipath error envelope, Comparison of MDR = −6 dB multipath error

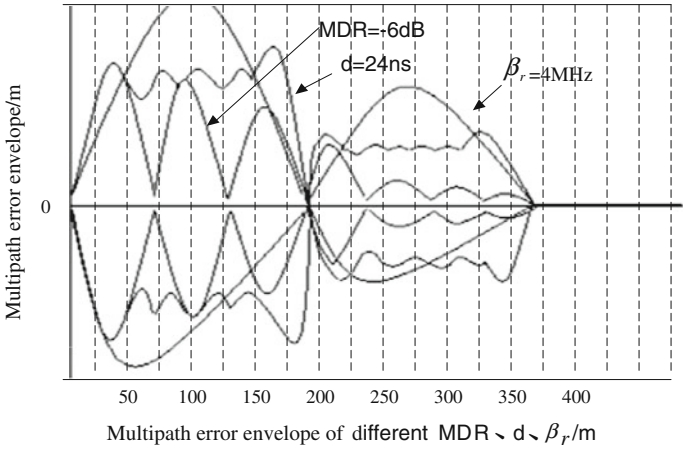

Fig. 21.2 The antenna design and data processing after will reduce the effect of multipath error

envelope, the smaller the MDR multipath signal amplitude is weak, the multipath error caused by multipath delay is small; Reduce the correlator spacing can reduce multipath error, the front end of the receiver bandwidth constraints, when the code spacing D tends to zero, the multipath error is not zero, and then increase the spacing of anti-multipath performance improvement is not obvious; For the receiver bandwidth, smaller bandwidth, easy to filter high frequency component is larger, in order to guarantee the performance of the two generation navigation Beidou multipath signals, must ensure that the receiver bandwidth is larger than 4 MHz, bandwidth is easy to cause the distortion. Considering the market hardware manufacturing level, on the basis of the above factors comparison parameters MDR = −6 dB, d = 24 ns, receiver = 24 MHz index.

21.4.4 Strategy Use Survey Ship Engineering

In order to detect, restrain and eliminate multipath, engineering application may take different strategies in the design of satellite signal receiving antenna design, and location, digital signal processing and navigation calculation of these four links. Measurement of ship engineering application tests except for processing the receiver receives the signal and also from the antenna design and location and navigation calculation using the optimization strategy for measuring the value of treatment.

21.4.4.1 The Design and Location of the Receiving Antenna

(1) using the right-hand circular polarization antenna to receive the left-hand circular polarization signal odd several times after the reflection, while the right-hand circular polarization signal strength even after the reflection can be attenuated greatly, so only the direct wave signal received by antenna. (2) high performance antenna using the choke antenna that has multiple path resistance, or by using antenna array to eliminate the multipath effect using space diversity technology. (3) the antenna measurement ship antenna mounted on the ship mast on the highest point, avoids around the antenna and deck building block. Anti-interference measures are taken for the maritime satellite communication signal: for maritime Satcom and GLONASS working frequency technology state take effective anti-interference measures on equipment; supporting the development of two kinds of antenna: Marine Beidou2 antenna and marine GNSS active antenna combined to adapt to different use environments.

21.4.4.2 Positioning and Navigation Calculation of Measured Values

Measurement of ship main through the average of Beidou2 signal measurement analysis, processing, reduce multipath error; carrier phase measurements on different time values with the same parabola approximation, using actual measured values close to and curve for evaluation and selection of measurement; Periodic of the Beidou2 satellite orbital motion and rotation of the earth, in the measurement of multiple cycles of estimated pseudorange multipath error and the use of multipath error on a cycle estimate to correct the cycle of the pseudo-range measurements; ④ by statistical analysis in the multipath error data, the establishment of a multipath error model, on the basis of this model to correct later in the measured values of multipath error method for measuring value.

21.5 Test Result

The Beidou2 navigation signal contains a variety of signal components, covering a wide range of MBOC (6,1,1/11) signal test. The MBOC included by BOC (1, 1) to BOC (6, 1) consists of the signal, at the same time the power ratio of the total signal for 1/11. Considering the high frequency carrier signal transmission of high intensity, autocorrelation performance is good, the QPSK modulated signal of high frequency 1,589 MHz satellite M1, multipath error directly receiving and processing two Beidou2 generation of public service signal and authorization signal as shown in Fig. 21.3, the use of narrow correlation processing technique, for digital signal processing and navigation computation at the receiver, the average multipath error signal as shown in Fig. 21.4.

The test results show that: in the above parameters, the calibration tower produce multipath delay 300 m as measuring reference point, the weather condition is good, the smaller the relative position of the sea waves, as shown in Fig. 21.4 position in the 5,871 position, the multipath delay exceeds 300 m, processing of measurement ship positioning and navigation calculation value later, the multipath

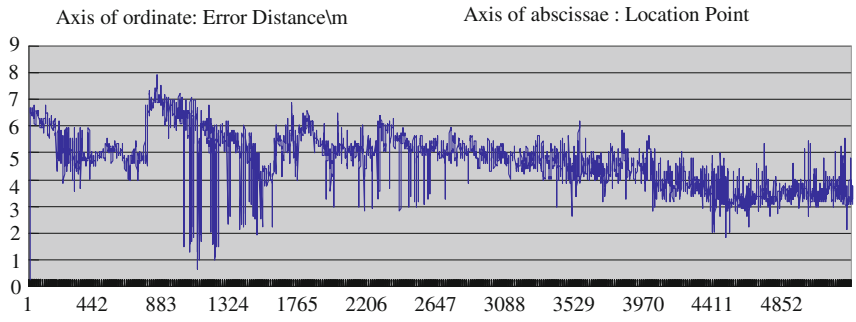

Fig. 21.3 Two Beidou2 generation of public service signal and authorization signal

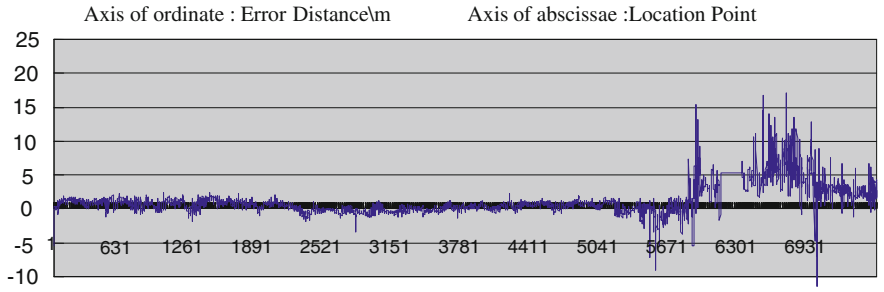

Fig. 21.4 The average multipath error signal

error on the Beidou2 navigation signal of the two generation of convergence in the vicinity of 0 m; multipath delay is less than 300 m (corresponding to 1), outliers position error caused by multipath effect of the two generation of the Beidou2 navigation signals within 4 m, illustrate the multipath receiver with narrow correlator processor can easily distinguish the Beidou2 navigation signal over two generations 300 m delay.

21.6 Conclusion

Stereotypes in the Beidou2 satellite signal receiving antenna design, design of measurement ship and the location of the space is limited, take a variety of measures in the receiver digital signal processing to suppress the multipath effect is very effective. In this paper, through the survey ship test, using digital signal processing technique using narrow and high resolution techniques appropriate analog filter RF front-end βr and phase discriminator type of receiver inside, can significantly improve the autocorrelation properties, effectively reduce the influence of multipath effect, with positioning and navigation measurement of certain value processing method, which can be further to meet the high precision positioning measurement ship needs.

References

1. Shusen T, Bing Z, Shengtao G (2010) Chinese science: physics, mechanics. Glob Des Satell Navig Signal 40(5):514–519
2. Fenton P (2005) Pseudorandom noise ranging receiver which compensates for multipath distortion by making use of multiple correlator time delay spacing. US Patent 5414729, 9 May 2005
3. Van Dierendonck AJ, Fenton P, Ford T (2011) Theory and performance of narrow correlator spacing. J Inst Navig 39(3):265–283 Fall 2011
4. Zuping T, Hongwei Z, Xiulin H (2010) Research on performance evaluation of Compass navigation signal Chinese sci: phys, mech, astron 40(5):592–602

Chapter 22
Regional PWV Estimation Using Interpolated Surface Meteorological Data from NCEP CFSv2

Xiufeng He and Junjie Wang

Abstract In addition to the GPS data, site-specific surface meteorological data is essential to derive the precipitable water vapor (PWV) using ground-based GPS. Furthermore, many GPS networks don't have the meteorological sensors installed together with the GPS antenna at all when built. This thesis has provided in detail a new method to interpolate the surface meteorological data of GPS sites by using National Centers for Environmental Prediction (NCEP) Climate Forecast System Version 2 (CFSv2) 6-hourly forecast products. Based on Hong Kong Satellite Positioning Reference Station Network (SatRef), the method is tested, and the results show that the method can be helpful to estimate the regional PWV even when there are no meteorological sensors.

Keywords GPS meteorology · NCEP CFSv2 · PWV · Interpolation

22.1 Introduction

Water vapor is the substrate between moisture and heat transfer, and it is a very unstable meteorological parameter, affecting the radiation balance, energy transportation, cloud formation and precipitation processes [1, 2]. The estimation of atmospheric water vapor from ground-based GPS started in 1992 [3] and is being continuously improved and evaluated [4–8]. In addition to the GPS data, site-specific surface meteorological data is essential to derive the precipitable water vapor

X. He (✉) · J. Wang
Institute of Satellite Navigation and Spatical Information System,
Hohai University, 210098 Nanjing, China
e-mail: xfhe@hhu.edu.cn

J. Wang
e-mail: wang_900328@hhu.edu.cn

J. Sun et al. (eds.), *China Satellite Navigation Conference (CSNC) 2013 Proceedings*, Lecture Notes in Electrical Engineering 243,
DOI: 10.1007/978-3-642-37398-5_22,

(PWV) from the atmospheric delay [9]. Ideally a dedicated meteorological sensor is installed together with the GPS antenna. However, this involves additional cost at the level of one-third or half of the geodetic GPS receiver cost [10]. Furthermore, many GPS networks don't have the meteorological sensors installed together with the GPS antenna at all when built. In order to take advantage of the existing regional GPS networks to estimate PWV, it is worthwhile seeking alternative solutions, for example, using surface meteorological data from other sources.

NCEP has developed the Climate Forecast System version 2 (CFSv2; [11]) fully coupled ocean–atmosphere-land model with advanced physics, increased resolution and refined initialization. The 6-hourly atmospheric, oceanic and land surface analyzed products and forecasts, available at 0.2, 0.5, 1.0, and 2.5 degree horizontal resolutions, became operational since 2011 (http://cfs.ncep.no-aa.gov/). This thesis proposes in detail a new method of spatial and temporal interpolation to derive the surface meteorological data of GPS sites from NCEP CFSv2 6-hourly forecast products which at a horizontal resolution of 0.5 degree. With the help of this method, we achieve the surface temperature and pressure of the 3 IGS tracking stations and 6 selected continuously operating reference stations in Hong Kong SatRef, and then the regional PWV of Hong Kong is estimated. The advantages of the new data source are presented by comparing the precision of the different interpolated meteorological data from CFSv2 and NCEP/NCAR (National Center for Atmospheric Research) reanalysis products. In order to verify the reliability of regional PWV estimation with this method, the interpolated meteorological data from CFSv2 is compared with the measured meteorological data, and the PWV estimated with interpolated meteorological data from CFSv2 is also compared with the PWV estimated with measured meteorological data.

22.2 Principles of Ground-Based GPS Sensing Atmospheric Water Vapor

When GPS signal transmits in the ionosphere and neutral atmosphere of the earth, it may produce speed delay and inflecting delay on account of atmosphere refraction. According to the dispersion of ionosphere, 99 % ionosphere delay can be eliminated using dual-frequency GPS receiver [12]. Then the neutral atmosphere delay can be expressed as:

$$T_D = 10^{-6} \int N_d \, ds + \int N_w \, ds = H_D + W_D \tag{22.1}$$

where N_d and N_w are the refractive indexes of dry and wet atmosphere, respectively; H_D is the hydrostatic delay; W_D is the wet delay. The neutral atmosphere delay can be converted to zenith direction with mapping function. Thus, the zenith total delay (ZTD) can be expressed as:

$$ZTD = ZHD + ZWD \tag{22.2}$$

ZTD can be resolved by using high-precision GPS data processing software such as GAMIT. ZHD can be well estimated using Saastamoinen model. The model can be expressed as:

$$ZHD = (2.2779 \pm 0.0024)P_s/f(\Phi, h) \tag{22.3}$$

where P_s is the surface pressure, and $f(\Phi, h)$ can be expressed as:

$$f(\Phi, h) = 1 - 0.00266\ \cos(2\Phi) - 0.00028h \tag{22.4}$$

where Φ is the geographic latitude, h is the altitude of GPS site (in km). Thus, ZWD can be isolated according to Eq. 22.2, and PWV is proportional to ZWD which can be expressed as:

$$PWV = \Pi \times ZWD \tag{22.5}$$

$$\Pi = \frac{10^6}{\left(K_2' + K_3/T_m\right)R_v} \tag{22.6}$$

where Π is the conversion coefficient; T_m is the surface weighted mean temperature; K_2', K_3 and R_v are constants.

22.3 Description of Meteorological Data Interpolation Method

22.3.1 Data Description

Figure 22.1 illustrates the 6 selected continuously operating GPS stations providing daily GPS data files available in Hong Kong SatRef and the neighboring radio sounding site. The daily GPS data files we collected include both observation files and meteorological files. The sampling interval of observation files is 5 s. Data on temperature, pressure, relative humidity (RH) are recorded every minute in meteorological files. For the radio sounding site, the PWV derived from the sounding observation data will be used for later comparison.

Duan et al. [5] point out that the PWV resolved in regional network is relative value based on difference method. By incorporating a few remote global tracking stations into the regional network (making some baselines over 500 km), the absolute value of PWV at each station in the augmented network can be estimated. Hence, there are 3 global tracking stations (BJNM, IISC and URUM) selected. Figure 22.2 shows the distribution of the three selected IGS tracking stations and their distance to Hong Kong.

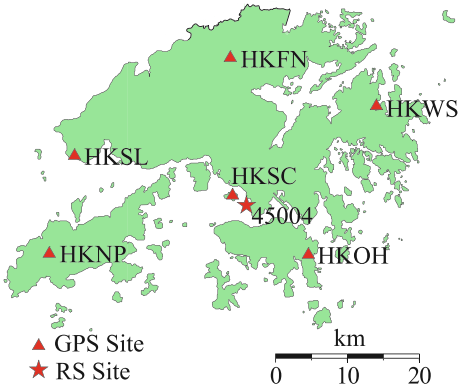

Fig. 22.1 Distribution of the selected *GPS sites* and the neighboring *radio sounding site* in Hong Kong

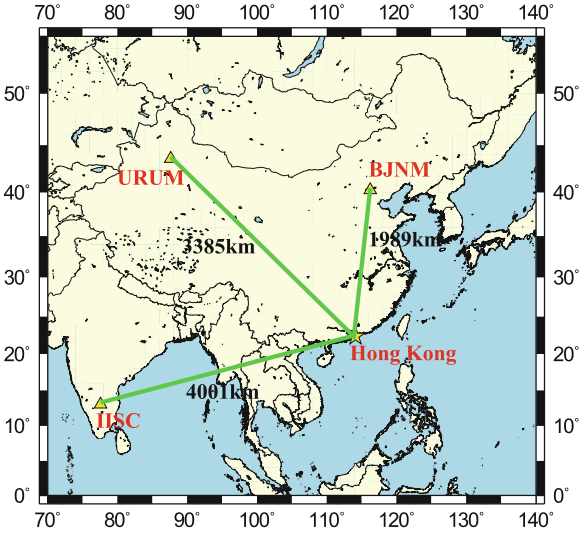

Fig. 22.2 Distribution of the three selected IGS tracking stations and their distance to Hong Kong

The NCEP CFSv2 6-hourly atmospheric, oceanic and land surface analyzed products and forecasts can be achieved freely. The data which is on "ground or sea surface" level at a horizontal resolution of 0.5 degree is chosen to be analyzed in this research. There are 3 variables in the data of "ground or sea surface" level, including temperature, pressure and geopotential height, which are used to interpolate the surface meteorological data of GPS sites, and then used to estimate the PWV of Hong Kong.

22.3.2 Interpolation Method

Interpolated surface meteorological data [10] from the Australian automatic weather station have been used for water vapor estimation from GPS data as GPS

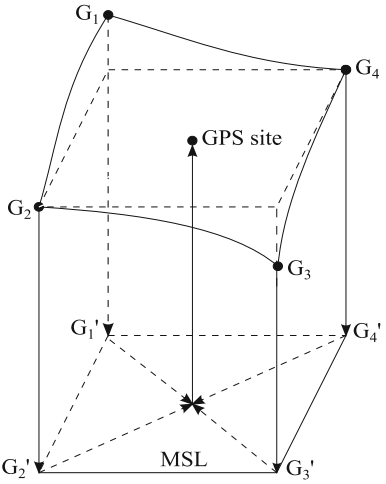

Fig. 22.3 Spatial distribution of GPS site and the four neighboring grid points

sites were not collocated with the weather stations. Jade et al. [9] has derived the PWV using the interpolated site-specific surface meteorological parameters from the numerical weather fields of the NCEP/NCAR reanalysis products, whose horizontal resolution is 2.5 degree. In this paper, the previous interpolation methods are integrated and improved, and the surface meteorological data is derived from a new data source which at a higher horizontal resolution of 0.5 degree. The main interpolation steps are expressed as follows.

1. As shown in Fig. 22.3, G_i ($i = 1, 2, 3, 4$) are the 4 neighboring grid points of a specific GPS site, G_i' ($i = 1, 2, 3, 4$) are the corresponding projection points to the grid points on mean sea level (MSL). For a given GPS site, we can easily find its four neighboring grid points according to its geographic coordinates and CFSv2 horizontal resolution.
2. According to the relationships between values at station level and MSL given by Klein et al. [13], taking the grid points' geopotential height as its altitude, deducting the MSL measurements from the Station Level meteorological data at all 4 grid points. The relationships are expressed as:

$$\begin{cases} P_s = P_{MSL}(1 - 2.26 \times 10^{-5} H)^{5.225} \\ T_s = T_{MSL} - 0.0065H \end{cases} \tag{22.7}$$

where H is the altitude of station height level (in m).

3. Horizontal interpolation. Using inverse distance weighted (IDW) interpolation method to obtain the meteorological data of the GPS site's projection point on MSL. That is

$$\begin{cases} P'_{GPS} = \sum_{i=1}^{4} \left(P'_i/d_i^2\right) / \sum_{i=1}^{4} \left(1/d_i^2\right) \\ T'_{GPS} = \sum_{i=1}^{4} \left(T'_i/d_i^2\right) / \sum_{i=1}^{4} \left(1/d_i^2\right) \end{cases} \tag{22.8}$$

4. According to Eq. 22.7, deducting the Station Level meteorological data at the GPS site from the MSL meteorological data.
5. Temporal interpolation. Using cubic spline interpolation method.

22.4 Test Results and Analysis

22.4.1 Comparison Between the Interpolated Meteorological Data and the Measured Meteorological Data

The 6 GPS sites and 3 IGS tracking stations are all equipped with meteorological sensors, so the interpolated meteorological data can be compared with the measured meteorological data in each GPS site. Figure 22.4 shows the time series of both interpolated and measured meteorological data in HKSL site.

Table 22.1 summarizes the Bias, RMS (Root Mean Square) and Std (Standard Deviation) between the interpolated results from CFSv2 and the measured results of each GPS sites. As can be seen from Fig. 22.4 and Table 22.1, the interpolated meteorological data from CFSv2 and the measured meteorological data are basically consistent, but the interpolated pressure is more correspond to the measured data than the interpolated temperature does. Besides, the Std between the interpolated and measured pressure is about 1hpa, the pressure error contribution in

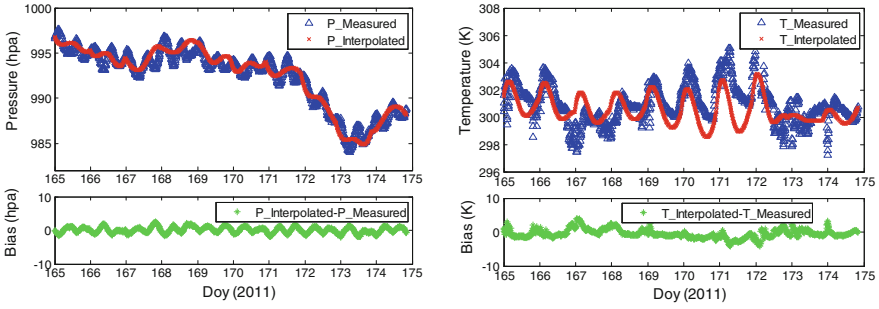

Fig. 22.4 HKSL's time series of surface pressure, temperature and the bias curve between the interpolated results from CFSv2 and the measured results

Table 22.1 The Bias, RMS and Std between the interpolated results from CFSv2 and the measured results of each GPS site

GPS sites	Pressure (kpa)			Temperature (K)		
	Bias	RMS	Std	Bias	RMS	Std
HKFN	0.42	1.03	0.94	−1.14	2.00	1.64
HKNP	−1.50	1.74	0.89	0.27	1.43	1.40
HKOH	−1.70	1.95	0.97	0.24	1.77	1.78
HKSC	−0.0017	0.94	0.93	−1.08	1.97	1.68
HKSL	0.093	0.88	0.88	−0.46	1.36	1.28
HKWS	−2.30	2.61	1.23	−1.43	2.38	1.91
BJNM	−0.30	1.17	1.13	0.33	5.09	5.08
IISC	−1.11	1.47	0.97	−0.52	2.60	2.55
URUM	0.23	1.05	1.02	−3.69	4.47	2.03

Table 22.2 The Bias, RMS and Std between the interpolated results from NCEP/NCAR reanalysis products and the measured results of each GPS site

GPS sites	Pressure (kpa)			Temperature (K)		
	Bias	RMS	Std	Bias	RMS	Std
HKFN	1.01	1.31	0.83	−1.14	2.00	1.65
HKNP	−0.78	1.19	0.90	0.095	1.33	1.32
HKOH	−0.35	0.94	0.87	−0.098	1.52	1.51
HKSC	0.85	1.90	0.84	−1.26	1.95	1.48
HKSL	0.54	0.99	0.83	−0.42	1.36	1.30
HKWS	0.27	1.13	1.10	−1.58	2.37	1.76
BJNM	11.44	11.52	1.41	4.21	4.91	2.53
IISC	−1.01	1.53	1.15	−2.74	3.43	2.05
URUM	−7.25	7.37	1.28	−0.30	2.34	2.32

PWV estimation will be within 0.5 mm according to the analysis of Bai and Feng [10]. Therefore, it is feasible to estimate the regional PWV with the interpolated meteorological data from CFSv2.

In order to show the advantages of the new data source, the precision of the interpolated results from CFSv2 is compared with the precision of the results from NCEP/NCAR reanalysis products using the same interpolation method. Table 22.2 summarizes the Bias, RMS and Std between the interpolated results from NCEP/NCAR reanalysis products and the measured results of each GPS sites. It can be seen from Tables 22.1 and 22.2 that the precision of the different interpolated results from CFSv2 and NCEP/NCAR reanalysis products are almost the same in the 6 selected GPS sites in Hong Kong SatRef, but for BJNM and URUM, the precision of the interpolated results from CFSv2 in the two IGS tracking stations is much better. It indicates that the precision of the interpolated results from CFSv2 is more stable and better, which may be due to the higher horizontal resolution and the new models adopted in developing CFSv2.

22.4.2 Comparison Between the PWV Estimated with Interpolated Meteorological Data and the PWV Achieved with Other Methods

In order to verify the reliability of regional PWV estimation with interpolated meteorological data from CFSv2 (PWV_Interpolated), it is compared with the PWV achieved with two other methods, one is estimated with measured meteorological data (PWV_Measured), and the other is estimated with the sounding observation data (PWV_RS). As can be seen from Fig. 22.1, HKSC is the nearest GPS site to the radio sounding station, and Fig. 22.5 shows the three kinds of PWV estimated in HKSC. For other GPS sites, the PWV_Interpolated are only compared with their PWV_Measured, the Bias, RMS and Std are summarized in Table 22.3.

As can be seen from Fig. 22.5, the change tend of the three kinds of PWV in HKSC is consistent, and the PWV time series estimated using ground-based GPS are more precise than the PWV estimated with the sounding observation data, showing the advantage of ground-based GPS in PWV estimation. From Table 22.3, it can be also found that the PWV_Interpolated and the PWV_Measured are basically consistent in each GPS sites with the bias under 1.5 mm, but the RMS and Std in some sites are nearly 5 mm, the probable reason is the cubic

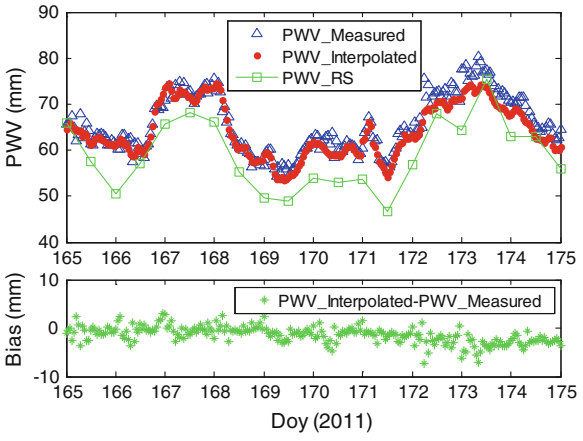

Fig. 22.5 HKSC's time series of PWV and the bias scatter between the interpolated PWV and the measured PWV

Table 22.3 The Bias, RMS and Std between PWV_interpolated and PWV_measured of each GPS site

GPS sites	Bias (mm)	RMS (mm)	Std (mm)
HKFN	−1.33	2.26	1.84
HKNP	−0.87	4.70	4.63
HKOH	−0.56	4.13	4.10
HKSC	−1.41	2.21	1.71
HKSL	−1.06	4.49	2.25
HKWS	−0.43	2.37	2.33

spline interpolation method adopted in the temporal interpolation, omitting some small changes in the real PWV time series.

22.5 Summary

This paper has experimentally demonstrated the feasibility of using surface interpolated temperature and pressure from the NCEP CFSv2 6-hourly forecast products which at 0.5 degree horizontal resolution for GPS PWV estimation. Data analysis with 3 IGS tracking stations and 6 GPS sites from Hong Kong region has demonstrated that the new method proposed in this study is available for pressure interpolation.

This study used data from all 9 GPS sites which have equipped with meteorological sensors over a period of 10 days. The results have shown that the PWV time series estimated using ground-based GPS agree with the PWV estimated with the sounding observation data, though the RMS and Std between the interpolated PWV and the measured PWV in some sites are nearly 5 mm, seems not perfect. In other words, the test results indicate a possible way to develop applications of GPS meteorology with the existing regional GPS networks which have no available site-specific surface meteorological data. This method can also take the place of using new meteorological sensors. This could save significant costs in installation of meteorological sensors.

References

1. Sun D, Yu Y, Zhang T (2009) Tropical water vapor and cloud feedbacks in climate models: a further assessment using coupled simulations. J Clim 22:1287–1304
2. Zhang W, Xue H, Chen G (2012) The three-dimensional structure of precipitating shallow cumuli. Part two: the effect of precipitation on water vapor distribution. Atmos Res 107:171–177. doi:10.1016/j.atmosres.2012.01.008
3. Bevis M, Businger S, Herring TA, Anthes RA, Ware R (1992) GPS meteorology: remote sensing of atmospheric water vapor using the global positioning system. J Geophys Res 97 (D14), 15787–15801
4. Bevis M, Businger S, Chiswell S et al (1994) GPS meteorology-mapping zenith wet delays onto precipitable water. J Appl Meteorol 33:379–386
5. Duan J, Bevis M, Fang P et al (1996) GPS meteorology: direct estimation of the absolute value of precipitable water. J Appl Meteorol 35:830–838
6. Rocken C, Van Hove T, Ware R (1997) Near real-time GPS sensing of atmospheric water vapor. Geophys Res Lett 24:3221–3224
7. Bar-Sever YE, Kroger PM, Borjesson JA et al (1998) Estimating horizontal gradients of tropospheric path delay with a single GPS receiver. J Geophys Res 103:5019–5035
8. Tregoning P, Boers R, O' Brien D et al (1998) Accuracy of absolute precipitable water vapor estimates from GPS observations. J Geophys Res 103:28701–28710

9. Jade S, Vijayan M (2008) GPS-based atmospheric precipitable water vapor estimation using meteorological parameters interpolated from NCEP global reanalysis data. J Geophys Res 113 (D03106). doi:10.1029/2007JD008758
10. Bai Z, Feng Y (2003) GPS water vapor estimation using interpolated surface meteorological data from Australian automatic weather stations. J Glob Positioning Syst 2(2):83–89
11. Saha S et al (2010) The NCEP climate forecast system reanalysis. Bull Am Meteor Soc 91:1015–1057. doi:10.1175/2010BAMS3001.1
12. Brunner FK, Gu M (1991) An improved model for the dual frequency ionospheric correction of GPS observations. Manuscr Geod 16:205–214
13. Klein B et al (1999) GPS water vapor meteorology, Beleids commissie remote sensing (BCRS), chapter 2: water vapor from GPS troposheric delay estimates, 3–11

Chapter 23
The Measurement of Wave Parameter Based on PPP Method

Huayi Zhang, Daolong Wang, Xinghua Zhou and Yanxiong Liu

Abstract Filtering method was selected to eliminate the impact of long-term errors which include the tide, systematic errors and other factors based on GPS Precise Point Positioning (PPP) data processing method, and accurate wave height was get finally. Fast Fourier Transform (FFT) analysis method was used to calculate average period of the wave, the average wave height and other parameters. At last sea test was made, we found that the results of GPS measurement and wave measurement are consistent. It proves that we can calculate correct wave parameters directly based on PPP method.

Keywords Precise point positioning (PPP) · The average wave height · The average period

23.1 Introduction

Wave is an important sports phenomenon in the ocean, it plays an important role on the marine project planning, construction operation and maintenance, offshore resources investigation, water recreation activities and sailing safety. So far, there are all kinds of waves, tide measuring instruments and methods.

While the existing methods can be used to measure the waves effectively, but the disadvantages are also obvious. Visual method and optical means can not meet the requirements of bad weather and night-time observation. Gravity, acoustic and water pressure measured wave devices have high precision, but the price is

H. Zhang (✉)
School of Geodesy and Geomatics, Wuhan University, Wuhan, China
e-mail: zhanghuayi@fio.org.cn

D. Wang · X. Zhou · Y. Liu
The First Institute of Oceanography, SOA, Qingdao, China

J. Sun et al. (eds.), *China Satellite Navigation Conference (CSNC) 2013 Proceedings*, Lecture Notes in Electrical Engineering 243,
DOI: 10.1007/978-3-642-37398-5_23,

dramatically expensive, and if you want to get the location information, you should install GPS device on the equipment.

With the development of GPS technology, its application in wave and tide observation has also been good development and improvement. Nagai et al. [1], Kato et al. [2], Jean et al. [3], Fujita et al. [4], Yoo et al. [5] use RTK to get vertical height to calculate wave height directly, tidal changes and even tsunami fluctuations. However, this method must be carried out under high density of GPS base station. Even if has a base station on the shore, the wave observations of RTK-GPS are still limited in the nearshore region. If it is applied to distant offshore in deep sea region, there would be relatively large observation error.

Chang [6] in National Cheng Kung University using GPS buoy measure wave dynamic information, to get vertical velocity, through spectral analysis method to calculate wave height and period projection, compared with data buoy to draw a correlation between the two proved accurate wave information which can reach more than 0.97. It shows we can get correct information of wave by GPS buoy. With the continuous development of GPS precise point positioning technology, Cheng and Zhang [7], Wuhan University, use Trip software to process measured buoy data, which can extract elevation change s caused by storm in sea surface. Chiu [8], Taiwan Sucess University, use precise point positioning technology to explore GPS buoy. Compared with DGPS observation data and tidal station observation, it proves the feasibility of using PPP technology to do wave measurement. This article attempts to use PPP technology to extract GPS buoy wave information, combine with spectral analysis method to obtain the parameters of significant wave height, average cycle waves and so on.

23.2 Data Processing Method

23.2.1 Acquisition of Wave Height

GPS plays a role of collecting data in the ocean wave measurements, the receiver was installed on the wave measurement platforms such as buoys, small tracking ship, based on Precise Point Positioning (PPP), the receiver can get WGS-84 coordinates XYZ coordinate changes in three directions, under coordinate system conversion, we can get a local level the three-dimensional coordinates of the coordinate system change. Due to buoys' wave motion, changes on the zenith direction is the sea height variation in buoy. The sea surface height variation contains waves, tides, and the measurement noise, so these factors must be separated out to obtain clean wave height variation.

23.2.2 Separation of Tide and Wave

Moving average method is to average the original time series among two or more time segments data, and obtain average value as a trend value for the middle time period, after gradually sequentially moving we get the average value of every time segment, thus obtain a new sequence. This sequence eliminate impact of uncertainty composition in the original sequence, and get long-term trends in the original sequence. The method is a common and simple method to analysis the long-term trends, and its essence is a simple filtering [9, 10].

Assume the time series Xi (i = 1,2,…, n), the sliding average is K (K = 2k +1) :

$$Y = \frac{X_{i-k} + \cdots + X_{i-1} + X_i + X_{i+1} + \cdots + X_{i+k}}{2k+1} (k < i < n-k) \tag{23.1}$$

The selections of parameters of the moving average method will directly affect the smooth effect on data. If the value of k is larger, the deterministic components of high-frequency changes will be weakened because more adjacent data is smoothed. Otherwise, the random fluctuation on the low frequency is not weakened because less adjacent data is smoothed. So we should choose the suitable k value according to the purpose of smoothing and the actual changes of objective. Then one or more moving average processing was carried out for the sea level changes to obtain the low frequency signal which is mostly tidal signal. After that, we get the high frequency signal which is mainly wave height through substracting the low frequency signal from original signal.

23.2.3 Calculation of Wave Parameters

The waves is usually regarded as a random process. The spectrum which describe the random process can be derived by wave elements (such as wave height, period) respecting some assumptions. Also it can be get from wave height in fixed-point using special spectrum analysis. And the later one has become the main method which obtain the wave spectrum gradually.

At present, there are mainly two kinds of spectrum estimation, one is obtained by the covariance function, another is get through the cycle graph.

Wave height can be substracted from the height variation of sea level. Then the wave elements can be calculated.

In order to facilitate Fast Fourier Transform (FFT) algorithm, in this article cycle map method was used. The reference documentation suggests that [11]: piecewise average FFT algorithm is better than average frequency method spectral estimation for its' shorter sampling step, and spectral estimation is much better.

Sub-average method is meaning dividing all the sampling length into m segments, and each segment length is $L = 2^q$, data of half segment between adjacent

sections. Fourier transform to obtain a crude spectrum of each segment, then averaged these coarse spectrum to obtain total spectral estimation. This kind of treatment improve the data availability and estimate accuracy.

The spectral moment can determine the average wave height $\overline{\mathrm{H}}$, average cycle $\overline{T}$ and spectrum width ε and other elements. Formula is as follows

$$M_0 = \left[\frac{1}{2}S(\omega_0) + \sum_{k=1}^{M-1} S(\omega_k) + \frac{1}{2}S(\omega_M)\right] \cdot \Delta\omega \tag{23.2}$$

$$M_2 = \left[\frac{1}{2}\omega_0^2 S(\omega_0) + \sum_{k=1}^{M-1} \omega_k^2 S(\omega_k) + \frac{1}{2}\omega_M^2 S(\omega_M)\right] \cdot \Delta\omega \tag{23.3}$$

$$M_4 = \left[\frac{1}{2}\omega_0^4 S(\omega_0) + \sum_{k=1}^{M-1} \omega_k^4 S(\omega_k) + \frac{1}{2}\omega_M^4 S(\omega_M)\right] \cdot \Delta\omega \tag{23.4}$$

$$\overline{\mathrm{H}} = \sqrt{2\pi M_0} \tag{23.5}$$

$$\overline{T} = 2\pi\sqrt{M_0/M_2} \tag{23.6}$$

$$\varepsilon = \sqrt{(M_0 M_4 - M_2^2)/M_0 M_4} \tag{23.7}$$

ω_i is circular frequency, $\omega_i = \frac{2i\pi}{N\Delta t}, s(\omega_i)$ is the spectrum of the frequency m_n is the n order matrix of the spectrum

$$m_n = \int_0^\infty \omega^n S(\omega) d\omega \tag{23.8}$$

23.3 Sea Test Verification

In order to verify the accuracy of GPS wave in actual observations at sea, we place GPS wave buoy in the nearby waters in Tianheng, eastern Qingdao, meanwhile place waves Knight synchronization wave measurement buoys in the vicinity of the GPS buoy for data comparison. The same observation time is from November 1st, 2012 the 8:16–10:16 (GPS time).

GPS data was processed by Trip software (precise ephemeris using cod17124. ehp, the precise clock using cod17124.clk_05 s), to get change of the BLH coordinates (as shown in Fig. 23.1). From the picture we can find tide changes slowly during the period because it is in the slack period. Under the coordinate system conversion, we get NEU 3D coordinate system changes in local horizontal coordinate. Some tests were carried out on the selection of k, and 15 is the best parameter

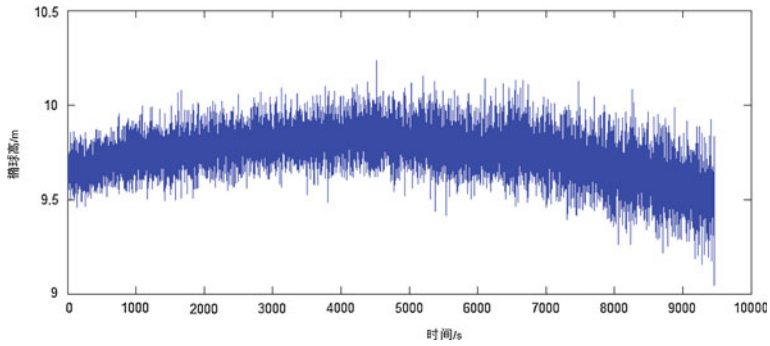

Fig. 23.1 Sea level changes (unfiltered)

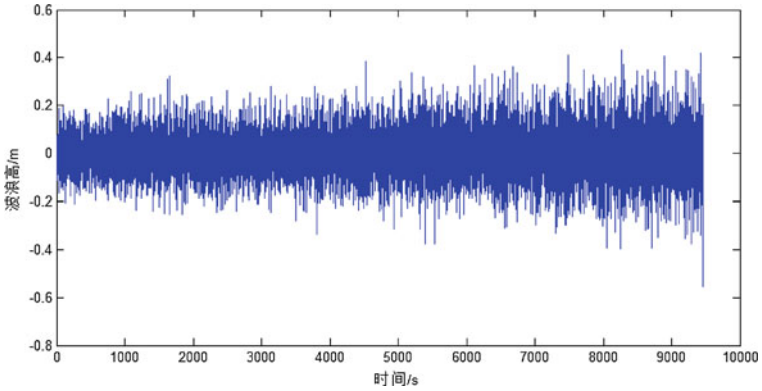

Fig. 23.2 Series of wave height

for k when separating the wave signal from the original signal because the wave height (Fig. 23.2) separated from the original signal fluctuates on the zero.

Using FFT spectrum analysis wave information, in accordance with the wave factor calculated as described in 23.3, calculate the average wave height $\overline{H}$, average cycle $\overline{T}$. The comparison result with wave buoy as Shown in Tables 23.1 and 23.2.

Comparing the wave measurement results between buoys and GPS, we can find they have nearly the same tendency, the maximum error of the average wave height, is 4.90 cm, minimum 3.62 cm, no more than 5 cm. The Maximum error of the average period 0.19 s, the minimum is only 0.02 s.

The error of result was mainly affected by two reasons. The first one was that PPP dynamic accuracy is only about 5 cm. The other one was that the character of wave spectrum is not obvious. Because the sea is well during the test, and the maximum height of wave is less than 50 cm (as shown in Fig. 23.2).

Table 23.1 The difference of average wave height between wave buy and GPS

Time	Wave buy (cm)	GPS buy (cm)	Error (cm)
8:16–8:46	35	36.62	1.62
8:46–9:16	37	40.62	3.62
9:17–9:46	38	42.90	4.90
9:47–10:16	44	48.83	4.83

Table 23.2 The difference of average period between wave buy and GPS

Time	Wave buy (s)	GPS buy (s)	Error (s)
8:16–8:46	3.84	3.65	−0.19
8:46–9:16	3.04	3.21	0.17
9:17–9:46	3.17	3.19	0.02
9:47–10:16	3.21	3.13	−0.08

23.4 Conclusion

Based on GPS Precise Point Positioning data processing method, filtering method also was carried out to eliminate the impact of the tide level, long-term systematic errors and other factors, and accurate wave height was get finally. Then Fast Fourier Transform (FFT) analysis method was used to calculate average period of the wave, the average wave height and other parameters. At last sea test was made, we found that the results of GPS measurement and wave instrument are consistent. The maximum error of average wave height is less than 5 cm, and the maximum error of average wave period is less than 0.19 s. It proves that we can calculate correct wave parameters directly based on PPP method which has a good prospect.

Acknowledgments This work is supported in part by the senior engineer of National Geomatics Center of China.

References

1. Nagai T, Satomi S, Terada Y et al (2005) GPS buoy and seabed installed wave gauge application to offshore tsunami observation. In: Proceedings of the international offshore and polar engineering conference. Seoul, pp 292–299
2. KatoT, TeradaY, Itoh T, et al (2001) A new tsunami detection system using RTK-GPS. In: Proceedings of the international tsunami symposium, Seattle, pp 645–651
3. Jeans G, Bellamy I, Vries JJ et al (2003) Sea trial of the new datawell GPS direction waverider. In: Proceedings of the IEEE/OES seventh working conference on current measurement technology, SanDiego, pp 145–147
4. Fujita T, Terada Y, Nagai T et al (2004) A development of GPS wave,tide and tsunami meter. In: Proceedings of workshop on wave, tide observation and modelings in the Asian-Pacific region (CD-ROM), Seoul

5. Yoo Y, Hou D, Kouguchi N et al (2004) Arrayed GPS-buoys wave observation system. In: Proceedings of Ocean'04-MTS/IEEE Techno-Ocean'04:bridges across the Ocean, Kobe, pp 1370–1375
6. Chang Y-W, Doong D-J, Lee B-C (2009) Wave measurement by GPS. Ocean Eng 27(4):73–80
7. Cheng S, Zhang X (2007) Simulation of tsunami forecasting with GPS buoy using PPP technology. Geomatics Inf Sci Wuhan Univ 32(9):764–766
8. Chiu K-W (2009) Near real-time GPS buoy positioning using precise point positioning techniques. Master's degree Thesis, The South of Taiwan, National Cheng Kung University
9. Changlong G, Chujin L (1996) Spectrum of the waves in the coordinate system of Sports. J Ocean Univ Qingdao 26(7):261–265
10. Yixuan P, Min G (2001) The fundamental principle and application of sliding average method. Gun Launch Control J 1:21–23
11. Cheng G (1990) Wave spectrum analysis using FFT. The state oceanic administration, institute for the protection of the marine environment 2:7–11

Chapter 24
The Method of Earth Rotation Parameter Determination Using GNSS Observations and Precision Analysis

Qianxin Wang, Yamin Dang and Tianhe Xu

Abstract Based on the principle of GNSS observation, the linear observation equations of earth rotation parameters (ERP) estimation using GNSS data are deduced. The general solution and precision evaluation function are obtained. According to the precision evaluation function, the major factors of effect ERP solution precision are analyzed. One is the geometric distribution of the satellites relative to the station; another is the geometric distribution of the stations relative to the geo-center. It is proved that ERP will not be solved if using one GNSS station. The solution precision of ERP will be the best when the vectors of two stations to geo-center are orthogonal, if two stations are used. For testing ERP estimation precision using GNSS data, two weeks GPS data from 295 and 21 IGS stations are processed, respectively. The results show that the precise ERP can be obtained whether 295 or 21 stations data are used, when the stations rational distribution. The estimation precisions of pole motion and length of day parameters are better than 0.04 mas and 0.03 ms respectively, where the results of IERS are taken as the reference values.

Keywords Global navigation satellite system · Earth rotation parameter · Linear observation equation · Precision factors · Optimal configuration

Q. Wang (✉) · Y. Dang
Chinese Academy of Surveying and Mapping, Lianhuachi West Road 28,
100830 Haidian District, Beijing, People's Republic of China
e-mail: wangqianxin8012@163.com

T. Xu
Xi'an Research Institute of Surveying and Mapping,
Yanta Middle Road 1, 710054 Xi'an, People's Republic of China

J. Sun et al. (eds.), *China Satellite Navigation Conference (CSNC) 2013 Proceedings*, Lecture Notes in Electrical Engineering 243,
DOI: 10.1007/978-3-642-37398-5_24,

24.1 Introduction

The earth rotation parameters (ERP) includes that the pole motion (PM) and length of day (LOD), which with the precession and nutation constitute together the earth orientation parameters (EOP). It is the most import theory basis of setting up high precision celestial reference system and terrestrial reference system. And it is necessary for the artificial satellite orbit determination, the autonomous navigation of space craft and high accurate time service. Additionally, ERP includes the potential information of the earth interior material motion and effect of the other celestial bodies on the earth motion. Therefore, ERP research attracts the great attention of geodesy, geodynamics, geophysics, astronomy.

The classical optical instruments were used at early stage of ERP observation, which have a precision of ± 1 m [1]. In the 1970s, the ERP observation precision had been improved by two orders of magnitude, with the rising of modern space measurement technology, such as VLBI, SLR, LLR and DORIS [2]. However, the temporal resolution of ERP is poor, because of the huge equipment and the low sample rate of VLBI and SLR [3]. It is not suitable for applications of high temporal and spatial resolution. Therefore, it becomes a key problem of improving the temporal resolution of ERP.

The GNSS technology has a wide station distribution, low equipment cost, high observation precision and high data sample rate. Therefore, it is very suitable for obtaining high precision and high temporal resolution of ERP [4–6]. With the building up of Compass satellite navigation system, it is very important of developing ERP monitoring system based on Compass observation for setting up Chinese independent space-time reference system. In this paper, the linear observation equations of ERP estimation using GNSS observation are deduced, as well as the general solution and precision evaluation function have been obtained. The major factors of effect ERP estimation precision are analyzed. Additionally the actual precision of ERP solution using GNSS data has been tested by the real GNSS data from 295 IGS stations.

24.2 Method of ERP Determination Using GNSS Observations

Based on the principle of GNSS observation, the GNSS observation equation can be written as [7]:

$$\rho + \triangle\rho = \bar{\rho} \tag{24.1}$$

where ρ is the observation distance between satellite and station; $\triangle\rho$ is the equivalent distance of observation error; $\bar{\rho}$ is the theory distance. The concrete expressions of three items as follows:

$$\rho = \lambda(\varphi + N) \tag{24.2}$$

$$\triangle\rho = dt_s + dt_r + dtrop + diono + dmulti + drel + d\varepsilon \tag{24.3}$$

$$\bar{\rho} = |RX_s - RX_r| \tag{24.4}$$

where $\lambda,\ \varphi,\ N$ are the wavelength, observation, integer ambiguity of carrier phase observation, respectively; dt_s, dt_r, $dtrop$, $diono$, $dmulti$, $drel$, $d\varepsilon$ are the equivalent distances of satellite clock error, receiver clock error, troposphere error, ionosphere error, multipath error, relativistic error and observation noise, respectively; X_s, X_r are the coordinates of satellite and receiver in the terrestrial reference system; R is the coordinate transformation matrix from terrestrial reference system to celestial reference system, which can be expressed as:

$$R = PNSU \tag{24.5}$$

where P, N, S, U are the rotation matrix of precession, nutation, sidereal time and polar motion. The detailed calculation formula of $PNSU$ can see the references [8]. The length of day and polar motion parameters $(\theta_t,\ \theta_x,\ \theta_y)$ are included in the rotation matrix S and U. Therefore, the observation equation needs to be linearized if estimating ERP using GNSS data. Using the Taylor series expansion to one order, Eq. (24.1) can be written as:

$$\rho + \triangle\rho = \bar{\rho}_0 + \frac{\delta\bar{\rho}}{\delta\theta_0}\delta\theta \tag{24.6}$$

where $\bar{\rho}_0$ is the approximate value using the initial ERP; $\delta\theta$ includes $\delta\theta_t, \delta\theta_x, \delta\theta_y$; the expressions of $\frac{\delta\bar{\rho}}{\delta\theta_0}$ as follows:

$$\frac{\delta\bar{\rho}}{\delta\theta_{x_0}} = -\frac{(R_0X_s - R_0X_r)^T}{\bar{\rho}_0} PNS_0 \frac{\delta U}{\delta\theta_{x_0}} X_r \tag{24.7}$$

$$\frac{\delta\bar{\rho}}{\delta\theta_{y_0}} = -\frac{(R_0X_s - R_0X_r)^T}{\bar{\rho}_0} PNS_0 \frac{\delta U}{\delta\theta_{y_0}} X_r \tag{24.8}$$

$$\frac{\delta\bar{\rho}}{\delta\theta_{t_0}} = -\frac{(R_0X_s - R_0X_r)^T}{\bar{\rho}_0} PN \frac{\delta S}{\delta\theta_{t_0}} U_0X_r \tag{24.9}$$

where $R_0,\ S_0,\ U_0$ are the approximate values of corresponding matrix based on the initial ERP. Ignoring the effect of micro items, $\frac{\delta U}{\delta\theta_{x_0}}$, $\frac{\delta U}{\delta\theta_{y_0}}$, $\frac{\delta U}{\delta\theta_{t_0}}$ can be written as:

$$\frac{\delta U}{\delta\theta_{x_0}} = \begin{bmatrix} 0 & 0 & 1 \\ 0 & 0 & 0 \\ -1 & 0 & 0 \end{bmatrix} \tag{24.10}$$

$$\frac{\delta U}{\delta \theta_{y_0}} = \begin{bmatrix} 0 & 0 & 0 \\ 0 & 0 & -1 \\ 0 & 1 & 0 \end{bmatrix} \tag{24.11}$$

$$\frac{\delta U}{\delta \theta_{t_0}} = \begin{bmatrix} -\sin(GAST) & -\cos(GAST) & 0 \\ \cos(GAST) & -\sin(GAST) & 0 \\ 0 & 0 & 0 \end{bmatrix} \times \gamma \times (t - t_0) \tag{24.12}$$

where $GAST$ is Greenwich apparent sidereal time; the calculation formula of $GAST$ see the references [9]. $\gamma = 1.0027379093$; t is the Julian date of observation time, and t_0 is the Julian date of reference time.

Based on the above formulas, the linear observation equations of ERP estimation using GNSS data can be obtained, when the initial values of ERP and observation time are given. If assuming there are n stations and m satellites are observed by each station, the observation equation set is written as:

$$A_{(n\times m)\times 3} X_{3\times 1} = L_{(n\times m)\times 1},\ P_{(n\times m)(n\times m)} \tag{24.13}$$

where A is the coefficient matrix; L is the constant matrix; X is the unknown parameter matrix; P is the weighting matrix; the expressions of each matrix as follows:

$$A_{(n\times m)\times 3} = \begin{bmatrix} \frac{\delta \overline{\rho_1^1}}{\delta \theta_{x_0}} & \frac{\delta \overline{\rho_1^1}}{\delta \theta_{y_0}} & \frac{\delta \overline{\rho_1^1}}{\delta \theta_{t_0}} \\ \cdots & \cdots & \cdots \\ \frac{\delta \overline{\rho_i^j}}{\delta \theta_{x_0}} & \frac{\delta \overline{\rho_i^j}}{\delta \theta_{y_0}} & \frac{\delta \overline{\rho_i^j}}{\delta \theta_{t_0}} \\ \cdots & \cdots & \cdots \\ \frac{\delta \overline{\rho_n^m}}{\delta \theta_{x_0}} & \frac{\delta \overline{\rho_n^m}}{\delta \theta_{y_0}} & \frac{\delta \overline{\rho_n^m}}{\delta \theta_{t_0}} \end{bmatrix} \tag{24.14}$$

$$L_{(n\times m)\times 1} = \begin{bmatrix} \rho_1^1 + \triangle \rho_1^1 - \overline{\rho_1^1} \\ \cdots \\ \rho_i^j + \triangle \rho_i^j - \overline{\rho_i^j} \\ \cdots \\ \rho_n^m + \triangle \rho_n^m - \overline{\rho_n^m} \end{bmatrix} \tag{24.15}$$

$$X_{3\times 1} = \begin{bmatrix} \delta \theta_x \\ \delta \theta_y \\ \delta \theta_t \end{bmatrix} \tag{24.16}$$

If assuming k epochs are observed, the k normal equations are added together and the iterative least square adjustment is used to estimate the ERP. The solution result and variance-covariance matrix as follows:

$$X = (\sum_{i=1}^{i=k} A_i^T P_i A_i)^{-1} \sum_{i=1}^{i=k} A_i^T P_i L_i \tag{24.17}$$

$$D = \sigma_0^2 (\sum_{i=1}^{i=k} A_i^T P_i A_i)^{-1} \tag{24.18}$$

$$\sigma_0^2 = \frac{V^T V}{n - t} \tag{24.19}$$

where n is the number of observation equation; t is the number of unknown parameter; V is the residual matrix; σ_0^2 is the variance of unit weight.

24.3 Major Factors of Effect ERP Solution Precision

For the simplicity of discussion, the initial values of ERP and observation time are given, where $\theta_{x_0} = 0.11881''$, $\theta_{y_0} = 0.26326''$, $\theta_{t_0} = 0.001355s/d$, $t = 2455927.5$, $t = 2455926.5$, and the mica item (10^{-6}) is ignored. The Eqs. (24.7–24.9) can be written as:

$$\frac{\delta \bar{\rho}}{\delta \theta_{x_0}} = \frac{[x_s - x_r \quad y_s - y_r \quad z_s - z_r]}{\bar{\rho}_0} \begin{bmatrix} -z_r \\ 0 \\ x_r \end{bmatrix} \tag{24.20}$$

$$\frac{\delta \bar{\rho}}{\delta \theta_{y_0}} = \frac{[x_s - x_r \quad y_s - y_r \quad z_s - z_r]}{\bar{\rho}_0} \begin{bmatrix} 0 \\ z_r \\ -y_r \end{bmatrix} \tag{24.21}$$

$$\frac{\delta \bar{\rho}}{\delta \theta_{t_0}} = \frac{[x_s - x_r \quad y_s - y_r \quad z_s - z_r]}{\bar{\rho}_0} \begin{bmatrix} y_r \\ -x_r \\ 0 \end{bmatrix} \tag{24.22}$$

If assuming m satellites are observed by one station, the coefficient matrix A can be written as:

$$A_{m\times 3} = \begin{bmatrix} \frac{x_s^1 - x_r}{\bar{\rho}_0} & \frac{y_s^1 - y_r}{\bar{\rho}_0} & \frac{z_s^1 - z_r}{\bar{\rho}_0} \\ \cdots & \cdots & \cdots \\ \frac{x_s^j - x_r}{\bar{\rho}_0} & \frac{y_s^j - y_r}{\bar{\rho}_0} & \frac{z_s^j - z_r}{\bar{\rho}_0} \\ \cdots & \cdots & \cdots \\ \frac{x_s^m - x_r}{\bar{\rho}_0} & \frac{y_s^m - y_r}{\bar{\rho}_0} & \frac{z_s^m - z_r}{\bar{\rho}_0} \end{bmatrix} \begin{bmatrix} -z_r & 0 & y_r \\ 0 & z_r & -x_r \\ x_r & -y_r & 0 \end{bmatrix} \tag{24.23}$$

The Eq. (24.23) can be simplified written as:

$$A_{m\times 3} = B_{m\times 3}\, C_{3\times 3} \tag{24.24}$$

Based on the Eq. (24.24), it can be known that the coefficient matrix A of ERP solution includes two parts: one is the direction cosine matrix of satellite and station; another is the coordinate matrix of stations. If assuming the weighting matrix P is the unit matrix, the precision matrix Q can be written as:

$$Q = (A^T A)^{-1} = (C^T B^T B C)^{-1} \tag{24.25}$$

From Eq. (24.25), it can be drawn that the major factors of effect ERP estimation precision are the geometric distribution of the satellites relative to the station and the geometric distribution of the stations relative to the geo-center.

If assuming $B^T B$ is the unit matrix, namely without considering of effect of satellite, the matrix $A^T A$ can be expressed as:

$$A^T A = C^T C = \begin{bmatrix} x_r^2 + z_r^2 & -x_r y_r & -z_r y_r \\ -x_r y_r & z_r^2 + y_r^2 & -z_r x_r \\ -z_r y_r & -z_r x_r & y_r^2 + x_r^2 \end{bmatrix} \tag{24.26}$$

According to the Eq. (24.26), the determinant of $A^T A$ can be calculated ($\det(A^T A) = 0$). The result shows the ERP can not be estimated if using one station. If there are two stations and m satellites are observed by each station, the matrix A can be written as:

$$A_{2m\times 3} = \begin{bmatrix} B_1 C_1 \\ B_2 C_2 \end{bmatrix} \tag{24.27}$$

where $B_1,\ C_1,\ B_2,\ C_2$ are the direction cosine matrix and coordinate matrix of two stations. And assuming (x_1, y_1, z_1) and (x_2, y_2, z_2) are the coordinates of two stations. The matrix $A^T A$ can be expressed as:

$$A^T A = C_1^T C_1 + C_2^T C_2 \tag{24.28}$$

$$A^T A = \begin{bmatrix} x_1^2 + z_1^2 + x_2^2 + z_2^2 & -(x_1 y_1 + x_2 y_2) & -(z_1 y_1 + z_2 y_2) \\ -(x_1 y_1 + x_2 y_2) & z_1^2 + y_1^2 + z_2^2 + y_2^2 & -(z_1 x_1 + z_2 x_2) \\ -(z_1 y_1 + z_2 y_2) & -(z_1 x_1 + z_2 x_2) & y_1^2 + x_1^2 + y_2^2 + x_2^2 \end{bmatrix} \tag{24.29}$$

If two stations are very close, namely $x_1 \approx x_2,\ y_1 \approx y_2,\ z_1 \approx z_2$, the determinant of matrix $A^T A$ is zero. The necessary and sufficient condition of ERP can be estimated by the Eq. (24.17) is $\det(A^T A) > 0$. And the solution precision is improving with the value of $\det(A^T A)$ is increasing. It can be proved that the value of determinant is maximal when the non diagonal elements are zero and the diagonal elements are equal [10]. Therefore, some condition equations can be obtained as follows:

$$x_1 y_1 = -x_2 y_2 \tag{24.30}$$

$$z_1 y_1 = -z_2 y_2 \tag{24.31}$$

$$z_1 x_1 = -z_2 x_2 \tag{24.32}$$

$$x_1^2 + z_1^2 + x_2^2 + z_2^2 = z_1^2 + y_1^2 + z_2^2 + y_2^2 \tag{24.33}$$

Based on above equations, if the coordinates of one station are given, the coordinates of another station will can be determined. For example, the coordinates of one station are $(r, 0, 0)$, the coordinates of another station are $(0, \pm r, 0)$. Therefore, it can be known that the solution precision of ERP will be the best when the vectors of two stations to geo-center are orthogonal.

If the number of stations is larger than two, the optimal condition of stations distribution for ERP estimation is more complicated than that. In this paper, it is not discussed.

24.4 Data Processing and Analysis

For testing ERP estimation precision using GNSS data, two weeks GPS data from 295 IGS stations are processed (11th–25th September 2007). For analysis of effect of station distribution on ERP solution, the data of 21 stations are tested, which are chosen from above stations and have a rational distribution.

The coordinates of stations, the orbit parameters of satellites, light pressure parameters are constrained strongly in the data processing. One set of ERP are estimated every 24 h and the results are compared with the value of IERS. Figure 24.1 shows the location of 21 tested stations. Figures 24.2, 24.3, 24.4 show the difference between the experimental results and the IERS results about pole motion and length of day, respectively. Table 24.1 is the precision statistics of ERP solution in two experiments.

Based on above experimental results, it can be known that there is light effect of satellite distribution on ERP estimation because the long time observation will

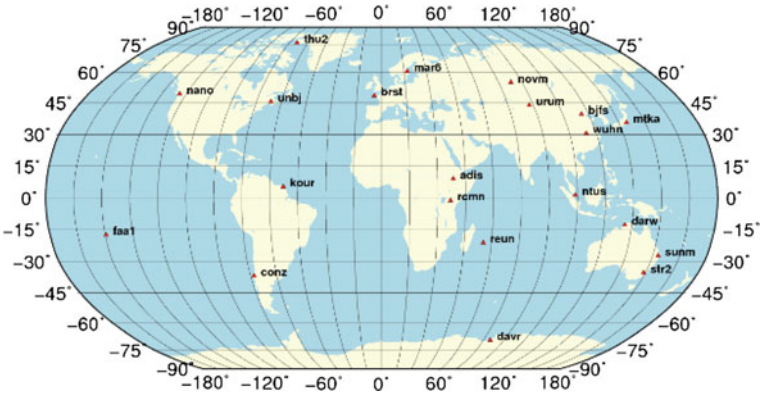

Fig. 24.1 The location of 21 tested stations

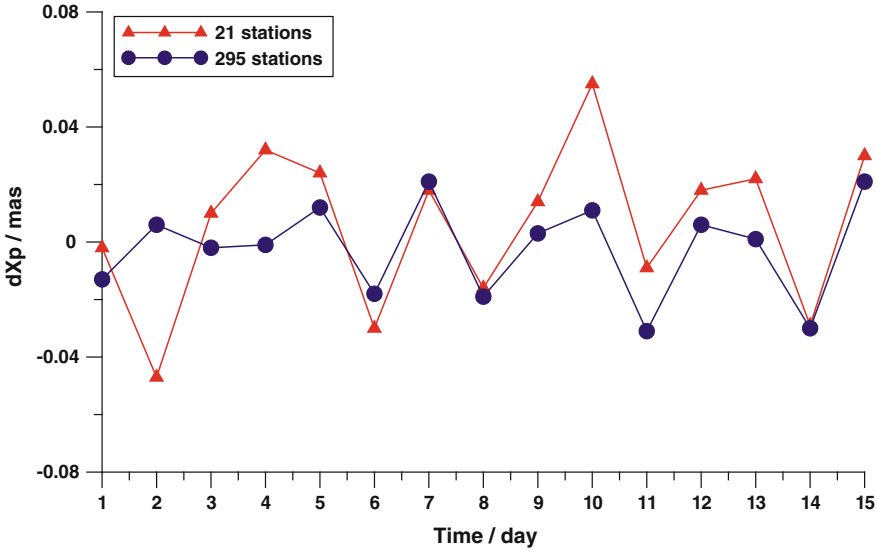

Fig. 24.2 The difference of PM between experimental results and IERS values on X component

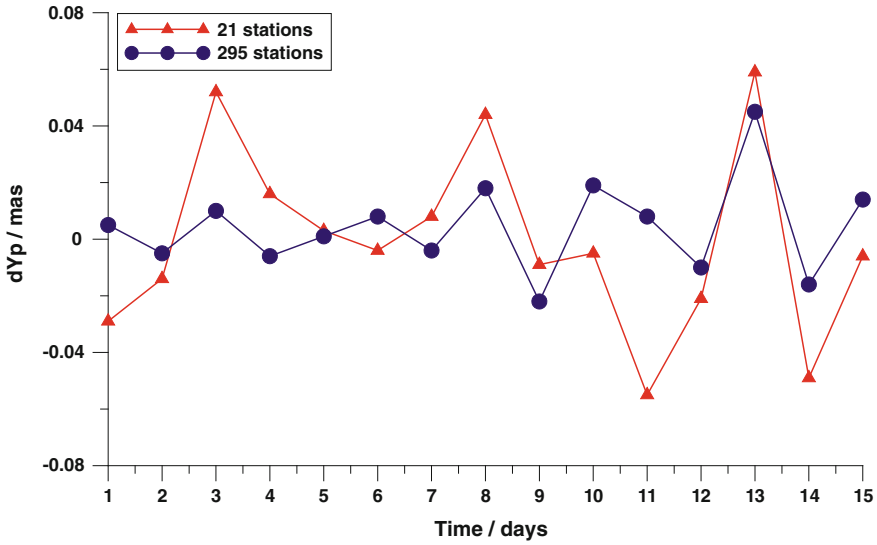

Fig. 24.3 The difference of PM between experimental results and IERS values on Y component

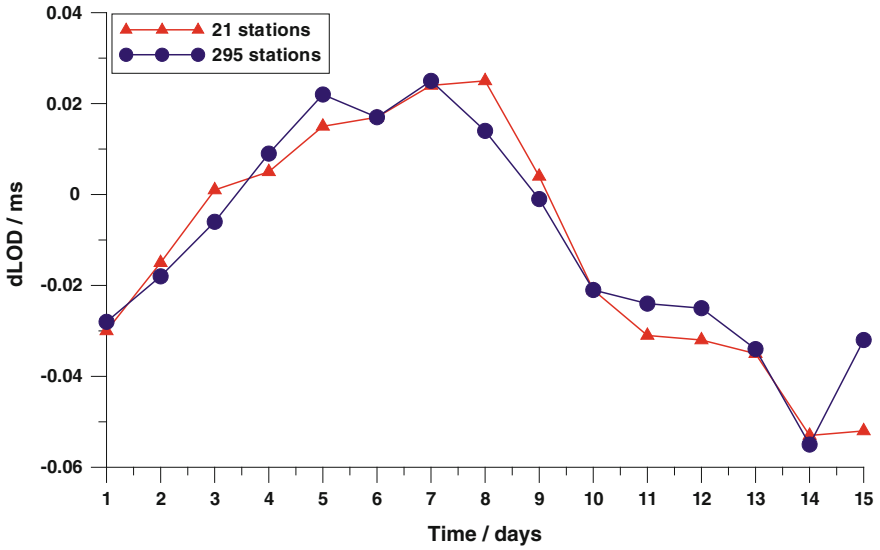

Fig. 24.4 The difference of LOD between experimental results and IERS values

Table 24.1 The precision statistics of two experimental results

	21 stations			295 stations		
	Xp/mas	Yp/mas	LOD/ms	Xp/mas	Yp/mas	LOD/ms
Max.	0.055	0.059	0.053	0.031	0.045	0.055
Min.	0.002	0.003	0.001	0.001	0.001	0.001
Std.	0.028	0.033	0.027	0.017	0.016	0.024

lead the geometry of satellites to change significantly. On the contrary, the location of stations is always invariable. Therefore, it is the decisive factor of ERP estimation precision using GNSS data that the stations distribution.

Because the stations have a rational distribution in two experiments, the precise ERP can be obtained whether 295 or 21 stations data are used. Comparing with the results of IERS, the estimation precisions of pole motion and length of day parameters are better than 0.04 mas and 0.03 ms, respectively

24.5 Conclusions

Based on above theoretical derivation and real data processing, some conclusions can be drawn.

1. There are two major factors which effect ERP estimation precision using GNSS data. One is the geometric distribution of the satellites relative to the station; another is the geometric distribution of the stations relative to the geo-center.

2. Because the long time observation will lead the geometry of satellites to change significantly, it has very light effect on ERP estimation that the geometric distribution of satellites. The location of stations is always invariable. Therefore, it has important effect on ERP estimation that the geometric distribution of stations.
3. The ERP will not be solved if using one GNSS station. The solution precision of ERP will be the best when the vectors of two stations to geo-center are orthogonal. And the solution precision is improving with the value of $\det(A^TA)$ is increasing, if using many stations data to estimate ERP.
4. If the distribution of stations is well, the high precision ERP can be obtain just using a small number of stations data. Therefore, for obtaining precise ERP using Compass satellite data, the key problem is stations geometric distribution rather than the number of stations.

Acknowledgments Thanks the international GNSS service (IGS) and international earth rotation and reference system service (IERS) for providing experimental data. This work was supported by the National High Technology Research and Development of China (2013AA122501), and the National Science and Technology Pillar Program (2012BAB16B01).

References

1. Zhao M, Gu Z (1986) Comparison and comment on the techniques for determination ERP. Acta Astronomica Sinica, 27(3): P181–P189 (Ch)
2. Zhu Y, Feng C, Zhang F (2006) Earth orientation parameter solved by Lageos Chinese SLR data[J]. Acta Astronomica Sinica 47(4), P441–P449 (Ch)
3. Zhu W, Zhang H, Feng C (1990) Determination of parameters of present global plate motion using SLR technique. Sci China, Ser A 35(12):P195–P197
4. Wang J, He M, Zhu W (1993) The applications of GPS to geodesy and geodynamics. Prog Astron 11(4):P303–P308 (Ch)
5. He Z, Yang X, Li Z, Cheng Z (2010) Estimation of earth rotation parameters based on GPS observations. J Time Freq 33(1):P69–P76 (Ch)
6. Englich S, Paulo JMC, Weber R, Schuh H (2007) Determination of earth ration variations by means of VLBI and GPS and comparison to conventional models. Vermessung and Geoinformation 2:104–112
7. Xu G (2002) GPS data processing with equivalent observation equations. GPS Solution 2002(6):P28–P33
8. Xu C, Shen W, Dingbo C (2006) Geophysical geodesy principle and methods. Wuhan University Press, Wuhan (Ch)
9. Zhang H, Xu H, Liu L (2006) The theory on earth rotation in dynamical geodesy. China Science and Technology Press, Beijing (Ch)
10. Zhao M, Zhu SY (1986) On the optimal conditions for determination of earth rotation parameters. Acta Astronomica Sinica 27(2):P96–P105 (Ch)

Chapter 25
Analysis and Application of Extracting GPS Time Series Common Mode Errors Based on PCA

Gao Han, Zhang Shuangcheng and Zhang Rui

Abstract Characteristics of daily position time series which dated from 2006 to 2011 in South Central of America GPS fiducial network are researched in this paper. A spatial filtering algorithm based on principal component analysis was employed to extract and remove the common mode errors from the coordinate time series. This method promoted the accuracy and reliability of the sites coordinate. Further, we discussed the differences influence in velocity field of GPS stations by test to wipe off the common-mode error. The result shows that the common mode errors can not be neglected in time series analysis, particularly when we deal with the micro deformation, the PCA method can get rid of the common mode errors effectively and improve the reliability of result.

Keywords GPS time series · Common mode error · Principal component analysis · Velocity field

25.1 Introduction

Nowadays GPS continuous observation has become one significant method of deformation monitoring. There are hundreds of global monitor stations and thousands of regional monitor stations have been built around the world, they can provide us with a unified reference frame to monitor the surface deformation of

G. Han (✉) · Z. Shuangcheng · Z. Rui
College of Geology Engineering and Geomatics, Chang'an University, Xi'an 710054, China
e-mail: gaohan_cd@163.com

Z. Shuangcheng
e-mail: shuangcheng369@vip.163.com

Z. Rui
e-mail: zhangruiwkk@163.com

J. Sun et al. (eds.), *China Satellite Navigation Conference (CSNC) 2013 Proceedings*, Lecture Notes in Electrical Engineering 243,
DOI: 10.1007/978-3-642-37398-5_25,

global, regional also even smaller scale range. It not only can monitor surface displacement and deformation which caused by the earthquake, but also can monitor tiny tectonic deformation such as post seismic deformation, tectonic movement deformation and so on [1]. However, through the analysis of stations' coordinate time series of GPS regional network we found that there was a kind of space–time correlation error between different stations which called the common mode error (CME) [2–4]. There is no clear conclusion for the source of CME nowadays. It reflects the change on reference framework and scale. Probably it was unsteadily caused by GPS satellite orbit biases, residual error of ocean tide correction and atmospheric pressure tidal (S1 and S2 tidal wave) in essence [5]. CME is the main error source of GPS daily solution, and has negative influence on the extraction of deformation characteristics. Therefore, how to remove the common mode error from the coordinate time series of GPS stations and improve the precision of sites coordinate are very important to the deformation analysis.

In this paper, we used the data of South Central of America GPS regional network which contains about thirteen stations, and utilize the principal component analysis (PCA) to extract and remove the common mode errors from the coordinate time series, improve the accuracy and reliability of the sites coordinate. Further we got the crustal deformation information of experiment region.

25.2 The Rationale of Principal Component Analysis

PCA is a multivariate statistics analysis method of selecting a few important variables from multiple variables by the linear transformation. With orthogonal transforms, it turns original random vectors of dependent fraction into new random vectors of independent fraction. The transpositional aim is turning the multiple indicators into a few comprehensive index which used the thought of dimension reduction.

For a GPS regional network which has n stations and observations are carried out for m days, each component (N, E and U) of the residual coordinate time series was expressed $\boldsymbol{X}(t_i, x_j)$ $(i = 1, 2, \cdots m;\ j = 1, 2, \cdots n)$, each column contains a direction data sequences which removed the trend and average, each line represents a component value of all stations in specified epoch, $\boldsymbol{B}$ is covariance matrix of $\boldsymbol{X}$, $b_{i,j}$ was defined by

$$b_{i,j} = \frac{1}{m-1}\sum_{k=1}^{m} \boldsymbol{X}(t_k, x_i)\boldsymbol{X}(t_k, x_j) \tag{25.1}$$

It is a matrix of $n \times n$, can be broken down into

$$\boldsymbol{B} = \boldsymbol{V}\Lambda\boldsymbol{V}^{\boldsymbol{T}} \tag{25.2}$$

where $\boldsymbol{V^T}$ is a $n \times n$ orthogonal matrix which consist of feature vector, Λ is a eigenvalue matrix which consist of k nonzero diagonal elements, $\boldsymbol{B}$ is a non-singular matrix, namely $k = n$, the feature vector of $\boldsymbol{B}$ can be written as$(\lambda_1, \boldsymbol{v_1}), (\lambda_2, \boldsymbol{v_2}), \cdots (\lambda_n, \boldsymbol{v_n})$, where $\boldsymbol{v}_1, \boldsymbol{v}_2, \cdots \boldsymbol{v}_n$ is a set of orthogonal basis, we describe $\boldsymbol{X}(t_i, x_j)$ with the set of orthogonal basis

$$\boldsymbol{X}(t_i, x_j) = \sum_{k=1}^{n} \boldsymbol{a}_k(t_i)\boldsymbol{v}_k(x_j) \qquad (j = 1, 2 \cdots n) \tag{25.3}$$

where $\boldsymbol{a}_k$ is the temporal amplitude of the kth principal component, as shown

$$\boldsymbol{a}_k(t_i) = \sum_{j=1}^{n} \boldsymbol{X}(t_i, x_j)\ \boldsymbol{v}_k(x_j) \qquad (k = 1, 2 \cdots n) \tag{25.4}$$

where $\boldsymbol{v}_k$ is its corresponding eigenvector. Usually the eigenvectors are arranged in the descending order so that the leading few PCs can account for the common mode signature of the entire network, while the higher-order PCs are related to local environmental effects [6]. Can use the cumulative contribution of characteristic value m_k to represent the contribution of each principal component, namely,

$$m_k = \frac{\sum_{i=1}^{k} \lambda_i}{\sum_{i=1}^{n} \lambda_i} \qquad (k = 1, 2, \cdots n) \tag{25.5}$$

Set a threshold value such as 0.85, when the cumulative contribution rate to achieve the threshold value, the first P is the primarily model component.

$$\varepsilon_j(t_i) = \sum_{k=1}^{p} \boldsymbol{a}_k(t_i)\, \boldsymbol{v}_k(x_j) \tag{25.6}$$

Since the first p principal components of the detrended time series explain the common mode variations on our network and their eigenvectors have a rather homogeneous spatial pattern, we treat the first p PC as CME.

25.3 Analysis of Extracting GPS Time Series CME Based On PCA

In this paper, the stable area's stations of South Central of America were considered in our experiment: primarily we obtained the residual error time series by getting rid of the mean and the trend from the original series; secondly we

Fig. 25.1 The station of SEU1 network

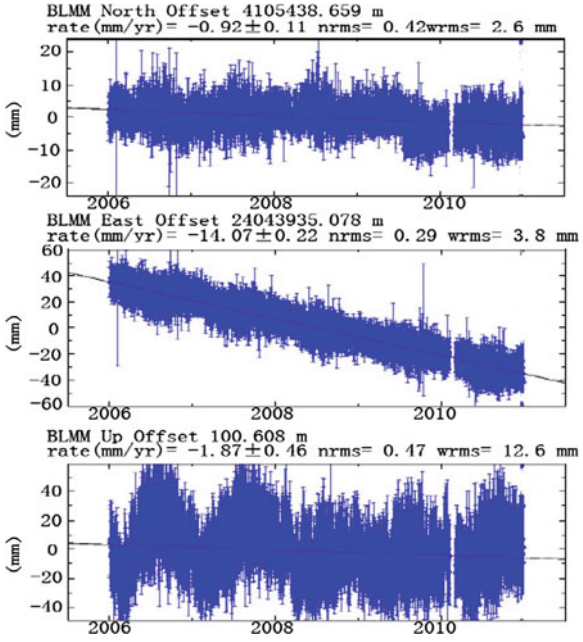

Fig. 25.2 Raw daily coordinate time series of BLMM

extracted the common-mode error of the experiment area by PCA method; lastly we analyzed the impact of common-mode error on the velocity field of the experiment area.

25.3.1 Obtain the GPS Residual Time Series

In the paper we selected thirteen stations of GPS continuous observation which dated from January 1, 2006 to January 1, 2011 in the South Central of America, the distribution of these stations are shown in Fig. 25.1. The daily sites coordinate was estimated from GPS observation by using the GAMIT/GLOBK software packages. In the first step, we obtained the relaxant solution each day with GAMIT software, we used in this solution nearby 4 IGS stations (ALGO, KOUR, GOL2, DRAO) in this solution which position and velocities were well determined in the ITRF2005 to serve as the linking of the local network and global IGS network. In the second step we combined our loosely constrained solution with the SOPAC global solution (igs1 - 1gs6) by using GLOBK softeware. Further, coordinates time series of stations were generated by using GLRED model to identify and remove the surveys or stations which are outliers. Finally, after the clean coordinates time series were got, internal constraints are applied by using a set of globally-distributed

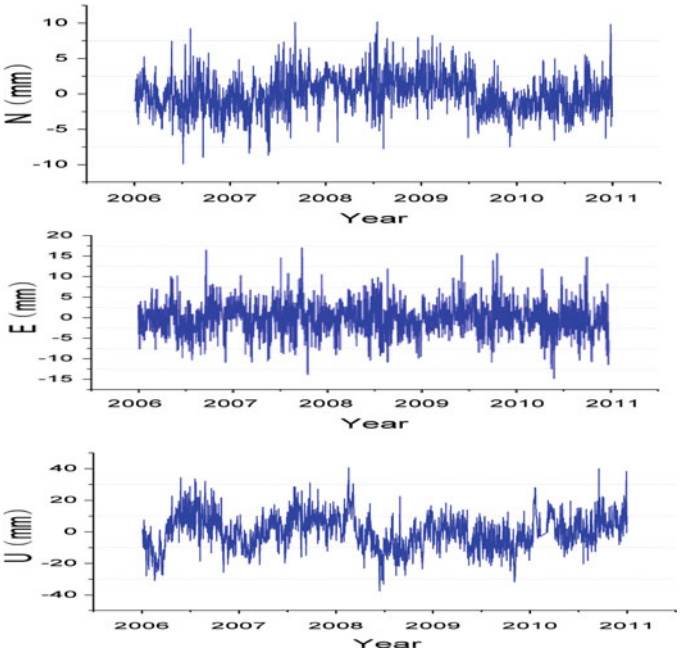

Fig. 25.3 The residual coordinate time series of BLMM

fiducial station coordinates to define the reference frame for daily station coordinate estimates. Then, we obtained the raw daily coordinate time series in the ITRF2005 (Fig. 25.2, BLMM, for example). Because of the data of some sites is missing seriously, we only process the data from January 1, 2006 to February 25, 2010 by using the PCA method in the subsequent.

When we filter the residual time series with PCA, it requires the time series should be uniformly-space sampling. But it is unlikely to meet such requests in the actual observation. There will always be some days missing. It needs the interpolation management for it to get the uniformly-space sampling time series. Therefore, the paper used cubic spline interpolation. This method is more effective for the continuous data which missing less than 5 days, and the less missing the better [7]. However, when the continuous volume data have bigger loss, the interpolation will appear abnormal after the cubic spline interpolation method was used. In our example, the most continuous lost quantity no more than 5 days in addition to the part of some stations after 2010. Therefore, we use the cubic spline interpolation to filling-in the date which missing below 5 days, and use the Fast Fourier Transform (FFT) interpolated algorithm to filling-in the date which missing more than 5 days. Because of the method of FFT has less damage to the time series and it is better for the situation of whose most continuous lost quantity no more than 50 days.

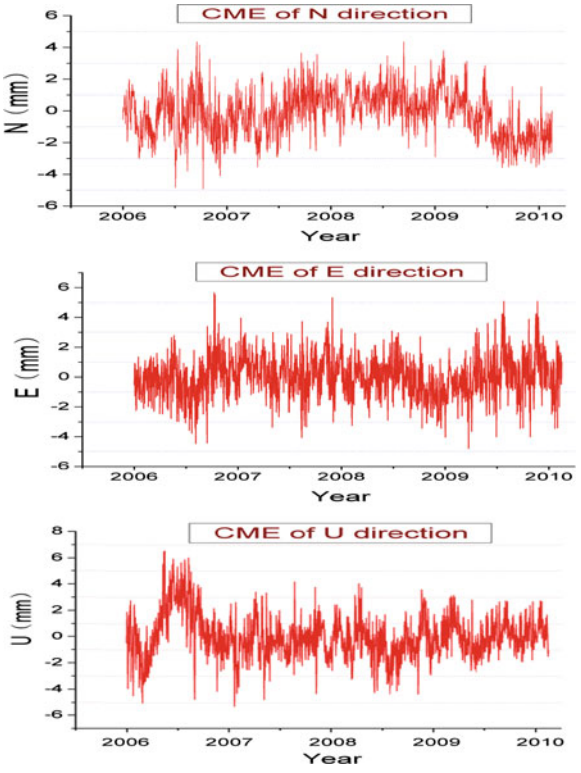

Fig. 25.4 Time series of common mode errors (N, E, U)

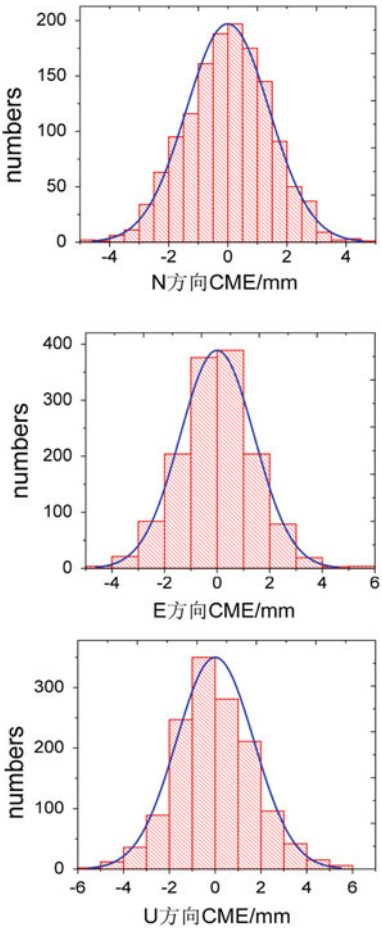

Fig. 25.5 Statistical graph of CME

After the interpolating, we used Nikolaidis model (see [8]) to fit the GPS coordinates time series and obtain the GPS residual coordinates time series which removed the mean and the trend. The result will be the input data of PCA in the subsequent. Due to the limit of paper, station of BLMM only be showed at here. Figure 25.3 is the residual coordinate time series of BLMM.

25.3.2 Extract of GPS Time Series CME with PCA

Using the above method which called Principal Component Analysis, we processed 13 sites residual time series on SEU1 area-network in the South Central of America. During the PCA analyzing, we extracted and eliminated the components whose accumulative contribution rate reached 85 %. That component represents

common mode error. In this experiment, we selected the first three principal components as the common mode error which present the directions of N, E and U. Their accumulative contribution rate was obtained respectively as 86.4, 87.8 and 90.1 % by using the formula (25.5). The common mode errors extracted on the SEU1 area-network which present the directions of N, E and U are shown in the Fig. 25.4. The mean value of N, E and U respectively is 5, 5 and 7 mm. From the following cartogram Fig. 25.5, we can see that common mode error has randomness obviously. Its characteristic is similar to the usual error we see later, CME of all the stations on the regional network were eliminated. The original result of site BLMN was shown in the Fig. 25.6. And by the PCA area filtering, the residual time series of BLMM which has dealed was shown in the Fig. 25.7. From the figure, we found that its horizontal direction is smooth, its height direction has slightly fluctuation. But from the overall view, its amplitude of fluctuation decreased. The method effectively eliminated the common mode errors which improves the precision and stability of the sites coordinate, enhances the robustness of coordinate series.

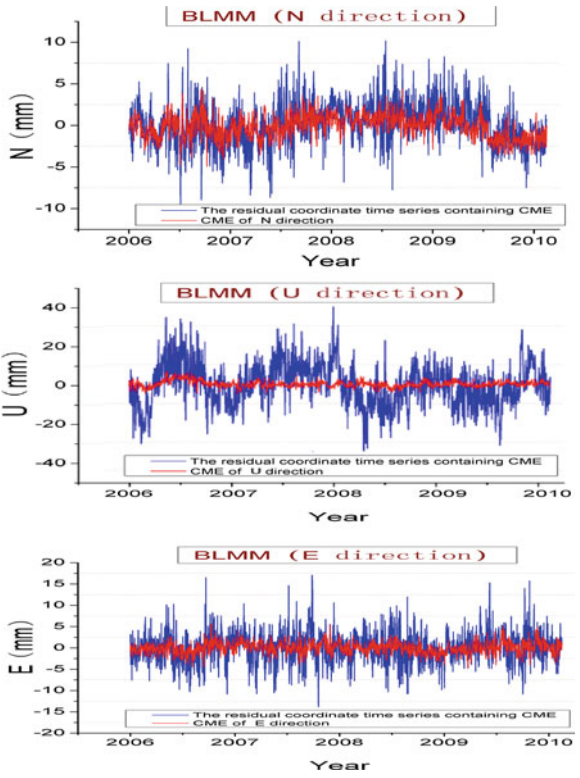

Fig. 25.6 The residual coordinate time series of BLMM before removing CME

25.3.3 Analysize the Impact of CME on Velocity Field

In order to further discuss the horizontal movement of the SEU1 area-network in the South Central of America, and impacts of the regional common mode error on horizontal velocity. To analyze the impact, in the view of weather or not contain the CME, the velocity field of the area should be achieved separately. Next, comparative analysis was got such as below.

When using GLOBK to obtain the velocity field, we chose the data of 20 days (dated from January 1st to January 20th) every year in 2006–2010. First of all, we combined the everyday relaxation solution of baseline and the global solution which ware calculated from GAMIT. Secondly, we computed the time series by using the GLRED model, and checked the repeatability of baseline and coordinate. Moreover, we eliminated outliers and the CME in the 3.2-part, got the clean time series. Finally, we combined the everyday solution by using the GLOBK modle. And then, the speed of each station in ITRF2005 framework (see Fig. 25.8) was

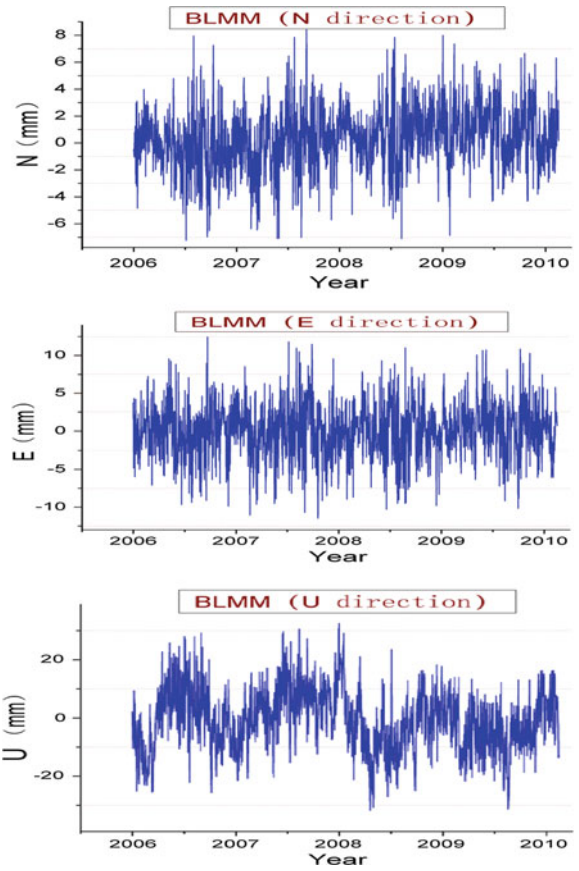

Fig. 25.7 The residual coordinate time series of BLMM after removing CME

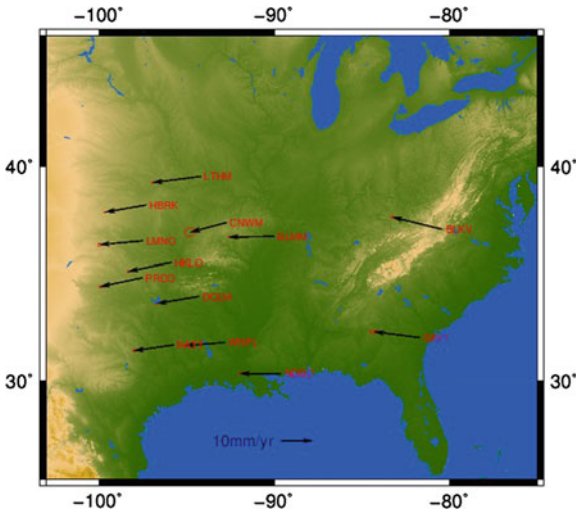

Fig. 25.8 Station horizontal velocities of North America area (relative ITRF2005) (Error *ellipse* is 95 % confidence level)

estimated. Further, the velocity filed was obtained which relating to the North America plate based on the plate motion model of ITRF2005VEL [9–11]. The horizontal velocity in the east–west direction is between −1.3 mm/a and 3.5 mm/a, and its mean velocity is 1.4 mm/a; the horizontal velocity in the north–south direction is between −3.7 and 2.5 mm/a, and its mean velocity is −2.2 mm/a. Using the same method but the only difference is not eliminating the CME, we can get the velocity filed which relating to the North America plate that including the CME. Comparing it with the velocity filed which eliminating the CME, we can find that the horizontal velocity in the E and direction N are about 1 mm/a. The biggest is 1.2 mm/a. As the Fig. 25.9 shows, blue arrows represent the velocity which

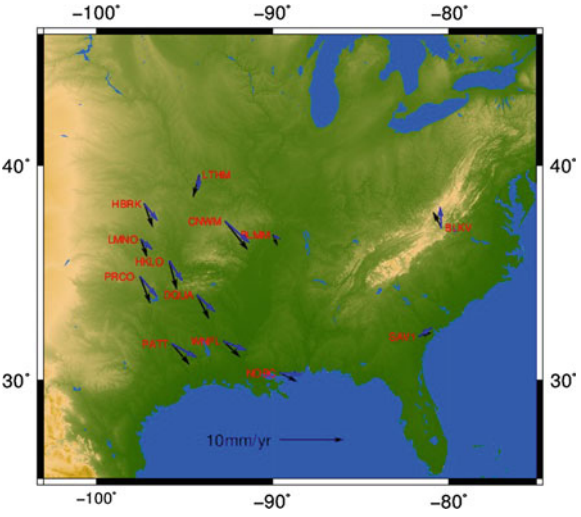

Fig. 25.9 Station horizontal velocities of SEU1 area (relative to the North America plate) (*blue arrows* represent before removing CME, *black arrows* represent after removing CME)

not removing CME, black arrows represent the velocity which removing CME. From the above results, we can see that the CME has influence on the horizontal velocity in the Central and South America and it can not be ignored when we extract the micro deformation of crustal.

25.4 Conclusions

In this paper, we effectively extracted the common mode error of coordinate time series on SEU1 area-network in the South Central of America, it improved the precision and stability of the sites coordinate and enhances the robustness of the coordinate series. Then after we eliminate the CME, the difference of velocity field was further discussed relative to North American Plate. As the result shows that the common-mode error has important influence on the station velocity in some extent, and so it cannot be ignored especially when we extract the micro deformation of crustal.

References

1. Wu J, SunY, Liu C (2008) Extraction of common mode errors for continuous GPS networks and deformation analysis. J Geodesy Geodyn 28(4):97–101
2. Dong DN, Fang P, Bock Y, Webb F, Prawirodirdjo L, Kedar S, Jamason P (2006) Spatiotemporal filtering using principal component analysis and Karhunen-Loeve expansion approaches for regional GPS network analysis. J Geophys Res 111:B03405
3. Yunfeng T, Zhengkang S (2009) Progress on reduction of non-tectonic noise in GPS position time series. Acta Seismol Sin 31(1):68–81
4. Zhang J et al (1997) Southern California permanent GPS geodetic array. Error analysis of daily position estimates and site velocities. J Geophys Res 102:18035–18055
5. Yunfeng T, Zhengkang S (2011) Correlation weighted stacking filtering of common-mode component in GPS observation network. Acta Seismol Sin 33(2):198–208
6. Savage J (1995) Principal component analysis of interseismic deformation in southern California. Geophy Res 100:12691–12701
7. Yanqiang W, Liren H (2004) A new interpolation method in time series analyzing. J Geodsy Geodyn 24(4):43–47
8. Nikolaidis R (2002) Observation of geodetic and seismic deformation with the global positioning system. University of California, San Digeo
9. Yian L, Liren H et al (2004) Present-day Crustal movement in China. Seismological Press, Beijing
10. Liu GY (2004) Some key issues relating to high precision GPS positioning and crustal deformation analysis. Institute of Geodesy and Geophysics, CAS, Wuhan
11. Rong M, Zhou W et al (2009) Global plate motion model based on ITRF2005. Hydrogr Surveying charting 29(1):1–3

Chapter 26
The Application of Smoothed Code in BeiDou Common View

Wei Guang and Haibo Yuan

Abstract The time transfer based on satellite navigation system is adopted widely in the international time comparison. The main methods of time laboratories comparison are GPS common-view and GPS PPP in the international comparison links. Because of its mature technology and standard specification in traditional method, GPS common view is the most convenient technology in the precise time transfer field. In this paper, four data processes methods are used to calculate the time difference between two time laboratories, such as direct common view, standard common view as CGGTTS, carrier phase smoothed code in direct common view and carrier smoothed code modifying the CGGTTS. At the end of paper, the comparison of these methods is analyzed on the precision and frequency stability. The results show that the phase smoothing method can get a better accuracy in time transfer.

Keywords Time transfer · Smoothed code · Slip detecting · BeiDou common view

W. Guang (✉) · H. Yuan
National Time Service Center, CAS, BOX 18, Lintong Xi'an Shaanxi 710600, China
e-mail: guangwei@ntsc.ac.cn; weiguang@foxmail.com

H. Yuan
e-mail: Yuanhb@ntsc.ac.cn

H. Yuan
Key Lab of Time-frequency Standard of the Chinese Academy of Sciences, Beijing, China

J. Sun et al. (eds.), *China Satellite Navigation Conference (CSNC) 2013 Proceedings*, Lecture Notes in Electrical Engineering 243,
DOI: 10.1007/978-3-642-37398-5_26,

26.1 Introduction

In the international time comparison, the time transfer based on satellite navigation system and two-way satellite time and frequency transfer (TWSTFT) are adopted widely. With its advantage on high precise and real-time features, TWSTFT is the main link between the time laboratory, and the time transfer based on satellite navigation system is adopted as its backup link. At present, with the benefit of its stable, reliable and high precision characteristics, GPS become the main GNSS time transfer based on in the international time comparison on the four global satellite navigation system. GPS CV and PPP time transfer technology is In-depth researched and developed. The GLONASS system is not used as common as GPS, because its stability and precision is not as well as GPS. The Galileo system is being tested at present, the time transfer based on this system is not developed yet. The Asia Pacific region covered BeiDou satellite navigation system is in the regional service stage now, which can provide a high precision positioning and Timing application. The principle of BeiDou navigation system is similar to the GPS system. The differences is the satellite constellation, there are three types of satellite in BeiDou system,such as five geostationary orbit synchronous satellite (GEO), five inclined orbit synchronous satellite (IGSO) and many middle earth orbit satellites (MEO). The different data processing methods on three kinds of BeiDou satellite for time transfer application is used in this paper, and the analysis and comparison among these methods is provided at the end of the paper.

26.2 The Introduction of Time Transfer Principle

Time transfer method Based on the navigation system is often using common view (CV), all in view (AV) and the precise point position (PPP). In the traditional common view method, GPS CV is widely used for its data processing algorithm standard. Due to the complex algorithm, no unified standard and the precise obit and Clock bias product not being real-time, AV and PPP is not widely used as CV before. But with the development of IGS product, the PPP time transfer is becoming the popular method in the international time comparison [1]. As the precise obit and Clock bias product is unavailable in BeiDou for us, the traditional common view is adopted in this paper. The direct common view, CGGTTS standard algorithm and phase smoothing pseudorange coed methods are used in the data processing for the remote time comparison. At the end of the paper, the result is shown and compared on different data processing. The principle of BeiDou common view is similar as GPS CV which shown at follow figure (Fig. 26.1).

Two remote time laboratories receive the same satellite signal at the same time, and compute the time difference between the local time and the satellite clock time. Compared the clock bias between the two laboratories computed above, the time bias can be get for the two time laboratories. Supposing the timing receiver

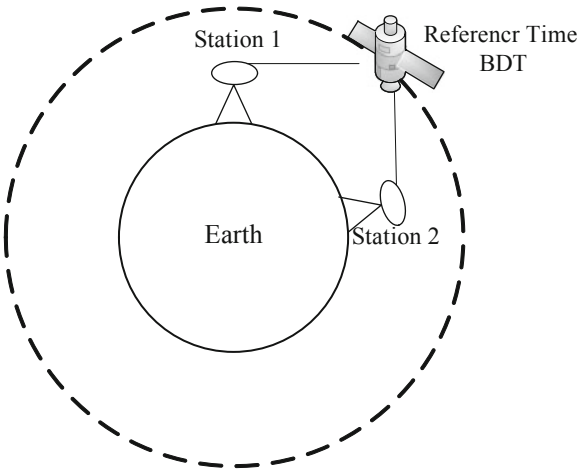

Fig. 26.1 The principle of common view

are placed on the two laboratories, such as station A and station B, and they receiving the signal of satellite S, the function can be written:

$$\Delta t_{AS} = (t_A - t_S) \tag{26.1}$$

$$\Delta t_{BS} = (t_B - t_S) \tag{26.2}$$

In the function, Δt_{AS} means the time bias between station A and the satellite S, t_S means the clock on satellite S, t_A means local time of station A; Δt_{BS} means the time bias between station B and the satellite S, t_B means local time of station B.

The time difference between station A and B can be got by formal (26.1) misusing (26.2):

$$\begin{aligned} \Delta T_{AB} &= \Delta t_{AS} - \Delta t_{BS} \\ &= (t_A - t_S) - (t_B - t_S) = t_A - t_B \end{aligned} \tag{26.3}$$

26.3 Data Processing Methods

The directing common view, CGGTT standard and carrier phase smoothing code data processing methods are implemented for the time transfer based on BeiDou navigation system.

26.3.1 The Direct Common View

Navigation system is by measuring the signal from the source from the known satellites to the user received to complete distance measurements and for the geometric positioning. This can be say that using TOA distance measurement to determine user location.

$$P_i = \rho + cdt_r - cdT_s + d_{orb} + d_{trop} + d_{ion/Pi} + d_{mult/Pi} + \varepsilon_{pi} \tag{26.4}$$

P_i means the pseudo-range code observation from frequency i. ρ means geometrical distance between station and satellite. cdt_r is the Receiver clock bias correction (m). cdT_s is satellite clock bias correction (m). d_{orb} is satellite orbit error correction (m). d_{trop} is tropospheric delay (m). $d_{ion/Pi}$ is ionospheric delay (m). $d_{mult/Pi}$ means Multipath delay (m). ε_{pi} means noise of pseudo-range phase and measurements.

In the direct common view calculation, we just need to take the acquisition date into the observation equations mentioned above to calculate the time bias between the local receiver's clock and the system time. Two time laboratory have got this result at the same time, then the difference between the two stations can be get by a simple subtraction.

26.3.2 Standard Common View Data Processing Method

The standard common view (CGGTTS file format formation) data processing procedure can be described as follows [2]: The satellites' elevation angle should be more than 20° on each Tracking in 16 min (two minutes for preparation, one minute for processing). Then, continuously record the data for 13 min, collecting 780 code pseudo-range observations (one per second) for a group as a common view data. Make the 780 data points into 52 groups, each group have 15 points. The 52 sets of each points (15 points) respectively be used the quadratic polynomial fitting values at the midpoint of the selected data. A linear fit applied to the results (shown on the following figure) the tropospheric delay, Ionospheric delay, Multipath delay and other delay are considered in the data processing to get time bias between the local time and the GPST(REFGPS) or satellite time (REFSV). For the two time laboratory clock difference can obtain by the REFGPS subtraction at the same time (Fig. 26.2).

26.3.3 Phase Smoothing Code Data Processing Method

In the traditional common view data processing, the code observations is used for calculation. The precision is limited on the code measurement. In order to improve

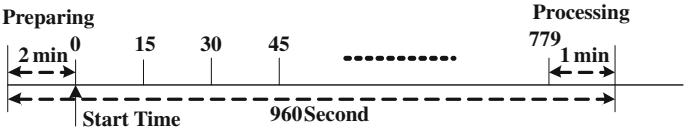

Fig. 26.2 The data and its group of once common view

the precision of the time transfer, here the phase observation is adopted into smoothing the code observation. The slip of the phase data may cause mistake without preprocessing, so the slip detecting is an indispensable procedure. In the paper the combination of Melbourne—Wübbena and ionospheric residual is used to detect the phase slip [3]. The combination of the equation (M-W) is as follow:

$$L_M = L_w - P_n = \frac{(f_1 L_1 - f_2 L_2)}{f_1 - f_2} - \frac{(f_1 P_1 + f_2 P_2)}{f_1 + f_2} = -\lambda_w N_w \tag{26.5}$$

L_1, L_2 means the phase with the unit m, $\lambda_w = {}^{c}/_{f_1 - f_2}$ is the wide combination wavelength, $N_w = N_1 - N_2$ means the wide ambiguity of the combination observation.the variance of the observation is:

$$\sigma^2_{L_M} = \frac{(f_1^2 \sigma^2_{L_1} - f_2^2 \sigma^2_{L_2})}{(f_1 - f_2)^2} - \frac{(f_1^2 P^2_{P_1} + f_2^2 P^2_{P2})}{(f_1 + f_2)^2} \tag{26.6}$$

In the practical data processing, the follow equations are used to remove unsuitable phase and code observation data, and for the wide ambiguity calculation.

$$\left.\begin{aligned} \langle N_w \rangle_i &= \langle N_w \rangle_{i-1} - \frac{1}{i}\left[N_{w,i} - \langle N_w \rangle_{i-1}\right] \\ \sigma_i^2 &= \sigma_{i-1}^2 + \frac{1}{i}\left[\left(N_{w,i} - \langle N_w \rangle_{i-1}\right)^2 - \sigma_{i-1}^2\right] \end{aligned}\right\} \tag{26.7}$$

$$\left|N_{w,i} - \langle N_w \rangle_{i-1}\right| \geq 4\sigma_i \tag{26.8}$$

$$\left|N_{w,i+1} - N_{w,i}\right| \leq 1 \tag{26.9}$$

If the formula (26.8) is satisfied, means the slip may be found, at the same time the formula is also satisfied, the data must be slip. Then, we mark this data point. One of these conditions appears, it means the data is gross.

Ionospheric residual combination is the difference between the adjacent epochs of phase observation, which is interrelated with the ionospheric noise and the noise of phase measurements. As the change between the adjacent epochs of phase observation is small, the slip can be detected more easily. The combination observation function can be written:

$$\left.\begin{aligned} L_{ion} = \lambda_1\phi_1 - \lambda_2\phi_2 = \lambda_1 N_1 - \lambda_2 N_2 + I_{f1} - I_{f2} \\ I_{diff} = L_{ion}(t_{i+1}) - L_{ion}(t_i) \end{aligned}\right\} \tag{26.10}$$

When the ionosphere is stable, and data sampling interval is short, the ionospheric changes is at cm level, then decision threshold is close to zero, if the residual value is greater than the threshold, the data can be mark as slip data. For the GEO and IGSO, the satellite moves slower than other navigation system satellites, the variation between each epoch is in a small scale [4]. The Ionospheric Residual combination is very suitable for GEO and IGSO carrier phase data processing.

The Ionosphere-free combination of pseudo-range and phase observations can be expressed as:

$$\left.\begin{aligned} \lambda(\varphi + N) = \rho + \Delta\rho_L + \varepsilon \\ P_{IF} = \rho + \Delta\rho_P + \varepsilon \end{aligned}\right\} \tag{26.11}$$

According to the relationship of the code and phase observation, two formals minus each other the combined ambiguity can be got, and then take the average of some epoch [5].

$$\left.\begin{aligned} P_{3smth} = \frac{1}{i}P(i) + \frac{i-1}{i}(P_{3smth}(i-1) + L_3(i) - L_3(i-1)) \\ P_{3smth}(1) = P_3(1) \end{aligned}\right\} \tag{26.12}$$

In the practical data processing, the formal (26.13) is adopted.

$$\left.\begin{aligned} \langle\lambda N\rangle_i = \frac{i-1}{i}\langle\lambda N\rangle_{i-1} + \frac{1}{i}(P_i - L_i) \\ P_{i,smth} = L_i + \langle\lambda N\rangle_i \end{aligned}\right\} \tag{26.13}$$

26.4 The Analysis and Comparison of the Result

According to the principle and algorithm, five days data from 2012.09.01 to 2012.09.05 of BeiDou geodetic receivers at NTSC and other time laboratories is selected in this experiment, the observation data of BD satellites (No.1 to No.10) are calculated. The following figures show the result of GEO satellites and IGSO satellites on 2012.09.03 (Figs. 26.3, 26.4, 26.5, and 26.6).

In these figures, 30 s CV means direct common view with the data interval of 30 s, STCV stands for standard common view method (that is, CGGTTS format formation method), SMCV means using phase smoothing code menthod before common view to process the data with the interval of 30 s, SMSTCV means using phase smoothing code method before standard common view. Base on the result of

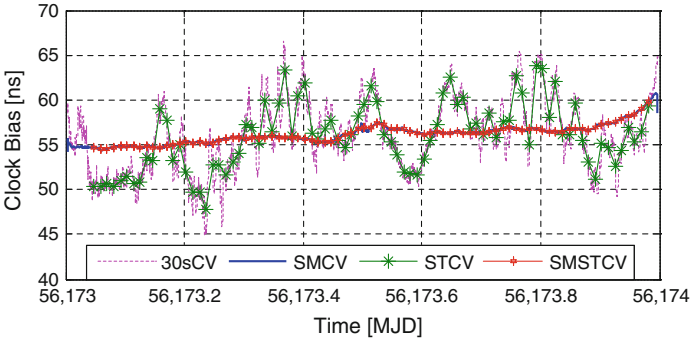

Fig. 26.3 The result of satellite GEO-03 on different method

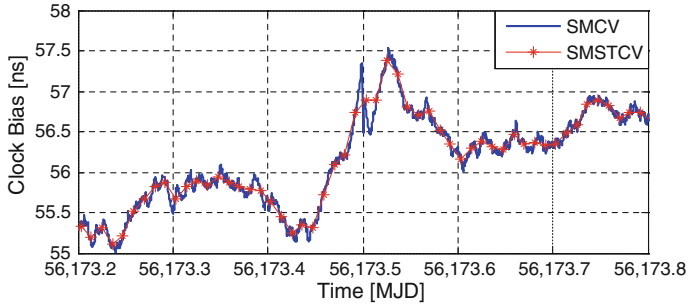

Fig. 26.4 The result of satellite GEO-03 between smoothed and standard method

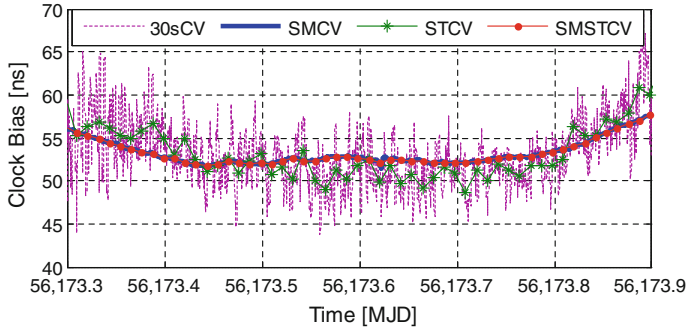

Fig. 26.5 The result of satellite IGSO-04 on different methods

signal satellite, it can be seen obviously that the method of phase smoothing code before common view is superior to the method of direct common view, the method of SMSTCV is better than SMCV because SMSTCV can remove the coarse value, and the data file of SMSTCV is smaller than SMCV so that it is easy to transmission.

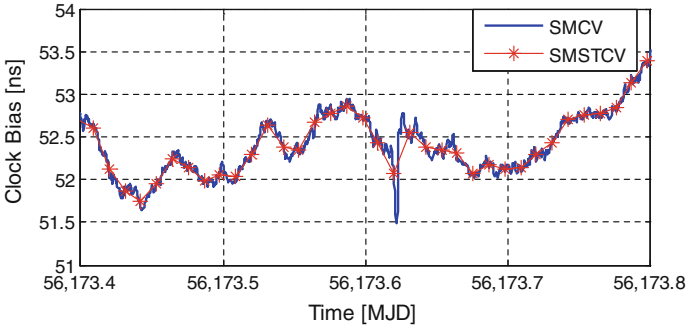

Fig. 26.6 The result of satellite IGSO-04 between smoothed and standard methods

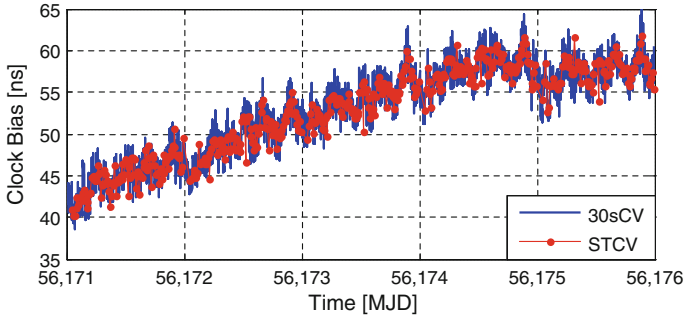

Fig. 26.7 Comparison between direct and standard common view

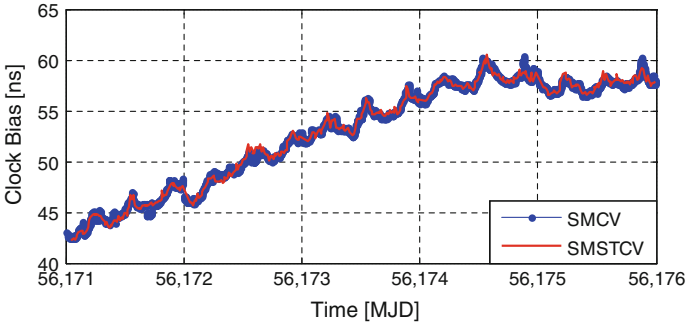

Fig. 26.8 Comparison between smoothed and modified common view

Following figure is the analysis on the stability of common view between two laboratories through averaging the result of No. 1 to No. 10 satellites in the 5 days.

Figures 26.7 and 26.8 show that the in the common view between two laboratories, the result of phase smoothing code is superior than traditional common

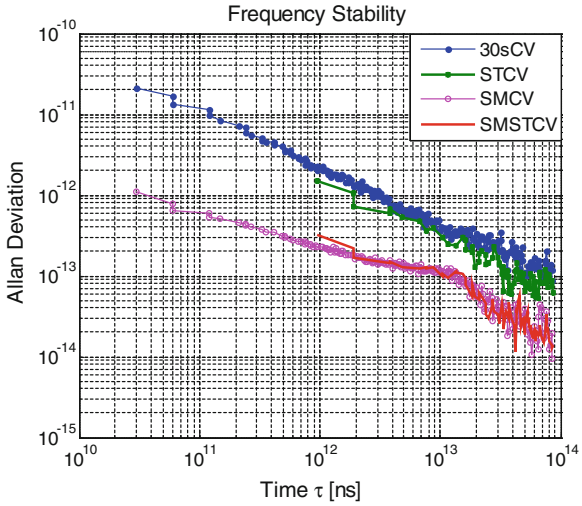

Fig. 26.9 The Frequency stability of all method

Table 26.1 The stability of different method

	30 s CV	Standard CV	Phase smoothed CV	Modified standard CV
1 min	1.65e–11	*	7.81e–13	*
1 h	8.52e–13	6.00e–13	1.44e–13	1.43e–13
1 day	8.75e–14	7.38e–14	9.27e–15	1.39e–14

Table 26.2 Comparison of the TIE RMS

	30 s CV	Standard CV	Phase smoothed CV	Modified standard CV
1 h	2.25 ns	1.87 ns	0.63 ns	0.61 ns

view, meanwhile the common view result corrected by phase data is better than traditional common view on the stability of time transfer link. In order to quantify the results, following tables give the time transfer stability (one minute stability, of hour stability, one day stability) and RMS of time interval error (TIE RMS). From Fig. 26.9, it can be seen that phase smoothing code method has obvious advantage in short-term stability, and its long-term stability is close to the pseudo-range method (Tables 26.1 and 26.2).

On the method of phase smoothing code, the minute stability is 7.8e–13, hour stability can reach 1.4e–13, and one day stability is 9.2e–15. The difference between the method of phase smoothing code and the method of modified standard common view by phase smoothing code is not obvious on the stability, however on the aspect of TIE RMS, the method of modified standard common view by phase

smoothing code has some improvement than method of directly phase smoothing code, meanwhile it is superior to traditional common view method.

26.5 Conclusion

This paper gives the time transfer method between two time laboratories. Different data processing methods is used for BeiDou common view principle. From the comparison of the different results, it can be concluded that phase smoothing code method can improve traditional common view algorithm, this method can get better time accuracy, which can be beneficial for improving BeiDou standard common view algorithm.

References

1. Shirong Y (2002) Theory and its realization of GPS precise point positioning using undifferenced phase observation. WuHan University, WuHan, pp 71–76
2. Petit G, Jiang Z (2008) GPS all in view time transfer for TAI computation. Metrologia 45:35–45
3. Allan DW, Thoms C (1994) Technical directives for standardization of GPS time receiver software. Metrologia 31:69–79
4. Peng HM, Liao CS (2004) GPS smoothed P3 code for time transfer, EFTF, pp 137–141
5. Defraigne P, Bruyninx C, Guyennon N (2007) PPP and phase-only GPS time and frequency transfer, EFTF, pp 904–908

Part II
BeiDou/GNSS Test and Assessment Technology

Chapter 27
Vulnerability Assessment for GNSS Constellation Based on AHP-FCE

Bo Qu, Jiaolong Wei, Shuangna Zhang and Liang Bi

Abstract The vulnerability of global navigation satellite system (GNSS) constellation is an important part of the vulnerability of GNSS. The vulnerability assessment for GNSS constellation is helpful to improve GNSS constellation. In this paper, the vulnerability of GNSS constellation is investigated and a vulnerability assessment model for GNSS constellation is suggested, then the vulnerability of GNSS constellation is evaluated by Analytical Hierarchy Process and Fuzzy Comprehensive Evaluation (AHP-FCE). The suggested assessment model concerns about the coverage of GNSS constellation in the situations that 1 satellite, 2 satellites, and 3 satellites are failure, and the mean coverage of GNSS constellation which is affected by satellite failures is used to be the assessment criterions. The vulnerability values of GNSS constellation can be calculated by AHP-FCE according to these criterions. In this paper, the vulnerability of GPS constellation and COMPASS constellation are evaluated, and the assessment results show that GPS constellation is slightly more vulnerable than COMPASS constellation which has more redundant satellites.

Keywords Vulnerability · GNSS constellation · AHP · FCE · Assessment

B. Qu (✉) · J. Wei (✉)
The Department of Electronic and Information Engineering,
Huazhong University of Science and Technology, Wuhan, China
e-mail: qb840528@163.com

J. Wei
e-mail: jlwei@mail.hust.edu.cn

S. Zhang · L. Bi
Space Star Technology Co. Ltd, Beijing, China

J. Sun et al. (eds.), *China Satellite Navigation Conference (CSNC) 2013 Proceedings*, Lecture Notes in Electrical Engineering 243,
DOI: 10.1007/978-3-642-37398-5_27,

27.1 Introduction

With the wide application of GNSS on various aspects of national defense and social life, the importance of GNSS is increasing apparently. Therefore, the research on the vulnerability of navigation satellite system is becoming more and more important.

The navigation satellite system typically consists of three segments [1]: a satellite constellation, ground control/monitoring networks and receivers. The satellite constellation includes satellites in orbit, which provide navigation ranging signals and navigation data messages for receivers. Therefore, GNSS constellation is the core of navigation satellite system, and the vulnerability of GNSS constellation is an important part of the vulnerability of GNSS. The vulnerability of GNSS can be mitigated by evaluating the vulnerability of GNSS constellation and improving GNSS constellation.

An assessment vulnerability method for GNSS constellation based on AHP-FCE is suggested in this article. Because the probability of more than 3 satellites failure is small [1], the vulnerability assessment model for GNSS constellation only concerns about the coverage performance of GNSS constellation in the case of 1 satellite failure, 2 satellites failure, and 3 satellites failure.

The paper is organized as follows: In the Sect. 27.2, AHP-FCE is briefly introduced. Section 27.3 suggests a vulnerability assessment model for GNSS constellation and provides the steps in which AHP-FCE is used to evaluate the vulnerability. Section 27.4 shows the vulnerability assessment results of COMPASS constellation and GPS constellation. Finally conclusions are drawn in Sect. 27.5.

27.2 AHP and FCE Method

AHP-FCE assessment method is a combination of Analytical Hierarchy Process and Fuzzy Comprehensive Evaluation.

Analytic Hierarchy Process (AHP) is a multi-attribute decision-making method which can be used for scheme selection, evaluation, and decision-making [2]. The main steps of AHP method are as follows [3]:

1. Establish a hierarchy model

An analytic hierarchy model is constructed on the basis of an actual problem. In the hierarchy model, a complex problem is broken down into many elements (or criteria), and the elements are divided into groups in different layers according to their attributes. The established hierarchy model should be able to reflect intrinsic attributes and all internal relations of the evaluated object, as shown in Fig. 27.1.

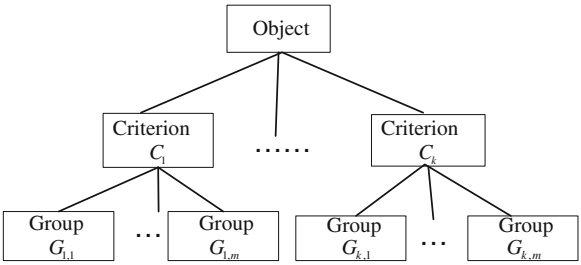

Fig. 27.1 Hierarchy model

2. Establish judgment matrices

After establishing the hierarchy model and determining the relationship between various criterions of the object to be evaluated, the relative importance of different criterions in the same layer should be determined, and then the judgment matrices can be constructed by making use of digital scales.

3. Calculate the weight of criterions in the same layer

This step is a process to compute the relative weight of criterions in the same layer according to the judgment matrices. The relative weight can be calculated by calculating the eigenvalue and the eigenvector of judgment matrices.

4. Calculate the weight of criterions in different layers

The above step is repeated, and eigenvalues and eigenvectors of the judgment matrices are calculated along the layers. The relative weight of criterions can be calculated to make decisions.

The fuzzy comprehensive evaluation (FCE), which is based on fuzzy math, makes use of the principles of fuzzy relation synthesis to evaluate an object [4]. The main steps of FCE method are as follows:

1. Determine the evaluation criterions

It is needed to identify criterions which characterize the objects to be evaluated. The main criterions which reflect the objects to be evaluated can be selected according to the evaluating purpose.

2. Determine a comment set or evaluation grades

A comment set or evaluation grades can be determined for each of evaluation criterions.

3. Generate fuzzy matrices

The ranges of different criterions are different due to the different dimensions of criterions, so the values of criterions need to be processed as a normalized one. The criterions with different physical meanings are normalized to be a dimensionless value in the interval [0, 1]. Before starting fuzzy synthesis calculation, fuzzy relationship matrices are calculated according to the membership function.

4. Fuzzy synthesis calculation

The membership degree of evaluation grades of the evaluated object can be calculated on the basis of a fuzzy matrix R and a weight vector W.

The vector of fuzzy comprehensive evaluation result is defined as $S = (s_1, s_2, \ldots, s_n)$, and S can be calculated by the fuzzy matrix R and the weight vector W through the fuzzy operator. It can be expressed as:

$$S = W \circ R \tag{27.1}$$

where $\circ$ is the fuzzy operator symbol. Different operator symbols correspond to different fuzzy comprehensive evaluation models.

27.3 Vulnerability Assessment for GNSS Constellation

27.3.1 Vulnerability Assessment Criterions for GNSS Constellation

The vulnerability assessment for GNSS constellation needs to evaluate the coverage performance of the GNSS constellation in the case of 1, 2, and 3 satellites failure. Failed satellites in different orbital positions have different impacts on the coverage performance of GNSS constellation. The assessment criterions mainly reflect the mean impact on the coverage performance in the case of satellites failure.

The coverage performance of GNSS constellation is mainly reflected by a global coverage of GNSS constellations. A receiver needs to receive signals from at least four satellites for the positioning function; a receiver needs to receive signals from at least five satellites to detect whether there is an unacceptable positioning error, and needs to receive signals from at least six satellites to exclude the data of failed satellites from the navigation solution [1]. Therefore, if some satellites of GNSS constellation were failure, the receivers would not be able to receive enough navigation signals, which would affect the autonomous integrity monitoring function or the positioning function. Thus, the vulnerability assessment for GNSS constellation mainly concerns about the coverage of 4 satellites, 5 satellites, and 6 satellites.

When GNSS constellation loses n satellites, the mean coverage of at least k navigation satellites can be defined as $CL(n, k)$, where n is the number of failed satellites, and k is the minimum number of satellites which can be received by receivers in one day. For example, when 2 satellites are failure, the mean coverage of 5 satellites can be expressed as $CL(2, 5)$.

The number of received signals by receivers on the ground varies at different times. When the number of received signals is less than the required number, the corresponding function can't work. The global coverage that the minimum number of satellites received on the ground isn't less than k in one day is used in the vulnerability assessment for GNSS constellation.

27.3.2 Vulnerability Assessment Model for GNSS Constellation

The vulnerability assessment model for GNSS constellation can be established according to AHP-FCE. The vulnerability assessment model for GNSS constellation is a three-layer assessment model, and the assessment model is shown in Fig. 27.2.

The ultimate goal is to assess the vulnerability of GNSS constellation. The middle layer is the vulnerability of GNSS constellation in the case of 1 satellite failure, 2 satellites failure, and 3 satellites failure. The bottom layer is the coverage performance of GNSS constellation.

27.3.3 Relative Weight Calculation

The 1–9 scale method is used in the vulnerability assessment for GNSS constellation, its meaning is shown in Table 27.1 [3]:

After determining judgment matrices, the weight vectors are calculated by using the eigenvalue method, the basic steps are as follows [5]:

1. Each column of the matrix A is normalized: $\tilde{w}_{ij} = a_{ij} / \sum_{i=1}^{n} a_{ij}$
2. Summing $\tilde{w}_{ij}$ according to row: $\tilde{w}_i = \sum_{j=1}^{n} \tilde{w}_{ij}$
3. $\tilde{w}_i$ is normalized: $w_i = \tilde{w}_i / \sum_{i=1}^{n} \tilde{w}_{ij}$
4. The weight vector is $w = (w_1, w_2, \ldots, w_n)^T$.

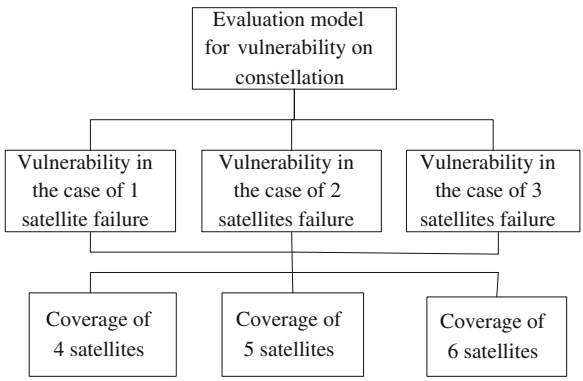

Fig. 27.2 Vulnerability assessment model

Table 27.1 Fundamental linguistic variables for pairwise comparisons

Scale	Definition
1	Equally important
3	Moderately more important
5	Strongly more important
7	Very strongly more important
9	Exceedingly more important
2, 4, 6, 8	Intermediate preferences
Reciprocal	If the importance of criterion i with respect to criterion j is a_{ij}, the importance of criterion j with respect to criterion i is $a_{ji} = 1/a_{ij}$

27.3.4 Generate Fuzzy Matrices

Fuzzy matrices are generated on the basis of the global coverage of GNSS constellation. Triangular fuzzy numbers are selected as membership functions in the process of assessment vulnerability for GNSS constellation. The comment set includes five grades: excellent, good, middle, poor, worst. The membership functions are as follows [5]:

$$S_1(x) = \begin{cases} (m_2 - x)/m_2 & 0 \le x \le m_2 \\ 0 & m_2 \le x \le 1 \end{cases} \tag{27.2}$$

$$S_i(x) = \begin{cases} 0 & 0 \le m_{i-1} \\ (x - m_{i-1})/(m_i - m_{i-1}) & m_{i-1} \le x \le m_i \\ (m_{i+1} + x)/(m_{i+1} - m_i) & m_i \le x \le m_{i+1} \\ 0 & m_{i+1} \le x \le 1 \end{cases} \tag{27.3}$$

$$S_5(x) = \begin{cases} 0 & 0 \le m_4 \\ (x - m_4)/(1 - m_4) & m_4 \le x \le 1 \end{cases} \tag{27.4}$$

where $i = 2, 3, 4$, $m_1 = 0$, $m_2 = 0.25$, $m_3 = 0.5$, $m_4 = 0.75$, $m_5 = 1$.

The fuzzy relation matrix of n satellites failure can be described as follow:

$$R_n = [\, S_{n,4} \quad S_{n,5} \quad S_{n,6} \,]^T \tag{27.5}$$

where $S_{n,4}$, $S_{n,5}$, $S_{n,6}$, are respectively the membership degrees of the coverage performance of 4 satellites, 5 satellites, 6 satellites in the case of n satellites failure.

27.3.5 Fuzzy Synthesis Calculation

The vulnerability assessment model for GNSS constellation is a three-layer assessment model. Therefore, 2 times of synthesis operations are needed to calculate the final assessment result.

The fuzzy relationship matrix of 1 satellite failure, 2 satellites failure and 3 satellites failure can be respectively expressed as R_1, R_2, R_3. The weights of $S_{n,4}$, $S_{n,5}$, $S_{n,6}$ are respectively expressed as $w_{n,4}$, $w_{n,5}$, $w_{n,6}$. After finishing the fuzzy synthesis calculation, the assessment results in the case of n satellites failure can be formulated as follow:

$$r_n = [\, w_{n,4} \quad w_{n,5} \quad w_{n,6} \,] R_n \tag{27.6}$$

The new fuzzy relation matrix consists of r_1, r_2, r_3. The weights of vulnerability caused by 1 satellite failure, 2 satellites failure, and 3 satellites failure are respectively described as w_1, w_2, and w_3. After the second fuzzy synthesis calculation, the final assessment results of GNSS constellation can be expressed as follow:

$$r = [\, w_1 \quad w_2 \quad w_3 \,] \begin{bmatrix} r_1 \\ r_2 \\ r_3 \end{bmatrix} \tag{27.7}$$

27.4 Vulnerability Assessment for COMPASS Constellation and GPS Constellation

COMPASS constellation is designed to have 27 medium earth orbit (MEO) satellites, 5 geostationary earth orbit (GEO) satellites and 3 inclined geosynchronous orbit (IGSO) satellites [6]. In the simulation, 27 MEO satellites in COMPASS constellation are assumed to locate in three orbital planes as Galileo constellation. GPS constellation consists of 31 satellites and these satellites locate in six orbital planes which have about five satellites.

When the shield angle is 5°, and 1, 2, 3 satellites are failure, the coverage performance of COMPASS constellation and GPS constellation can be simulated by STK and the simulation results are shown in Tables 27.2 and 27.3:

Table 27.2 The mean coverage of COMPASS constellation

Coverage	Satellites failure		
	1 satellite failure	2 satellite failure	3 satellite failure
At least 4 satellites	1	1	0.999
At least 5 satellites	1	0.994	0.981
At least 6 satellites	0.948	0.908	0.863

Table 27.3 The mean coverage of GPS constellation

Coverage	Satellites failure		
	1 satellite failure	2 satellite failure	3 satellite failure
At least 4 satellites	1	1	0.999
At least 5 satellites	0.998	0.978	0.977
At least 6 satellites	0.929	0.820	0.763

27.4.1 Calculate Relative Weights

It is known that the main function of GNSS is the positioning function which needs at least four navigation signals. Therefore, the coverage performance of four satellites is more important than the coverage performance of five satellites. Similarly, the coverage performance of five satellites is more important than the coverage performance of six satellites. The relative importance is shown in Table 27.4:

The weight vector can be obtained by the eigenvalue method:

$$\mathrm{w} = [0.6333,\ 0.2605,\ 0.1062]$$

In the process of the vulnerability analysis, the probability of 1 satellite failure is higher than the probability of 2 satellites failure, and the probability of 2 satellites failure is higher than the probability of 3 satellites failure, so the relative importance of 1 satellite failure, 2 satellites failure, and 3 satellites failure is shown in Table 27.5:

The weight vector can be obtained by the eigenvalue method:

$$\mathrm{w} = [0.7235,\ 0.1932,\ 0.0833]$$

27.4.2 Generate Fuzzy Matrices of COMPASS Constellation

The fuzzy matrices of COMPASS constellation can be calculated by the fuzzy membership function mentioned above.

When 1 satellite is failure, the fuzzy relation matrix can be described as follow:

Table 27.4 The relative importance of criterions

	$CL(n,4)$	$CL(n,5)$	$CL(n,6)$
$CL(n,4)$	1	3	5
$CL(n,5)$	1/3	1	3
$CL(n,6)$	1/5	1/3	1

Table 27.5 The relative importance of satellites failure

	1 satellite failure	2 satellites failure	3 satellites failure
1 satellite failure	1	5	7
2 satellites failure	1/5	1	3
3 satellites failure	1/7	1/3	1

$$R_1 = \begin{bmatrix} 0 & 0 & 0 & 0 & 1 \\ 0 & 0 & 0 & 0 & 1 \\ 0 & 0 & 0 & 0.208 & 0.792 \end{bmatrix}$$

When 2 satellites are failure, the fuzzy relation matrix can be described as follow:

$$R_2 = \begin{bmatrix} 0 & 0 & 0 & 0 & 1 \\ 0 & 0 & 0 & 0.024 & 0.976 \\ 0 & 0 & 0 & 0.368 & 0.632 \end{bmatrix}$$

When 3 satellites are failure, the fuzzy relation matrix can be described as follow:

$$R_3 = \begin{bmatrix} 0 & 0 & 0 & 0.004 & 0.996 \\ 0 & 0 & 0 & 0.076 & 0.924 \\ 0 & 0 & 0 & 0.548 & 0.452 \end{bmatrix}$$

Similarly, the fuzzy matrices of GPS constellation can also be calculated by the fuzzy membership function.

27.4.3 Fuzzy Synthesis Calculation

The weight vector $[w_{n,4}, w_{n,5}, w_{n,6}] = [0.6333, 0.2605, 0.1062]$ is applied during fuzzy synthesis calculation. According to the fuzzy synthesis steps, the results of constellation vulnerability which are caused by 1, 2, 3 satellites failure can be calculated in the first fuzzy synthesis calculation.

When 1 satellite is failure, the fuzzy synthesis result is shown as follow:

$$r_1 = [\, w_{n,4} \quad w_{n,5} \quad w_{n,6} \,] \cdot R_1 = [\, 0 \quad 0 \quad 0 \quad 0.0221 \quad 0.9779 \,]$$

When 2 satellites are failure, the fuzzy synthesis result is shown as follow:

$$r_2 = [\, w_{n,4} \quad w_{n,5} \quad w_{n,6} \,] \cdot R_2 = [\, 0 \quad 0 \quad 0 \quad 0.0453 \quad 0.9547 \,]$$

When 3 satellites are failure, the fuzzy synthesis result is shown as follow:

$$r_3 = [\, w_{n,4} \quad w_{n,5} \quad w_{n,6} \,] \cdot R_3 = [\, 0 \quad 0 \quad 0 \quad 0.0805 \quad 0.9195 \,]$$

These calculation results can be combined as the input of the fuzzy synthesis calculation in the second time. The fuzzy relationship matrix can be established as follow:

$$R = \begin{bmatrix} 0 & 0 & 0 & 0.0221 & 0.9779 \\ 0 & 0 & 0 & 0.0453 & 0.9547 \\ 0 & 0 & 0 & 0.0805 & 0.9195 \end{bmatrix}$$

The weight vector w = [0.7235, 0.1932, 0.0833] is used during the second fuzzy synthesis calculation, and the assessment result is as follow:

$$r = w \cdot R = [0 \quad 0 \quad 0 \quad 0.0314 \quad 0.9686]$$

The membership degrees of the vulnerability of COMPASS constellation in five grades are respectively 0, 0, 0, 0.0314, and 0.9686. According to the principle of maximum membership degree, the comment of the vulnerability of COMPASS constellation is "excellent".

Similarly, the membership degrees of the vulnerability of GPS constellation in five grades are respectively 0.0000, 0.0000, 0.0000, 0.0529, and 0.9471. According to the principle of maximum membership degree, the comment of the vulnerability of GPS constellation is also "excellent".

Although the comments of COMPASS constellation and GPS constellation are both "excellent", the membership degree of GPS constellation is 0.9471, and the membership degree of COMPASS constellation is 0.9686. It means that GPS constellation is slightly more vulnerable than COMPASS constellation.

27.5 Conclusions

GNSS plays an important role in the national defense and economy, the vulnerability assessment for GNSS is becoming more and more important. GNSS constellation is the core of the navigation satellite system, and the vulnerability of GNSS constellation is an important part of the vulnerability of GNSS.

A vulnerability assessment method for GNSS constellation based on AHP-FCE is suggested in this paper. The probability of more than 3 satellites failure is lower, so the vulnerability assessment model for GNSS constellation only concerns about 1 satellite failure, 2 satellites failure, and 3 satellites failure. Failed satellites in different orbital positions have different impacts on the global coverage performance of GNSS constellation, so the assessment criterions need to reflect the mean impact on the coverage performance in the case of satellites failure. Although the vulnerability assessment model for GNSS constellation only includes the situation that 1, 2 and 3 satellites are failure in this paper, it's very easy to add criterions reflecting 4 or more satellites failure into the assessment model. The assessment model mainly concerns about the impacts on the coverage performance of GNSS

constellations in the case of satellites failure, which provides a new way to evaluate the vulnerability of GNSS constellations.

Acknowledgments This work was supported by the National High Technology Research and Development Program of China (863 Program). The fund number is 2011AA120503.

References

1. Kaplan ED, Hegarty CJ (2008) Understanding GPS: principles and applications, 2nd edn. Publishing House of Electronics Industry, Beijing (In Chinese)
2. Vaidya OS, Kumar S (2006) Analytic hierarchy process: an overview of applications. Eur J Oper Res 169(1):P1–P29
3. Saaty L (1980) The analytic hierarchy process. McGraw-Hill, New York
4. Zhu M (2008) Evaluating destination competitiveness based on integrated fuzzy AHP and FCE. In: Proceedings of the seventh international conference on information and management sciences, Urumchi, China, pp 289–294
5. Haitao Yang (2007) Research on methods of constellation satellite communication system effectiveness evaluation. National University of Defense Technology, Changsha
6. China Satellite Navigation Office (2012) BeiDou navigation satellite system signal in space interface control document open service signal B1I (1.0)

Chapter 28
Research on Spare Satellites Strategy of Navigation Constellation Based on System Availability

Haisheng Li, Heng Zheng, Wei Wang, Bo Zhou and Laiping Feng

Abstract The satellite reliability and the service performance of the navigation system will both decrease gradually as the satellite on-orbit operation time increases. In order to guarantee the system always in a stable and reliable operation status, the satellites strategy is necessary. Learning from GPS experience, an improved satellite reliability model is proposed, and then the system availability model is constructed by using the Bayesian network. Finally, according to the requirement of the system availability, the rational spare satellites strategy which includes the spare mode, the spare satellite number, and the spare satellite launch plan is developed. Moreover, the simulation results can provide an important technical support for engineering decisions.

Keywords Navigation constellation · System availability · Spare satellites strategy · Satellite reliability · Bayesian network

28.1 Introduction

The satellite navigation system plays an increasingly significant role in national defence construction and economic development. Thus it is crucial to ensure the system working in stable operation [1]. The spare satellites strategy directly affects

H. Li (✉) · H. Zheng · B. Zhou
China Academy of Aerospace Standardization and Product Assurance, Beijing, China
e-mail: leehaisheng@126.com

W. Wang
Beijing Institute of Tracking and Communication Technology, Beijing, China

L. Feng
Xi'an Research Institute of Surveying and Mapping, Xi'an, China

J. Sun et al. (eds.), *China Satellite Navigation Conference (CSNC) 2013 Proceedings*, Lecture Notes in Electrical Engineering 243,
DOI: 10.1007/978-3-642-37398-5_28,

the realization of system availability, continuity and integrity. It is also the key factor to ensure the stability of the system when some satellite fails.

According to the experience of the construction and operation of GPS and GLONASS, spare satellites are necessary to ensure the system working in continuous and stable operation. The designed GPS constellation consists of 24 satellites, but since the system runs from 1993, the actual number of satellites is always more than 27, which effectively guarantees the system performance. In comparison, because of financial problems, the full constellation of GLONASS is not timely completed, resulting in system performance declining and loosing the broad application market. According to the constellation design of Galileo scheme, in order to meet the stringent requirements of system availability, continuity and integrity, each orbital plane are emplaced a spare satellite. The spare satellite usually does not transmit signal, but drifts to complete the supplement under the control of the ground system when an operating satellites fails, ensuring the design specifications requirements [2].

In view of the spare satellites strategy's important effect, it is necessary to carry out the research on spare satellites strategy to ensure the system performance. It will provide a technical support for the long-term stable operation of the satellite navigation system. A method with spare satellites of navigation constellation is presented in this paper. First, learning from the GPS experience, and considering both the random failure and the wear-out failure, the improved satellite reliability is modelled. Second, the satellite reliability changes are analyzed and compared with the exponential model throughout the whole life. Then, the system availability is modelled and analyzed by using the Bayesian network. And then, combining the satellite reliability and the contribution of different satellites, the key satellite of the constellation can be identified with the enumeration method. Finally, considering the requirement of system availability, the rational spare satellites strategy which includes the spare mode, the spare satellite number, and the spare satellite launch plan is developed. Moreover, the simulation results can provide an important technical support for spare design alternatives trade-off and engineering decisions at the system operation stage.

28.2 System Availability Modeling

28.2.1 The Satellite Reliability Model

The satellite reliability which is the input condition of the spare satellites strategy is the key factor affecting the system stable operation and reflects it's the failure probability of the satellite. The satellite reliability's small changes may lead to the expected replacement satellite changing greatly. Even though the satellite reliability is known as statistical values, uncertainty changes also affect the anticipated replacement satellite time. The satellite replacement program risk level can be

evaluated by simulating the actual life of satellite random changes, thus this requires the precise satellite reliability model.

The satellite traditional reliability exponential model can simplify the analysis, but its hypothesis which the fault rate is constant contraries to the process of satellite waste accumulation and aging. In addition, the exponential distribution can not well describe the early failure and the failure depletion. In short, the reliability exponential model can not be a good reflection of the variation of the satellite reliability.

According to the GPS experience [3], an improved satellite reliability model is presented in this paper. The model is the product of the two models random fault model and depletion fault model. The random fault model mainly considers the random failures caused by the component failure, while the depletion fault model mainly considers the impact of loss device components.

The reliability function of the random fault model is expressed as:

$$R_r(t) = e^{-(t/\alpha)^{\beta}} \tag{28.1}$$

where α is the scale parameter related to the failure rate, β is the shape parameter determining the distribution, according to the different value of β, different failure rate curve can be obtained.

The reliability function of the depletion fault model is expressed as:

$$R_w(t) = \int_t^{\infty} \frac{1}{\sqrt{2\pi}\sigma} e^{-\frac{(t-\mu)^2}{2\sigma^2}} dt \tag{28.2}$$

where μ is the mean, σ is the standard deviation, and t is the usage time of the satellite.

So, the satellite reliability function is got:

$$R(t) = R_r(t)R_w(t) \tag{28.3}$$

While the satellite traditional reliability exponential model is:

$$R(t) = e^{-\lambda t} \tag{28.4}$$

where λ is the failure rate which is constant in the satellite's lifetime.

Figure 28.1 shows the comparison of the satellite improved reliability model and the satellite exponential model. It can be seen that the satellite improved reliability model takes into account the process of satellite waste accumulation and aging. The reliability is relatively stable during the satellite lifetime but with a sharp decline beyond the design life, which is more in line with the actual state of the satellite and better describes the satellite reliability.

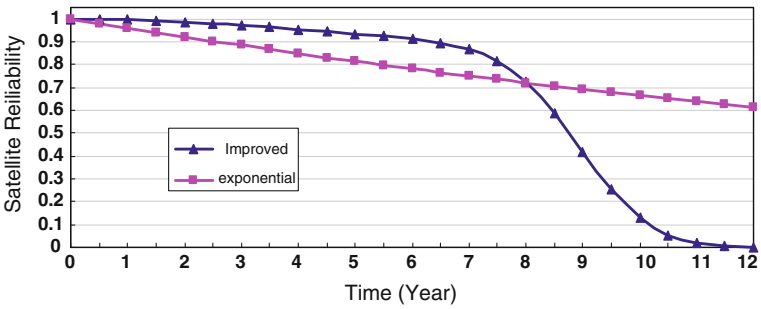

Fig. 28.1 Curve: comparison of two reliability model of satellite

28.2.2 The Constellation State Probability

There are $(N+1)$ kinds of possible states in the constellation of N satellites. S_0 is the state with no failure satellite, S_1 is the state with one failure satellite, and so on. Then the occurrence possibility of S_k is a probability value P_k. P_k is defined as the constellation state probability of k failure satellite. It determines the reliability of each satellite and all combinations, and there must be $\sum P_k = 1$. In order to describe the constellation state probability's dynamic changes over satellite reliability and adding the time information, it can be expressed as $P_k(t)$.

As the reliability of each satellite is different, the constellation state probability with different failure satellite combination is also different. There is

$$\begin{cases} P_k(t) = \sum\limits_{n=1}^{C_N^k} P_{k,n}(t) \\ P_{k,n}(t) = \left(\prod\limits_{m=1}^{N-k} R_{n,m}(t) \right) \left(\prod\limits_{i=N-k+1}^{N} (1 - R_{n,i}(t)) \right) \end{cases} \tag{28.5}$$

where C_N^k is the combination number of k satellites in N, $P_{k,n}(t)$ is the constellation state probability of n case with k failure satellites, $R_{n,m}(t)$ is the reliability of each satellite of the $(N-k)$ satellites, and $(1 - R_{n,i}(t))$ is the corresponding failure probability.

28.2.3 The Constellation Performance Simulation Model

The constellations performance which reflects the pros and cons of the constellation configuration changes over time and space. In the process of the constellation design, the concerned indicators must be obtained by statistical methods, and optimized as the design goals or boundary conditions [4]. In the field of satellite navigation, the space signal accuracy is usually assumed to be known, so

it is generally designed basing on dilution of precision (referred to as DOP) value to measure the constellation performance.

According to GPS experience, the constellation value (referred to as CV) is chosen as the objective function to evaluate the constellation performance. CV which reflects the constellation geometry characteristics and continuous visibility is an important manifestation of the constellation performance.

CV is calculated as:

$$CV = \frac{\sum_{t=t_0}^{t_0+\Delta T} \sum_{i=1}^{L} bool(DOP_{t,i} \leq DOP_{\max}) \times area_i}{\Delta T \times Area} \times 100\,\% \tag{28.6}$$

where ΔT is the total simulation time, t_0 is the initial time, L is the total number of grid points, $bool(x)$ is Boolean function, when x is true, $bool(x) = 1$, when x is false, $bool(x) = 0, DOP_{t,i}$ is the DOP value of the i grid point at time t, $Area$ is total service area, $area_i$ is the area of the i grid point.

28.2.4 The System Availability Model

The system availability is affected by two factors: constellation state and constellation configuration. In the constellation state aspect, due to the satellite reliability changes over time, the constellation state probability is also in dynamic change. In the constellation performance aspect, the constellation performance will be affected by the constellation configuration with failure satellite. Therefore, the system availability will vary with the changes of system operation time.

For generality, assuming the constellation as non-uniform configuration, then each state will have a different impact on the system performance. And the system can be calculated by the constellation state probability and the constellation value. There is:

$$A(t) = \sum_{k=0}^{N} \sum_{n=1}^{C_N^k} P_{k,n}(t) \cdot \alpha_{k,n}(t) \tag{28.7}$$

where N is the total number of satellites, C_N^k is combination number of k failure satellites of N satellites, $P_{k,n}(t)$ is the constellation state probability with k failure satellites in n combination case, $\alpha_{k,n}(t)$ is the constellation value.

The Bayesian network model which is constituted by the network topology and the mathematical model (conditional probability tables, referred to as CPT) have the ability to express the complex relationship between the multi-state nodes (including the uncertainty relation). It is convenient to use Bayesian network for the system modelling, and to describe the influence relationship among satellites. And CPT is usually used to characterize it.

According to the constellation state probability model, it is narrowed to each satellite. That is to consider each satellite as a 'constellation'. Then the constellation state probability is transformed to the satellite reliability. CPT represents the constellation values of different failure satellites, which can be got by the constellation performance simulation.

Figure 28.2 shows the system availability model by using the Bayesian network.

It can be seen from Fig. 28.2 that in the system availability model, each satellite is parent node, and the reliability of each satellite is the marginal probability. Every node points to the "system availability" child node, and CPT is the constellation value of different failure satellites.

Assuming that the satellite reliability is $P(X_k)$, $k = 1, 2, \ldots, N$, which is also the marginal probability of the k node. The constellation value of different failure satellites can be got by the constellation performance simulation which is the conditional probability $P(X_{N+1}|parent(X_{N+1}))$. And $parent(X_{N+1})$ is the parent node set of "system availability" X_{N+1}. Using the Bayesian network chain rule, the joint probability distribution of all nodes is calculated as:

$$P(X) = \prod_{k=1}^{N+1} P(X_k|parent(X_k)) \tag{28.8}$$

The Bayesian network inference mainly adopts the expression of the joint probability distribution. Given the observation (or evidence) of a set of variables E, that is the process of calculating the posterior probability distribution $(P(Q|E))$ of the set of variables Q. Researchers have made a lot of efficient algorithms for reasoning, including the exact algorithms and approximation algorithms [5, 6]. Therefore, it is possible to calculate the 'system availability' under the conditions of knowing the reliability of each satellite.

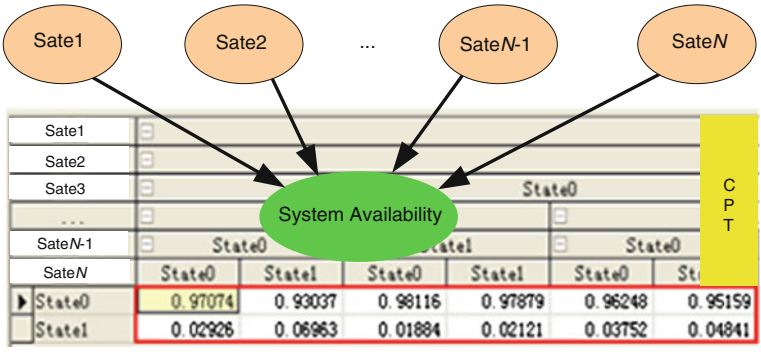

Fig. 28.2 System availability model based on Bayesian network

28.3 Satellites Spares Strategy

The satellite reliability is a time-changing function, whose changes at different time may cause the changes of system availability. Based on the satellite reliability model, the system availability can be got by using the Bayesian network. Combined with the user demand, it can be judged to determine what time and which satellite to be supplemented. According to the value of system availability of user demand, it should be considered to launch spare satellites when the system doesn't meet the index requirements.

For uneven constellation, assuming that it consists of three types of orbits (the GEO, IGSO and MEO satellites). Considering the different launching time of each satellite, the contribution of the three types of satellites to the system availability is also different. So it should not simply replace the first launching satellite, but give a comprehensive consideration of the satellite launching time and the contribution to the system availability. In order to examine the contribution of a satellite to system availability at different time, the brute-force method is used to select the satellite needed spares to enhance the maximum system availability.

28.4 Simulation Examples

Without loss of generality, the non-uniform constellation is chosen for simulation. Assuming that there are 12 satellites of different orbits (e.g. S1–S12). Our country is defined as the service area. Position dilution of precision (referred to as PDOP) is considered as the criterion of the constellation simulation model, here PDOP threshold is supposed at 6. The satellite design life is set as 10 years, and the end-of-life reliability is 0.6. The successful completion of constellation networking is within 2 years, and a satellite is launched in accordance with the serial satellite number every 6 months. Due to the satellite design life of 10 years, the launching satellite time of about 2 years, giving a comprehensive consideration of satellite life and launching satellite time, the spares satellite strategy will provide measures to maintain the system working in stable operation for 8 years. Then the constellation will be in the replacement stage, and the satellite reliability will be gradually restored and improved, so it no longer needs spares.

For fully and accurately reflecting the changes of each satellite reliability and system availability, the time of last launching satellite (that is the system networking success) is considered as the beginning time of computational analysis. According to the improved satellite reliability model, the reliability of every satellite at the time of system networking success can be got. Then the satellite reliability results will be listed after every 6 months, as shown in Table 28.1. The changes of satellite reliability over time are as shown in Fig. 28.3.

It can be seen from Fig. 28.3 that the earlier satellite is launched the lower reliability it is at the beginning time of system operation. The reliability is

Table 28.1 Satellite reliability after system operation

Running time (year)	Satellite reliability											
	S1	S2	S3	S4	S5	S6	S7	S8	S9	S10	S11	S12
0	0.976	0.979	0.982	0.985	0.987	0.990	0.992	0.994	0.996	0.998	0.999	1.000
0.5	0.965	0.969	0.972	0.976	0.979	0.982	0.985	0.987	0.990	0.992	0.994	0.996
1.0	0.954	0.958	0.962	0.965	0.969	0.972	0.976	0.979	0.982	0.985	0.987	0.990
1.5	0.941	0.945	0.950	0.954	0.958	0.962	0.965	0.969	0.972	0.976	0.979	0.982
2.0	0.928	0.932	0.937	0.941	0.945	0.950	0.954	0.958	0.962	0.965	0.969	0.972
2.5	0.913	0.918	0.923	0.928	0.932	0.937	0.941	0.945	0.950	0.954	0.958	0.962
3.0	0.898	0.903	0.908	0.913	0.918	0.923	0.928	0.932	0.937	0.941	0.945	0.950
3.5	0.882	0.887	0.893	0.898	0.903	0.908	0.913	0.918	0.923	0.928	0.932	0.937
4.0	0.865	0.871	0.876	0.882	0.887	0.893	0.898	0.903	0.908	0.913	0.918	0.923
4.5	0.848	0.854	0.860	0.865	0.871	0.876	0.882	0.887	0.893	0.898	0.903	0.908
5.0	0.831	0.837	0.843	0.848	0.854	0.860	0.865	0.871	0.876	0.882	0.887	0.893
5.5	0.813	0.819	0.825	0.831	0.837	0.843	0.848	0.854	0.860	0.865	0.871	0.876
6.0	0.794	0.800	0.807	0.813	0.819	0.825	0.831	0.837	0.843	0.848	0.854	0.860
6.5	0.772	0.780	0.787	0.794	0.800	0.807	0.813	0.819	0.825	0.831	0.837	0.843
7.0	0.742	0.753	0.763	0.772	0.780	0.787	0.794	0.800	0.807	0.813	0.819	0.825
7.5	0.692	0.712	0.728	0.742	0.753	0.763	0.772	0.780	0.787	0.794	0.800	0.807
8.0	0.611	0.642	0.669	0.692	0.712	0.728	0.742	0.753	0.763	0.772	0.780	0.787

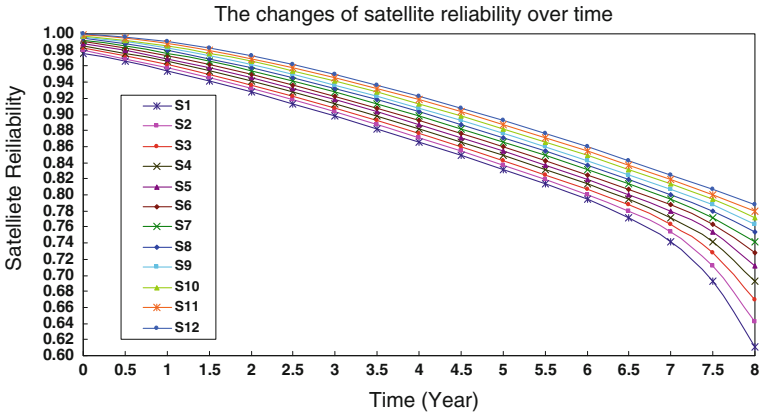

Fig. 28.3 Curve: changes of satellite reliability after system operation

relatively stable during the satellite lifetime but with a sharp decline beyond the design life.

According to the constellation configuration and the constellation performance simulation results, the application of GeNIe software developed by the Decision Systems Laboratory of the University of Pittsburgh is used for the system availability modelling, as shown in Fig. 28.4.

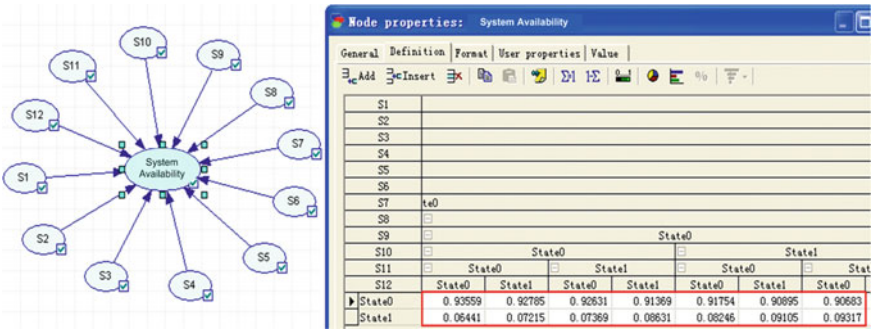

Fig. 28.4 System availability model of a navigation constellation

Table 28.2 Analysis results of system availability

Running time (year)	System availability	Running time (year)	System availability	Running time (year)	System availability
0	0.9936	3.0	0.9518	6.0	0.8437
0.5	0.9894	3.5	0.94	6.5	0.8134
1.0	0.9842	4.0	0.9261	7.0	0.7745
1.5	0.978	4.5	0.91	7.5	0.7169
2.0	0.9706	5.0	0.8911	8.0	0.6201
2.5	0.9619	5.5	0.8692	—	

Combined with the reliability of every satellite, the system availability analysis results can be calculated, as shown in Table 28.2.

And it is also described in curve, as shown in Fig. 28.5.

Assuming the designed system availability is set at 0.9, and then it can be seen from Fig. 28.5 that the system availability will drop to 0.8911 after 5 years which will no longer meet the target requirements. Therefore, in order to ensure the system's normal operation, to meet the user requirements, spare satellites should be launched to improve the satellite reliability, ensuring the system availability remaining above 0.9.

In order to examine the contribution of a satellite to system availability at different time, the brute-force method is used to select the satellite needed spares to enhance the maximum system availability. Results are shown in Table 28.3 and described in Fig. 28.6.

As can be seen from Table 28.3 and Fig. 28.6, after 5 years of system operation, it will get the maximum system availability to replace S1. After 6 years of system operation, it will get the maximum system availability to replace S4. After six point 5 years of system operation, it will get the maximum system availability to replace S3. After seven point 5 years of system operation, it will get the maximum system availability to replace S6. Therefore, it can be got the replaced satellite sequence: S1, S4, S3 and S6.

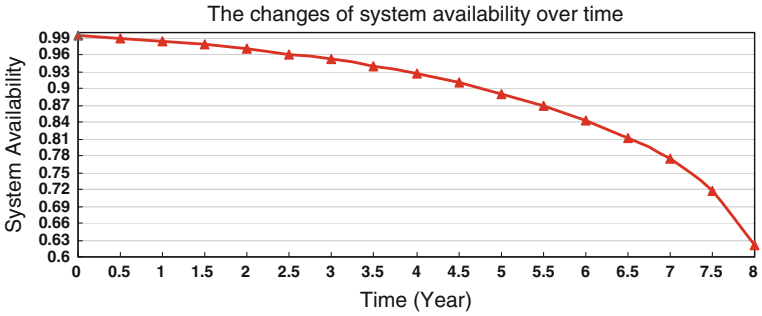

Fig. 28.5 Curve: changes of system availability after system operation

Table 28.3 Analysis results of system availability after substituting different satellites

Running time (year)	System availability								
	S1	S2	S3	S4	S5	S6	S7	S8	S9–S12
5.0	0.918	0.909	0.911	0.91	0.908	0.91	0.906	0.908	0.896
6.0	0.883	0.901	0.908	0.91	0.905	0.908	0.904	0.906	0.891
6.5	0.893	0.915	0.923	0.893	0.912	0.922	0.917	0.919	0.902
7.5	0.887	0.914	0.885	0.886	0.908	0.924	0.918	0.921	0.898

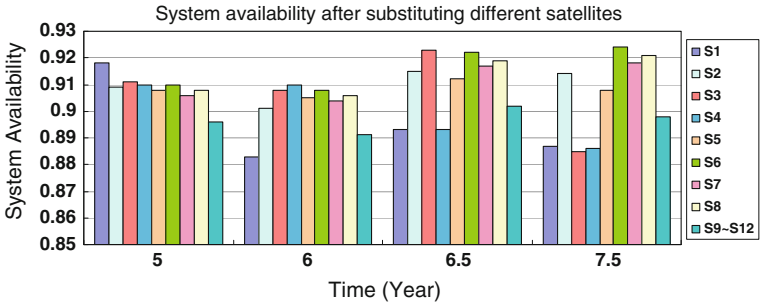

Fig. 28.6 Chart: analysis results of system availability after substituting different satellites

According to the spares satellite program, the system availability analysis results are as shown in Table 28.4 and described in Fig. 28.7.

As can be seen from Table 28.4 and Fig. 28.7, according to the spare program, the system availability is maintained at 0.8985 after 5 years of system operation, which could meet the requirements.

The above example shows that under the given reliability of every satellite, in order to meet the user requirements, it should be considered to replace the first launching satellite with S1 after 5 years of system operation. Then the second launching satellite should be replaced with S4 after 6 years of system operation.

Table 28.4 Analysis results of system availability based on spare program

Running time (year)	System availability
0	0.9936
0.5	0.9894
1.0	0.9842
1.5	0.978
2.0	0.9706
2.5	0.9619
3.0	0.9518
3.5	0.94
4.0	0.9261
4.5	0.91
5.0	0.918 (substituting S1)
5.5	0.9016
6.0	0.9102 (substituting S4)
6.5	0.9226 (substituting S3)
7.0	0.907
7.5	0.9243 (substituting S6)
8.0	0.8985

Note 0.918 represents system availability after substituting S1

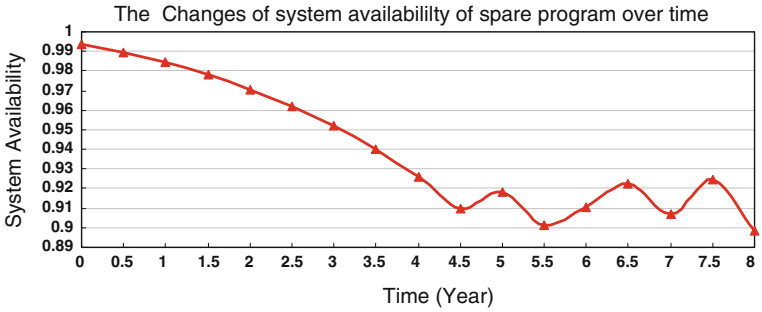

Fig. 28.7 Curve: results of system availability of spare program

After six point 5 years of system operation, the third launching satellite should be replaced with S3. Finally, the fourth launching satellite should be replaced with S6 after seven point 5 years of system operation. The spare program can ensure the system availability to meet the requirements in 8 years. According to the satellite design life, most of the satellites will go to the end of life after 8 years of system operation, and then it will need the constellation replacement.

28.5 Conclusions

The spare satellites strategy directly affects the realization of system availability, continuity and integrity, and is also the key factor to ensure the system working in stable operation when some satellite fails. In view of the important role of the spare satellites strategy, a rational spare program is proposed to ensure the system reliability to meet users' requirements in this paper.

First, learning from the GPS experience, and considering both the random failure and the wear-out failure, the improved satellite reliability is modelled. Second, the satellite reliability changes are analyzed and compared with the exponential model throughout the whole life. Then, the system availability is modelled and analyzed by using the Bayesian network. And then, combining the satellite reliability and the contribution of different satellites, the key satellite of the constellation can be identified with the enumeration method. And the spare satellite launch plan is developed. Finally, an example of a navigation constellation is given, which effectively verifies the system availability-based spare satellites method. And the simulation results can provide an important technical support for spare design alternatives trade-off and engineering decisions.

References

1. Tan S (2010) Satellite navigation and positioning engineering, 2nd edn. National Defense Industry Press, Beijing
2. Liu G, Shen H (2005) Satellite spare strategy with confidence in the constellation design. J Acad Equip Command Technol 16(1):67–70
3. James M (1998) Revised block II/IIA lifetime predictions and the impact on block IIR/IIF replenishment planning. In: Proceedings of ION national technical meeting, San Diego
4. Zhang Y, Fan L, Zhang Y (2008) Satellite constellation theory and design. Science Press, Beijing
5. Jesen FV (2001) Bayesian networks and decision graphs. Springer, New York
6. He M, Qiu H, Jiang H (2009) Research on system reliability evaluation method based on Bayesian network. J Syst Simul 21(16):4934–4937

Chapter 29
Space Coverage Analysis of BeiDou Navigation Satellite System Regional Constellation

Zhenhai Li, Wenhai Jiao, Jin Fan, Changjiang Geng and Yu Bai

Abstract Satellites constellation space coverage analysis plays an important reference role in GNSS spatial positioning, navigation and timing, guides the designing of future constellation. This paper used regional constellation of BeiDou navigation satellite system composed of 5GEO, 5IGSO and 4MEO satellites, based on geometric relationship between satellite, earth and focused point, computed worldwide spatial visible satellites number and PDOP, analyzed the statistical results, and showed the spatio-temporal distribution. Computational results showed that: BeiDou regional navigation satellite system could provide effective PNT services for Asia–Pacific region and spatial south and north Polar Regions under 1,000 km, satisfied the designed requirements, but not the space above 1,000 km because of the promptly reducing of spatial coverage range, increasing of effective continual time segments, decreasing of maximum continual time and total time in all segments.

Keywords BeiDou · Space coverage · PNT services · Visible satellites number · PDOP

29.1 Introduction

BeiDou is a global navigation satellite system which is self-dependent developed and operated by China, and it is one of four main GNSS in the world. BeiDou will provide positioning, navigation and timing (PNT) services for global users by

Z. Li (✉) · W. Jiao · J. Fan · C. Geng · Y. Bai
Test and Assessment Research Center, China Satellite Navigation Office,
Beijing 100094, China
e-mail: lizhenhai666@163.com

W. Jiao
Beijing Institute of Tracking and Telecommunication Technology,
Beijing 100094, China

J. Sun et al. (eds.), *China Satellite Navigation Conference (CSNC) 2013 Proceedings*, Lecture Notes in Electrical Engineering 243,
DOI: 10.1007/978-3-642-37398-5_29,

2020. According to the development plan [1, 2], the working satellites of BeiDou include 5GEO (Geosynchronous orbit) satellites, 5IGSO (Inclined Geosynchronous Orbits) satellites and 4MEO (Medium Earth Orbit) satellites in December 2012, and will completely provide stable and reliable PNT services for the Asia–Pacific region by early 2013.

Space coverage analysis is one of the important characteristics for GNSS constellation performance evaluation, which plays an important role in the world-wide terrestrial and spatial PNT services and guides the future constellation design of BeiDou system. Jiejuan et al. [3] established the geometrical models between GPS satellites and LEO, MEO and HEO satellite respectively, and simulated the coverage performance of 32 GPS satellites constellation. Zhang et al. [4] analyzed the constellation's observation region, summarized the main influential factors on space coverage performance, illuminated the judgment approaches, lastly analyzed the coverage performance in spatio-temporal domain based on theoretical constellation. Besides, GPS space service volume and spatial navigation experiments [5–7] were deeply researched in foreign countries.

With the development of spatial technologies, spatial navigation is increasingly concerned in the satellite navigation fields at present. The GPS navigation capabilities for LEO even HEO are focused by more and more researchers, and achieved engineering application gradually. Because BeiDou was developed and started to provide Initial Operational Capability (IOC) lately, its spatial navigation capabilities are less concerned. This paper mainly discusses the world-wide spatial coverage performance based on the regional constellation of BeiDou navigation satellite system, firstly develops several computational models of spatial visible satellites number and DOPs, then computes these values in world-wide spatial domain, and analyzes the spatial distribution and characters of these factors lastly.

29.2 Basic Principles

Satellite visibility and DOPs are two key factors in GNSS service performance evaluation. The former one denotes the number of satellites observed by a receiver, represents the PNT services capabilities that GNSS can provide for special spatio-temporal users, and the later one denotes the scale coefficient between pseudo-range errors and user positioning accuracy, that is varied with the spatial geometrical distribution between satellites and receiver [8]. Both visible satellites number and DOPs can be expressed as functions of time and space, that is to say, two factors will vary with the changing of spatio-temporal domain.

29.2.1 Spatial Satellites Visibility

In order to conveniently analyze the visibility of satellite S on a spatial focused point F, the space above the earth surface is divided into three independent research spaces, including the LEO space (Space I) from earth surface to h_1 which is the altitude of a tangency point of satellite's conical signal to earth's concentric circles, the MEO space (Space II) from h_1 to h_0 which is the orbit altitude of navigation satellite S, and the HEO space (Space III) beyond h_0. These three areas are shown from Figs. 29.1, 29.2 and 29.3, O is the earth geocentre, θ denotes the angle between SO which is a line from satellite to earth center and tangency line which is satellite to the earth surface, φ denotes half beam width angle of satellite's transmitting signal, α and β are two internal angles corresponding to two vertexes F and S in ΔSFO, h_0 and h_1 denotes the boundary altitude of three independent spaces. Assuming the coordinates of the spatial focused point F and satellite S are (x_F, y_F, z_F) and (x_S, y_S, z_S) under ECEF respectively, then the distances R_S between satellite and earth geocentre, R_F between focused point F and earth geocentre, R_{SF} between satellite S and focused point F can be expressed as

$$R_S = \left(x_S^2 + y_S^2 + z_S^2\right)^{1/2}$$

$$R_F = \left(x_F^2 + y_F^2 + z_F^2\right)^{1/2}$$

$$R_{SF} = \left[(x_S - x_F)^2 + (y_S - y_F)^2 + (z_S - z_F)^2\right]^{1/2} \tag{29.1}$$

Internal angles α and β can be described as

$$\alpha = \arccos\left(\frac{R_{SF}^2 + R_F^2 - R_S^2}{2R_{SF}R_F}\right)$$

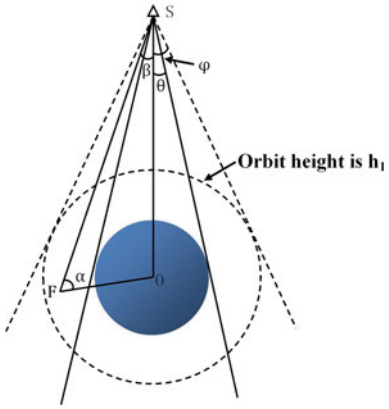

Fig. 29.1 Object point F in space I

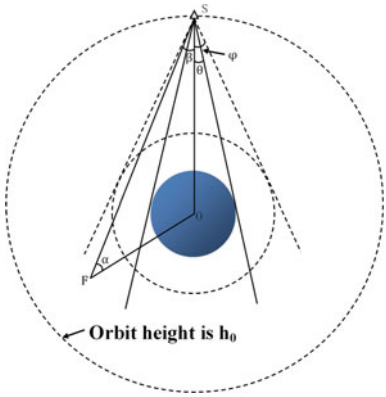

Fig. 29.2 Object point F in space II

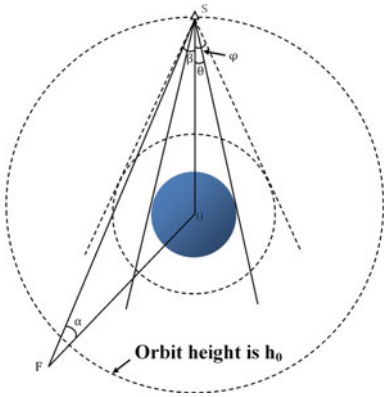

Fig. 29.3 Object point F in space III

$$\beta = \arcsin\left(\frac{R_F}{R_S}\sin\alpha\right) \tag{29.2}$$

Satellite S's visibility on spatial focused point F can be derived from α and β, the visibility on the focused point F in Space I ($0 \le h < h_1$, Fig. 29.1) is defined as

$$\text{Vis} = \begin{cases} \text{True}, & \alpha \le 90^\circ \text{ and } \theta \le \beta \le \varphi \\ \text{True}, & \alpha > 90^\circ \textit{ and } \theta \le \beta < \varphi \\ \text{True}, & \alpha > 90^\circ \textit{ and } 0^\circ \le \beta < \theta \\ \text{False}, & \alpha \le 90^\circ \text{ and } 0^\circ \le \beta < \theta \end{cases} \tag{29.3}$$

The visibility on the focused point F in Space II ($h_1 \le h < h_0$, Fig. 29.2) is

$$\text{Vis} = \begin{cases} \text{False}, & \alpha \le 90^\circ \text{ and } \beta > \varphi \\ \text{True}, & \alpha \le 90^\circ \text{ and } \theta \le \beta < \varphi \\ \text{False}, & \alpha \le 90^\circ \text{ and } 0^\circ \le \beta < \theta \\ \text{False}, & \alpha > 90^\circ \textit{ and } \beta \ge \varphi \\ \text{True}, & \alpha > 90^\circ \textit{ and } \theta \le \beta < \varphi \\ \text{True}, & \alpha > 90^\circ \textit{ and } 0^\circ \le \beta < \theta \end{cases} \tag{29.4}$$

The visibility on the focused point F in Space III ($h_0 \le h$, Fig. 29.3) is

$$\text{Vis} = \begin{cases} \text{False}, & \alpha < 90^\circ \textit{ and } \beta \ge \varphi \\ \text{True}, & \alpha < 90^\circ \textit{ and } \theta \le \beta < \varphi \\ \text{False}, & \alpha < 90^\circ \textit{ and } 0^\circ \le \beta < \theta \end{cases} \tag{29.5}$$

Without consideration of spatial point's masking angle, satellite S's visibility on spatial focused point F can be concluded through formula (29.3)–(29.5), then the number of visible satellites of constellation can be calculated.

29.2.2 DOP Computation

Dilution of precision (DOP) is a term used in GNSS to specify the additional multiplicative effect of GNSS satellite geometry on GNSS precision. GDOP, HDOP, VDOP, PDOP and TDOP are Geometric, Horizontal, Vertical, Positional, and Time dilution of precision respectively, and can be computed by observation equations coefficient matrix H and coordinate system translation matrix T.

The coefficient matrix H of pseudo-range observation equations in GNSS absolute positioning can be described as

$$\mathrm{H} = \begin{bmatrix} \frac{X_1^s - X_0}{\rho_1} & \frac{Y_1^s - Y_0}{\rho_1} & \frac{Z_1^s - Z_0}{\rho_1} & -1 \\ \frac{X_2^s - X_0}{\rho_2} & \frac{Y_2^s - Y_0}{\rho_2} & \frac{Z_2^s - Z_0}{\rho_2} & -1 \\ \vdots & \vdots & \vdots & \vdots \\ \frac{X_n^s - X_0}{\rho_n} & \frac{Y_n^s - Y_0}{\rho_n} & \frac{Z_n^s - Z_0}{\rho_n} & -1 \end{bmatrix} \tag{29.6}$$

where $\left(X_n^s, Y_n^s, Z_n^s\right)$ is the nth satellite's position, (X_0, Y_0, Z_0) is the receiver's spatial position, and ρ_n is the observed pseudo-range between the satellite and the receiver.

The coordinate system translation matrix T from ECEF to ENU is

$$\mathrm{T} = \begin{bmatrix} -\sin\lambda & \cos\lambda & 0 \\ -\sin \mathrm{L} \cos\lambda & -\sin \mathrm{L} \sin\lambda & \cos \mathrm{L} \\ \cos \mathrm{L} \cos\lambda & \cos \mathrm{L} \sin\lambda & \sin \mathrm{L} \end{bmatrix} \tag{29.7}$$

where L and λ is receiver's geodetic latitude and longitude respectively.

Two transitional matrix A and B are introduced as

$$A = (H'H)^{-1} \tag{29.8}$$

$$B = TA_{1:3,1:3}T' \tag{29.9}$$

where $A_{1:3,1:3}$ is improved 3 × 3 matrix subtracted last row and column by A, then

$$GDOP = \sqrt{A_{11} + A_{22} + A_{33} + A_{44}} \tag{29.10}$$

$$PDOP = \sqrt{A_{11} + A_{22} + A_{33}} \tag{29.11}$$

$$TDOP = \sqrt{A_{44}} \tag{29.12}$$

$$HDOP = \sqrt{B_{11} + B_{22}} \tag{29.13}$$

$$VDOP = \sqrt{B_{33}} \tag{29.14}$$

29.3 Computational Results and Analysis

This paper employed BeiDou broadcast ephemeris (5GEO+5IGSO+4MEO) to compute spatial number of visible satellites and DOPs from UTC 2012-06-28 00:00:00 to UTC 2012-07-05 00:00:00. Temporal sampling was 5 min and spatial sampling was 5° × 2.5° × 100 km (longitude, latitude and elevation intervals). The half-beam width angle was ±10° for GEO and IGSO satellites and ±15° for MEO satellites. It is noticed that the masking angle was not considered in these computations.

29.3.1 Spatial Distribution at a Certain Time

The spatial distribution for number of visible satellites and PDOP at UTC 2012-06-28 00:00:00 are shown in Figs. 29.4 and 29.5 respectively: the effective coverage areas of BeiDou regional constellation are eastern hemisphere and south and north Polar Regions, and the spatial altitude is under 1,000 km above the earth surface, these areas can meet the minimum requirements of PNT services because the number of visible satellites is more than 4 and PDOP is less than 8. The space beyond 1,000 km may not meet the minimum requirements because effective coverage areas for eastern hemisphere are decreasing, and number of visible satellites in some area for western hemisphere is less than 3. For the computation of PDOP is closely related to the number of visible satellites, the spatial distribution for these two factors are similar.

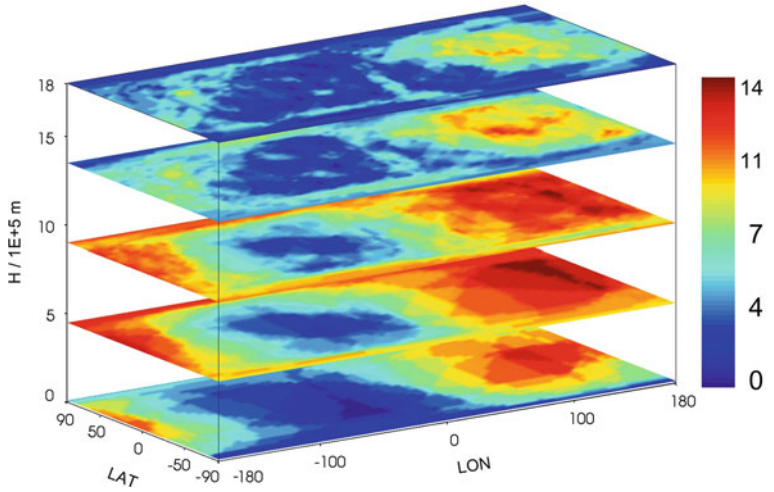

Fig. 29.4 Spatial distribution of visible satellites number at a certain time

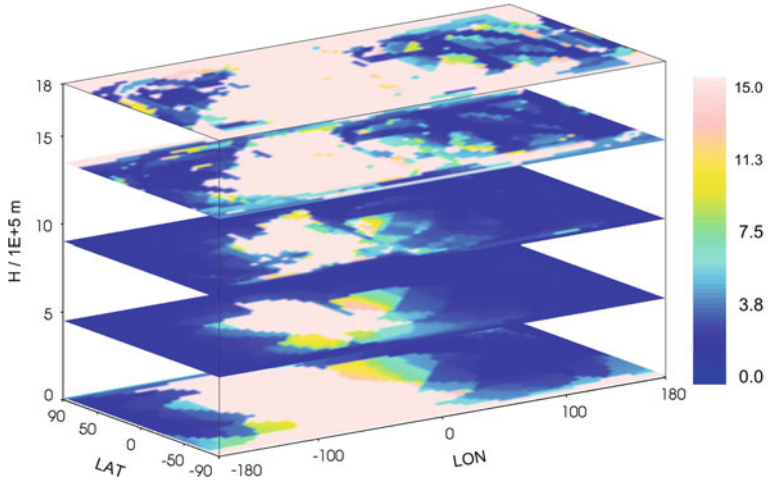

Fig. 29.5 Spatial distribution of PDOP at a certain time (High light areas were not covered by satellites)

29.3.2 Temporal Distribution of Statistical Results

To analyze the time-varying character of spatial coverage for BeiDou regional constellation, the number of visible satellites, worst PDOP, mean number of visible satellites, spatial effective continual time in total one week from UTC 2012-06-28 are computed respectively, and the results are shown from Figs. 29.6, 29.7, 29.8 and 29.9. Then the effective continual time segments ($N \geq 4$ and $PDOP \leq 7$)

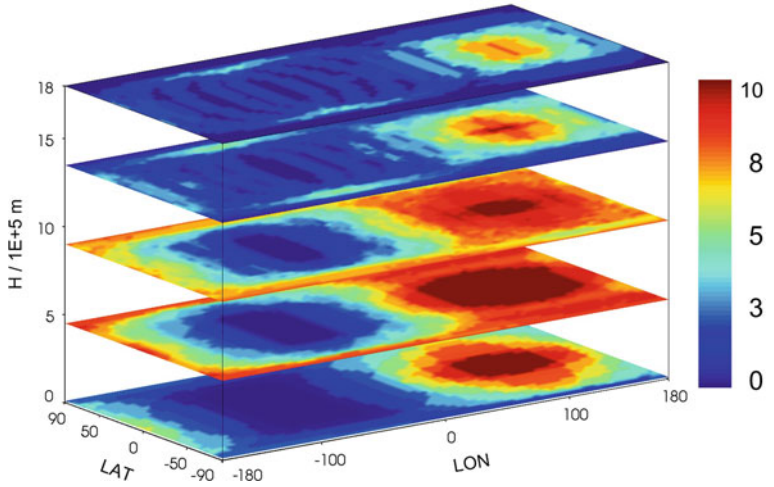

Fig. 29.6 Distribution of least visible satellites number

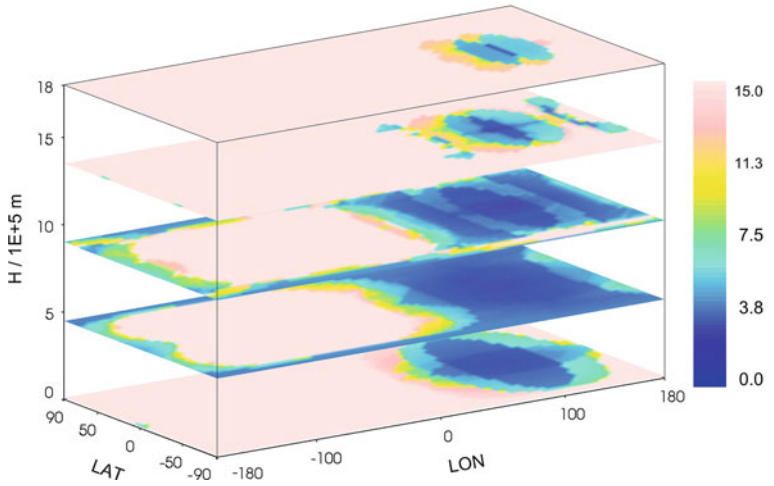

Fig. 29.7 Distribution of worst PDOP (High light areas were not covered by satellites)

are computed and analyzed at 60 spatial points which are evenly distributed. The spatial points' distribution is shown in Fig. 29.10, and the statistical results are listed in Table 29.1.

The least number of visible satellites and the worst PDOP reflects the minimum effective PNT services performance that constellation can supply to special spatio-temporal domain. As showed in Figs. 29.6 and 29.7, the space that BeiDou regional constellation can continually supply effective PNT services in one week include: eastern hemisphere and south and north Polar Regions under 1,000 km

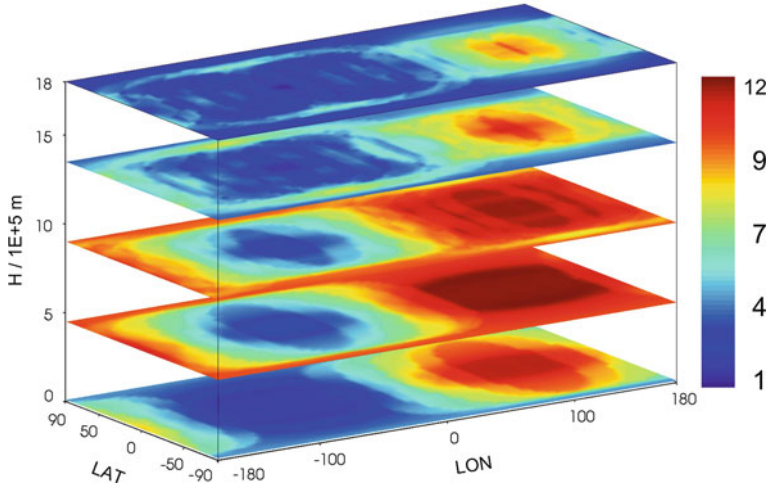

Fig. 29.8 Distribution of mean number of visible satellites

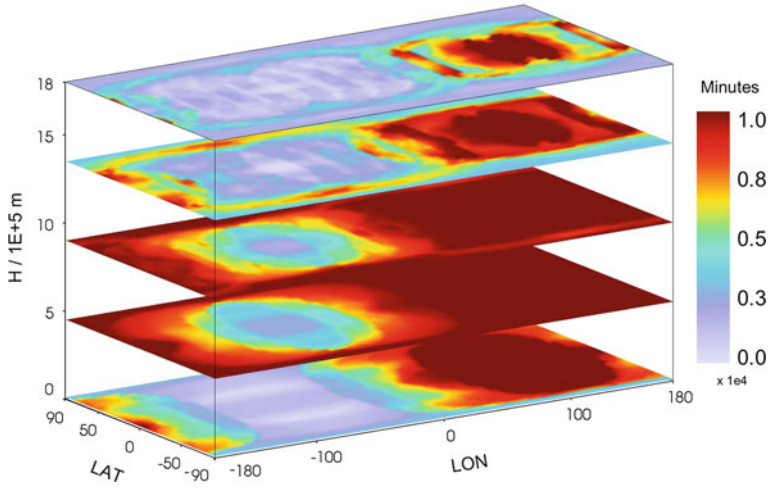

Fig. 29.9 Statistics of spatial continual time (N $\geq$ 4, PDOP $\leq$ 7)

above the earth surface. The space from 500 km to 1,000 km reach the most effective coverage, and the coverage will reduce rapidly beyond 1,000 km.

The mean number of visible satellites reflects the general distribution during certain time span, and the computed results can only for reference. As showed in Fig. 29.8, BeiDou regional constellation could provide effective PNT services for Asia–Pacific region on the ground and spatial south and north Polar Regions under 1,000 km above the earth surface.

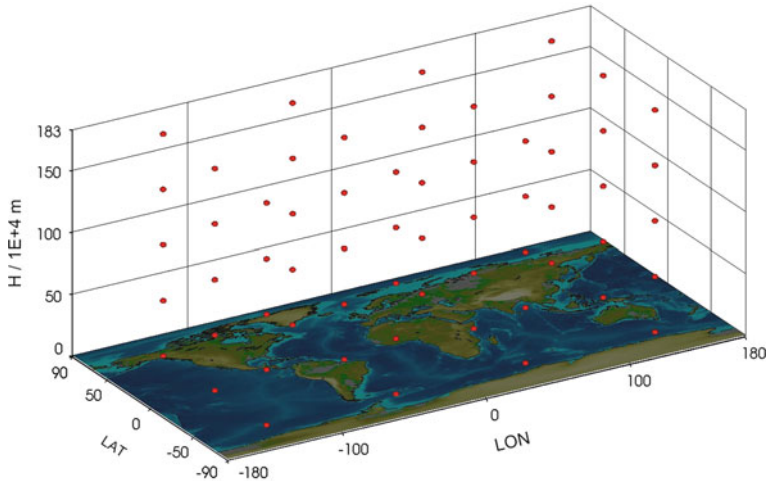

Fig. 29.10 Spatial points distribution employed for statistical results (N $\geq$ 4, PDOP $\leq$ 7)

The spatial continual time reflects the continual capability that constellation can provide effective PNT services to the spatial focused point. Figure 29.9 shows that: in the most regions of eastern hemisphere and south and north polar under 1,000 km, the continual time is no less than 1,000 min (about 6.9 days), and the regions above 1,000 km which can meet the above performance will decrease rapidly.

The statistical results in Table 29.1 show that: (1) All specifications in continual time segments statistics are symmetry in North–South direction, and this character has no correlation with elevation. (2) In the space under 1,000 km, segments in the western hemisphere are much more than the eastern hemisphere. In the spatial domain above 1,000 km, the segments in the eastern hemisphere increase rapidly with the increment of altitude, and even exceed the western hemisphere in some area. So the spaces above 1,000 km are not suitable for spatial continual navigation. (3) "Maximum continual time" performs the best in space from 500 km to 1,000 km and will decrease rapidly above 1,000 km. (4) The results of "Sum of continual time" are consistent with Fig. 29.9.

From the analysis of the above computed results of visible satellites number, PDOP, spatial distribution at a certain time, and temporal distribution, some conclusions can be summarized as follows: BeiDou regional constellation could provide effective PNT services for Asia–Pacific region mainly, for the restriction of smaller half-beam width signal to GEO and IGSO and the quantity of MEO, the spatial scope limitation is from the earth surface to an altitude of 1,000 km above the earth surface. For the higher altitude (36,000 km) of GEO and IGSO, the space from 500 km to 1,000 km above the earth surface in south and north Polar Regions

Table 29.1 Statistical results of continual time segments ($N \geq 4$, $PDOP \leq 7$, minutes)

Height (km)	Longitude	Latitude	Number of segments	Maximum continual time	Minimum continual time	Sum of continual time	Per centum (%)
10	−135	−60	38	575	0	4,650	46
	−45	−60	26	140	0	1,200	12
	45	−60	28	1,005	0	8,145	81
	135	−60	1	10,075	10,075	10,075	100
	−135	0	13	715	0	4,015	40
	−45	0	12	210	25	1,400	14
	45	0	7	2,080	5	9,675	96
	135	0	1	10,075	10,075	10,075	100
	−135	60	40	400	0	4,585	46
	−45	60	26	140	0	1,180	12
	45	60	29	1,000	0	8,105	80
	135	60	1	10,075	10,075	10,075	100
460	−135	−60	13	1,905	5	8,775	87
	−45	−60	32	895	0	6,480	64
	45	−60	1	10,075	10,075	10,075	100
	135	−60	1	10,075	10,075	10,075	100
	−135	0	13	1,265	30	6,930	69
	−45	0	14	325	65	2,470	25
	45	0	1	10,075	10,075	10,075	100
	135	0	1	10,075	10,075	10,075	100
	−135	60	14	1,905	5	8,785	87
	−45	60	34	895	0	6,450	64
	45	60	1	10,075	10,075	10,075	100
	135	60	1	10,075	10,075	10,075	100
910	−135	−60	35	1,340	0	8,160	81
	−45	−60	34	1,295	0	7,700	76
	45	−60	1	10,075	10,075	10,075	100
	135	−60	1	10,075	10,075	10,075	100
	−135	0	33	1,100	0	7,705	76
	−45	0	25	490	0	3,260	32
	45	0	1	10,075	10,075	10,075	100
	135	0	1	10,075	10,075	10,075	100
	−135	60	34	1,335	0	8,165	81
	−45	60	33	1,300	0	7,685	76
	45	60	1	10,075	10,075	10,075	100
	135	60	1	10,075	10,075	10,075	100

(continued)

Table 29.1 (continued)

Height (km)	Longitude	Latitude	Number of segments	Maximum continual time	Minimum continual time	Sum of continual time	Per centum (%)
1,360	−135	−60	49	500	0	4,890	49
	−45	−60	45	95	0	1,700	17
	45	−60	65	715	0	6,670	66
	135	−60	63	540	0	7,500	74
	−135	0	36	365	0	3,355	33
	−45	0	23	200	0	1,260	13
	45	0	35	625	0	8,240	82
	135	0	1	10,075	10,075	10,075	100
	−135	60	53	490	0	4,875	48
	−45	60	48	95	0	1,715	17
	45	60	65	715	0	6695	66
	135	60	63	545	0	7,545	75
1,810	−135	−60	44	290	0	3,065	30
	−45	−60	44	250	0	2,840	28
	45	−60	57	150	0	1,945	19
	135	−60	75	260	0	3,915	39
	−135	0	29	205	0	2,230	22
	−45	0	5	135	45	425	4
	45	0	36	480	5	6,580	65
	135	0	1	10,075	10,075	10,075	100
	−135	60	45	290	0	3,030	30
	−45	60	45	250	0	2,810	28
	45	60	56	180	0	1,915	19
	135	60	73	255	0	3,890	39

Note "0" in "Minimum continual time" specifies that statistical segment (meet $N \geq 4$, $PDOP \leq 7$) is just one time point

can obtain effective PNT services. Relative to eastern hemisphere, the western hemisphere where the number of effective continual time segments is lager, the sum of continual time is fewer, so it is not suitable for spatial continual and long time navigation.

29.4 Conclusions

Without considering of the effect of signal in space (SIS) power, this paper employed BeiDou regional constellation (5GEO+5IGSO+4MEO) to compute and analyze the spatial number of visible satellites and DOPs. The computational results showed that: BeiDou regional navigation satellite system could provide effective PNT services for Asia–Pacific region, south and north Polar Regions

under 1,000 km, satisfied the designed service performance of BeiDou regional constellation. The computational and statistical results of the least visible satellites number, the worst PDOP, and the effective continual time segments reflected that: the space from 500 km to 1,000 km above the earth surface could acquire the best PNT services, and the coverage area is larger than the earth surface. Because of the promptly reducing of spatial coverage area, increasing of effective continual time segments and decreasing of maximum continual time and total time in all segments, the space above 1,000 km could not acquire effective PNT services.

This paper just discussed two main factors that are number of visible satellites and PDOP in spatial coverage performance evaluation. In further research, another factor that is signal power should be taken into consideration. Moreover, the impact of spatio-temporal resolutions on the computing results of spatial coverage performance deserves further study.

Acknowledgments The authors wish to acknowledge the support of Wuhan University for providing BeiDou broadcast ephemeris in developing this paper.

References

1. Chengqi R (2012) Development and application of BeiDou navigation satellite system. In: Proceedings of 3rd China satellite navigation conference, Guangzhou
2. China satellite navigation office (2012) Report on the development of BeiDou navigation satellite system (Version 2.0). www.beidou.gov.cn
3. Jiejuan W, Diao H, Dong ZH (2009) Modeling and simulation of coverage performance of 32 GPS satellites constellation. Aerosp Control 27(6):52–55
4. Zhang Q, Zhao Y, Xu M (2011) Computation model of constellation space coverage performance. J Spacecraft TT&C Technol 30(1):6–10
5. Bauer FH, Moreau MC, Dahle-Melsaether ME et al (2006) The GPS space service volume. ION GNSS, Fort Worth
6. Moreau M, Davis E, Carpenter JR et al (2002) Results from the GPS flight experiment on the high earth orbit AMSAT AO-40 Spacecraft. ION GPS, Portland
7. Kronman JD (2000) Experience using GPS for orbit determination of a geosynchronous satellite. In: Proceedings of institute of navigation GPS, Salt Lake City, UT
8. Zuohu Li (2012) Research on monitoring and assessment of satellite navigation system performance. PLA Information Engineering University, Zhengzhou

Chapter 30
Global Coverage Performance Analysis Based on 4 BeiDou MEO Satellites

Xin Liu, Wenhai Jiao, Yu Bai and Jin Fan

Abstract Constellation coverage performance is an important indicator of assessing constellation design, therefore this paper intended to provide reference for the deployment of BeiDou Navigation Satellite System in the future by analyzing the coverage performance of BeiDou navigation satellites. This paper studied two navigation constellation performance indicators which are continuous coverage and spatial configuration, and studied the design method for global coverage performance simulation based on 4 BeiDou MEO satellites constellation. Firstly, this paper analyzed global area which can be quadruple covered, time percentage of navigation availability and the PDOP average value within time of navigation availability; Secondly, this paper calculated PDOP value of observation points sharing the same longitude within one regression cycle, made statistical analysis of maximum coverage gap and average coverage gap of each point, and analyzed the variation of PDOP value in different latitudes; Finally, this paper analyzed periodic changes of global coverage area of navigation availability.

Keywords BeiDou navigation satellite system · MEO navigation satellite · PDOP value · Continuous coverage indicator · Spatial configuration indicator

30.1 Introduction

With more and more BeiDou navigation satellites launched successfully, BeiDou Navigation Satellite System basically has had the capability of providing regional passive services, and On December 27, 2011, BeiDou system declared to provide Initial Operational Capability (IOC) officially. Meanwhile, through One Launch

X. Liu (✉) · W. Jiao · Y. Bai · J. Fan
Test and Assessment Research Center of China Satellite Navigation Office, Beijing, China
e-mail: jmdliuxin@hotmail.com

J. Sun et al. (eds.), *China Satellite Navigation Conference (CSNC) 2013 Proceedings*, Lecture Notes in Electrical Engineering 243,
DOI: 10.1007/978-3-642-37398-5_30,

Vehicle technology in launching double MEO Satellites, BeiDou System is still working on expanding service area, improving system performance and perfecting BeiDou regional constellation gradually. In line with the development plan, BeiDou system will complete the transition from regional constellation to global constellation by 2020. In view of the essential role of these 4 MEO satellites of BeiDou regional constellation in enhancing regional constellation (GEO + IGSO) and carrying-out of global constellation technology tests, the analysis of global coverage performance will be significant and provide indispensible reference value for further research.

As constellation coverage performance is an important indicator of assessing constellation design, the analysis of coverage performance of BeiDou navigation satellites in this paper will provide reference for the deployment of BeiDou Navigation Satellite System in the future. In 1970s, many experts aboard have done systematic research on the global constellation coverage, Walker [1] studied circular orbit patterns to provide continuous whole earth coverage and some different constellations to meet various performance requirements. In 1990s, many experts at home had begun to carry out the research of MEO satellite coverage performance. Sudan [2] studied the optimal method for constellation parameters of MEO communication regional satellite based on the analysis of major parameters of orbit, and analysed the global coverage capability of an optimal 5 MEO satellite constellation.

For the present however, few researches have been done on BeiDou MEO navigation satellites at home and aboard, because they are newly networked satellites. Considering that BeiDou system is still on its way to global continuous coverage due to only 4 MEO satellites launched, this paper intended to investigate the performance based on 4 BeiDou MEO satellites constellation in order to ensure its global coverage performance in future. By the simulation of continuous coverage and spatial configuration performance indicators, this paper gave preliminarily statistics of 4 BeiDou MEO satellites constellation, including worldwide coverage area, coverage period and navigation available range, in order to lay the foundation for the more in-depth studies of BeiDou global constellation and provide reference for subsequent deployment strategies of BeiDou system.

30.2 BeiDou Navigation Satellite System Development Plan

According to the overall planning of the “three-step” development strategy [3, 4], BeiDou is in the implementation of the “Phase II”. Up to November 2012, there are 14 effective BeiDou navigation satellites in-orbit, including 4 GEO, 5 IGSO and 4 MEO satellites. Each satellite’s design parameters are shown in Table 30.1.

Table 30.1 The designed parameters of BeiDou navigation satellite system

Satellite type	Satellite number	Orbit latitude	Orbit number	Orbit inclination	Serial number	RAAN
GEO	5	36000	1	0	GEO-1	58.75°E
					GEO-2	80°E
					GEO-3	110.5°E
					GEO-4	140°E
					GEO-5	160°E
IGSO	5	36000	5	55	IGSO-1	118°E
					IGSO-2	118°E
					IGSO-3	118°E
					IGSO-4	95°E
					IGSO-5	95°E
MEO	4	21500	2	55	MEO-1	0°E
					MEO-2	0°E
					MEO-3	120°E
					MEO-4	120°E

30.3 Simulation of 4 BeiDou MEO Satellites Constellation

30.3.1 Navigation Constellation Performance Indicators

Navigation constellation performance indicators are the fundamental basis of constellation design and navigation performance assessment, which include continuous coverage indicator, spatial configuration indicator, redundancy maintain indicator, configuration maintain indicator, independent performance indicator, etc. [5, 6]. Among them, navigation satellite systems are directly associated with the analysis of continuous coverage indicator and spatial configuration indicator. The analysis of 4 BeiDou MEO satellites constellation in this paper is mainly based on these two indicators by numerical simulation method.

30.3.1.1 Continuous Coverage Indicator

Continuous coverage indicator mainly estimates quadruple coverage capability of navigation constellation [7]. It includes some quantitative evaluation parameters, which are time percentage of navigation availability, maximum coverage gap and average gap [8].

Time percentage of navigation availability is the ratio of time with not only quadruple covered but also PDOP value under given threshold to total simulation time of point (i,j) in the grid of earth, which can be described as follows:

$$A_{tpna} = \frac{\int_{i=0}^{i=T_s} \{t | n_{tvs} \geq 4 \& PDOP_i \leq k\} dt}{T_s} \times 100\,\% \tag{30.1}$$

In Eq. 30.1, n_{tvs} is the number of visible satellites, T_s is total simulation time, k is the threshold of PDOP value.

Coverage gap is the period of point (i,j) which cannot be covered by more than 3 satellites.

Maximum coverage gap is the maximum coverage gap of point (i,j) in the grid of earth during some period of time, which can be described as follows:

$$Tg_{\max} = \max\left\{Tg_{ij}^1, Tg_{ij}^2, \quad , Tg_{ij}^n\right\}, (i \in [-180, 180], j \in [-90, 90]) \tag{30.2}$$

In Eq. 30.2, Tg_{ij}^k is the k-th coverage gap of point (i,j) within total simulation time.

Average coverage gap is the ratio of total time of point (i,j) 's coverage gap and the number of coverage interrupts during some period of time, which can be described as follows:

$$Tg_{ave} = \frac{\sum_{i=1}^{i=n_{nci}} Tg_{ij}^k}{n_{nci}} \tag{30.3}$$

In Eq. 30.3, n_{nci} is the number of coverage interrupts during some period of time.

30.3.1.2 Spatial Configuration Indicator

Spatial configuration indicator mainly estimates spatial location and geometry strength of navigation satellites which are used in position calculation. We usually use dilution of precision (DOP) as metrics. DOP includes geometric dilution of precision (GDOP), horizontal dilution of precision (HDOP), vertical dilution of precision (VDOP), position dilution of precision (PDOP) and time dilution of precision (TDOP). The factors above can be calculated from locations of satellites known by users. The correspondence between DOP values and navigation performance is shown in Table 30.2 [9].

The equations of GDOP, PDOP, HDOP, VDOP and TDOP are shown as follows:

$$GDOP = (g_{11} + g_{22} + g_{33} + g_{44})^{1/2} = \sigma_g / \sigma \tag{30.4}$$

Table 30.2 The correspondence between DOP values and navigation performance

DOP value	<1	1–2	2–5	5–10	10–20	>20
Rating	Ideal	Excellent	Good	Moderate	Fair	Poor

$$PDOP = (g_{11} + g_{22} + g_{33})^{1/2} = \sigma_p/\sigma \tag{30.5}$$

$$HDOP = (g_{11} + g_{22})^{1/2} = \sigma_h/\sigma \tag{30.6}$$

$$VDOP = (g_{33})^{1/2} = \sigma_v/\sigma \tag{30.7}$$

$$TDOP = (g_{44})^{1/2} = \sigma_t/\sigma \tag{30.8}$$

In Eqs. 30.4–30.8, σ is ranging error, σ_g is geometric error, σ_p is position error, σ_h is horizontal error, σ_v is vertical error, and σ_t is time error. $g_{ii}(i = 1, \cdots, 4)$ are diagonal elements of $G = (H^T \cdot H)^{-1}$, in which H is observation matrix.

30.3.2 Simulation Design of 4 BeiDou MEO Satellites Constellation

In order to examine the impact of 4 MEO satellite on global coverage performance more clearly, BeiDou GEO an IGSO navigation satellites were not included in the simulation.

30.3.2.1 Input Variables and Conditions

As the simulation inputs, all orbital parameters of 4 BeiDou MEO satellites are shown in Table 30.1.

As the orbit of BeiDou MEO navigation satellite is the regression orbit of 7 days/13 circles, this paper set 7 days as the total simulation time, calculated grid points with the sampling frequency of every 5 min and the sampling grid of 5° × 5°, and set 7 as the threshold of PDOP.

30.3.2.2 Definition

If the PDOP value of grid point is blow 7 at the time t, we define that this point is available for navigation; that the area formed by all the navigation available points is navigation available area; and that the point with the best PDOP in navigation available area (or the best geometric point of constellation) is the centre of navigation available area.

30.3.3 Simulation Results

30.3.3.1 Result 1

Limited by the number of BeiDou MEO navigation satellites, the coverage area and coverage time of 4 BeiDou MEO satellites constellation is small and short. Figure 30.1 shows the global area which can be quadruple covered within one regression cycle; Fig. 30.2 shows each point's time percentage of navigation availability within one regression cycle; and, Fig. 30.3 shows each point's PDOP average value within the time of navigation availability.

30.3.3.2 Result 2

The PDOP value of the observation points on the equator changed irregularly, from which we can obtain the statistics of maximum coverage gap and average gap. Figure 30.4 shows each point's PDOP value in different latitude sharing the same longitude within one regression cycle, which are (0°E, 15°N), (0°E, 10°N), (0°E, 5°N), and (0°E, 0°N).

30.3.3.3 Result 3

In one regression cycle, the geometry configuration of 4 BeiDou navigation satellites in space changes periodically. So the navigation available area, navigation available time and the centre of navigation available area also changes periodically. Figure 30.5 shows the changes of navigation available area at different times within the same cycle.

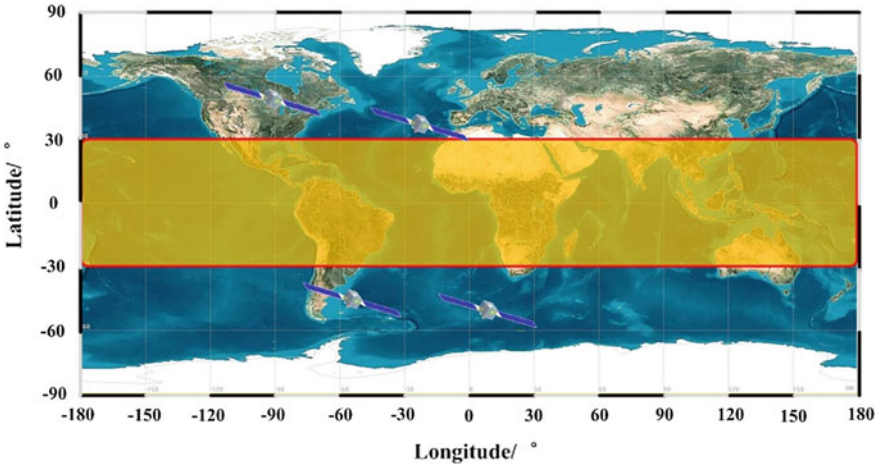

Fig. 30.1 The global area which can be quadruple covered within one regression cycle

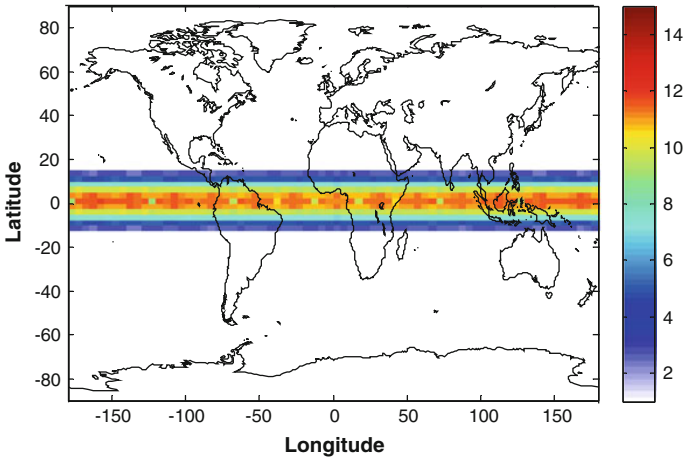

Fig. 30.2 Each point's time percentage of navigation availability within one regression cycle

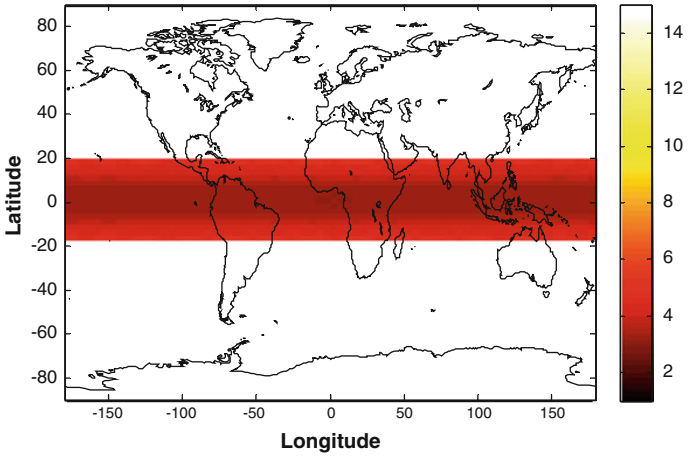

Fig. 30.3 Each point's PDOP average value within the time of navigation availability

30.3.4 Simulation Analysis

30.3.4.1 Analysis 1

From Result 1 in 3.3.1, we can obtain three points as follows:

Firstly, we can see that the global area which can be quadruple covered within one regression cycle is from 180°W to 180°E in longitude and from 20°N to 20°S in latitude; and that the navigation available area is from 180°W to 180°E in longitude and from 15°N to 15°S in latitude.

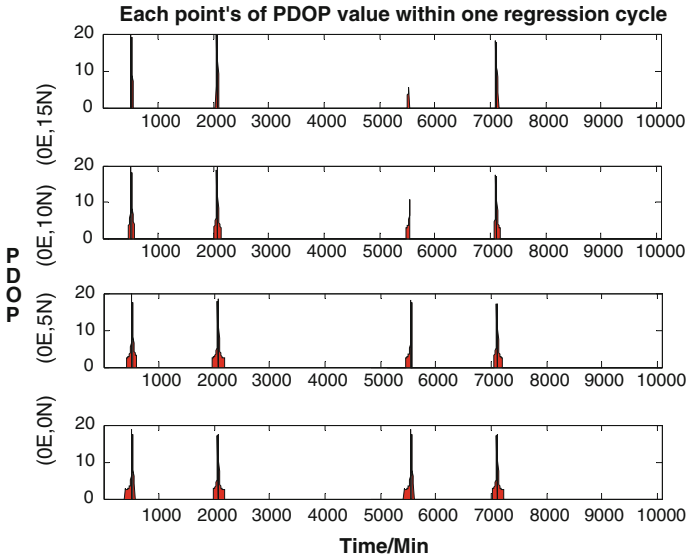

Fig. 30.4 Each point's PDOP value in different latitude sharing the same longitude within one regression cycle

Secondly, we can also see that navigation available time decreases toward both poles setting the equator as the boundary. The observation points on the equator have the longest time of navigation availability, approximately 19.5 h/7 days; meanwhile, the ones on latitude 15°N or 15°S have the shortest time of navigation availability, approximately 1.7 h/7 days.

Thirdly, we can also see that PDOP average value of the observation points within navigation available time increases toward both poles setting the equator as the boundary. PDOP average value of the observation points on the equator is the minimum, approximately 3.25; meanwhile, the one on latitude 15°N or 15°S is the maximum, approximately 4.90.

30.3.4.2 Analysis 2

From Result 2 in 3.3.2, we can obtain two points as follows: we can see that the maximum coverage gap of each observation point decreases toward both poles setting the equator as the boundary. The observation points on the equator have the shortest time of maximum coverage gap, approximately 54 h; meanwhile, the ones on latitude 15°N or 15°S have the longest time of maximum coverage gap, approximately 59 h.

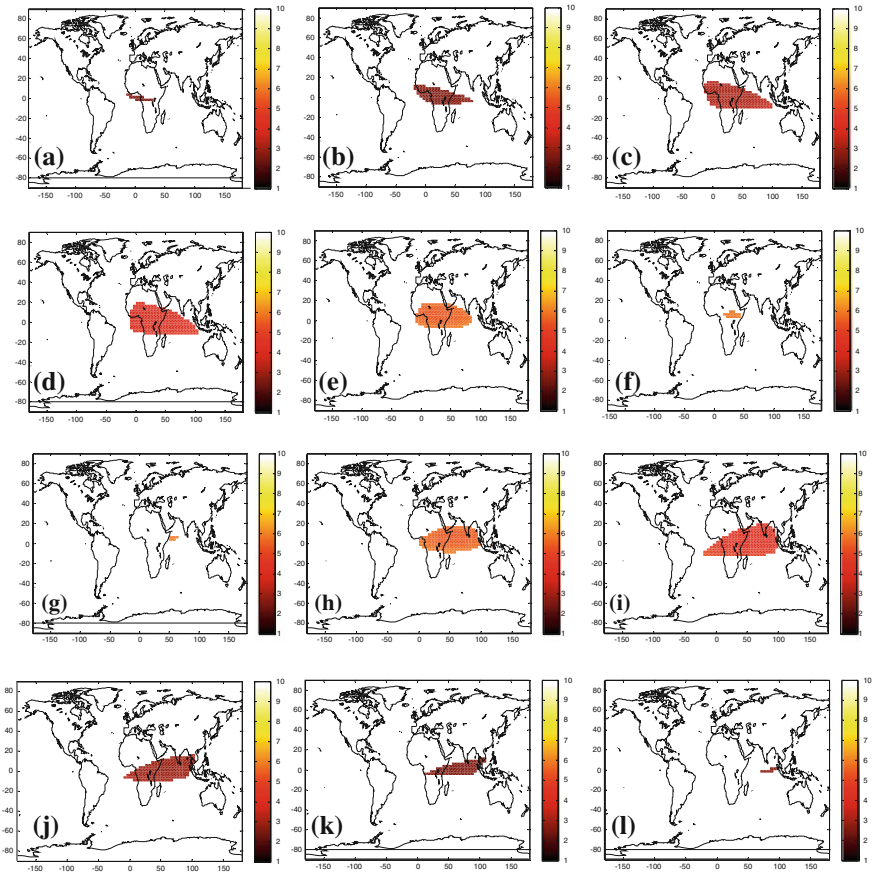

Fig. 30.5 The changes of navigation available area at different times within the same cycle. **a** t = 0 min. **b** t = 65 min. **c** t = 95 min. **d** t = 110 min. **e** t = 122 min. **f** t = 124 min. **g** t = 170 min. **h** t = 172 min. **i** t = 180 min. **j** t = 205 min. **k** t = 235 min. **l** t = 300 min

30.3.4.3 Analysis 3

From Result 3 in 3.3.3, we can obtain the periodic variation of navigation available area in different time:

The variation period is approximately 12.9 h, as same as the time of MEO satellite orbiting the earth one circle. The centre of navigation available area moves $14\pi/13$ westward in longitude during the variation period.

We can see in terms of the variation tendency of the size of navigation available area. In the beginning, the area appeared and expanded slowly until the maximum, and then reduced rapidly until disappeared, and after that it appeared again after a vanished period and expanded rapidly until the maximum, and then reduced slowly until disappeared again.

We can also see the variation tendency of the centre of navigation available area is that the centre firstly moved $2\pi/13$ westward in longitude during the first expansion period, and then moved $\pi/13$ westward in longitude during the first reduction period, and secondly moved $\pi/13$ westward in longitude during the first vanished period, and thirdly moved $\pi/13$ westward in longitude during the second expansion period, and then moved $2\pi/13$ westward in longitude during the second reduction period, and finally moved $8\pi/13$ westward in longitude during the second vanished period.

30.4 Conclusions

To sum up the simulation results above, we can come to four conclusions as follows:

1. 4 BeiDou MEO satellites constellation can offer discontinuous PNT services in navigation available area, which is from 180°W to 180°E in longitude and from 15°N to 15°S in latitude. In region of navigation available area, the navigation available time of each point is from 1.7 to 19.5 h per 7 days, within which the PDOP average value is below 5.
2. During the regression cycle, setting the equator as the boundary, the navigation available time of each point in navigation available area decreases toward both poles; and the PDOP average value of each point in navigation available area within its navigation available time increases toward both poles; and the maximum coverage gap of each point in navigation available area decreases toward both poles; and the average coverage gap of each point in navigation available area decreases toward both poles.
3. The variation period of navigation available area is approximately 12.9 h, as same as the time of MEO satellite orbiting the earth in one circle. During the variation period, the size of navigation available area expands and reduces twice, and the centre of navigation available area moves $14\pi/13$ westward in longitude.
4. Although 4 BeiDou MEO satellites cannot meet the requirement of global continuous coverage temporarily, they are enough to perform a variety of in-orbit test missions such as multi-satellite positioning test, heterogeneous satellite networking test, navigation signal debugging and so on.

References

1. Walker JG (1973) Continuous whole-earth coverage by circular-orbit satellite patterns. In: Proceedings of international conference on satellite systems for mobile communications and surveillance, institution of electrical engineers, London, England, pp 33–38
2. Sudan L, Jiang Z, Guangxia L (2005) A MEO regional communication constellation design wit multi-object GA. Aerospace Shanghai, No. 5

3. Chengqi R (2012) Development and application of BeiDou navigation satellite system. 3rd China satellite navigation conference, Guangzhou
4. China satellite navigation office report on the development of BeiDou navigation satellite system (Version 2.0) (2012). www.beidou.gov.cn
5. Yulin Z, Li F, Yan Z (2008) Theory and design of satellite constellations. Science
6. Lu H, Liu X (2012) Compass augmented regional constellation optimization by a multi-objective algorithm based on decomposition and PSO. Chin J Electron 21(2):374–378
7. Hanghua Y, Yuncheng H, Shihong C (2010) Analysis of coverage and positioning dilution of precision of navigation constellations. GNSS World of China
8. Min X, Fengzhou C, Shilu C (2000) Numerical simulation of coverage performance for satellite constellation. J Astronaut 21(51):19–26
9. Hegarty CJ (2007) Understanding GPS: principles and applications. In: Yanhong K (ed) Publishing house of electronics industry, 2nd edn. Beijing

Chapter 31
Research on Performance Evaluation of Receiver Combining Measurements from RDSS and RNSS for Position Fixing and Report

Jianwei Zhan, Yonghu Zhang, Haibo Tong, Guozhu Zhang and Gang Ou

Abstract In recent years, navigation signal simulator with different functions has been playing a very important role in meeting the performance requirement of the research, test and evaluation of the different navigation receiver, such as RDSS, RNSS and dual-mode receivers. Compared with the simulator of GPS, BeiDou Navigation Satellite System (BDS) have some different unique characteristics, especially in RDSS determination. First, the principle of comprehensive RDSS position and report is elaborated and then requirements of the dynamic navigation signal simulation are analyzed. Finally, two key mathematical models are established to simulate the signals arriving at the receiver antenna for dual-mode receiver test, which are: the transmitting time iterative model and satellite orbit approximation model. The results show that the BDS dual-mode simulator can satisfy dual-mode receiver's test requirements.

Keywords Satellite navigation · BeiDou navigation satellite system · Simulation model · Hermit interpolation · Dual-mode receiver · Test

31.1 Introduction

During the past few years there has been growing interest in the Chinese regional satellite navigation system of BeiDou Navigation Satellite System (BDS) and in navigation receivers that use RNSS and a combination of RDSS and RNSS signals. The most important reasons for this interest are the advantages of quick position fixing and position report. So combination technologies of RDSS and RNSS in the commercial world appear very promising.

J. Zhan (✉) · Y. Zhang · H. Tong · G. Zhang · G. Ou
Satellite Navigation Research and Development Center, National University of Defense Technology, Changsha, China
e-mail: sophy_zjw@nudt.edu.cn

J. Sun et al. (eds.), *China Satellite Navigation Conference (CSNC) 2013 Proceedings*, Lecture Notes in Electrical Engineering 243,
DOI: 10.1007/978-3-642-37398-5_31,

The dual-mode receivers have three work modes, which are RDSS, RNSS and combination of the two. RDSS is an active positioning subsystem, which provides short message communication and two-dimensional positioning service, needs to transmit burst signal, whereas RNSS differs significantly from RDSS, is a passive positioning subsystem like GPS and GLONASS, which provides PNT service, needs not to transmit signal. And the most important mode is the combination, which contains fast RNSS signal acquisition depending on RDSS which can reduce the time uncertainty, comprehensive position and report technology which has high-security, precise point positioning, dual-frequency ionospheric delay correction.

Navigation signal simulator can simulate and generate the standard navigation signal. Comparing to the signal acquired from the navigation system, the signals generated by a simulator is repeatable and controllable and as a result they can be applied to support more flexible and configurable test scenarios. For this reason, signal simulator technology has been widely applied in testing and verifying BDS receiver performance.

At present, there are many types of commercial GPS or GNSS simulator in the market [1–5]. However, due to the complete specific details of signal in space interface control document (ICD) of BDS has not yet provided by research of simulators for BDS lagging behind [6, 7]. Even more importantly, there are no commercial simulator which can satisfy the verification and assessment of the receiver combining measurements from RDSS and RNSS for position fixing and report now. The simulator in [6] is designed only for the active receiver. Zhang and Sun [7] briefly introduces the principles and the structures of the RDSS system, but not establishes simulation models.

This paper is concerned with the test requirements of the dual-mode receiver. By analyzing and establishing the key models such as the transmitting time iterative model, satellite orbit approximation model, design and implement a kind of BDS dual-mode simulator which can simulate satellite dynamic signals arriving at the antenna simultaneously. Compared with the traditional simulator, it can provide navigation signal for the function evaluation and validation of RDSS and RNSS receiver, especially for dual-mode receivers. This paper focuses on the simulation modeling and the test result analysis.

31.2 Comprehensive RDSS Position and Report Theory

BDS is a hybrid constellation navigation with GEO/IGSO/MEO [8]. A major difference is that GEO satellites carry RDSS and RNSS payloads simultaneously. Like GPS, RNSS signals are generated on satellites, while RDSS signals are constructed and disseminated on the ground, and the satellites only transfer the signals to the ground by transponders. As would be expected, considerations for the advantage of GEO, a new method for position fixing and report is proposed [9], which is shown in Fig. 31.1.

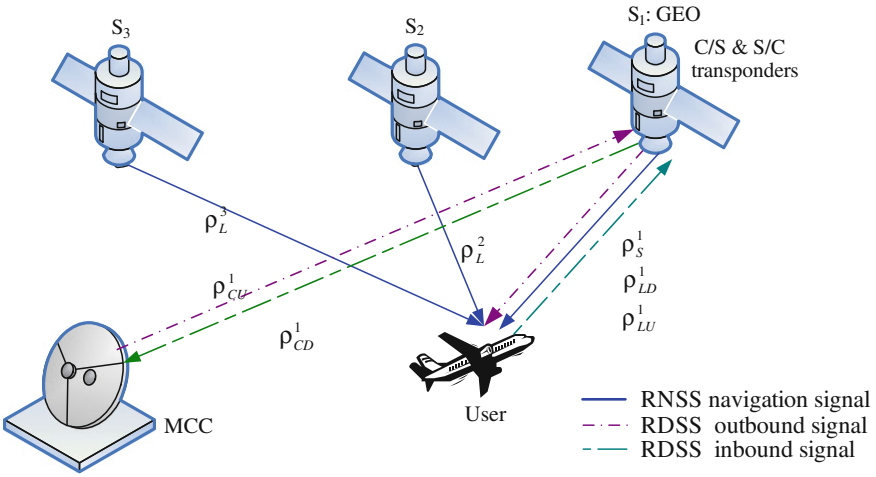

Fig. 31.1 The theory of comprehensive RDSS position and report

In order to determine user position (x_u, y_u, z_u) in three dimensions, measurements are made to at least three satellites S1, S2 and S3 by user receiver. More specifically, at any epoch t_k, the pseudorange difference $\Delta\rho^{i,j}{}_L(t_k) = \rho^i_L(t_k) - \rho^1_L(t_k)$ (i and j are the satellite PRN number of BDS, $i \,!= j$, and j is limited to a visible GEO PRN number, for example, $j = 1$ is assumed here), and $\rho^1_s(t_k)$ are measured. Meanwhile, $\rho^1_s(t_k)$ is assumed to be consistent with the pseudorange $\rho^1_L(t_k)$ after calibrated ionosphere errors caused by different frequencies between RDSS S and RNSS L using MCC precision ephemeris, ionosphere model parameters. As soon as observations are accomplished, the user receiver transmits to MCC using a transmission burst through inbound channel in response to a message request. The transmission parameters would include all the $\Delta\rho^{i,1}{}_L(t_k)$. It is noted that the actual measurements are ρ^1_{LD} and $\Delta\rho^{i,1}_L$. Hence, in the absence of measurement errors, the basic set of positioning equations and the geometry matrix **H** can be expressed as

$$\begin{cases} \rho^1_{LD} = f(\rho^1_{CU} + \rho^1_S + \rho^1_{LU} + \rho^1_{CD}) = f(x_u, y_u, z_u) \\ \Delta\rho^{2,1}_L = \rho^2_{LD} - \rho^1_{LD} \\ \cdots\cdots\cdots\cdots \\ \Delta\rho^{n,1}_L = \rho^n_{LD} - \rho^1_{LD} \end{cases} \tag{31.1}$$

$$\mathbf{H} = \begin{bmatrix} \frac{\partial F_1}{\partial x_u} & \frac{\partial F_1}{\partial y_u} & \frac{\partial F_1}{\partial z_u} \\ \frac{x_2 - x_u}{r_2} - \frac{\partial F_1}{\partial x_u} & \frac{y_2 - y_u}{r_2} - \frac{\partial F_1}{\partial y_u} & \frac{z_2 - z_u}{r_2} - \frac{\partial F_1}{\partial z_u} \\ \cdots & \cdots & \cdots \\ \frac{x_n - x_u}{r_n} - \frac{\partial F_1}{\partial x_u} & \frac{y_n - y_u}{r_n} - \frac{\partial F_1}{\partial y_u} & \frac{z_n - z_u}{r_n} - \frac{\partial F_1}{\partial z_u} \end{bmatrix} \tag{31.2}$$

where $f(\cdot)$ in (31.1) is the nonlinear observation function, ρ_{LD}^{i} is the pseudorange to the ith satellite, $\Delta\rho^{i,1}{}_{L}$ is the RNSS pseudorange difference between the ith satellite and GEO satellite. The sum of $\rho^{1}{}_{\mathrm{CU}}$, $\rho^{1}{}_{\mathrm{s}}$, $\rho^{1}{}_{\mathrm{LU}}$ and ρ_{CD}^{1} are MCC-satellite-user back and forth pseudorange measurements.

31.3 Simulation Model

31.3.1 Architecture of Simulator

Consider the architecture and the simulation algorithm. BDS dual-mode simulator simulates satellite and receiver trajectories, signal measurement errors and receiver measurement errors. The simulator consists of two main parts. The first one is the signal parameter calculation unit which calculates observation data according to the satellite orbit model, the target trajectory calculation model and the signal propagation error model. The second one is signal generator unit, which uses observation data to generate RF navigation signal (Fig. 31.2).

Figures 31.3 and 31.4 further describe the details on the architecture and flowchart of the simulator. The GUI interface allows the user to set/input various parameters, such as constellation parameters, simulation start time, receiver trajectory, environment error, effects, etc. The simulator uses special orbit integration or interpolation techniques for the computation of the satellite positions. For a realistic modeling of the measurements, signal propagation effects, such as ionosphere, troposphere and delays due to errors caused by the satellites are simulated. As an output either pseudorange and navigation data or a RF signal is provided to the user receiver.

31.3.2 Signal Transmitting Time Iterative Model

The BDS dual-mode simulator designed in the paper consist of four simulation models, satellite transmitting iterative model, satellite orbit approximation model, signal propagation delay model and the target trajectory calculation model. For a limited length of the paper, the first two models would be analyzed and established.

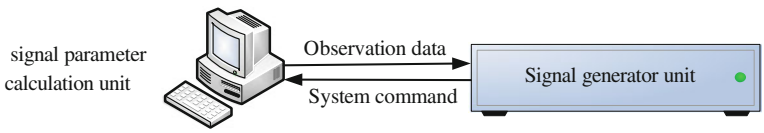

Fig. 31.2 A schematic graph show BDS dual-mode simulator's composing

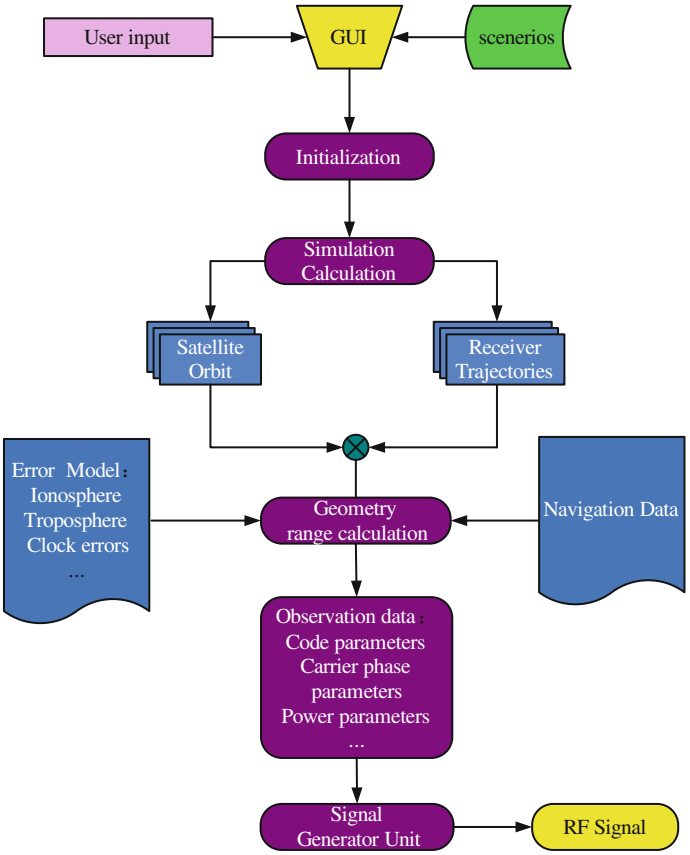

Fig. 31.3 BDS dual-mode simulator flowchart

According to the principle of position determination, the signal received by the receiver at time t_r is transmitted by the satellite at time t_t. In order to simulate the signal appropriately, the satellite position and the delay should be calculated iteratively. Therefore, obtaining the time t_t when the satellite transmits the signal is the key point of the algorithm. As an example of how to use the model to calculate time, the process of calculating t_t is given as follows.

Assuming t_t is expressed in BDT. r is the geometric satellite-to-receiver distance. c is the speed of light in vacuum. Then the transmitting time is calculated as

$$t_t = t_r - \frac{r}{c} - I - T - \tau_{sag} \tag{31.3}$$

where I is the ionospheric delay, T is the tropospheric delay, and τ_{sag} is the delay caused by the earth rotation.

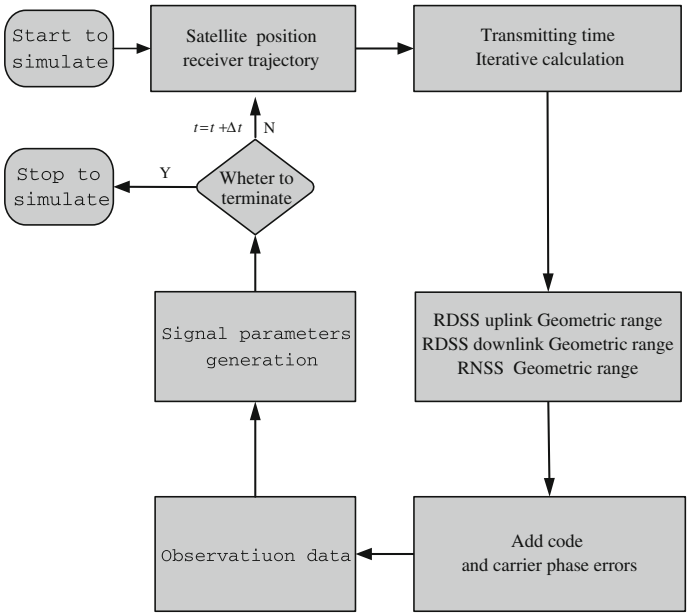

Fig. 31.4 Pseudorange calculation flowchart

Given the geometric range r is computed in a CGCS2000 coordinate frame. t_t $(k + 1)$ is the transmitting time calculated iteratively by $k + 1$ times. The initial value is $t_t = t$ and the iteration finishes when Eq. (31.4) condition is satisfied.

$$|r(t_s(k+1)) - r(t_s(k))| < \varepsilon \tag{31.4}$$

ε denotes the precision, and it is always equal to or less than 10e-10. Simulation shows that in the condition of $\varepsilon =$ 1e-10, the calculation will converge in $3 \sim 4$ iterative times and, therefore, t_t $(k + 1)$ is the signal transmitting time.

31.3.3 Efficient Satellite Orbit Approximation Model

Since the broadcast ephemeris is used to determine satellite positions, orbital errors must be simulated, which would affect the navigation accuracy directly.

Given ephemeris, the best estimate is achieved by directly calculating the satellite's position and velocity from the model. However, a major issue for a realistic signal modeling is the computation of the Keplerian orbit parameters including their correction terms based on the simulated orbits is a crucial task, since they have to fulfill specific accuracy of navigation solution. So in order to speed up position and velocity computation and get good quality of satellite

position and velocity estimates, orbit. Interpolation is appropriate. Among many interpolation methods, the 3 order Hermit interpolation has high efficiency in both position and velocity [10]. For a detailed description of the Hermit interpolation algorithm refer to [11]. In general, Hermit interpolation can be set up as:

$$H(t) = a_i + b_i(t - t_i) + c_i(t - t_i)^2 + d_i(t - t_i)^3 \tag{31.5}$$

$$\begin{aligned} a_i &= f(t_i) \\ b_i &= f'(t_i) \\ c_i &= \frac{3f[t_i, t_{i+1}] - 2f'(t_i) - f'(t_{i+1})}{t_{i+1} - t_i} \\ d_i &= \frac{f'(t_i) - 2f[t_i, t_{i+1}] + f'(t_{i+1})}{(t_{i+1} - t_i)^2} \end{aligned} \tag{31.6}$$

where t_i is the sample instants, and they are assumed to be in strictly increasing order, i.e., $t_i < t_i + 1$ for all i. $H(t)$ is the function evaluated at value t. a_i, b_i, c_i and d_i are the coefficients of the polynomial. $f(t)$ is Hermit polynomial and $f'(t)$ is the derivative of $f(t)$, in our case is the ECEF satellite position and velocity coordinate X, Y or Z, respectively.

Here, 1 min interval sampled data for the time span from 04 h through 24 h of 06 September 2007 is calculated from ephemeris. Then sampled data is subdivided into two 2 min interval observation data. One is used for sampling instants, the other is developed as the reference sampled data.

It is seen from the plots in Fig. 31.5 that for reasonable position error of 1–5 mm and velocity error of 4–6 mm/s, the shorter interpolation time span, the more efficient of Hermit interpolation. So piecewise polynomial interpolation is needed for long interpolation area [10]. In order to validate the precision, the comparisons between GEO, IGSO and MEO with above data for time span from 04 h through 05 h are made, as shown in Figs. 31.6 and 31.7.

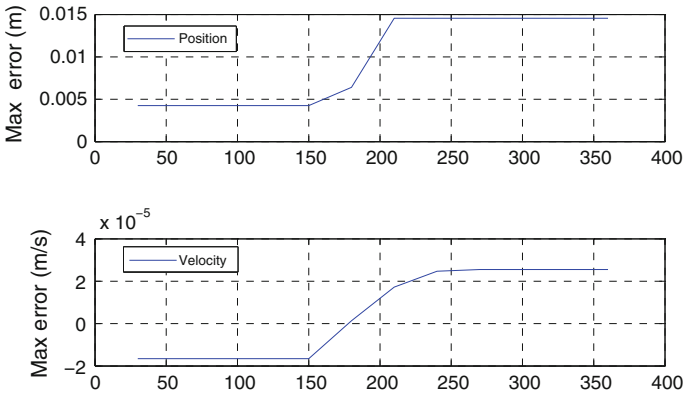

Fig. 31.5 Max. error of MEO satellite in x position and velocity versus different time span

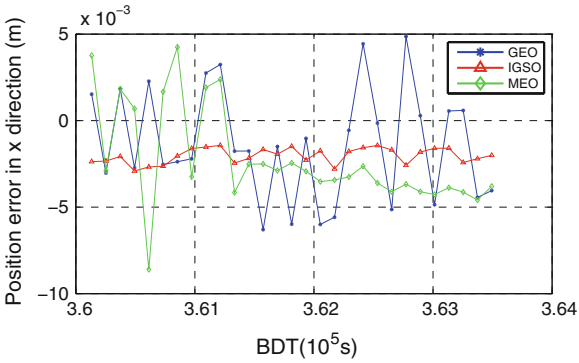

Fig. 31.6 Position error versus different satellite types

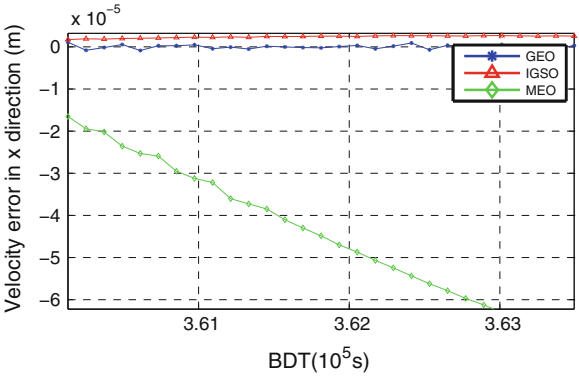

Fig. 31.7 Velocity error versus different satellite types

From the summary in Table 31.1, for either satellite type, the precision is less than 1e-2 m and 1e5 m/s. Therefore, the effect on navigation solution can be neglected.

As a conclusion, Hermit interpolation reduces the cost of satellite location and velocity determination remarkably, also satisfies orbit approximation curve's continuity, precision requirements. So the Hermit interpolation is appropriate for navigation satellite orbit calculating, also a compromise between computational burden and precision.

Table 31.1 Precision of different type satellite with Hermit interpolation (m, m/s)

Sat. type	Max error		Min error		RMS error	
	Position	Velocity	Position	Velocity	Position	Velocity
GEO	6.303e-3	1.097e-6	1.424e-4	1.355e-8	3.512e-5	5.114e-9
IGSO	2.913e-3	2.678e-5	1.431e-3	1.736e-6	2.113e-5	2.452e-8
MEO	8.604e-3	6.916e-5	6.850e-4	1.6534e-5	3.692e-5	4.784e-7

31.4 Experiments and Analysis

To meet the accuracy test requirements of all types of BDS dual-mode receivers, the BDS dual–mode simulator integration with evaluation function shows in Fig. 31.8 is designed and implemented with high performance. The key performance is shown here:

1. Pseudorange accuracy: ±0.003 m.
2. Pseudorange rate: ±0.003 m/s.
3. Interchannel bias: ≤0.167 ns (code), ≤0.001 m (carrier).
4. Equipment delay stability: 1 ns/month.

To evaluate the performance of the dual-mode receiver, for example, two simulator-based experiments, the dynamic position accuracy and the difference pseudorange, are carried out. Experiments are conducted in cable connect environment based on the above navigation receiver integrated test system, as shown in Fig. 31.8, which consists of BDS dual simulator and a prototype receiver with CRDSS.

In the experiment, the simulation beginning time of scenarios is at 314 BD week number and 3.6e4 s of week, the constellation configure is BDS (Phase I), the rate of observation data is set to 1 Hz, and the average number of visible

Fig. 31.8 A schematic graph show BDS dual-mode simulator

satellites is 7. It should be noted that the second experiment's observation data is the difference pseudorange measurement only, without MCC-satellite-user back and forth pseudorange measurements. For the receiver is unable to simulate the signal arriving at MCC's antenna with actual pseudorange in the simulation environment. If pseudorange measured from the receiver inbound signal, large error will be caused which, furthermore, affected the navigation solution's reality. Therefore, limited the simulation environment, the position fixing and report of the receiver can be only assessed indirectly by measuring difference pseudorange.

Equation (31.7) is the trajectory expression of the dynamic position accuracy scenario, which is a sinusoidal movement curve in the altitude direction of geodetic coordinates. The center position is set to (40°N, 112°E, 1,000 m)

$$s = s_0 + A\sin(wt + \varphi) \tag{31.7}$$

where s is the real time pseudorange from satellites. s_0 is the initial pseudorange determined by the initial user receiver position. A is a constant amplitude with a value 2,296 m. Angular frequency ω is set to 0.1307 rad/s. The initial phase φ is zero rad.

Figures 31.9, 31.10, 31.11, 31.12 and Table 31.2 present the test result of the dynamic position and velocity accuracy in different direction by RNSS alone

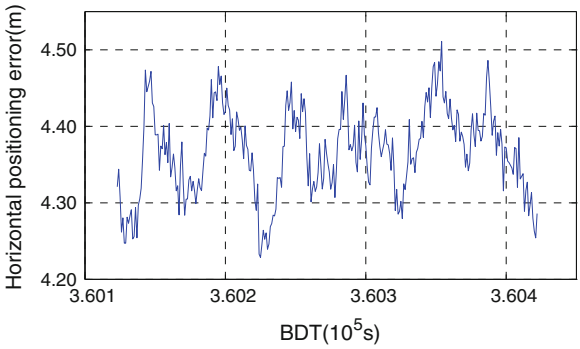

Fig. 31.9 Horizontal positioning errors

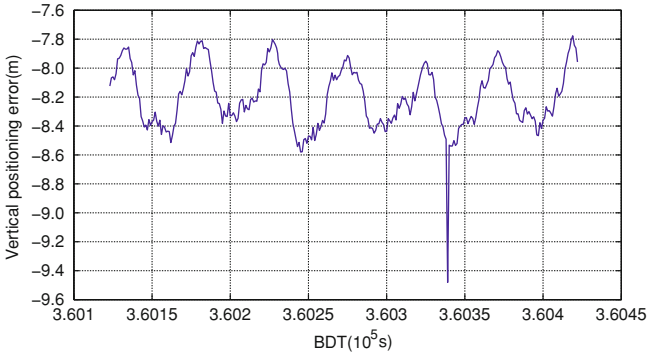

Fig. 31.10 Vertical positioning errors

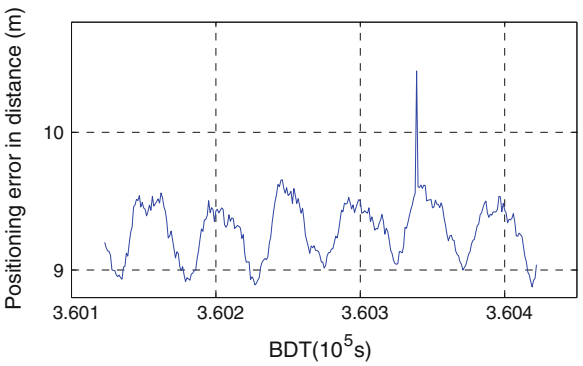

Fig. 31.11 Positioning errors in distance

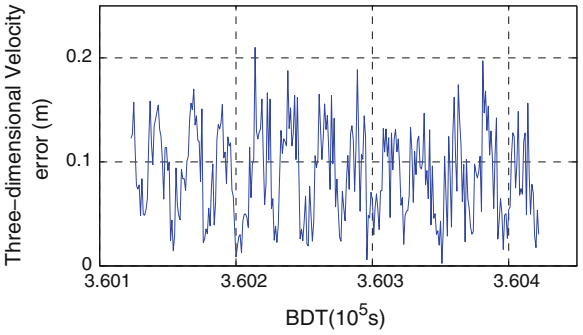

Fig. 31.12 Three dimensional velocity error

Table 31.2 Accuracy of dynamic position and velocity test

Item	RMS error (m)				
	Horizontal	Vertical	Distance	Max	Min
Position error	4.374	8.217	9.309	10.446	8.877
Velocity error	–	–	0.099	0.210	0.002

solution, which is in accordance with the one provided by BDS. It can be noted that there is a pseudorange jump during the test, which is caused by the receiver itself through comparison test with other receivers under the same scenario.

As shown in Figs. 31.13, 31.14 and Table 31.3, the accuracy of the difference pseudorange and double zero value is less than 0.1 and 1 ns. That is, the accuracy of comprehensive RDSS position fixing and report would be improved when compared with RDSS standalone solutions and, also better than RNSS by using MCC precision ephemeris, ionosphere model parameters. Furthermore, all the test result proves the signal simulator can satisfy dual-mode receiver's test requirements completely.

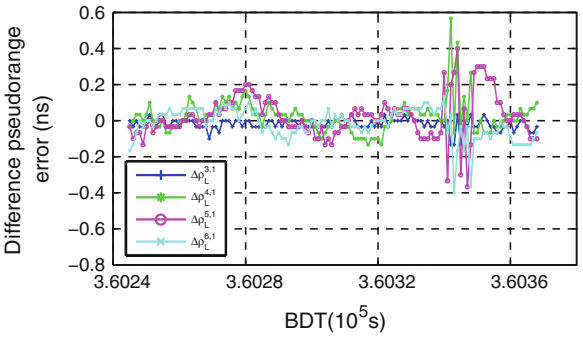

Fig. 31.13 Different pseudorange versus time

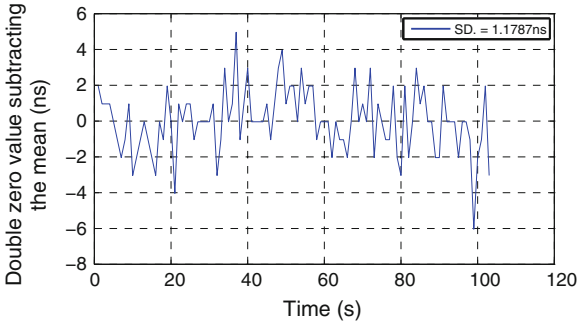

Fig. 31.14 RDSS double zero versus time

Table 31.3 Difference pseudorange accuracy of CRDSS position fixing and report

Difference pseudorange	$\Delta\rho_L^{3,1}$	$\Delta\rho_L^{4,1}$	$\Delta\rho_L^{5,1}$	$\Delta\rho_L^{6,1}$	$\Delta\rho_L^{7,1}$	$\Delta\rho_L^{8,1}$	$\Delta\rho_L^{12,1}$
RMS error (ns)	0.0360	0.095	0.122	0.0856	0.0968	0.107	0.165

31.5 Conclusions

As a conclusion, the simulation models are proposed and analyzed based on the dual-mode receiver's test requirements. The discussion here focuses on the transmitting time iterative model, satellite orbit approximation model and the ways to improve model accuracy. Finally, the implementation of the simulator and the analysis of the two simulator-based experimental result with the prototype receiver are given. Compared with the existing simulator, the BDS dual-model simulator can simulate the RDSS and RNSS signal simultaneously to support all types of BDS receiver's performance evaluation, such as RDSS, RNSS and dual-mode receiver. The test results indicate that the accuracy of position and velocity is 9.3 m and 0.099 m/s, respectively. Even more importantly, the function of CRDSS can also be validated, with the accuracy of difference pseudorange and double zero value less than 0.1 and 1 ns. Therefore, the BDS dual-model's design completely meets the test requirements.

References

1. Winkel J, Wolf R et al (2006) The merlin signal generator—a powerful, low-cost constellation Galileo/GPS signal simulator. 19th ION GNSS, TX
2. Guenter H, Markus I et al (2007) NavX®-NCS—the first Galileo/GPS full RF navigation constellation simulator. 20th ION GNSS, TX
3. Artaud G, de Latour A et al (2010) A new GNSS multi constellation simulator: NAVYS. 23rd ION GNSS, Portland, USA
4. Rui Li, Dazhi Zeng et al (2010) Architecture and implementation of an universal real-time GNSS signal simulator. ION 2010 international technical meeting, San Diego, CA
5. GéBerglez P, Wasle E et al (2009) GNSS constellation and performance simulator for testing and certification. 22nd ION GNSS, Savannah, GA
6. Li G, Zhu M (2001) The study of real-time simulation for the radio determination satellite service (RDSS). Modeling and simulation in distributed applications, Changsha, CA
7. Zhang G, Sun C (2005) Simulation and implementation of BD-1 dynamic navigation signals. J Syst Simul 17(11):2731–2733
8. China Satellite Navigation Office (2011) Development of BeiDou navigation satellite system: NAVYS. 24th ION GNSS, Portland, USA
9. Tan S (2009) Theory and application of comprehensive RDSS position and report. Acta Geodaetica et Cartographica Sinica. 38(1):1–5
10. Lee WJ, Ronald DR (1982) Numerical analysis. Addison-Wesley Publishing Company, Massachusetts
11. Tong H, Sha H et al (2012) A high-precision and real-time interpolation method for satellite orbit in GNSS. J Navig Univ Defense Technol 34(2):59–63

Chapter 32
Analysis of Ranging and Positioning Performance Influenced by Signal Coherence Parameters

Chengtao Xu, Xiaomei Tang, Xiaofeng Ouyang and Feixue Wang

Abstract Multi-band, multi-service and multi-modulation are new trends of GNSS development. Since novel modulation types like BOC/MBOC and multiplex techniques of navigation signals have been utilized, the composite navigation performance is indeed improved. With increased modulated signals broadcasting on single frequency in satellite, Signal coherence parameter has become one of the most important monitoring parameter. For satellite navigation system, the coherence of phases between pseudo-random codes and between carriers are the prerequisite for realization to pseudo-random code ranging and carrier phase ranging, and they are also two of the main factors affecting on the satellite signal system. This paper discusses how the coherence of phases between pseudo-random codes, between carriers and between carrier and code affect pseudo-random range measurement, carrier phase range measurement and carrier phase smoothing pseudo range process. Furthermore, the relationship between code minus carrier and code phase carrier phase coherence is discussed. Then, the positioning error and code minus carrier measurement is given by the simulation of carrier phase smoothing pseudo range process. In the end, we test code minus carrier parameter and code phase carrier phase coherence parameter using the system built by ourselves.

Keywords Carrier phase · Code phase · Carrier code coherence · CMC (code minus carrier) · Signal quality monitoring

32.1 Introduction

GNSS (Global Navigation Satellite System) signal quality monitoring and evaluation is one significant part in navigation system design and operation as it can

C. Xu (✉) · X. Tang · X. Ouyang · F. Wang
Satellite Navigation and Positioning Research and Development Center,
Electronic Science and Engineering School, National University of Defense Technology,
Changsha, China
e-mail: xct1130@gmail.com

J. Sun et al. (eds.), *China Satellite Navigation Conference (CSNC) 2013 Proceedings*, Lecture Notes in Electrical Engineering 243,
DOI: 10.1007/978-3-642-37398-5_32,

Table 32.1 List of signal quality monitoring parameters

Classification	Parameters
Frequency	Power spectrum, stray in-band, stray out-of-band, phase noise
Modulation	Constellation, vector graph phase error, magnitude error, error vector magnitude, IQ offset, peak to average envelope ratio
Correlation	Correlation peak, S curve, correlation loss, T offset, signal power, eye diagram, group delay
Ranging	Code phase coherence, IQ quadrature, code phase carrier phase coherence
Time	Ranging code, navigation data, signal voltage distribution histogram

support the signal design and gordian technique in-orbit test verification. Though the navigation signal monitoring and evaluation is mainly a comprehensive measurement of satellite navigation system own performance, it is related to the user application performance [1, 2]. Frequently used monitoring parameters are listed in Table 32.1.

The system performance requirement from users can be separated into four areas—precision, integrity, consistency and availability [3], in which the precision is the foundation of other performance requirements. In the signal monitoring system, signal coherence is of great value since and its inner connection to the navigation performance needs to be studied (Fig. 32.1).

This paper analysed the relationship between signal coherence parameter and ranging precision based on a software receiver and tests is performed using signals from different navigation systems.

32.2 Theory Analysis

32.2.1 Code Coherence Parameter

In modernized system, satellite multiplex efficiency has been enhanced as several signals are broadcast from one satellite frequency band. Ideally, different signals from the same satellite should keep in synchronization. Thus, the phase offset between different codes is defined as code coherence. Now presume that one satellite broadcasts m synchronized signals, and the number k signal in the number i satellite has a phase offset δ_{ck} following the normal distribution as $\delta_{\mathrm{ck}} \sim \mathrm{N}(\mu_{\mathrm{k}}, \sigma_{\mathrm{k}}^2)$. Then the code coherence between k2 signal and k1 signal is $\varepsilon_{c_{k1,k2}}^{(i)} = \delta_{ck2} - \delta_{ck1}$. Assuming that different δ_{ck} are mutual independent, therefore the code coherence parameter is normal distributed as $\varepsilon \sim \mathrm{N}(\mu_{\mathrm{k2}} - \mu_{\mathrm{k1}}, \sigma_{\mathrm{k1}}^2 + \sigma_{\mathrm{k2}}^2)$. We believe $\mu_{\mathrm{k}} = 0$ in general situations.

When the error parts from satellite to receiver measurements is mutual independent, the user ranging error of k1 signal will increase $\sigma_{\mathrm{k1}}^2 - \sigma_{\mathrm{k2}}^2$ compared to k2 signal. Meanwhile, the pseudo range will shift

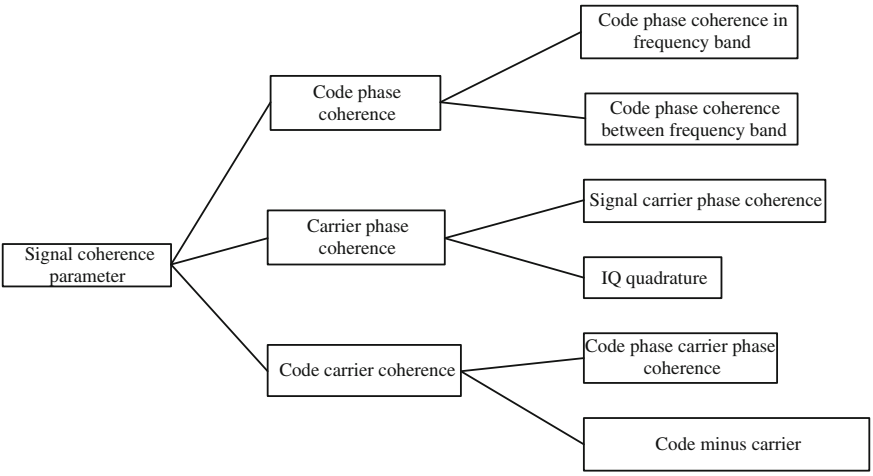

Fig. 32.1 Classification of signal coherence parameter

$$\delta_R = c(\mu_{k2} - \mu_{k1}) \tag{32.1}$$

However, this range offset will be included in the clock error if receiver uses same signal from each satellite in positioning operation. Inversely, the range offset will not be absorbed in clock error if the receiver uses different signals from different satellites, as they have unequal distribution in different satellites.

32.2.2 Code Carrier Coherence Parameter

In high-precision positioning applications, carrier phase smoothing pseudo range technique is often involved to improve measurement precision. Code carrier coherence parameter implies the coherence between code phase and carrier phase [4–6].

Assume the pseudo range measurement of GNSS receiver is ρ and the carrier phase measurement is Φ, and they can be expressed as,

$$\rho(t) = \begin{cases} r(t) + c[\delta t_u(t) - \delta t^s(t-\tau)] \\ +I(t) + T(t) + \varepsilon_\rho(t) \end{cases} \tag{32.2}$$

$$\Phi(t) = \lambda\phi(t) = \begin{cases} r(t) + c[\delta t_u(t) - \delta t^s(t-\tau)] \\ -I(t) + T(t) + \lambda N + \varepsilon_\phi(t) \end{cases} \tag{32.3}$$

in which, r represents the distance between satellite and receiver, I represents the Ionosphere error, T represents the Troposphere error, N represents the carrier phase ambiguity, $\delta t_u(t) - \delta t^s(t-\tau)$ represents clock error of satellite and receiver, c represents light speed, λ represents the wavelength of carrier, ε_ρ(t) represents the

measurement error of code caused by receiver and multipath, $\varepsilon_\Phi(t)$ represents the measurement error of carrier caused by receiver and multipath. Code carrier coherence parameter consists of two items according to the calculation methods, and they are code minus carrier and code phase carrier phase coherence.

Code minus carrier measurement is defined as

$$\delta_{CMC}(t) = \rho(t) - \Phi(t) \tag{32.4}$$

Code phase carrier phase coherence is defined as [2]

$$\delta_{cc} = \left| \frac{f_{code}}{f_{code0}} - \frac{f_{carrier}}{f_{carrier0}} \right| = \left| \frac{\Delta f_{code}}{f_{code0}} - \frac{\Delta f_{carrier}}{f_{carrier0}} \right| \tag{32.5}$$

This comes from the requirement of WAAS (Wide Area Augmentation System) from the USA authority. Δf represents the anomalous variation of code or carrier frequency. To do the differential of code minus carrier,

$$d\frac{\delta_{CMC}}{dt} = \frac{\frac{d\rho}{\lambda} * 360 - d\Phi}{dt} = \frac{\frac{dc_p}{\lambda} * c * 360 - d\phi}{dt} \tag{32.6}$$

c_p represents the code phase measurement, φ represents the carrier phase measurements with unknown phase ambiguity. Further analysis shows,

$$\begin{aligned} d\frac{\delta_{CMC}}{dt} &= \frac{\frac{dc_p}{\lambda} * c * 360 - d\phi}{dt} \\ &= \frac{[(f_{code} + \Delta f_{code} - f_{code})dt/f_{code0}] * f_{carrier0} - (f_{carrier} + \Delta f_{carrier} - f_{carrier})dt}{dt/360} \\ &= 360 * f_{carrier0}\left(\frac{\Delta f_{code}}{f_{code0}} - \frac{\Delta f_{carrier}}{f_{carrier0}}\right) \\ &= 360 * f_{carrier0}\delta_{cc} \end{aligned} \tag{32.7}$$

Accordingly, the differential of code minus carrier equals code phase carrier phase coherence times a constant. The code minus carrier measurement represents the difference between code and carrier ranging results, while the code phase carrier phase coherence represents the variance ratio of ranging results. Moreover, they differ in calculation methods. Code minus carrier measurement is calculated using results from information processing level and code phase carrier phase coherence measurement is calculated using results from signal processing level.

One real-time application of carrier phase smoothing pseudo range can be expressed as

$$\overline{\rho(t_i)} = \frac{1}{i}\rho(t_i) + \frac{i-1}{i}\left[\overline{\rho(t_{i-1})} - \Delta\Phi(t_{i-1}, t_i)\right] \tag{32.8}$$

An afterwards application of carrier phase smoothing pseudo range can be expressed as

$$\overline{\rho(t_i)} = \overline{\rho(t_1)} + \Delta\Phi(t_i, t_1) \tag{32.9}$$

In which, $\overline{\rho(t_i)}$ represents the smoothed pseudo range in i epoch, $\overline{\rho(t_1)}$ represents the smoothed pseudo range in start epoch.

$$\overline{\rho(t_1)} = \frac{1}{M}\sum_{i=1}^{M}[\rho(t_1)]_i \tag{32.10}$$

And M is a preset constant.

It can be proved that the results of real-time carrier phase smoothing pseudo range could be represented by code minus carrier measurement from several epochs as shown in Eq. 32.11.

$$\overline{\rho(t_i)} = \frac{1}{i}\sum_{j=1}^{i}\delta_{CMC}(t_j) + \Phi(t_i) \tag{32.11}$$

Similarly, we have the results of afterwards carrier phase smoothing pseudo range could be represented by code minus carrier measurement from several epochs as shown in Eq. 32.12.

$$\overline{\rho(t_i)} = \sum_{j=1}^{k}\frac{1}{k}\delta_{cc}(t_j) + \Phi(t_i) \tag{32.12}$$

It shows that the results of carrier phase smoothing pseudo range uses the code minus carrier measurement from several epochs to estimate the pseudo range.

The carrier phase measurement can provide more accurate ranging results under a stable condition, thus improve the precision of carrier phase smoothing pseudo range than the pure pseudo range measurement. In the calculation, the carrier phase ambiguity is cancelled out by carrier phase differentiation and only carrier cycle jump should be taken into consideration, which makes it easier to use. Consequently, the code carrier coherence becomes the precondition to improve the precision of carrier smoothing pseudo range. If there is an abnormal phase error happens, the code minus carrier measurement will be affected and introduces a ranging error into positioning results [7].

Assume the code minus carrier measurement varies near the theoretical value, and the standard error is σ_{CMC} angle. Thus the precision of real-time carrier phase smoothing pseudo range is,

$$\sigma = \frac{c}{360f}\frac{\sigma_{CMC}}{\sqrt{L}} \tag{32.13}$$

And the precision of afterwards carrier phase smoothing pseudo range is

$$\sigma = \frac{c}{360 \cdot f}\frac{\sigma_{CMC}}{\sqrt{k}} \tag{32.14}$$

In which, t represents the smoothing length, c represents light speed, f represents carrier frequency, L represents epoch number per smooth period. The simulation of relationship between carrier phase smoothing pseudo range and code minus carrier is shown in Figs. 32.2, 32.3 and 32.4. A section data of 2000s containing pseudo range and carrier phase from GPS L1 receiver is utilized in the simulation calculating code minus carrier in the carrier phase smoothing pseudo range. Multipath error, ionosphere error and other errors are included in the pseudo range and carrier phase. Assuming the variance of code multipath error is 0.3 m; the variance of carrier multipath error is 0.002 m, the variance of code ionosphere error is 1 m and the variance of other error is 4 m. Moreover, an inherent error of code minus carrier is added, which has an expectation of 1 m and a standard error of 20 m.

From the simulation results we can derive that the average error of code minus carrier measurement caused by signal will greatly influence the carrier smoothing pseudo range results by accumulation of each epoch results. Specifically, the bias of code minus carrier can be accumulated during the smoothing process which lead to an increasing error in the pseudo range.

The standard error of code minus carrier measurement has a slightly influence on the precision of smoothing results because carrier phase smoothing process significantly decrease the variance of pseudo range. And the variance of code minus carrier measurement is mainly affected by the variance of carrier phase.

32.2.3 Carrier Phase Coherence

Traditional IQ quadrature parameter represents the imperfection of carrier phase difference between in-phase and quadrature-phase signal. Consequently, it will affect the ranging precision and positioning accuracy. As for modernized signal, more than two signals are modulated on the carrier, therefore the IQ quadrature

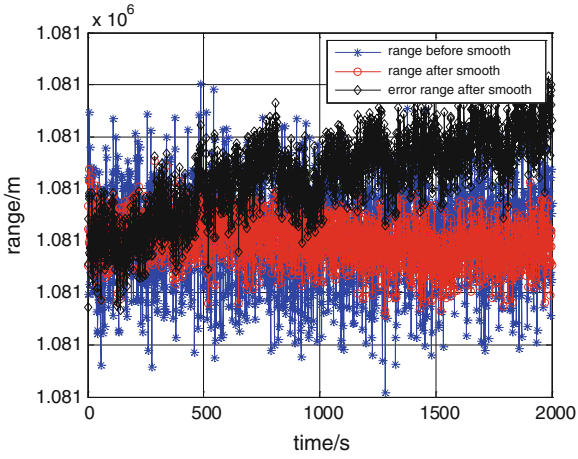

Fig. 32.2 Simulation results of carrier smooth pseudo-range

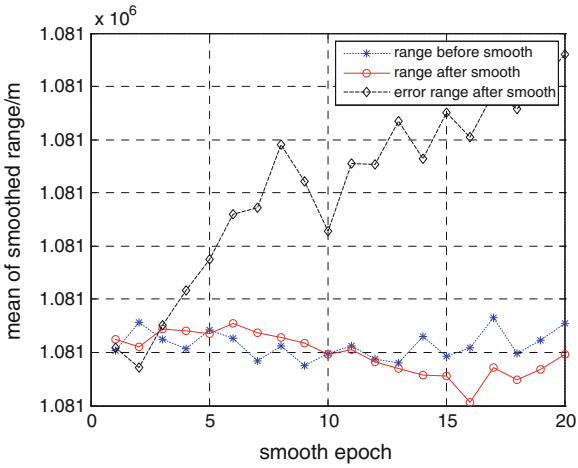

Fig. 32.3 Expectation of pseudo-range after smoothing

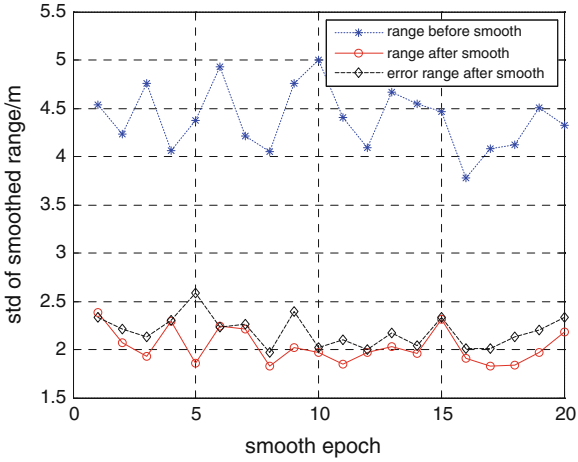

Fig. 32.4 Standard error of pseudo-range after smoothing

parameter can be redefined here as signal carrier phase coherence measurement. The deterioration of carrier phase coherence affect range measurement in a way similar to the code phase coherence.

32.2.4 Test Results

To fully exploit the flexibility of software and high gain signal, a high-gain antenna with software receiver system was adopted to monitor the signal quality from different satellites. The structure of it is shown in Fig. 32.5.

The results of GPS code phase carrier phase coherence is shown in Figs. 32.6 and 32.7.

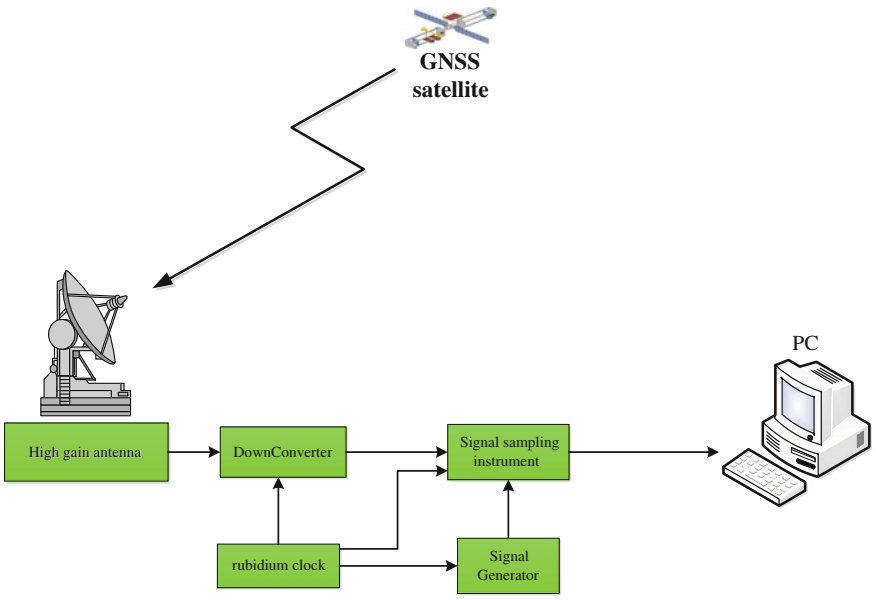

Fig. 32.5 Structure of test system

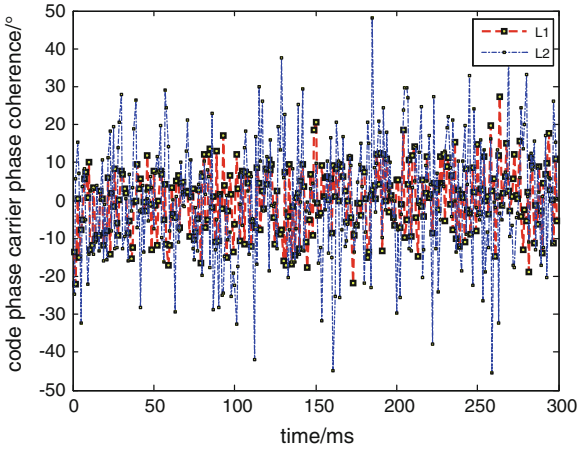

Fig. 32.6 Results of GPS code carrier coherence parameter

It can be concluded that the code phase carrier phase coherence possesses a feature like white noise with a zero mean. The result of code minus carrier measurement after cleaning ionosphere error is shown in Fig. 32.8.

The results of code minus carrier measurement reply the multipath error and measurement precision of receiver, and its fresh frequency is much slower than the code phase carrier phase coherence. Due to the huge difference between code minus carrier and code carrier coherence parameter in time scale, the linearity is

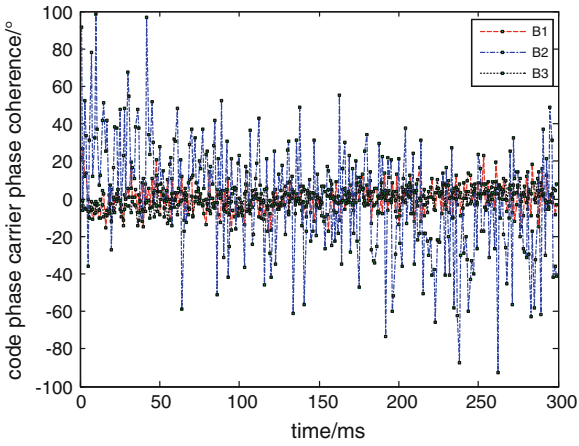

Fig. 32.7 Results of Beidou code carrier coherence parameter

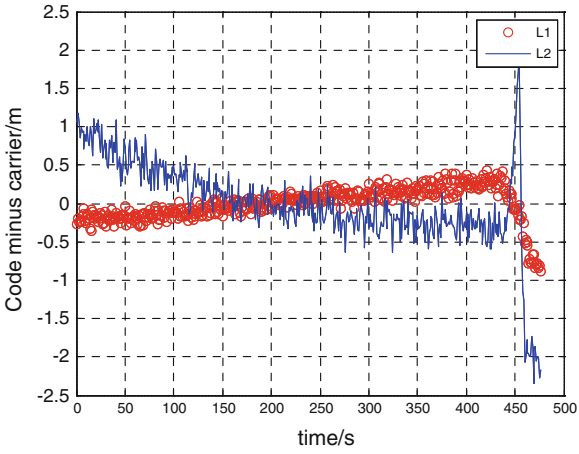

Fig. 32.8 Results of GPS CMC parameter

not verified here. However, it can be seen that the variation of code minus carrier tend to have a zero mean randomness.

32.3 Conclusion

Signal coherence parameter has a direct influence on the code phase ranging and carrier phase ranging and is one of the most important monitoring parameter. This paper discusses how the coherence of phases between pseudo-random codes and carriers affect pseudo-random range measurement and carrier phase range measurement.

The results of carrier phase smoothing pseudo range uses the code minus carrier measurement from several epochs to estimate the pseudo range. Therefore an

abnormal phase error will affect the code minus carrier measurement and introduce a ranging error into positioning results.

Equations show that the differential of code minus carrier has a linear relation of code phase carrier phase coherence. The code minus carrier measurement represents the difference between code and carrier ranging results, while the code phase carrier phase coherence represents the variance ratio of ranging results.

Then, the positioning error and code minus carrier measurement is given by the simulation of carrier phase smoothing pseudo range process. The simulation result shows that the bias of code minus carrier can cause an increasing error of smoothed pseudo range.

In the end, we test code minus carrier parameter and code phase carrier phase coherence parameter using the system built by ourselves. The result shows that code phase carrier phase coherence's feature is similar to white noise and has high precision in time domain. Code minus carrier measurement has a larger time scale than code phase carrier phase coherence and directly linked to the multipath error and noise of receiver.

References

1. Wang H (2010) The study of key technologies of the GNSS navigation signal monitoring, TianJing
2. Jing G, Wang M, Fan J, Feng X (2012) Image of satellite signal quality monitoring. J Guilin Univ Electron Technol 32(5):358–363
3. Xie G (2009) Principles of GPS and receiver design. Publishing House of Electronics Industry, Beijing, p 7
4. Yang Z, Wang W, Meng Y, Geng S, Huang Z (2011) Research of GNSS signal quality assessment and measurement methods. CSNC2011, Shanghai
5. Li C, Huang Z, Wang S, Wang H, Gao S (2012) The Application of carrier phase smoothing Pseudo-range in GPS point positioning, CSNC2012, Guanzhou
6. Cheng F, Lu X, Wang X (2010) Analysis of positioning accuracy affected by signal coherence from satellites, CSNC2010, Beijing
7. Soellner M, Kurzhals C, Hechenblaikner G, Rapisarda M, Burger T, Erker S et al (2008) GNSS offline signal quality assessment, ION GNSS 21st international technical meeting of the satellite division, Savannah, GA

Chapter 33
Analysis of the Pseudorange Multipath Impact on Dual-Frequency Ionospheric Delay Correction in Compass System

Wei Zhao, Na Zhao, Haixing Zhao, Jinxian Zhao, Feng Xue, Caibo Hu and Yan Wang

Abstract The multipath error is the primary pseudorange measuring error factor in Compass system, in dual-frequency positioning mode, it is difficult to be eliminated by modeling methods, and on the contrary, it is always amplified because of the combination of measuring error. As a result, certain kind of user terminal has lower vertical positioning precision under dual-frequency mode than under single-frequency mode. This paper makes simulation of the impact of multipath error on pseudorange UERE under single-band mode and dual-band mode, obtains the interrelation of ionosphere modeling error, multipath error and the vertical positioning precision of single-band and dual-band respectively. This paper extracts multipath error in pseudorange of GEO and IGSO satellite by pseudorange carrier phase combination method, and uses the ionosphere delay calculated by dual-band carrier phase measurements as a benchmark, makes assessment of the ionosphere delay calculated by dual-band pseudorange combination method and ionospheric delay model correction method, analyses the amount of error correction brought into the Compass system by pseudorange of distinct orbit satellite. Data processing results show that, under current multipath mitigation measures, the pseudorange multipath error will cause that the error of GEO satellite ionosphere delay correction measured by dual-band is larger than by single-band, make a reasonable interpretation of the phenomena that dual-band vertical positioning accuracy is lower than single-band vertical positioning accuracy, and the ionospheric delay correction errors brought by pseudorange multipath error of GEO satellites are greater than the IGSO satellites, verify the phenomenon of "standing multipath error" brought by GEO satellite orbital characteristics.

W. Zhao (✉) · N. Zhao · H. Zhao · J. Zhao · F. Xue · C. Hu
The Beijing Satellite Navigation Center, Beijing 100094, China
e-mail: joypla@163.com

Y. Wang
Beijing Institute of Spacecraft System Engineering, Beijing 100094, China

J. Sun et al. (eds.), *China Satellite Navigation Conference (CSNC) 2013 Proceedings*, Lecture Notes in Electrical Engineering 243,
DOI: 10.1007/978-3-642-37398-5_33,

Keywords Compass system · Pseudorange multipath effect · Vertical positioning accuracy · Dual-band ionosphere delay correction

33.1 Introduction

Global Navigation Satellite Systems (GNSS) is a spatial information infrastructure which could provide a variety of users high-precision positioning and timing (PNT) and other navigation services all times all day. The positioning error of the user in satellite navigation systems is affected by various factors, such as tropospheric and ionospheric delay error, broadcast clock error, broadcast ephemeris error and multipath error, which are the primary factor of restricting the precision of the navigation receivers.

Broadcast clock error, broadcast ephemeris error can be eliminated by difference correction; tropospheric error can be eliminated by simulated modeling. Ionosphere delay error correction is an important part of the user terminal positioning in satellite navigation system. Generally speaking, single-band terminal uses ionospheric model to calculate ionospheric delay, the correction accuracy depends on the accuracy of the ionosphere model used; meanwhile dual-band terminal uses pseudorange combination method to calculate ionospheric delay, the correction accuracy is affected by the pseudorange measuring precision. The ionospheric delay model error of the GPS system is about 1–5 m which could substantially correct 50 % real ionospheric delay error, meanwhile the ionospheric delay error measured by the dual-band pseudo-ranges measurement is only about 1 cm which is much smaller, and therefore precision positioning users generally use the dual-band pseudo-ranges measurement to calculate ionosphere delay.

Different from the Single MEO satellite constellation in the GPS system, the Compass satellite navigation system constellation is mixed with GEO, IGSO, and MEO satellite. Limited by the number of satellites (five GEO satellites, five IGSO satellite, and four MEO satellite) and satellite orbits, GEO and IGSO satellites is longer visible meanwhile the positioning accuracy is widely influenced by GEO and IGSO satellites to the Compass system users. About the MEO satellite pseudorange multipath effects in the measurement error the domestic and foreign scholars have already done a lot of research on the GPS system and brought forward a lot of multipath mitigation method of pseudorange measurement. For the GEO satellites, foreign satellite-based augmentation system experts discovered the "standing multipath error" phenomenon in GEO satellite pseudorange in GEO navigation signals ranging study [1]. For the IGSO satellite pseudorange measurement error, there are few research at home and abroad, along with the completion of Compass system in recent years, the research on GEO and IGSO satellite pseudorange measurement errors are gradually increased [2].

According to the importance of the dual-frequency pseudo-range positioning in the high-precision measurement, it is significant to study the effect of different

types satellite pseudorange multipath error on the dual-frequency ionosphere delay calculated error in Compass System, it can guide the user machine manufacturers take corresponding multipath mitigation measures for different multipath errors.

33.2 Analysis of the Multipath Error Impact on Vertical Positioning Accuracy of Single-Band and Dual-Band Mode

33.2.1 Multipath Signal Characteristic

In Satellite navigation system, the navigation signal will become reduced, reflected and phasic deflexed in broadcasting procession from the satellite to the receiver due to buildings, trees, and other obstacles. This effect makes the signal which arrives at the receiver antenna superimposed to a plurality of propagation path signal. Due to the difference of the transmission paths, it exists relative phase and the relative delay among the direct signals, the reflected and the scattered signals in addition to the amplitude characteristics differences which resulting in signals entry into the receiving loop distorted and the correlation peak identification curve zero offsets, thus it could affect the users in measuring ranging accuracy. The multipath signal generation mechanism and variation cannot be described in specific environmental model as the random characteristics [3].

33.2.2 Test Results

To verify the effect multipath error on the single dual-frequency positioning accuracy, a single dual-frequency positioning test is practiced in Beijing area. As single dual-frequency positioning mode mainly varies in ionospheric delay calculation, the test mainly focuses on analyzing the difference of the vertical positioning accuracy between the two modes. The user terminal uses the basic multipath mitigation measures during the test. The vertical positioning results of single-band and dual-band in 24 h are showed below (Fig 33.1).

Under single-frequency mode, vertical positioning errors RMS statistics results within 24 h are 5.21 m (1σ). Under dual-frequency mode, vertical positioning errors RMS statistics results within 24 h are 8.20 m (1σ). It will be seen that in the case of consistent VDOP value and basic multipath mitigation measures, the vertical positioning accuracy of dual-band is less than single-band.

In Compass system, single-band receiver makes use of ionosphere model parameters from navigation message to calculate vertical ionospheric delay, so the calculation accuracy of ionospheric delay is not related to pseudorange

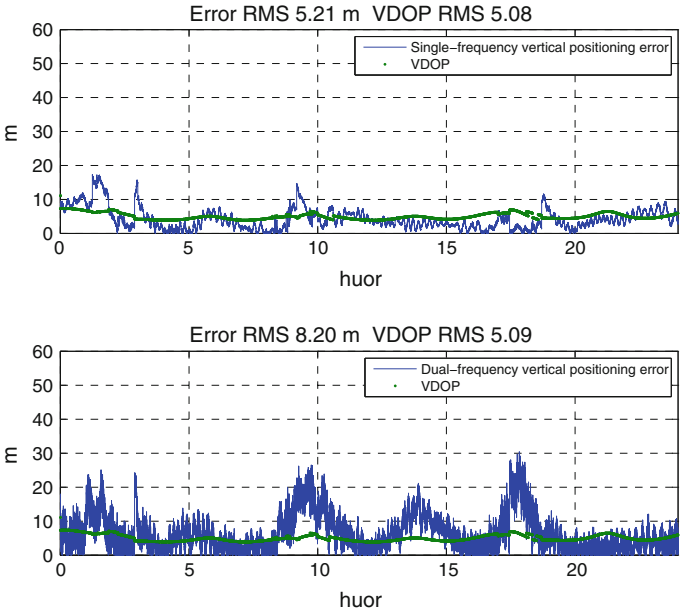

Fig. 33.1 Stat: vertical positioning error results of *single-band* and *dual-band* in 24 h

measurement accuracy. Under the B1B3 dual-frequency pseudorange positioning mode, B1 ionospheric delay could be calculated as following:

$$\Delta S_{B1} = \left(\frac{f_{B3}^2}{f_{B3}^2 - f_{B1}^2}\right)(\rho_{B1} - \rho_{B3}) \tag{15.1}$$

Where ΔS_{B1} is the ionospheric delay value in the B1 pseudorange measurement, f_{B1} is the frequency value of B1, f_{B3} is the frequency value of B3, ρ_{B1} and ρ_{B3} are the pseudorange measuring value of B1 and B3. The ionosphere delay value in B3 could be calculated through the ionosphere delay value in B1 multiplied with a constant.

$$\Delta S_{B3} = (f_{B1}/f_{B3})^2 \cdot \Delta S_{B1} \tag{15.2}$$

After using the ionospheric delay correction amount respectively calculated in the formula (15.1) and formula (15.2) to correct the pseudorange measurements amount in B1 and B3, the corrected pseudorange measurement values could be marked as ρ'_{B1} and ρ'_{B3}.

$$\begin{aligned}\rho'_{B1} &= \rho_{B1} - \Delta S_{B1} = \frac{f_{B1}^2}{f_{B1}^2 - f_{B3}^2}\rho_{B1} - \frac{f_{B3}^2}{f_{B1}^2 - f_{B3}^2}\rho_{B3} \\ &= 2.944\rho_{B1} - 1.944\rho_{B3}\end{aligned}$$

$$\rho'_{B3} = \rho_{B3} - \Delta S_{B3} = \frac{f_{B1}^2}{f_{B1}^2 - f_{B3}^2}\rho_{B1} - \frac{f_{B3}^2}{f_{B1}^2 - f_{B3}^2}\rho_{B3}$$
$$= 2.944\rho_{B1} - 1.944\rho_{B3}$$

According to the formula above, the corrected pseudorange measurements amount in B1 is equal to the corrected pseudorange measurements amount in B3. Assuming the pseudorange measurement error and receiver noise is unrelated with each other meanwhile they have equal variances in B1 and B3 frequency point, then the measurement error of corrected pseudorange measurement value ρ'_{B1} or ρ'_{B3} is 3.528 times ($\sqrt{2.944^2 + 1.944^2}$) of single-frequency pseudorange measurement error variance.

There are two factors which could affect the user machine pseudorange measurement accuracy: the receiver noise resolution and multipath effects error. The noise and resolution error of a typical modern receiver is about 1 dm (1σ) and it is much smaller under the normal condition (no external interference) which is negligible compared with the error caused by the multipath effect.

33.2.3 UERE Error Factors Simulation in Ionosphere Delay Correction Calculation

To analyze the reason that results in the vertical accuracy of dual-band less than single-band, a thematic simulation test is made to verify how the single dual-frequency positioning accuracy impacted by the multipath error. The pseudorange error distribution follows the rule of Gaussian; therefore the vertical error distribution follows the rule of Gaussian too. It could be expressed as following:

$$V_{Error} = VDOP \cdot \sigma_{UERE} \tag{15.3}$$

Where VDOP is vertical accuracy factor, σ_{UERE} is the pseudorange error factor. In the test in Sect. 33.2.2, the VDOP values are basically the same in both positioning mode, therefore the pseudorange error factor is the main factor resulting in difference between dual-band and single-band vertical positioning accuracy. The single-band and dual-band pseudorange error factor can be expressed as following:

$$\begin{cases} \sigma_{UERE,s} = \sqrt{\sigma_{Clock}^2 + \sigma_{Eph}^2 + \sigma_{Ion,s}^2 + \sigma_{Tro}^2 + \sigma_{Mp}^2 + \sigma_{Noise}^2} \\ \sigma_{UERE,d} = \sqrt{\sigma_{Clock}^2 + \sigma_{Eph}^2 + \sigma_{Ion,d}^2 + \sigma_{Tro}^2 + \sigma_{Mp}^2 + \sigma_{Noise}^2} \end{cases} \tag{15.4}$$

Where σ_{Clock} is broadcast clock error factor, σ_{Eph} is broadcast ephemeris error factor, $\sigma_{Ion,s}$ and $\sigma_{Ion,d}$ represent single-band ionospheric delay error factor and ionospheric delay model error factor respectively, σ_{Tro} is tropospheric delay error factor, σ_{Mp} is Multipath error factor and σ_{Noise} is receiver noise error. So it is

obvious that the single and dual positioning mode is only different in the error term of the ionospheric delay correction.

Assuming the pseudorange measurement error and receiver noise is unrelated with each other meanwhile they have equal variances in B1 and B3 frequency point, the relationship between the ionospheric delay correct error and the multipath error in dual-frequency positioning mode could be concluded through formula (15.1) in the case that the receiver noise error is ignored. Take B1 frequency point as an example.

$$\sigma_{Ion,d} = \sqrt{2} \cdot \left(\frac{f_{B3}^2}{f_{B1}^2 - f_{B3}^2} \right) \cdot \sigma_{Mp} = 2.749 \sigma_{Mp} \tag{15.5}$$

Substitute formula (15.5) into formula (15.4), the result is as following:

$$\sigma_{UERE,d}^2 - \sigma_{UERE,s}^2 = 7.55 \sigma_{Mp}^2 - \sigma_{Icon,s}^2 \tag{15.6}$$

According to the typical UERE budget of GPS precise positioning service and standard positioning service in Ref. [3], if we take the $\sigma_{Ion,s}$ as the maximum value of 7 and take the σ_{Mp} as the maximum value of 3, the value of $\sigma_{UERE,d}^2 - \sigma_{UERE,s}^2$ could be expressed in the figure following below.

In Fig. 33.2, the X-axis represents σ_{Mp}, Y-axis represents $\sigma_{Ion,s}$, Z-axis represents $\sigma_{UERE,d}^2 - \sigma_{UERE,s}^2$. Therefore, in the diagram the region above 0 in Z-axis indicates that the dual-frequency pseudo-range error factor is larger than the ionosphere delay model error factor, according to the formula (15.3), the region above 0 in Z-axis represents dual-frequency vertical positioning error is greater

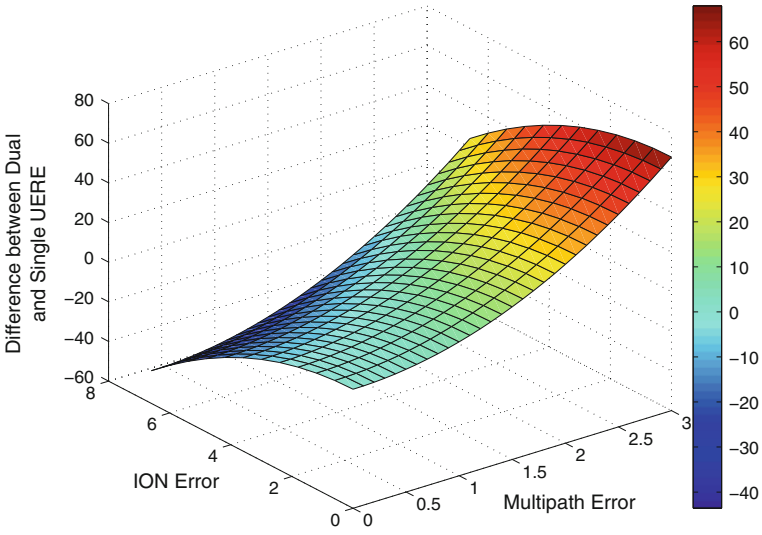

Fig. 33.2 *Curve* analysis of the impact of multipath error factor and ionosphere delay model error factor on *single-band* and *dual-band* pseudorange UERE

than single-frequency vertical positioning error. According to Fig. 33.2 although the UERE budget value of the ionospheric delay model error factor is greater than the UERE budget value of the multipath error factor, σ_{Mp} still has bigger influence than $\sigma_{Ion,s}$ to the $\sigma^2_{UERE,d} - \sigma^2_{UERE,s}$ because of 7.55 times coefficient to the multipath error factor. In another word, the increased multipath error factor has greater influence to the dual-band UERE than ionospheric delay model error factor to single frequency UERE. As the fitting accuracy of single frequency ionospheric model is a little higher in Beijing Area, under the condition of without taking effective multipath mitigation measures, the situation in Sect. 33.2.2 that dual-frequency vertical positioning accuracy is lower than single-frequency vertical positioning accuracy in the single dual-frequency positioning test will happen.

33.3 Analysis of Multipath Error Effect on Ionosphere Delay Correction Calculation

33.3.1 Analysis of Multipath Error Characteristics for Satellites of Different Orbit

In order to analyze the influence of multipath error in pseudorange to the ionospheric delay correction amount, multipath error should be extracted from the pseudorange measurements value.

According to the pseudorange multipath error analysis method through dual-frequency pseudorange and carrier phase combination observations [4] put forward by professor Kee and Parkinson, the pseudo-range carrier phase observations measurements of B1 and B3 could be defined as followed:

$$M_{P1} = P_1 + \frac{1+\alpha_{13}}{1-\alpha_{13}}\varphi_1 \cdot \lambda_1 - \frac{2}{1-\alpha_{13}}\varphi_3 \cdot \lambda_3$$

$$M_{P3} = P_3 + \frac{2\alpha_{13}}{1-\alpha_{13}}\varphi_1 \cdot \lambda_1 - \frac{1+\alpha_{13}}{1-\alpha_{13}}\varphi_3 \cdot \lambda_3$$

Where P_1 and P_3 are pseudorange measurements of B1 and B3, φ_1 and φ_3 are carrier phase measurements of B1 and B3, λ_1 and λ_3 are the wavelength of B1 and B3. $\alpha_{13} = f_1^2/f_3^2, f_1, f_3$ are the frequencies of B1 and B3.

Under the circumstances of no cycle slips phenomenon in the carrier phase observations, M_{P1} and M_{P2} reflect the other external environmental effect on pseudorange data at each frequency point, i.e., multipath error.

Based on the multipath error extraction methods above, we calculate the pseudo-range multipath error in 24 h of two GEO satellites and two IGSO satellites in Beijing area according to the receiver data in the test (as the visual arc of MEO satellite is less than four hours, so it is not included in the statistical result). The result is displayed in Fig. 33.3.

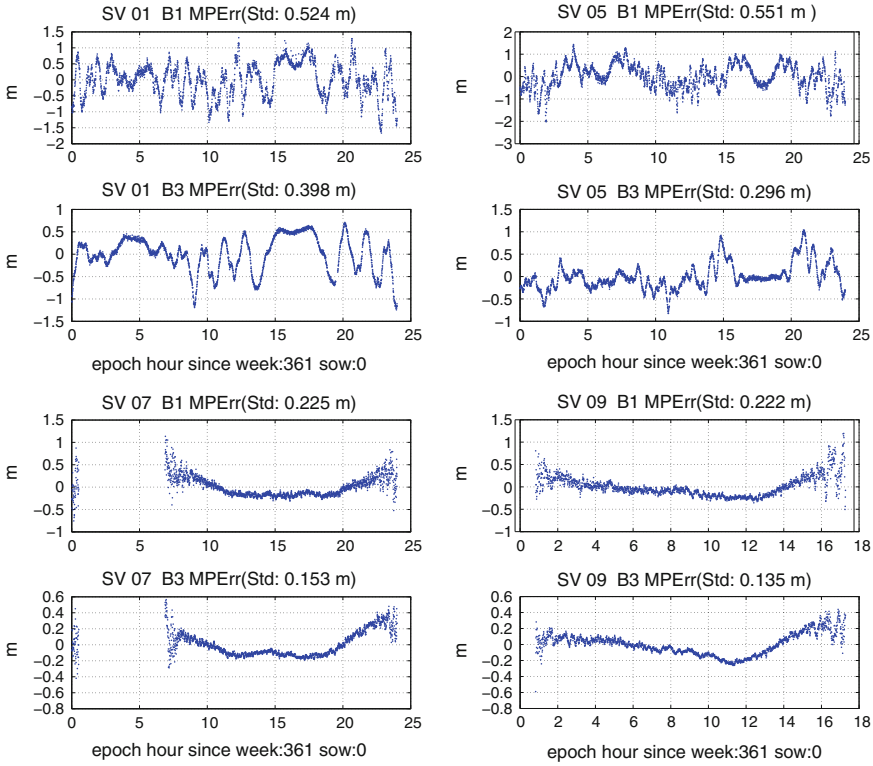

Fig. 33.3 Stat: standard error of GEO/IGSO pseudorange multipath error in 24 h

In Fig. 33.3 the upper two diagrams are the results of the GEO satellite multipath error extraction, and the below two diagrams are the results of the IGSO satellite multipath error extraction. According to diagram, the GEO satellite multipath shows cycle characteristics obviously. As the multipath error is related to the observation angle, the multipath error of the IGSO satellite is increased obviously during immigration and departure. The statistical results of the multipath error are showed in Table 33.1.

In Table 33.1, SV01 and SV02 are GEO satellites, SV03 and SV04 are IGSO satellites. According to Table 33.1, as the multipath signals are influenced by code rate, in the case that code rate in B1 frequency is less than that in B3 frequency, the multipath error standard deviation statistical results of B1 frequency is always

Table 33.1 The statics result of standard error of GEO/IGSO satellite pseudorange multipath error in 24 h

Satellite no	SV01	SV02	SV03	SV04
B1	0.52	0.55	0.23	0.22
B3	0.40	0.30	0.15	0.14

greater than B3 frequency for both GEO and IGSO satellite, meanwhile the multipath error standard deviation statistical results of B1 and B3 frequency points of GEO satellite are always greater than IGSO satellite. For the multipath errors caused by the moving-orbit satellite (IGSO satellite), as its signal time disguise is comparatively faster to the constant of receiver track ring, it would be smoothing processed in the receiver end. But as the multipath signal of the GEO satellite is slowly time disguised, it could not be smoothing processed in the receiver end, as a result it will cause a time-invariant error term which could verify the "standing multipath error" of GEO satellite mentioned in Ref. [1].

33.3.2 The Comparison of Ionosphere Delay Calculation Error Between Single-Band and Dual-Band Mode

In order to verify the error value which is brought by the multipath error when using dual-frequency pseudorange method to measure the ionosphere delay error, we design the tests following below to calculate the ionospheric delay amount measured by the ionospheric delay model method and dual-frequency pseudo-range method of different types of satellites. While using the dual-band carrier phase measurements to calculate the amount of ionospheric delay, we complete the ionospheric delay calculation accuracy evaluation in the single and dual-frequency model through compared the ionospheric delay amount measured by the ionospheric delay model method, dual-frequency pseudo-range method to dual-frequency carrier phase method respectively.

Using dual-band ionosphere delay calculation method in Sect. 2.3, choosing two GEO satellites and two IGSO satellite which involved in positioning test in Sect. 2.2 (MEO satellites' visual arc less than four hours, not included in the statistics), calculate the ionospheric delay amount, indicated in Fig. 33.4 by the red curve; calculate ionosphere delay amount of B3 using the ionospheric model parameters at the same time segment, indicated in Fig. 33.4 by the blue curve; calculate ionospheric delay amount of B3 using dual-band carrier phase, indicated in Fig. 33.4 by the green curve.

Eliminate cycle slips in the carrier phase measurements; take the amount of ionosphere delay calculated by the dual-band carrier phase mode as a benchmark, make statistics of the ionospheric delay errors for each satellite calculated by ionospheric model parameters and dual-band pseudorange method respectively. The calculation results are shown in Table 33.2.

According to Table 33.2, the ionospheric delay error calculated through dual-frequency pseudorange measurements of GEO satellite is greater than IGSO satellite. It verifies that the characteristics of GEO satellite orbit causes its pseudo-range multipath signals have periodic slowly changing characteristic which make it could be hardly eliminated at the receiver end. Meanwhile it results in ionospheric delay error measured by the dual-frequency pseudorange calculation of

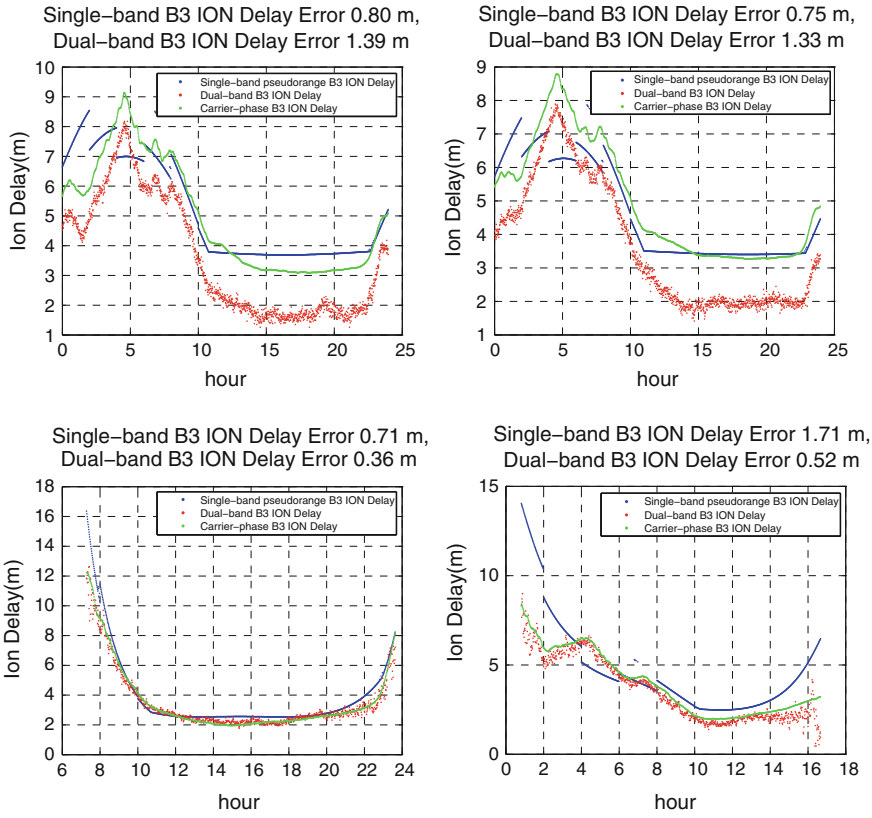

Fig. 33.4 Stat: the standard error of ionosphere delay error of GEO/IGSO satellites in 24 h

Table 33.2 The resulting data of ionosphere delay error for different calculation mode

Satellite no	SV01	SV02	SV03	SV04
Single-band model method	0.80	0.75	0.71	1.71
Dual-band pseudorange method	1.39	1.33	0.36	0.52

GEO satellite is greater than ionospheric delay error measured by ionospheric delay model method. As the fading frequency rate of the pseudorange multipath signal of IGSO satellite is greater, the receiver could filters the signals out during processing it, so the ionospheric delay accuracy measured by the dual-frequency pseudo-range method of IGSO satellite is greater than ionospheric delay model method. In Compass system, due to the limited visible time of the IGSO and MEO satellite, in order to receive a better observation DOP value, it is inevitable to select more GEO satellite to position. When the ionospheric delay accuracy measured by the dual-frequency pseudorange method of GEO satellite is lower than ionospheric delay accuracy measured by the ionospheric delay model method,

the dual-frequency positioning vertical accuracy could be lower than the single frequency positioning vertical accuracy.

33.4 Conclusions

The multipath error is the main pseudorange measuring error factor in Compass system, under dual-band positioning mode; it does not only affect the pseudorange ranging accuracy, but will be amplified because of the combination of measuring, resulting in the phenomenon that vertical positioning accuracy of dual-band less than single-band when proceeding dual-band positioning. This article makes a reasonable interpretation for the phenomenon that multipath errors leading to the dual-band vertical positioning accuracy less than single-band from pseudorange UERE error factor simulation, pseudorange multipath extraction and analysis of ionospheric delay error, and gives the multipath error characteristics of different orbit satellites, thus provides a useful reference for the research of multipath mitigation in receiver end.

References

1. Schempp T, Burker J, Rubin A (2008) WAAS Benefits of GEO Ranging. Proceedings of ION GNSS 2008:1903–1910
2. Gao Y, Cui M (2012) The analysis and simulation of multipath error fading characterization in different satellite orbits. China satellite navigation conference (CSNC) 2012 proceedings, LNEE 161, p 297
3. Kaplan ED (2002) Understanding GPS principles and applications, Publishing House of Electronics Industry in 2002, Beijing, pp 208–210
4. Kee C, Parkinson B (1994) Calibration of multipath errors on GPS pseudorange measurements. In: Proceedings of the 7th international technical meeting of the satellite division of the Institute of Navigation, pp 353–362, Salt Lake, UT, 20–23 Sep 1994

Chapter 34
A Practical Reduced-Rank Anti-Jamming Algorithm Based on Variable Diagonal Loading Method

Guangwei Fan, Baoguo Yu, Lei Chao and Zhixin Deng

Abstract In the space–time anti-jamming practice of GNSS, the amplitude-phase error of array antenna and the relative motion of interference source might cause position deviation of null or theoretical null in anti-jamming algorithms, and consequently to affect the anti-jamming performance of anti-jamming algorithm severely. For this problem, a space–time 2D anti-jamming algorithm based on reduced-rank variable diagonal load was proposed. This algorithm is purposed to widen and correct the established null under the orthogonality principle of signal subspace and noise subspace, thereby to eliminate the effect to anti-jamming algorithm resulting from the space domain mismatch of signal subspace and the mismatch of signal covariance matrix and eventually to improve the robustness of anti-jamming algorithm. The simulation result validated the correctness of the theoretical analysis and the algorithm robustness.

Keywords Diagonal load · Space–time adaptive · Steering vector · Power inversion

34.1 Section Heading

The electromagnetic environment of GNSS is becoming increasingly complicated. The receiving system of GNSS usually uses space–time 2D anti-jamming algorithm for adaptive signal processing. However, this algorithm might be affected

G. Fan (✉) · B. Yu · L. Chao · Z. Deng
The 54th Research Institute of CETC, Shijiazhuang, People's Republic of China
e-mail: fgweihb@163.com

G. Fan · B. Yu · L. Chao · Z. Deng
Satellite Navigation Technology and Equipment Engineering Technology Research Center of Hebei Province, Shijiazhuang, People's Republic of China

J. Sun et al. (eds.), *China Satellite Navigation Conference (CSNC) 2013 Proceedings*, Lecture Notes in Electrical Engineering 243,
DOI: 10.1007/978-3-642-37398-5_34,

due to vibration or motion of antenna receiving platform, quick change of interference location or array-element position error resulting from poor antenna manufacturing quality or installation-sourced mutual coupling, consequently causing mismatch of null position and jamming direction [1] or even complete failure of the anti-jamming algorithm.

To implement the space–time anti-jamming technique of GNSS, it is required to eliminate the affect to space–time 2D anti-jamming algorithm resulting from amplitude-phase error and receiver or interference motion. The feasible solution is to widen the null around the jamming signal with more robust adaptive processing algorithm. A common technique widening the null of jamming signal is diagonally-loading method. Diagonal loading algorithm is also known as artificial noise injection method [2]. The basic idea of this algorithm is to establish wider null in the jamming direction so as to avoid the interference location moving out of the null in the weight processing period, thereby to suppress the interference effectively. The method has good robustness in the case of small snapshot number and signal response error of random array [3]. It was firstly proposed by B. D. Carlson in 1988 [2], and later, Ma and Goh proposed variable diagonal loading method [4]. But all these loading algorithms need matrix inversion, which require complex computation and is not in favor of real-time implementation. After Goldstein proposed reduced-rank multi-level Wiener filtering algorithm [5], some researches were given to diagonal loading anti-jamming method with multi-level Wiener filtering in the backward synthetic process [6].

Based on an in-depth analysis of diagonal loading algorithm and making full use of the orthogonality of interference subspace and noise subspace, this paper introduced the variable diagonal loading method into the simplified reduced-rank multi-level Wiener filtering space–time 2D anti-jamming algorithm. In addition to algorithm principle and derivation process, the effectiveness of this new algorithm was validated with simulation experiment.

34.2 Diagonal Loading Anti-Jamming Principle

As its name suggests, diagonal loading method is defined as the algorithm that introduce a certain noise constant along the diagonal line of the covariance matrix of received signal and then substitute the regular sampling covariance matrix with diagonal loading covariance matrix. This method remains good robustness in the condition of small snapshot number.

$$R_{x,M} = \frac{1}{K}\sum_{k=1}^{K} X(k)X^H(k) + \sigma_L^2 I \tag{34.1}$$

where, $R_{x,M}$ represents the covariance matrix after diagonal loading; $X(k)$ represents the received satellite navigation signal; M represents the element number of

receiving array; K represents the length of the received data given with covariance computation; I represents unit matrix; σ_L^2 represents diagonal loading quantity.

In space–time 2D anti-jamming applications, the algorithm based on linear-constraint minimum variance (LCMV) criterion [7] is very popular. Taking advantage of the characteristic that navigation signal power is far below noise and interfering power, it constrains the space domain and time domain simultaneously under the condition of space–time joint processing and adjust the weight to have the minimum output signal variance, so as to weaken the jamming energy significantly. The essence of diagonal loading space–time 2D anti-jamming algorithm is to add one secondary compensation term to adjust the weight vector for the objective function of linear constraint minimum variance algorithm [7], which is expressed as follows:

$$\begin{cases} \underset{w}{\text{Min}} & w^{\text{H}} R w + \sigma_L^2 w^{\text{H}} w \\ \text{s.t.} & S^{\text{H}} w = b \end{cases} \tag{34.2}$$

where, σ_L^2 is the loading value.

Based on the Lagrange in equation, the space–time 2D anti-jamming optimal weight under this criterion is expressed as follows:

$$W_{opt} = \left(S^H (R + \sigma_L^2 I)^{-1} S \right)^{-1} (R + \sigma_L^2 I)^{-1} S. \tag{34.3}$$

where, W_{opt} W_{opt} represents $MP \times 1$th dimension vector; M represents the element number of array antenna; P represents the number of time cells; R represents the covariance matrix of $MP \times MP$-dimension received signal; $\boldsymbol{S}$ represents the constrained vector of $MP \times 1$ dimension. When the signal direction is unknown, $\boldsymbol{S} = [1, 0, \cdots, 0]^T$. The output signal, after anti-jamming processing, can be expressed as follows:

$$\boldsymbol{y} = \boldsymbol{W}^H \boldsymbol{X} \tag{34.4}$$

Diagonal loading algorithm is able to enhance the performance of space–time 2D anti-jamming algorithm when random array signal response error exists. By diagonal loading and choosing appropriate diagonal loading quantity, larger characteristic value corresponding to jamming signal will not be affected significantly, but the small characteristic value corresponding to noise signal will have an additional noise substrate σ_L^2 σ_L^2. The diagonally-loaded noise characteristic values will be distributed around σ_L^2 σ_L^2, which can reduce the diffusion level of noise characteristic values and thereby to reduce the affect of noise characteristic vector to adaptive weight vector [6].

34.3 Implementation Process of Diagonal Loading Reduced-Rank Filtering Algorithm

The multi-level Wiener filter uses a nested link composed of scalar Wiener filters that has very good reduced-rank processing capacity and does not require resolution to the characteristic values of covariance matrix. This feature gives it lower complexity of computation; therefore, it is an important breakthrough in reduced-rank adaptive filtering technology.

Multi-level Wiener filtering technique takes the system as dual input and implement it with multi-level resolution on the basis of regular cross-correlation. To lower the noise diffusance and the affect of loading quantity to large characteristic values and w_d^D, a processing method similar to diagonal loading method was considered for covariance matrix R_{X_0}, i.e., to add one more diagonal matrix to the covariance matrix R_D after reduced-rank processing and replace the covariance matrix R_D before diagonal loading with the diagonally loaded one.

Since the optimum block matrix $B_i = I - t_i t_i^H$, $[t_1, t_2, \ldots, t_D]$ belong to orthonormal vectors. Therefore, it is allowed to complete three diagonalization to the diagonally-loaded covariance matrix R_{dl} with matrix T_D.

$$R_D = T_D^{\mathrm{H}} R_{dl} T_D = T_D^{\mathrm{H}} (R_{X_0} + \gamma I) T_D = \begin{bmatrix} r_{1,1} + \gamma & r_{1,2} & & \\ r_{1,2}^* & r_{2,2} + \gamma & \ddots & \\ & \ddots & \ddots & r_{D-1} \\ & & r_{D-1,D}^* & r_{D,D} + \gamma \end{bmatrix} \tag{34.5}$$

I.e., the diagonal loading effect to rank-reduced covariance matrix R_D is equivalent to that to the covariance matrix R_{X_0} before reduced-rank processing is given.

Since R_D R_D is a Hermitian matrix, the rank-reduced matrix R_D is a given Hermitian matrix and the column vector of rank-reduced matrix T_D forms Krylov subspace. Therefore, it is allowed to derive the iteration structure of weighted multi-level Wiener filtering with Lanczos iterative algorithm [8].

$$R_D = \begin{bmatrix} T_{D-1}^{\mathrm{H}} R_{dl} T_{D-1} & \mathbf{0} \\ \mathbf{0}^{\mathbf{T}} \quad r_{D-1,D}^* & r_{D-1} \\ & r_{D,D} + \gamma \end{bmatrix} \tag{34.6}$$

The cross correlation with the desired signal $d_0(k)$ is $\mathbf{r}_{\mathbf{X}_T d_0}^{(D)} = \mathbf{T}_D^{\mathrm{H}} \mathbf{r}_{\mathbf{X}_0 d_0} = \begin{bmatrix} \|\mathbf{r}_{\mathbf{X}_0 d_0}\| \\ \mathbf{0} \end{bmatrix} \in \mathbb{R}^D$, where $\mathbb{R}^D$ represents real D-dimension space. The covariance matrix $R_{D-1} = T_{D-1}^{\mathrm{H}} R_{\mathbf{X}_0} T_{D-1}$ is already known, then the new term in R_D is $r_{D-1,D} = t_{D-1}^{\mathrm{H}} R_D t_D$. To solve Wiener filter $W_D = R_D^{-1} r_{\mathbf{X}_T d_0}^{(D)} \in \mathbb{C}^D$ with $r_{D,D} = t_D^{\mathrm{H}} R_D t_D$, considering only the first element in $r_{\mathbf{X}_T d_0}^{(D)}$ is not zero, only the

first column in $C^{(D)} = R_D^{-1} = \left[c_1^{(D)}, c_2^{(D)}, \ldots, c_D^{(D)}\right]$ is therefore prerequisite. With reference to the matrix inversion lemma [9] of partitioned matrix, it is allowed to use recursion method to work out $C^{(D)}$.

$$C^{(D)} = \begin{bmatrix} C^{(D-1)} & 0 \\ 0^{\mathrm{T}} & 0 \end{bmatrix} + \beta_D^{-1} b^{(D)} b^{(D),\mathrm{H}} \tag{34.7}$$

where, $b^{(D)} = \begin{bmatrix} -r_{D-1,D} c_{D-1}^{(D-1)} \\ 1 \end{bmatrix} \in \mathbb{C}^D$, $\beta_D = r_{D,D} - \left|r_{D-1,D}\right|^2 c_{D-1,D-1}^{(D-1)}$ and $c_{D-1,D-1}^{(D-1)}$ is the last element in the last column $c_{D-1}^{(D-1)}$ of $C^{(D-1)}$. Therefore, the new first column $c_1^{(D)} \in \mathbb{C}^D$ at the Dth step may be expressed as:

$$c_1^{(D)} = \begin{bmatrix} c_1^{(D-1)} \\ 0 \end{bmatrix} + \beta_D^{-1} c_{1,D-1}^{(D-1),*} \begin{bmatrix} \left|r_{D-1,D}\right|^2 c_{D-1}^{(D-1)} \\ -r_{D-1,D}^* \end{bmatrix} \tag{34.8}$$

where, $c_{1,D-1}^{(D-1)}$ is the first element in the last column $c_{D-1}^{(D-1)}$ of $C^{(D-1)}$. The updating of Wiener filter W_D at the Dth step requires the first column $c_1^{(D-1)}$ at the $D-1$ step and the two new terms of covariance matrix, i.e., $r_{D-1,D}$ and $r_{D,D}$. The updating of the last matrix column only depends on the last column of the previous matrix and the new term of matrix R_D.

$$c_D^{(D)} = \beta_D^{-1} \begin{bmatrix} -r_{D-1,D} c_{D-1}^{(D-1)} \\ 1 \end{bmatrix} \tag{34.9}$$

Therefore, it is required to update vectors $c_1^{(D)}$ and $c_D^{(D)}$ at every step in a complete interactive process. The MSE of multi-level Wiener filter is defined as follows, where D represents the level.

$$MSE^{(D)} = \mathrm{E}\left[\left|e_0(k)\right|^2\right] = \mathrm{E}\left[\left|d_0(k) - W_{MWF}^{(D)} X_0(k)\right|^2\right] \tag{34.10}$$

It is easy to know that $MSE^{(D)}$ may be represented by the first element $c_{1,1}^{(D)}$ of $c_1^{(D)}$.

$$MSE^{(D)} = \sigma_{d_0}^2 - \left\|r_{\mathbf{X}_0 d_0}\right\|_2^2 c_{1,1}^{(D)} \tag{34.11}$$

$$\omega_0^{(D)} = \left\|r_{x_0,d_0}\right\|_2 T^{(D)} c_1^D \tag{34.12}$$

As shown in the above formula derivation process, only $\beta_D = r_{D,D} - \left|r_{D-1,D}\right|^2 c_{D-1,D-1}^{(D-1)}$ is directly affected by diagonal loading process in the above procedure. Since diagonal loading only affects the value of $r_{i,i}$ and no change happens to the value of $r_{i-1,i}$, the phase difference γ between the diagonally-loaded

β_i and the not-diagonally-loaded β_i is {FLD6} and γ represents diagonal loading quantity.

β_i will decrease along with the increase of the number of reduced-rank dimensions; the effect of diagonal loading quantity γ to β_i therefore become more and more stronger along with the number of reduced-rank dimensions. The diagonal loading quantity reduces the updating weight of high-order c_1^i and c_D^i, thereby to affect the contribution of the number of rank-reduced dimensions to the final weight. The more large the diagonal loading quantity is, the more noticeable such offsetting effect is. Before the number of rank-reduced dimensions reaches the optimum, its side effect will appear, i.e., lowering the output SINR. However, if the loading level is too low and the performance after and before diagonal loading gives no difference, the diagonal loading effect is not satisfactory.

Therefore, to achieve satisfactory diagonal loading effect, it is required to manage the diagonal loading quantity γ to decrease at every step of the algorithm along with the increase of the iteration times.

$$\gamma_i = \frac{\beta_i}{\beta_{i-1}} \gamma_{i-1} \tag{34.13}$$

The typical level loading method often used in engineering is 5–10 dB higher than the noise background. The procedure to implement diagonal-loading-based adaptive rank-reduced multi-level nesting Wiener filtering algorithm is specific as follows:

1. Data initialization:

Choose the maximum number of dimensions D.

Set $t_0 = 0, \quad d_0(k) = S^H X_{MN}(k), \quad X_0(k) = X_{MN}(k) - S d_0(k), \quad r_{1,1} = E\{d_1(k) d_1^*(k)\}$

$$c_{first}^{(1)} = r_{1,1}^{-1} \quad c_{last}^{(1)} = r_{1,1}^{-1}$$

$$\gamma_0 = \sigma_L^2$$

2. Interactive process:

$$i = 2, \ldots, D$$

$$r_{X_i d_i} = \frac{1}{K} \sum_{k=1}^{K} X_i(k) d_i^*(k)$$

$$t_{i+1} = r_{X_i d_i} \Big/ \sqrt{r_{X_i d_i}^* r_{X_i d_i}}$$

$$r_{i,i} = \frac{1}{K} \sum_{k=1}^{K} |d_i(k)|^2$$

$$r_{i-1,i} = \frac{1}{K}\sum_{k=1}^{K} d_{i-1}(k)d_i^*(k)$$

$$\beta_i = r_{i,i} - \left|r_{i-1,i}\right|^2 c_{last,i-1}^{(i-1)}$$

$$\gamma_i = \frac{\beta_i}{\beta_{i-1}}\gamma_{i-1}$$

$$\widehat{\beta}_i = \beta_i + \gamma_i$$

$$c_{first}^{i} = \begin{bmatrix} c_{first}^{(i-1)} \\ 0 \end{bmatrix} + \widehat{\beta}_i^{(i-1)} c_{first,1}^{(i-1)} \cdot \begin{bmatrix} \left|r_{i-1,i}\right|^2 c_{first}^{(i-1)} \\ -r_{i-1,i}^* \end{bmatrix}$$

$$c_{last}^{i} = \widehat{\beta}_i^{(i-1)} \cdot \begin{bmatrix} \left|r_{i-1,i}\right|^2 c_{last}^{(i-1)} \\ 1 \end{bmatrix}$$

$$MSE^{(i)} = \sigma_{d_0}^2 - \left\|r_{x_0,d_0}\right\|_2^2 c_{first}^{(i)}$$

3. Weight estimation:

$$T^{(D)} = [t_1, \ldots, t_\Delta]$$

$$\omega_0^{(D)} = \left\|r_{x_0,d_0}\right\|_2 T^{(D)} c_{first}^{(i)}$$

$$W_{MWF} = \begin{bmatrix} 1 \\ -\omega_0^D \end{bmatrix}$$

34.4 Analysis of Performance Simulation

To validate the algorithm performance, the following simulation was given. In the simulation, a 5-element circular array (with the center of circle is provided) of GNSS receiver was set. One of the elements was at the centre of the circle and other four elements were uniformly distributed around the circumference of the circle. The radius of the circle was $\sqrt{2}\lambda/4$, and λ was the signal wavelength. In this case, the interval between the adjacent elements along the circumference was $\lambda/2$. $\theta \in [0, \pi/2]$ and $\varphi \in [0, 2\pi]$ were the elevation angle and the azimuthal angle of the received signal. Let's assume that P code is used as the spread-spectrum code for the modulation of satellite navigation signal, the noise is additive white Gaussian noise, the code rate is 10.23 MHz/s, the input SNR is -15 dB and all the

SINR is 40 dB. Under the condition of meeting the performance requirements, set the number of delay tap $N = 3$ considering the purpose of simplifying computation workload and improving the real-timeness. The elevation angle of the incoming signal is 80° and the azimuthal angle is 180°. Zero IF baseband signal was used directly in the simulation, which was represented with normalized frequency bandwidth in the chart. Normalized frequency bandwidth refers to the ratio of actual interference bandwidth to receiver bandwidth.

Simulation Experiment 1: output SINR changing along with the angular error.

Provide a single broadband jamming source and set the number of snapshots $L = 500$. In the real applications, the estimation error of the signal arrival direction might cause mismatch between the steering vector of the estimated desired signal and the steering vector of the real signal source; therefore, the pointing error of the desired signal was set to a variation range of $-5°$ to $5°$.

Figure 34.1 shows the curves of output SINR changing along with the pointing error in three algorithm cases: rank-reduced multi-level Wiener filtering algorithm without diagonal loading under linear constraint, rank-reduced algorithm based on fixed diagonal loading and the algorithm proposed in this paper. As shown in the figure, the algorithm proposed by this paper provided the best performance, the fixed diagonal loading rank-reduced algorithm was next, and both algorithms were superior to the rank-reduced multi-level Wiener filtering algorithm without diagonal loading. Conclusively, adaptive diagonal loading algorithm is able to effectively improve the filtering performance of anti-jamming algorithm in case of pointing error.

Simulation Experiment 2: Output SINR changing along with the number of rank-reduced dimensions.

Provide single broadband jamming source. Set the number of snapshots to 500. Simulate the output SINR changing along with the number of snapshots in three algorithm cases: rank-reduced multi-level Wiener filtering algorithm without

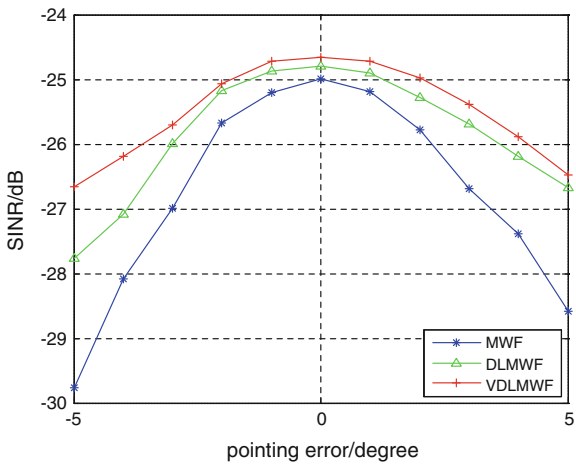

Fig. 34.1 Curve of output SINR changing along with pointing error

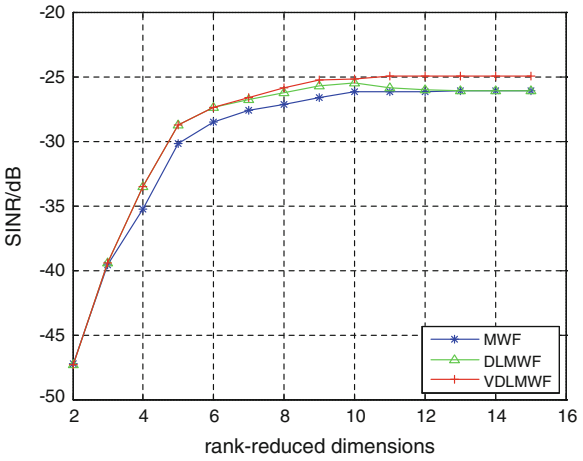

Fig. 34.2 Curve of output SINR changing along with rank-reduced dimensions

diagonal loading, the one based on fixed diagonal loading and the one based on variable diagonal loading (Fig. 34.2).

As shown in the figure, the algorithm based on variable diagonal loading provided the best performance, the algorithm based on fixed diagonal loading gave somewhat declined performance when the number of rank-reduced dimensions got to some extent, and both the algorithms were superior to the rank-reduced space–time anti-jamming algorithm without diagonal loading in filtering performance.

Simulation Experiment 3: Output SINR changing along with the number of snapshots.

Provide a single broadband jamming source. Set the number of snapshots to 500 from 50. Simulate the variation curves of output SINR changing along with the number of snapshots in the three algorithm cases (Fig. 34.3).

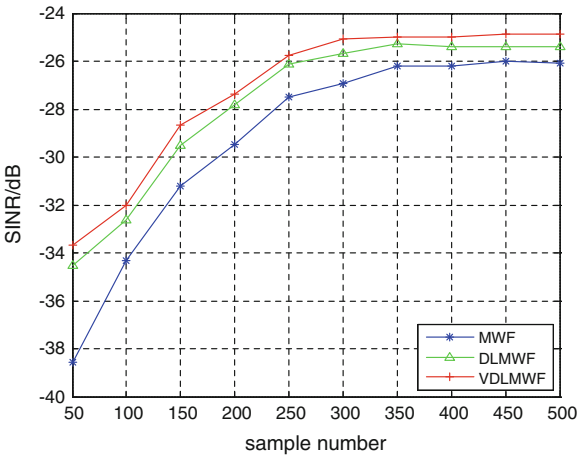

Fig. 34.3 Curve of output SINR changing along with sample number

As shown in the figure above, the algorithm proposed in this paper was superior to the anti-jamming method based on fixed diagonal loading algorithm and the one without diagonal loading. The algorithm proposed in this paper supports adaptive selection of loading quantity. It is able to reduce the diffusance of noise characteristic value without affecting the interference characteristic value. Therefore, this algorithm has better anti-jamming filtering performance. The computational complexity of the algorithm proposed in this paper is approximately $O\left((MN)^2 + 5(MN)\right)$, which is much reduced in comparison with the one using matrix inversion diagonal loading algorithm $O\left((MN)^4 - 2(MN)^3 + 2(MN)^2 - 1\right)$. Therefore, the former has better real-timeness and engineering reliability.

34.5 Conclusion

To reduce the effect of motion and error to the robustness of space–time adaptative anti-jamming algorithm and improve the performance of space–time 2D anti-jamming algorithm, this paper proposed a variable diagonal loading rank-reduced multi-level Wiener anti-jamming algorithm based on diagonal loading method. This algorithm does not require matrix inversion and thereby simplifies the computational complexity. Comparing with the algorithm based on fixed diagonal loading method, it has better anti-jamming performance and robustness. Under the condition of small snapshot number, it still show good anti-jamming performance. The simulation result also demonstrated the excellent performance of this algorithm. It is of important the theoretical value and engineering applications value for the design of GNSS anti-jam receiver.

Acknowledgment The work of this article is supported by National Science and Technology Ministry (No. 2011BAH24B04).

References

1. Lin ZW, Premkumar AB, Madhkumar AS (2006) Diagonally loaded linear MMSE equalization for UWB multipath channel under limited training sample. IEEE 63rd vehicular technology conference, vol 5. pp 2359–2363
2. Carlson BD (1988) Covariance matrix estimation errors and diagonal loading in adaptive arrays. IEEE Trans Aerosp Electron Syst 24(4):397–401
3. Mestre X, Agunas MA (2006) Finite sample size effect on minimum variance beam formers: optimum diagonal loading factor for large arrays. IEEE Trans Signal Process 54(1):69–82
4. Zatman M (1995) Production of adaptive array troughs by dispersion synthesis. Electron Lett 21(25):2141–2142
5. Goldstein JS, Reed IS, Scharf LL (1998) Multistage representation of the Wiener filter based on orthogonal projections. IEEE Trans Inf Theory 44:2943–2959

6. Cao JS, Wang XG (2009) An improved error loading method for multistage Wiener filter. Signal Proces 25(04):618–621
7. Nan H (2010) Research and comparison of anti-jamming performances of LMS and LCMV algorithm based on MATLAB simulation. Electron Meas Technol 33(9):29–32
8. Witzgall HE, Goldstein JS (2003) Detection performance of the reduced rank linear predictor ROCKET. IEEE Trans Signal Process 51(7):1731–1738
9. Dong ZF (2010) Matrix analysis. Publishing House of Harbin Institute of Technology, Harbin, 2009

Chapter 35
Title Research on Key Technology of Testing and Verification Multi GNSS Simulator

Hongjun Ye, Liqiao Dong and Haitao Wei

Abstract Multi GNSS Simulator provides the technical means and environments in those areas as the framework designing for navigation systems, study of effects of signal propagation environments, ground testing and verification of Compass navigation system. As a satellite navigation testing device, high-performance multi-mode satellite navigation signal generators includes many essential technologies as multi-system constellation simulation, signal propagation environment effects simulation, user movement characteristic simulation, antenna characteristic simulation, high-precision navigation signal simulation, thus brings the challenges for the high-precision, accurate, objective and just assessment and testing. The article based on the generator project, studies the testing and assessment system for the generators and preliminarily determines complete assessment means and testing guidelines, particularly in the study of processing and analysis method of applying standard equipments such as high-speed signal sampler. The generator has gone through the testing of the control resolution of generator's pseudo ranges and passed the actual testing and verifications.

Keywords GNSS · GNSS simulator · Testing and assessment · High-speed signal sampler

H. Ye (✉) · L. Dong · H. Wei
The 54th Institute of China Electronic Technology Corporation, Zhongshan West Road No. 589, Shijiazhuang Hebei 050081, China
e-mail: yehongjun563@163.com

H. Ye · L. Dong · H. Wei
Hebei Satellite Navigation Technology and Equipment Engineering Technology Research Centre, Shijiazhuang Hebei 050081, China

J. Sun et al. (eds.), *China Satellite Navigation Conference (CSNC) 2013 Proceedings*, Lecture Notes in Electrical Engineering 243,
DOI: 10.1007/978-3-642-37398-5_35,

35.1 Introduction

As a signal framework verification means that is the most close to practical considerations, multi-mode GNSS simulator is used to help with the verification of the design rationality of navigation signal system, the assessment of navigation signal stream, the rationality verification of information stream and other specification verification in addition to supporting the development of ground receiver terminal and other related application products.

As test equipment particularly for navigation equipment, GNSS simulator is required to have high accuracy, good measurability and calibration capability. Its navigation test capability is based on overall testing and assessment to itself. However, GNSS simulator is classified as high-end test equipment and involved in many sensitive applications and technologies, and almost no open literature is available internationally about the testing and assessment methods. In China, along with the construction of navigation system, some navigation simulators were developed, of which the testing and assessment is still in exploratory experiment stage. In a simulator development project we undertook, an in-depth research and analysis and verification test were given to the testing and assessment methods for simulator, so as to assure the testing accuracy and objectivity.

35.2 Test and Assessment of GNSS Simulator

35.2.1 Key Test Items of Simulator

Considering the characteristics of GNSS simulator, the tests are divided into functional and performance tests to mathematic simulation software and hardware performance test of simulator. The simulator hardware tests are performance tests particular for high-accuracy signal, which is quite different from the ones for general signal simulator.

1. Mathematic simulation test.

- In terms of navigation constellation and orbit simulation function, the simulated orbital data should be in agreement with the Ephemeris data that are used to generate navigation message.
- In terms of satellite clock error simulation function, the simulated satellite clock error should be in agreement with the clock error model set by user and the satellite clock parameters in the generated navigation message.
- In terms of ionospheric delay simulation function, the simulated ionospheric delay should be in agreement with the ionospheric model set by user and the ionospheric parameters in the navigation message.

- In terms of tropospheric delay simulation function, the simulated tropospheric delay should be in agreement with the tropospheric model set by user and the tropospheric parameters.

2. Key test items for signal simulation precision.

- RF signal precision.

– Pseudo range zero value and its stability.
– Pseudo range precision.
– Pseudo-range control resolution.
– Pseudo-range rate precision.
– Carrier-phase change precision.
– Intersignal code phase consistence.
– Code-phase interchannel consistence.
– Carrier-phase interchannel consistence.
– Coherence between carrier and pseudo code.

- Dynamic control precision of RF signal.

– Speed resolution.
– Acceleration resolution and Jerk resolution.

35.2.2 Key Test Items of Simulator

Since the present requirement for pseudo-range control accuracy of simulator has reached centimeter level and the requirements for carrier control accuracy has reached millimeter level, it brings about challenges for the tests based on standard instrument, especially for the tests under dynamic signal conditions and the tests for modern navigation signals based on complicated modulation. The popular test proposals are mainly based on standard instrument or software receiver. Neither method is perfect. The standard instrument method is the easiest to be acceptable, but it requires corresponding research and strict test and assessment method. The software receiver method depends on signal acquisition and mathematical statistics of observed quantity; it is thereby applicable to the tests related to statistics.

35.2.2.1 Software Receiver Method

Signal simulator is mainly designed to give function verification and performance test to receiver. To complete specification and performance tests for multi-system signal simulator, the test instruments of higher resolution are required. If software receiver is to be used in testing signal simulator, then the software receiver must have excellent performance or accuracy to be qualified.

1. Pseudo-range zero value(accuracy) test

Pseudo-range zero value and stability test is mainly used to verify if the pseudo-range zero value and the stability of navigation signal simulation meet the requirements or not. Software receiver testing method uses the directly obtained pseudo range for assessment, which has the following weakness:

- Since software receiver has no reference 1PPS input, it is very difficult to acquire the time point information for synchronization with the simulator. It has no choice but to preestimate a local time after the receiver acquires and tracks the downlink signal and restores the emission time, and then acquire a pseudo-range value based on the time difference between the preestimated local time and the subsequently received emission time, which is used to compare with the theoretical value provided by the simulator and the value measured by the software receiver.
- After obtained the measurement pseudo range, software receiver may acquire the simulator error based on the difference between the measuring pseudo range and the real pseudo range. However, it is very difficult to eliminate the receiver error or to justify that the receiver error is much less than the simulator error; in other words, the challenge is no way to eliminate the system error.

2. Pseudo-range accuracy test

After the software receiver is given coarse alignment, if the alignment accuracy is inadequate, fine alignment should follow. In the process of fine alignment, it is required to shift the local sampled data to complete the test. If pseudo-range accuracy requirement is 0.01 m, then the resolution of data point after sampling must be higher than 0.01 m. To implement such a high accuracy, the sampling rate of receiver might have to be above 30 GHz and a series of design issues must be considered such as how to sample the receiver processing data, how to store and how to generate pseudo code and carrier of software receiver. In addition, even if post-processing mode is used, it needs a very long processing time to process the sampled data in unit time.

3. Pseudo-range rate accuracy test

In the measurement of pseudo-range rate, pseudo range is also used for being agreement with signal simulator, which is related to sampling rate as well. The more critical fact is that the assessment of pseudo-range rate accuracy is essentially the assessment of Doppler accuracy. The reference value provided by the signal simulator is an instant Doppler value, while receiver can only measure the average Doppler rather than the instant Doppler with the full-cycle carrier count traveled in unit time. When testing this specification, receiver is required to complete PVT solution to acquire local reference time accurately. The accuracy is required to be mill microsecond level at least. It is really difficult for a receiver to maintain mill microsecond-level accuracy.

4. Carrier Phase Modulation Orthogonality

In the testing process of carrier phase, to assure the same phase and the phase accuracy of orthogonality higher than 1 degree, the carrier loop accuracy must be much higher than 0.003 cycle. To reach such a high accuracy with software receiver or to assure the PLL to reach such a high accuracy, the requirements for the clock accuracy of the local AD capture card and for the local RF phase noise must be very high. In other words, it is very difficult to reach such a high accuracy with software receiver.

35.2.2.2 High-Speed Broadband Storage Oscilloscope Method

Along with the rapid development of high-speed broadband digital storage oscilloscope, it becomes possible to directly measure the high-accuracy signal characteristics in the delay test of BPSK modulator. It includes two types of test: modulation domain test and time domain test [1].

Essentially, modulation domain testing method is a method that integrates time domain and modulation domain together. It acquires baseband signal and RF signal simultaneously with oscilloscope, and then analyze the RF signal with vector analysis software and restore the baseband signal, which is finally compared with the original baseband signal in time domain to obtain the delay parameter. The major weakness of this method is that an inherent inconsistence exists between the acquired baseband signal and the finally modulated signal, which makes it impossible to precisely characterize the characteristics of the baseband signal finally modulated. Besides, vector analysis software is required to set such parameters as reference filter and testing filter. The setting accuracy of these parameters is directly related to the detail accuracy of the baseband signal waveform finally demodulated, and consequently affects the final test results [2]. In working practice, it is hard to obtain the accurate parameters of modulator, and the approximate value is usually used; therefore, it is not easy to evaluate the accuracy of this testing method. Besides, since digital down conversion is introduced for demodulation analysis, the time resolution might suffer from loss. Moreover, this method requires complicated operations, and changes take place twice in time domain and modulation domain. It will be extremely inefficient to work out the mean value by manual measurements for many times.

The theoretical basis of time-domain test is the assumption that the point of smallest amplitude on the signal envelope is the phase reversal point after modulation and filtering, for the frequency band of BPSK signal is the widest at the phase reversal point. For an ideal BPSK modulated signal, theoretically, the phase change of sinusoidal wave should take place at the change time of modulated signal, and the sinusoidal wave should be undamped before and after modulation. In actual measurement, however, there is no ideal waveform, but a point of minimum amplitude (envelope zero point) exists, because the frequency band is the widest at modulation time and the energy attenuation resulting from the finite

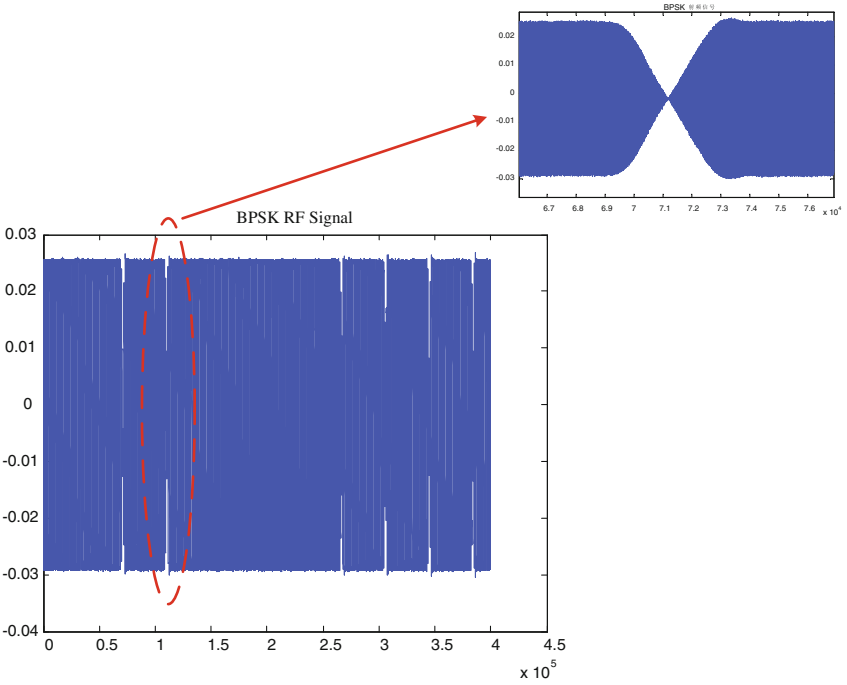

Fig. 35.1 Phase reversal point of BPSK signal

bandwidth of filter is the maximum [3]. The practice in the past was to directly measure the time difference between the signal edge and the phase reversal point with an oscilloscope. This measurement is generally taken with cursor manually. The weakness of this method is the difficulty to locate the phase reversal point. Besides, subjective factor of test operator is introduced in the test and the requirement for the output level of RF signal is definite to assure the observation with oscilloscope. Conclusively, it is difficult to guarantee the measuring accuracy and consistence in this method. In particular, it is really hard to directly observe and test the non-BPSK complex-modulated signals among the navigation signals (Fig. 35.1).

35.3 Research of Key Techniques

35.3.1 Test of BOC Signal

For BPSK, BOC and TMBOC signals, they have the same time domain characteristic as BPSK signal but subcarrier makes the chip width of BOC and TMBOC signals narrower. Currently, the oscilloscope testing method is based on the

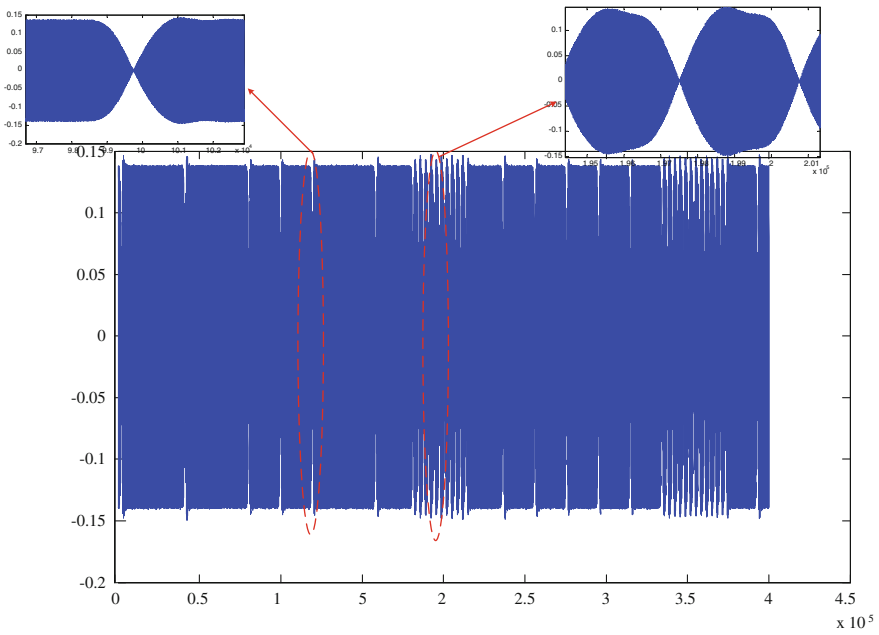

Fig. 35.2 Phase reversal point of MBOC signal

monitoring to the phase reversal point of chip variation. BPSK, BOC and TMBOC signals have the same phase reversal point of chip; therefore, they share the same testing basis (Fig. 35.2).

MBOC signal is based on the sum of one BOC(1,1) and one BOC(6,1). The power of BOC(6,1) is only 1/10 of that of BOC(1,1) and their subcarrier phases are aligned with each other; therefore, the oscilloscope testing method for BOC(1,1) is used when testing CBOC signal and BOC(6,1) is ignorable.

35.3.2 Dynamic Signal Tested with Oscilloscope

When testing the velocity related performance of simulator in response to dynamic signal, the frequency meter method is often used currently. In principle, velocity will generate Doppler that may cause frequency offset. It is allowed to measure the frequency offset to test the velocity related specifications. Specifically, it is implemented by setting the simulator under test to output single carrier plus the frequency offset generated by Doppler. However, since it is single-carrier signal directly generated by simulator, which has lost the intension of navigation signal as spread-spectrum signal to complete velocity measurement of user terminal, this method has certain limitation. Based on a research, Doppler will also pose offset of pseudo code

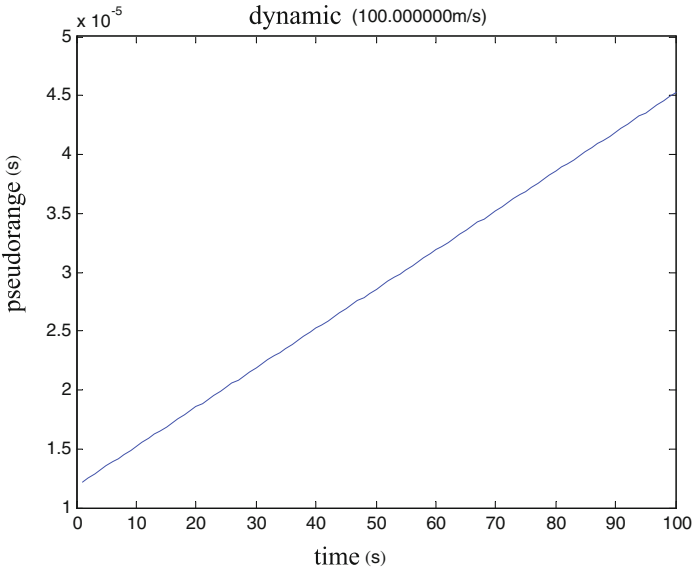

Fig. 35.3 100 m/s velocity test

and carrier relative to simulator reference signal; therefore, it is possible to carry out statistical test with oscilloscope method. The procedure is as follows:

Set the simulator under test to single satellite stationary state and the satellite and simulated user receiver keep overhead vertically (receiver antenna pointing at satellite transmitter antenna all the time). Couple the 10 MHz simulator output with the 10 MHz external synchronization of an oscilloscope. Regulate the reference frequency of the oscilloscope to external 10 MHz reference. Input the 1PPS simulator output and the RF signal from the simulator calibration port into the high-speed storage oscilloscope via two channels. 1PPS signal serves as trigger signal and RF signal as tested signal. Set the receiver to static state and set the initial pseudo range of satellite and receiver to P0; set the dynamic scenario of receiver to uniform rectilinear translation; set the direction towards or back on to the diametric connection direction(forward direction/backward direction); and set the velocity amplitude to the resolution of velocity. Test the first phase reversal point with oscilloscope and then estimate the velocity amplitude based on simulator setting and go on setting to measure the pseudo-range values at the subsequent 100 phase reversal points. Thereby, it is possible to acquire the relation between pseudo-range change and time, i.e., velocity.

The results of several typical velocity-control accuracies are as follows when the simulator under test outputs GPS-L1 signal (Fig. 35.3):

- Set velocity: 100.000000 m/s
- Test acquired velocity: 10.000057 m/s

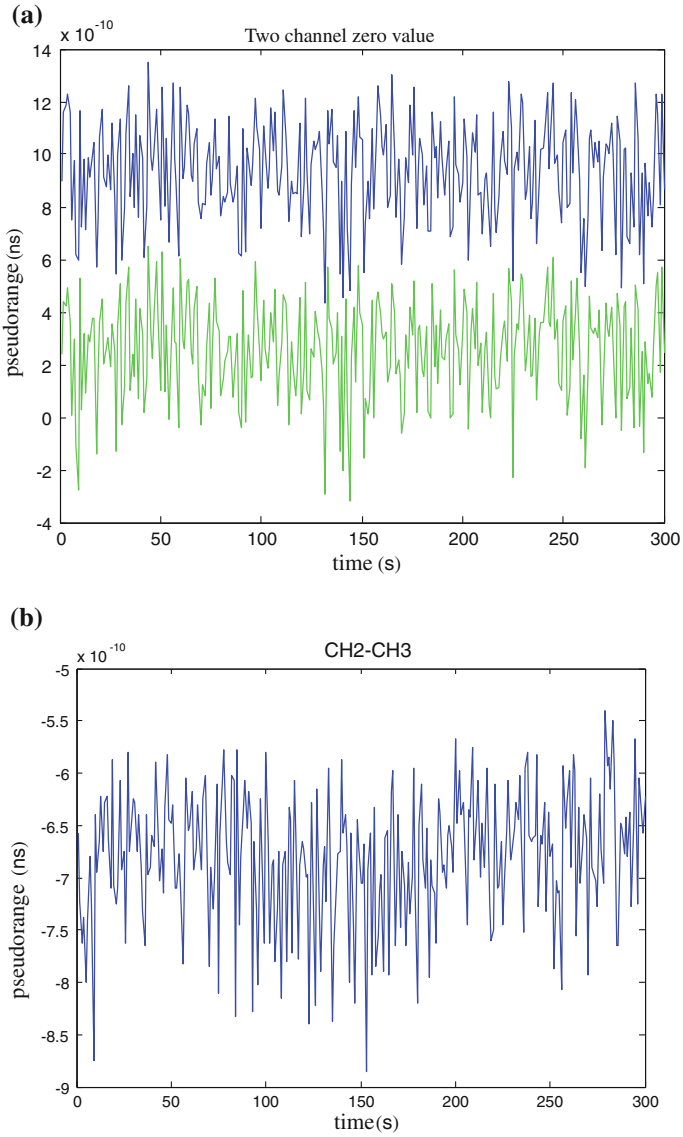

Fig. 35.4 Test results of pseudo-range control accuracy and interchannel deviation. **a** Two-channel zero value. **b** Interchannel deviation

As shown in the figures above, it is possible to measure the velocity control accuracy of simulator by measuring and summarizing the velocity at the reversal points of signal, which is applicable to testing dynamic signal accuracy.

Table 35.1 Test results of pseudo-range control accuracy and interchannel deviation

CH1 1PPS	CH2 GPS L1	CH3 B1	Interchannel deviation
Time calculating variance (ns)	0.188563	0.188243	0.062805
Time calculating variance after ten-point averaging (ns)	0.042881	0.044493	0.025107

Table 35.2 Test results with modified time frequency

CH1 1PPS	CH2 GPS L1	CH3 B1	Interchannel deviation
Time calculating variance (ns)	0.052826	0.055357	0.079713
Time calculating variance after ten-point averaging	0.010896	0.011469	0.013501
Time calculating variance after 60-point averaging	0.003581	0.005676	0.001717

35.3.3 Effect of Simulator Time–Frequency Signal to Measuring Accuracy

In the process of simulator specification test, it was found time–frequency signal had important effect to such specifications as pseudo-range control accuracy. Comparison tests were given for further analysis.

Test 1: 300 s test to two-channel data. Set oscilloscope CH1 to 1PPS, CH2 to GPS signal and CH3 to B1 signal (Fig. 35.4). The test results were as follows (Table 35.1).

The interchannel deviation satisfies the required specification of 0.02 m, but the single-channel deviation is poor, which might be related to the jitter of 1PPS signal. The good specification for 1PPS self jitter is 0.1 ns in China (a nominal performance index is higher than tens of ps abroad), it will introduce effect to signal accuracy test. It is concluded based on test that n-point data averaging is necessary to eliminate this effect. It is suggested to use external clock method (providing 10 M, 1PPS) when testing the accuracy specification, so as to eliminate the effect of 1PPS jitter.

Therefore, the following tests were conducted. Changed the time frequency and used Timetech Rb. oscillator and 10 MHz input instead of internal time frequency. The test results were as follows (Table 35.2):

As shown in the table above, after external time frequency was used, the jitter of self channel becomes smaller, which was in agreement with the result after 10-point averaging; conclusively, 1PPS jitter or internal time frequency affects the uncertainty of channel and deteriorates the jittering.

35.4 Conclusion

Based on the analyses and verification tests to simulator testing methods and the comparative analysis to the weakness of conventional methods, an exploratory research was given to the new navigation signal architecture and dynamic signal test with high-speed oscilloscope and by means of data statistic analysis. The proposed testing method was verified with tests that could improve the measurement accuracy significantly up to tens of ps. Comparing with the conventional methods, this method has the following features: directly testing in time domain, simple and easy to operate, direct output of results based on the characteristics of BPSK signal in time domain and the waveform sync calculation function, avoiding the factors that affect measuring accuracy by using digital down converter or filter in modulation domain test, and also avoiding the subjective uncertainty resulting from artificially reading the phase reversal points. On the basis of verification, this method may also be used to test such signals as BOC. It requires only to modify the test analysis program somewhat in working practice.

References

1. Plumb J, Larson KM, White J et al (2005) Absolute calibration of a geodetic time transfer system. IEEE Trans Ultrason Ferroelectr Frequecy Control 52:1904–1911
2. Chen Z, Guo T, Jiang C (2007) A new method for time synchronization between MEO satellite and the Earth. J Univ Electron Sci Technol China 36(1):3–35
3. Li X, Zhang Q, Xi Q et al (2008) A technical research of AFF inter-satellite baseline measurement based on asynchronous communication link. Acta Astronaut 29(4):1369–1374

Chapter 36
Analysis of Positioning Accuracy for COMPASS Based on Single/Multi Frequency Pseudo-Range

Yongxing Zhu, Xiaolin Jia and Yu Liang

Abstract Compass/Beidou satellite navigation system makes it possible for positioning using three frequencies for the first time. Single frequency pseudo-range measurement and multi-frequency combination pseudo-range measurement are introduced; single & dual frequency positioning accuracy of raw & smooth pseudo-range are analyzed; and the single point availability for different accuracy demands at Lintong station is counted. Results show that: the noise of the ionosphere free using triple-frequency combination is amplified as much as the one using dual frequency combination by eliminating only the first order ionosphere delay; and the amplification is 30 times by eliminating both the first and second order ionosphere delay; pseudo-range positioning errors less than 10 m takes up about 95 % for single & dual frequency pseudo-range; and the single point availability for 10, 15 and 20 m (both level and height errors) take up about 95, 99 and 100 % at the this station.

Keywords Beidou satellite navigation system · Multi-frequency combination pseudo-range measurement · Smooth pseudo-range positioning · Positioning accuracy · Availability

36.1 Introduction

Compass is a self-developed, independent satellite navigation system which is being implemented and independently run by China [1]. Its goal is providing positioning, navigation and timing (PNT) service, as well as short-message communication service, for most Asia–Pacific region users in 2012, and realizing global coverage around 2020.[1] After completion, it will provide users integrated

[1] http://www.beidou.gov.

Y. Zhu (✉) · X. Jia · Y. Liang
Xi'an Research Institute of Surveying and Mapping, Xi'an, People's Republic of China
e-mail: chxyzyx_2008@126.com

J. Sun et al. (eds.), *China Satellite Navigation Conference (CSNC) 2013 Proceedings*, Lecture Notes in Electrical Engineering 243,
DOI: 10.1007/978-3-642-37398-5_36,

services of PNT and short-message. The capacity of compatibility and interoperability enables it to take advantage of multi-system observation data, which will greatly improve observation redundant degree as well as navigation and positioning accuracy [2]. Now the service performance has become a great concern for system builders, related scholars and many future users.

In the early stage of the system construction, many researches has presented on the service performance of Compass based on simulation data. For example, Yang Xinchun analyzed the system's satellite visibility, DOP values and positioning accuracy in China mainland based on the Compass global constellation. And the XPL value provided in China mainland is studied using the Space-Based Augmentation System's (SBAS) integrity algorithm. Results show that the simulation meets the predetermined demand [3].

In the process of system-building, a number of studies are carried out based on measured data by scholars who show strong interests in Compass. Wu et al. has analyzed the ionosphere parameters correction accuracy using measured ionosphere model and positioning accuracy indicators. Results show that the ionosphere parameters correction accuracy is better than 65 % and GPS positioning accuracy (3-dimension) is improved 7.8–35.3 % in the Northern Hemisphere [4]. Chen et al. analyzed the pseudo-range quality and position accuracy with Compass constellation of seven satellites. Results show that multipath and observation noise is in the magnitude of 0.5–3 m, B1/B2 dual-frequency pseudo-range position accuracy is 15.92 m [5]; Professor Shi Chuang also carried out some studies based on the Compass constellation of eight satellites, Compass satellite observations experimental network (Beidou Experimental Tracking Stations, BETS) data and PANDA software. The results show that the radial accuracy of Compass satellite precise orbit determination is better than 10 cm, static precise point positioning accuracy is of centimeter level, baseline relative positioning is of a millimeter; dynamic pseudo-range differential positioning accuracy is of 2.0–4.0 m, and RTK positioning accuracy is of 5–10 cm, close to the current level of GPS [6]. At the same time, foreign scholar Oliver Montenbruck do some research using a small regional Compass monitoring network and its triple-frequency data in March of 2012 and results show that RMS of Overlap differences for Compass satellite precise orbit determination is about 1–10 m, that horizontal and vertical errors achieve 12 cm in single frequency single point positioning (PPP) and that baseline relative position error, north, east and up are 2, 4 and 9 mm, reaching the GPS dynamic positioning level [7].

Compass has owned the ability to provide regional service with the 16th Beidou navigation satellite launched on October 25, 2012 and other early launched satellites, and formal services will be opened early next year in most parts of the Asia–Pacific (see footnote 1). It transmits three frequency signals which are two open service signals B1 and B2, with their frequency 1561.098 and 1207.14 MHz, code rate 2.046 Mcps, and bandwidth 2.046 MHz and one authorized service signals B3, with its frequency 1268.52 MHz, code rate 10.23 Mcps, and bandwidth 10.23 MHz. Compass is the first tri-frequency satellite navigation system, will provide reliable and high-precision services for users, together with GPS, GLONASS, GALILEO [1].

This paper first introduces the Compass single-frequency measurement and muti-frequency combination measurement and its observation noise, and then analyzes the raw & smooth pseudo-range single & dual positioning accuracy based on the measured data and the reasons for precision changes; finally the single point availability is analyzed for different users in the region.

36.2 Combination Pseudo-Range Measurement

For civilian users, Compass provides three frequency signals. These signals can form a variety of measurements. As the ionosphere delay is one of the most important error sources of the satellite navigation and positioning, the combination of multi-frequency measurement generally used the ionosphere-free style. These styles include the following:

36.2.1 Single-Frequency Pseudo-Range Measurement

The form of Compass's three single-frequency pseudo-range measurements $P1$ is as follows:

$$P1 = \rho_0 + C(\Delta t - \Delta T) + \Delta I_i + \Delta D_{trop} + \delta_i \qquad (i = 1, 2, 3) \tag{36.1}$$

ρ_0 for the geometric distance to the satellite receiver. C for the speed of light, Δt for the receiver clock error, ΔT for the satellite clock error, ΔI_i for the ionosphere delay, ΔD_{trop} for the troposphere delay, δ_i for the pseudo-range measurements noise. Assumed that the pseudo-range measurements noise of each frequency data are white noise and independent to each other. The size of the noise is δ.

36.2.2 Dual-Frequency Combination Pseudo-Range Measurement

The general form of dual-frequency combination pseudo-range measurements of the Compass are as follows:

$$P2 = \alpha\rho_i + \beta\rho_j + C(\Delta t - \Delta T) + \Delta D_{trop} + \sqrt{\alpha^2 + \beta^2}\delta \qquad (i, j = 1, 2, 3; i \neq j) \tag{36.2}$$

$P2$ for the dual-frequency pseudo-range measurements, $\alpha = \frac{f_i^2}{f_i^2 - f_j^2}, \beta = \frac{-f_j^2}{f_i^2 - f_j^2}$, the noise is larger $\sqrt{\alpha^2 + \beta^2}$ times after combination.

36.2.3 Tri-frequency Combination Pseudo-Range Measurement

The tri-frequency pseudo-range measurements can eliminate the first-order ionosphere delay or the second-order ionosphere delay [8].

1. The combination to eliminate the first-order ionosphere delay of tri-frequency measurements is P3:

$$P3 = \alpha\rho_1 + \beta\rho_2 + \gamma\rho_3 + C(\Delta t - \Delta T) + \Delta D_{trop} + \sqrt{\alpha^2 + \beta^2 + \gamma^2}\delta \qquad (36.3)$$

While $\alpha = \frac{D_2 - D_1/f_1^2}{3D_2 - D_1^2}, \beta = \frac{D_2 - D_1/f_2^2}{3D_2 - D_1^2}, \gamma = \frac{D_2 - D_1/f_3^2}{3D_2 - D_1^2}, D_1 = \frac{1}{f_1^2} + \frac{1}{f_2^2} + \frac{1}{f_3^2}, D_2 = \frac{1}{f_1^4} + \frac{1}{f_2^4} + \frac{1}{f_3^4}$, the combination of noise amplification is larger $\sqrt{\alpha^2 + \beta^2 + \gamma^2}$ times.

2. The combination to eliminate the second-order ionosphere delay of tri-frequency measurements is P4:

$$P4 = \alpha\rho_1 + \beta\rho_2 + \gamma\rho_3 + C(\Delta t - \Delta T) + \Delta D_{trop} + \sqrt{\alpha^2 + \beta^2 + \gamma^2}\delta \qquad (36.4)$$

While $\alpha = \frac{f_1^3(f_2 - f_3)}{D}, \beta = \frac{f_2^3(f_3 - f_1)}{D}, \gamma = \frac{f_3^3(f_1 - f_2)}{D}$, $D = (f_1 - f_2)(f_2 - f_3)(f_1 - f_3)(f_1 + f_2 + f_3)$, The combination of noise amplification is larger $\sqrt{\alpha^2 + \beta^2 + \gamma^2}$ times.

36.2.4 Coefficients of Combination Pseudo-Range Measurement

The coefficients of various combine measurements for compass and noise magnification are shown in the following Table 36.1:

The table shows that the observation noise magnification of dual-frequency combination measurement of B1/B2 and B1/B3 is 2.90 times and 3.53 times. For tri-frequency combination measurement, the observation noise magnification is roughly equal to the dual-frequency combination measurements by eliminating only the first order ionosphere delay. While the first and second order ionosphere delay is eliminated, the magnification is 35.75 times. Usually the high order

Table 36.1 Coefficients of compass combined pseudo-range measurements

Measurements	α	β	γ	Noise magnification
$P2_{B1/B2}$	2.49	−1.49	/	2.90
$P2_{B1/B3}$	2.94	−1.94	/	3.53
P3	2.57	−1.23	−0.34	2.87
P4	9.10	20.06	−28.16	35.75

ionosphere delay is far less than 1 % of the total delay. The observation noise is largely magnified when using the combination of tri-frequency measurements to eliminate the ionosphere delay. It is always used in cycle slip detection and ambiguity resolution fixed. This article analyzes the single & dual positioning accuracy of the raw & smooth pseudo-range measurement.

36.3 Pseudo-Range Positioning Accuracy

36.3.1 Data Processing Strategy

This article analyzed the Compass positioning accuracy using the 3 days data of Lintong Station (CLIN) in the 254, 255, 256 day of year. Data acquisition equipment is developed by CLP 20. The troposphere corrections are based on model SAASTAMOINEN zenith and NELL projection function. The Klobuchar 8 parameters model is used for single frequency ionosphere delay correction, and combination of deionization layer is used for dual-frequency. The satellite clock error correction parameters stems from the navigation message relativistic corrections and the earth's rotation effect corrections are related to corresponding models. The cut-off angle of the data is 5°. Positioning results are validated according to GPS precise point positioning result.

36.3.2 Raw Pseudo-Range Positioning Accuracy

Single & dual frequency of raw pseudo-range positioning results are as follows:

Analysis found that for 10 m positioning accuracy, the percentage of B1, B3 single frequency and B1/B3 ionosphere combination pseudo-range were 98.98, 96.48 and 95.37 %. The variation of the positioning accuracy is basically consistent with the PDOP value. Overall the positioning results of B1 single frequency are better than those of B1/B3 dual-frequency and B3 single frequency. Analysis found that dual-frequency combination enlarges the multipath and noise, that the positioning error is greater than that in B1 single frequency positioning; the positioning error of B3 single frequency pseudo-range is greatly influenced by ionosphere delay. If the positioning results for the 12–14 h (BDT 4–6 h) are neglected; the proportion of the three-dimensional error better than 10 m is up to 99 %.

From the Fig. 36.1 we also can get that: single-frequency positioning errors of B3 single frequency is particularly evident around BDT 5 h, while dual-frequency positioning is not. Analysis found that this phenomenon is related to the correction accuracy of Compass Klobuchar 8 parameters model. The ionosphere correction

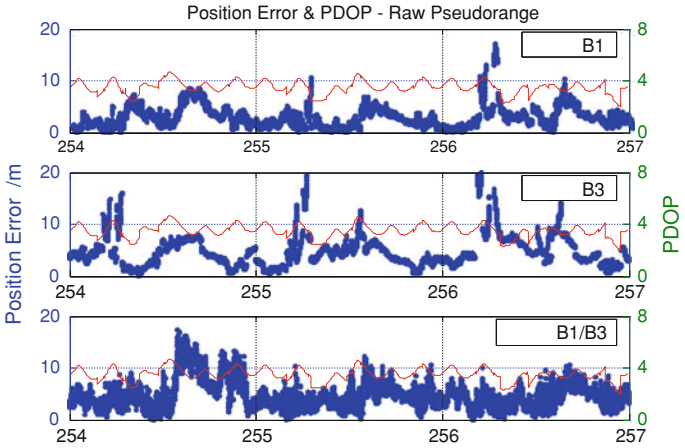

Fig. 36.1 Time serial of position error and PDOP value for raw pseudo-range

error of 1 TECU to the B3 frequency pseudo-range delay is about 25 cm. The impact is greater than the influence to B1 pseudo-range. And the ionosphere activity happens to be most intense around this time (around 14 h local time). The positioning error of single & dual frequency is large around BDT 15 h caused by poor constellation structure. This time the visible satellites number of CLIN station is 8, which C06 and C09 satellite over the southerly, C07 and C10 just entering the field of view in the south of the station. All GEO satellites are in the south of the station, the constellation structure presented "one-sided", and positioning error is large.

36.3.3 Smooth Pseudo-Range Positioning Analysis

Single & dual frequency smooth pseudo-range positioning results is as follows (Fig. 36.2):

The analysis found that the positioning accuracy using the smooth pseudo-range single & dual frequency is significantly improved. The positioning accuracy of dual-frequency is better than 10 m, most obviously improved. The proportion of the positioning accuracy for B1, B3 single frequency and B1/B3 combination pseudo-range better than 10 m is 98.74, 96.33 and 99.03 %.

The observation noise is greatly reduced of smooth pseudo-range, so the positioning accuracy of dual-frequency improved is better than single-frequency. The positioning error of single frequency is still large around BDT 5 h, proving that positioning errors are mainly due to ionosphere delay. Meanwhile, the positioning accuracy of smooth pseudo-range around BDT 15 h is not highly improved, which is an approval that constellation structure within this period is the reason for it.

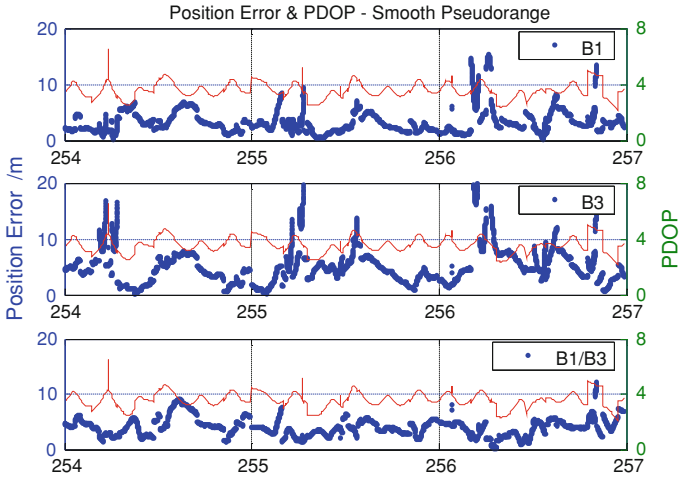

Fig. 36.2 Time serial of position error and PDOP value by smooth pseudo-range

36.4 Availability Analysis

Availability refers to the probability of the system that can provide the navigation service, which is one of the system's performance indicators [9]. It can be divided into instantaneous availability, single point availability and service area availability. Single point availability is available statistics of a point in different time [9]. Generally, analyzing availability is based on DOP values or positioning accuracy. In the section, it is analyzed through positioning accuracy.

Single point availability is calculated using the following formula:

$$P_{A,i} = \frac{\sum_{t=t_{start},inc=T}^{t_{end}} \{Bool(t) = True\}}{1 + \frac{t_{end} - t_{start}}{T}} \tag{36.5}$$

While, t_{start} and t_{end} for the start and end time of the test respectively; T for sampling interval; If positioning accuracy on t epoch meet the requirements then $Bool(t) = 1$, otherwise $Bool(t) = 0$.

Horizontal and vertical errors of the raw pseudo-range positioning in 3 days are as follows (Figs. 36.3 and 36.4):

Horizontal and vertical errors of the smooth pseudo-range positioning in 3 days are as follows (Figs. 36.5 and 36.6):

In order to analyze single point availability of the Compass system in CLIN station, it has divided accuracy demands into five levels, including 5, 8, 10, 15 and 20 m of both horizontal errors and vertical errors. The results are as follows: (Tables 36.2 and 36.3).

Results show that: for 10 m positioning accuracy demands, B1 single frequency raw pseudo-range, B1 frequency and B1/B3 dual-frequency smooth pseudo-range can reach 98 %. The availability for 10, 15 and 20 m is 95, 99 and 100 % of both

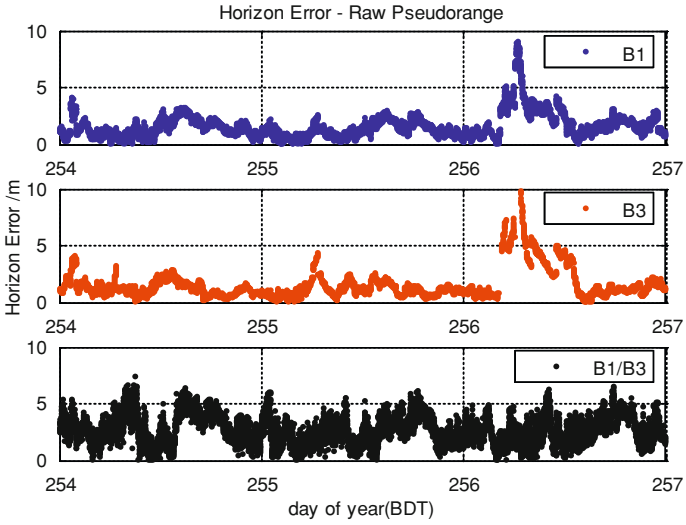

Fig. 36.3 Time serial of horizon error by raw pseudo-range

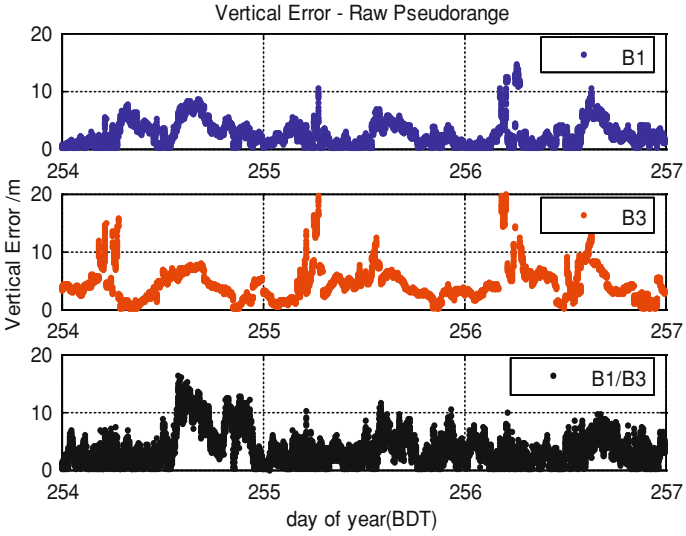

Fig. 36.4 Time serial of vertical error by raw pseudo-range

raw and smooth pseudo-range of single & dual frequency positioning. The B3 single-frequency is influenced largely by the ionosphere delay and the availability is slightly low.

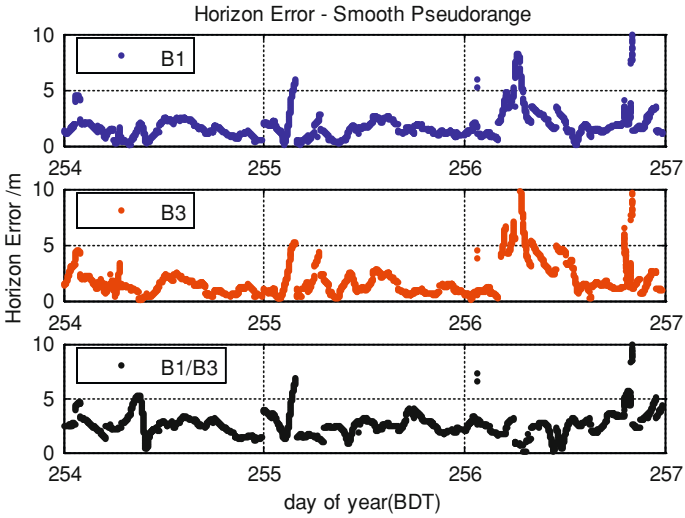

Fig. 36.5 Time serial of horizon error by smooth pseudo-range

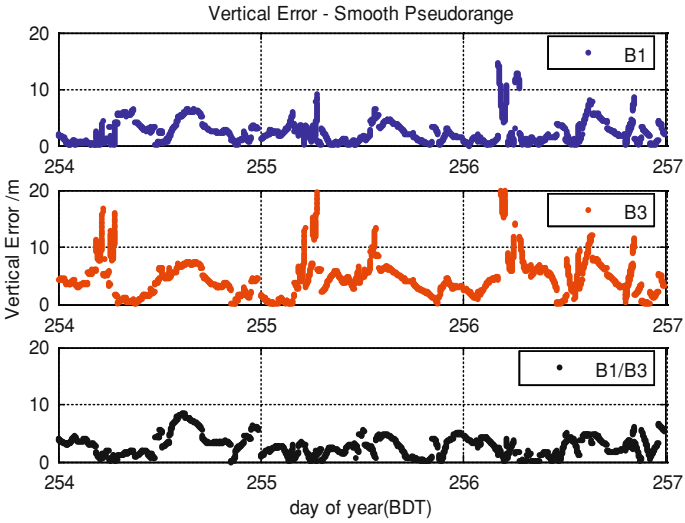

Fig. 36.6 Time serial of vertical error by smooth pseudo-range

Results also show that B3 single-frequency positioning vertical error is large. Also B1 single-frequency and B1/B3 dual-frequency positioning are affected by ionosphere delay in time BDT 4–6 h (local time 12–14 h). The single & dual

Table 36.2 Single point availability of different accuracy demands by raw pseudo-range (%)

H/V (m)	5	8	10	15	20
B1	84.07	97.08	98.90	99.64	100
B3	63.09	91.37	96.01	98.69	99.93
B1/B3	63.08	89.18	94.20	99.79	100

Table 36.3 Single point availability of different accuracy demands by smooth pseudo-range (%)

H/V (m)	5	8	10	15	20
B1	84.29	97.87	98.36	99.81	100
B3	60.99	91.57	95.62	98.82	99.93
B1/B3	78.54	97.43	99.78	100	100

frequency positioning vertical error is large around BDT 15 h by influence of constellation structure. Therefore, we suggested that users can avoid these two time periods for high accuracy requirements in Lintong region.

36.5 Conclusion

Compass is the first tri-frequency positioning satellite navigation system. This article first introduces the Compass's single-frequency pseudo-range measurement and multi-frequency pseudo-range measurements, then analyze the single & dual frequency positioning accuracy, finally analyze the single point availability in Lintong station for different accuracy requirements. Conclusions are as follows:

1. The noise of pseudo-range measurement increases up to 3 times when eliminating the first-order ionosphere delay. It is roughly equal to the accuracy of dual-frequency combination measurement. The noise of pseudo-range measurement increases 30 times when eliminating up to first-order and second-order ionosphere delay;
2. The proportion of the pseudo-range positioning accuracy of B1, B3 single frequency and B1/B3 dual-frequency better than 10 m: 98.98, 96.48 and 95.37 % for raw pseudo-range; 98.74, 96.33 and 99.03 % for smooth pseudo-range;
3. The positioning accuracy is slightly deteriorated in Lintong region around BDT 5 and 15 h by the influence of ionosphere delay and the constellation.
4. For the demands of 10, 15 and 20 m positioning accuracy, the single point availability of Lintong station are 95, 99 and 100 %. The B3 ingle-frequency positioning accuracy is influenced by the ionosphere delay and its availability is slightly lower.

This article is analyzed based on 4G +5I +2M Compass constellation. The results show that the single & dual frequency positioning can achieve high accuracy and high stability. The system performances will be better with full Compass area constellation of 5G +5I +4M.

References

1. Yang YX, Li JL, Xu JY et al (2011) Contribution of the compass satellite navigation system to global PNT users. Chin Sci Bull 56(26):1734–1740
2. Yang YX (2010) Review on progress, contribution and challenges of Beidou satellite navigation system. Acta Geodaetica et Cartographica Sinica 39(1):1–6
3. Yang XC, Li ZH, Wu Y (2011) The performance analysis of constellation and XPL for compass. Acta Geodaetica et Cartographica Sinica 40:68–72
4. Wu X et al (2012) Application of compass ionospheric model in GNSS positioning. Proceedings of CSNC 2012. May 2012
5. Chen L et al (2012) Preliminary analysis of compass navigation system pseudo-range data quality and positioning accuracy. Proceedings of CSNC 2012. May 2012
6. Shi C, Zhao QL, Li M et al (2012) Precise orbit determination of Beidou Satellites with precise positioning. Sci China Earth Sci 55:1079–1086. doi:10.1007/s11430-012-4446-8
7. Montenbruck O, Hauschild A, Steigenberger P et al (2012) Initial assessment of the Compass/BeiDou-2 regional navigation satellite system. GPS Solut, 12 June 2012. doi:10.1007/s10291-012-0272-x
8. Wang M, Wang F (2008) Three multi-frequency correction methods' comparison of ionospheric delay. Sci Surveying Mapp 33(4):58–60
9. Chen JP, Zhou JH, Zhao WW (2005) Analysis the concept of satellite navigation system performance. Radio Eng 35(1):30–32

Chapter 37
Antenna Circular Rotation Method for Detecting Receiver Dynamic Positioning Accuracy

Haisong Jiao, Shentang Li, Haiqiang Yang, Liangjian Jiang and Lili Wang

Abstract The paper introduces circular rotation testing system by which GPS receiver's dynamic performance can be examined, analyzes the change rule of Doppler frequency shift caused by the circular rotation of antenna, compares the states of antenna circular rotation and the linear moving of airborne by investigating the Doppler shift and Doppler shift changing rate, then puts forward the basic method for detecting receiver dynamic positioning accuracy via antenna circular rotation to simulate the state of the airborne linear motion by investigating Doppler shift changing rate. As an example, by using a NovAtel RT2 GPS receiver, the paper gives accuracy analysis of the GPS receiver point positioning and carrier phase differential positioning under the condition of antenna circular rotation with the proposed method, and gives the Receiver's accuracy of point positioning and carrier phase differential positioning under different moving states as well. Finally, points out the application and popularization of the proposed method in detecting dynamic accuracy and tracking performance of Compass and GPS of other types.

Keywords Receiver · Dynamic accuracy · Circular rotation · Detection

H. Jiao (✉)
State Key Laboratory of Complex Electromagnetic Environment Effects on Electronics and Information System, Luoyang 471003, China
e-mail: jiaohs888@163.com

H. Jiao · H. Yang · L. Jiang · L. Wang
The 63880 troop, Luoyang 471003, China

S. Li
The 27nd Research Institute of CETC, Zhengzhou 450005, China

J. Sun et al. (eds.), *China Satellite Navigation Conference (CSNC) 2013 Proceedings*, Lecture Notes in Electrical Engineering 243,
DOI: 10.1007/978-3-642-37398-5_37,

37.1 Introduction

In view of GPS and Compass measurement receiver's high precision, it is difficult to find higher precision dynamic measuring equipment to examine their accuracy. Thus, the evaluation of receiver dynamic positioning precision has been difficult at home and abroad. At present, many domestic research institutes have been trying to study on this problem, the common method is to use the signal simulator for measurement dynamic simulation environment [1]. While, the cost of which is expensive and inconvenient to use. Furthermore, it can not simulate the real working environment, the test results are often in doubt as well. This paper presents a method using antenna circumferential rotation to detect and analyze the receiver dynamic positioning accuracy, trying to solve the difficult problem of receiver dynamic accuracy testing.

37.2 Design of Antenna Rotating Test System

37.2.1 Design Ideas

The receiver is mounted on the rotating platform, the antenna on the edge of rotating arm, continuously improve the antenna rotation speed by adjusting the motor, research the dynamic positioning accuracy by investigating the deviation of the dynamic positioning data relative to fixed position, by observing the receiver positioning and the change of Doppler shift of original measurements to study the receiver dynamic tracking performance [2].

37.2.2 System Consist

Antenna rotation test system, shown in Fig. 37.1, consists of a rotating platform test subsystem, differential reference station subsystem and the dynamic performance test subsystem.

Subsystem composition and function:

1. Rotating platform test subsystem mainly consists of a rotating platform (motor, rotating shaft, etc.), receiver (for recording), data transmission system and a photoelectric sensor. The main task of which is to simulate the operating state of receiver, to complete the measurement precision and tracking performance test under dynamic condition.
2. Differential reference station subsystem mainly consists of the receiver whose antenna is arranged at the reference point, the records with a laptop and data transmission radio. The main work of which is to record the original measurement data of the reference station and to transmit the differential information [3].

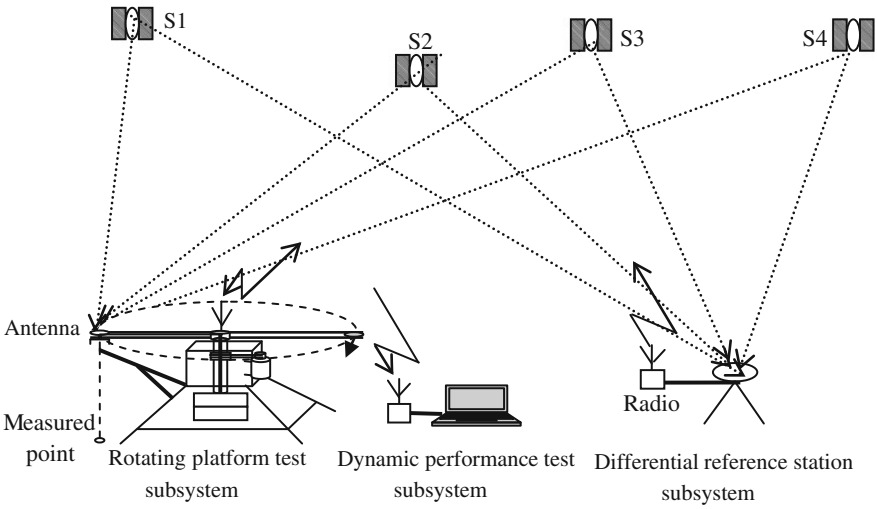

Fig. 37.1 Working scenario of antenna rotation test system

3. Dynamic performance test subsystem mainly consists of the laptop installed with dynamic test software, data radio to receive, process and display the real-time positioning information and original measurement information

37.3 Comparison of Antenna Circular Motion and Airborne Linear Motion State

37.3.1 Analysis of Doppler Frequency Shift Changes

37.3.1.1 Analysis and Test of Doppler Frequency Shift Caused by the Antenna Circular Motion

Set the disk center point is O, satellite S in ground projection point is E, EO connection with the disc for the intersection of A and C, B and D as the intersection point of circular and vertical line of AC that passes O, the angle between planar BDS and horizontal is θ ($\theta \leq 90°$), as shown in Fig. 37.2.

The Doppler frequency shift caused by relative motion of satellite and the target can be expressed as [4]:

$$f_d = f_s - f_r = -f_s \frac{V_R}{C} \tag{37.1}$$

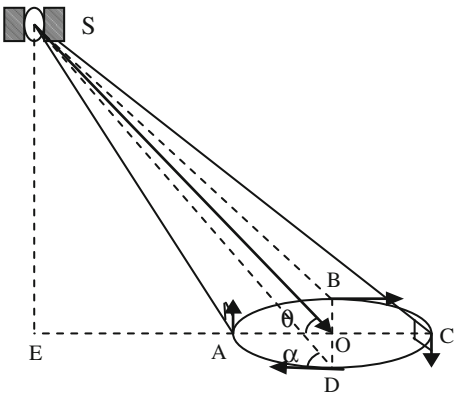

Fig. 37.2 Analysis diagram of Doppler frequency shift changes

where, f_s is the satellite transmitting frequency, f_r is the received satellite signal frequency, C is the velocity of light, V_R is the radial velocity of satellite and target's relative movement.

Suppose Satellite is stationary, namely the Doppler frequency shift is caused only by the antenna rotating, the GPS antenna line speed is V, the angle between the line SD and tangential component is α, then the radial velocity of D relative to satellite S is $V_R = V * COS\ \alpha$. When $\alpha > 90°$, the point D moves away from S, namely Doppler frequency shift is positive. When $\alpha < 90°$, the point is close to S, namely Doppler frequency shift is negative. When $\alpha = 90°$, $V_R = 0$, namely Doppler frequency shift is 0.

Let turntable arm rotate clockwise, the Doppler frequency shift caused by the antenna rotation is analyzed as follows:

1. From A to B, α increases from 90° to maximum gradually (obtuse angle). The radial velocity is reduced from 0 to negative maximum, Doppler frequency shift decreases gradually from 0 to positive maximum;
2. From B to C, α decreases from maximum to 90° gradually. The radial velocity is increased from negative maximum to 0, Doppler frequency shift decreases gradually from positive maximum to 0;
3. From C to D, α decreases from 90° to a minimum gradually f (acute angle). The radial velocity is increased from 0 to a positive maximum, Doppler frequency shift decreases gradually from 0 to a negative maximum;
4. From D to A, α increases from minimum 90° gradually. The radial velocity is decreased gradually from a positive maximum to 0, Doppler frequency shift increases gradually from a negative maximum to 0.

The Doppler frequency change shift caused by the relative movement of a certain GPS satellite and the turning antenna and the reference station is shown in Fig. 37.3, The Doppler frequency shift change caused only by the GPS antenna turning is shown in Fig. 37.4, where the satellite movement is canceled out.

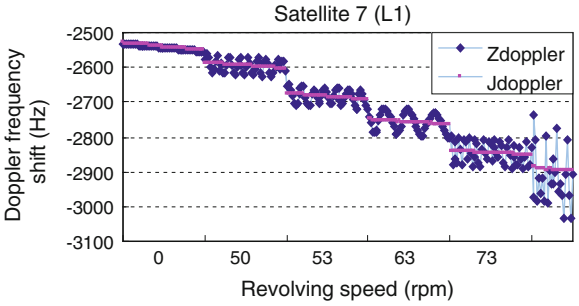

Fig. 37.3 Doppler frequency shift of antenna and reference station relative to satellite

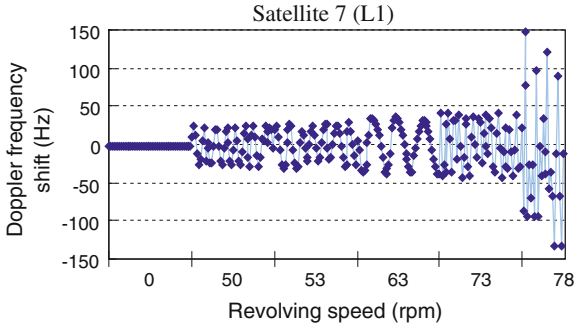

Fig. 37.4 Doppler frequency shift caused only by GPS antenna turning

As shown in Figs. 37.3, 37.4, with the GPS antenna rotating, the Doppler frequency shift caused by the antenna circular motion is changed periodically. Moreover, with the increase of rotation speed, the Doppler shift frequency caused by antenna rotation increases accordingly.

37.3.1.2 Analysis of Doppler Frequency Shift Caused by Airborne GPS Motion

The NovAtel GPS receiver is commercial receiver, which uses a carrier phase locked loop for carrier tracking, a code delay locked-loop for code tracking. At present the aircraft speed varies from tens of meters per second (helicopter) to 250 meters per second or so (fighter, transport models ranging), which belongs to the low and middle dynamic range. The Doppler frequency shift change received by airborne GPS and reference station (nearly to turn the corner section) is shown in Fig. 37.5; Figure 37.6 shows Doppler frequency shift change caused only by the movement of plane relative to the GPS satellite.

Analysis: It can be got from Figs. 37.5, 37.6 that, the range of Doppler frequency shift caused only by aircraft movement is about ±700 Hz (The turning section for a maximum of ±1000 Hz). On the receiver under static condition, Doppler frequency shift caused by the motion of the satellite lies in ±4.5 kHz, the range of Doppler shift frequency caused by turntable rotation is ±100 Hz. If we

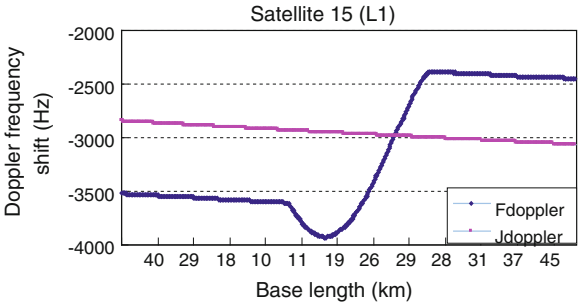

Fig. 37.5 Doppler frequency shift of airborne GPS and reference station relative to satellite

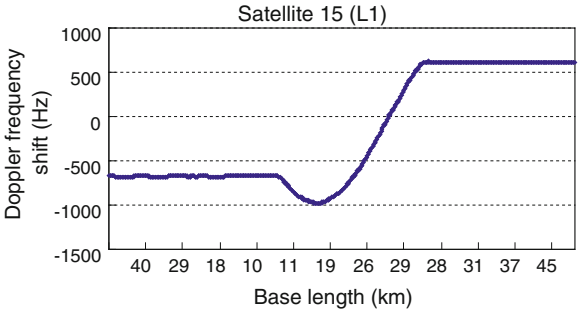

Fig. 37.6 Doppler frequency shift caused by airborne GPS moving

verify the receiver precision only by Doppler frequency shift, the dynamic range of the measurement via turntable is low. In comparison with Doppler frequency caused only by the motion of the satellite on the receiver under static condition. The variation range of Doppler shift caused by the aircraft motion is not big, If the double difference positioning accuracy of GPS receiver under static condition is very high, which is verified, then the linear change of Doppler frequency caused by aircraft moving uniformly in a straight line will not affect the dynamic positioning accuracy of airborne receiver.

37.3.2 Analysis of Doppler Frequency Shift Change Rate

The Doppler frequency shift change rate caused by GPS antenna's circumferential rotation (one revolution) relative to a certain satellite is shown in Fig. 37.7. Figure 37.8 for the Doppler frequency shift change rate caused by the airborne GPS antenna movement (intermediate for turning) relative to satellite No. 15.

Analysis: It is shown in Fig. 37.7 that, the minimum scope of Doppler frequency change rate caused by GPS circular motion is within 250 Hz/s under the rotation condition (53 RPM). In Fig. 37.8, the Doppler change rate caused by airborne GPS in uniform motion (V = 220 m/s) is within a range of about 2 Hz/s, the maximum of which is 20 Hz/s at turning section. Thus, by investigating the

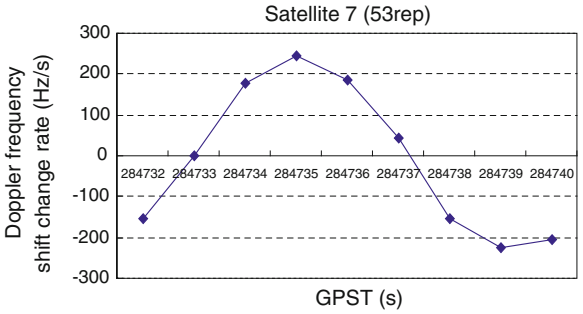

Fig. 37.7 Doppler frequency shift change rate caused by GPS antenna turning

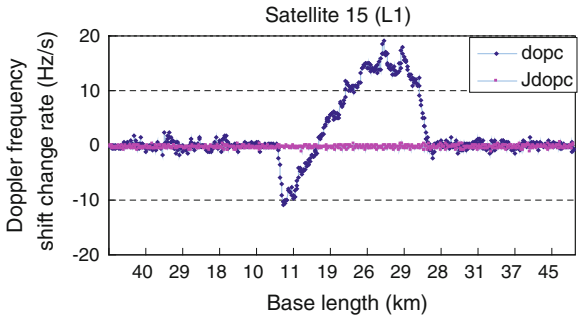

Fig. 37.8 Doppler frequency shift change rate caused by airborne GPS moving

Doppler frequency change rate, the method can fully simulate and detect receiver positioning accuracy under high dynamic conditions.

37.4 Positioning Precision Detection of GPS Receiver Under Dynamic Circular Motion Conditions

37.4.1 Detection and Analysis of GPS Single Point Positioning Accuracy

Test method: Let the receiver record or transmit the real time single point positioning data PRTKA (or GPGGA), the ground station then receives and displays the deviation curve of the data through GPS dynamic measurement precision test software in real time. Figure 37.9 shows real-time point positioning deviation relative to a fixed point on different speed conditions.

Accuracy analysis: As seen from Fig. 37.9, with the increasing of rotation speed, the dynamic point positioning deviation increases gradually, which is from 5 to 30 m or so. The increasing of the observation noise leads to the gradual increasing of Random deviation, which indicates that the GPS receiver point positioning is greatly affected by the circular motion environment. In the Figure, the deviation value is for

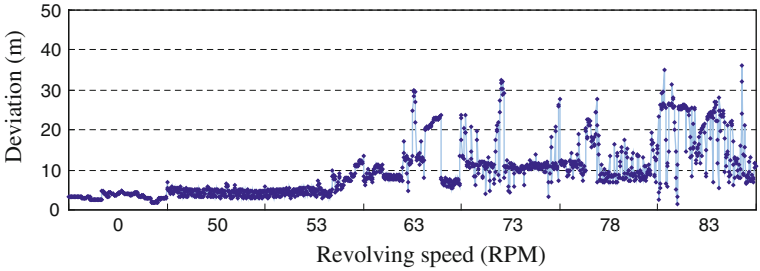

Fig. 37.9 Point positioning deviation on different rotation speed conditions

the distance the antenna away from a certain fixed point during real time rotating (In this test, the antenna from the shaft center distance is 0.99 m).

37.4.2 Detection and Analysis of Dynamic Positioning Accuracy of Carrier Phase Differential Data

37.4.2.1 Accuracy Detection

Test method A: Reference receiver and the GPS receiver on turntable record RGEB (the original measurement data) and REPB (satellite ephemeris) simultaneously, change the rotating speed, by afterwards processing via double difference processing software, the deviation from a fixed point can be got, the values of which reflect the dynamic data accuracy. Figure 37.10 shows the deviation of double difference carrier phase data relative to a fixed position on conditions of different rotating speed (from static until not positioning).

Test method B: Reference receiver transmit difference data (RTCAOBS and RTCAREF) to the receiver on turntable in real time, the receiver on turntable then process the data and send out the result, the ground radio station receives the double differential positioning data and displays the deviation curve of the received data by Dynamic Measurement Precision Test software in real time.

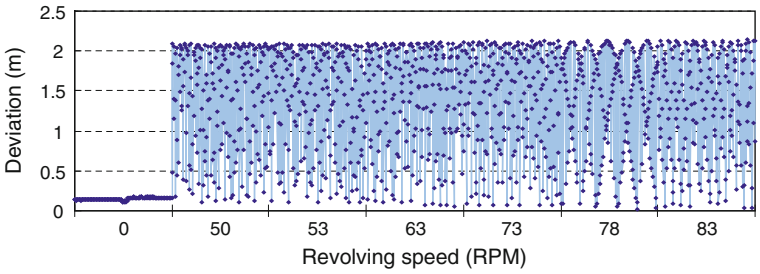

Fig. 37.10 Carrier phase differential positioning deviation on different rotation speed conditions

37.4.2.2 Accuracy Analysis

Below, taking rotation speed of 78 rpm as an example to analyze the actual position of the receiver antenna at each moment. Due to the max sampling rate of the receiver is 4 times/s, the analysis interval is 0.25 thereby. Table 37.1 and Fig. 37.11 show the corresponding relationship between each positioning time and actual position of the circular rotating antenna.

Theoretical analysis: As can be seen in Table 37.1 and Fig. 37.11, when the rotation speed is 78 rpm, the antenna is located adjacent to position on the

Table 37.1 Corresponding relationship between each epoch and actual position of rotating antenna

Numerical order	Record epoch (second)	Number of bars per second (bar)	Location in chart (bar)	Mark in chart
1	0	–	1	O
2	0.25	19.5	19.5	①
3	0.5	39	39	②
4	0.75	58.5	58.5	③
5	1	78	18	④
6	1.25	97.5	37.5	⑤
7	1.5	117	57	⑥
8	1.75	136.5	16.5	⑦

Note Assum set 1 revolution = 60 bars, then: 78 rpm= 78 bar/s

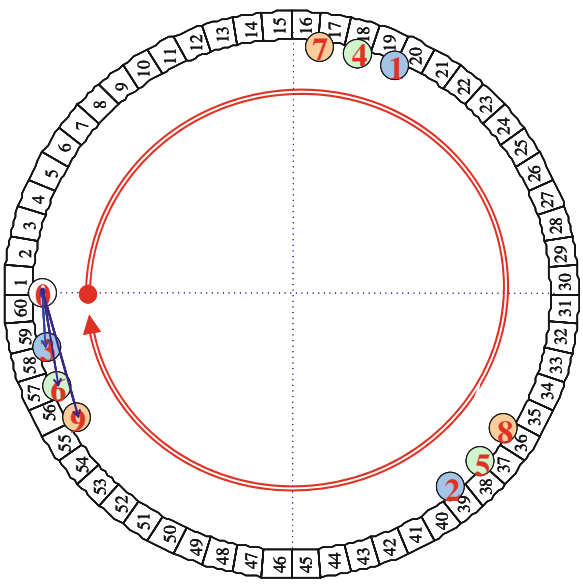

Fig. 37.11 Aided analysis diagram of positioning accuracy on circular rotation conditions

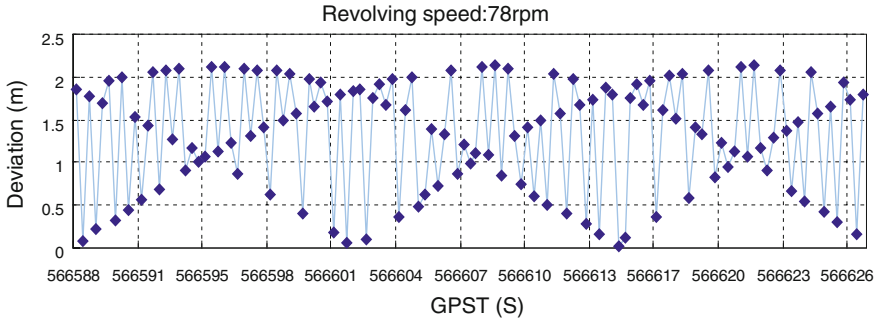

Fig. 37.12 Deviation of carrier phase differential data relative to fixed point on rotation conditions

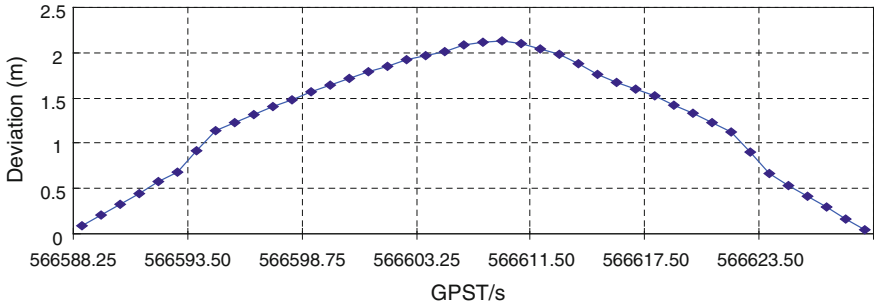

Fig. 37.13 Deviation of carrier phase differential data relative to fixed point on rotation conditions

turntable every 0.75 s and counterclockwise postponed. With the increase of rotation time, the distance between antenna's current position and initial position increases from the scale range 60 to 31 and decreases from the scale 30 to 1.

Figures 37.12, 37.13 for the position deviation curve of the GPS receiver on turntable away from a fixed point by the post carrier phase difference processing. Figure 37.12 for recording interval of 0.25 s of the differential data position deviation, Fig. 37.13 for the interval of 0.75 s.

Conclusion can be drawn from the above analysis, when the rotating speed is 78 rpm, the accuracy of GPS dynamic carrier phase differential data is high, the circular motion trajectory of antenna can be accurately plotted to a degree of centimeter precision level. It can be seen from Fig. 37.10, the accuracy of carrier phase differential dynamic data changes little with the increase of antenna rotation speed, which further indicates that dynamic measuring precision of the present system is high and fully meet the mission accuracy requirements.

37.5 Conclusions

Besides the application in verifying GPS or Compass user machine dynamic positioning precision and dynamic tracking performance, the rotating test platform can be applied not only to examine and check before acceptance the afterwards difference processing software's performance of dynamic solution, ambiguity and cycle-slip detection and repair ability as well, but also to test the anti-jamming ability of the receiver under dynamic conditions, etc.

References

1. Yanhong K, Qing C, Qishan Z (2004) System architecture and software design of high-dynamic GPS signal simulator. J Beijing Univ Aeronaut Astronautics 30(6):534–538
2. Jiao HS (2007) The test and analysis of GPS survey precision. Master's thesis, Electron Sci Eng Nat Univ Defense Technol
3. Wen YL (2009) Analysis and simulation technology of satellite navigation system. Aerospace Press, Beijing
4. Jiyu L (2008) GPS satellite navigation locating principle and methods, 2nd edn. Science Press, Beijing

Chapter 38
Comparison of Methods on Computing Ionospheric Delays in GNSS System Time Offset Determination

Xue Zhang, Huijun Zhang and Xiaohui Li

Abstract Ionospheric delay error is one of the main factors that have significant impact on GNSS system time offset determination. Two methods are adopted to calculate the ionospheric delays in the monitoring of the GNSS system time offset. The first one is Total Electron Content (TEC) map provided by International GNSS Service (IGS) and the other one is the dual-frequency measure correction. The different effects of these two calculating methods are compared and analyzed in this paper. The results show that the ionospheric delays are corrected using dual-frequency observation is better than using the IGS TEC MAP. The monitoring results of the GPS/GLONASS system time offset compared with GPS/GLONASS system time offset published by Circular T, the accuracy of the former one is increased by 15 % than the latter one.

Keywords Ionospheric delays · TEC map · Dual-frequency measure · System time offset

38.1 Introduction

With the development of multiple Global Navigation Satellite Systems, the navigation based on the combination of more than one satellite navigation system will be the important development direction in the future. By choosing the

X. Zhang (✉) · H. Zhang · X. Li
National Time Service Center, The Chinese Academy of Sciences, 710600 Xi'an, China
e-mail: yingtaoxinyu@126.com

X. Zhang · H. Zhang · X. Li
Key Laboratory of Precision Navigation Positioning and Timing, The Chinese Academy of Sciences, 710600 Xi'an, China

X. Zhang
University of Chinese Academy of sciences, 100039 Beijing, China

J. Sun et al. (eds.), *China Satellite Navigation Conference (CSNC) 2013 Proceedings*, Lecture Notes in Electrical Engineering 243,
DOI: 10.1007/978-3-642-37398-5_38,

combination of different navigation system based on their actual needs, the users can avoid excessive reliance on the only one system. However, since every GNSS system has their own time reference system, the time differences between two GNSS system will cause the deviation of positioning. The positioning precision can be highly improved in the multi-GNSS applications if we take the GNSS system time offset into consideration [1]. Therefore, the GNSS system time offset determination is a very important issue in the multi-GNSS application.

Nevertheless, the ionospheric delay error is one of the main factors that influence the result in the monitoring of the GNSS system time offset. When the electromagnetic signals go through the ionosphere, the path of the signal will be bend and the propagation velocity will be change because ionospheric is a diffuse medium for propagation of electromagnetic waves. As can be seen based on the actual data analysis, the distance difference of the electromagnetic wave propagation path along the zenith direction up to 50 m, in the horizontal direction up to 150 m due to ionospheric refraction for GNSS system. Such a large deviation must be considered for the calculation of the GNSS system time offset [2].

Two methods are mainly used to determine the ionospheric delay in the monitoring of the GNSS system time offset, the first one is Total Electron Content (TEC) map provided by International GNSS Service (IGS) and the other one is the dual-frequency measurement. This paper will evaluate these two methods in term of analyzing the accuracy and precision of the GNSS system time offset.

38.2 GPS/GLONASS System Time Offset Detection Principles

Because Standard Time in China is produced in National Time Service Center (NTSC), we can take the advantage of GNSS timing receiver to measure the difference between GPST with UTC (NTSC), and the difference between GLONASST with UTC (NTSC). We can obtain the system time offset by that indirectly.

Figure 38.1 shows the schematic diagram of GNSS system time offset monitoring system. The precision time interval counter measures the time difference of UTC (NTSC) 1pps signal and 1pps signal of the GNSS timing receiver output. Timing receiver receives GNSS satellite signal. After processing pseudorange data and Ephemeris data, the timing receiver can obtain the time offset between the navigation system and receiver. And then, by doing a simple arithmetic calculation, we can get the time deviation of UTC (NTSC) and GPST as well as the time deviation of UTC (NTSC) and GLONASST [3].

We need to consider variety of factors in this monitoring approach, such as the pseudorange measurement error, ephemeris error, tropospheric delay error, ionospheric delay error, receiver delay, and local clock delay. Among these factors, the

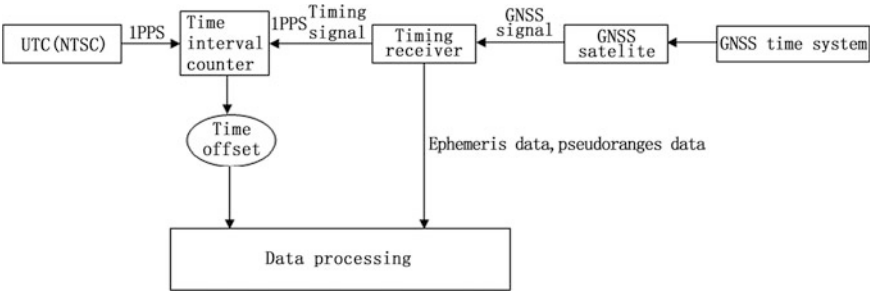

Fig. 38.1 Schematic diagram of monitoring GNSS system time offset

ionospheric delay error is one of the most important factors, which will influence GNSS system time offset monitoring results.

38.3 Ionospheric Delays Algorithm

38.3.1 Ionospheric Delays Determination by IGS TEC Map

IGS provides a global range of ionospheric TEC figure every 2 h. This figure is given in each 5° of longitude direction and each 2.5° of latitude direction in grid form. The total electron content of some region at t moment is interpolated by TEC map at T_i and T_{i+1} moment ($T_i < t < T_{i+1}$) [4]. The four points grid interpolation as shown in Fig. 38.2:

The detailed steps are as follows:

Firstly, we calculate the tec of T_i moment and T_{i+1} moment by spatial interpolation through the surrounding four points. E_i and E_{i+1} can be calculated by:

$$E(\lambda, \beta) = (1-p)(1-q)E_{00} + p(1-q)E_{10} + q(1-p)E_{01} + pqE_{11} \qquad (38.1)$$

where (λ, β) is the latitude and longitude of the puncture point. $E_{00}, E_{01}, E_{10}, E_{11}$ is the TEC of surrounding four points (λ_0, β_1), (λ_0, β_0), (λ_1, β_1), (λ_1, β_0) provided by IGS TEC map. ($\Delta\lambda$, $\Delta\beta$) is the latitude and longitude intervals of ionosphere

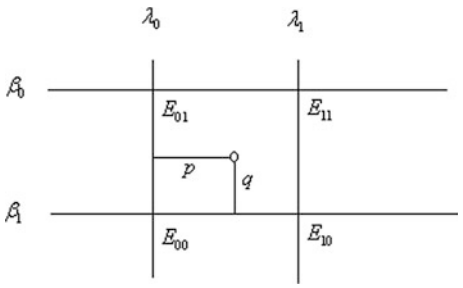

Fig. 38.2 Diagram of the four points grid interpolation

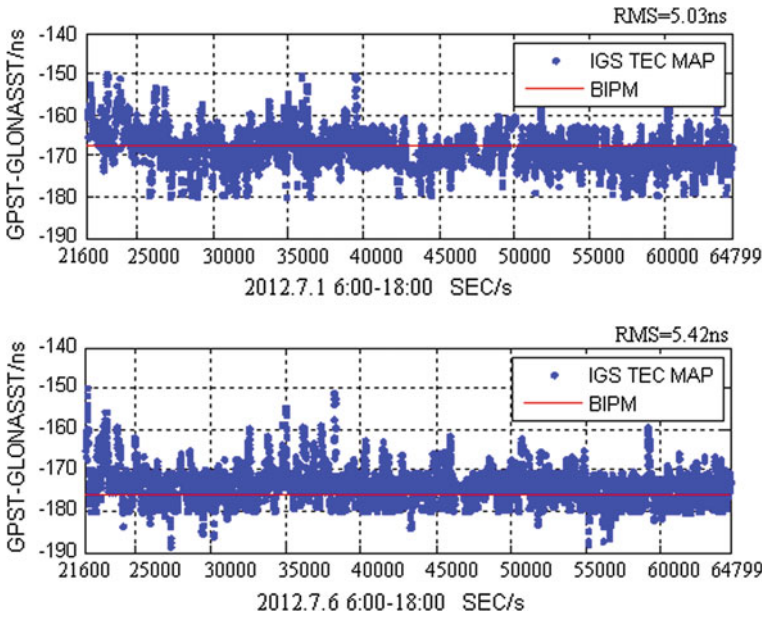

Fig. 38.3 Result of GPS/GLONASS system time offset (TEC map)

map grid point. $p = (\lambda - \lambda_0)/\Delta\lambda$, $q = (\beta - \beta_0)/\Delta\beta$, E_i and E_{i+1} are the tec at T_i, T_{i+1} moment.

Secondly, bilinear interpolation is calculated in two epochs, which t as a variable. The TEC along zenith direction at t moment is expressed as $E(\lambda, \beta, t)$, it can be calculated by:

$$\frac{T_{i+1} - t}{T_{i+1} - T_i} E_i + \frac{t - T_i}{T_{i+1} - T_i} E_{i+1} \tag{38.2}$$

Lastly, we select the appropriate mapping function to obtain each direction of the ionospheric delay.

Using the IGS TEC map for ionospheric delay determination in calculating the GPS/GLONASS system time offset. Figure 38.3 shows a part of the experimental results, and the RMS of about 5 ns.

38.3.2 Ionospheric Delays Determination by Dual-Frequency Observation

The difference of L1 and L2 pseudorange measurement is reflecting the changes in ionospheric delays because they are related to frequency. Do observe with dual-frequency receivers will be able to basically eliminate the ionospheric delays (the

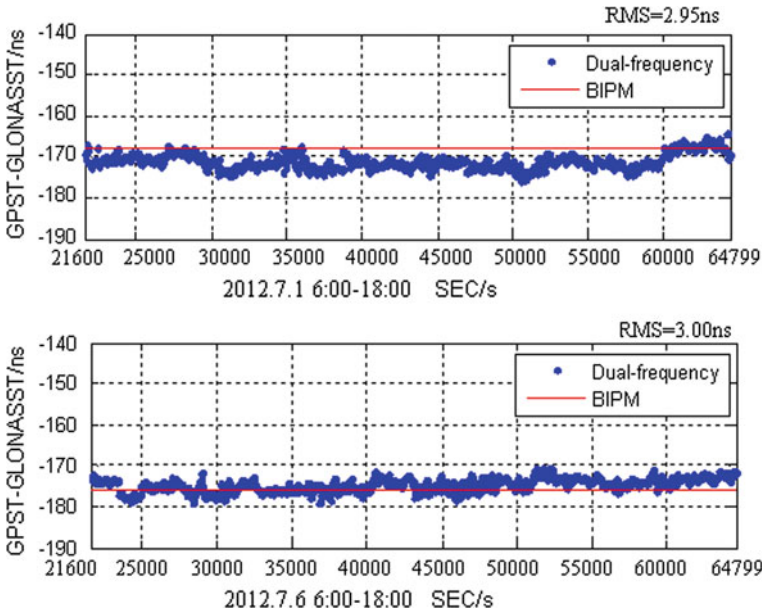

Fig. 38.4 Result of GPS/GLONASS system time offset (dual-frequency)

accuracy of the ionospheric delay measurement up to 1.2 m (about 4 ns)). Pseudoranges have no ionospheric influence can be expressed as:

$$\rho = \frac{\rho_{L2} - \rho_{L1}}{1 - \gamma} \tag{38.3}$$

where $\gamma = (f_{L1}/f_{L2})^2$. ρ is the ionospheric-free pseudarange. f_{L1} is the Carrier frequency of L1 as well as f_{L2} is the Carrier frequency of L2. ρ_{L1} is the measured value of pseudorange in L1 and ρ_{L2} is the measured value of pseudorange in L2. The disadvantage of this method is that the measurement error is enlarged although ionospheric delay error is erased. Based on a better method produced, the ionospheric delay error on L1 estimated in accordance with the following formula 38.4 [5]:

$$\Delta s_{iono,L1} = \left(\frac{f_{L2}^2}{f_{L2}^2 - f_{L1}^2}\right)(\rho_{L1} - \rho_{L2}) \tag{38.4}$$

Owing to ionospheric delays usually change slowly and a correction value Estimated should be subtracted from the pseudorange values, these corrected values must be smoothed [6].

Using the dual-frequency observation for ionospheric delay determination in calculating the GPS/GLONASS system time offset. Figure 38.4 shows a part of the experimental results, and the RMS of about 3 ns.

38.4 Analysis of the Results of GPS/GLONASS System Time Offset that Using the Different Methods to Calculate the Ionospheric Delays

Analyzing the results of GPS/GLONASS system time offset that using the different methods to calculate the ionospheric delays (shown in Fig. 38.5), it can be seen that dual-frequency correction works better than correction by IGS TEC map, the accuracy [7] of the former (the RMS about 3 ns) is higher than the latter one (the RMS about 5 ns). Figure 38.6 shows the results are compared with GPS/GLONASS system time offset published by circular T.

Determining GPS/GLONASS system offset by taking these two ionospheric delay corrections from July 2012 to September 2012, the RMS is shown in Table 38.1.

From Table 38.1, it can be concluded: After a dual-frequency measure correction, the RMS of GPS/GLONASS system time offset results is smaller about 2 ns and its accuracy improved by about 15 % compared with correction by IGS TEC map.

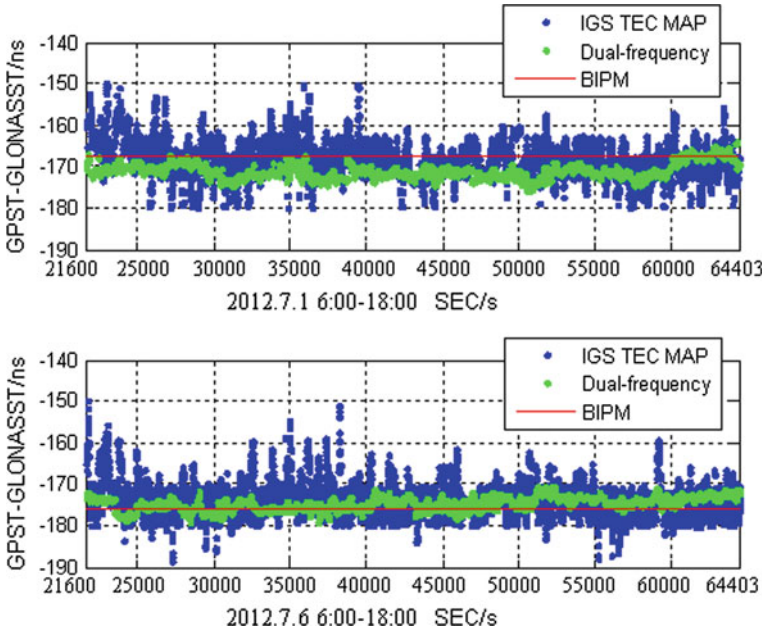

Fig. 38.5 Result of GPS/GLONASS system time offset in July 1 2012, July 6 2012 compared with the BIPM circular T

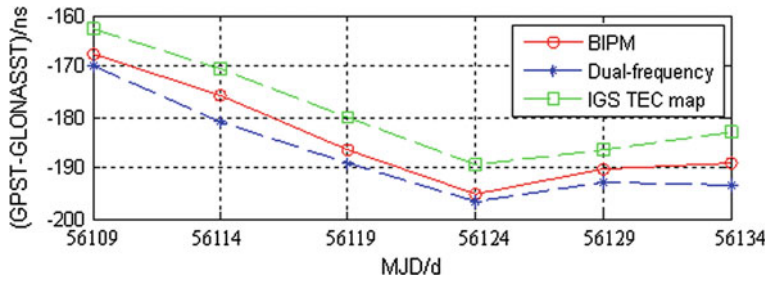

Fig. 38.6 Result of GPS/GLONASS system time offset in July 2012 compared with the BIPM circular T

Table 38.1 The RMS data compared by the two methods correction of GPS/GLONASS system time offset

	TEC map (RMS/ns)	Dual-frequency (RMS/ns)
2012.7	5.49	3.34
2012.8	5.23	3.12
2012.9	5.02	2.95

38.5 Conclusions

Ionospheric delay error has significant impact on GNSS system time offset determination. The Main objective of this article is to analyze two methods to measure the ionospheric delays in the monitoring of the GNSS system time offset, the one is TEC map provided by IGS and the other one is the dual-frequency measurement. From the experiment result, we can see that the ionospheric delays are corrected using dual-frequency observation is better than using the IGS TEC MAP. The accuracy of the former one is increased by 15 % than the latter one in monitoring results of the GPS/GLONASS system time offset.

Although the TEC map estimated ionospheric delays are not as good as dual-frequency measured ionospheric delays, the TEC map method is much simpler and cheaper. However, the reliability of IGS TEC map is not high due to there are no enough IGS sites. Besides, that will result in the estimated ionospheric delays drop in accuracy. In addition, the TEC map ionospheric delays are estimated by lag calculation, it is not recommended in real-time calculation. The ionospheric delay correction calculated by the dual-frequency measure is higher, but the L2 carrier signal of dual-frequency receivers is relatively weak and the cost is high. From this point of view, both of these two methods have their advantages and disadvantages. Therefore, when we determine the receiver delay [8] and the inter system hardware delay in monitoring the GNSS system time offset, it may be a better way to have these two methods combined.

References

1. Vanschoenbeek I, Bonhoure B, Boschetti M et al (2007) GNSS time offset: effects on GPS-Galileo interoperability performance. Inside GNSS 60–70
2. Dang Y, Bi J, Cheng Y (2007) Principles and applications of Global Navigation Satellite System, vol 9. Publishing House of Surveying and Mapping, Beijing, p 103
3. Zhang H, Li X, Xu L (2010) Monitoring and prediction of GNSS system time difference. The 1st China satellite navigation conference
4. Wu W, Li Z, Li X, Yang X (2012) The application of IGS ionosphere product in TWSTFT. J Astronaut Metrol Meas 32(4):51–54
5. Xie G (2009) GPS principles and receiver design. Publishing House of Electronic industry, Beijing, p 85
6. Kaplan ED, Hegarty CJ (2010) Understanding GPS principles and applications, vol 3. 2nd edn. Publishing House of Electronics Industry, Beijing, p 232
7. Qi G (2006) Fundamentals of time science. Higher Education Press, Beijing, p 110
8. Li X, Liu Y, Zhang H, Shi S (2009) Measurement of time delay of GPS timing receiver based on UTC (NTSC). J Time Freq 6:18–21

Chapter 39
Study on Signal-In-Space Errors Calculation Method and Statistical Characterization of BeiDou Navigation Satellite System

Liang Chen, Wenhai Jiao, Xiaorui Huang, Changjiang Geng, Lun Ai, Lu Lu and Zhigang Hu

Abstract BeiDou Navigation Satellite System (BDS), currently including valid 14 in-orbit satellites-5GEOs, 5IGSOs and 4MEOs, had provided formal operation service in the late of 2012. Different type BeiDou satellite's Signal-In-Space Range Errors (SISRE) calculation formulation is derived in this paper according to navigation satellite's Signal-In-Space Range Errors definition. SISRE of Different type BeiDou satellites are assessed and analyzed on the basis of this SISRE calculation formulation by using broadcast ephemeris data and precise orbit products from January to October, 2012 (day of year 001–303, 2012). The results show: the broadcast ephemeris orbit accuracy of BeiDou system non-GEO satellites is better than GEO satellites; the accuracy of BeiDou satellites broadcast ephemeris orbit errors in radial direction, GEO is better than 1.5 m and non-GEO is better than 1.0 m, is the best; the average of GEO satellites rms Signal-In-Space Range errors including orbit errors only is better than 2.0 m, while non-GEOs is better than 0.8 m.

Keywords BeiDou system · SISRE · Formula derivation · Signal-in-space · Accuracy statistical characterization

L. Chen (✉) · W. Jiao · C. Geng · L. Lu
Test and Assessment Research Center, China Satellite Navigation Office,
1 Fengyingdong Road, Beijing 100094, China
e-mail: sdkdchenliang@163.com; chenliang880905@163.com

L. Chen · C. Geng · L. Lu
GNSS System Engineering Center, China Academy of Aerospace Electronics Technology,
1 Fengyingdong Road, Beijing 100094, China

X. Huang · L. Ai
Beijing Research Institute of Telemetry, Nandahongmen Road, Beijing 100076, China

Z. Hu
GNSS Research Center, Wuhan University, 129 Luoyu Road, Wuhan 430079, China

J. Sun et al. (eds.), *China Satellite Navigation Conference (CSNC) 2013 Proceedings*, Lecture Notes in Electrical Engineering 243,
DOI: 10.1007/978-3-642-37398-5_39,

39.1 Introduction

BeiDou Navigation Satellite System developed and operated by China independently, can provide high-precision and high-reliability Position, Navigation and Timing service (PNT) and will be completed to be BeiDou-II, which include 35 satellites and can overlap the earth surface in 2020s [1, 2]. BeiDou Navigation Satellite System had provided trial service for Asia-pacific area users in the late of 2011. The event that 16th satellite was successfully launched on October 25, 2012 respected that the second-stage satellite network had completed, which will further promote and improve the BeiDou system service performance immensely. With the ICD formal version publishing, BeiDou had provided formal operation service for Asia–pacific area users in Dec 27, 2012.

BeiDou Navigation Satellite System currently includes valid 14 in-orbit working satellites-5 Geostationary Orbit satellites (GEOs), 5 inclined Geo-synchronization orbit satellites (IGSOs) and 4 Medium Earth Orbit Satellites (MEOs). The Fig. 39.1 shows the BeiDou system footprints and coverage (reference time–0:00:00 November 11, 2012). As can be seen from the figure, the number of visible BeiDou satellites is more than 8 in the area of Asia-pacific. The satellite marked red is GEO (C02), which was launched on October 25 and is in on-orbit tests now; The GEO (C03) satellite is adjusting to 110.5°E.

Currently, Signal-In-Space Ranging Error (SISRE) is one of key indicators which can assess the system service performance of navigation satellite system effectively. Different type BeiDou satellite's Signal-In-Space Range Errors (SISRE) calculation formula is derived in this paper according to navigation satellite's Signal-In-Space Range Errors definition. Broadcast orbit and Signal-In-Space accuracy of BeiDou system are analyzed by those calculation formulae and a series of results and conclusions are got in this paper too.

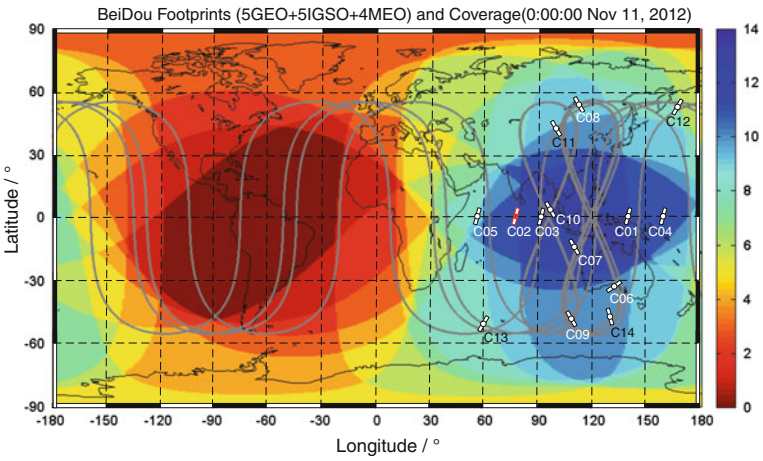

Fig. 39.1 BeiDou satellites footprints and depth of coverage (reference time–0:00:00 2012-11-11)

39.2 Calculation Method of BeiDou Signal-In-Space Errors

39.2.1 Navigation Satellite SISRE

The Signal-In-Space Ranging Error (SISRE) is a key performance indicator for assessing the performance of the BeiDou Navigation Satellite System. SISRE can be defined as the difference between the satellite position based on the broadcast navigation data (position and clock) and the truth, projected on the line-of-sight to the user [3]. The instantaneous SISRE values can be evaluated at a large number of spatial points spread evenly across the satellite's coverage on the surface of Earth, and the global average SISRE can be computed as the rms of the instantaneous SISRE value at each of those spatial points [4].

As shown in Fig. 39.2, R_S is orbital radius of navigation satellite, r_E is the average radius of the Earth; $\overrightarrow{E} = (-C,\ A,\ -R)$ is the deviation vector of broadcast orbit error in the Cross, Along, Radial direction, respectively. A space Cartesian coordinate system is created as shown in the figure. A point D, the projection of which in xoy plane is D', is selected arbitrarily in the satellite S coverage on the earth surface. Assuming the angle between OD and the z-axis is α, OD′ and x-axis β. From those, $\overrightarrow{SD}$ direction normalized vector can be got as follow:

$$\overrightarrow{l} = \frac{\overrightarrow{SD}}{\left|\overrightarrow{SD}\right|} = \frac{(r_E \sin\alpha \cos\beta,\ r_E \sin\alpha \sin\beta,\ r_E \cos\alpha - R_S)}{\sqrt{r_E^2 - 2r_E R_S \cos\alpha + R_S^2}} \tag{39.1}$$

If we assume uniform distribution of positions on the surface of Earth [5, 6], for the point $D\ (\alpha,\ \beta)$ on the surface of Earth the superficial area in the range of $[\alpha,\ \alpha + \mathrm{d}\alpha]$, $[\beta,\ \beta + \mathrm{d}\beta]$ is $[\beta,\ \beta + \mathrm{d}\beta]$, then the superficial area of satellite S coverage on the surface of Earth is $\int_0^{2\pi}\int_0^{\frac{\pi}{2}-\theta} r_E^2 \cdot \sin\alpha\,\mathrm{d}\alpha\,\mathrm{d}\beta$. So the joint probability distribution of the point in satellite coverage on the surface of Earth is:

$$p(\alpha,\ \beta) = \frac{r_E^2 \cdot \sin\alpha\,\mathrm{d}\alpha\,\mathrm{d}\beta}{\int_0^{2\pi}\int_0^{\frac{\pi}{2}-\theta} r_E^2 \cdot \sin\alpha\,\mathrm{d}\alpha\,\mathrm{d}\beta} = \frac{\sin\alpha\,\mathrm{d}\alpha\,\mathrm{d}\beta}{2\pi(1 - \sin\theta)} \tag{39.2}$$

According to the definition of "Global Positioning System Standard Positioning Service Performance Standard 2008" for resolving the global average SISRE formula, the global average SISRE is RMS statistical value of the projection error of satellite signal-in-space error (orbit error $\overrightarrow{E}$ and satellite clock error T) on the signal propagation direction $\overrightarrow{l}$ [6, 7]. From Fig. 39.2, variable range of α is $\left[0,\ \frac{\pi}{2} - \theta\right]$, and the β is $[0,\ 2\pi]$. Thus, the RMS formula of SISRE is as follows:

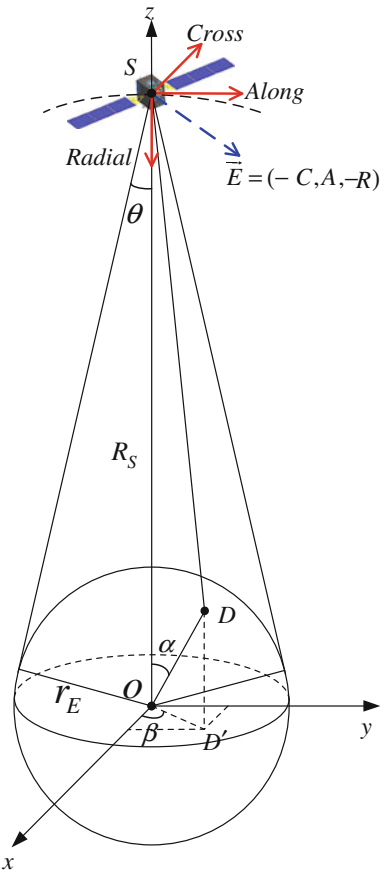

Fig. 39.2 Diagram of orbit errors in *Radial*, *Along*, *Cross* direction and Signal-In-Space range errors formula derivation

$$rms\,SISRE = \sqrt{\int_0^{2\pi}\int_0^{\frac{\pi}{2}-\theta}\left[\vec{E}\cdot\vec{l}-c\cdot T\right]^2\sin\alpha\,\mathrm{d}\alpha\,\mathrm{d}\beta \Big/ 2\pi(1-\sin\theta)} \tag{39.3}$$

where, c is the speed of the light in vacuum, T is the satellite clock error.

39.2.2 SISRE Formulation of BeiDou System

BeiDou satellite navigation constellation consists of GEO satellites, IGSO satellites and MEO satellites. Because orbit height of different type BeiDou satellites is different with GPS, the SISRE calculation formula is different. In order to get the BeiDou system SISRE approximate calculation formula, we assume that the Earth

is a uniform sphere, average radius of which is 6,371 km; BeiDou GEO and IGSO satellite's average orbit height are 35,786 km, and the MEO's is 21,528 km [8, 9].

According to those assumptions, we can obtain the BeiDou GEO and IGSO satellite's $\theta = 8.69°$, MEO satellite's $\theta = 13.21°$ in the Fig. 39.2. Substituting θ into the formula (39.3), different type BeiDou navigation satellite's SISRE approximate calculation formula can be obtained as follows:

$$\begin{aligned} rms\,SISRE_{GEO\&IGSO} &= \sqrt{0.9842 \cdot R^2 - 1.9841 \cdot R \cdot cT + (c \cdot T)^2 + 0.0079 \cdot (A^2 + C^2)} \\ &\approx \sqrt{(0.99 \cdot R - c \cdot T)^2 + \frac{1}{127} \cdot (A^2 + C^2)} \end{aligned} \tag{39.4}$$

$$\begin{aligned} rms\,SISRE_{MEO} &= \sqrt{0.9631 \cdot R^2 - 1.9627 \cdot R \cdot cT + (c \cdot T)^2 + 0.0185 \cdot (A^2 + C^2)} \\ &\approx \sqrt{(0.98 \cdot R - c \cdot T)^2 + \frac{1}{54} \cdot (A^2 + C^2)} \end{aligned} \tag{39.5}$$

The statistics results SISRE in this paper only consider the satellite's broadcast orbit error, that is:

$$rms\,SISRE_{G\&I-Orbit-error-only} = \sqrt{(0.99 \cdot R)^2 + \frac{1}{127} \cdot (A^2 + C^2)} \tag{39.6}$$

$$rms\,SISRE_{M-Orbit-error-only} = \sqrt{(0.98 \cdot R)^2 + \frac{1}{54} \cdot (A^2 + C^2)} \tag{39.7}$$

39.3 Data Sources

39.3.1 WHU's Precise Ephemeris

Some data used in this paper are based on the international GNSS monitoring and assessment system (iGMAS). As the Data and Analysis Center of the iGMAS, Wuhan University (WHU) set out to establish the BeiDou Experimental Tracking Stations (BETS, as shown in Fig. 39.3) worldwide at the beginning of 2011 to carry out comprehensive scientific and application studies about the BeiDou Navigation Satellite System. Currently, a continuous tracking network for BeiDou in-orbit satellites has been basically formed. Currently, the BETS network consist of nine domestic stations and seven overseas continuous tracking stations, which are equipped with UR240-CORS, independently developed by China and supporting Beidou/GPS dual system quadruple frequency high-accuracy receivers. By PANDA (Position And Navigation Data Analysis) software processing the observations of BETS network, BeiDou system precise orbit products can be obtained in format sp3. From the orbit results, the radial accuracy of the BeiDou satellite precise orbit is better than 10 cm, the other directions accuracy of

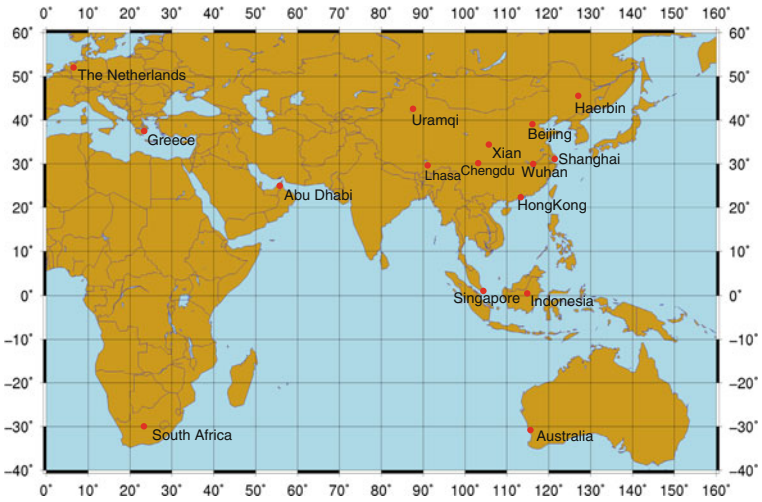

Fig. 39.3 BeiDou experimental tracking stations (BETS) for producing precise ephemeris products

overlapping arcs can reach to 10–20 cm [10]. Relative to the meters accuracy of BeiDou broadcast ephemeris orbit, the precise ephemeris products can be used as its reference true value absolutely.

What need to mention is that the precise orbit accuracy of IGSO satellite is better than GEO satellite's from the orbit results. Some reasons are as follow: firstly, because flare angle of the GEO satellite relative to the earth is very small (less than 18°) and BETS network belongs to a local distribution tracking network currently, observation geometry structure strength to the GEO satellites is poor. Secondly, the GEO satellite is a kind of Geostationary Orbit satellite and keep stationary relative to the ground tracking stations, the geometry changes of satellite-to-station are very small, the information increased by increasing the observation time is limited, so some system errors (such as clock error and tracking station position deviation) are hard to be resolved and separated, which makes the GEO satellite orbit errors in along track direction are large. These factors may affect the statistical analysis result of BeiDou broadcast ephemeris orbit accuracy in the following paper.

39.3.2 Data Selection and Processing Strategies

In order to assess and analyse the accuracy of the BeiDou system signal-in-space effectively, consecutive ten months broadcast ephemeris data are selected since BeiDou system began to provide trial service in the late of last year (Day of Year 001-303, 2012). The selected satellite data arcs are shown in Table 39.1. Taking

Table 39.1 Data arc selected in this paper

Satellite no.	Satellite type	Start time	End time
C01	GEO	2012.1.1	2012.10.29
C02	GEO	–	–
C03	GEO	2012.1.1	2012.10.29
C04	GEO	2012.1.1	2012.10.29
C05	GEO	2012.5.1	2012.10.29
C06	IGSO	2012.1.1	2012.10.29
C07	IGSO	2012.1.1	2012.10.29
C08	IGSO	2012.1.1	2012.10.29
C09	IGSO	2012.1.1	2012.10.29
C10	IGSO	2012.1.1	2012.10.29
C11	MEO	2012.7.1	2012.10.29
C12	MEO	2012.7.1	2012.10.29
C13	MEO	–	–
C14	MEO	–	–

the BeiDou precise ephemeris provided by iGMAS Data and Analysis Center (WHU) as the reference true value and following the BeiDou SISRE calculation formula obtained above, BeiDou system present broadcast ephemeris orbit accuracy and SISRE are assessed in the follow paper.

39.4 Statistical Characterization of BeiDou Signal-In-Space Errors

39.4.1 Statistics and Analysis of Broadcast Ephemeris Orbit Error

In order to analyze the change rules of different type BeiDou satellite's broadcast orbit error in each direction over time, GEO (C04), IGSO (C06) and MEO (C11) orbit data in September, 2012 (Day of Year 245–274) are selected to give typical examples in this part, as shown in Fig. 39.4.

At the same time, we also statistic the mean and standard deviation of BeiDou in-orbit working satellite's ephemeris errors in Radial, Along and Cross direction from January to October, 2012, which is shown in Fig. 39.5, and the RMS of BeiDou ephemeris in each direction according to the formula (39.8), as shown in Table 39.2.

$$RMS = \sqrt{\sum_{i=1}^{n} v_i \cdot v_i \Big/ n - 1} \tag{39.8}$$

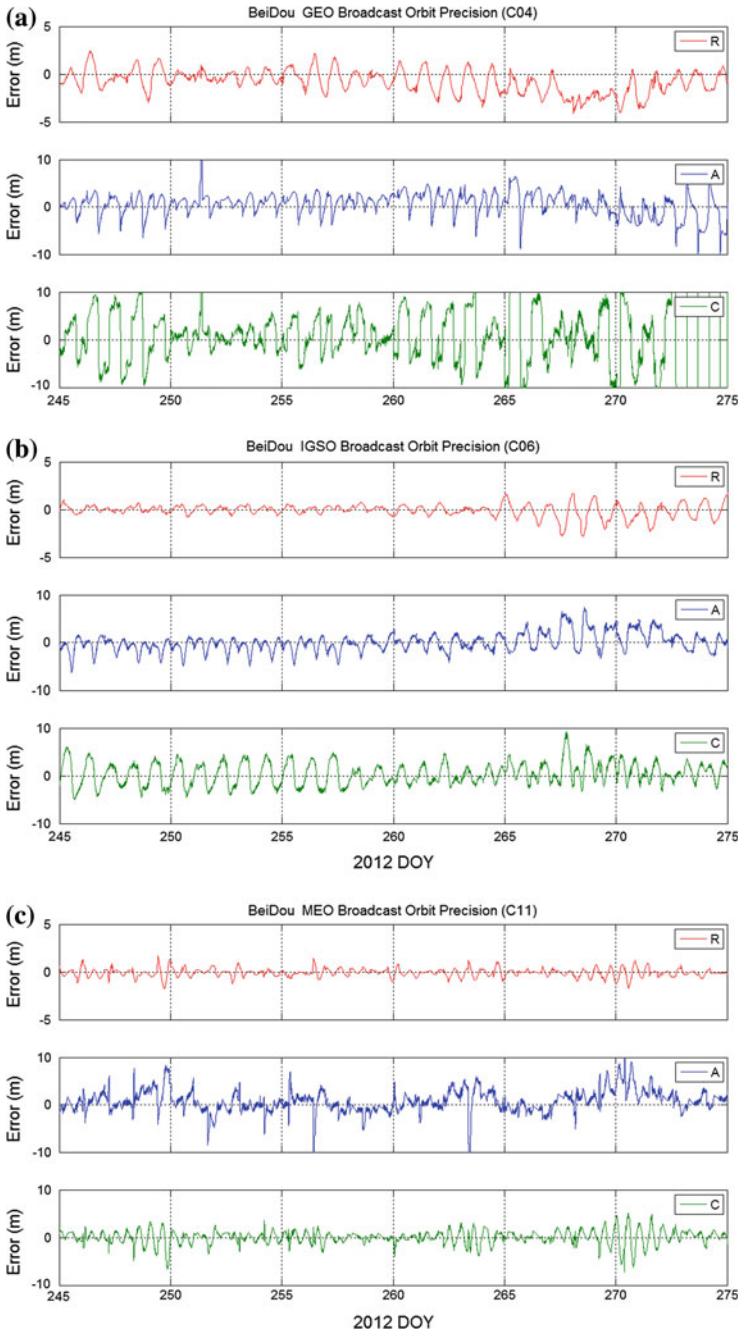

Fig. 39.4 Broadcast ephemeris errors change curve versus time of Different type BeiDou satellites are BeiDou MEO Broadcast Orbit Precision **a** C04, **b** C06, and **c** C11

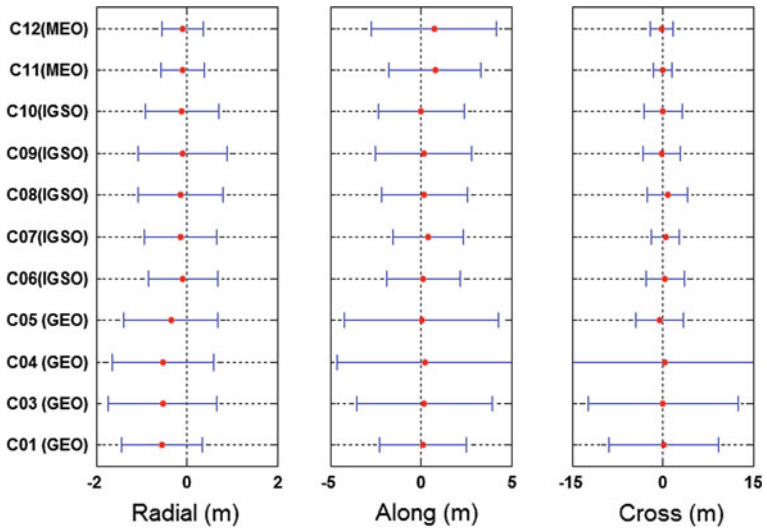

Fig. 39.5 Mean and once standard deviation of BeiDou Navigation Satellite System broadcast ephemeris errors

Table 39.2 RMS Accuracy statistic of BeiDou satellites broadcast orbit errors in Radial, along and cross direction

Satellite no.	Satellite type	Radial (m)	Along (m)	Cross (m)
C01	GEO	1.041	2.417	9.063
C03	GEO	1.310	3.744	12.471
C04	GEO	1.231	4.867	20.434
C05	GEO	1.109	4.238	3.935
C06	IGSO	0.774	2.051	3.191
C07	IGSO	0.807	1.972	2.342
C08	IGSO	0.953	2.372	3.341
C09	IGSO	0.991	2.648	3.132
C10	IGSO	0.817	2.384	3.172
C11	MEO	0.492	2.654	1.519
C12	MEO	0.470	3.540	1.914

Combining Figs. 39.4, 39.5 and Table 39.2, what can be obtained as follow:

1. The broadcast orbit errors in each direction exit significant periodic fluctuation. Figure 39.4 shows that there are obvious fluctuations in all directions since DOY265.
2. Although ephemeris errors are generally assumed to be zero-mean, the reality may be different. Figure 39.5 indicates the mean of Radial, Along and Cross normalized by the standard deviation. In Fig. 39.5, the red dots denote the mean, while the blue lines with a length of once the standard deviation are centered at the red dots. From the figure, we can get that most of the mean of

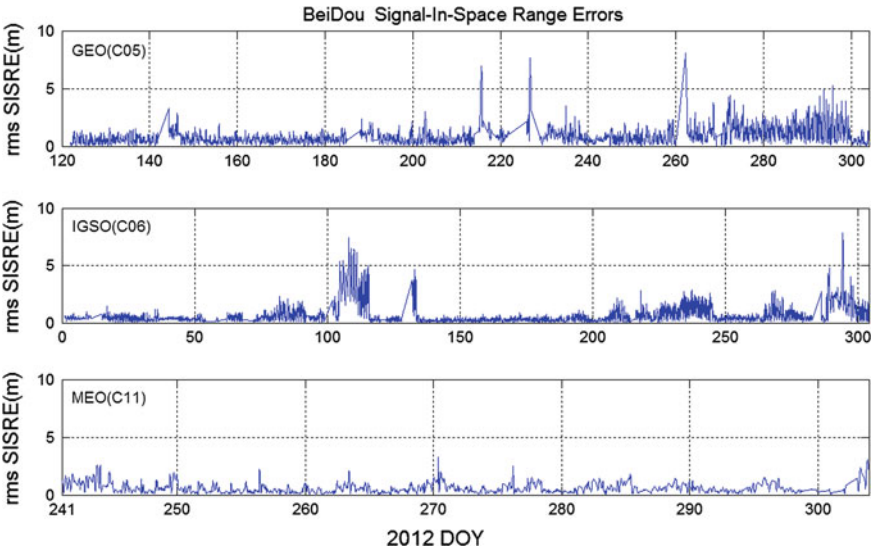

Fig. 39.6 Orbit-error-only SISRE change curve versus time of different type BeiDou satellites

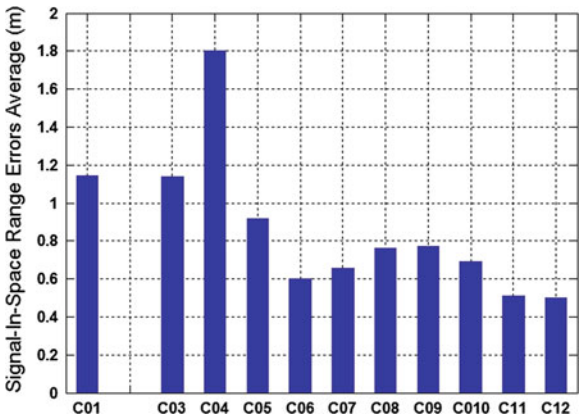

Fig. 39.7 Mean of BeiDou system Orbit-error-only SISRE from DOY 001-303, 2012

BeiDou non-GEOs ephemeris errors in each direction are near zero, while radialtrack errors usually have a negative mean.

3. Table 39.2 indicates the accuracy of radial ephemeris errors is the best, with GEOs is better than 1.5 m, IGSOs precedes 1.0 m and MEOs is superior to 0.5 m. This is because the ground tracking stations to satellite observations changes in the radial is more sensitive than the other two directions, and the force model in along track and cross track is not perfect.
4. Figure 39.5 and Table 39.2 indicate the ephemeris errors accuracy of IGSOs and MEOs in each direction is better than GEOs'. In Fig. 39.5, there is a larger standard deviation of the C04 (GEO) ephemeris error in cross direction, which is 20.43 m.

39.4.2 SISRE Statistics and Analysis

By the formula (39.6, 39.7), what can be obtained is that radial errors have a greater impact on SISRE; better radial error can obtain better SISRE. Using the data in Table 39.1, we calculate and analyze the orbit-error-only SISRE ($SISRE_{Orbit\text{-}error\text{-}only}$) of different type BeiDou satellites. Figure 39.6 shows orbit-error-only SISRE change curve versus time of Different type BeiDou satellites, taking GEO(C05), IGSO(C06) and MEO(C11) as typical examples.

As can be seen from the Fig. 39.5, the orbit-error-only SISRE changes of different type BeiDou satellites are smooth; Most of GEO and IGSO satellite's orbit-error-only SISRE is better than 3.0 m, while MEO satellite's is superior to 2.0 m.

Figure 39.7 shows the statistic mean of BeiDou satellites orbit-error-only SISRE from DOY 001-303, 2012. From that, the mean of GEOs orbit-error-only SISRE, better than 2.0 m, is larger than non-GEO satellite's, which is superior to 1.8 m. From the statistical results, the BeiDou system's orbit-error-only SISRE has keep the same level with GLONASS [5].

39.5 Conclusions

Now BeiDou Navigation Satellite System has completed the work of second-stage satellite network (5GEO+5IGSO+4MEO). Based on the characteristics of the BeiDou satellite orbit, Different type BeiDou satellite's Signal-In-Space Range Errors (SISRE) calculation formula, as the key, is derived in this paper. Using the broadcast ephemeris data and precise ephemeris product from January to October, 2012 (Day of Year 001-303, 2012), broadcast orbit accuracy and Signal-In-Space performance of BeiDou system are elevated and analyzed by those calculation formulae. Statistical analysis results show as follow:

1. The broadcast ephemeris orbit accuracy of BeiDou system non-GEO satellite is better than GEO satellite;
2. The radial ephemeris error accuracy of each BeiDou satellites is the best, GEO is better than 1.5 m, non-GEO is superior to 1.0 m;
3. The mean of GEO satellite's Orbit-error-only SISRE is better than 2.0 m, while non-GEOs' is superior to 0.8 m.
4. BeiDou system broadcast ephemeris orbit-error-only SISRE has keep the same level with GLONASS. But comparing to GPS system's better than 1.0 m broadcast ephemeris orbit-error-only SISRE [11], there is still room for further improvement for the BeiDou system's broadcast ephemeris orbit accuracy.

With the further development of the BeiDou Navigation Satellite System, the broadcast ephemeris orbit accuracy will be further improved and enhanced to provide better positioning and navigation services for global users

Acknowledgments The author is grateful for receiving the support from China Satellite Navigation Conference 2012 youth outstanding papers found (CSNC2012-QY-4) project and the help and guidance from Doctor Jiao Wenhai coming from Chinese Satellite Navigation Office. The author is also thankful for BeiDou precise ephemeris products provided iGMAS Data and Analysis Center-Wuhan University.

Funding Information

China Satellite Navigation Conference 2012 youth outstanding papers found project (CSNC2012-QY-4).

References

1. Sun J (2010) Evolution of compass. Xidian University, Xi'an
2. Ran C (2010) Plan of compass development. Chinese Satellite Navigation Office, Beijing
3. Gaetano G, Manuel S, Francisco G et al (2009) GIOVE-B navigation message performance analysis and single in space user ranging error (SISRE) characterization. ION GNSS 2009, Savannah, GA
4. US DoD (2008) Global positioning system standard positioning service performance standard, 4th edn. Sept 2008
5. Zumberge JF, Bertiger WI (1996) Ephemeris and clock navigation message accuracy. Global positioning system theory and applications, vol 1, Chapter 16, Parkinson BW ed. American institute of aeronautics and astronautics, Cambridge
6. Heng L, Gao GX, Walter T et al (2011) Statistical characterization of GLONASS broadcast ephemeris errors. In: Proceedings of the 24th international technical meeting of the satellite division of the institute of navigation (ION GNSS 2011), Portland, OR, pp 3109–3117
7. Malys S, Lazeros M, Gottschalk S et al (1997) The GPS accuracy improvement initiative. In: Proceedings of the 10th international technical meeting of the satellite division of the institute of navigation, ION-97, Kansas City
8. BDS-SIS-ICD (2012) BeiDou navigation satellite system signal in space interface control document open service signal B1I (Version 1.0), China Satellite Navigation Office, December 2012
9. Holfman-Wellenhof B, Lichtenegger H, Wasle E (2007) Global navigation satellite systems-GPS, GLONASS, Galileo and more. Springer, New York
10. Shi Chuang, Zhao Qile, Li Min et al (2012) Precise orbit determination of Beidou satellites with precise positioning. Sci Chin Earth Sci 55(7):1079–1086
11. Heng L, Gao GX, Walter T et al (2011) Statistical characterization of GPS signal-in-space errors. In: Proceedings of the 2011 international technical meeting of institute of navigation (ION ITM 2011), San Diego, pp 312–319

Chapter 40
A New EIRP Measurement for User Equipments Based on CRDSS

Qian Wang and Chao Xie

Abstract The radiated signal of user equipment enters into the station effectively only with the proper power, so effective isotropic radiated power (EIRP) is the main factor for design of user equipment. The precise value of EIRP is measured in the two dimensional plane condition of darkroom. While in outside circumstance, ERIP is calculated complicatedly by many parameters of communication route, but the final result is not right. In this paper, to satisfy the operation need of Comprehensive Radio Navigation Satellite Service (CRDSS), emission route is abstracted into mathematical models, apart from the circumstance, distance and device factor, the angle formed by antenna and satellite is taken and the right valve of EIRP of multiple satellites is got simultaneously by the geometry relation of solid space. EIRP measurement is executed on the GEO and IGSO satellite by this way, it is useful for evaluation of effective entrance range to the station and design of satellite constellation. On the basis, the concept of extended angle is proposed to testify the practicableness of satellite. Experiment data in the east and west polar region of china proves out this measurement way. The conclusion is that ERIP of 4dBw is proper lower limit for signal to enter into the station in the condition of satellite constellation and signal processing.

Keywords CRDSS · EIRP · Effective extended angle · Link calculation

40.1 Introduction

CRDSS [1] is the special operation of Compass navigation system. The function of position service share was performed only by the technique of GPS position and communication in the past time, but it is totally substituted by CRDSS. CRDSS

Q. Wang (✉) · C. Xie
Beijing Satellite Navigation Center, Beijing 100094, China
e-mail: wqaloha@139.com

J. Sun et al. (eds.), *China Satellite Navigation Conference (CSNC) 2013 Proceedings*, Lecture Notes in Electrical Engineering 243,
DOI: 10.1007/978-3-642-37398-5_40,

combines measurement, orientation and position report, simplifies the different demand of user and complex math processing into the unified manipulation. Complexity of user equipment and the basic facilities is reduced by CRDSS. The technique is not the simple mixture of navigation and communication, but a entirely new mode and service idea to meet the diversified needs of the application.

CRDSS is a radio positioning system of measuring distance among multiple reference stations, which includes the parts of RDSS of two satellites, RDSS of three satellites and Radio Navigation Satellite System (RNSS). The most distinctive difference with RNSS is that user equipment need transmit a response signal to different type of satellites (2 GEO satellites and 1 IGSO satellite). It is urgent to measure EIRP of user equipment accurately and quickly by practical way to ensure that transmitting signal is received and relaid through satellite transponder. The classical calculation method based on communication link involves many application parameters and link processing, so this way is not practical in the project realization due to parameter accuracy and computational complexity.

In view of the above problems, this paper analyses the systematical transmission link of CRDSS device, and sets up a model way of EIRP measurement and quantitative expression making direct use of signal factors and orbital elements apart from the circumstance, distance and device factor. The concept of effective extended angle is proposed to reflect satellite availability, and field test data proves the effectiveness of the method. The research method and conclusion provides basis for design of user equipment. It is the reference to the design of constellation of navigation system.

40.2 Analysis of Transmission Link

40.2.1 Explain of Process

Link Composition of CRDSS is shown in Fig. 40.1. Measurement and control center (MCC) in the ground transmits signal of measuring distance. After receiving the forward signal through any satellite, user equipment transmits response signal to three satellites. MCC receives the response signal through three satellites, gets the

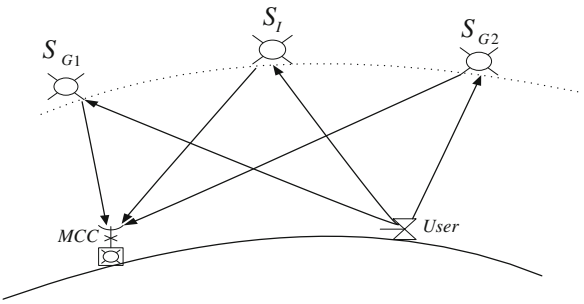

Fig. 40.1 Composition structure of CRDSS system

round trip distance from MCC to user, and completes the solution of user position finally. From the above processing, three satellites compose the certain geometric relationships and relay the signal from the user equipment to get good position results. It is very important to set proper value of EIRP.

40.2.2 Calculation in Theory and Limitation

It is an usual computing method [2] that EIRP is deducted according to received electrical level and state of link from the ground to satellite. Input link of CRDSS is random access for multiple user signals. Due to power difference of user, the cross-correlation value produced by large power and small power is so much larger than the autocorrelation value that the signal of small power does not enter into the station [3, 4]. So it is very important to set the proper EIRP and the acceptable lower level respectively for user and MCC. In addition, these factors such as G/T of satellite, signal gain of satellite channel, loss of free space, and loss of weather produce the influence of ERIP calculation. The measure method of G/T of satellite can be found in the paper [5].

Table 40.1 shows the calculation value of electronic level and ERIP while the user equipments of 5 and 10 W power amplifier work in Beijing region. From the test, the EIRP value of 10 W power is 2 times as much as that of 5 W power, which is matching to the true ratio. The problem is that EIRP value is 2 or 3 dB larger than the true power. There are two reasons to explain why it happens. One is that many indefinite factors cause the complex test in the outdoor environment. ERIP calculation involves many parameters, which are defined by the typical and statistical value as described in the parameter Table 40.2, but these values are not ac-curate number in the certain environment only to express theoretical significances. The other is the error caused by difference of processing equipment in the station and volatility of level in calculation of electronic level.

Table 40.1 Electronic level of entering into the station and EIRP value

Power amplifier (W)	Designed angle	Inbound electrical level			Calculation value of EIRP		
		Beam 1	Beam 3	Beam 5	East	West	Middle
10	180/90	53.9	51.8	51.7	15.9	13.8	13.8
	180/80	53.9	51.7	51.7	15.9	13.7	13.8
	180/70	53	49.3	53.4	15	11.3	15.5
	180/50	52.5	49.3	53.5	14.5	11.3	15.6
	180/30	53.65	49.9	52.5	15.6	11.8	14.6
5	180/90	0	46.85	47.3	0	8.8	9.3
	180/80	49	48.39	50	11	10.5	12
	180/70	50.34	49.4	50	12.3	11.5	12
	180/50	50.7	48.3	50.6	12.7	8.8	12.5
	180/30	43.57	47.5	49	0	9.5	11

Table 40.2 Working parameters of link calculation

Parameter of uplink	Parameter of downlink
User EIRP	Receiving power
Free Space loss of uplink	Free space loss of downlink
Loss of weather (T1)	Loss of weather (T2)
G/T1 of satellite	G/T2 of central station
Carrier noise ratio of uplink	Carrier noise ratio of downlink

40.3 Modeling of Included Angle Factor and Actual Calculation

Based on the definition of EIRP, the value of EIRP is measured and calculated by the model of included angle. On the basis, the actual prediction is executed. The definition [6] is as follows:

$$EIRP = P_T(f)G_T(f) \tag{40.1}$$

where P_T is power density of transmission signal, G_T is power gain, which is directly related with included angle between the antenna and the satellite (Fig. 40.2).

40.3.1 Calculation of Satellite Angle [7]

From the above figure, the coordinate of user position in Earth centered Earth fixed frame system is (x,y,z), the coordinate of satellite position is (x^s,y^s,z^s), the observation vector from user to satellite is

$$\begin{bmatrix} \Delta x \\ \Delta y \\ \Delta z \end{bmatrix} = \begin{bmatrix} x^s \\ y^s \\ z^s \end{bmatrix} - \begin{bmatrix} x \\ y \\ z \end{bmatrix} \tag{40.2}$$

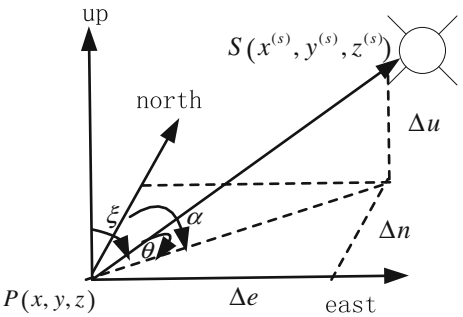

Fig. 40.2 Diagram of satellite angle

The observation vector $[\Delta x \quad \Delta y \quad \Delta z]^T$ is substituted for vector in the local level frame system as point p is base point, the alteration relationship is

$$\begin{bmatrix} \Delta e \\ \Delta n \\ \Delta u \end{bmatrix} = S \bullet \begin{bmatrix} \Delta x \\ \Delta y \\ \Delta z \end{bmatrix} \tag{40.3}$$

In the expression, $S = \begin{bmatrix} -\sin\lambda & \cos\lambda & 0 \\ -\sin\varphi\cos\lambda & -\sin\varphi\sin\lambda & \cos\varphi \\ \cos\varphi\cos\lambda & \cos\varphi\sin\lambda & \sin\varphi \end{bmatrix}$ (ϕ is latitude in location, λ is longitude in location).

Based on the principle of trigonometry as described in the figure, the expression of elevation and azimuth angle of the satellite is as follows:

$$\theta = \arcsin\left(\frac{\Delta u}{\sqrt{(\Delta e)^2 + (\Delta n)^2 + (\Delta u)^2}}\right) \tag{40.4}$$

$$\alpha = \arctan\left(\frac{\Delta e}{\Delta n}\right) \tag{40.5}$$

40.3.2 Elevation Angle of GEO Satellite

As an example of the middle latitude region of 40°, the range of longitude is from 70 to 140°, which covers the entire region of china from the east to the west. The variety of elevation angle of east, west and middle satellite by above calculation is shown in the Fig. 40.3. From the figure, the elevation angle of middle spare satellite is more than 30° in the whole region. The elevation angle of east satellite

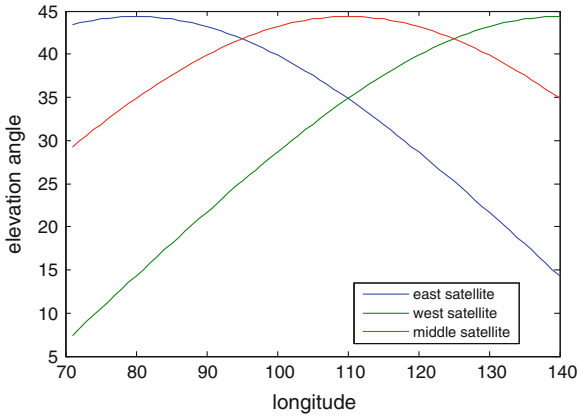

Fig. 40.3 Changes of GEO satellite elevation angle

is pairing with that of west satellite. In the any region, there are two available satellites of high elevation angle for users. The results show three GEO satellites can complete the RDSS operation of double satellites in the whole region of china and surrounding areas.

40.3.3 Elevation Angle of IGSO Satellite

To be the certain geometric shape, CRDSS system usually involves one IGSO satellite. The intersection formed by the earth surface and connection between satellite and earth center is called point under satellite. The point shape of IGSO is "8" through crossover point of the equator. The moving cycle is 24 h. Variety of IGSO elevation angle in the region of high latitude, middle latitude, and low latitude is shown with the passage of time. The lower is latitude, the longer is the effective duration time of elevation angle. The effective duration time of elevation angle is more than 12 h in the region of high latitude (60°). Two alternate IGSO satellites provide effective CRDSS service for users in the above place (Fig. 40.4).

40.3.4 Calculation of Included Angle

Provided that the angles of satellites and users are known, the included angle between user and satellite can be estimated. In the Fig. 40.5, point A expresses antenna of receivers, P0 expresses horizontal plane that the receiver is located in. P1 expresses vertical plane that satellite is located in. Point B expresses the point that Plane P1 intersects with connecting line between satellite and receiver. Point

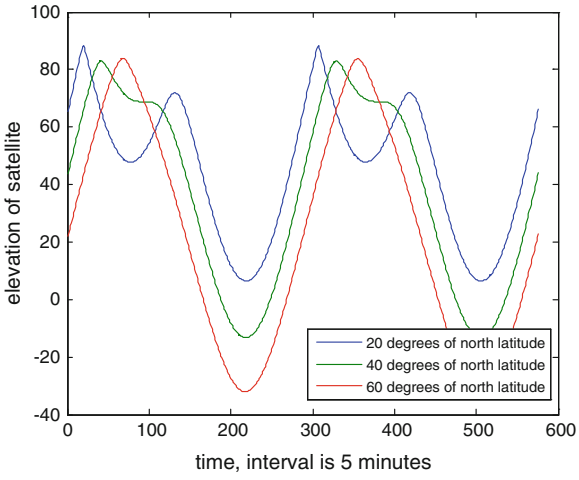

Fig. 40.4 Changes of IGSO satellite elevation angle

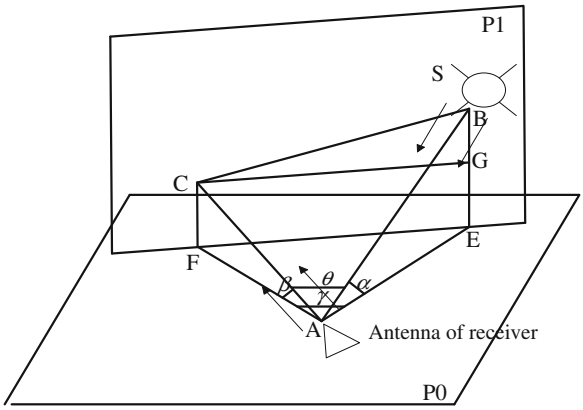

Fig. 40.5 Diagram of included angle calculation

C expresses point that antenna normal intersects with plane P1. E expresses the vertical point of B in the plane P0. F expresses the vertical point of C in the plane P0. G expresses vertical point of C in the line BE. α expresses elevation angle of satellite, β expresses elevation angle of antenna. γ expresses horizontal azimuth angle of satellite and antenna. θ expresses included angle of satellite and antenna, which is the last destination. To ensure the uniqueness of plane P1, P1 is perpendicular to P0. Projection length of Line AC in the plane P0 with the direction of antenna normal line is the same as that of line AB with the direction of satellite and user. This design simplifies subsequent calculation.

$$AB = \frac{AE}{\cos(\alpha)} \tag{40.6}$$

$$AC = \frac{AF}{\cos(\beta)} \tag{40.7}$$

Based on Eqs. (40.6) and (40.7), according to Cosine theorem,

$$EF = \sqrt{AE^2 + AF^2 - 2 \cdot AE \cdot AF \cdot \cos(\gamma)} \tag{40.8}$$

$$CG = EF \tag{40.9}$$

$$BC = \sqrt{BG^2 + EF^2} \tag{40.10}$$

If the length of line the AB, AC, and BC is known, according to cosine theorem, the angle value of θ is found.

The analysis Fig. (40.6a–d) are shown in the different region based on the above theory. Provided that the azimuth angle is stationary and the elevation angle of satellite is small, the larger is the elevation angle of antenna, the smaller is angle between antenna and satellite. Conversely, when the elevation angle is large, the variety of antenna elevation angle has small effect on the above angle. Or the larger is elevation angle, the larger is the above included angle.

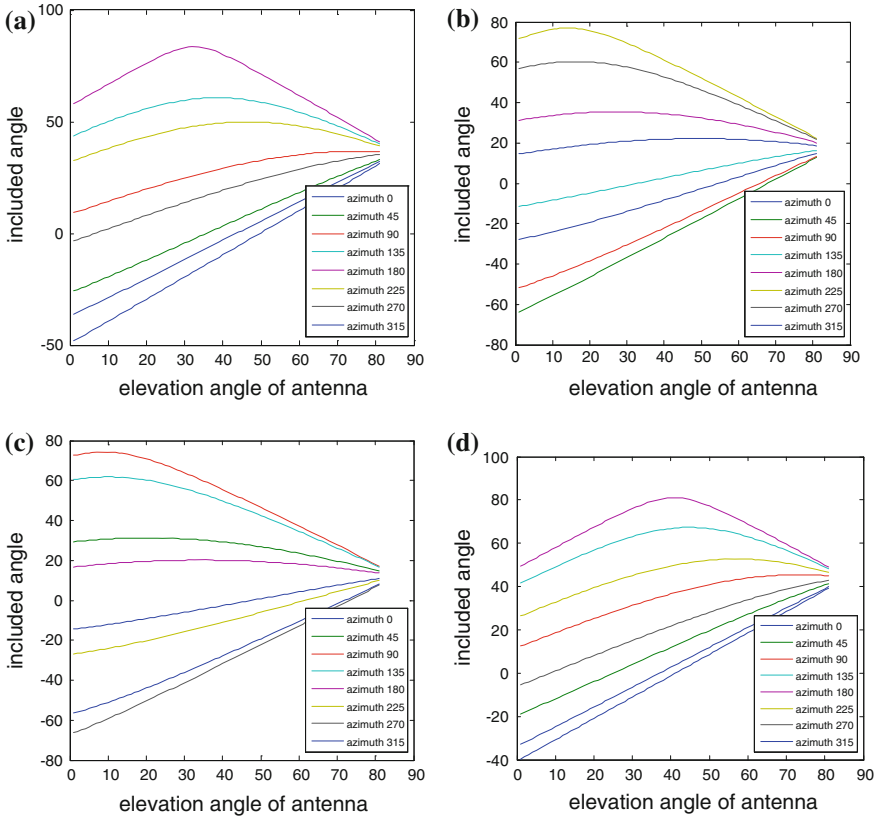

Fig. 40.6 **a** Analysis of east sat. in Fy. region. **b** Analysis of west sat. in Fy region. **c** Analysis of east sat. in KS. region. **d** Analysis of west sat. in KS. region

When the elevation angle of antenna is stationary, the angle range from 30 to 60° is suitable according to using habit. Corresponding to the included angle (more than 30°), the range of azimuth angle is called "effective extended angle". Effective extended angle is 135 and 90° respectively corresponding to east and west satellite in fuyuan region. Effective extended angle is 90 and 180° respectively corresponding to east and west satellite in kashi region. The large range of effective extended angle shows that the receivers produce good results of entering into the station in the region.

40.4 Verification of Actual Measurement Data

40.4.1 Performance Detection of Transmission Antenna

To get high power gain of transmission, entire directional antenna is used in the receiver. Out of roundness of antenna is 1 as far as possible. Variety of power gain in the different elevation angle is small. Restricted with the technical and productive factor, circularly polarized microstrip antenna in use produces the certain deviation. Experiment results show that from the directional diagram of antenna in the dark-room the range of power gain is within 3 dB in the elevation range from 30 to 90°.

40.4.2 Analysis of Actual Data

To verify the practical results of receiver ERIP in the outside environment, the representative test regions such as kashi in xinjiang province and fuyuan province in Heilongjiang are selected in this paper. These two places are located in the west and east bottom of china to test service performance of GEO satellite in the edge of position.

Experiment is done in the open region without the obvious interference. Horizontal calibration instrument is used to define base level. Receiver is placed on the horizontal framework, continuous position is applied after setting certain azimuth and pitch. After the test is finished, the dependent level data of entering into the station is extracted from the center control system, data valve of included angel is got in the principle described in the second part of paper. These above kinds of data are filled in the Tables 40.3 and 40.4.

Due to difference of the region that satellite wave beams of entering into the station cover, beam 1, 3, and 5 are main waves in fuyuan, beam 2, 4, and 6 are main waves in kashi. From the table, included angle in theory is larger, the electrical level valve of entering into the station is larger. This phenomenon proves exactness of theoretical calculation. When the included angle is more than 25°, the corresponding electrical level is effective, the corresponding azimuth of receiver is called effective azimuth. Effective azimuth range of east satellite in fuyuan is from 90 to 270°. Effective azimuth range of West Satellite in fuyuan is from 180 to 270°, the above value of Ready Satellite is in the middle of two above ranges. Effective azimuth range of west satellite in kashi is from 45 to 270°. Effective azimuth range of east satellite in kashi is from 45 to 135°, the above value of Ready satellite is so. This result is similar to the theoretical calculation value in the Sect. 3.4.

Comparing the level data of kashi with that of fuyuan, the level of entering into station is also similar when the included angle is identical. In the same place, the level of different satellites is similar when the included angle is similar. The important inference is that included angle is main factor of determining ERIP irrelevant to the certain user position and satellite.

Table 40.3 Test resulting data in Fuyuan region

Azimuth/elevation		Included angle calculation			Inbound Electrical level in Fuyuan		
		Beam 1	Beam 3	Beam 5	Beam 1	Beam 3	Beam 5
0	30	−25.37	−15.86	−23.29	0	0	0
0	60	4.43	−0.815	3.33	24.98	29.5	35.5
45	30	−8.83	−42.77	−28.82	0	0	0
45	60	13.66	−14.388	0.462	27.9	38.8	32.4
90	30	22.09	−37.89	−8.11	38.5	33.49	32.63
90	60	32.81	−12.18	11.83	46.31	31.82	41.71
135	30	58.23	−6.70	25.33	49.2	0	42.33
135	60	54.65	4.37	32.24	48.74	19.63	46.7
180	30	82.29	31.47	63.06	42.74	47.24	45.84
180	60	63.75	26.42	53.24	46.7	46.87	45.89
225	30	45.73	68.09	78.00	46.05	49.31	46.6
225	60	47.5	42.78	58.33	46.93	49.85	47.2
270	30	10.74	59.64	39.58	0	49.87	47.12
270	60	25.62	39.92	40.86	46.26	49	44.85
315	30	−16.71	21.43	3.90	0	0	0
315	60	9.13	20.77	19.01	33.6	0	37.4

Table 40.4 Test resulting data in Kashi region

Azimuth/elevation		Included angle calculation			Inbound electrical level in Kashi		
		Beam 1	Beam 3	Beam 5	Beam 1	Beam 3	Beam 5
0	30	−8.83	−15.61	−13.42	0	38.67	32.17
0	60	1.39	14.29	10.14	8.24	50.18	36.03
45	30	29.59	−2.315	16.88	48.93	49.12	44.4
45	60	23.45	22.27	28.55	47.1	48.26	45.24
90	30	65.38	24.59	53.16	47.64	51.52	46.38
90	60	39.63	39.98	50.56	50.25	50.95	49.48
135	30	58.12	56.39	87.10	46.2	51.37	47.88
135	60	37.10	62.02	62.48	50.37	51.82	48.98
180	30	20.43	74.99	50.31	12.41	50.26	47.22
180	60	18.33	73.73	48.98	35.21	48.98	45.71
225	30	−17.35	47.49	14.29	40.3	50.94	41.92
225	60	−3.39	55.88	26.92	5.56	49.34	45.3
270	30	−45.52	16.30	−15.25	0	45.70	0
270	60	−17.40	34.36	9.11	0	47.8	15.9
315	30	−40.81	−7.82	−27.48	0	38.39	21.46
315	60	−15.33	18.89	2.51	0	50.53	44.49

40.5 Conclusions

Not using the complicated way of link analysis, a practical calculation model of ERIP is set up in the outer three Dimensional spaces. According to the position angle of receiver, the included angle between antenna and satellite is calculated through the geometry model. Combined with power amplifier and electrical level value of entering into station, the basic conclusion is that when the power is 5 W and the angle between receiver antenna and satellite is more 30°, corresponding ERIP of 4dBw can ensure that transmission signal enters into station effectively. The concept of effective extended angle is proposed. The test in the east and west bottom of china shows the effective extended angle of satellite with high elevation angle is more than 180°, which of satellite with low elevation angle is more than 90°. The value of extended angle shows the availability of satellite. Based on the running orbit of satellite, 3 GEO satellites and 2 IGSO satellites can satisfy the needs of CRDSS service in china and nearby region.

Acknowledgments This work is supported by Zhong Sen communication science and technology corporation of ChengDu.

References

1. Tan S (2011) The comprehensive RDSS global position and report. National Defence Industry Press, China
2. Tan S (2010) The engineering of satellite navigation and positioning. National Defense Industry Press, China
3. Behrens RT, Scharf LL (1994) Signal processing applications of oblique projection operators. IEEE Trans Sig Proc 42(6):P1413–P1423
4. Morton YT, Tsui J, Lin D (2003) Assessment and handling of CA code self-interference during weak GPS signal acquisition. ION GPS-03 2003, Portland, pp P646–P653
5. Wen R, Pan Y (2005) On-orbit calibration of G/T value of effective load on the synchronous satellite. Radio Eng 35(1):P33–34
6. Mirshafiei M, Abtahi M, LaRochelle S (2008) Wideband antenna EIRP measurements for various UWB waveforms. In: Proceedings of the 2008 IEEE international conference on ultra-wideband, vol 1, pp P125–128
7. Xie G (2009) Principles of GPS and receiver design. Electronics Industry Press, China

Chapter 41
BeiDou Positioning and Multipath Analysis for Short Baselines

Xuying Ma and Yunzhong Shen

Abstract In this paper, we carried out GPS and BeiDou relative positioning with our developed software using the real data collected in Beijing and Shanghai, respectively, and assessed the accuracy of single epoch baseline solution of the two systems. For short baseline, the relative positioning accuracies of the two systems are basically the same, and the vertical accuracy of the baseline of BeiDou is better than that of GPS. The solved time series errors mainly contain the multipath error and random noise. We used wavelet filtering to extract multipath error according to the frequency characteristics of the random noise and multipath errors. Subsequently, the analysis of GPS and BeiDou multipath was carried out to find the differences between them. Finally, sidereal filtering based on the orbit characteristics of BeiDou was used to eliminate multipath error and improve the relative positioning accuracy. The results showed that the accuracy of relative positioning for short baselines can improve up to 10 % after the multipath error is filtered out.

Keywords BeiDou · GPS · Relative positioning · Multipath effects · Sidereal filtering

41.1 Introduction

BeiDou Navigation Satellite System is China's global navigation satellite system which has been developed independently. By the end of 2012, a regional navigation satellite system providing service for areas in China and its surrounding areas has

X. Ma (✉)
College of Surveying and Geo-Informatics, Tongji University,
Shanghai 200092, China
e-mail: voldemortpotter@sina.com

Y. Shen
Center for Spatial Information Science and Sustainable Development,
Shanghai 200092, China
e-mail: yzshen@tongji.edu.cn

J. Sun et al. (eds.), *China Satellite Navigation Conference (CSNC) 2013 Proceedings*, Lecture Notes in Electrical Engineering 243,
DOI: 10.1007/978-3-642-37398-5_41,

been established and there are 14 satellites in orbit including 5 geostationary orbit (GEO) satellites, 5 inclined geostationary orbit (IGSO) satellites and 4 median elevation orbit (MEO) satellites. The open service is free to all users with point positioning accuracy of 10 m, timing accuracy of 20 ns and velocity accuracy of 0.2 m/s currently [1]. BeiDou works as the third mature navigation satellite system following the former GPS and GLONASS. With the construction and development of BeiDou system, its data processing and application becomes a hot spot and focus of GNSS positioning. In recent years, numerous studies related to positioning and its error sources using BeiDou system have been carried out by many institutions and scholars. For instance, the error sources such as satellite clock error, ionosphere delay, troposphere delay and multipath error were analyzed and single point positioning was carried out after correcting these errors [2]. Performance of precise point positioning and relative positioning based on BeiDou system were initially assessed and the results are compared and analyzed using real GPS/BeiDou data collected from UR240-CORS Dual-System receivers [3, 4]. In this paper, we carry out GPS and BeiDou relative positioning with our developed software using the real data collected in Beijing and Shanghai, respectively, and assessed the accuracy of single epoch baseline solution using the two systems. Subsequently, sidereal filtering based on the orbit characteristics of BeiDou system are carried out and the positioning accuracy is significantly improved.

41.2 GNSS Baseline Solution Principle

The accuracy of GNSS point positioning will be affected by many factors such as satellite orbit errors, clock errors and signal propagation errors. The relative positioning, which is widely used in precision positioning, can effectively weaken the impact of these errors. The receiver and satellite clock biases can be eliminated using double differenced observations, the equations of pseudo-range and carrier phase read [5]

$$P_{AB}^{ij} = \rho_{AB}^{ij} + (l_B^j - l_B^i)dX_B + (m_B^j - m_B^i)dY_B + (n_B^j - n_B^i)dZ_B + I_{AB}^{ij} + T_{AB}^{ij} + M_P + \varepsilon_P \tag{41.1}$$

$$L_{AB}^{ij} = \rho_{AB}^{ij} + (l_B^j - l_B^i)dX_B + (m_B^j - m_B^i)dY_B + (n_B^j - n_B^i)dZ_B + \lambda_f N_{AB}^{ij} - I_{AB}^{ij} + T_{AB}^{ij} + M_L + \varepsilon_L \tag{41.2}$$

where, P_{AB}^{ij} and L_{AB}^{ij} are the double differenced pseudo-range and carrier phase measurements, the subscript A, B represent stations and superscript i, j represent satellites, A denotes the reference station and i is the reference satellite. dX, dY and dZ represent three coordinate corrections of baseline vectors; l, m and n represent direction cosines of three coordinate components; λ_f is wavelength of f frequency,

N represents ambiguity; I and T represent ionosphere and troposphere delays respectively, which can be neglected when the baseline is short. The double differenced constant term

$$\rho_{AB}^{ij} = \rho_{AB}^{j} - \rho_{AB}^{i} = \rho_{B}^{j} - \rho_{A}^{j} - \rho_{B}^{i} + \rho_{A}^{i} \tag{41.3}$$

where, ρ is the distance between station and satellite. M_P and M_L represent multipath of pseudo-range and phase, respectively. ε_P and ε_L represent the pseudo-range and carrier phase measurement errors respectively. The weight matrix of double differential observations is [6]:

$$\mathbf{P}_s = \frac{1}{2n_s}\left(n_s\mathbf{I}_{n_s-1} - \mathbf{e}_{n_s-1}\mathbf{e}_{n_s-1}^T\right) \tag{41.4}$$

where, **I** and **e** denote diagonal matrix and unit matrix correspondingly. s represent the observation type and n_s represent satellite number of this observation type.

41.3 Data Processing and Analysis

41.3.1 Data Collection

We collected two short baselines data using UB240-CORS BD-2/GPS Dual-System Quad-Frequency (GPS: L1, L2; BD-2: B1, B2) receivers produced by UNICORE Communications Incorporation. One ultra-short baseline in Beijing is 3.0669 m and the observation period is from Nov 8, 2012 to Nov 10, 2012. Another short baseline in Shanghai is 470.3009 m and the observation period is from Nov 8, 2012 to Nov 15, 2012. The sampling interval of all the data is 1 s.

41.3.2 Analysis of Baseline Solution Results Based on Different Systems

By using self-developed BeiDou/GPS data processing software, we calculated all the data. Meanwhile, we also computed the baseline with all the GPS data using Bernese software, which are used as reference values for analyzing the accuracy of our epoch-wise solutions. Figure 41.1 presents the error time series for the short baselines of both BeiDou and GPS in Shanghai at Nov 08, 2012.

The root mean squared (RMS) errors, which are calculated from the error time series of the BeiDou system in Fig. 41.1, are 0.41, 0.30 and 0.71 cm respectively for north (N, *blue*), east (E, *red*) and up (U, *green*) coordinate components; and the RMS errors for the GPS system are 0.33, 0.28 and 1.26 cm respectively. Figure 41.2 illustrates the RMS errors of all day's solutions for the short baselines

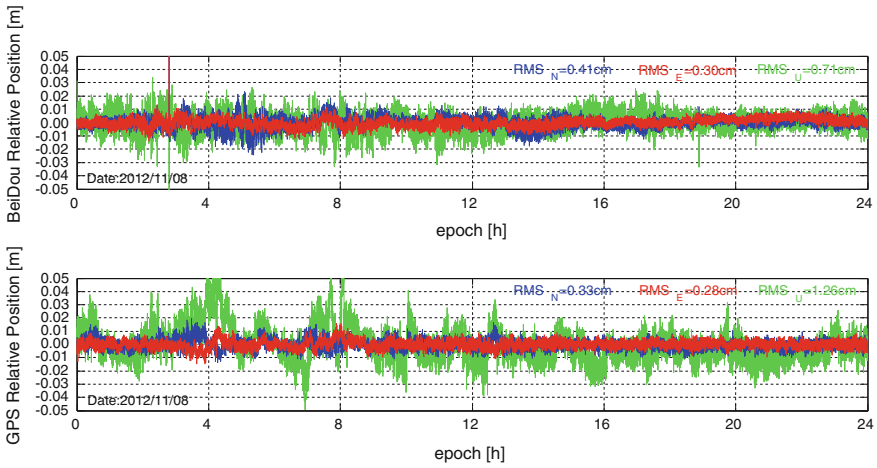

Fig. 41.1 Error time series of BeiDou, GPS baseline of Shanghai station (2012/11/08, 86400 epochs)

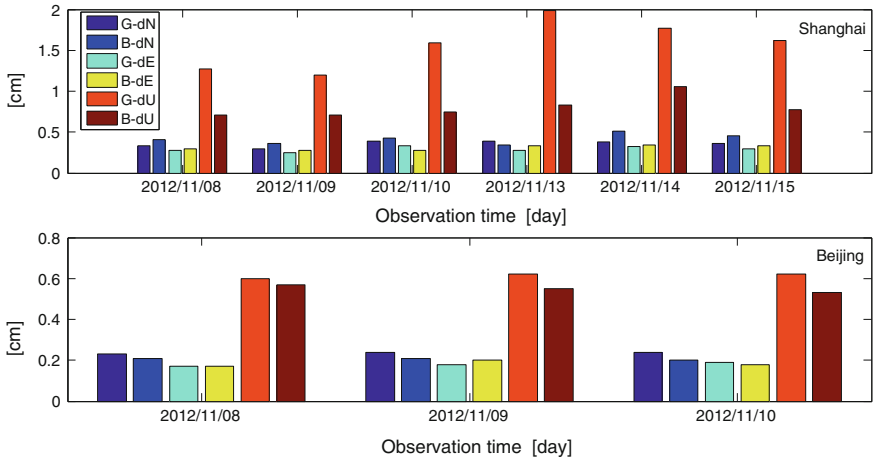

Fig. 41.2 RMS errors of each coordinate components for the baselines in Shanghai (*Up*) and Beijing (*Down*)

both in Shanghai and Beijing. The average RMS errors of the short baseline in Shanghai are 0.36, 0.29, 1.57 cm and 0.42, 0.31, 0.80 cm for the N, E and U coordinate components of GPS and BeiDou systems, respectively. The average RMS errors of the short baseline in Beijing are 0.24, 0.18, 0.61 cm and 0.21, 0.18, 0.55 cm for N, E and U coordinate components of GPS and BeiDou systems, respectively. We find that the relative positioning errors of the two systems are basically at the same level. For the baseline in Shanghai, GPS performs better than BeiDou for the N, E coordinate components but inferior to BeiDou for the U

coordinate component; for the baseline in Beijing, BeiDou performs slightly better than GPS for the N, U coordinate components and almost the same for the E coordinate component. In summary, for short baseline, the relative positioning errors of the two systems are basically at the same level for the N, E coordinate components, and the accuracy of BeiDou is better than that of GPS for the U coordinate component, especially in Shanghai, the lower latitude area.

41.3.3 Analysis of DOP Value for Different Systems

In order to compare the difference of satellite constellations between GPS and BeiDou system, we count visible satellites and DOP values of GPS and BeiDou in Shanghai and Beijing on Nov 8, 2012, respectively. The results are shown in Fig. 41.3.

As can be seen from Fig. 41.3, the number of visible satellites of BeiDou (*green*) in Shanghai and Beijing areas are from 6 to 11 and the average numbers are 8 and 7 in Shanghai and Beijing, respectively. While the average numbers of GPS (*blue*) are 8.5 and 9 respectively in Shanghai and Beijing. The number of BeiDou satellites is less than that of GPS, especially in the higher latitudes areas. Because BeiDou constellation consists of three different types of satellites: GEO, IGSO and MEO satellites, there are only two MEO satellites providing services at present and we carried out positioning using GEO + IGSO satellites mode in most times, which causes less visible satellites in higher latitudes areas. The total visible satellites of the two systems (*red*) in Shanghai and Beijing areas are from 13 to 20, therefore, the satellites constellation will be significantly improved when we carry out integrated positioning by using the GPS/BeiDou systems.

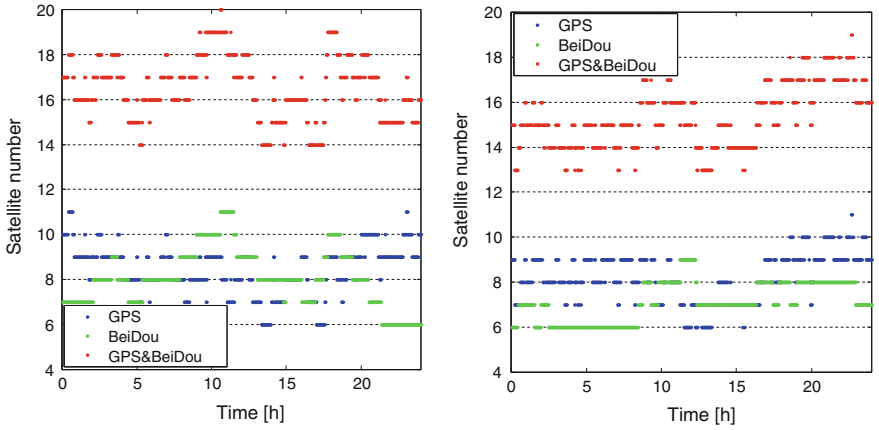

Fig. 41.3 Visible satellite statistics of different systems for Shanghai (*Left*) and Beijing (*Right*) areas

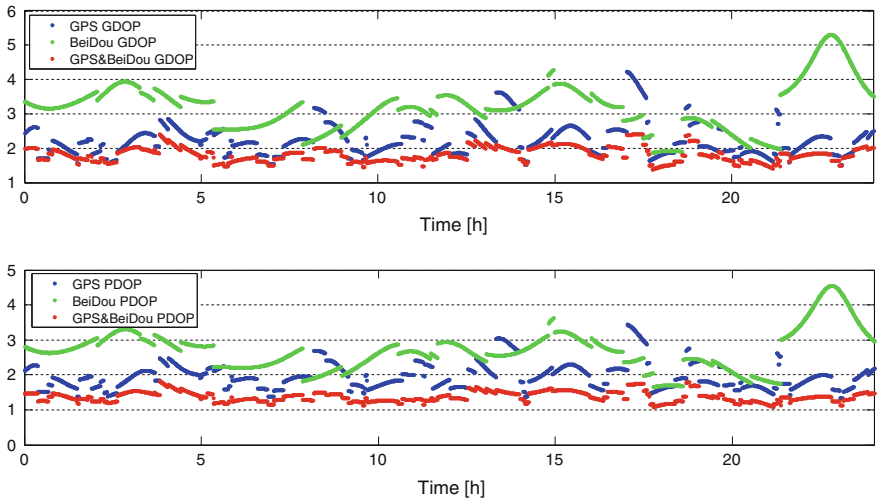

Fig. 41.4 DOP value condition of Shanghai area

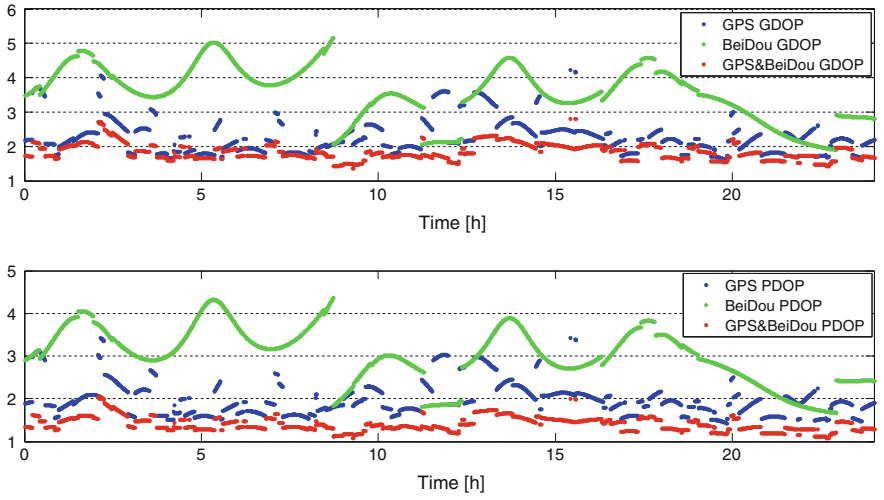

Fig. 41.5 DOP value condition of Beijing area

The DOP values in Shanghai and Beijing areas of the two systems are drawn in Figs. 41.4, 41.5, respectively. Comparing Figs. 41.4 and 41.5, we can find that both the GDOP and PDOP values of BeiDou are larger than that of GPS. The DOP values of BeiDou is large but the alteration trend smooth and consecutive. When a IGSO satellite arise or fall down, the DOP value will vary significantly (As shown 9:00 am in Figs. 41.3 and 41.5).The DOP value will be significantly improved when combine the two systems.

Table 41.1 Statistic of the multipath correlation delay for BeiDou and GPS (Beijing and Shanghai area)

System	Relevant date	Direction	Beijing area		Shanghai area	
			Correlation lag (s)	Max. corr. coefficient	Correlation lag(s)	Max. corr. coefficient
BeiDou	Day1-Day2	N	244	0.513	252	0.622
		E	253	0.455	239	0.573
		U	247	0.469	245	0.501
	Day2-Day3	N	243	0.598	241	0.575
		E	246	0.623	243	0.592
		U	242	0.590	245	0.611
	Day1-Day3	N	491	0.410	490	0.584
		E	487	0.396	483	0.416
		U	488	0.322	485	0.409
GPS	Day1-Day2	N	245	0.712	250	0.663
		E	245	0.675	246	0.683
		U	248	0.757	247	0.766
	Day2-Day3	N	250	0.697	248	0.717
		E	247	0.657	249	0.632
		U	248	0.743	243	0.710
	Day1-Day3	N	488	0.677	485	0.579
		E	491	0.623	493	0.634
		U	488	0.732	487	0.601

41.3.4 Multipath Error Analysis for BeiDou and GPS

The error time series mainly contain the multipath error and random noise. We extract the multipath errors of GPS and BeiDou measurements by using wavelet filtering according to the frequency characteristics of the random noise and multipath errors. Since the observation environment of the permanent stations are not change, the multipath errors must be periodic. We can improve the accuracy of daily baseline solution by filtering the periodic multipath errors. In this example, the single epoch solution of the two systems for Beijing and Shanghai has been carried out using three consecutive days' measurements from Nov 8 to Nov 10, 2012. We use the 10 order daubechies (db10) wavelet to extract the multipath errors according to the low-frequency characteristics from three days' error time series of the N, E and U coordinate components, respectively.

The cross-correlation lags and coefficients between pairs of results are shown in Table 41.1. The cross-correlation lags indicate the shifts from ~239 to 253 s. These shifts are roughly indicative of the sidereal repeat period (~236 s less than 1 solar day), which indicate that the multipath errors significantly exist. As shown in Table 41.1, the correlation coefficients of BeiDou are smaller than that of GPS, which indicates that the change of constellation geometry of BeiDou is more significant than that of GPS. The cross-correlation lag of BeiDou are slightly shorter than that of GPS, and the cross-correlation lag between the adjacent two

days is centered at about 240 s, which is longer than the theoretical value 236 s. With the increase of interval days, the max correlation coefficient decrease gradually [7]. For instance, the max correlation coefficient of day1 and day3 is smaller than that of day1 and day2 or day2 and day3. It indicates that the geometry structure of satellites will change at the same place as the increase of interval days.

41.4 Sidereal Filtering Based on Orbit Characteristics of BeiDou

41.4.1 Multipath Period of BeiDou

For a fixed station, the period of satellite-receiver geometry mainly depends on satellites orbit period. We can calculate satellite orbit period according to the broadcast ephemeris, the equation is [8]

$$\begin{aligned} n &= \sqrt{GM}/a^{\frac{3}{2}} + \Delta n \\ T &= 2\pi/n \end{aligned} \tag{41.5}$$

where, $\sqrt{GM}$ is the Earth, a and Δn are the semi-major axis of orbit ellipse and the perturbation of mean velocity, T is orbit period.

GPS constellation only consists of several MEO satellites; the orbit period, which can be calculated with (41.5), is 11 h 58 m. For a fixed station on the Earth, the visible satellites in the sky will be exactly the same after 23 h 56 m 4 s (the sidereal day). Since the multipath errors are related to satellite-receiver geometry, we can mitigate these errors by correct them according to the periodic characteristics, we call this method sidereal filtering [7]. The sidereal filtering has two steps and its implementation requires two or more day's data. The first step is to estimate multipath errors with the measurement of the first day, the second step is to subtract the estimated multipath errors, shifted by one sidereal period (23 h 56 m 4 s), from the estimated positions of the second day [9–11].

We calculate orbit repeat times for all BeiDou satellites with the broadcast ephemerides from Jul. 13 to Aug. 1, 2012, the results are shown in Fig. 41.6.

In Fig. 41.6, the SatID 1-5, SatID 6-10 and SatID 11, 12 are GEO, IGSO and MEO satellites, respectively. We can find that orbit periods of each kind satellite are different, and for one satellite, each day's orbital period is also different. The orbit periods of GEO, IGSO and MEO satellites are 86163, 86162 and 46391 s, respectively, which basically coincide with that of the multipath periods [12]. Namely, GEO, IGSO and MEO satellites appear a period ahead of time 237, 238 and 245 s every day (MEO satellites orbit around the earth 13 cycles every week, taking the 1715 s shift-seconds relative to one week into account, average 245 s for one day and it is basically consistent with the results of GPS).

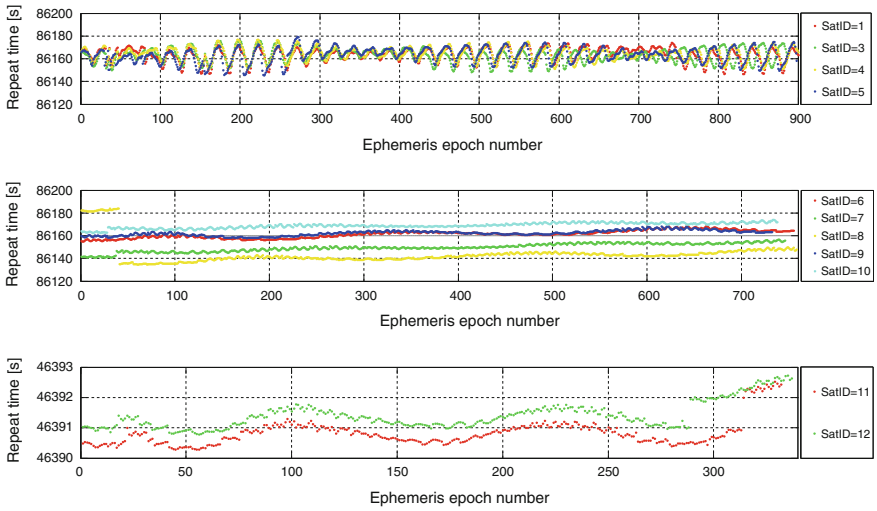

Fig. 41.6 Orbit repeat times found from the broadcast ephemerides of all BeiDou satellites from Jul. 13st to Aug. 1st, 2012 (The broadcast ephemerides interval of BeiDou is 1 h, the ephemerides epoch number in one day are about 24, 19 to 21, 8–10 for GEO, IGSO and MEO satellites, respectively)

41.4.2 Sidereal Filtering Based on Multipath Error Periods of BeiDou

The satellite constellation of BeiDou consists of three different types of satellites: GEO, IGSO and MEO satellites, it contributes to the different orbit periods. So the sidereal filtering based on GPS constellation is not suitable for BeiDou.

We carried out sidereal filtering for baseline solution according to the average orbit period previously obtained. In this example, two consecutive days' dating from Nov 13 to Nov 14, 2012 single epoch baseline solution for the short baselines in Beijing and Shanghai were carried out with BeiDou measurements. The error time series of N, E, and U coordinate components before and after sidereal filtering (2012/11/14) are drawn in Fig. 41.7, and the statistics of baseline solution in Shanghai and Beijing are listed in Tables 41.2 and 41.3 respectively.

From the results, we can find that sidereal filtering partly eliminate period errors related to satellite-receiver geometry, the accuracy of relative positioning for short baselines is significantly improved. This illustrates that this sidereal filtering based on orbit characteristic of BeiDou is useful for improving the daily BeiDou solution of fixed stations.

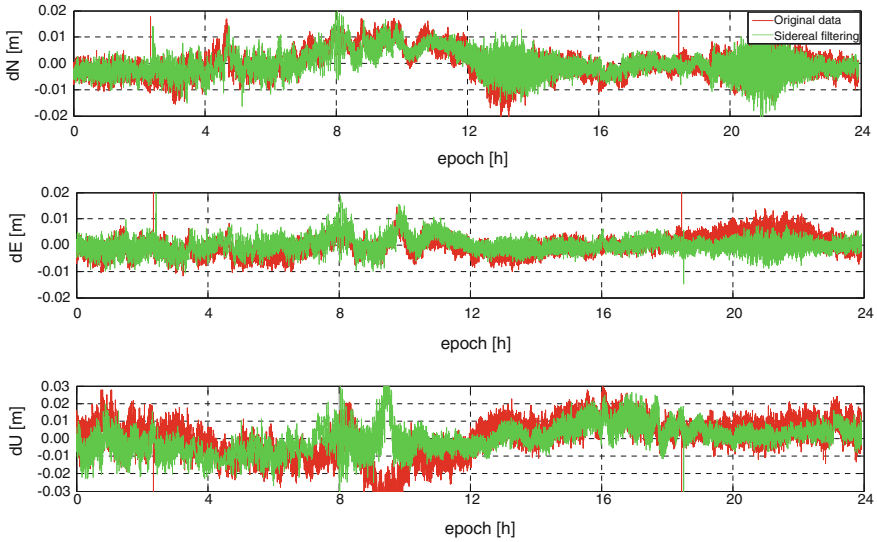

Fig. 41.7 Time series of coordinate error in each orientation before and after sidereal filtering (2012/11/14, Shanghai)

Table 41.2 Results statistics before and after sidereal filtering of Shanghai station

	RMS N (cm)	RMS E (cm)	RMS U (cm)
Original results	0.51	0.34	1.06
Sidereal filtering results	0.43	0.27	0.82
Improvement proportion (%)	15.69	20.59	22.64

Table 41.3 Results statistics before and after sidereal filtering of Beijing station

	RMS N (cm)	RMS E (cm)	RMS U (cm)
Original results	0.23	0.20	0.62
Sidereal filtering results	0.19	0.18	0.55
Improvement proportion (%)	17.39	10.00	11.29

41.5 Conclusions

In this paper, we carry out GPS and BeiDou relative positioning using the real data and assess the positioning performance of the two systems in China. Subsequently, sidereal filtering based on the orbit characteristics of BeiDou is used to eliminate multipath error and improve the accuracy of relative positioning. We can draw the following conclusions from our results:

1. For the two short baselines calculated in this paper, the relative positioning accuracies of the two systems are basically at the same level; the BeiDou can get better accuracy for U coordinate component than GPS.
2. Currently, BeiDou has been able to provide high-precision positioning, its visible satellites keeps about 6–11. Since BeiDou constellation is not yet completed, the average visible satellites are less than that of GPS, and the DOP conditions are inferior to GPS as well.
3. The multipath effect correlation characteristics of BeiDou and GPS are similar to some extends. The periods of multipath of the GEO, IGSO and MEO satellites are 86163, 86162 and 46391 s respectively, which are basically consistent with their orbit periods.
4. Under the circumstance of heavy multipath effect, sidereal filtering based on orbit periods characteristic of BeiDou can significantly improve the accuracy of positioning, which is meaningful to its data processing.

Acknowledgments This work was sponsored by Natural Science Foundation of China (Projects: 41074018). Thanks Li Jianwen, Li Bofeng and Zhu Yongxing for the great support of this paper. Liu Weizhou and Tang Chengpan provided useful guidance during data processing and paper writing. The writers thank UNICORE company for their relevant hardware support.

References

1. China Satellite Navigation Office (2011) Report on the development of BeiDou(COMPASS) Navigation satellite system(V1.0), Beijing
2. Cao Y, Hu X, Wu B et al (2012) The wide-area difference system for the regional satellite, SCIENCE CHINA(Physics, Mechanics and Astronomy), July vol 55(7):1307–1315, doi: 10.1007/s11433-012-4746-1
3. Montenbruck O, Hauschild A, Steigenberger P, Hugentobler U, Teunissen P, Nakamura S (2012) Initial assessment of the COMPASS/BeiDou-2 regional navigation satellite system, GPS Solutions. doi:10.1007/s10291-012-0272-x. Published online: 12 June
4. Shi C, Zhao Q, Hu Z, Liu J (2013) Precise relative positioning using real tracking data from COMPASS GEO and IGSO satellites. GPS solut 17(1):103–119. doi:10.1007/s10291-012-0264-x
5. Li Z, Huang J (2005) GPS surveying and data processing. Wuhan University Press, Wuhan
6. Wei Z, Ge M (1998) Mathmatic model of GPS relative positioning. Surveying and Mapping Press, Beijing
7. Yuan L, Huang D, Ding X, Xiong Y, Zhong P, Li C (2004) On the influence of signal multipath effects in GPS carrier phase surveying. Acta Geodaetica et Cartographica Sinica 33(3):1001–1595
8. Agnew DC, Larson KM (2006) Finding the repeat times of the GPS constellation, GPS solutions, vol 11(3):71–76. doi:10.1007/s10291-006-0038-4. Published online: 31 August
9. Choi K, Bilich A, Larson KM, Axelrad P (2004) Modified sidereal filtering: implications for high-rate GPS positioning, Geophysical research letters, vol 31, L22608, doi:10.1029/2004GL021621
10. Yin H, Gan W, Xiao G (2011) Modified sidereal filter and its effect on high-rate GPS positioning. Geomatics Inf Sci Wuhan Univ 36(5):608–611

11. Ragheb E, Clarke PJ, Edwards SJ (2007) GPS sidereal filtering: coordinate- and carrier-phase-level strategies. J Geodesy 81(5):325–335. doi:10.1007/s00190-006-0113-1
12. Ma X, Shen Y (2012) Multipath analysis of COMPASS triple frequency observations, The international symposium on GPS/GNSS, Oct. 31st-Nov. 2nd, Xi'an, China

Chapter 42
Research on High-Precision Measurement and Calibration Technology for Carrier Phase Consistency of Digital Beam Array Navigation Signal Simulator

Dexiang Ming, Yangyang Liu, Xiaopeng Zhong and Xiye Guo

Abstract Digital beam array navigation signal simulator is a kind of important equipment to develop, test and verify multi-element anti-jamming satellite navigation terminal with cables. According to the working principle of anti-jamming satellite navigation terminal, the carrier phase consistency is a key indicator to signal simulator. Thus, measurement and correction of carrier phase consistency is an important part in the design of digital beam array signal simulator. In this paper, for this problem, an innovative technical solution is proposed for high-precision calibration based on carrier interferometer. This solution uses two array elements to measure delay mutually, based on the signal phase of one, directly detecting the phase of another. After analysis of theory and validation of experiment, the solution can achieve high measurement accuracy that is less than 0.1° of the relative phase among the array elements, and the price is small.

Keywords GNSS · Digital beam array navigation signal simulator · Carrier phase consistency · High precision · Measurement and calibration

42.1 Introduction

Digital beam array navigation signal simulator is a kind of important equipment to develop, test and verify multi-element anti-jamming satellite navigation terminal with cables, and is also guarantee and support to improve the anti-jamming

D. Ming (✉) · X. Zhong · X. Guo
College of Mechatronics Engineering and Automation, National University Defense Technology, Changsha 410073, People's Republic of China
e-mail: mdxnihao@263.net

Y. Liu
College of Physical and Electronics, Central South University, Changsha 410083, People's Republic of China

J. Sun et al. (eds.), *China Satellite Navigation Conference (CSNC) 2013 Proceedings*, Lecture Notes in Electrical Engineering 243,
DOI: 10.1007/978-3-642-37398-5_42,

capability of weapons and equipment. In order to ensure the precision of the phase consistency, we need to take measurement adjusting and periodic calibration. Therefore, measurement and correction of zero value [1–3] of carrier phase is an important part in the design of digital beam array signal simulator. The zero value is a relative value between each array element, not absolute value that is from baseband to the antenna, and generally requires less than one degree. The traditional method [4–6] of measurement measures the absolute delay of phase by tracking loop, and this requires the closed-loop measurement system as a reference. Using the closed-loop measurement system will make error larger, and requires high synchronized performance of the closed-loop measurement. The conventional closed-loop measurement cannot achieve high measurement accuracy. In response to this problem, an innovative technical solution is proposed for high-precision calibration based carrier interferometry in the design of digital beam array signal simulator. The solution uses two array elements to measure delay mutually, based on signal phase of one, directly detecting the phase of another, and can achieve high measurement accuracy that is less than 0.1° with small price.

42.2 Principles of Measurement and Calibration

The schematic diagram of high-precision measurement and calibration based on the carrier interferometry measurement is shown in Fig. 42.1. The emitting unit of simulator has a total of k ports, and the signal waveform that is output by DAC at each emitting port is: $x_k(t) = \sin((\varpi - \varpi_{LO})t + \varphi_k)$. The phase delay caused by down-conversion and filtering system is: $\phi_k - \varphi_k$. The signal waveform that reaches antenna aperture is: $A_1 \sin(\varpi t + \phi_1)$.

The synthesized signal is $y(t) = \sum_{k=1}^{K} A_k \sin(\varpi t + \phi_k)$, formed by the signal of k ports. Since each signal has completely the same frequency, the k and j channel

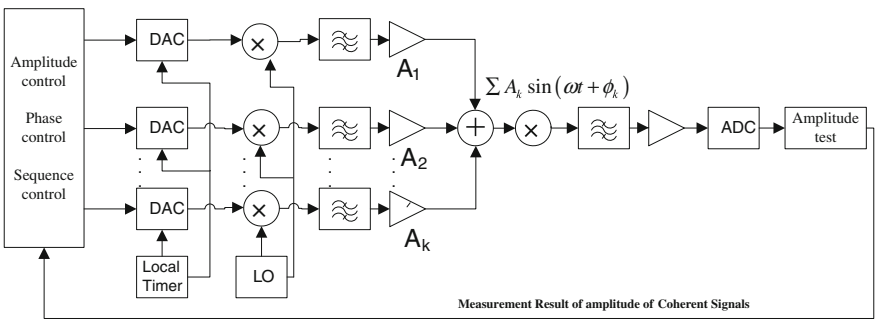

Fig. 42.1 Schematic of high-precision measurement and calibration

signal, only has the phase difference, that is $\phi_k - \phi_j$, and amplitude difference, so each signal is actually fully coherent signal. We can take full advantage of this coherence to achieve the detection of the phase difference, that is $\phi_k - \phi_j$.

The following example illustrates the high-precision measurement principle of phase difference, $\phi_k - \phi_j$, using two channel signals.

42.2.1 Principle of Coherent Measurement of Carrier Phase Consistency

Firstly we study phase measurement principle of two coherent signals. Without loss of generality, suppose the waveform of first channel signal that arrives at the antenna aperture planes as a reference waveform, the waveform is:

$$x_1(t) = A_1 \sin(\varpi t + \phi_1) \tag{42.1}$$

The waveform of k channel:

$$x_k(t) = A_k \sin(\varpi t + \phi_k) \tag{42.2}$$

The synthesized signal of 1 and k channel is:

$$\begin{aligned} y(t) &= A_1 \sin(\varpi t + \phi_1) + A_k \sin(\varpi t + \phi_k) \\ &= A_1 \left(\sin(\varpi t + \phi_1) + \frac{A_k}{A_1} \sin(\varpi t + \phi_k) \right). \end{aligned} \tag{42.3}$$

After trigonometric transform:

$$\begin{aligned} y(t) = A_1 \Big\{ & \sin(\varpi t)\cos(\phi_1) + \cos(\varpi t)\sin(\phi_1) \\ & + \frac{A_k}{A_1} [\sin(\varpi t)\cos(\phi_k) + \cos(\varpi t)\sin(\phi_k)] \Big\} \end{aligned} \tag{42.4}$$

$$\begin{aligned} y(t) = A_1 \Big\{ & \sin(\varpi t) \left[\cos(\phi_1) + \frac{A_k}{A_1} \cos(\phi_k) \right] \\ & + \cos(\varpi t) \left[\sin(\phi_1) + \frac{A_k}{A_1} \sin(\phi_k) \right] \Big\} \end{aligned} \tag{42.5}$$

$$y(t) = A_1 \sqrt{\left[\cos(\phi_1) + \frac{A_k}{A_1} \cos(\phi_k) \right]^2 + \left[\sin(\phi_1) + \frac{A_k}{A_1} \sin(\phi_k) \right]^2} \sin(\varpi t + \delta\phi_k) \tag{42.6}$$

Merge the Eq. (42.6), we get:

$$y(t) = A_1\sqrt{1 + 2\frac{A_k}{A_1}\cos(\phi_1 - \phi_k) + \left(\frac{A_k}{A_1}\right)^2}\sin(\varpi t + \delta\phi_k) \tag{42.7}$$

It can be seen that the synthesized waveform relative to the first channel signal $x_1(t) = A_1\sin(\varpi t + \phi_1)$, the amplitude enhancement factor is:

$$\begin{aligned}\sqrt{P_k(\phi_1 - \phi_k)} &= \frac{A_1\sqrt{1 + 2\frac{A_k}{A_1}\cos(\phi_1 - \phi_k) + \left(\frac{A_k}{A_1}\right)^2}}{A_1} \\ &= \sqrt{1 + 2\frac{A_k}{A_1}\cos(\phi_1 - \phi_k) + \left(\frac{A_k}{A_1}\right)^2}\end{aligned} \tag{42.8}$$

That is:

$$P_k(\phi_1 - \phi_k) = 1 + 2\frac{A_k}{A_1}\cos(\phi_1 - \phi_k) + \left(\frac{A_k}{A_1}\right)^2 \tag{42.9}$$

Therefore, the power enhancement factor of the synthesized signal waveform is a function of the phase error $\phi_1 - \phi_k$. We can get $\phi_1 - \phi_k$ by $P_k(\phi_1 - \phi_k)$. Since $\frac{A_k}{A_1}$ can be accurately measured and only $\cos(\phi_1 - \phi_k)$ is unknown in the Eq. (42.9), so $\phi_1 - \phi_k$ can be calculated as Eq. (42.10).

$$\cos(\phi_1 - \phi_k) = \frac{P_k(\phi_1 - \phi_k) - 1 - \left(\frac{A_k}{A_1}\right)^2}{2\frac{A_k}{A_1}} \tag{42.10}$$

Define the right side of Eq. (42.10) as a concept d_k:

$$d_k \triangleq \frac{P_k(\phi_1 - \phi_k) - 1 - \left(\frac{A_k}{A_1}\right)^2}{2\frac{A_k}{A_1}}. \tag{42.11}$$

We can get the measurement equation:

$$\cos(\phi_1 - \phi_k) = d_k \tag{42.12}$$

Based on $P_k(\phi_1 - \phi_k)$, d_k can be calculated; thereby $\phi_1 - \phi_k$ can be calculated.

There is only one observed quantity in this measurement principle, so the measurement accuracy cannot meet the demand. In order to improve the measurement accuracy, we should better use more observed quantities.

In order to obtain more observations, the best method is to change the phase of reference signal of the first channel manually, forming M corrections of observations $\phi_1(m), m \in [1, M]$ Suppose the M scanning phases generated manually of the first channel can scan 2π phase angles.

$$\phi_1(m) = \frac{2\pi}{M}m, \quad m = 1, 2, 3, \ldots, M \tag{42.13}$$

For each correction value $\phi_1(m), m \in [1, M]$, after observing for a few times, we can get one observed value that is $d_k(m)$. And we also will get a measurement sequence as shown in Eq. (42.14):

$$\cos(\phi_1(m) + \phi_1 - \phi_k) = d_k(m) \tag{42.14}$$

Reference [7] describes the sine phase detection method: obtain $\tan(\phi_1 - \phi_k)$ through the orthogonal measurement method, and then through $\tan(\phi_1 - \phi_k)$ we can obtain $\phi_1 - \phi_k$. Thus, here directly give $\tan(\phi_1 - \phi_k)$ according to $d_k(m)$:

$$\tan(\phi_1 - \phi_k) = \frac{\sum_{m=1}^{M} d_k(m)\sin(\phi_1(m))}{\sum_{m=1}^{M} d_k(m)\cos(\phi_1(m))} \tag{42.15}$$

If $\phi_1(m) = \frac{2\pi}{M}m, \quad m = 1, 2, 3, \ldots, M$, we get:

$$\sum_{m=1}^{M} \sin(\phi_1(m)) = 0 \tag{42.16}$$

$$\sum_{m=1}^{M} \cos(\phi_1(m)) = 0 \tag{42.17}$$

Take Eqs. (42.16) and (42.17) into the expression $\tan(\phi_1 - \phi_k)$, and remove $-1 - \left(\frac{A_k}{A_1}\right)^2$, we can obtain:

$$\tan(\phi_1 - \phi_k) = \frac{\sum_{m=1}^{M} P_k(\phi_1 - \phi_k, m)\sin(\phi_1(m))}{\sum_{m=1}^{M} P_k(\phi_1 - \phi_k, m)\cos(\phi_1(m))} \tag{42.18}$$

This $\phi_1(m) = \frac{2\pi}{M}m, \quad m = 1, 2, 3, \ldots, M$experimental phase scanning process is necessary, not only to improve the precision of the phase measurement, and eliminate various amplitude error. In fact, $\sin(\phi_1(m))$, $\cos(\phi_1(m))$, is a narrow-band filter, and can eliminate most of the DC noise, like $P_k(\phi_1 - \phi_k, m)$.

42.2.2 Procedure of Measurement

According to the above principle, the method of calibration process is described as follows:

Step 1: Measuring the reference signal power, P_1, of the first channel.

Fix the first channel signal, as a reference signal, and calculate its power by self-measurement loop.

Step 2: Measure the relative power $P_k(\phi_1 - \phi_k, m)$ of the total M experimental synthetic signal of the k channel.

Holding the first channel signal power, open the k channel, close the other signals except the first and k channel signal.

For the k channel signal, change the phase of the baseband carrier signal of the first channel signal, $\phi_1(m) = \frac{2\pi}{M}m, \quad m = 1, 2, 3, \ldots, M$, in which $M = 16$. Each channel signal holds 50 ms to calculate the signal power for self-measurement loop. Within a cycle of 50 ms, calculate enhancement factor, $P_k(\phi_1 - \phi_k, m)$, that is the power of the synthesized signal by measurement loop respect to the power of the first channel signal.

Step 3: calculate the relative phase difference $\phi_1 - \phi_k$.

According to $P_k(\phi_1 - \phi_k, m)$, calculate $\tan(\phi_1 - \phi_k)$ by Eq. (42.18), then look up the tan table, and $\phi_1 - \phi_k$ can be obtained.

42.2.3 Analysis of Measurement Accuracy

According to the Reference [7], we estimate the accuracy of the formula (42.18). If the observation noise variance is σ_P, the measurement accuracy of the phase is:

$$\sigma(\phi_1 - \phi_k) \approx \sqrt{\frac{2}{M}}\sigma_P \times \frac{180}{\pi} \text{ (Degree)} \tag{42.19}$$

If we take $P_s = -40\text{dBmW}$, $N_0 = -174\text{dBmW}$, and B = 20 Hz, σ_P, can be estimated as Eq. (42.20):

$$\sigma_P = \sqrt{\frac{N_0 B}{P_s}} \approx 10^{-6} \tag{42.20}$$

$$\sigma(\phi_1 - \phi_k) \approx 2.0 \times 10^{-5} \text{ (Degree)} \tag{42.21}$$

Thus, this phase detecting method can achieve high accuracy.

42.3 Tests and Analysis of Results

In order to verify the above theory, we take the experimental instruments as follows to test:

Signal Source: IFR2025
Power divider: Mini—ZAPD-2-21-3 W
Synthesizer: Mini—ZAPD-2-21-3 W
Spectrum analyzer: Agilent 8563E
Phase shifter: Spectrum LS-0170-1121

42.3.1 Test Results of Power Synthesis

Experimental connection relationship is shown in Fig. 42.2. The signal source sends 1.5 GHz single carrier with low phase noise to the power divider, forming completely same phase signals of two ways. The synthesized signal is then fed into a spectrum analyzer to measure the power of the synthesized signal.

According to Fig. 42.2, firstly measure power of the synthesis signal of two channels. Then remove one, and measure power of the remaining channel signal. The experimental results measured are shown in Table 42.1.

From Table 42.1, we can get that the power of two completely same phase coherent signal respect to without synthetic beam, will be enhanced 6 dB. Since the power divider is a linear device, and the correctness of the synthesis formula (42.3) is also verified.

42.3.2 Test Results of Amplitude Changing Caused by Phase Changing

The connection relationship of verification test of amplitude variations caused by phase changes is shown in Fig. 42.3.

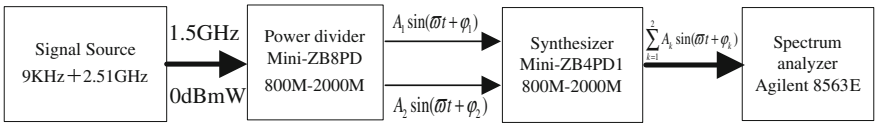

Fig. 42.2 Test schematic of power synthesis of two channels

Table 42.1 Test results of power synthesis of two channels

	Synthesis of two channels (dB)	Synthesis of one channels (dB)
Relative power of synthesized signal	0	−6.33
Theoretical value	0	−6

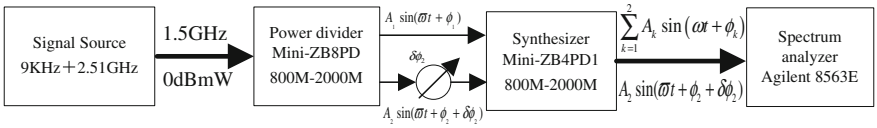

Fig. 42.3 Test schematic of amplitude changing caused by phase changing

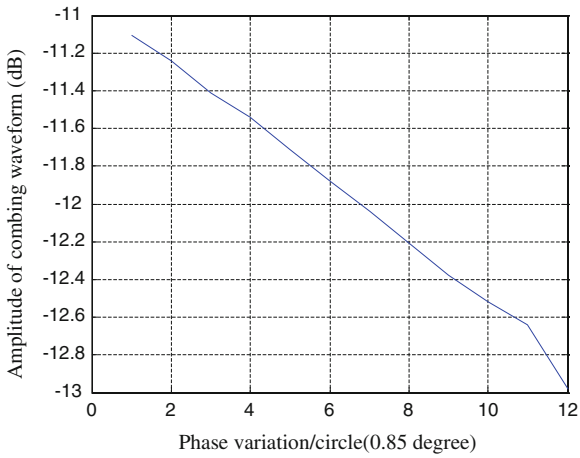

Fig. 42.4 Line of relationship of phase change and synthesis waveform (connect one SMA)

1. **Test after connecting one SMA**

Spectrum phase shifter moves only 7°. Therefore, connect an SMA connector in front of the synthesizer to increase the signal delay, and compensate insufficient of the Spectrum phase shifter. The phase shifts 45°. After connecting, change the phase shifter of Spectrum phase shifter, we can get the relationship between the relative power change of synthesized waveform and number of turns of Spectrum phase shifter that is shown in Fig. 42.4.

As shown in Fig. 42.4, the Spectrum's phase shifter changes one lap (0.85°), the amplitude substantially changes 0.13 dB. At this time, the phase difference is relatively small, at the peak of the cosine wave, and is not very sensitive to the change in phase. DSP can sense 0.13 dB amplitude variations. It proves that we can detect the phase difference changes by detecting the power change of synthesized signal.

2. **Test after connecting two SMA**

Spectrum phase shifter moves only 7°. Therefore, connect two SMA connectors in front of the synthesizer to increase the signal delay, and compensate insufficient of the Spectrum phase shifter. The phase shifts 90°. After connecting, change the phase shifter of Spectrum phase shifter, we can get the relationship between the relative power change of synthesized waveform and number of turns of Spectrum phase shifter that is shown in Fig. 42.5.

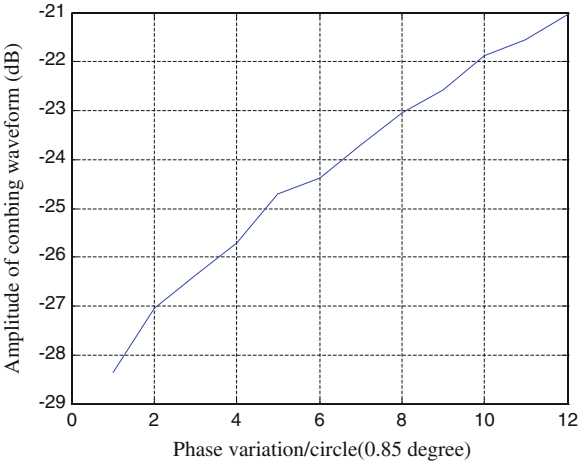

Fig. 42.5 Line of relationship of phase change and synthesis waveform (connect two SMA)

As shown in Fig. 42.5, the Spectrum's phase shifter changes one lap (0.85°), the amplitude substantially changes 0.67 dB. At this time, the phase difference is large, at the middle of the cosine wave, and is sensitive to the change in phase. DSP can sense 0.67 dB amplitude variations. It proves that we can detect the phase difference changes by detecting the power change of synthesized signal.

3. **Test after connecting three SMA**

Spectrum phase shifter moves only 7°. Therefore, connect three SMA connectors in front of the synthesizer to increase the signal delay, and compensate insufficient of the Spectrum phase shifter. The phase shifts 135°. After connecting, change the phase shifter of Spectrum phase shifter, we can get the relationship between the relative power change of synthesized waveform and number of turns of Spectrum phase shifter that is shown in Fig. 42.6.

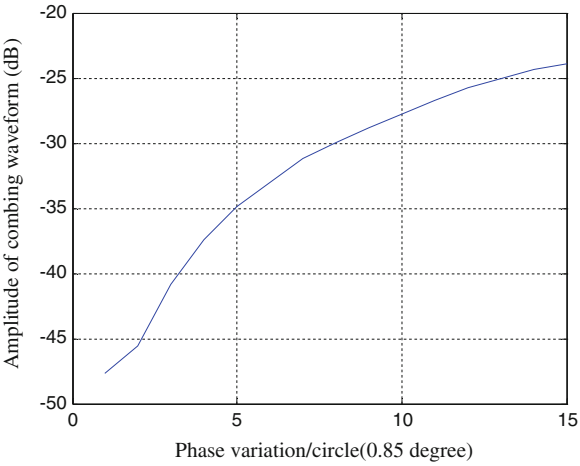

Fig. 42.6 Line of relationship of phase change and combining waveform (connect three SMA)

As shown in Fig. 42.6, the Spectrum's phase shifter changes one lap (0.85°), the amplitude substantially changes 4–2 dB. At this time, the phase difference is relatively large, at the down of the cosine wave, and is very sensitive to the change in phase. DSP can sense 2–4 dB amplitude variations. It proves that we can detect the phase difference changes by detecting the power change of synthesized signal.

42.3.3 Conclusions

In this paper, an innovative solution of high-precision measurement calibration is presented based on carrier interferometry to measure and correct carrier phase consistency in the design of digital beam array signal simulator. This solution can measure the relative phase difference of each synthesis signal precisely and in real time, and is irrespective of other zero-value error interferences. After test and analysis, the algorithm has high measurement accuracy that is less than 0.1° of phase difference and good anti-jamming performance, which demands less to the amplitude of the reference signal, and reduces the requirements to self-correction circuit. It is a kind of good measurement correction method of carrier phase consistency.

References

1. Jaffer AG (2002) Sparse mutual coupling matrix and sensor gain phase estimation for array auto-calibration. In: Proceedings of IEEE rader conference 2002, pp 294–297
2. Wang B, Wang Y, Guo Y (2004) Mutual coupling calibration with instrumental sensors. Electron Lett 40(7):406–408
3. Jun Y (2007) The research of the signal simulation theory and technologies for satellites navigation. School of National University of Defense Technology, Changsha
4. Kohei M (2001) Experiments of DOA estimation by DBF array antenna at 2.6 GHz. IEICE Trans on Commu E84-B(7):1871–1875
5. Godara LC (1997) Application of antenna to mobile communication, Part II: beamforing and direction arrival consideration. Proc IEEE 85(8):1195–1245
6. Ertel R, Hu Z, Reed J (1999) Antenna array hardware amplitude and phase compensation using baseband antenna array outputs. IEEE Veh Technol Conf 3:1763–1795
7. Kay SM (2011) Fundamentals of statistical signal processing: estimation and detection theory. Publishing House of Electronics Industry, Beijing, p 2

Chapter 43
A Study on High Precision Calibration of Zero Value for Navigation Signal Simulator

Xiaopeng Zhong, Zhenwu Tang, Zhijun Meng and Dexiang Ming

Abstract As a high precision source, the navigation signal simulator is possible to simulate the navigation signal which arrived at the antenna of receivers in all kinds of dynamic or static scene, providing a realistic and controllable environment for receiver performance testing. It not only needs higher signal simulation accuracy, but also needs methods and means of high-precision test measurement for itself. The measurement of zero value which is a key indicator has an important effect on its testing as well as the correctness and reliability of receiver's measurement. The traditional measurement of zero value is to make use of an oscilloscope to observe the measured waveform and manually measure the time delay between of flip point and the rising edge of 1PPS signal, and average the measurements. This method will not only introduce measurement errors, but also difficult to locate the flip point accurately due to the low power signal. In this paper, the analysis of the measurement principle of zero value was first introduced, and then a new method was proposed which oscilloscope was used to store the measurement data. In this method, interpolation was first applied to the sampled data, and then the Hilbert transform and polynomial interpolation fitting were used to extract the envelope to find the zero value. The actual results show that the method can improve work efficiency, and is capable to raise the zero value measurement accuracy up to 1 cm.

Keywords GNSS · Beidou · Navigation signal simulator · Zero value · Calibration · Hilbert transform · High precision

X. Zhong (✉) · Z. Meng · D. Ming
College of Mechatronics Engineering and Automation, National University Defense Technology, Changsha 410073, People's Republic of China
e-mail: 13874801824@139.com

Z. Tang
College of Physics and Electronics, Center South University, Changsha 410083, People's Republic of China

J. Sun et al. (eds.), *China Satellite Navigation Conference (CSNC) 2013 Proceedings*, Lecture Notes in Electrical Engineering 243,
DOI: 10.1007/978-3-642-37398-5_43,

43.1 Introduction

The Satellite Navigation Signal simulator is a high precision integrated testing and simulation equipment, which not only provides a critical test and supports for various types of military and civilian navigation receiver equipment [1], as well as other aspects of scientific research, production, application, testing, inspection, simulation training, but also provide an important tool for the study of the compatibility and interoperability features between China's second-generation Beidou satellite navigation system and other navigation system, such as GPS, GLONASS, Galileo.

As high-precision navigation signal source, the signal accuracy of the simulator itself should be higher than the tested devices. However, on the one hand, due to the inherent characteristics of its own design and hardware, there are some deviations between the output signal and ideal value; on the other hand, by the external impact of electromagnetic environment, random error also will be found in the output signal. Therefore, the research on calibration method of output signal of simulator is of great significance for the protection of its reliability and credibility.

Among all the calibration items, the zero value measurement directly impact the control precision of pseudo range, the consistency between the code and carrier channels also will be greatly reduced, which will introduce additional errors, affecting the truthfulness and accuracy of the receiver performance testing. Therefore, among the formal production and testing, a zero calibration will be needed, and the zero value will be deducted from the system.

This article briefly describes the basic principles of the cause of zero value of the navigation signal simulator zero value and measurement with oscilloscope. Heavy workload against the traditional methods of measurement, the efficiency is low, there is the disadvantage of manual measurement error, and this paper describes an oscilloscope store measurement for zero value calibration. Using this method can not only improve work efficiency, reduce manual measurement error, but also improve the accuracy of the zero value measurement up to 1 cm (RMS, 60 s).

43.2 The Basic Principles of Zero Value Measurement

43.2.1 Cause of Zero Value

According to the principle of simulators [2], the RF cell need to produce satellite signal follow the pseudorange computed by the mathematical simulation cell, and the deviation should match the index commanded. But, there are still more deviation between theoretical value and actual value, for the signal producer will finish several parts such as mathematical computation, baseband combination and up-conversion.

The system zero value usually should be several ten microseconds, and changes according to the cable length. In the case of zero-pseudorange, the zero value means the time delay between the head of pseudocode and 1PPS, as shown in Fig. 43.1.

In the design of GNSS simulator, zero value would have a big effect while the existence of different channel in same frequency or different frequency which is a key index, and used in navigation terminate. It a base method for BeiDou/GPS and other system to get the code phase measured using usual device [3].

43.2.2 Measurement Through Flip Point

Most navigation signal using BPSK modulation scheme. In this modulation scheme, when the baseband signal sequence change from "1" to "0" or in reverse, the carrier will have a phase flip of π radian, as shown in Fig. 43.2.

Ideally, the amplitude of the carrier maintains the same at the both side of the flip point. However, in order to reduce the effect of Inter-Symbol Interference, the baseband signal uses a cosine roll off for processing before up conversion [4, 5]. In the actual signal testing, there is a transition area near the flip point [6] shown in Fig. 43.3, the center of the recess is the "turning" point.

Using the oscilloscope to observe the navigation RF signal out from simulator, and set the oscilloscope triggered by the channel which 1PPS signal coming from, then we can observe the waveform on the oscilloscope. When the head and tail has the same symbol, the wave shows in Fig. 43.3a, while different, the wave shows in Fig. 43.3b. And due to the cyclical changes of the navigation message, the figure will alternate between 43.3a and 43.3b. This phenomenon always appears at the

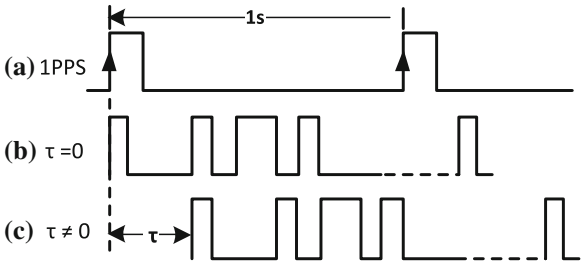

Fig. 43.1 Relationship between 0 phases of Pseudo code and 1PPS

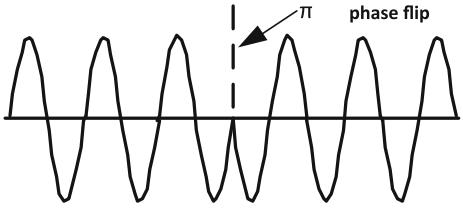

Fig. 43.2 Phase flip diagram of BPSK modulation

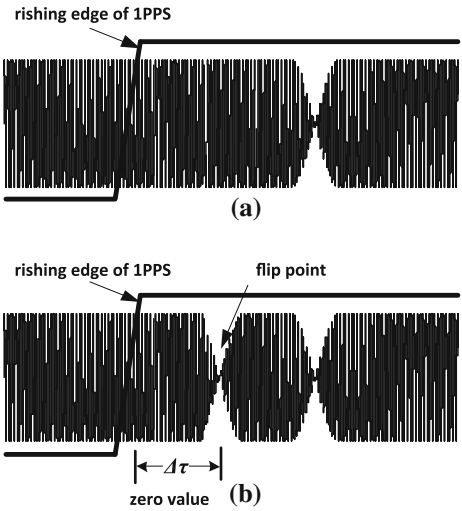

Fig. 43.3 Diagram of flip point

beginning of the navigation message. The point which closing and opening with time go by is the so-call "flip point". As show in Sect. 43.2.1, the zero value turn out to be the time delay between the point and rising edge of 1PPS signal. So, the zero value can be measure using the message of this point and the message of the 1PPS.

43.3 Zero Value Measurement Method

43.3.1 Oscilloscope Manual Measurements

The key of system zero value measurement is to position the flip point exactly, and measuring the distance of the turning point to the center of rising edge of 1PPS. In order to obtain the distance, a direct measurement of the time-domain by oscilloscope can be used. Because the oscilloscope needs to sample the RF navigation signal which has a very high frequency, the oscilloscope requires a higher sampling rate. Its measurement connection relationship is shown in Fig. 43.4.

The actual measurement following these steps: (1) First, the channel 1 of oscilloscope is connected to the 1PPS signal output port which has the same source

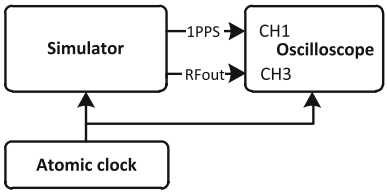

Fig. 43.4 Connection of direct measuring

with the DAC clock, channel 3 is connected to the RF output of the oscilloscope, and the oscilloscope is set to be triggered by channel 1; (2) In the case that pseudo ranges has been set to zero, set the signal output as a single frequency and static BPSK modulation with signal satellite; (3) When the oscilloscope has a stable display, locate the 1PPS rising edge, and find the start of the Barker code in this vicinity, reads out the time span between flip point and the rising edge of 1PPS; (4) track the position of the flip point for a long period of time, and recorded on the oscilloscope readings; (5) Repeat (1) to step (4), using the formula (43.1) averaging several measurements, and using the root mean square error [formula (43.2)] to calculate the value of zero uncertainty.

$$E(\tau) = \frac{1}{n}\sum_{i=1}^{n}\tau_i \tag{43.1}$$

$$D(\tau) = \sqrt{\frac{1}{n-1}\sum_{i=1}^{n}[\tau_i - E(\tau)]^2} \tag{43.2}$$

Table 43.1 shows the zero-value test results using this method of B1 frequency.

Using the method for measurement, we need to manually adjust the time axis of the oscilloscope to get the time span; also we get the estimation by our eyes directly. This kind of measurement makes a heavy workload, and because of the error introduced by manual adjustment and visual cannot be eliminated, the measured results have some uncertainties. Also, because this method can only measure a 1PPS pulse rising edge each time, it cannot provide a long time, continuous observation of the zero value which jitters and wanders as time goes by.

43.3.2 Oscilloscope Sampling Storage Measurement

In order to reduce the error cause by manual adjustment and visual deviation, the method shown in Fig. 43.5 can be used to get zero. First, we store the sample data for a long time by the high speed storage oscilloscope. After the data has been prepared, we used software to analysis and process the data, finding the time distance between flip point and the center of the rising edge; finally we get the zero value by compute the average value we have obtained.

Table 43.1 Zero value test data (after calibration)

Times	1	2	3	4	5
Zero value (ns)	112.5886	112.4604	112.2022	112.3112	112.2748
Times	6	7	8	9	10
Zero value (ns)	112.2330	112.5386	112.1704	112.5204	112.2294
Mean (ns)	112.3529		Standard deviation	0.149377 ns (0.0448 m)	

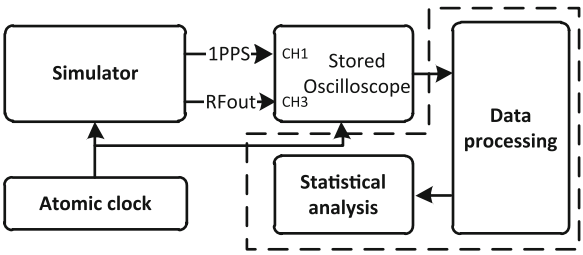

Fig. 43.5 Connection of stored-measuring

The processing of sampled data is the key of data storage measurement method. In order to get the precise value of zero, some procession are needed, including the data interpolation, envelope extraction process, envelope polynomial fitting and statistical analysis.

1. Data interpolation

If the sampling rate of the channel of oscilloscope has only reach 20 GHz, the resolution between two points can only be 0.015 m. In order to improve the processing accuracy of the collected signal, the data was process with interpolation before calculating.

The common interpolation processing includes Lagrange interpolation, Newton interpolation, Hermiter interpolation. Although the Hermiter interpolation method can equal the derivative values of the interpolation-node, but the solution of the base function is still to be known and it also need much computation, this paper mainly consider the first two methods. In this paper, the Lagrange linear interpolation was used, and data was processed in pieces of segment (Fig. 43.6).

For the two adjacent data points $P_k(t_k, \tau_k)$, $P_{k+1}(t_{k+1}, \tau_{k+1})$, the Lagrange interpolation function is created as

$$L(t) = \tau_k \cdot l_k(t) + \tau_{k+1} \cdot l_{k+1}(t), t_k < t < t_{k+1} \tag{43.3}$$

While $l_k(t) = \frac{t - t_{k+1}}{t_k - t_{k+1}}$ and $l_{k+1}(t) = \frac{t - t_k}{t_{k+1} - t_k}$ are the base functions. For M times interpolation, the n-th interpolation point is represented as

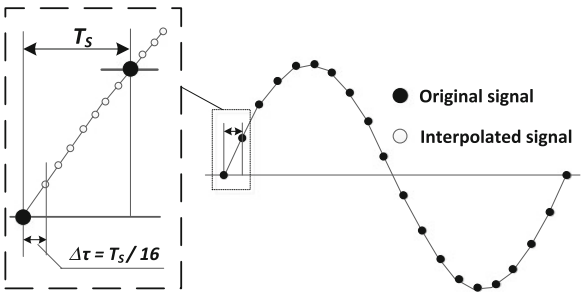

Fig. 43.6 Diagram of data interpolation

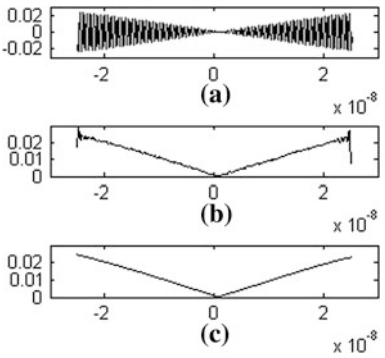

Fig. 43.7 Processing of discrete data

$$P_n\left(t_k + n \cdot \frac{T_s}{M}, L\left(t_k + n \cdot \frac{T_s}{M}\right)\right) \tag{43.4}$$

If $M = 16$, the virtual sampling rate would be 320 GHz, and signal processing accuracy raising up to 1 mm at this time.

2. Envelope extraction by Hilbert Transform

Figure 43.7a shows a piece of the data sampled by oscilloscope, where the 0 moment corresponds to the center of rising edge center of 1PPS, the flip point located at the intersection of the envelope of the RF sample waveform.

The envelope can be extracted using the Hilbert transform method [7]. For a real signal, the Hilbert transform is defined as

$$\hat{x}(t) = x(t) * \frac{1}{\pi t} = \frac{1}{\pi} \int_{-\infty}^{+\infty} \frac{x(\tau)}{t - \tau} d\tau \tag{43.5}$$

Take the Fourier transform of $\hat{x}(t)$ and we can be obtained

$$\begin{aligned} \hat{X}(f) &= F[x(t) * 1/(\pi t)] = X(f) \cdot F[1/(\pi t)] \\ &= X(f) \cdot [-j\mathrm{sgn}(f)] \end{aligned} \tag{43.6}$$

Which $F[\cdot]$ represent Fourier Transform, and $\mathrm{sgn}(\cdot)$ represents the sign function. It is shown that the Hilbert transform is equivalent to a 90° phase shifter. So, for a narrowband signal $f(t)=A(t)\cos(\omega t+\varphi(t))$ with slowly changing envelop $A(t)$, the Hilbert transform can be

$$\hat{f}(t) = A(t)\sin(\omega t + \varphi(t)) \tag{43.7}$$

and we can get its analytical signal as

$$\begin{aligned} \bar{f}(t) &= f(t) + j\hat{f}(t) \\ &= A(t)\cos(\omega t + \varphi(t)) + j \cdot A(t)\sin(\omega t + \varphi(t)) \\ &= A(t)e^{j[\omega t + \varphi(t)]} \end{aligned} \tag{43.8}$$

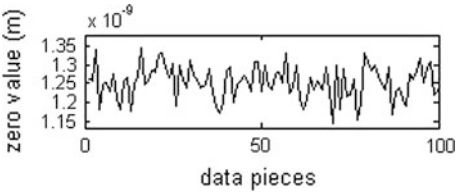

Fig. 43.8 Statistic values of 100 pieces sample data

so we can get the signal envelop according the following formula

$$A(t) = \sqrt{f^2(t) + \hat{f}^2(t)} = \left|\bar{f}(t)\right| \tag{43.9}$$

For each period of the signal acquisition, the Hilbert transform is used to extract the envelope, the results is shown in Fig. 43.7b.

3. Envelope Polynomial Fitting

The envelop extracted by Hilbert transform is not smooth, and there still has a small ripple in the envelope, the direct use of the intersection of the envelope to estimate the zero value will make the introduction of a larger error.

Because the envelope is approximately linear change at the flip point, so the one-order linear fit can be used to process the envelopes of both sides, and the fit polynomial is

$$f(t) = a + b \cdot t \tag{43.10}$$

The fitting result is shown in Fig. 43.7c. In this case, the obtained intersection of two curves of the horizontal axis value should be the zero value.

43.4 Results

The zero value determination takes a long time to track the measurement, it's a statistical value. Figure 43.8 shows the change of zero value obtained using oscilloscope storing measurement way.

During curve fitting, the fitting lines of the envelope will cause large errors due to truncation of the both ends. The use of these data will affect the precision of curve fitting, thus affecting the extraction of zero values. In order to improve the handling of precision, the actual data processing is required to strike out the part of the point. The relationship of the removed points and the zero value is shown in Table 43.2.

Table 43.2 shows us that the using of the data storage means to get the zero value can obtained a high processing accuracy.

Table 43.2 Relationship between excluding point and standard deviation of zero value

Excluding point	0	20	40	60	80
Standard deviation (m)	0.00988	0.00965	0.00932	0.00929	0.00958

43.5 Conclusions

The accurate measurement of the zero value makes a very important meaning for the precision of the control of pseudoranges, channel consistency and stability of the zero value. Using oscilloscope to measure the zero value directly is not only inefficient, but also will introduce artificial measurement error, the measurement accuracy cannot be guaranteed. And the store measurement mode can simplify the measurement steps, and make full use of the software and signal processing algorithms, we can optimize the processing of the sampled data. Actual measurements show that the zero value can be estimated using the stored measurement mode to achieve high accuracy and improve the figure to 1 cm, it is possible to meet the needs of some testing occasions.

References

1. Jaroslaw M (2012) Design and implementation of GPS signal simulator 2012. International conference on localization and GNSS (ICL-GNSS) 2012, P1–4
2. Jun Y (2007) The research of the signal simulation theory and technologies for satellites navigation. School of National University of Defense Technology, Changsha
3. Zhuang C, Wang L, Li T, Wang J (2012) Research on testing technology and accurate measuring method of satellite navigation signal simulator time delay. The 3rd China satellite navigation conference
4. Pitakdumrongkija B, Suzuki H, Suyama S, Fukawa K (2008) Coded single-sideband QPSK and its turbo detection for mobile communication systems. IEEE Trans Veh Technol 57(1):P311–P323
5. Sharma OP, Janyani V, Sancheti S (2007) Analysis of raised cosine filtering in communication systems. Third international conference on wireless communication and sensor networks, pp 9–12
6. Li XH, Bian YJ (2003) Analysis of AM phenomenon in BPSK signals. J Time Freq, 12, 26(2), P111–118
7. Wei F, Yan Z (2011) Harmonic and inter-harmonic signal analysis based on Hilbert-Huang transform. Second international conference on digital manufacturing and automation (ICDMA) 2011, pp 572–575

Chapter 44
An Initial Evaluation About BDS Navigation Message Accuracy

Zhihang Hu, Guo Chen, Qiang Zhang , Jing Guo, Xing Su, Xiaotao Li, Qile Zhao and Jingnan Liu

Abstract In this paper, the accuracy of the trial operation stage BeiDou Navigation Satellite System (BDS) navigation message was analyzed and evaluated from January to December in 2012. The main content of the Beidou performance assessment was briefly introduced together with availability of Beidou precise ephemeris. Then, according to the Beidou mixed multi-satellite constellation characteristics, calculation formula of signal in space was derived, which is exactly suitable for Beidou system. Based on the Beidou precise ephemeris which derived from Position And Navigation Data Analysis software (PANDA) and BeiDou Experimental Tracking Stations (BETS), the accuracy of Beidou broadcast ephemeris, clock errors, Beidou system ionospheric correction model (BeiDou Klobuchar) and the pseudorange Single Point Positioning (SPP) were analyzed in details.

Keywords BeiDou/BDS/Compass · SISRE/URE · BeiDou Klobuchar · Single point positioning · PANDA

44.1 Introduction

Global Navigation Satellite System (GNSS) signal in space performance plays a key role in the accuracy of satellite navigation message and integrity monitoring [1]. GNSS Signal in Space Range Error (SISRE) is the fidelity between the actual

An erratum to this chapter is available at 10.1007/978-3-642-37398-5_70

Z. Hu (✉)
School of Geodesy and Geomatics, Wuhan University, Wuhan 430079, China
e-mail: zhigang.hu@whu.edu.cn

Z. Hu · G. Chen · Q. Zhang · J. Guo · X. Su · X. Li · Q. Zhao · J. Liu
GNSS Research Center of Wuhan University, Wuhan 430079, China

J. Sun et al. (eds.), *China Satellite Navigation Conference (CSNC) 2013 Proceedings*, Lecture Notes in Electrical Engineering 243,
DOI: 10.1007/978-3-642-37398-5_44,

value and the predictive value of the navigation message. It reflects the accuracy of predicted navigation ephemeris and clock error, and ultimately affects the positioning accuracy of real-time navigation users. BeiDou Navigation Satellite System (BDS), which is self-constructed, independently operated and compatible with other satellite navigation systems in the world, is steadily being built as the "three-step plan [2]", As a result, evaluating the signal in space performance of the rapid development of the BeiDou System is of great significance for people to understand the BeiDou System itself running status and its follow-up development.

On the basis of accumulating successful experience of Beidou I experiment satellite system (Beidou-1), China started the construction of the BeiDou phase II (BeiDou-2) in 2004. China successfully sent the first MEO satellite Compass M-1 into orbit in 2007, which indicates that the construction of China's satellite navigation system substantively entered the second step of the "three-step plan". In 2011, there has been 3 GEOs and 4 IGSOs successfully being placed into their slots, with initially regional navigation and positioning capacity. At the end of year 2011, China announced Beidou regional satellite system stepped into trial operation stage. Until December in 2012, 5 synchronous geostationary satellites (GEO), 5 inclined geosynchronous satellites (IGSO) and 4 medium earth orbit

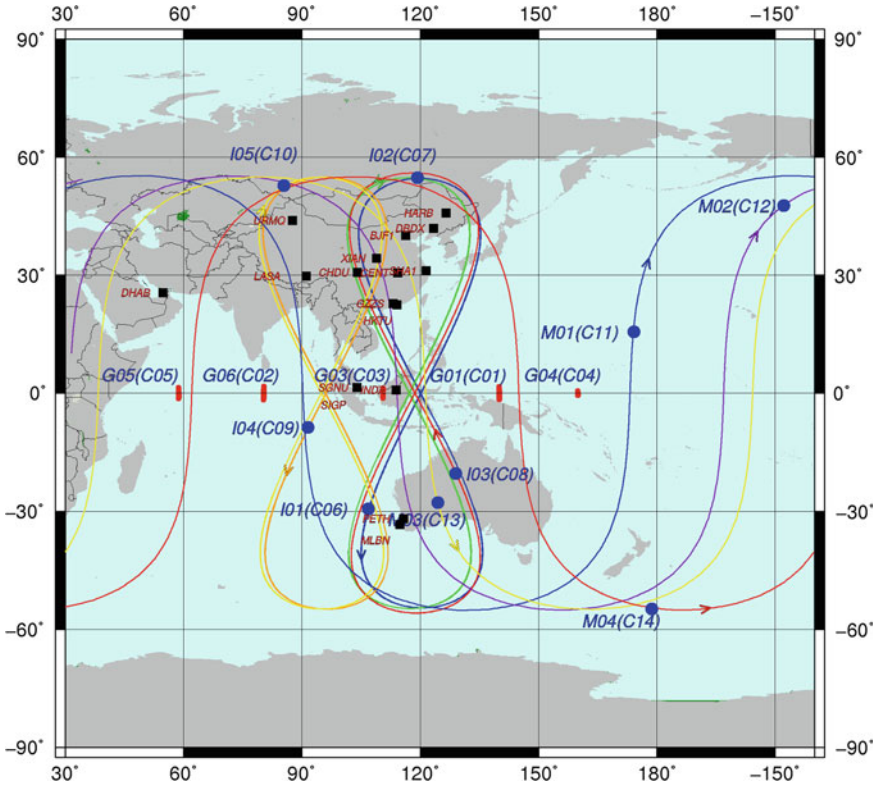

Fig. 44.1 5GEO + 5IGSO + 4MEO Beidou satellite footprint and BETS station distribution

satellites (MEO) have been put into their slots, which achieved the goal of building "5GEO + 5IGSO + 4MEO" regional satellite system (See Fig. 44.1). And the Signal in Space Interface Control Document (ICD) of the Beidou system was announced in detail.

In this paper, the accuracy of the trial operation stage BDS navigation message was analyzed and evaluated from January to December in 2012. Firstly, the main content of the BDS performance assessment and availability of BDS precise ephemeris are briefly introduced respectively. Then, according to the characteristics of BDS mixed multi-satellite constellation, calculation formula of space signal accuracy is derived, which is exactly suitable for BDS. Last but not least, based on the BDS precise ephemeris and BDS Experimental Tracking Stations (BETS), which is established by Wuhan University, the accuracy of BDS predicted ephemeris, clock errors, BDS ionospheric correction model (BDS Klobuchar) and the pseudorange Single Point Positioning (SPP) are analyzed in details.

44.2 BDS Performance Evaluation Content and Precise Ephemeris

The satellite position error and clock error of the navigation message are the important component of SISRE and may influence the precision of navigation and positioning for real-time navigation user. Additionally, lacking of double frequency observation data, the precision of navigation and positioning calculated by single frequency will be under the influence of ionospheres' error. The main contents of this article will be analyzed as follow:

- BDS Broadcast ephemeris accuracy

For the pos-processing reason, the precise ephemeris is not available for real time positioning users. Master Control Station forecasts the orbit and clock error of the navigation satellites according to the field data provided by the ground monitoring station and transfers them to satellites in advance, then broadcasts to users. But this may lead to an error between satellites' real orbits and the prediction. The usually evaluation method is to compare navigation ephemeris with the post-processing precise one in the orbit coordinate system (namely, the radial, tangential and normal direction) accuracy.

- BDS Broadcast clock error accuracy

The clock error accuracy is the important component of the Space signal accuracy. The clock error precision will be calculated based on the precise clock offset.

- BDS Klobuchar ionospheric model accuracy

Ionospheric error mainly influence the single frequency users' positioning accuracy. The BDS provides modified Klobuchar eight parameters ionospheric

model, the refresh rate is 2 h. Base on the GIM Ionospheres model published by CODE center, the BDS Klobuchar ionospheric model accuracy evaluation will be conducted.

The assessment of the BDS broadcast ephemeris needs the higher accuracy satellite position and clock error as reference. As BDS now is trial operation phase, there are no available precise orbit and precise clock error released by BDS official. With the help of the observation data from "BeiDou observation and experiment network (BETS)" built by Wuhan University for scientific research purpose, the BDS satellites precise orbit and clock error are derived using PANDA software, which is self-developed by Wuhan University. BETS consist of 20 ground tracking stations, 11 stations are uniform distribution in China, and another stations distribute in Asia–pacific countries such as Australia, Singapore, and Indonesia and so on. The BETS ground tracking stations distribute in Asia–pacific area properly and quite a number of data can be achieved, which is useful for BDS precise orbit determination (POD). The radial precision of 10 cm [3] is achieved from BeiDou POD, which satisfies the evaluation of BeiDou SISRE.

44.3 Methods of BDS Performance Evaluation

- Beidou SISRE derivation

Signal in space accuracy is the fidelity of the navigation information (navigation ephemeris and clock errors) accuracy. There are a lot of literatures about the performance and features of GPS and GLONASS space signals [4–6], having deduced the corresponding formula of the space signal accuracy. For example, the formula of GPS SISRE is:

$$SISRE = \sqrt{(R - T)^2 + \frac{1}{49}(A^2 + C^2)} \tag{44.1}$$

where, A, C, R, T are respectively the ephemeris position errors and satellite clock in the satellite orbit coordinate system.

At present, BeiDou Satellite System constellations are mainly composed of GEOs and IGSOs composition with high orbital altitude, and is obvious different from GPS and other satellite navigation systems. The formula (44.1) is not suitable to calculate current BeiDou Satellite System SISRE.

Assuming that the Earth as an ideal sphere, orbital coordinate system is established (see Fig. 44.2), with the Earth's mass of center as an origin, connecting geocentric and satellite $\boldsymbol{S}$ mass of center and pointing to satellite setting up $\boldsymbol{r}$ axis (radial), the satellite $\boldsymbol{S}$'s flight direction (tangential) as $\boldsymbol{a}$ axis, and according to the right-hand rule established $\boldsymbol{c}$ axis (normal). Assuming the distance of the satellite to the geocentric and the radius of the earth are D_s and D_e, arbitrary $\boldsymbol{P}$ with the zenith distance and azimuth θ, is satisfied with the joint density probability $\rho(\theta) \propto \sin\theta$ in the satellite signal coverage $(0 \le \theta \le 2\pi,\ \ 0 \le \theta \le \theta_{max} = \cos^{-1}(D_e/D_s))$. According to the literature [4], the general formula of the GNSS average SISRE is:

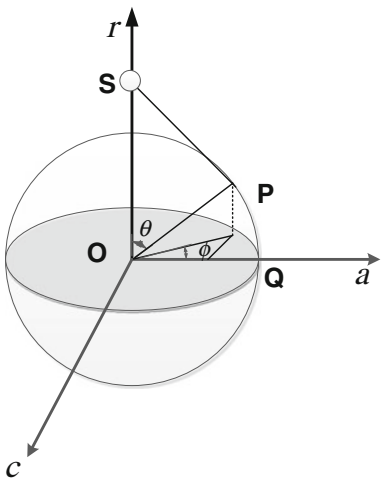

Fig. 44.2 The orbit coordinate system position error projection

$$SISRE = \sqrt{(\alpha R - T)^2 + \beta(A^2 + C^2)} \tag{44.2}$$

$$\alpha = \frac{1}{D}\int_0^{\theta_{\max}}\int_0^{2\pi} \frac{D_s - D_e\cos\theta}{\sqrt{D_e^2 + D_s^2 - 2D_eD_s\cos\theta}}\sin\theta d\phi d\theta$$

$$\beta = \frac{1}{D}\int_0^{\theta_{\max}}\int_0^{2\pi} \frac{D_e^2\sin^2\theta\cos^2\phi}{\sqrt{D_e^2 + D_s^2 - 2D_eD_s\cos\theta}}\sin\theta d\phi d\theta$$

where, $D = 2\pi(1 - \cos(\theta_{\max}))$ is the coverage area of the satellite footprint.

Supposing that the Earth's radius is 6,371 km, the height of MEO orbit is 21,500 km, the GEO orbit height of 21,500 km, using the above formula we can get the formula for the BeiDou system SISRE:

$$\begin{aligned} SISRE_{BDS(GEO,IGSO)} &= \sqrt{(0.99R - T)^2 + \frac{1}{128}(A^2 + C^2)} \\ SISRE_{BDS(MEO)} &= \sqrt{(0.98R - T)^2 + \frac{1}{54}(A^2 + C^2)} \end{aligned} \tag{44.3}$$

If satellite clock error is removed, then, we obtain:

$$\begin{aligned} SISRE^{Orbit\ only}_{BDS(GEO,IGSO)} &= \sqrt{(0.99R)^2 + \frac{1}{128}(A^2 + C^2)} \\ SISRE^{Orbit\ only}_{BDS(MEO)} &= \sqrt{(0.98R)^2 + \frac{1}{54}(A^2 + C^2)} \end{aligned} \tag{44.4}$$

The formula (44.3–44.4) will be used to evaluate the Beidou SISRE performance.

In addition, to evaluate the Beidou SISRE also need considering the following issues:

- Satellite antenna phase center offset

The satellite position calculated by the BeiDou navigation ephemeris is relative to the position of the satellite antenna phase center offset (PCO), while BeiDou precise orbit is relative to the mass center of satellite. Thus the transformation is needed from the mass of center to the satellite antenna phase center.

- The unification of the time system and the coordinate system

The BeiDou broadcast ephemeris time is BeiDou Time (BDT). Duo to using different reference clock for orbit determination, there exists an offset between the precision clock error and broadcast clock error. It can be removed by standard deviation (STDEV) statistical method. The BeiDou broadcast ephemeris is based on China Geodetic Coordinate System 2000 (CGCS2000) coordinate system and the precise orbit data is based on ITRF2008 coordinate system. Both of them exist differences. However, this difference is only a few centimeters of the order of magnitude [7, 8], so this difference will be neglected in this paper analysis.

- The calculation of the BeiDou system GEO satellite position

The GEO satellite orbital inclination and eccentricity are very close to zero, so following GPS broadcast ephemeris parameters form to fit the BeiDou GEO satellite orbit may diverge due to the matrix singularity. The BeiDou GEO satellite ephemeris parameters use the so-called coordinate rotation method to reduce the parameter fitting error. When the BeiDou users use the BeiDou GEO navigation ephemeris, it also required the corresponding coordinate rotation in order to calculate the correct position of the satellite. The detailed algorithm please refers to BeiDou ICD [9].

44.4 Results and Discussion of BeiDou Performance Evaluation

The BDS SISRE accuracy and positioning accuracy were assessed for the whole year of 2012. Observation data was collected from the BETS, while BDS precise orbit and clock products were obtained with PANDA in post-processing mode.

1. Analysis of BDS SISRE

SISRE depends mainly on the broadcast ephemeris error and clock error. In normal scenarios, ephemeris of GEO and IGSO of BDS navigation message updates every 60 min, including the forecast clock error. Frequently updating ephemeris is helpful to improve broadcast satellite orbit and clock precision. Shown in Fig. 44.3 was the standard deviation of differences between broadcast and precise clock products, and standard deviation of most broadcast clock error falls in the range of 2 - 8 ns during the day 001 to 336 of year 2012.

Standard deviation of clock error for C01 was large (about 12 ns) during the first 3 months, and the precision increased to 4 - 8 ns from April on. For C03, the standard deviation fluctuated from 2 - 4 ns to 12 ns (in the middle period), and the precision was then improved (2 - 4 ns) near the end year of 2012. The precision of clock error for IGSOs (C06 - C10) is generally better compared to GEOs (C0 - C05), most of which are stably within 2 - 6 ns (STDEV). However, the precision of forecast clock errors for MEO C11 - C12 increased sharply after their working well for 3 months.

According to Eq. (44.3), statistics of SISRE for each satellite of BDS is shown in Fig. 44.4. Since IGSO could be tracked for a long time in China area and broadcast ephemeris updates every hour, the precision of SISRE is 1.2 m (RMS) on average and keeps relatively stable. Different from IGSOs, GEOs stay "static" at equatorial plane and geometry changed slowly, leading to worse clock precision than IGSOs. The SISRE of MEOs built in June of 2012 was gradually improved from 3.5 to 1.2 m. Generally speaking, SISREs of all three types (GEOs, IGSOs and MEOs) were increasing continuously, with the improvement in number and distribution of BDS tracking stations, as well as that in system performance of BDS. Up to December in 2012, the average precision of 5GEO/5IGSO/4MEO is about 1.5 m (RMS).

Shown in Fig. 44.5 is the statistical result of SISRE, only with orbit forecasting error taken into account. Among the three types of constellation, MEOs had the best precision, and GEOs the worst. Compared with Fig. 44.4, SISRE with forecasting clock error not taken into account was obviously better than the opposite, which indicated that clock error accounted the main part of the SISRE.

2. BeiDou Klobuchar ionosphere model accuracy

To improve the navigation and positioning precision for the regional single frequency users, BDS has built the BeiDou Klobuchar model for ionospheric

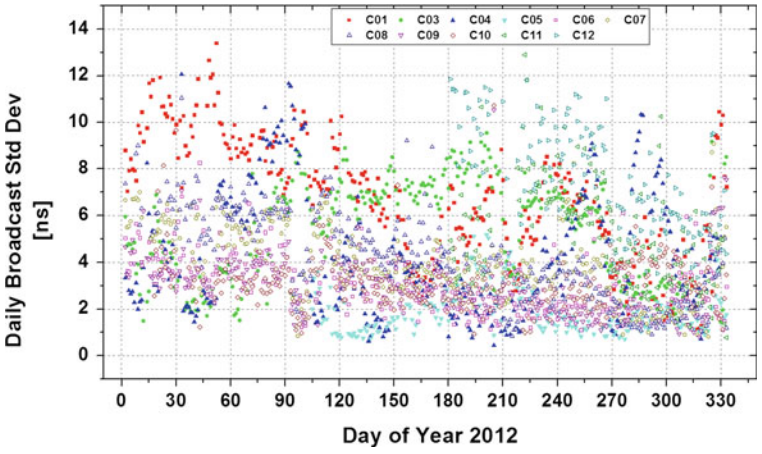

Fig. 44.3 Daily broadcast clock residual w.r.t WHU precise clock

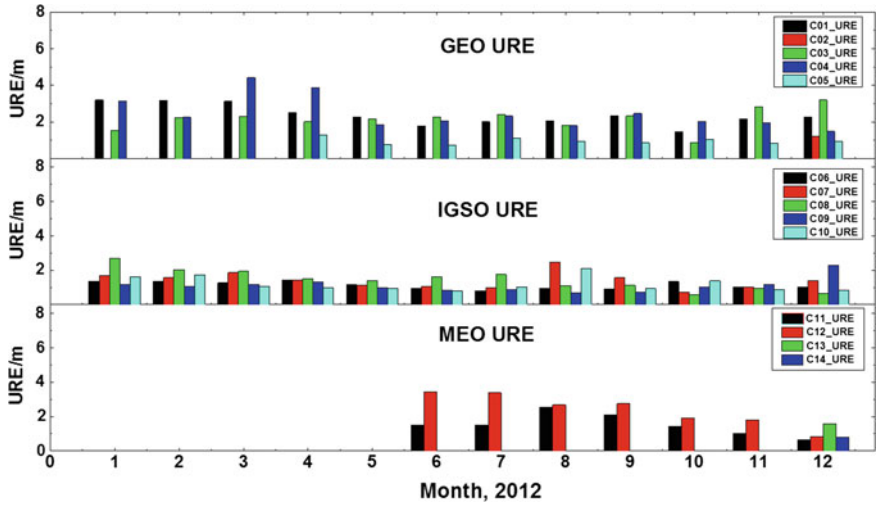

Fig. 44.4 Statistics of BeiDou SISRE accuracy

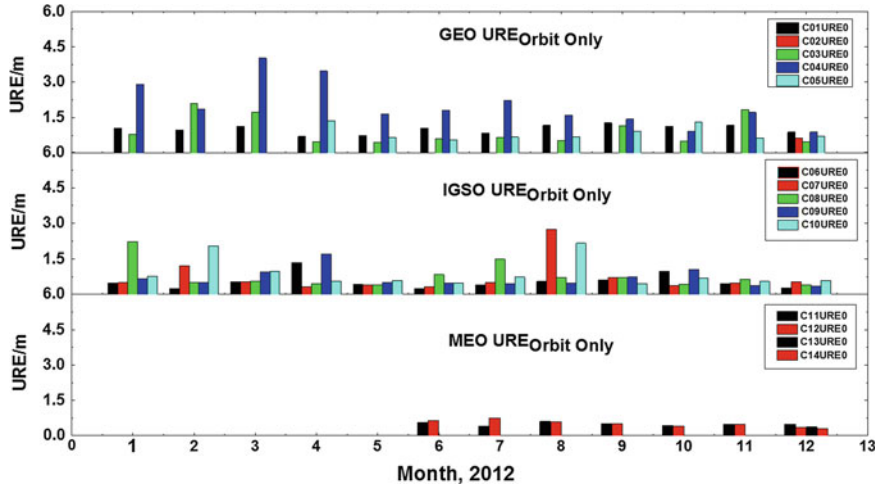

Fig. 44.5 Statistical result of SISRE only with forecasting clock error taken into account

correction. The model is obtained by solving the real dual-frequency GNSS observations from a regional tracking network in China. Due to the lack of data in the southern hemisphere, the ionospheric corrections in the southern hemisphere are calculated by means of symmetry with the northern hemisphere.

The Global Ionosphere Maps (GIM) provided by CODE is used as the reference ionospheric correction values in this paper. And then the vertical ionospheric correction residuals of BeiDou Klobuchar model are calculated for December 2012, which is shown in Fig. 44.6. It is can be seen from Fig. 44.6 that the

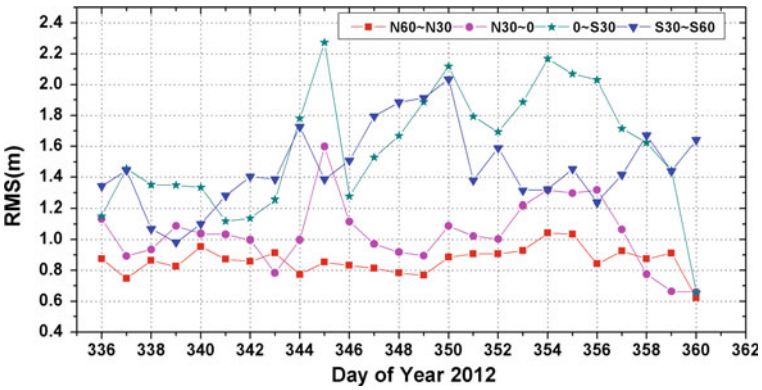

Fig. 44.6 The precision of BeiDou Klobuchar model in different latitude zone. The *horizontal axis* is the Day of Year in 2012 (unit: day) and the *vertical axis* is the RMS of BeiDou Klobuchar ionospheric delay correction residuals (unit: m). The *red symbol* is mean RMS from N60° to N30°, respectively, the *pink symbol* is the mean RMS from N30° to 0°, the *green symbol* is the mean RMS from 0° to S30°, and the *blue symbol* is the mean RMS from S30° to S60°

correction precision of BeiDou Klobuchar model is about 1.0 m in the northern hemisphere, while in the southern hemisphere the precision decreases to 1.5 m. This is mainly because that in BeiDou Klobuchar model the southern hemisphere adopts the same parameters with the northern hemisphere by means of symmetry.

For further analysis, the correction ratio of BeiDou Klobuchar model is calculated for 5 chosen stations from BETS tracking network. The correction ratio equation used in the paper is:

$$Ratio = \frac{1}{n}\sum_{i=1}^{n}\left(1 - \frac{|Klobuchar_{BDS} - GIM_{GPS}|}{GIM_{GPS}}\right) \times 100\,\% \qquad (44.5)$$

As shown in Fig. 44.7, the correction ratio of BeiDou Klobuchar model in China is almost above 70 %. This is convinced by using the real dual-frequency BeiDou observations as the reference value, and [10] shares the same conclusion. By comparing the ratios of stations in the perspective of latitude, it can be seen that the correction precision is higher in the mid-latitude area than in the low latitude area.

3. Analysis of BDS pseudorange positioning accuracy

In 2012, 6 BeiDou satellites were launched, including 2 GEOs and 4 MEOs, lending to a significant change in the constellation structure and a dramatic improvement in DOP value. Table 44.1 listed the change of constellation, so as to analyze the impact of constellation on positioning accuracy. The service area covers 55°E ∼ 160°E, 55°S ∼ 55°N. Three typical observing stations were selected to analyze the positioning accuracy of BDS in 2012, and the information of these stations was shown in Table 44.2.

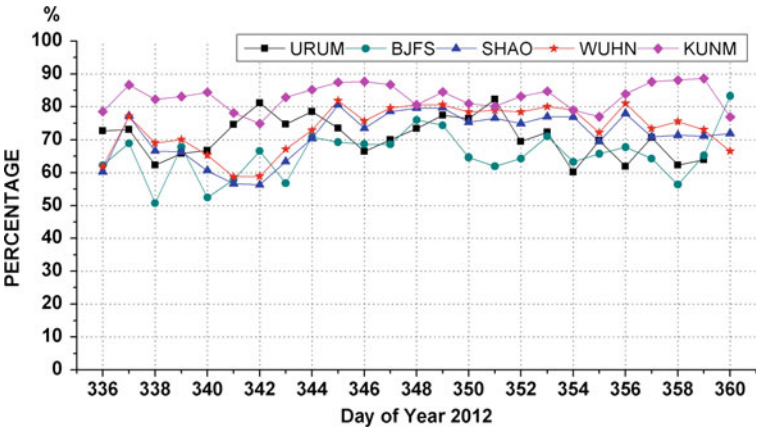

Fig. 44.7 BeiDou Klobuchar model ionospheric delay correction precision. The *horizontal axis* is the Day of Year in 2012 (unit: day) and the *vertical axis* is the correction percentage of BeiDou Klobuchar ionospheric model. The *black symbol* is the correction of URUM station, respectively, the *green* represents BJFS, the *blue* represents SHAO, the *red* represents WUHN, and the *pink* represents KUNM

Table 44.1 Beidou construction stages

Number	Constellation	Duration
1	3G + 4I	2012.01.01–2012.02.06
2	3G + 5I	2012.02.07–2012.04.15
3	4G + 5I	2012.04.16–2012.06.29
4	4G + 5I + 2 M	2012.07.01–2012.10.31
5	5G + 5I + 4 M	2012.11.28–now

Table 44.2 Typical BeiDou tracking station information

Site	ID	Obs. type	Latitude	Longitude	Receiver privider
Beijing	BJF1	B1I/B2I	+40.0	+116.3	UNICORE
Wuhan	CENT		+30.5	+114.4	UNICORE
Perth (Australia)	PETH		−31.9	+115.8	UNICORE

The positioning algorithm for BDS pseudo range was a little different from GPS: (1) Coordinates transformation was required when computing GEO satellite position with broadcast ephemeris; (2) Beidou Klobuchar ionosphere model could be use to correct ionospheric delay in single-frequency positioning, which is computed in a different way from GPS [10].

Figures 44.8, 44.9 and 44.10 show the pseudo range stand-alone result of single frequency (B1I). When the constellation was 3GEO + 4IGSO, positioning precision was about 10 m in horizontal and 15 m in vertical (95 %). When another GEO (C05) was added and the structure became 4GEO + 5IGSO, geometric

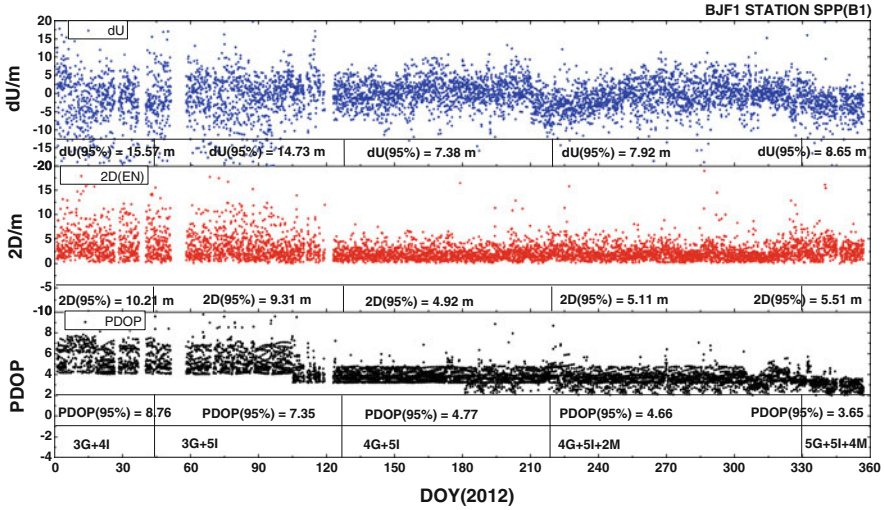

Fig. 44.8 Beijing station SPP precision (January–December, 2012)

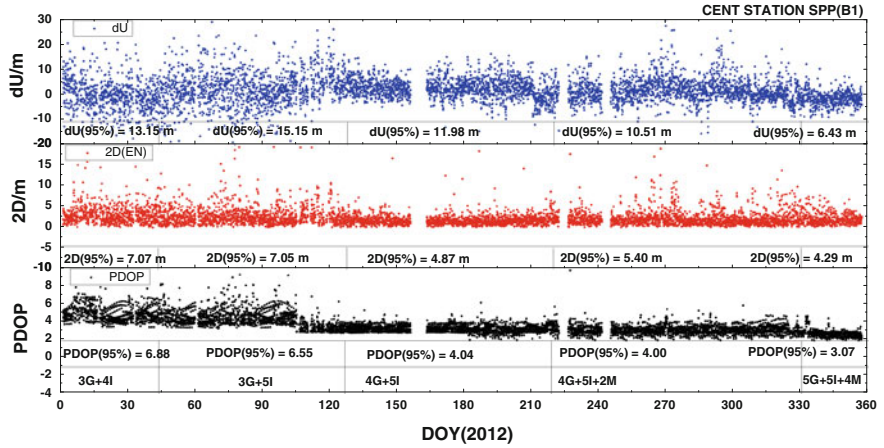

Fig. 44.9 Wuhan station SPP precision (January–December, 2012)

condition at observing station was improved dramatically, and the PDOP value was reduced by half. Correspondingly, the positioning precision improved. In 4GEO + 5IGSO + 2MEO constellation, the contributions of additional two MEOs to geometric conditions and positioning precision were not that obvious, since tracking time is relatively short and interval of ephemeris uploading is longer than GEOs and IGSOs. Precision of pseudo range positioning at the condition of 5GEO + 5IGSO + 4MEO is improved, with horizontal precision better than 6 m (95 %) and vertical precision better than 10 m (95 %). The results show that the

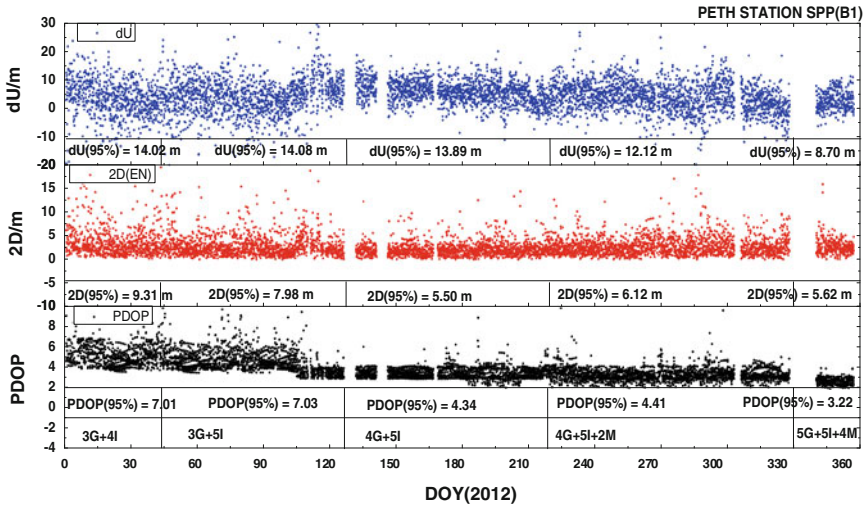

Fig. 44.10 Perth station SPP precision (January–December, 2012)

precision of BeiDou pseudo range positioning for choosen stations has meets the service specification of horizontal 10 m and vertical 10 m.

44.5 Conclusion

Based on the large BeiDou observation data from January to December in 2012, the BeiDou broadcast ephemeris and clock precision is assessed with BeiDou precise ephemeris and clock computed by PANDA software. The BeiDou Klobuchar ionosphere model is also compared with higher precise GIM released by CODE and the navigation positioning accuracy is investigated as well choosing typical tracking stations in the BeiDou service volume. From the statistics result, we can draw conclusions as follows:

- Compared with precise clock data, the broadcast clock error precision ranges from 4 to 6 ns (STDEV)
- Signal in Space error accuracy better than 1.5 m
- BeiDou ionosphere Klobuchar model correction ratio is approximately 70 %. And northern sphere is generally better than southern sphere duo to lack of southern ionosphere monitor observation data.
- With rapid constellation development of the BDS the signal in space performance of BDS becomes better and better. The positioning accuracies of initial stage (3GEO + 4IGSO) are 10 m (Horizontal) and 15 m (Vertical). And these accuracies are further improved up to 6 and 10 m respectively. The typical SPP

statistical results show that the single frequency receiver positioning accuracy generally meets the Asian–pacific region service specification of horizontal 10 m and vertical 10 m.

References

1. Heng L, Gao GX, Walter T et al (2010) GPS signal-in-space anomalies in the last decade: data mining of 400,000,000 GPS navigation messages, paper presented at Proceedings of the 23rd international technical meeting of the satellite division of the institute of navigation (ION GNSS 2010), Portland, September 2010
2. CSNO (China Satellite Navigation Office) (2012a) Report on the development of BeiDou navigation satellite system, edited by C. S. N. Office, Beijing
3. Shi C, Zhao Q, Li M et al (2012) Precise orbit determination of Beidou Satellites with precise positioning. Science China Earth Sciences 55(7):1079–1086, doi:10.1007/s11430-012-4446-8
4. Warren DM, Raquet J (2003) Broadcast vs. precise GPS ephemerides: a historical perspective. GPS Solutions 7(3):151–156. doi:10.1007/s10291-003-0065-3
5. Zumberge J, Bertiger W (1996) Ephemeris and clock navigation message accuracy. In: Parkinson B, Spilker J, Axelrad P et al (eds) Global positioning system: theory and applications. American Institute of Aeronautics and Astronautics, Washington, DC, pp 585–699
6. Heng L, Gao GX, Walter T et al (2011) Statistical characterization of GLONASS broadcast ephemeris errors, paper presented at Proceedings of the 24th international technical meeting of the satellite division of the institute of navigation (ION GNSS 2011), Portland, OR
7. Yang Y (2007) National 2000's GPS control network of China. Prog Nat Sci 17(8):983–987
8. Yang Y (2009) Chinese geodetic coordinate system 2000. Chin Sci Bull 54(15):2714–2721 doi:10.1007/s11434-009-0342-9
9. CSNO (China Satellite Navigation Office) (2012b) BeiDou navigation satellite system signal in space interface control document open service signal B1I (version 1.0), edited by C. S. N. Office, Beijing
10. Wu X, Hu X, Wang G et al (2012) Evaluation of COMPASS ionospheric model in GNSS positioning. Adv Space Res 51(6):959–968, doi:http://dx.doi.org/10.1016/j.asr.2012.09.039

Chapter 45
Analysis of Signal Characteristic and Positioning Performance Affected by Pseudorange Multipath for COMPASS

Feng Zhang, Haibo He, Bin Tang, Fei Shen and Rong Chen

Abstract With the GNSS modernization, the satellite orbit error, the ionospheric delay and the tropospheric delay has been effectively eliminated or reduced, but the multipath error for different users is non-correlation, which can not be removed through differential technique, and then it will be the major error source for GNSS navigation and positioning. Considering COMPASS constellation contains GEO and IGSO satellites, which are high-orbiting satellites, so the multipath effect of COMPASS is different from that of GPS. In order to analyze the multipath effect of high-orbiting satellites, three schemes are adopted in this paper. (1) Model of code tracking multipath error is deduced based on coherent early minus-late delay lock loop, multipath error envelopes are achieved for different bandwidth and different correlation space. (2) The multipath effects on pseudo-range is quantitative analyzed based on the satellite signals and multipath signals simulated by the signal source. The performance of anti-multipath is analyzed for the first time with different receivers. (3) The pseudorange multipath effect on the navigation and positioning is analyzed with the observations of Compass receiver through differential algorithm of short line. The calculation and analysis shows that: Pseudorange Multipath of B1 is larger than B3, and Pseudorange Multipath of GEO is larger than IGSO and MEO. In static positioning, RMS of Multipath of B1 can reach up to 2.53 m, and RMS of Multipath of B3 can reach up to 0.73 m.

Keywords Multipath error · Code tracking · Simulation analysis · Narrow correlator · Pseudorange difference

F. Zhang (✉) · H. He · B. Tang · F. Shen · R. Chen
Beijing Satellite Navigation Center, Beijing 100094, China
e-mail: zhangfengchxy@163.com

J. Sun et al. (eds.), *China Satellite Navigation Conference (CSNC) 2013 Proceedings*, Lecture Notes in Electrical Engineering 243,
DOI: 10.1007/978-3-642-37398-5_45,

45.1 Introduction

COMPASS has been basically completed for regional navigation and positioning, which includes 5 GEO, 5 IGSO and 4 MEO satellites, so application research has attracted attention of many scholars based on hybrid constellation.

On the analysis and assessment of Beidou position performance, it is found pseudorange multipath error is the main error sources causing dual positioning bad. The Beidou pseudorange multipath not only correlate to satellite constellation and environment of application, but also correlate to signal bandwidth, receiver bandwidth and internal resources. Because of the small spatial correlation, it can not be corrected by differential technique [1]. Despite many methods of anti-multipath have been used, it is still difficult to eliminate multipath error.

At present, code tracking multipath error envelope based on coherent early minus-late delay lock loop is recognized as the evaluation standard [2, 3]. There have been many domestic and foreign papers researching on multipath of GPS signal, but multipath characteristics of Beidou II signal have not been studied in depth, the performance of anti-multipath have not been demonstrated, the multipath effect on positioning performance has not been comprehensively analyzed.

Concerning these problems and needs, in this paper, characteristics and related factors of Beidou civil signals are researched theoretically, performance of anti-multipath is analyzed through simulation for different receivers, and the pseudorange multipath analysis on the navigation and positioning is done with the observations of Compass receiver. It is helpful to study multipath characteristics and improve performance of anti-multipath of receivers.

45.2 Model of Multipath Error Envelope

The composite signal of Direct and multipath signal can be expressed as [4]:

$$r(t) = a_0 e^{j\varphi_0} g(t - \tau_0) + \sum_{i=1}^{N} a_i e^{j\varphi_i} g(t - \tau_i) \tag{45.1}$$

where, $g(t)$ is the complex envelope of emitted signal; a_0, φ_0, τ_0 are amplitude, phase and delay of direct signal; a_i, φ_i, τ_i are amplitude, phase and delay of the ith multipath signal; N is number of multipath signals. To simplify the discussion, considering $N = 1$.

Multipath effects are mainly reflected in the correlation characteristics of synthetical signal with multipath and direct signal [5]. On condition that amplitude of direct signal is 1, amplitude of multipath signal is 0.5, multipath delay are 0.4 chips, correlation properties of synthesized signal as shown in Fig. 45.1.

In actual uses, the relative phase and amplitude changes ceaselessly for the multipath signal relative to the direct signal, which cause the code loop

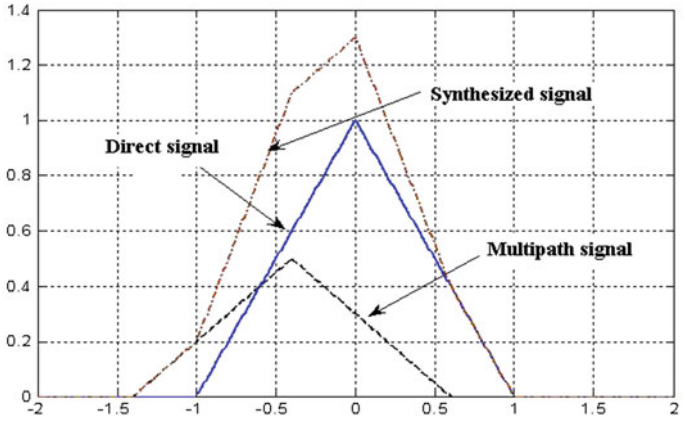

Fig. 45.1 Correlation properties of synthesized

discriminator deviates from the equilibrium tracking point, so tracking error is introduced in PRN code [6]. Code loop is usually designed to be coherent early minus-late delay lock loop, and multipath error envelope of code loop discriminator output as:

$$D(\varepsilon_\tau) = a_0[R(\varepsilon_\tau - d/2) - R(\varepsilon_\tau + d/2)] \pm a_1[R(\varepsilon_\tau - \tau - d/2) - R(\varepsilon_\tau - \tau + d/2)] \tag{45.2}$$

where, $R(\tau)$ is the code correlation function, ε_τ is time delay estimation of direct signal, d is space of coherent early minus-late delay correlator, multipath error is ε_τ when Discriminator output is zero, equal to resolving the following equation:

$$D(\varepsilon_\tau) = 0 \tag{45.3}$$

The first order Taylor series expansion of $D(\varepsilon_\tau)$ in the vicinity of 0 is:

$$D(\varepsilon_\tau) = D(0) + D^{'}(0) \times \varepsilon \tag{45.4}$$

Considering signal bandwidth, the relationship between code correlation function and power spectrum density is:

$$R(\tau) = \int_{-\beta_r/2}^{\beta_r/2} S(f) e^{j2\pi f\tau} df \tag{45.5}$$

where, β_r is signal bandwidth, $S(f)$ is power spectrum density. From Eqs. (45.2) to (45.5) we can attain multipath error:

$$\bar{\varepsilon}_\tau = \frac{\pm a \int_{-\beta_r/2}^{\beta_r/2} S(f) \sin(2\pi f\tau) \sin(\pi f d) df}{2\pi \int_{-\beta_r/2}^{\beta_r/2} f S(f) \sin(\pi f d)[1 \pm a\cos(2\pi f\tau)] df} \tag{46.6}$$

where, $a = a_1/a_0$ is amplitude ratio of multipath and direct signal, when the $\pm$ are the $+$ and $-$ according to the phase difference, Eq. (45.6) is multipath error envelope, and all actual multipath errors should be located within the envelope.

Based on formula (45.6), multipath error envelopes are achieved for different bandwidth and different correlation space. Results are as shown in Fig. 45.2.

As can be seen from Fig. 45.2, multipath error is related to signal bandwidth and correlation space. Performance of anti-multipath is limited only by reducing correlation space on condition that signal bandwidth is narrow. Anti-multipath effect of narrow correlator technology is obvious for signal of wide bandwidth [7]. The code rate of B1 is 2.046, and B3 is 10.023 MHz, which is 5 times larger than B1. From the simulation results we can see that B3 is better than B1 on performance of anti-multipath.

45.3 Analysis on Simulation Data

Signals of two satellites are simulated with signal source. One channel signal is pseudorange of 1 satellite, which do not contain multipath, as the reference signal. Second channel is 2 satellite which is placed in the same position to 1 satellite. At the same time, one multipath signal is simulated for 2 satellite using the third channel, its amplitude is half of direct signal, signal delay increase gradually from 0 to 1.5 chips by step of 0.01 m/s.

Beidou receivers track and achieve pseudorange observation of 1 and 2 satellite, and pseudorange of 2 satellite will be affected by multipath.

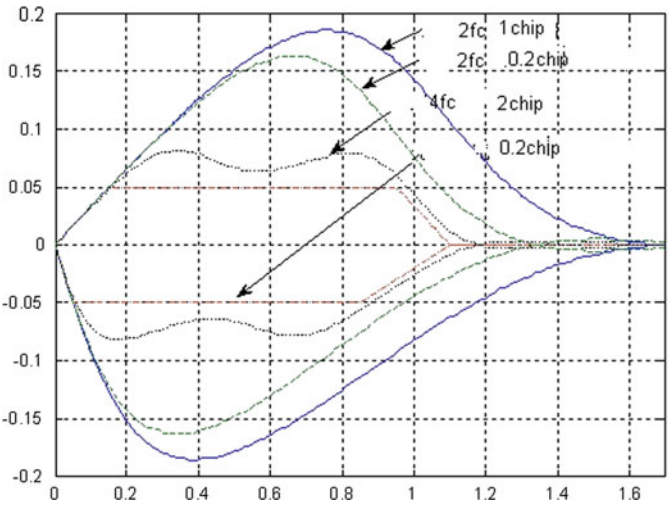

Fig. 45.2 Multipath error envelopes for different bandwidth and different correlation space

Through pseudorange of satellite 1 minus pseudorange of satellite 2, we can attain pseudorange error of different time and multipath value, and then generate picture of multipath error envelope. It can be used to analyze effect on pseudorange accuracy for known multipath value.

The results of B1 and B3 frequencies are as shown in Figs. 45.3, 45.4, 45.5, 45. 6, 45.7, 45.8.

1. Results of multipath simulation for B1
2. Results of multipath simulation for B3

In Figs. 45.3, 45.4, 45.5, 45. 6, 45.7, and 45.8, abscissa represents simulated multipath errors, longitudinal coordinates are pseudorange measuring errors. As can be seen from the result:

1. The multipath error of pseudorange is related to signal Bandwidth. Bandwidth of B1 is narrow, so the effect of multipath is serious; B3 frequency bandwidth is wide, so the multipath effect is relatively small.
2. Effect of multipath is different for different receivers, which may be related to baseband algorithm and correlation space in receiver. The correlation space of corporation C is smaller, which can remarkably reduce multipath effect of B3.
3. Comparing with simulated multipath, real received pseudorange multipath is reduced in different degree, which indicates that Beidou receivers have certain ability of anti-multipath.

45.4 Analysis on Practical Test Data

Based on the real measuring data of Beidou receivers for civil navigation, differential method of short baseline is designed in this paper. First of all, double difference observation equation is achieved using two stations and their known

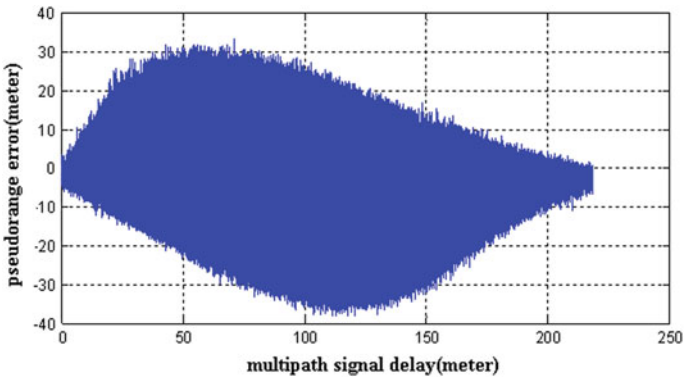

Fig. 45.3 Results of multipath simulation of B1 for corporation A

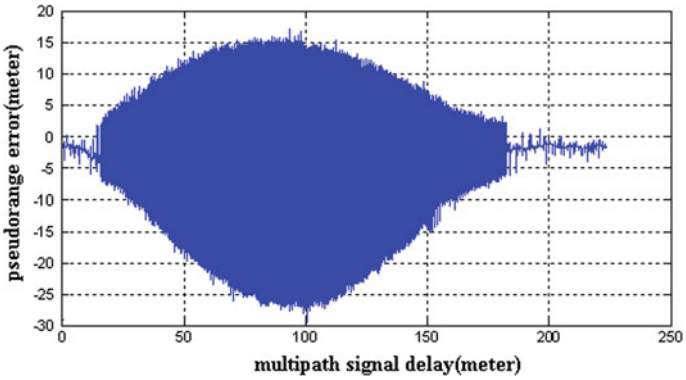

Fig. 45.4 Results of multipath simulation of B1 for corporation B

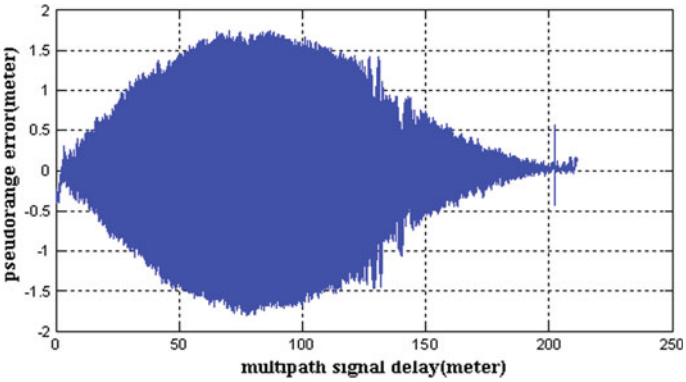

Fig. 45.5 Results of multipath simulation of B1 for corporation C

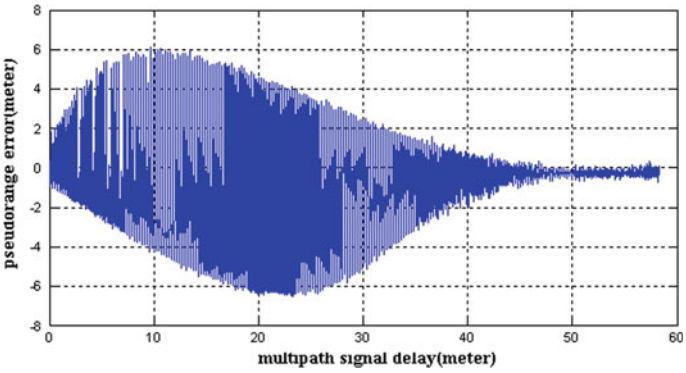

Fig. 45.6 Results of multipath simulation of B3 for corporation A

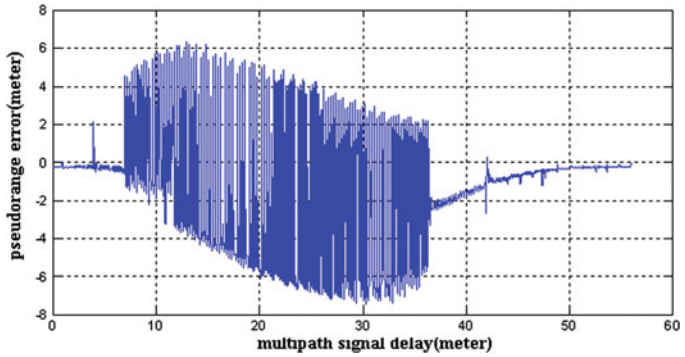

Fig. 45.7 Results of multipath simulation of B3 for corporation B

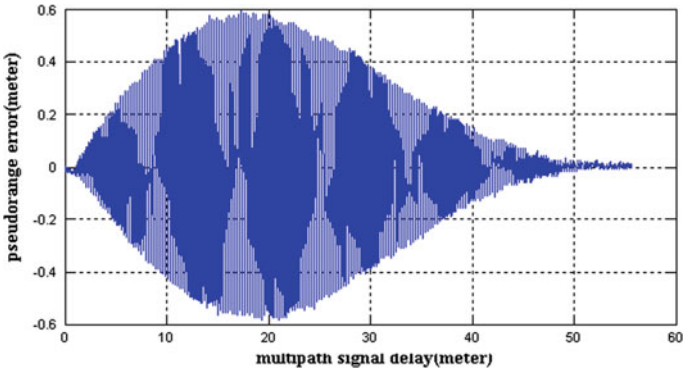

Fig. 45.8 Results of multipath simulation of B3 for corporation C

coordinates [8], which can eliminate errors such as satellite clock error, receiver clock error, ionospheric delay, tropospheric delay and hardware delay. Secondly, based on the double difference observation equation and error propagation law, the single difference equation is separated, whose residuals only contain multipath and noise of pseudorange. According to the propagation law of random errors, non differential multipath and noise of pseudorange can be attained by dividing $\sqrt{2}$. This method can completely eliminate hardware delay and other errors [9], and can reflect the multipath and noise value of pseudorange more intuitively.

Experimental data is obtained in Beijing using two navigational receivers away from 34 m, and they record original pseudorange and navigation data in double frequency positioning mode of B1 and B3. The time span of data is 06:00, 27/8/2012 to 06:20, 28/8/2012 in Beidou time, which is about 24 h, and the interval is 1 s, the cut-off angle is 5°.

Residuals of differential pseudorange for B1 and B3 are computed. Results of some visible satellite are as shown in Figs. 45.9, 45.10, 45.11, 45.12, 45.13, 45.14).

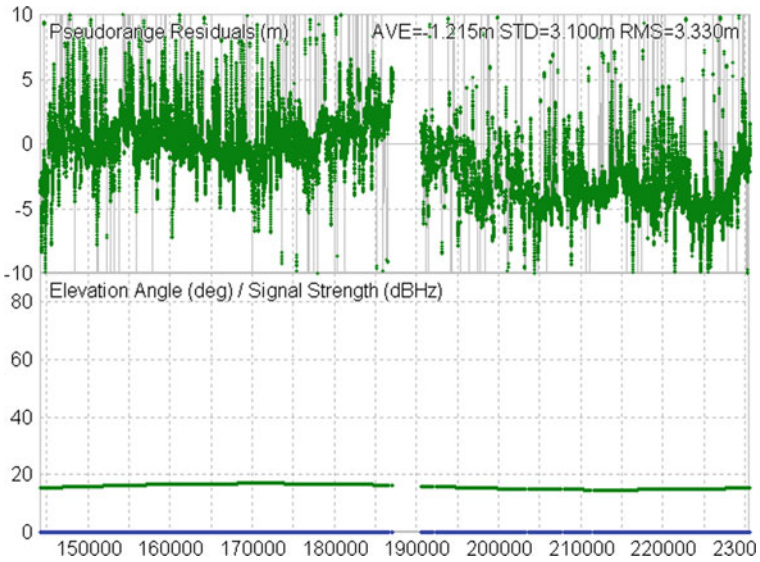

Fig. 45.9 Pseudorange multipath errors of C05 satellite on B1

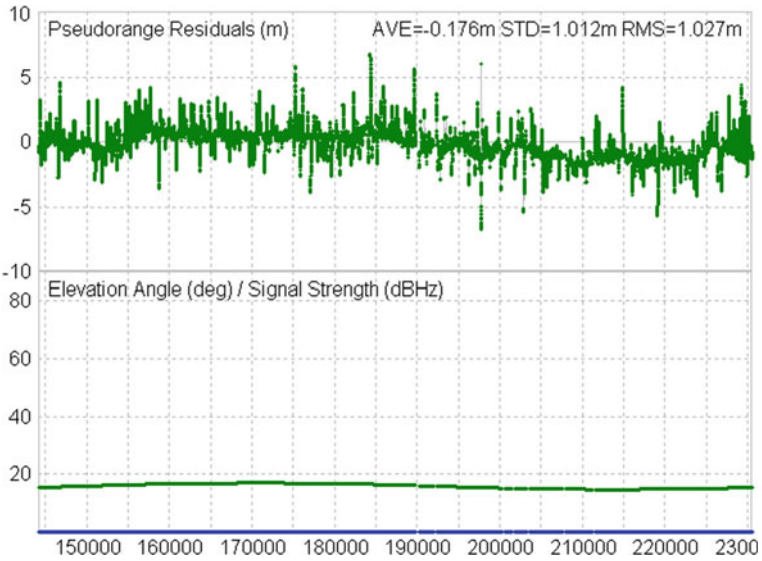

Fig. 45.10 Pseudorange multipath errors of C05 satellite on B3

In the figure, abscissa represents time (seconds in Beidou week), and ordinate respectively represent multipath value of pseudorange (m) and elevation angle of satellite (degrees). As shown in the figure: Multipath value of pseudorange is related to satellite. Multipath of GEO is larger than IGSO and MEO satellite. RMS

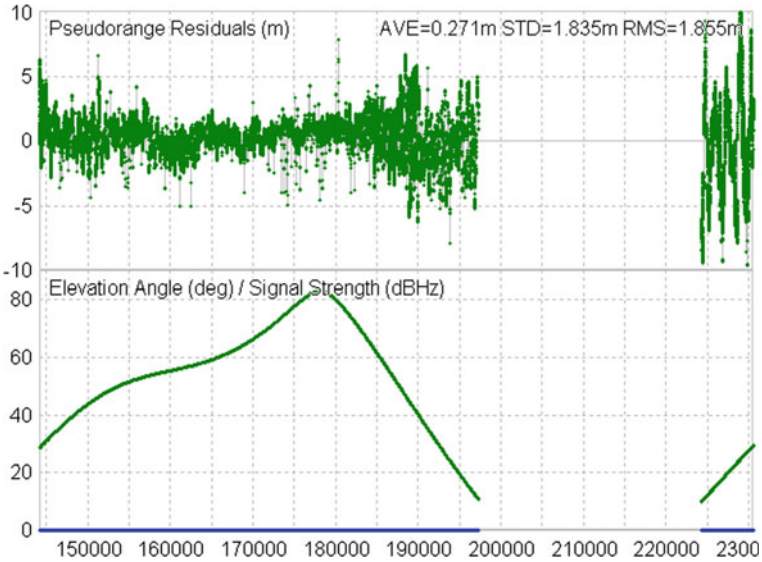

Fig. 45.11 Pseudorange multipath errors of C10 satellite on B1

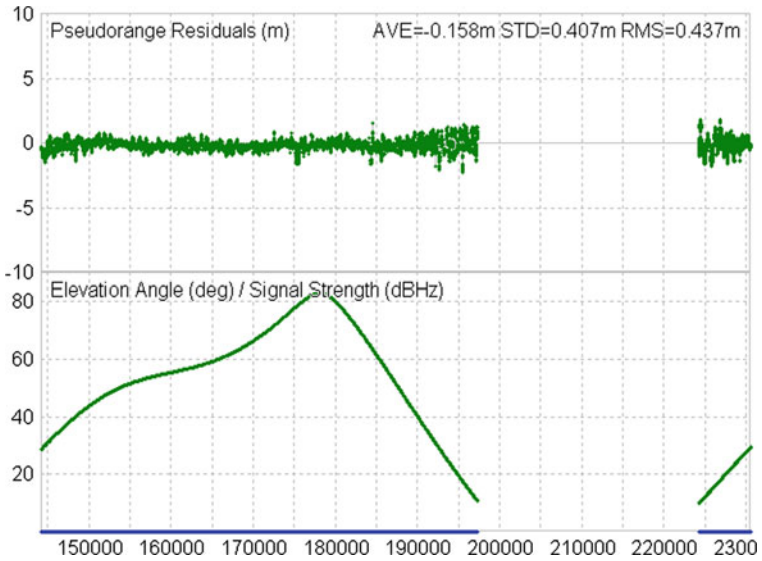

Fig. 45.12 Pseudorange multipath errors of C10 satellite on B3

of Multipath of B1 can reach up to 2.53 m, and RMS of Multipath of B3 can reach up to 0.73 m. Multipath value of pseudorange is also related to frequency, and multipath of B1 is larger than B3 for all satellites, which is caused by narrow bandwidth of B1.

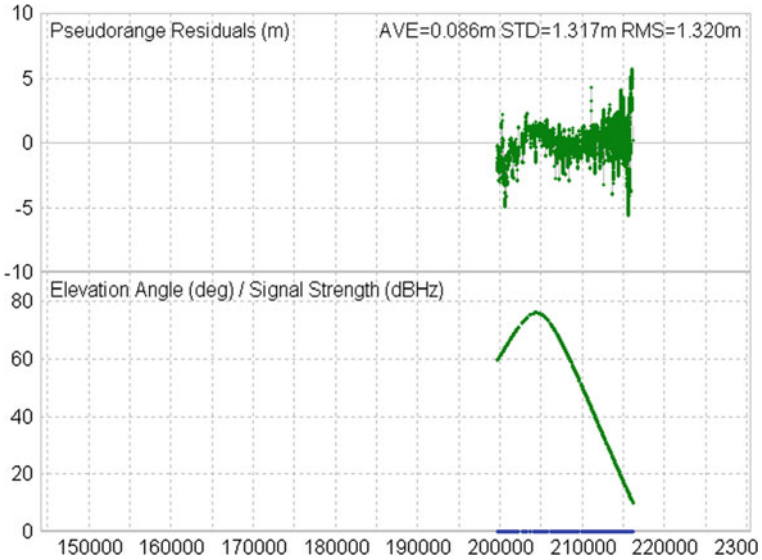

Fig. 45.13 Pseudorange multipath errors of C12 satellite on B1

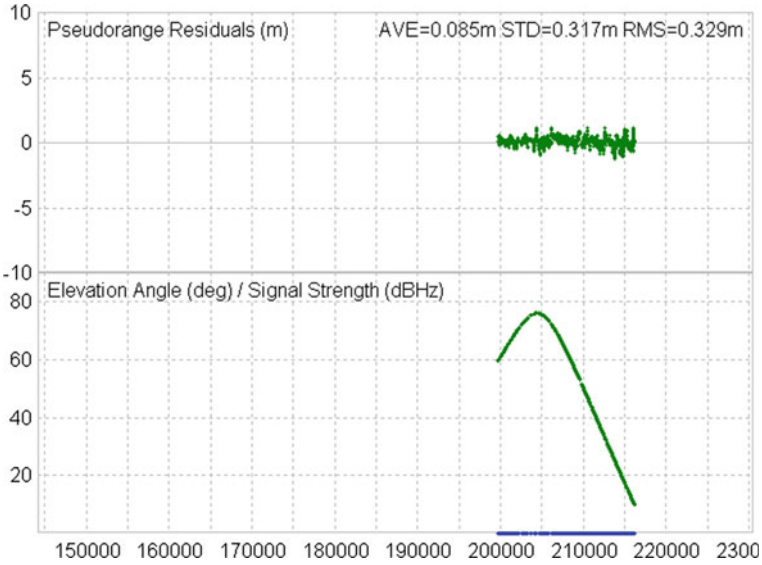

Fig. 45.14 Pseudorange multipath errors of C12 satellite on B3

45.5 Conclusions

Based on the characteristic of Beidou signal system and constellation, pseudorange multipath characteristics and effect on positioning performance are analyzed in detail, and the performance of anti-multipath is analyzed for the first time with different receivers. The conclusions are as follows:

1. Multipath value of B1 is greater than B3 for COMPASS, because bandwidth of B1 is narrow, so it is susceptible to multipath error.
2. Multipath of GEO is larger than IGSO and MEO satellite. RMS of Multipath of B1 can reach up to 2.53 m, and RMS of Multipath of B3 can reach up to 0.73 m.
3. On condition that signal bandwidth is wide, narrow correlator technology can effectively inhibit the effect of multipath error on pseudorange. Simulation results show that multipath of B3 can be significantly reduced through technology of narrow correlator for COMPASS receivers.

Acknowledgments This work is supported by the National Natural Science Funds of China (Grant Nos. 41020144004; 41104022), the National "863 Program" of China (No: 2013AA122501), and the 2nd and 3rd China Satellite Navigation Conference (Grant Nos. CSNC-2011-QY-13; CSNC-2012-QY-03).

References

1. Qifeng X. GPS satellite navigation and precise positioning. Publ PLA 1994:12–20
2. Huicui Liu, Xiao Cheng (2011) Evaluation of multipath mitigation performances based on error envelope. J Nat Univ Def Technol 33(1):72–75
3. Bao Li, Jiangning Xu (2012) Analysis and simulation on anti-multipath performance of Beidou2 navigation. J Chin Inertial Technol 20(3):339–342
4. Sennott JW, Pietraszewski D (1987) Experimental measurement and characterization of ionospheric and multipath errors in differentical GPS. Navigation 34(2)
5. Mengyang Z, Baoxiong L, Wenshen S (1998) Analysis on multipath in GPS system. J Xidian Univ 26(3):10–14
6. Goldhirsh J, Vogel WJ (1989) Mobile satellite system fade statistics for shadowing and multipath from roadside trace at UHF and L-band. IEEE Trans Antennas Propag 37(4):489–498
7. McGraw GA, Braasch MS. GNSS multipath mitigation using gated and high resolution correlator concepts. Proc Inst Navig NTM 1999: 333–342
8. Ziqing W (1998) The mathematic model of relative positioning for GPS, vol 1998. Publication of Surveying and Mapping, Beijing, pp 33–62
9. Lachapelle G, Falkenberg B, Neufeldt D, Kielland P (1989) Marine DGPS using code and carrier in a multipath environment. In: Proceedings of the second international technical meeting of the satellite division of the ION, GPS-89, Colorado Springs, 26–29 Sept 1989

Part III
BeiDou/GNSS User Terminal Technology

Chapter 46
Effect of Frequency Domain Anti-Jamming Filter on Satellite Navigation Signal Tracking Performance

Tianqiao Zhang, Xiaoming Zhang and Mingquan Lu

Abstract Among the satellite navigation anti-jamming techniques, frequency domain anti-jamming (FDAJ) filter is a simple-realized method to suppress multi-tone continuous wave, sweep continuous wave and narrowband interference quickly and efficiently, without convergence problems, so it has been widely utilized to the GNSS receivers in practice. FDAJ filter will distort useful navigation signal while suppressing interference, when it is inserted into a receiver. The effect of the FDAJ filter on the observation quality of navigation signal is worth attention, especially now that more and more high-precision receivers use anti-jamming filter. In this paper, the FDAJ filter is modeled as a band rejection filter ideally firstly. Then the impact of FDAJ filter on pseudo-code tracking accuracy and the output signal-to-noise ratio (SNR) is derived, based on the mathematical models of the receiver tracking loop phase detector and loop filter. At the end, according to the mathematical simulation and analysis, it is showed that the FDAJ filter will not cause tracking error bias for pseudo-code phase, but a decline of tracking accuracy and output SNR.

Keywords Frequency domain anti-jamming · GNSS · Pseudo-code tracking accuracy · Delay lock loop

T. Zhang (✉) · X. Zhang
Beijing Satellite Navigation Center, Beijing 100094, China
e-mail: zhangtqee@gmail.com

M. Lu
Department Electronic Engineering, Tsinghua University,
Beijing 100084, China

J. Sun et al. (eds.), *China Satellite Navigation Conference (CSNC) 2013 Proceedings*, Lecture Notes in Electrical Engineering 243,
DOI: 10.1007/978-3-642-37398-5_46,

46.1 Introduction

For satellite navigation receivers, the bit error rate (BER) is not the most concerned performance indicator, which is different from the traditional communication receiver. The accurate navigation message can be obtained through a variety of assisted means in a satellite navigation receiver. And it's repeated at a certain period of time in the signal in space (SIS), so the navigation receiver is generally not very dependent on the navigation message bit error rate, but more concerned about the pseudo-code tracking error which affects the navigation signal ranging accuracy directly [1–3]. In this paper, it is analyzed deeply how the frequency domain anti-jamming filter effects on the satellite navigation signal tracking performance in receivers, as well as its impact on the relevant output signal-to-noise ratio is studied.

46.2 Effect of FDAJ Filter on Code Tracking Performance

The basic algorithm of a FDAJ filter is that the interference spectrum will be set to null in frequency domain and then transformed back into the time domain [4–5]. If the negative impact of overlap windowing and residual interference is ignored, any FDAJ filter can be equivalent to a cascade of some ideal band-stop filters as follows:

$$H_i(f) = \begin{cases} 0, & |f - f_i| \le B_i/2 \\ 1, & other \end{cases} \tag{46.1}$$

where f_i is the center frequency of the filtered narrow-band interference, and B_i is the bandwidth of the filtered narrow-band interference. Assuming the total number of the filtered narrow-band interference is N, then the final filter transfer function can be expressed as below, and the time domain impulse response function is denoted as h(t).

$$H(f) = \prod_{i=1}^{N} H_i(f) \tag{46.2}$$

The mixed signal before FDAJ filter is denoted as x(t) = s(t) + n(t) + j(t), where s(t) is the input pure navigation signal which also is direct sequence spread spectrum signal, n(t) is environmental thermal noise satisfying Gaussian distribution, j(t) is interference signal. So the useful signal after interference being filtered can be expressed as $s'(t) = s(t) \otimes h(t)$, the filtered noise is $n'(t) = n(t) \otimes h(t)$. Then the filtered mixed signal is $x'(t) = s'(t) + n'(t)$.

In the code tracking loop, the early/late I-branch coherent integration results can be presented as below, after the carrier is synchronized accurately.

$$I_E = R\left\{\frac{1}{T}\int_0^T s'(t-t_0)s^*(t-\hat{t}_0-\Delta/2)dt + \frac{1}{T}\int_0^T n'(t-\hat{t}_0)s^*(t-t_0-\Delta/2)dt\right\} \tag{46.3}$$

$$I_L = R\left\{\frac{1}{T}\int_0^T s'(t-t_0)s^*(t-\hat{t}_0+\Delta/2)dt + \frac{1}{T}\int_0^T n'(t-\hat{t}_0)s^*(t-t_0+\Delta/2)dt\right\} \tag{46.4}$$

where T is the coherent integration time, Δ is the early-late space, t_0 is the actual code phase, $\hat{t}_0$ is the local estimated code phase, and $\varepsilon = t_0 - \hat{t}_0$ is the code phase tracking error.

The early I-branch coherent integration result is derived as below without interference or environmental thermal noise.

$$\begin{aligned}
I_{E,s} &= R\left\{\frac{1}{T}\int_0^T s'(t-t_0)s^*(t-\hat{t}_0-\Delta/2)dt\right\} \\
&= R\left\{\frac{1}{T}\int_0^T \left(\int_{-\beta_r/2}^{\beta_r/2} S'(f)e^{i2\pi ft}df\right)s^*(t-\hat{t}_0-\Delta/2)dt\right\} \\
&= R\left\{\frac{1}{T}\int_{-\beta_r/2}^{\beta_r/2} H(f)S(f)\int_0^T s^*(t-\hat{t}_0-\Delta/2)e^{i2\pi ft}dtdf\right\} \\
&= R\left\{\frac{1}{T}\int_{-\beta_r/2}^{\beta_r/2} H(f)S(f)\int_0^T s^*(t-t_0+t_0-\hat{t}_0-\Delta/2)e^{i2\pi ft}dtdf\right\} \\
&= R\left\{\frac{1}{T}\int_{-\beta_r/2}^{\beta_r/2} H(f)S(f)\int_{\varepsilon-\Delta/2}^{T+\varepsilon-\Delta/2} s^*(u-t_0)e^{i2\pi f(u-\varepsilon+\Delta/2)}dudf\right\}
\end{aligned} \tag{46.5}$$

where $S(f)/S'(f)$ is the navigation signal before/after FDAJ filter, and β_r is the front bandwidth. According to the expression $\varepsilon - \Delta/2 \ll T$, therefore Eq. (46.5) can be approximated as follows.

$$
\begin{aligned}
I_{E,s} &\cong R\left\{\frac{1}{T}\int_{-\beta_r/2}^{\beta_r/2} H(f)S(f)\int_{0}^{T} s^*(u-t_0)e^{i2\pi f(u-\varepsilon+\Delta/2)}dudf\right\} \\
&= R\left\{\frac{1}{T}\int_{-\beta_r/2}^{\beta_r/2} H(f)S(f)S^*(f)e^{-i2\pi f(\varepsilon-\Delta/2)}df\right\} \\
&= R\left\{C_s\int_{-\beta_r/2}^{\beta_r/2} H(f)G_s(f)e^{-i2\pi f(\varepsilon-\Delta/2)}df\right\}
\end{aligned}
\tag{46.6}
$$

where C_s is the power of the input navigation signal, and $G_s(f)$ is the normalized power spectral density function. The late I-branch coherent integration result is obtained with the same as the above derivation.

$$
I_{L,s} \cong R\left\{C_s\int_{-\beta_r/2}^{\beta_r/2} H(f)G_s(f)e^{-i2\pi f(\varepsilon+\Delta/2)}df\right\} \tag{46.7}
$$

Based on Eqs. (46.6) and (46.7), the normalized discriminator characteristic curve can be obtained for $E-L$ coherent phase detector and E^2-L^2 non-coherent phase detector, assuming the received navigation signal is GPS C/A signal, and the code rate is 1.023 MHz, the receiver front bandwidth is 24 MHz, the pre-detection integration time is 1 ms, the early-late space is one code chip, and the stop-band width is 10 % signal bandwidth of the main lobe. Then two cases are analyzed below, when the narrow band interference center frequency is coincides with the useful signal center or deviated from 511.5 kHz (Figs. 46.1, 46.2).

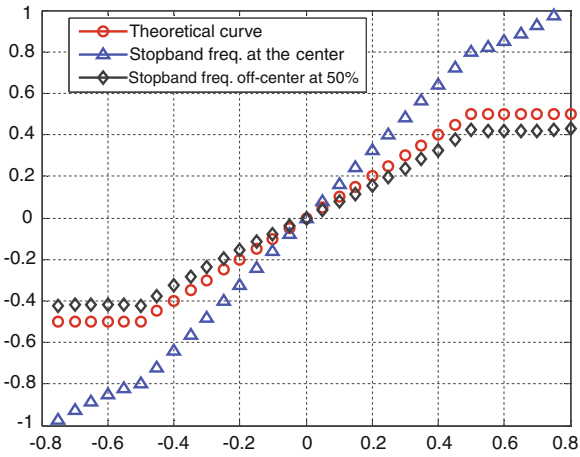

Fig. 46.1 Discriminator characteristic curves on E–L

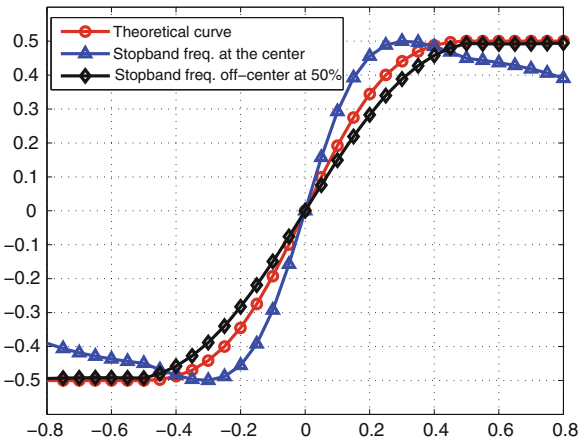

Fig. 46.2 Discriminator characteristic curves on $E^2 - L^2$

As shown in the figures above, the discriminator characteristic curves all are odd symmetry, so the discriminator result of the code tracking loop after FDAJ filtering is still unbiased, whether coherent phase discriminator or non-coherent phase discriminator. This indicates that the FDAJ will not give a biased error of code tracking, so it will not bring bias to the pseudo-range measurement or position result.

Then the code loop tracking error after frequency domain anti-jamming filter is derived as follows. Firstly, the discriminator result from coherent phase discriminator without interference or environmental thermal noise can be written as

$$e_s(\varepsilon) = I_{E,s} - I_{L,s} = R\left\{ C_s \int_{-\beta_r/2}^{\beta_r/2} H(f)G_s(f)\sin(\pi f\Delta)\sin(2\pi f\varepsilon)df \right\} \cong C_s K\varepsilon$$
$$\text{where } K = \int_{-\beta_r/2}^{\beta_r/2} 4\pi f H(f)G_s(f)\sin(\pi f\Delta)df \tag{46.8}$$

The discriminator result in environmental thermal noise without interference can be presented by the equation below.

$$e(t_0 - \hat{t}_0) = I_E - I_L$$
$$\cong C_s K(t_0 - \hat{t}_0) + R\left\{ \frac{1}{T}\int_0^T n'(t - \hat{t}_0)[s^*(t - t_0 - \Delta/2) - s^*(t - t_0 + \Delta/2)]dt \right\} \tag{46.9}$$

In the $E - L$ code tracking loop, the local estimated code phase before the smoothing loop filter can be written as

$$\hat{t}_0 = t_0 - \frac{e(t_0 - \hat{t}_0)}{C_s K} \tag{46.10}$$

Getting the conditional variance of $\hat{t}_0$

$$\mathrm{var}\{\hat{t}_0|t_0\} = \frac{\mathrm{var}\{e(t_0 - \hat{t}_0)|t_0\}}{C_s^2 K^2} \tag{46.11}$$

The molecule expression in the Eq. (46.11) is derived as follows, where $G_h(f)$ is the normalized power spectral density function of the FDAJ filter, the $G_n(f)$ is the normalized power spectral density function of the environmental thermal noise.

$$\begin{aligned}
&\mathrm{var}\{e(t_0 - \hat{t}_0)|t_0\} \\
&= \mathrm{var}\left\{\mathbb{R}\{\tfrac{1}{T}\int_0^T n'(t - \hat{t}_0)[s^*(t - t_0 - \Delta/2) - s^*(t - t_0 + \Delta/2)]dt\}|t_0\right\} \\
&= \tfrac{1}{2}\mathrm{var}\left\{\tfrac{1}{T}\int_0^T n'(t - \hat{t}_0)[s^*(t - t_0 - \Delta/2) - s^*(t - t_0 + \Delta/2)]dt|t_0\right\} \\
&= \tfrac{1}{2}E\left\{\left|\tfrac{1}{T}\int_0^T n'(t - \hat{t}_0)[s^*(t - t_0 - \Delta/2) - s^*(t - t_0 + \Delta/2)]dt\right|^2|t_0\right\} \\
&= \tfrac{1}{2}E\left\{\begin{array}{l}\dfrac{1}{T^2}\displaystyle\int_0^T\int_0^T n'(t - \hat{t}_0)n'^*(u - \hat{t}_0)[s^*(t - t_0 - \Delta/2) - s^*(t - t_0 + \Delta/2)] \\ \quad [s^*(t - t_0 - \Delta/2) - s^*(t - t_0 + \Delta/2)]dtdu|t_0\end{array}\right\} \\
&\cong \tfrac{2}{T}\int_{-\beta_r/2}^{\beta_r/2} C_s G_h(f)G_s(f)G_n(f)\sin^2(\pi f\Delta)df
\end{aligned} \tag{46.12}$$

Then the variance of code phase tracking error without the smoothing loop filter can be obtained.

$$\sigma_{c,u}^2 = \mathrm{var}\{\hat{t}_0|t_0\} = \frac{\displaystyle\int_{-\beta_r/2}^{\beta_r/2} G_h(f)G_s(f)\sin^2(\pi f\Delta)df}{2(2\pi)^2 T\frac{C_s}{N_0}\left(\displaystyle\int_{-\beta_r/2}^{\beta_r/2} fH(f)G_s(f)\sin(\pi f\Delta)df\right)^2} \tag{46.13}$$

B_L is marked as the bandwidth of the smoothing loop filter in the code tracking loop, and the effect factor on tracking error can be approximated as $2B_L T(1 - 0.5B_L T)$, so the variance of final tracking error from the coherent phase discriminator can be presented by the equation below.

$$\begin{aligned}\sigma_c^2 &\cong 2B_L T(1-0.5B_L T)\sigma_{c,u}^2 \\ &= \frac{B_L(1-0.5B_L T)\int_{-\beta_r/2}^{\beta_r/2} G_h(f)G_s(f)\sin^2(\pi f\Delta)df}{(2\pi)^2\frac{C_s}{N_0}\left(\int_{-\beta_r/2}^{\beta_r/2} fH(f)G_s(f)\sin(\pi f\Delta)df\right)^2}\end{aligned} \tag{46.14}$$

The non-coherent phase code loop tracking error variance is expressed as below from similar derivation method.

$$\begin{aligned}\sigma_n^2 \cong & \frac{B_L(1-0.5B_L T)\int_{-\beta_r/2}^{\beta_r/2} G_h(f)G_s(f)\sin^2(\pi f\Delta)df}{(2\pi)^2\frac{C_s}{N_0}\left(\int_{-\beta_r/2}^{\beta_r/2} fH(f)G_s(f)\sin(\pi f\Delta)df\right)^2} \\ & \cdot\left[1+\frac{\int_{-\beta_r/2}^{\beta_r/2} G_h(f)G_s(f)\cos^2(\pi f\Delta)df}{\frac{C_s}{N_0}\left(\int_{-\beta_r/2}^{\beta_r/2} H(f)G_s(f)\cos(\pi f\Delta)df\right)^2}\right]\end{aligned} \tag{46.15}$$

In the end, the effect of FDAJ filter on the code tracking error can be gained, when 10 % of spread spectrum signal main lobe bandwidth is filtered out. And the smoothing loop filter bandwidth is 1 Hz in the code tracking loop (Figs. 46.3, 46.4).

As the figures shown, the tracking error gets the maximum when the narrow band interference center frequency is between the main lobe center and the zero-to-zero point, as well as deviating from the main lobe center 511.5 kHz.

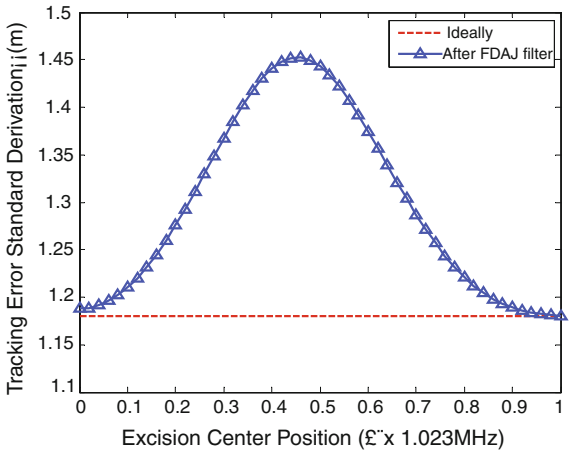

Fig. 46.3 CELL tracking error with 10 % signal bandwidth cut in different positions

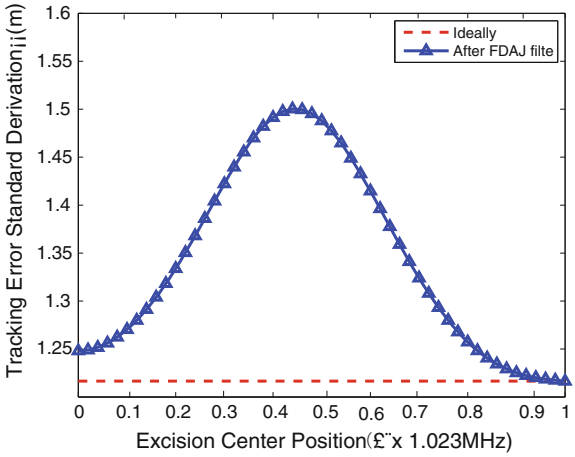

Fig. 46.4 NELL tracking error with 10 % signal bandwidth cut in different positions

46.3 Effect of FDAJ Filter on Output SNR

In the code tracking loop, the I-branch coherent integration results can be presented as below, when the carrier and pseudo-code all are synchronized accurately.

$$\begin{aligned} I_P &= R\left\{\frac{1}{T}\int_0^T s'(t)s^*(t)dt + \frac{1}{T}\int_0^T n'(t_0)s^*(t)dt\right\} \\ &= \frac{1}{2}\left\{\frac{1}{T}\int_0^T s'(t)s^*(t)dt + \frac{1}{T}\int_0^T s'^*(t)s(t)dt + \frac{1}{T}\int_0^T n'(t_0)s^*(t)dt + \frac{1}{T}\int_0^T n'^*(t_0)s(t)dt\right\} \end{aligned} \tag{46.16}$$

Then the expectation of coherent integration and the expectation of the square of coherent integration can be expressed as below.

$$E\{I_P\} = \frac{1}{2T}\left(\int_0^T s'(t)s^*(t)dt + \int_0^T s'^*(t)s(t)dt\right) = C_s \int_{-\beta_r/2}^{\beta_r/2} H(f)G_s(f)df \tag{46.17}$$

$$E\{I_P^2\} = \frac{C_s}{2T}\int_{-\beta_r/2}^{\beta_r/2} G_h(f)G_w(f)G_s(f)df + \left(C_s \int_{-\beta_r/2}^{\beta_r/2} H(f)G_s(f)df\right)^2 \tag{46.18}$$

where $G_w(f)$ is the mixed power spectrum of the input noise and interference, so the variance of the coherent integration result is expressed as below.

$$\mathrm{var}\{I_P\} = \frac{C_s}{2T}\int_{-\beta_r/2}^{\beta_r/2} G_h(f)G_w(f)G_s(f)df \tag{46.19}$$

The output signal-to-noise ratio after frequency domain filtering is derived as below.

$$\begin{aligned} SNR_{post} &= \frac{(E\{I_P\})^2}{\mathrm{var}\{I_P\}} = \frac{2TC_s\left(\int_{-\beta_r/2}^{\beta_r/2} H(f)G_s(f)df\right)^2}{\int_{-\beta_r/2}^{\beta_r/2} G_h(f)G_w(f)G_s(f)df} \\ &= \frac{2T\frac{C_s}{N_0}\left(\int_{-\beta_r/2}^{\beta_r/2} H(f)G_s(f)df\right)^2}{\int_{-\beta_r/2}^{\beta_r/2} G_h(f)G_s(f)df + \frac{C_j}{N_0}\int_{-\beta_r/2}^{\beta_r/2} G_h(f)G_j(f)G_s(f)df} \end{aligned} \tag{46.20}$$

where C_j is the power of the interference before FDAJ filter, and $G_j(f)$ is the normalized interference power spectral density function. If the influence of the residual interference is ignored, the above equation can be simplified as below.

$$SNR_{post} \cong \frac{2T\frac{C_s}{N_0}\left(\int_{-\beta_r/2}^{\beta_r/2} H(f)G_s(f)df\right)^2}{\int_{-\beta_r/2}^{\beta_r/2} G_h(f)G_s(f)df} \tag{46.21}$$

Then the effect of the FDAJ filter on the output SNR is gained.

$$Loss_{AJ\_filter} \cong \frac{\left(\int_{-\beta_r/2}^{\beta_r/2} H(f)G_s(f)df\right)^2}{\int_{-\beta_r/2}^{\beta_r/2} G_h(f)G_s(f)df} \tag{46.22}$$

Figure 46.5 shows the effect of the FDAJ filter on the output SNR when different positions 10 % main lobe bandwidth is filtered. The SNR loss gets worst when the narrow band interference center frequency is at the main lobe center, as −1 dB approximately.

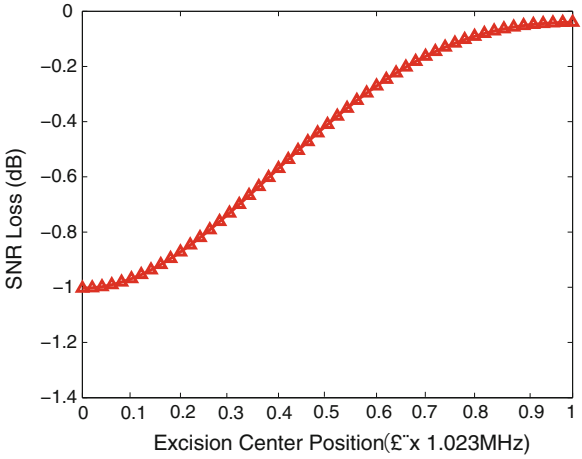

Fig. 46.5 Output SNR with 10 % signal bandwidth cut in different positions

46.4 Conclusion

The effect of FDAJ filter on the navigation performance is studied in this paper, while the frequency domain anti-jamming receiver is considered as a whole. The pseudo-code tracking error and output signal-to-noise ratio are utilized to evaluate the effect of FDAJ filter. According to theoretical derivation and mathematical simulation, it is elaborated that the FDAJ will not cause pseudo-code phase tracking bias, but will bring a decline to tracking accuracy and output signal-to-noise ratio. In the end, the effect results of FDAJ filter is gained in different stop-band cases.

References

1. Parkinson BW, Spilker JJ (1996) Global positioning system: theory and applications. American Institue of Aeronautics and Astronautics, Washington
2. Betz JW, Kolodziejski KR (2000) Extended theory of early-late code tracking for a band-limited GPS receivers. J Inst Navig 47(3):211–226
3. Chang H (1982) Presampling filtering, sampling and quantization effects on the digital match filter performance. In: Proceedings of international telemetering conference, San Diego, pp 889–915
4. Borio D (2008) A statistical theory for GNSS signal acquisition. Polytecnico di Torino NavSAS Group, Torino
5. Feng Jining W, Siliang WJ (2009) Narrow-band interference excision in spread spectrum systems using new n-sigma algorithm based on fuzzy threshold. J Sys Eng Electron 20(1):20–26

Chapter 47
An Improved Algorithm for Single Point Positioning of COMPASS

Guorui Xiao, Lifen Sui, Bing Wang, Yu Gan, Qinghua Zhang, Yu Duan and Guobin Qi

Abstract The BeiDou (COMPASS) Navigation Satellite System has been able to provide service for areas in China and its surrounding areas. However, due to the limited number of satellites and the low accuracy, its application is greatly limited. The global nonlinear least squares algorithm (Bancroft algorithm) is applied in COMPASS single point position in this paper. The Bancroft algorithm based on the Lorentz inner product is mainly in four-dimensional space. In consideration of the constellation of COMPASS is composed of Geostationary Earth Orbit (GEO) satellites and Non-Geostationary Earth Orbit (Non-GEO) satellites, A new method to get the COMPASS observation weights is introduced base on the Lorentz inner product. The observation data is computed to demonstrate the ideas involved. The results indicates that the method can improve the accuracy of COMPASS single point positioning.

Keywords Bancroft · Single point positioning · COMPASS · Weighting algorithm · Nonlinear least squares

47.1 Introduction

In global positioning system applications several error sources affect the observations. Tropospheric delay that occurs during the propagation of the wave through the troposphere and multipath taking place as a result of signal reflection are the most important error sources [1]. One way to overcome this problem is to introduce of new

G. Xiao (✉) · L. Sui · B. Wang · Y. Gan · Q. Zhang · Y. Duan · G. Qi
Geospatial Information Institute, Information Engineer University,
Zhengzhou 450052, China
e-mail: xgr@whu.edu.cn

J. Sun et al. (eds.), *China Satellite Navigation Conference (CSNC) 2013 Proceedings*, Lecture Notes in Electrical Engineering 243,
DOI: 10.1007/978-3-642-37398-5_47,

stochastic models. Ward [2] gives the $Sigma - \varepsilon$ model as a function of the measured C/N_0 values. In addition to this stochastic model, another model based on elevation cut-off angles has been applied by Rothacher [3]. Both models mentioned above are applied to GPS data at zero difference level, where the observations are undifferenced. The second model was implemented into the 4.2 version of Bernese GPS processing software. The constellation of GPS is composed of 24 MEO satellites located 20,231 km height in space while the constellation of COMPASS is composed of Geostationary Earth Orbit (GEO) satellites and Non-Geostationary Earth Orbit (Non-GEO) satellites [4]. The weighting algorithms used in GPS is not applicable in COMPASS because the satellites height are different.

For GPS single point positioning, the local area optimal solution is solved by the iteration of linearized least square [5]. But it may get different results and even can make the result incorrect because of the different approximate coordinates in the linearized process or the different receivers' positions (such as the receiver is not on the ground of the earth). Thus the American scholar Steven Bancroft [6] puts forward a global nonlinear least squares algorithm called the "closed-form" solution for GPS pseudorange equations in 1985. This algorithm does not need linearization, and it is one of nonlinear solution methods having the algebraic and analytic noniterative characteristics [7–9].

Global nonlinear least squares algorithm (Bancroft algorithm) is applied to COMPASS single point positioning in this paper and a new weighting algorithm is introduced base on the Lorentz inner product in Bancroft algorithm. The observation data is computed to demonstrate the ideas involved. The results indicates that the method can improve the accuracy of COMPASS single point positioning.

47.2 Improvement of Bancroft Algorithm

47.2.1 Bancroft Algorithm

The Bancroft algorithm based on the Lorentz inner product is mainly in R^4 dimensional space. The Lorentz inner product is defined as: in the R^4 dimensional space, we have

$$\underset{4\times1}{g} = \left[\underset{3\times1}{u^T}, \alpha\right]^T, \quad \underset{4\times1}{h} = \left[\underset{3\times1}{v^T}, \beta\right]^T \tag{47.1}$$

$$< g, h > \; = g^T M h = u^T v - \alpha\beta \tag{47.2}$$

The pseudorange observation between the *j*th satellite and the user station in GPS pseudorange positioning has such a nonlinear equation written according to the Lorentz inner product

$$\tilde{\rho}^j - b = \sqrt{(x^j - x)^2 + (y^j - y)^2 + (z^j - z)^2} \tag{47.3}$$

Let the position vectors of the GPS satellite be

$$S^j = \begin{bmatrix} x^j & y^j & z^j \end{bmatrix}^T,\ T^j = \begin{bmatrix} (S^j)^T & \tilde{\rho}^j \end{bmatrix}^T \tag{47.4}$$

and the user position vectors are

$$\mu = \begin{bmatrix} x & y & z \end{bmatrix}^T,\ X = \begin{bmatrix} \mu^T & b \end{bmatrix}^T \tag{47.5}$$

Then Eq. (47.3) can be expressed according to the Lorentz inner product

$$\frac{1}{2} < T^j,\ T^j > \ - < T^j, X > \ + \frac{1}{2} < X, X > \ = 0 \tag{47.6}$$

For every pseudorange observation $\tilde{\rho}^j$ and the corresponding satellite, we can list one equation that is similar to Eq. (47.6) without exception. When $d (d \geq 4)$, Eq. (47.6) through d observed satellites and pseudo-range can be expressed as

$$B^T P\theta - B^T PBMX + B^T P\lambda\tau = 0 \tag{47.7}$$

where

$$\underset{d\times 1}{\tau} = \begin{bmatrix} 1 & 1 & \cdots & 1 \end{bmatrix}^T,\ \lambda = \frac{1}{2} < X, X >$$

$$\theta = \begin{bmatrix} \theta^1 & \theta^2 & \cdots & \theta^d \end{bmatrix}, \theta^j = \frac{1}{2} < T^j,\ T^j >$$

$$B = \begin{bmatrix} x^1 & y^1 & z^1 & \tilde{\rho}^1 \\ x^2 & y^2 & z^2 & \tilde{\rho}^2 \\ \vdots & \vdots & \vdots & \vdots \\ x^d & y^d & z^d & \tilde{\rho}^d \end{bmatrix}$$

Then unknown parameters can be solved by Eq. (47.7)

$$\hat{X} = \begin{bmatrix} \hat{\mu} \\ \hat{b} \end{bmatrix} = MF(\lambda\tau + \theta) \tag{47.8}$$

where $F = (B^T PB)^{-1} B^T P$ and λ is still the unknown parameter, so it must be firstly solved.

From Bancroft algorithm, we have

$$< F\tau, F\tau > \lambda^2 + 2(< F\tau, F\theta > \ - 1)\lambda + < F\theta, F\theta > \ = 0 \tag{47.9}$$

We can get two solutions λ_1 and λ_2 by solving Eq. (47.9). Then substitute λ_1, λ_2 into Eq. (47.8), and get a group of solutions corresponding with pseudo-range that are consistent with the original pseudorange measurements.

47.2.2 Weighting Algorithm

From Ref. [2], we can see that Eq. (47.9) is a form of global nonlinear LS solution with the Lorentz norm

$$\sum_{i=1}^{n} <T^j - X, T^j - X>^2 = \min \tag{47.10}$$

Then

$$V = <T^j - X,\ T^j - X> = <T^j,\ T^j> - 2<T^j,\ X> + <X,\ X> \tag{47.11}$$

We can substitute B, θ, τ into Eq. (47.11)

$$V = \theta + \lambda\tau - BM\hat{X} \tag{47.12}$$

The weighting algorithm is based on prior information of pseudorange in tradition method which is rigorous in linear LS solution [10]. But when we write GPS pseudorange equation with Lorentz inner product, we need to change weighting algorithm based on Lorentz inner product.

According to Eq. (47.12), we can treat θ as virtual observation

$$\theta^j = \frac{1}{2} <T^j,\ T^j> = \frac{1}{2}\left[(S^j)^T S^j - \tilde{\rho}^j\tilde{\rho}^j\right] \tag{47.13}$$

In consideration of error propagation law, we can get the weight matrix of Lorentz inner product

$$P_L^j = \frac{\delta_0^2}{D(\tilde{\rho}^j)}\frac{1}{\tilde{\rho}^j\tilde{\rho}^j} \tag{47.14}$$

where δ_0^2 is mean square error, $D(\tilde{\rho}^j)$ is variance.

From the model based on elevation cut-off angles, the weight of j satellite can be expressed as

$$p_E^j = \frac{\delta_0^2}{D(\tilde{\rho}^j)} = \sin^2(e) \tag{47.15}$$

Then the weight matrix of Lorentz inner product

$$P_L^j = \frac{\sin^2(e^j)}{\tilde{\rho}^j\tilde{\rho}^j} \tag{47.16}$$

Compare Eq. (47.16) with Eq. (47.15), we can see that the new weighting algorithm takes the distance into consideration which is more accurate when satellites are at different heights.

47.3 Numerical Examples

We process the two-frequency COMPASS static observe data of four areas (urumqi, kashi, kunming, changchun) which was observed from October 7 to October 21 in 2012 year, interval is 1 s. Station coordinates are already known.

In data processing the following four schemes are adopted:

Scheme 1: least squares solution using ionosphere-free linear combination of two-frequency pseudorange, each observation weighted based on its satellite elevation angle;

Scheme 2: least squares solution using the original pseudorange observation, each observation weighted based on its satellite elevation angle;

Scheme 3: Bancroft solution using the original pseudorange observation, each observation weighted based on its satellite elevation angle;

Scheme 4: Bancroft solution using the original pseudorange observation, each observation weighted based on the method in this paper.

In order to see the results clearly, we choose data of urumqi station on October 7, 2012 to analysis. The result of other station and time are similar.

Based on Fig. 47.1 and Table 47.1, we can draw a conclusion that:

1. Compare scheme 1 with other schemes, we can see that the ionosphere-free linear combination can not improve SPP accuracy in COMPASS.
2. Bancroft algorithm improve the accuracy slightly than least square algorithm when both of their observations are weighted based on satellite elevation angle, mainly because Bancroft solution is global nonlinear least squares solution and the iterative least square are susceptible to the influence of its approximation.
3. Compared with other schemes, scheme 4 get the best result which shows that new weighting algorithm based on Lorentz inner product is more accurate and

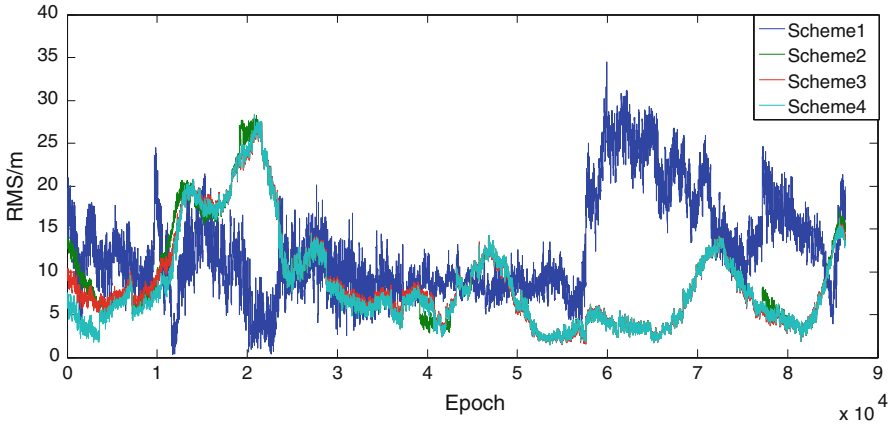

Fig. 47.1 RMS of four schemes

Table 47.1 N, E, U bias of four schemes/m

方案	N	E	U	RMS
Scheme 1	4.65613	4.81255	11.25848	13.09937
Scheme 2	2.10627	1.46580	10.18285	10.50121
Scheme 3	2.15792	1.49941	10.08553	10.42223
Scheme 4	2.03678	1.44668	9.87218	10.18339

Table 47.2 Satellites in epoch 1

PRN	Type	Altitude/m	Elevation angle/°	Weight ratio
1	GEO	35,770,412	44.93437	0.09527
3	GEO	35,779,901	42.12005	0.38142
5	GEO	35,793,493	30.47598	0.35802
7	IGSO	35,706,817	62.88308	0.25868
8	IGSO	35,853,064	58.11976	0.50603
10	IGSO	35,720,130	28.91402	0.48030
11	MEO	21,598,858	44.95042	0.61723
12	MEO	21,589,266	11.85839	1.00000

Table 47.3 N, E, U bias of four schemes in first 10,000 epochs

Scheme	N	E	U	RMS
Scheme 1	3.40756	2.69697	12.80179	13.51927
Scheme 2	1.40868	1.18814	7.46394	7.68807
Scheme 3	1.65410	1.22378	7.75057	8.01904
Scheme 4	0.78356	0.82774	6.15850	6.26309

rigorous than the weighting algorithm based on satellite elevation angle in Bancroft algorithm.

Through the analysis of result, we can be see Bancroft improve the accuracy of COMPASS single point positioning, but the result was not obvious. In order to further analysis, we selected first 10,000 epochs data to be analysis again. In this period, eight satellites have been observed and the satellite information of epoch 1 is listed in Table 47.2. The weight of every satellite observation is compared to the weight of 12th satellite observation.

Based on Tables 47.2 and 47.3, we can draw a conclusion that:

1. GEO satellites are about same altitude with IGSO satellites and higher than MEO satellites.
2. When GEO, IGSO and MEO satellites are observed at the same time, improved Bancroft algorithm improves the accuracy obviously. This is mainly because that MEO satellites are lower than other satellites and the new weighting algorithm based on Lorentz inner product takes the distance into consideration.
3. As MEO satellite increases, the constellation will be more complex, improved Bancroft will get higher accuracy.

47.4 Conclusion

Global nonlinear least squares algorithm (Bancroft algorithm) is applied to the COMPASS single point positioning in this paper. In consideration of the different altitude of satellites, a new weighting algorithm is introduced base on the Lorentz inner product. A lot of observation data is computed to demonstrate the ideas involved. The results indicates that the method can improve the accuracy of COMPASS single point positioning.

Along with development of COMPASS and MEO satellite increases, the new algorithm will be more and more useful.

References

1. Tevfik M (2004) The stochastic modeling of GPS observations. Tuikish J Eng Env Sci 28:223–231
2. Ward P (1996) GPS satellite signal characteristics. In: Understanding GPS principles and applications. Artech House Publishers, pp 83–117
3. Rothaceher M (1997) Processing strategies for regional GPS networks. In: Proceedings of the IAU General Assembly
4. China Satellite Navigation Office (2011) BeiDou navigation satellite system signal in space interface control document
5. Xu G (2007) GPS theory, algorithms and applications, 2nd edn. Springer, Berlin, pp 39–40
6. Bancroft S (1985) An algebraic solution of the GPS equation. IEEE Trans Aerosp Electron Syst AES-21:56–59
7. Zhang Q (2002) Research on nonlinear least square theory and its applications in GPS positioning. Wuhan University, pp 138–144
8. Zhang Q et al (2005) Nonlinear filter method of GPS dynamic positioning based on Bancroft algorithm. Transactions of Nanjing University of Aeronautics & Astronautics, June 2005, pp 170–176
9. Yang Y et al (2005) Analyses and comparisons of some strategies for nonlinear Kalman filter in GPS navigation. Eng Surveying Mapp 14(3):4–7
10. Rengui R et al (2008) Improvement of Bancroft algorithm. J Geodesy Geodyn 28(5):87–90

Chapter 48
The Study on Pseudorange Error Caused by Sampling Process for GNSS Receiver

Chao Yuan, Hong Yuan, Ying Xu, Xiaokun Zhang and Liang Li

Abstract This paper explore pseudorange error caused by sampling process in GNSS Receiver, and analyze the quantitative relationship between the pseudorange error and the sampling rate, and a performance evaluation criterion and calculation algorithm of the pseudorange error was proposed. The simulation results reveals that the pseudorange error is larger when the sampling rate is an integer multiple of the code rate or some special values, and the detailed analysis of the features was also given. The proposed algorithm can be applied for GNSS digital receiver designing to select a suboptimal sampling rate, and thus it can be able to achieve less pseudorange error caused by sampling process when the GNSS digital receiver was designed with lower cost.

Keywords GNSS · Pseudorange error · Non-commensurate sampling · Sampling rate · Receiver design

48.1 Introduction

As we all know that the technology, using digital format to processing baseband signal, is adopted on GNSS receiver so far, which takes integral-accumulation operation, code tracking, with the sampling sequence signal. As a result of this, it would make code phase discrimination error caused by sampling process [1, 2], which is called time discrimination error in this paper. What's more, the pseudorange measuring precision is determined by the accuracy of code tracking, which makes the time discrimination error transform to pseudorange error at last.

C. Yuan (✉) · H. Yuan · Y. Xu · X. Zhang · L. Li
Academy of Opto-electronics, Chinese Academy of Sciences, Beijing 100094, China
e-mail: yuanchao_yx@aoe.ac.cn

J. Sun et al. (eds.), *China Satellite Navigation Conference (CSNC) 2013 Proceedings*, Lecture Notes in Electrical Engineering 243,
DOI: 10.1007/978-3-642-37398-5_48,

Quirk et al. pointed out in 2002 that the time discrimination performance of code tracking loop was limited to the time of sampling interval when sampling rate is integer multiple of code rate [3] which is used in commensurate sampling technology to select sampling rate. However, in this method, the sampling rate should be 100 multiple of code rate to realize time discrimination performance for 1 % code width, which is hardly achieved in project for so high sampling rate.

Corresponding to commensurate sampling technology, the non-commensurate sampling (NCS) technology is the method whose sampling rate is not integer multiple of code rate which could achieve better time discrimination performance with lower sampling rate [3, 4]. Almost all of the GNSS receivers adopt NCS technology at present [5, 6]. Although there is only one public publish paper [7] which studies the quantitative relation between time discrimination performance and sampling rate, whose defect is that he has not took code tracking loop into consideration. Moreover, the name "time discrimination performance" called in the other paper is just a same physical quantity with the name "time discrimination error" in this paper.

The study, taking the quantitative relation between time discrimination error and sampling rate, which is different from paper [7], starts with the side of code tracking loop. Moreover, the paper explains the quantitative relation between pseudorange error and sampling rate.

48.2 Analysis of Pseudorange Error Caused by Sampling Process

This section analyses the limitation of commensurate sampling technology at first; and then, it would declare the better time discrimination performance of NCS technology; finally, the paper would bring forth the performance estimating rule for the pseudorange error caused by sampling process.

48.2.1 Commensurate Sampling Technology and NCS Technology

Figure 48.1 shows the commensurate sampling technology (x indicates the sampling point). Impose the integral time is $T_P = k_P N_C T_C$, in which k_P is a positive integer, T_C is one code width, N_C is number of code period; then impose the T_S is sampling interval, and τ_C is the phase difference between the local code and the receiving code. Figure 48.1 indicates that the value of the receiving code is keep same with all the sampling points on the local code. Therefore, it's hardly to distinguish the changing of the phase difference in the range of $[0, T_S)$. Thus it can be seen that the time discrimination performance for commensurate sampling technology is confined by sampling interval T_S.

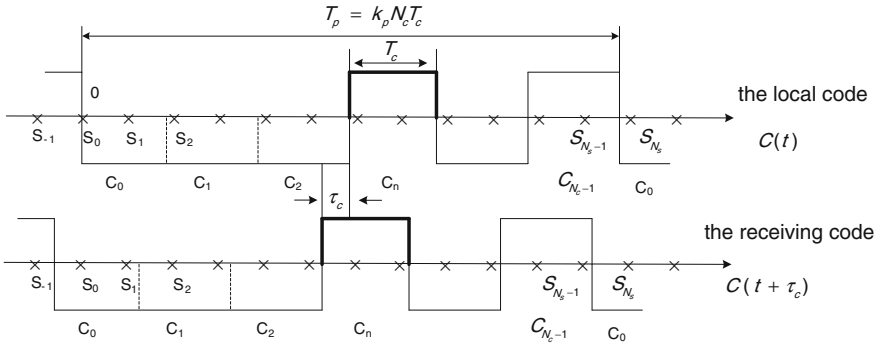

Fig. 48.1 Illustration of Commensurate sampling technology

Compass navigation satellite system is composed by GEO satellite, IGSO satellite, MEO satellite. The Doppler effect of MEO satellite is serious than the Doppler effect of IGSO satellite, and the Doppler effect of GEO satellite is least. When using commensurate sampling technology, the doppler frequency generated by the doppler effect can improve time discrimination performance, and the larger the Doppler frequency, the better the effect of improving, therefore, when Processing GEO satellite signal by use of commensurate sampling technology, time discrimination performance is worst.

Figure 48.2 shows the NCS technology in which the ratio between code width T_C and sampling interval T_S is not a integer, and the distribution character of sampling point in every code is not all the same. On the other side, there are many sampling points that their value are changing on the receiving code when τ_C is changing in the range of $[0, T_S)$, which makes some relevant performance change. Hence one can see that it is possible to distinguish the phase difference which is smaller than T_S with the help of some relative curve, which is to say, the NCS technology has the potential of distinguishing the phase difference accurately.

48.2.2 Evaluation Criterion for Pseudorange Error Caused by Sampling Process

As shown in Fig. 48.2, we impose that it does the integral accumulating operation at the beginning of time which the local code begins to recurrent, then sign the first n sampling point on the right of origin as S_n, mark the value of first n code as C_n, which n is counted from 0.

Impose the number of sampling points in sampling discrete sequence which are used to take the integral accumulating operation within the integral time is:

$$N_s = ceil[(T_P - \tau_s)/T_s] \tag{48.1}$$

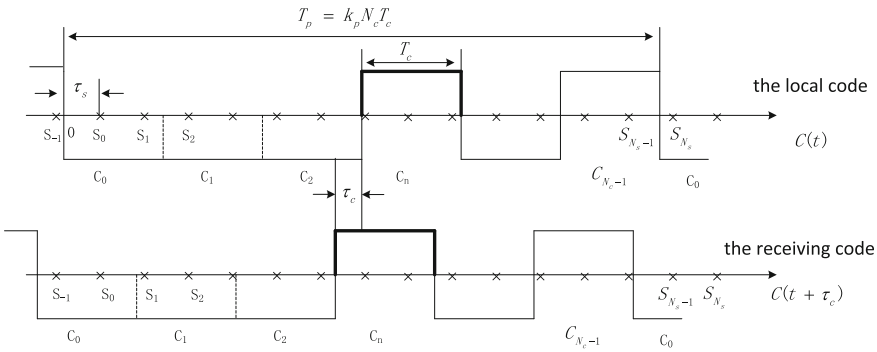

Fig. 48.2 Illustration of non-commensurate sampling technology

The operator $ceil(\bullet)$ in the equation above indicates upward rounding, τ_s is the interval between the first sampling point and the edge of the first code.

We take the receiving code to accumulate the sequence signal which is processed by sampling on the local code, and then, the operation result of integral accumulation could be computed as following:

$$R_{sample}(f_s, t_s, t_c, T_P) = \sum_{n=0}^{N_s} C(t_s + nT_s)C(t_s + t_c + nT_s) \tag{48.2}$$

In which f_s is sampling rate.

The code tracking loop of GNSS receiver is usually using normalizing E-L DLL, so does the research in this paper, moreover, we impose the correlative interval is 1 chip, and take the local early code and the local late code to make integral accumulate operation with the receiving code respectively, thus the integral accumulate value could be described as following [8]:

$$E_{sample}(f_s, \tau_s, \tau_c, T_P) = \sum_{n=0}^{N_s} C(\tau_s - 0.5T_c + nT_s)C(\tau_s + \tau_c + nT_s) \tag{48.3}$$

$$L_{sample}(f_s, \tau_s, \tau_c, T_P) = \sum_{n=0}^{N_s} C(\tau_s + 0.5T_c + nT_s)C(\tau_s + \tau_c + nT_s) \tag{48.4}$$

Then, the estimated value of code phase difference [8], which is produced by code demodulation with the integral accumulation value $E_{sample}(f_s, \tau_s, \tau_c, T_P)$ and $L_{sample}(f_s, \tau_s, \tau_c, T_P)$, is:

$$\hat{\tau}_c(f_s, \tau_s, \tau_c, T_P) = \frac{1}{2}\frac{E_{sample}(f_s, \tau_s, \tau_c, T_P) - L_{sample}(f_s, \tau_s, \tau_c, T_P)}{E_{sample}(f_s, \tau_s, \tau_c, T_P) + L_{sample}(f_s, \tau_s, \tau_c, T_P)} \tag{48.5}$$

$$\varepsilon(f_s, \tau_s, \tau_c, T_P) = \hat{\tau}_c(f_s, \tau_s, \tau_c, T_P) - \tau_c \tag{48.6}$$

In this paper, $\varepsilon(f_s, \tau_s, \tau_c, T_P)$ is defined as time discrimination error, which is also pseudorange error caused by sampling process.

As the analysis above, we could study the quantitative relation between time discrimination error and sampling rate. First of all, it must remove the affection of

τ_s, τ_c and T_P. If we fix the value of T_P, and enumerate N_{τ_s} values of τ_s which is described as following:

$$\tau_s(i) = (i/N_{\tau_s}) \times T_s \quad i = 0, 1, 2, \ldots, N_{\tau_s} - 1 \tag{48.7}$$

Taking the same method for τ_c, enumerating N_{τ_c} values which is described as following:

$$\tau_c(i) = (i/N_{\tau_c}) \times (T_c/100) \quad i = 0, 1, 2, \ldots, N_{\tau_c} - 1 \tag{48.8}$$

In which $T_c/100$ is because the accuracy of code tracking is better than 1 % chip generally.

If we define the criterion for assessing the relation between time discrimination error $\varepsilon(f_s)$ and sampling rate f_s as:

$$\varepsilon(f_s) = RMS(\varepsilon(f_s, \tau_s, \tau_c, T_P)) \tag{48.9}$$

In which $RMS(\bullet)$ is Root Mean Square (RMS) operation.

Then the pseudorange error caused by sampling process is defined as:

$$\rho_\varepsilon(f_s) = \varepsilon(f_s) \times C \tag{48.10}$$

In which C is speed of light.

48.3 Pseudorange Error Evaluation on GPS C/A Code

As we have analyzed the evaluation criterion for the pseudorange error caused by sampling process. Now we take the actual GNSS PRN code signal for example to study the relation between sampling rate and pseudorange error with computer simulation. We note that there are 3 important factors which could effect pseudorange error in GNSS receiver: sampling rate, code rate and code sequence, which are all infinitive. For example, there are different PRN code sequence in different navigating satellites; and the PRN code rate with different navigation frequencies are also different, meanwhile, the PRN code rate of receiving signal could deviate from the nominal value as a result of Doppler Effect; moreover, the sampling rate could be chosen at random by the designer. Therefore, it must take the above every factors into overall consideration while studying the sampling performance in GNSS receiver.

In this research, we take the 1.023 Mcps C/A code to study the relation between sampling rate and pseudorange error with the above evaluation criterion. We set the N_{τ_s} and N_{τ_c} as 100 and 200 respectively; what's more, the sample rate is a group of data. In order to compare the simulation situation with different PRN code sequence, the paper make 3 different kinds of PRN code sequence with the different PRN which is 1, 10 and 25 respectively.

What's shown in Fig. 48.3 is the pseudorange error while the sampling rate is changing from 5 to 7.4 MHz whose sampling interval is 1,000 Hz, that is to say,

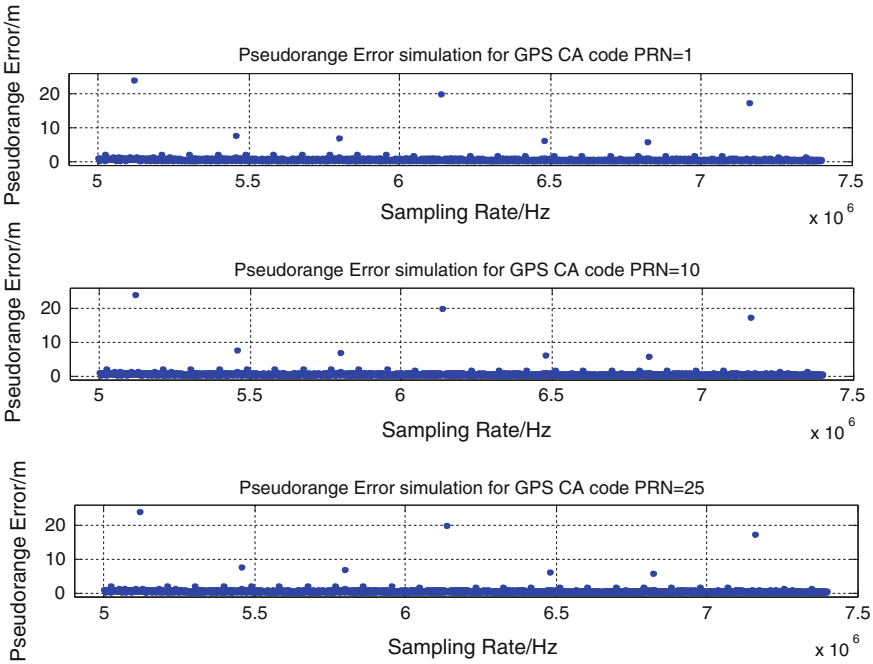

Fig. 48.3 Pseudorange error with sampling rate between 5 and 7.4 MHz

there are 2,400 values of sampling rate between 5 and 7.4 MHz. The simulation shows that the pseudorange error at some special sampling rates are more larger than any other sampling rates' which are recorded in Table 48.1, which we will probe into this problem later. On the other hand, most of the pseudorange errors are keeping in the range of 0.4–0.9 m. Table 48.1 shows that some sampling rate are integer multiple of code rate and the other are not, which is different from the paper [7] whose conclusion is that the pseudorange error would be more larger only when the sampling rate is integer multiple of code rate, but the other situation would be very small.

What's shown in Fig. 48.4 is the changing trend of pseudorange error while sampling rate is changing from 6.135 to 6.141 MHz whose sampling interval is 25 Hz, that is to say, there are 240 sampling values between 6.135 and 6.141 MHz. The simulation indicates that the pseudorange error at the sampling rate of 6.138 MHz is larger, however, the pseudorange error would become less while the sampling rate is deviating from 6.138 MHz, moreover, the pseudorange error would be smooth and steady when the distance from 6.138 MHz is more than 1,000 Hz whose pseudorange error keeps between 0.5 and 2 m.

Table 48.1 Pseudorange error with special sampling rate

Pseudorange error (m)		Sampling rate (MHz)						
		5.115	5.456	5.797	6.138	6.479	6.82	7.161
PRN	1	24.032	7.5133	7.0816	20.037	6.3334	5.9895	17.176
	10	24.035	7.5138	7.0813	20.036	6.3338	5.9894	17.177
	25	24.036	7.5137	7.0818	20.032	6.3334	5.9899	17.173

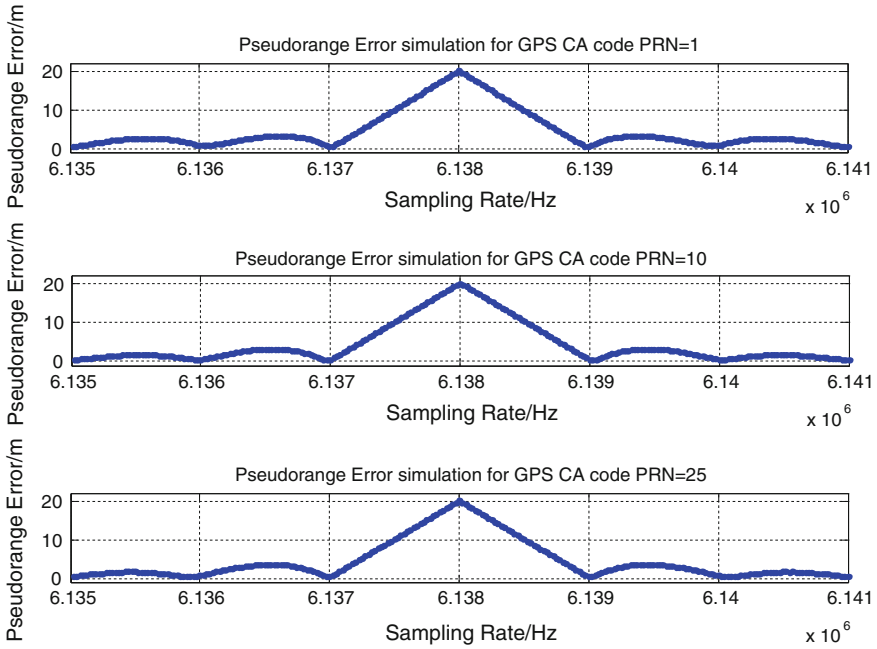

Fig. 48.4 Pseudorange error when sampling rate is nearby 6.138 MHz

What's shown in Fig. 48.5 is the pseudorange error when the sampling rate is nearby 5.797 MHz, whose sampling rate is changing from 5.794 to 5.8 MHz, sampling interval is 25 Hz, that is to say, there are also 240 sampling values while the sampling rate is changing from 5.794 to 5.8 MHz. From this simulating result, we could see that the pseudorange error is the most when the sampling rate is 5.797 MHz, moreover, the pseudorange error would become small along with the sampling rate deviating from 5.797 MHz, and the pseudorange error would be smooth and steady after the distance from 5.797 MHz is more than 300 Hz whose pseudorange error keeps between 0.5 and 1.5 m.

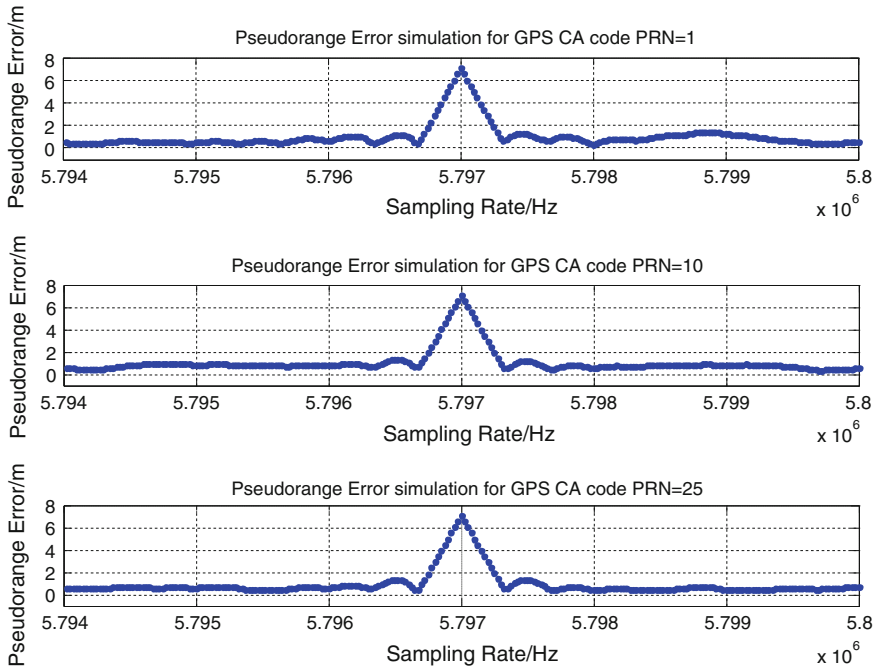

Fig. 48.5 Pseudorange error when sampling rate is nearby 5.797 MHz

48.4 Analysis for Some of Larger Pseudorange Error

As we discovered in the simulation above that the pseudorange error would become larger than any other sampling rates' when the sampling rate is integer multiple of code rate, or some particular sampling rate. And now, we may probe into this problem.

Impose the sampling rate is f_s, and code rate is r_s, thus the ratio of sampling rate and code rate is $\mathrm{R}_s = \frac{f_s}{r_s} = \frac{k_N}{k_M}$, in which k_N and k_M are mutually prime number, so $f_s = \frac{k_N * r_s}{k_M}$, then extracting the signal with the factor of k_M to the sampling sequence which is sampled with the rate of $k_N * r_s$ for code signal is equivalent to that taking f_s to sample for code signal. Thus the best time discrimination ability with the sampling rate of $k_N * r_s$ is $\frac{T_c}{k_N}$, in which T_c is width of code width, so we can know that the best time discrimination ability with the sampling rate of f_s would hardly better than sampling with the sampling rate of $\frac{T_c}{k_N}$. However, this is a special situation that the sampling rate is integer multiple of code rate since $k_M = 1$ at this time, which is the conclusion that integer multiple of sampling rate and some other particular non-integer multiple sampling rate would make more larger pseudorange error.

As seen in Table 48.1 that the large pseudorange errors whose sampling rate is not integer multiple of code rate are 5.456, 5.797, 6.479, 6.820 MHz, then according to R_s, their values are 16/3, 17/3, 19/3 and 20/3, and their corresponding pseudorange error shown in Table 48.1 become smaller and smaller in proper orders, which is completely in conformity with our conclusion.

As we have said that what's shown in Fig. 48.5 is the pseudorange error when the sampling rate is nearby 5.797 MHz. If we analyze this situation with the above conclusion, thus, the result of R_s is 17/3 when sampling rate f_s is 5.797 MHz, that is to say, the best time discrimination ability at this sampling rate is $\frac{T_c}{17}$, to which converted pseudorange error is about 17.5 m. This method is taking the maximum to calculate pseudorange error, but the method calculating pseudorange bought forward in this paper is using RMS operation, so the pseudorange error at the sampling rate of 5.797 MHz is smaller than 17.5 m.

We would discuss the relation of sampling rate selection and Nyquist theorem at next time, since the sampling rate selection of GNSS receiver must be satisfied with Nyquist theorem, and the sampling rate must not be the integer multiple of code rate at the same time, and Why? On the other hand, as we know that the signal processed with large sampling rate would contain more abundant frequency component than the signal processed with small sampling rate while taking the analog signal to sampling, but why the pseudorange error produced by large integer multiple sampling rate is larger than the pseudorange error produced by the samall non-integer multiple sampling rate? Can the questions above explain that there are any defects for the Nyquist theorem?

First, we know that there are two prerequisites that Nyquist theorem required: (1) the sampled signal must be band-limited signal; (2) the sampling rate must be more than 2 multiple of the highest frequency. If these two prerequisites could be satisfied at the same time, the sampling sequence could be stand for the signal sampled completely.

As is known to all that the inputting signal in GNSS receiver is band-limited signal, and the local code signal is not band-limited signal. So taking the inputting signal for sampling procession in GNSS receiver just like digital signal, that is to say, the digital signal which has been sampled could not stand for the original analog signal, which is also the reason for why the sampling rate could not be selected only by Nyquist theorem, but must be satisfied with that sampling rate could not be integer multiple of the code rate at the same time.

48.5 Suboptimal Sampling Rate Selecting Algorithm

The conclusion above indicates that the sampling of receiver could make larger pseudorange error when the sampling rate is selected as integer multiple code rate or some other particular sampling rate, which is the reason that selecting a better sampling rate is very important to the GNSS receiver. For this reason, we may

make a group of choice sampling rate according to hardware, prime cost and so on to design GNSS receiver first, and then select a better sampling rate based on the performance evaluation criterion and its algorithm in this paper, which must be satisfied with the minimize pseudorange error. Meanwhile, it also must take the Doppler Effect into consideration. For example, ignoring the doppler offset caused by clock oscillator drift, impose the code rate is r_s Hz, and the maximum deviation affected by doppler effect is f_d Hz, thus the value of actual code rate of receiver must be considered between the range of $r_s - f_d$ Hz and $r_s + f_d$ Hz.

48.6 Conclusion

The paper studied the pseudorange error caused by sampling process in GNSS receiver, and brought forward the performance evaluation criterion for pseudorange error produced by sampling process and its algorithm, besides that, the paper analyzed the reason that the selection of sampling rate in receiver must be satisfied with not only Nyquist theorem, but also that the sampling rate could not be integer multiple of code rate.

The simulating experiment processed with the algorithm put forward in this paper indicates that the pseudorange error would become larger when the sampling rate is integer multiple of code rate or some particular sampling rate; moreover, the pseudorange error computed by RMS operation is about 20 m when the sampling rate is 6 multiple of code rate; and with the same operation, the pseudorange error is about 7 m when the sampling rate is 5.797 MHz. What's more, the pseudorange error computed by RMS operation would become small when the sampling rate is deviating from integer multiple of code rate or some particular sampling rate to 1,000 Hz, whose pseudorange error would achieve the order of decimeter.

As the reason that the logical relation between pseudorange error and sampling rate could not be described by simple function, the paper provides method for selecting better sampling rate which could be applied to the designing of GNSS digital receiver, and it can take cheap hardware cost to design GNSS digital receiver which also has the advantage of small pseudorange error caused by sampling process.

Acknowledgments This work is supported by the National Natural Science Foundation of China (Grant No. 61102130).

References

1. Kaplan ED, Hegarty CJ (2006) Understanding GPS principles and applications. Artech House, Boston
2. Misra P, Enge P (2006) Global positioning system signals, measurements, and performance. Ganga-Jamuna Press, Lincoln

3. Quirk KJ, Srinivasan M (2006) PN code tracking using non-commensurate sampling. IEEE Trans Commun 54(10):1845–1856
4. Hegarty CJ (2009) Analytical model for GNSS receiver implementation losses. In: ION GNSS 2009, Washington
5. Ilie I, Fortin D, Landry JR et al (2009) Realworld interferences' impacts analysis using high dynamic range GNSS RF/IF signals record and playback. In: ION GNSS 2009, Washington
6. Ke T, Hu X, Liu Y, Ran Y (2010) Influence of sampling rate on time discrimination in GNSS receiver. J Astronaut 31(12):2722–2729
7. Quirk KJ, Srinivasan M (2002) Analysis of sampling and quantization effects on the performance of PN code tracking loops. In: IEEE international conference on communications, Washington
8. Parkinson B, Spilker J (1996) Global positioning system: theory and applications. American Institute of Aeronautics and Astronautics, Reston

Chapter 49
Solutions for False Lock of FLL in GNSS Receiver

Ting Ke, Xingguo Li, Xianhui Wang and Fuzhan Yue

Abstract The first stage of processing with a Global Navigation Satellite System (GNSS) receiver is signal acquisition process, while the second stage is Frequency Lock Loop (FLL) process. It was found that when sequentially adopting the "sliding correlation" acquisition strategy and the "dual-quadrant" frequency discrimination strategy, the FLL occasionally operates abnormally with hundreds Hz false lock error, while the sequential Phase Lock Loop (PLL) would steadily tracking but with incorrect output bit phase. Two simple and universal methods are proposed to solve above problem: A. Instead adopting the "four-quadrant" frequency discriminator; B. Inserting frequency false lock detecting and correction mechanism between "dual-quadrant" FLL and Phase Lock Loop (PLL). Theory analysis and simulation test show the validation of the solutions.

Keywords Global navigation satellite system (GNSS) · Frequency lock loop (FLL) · Frequency tracking discriminator · False lock

49.1 Introduction

The first stage of processing with a Global Navigation Satellite System (GNSS) receiver is signal acquisition process, while the second stage is Frequency Lock Loop (FLL) process. It was found that when sequentially adopting the "sliding correlation" acquisition strategy and the "dual-quadrant" frequency discrimination strategy, the FLL occasionally operates abnormally with hundreds Hz false lock error.

T. Ke (✉) · X. Li · X. Wang · F. Yue
Space Star Technology Co. Ltd., Beijing 100086, China
e-mail: greatcottus@gmail.com

J. Sun et al. (eds.), *China Satellite Navigation Conference (CSNC) 2013 Proceedings*, Lecture Notes in Electrical Engineering 243,
DOI: 10.1007/978-3-642-37398-5_49,

As discussed in [1], the PLL could not detect and correct the frequency false lock phenomenon induced by FLL with "dual-quadrant" frequency discriminator. Taking GPS L1 C/A code as an example, under the condition of frequency false lock, the PLL can tracking steadily but with false and alternately-rolling predetection integration value, which result in the false recovered information bits. Base on above observation of alternately-rolling predetection integration value, a detecting and correcting mechanism for FLL frequency false lock problem was proposed in [1].

Limited application scope is the main drawback of [1] since it could NOT work for the situations of only one or two PRN code periods existing in one information bit (such as GALILEO E1-B), or the situations of high rate secondary code being modulated (such as GPS L5, GALILEO E1-C, E5a, and E5b).

To overcome the shortcoming of [1], two simple but universal solutions were proposed in this paper.

49.2 Mechanism Analysis for FLL Frequency False Lock Phenomenon

Well known by GNSS signal acquisition theory [2], the detection probability P_D is a function of predetection integration SNR C/N and acquisition threshold Th. For a given Th, P_D increases with C/N.

Predetection integration SNR is defined as $C/N = \beta\ (C/N_0)T_p$, where C/N_0 is the Carrier-to-Noise Ratio (Hz), T_p is the predetection integration time (s), β is the power loss caused by mismatch of PRN code phase and carrier frequency, which defined as

$$\beta = R_c^2(\varepsilon_{code})\frac{\sin^2(\pi f_d T_p)}{(\pi f_d T_p)^2} \tag{49.1}$$

where ε_{code} and f_d are the synchronization errors of PRN code phase (chips) and carrier frequency (Hz) respectively. Figure 49.1 gives the curve of β versus ε_{code} and f_d. Referring to Fig. 49.1, error patterns of <0.25 chips, 333.3 Hz> and <0 chips, 527.8 Hz> corresponding to the same power loss of $\beta = 0.38$.

Assuming the predetection integration time being $T_p = 1$ ms, the PRN code searching step during signal acquisition being $\Delta_{code} = 0.5$ chips, the carrier Doppler frequency searching step being $\Delta_{freq} = 2/(3T_p) = 667$ Hz. Generally speaking, conservation design expects the error pattern of $<\Delta_{code}/2,\ \Delta_{freq}/2>$ (i.e., <0.25 chips, 333.3 Hz>) being success acquired, resulting in β corresponding to designed acquisition threshold Th being lower than 0.38. Under such acquisition threshold, some error patterns with residual carrier Doppler frequency larger than $1/(2T_p) = 500$ Hz (such as <0 chips, 527.8 Hz>) could be false judged as "success acquisition".

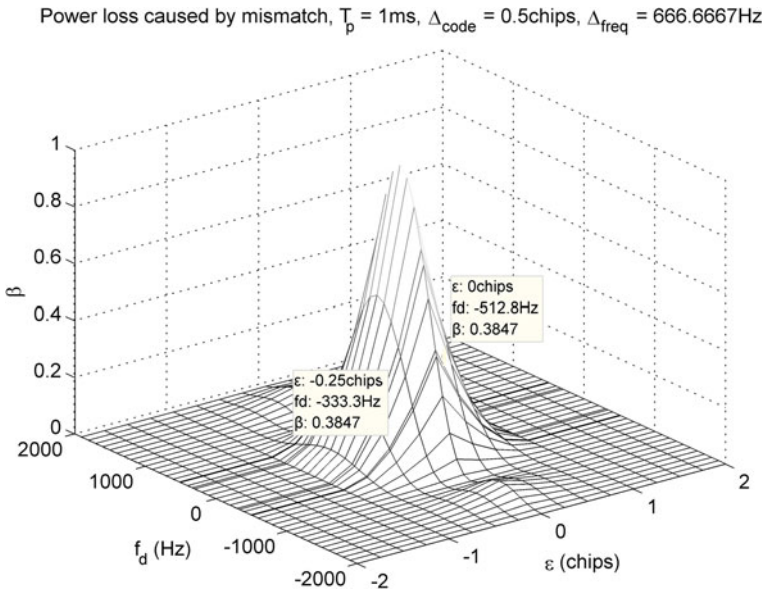

Fig. 49.1 Curve: β versus ε and f_d

Figure 49.2 gives the FLL discriminator curves of "four-quadrant" frequency discriminator $D_{FLL,4}$ and "dual-quadrant" frequency discriminator $D_{FLL,2}$ simultaneously.

$$D_{FLL\_4} = \frac{\text{atan2}(\text{Cross}, \text{Dot})}{2\pi T_p} \tag{49.2}$$

$$D_{FLL\_2} = \frac{1}{\sqrt{\text{Cross}^2 + \text{Dot}^2}} \frac{\text{Cross} \cdot \text{sgn}(\text{Dot})}{2\pi T_p} \tag{49.3}$$

where T_p is the predetection integration time, sign(.) denotes signum function, Cross and Dot are called as cross item and dot-product item respectively, with definition as

$$\text{Cross} = I_P(n-1)Q_P(n) - I_P(n)Q_P(n-1) \tag{49.4}$$

$$\text{Dot} = I_P(n-1)I_P(n) + Q_P(n-1)Q_P(n) \tag{49.5}$$

with I_P and Q_P being the in-phase and quadrature-phase correlation values respectively.

As shown in Fig. 49.2, giving $T_p = 1$ ms, the normal operation range of dual-quadrant discriminator $D_{FLL,2}$ is -250 to 250 Hz. If the absolute value of residual carrier Doppler frequency falls into the abnormal range of 250–750 Hz, then the FLL would false lock at ± 500 Hz [i.e., $1/(2T_p)$].

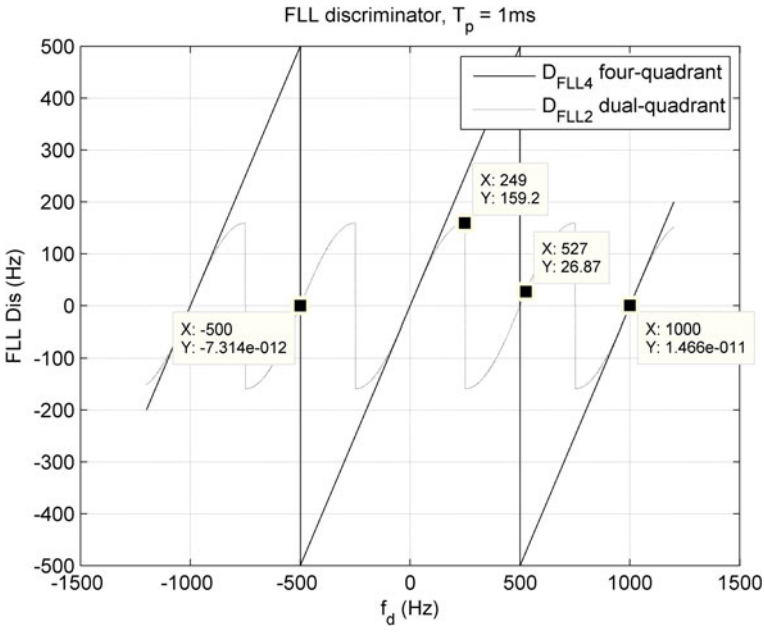

Fig. 49.2 FLL discriminator curve

Since the FLL and DLL work simultaneously, the last stabilized error pattern caused by FLL frequency false locked problem is <0 chips, ±500 Hz>, which has corresponding power loss of $\beta = 0.41$, larger than the acquisition threshold of $\beta = 0.38$, so the traditional Lose Loop Detector based on correlator power fading detection can NOT detect FLL frequency false lock phenomenon. Referring to [1], the PLL can NOT detect above anomaly too. Therefore, it is necessary to propose new methods to solve above problem.

49.3 Solutions

Referring to Sect. 49.1, a simple but application limited solution was first proposed by Li et al. [1], which could NOT work for the situations of only one or two PRN code periods existing in one information bit (such as GALILEO E1-B), or the situations of high rate secondary code being modulated (such as GPS L5, GALILEO E1-C, E5a, and E5b).

To overcome the shortcoming of [1], following two simple but universal solutions were proposed in this paper: A. Instead adopting the "four-quadrant" frequency discriminator; B. Inserting a novel frequency false lock detecting and correction mechanism between "dual-quadrant" FLL and Phase Lock Loop (PLL).

49.3.1 Solution A: Instead Adopting the "Four-Quadrant" Frequency Discriminator

Adopting the "four-quadrant" frequency discriminator can completely eliminate the FLL frequency false lock phenomenon.

Referring to Fig. 49.2, under the condition of four-quadrant discriminator $D_{FLL,4}$ being adopted, if the absolute value of residual carrier Doppler frequency larger than 500 Hz (e.g. 527 Hz), then the FLL would false lock at ±1,000 Hz, resulting in the correlator power fading to zeros. At that time, the traditional Lose Loop Detector based on correlator power fading detection will work and assert that tracking loops lose lock, and then the re-acquisition procedure would restart subsequently. After searching all the remaining PRN code phases, re-acquisition procedure would step into a new frequency (e.g., $527-627 = -100$ Hz) and continue to search the total PRN code phases until acquisition succeed. Since −100 Hz falls into the normal operation range of dual-quadrant discriminator $D_{FLL,4}$, the FLL will work normally. Therefore, the dual-quadrant discriminator can completely eliminate the FLL frequency false lock phenomenon, with the cost of acquisition time being obviously extended, which caused by an extra loop lose lock and re-acquisition procedure.

49.3.2 Solution B: Inserting a Novel Frequency False Lock Detecting and Correction Mechanism

Figure 49.3 gives the state flow of frequency false lock detecting and correction mechanism which is based on power judgment. After acquisition completion, "FLL State" is first executed. At FLL State, "dual-quadrant" frequency discrimination strategy is adopted, and the carrier frequency tends to lock at 0 or ±500 Hz. After A seconds, setting reference frequency (RefFreq) equal to the current frequency control word (FW), and then jumping into "Frequency False Lock Detecting and Correction State".

"Frequency False Lock Detecting and Correction State" consists of four substates with "Current Frequency Power Calculation State" being first executed. At that State, simply setting FW equal to RefFreq, and calculating the signal power of current frequency point (denotes as CurPower). After B seconds, it jumps into "+500 Hz Frequency Power Calculation State". At that State, simply setting FW equal to RefFreq plus 500 Hz, and calculating the signal power of current frequency point (denotes as PlusPower). After B seconds, it jumps into "−500 Hz Frequency Power Calculation State". At that State, simply setting FW equal to RefFreq minus 500 Hz, and calculating the signal power of current frequency point (denotes as MinusPower). After B seconds, it finally jumps into "False Lock Detecting and Correction State". At that State, finding the max value among

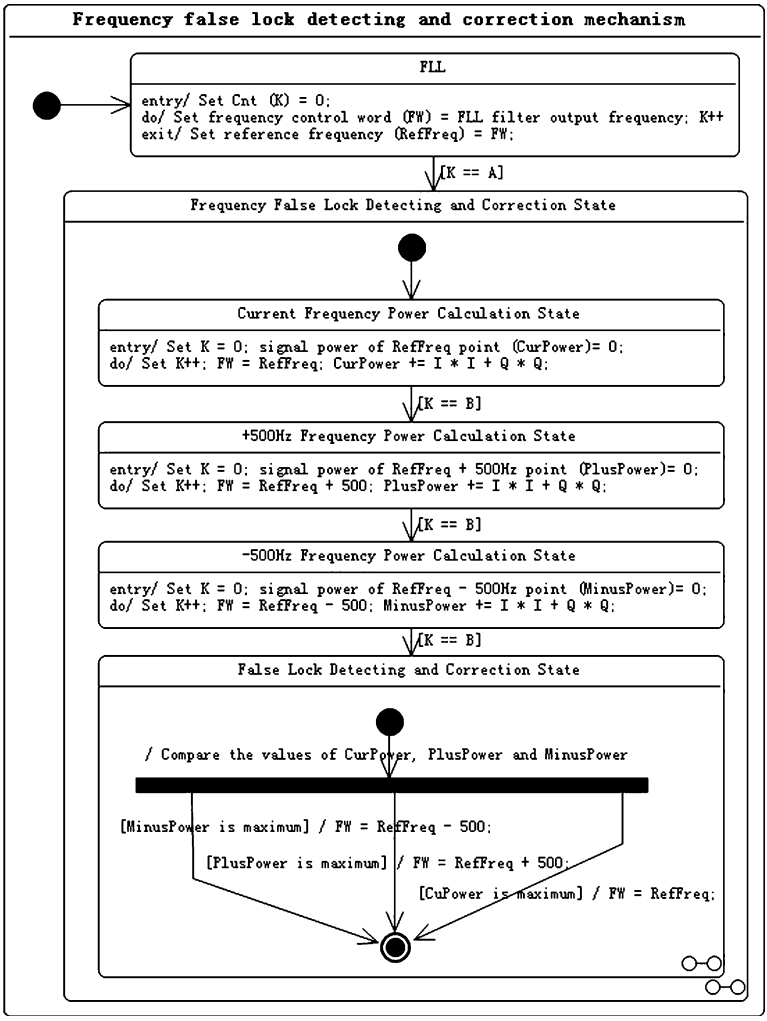

Fig. 49.3 State flow for frequency false lock detecting and correction algorithm

CurPower, PlusPower and MinusPower, and then setting FW equal to the right frequency corresponding to the maximum one.

Computer simulation was carried out to validate solution B. The simulation conditions are as follows: setting C/N_0 as 39 dB-Hz, the residual carrier Doppler frequency as 700 Hz, and the predetection integration time as 1 ms, which resulting the normal operation range of dual-quadrant discriminator being −250 to 250 Hz. Taking second-order FLL filter, with filter bandwidth as 12 Hz. Setting A equal to 2 s, B equal to 10 ms.

Figure 49.4 gives the Simulation result, with Fig. 49.4a being the global frequency tracking error curve, while Fig. 49.4b is the partial curve before frequency

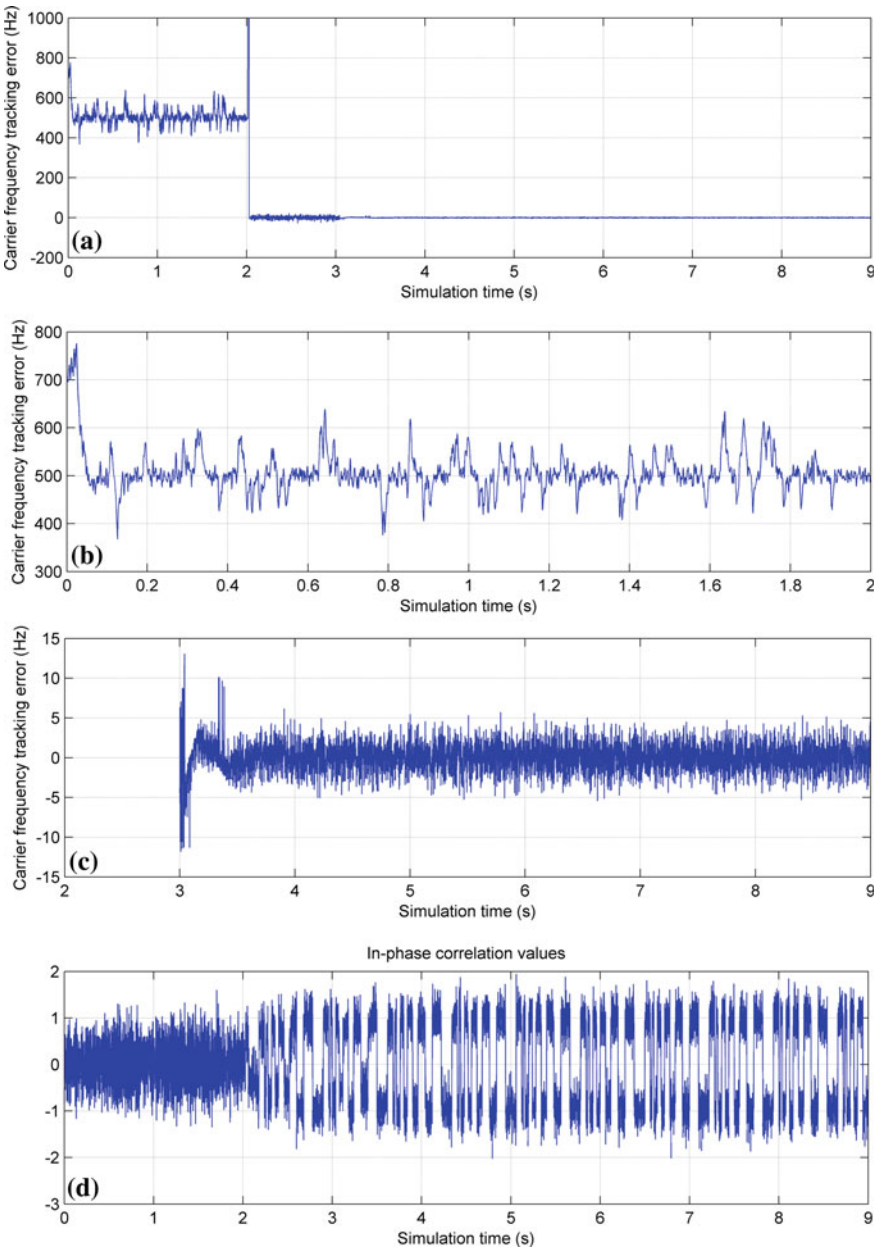

Fig. 49.4 Simulation for frequency false lock detecting and correction algorithm. **a** Carrier frequency tracking error (*global curve*). **b** Carrier frequency tracking error (*partial curve*, *before correction*). **c** Carrier frequency tracking error (*partial curve*, *after correction*). **d** In-phase correlation values

false lock correction, and Fig. 49.4c is the partial curve after the correction. Figure 49.4d is the in-phase correlation values. As shown in Fig. 49.4b, from 0 to 2 s, "dual-quadrant" frequency discriminator was adopted, and carrier frequency error was false locked from 700 to 500 Hz. As shown in Fig. 49.4a, from 2 to 2.03 s, frequency false lock detecting and correction mechanism was executed, and the carrier frequency error was corrected to 0 Hz around. As shown in Fig. 49.4c and d, from 3 to 9 s, FLL assist PLL frequency tracking algorithm was executed, and the carrier frequency error works normally with ±5 Hz jittering. At this time, bit synchronizes normally.

49.4 Conclusion

It was found that when sequentially adopting the "sliding correlation" acquisition strategy and the "dual-quadrant" frequency discrimination strategy, the FLL occasionally operates abnormally. The solutions found in literature have limitation that could NOT work for the situations of only one or two PRN code periods existing in one information bit, or the situations of high rate secondary code being modulated. To overcome above shortcomings, two simple but universal solutions were proposed in this paper: A. Instead adopting the "four-quadrant" frequency discriminator instead; B. Inserting a novel frequency false lock detecting and correction mechanism between "dual-quadrant" FLL and Phase Lock Loop (PLL). Theory analysis and simulation test show that the proposed solutions can effectively solve the FLL frequency false lock problem. The implementations are simple but universal, and they apply to all GNSS signal structures.

References

1. Li G, Cui X, Yin X, Feng Z (2007) Sensing of false locks of the AFC loop in GPS receivers. J Tsinghua Univ (Sci Technol) 47(1):69–72
2. Kaplan ED, Hegarty CJ (2006) Understanding GPS: principles and applications, 2nd edn. Artech House, Boston

Chapter 50
Research on Fast Satellite Selection Algorithm Based on Geometry

Pengfei Zhang, Chengdong Xu, Chunsheng Hu and Ye Chen

Abstract The positioning accuracy with Global Navigation Satellite System (GNSS) depends on both the pseudorange error and the geometric dilution of precision (GDOP), and GDOP is depended on the geometry of user/satellites which are selected. Positioning with a GNSS needs at least four satellites which are visible for the user so that at least four pseudorange measurements can be provided to determine the user position in three dimensions and the receiver clock offset. In order to select as few as visible satellites whose geometry is better, a new fast satellite selection algorithm based on geometry is come up with by this paper through analyzing geometry characteristics of the optimal visible satellites combination. The expected visible satellites are selected based on the distribution characteristics of elevation angles and azimuth angles combined with tetrahedron volume. Taking GPS, GLONASS and GALILEO system for examples, this paper compares the algorithm proposed by this paper with the best geometry satellite selection algorithm through simulation. The simulation results show that the algorithm proposed by this paper solves the problem that there are a lot of matrix multiplications and matrix inversions in the best geometry satellite selection algorithm. So the new algorithm can reduce computational complexity and increase receiver processing speed. The theory of the algorithm is simple and easy to use. Meanwhile, the algorithm can satisfy the real time requirements for users.

Keywords GNSS · GDOP · Geometry · Satellite selection algorithm

P. Zhang (✉) · C. Xu · C. Hu
Key Laboratory of Dynamics and Control of Flight Vehicle, Ministry of Education, School of Aerospace Engineering, Beijing Institute of Technology, No.5 South Zhongguancun Street, Haidian District 100081 Beijing, China
e-mail: successful.2008@163.com

Y. Chen
School of Information and Communication Engineering, North University of China, No.3 Xueyuan Road, Taiyuan 030051 Shanxi, China

J. Sun et al. (eds.), *China Satellite Navigation Conference (CSNC) 2013 Proceedings*, Lecture Notes in Electrical Engineering 243,
DOI: 10.1007/978-3-642-37398-5_50,

50.1 Introduction

The four Global Navigation Satellite Systems (GNSSs) which are currently on-orbit operation include the American GPS, the Russian GLONASS, the European GALILEO system and the Chinese BD2 system (the Second Generation of BeiDou Navigation System) [1]. The positioning accuracy with GNSS mainly depends on pseudorange error and geometric dilution of precision (GDOP), and GDOP is depended on user/satellites geometry [2]. In order to determine user position in three dimensions and the receiver clock offset, at least four satellites should be visible to provide four pseudorange measurements [3]. So it is important that how to select the visible satellites with better geometry and less quantity fast. The best geometry satellite selection algorithm is described simply as follows: find all combinations with four satellites in all visible satellites and calculate GDOP or tetrahedron volume in all combinations firstly, and then select the combination with minimal GDOP or maximal tetrahedron volume as final satellite selection result. The result of best geometry satellite selection algorithm is optimal and the corresponding positioning accuracy is best. However, it has a heavy calculation burden and it is time-consuming. Especially for the high-dynamic user, it has a disadvantage in real time performance. Therefore, it is significant to find out a fast satellite selection algorithm with less calculation on the premise that it has little influence on positioning accuracy. This paper analyzes the geometry characteristics of the optimal combination which is selected by best geometry satellite selection algorithm and summarizes the distribution regularities of elevation angles and azimuth angles in the combination. Then a new fast satellite selection algorithm based on geometry is come up with. At last, taking GPS, GLONASS and GALILEO system as examples, this paper compares the algorithm proposed by this paper with the best geometry satellite selection algorithm trough simulation.

50.2 Best Geometry Satellite Selection Algorithm

In GNSS, the positioning error can be expressed as a product of GDOP and pseudorange error [4].

$$\sigma_p = GDOP \times \sigma_{UERE} \tag{50.1}$$

where σ_p is the positioning error and σ_{UERE} is the pseudorange error. As is shown in formula (50.1), GDOP is a linear mapping from peseudorange error to positioning error. On the condition of the same pseudorange error, the less the GDOP, the less the positioning error. Therefore, a basic principle of satellite selection is to make GDOP of the selected combination as small as possible.

If there are $n(n \geq 4)$ simultaneous and continuous satellites of one GNSS in view of users in one area at one moment, a best geometry satellite selection algorithm is to go through the entire four satellites combinations in all visible

satellites and select the combination with minimal GDOP as a final satellite selection result. GDOP is inversely proportional to tetrahedron volume which consists of the end points of unit vectors between a user and satellites. So another best geometry satellite selection algorithm is to select the combination with maximal tetrahedron volume as a final satellite selection result [5]. Assuming that positions of the selected four satellites in Earth-Centered Earth-Fixed (ECEF) coordinate system are $(x_i, y_i, z_i)\,(i = 1, 2, 3, 4)$, the position of user in ECEF coordinate system is (x_u, y_u, z_u), the calculation formula of GDOP is as follows [6]:

$$GDOP = \sqrt{trace(H^T H)^{-1}} \tag{50.2}$$

Where,

$$H = \begin{bmatrix} a_{x1} & a_{y1} & a_{z1} & 1 \\ a_{x2} & a_{y2} & a_{z2} & 1 \\ a_{x3} & a_{y3} & a_{z3} & 1 \\ a_{x4} & a_{y4} & a_{z4} & 1 \end{bmatrix}$$

$$a_{xi} = \frac{x_i - x_u}{r_i},\ a_{yi} = \frac{y_i - y_u}{r_i},\ a_{zi} = \frac{z_i - z_u}{r_i}$$

$$r_i = \sqrt{(x_i - x_u)^2 + (y_i - y_u)^2 + (z_i - z_u)^2} \quad (i = 1, 2, 3, 4)$$

The calculation formula of tetrahedron volume V is as follows [7]:

$$V = \frac{1}{6}|H| \tag{50.3}$$

There are C_n^4 times calculation of GDOP or tetrahedron volume in best geometry satellite selection algorithm. Taking GPS as an example, there are 6–12 simultaneous and continuous satellites in view of a user in one area at one moment. That is, there are 15–495 times calculation of GDOP or tetrahedron volume in best geometry satellite selection algorithm. As is shown in formula (50.2) and formula (50.3), it involves matrix multiplication, matrix inversion or determinant computation in every time of calculation, the computation burden is heavy and it is time-consuming.

50.3 Analysis of Best Geometry Characteristics

Taking GPS as an example, the reference time of ephemeris and start time of simulation are set as 0 h 0 min 0 s January 1, 2012 UTC, the total time of simulation is set as 24 h. The observation site is set as 39°N and 116°E and the mask angle is set as 5°. The satellite selection result of best geometry satellite selection

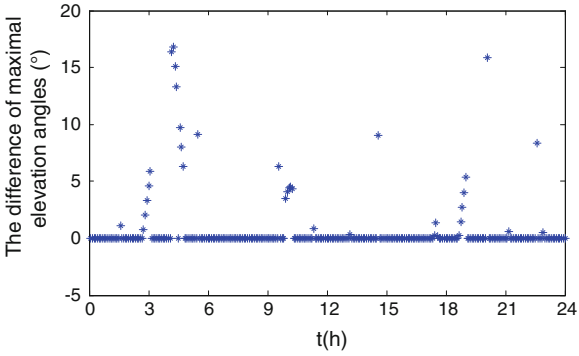

Fig. 50.1 The difference of maximal elevation angles between satellite selection result and all the visible satellites

algorithm is analyzed and the difference between maximal elevation angles of the satellite selection result and that of all the visible satellites is shown statistically in Fig. 50.1.

As is shown in Fig. 50.1, there is nearly 90 % simulation time that the satellite with maximal elevation angle in satellite selection result and the satellite with maximal elevation angle in all the visible satellites are the same, and there is more than 95 % simulation time that the difference of maximal elevation angle between them is less than 10°. It indicates that there should be a satellite with greater elevation angle in best geometry. Next, the geometry characteristics of the other three satellites are analyzed according to vertex distribution of tetrahedron. The tetrahedron which consists of the end points of unit vectors between a user and satellites is shown in Fig. 50.2.

In Fig. 50.2, the tetrahedron ABCD is consisted of four projective points of the four satellites located on the unit sphere whose center is the user [8]. The size of

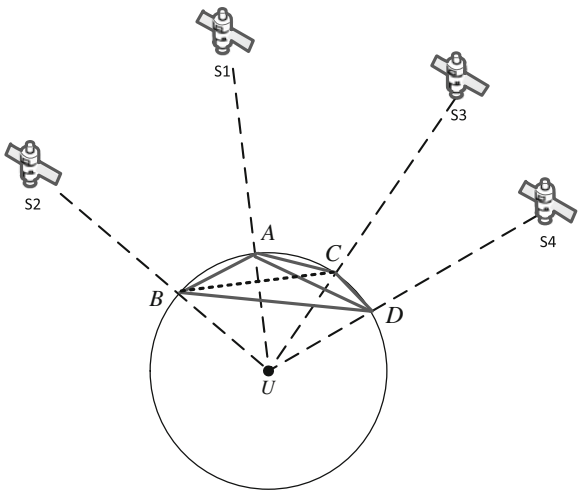

Fig. 50.2 Tetrahedron geometry of four satellites

tetrahedron volume reflects the quality of satellite selection result. The larger the volume, the better the result. In order to make the tetrahedron volume as large as possible, when a satellite with a greater elevation angle is determined, other three satellites should be selected as follows: the elevation angles of the three satellites should be small and the difference between that of each other should be also small, then the azimuth angles of them should be distributed uniformly.

50.4 Fast Satellite Selection Algorithm Based on Geometry

Through analyzing the geometry characteristics of the optimal visible satellites combination, the expected visible satellites are selected based on the distribution characteristics of elevation angles and azimuth angles combined with tetrahedron volume. The selection result is not optimal, but it can increase the satellite selection speed with less calculation on the premise that it has little influence on positioning accuracy. The detailed satellite selection process is shown in Fig. 50.3.

Step 1 Set the mask angle according to the field of vision to the satellites in the location of the receiver. The mask angle is inversely proportional to the field of vision. The wider the field of vision, the lower the mask angle should be set.

Step 2 Eliminate the unhealthy satellites in GNSS according to the parameters which represent the health state in ephemeris, calculate the position coordinates of the health satellites in ECEF coordinate system and get the total number of the visible satellites n according to the mask angle set in step 1.

Step 3 Transform the visible satellites coordinates in ECEF coordinate system to ENU coordinate system (the origin is the user, X-axis points to east orientation, Y-axis points to north orientation and Z-axis points to zenith orientation) and get the unit vector [9].

Step 4 Calculate the elevation angles and azimuth angles of all visible satellites in ENU coordinate system and select the satellites with maximal and the second maximal elevation angle as the first alternative satellite S1 in satellite selection result. Judge the difference between elevation angles of the two satellites, if it is less than 10°, select two combinations according step 5–step 8, if not, determine the satellite with maximal elevation angle as the first satellite S1 in satellite selection result.

Step 5 If $n \leq 6$, go through the entire three satellites combinations in the rest of visible satellites and select the satellites with maximal tetrahedron volume combined with S1 as the second S2, the third S3 and the fourth satellite S4 in satellite selection result respectively, and then turn to step 9; if $n > 6$, turn to step 6.

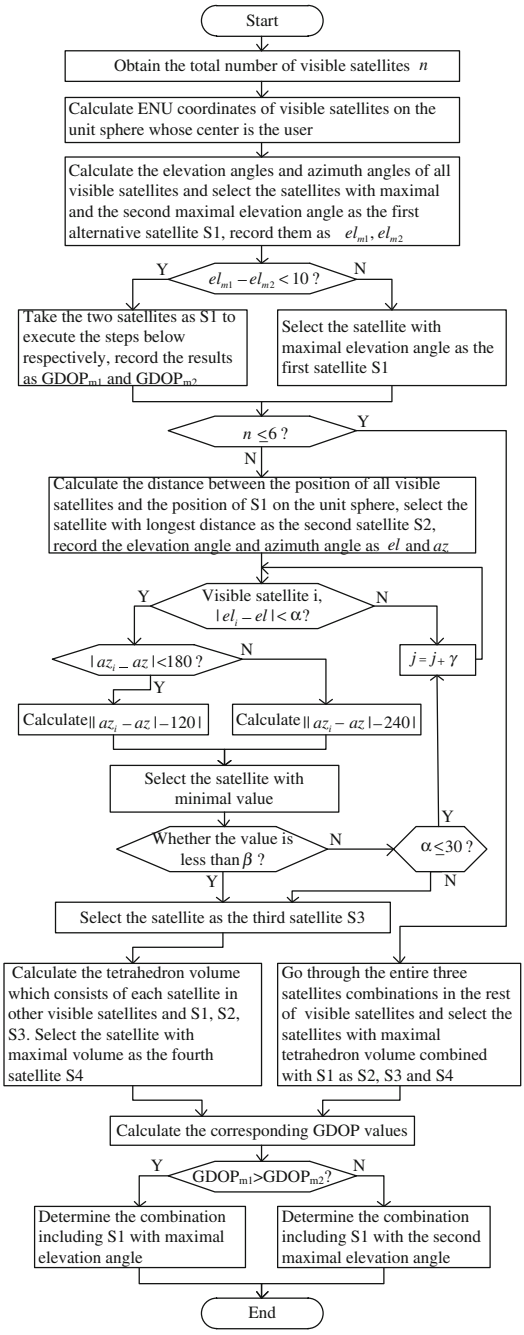

Fig. 50.3 Process of satellite selection

Step 6 Calculate the distance between the position of all visible satellites and the position of S1 on the unit sphere, select the satellite with longest distance as the second satellite S2 in satellite selection algorithm.

Step 7 Select the third satellite S3.

Step 7.1 Calculate the difference between elevation angle of S2 and that of other visible satellites except S1 and get the satellites whose absolute values of difference are less than α. In order to make the tetrahedron volume as large as possible, the elevation angles of S3 and S2 should be in the same range, that is, the smaller α, the better the result. In general, α is less than 30°;

Step 7.2 Calculate the difference between azimuth angle of S2 and that of other visible satellites obtained in step 7.1. If absolute value of the difference is greater than 180°, calculate the difference between the absolute value and 240°; if not, calculate the difference between the absolute value and 120°;

Step 7.3 Find out the minimal absolute value in the difference calculated in step 7.2, judge whether the minimal value is less than β (the size of β reflects azimuth angles distribution of S3 and S2, the smaller β, the more uniform azimuth angles distribution of S3 and S2, the larger the tetrahedron volume). If it is less than β, select this satellite as the third satellite S3 in satellite selection result. If not, increase the value of α by a certain step and repeat step 7.1–7.2 until find out the third satellite. If the third satellite met the conditions is not selected when the value of α increases to 30°, select the satellite with minimal β when α is 30° as the third satellite S3 in satellite selection result.

Step 8 Calculate the tetrahedron volume which consists of each satellite in other visible satellites and S1, S2, S3. Select the satellite with maximal volume as the fourth satellite S4 in satellite selection result.

Step 9 If there are two schemes in step 4 about S1, judge the GDOP size of the two schemes. Select the combination with the minimal GDOP as the satellite selection result.

50.5 Simulation Analysis

In the simulation, 32 GPS satellites (according to Yuma almanac), 24 GLONASS satellites (uniformly locate in 3 orbital planes 120° apart in right ascension) and 27 GALILEO satellites (3 orbital planes, equally spaced and with 56° nominal inclination and 9 satellites per plane) are chosen respectively [10]. The reference time of ephemeris and start time of simulation are set as 0 h 0 min 0 s January 1, 2012 UTC, the total time of simulation is set as 24 h. The observation site is set as 39°N and 116°E and the mask angle is set as 5°. Both α and β are set as 30°, γ is set

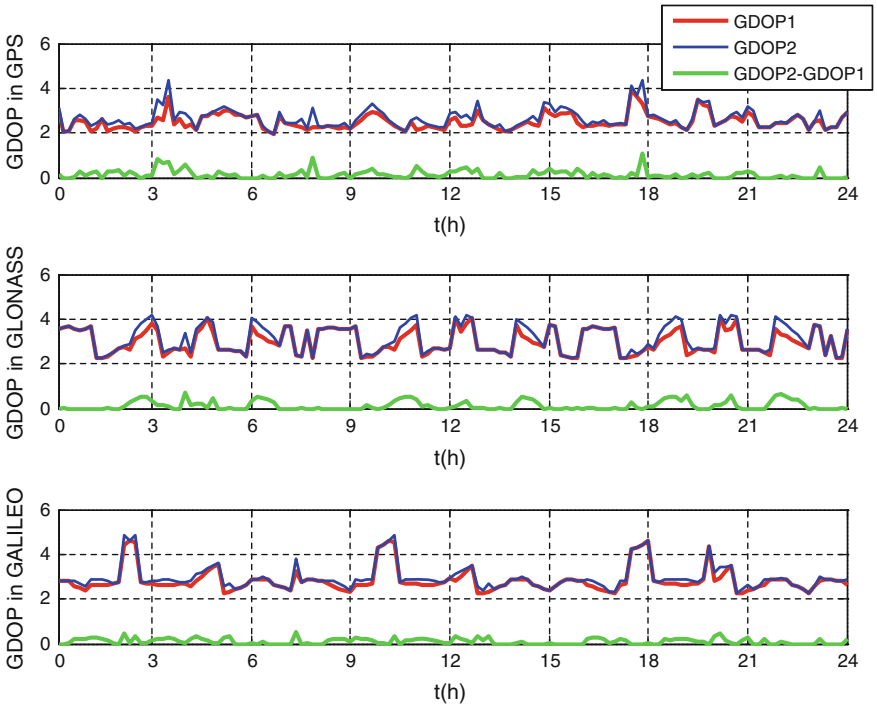

Fig. 50.4 Comparison of the corresponding GDOP values in the two algorithms

as 5°. The satellite selection results of best geometry satellite selection algorithm and fast satellite selection algorithm based on geometry proposed by this paper are simulated. The corresponding GDOP and consuming time are compared respectively. The comparison results are shown in Figs. 50.4 and 50.5.

In Figs. 50.4 and 50.5, GDOP1 and T1 represent the GDOP value and consuming time of satellite selection result in best geometry satellite selection algorithm respectively. GDOP2 and T2 represent the GDOP value and consuming time of satellite selection result in fast satellite selection algorithm based on geometry proposed by this paper respectively. The mean values of the difference between GDOP1 and GDOP2 in GPS, GLONASS and GALILEO system are 0.1470, 0.1377 and 0.1097 respectively. The mean increase of corresponding positioning error is less than 5 %. So it is an acceptable influence on positioning in fast satellite selection algorithm based on geometry. In addition, the calculation time is reduced obviously and the speed of satellite selection is increased about ten times. Therefore, it achieves the purpose that as few as visible satellites are selected fast with less calculation on the premise that it has little influence on positioning accuracy.

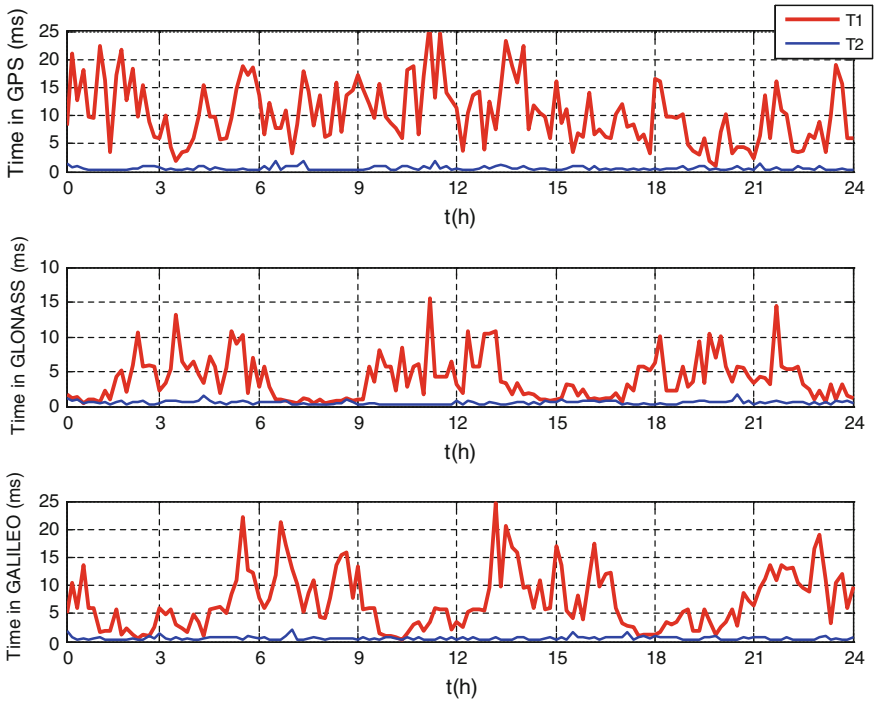

Fig. 50.5 Comparison of satellite selection time in the two algorithms

50.6 Conclusion

This paper analyzes the geometry characteristics of the optimal combination which is selected by best geometry satellite selection algorithm and summarizes the distribution regularities of elevation angles and azimuth angles in the combination. The selection result of the best geometry satellite selection algorithm is optimal, but it has a heavy calculation burden and it is time-consuming. Therefore, a fast satellite selection algorithm based on geometry is come up with by this paper. In this algorithm, the expected visible satellites are selected based on the distribution characteristics of elevation angles and azimuth angles combined with tetrahedron volume. At last, taking GPS, GLONASS and GALILEO system as examples, this paper compares the algorithm proposed by this paper and best geometry satellite selection algorithm trough simulation. The simulation results show that the algorithm proposed by this paper solves the problem that there are a lot of matrix multiplications and matrix inversions in the best geometry satellite selection algorithm so that it can satisfy the real time requirements for users. The algorithm proposed by this paper can be used in any one of the GNSSs and it can also be expanded to the satellite selection of multi-GNSSs.

Acknowledgments This work was supported by the National High-Tech. R&D Program, China (No.2011AA120505) and the National Natural Science Foundation, China (No.61173077).

References

1. Zhang P, Xu C, Hu C, Chen Y (2012) Time scales and time transformations among satellite navigation systems. The 3rd China satellite navigation conference (CSNC2012), Springer, Berlin, pp 491–502
2. Misra P, Enge P (2006) Global positioning system, signals, measurements, and performance, 2nd edn. Artech House Publisher, USA, pp 81–89
3. Kaplan ED, Hegarty CJ (2006) Understanding GPS: principles and applications, 2nd edn. Artech House Publisher, USA, pp 240–247
4. Chen C, Zhang X (2010) A fast satellite selection approach for satellite navigation system. Chin J Electron 38(12):2887–2891 (In Chinese)
5. Jin L, Huang Z, Li R, Ma Y (2009) Study on fast satellite selection algorithm for integrated navigation. Chin J Electron 37(9):1931–1936 (In Chinese)
6. Guangyao Li, Chengdong Xu, Zhang P, Hu C (2012) A modified satellite selection algorithm based on satellite contribution for GDOP in GNSS. International conference on mechanical and electronic engineering (ICMEE 2012), Springer, Berlin, pp 415–421
7. Zhang Q, Zhang X, Li H, Chang X (2007) Satellite selection algorithm for combined satellite receivers. J Beijing Univ Aeronaut Astronaut 33(12):1424–1427 (In Chinese)
8. Zhang M, Zhang J (2009) A fast satellite selection algorithm: beyond four satellites. IEEE J Sel Top Signal Process 3(2):P740–P747
9. Zhang P, Xu C, Hu C, Chen Y (2011) Coordinate transformations in satellite navigation systems. International conference on electronic engineering, communication and management (EECM2011), Springer, Berlin, pp 249–257
10. Zhang M, Zhang J, Qin Y (2008) Satellite selection for multi-constellation. 2008 IEEE/ION Position, Location and Navigation Symposium, Monterey, USA, pp 1053–1059

Chapter 51
Application of Improve Subspace Projection Technique in of GNSS Space–Time Anti-Jam Receiver

Xudong Zhang

Abstract According to the characters of GNSS receiver received interference signal is much stronger than the noise and the satellite signal. We apply subspace projection to space–time process. Improve the method of subspace projection based on the CCS-MSWF structure. It can estimate space–time two-dimensional subspace more quickly and exactly in the case of the limited data precision. Further obtain the optimal weight. This method is also suitable for small samples and signal changing scene. Compared with the original method. The accuracy of interference subspace estimate is improve without additional computational cost. Numerical simulation demonstrates that is effective and efficient to both narrow-band and wideband interference. The performance of anti-jamming is excellent and stable.

Keywords GNSS · Anti-jam · Space–time process · Improve subspace projection · Modify multistage Wiener filter

51.1 Introduction

A key issue in the satellite navigation system anti-jamming technology field is how to suppress interference in a complex electromagnetic environment of multiple interference type. Currently use of Adaptive null antennas can inhibit the number of interference is the number of antenna elements minus one. However, the number of antenna elements by the limit of the receiver's size, cost and other requirements. So that it lack of the number of the degrees of freedom in the presence of multiple interference. Therefore, the use of some certain limitations.

X. Zhang (✉)
Research Institute of Electronic Science and Technology, University of Electronic Science and Technology of China, Chengdu, China
e-mail: hehe19851027@126.com; zhangxudongg@hotmail.com

J. Sun et al. (eds.), *China Satellite Navigation Conference (CSNC) 2013 Proceedings*, Lecture Notes in Electrical Engineering 243,
DOI: 10.1007/978-3-642-37398-5_51,

In order to suppress multiple interference, we shall take advantage of the freedom of time and space domain.

Space–time (ST) processing methods used in the navigation receiver can provide a sufficient number of degrees of freedom to cancel a large number of wideband and narrowband interferers or jammers [1–3]. Although the research of Space–time (ST) theory have been researched long before. But In the early phases, be used to eliminate radar clutter [4]. Until 2000, Fante first applied Space–time (ST) technology to the anti-jamming receiver [5], and achieve good effects. In the development and application of space–time technology. Space–time technology has become an important method for signal processing. Adaptive algorithm design more flexible, effective and strengthen the capacity of anti-jamming.

This paper improve the traditional subspace projection methods. So that it can maintain good interference suppression effect though data accuracy is limited. Simulation results show that the improved method is effective.

51.2 The Principle of Space–Time Processing

The thought of Space–time adaptive processing (STAP) can handling signal in space domain and time domain. From each antenna element, the structure of delay unit form FIR filter architecture. It can be filter interference in time domain. From the same node on the delay, different elements constitute the spatial adaptive filtering. It can be distinguish interference from different direction. An adaptive array is able to form a pattern null in the direction of interfering signal. This method has the properties of strong resistance against interference in space area and time area. STAP might achieve better performance than a single time domain, frequency domain or spatial filtering methods.

51.2.1 Space–Time Processing Array Models

The structure of Space–time processing structure shown in Fig. 51.1. Set the antenna array system with M elements. The number of delay unit of an element is L. the weight coefficient as follow:

$$w = \left[w_1^T, w_2^T, \ \ldots \ w_L^T\right]^T. \tag{51.1}$$

Among them, $w_i = [w_{i,1}, w_{i,2}, \ldots \ w_{i,M}]^T$ represent the weight coefficient of filter of each element. The array received signals can be expressed as:

$$x(k) = Ss(k) + \sum_{i=1}^{P} a_i j_i(k) + n(k) \tag{51.2}$$

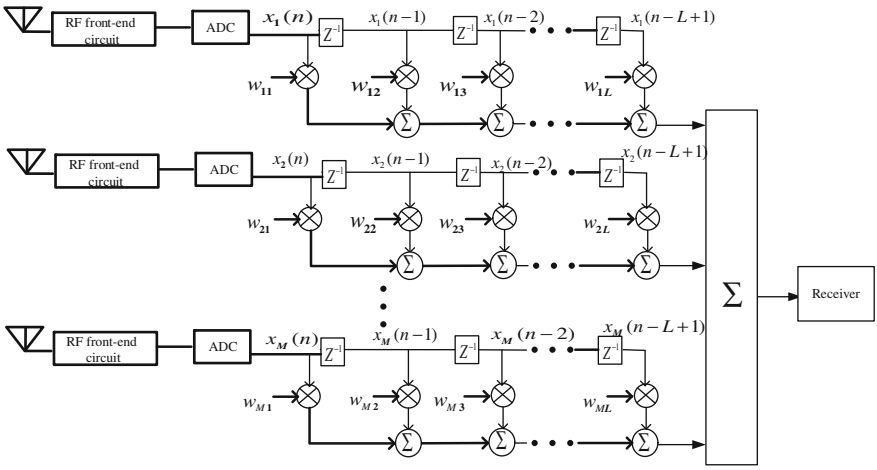

Fig. 51.1 The structure of STAP

$s(k)$, S represent the navigation signals and their space–time direction vector respectively. $j_i(k)$, a_i represent the interference signals and their space–time direction vector respectively. $n(k)$ represent the received signal of array antennas. $r = E(xx^H)$ is the covariance matrix of the received signal of array antennas.

This structure can be described as a constrained optimization problem.

$$\begin{cases} W_{opt} = \arg\min_W W^H R W \\ W^H S = 1 \end{cases} \tag{51.3}$$

S is space–time two dimensional steer vector. Combined with Lagrangian quantitative, we can push out the optimal weights of the two-dimensional processor as follow:

$$W_{opt} = (S^H R^{-1} S)^{-1} R^{-1} S = P_{o\min} R^{-1} S \tag{51.4}$$

In formula (51.4), $P_{o\min}$ is a constant, represents minimum output power.

51.3 Improved Subspace Projection Method

According to the character of satellite signals are weak than noise and interference signals, when calculate the formula (51.4) can be omitted $P_{o\,\min}$ so the formula (51.4) becomes:

$$w_{opt} = R^{-1} S = (\sigma^2 \mathrm{I} + A_J R_J A_J^H)^{-1} S \tag{51.5}$$

where: $A_J = [a_1\ a_2\ \cdots\ a_D]$, $R_J = E(JJ^H)$.

Under the matrix inversion lemma [6]:

$$\begin{aligned}\sigma^2 R^{-1} &= (\mathrm{I} + \sigma^{-2} A_J R_J A_J^H)^{-1} \\ &= \mathrm{I} - A_J(\sigma^2 R_J^{-1} + A_J^H A_J)^{-1} A_J^H.\end{aligned} \tag{51.6}$$

Because the interference signal power is also much larger than the noise power in the practical application. So we can omit the noise. Then the formula (51.4) becomes:

$$\sigma^2 R^{-1} = \mathrm{I} - A_J(A_J^H A_J)^{-1} A_J^H = P_{A_J}^{\perp} \tag{51.7}$$

$P_{A_J}^{\perp}$ is subspace projection matrix which orthogonal to the interference subspace. Then the formula (51.5) becomes:

$$w_{opt} = P_{A_J}^{\perp} S = (I - P_{A_J})S. \tag{51.8}$$

So we can apply the subspace projection technology in space–time domain process. Use the receive data to construct the interference subspace. In order to calculate the optimum weights, the signal steer vector projected onto the interference subspace. Document [7] give a subspace projection method based on the relevant multi-stage Wiener filter structure (CCS-MSWF). In this paper, we present a subspace projection method base on improve the multi-stage Wiener filter base on correlation subtraction structure.

51.3.1 Improve the Multi-Stage Wiener Filter Base on Correlation Subtraction Structure (MCCS-MSWF)

Blocking matrix which is based on the structure of the CCS-MSWF is calculated as follows:

$$B = \mathrm{I} - P_i P_i^H. \tag{51.9}$$

During the implementation of multi-stage Wiener filter. There are lots of methods to realize the blocking matrix [8]. However, the choice of blocking matrix has close relationship to the stability of the algorithm. In the condition of the data is more accurate, we can use formula (51.9) to make algorithm presents stable and reliable. However, in practical applications it is not perfect. It is necessary to consider the question about the finite word-length effect during the Digital signal processing. Under this situation, there are many problems in rationally using formula (51.9) to calculate blocking matrix. Because the normalized cross-correlation vector is very difficult to meet $||P_i|| = 1$, this will lead to the subspace projection which calculated through the blocking matrix and subspace which consists of cross-correlation vector might be not always orthogonal. Through the

above study, we have some major finding that CCS-MSWF anti-interference performance will decline when the demand of data precision is not very high. From the view of engineering application, in this paper, a improved calculation method is proposed. The modified algorithm does not need to satisfy $||P_i|| = 1$, but has block effect as well.

A new method for calculating the blocking matrix is presented as follow:

$$B = \mathrm{I} - P_i P_i^H / P_i^H P_i. \tag{51.10}$$

We had to multiple cross-correlation vector with formulas (51.9) and (51.10) separately, We can obtain formulas (51.11) and (51.12):

$$B * P_i = (\mathrm{I} - P_i P_i^H) * P_i = P_i - P_i P_i^H P_i \tag{51.11}$$

$$\begin{aligned} B * P_i &= (\mathrm{I} - P_i P_i^H / P_i^H P_i) * P_i \\ &= P_i - P_i P_i^H P_i / P_i^H P_i \\ &= P_i - P_i = 0 \end{aligned} \tag{51.12}$$

Compare with formulas (51.11) and (51.12), it can be seen that even if its condition of $||P_i|| = 1$ is not satisfied, formula (51.12) can also guarantee the blocking matrix and correlation matrix orthogonal to each other. The results showed that the improved algorithm was feasible, effective, and practicable under limited data accuracy. The method improved was MCSS-MWFD.

51.3.2 The Step of Subspace Projection Anti-Jamming Technology Base on MCCS-MSWF

By the document [7] analysis, using the multi-level decomposition characteristics of the multistage Wiener filter can form the noise subspace and interference subspace structure in the joint space–time domain, optimal weight vector can be calculated according to Eq. (51.8). In this paper, we take advantage of the MCS-MSWF structure of the multistage Wiener filter to decompose. The benefits of using this structure can guarantee the stability of the algorithm in the condition of data accuracy with restricted. It Suitable for small sample data and signal changing scene.

If the rank of receive data covariance matrix R is D, Afterward the data are deal with Multistage Wiener decomposition, data can be seen as white noise after the D-level. Almost does not contain any interference components. However, in practical applications, does not know the rank of receive data covariance matrix. But we can fixed threshold Δ based on practical experience in engineering design. As long as the power of the observational data is less than or equal to Δ stop iterative calculation. We select $\Delta = 2\mathrm{ML}\sigma^2$ in the simulation.

The following gives the detailed steps:
Initialization: $d_0(n) = x_1(n); x_0(n) = x(n), i = 1;$
Iteration: For i = 1:D do

$$p_i = E\{d_{i-1}^*(n)x_{i-1}(n)\}/\|E\{d_{i-1}^*(n)x_{i-1}(n)\}\| \; d_i(n) = p_i^H x_{i-1}(n);$$
$$B_i = \mathrm{I} - P_i P_i^H / P_i^H P_i;$$
$$x_i(n) = B_i x_{i-1}(n) = x_{i-1}(n) - p_i d_i(n) / P_i^H P_i;$$

If $|x_i(n)|^2 \leq \Delta$, stop;
Else i = i + 1;
Calculate Weight: $T = [p_1 \; p_2 \; \ldots \; p_D]$;

$$W_{opt} = (I - TT^H) * S$$

51.4 Simulation

A computer analysis is now made to demonstrate the performance of the above MCS-MSWF and to compare its performance with CCS-MSWF.

For the purpose of the analysis, A uniform linear space–time array with M = 3 antenna elements is used with $\lambda/2$ interelement spacing. Each element has a tapped delay line of L = 4 taps.

According to IDC-GPS-200, a minimum power of GNSS receiver signal approximately is −160 dBW, the thermal noise density is −205 dBW/Hz, sampled at Chip rate, so the SNR is −20 dB.

Navigation data was received form one satellite with a DOA (0)deg and a randomly chosen C/A code. The frequencies of two narrowband interference are {6, 10} MHz respectively, and the DOA is {−30°, 40°}, all the INR of narrowband interference are 50 dB. The bandwidth of two wideband interference is {10, 20} MHz, the INR of wideband interference both are 50 dB.

51.4.1 The Comparison of Resist Interference Performance in the Conditions of Double-Precision Floating-Point

See from Fig. 51.2, in the condition of double-precision floating-point. The resist interference performance of two algorithms are basically consistent. When the order was 6 has a very good performance in rejecting interference.

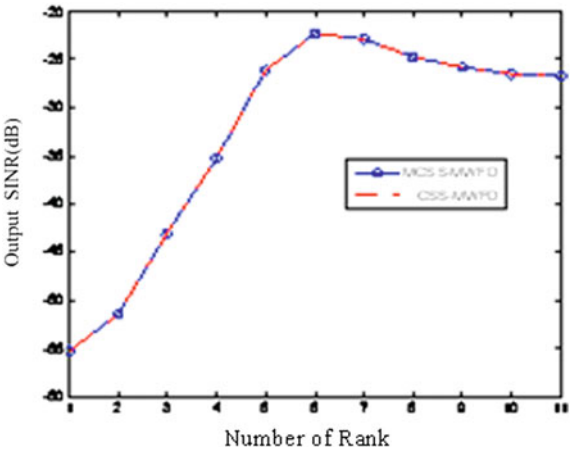

Fig. 51.2 Output SINR changes with the number of rank

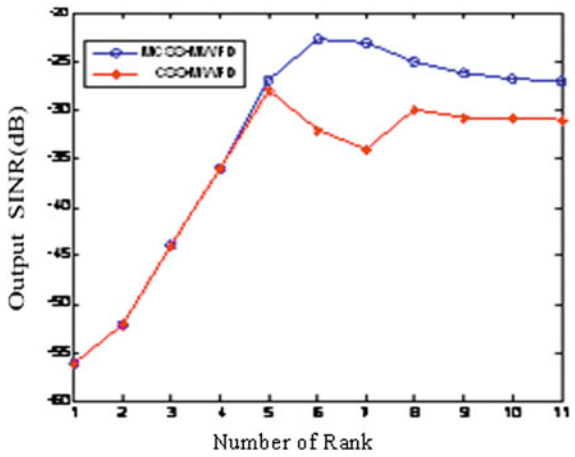

Fig. 51.3 Output SINR changes with the number of rank

51.4.2 The Comparison of Resist Interference Performance in the Conditions of Fix-Point

See from Fig. 51.3, the resist interference performance of MCS-MSWF in the conditions of fix-point is consistent with Fig. 51.2, Due to limited data accuracy, the anti interference performance of CCS-MSWF will be degraded greatly when the order is larger than 5.

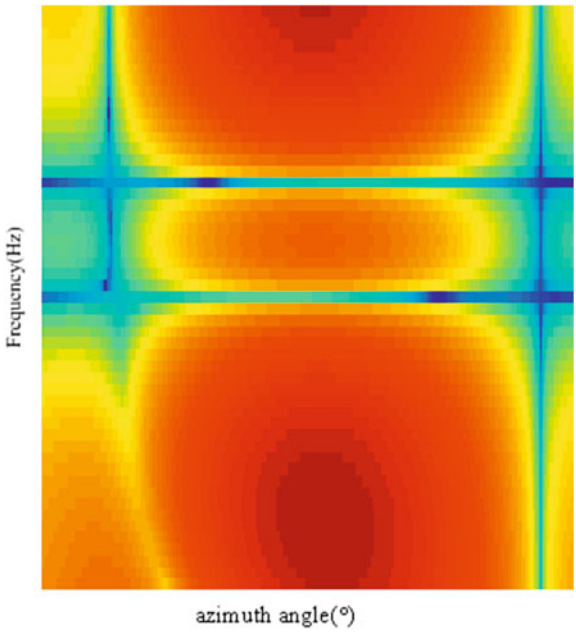

Fig. 51.4 Two-dimensional antenna pattern

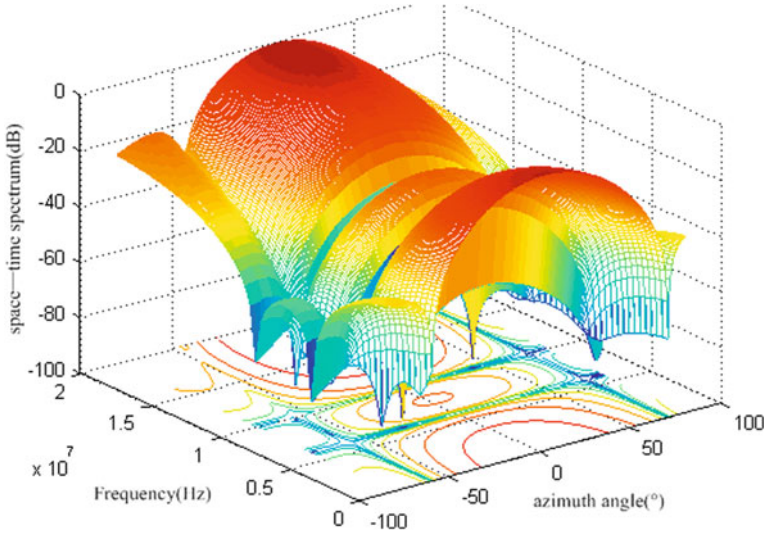

Fig. 51.5 Three-dimensional antenna pattern

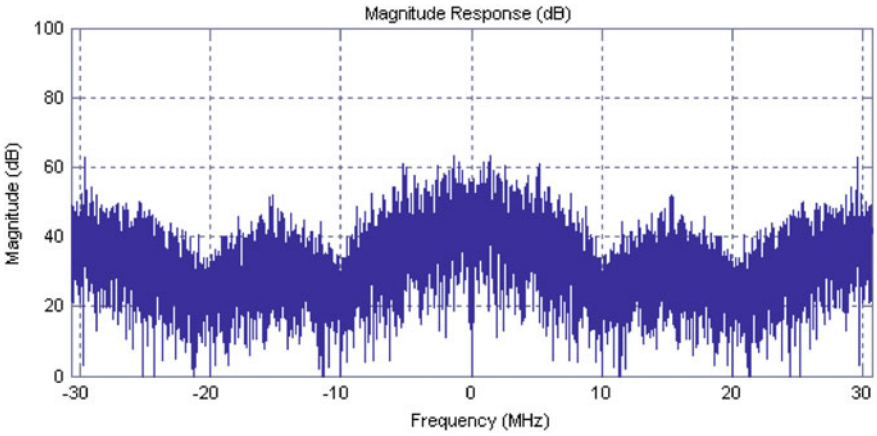

Fig. 51.6 Signal spectrum after the anti-jamming

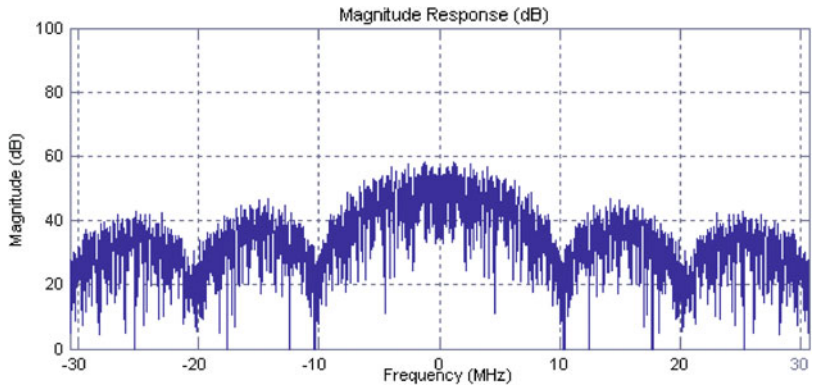

Fig. 51.7 GNSS signal spectrum

51.4.3 Space-Frequency Response

Two pits formed in the two narrow-band interference corresponding to the space-frequency. The direction of desire signal corresponds to a raised. This illustrates the algorithm to effectively suppress interference at the same time to ensure that the signal without distortion. Also proved that the space–time array has more freedom to destructive interference than the spatial filter (Figs. 51.4, 51.5).

Compare with Figs. 51.6 and 51.7, we can conclude that the interferences are inhibited.

51.5 Conclusion

In this paper, Base on the subspace projection anti-jamming technology, propose an improved subspace projection method. The simulation results demonstrate that it can be improved the capability of suppress interference in the condition of data accuracy with restricted and that the improved method is more conducive to used in actual project.

References

1. Farina A, Lombardo P, Pirri M (1999) Nonlinear STAP processing. IEE Electron Comm Eng J 2:41–48
2. Goldstein JS, Guerci JR, Reed IS (200) Advanced concepts in STAP. IEEE international radar conference, pp 699–704
3. Zatman M (2000) Circular array STAP. IEEE Trans Aerosp Electron Syst 36(2):510–517
4. Himed B, Kim K, Zhang Y, Hajjari A (2004) A New Approach to Wideband Space-Time Adaptive Processing (W-STAP). 2004 IEEE sensor array and multichannel signal processing workshop, pp 672–676
5. Fante RL, Vaccro JJ (200) Wideband cancellation of interference in a GPS receive array. IEEE Trans AES 36(2):549–564
6. Zhang X (2004) Matrix analysis and applications. Tsinghua University press, Beijing, p 9
7. Guo Y, Zhang EY (2007) Interference suppression in GPS receiver using space-tine subspace projection techniques. J Commun 5:62–66
8. HayKin S (2001) Adaptive filtertheory. 4th edn. Prentice-Hall, NJ
9. Ricks DC, Goldstein JS (2000) Efficient architectures for implementing adaptive algorithms. In: Proceedings of the 2000 applications symposium, pp 29–41
10. Guo Yi, Zhang E, Shen R (2007) Application of subspace tracking technique in interference suppression of GPS space-time receiver. J Astronaut 28(5):100–104
11. Goldstein JS, Guerci JR, Reed IS (2000) Advanced concepts in STAP. IEEE international radar conference, pp 699–704
12. Kohko R (1998) Spatial and temporal communication theory using adaptive antenna array. IEEE/ACM Pers Commun-Mag Nomadic Commun Comput 2:28–35

Chapter 52
A New SIMD Correlator Algorithm for GNSS Software Receivers to Process Complex IF Data

Liangchun Xu, Hongping Zhang, Wenfei Guo and Di Zhang

Abstract GNSS software receivers implement digital signal processing algorithms on programmable software platform (such as PC, DSP), which traditional ones execute on dedicated hardware. It is highly flexible, convenient for debug and could be adapted to a platform for GNSS algorithm research. However, the computation of down shifting of the GNSS signal to baseband and correlation with the locally generated ranging code is too expensive for normal GNSS software receivers to work in real time. The computational cost could be reduced by utilizing Single Instruction Multiple Data (SIMD) operations. The article proposes a new SIMD correlator algorithm for complex GNSS IF signal processing on x86 processors. It firstly demonstrates why normal GNSS software receivers couldn't achieve real-time processing by using Single Instruction Single Data (SISD) operations and the improvements achieved by using existing SIMD algorithms; then proposes a new SIMD correlator algorithm, outlines its implementation principle and compares it with the SISD and the existing SIMD algorithms. Performance gains achieved via the new SIMD algorithms are then demonstrated in an analysis. Finally, the implementation and experimental results of the new algorithm are presented. The experimental results show that compared to the SISD and existing SIMD algorithms the new SIMD algorithm can effectively reduce the computation of down shifting of the GNSS signal to baseband and correlation with the locally generated ranging code.

Keywords GNSS software receivers · SIMD · CPU pipelines · Intel AVX

L. Xu (✉) · H. Zhang (✉) · W. Guo · D. Zhang
GNSS Research Center of Wuhan University, Wuhan, China
e-mail: maiar@whu.edu.cn

H. Zhang
e-mail: hpzhang@whu.edu.cn

J. Sun et al. (eds.), *China Satellite Navigation Conference (CSNC) 2013 Proceedings*, Lecture Notes in Electrical Engineering 243,
DOI: 10.1007/978-3-642-37398-5_52,

52.1 Introduction

GNSS software receivers are built on PC in a compiled programming language, such as C or C++, it's developed for testing new GNSS related algorithms that used to be modified on the hardware found in a traditional receiver [1].

Though GNSS software receivers are convenient for debugging, it cannot work in real time without any optimization on a generic x86 processor. The most time-consuming part of GNSS software receivers is the correlator. Traditional GNSS Receivers implement the correlation algorithm on an FPGA which performs much faster than x86 processors. A more detailed analysis of the reason why GNSS software receivers cannot operate in real time can be seen in Heckler and Garrison's [1] paper which presents a SIMD correlator library for real GNSS IF data processing. The library contains the functions of vector addition, multiplication and their loop unrolling version. And a SIMD library for GNSS software receivers to process with complex IF data has also been demonstrated. Heckler's method is simple and easy to understand. However, it's not the most efficient one and implemented with SSE code. In this article firstly an efficient algorithm is designed for the correlation of complex IF data. Then the AVX code implementation of the algorithm and its loop unroll version are presented. Lastly there is a comparison of the processing time between the software GNSS receiver with the new SIMD library and the one with Heckler's code.

52.2 Demand Analysis

When complex GNSS IF data are put into a conventional correlator, firstly the digital IF data are stripped of the carrier with Doppler by mix the replica carrier generated by local carrier numerically controlled oscillator (NCO). The outputs are in-phase (i) and quadra-phase (q) sampled data. Then i and q signals are stripped of code by multiply the replica code generated by local code NCO. In order to keep carrier and code loop tracking, the i and q signals are correlated with early, prompt, and late replica code. Every correlation should be integrated until the code phase accumulates a whole cycle. Figure 52.1 illustrates a block diagram to demonstrate how GNSS software receivers work with the input complex IF data. Furthermore, the dashed box shows the bound of the correlator.

Assuming the input complex IF data $S_{IF} = a + b * k(k^2 = -1)$, local carrier NCO generates $\cos\theta$ and $\sin\theta$ for wiping off the carrier of the signal, the output phase result $S_{iq} = i + q * k(k^2 = -1)$. The relationships among the variables above can be described by the following equation [2]:

$$\begin{aligned} i &= a * \cos\theta + b * \sin\theta \\ \mathrm{q} &= \mathrm{b} * \cos\theta - \mathrm{a} * \sin\theta \end{aligned} \tag{52.1}$$

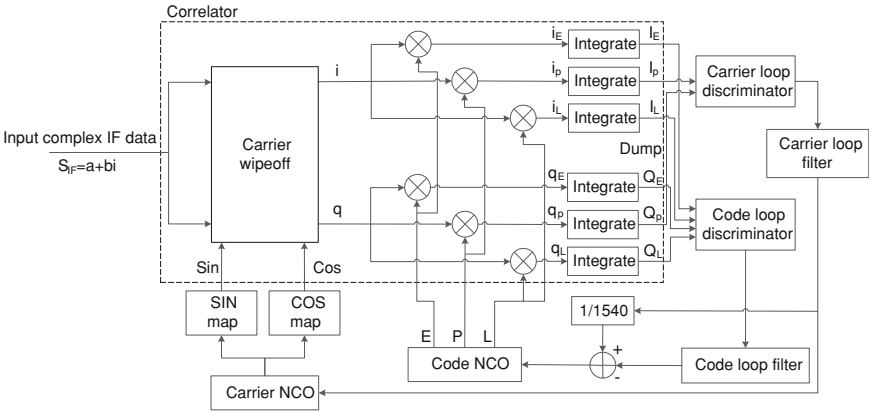

Fig. 52.1 The correlator in a typical software GNSS receiver

It can be abstracted into a complex multiplication. Then (52.1) can be rewritten as follows:

$$S_{iq} = S_{IF} * (\cos\theta - \sin\theta * k), \quad k^2 = -1 \tag{52.2}$$

The work of stripping off the code and integrating the correlation result can be easily achieved by real multiplication and addition. So the problem is simplified to how to design a SIMD complex multiplication algorithm for the correlator of software GNSS receivers.

52.3 Algorithm Design

The complex multiplication could be divided into a combination of real multiplication and addition according to (52.1). The design of algorithm varies. Before presenting the detailed algorithm, the SIMD instructions utilized in this article would be introduced.

52.3.1 Intel Advanced Vector Extensions

Intel AVX introduces support for 256-bit wide SIMD registers (YMM0-YMM7 in operating modes that are 32-bit or less, YMM0-YMM15 in 64-bit mode) [3]. It is a 256-bit floating-point instruction set with enhancement of up to 2X performance gain relative to 128-bit streaming SIMD extensions. Intel AVX only supports operations of floating-point arithmetic. Operations of integer arithmetic will be supported in the next generation of AVX named AVX2 (Fig. 52.2).

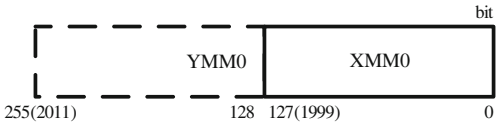

Fig. 52.2 A register of AVX

52.3.2 Complex Multiplication Algorithm Design

AVX supports a minimum of 32-bit wide floating-point operations. However, the imaginaries and reals of GNSS IF data are integer numbers. There must be a cast from integer to floating-point type. For Intel C++ compiler, the float type is 32-bit wide. The real and imaginary of a complex can be defined as a float type. Then a complex is totally 64-bit wide.

As the register of AVX is 256-bit wide, a register of AVX is able to contain 4 complex numbers. To complete a complex multiplication in full use of the register, there should be two complex arrays with length of 4 filling in. Assuming A0-A3, B0-B3 are the reals, imaginaries of 1st array and a0-a3, b0-b3 are the reals, imaginaries of 2nd array, the procedure of a complex multiplication in registers can be divided into five steps [4]:

(1) Load complex numbers from two complex arrays to YMM0, YMM1 (Fig. 52.3).
(2) Duplicate imaginaries of array 2 from YMM0 to YMM2 and reals of array 2 from YMM0 to YMM0 as follows (Fig. 52.4).
(3) Multiply array1 times reals of array 2. The operation of registers is a 32-bit wide multiplication of YMM0 and YMM1 with the result stored in YMM0 (Fig. 52.5).
(4) Shuffle to reverse order of array 1, multiply reversed array 1 times imaginaries of array 2. Firstly reverse the order of YMM1, then store the result of multiplying YMM1 times YMM2 in YMM2 (Fig. 52.6).

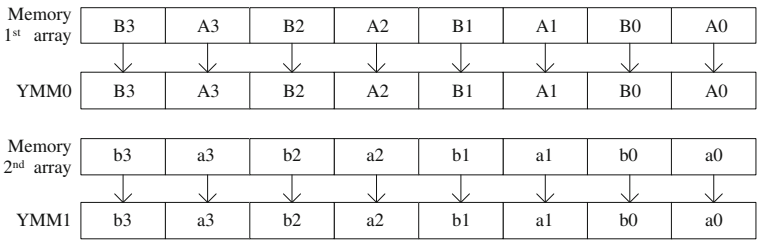

Fig. 52.3 Load data to YMM0, YMM1 form array 1 and array 2

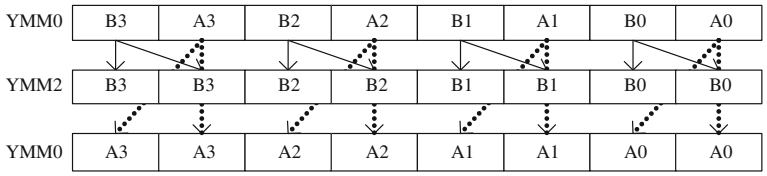

Fig. 52.4 Duplicate the imaginaries and reals of array 2

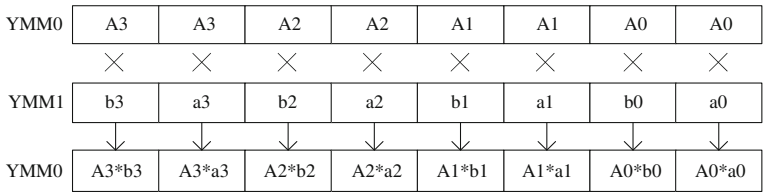

Fig. 52.5 Multiply array1 times reals of array 2

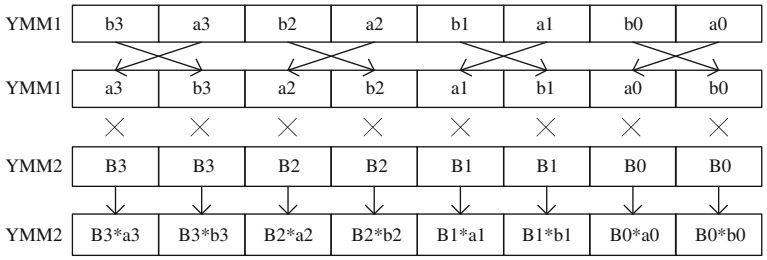

Fig. 52.6 Shuffle to reverse order of array1 and then multiply it times imaginaries of array 2

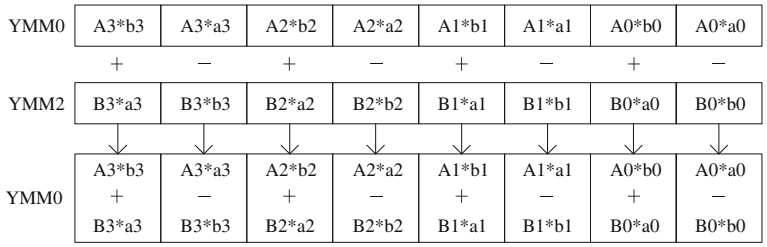

Fig. 52.7 Output the array result

(5) Calculate the product of reals and the product of imaginaries. It can be achieved by utilizing the instruction of a 32-bit wide cross addition and subtraction (Fig. 52.7).

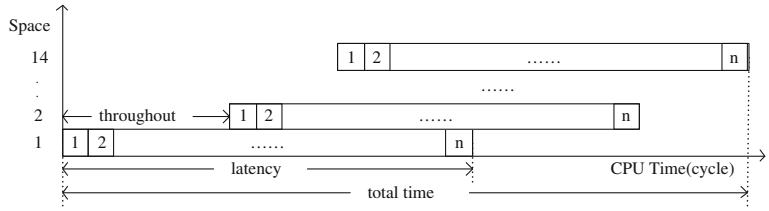

Fig. 52.8 CPU pipelines

52.3.3 Pipelines Version

To complete complex multiplication more efficiently, the CPU pipelines must be utilized. Modern processors break operations into multiple micro operations (μ-ops). Each micro operation has a given latency and throughput. The latency is how many cycles are required to fully complete the instruction, whereas the throughout is how many cycles are required to wait before introducing the next μ-op in the pipeline [1]. Figure 52.8 shows how CPU pipelines work.

For the algorithm proposed above, each process of complex multiplication consumes 3 registers. There are 8 registers in the mode of x86. Two pipelines can be manufactured with 6 registers. One of the remaining two registers can be used for storing the accumulation result.

52.3.4 Time Complexity Analysis

The following gives a simple time complexity analysis of the algorithm. Due to the presence of AVX registers, the complex multiplication can be done four by four. Each complex contains two single float-point numbers, which results in an 8X gain in performance over the compiler generated code. Two pipelines would contribute less than 2X gain in performance. So the whole design of algorithm is expected to achieve 16X gain in performance over the compiler generated code.

52.4 Code Implementation and Test

The code is implemented on a PC with 3.4 GHz, 4 CPUs processor and 8 GB DDR3 RAM. Figure 52.9 demonstrates the performance gains realized by the new algorithm and Heckler's algorithm. The benchmark is created by repeatedly multiplying two vectors of length N and measuring the time required to perform the operation. The lengths are between 3.6e7 and 4.6e7. Assuming the performance gain of raw C/C++ code is 1.

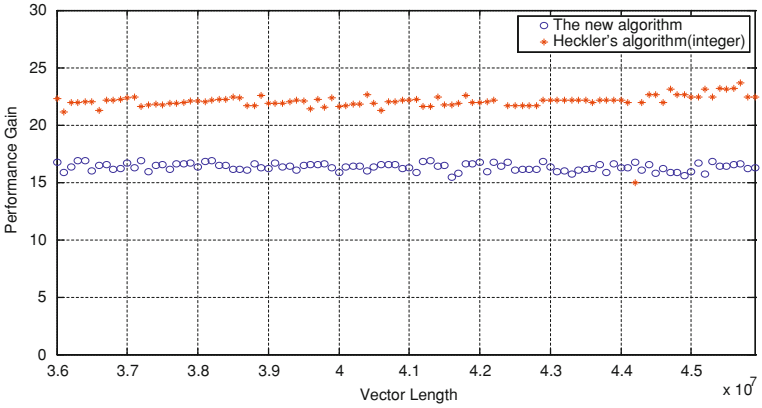

Fig. 52.9 The comparison of the new algorithm and Heckler's algorithm (integer version)

From Fig. 52.9, the new algorithm's performance gain isn't larger than that of Heckler's. That's because the implementation of the new algorithm is based on float type, while Heckler's algorithm is implemented on a short integer type. The latency of float-point arithmetic operations is much larger than that of the same operations in integer arithmetic (e.g. addps and paddd). So there is a comparison between the implementation of the new algorithm and that of Heckler's algorithm which is rewritten in AVX based on float type (Fig. 52.10).

Now the new algorithm has produced a higher performance gain than Heckler's algorithm under the same experimental conditions. The detailed statistics are put into Table 52.1.

The new algorithm's average improvement is 16.20X. It's almost twice the performance gain produced by Heckler's algorithm. However, because AVX

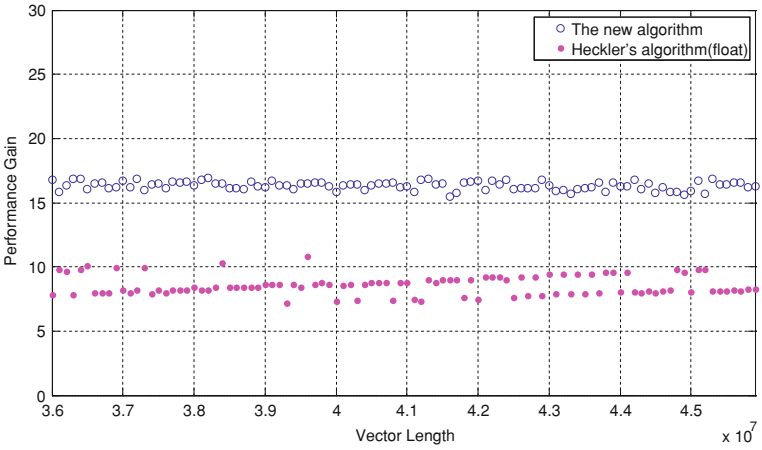

Fig. 52.10 The comparison of the new algorithm and Heckler's algorithm (float-point version)

Table 52.1 Summarize the test results of different methods

Processor	C++ compiler	Algorithm	Average processing time(s)	Average improvement
Core i7-3770 k (Ivy Bridge, 3.4 GHz) 8 GB RAM	Intel C++ 13.0	Raw c/c++ code	0.67822	1X
		Heckler's algorithm (integer)	0.02979	22.77X
		Heckler's algorithm (float)	0.08144	8.33X
		The new algorithm	0.04187	16.20X

doesn't support integer arithmetic operations now, the implementation of Heckler's algorithm based on short integer type achieves the highest average improvement.

52.5 Conclusion and Future Work

Heckler's algorithm with an integer arithmetic implementation performs best so far. The new algorithm proposed in the article has the minimum time complexity while it can only be achieved with float-point arithmetic.

The next generation of AVX named AVX2 would be introduced with the next generation of Intel processors in 2013. Its reference has been published for developers [3]. From the Intrinsics Guide for Intel Advanced Vector Extensions 2, the operations of integer arithmetic are introduced. Furthermore, AVX2 supports 16-bit wide integer operations, which is expected to finish a multiplication of 8 complex numbers (the reals and imaginaries can be defined as short type) in a single process. Despite the gap between the performance of integer and float-point arithmetic operations, the decrease in the operable bit width is expected to gain a 2X performance than the float-point version.

Fused Multiply Add (FMA) is an instruction set which is going to be introduced with AVX2. It performs a set of SIMD multiply-add computation on packed double-precision floating-point values [4]. For the design of a correlator, the multiplication and addition can be fused into one operation. The computing time of a correlator would be further reduced.

References

1. Heckler GW, Garrison JL (2006) SIMD correlator library for GNSS software receivers. GPS Solutions 10:269–276
2. Xie G (2009) Principles of GPS and receiver design (in Chinese). Publishing House of Electronics Industry, Beijing
3. Intrinsics Guide for Intel Advanced Vector Extensions2—v2.6.4. Available from http://software.intel.com/zh-cn/avx

4. How to optimize your software via AVX (In Chinese: 如何适用即将面世的英特尔高级矢量扩展指令集优化您的软件).Available from http://software.intel.com/zh-cn/avx
5. Intel 64 and IA_32 architectures software developer's manual. Available from http://software.intel.com/zh-cn/avx
6. Intel architecture instruction set extensions programming reference. Available from: http://software.intel.com/zh-cn/avx
7. Microsoft Corporation (2012) C++ language reference, inline assembler. Available from: http://msdn.microsoft.com/zh-cn/library/vstudio/ddz712yw.aspx
8. Charkhandeh S, Petovello MG, Watson R, Lachapelle G (2006) Implementation and testing of a real-time software- based GPS receiver for x86 processors. In: Proceedings of ION navigational technical meeting, Monterey, CA, 18–20 January 2006

Chapter 53
Improved Satellite Selection Algorithm Based on Carrier-to-Noise Ratio and Geometric Dilution of Precision

Zhong-liang Deng, Hui Dong, Zhong-wei Zhan, Guan-yi Wang, Lu Yin and Yue Xi

Abstract Based on the traditional fuzzy arithmetic and concerned about the influence of carrier-to-noise ratio (C/N0) to positioning accuracy, this paper proposes an improved satellite selection algorithm based on C/N0 and geometric dilution of precision (GDOP). Positioning accuracy is mainly influenced by GDOP and the error of pseudo range measurement, and C/N0 is one of the primer factors influence the latter one. Both the error of pseudo range measurement and GDOP should be concerned in order to decrease the positioning error, instead of separate consideration. Traditional satellite selection algorithms, such as the algorithm of minimum GDOP, the algorithm of max volume of tetrahedron and so on, they just concentrated on the influence of GDOP and ignore the error of pseudo range measurement. This paper chooses the first two satellites with the highest and lowest elevation angle based on the principle of minimum GDOP, and then consider C/N0 and the satellite geometric distribution both when choosing the others. Use fuzzy satellite selection algorithm based on entropy method to weight the two factors. Pick out the satellite combination with smaller GDOP and higher C/N0 in the end. Compare and analyze the two results separately get from the method proposed in this paper and the traditional one, the simulation result shows that the improved satellite selection algorithm that considered GDOP and C/N0 both, compared to the traditional ones, can lead to smaller positioning error and better positioning result.

Keywords C/N0 · GDOP · Positioning error · Entropy method · Fuzzy arithmetic

Z. Deng · H. Dong (✉) · Z. Zhan · G. Wang · L. Yin · Y. Xi
Beijing University of Posts and Telecommunications, Beijing 100876, China
e-mail: 742880734@qq.com

J. Sun et al. (eds.), *China Satellite Navigation Conference (CSNC) 2013 Proceedings*, Lecture Notes in Electrical Engineering 243,
DOI: 10.1007/978-3-642-37398-5_53, © Springer-Verlag Berlin Heidelberg 2013

53.1 Introduction

Global Positioning System is radio navigation system based on satellite, characterized by pluripotency, globalization, all-weather, continuity and instantaneity, which has been widely used in both military and civil fields.

By the end of 1994, the layout of GPS consisted of 24 satellites had been completed, which can reach up to 98 % of global covered ratio; at present, receiver can use ephemeris of 32 satellites to accomplish positioning. So, if use all these ephemeris to calculate, not only the accuracy of positioning would not improve obviously but the consumption of time would increase largely, influence the performance of fast positioning. How to choose the combination of satellites which has the highest accuracy of positioning fast and effectively, makes a lot sense to improve the whole performance of software receiver.

There are mainly two factors that influence the accuracy of positioning: measurement error of pseudo range and GDOP. Traditional algorithm of satellite choosing, such as the algorithm of minimum GDOP, the algorithm of max volume of tetrahedron and so on, they just concentrated on the influence of GDOP and ignore the error of pseudo range measurement. This paper chooses the first two satellites with the highest and lowest elevation angle based on the principle of minimum GDOP, and then consider C/N0 and the satellite geometric distribution both when choosing the others. Use fuzzy satellite selection algorithm based on entropy method to weight the two factors. Pick out the satellite combination with smaller GDOP and higher C/N0 in the end.

53.2 Factors Influenced the Accuracy of Positioning

53.2.1 Geometric Dilution of Precision (GDOP)

GDOP measures the geometric distribution of the satellites, it represents space geometric distribution performance between users and satellites. If see the pseudo range measurement error factor as an independent and constant error, variances are all σ_0, then the positioning error can be expressed as: $\delta_{PVT} = GDOP * \sigma_0$, so GDOP plays a part in magnifying δ_{PVT}.

In order to improve the accuracy of positioning, we should choose the combination of satellites with lower GDOP, that means the satellite with larger space distribution range and better geometric distribution with users is better.

Document [1] proves that with the increase of satellites used in the calculation of positioning, GDOP decreased largely, and this trend tends to be un-conspicuous when the sum of satellites comes to 6.

53.2.2 Measurement Error of Pseudo Distance

In order to analyze the influences of all kinds of errors to the accuracy of positioning, a basic assumption is usually made: attribute the errors to the pseudo distances of every satellite and see them as equivalent error of pseudo distance values. The main error source include: the delay caused by atmosphere, noise and disturbance of receiver, deviation of multipath and hardware. Typical estimation of UERE listed in Table 53.1.

The error sources listed above influence the accuracy of positioning directly in different degree, the errors from user are much larger than that from space and control, and that would badly influence C/N0, which is the ratio between the power of receiver and noise, the bigger C/N0 is, the better signal received. This paper is mainly discussed the influence to the accuracy of positioning that C/N0 made.

Document [2] proves that the bigger SNR is, the smaller error of positioning is; on the contrary, the same conclusion can be got. On the other hand, document [3] gives a relation between C/N0 and SNR:

$$SNR = C/N0 * T_{coh}$$

Here, T_{coh} is coherent integration time. So the conclusion is: the bigger C/N0 is, the smaller error of positioning is, the higher accuracy is; the smaller C/N0 is, the bigger error of positioning is, the lower accuracy is.

53.3 Algorithm of Choosing Satellites Based on Entropy

53.3.1 Analysis of Algorithm

Based on the number of satellites of GPS that can be seen in BUPT, which mostly ranges from 6 to 12, according to the conclusion made before, 6 is the best choice.

From document [4] we can see that, the higher the top satellite (with biggest elevation) is, the smaller GDOP is; the lower the bottom satellite (with lowest elevation) is, the higher accuracy of positioning is. So, at first, we choose the

Table 53.1 Typical estimate of UERE of standard positioning service

Section source	Error source	1σ error (m)
Space/control	Broadcast clock	1.1
	L1 P(Y)-L1 C/A group delay	0.3
	Broadcast ephemeris	0.8
User	Ionospheric delay	7.0*
	Tropospheric delay	0.2
	Noise of receiver	0.1
	Multipath	0.2
System UERE	Total (RSS)	7.1*

satellite with biggest elevation to be the first one and the one with second biggest elevation be the next, the third satellite is the one with lowest elevation. After that, we use entropy method to balance the ratio among elevation, azimuth and C/N0 in order to choose the next three satellites.

53.3.2 Using Entropy Method to Weight

(1) Make sure the factors:

$$\text{Factors set}: E = [x1 \quad x2 \quad x3]$$

Here, $x1$ represents azimuth angle Al, $x2$ represents elevation angle E and $x3$ represents C/N0.

(2) Make sure the judges:

$$F = [f_1 \quad f_2 \quad \cdots \quad f_m]$$

Here, $f_i = [Al_i \quad E_i \quad C/N0_i]^T$, m represents the number of satellites that can be seen.

(3) Judge every factors and get fuzzy vectors:

$$R_1 = [CAl_1 \quad CAl_2 \quad \cdots \quad CAl_m]$$

$$R_2 = [CE_1 \quad CE_2 \quad \cdots \quad CE_m]$$

$$R_3 = [CN0_1 \quad CN0_2 \quad \cdots \quad CN0_m]$$

$$R = \left[R_1^T \quad R_2^T \quad R_3^T\right]^T$$

$$CAl_i = Al_3 + 90^\circ * (i-3) - Al_i,\ CE_i = E_i - E_3,\ CN0_i = C/N0_i - C/N0_{\min}, \quad i \in (4,5,6).$$

$CAl_i\ (i = 4,5,6,)$ represents adding 90°, 180° and 270° respectively to the third azimuth that had been chosen before. Then minus it with last azimuths, choose the one with bigger difference which means more uniform distribution. For the index which is the bigger the better:

$$R_1 = \frac{Al_{1j} - \min\{Al_{1j}\}}{\max\{Al_{1j}\} - \min\{Al_{1j}\}}$$

$CE_i\ (i = 4,5,6,)$ represents the minus difference between the last elevations and the third one, the smaller the value is, the little elevation for chosen is. For the index which is the smaller the better:

$$R_2 = \frac{\max\{E_{2j}\} - E_{2j}}{\max\{E_{2j}\} - \min\{E_{2j}\}}$$

$CN0_i$ $(i = 4, 5, 6,)$ represents the minus difference between the last values of C/N0 and the smallest one, the bigger the value is, the better signal the satellite owns. So the same as above, for the index which is the bigger the better:

$$R_3 = \frac{CN0_{3j} - \min\{CN0_{3j}\}}{\max\{CN0_{3j}\} - \min\{CN0_{3j}\}}$$

(4) Define entropy

In the case of n evaluated objects and m indexes, the entropy of the index ranked I is defined:

$$H_i = -k \sum_{j=1}^{n} f_{ij} \ln f_{ij}, \quad i = 1, 2, \ldots, m$$

Here, $f_{ij} = r_{ij} \Big/ \sum_{j=1}^{n} r_{ij}$, $k = 1/\ln n$, when $f_{ij} = 0$, let $f_{ij} \ln f_{ij} = 0$.

(5) Use "Entropy Method" to stricter weight set:

$$P = [\, w_1 \quad w_2 \quad w_3 \,]$$

Here, $w_i = \frac{1 - H_i}{m - \sum_{i=1}^{n} H_i}$, $0 \le w_i \le 1, \sum_{i=1}^{n} w_i = 1$

(6) Fuzzy change:

$$Q = P \bullet R$$

Choose the one with bigger Q value in the end.

53.4 Analysis of Simulated Results

On the basis of theoretical analysis above, this paper uses the simulated tool of MATLAB to test and verify the data got from satellite signal simulator in the two different conditions: results got from traditional and modified method on the condition that the C/N0 value of every satellite differs less than 2db; use satellite signal simulator to minus 5db from one of the satellites chosen from the smallest GDOP combination, then compare the performances of two different method again.

53.4.1 Result of Un-Conspicuous Difference of C/N0 Values

At the observed point, the number of satellites that can be seen is 12, the elevations, azimuths and C/N0 values are listed below:

PRN	Elevations	Azimuths	C/N0
1	7.100574	317.1562	45.6889
5	68.42472	249.8318	45.1346
9	14.60859	53.85035	45.2436
10	51.12814	174.5211	44.9057
12	41.17076	64.32487	44.7321
15	59.03869	81.71412	45.4117
18	31.44686	162.0777	44.4217
25	53.54906	131.2996	45.5653
27	78.37755	340.0934	45.6102
28	50.48001	131.3614	45.7455
31	34.85086	245.0932	45.6404
32	5.120772	319.7330	45.6319

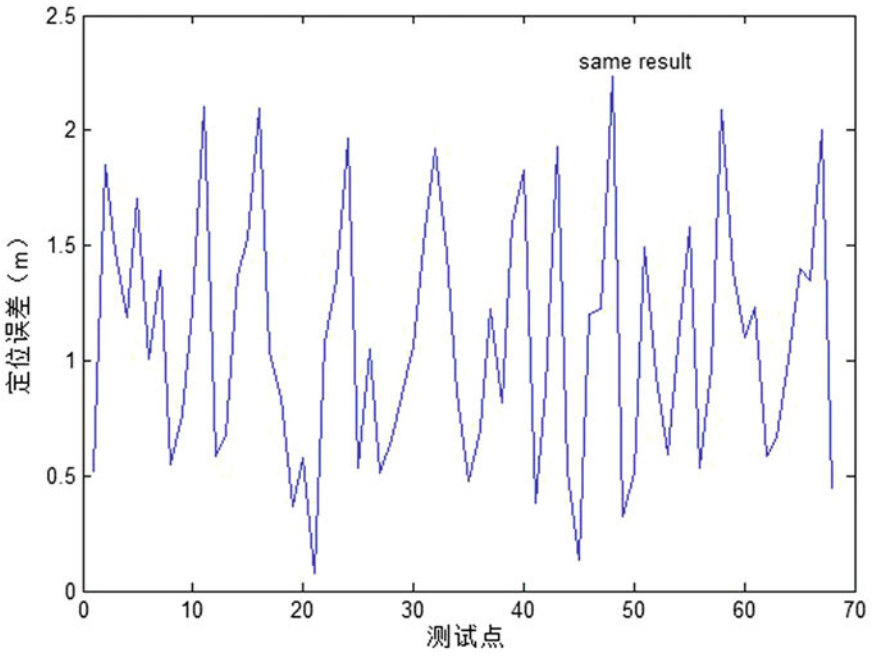

Fig. 53.1 Error line of positioning

Make simulation of the method mentioned in document [5], we can get the combination of satellites with smallest GDOP, this method cut down the cost of calculation, results are listed below, which are the same to the results got from the method mentioned in this paper (Fig. 53.1):

Satellite combination (PRN)	GDOP	Mean value of C/N0	Error of positioning (m)
1, 5, 18, 27, 31, 32	2.54576	45.3546	1.0914

53.4.2 Result of Conspicuous Difference of C/N0 Values

Use satellite signal simulator to minus 5db from one of the satellites chosen from the smallest GDOP combination (here, we choose PRN 18), data and the simulation listed below:

PRN	Elevations	Azimuths	C/N0
1	7.100574	317.1562	45.6889
5	68.42472	249.8318	45.1346
9	14.60859	53.85035	45.2436
10	51.12814	174.5211	44.9057
12	41.17076	64.32487	44.7321
15	59.03869	81.71412	45.4117
18	31.44686	162.0777	39.4217
25	53.54906	131.2996	45.5653
27	78.37755	340.0934	45.6102
28	50.48001	131.3614	45.7455
31	34.85086	245.0932	45.6404
32	5.120772	319.7330	45.6319

	Satellite combination (PRN)	GDOP	Mean value of C/N0	Error of positioning (m)
Traditional method	1, 5, 18, 27, 31, 32	2.5457	44.5212	1.8428
Modified method	1, 5, 9, 27, 31, 32	3.0927	45.4916	1.2916

In Fig. 53.2, red-real line represents the errors of positioning got from the traditional algorithm, blue-broken line represents the errors of positioning got from the modified method. We can see that use the modified method, which blends C/N0 in the index that valued by entropy, to choose the combination of satellites can lead to bigger mean C/N0 value and better effect of positioning which improved by about 30 %, although GDOP is bigger than the traditional one.

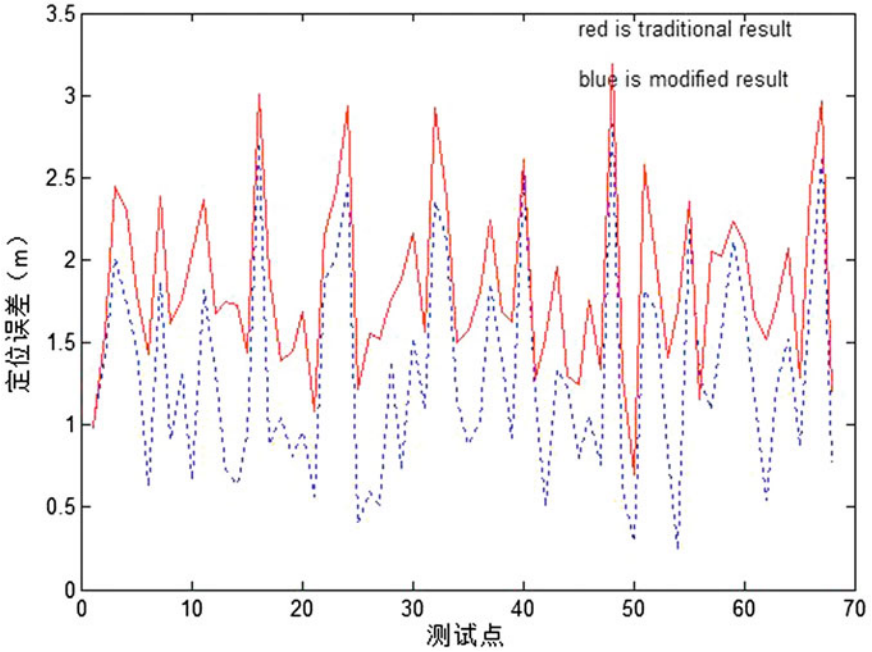

Fig. 53.2 Error line of positioning

53.4.3 Compare and Analyse

Compare and analyze the results above, we can get the conclusions:

(1) The final result of two methods are the same under the condition that the C/N0 value of every satellite differs less than 2db;
(2) When C/N0 value of one or more satellites differs largely (>2db) than the others, although the GDOP still is the smallest got from the traditional method, if the combination contains the satellite of low C/N0 value, the final error of positioning would be large. On the contrary, the accuracy of positioning calculated through the satellites chose by the modified method is the highest even if the GDOP is not the smallest, because the C/N0 value is higher.

For the case of multi-system, the number of satellites grows bigger, if spreading this method mentioned here to this situation, not only the cost of calculation would be definitely cut down, the accuracy of positioning would be guaranteed powerfully as well.

53.5 Conclusion

This paper mainly discussed the influence of GDOP and C/N0 on positioning accuracy respectively from the angel of positioning error, and proposed a modified method of choosing satellites, which used entropy method to weight both GDOP and C/N0, on the basis of traditional fuzzy method. The simulated result proves that: this modified method not only owns the traditional advantage of lower cost of calculation, but also the final effect of positioning is improved obviously.

References

1. Cong L, Tan Z (2008) Satellite selection algorithm to improve precision and real time performance of GPS positioning. Coll Electron Inf Eng 30(10):1914–1917
2. Wang M, Lu L (2007) GPS positioning error evaluation based on fuzzy algorithm. Department of Automation, Beijing Institute of Technology, Beijing, 100081, China
3. Yu F (2011) Research on Satellite Navigation Receiver C/N0 Estimation Method. Hebei Satellite Navigation Technology and Equipment Engineering Technology Research Center, Shijiazhuang, Hebei, 050081, China, Xidian University, Xi'an Shaanxi, 710071, China
4. Yuan J, Luo J, Yue X (2003) Satellite navigation system: principle and application. China Aerospace Press, Beijing
5. Zhang L, Deng Z, Yang L (2011) An improved satellite selection algorithm based on fuzzy comprehensive evaluation method and the entropy method for determining the weight of evaluation indicators. In: Proceedings of IEEE IC-BNMT, 2011

Chapter 54
Design and Implementation of a Real-Time Three-Frequency COMPASS Software Receiver

Weihua Xie, Jun Zhang, Chao Xie and Qian Wang

Abstract GNSS software-defined receiver is of importance in satellite navigation system, especially in the fields of receiver design and satellite navigation system scheme validating. The general scheme of COMPASS software receiver has been proposed, and the main software functional modules were designed using XML language. A real-time software receiver with 12 channels on PC platform has been implemented, which can process COMPASS B1/B2/B3 C (civil) code signal. The receiver can be capable of post-processing datasets from collection hardware or real-time processing data stream through PCI bus interface. A lot of performance improvement approaches have been proposed to enhance the speed of the software receiver, which include computational platform choosing, acquisition and correlator arithmetic optimization, program code optimization with SIMD instructions on CPU and CUDA instructions on GPU. Using this methods, the software receiver can reach real-time processing capacity under 80 MHz sampling rate and 2 bit quantization conditions. The positioning results show that the software receiver's three-dimensional positioning accuracy is superior to 10 m under 95 % confidences.

Keywords COMPASS navigation system · Software receiver · Real time · XML language · Speed optimization

54.1 Introduction

Software-defined radio receiver (SDR) is a concept for transceivers in which the signal processing is accomplished via a programmable general-purpose microprocessor or digital signal processor (DSP), as opposed to an application-specific

W. Xie (✉) · J. Zhang · C. Xie · Q. Wang
Beijing Satellite Navigation Center, Beijing, China
e-mail: 18901080599@163.com

J. Sun et al. (eds.), *China Satellite Navigation Conference (CSNC) 2013 Proceedings*, Lecture Notes in Electrical Engineering 243,
DOI: 10.1007/978-3-642-37398-5_54,

integrated circuit (ASIC). A software receiver differs from a hardware receiver by performing correlations in software running on a general purpose microprocessor. It can afford batch data processing options that are not available in hardware implementations. New frequencies and new pseudo-random number (PRN) codes can be used simply by making software changes. SDR are not only research tools for the development and test of new navigation and positioning algorithms. The flexibility of software architectures enables them to record several pieces of information that are not limited to position and velocity. Correlator and discriminator outputs, frequency and phase lock indicators and several synchronization messages are just a few examples of the parameters that a software receiver makes available to users and researchers. And the software receiver could be reprogrammed to adjust a new navigation system, which provides an added benefit from the use of the software radio architecture. It played an important role in GSSF (Galileo System Simulation Facility) and GSTB (Galileo Satellite Test Bed). Along with the decrease of the required processing time, the high configurability, high development speed, low cost software receiver is obtaining more people's favors.

In this paper, a complete COMPASS software receiver has been developed using C/C ++ and C# language code in Visual Studio 2010 environment. It can be used for acquisition, tracking, and calculating position for COMPASS B1,B2 and B3 civil code signals.

54.2 Architecture of Software Receiver

The architecture of software receiver is shown in Fig. 54.1. It consists of eight modules, which include an antenna, a RF front-end, acquisition module, tracking module, correlator module, navigation message decoding, position calculation module and GUI module. The antenna and RF front-end devices are the only hardware devices of the system. The RF front-end device is necessary to down convert the COMPASS signal to an intermediate frequency (IF), sample the IF signal and digitize it [1–5]. The present CPU capacity is still unable to process the COMPASS signal directly from the antenna in completely software-based

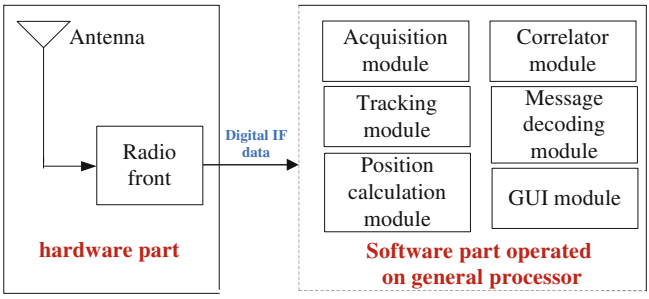

Fig. 54.1 Architecture diagram of software receiver

approach. Thus a RF front-end device is still necessary. In conventional hardware-based receiver, the six modules in the right textbox in Fig. 54.1 [6] are implemented in an IC chip and hence the user does not have a free access to the algorithms built inside the chips. In software-defined receiver, these blocks are fully implemented using high level programming languages and hence the user has complete control over the algorithms. This is the main difference between the software receiver and a conventional hardware receiver.

54.3 General Scheme of COMPASS Three-Frequency Software Receiver

54.3.1 Components of COMPASS Three-Frequency Software Receiver

The components of COMPASS three-frequency software receiver are shown in Fig. 54.2. It includes three parts: three-frequency antenna, digital IF signal sampling card and PC with graphic card. The function of three-frequency antenna is to receive COMPASS B1, B2 and B3 signals. The function of RF (radio frequency) is to amplify and filter the RF signal and down convert to analog IF (immediate frequency) signal. The function of sampling card is to sample and digitize the analog IF signal and transfer digital data stream to PC through PCI bus interface.

54.3.2 Functional Module Design of Software Receiver

The software design of COMPASS software receiver is divided into two layers, as showed in the Fig. 54.3. One is user interface layer and the other is arithmetic layer. The function of client layer is to interface to user, through which users can configure all kinds of receiver's parameters. And all kinds of results can be displayed on it. The function of arithmetic layer is to finish all kernel algorithms. The benefit of this two-layer software design method is that user interface and kernel can be developed and upgraded separately.

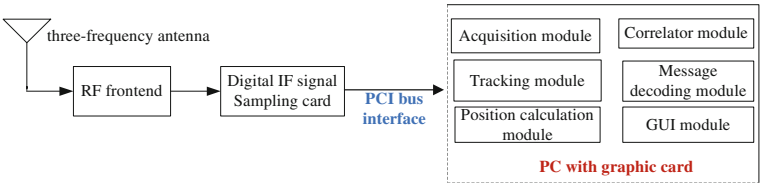

Fig. 54.2 Components of COMPASS three-frequency software receiver

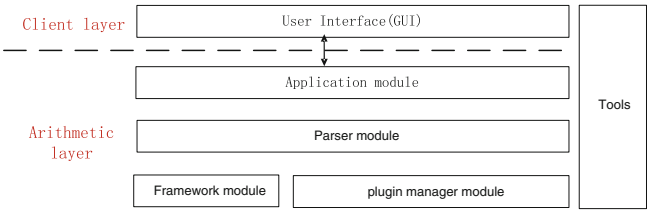

Fig. 54.3 Software design of COMPASS software receiver

54.3.2.1 Design of User Interface Module

User interface module consists of two parts: design of interface display and design of user configuration. Design of interface display mostly shows all kinds of information, such as receiver channel information, signal C/No information, on-viewed satellite information, position information etc. Design of user configuration mostly includes all kinds of setup parameters in each module of software receiver.

54.3.2.2 Design of Framework Module

Framework module mainly includes receiver component (denoted as IReceiver), as showed in Fig. 54.4. IReceiver component is an abstract class of receiver, which consists of four components: channel component (denoted as IChannel), channel allocated component (denoted as IChannelAllocator), navigation computation component (denoted as INavigator), satellite status tracking component (denoted as ISatelliteTracker) and receiver clock component (denoted as IRcvclk). IChannel component is an abstract class of receiver channel, the function of which is to process the signal acquisition and tracking operation. It consists of five components: signal detection component (denoted as IDetector), signal tracking component (denoted as ISignalTracker), signal correlation component (denoted as ICorrelator), bit synchronization component (denoted as IBitSyncer) and frame synchronization component (denoted as IFrameSyncer).

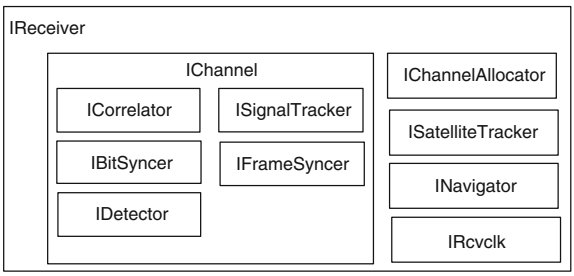

Fig. 54.4 Framework module design of software receiver

```
<receiver ionospheric = "true" troposphere = "true">
     <channel id="0" type="gps" carrierFrequency="4.309e6" >
          <detector class="GpsDetector" doppler="10e3" />
          <correlator class="GpsCorrelator" plugin="Gps"/>
          <signal-tracker class="GpsSignalTracker" >
               <carrier-tracker class="DefaultPhaseLockLoop" bandwidth="15">
                    <discriminator class="DefaultCarrierDiscriminator" type="0" />
               </carrier-tracker>
               <code-tracker  class="DefaultPhaseLockLoop" bandwidth="0.5">
                    <discriminator class="DefaultCodeDiscriminator" type="0" />
               </code-tracker>
          </signal-tracker>
          <bit-syncer class="GpsBitMatcher" />
          <frame-syncer class="GpsFrameMatcher" />
     </channel>
     <navigator class="GpsNavigator" />
     <clock sample-frequency="5.714e6" tic="0.100" navigation-interval="1" />
     <ins-auxiliary class="InsAuxiliary" />
</receiver>
```

Fig. 54.5 Description of receiver structure using XML

54.3.2.3 Design of Parser Module

The function of parser module is to parse the configuration file using XML (Extensible Markup Language). XML is adopted to describe the receiver structure in this paper. Figure 54.5 is an example to describe GPS receiver structure using XML. The 'receiver' is the root node and corresponding to 'IReceiver' component in Fig. 54.4, and the 'channel' is corresponding to 'IChannel' component in Fig. 54.4. Dynamic configuration of software receiver can be implemented using XML to descript the receiver. It can greatly improve the software's flexibility.

54.3.2.4 Design of Plugin Manager Module

Plugin manager module consists of two components: plugin manager component (denoted as IPluginManager) and plugin component (denoted as IPlugin). The function of IPluginManager is to create IPlugins. One IPlugin is corresponding to a DLL (dynamic link library) in Windows operating system. The magnitude of a IPlugin can be very small, such as including only an algorithm. It can also be very big, such as including all components of receiver.

54.3.2.5 Design of Application Module

The function of application module is to provide an interface to access software receiver. Figure 54.6 shows the relationship between application module and other module of software receiver.

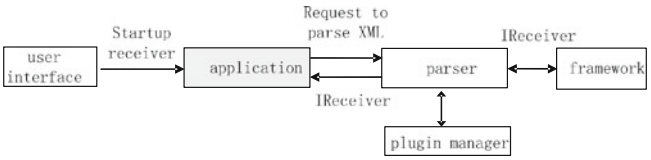

Fig. 54.6 Relationship diagram between application module and other module

54.3.2.6 Design of Tools Module

Tools module mainly include some often use tool, such as coordinate datum conversion, time datum conversion, software running log etc.

54.4 Class Diagram Design of Receiver Module using XML

54.4.1 Design of Receiver Class Using XML

The design diagram of receiver class (denoted as IReceiver) is showed in Fig. 54.7. IReceiver defines the interface of software receiver, which is the parent

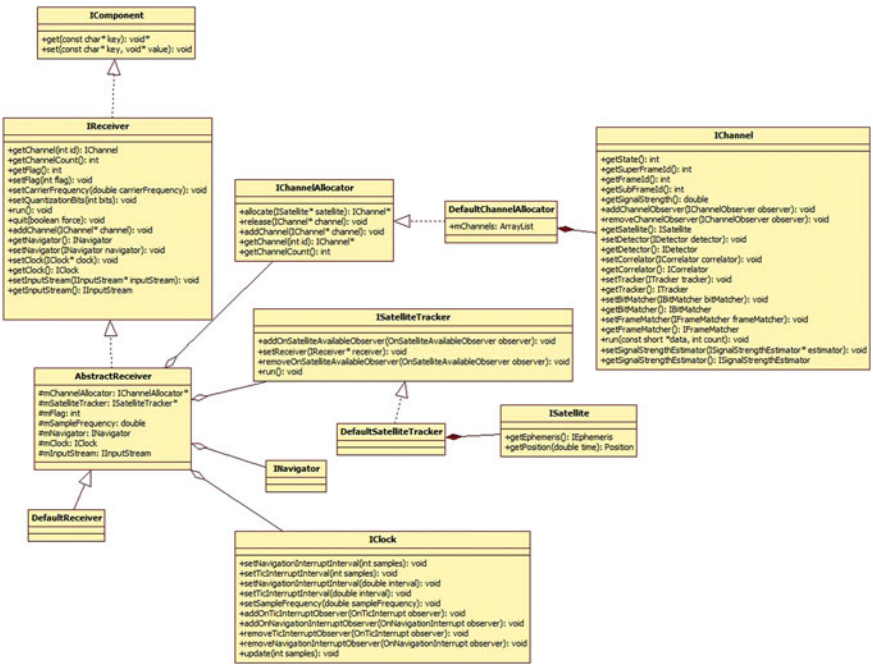

Fig. 54.7 Design diagram of receiver class using XML

class of 'AbstractReceiver' class. 'AbstractReceiver' class provides default implement of the IReceiver's methods. Similarly, 'AbstractReceiver' class is the parent class of the 'DefaultReceiver' class. The 'DefaultReceiver' class provides default implement of the 'AbstractReceiver' methods.

54.4.2 Design of Receiver Channel Class Using XML

The design approach of receiver channel is the same as receiver class and the design diagram is showed in Fig. 54.8.

54.4.3 Design of Channel Tracking Class Using XML

The design approach of channel tracking is the same as receiver class and the design diagram is showed in Fig. 54.9.

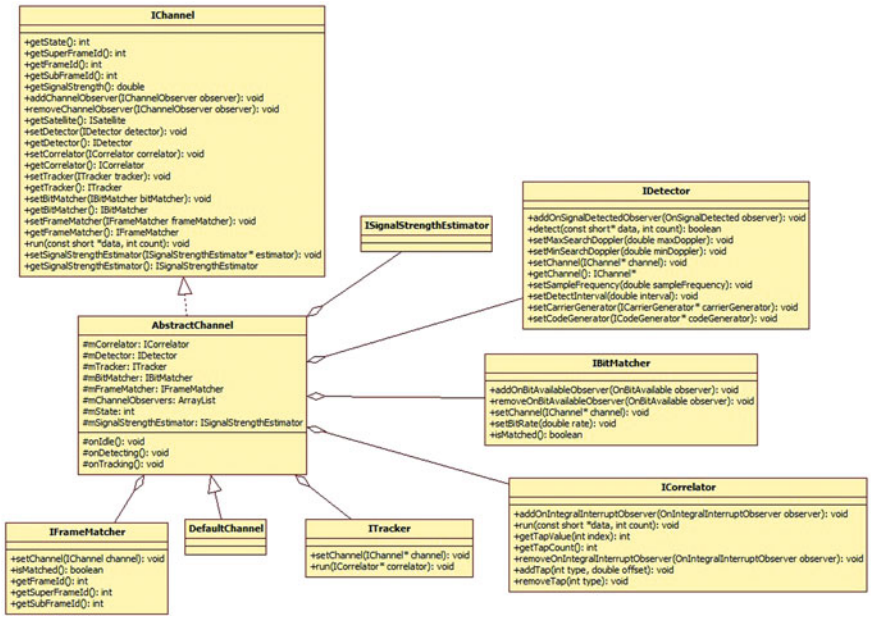

Fig. 54.8 Design diagram of receiver channel class using XML

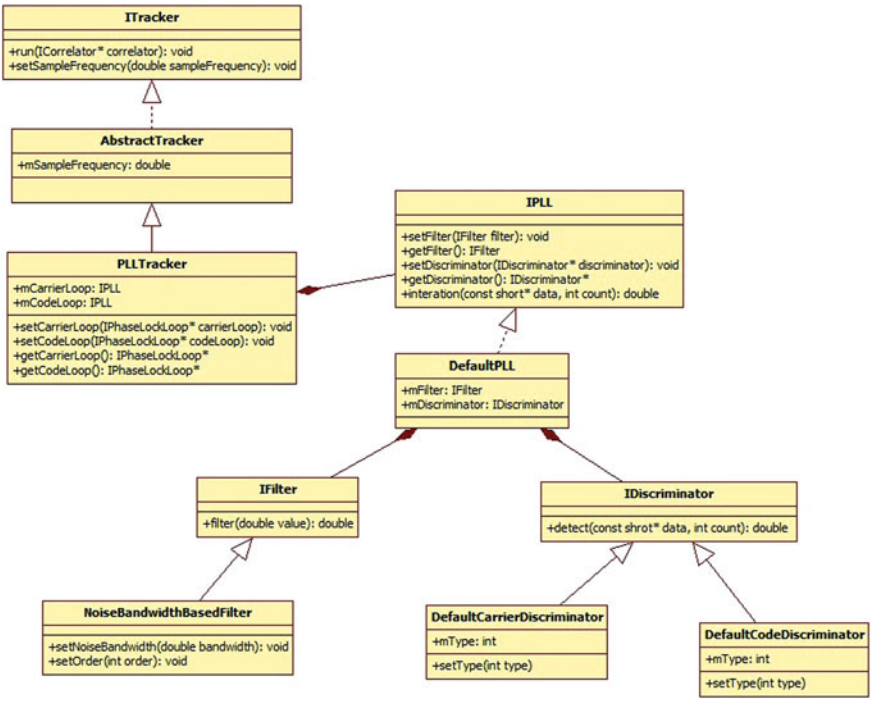

Fig. 54.9 Design diagram of channel tracking class using XML

54.4.4 Design of Input Stream Class Using XML

The design approach of input stream is the same as receiver class and the design diagram is showed in Fig. 54.10. Input Stream class defines the data interface from sampling card to PC. The function of FileInputStream class is to read data from file in disk. The function of DeviceInputStream class is to read data from sampling card.

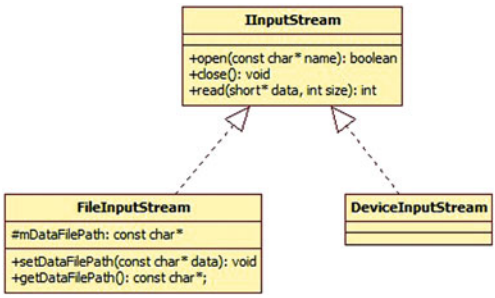

Fig. 54.10 Design diagram of input stream class using XML

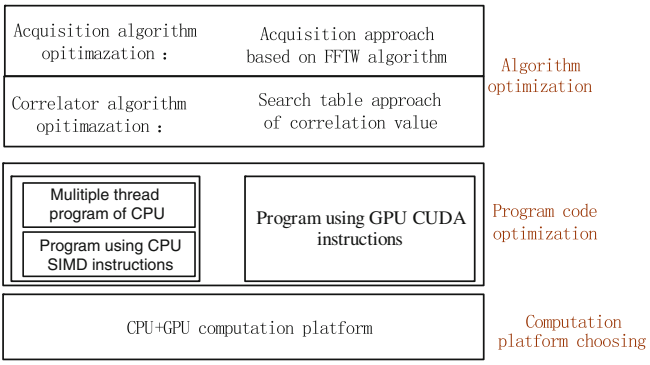

Fig. 54.11 Speed optimization scheme of software receiver

54.5 Speed Optimization Approaches of COMPASS Software Receiver

For COMPASS three frequencies software receiver based on the PC platform, signal capture, tracking and position calculating are all implemented by software code instead of hardware. Calculation quantity of signal capture and correlation operation is very large, which is the most time-consuming module in the receiver. To satisfy real time demands of processing signal, a series of speed optimization methods were proposed, which included arithmetic optimization, program code optimization and calculation platform choosing. The optimization scheme is shown in Fig. 54.11.

54.5.1 Computation Platform Choosing of Software Receiver

The programmable GPU has been developed into a processor of high parallel, multithreading and multicore. It has outstanding operating speed and high store bandwidth. The performance of GPU in aspect of floating-point operation is much better than that of CPU, which is more than 1Tflops/s. Because of the powerful parallel computing capability of GPU, the CPU and GPU are chosen as the computation platform of software receiver. And the parallel correlation operation of the most time-consuming in the software receiver is implemented by GPU.

54.5.2 Program Code Optimization of software receiver

Program code optimization was executed from three aspects:

(1) Technology of multithread program is used. At present, CPU of the PC has general more than two cores and four physical threads. And the CPU of Workstation has even 24 cores. Twelve threads were created in the software receiver, each of which separately executes the operation of one receiver channel. To acquire more time clock cycles of CPU, the highest priority of each thread is set. The test results show that processing speed of the software receiver has been improved five times on the CPU with more than six cores after the technology of multithread program is used.
(2) Technology of program code optimization based on CPU's SIMD (Single Instruction Multiple Data) is used. SIMD is a special instruction collection of CPU designed by Intel Company, which can simultaneously process multiple data in one clock cycle of CPU. At present, five kinds of SIMD, including MMX, SSE, SSE2, SSE3 and SSE4, have been presented by Intel Company.
(3) Technology of program code optimization based on GPU's CUDA (Compute Unified Device Architecture) is used. CUDA is a general parallel computing architecture designed by NVIDIA Company, which can solve complicated problem. It includes Instruction Set Architecture (ISA) of CUDA and the inner parallel calculation engine of GPU. Programmer can use c language code to develop program based on CUDA, which can be run effectively on the GPU processor. In this article, the correlation module of the most time-consuming in the software receiver is implemented on GPU based on CUDA. The test results show that the operation speed can be improved ten times on the display card of NVIDIA GeForce GT650 M after applying this technology.

54.5.3 Algorithm Optimization of Software Receiver

Algorithm optimization includes two methods. One is signal acquisition algorithm and the other is signal correlation algorithm.

(1) Algorithm optimization of signal acquisition

Because of using FFT algorithm in signal acquisition module, the processing time of FFT is crucial to the arithmetic. The acknowledged FFT optimization arithmetic on PC platform in the world is FFTW method designed by MIT, which is described in detail in paper [7] and [8]. The signal acquisition speed can be improved two or three times after using the FFTW method in this paper.

(2) Algorithm optimization of signal correlation

In traditional way, the correlation value of one sampling data need separately compute the product of Early-arm, Prompt-arm and Late-arm in in-phase way and quadrature-phase way. Because each arm (Early, Prompt or Late) product operation includes two multiplications and one calculation of trigonometric function, one sampling data includes twelve multiplications and six calculations of trigonometric

function. So the computing quantity of correlator is very large due to high sampling frequency. A look-up table method has been presented in this article, which in advance stores correlator value in a three dimensional table and replace the above twelve multiplications and six calculations of trigonometric function.

54.6 Conclusions

The software receiver adopted Visual studio 2010 as development tool. The core arithmetic was designed by C/C ++ language code, and the user interface was designed by C# language code. The software receiver can reach real-time processing capacity under 80 MHz sampling rate and 2 bit quantization conditions. It can process COMPASS B1/B2/B3 civil-code signals at the same time. The positioning results show that the software receiver's three-dimensional positioning accuracy is less than 10 m (95 %) under the condition of GDOP < 4. The following figure shows the results that software receiver processed COMPASS B3 civil signal (Fig. 54.12).

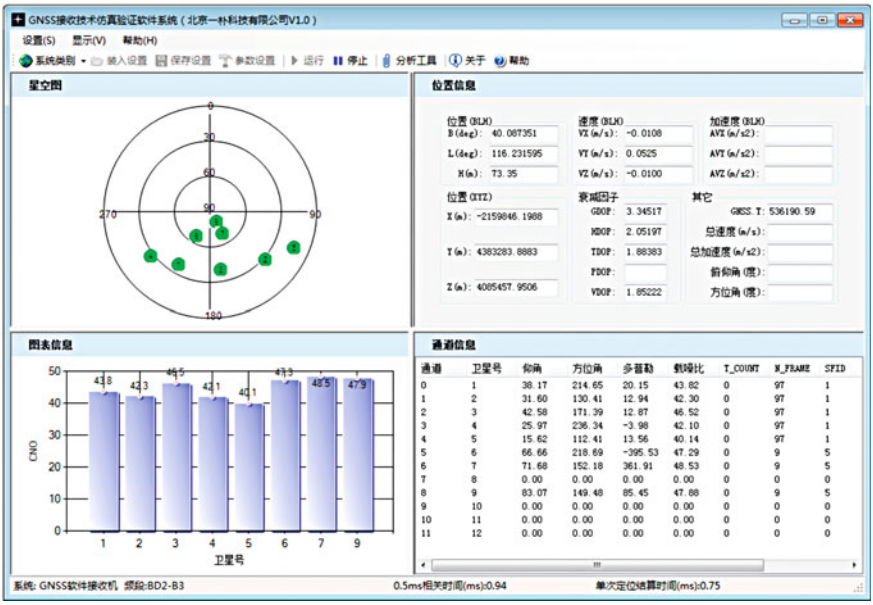

Fig. 54.12 Graph of COMPASS software receiver for processing B3 civil-code signal

In the above picture, satellites graph in view is shown at the top left corner. The ratio of carrier-to-noise of visible satellites is shown at the down left corner. The positioning result is shown at the top right corner. The channel information,

including elevation, azimuth, Doppler frequency, frame ID number, acquisition time and correlating time, are shown in the down right corner.

References

1. Strodl K, Naddeo G, Samson J, et al (2003) System verification approach, methods, and tools for Galileo. In: ION GPS/GNSS 2003, Portland, 9–12 Sept 2003, pp 2446–2456
2. Tsui JBY (2005) Fundamentals of global positioning system receivers-a software approach, 2nd edn. Wiley, New York
3. Borre K, Akos DM, Bertelsen N, Rinder P, Jensen SH (2007) A software-defined GPS and Galileo receiver. Birkhauser, Boston
4. Wei Z, Ke Z, Binbin W, Heejong S (2010) Simulation and analysis of GPS software receiver. In: 2nd international conference on computer modeling and simulation, pp 314–317
5. Chen Y-H, De Lorenzo DS, Juang JC, et al (2011) Real-time dual-frequency (L1/L5) GPS/WAAS software receiver. In: Proceedings of ION ITM 2011, Portland, OR, pp 767–774
6. Fern'andez–Prades C, Arribas J, Closas P, et al (2011) GNSS-SDR: an open source tool for researchers and developers. In: Proceedings of ION ITM 2011, Portland, OR, pp 780–794
7. Frigo M, Johnson SG (2005) The design and implementation of FFTW3. Proc IEEE 93(2):216–231
8. Johnson SG, Frigo M (2007) A modified split-radix FFT with fewer arithmetic operations. IEEE Trans Signal Process 55(1):111–119

Chapter 55
Analysis of Multipath Parameter Estimation Accuracy in MEDLL Algorithm

Yuan Gao, Feng Liu and Teng Long

Abstract MEDLL (Multipath Estimating Delay Lock Loop) is an excellent multipath mitigation algorithm, the core of the algorithm is estimated multipath parameters, and parameter estimation accuracy determines the actual performance of the algorithm. Previous studies and experiments have demonstrated the anti-multipath MEDLL algorithm performance, lack of research but for its observations on the multipath performance, multipath parameter estimation performance. Studied MEDLL algorithm the multipath estimation accuracy and thermal noise, front-end bandwidth, the correlator spacing and sampling rate and other parameters of the relationship obtained MEDLL algorithm under different conditions, the accuracy of the estimate of the multipath parameters.

Keywords MEDLL · Multipath parameter estimation · GNSS receiver

55.1 Introduction

Improvements due to GNSS (Global Navigation Satellite System) augmentations and GNSS modernization are reducing many source of error leaving and shadowing as significant and sometimes dominant contributors to error [1]. As a result, the multipath rejection performance of GNSS receiver becomes more and more important. The MEDLL (Multipath Estimating Delay Lock Loop) algorithm is a multipath mitigation algorithm which was first proposed in Ref. [2].

Y. Gao · F. Liu (✉) · T. Long
School of Information and Electronics, Beijing Institute of Technology, 5 South Zhongguancun Street, Haidian, Beijing 100081, People's Republic of China
e-mail: bit_liufeng@bit.edu.cn

Y. Gao
e-mail: fyuan1986@bit.edu.cn

J. Sun et al. (eds.), *China Satellite Navigation Conference (CSNC) 2013 Proceedings*, Lecture Notes in Electrical Engineering 243,
DOI: 10.1007/978-3-642-37398-5_55,

The performance of MEDLL algorithm applied in NovAtel GPS receiver is analysed in Ref. [3, 4]. It has been proved the MEDLL algorithm is an effective way to mitigate errors caused by multipath. The basic idea of MEDLL algorithm is mitigating multipath by separating direct signal from multipath by estimating parameters of multipath. As a result, MEDLL algorithm is also applied in multipath monitoring [5].

From above we know previous studies are mainly concentrated in performance of MEDLL algorithm and how to improve the performance. Some studies are also focused on how to reduce resource consumption due to highly complexity of MEDLL algorithm. However, this is rare study on multipath parameter estimation accuracy. In fact, multipath parameter estimation whose accuracy determines performance of multipath mitigation is the key to MEDLL algorithm especially in application using MEDLL algorithm for multipath monitoring.

55.2 Multipath Models and MEDLL Algorithm

55.2.1 Multipath Signal Models

Multipath is the reception of reflected or diffracted of the desired signal as shown in Fig 55.1. Multipath is divided into two kinds: reflected one and scattering on. Scattering signal often performs as an additional noise channel, which has little effects on GNSS receiver working. Therefore, only reflected signal is in consideration when studying multipath parameter estimation accuracy. The reflected signal can be approximately considered as the direct signal with changes of amplitude, phase and time delay. Then a simple model for the complex envelope of a received signal $r(t)$ with multipath after frequency down conversion is

$$r(t) = \sum_{n=0}^{N} A_n e^{j(2\pi fct + \phi_n)} p(t - \tau_n) + n_r(t) \tag{55.1}$$

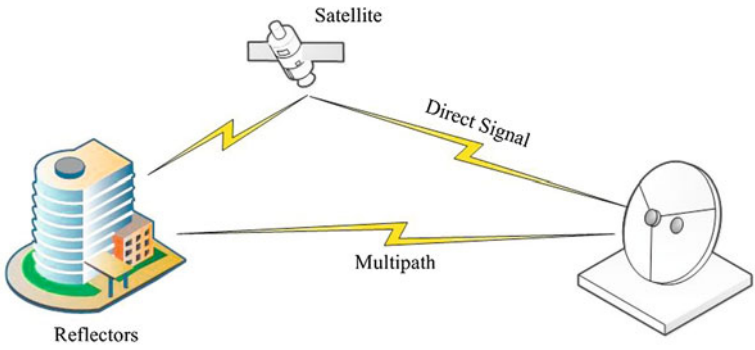

Fig. 55.1 Generation of multipath

where, $p(t)$ is the spreading code of the transmission signal, f is the carrier frequency, A_n is the amplitude of the nth signal, ϕ_n is the carrier phase of the nth signal, τ_n is the time delay of nth signal, when $n = 0$, it means signal is the direct one; $n_r(t)$ is the complex envelope of receiver front-end noise; it is a narrowband random process which can be represented by the quasi-sinusoidal form as shown in Eq. (55.2).

$$n_r(t) = [n_{rc}(t) + jn_{rs}(t)]e^{j(2\pi fct+\phi_0)} \tag{55.2}$$

It's known from Eq. (55.2) that one multipath signal will be determined and separated from the direct signal once parameters of amplitude, time delay and carrier phase has been calculated by estimating. Therefore, the main task of MEDLL algorithm is determining these three parameters of multipath.

55.2.2 Principle of MEDLL Algorithm

MEDLL loop which is a group of correlator with different local replica code phase is the hard foundation of performing MEDLL algorithm. MEDLL loop is shown in Fig. 55.2. A group of

The equation of $s(t)$ can be obtained from Eq. (55.1) assuming the carrier frequency has been estimated accurately during carrier stripping.

$$s(t) = \sum_{n=0}^{N} A_n e^{j\phi_n} p(t - \tau_n) + n(t), n(t) = [n_c(t) + jn_s(t)]e^{j\phi_o} \tag{55.3}$$

This group of integrated sum obtained from MEDLL loop which is called measured correlation function $R_s(\tau)$ is actually a group of measurement of $s(t)$. That is:

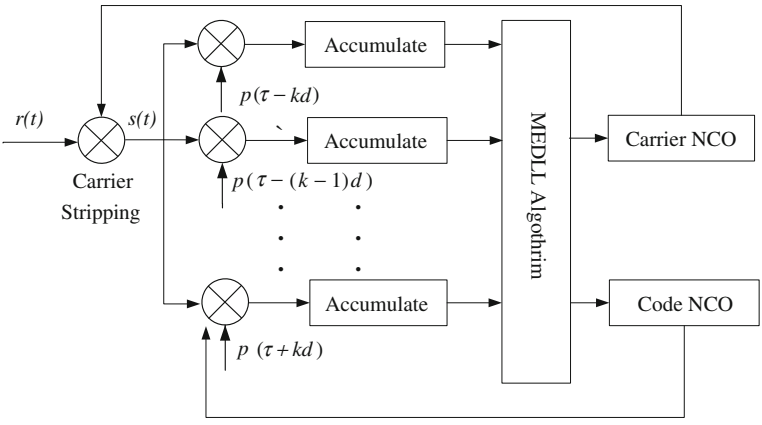

Fig. 55.2 MEDLL loop block diagram

$$R_s(\tau) = \sum_{n=1}^{k} [s(\tau) \otimes p(\tau + \tau_k)] \tag{55.4}$$

Assuming $\hat{N}$ set of parameters obtained from MEDLL algorithm is $(A_n, \tau_n, \phi_n)(n = 0, 1, \ldots \hat{N})$, $\hat{N}$ is estimated value of multipath signal's number. Ignoring noise, the estimated values $\hat{s}(t)$ of $s(t)$ is:

$$\hat{s}(t) = \sum_{n=0}^{\hat{N}} \hat{A}_n e^{j\hat{\phi}_n} x(t - \hat{\tau}_n), M(\hat{A}, \hat{\tau}, \hat{\phi}) = \int_{t-T_p}^{t} [s(t) - \hat{s}(t)]^2 dt \tag{55.5}$$

where, T_p is predetection correlation time and $M(\hat{A}, \hat{\tau}, \hat{\phi})$ is mean square error of $\hat{s}(t)$.

According to maximum likelihood estimation (MLE) rule, $M(\hat{A}, \hat{\tau}, \hat{\phi})$ should be minimum, that is:

$$\frac{\partial M\left(\hat{A}, \hat{\tau}, \hat{\phi}\right)}{\partial \hat{A}} = 0, \frac{\partial M\left(\hat{A}, \hat{\tau}, \hat{\phi}\right)}{\partial \hat{\tau}} = 0, \frac{\partial M\left(\hat{A}, \hat{\tau}, \hat{\phi}\right)}{\partial \hat{\phi}} = 0 \tag{55.6}$$

According references [2, 3], Eq. (55.6) can be solved:

$$\begin{matrix} \\ \hat{\tau}_i \\ \\ \hat{A}_i \end{matrix} = \max \left\{ \mathrm{Re} \left[R_s(\tau) - \sum_{\substack{n=0 \\ n \neq i}}^{\hat{N}} \hat{A}_k R_{ref}(\tau - \hat{\tau}_k) e^{j\hat{\phi}_i} \right] \right\} \tag{55.7}$$

where $R_{\mathrm{ref}}(\tau)$ which is named with reference correlation function in MEDLL algorithm is the correlation function of $p(t)$ in this receiver channel [2]. The reference correlation function reflects the characteristics of the receiver's channel.

55.2.3 Multipath Parameters Solving

It is hard to solve Eq. (55.7) directly because parameters are tightly coupled. Therefore, Eq. (55.7) is usually solved with method of iterative calculation.

We just take one multipath in consideration in order to simplify the analysis. That is:

$$s(t) = s_o(t) + s_1(t) \tag{55.8}$$

where, $s_0(t)$ is the direct signal with correlation function of $R_0(\tau)$ and $s_1(t)$ is the direct signal with correlation function of $R_1(\tau)$. Known by the linear characteristics of correlation function:

$$R_s(\tau) = R_0(\tau) + R_1(\tau) \tag{55.9}$$

The general iterative solver process is:

Step 1 Assuming $R_0(\tau) = R_s(\tau)$, the first set estimated parameters $(\hat{A}_0, \hat{\tau}_0, \hat{\phi}_0)_1$ of $R_0(\tau)$ will be obtained. Then, combining this set parameters with reference correlation function, the first estimated value $\hat{R}_0(\tau)_1$ of $R_0(\tau)$ will be obtained;

Step 2 Assuming $R_1(\tau) = R_s(\tau) - \hat{R}_0(\tau)_1$, the first set estimated parameters $\left(\hat{A}_1, \hat{\tau}_1, \hat{\phi}_1\right)_1$ of $R_1(\tau)$ will be obtained. Then, combining this set parameters with reference correlation function, the first estimated value $\hat{R}_1(\tau)_1$ of $R_0(\tau)$ will be obtained. Assuming $R_0(\tau) = R_s(\tau) - \hat{R}_1(\tau)_1$, the second set estimated parameters $\left(\hat{A}_0, \hat{\tau}_0, \hat{\phi}_0\right)_2$ of $R_0(\tau)$ will be obtained. Then, combining this set parameters with reference correlation function, the second estimated value $\hat{R}_0(\tau)_2$ of $R_0(\tau)$ will be obtained;

Step 3 Assuming $R_1(\tau) = R_s(\tau) - \hat{R}_0(\tau)_2$, the second set estimated parameters $\left(\hat{A}_1, \hat{\tau}_1, \hat{\phi}_1\right)_2$ of $R_1(\tau)$ will be obtained. Then, combining this set parameters with reference correlation function, the second estimated value $\hat{R}_1(\tau)_2$ of $R_1(\tau)$ will be obtained;

Repeat Step 2, 3 until the mean square $E(V_\mathrm{n})$ of iteration residuals V_n has met expectations. V_n is defined in Eq. (55.10)

$$V_n = R(\tau) - \hat{R}_0(\tau)_n - \hat{R}_1(\tau)_n, E(V_n) = \int_{-D}^{D} \left|R(\tau) - \hat{R}_0(\tau)_n - \hat{R}_1(\tau)_n\right|^2 d\tau \tag{55.10}$$

55.2.4 Algorithm of Parameters Estimation

Assuming that a correlation function $R_\mathrm{s}(\tau)$ contains only one path signal, in order to estimate its parameters, we should first find the maximum energy point τ_max make Eq. (55.11) established.

$$\left\{[\mathrm{Re}(R_s(\tau_\mathrm{max})]^2 + [\mathrm{Im}(R_s(\tau_\mathrm{max})]^2\right\} = \max\left\{[\mathrm{Re}(R_s(\tau)]^2 + [\mathrm{Im}(R_s(\tau)]^2\right\} \tag{55.11}$$

Carrier phase estimated value is obtained through four quadrant arctangent at this point as shown in Eq. (55.12).

$$\hat{\phi}_s = arc\tan 2\left(\frac{\mathrm{Im}(R_s(\tau_{\max}))}{\mathrm{Re}(R_s(\tau_{\max}))}\right) \tag{55.12}$$

Then, at the same point time delay estimated value is obtained through incoherent early-late code discriminator as shown in Eq. (55.13).

$$\begin{aligned} I_E &= \mathrm{Re}(R_s(\tau_{\max} - dT_c)), Q_E = \mathrm{Im}(R_s(\tau_{\max} - dT_c)) \\ I_L &= \mathrm{Re}(R_s(\tau_{\max} + dT_c)), Q_L = \mathrm{Im}(R_s(\tau_{\max} + dT_c)) \\ \tau_{EMLP} &= \left[\left(I_E^2 + Q_E^2\right) - \left(I_L^2 + Q_L^2\right)\right] \end{aligned} \tag{55.13}$$

where, T_c is the chip length of spreading code.

At last, the amplitude estimated value is obtained through reference correlation function as shown in Eq. (55.14).

$$\hat{A}_s = \sqrt{\mathrm{Re}(R_s(\tau_{\max}))^2 + \mathrm{Im}(R_s(\tau_{\max}))^2}\,\frac{R_{ref}(0)}{R_{ref}(\hat{\tau}_s)} \tag{55.14}$$

55.3 Error Analysis of Multipath Parameters Estimation

It's known in Eq. (55.7) that time delay plays a more important part because it determines if the estimating point is right. On the other hand, time delay gets more concerned in applications which apply MEDLL algorithm into multipath mitigation (actually most applications are such). Therefore, in this paper estimation accuracy of time delay is mainly discussed.

55.3.1 Error Source of Estimation

It's known from Sect. 55.2.4 that estimation of time delay is similar to code tracking in normal GNSS receiver. Therefore, the source of estimation is mainly thermal noise, front-end bandwidth and correlator spacing [1, 6]. There is another source named with iteration residuals because iteration calculation is applied into.

Iteration residual is similar to multipath when estimating time delay. In the following analysis we first analyze other sources then take iteration residual into consideration.

55.3.2 Error Brought by Noise and Limited Bandwidth

Without consideration of iteration, assume the theoretical time delay in Eq. (55.13) is ε, and then the linear model of EMLP's output is:

$$\tau_{EMLP} = K\varepsilon_\tau + n_\tau, |\varepsilon_\tau - \tau_{EMLP}| \to 0 \tag{55.15}$$

where, K is slope of discriminator around theoretical value independent of noise. n_τ is the output noise of discriminator whose bandwidth is greater than predetection correlation bandwidth $1/T_p$. As a result, n can be considered as zero mean and independent in each output, and then mean square of discrimination error is [6]:

$$\sigma_{EL}^2 = \frac{2N_\tau T_p}{K^2} \tag{55.16}$$

where, N_τ is power of n_τ. Then Eq. (55.13) is rewritten as follow:

$$\begin{aligned} I_E &= \mathrm{Re}\big(R_{ref}(\tau_{\max} - dT_c) + n_E\big), I_L = \mathrm{Re}\big(R_{ref}(\tau_{\max} + dT_c) + n_L\big) \\ Q_E &= \mathrm{Im}\big(R_{ref}(\tau_{\max} - dT_c) + n_E\big), Q_L = \mathrm{Im}\big(R_{ref}(\tau_{\max} + dT_c) + n_L\big) \end{aligned} \tag{55.17}$$

where, the noise term is obtained in following equation:

$$n_E = n(t) \otimes p(\tau_{\max} - dT_c), n_E = n(t) \otimes p(\tau_{\max} + dT_c) \tag{55.18}$$

Then the output of discriminator can be presented as follow:

$$\begin{aligned} \tau_{EMLP} &= \left[\left(I_E^2 + Q_E^2\right) - \left(I_L^2 + Q_L^2\right)\right] \\ &= \left|R_{ref}(\tau_{\max} - T_c d) + n_E\right|^2 - \left|R_{ref}(\tau_{\max} + T_c d) + n_L\right|^2 \\ &= \left|R_{ref}(\tau_{\max} - T_c d)\right|^2 - \left|R_{ref}(\tau_{\max} + T_c d)\right|^2 + |n_E|^2 - |n_L|^2 \\ &\quad + R_{ref}(\tau_{\max} - T_c d)n_E^* - R_{ref}(\tau_{\max} + T_c d)n_L^* \\ &\quad + R_{ref}^*(\tau_{\max} - Tcd)n_E - R_{ref}^*(\tau_{\max} + T_c d)n_L \end{aligned} \tag{55.19}$$

Because expectation of terms containing noise in above equation is zeros [7], the expectation of τ_{EMLP} is:

$$E(\tau_{EMLP}) = E\left(\left|R_{ref}(\tau_{\max} - T_c d)\right|^2 - \left|R_{ref}(\tau_{\max} + T_c d)\right|^2\right) \tag{55.20}$$

Then

$$K = E'(\tau_{EMLP})|_{\tau_{EMLP}=\tau_{\max}}, N_\tau = Var(\tau_{EMLP}) \tag{55.21}$$

Equations (55.19–55.21) substituted into Eq. (55.16) after finishing is [1, 6, 8]:

$$\sigma_{EL}^2 = \frac{\frac{1}{4\pi^2}\int_{-\beta_s/2}^{\beta_s/2} S_s(f)\sin^2(\pi f d T_c)df}{(P_s/N_0)\left(\int_{-\beta_s/2}^{\beta_s/2} f S_s(f)\sin(\pi f d T_c)df\right)^2} \times \left[1 + \frac{\int_{-\beta_s/2}^{\beta_s/2} S_s(f)\cos^2(\pi f d T_c)df}{(T_P P_s/N_0)\left(\int_{-\beta_s/2}^{\beta_s/2} S_s(f)\cos(\pi f d T_c)df\right)^2}\right] \tag{55.22}$$

where, $S_s(f)$ is transmit spectrum of navigation signal, P_s is received power, N_0 is single band power spectral (assuming noise is white), β_s is front-end bandwidth.

55.3.3 Error Brought by Iteration Residual

Because iteration residual is similar to multipath when estimating time delay, we assuming error brought by iteration residual is $\sigma_{ir}(V_n)$, that is:

$$\sigma_\tau = \sigma_{mp}(V_n) + \sigma_{EL} \tag{55.23}$$

According to MLE rules:

$$\frac{\partial}{\partial \tau_1}\int_{t-T_p}^{t} [s(t) - \hat{s}_0(t) - \hat{s}_1(t)]^2 dt = \frac{\partial}{\partial \tau_1}\int_{t-T_p}^{t} [V_n]^2 dt = 0 \tag{55.24}$$

From Eq. (55.24) we can know that V_N is considered independent of τ_1 when estimating delay τ_1 of $s_1(t)$, that is:

$$V_n = R_{ref}(\tau_0) - R_{ref}(\tau_0 + \sigma_{EL}), \sigma_\tau = \sigma_{mp}\left(R_{ref}(\tau_0) - R_{ref}(\tau_0 + \sigma_{EL})\right) + \sigma_{EL} \tag{55.25}$$

55.4 Analysis of Accuracy and Simulation

Correlation spacing d is usually tiny in MEDLL loop. Therefore, make $d \to 0$, known from Eq. (55.22), when received power is constant and $T_p \to \infty$,

$$\sigma_{EL}^2 \to \frac{1}{(2\pi)^2 (P_\beta/N_0)\omega_{RMS}^2}$$
$$P_\beta = P_s \int_{-\beta_s/2}^{\beta_s/2} S_s(f)df,\ \omega_{RMS} = \sqrt{\int_{-\beta_s/2}^{\beta_s/2} f^2 S_s(f)df} \tag{55.26}$$

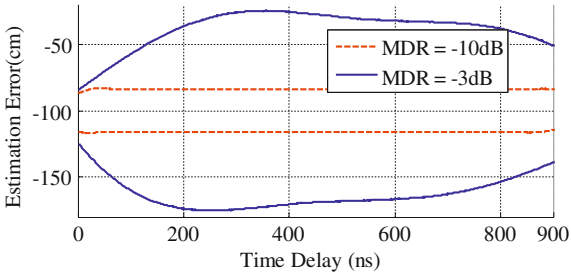

Fig. 55.3 Accuracy of GPS L1C/A code delay estimation under different MDR

where, ω_{RMS} is named with root-mean-squared bandwidth [1] or Gabor bandwidth [9]. It is useless when $d \to 0$ because of Gabor bandwidth.

Take BPSK-R(n) modulation which is used in most running satellite navigation system as an example. C/A code of GPS L1 is BPSK-R(1), when $d \to 0$:

$$\sigma_{EL}^2 \cong \frac{1}{2P_\beta/N_0\beta_s T_c}\left(1+\frac{1}{T_p P_\beta/N_0}\right), \quad d \le \frac{1}{T_c\beta_s} \tag{55.27}$$

From above equation we know that when front-end bandwidth is determined and correlator spacing is smaller than $1/T_c\beta_s$ accuracy of time delay estimation tends to a value independent of correlator spacing. Figure 55.3 shows accuracy of GPS L1C/A code delay estimation under different MDR (Multipath-to-direct Ratio).

From Fig. 55.3 we can see that accuracy of time delay estimation is mainly determined by thermal noise and front-end bandwidth and tends to a constant value when MDR is small. However, when MDR is large that accuracy is mainly determined by iteration residual instead and its envelope tends to envelope of error caused by multipath.

55.5 Conclusions

In this paper, we first analyze the accuracy of multipath parameter estimation from principle and implementation of MEDLL. Then error source of estimation is analyzed and equation of accuracy is given and proved to be correct by simulation. Otherwise, the theoretical limit of accuracy is given under various conditions. It is helpful to design of application using MEDLL algorithm.

References

1. Kaplan ED, Hegarty CJ (2006) Understanding GPS: principles and applications, 2nd edn. Artech House, Boston
2. Van Nee RDJ (1992) The multipath estimating delay lock loop. In: IEEE 2nd internal symposium on spread spectrum techniques and applications (ISSSTA'92), Yokohama, Japan, 29 Nov to 2 Dec 1992

3. Van Nee RDJ, Siereveld J, Fenton PC, Townsend BR (1994) The multipath estimating delay lock loop: approaching theoretical accuracy limits. In: Proceedings of the IEEE position, location and navigation symposium, Las Vegas, NV, USA
4. Townsend BR, Van Nee RDJ, Fenton PC, Van Dierendonck KJ (1995) Performance evaluation of the multipath estimating delay lock loop. In: ION NTM, 18–20 Jan 1995, Anaheim, California
5. Townsend B, Wiebe J, Jakab A (2000) Results and analysis of using the MEDLL receiver as a multipath meter. In: ION NTM, 26–28 Jan 2000, Anaheim, CA
6. Betz JW, Kolodziejski KR (2000) Generalized theory of GPS code-tracking accuracy with an early-late discriminator. IEEE Trans Aerospace Electron Syst 45:1538–1556
7. Tang Z (2009) Research on relevant theory for GNSS signal design and evaluation. Huazhong University of Science and Technology, Wuhan
8. Betz JW, Kolodziejski KR (2000) Extended theory of early-late code tracking for a bandlimited GPS receiver. Navigation: J Inst Navigation 47(3):211–226
9. Eissfeller B, Hein GW, Winkel J, et al (2000) Requirements on the Galileo signal structure. In: ION GPS 2000, Salt Lake City, UT

Chapter 56
Research of a Low Complexity Spoofing Mitigation Method Based on a Moving Antenna

Long Huang, Junwei Nie, Rui Ge and Feixue Wang

Abstract Spoofing to GNSS receivers becomes to a majority threat to satellite navigations systems in civil safety critical applications. By weighing the groups of samples from a single moving antenna precisely, an equivalent adaptive beam forming antenna array is synthesized. Corresponding to the scenario that all spoofing pseudo random noise (PRN) codes are transmitted from the same source in space, the different spatial signatures of spoofing and authentic signals are analyzed. With a low complexity weighing parameters calculations algorithm, a null is steered in the direction where spoofing signals come from. This is an effective spoofing mitigation method which greatly suppresses the energy of spoofing signals in the conventional GNSS receiver procedures. And simulation results are given in the end to the valid the performance of the proposed method.

Keywords GNSS · Satellite navigation receiver · Spoofing interference · Spoofing mitigation

56.1 Introduction

Spoofing to civil GNSS receiver aim to mislead the target receiver to a false position/timing solution, which becomes to a major threaten to the satellite navigation systems [1]. Plenty of anti-spoofing techniques have been proposed in the open literature recently. These methods can be generally divided into two main categories, namely spoofing detection and spoofing mitigation.

Spoofing detection techniques refer to discriminate the spoofing signals from the authentic ones, and exclude them off the position/timing calculation. The widely

L. Huang (✉) · J. Nie · R. Ge · F. Wang
Satellite Navigation R&D Center, National University of Defense Technology, Changsha, China
e-mail: huangl386@hotmail.com

J. Sun et al. (eds.), *China Satellite Navigation Conference (CSNC) 2013 Proceedings*, Lecture Notes in Electrical Engineering 243,
DOI: 10.1007/978-3-642-37398-5_56,

discussed signal power discrimination, time of arrival (TOA) discrimination, polarization discrimination, angle of arrival (AOA) discrimination, cross-check of IMU and cryptographic authentication are all belong to this category [2–6].

Spoofing mitigation techniques refer to remove the spoofing signals in front of conventional GNSS receiver acquisition and tracking processing, which can eliminate the impact of spoofing to receiver radically. Dr. Daneshmand [7] in university of Calgary proposed a spoofing mitigation technique using multiple antennas and proved to be effective to remove spoofing signals coming from a point transmitting source. Multiple antennas technique is one of the most powerful techniques that have been devised against spoofing threat, but it increase the size and cost of GNSS receivers, which restricts the use of multiple antennas in civil domain.

In this paper, a new equivalent adaptive beam forming antenna array technique is proposed to migration spoofing signals coming from a point transmitting source. By weighing the groups of samples from a single moving antenna precisely, an equivalent adaptive beam forming antenna array is synthesized. Corresponding to the scenario that all spoofing pseudo random noise (PRN) codes are transmitted from the same source in space, the different spatial signatures of spoofing and authentic signals are analyzed. With a low complexity weighing parameters calculations algorithm, a null is steered in the direction where spoofing signals come from. This is an effective spoofing mitigation method which greatly suppresses the energy of spoofing signals in the conventional GNSS receiver procedures.

56.2 System Model

56.2.1 Receiver Signal Model

In this paper, it is assumed that the spoofer transmitting several PRN codes through a single antenna, each of which having a comparable power level to that of the authentic signals. And the spoofing and authentic signals all use periodicity PRN codes in their structures. A typical spoofing scenario is shown in Fig. 56.1.

The baseband samples of authentic and spoofing signals in GNSS receivers can be written as:

$$r(n) = \sum_{m=1}^{N_A} a_{mn}\sqrt{P_m^a}F_m^a(n) + \sum_{k=1}^{N_S} b_{kn}\sqrt{P_k^s}F_k^s(n) + \omega(nT_s) \tag{56.1}$$

where N_A and N_S are the number of authentic and spoofing PRNs respectively and

$$\begin{aligned} F_m^a(n) &= d_m^a\left(nT_s - \tau_m^a\right)c_m^a\left(nT_s - \tau_m^a\right)e^{j\phi_m^a + j2\pi f_m^a nT_s} \\ F_k^s(n) &= d_k^s\left(nT_s - \tau_k^s\right)c_k^s\left(nT_s - \tau_k^s\right)e^{j\phi_k^s + j2\pi f_k^s nT_s} \end{aligned} \tag{56.2}$$

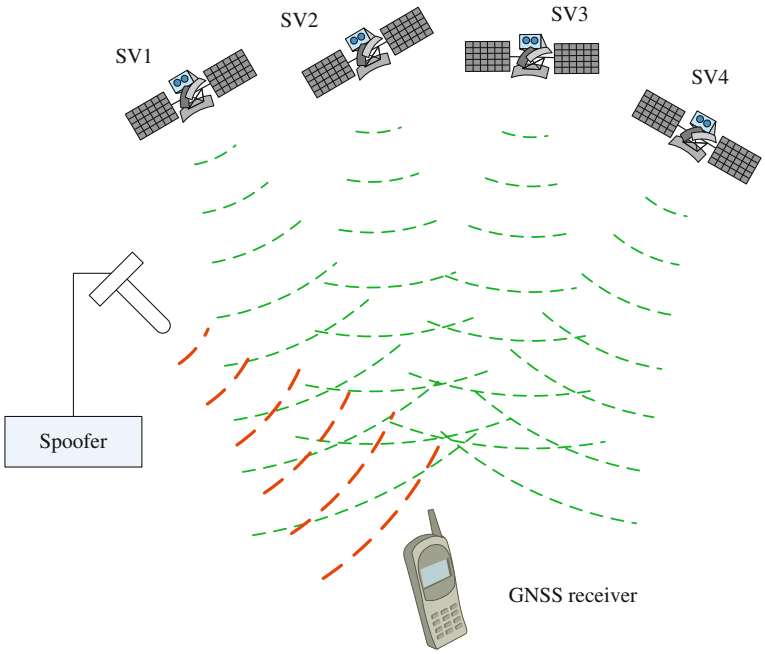

Fig. 56.1 A typical spoofing scenario

In (56.1) and (56.2), the superscripts a and s refer to the authentic and spoofing signals respectively. T_s is the sampling interval and ϕ, f, P and τ are the phase, Doppler frequency, signal power and code delay of the received signals respectively. Symbols a_{mn} and b_{kn} present the spatial attenuation-delay characteristic of the authentic and spoofing signals, while ω is the additive white Gaussian noise with variance σ^2.

56.2.2 Spoofing Mitigation Model

For a moving GNSS receiver, taking N samples out of the input sequence in (56.1) can form an equivalent N-element array antenna output vector:

$$\mathbf{R_N}(n) = \left[r(n)\ r(n-\Delta)\ r(n-\Delta)\ \ldots\ r(n-(N-1)\Delta)^T\right] \tag{56.3}$$

Without loss of generality assuming that the reference coordinate system is located at the receiver antenna at the time of r(n), as shown in Fig. 56.2.

where $\hat{\mathbf{d}}_m^A$ and $\hat{\mathbf{d}}^S$ are unit vectors pointing from the origin of the coordinate system towards the mth GNSS satellite and the spoofer respectively. $\mathbf{d}_{i1}^{ant}$ is the vector

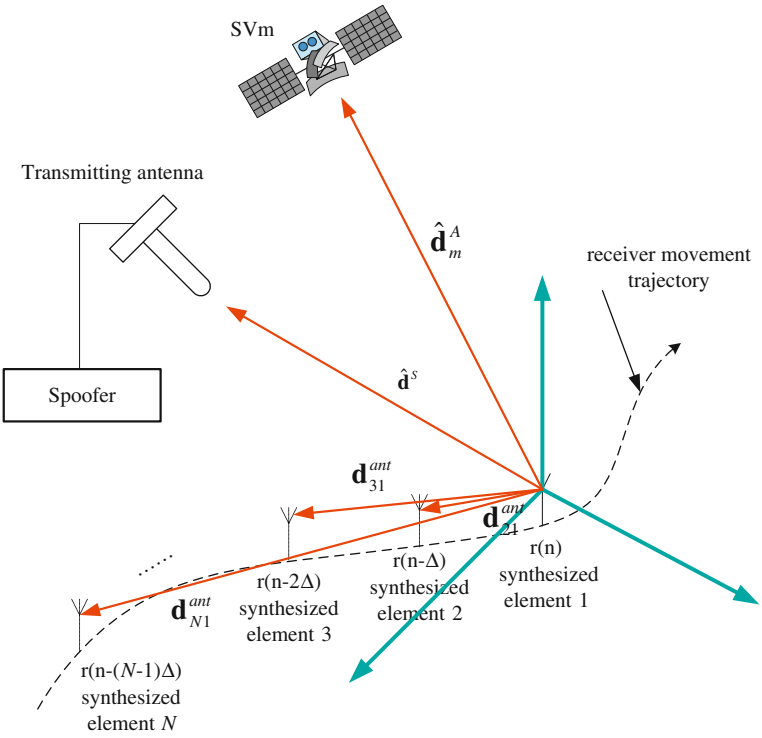

Fig. 56.2 Equivalent N-element antenna configuration

pointing from the origin to the *i*th equivalent antenna element phase center and λ is the GNSS carrier wavelength.

Taking Eqs. (56.1) and (56.2) into Eq. (56.3), the equivalent array antenna output vector can be written as:

$$\mathbf{R_N}(n) = \sum_{m=1}^{N_A} \mathbf{a_m} \sqrt{P_m^a} F_m^a(n) + \mathbf{b} \sum_{k=1}^{N_s} \sqrt{P_k^s} F_k^s(n) + \boldsymbol{\eta}(n) \tag{56.4}$$

where η is the complex additive white Gaussian noise vector with covariance matrix $\sigma^2\mathbf{I}$. $\mathbf{b}$ and $\mathbf{a_m}$ are spatial characteristic vector (SCV) of spoofing PRNs and *m*th authentic signal respectively:

$$\mathbf{a_m} = \mathbf{C}\overline{\mathbf{a}}_\mathbf{m}$$
$$\mathbf{b} = \mathbf{C}\overline{\mathbf{b}}$$
$$\mathbf{C} = \begin{bmatrix} 1 & 0 & \cdots & 0 \\ 0 & C_2 & \cdots & 0 \\ \vdots & \vdots & \ddots & \vdots \\ 0 & 0 & \cdots & C_N \end{bmatrix} \quad \overline{\mathbf{a}}_\mathbf{m} = \begin{bmatrix} 1 \\ a_{m2} \\ \vdots \\ a_{mN} \end{bmatrix} = \begin{bmatrix} 1 \\ e^{-j\frac{2\pi \mathbf{d}_{21}^{ant} \bullet \hat{\mathbf{a}}_m^A}{\lambda}} \\ \vdots \\ e^{-j\frac{2\pi \mathbf{d}_{N1}^{ant} \bullet \hat{\mathbf{a}}_m^A}{\lambda}} \end{bmatrix} \quad \overline{\mathbf{b}} = \begin{bmatrix} 1 \\ b_2 \\ \vdots \\ b_N \end{bmatrix} = \begin{bmatrix} 1 \\ e^{-j\frac{2\pi \mathbf{d}_{21}^{ant} \bullet \hat{\mathbf{d}}^S}{\lambda}} \\ \vdots \\ e^{-j\frac{2\pi \mathbf{d}_{N1}^{ant} \bullet \hat{\mathbf{d}}^S}{\lambda}} \end{bmatrix} \tag{56.5}$$

Consequently, the problem of spoofing mitigation with a synthesized antenna array is to find an optimal gain vector which is denoted by $\mathbf{f}$ to satisfy the following conditions:

$$\mathbf{f}^H\mathbf{b} = 0 \text{且} \|\mathbf{f}\| \neq 0 \tag{56.6}$$

By applying the vector $\mathbf{f}$ to the synthesized antenna array signals, the spoofing signal is suppressed in the beam former output as:

$$\begin{aligned} v(n) &= \mathbf{f}^H\mathbf{R_N}(n) \\ &= \sum_{m=1}^{N_A} \mathbf{f}^H\mathbf{a_m}\sqrt{P_m^a}F_m^a(n) + \mathbf{f}^H\mathbf{b}\sum_{k=1}^{N_S}\sqrt{P_k^s}F_k^s(n) + \mathbf{f}^H\boldsymbol{\eta}(n) \\ &= \sum_{m=1}^{N_A} \mathbf{f}^H\mathbf{a_m}\sqrt{P_m^a}F_m^a(n) + \mathbf{f}^H\boldsymbol{\eta}(n) \end{aligned} \tag{56.7}$$

56.3 Spoofing Mitigation

The proposed spoofing mitigation technique based on a moving single antenna receiver consists of two main modules, namely spoofing SCV estimation and null steering, which are described in the following subsections.

56.3.1 Spoofing SCV Estimation

As mentioned above, the key problem of the proposed method is to find a non-zero orthogonal vector of spoofing SCV, so it's necessary to estimate the spoofing SCV at the beginning.

In order to avoid the computational complexity of the conventional two-dimensional time and frequency search for the authentic and spoofing signals, a approximate despreading processing is conducted by multiplying samples with space of Δ and one period of the PRN code.

Assume vector $\mathbf{y}$ is constructed as:

$$\mathbf{y} = \begin{bmatrix} \beta_1 e^{j\theta_1} \\ \beta_2 e^{j\theta_2} \\ \vdots \\ \beta_N e^{j\theta_N} \end{bmatrix} \tag{56.8}$$

where

$$\theta_i = \begin{cases} 1 & i = 1 \\ \angle\left(\sum_{n=0}^{K-1} r(n - i\Delta) r^*(n)\right) & i = 2, \ldots, N-1 \end{cases}$$

$$\beta_i = \sqrt{\sum_{n=0}^{K-1} r(n - i\Delta) r^*(n - i\Delta - T_0)} \quad i = 1, \ldots, N-1$$

and K is the number of samples which are averaged and T_0 is one epoch interval.

Based on the different spatial characteristic of authentic and spoofing signals, the energy of spoofing signals from the same direction can be accumulated constructively while authentic signals from different directions can not. So the phase angles of vector $\mathbf{y}$ can be approximated as:

$$\begin{aligned} \theta_i &= \angle\left(\sum_{n=0}^{K-1} r(n - i\Delta) r^*(n)\right) \\ &\approx \angle\left(C_i \sum_{n=0}^{K-1} \left(\sum_{m=1}^{N_A} P_m^a a_{mi} + b_i \sum_{k=1}^{N_S} P_k^s\right)\right) \\ &\approx \angle\left(C_i b_i K \sum_{k=1}^{N_S} P_k^s\right) = \angle C_i + \angle b_i \end{aligned} \tag{56.9}$$

Based on the periodic characteristic of the PRN codes in the signals, the amplitude of vector $\mathbf{y}$ can be approximated as:

$$\begin{aligned} \beta_i &= \sqrt{\sum_{n=0}^{K-1} r(n - i\Delta) r^*(n - i\Delta - T_0\Delta)} \\ &\approx |C_i| \cdot \left(K\left(\sum_{m=1}^{N_A} P_m^a + \sum_{k=1}^{N_S} P_k^s\right)\right) \triangleq q|C_i| \end{aligned} \tag{56.10}$$

Taking Eqs. (56.9) and (56.10) into Eq. (56.8), the assumed vector $\mathbf{y}$ can be written as:

$$\mathbf{y} = \begin{bmatrix} q \\ q|C_2|e^{j(\angle C_2 + \angle b_2)} \\ \vdots \\ q|C_N|e^{j(\angle C_N + \angle b_N)} \end{bmatrix} = q\mathbf{C}\bar{b} = q\mathbf{b} \tag{56.11}$$

which concludes to a linear estimation of the spoofing SCV **b**.

56.3.2 Null Steering of the Synthesized Antenna Array

From Eq. (56.11), it is obvious that the orthogonal vector of vector **y** is orthographic to spoofing SCV. The orthogonal projection to the spoofing subspace can be obtained as:

$$P_{\perp} = I_N - \mathbf{y}\left(\mathbf{y}^H\mathbf{y}\right)^{-1}\mathbf{y}^H \tag{56.12}$$

so any vector in the subspace $P_{\perp}$ is orthographic to the vector **y** and also orthographic to the spoofing SCV **b**.

Taking an arbitrary vector **h** and define:

$$\mathbf{f} = P_{\perp}\mathbf{h} \in P_{\perp} \tag{56.13}$$

and the vector **f** is orthographic to the spoofing SCV **b**:

$$\begin{aligned} \mathbf{f}^H\mathbf{b} &= \mathbf{h}^H(P_{\perp})^H\mathbf{b} = \mathbf{h}^H P_{\perp}\mathbf{b} \\ &= \mathbf{h}^H\left(I_N - \mathbf{y}\left(\mathbf{y}^H\mathbf{y}\right)^{-1}\mathbf{y}^H\right)\mathbf{y}/d \\ &= \mathbf{h}^H\left(\mathbf{y} - \mathbf{y}\left(\mathbf{y}^H\mathbf{y}\right)^{-1}\mathbf{y}^H\mathbf{y}\right)/d \\ &= \mathbf{h}^H(\mathbf{y} - \mathbf{y})/d = 0 \end{aligned} \tag{56.14}$$

Applying the vector f to the synthesized antenna array output vector, the spoofing signals are removed from the original signals and an equivalent antenna direction pattern null is formed at the direction of spoofing signals:

$$\begin{aligned} v(n) &= \mathbf{f}^H\mathbf{R}_{\mathbf{N}}(n) \\ &= \sum_{m=1}^{N_A}\mathbf{h}^H P_{\perp}\mathbf{a}_{\mathbf{m}}\sqrt{P_m^a}F_m^a(n) \\ &\quad + \mathbf{h}^H P_{\perp}\mathbf{b}\sum_{k=1}^{N_S}\sqrt{P_k^s}F_k^s(n) + \mathbf{h}^H P_{\perp}\boldsymbol{\eta}(n) \\ &\approx \sum_{m=1}^{N_A}\mathbf{h}^H P_{\perp}\mathbf{a}_{\mathbf{m}}\sqrt{P_m^a}F_m^a(n) + \mathbf{h}^H P_{\perp}\boldsymbol{\eta}(n) \end{aligned} \tag{1.15}$$

v(n) is the signal sequence after spoofing mitigation, and can be fed to the conventional GNSS receivers.

56.3.3 *Structure of Anti-spoofing Receivers*

An anti-spoofing receiver structure based on the proposed technique above can be configured as (Fig. 56.3):

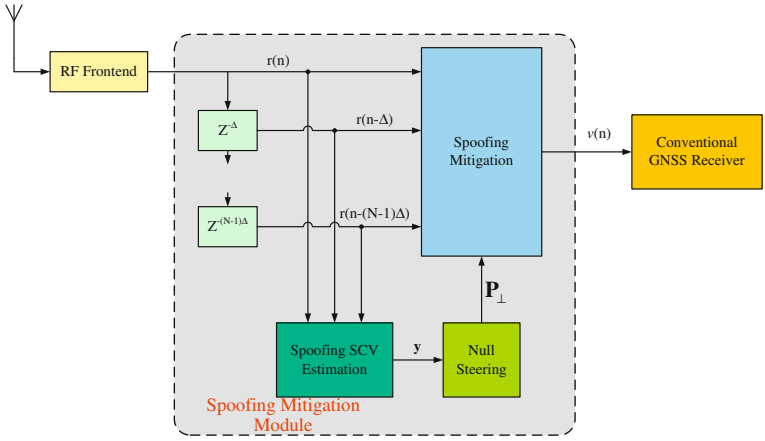

Fig. 56.3 Configuration of anti-spoofing GNSS receiver

56.4 Simulation Results

A simulation environment based on Matlab is setup to verify the effectiveness of the proposed anti-spoofing technique. Herein, four authentic and nine spoofing GPS L1 C/A PRNs are simulated, with CNRs (carrier power-to-noise density ratio) at 45 and 47dBHz respectively, while the velocity of receiver is 30 m/s and a two-element antenna array is synthesized.

Figures 56.4 and 56.5 show the cross ambiguity functions (CAF) for a certain PRN code before and after spoofing mitigation. It is observed that before spoofing mitigation (Fig. 56.4) there are two remarkable signal peaks in the time–frequency space and the authentic signal peak is weaker than the spoofing one, which could induce to a mistake signal acquisition. After spoofing mitigation (Fig. 56.5), it is obvious that only the authentic signal peak is reserved in the time–frequency space, which prevents the conventional receiver being affected by the spoofing interfere.

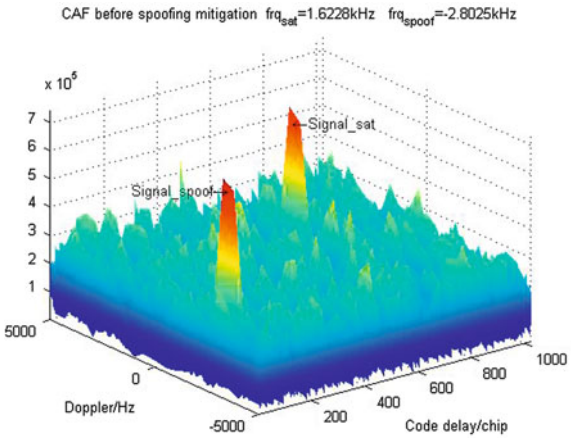

Fig. 56.4 CAF before spoofing mitigation

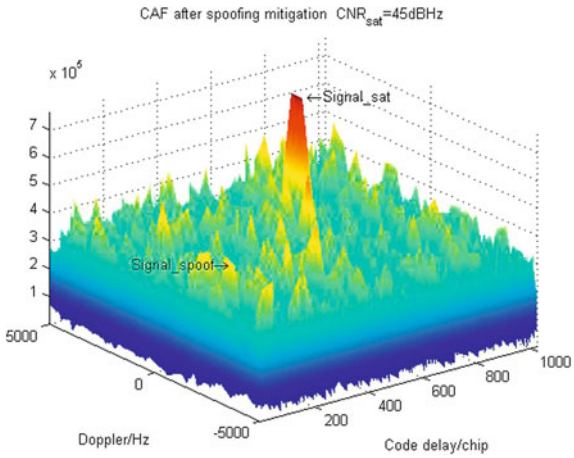

Fig. 56.5 CAF after spoofing mitigation

It can also be observed by compare the Figs. 56.4 and 56.5 that after spoofing mitigation, the noise floor of the CAF increases obviously, which results in 2 dB deterioration in the CNR of the authentic signal. Lightening the deterioration of spoofing mitigation to the authentic signals would be a major future work.

56.5 Conclusions

A low complexity spoofing mitigation method based on a moving antenna is proposed in this paper, which could effectively mitigate the spoofing signals from a point transmitter. The advantages in receiver cost and size make it suitable in civil navigation and timing domain.

References

1. Basker S (2010) Jamming: a clear and present danger. GPS World 21(4):8–9
2. Volpe JA (2001) Vulnerability assessment of the transportation infrastructure relying on the global positioning system. National Transportation Center, p 8
3. Broumandan A, Lin T, Moghaddam A, et al. (2007) Direction of arrival estimation of GNSS signals based on synthetic antenna array. In: Proceeding of ION GNSS 2007, pp 728–738
4. Pozzobon O (2011) Keeping the spoofs out. Inside GNSS 6(3):55
5. Wesson K, Shepard D, Humphreys T (2012) Straight talk on anti-spoofing. GPS World 23(1):32–39
6. Jafarnia-Jahromi A, Nielsen J, Lachapelle G (2012) GPS spoofer countermeasure effectiveness based on using signal strength, noise power and C/No observables. Int J Satell Commun Network 30:181–188
7. Daneshmand S, Jafarnia-Jahromi A, Lachapelle G (2012) A low-complexity GPS anti-spoofing method using a multi-antenna array. in: Proceeding of ION GNSS 2012

Chapter 57
DVFS Energy-Saving Scheduling of Navigation Receiver Based on Equilibrium Optimization

Wei Wu, Rui Ge, Shao-jie Ni and Fei-xue Wang

Abstract Hand-held or portable navigation receivers are powered by battery. The energy-saving design is very important to extend battery life. High-precision geodesic navigation receivers can be installed in fixed ground station. Dynamic-adaptive navigation receivers can be carried in a ship, aircraft, missile, or other vehicle. Although those carriers can supply sufficient power, low power design is of great benefit to system cooling, thus improves the receiver life cycle. Receiver processor can schedule task in busy or idle state. Dynamic Voltage and Frequency Scaling (DVFS) technology adjusts system voltage and frequency dynamically to make use of idle state, thus effectively saves system energy. This paper analyses the energy-saving scheduling design of multi-channel receivers, where the power consumption is remarkably reduced based on DVFS, meanwhile receiver works well in real-time. A DVFS energy-saving scheduling method based on equilibrium optimization is proposed, where the receiver clock frequency is dynamically adjusted corresponding to the number of satellites available using utilization equilibrium rule and its reverse counterpart. Our method optimizes the energy-saving factor based on utilization feedback approach and schedulability condition approach, and voltage and frequency adjusting is transformed into execution time increase. Monte Carlo simulations and experiment results show that our method is independent of scheduling algorithm and schedulability condition, and has low time complexity. Utilization equilibrium rule can obtain more balanced energy-saving factor compared with its reverse counterpart, and schedulability condition approach can acquire higher total utilization compared with utilization feedback approach, thus effectively reduce receiver power consumption.

Keywords Navigation receiver · Dynamic voltage and frequency scaling (DVFS) · Task scheduling · Energy-saving · Equilibrium optimization

W. Wu (✉) · R. Ge · S. Ni · F. Wang
Satellite Navigation R&D Center, National University of Defense Technology, Changsha, China
e-mail: wuwei198106@163.com

J. Sun et al. (eds.), *China Satellite Navigation Conference (CSNC) 2013 Proceedings*, Lecture Notes in Electrical Engineering 243,
DOI: 10.1007/978-3-642-37398-5_57,

57.1 Introduction

For battery-powered hand-held or portable navigation receivers, the energy-saving design is very important to extend battery life. High-precision geodesic navigation receivers can be installed in fixed ground station. Dynamic-adaptive navigation receivers can be carried in a ship, aircraft, missile, or other vehicle. Although the carriers can supply sufficient power, low power design is of great benefit to system cooling, thus increases receiver life cycle. Modern embedded design widely uses Dynamic Voltage and Frequency Scaling (DVFS) technology, along with Dynamic Power Management (DPM) technology such as hibernate, sleep and shutdown, achieves system low-power design [1, 2].

Power optimization design of visible satellites' signal receiving is important for receiver energy-saving design. Literature [3] models DVFS power consumption based on low-power System on Chip (SoC), two scheduling approaches Cycle conserving EDF (CCEDF) and Look Ahead EDF (LAEDF) are applied to verify the power optimization. Literature [4] considers task preemptive scheduling in hard real-time system, uses multiple voltage levels for task set to obtain low power. Literature [5] illustrates that DVFS is suitable for thermal management, and is able to achieve a square or cubic reduction in power relative to the performance loss. Those known DVFS methods pay little attention to the task sets with dynamic timing parameters.

DPM configures processor into extreme low power mode, lets part/all of the circuit modules hibernate, sleep or shutdown, reduces the power consumption in system idle [1, 6]. The navigation tasks should always keep working, so that navigation receiver continually tracks the visible satellites. On the other hand, the user interface, such as LCD display and instruction control module, can operate under extreme low power mode when not used.

We propose a DVFS energy-saving scheduling method based on equilibrium optimization. The receiver working channel number is determined according to the visible navigation satellite number. Navigation task execution time optimization is achieved by adjusting voltage and frequency, and the optimal task working frequency is calculated. The power consumption of receiver processor is reduced as much as possible, meanwhile receiver works well in real-time.

57.2 Fundamentals and Modeling

57.2.1 DVFS Fundamentals

As for modern processor based on CMOS technology, the core power consumption can be composed of dynamic power and static power [3]:

$$P_{DD} = P_{Dynamic} + P_{static} \tag{57.1}$$

$$P_{Dynamic} = \alpha C_S V_{DD}^2 f_{clk} \tag{57.2}$$

$$P_{static} = I_{leak} V_{DD} \tag{57.3}$$

where α denotes activity factor, C_S denotes switching capacity, V_{DD} denotes core voltage, f_{clk} denotes clock frequency, I_{leak} denotes leakage current. The leakage current works at the level of mA or uA, so the dynamic power is ignored in our model.

Instruction cycles per unit time are calculated as:

$$n = f_{clk} t \tag{57.4}$$

With (57.2) and (57.4), the core energy per unit time is:

$$E_{DD} = \alpha C_S V_{DD}^2 n \tag{57.5}$$

When the core voltage is reduced, its power consumption achieves a square or cubic reduction. The core voltage should be higher than the threshold voltage of the transistor (when it starts conducting). In working region of CMOS circuits, clock frequency f_{clk} is approximately proportional to the core voltage V_{DD} [7]. As the supply voltage is reduced, working frequency also reduces, which is the fundamentals of DVFS technology. Meanwhile, frequency reduction increases the task execution time, which may influence the system real-time performance.

57.2.2 Receiver Task Analysis

Consider the navigation receiver with maximal M channels: Fig. 57.1.

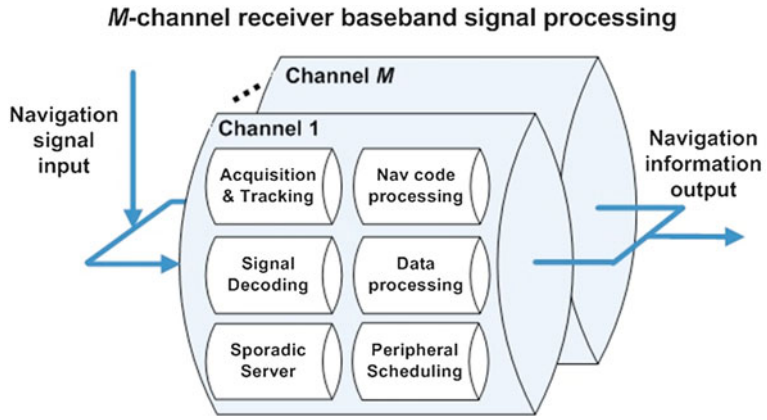

Fig. 57.1 Block of navigation receiver signal processing tasks

The receiver runs with m ($0 < m \leq M$) channels working, while the value of m can be dynamically adjusted according to the number of satellites available. Each working channel operates signal acquisition, tracking, decoding and processing tasks of the corresponding satellite.

57.2.3 Task Scheduling Modeling

Consider scheduling N periodic tasks. Task set is $T = \{\tau_1, \tau_2, \ldots, \tau_N\}$. Tasks can be modeled as

$$\tau_i = \{C_i, T_i, D_i\} \quad i = 1, 2, \ldots, N \tag{57.6}$$

where C_i denotes the worst-case execution time of τ_i. T_i denotes the period of τ_i. D_i denotes the relative deadline of τ_i. The utilization of τ_i is defined as:

$$U_i = C_i/T_i \qquad i = 1, 2, \ldots, N \tag{57.7}$$

In order to schedule receiver in the right way, parameters C_i, T_i and D_i need to be properly designed. The task set is schedulable if all tasks can achieve deadline without overhead. Assume $\mathbf{\Psi}$ denotes the scheduling algorithm. The period and deadline of receiver tasks are decided by system requirement, T_i and D_i are fixed parameters, so the scheduling algorithm of a receiver can be denoted as:

$$\mathbf{\Psi}\{\boldsymbol{T}\} = \mathbf{\Psi}\{C_i\}|_N \quad i = 1, 2, \ldots, N \tag{57.8}$$

57.2.4 DVFS Energy-Saving Scheduling

Consider m-channel working simultaneously. Using inter-task approaches [2], frequency reduction linearly increases task execution time. For a single channel, assume the worst case instruction cycles of task τ_i is denoted as n_i, the working frequency is f_i, than its WCET (Worst Case Execution Time) is n_i/f_i. thus the WCET of m-channel is:

$$C_i = mn_i/f_i \quad i = 1, 2, \ldots, N \tag{57.9}$$

Our goal is to minimize the system power consumption, meanwhile guarantee receiver task schedulable:

$$\textbf{Min} \qquad E_{DD} \tag{57.10}$$

$$\text{Subject to } \Psi\left\{\left(\tfrac{1}{f_i}\right)mn_i\right\}|_N \text{ schedulable}$$

57.3 Energy-Saving Algorithm

57.3.1 Energy-Saving Factor Optimization Based on Equilibrium

According to (57.10), m and n_i are already known, suitable f_i is the key of energy-saving scheduling. The energy-saving factor of task τ_i is defined as:

$$\eta_i = 1/f_i = Weight_i \eta_0 \quad i = 1, 2, \ldots, N \tag{57.11}$$

Different weighting schemes influence our chosen $Weight_i$. With utilization equilibrium rule, the obtained utilization is proportional to single-channel utilization, so the weighting factor is:

$$Weight_i \equiv 1 \tag{57.12}$$

With utilization reverse-equilibrium rule, the obtained utilization of each task is equal to $1/N$, which is inversely proportional to single-channel utilization, so the weighting factor is:

$$Weight_i = \sum U_j / U_i \quad i = 1, 2, \ldots, N \tag{57.13}$$

57.3.2 Scheduling Based on Utilization Feedback Approach

When the scheduling algorithm $\boldsymbol{\Psi}$ is Rate Monotonic (RM) or Earliest Deadline First (EDF), the energy-saving factor can be calculated according to utilization. The upper bound of total utilization is denoted as $Bound_{\boldsymbol{\Psi}}$. For RM and EDF, we have [8]:

$$Bound_{RM} = N(2^{1/N} - 1) \tag{57.14}$$

$$Bound_{EDF} = 100\%$$

With (57.7), (57.9), (57.11) and (57.14), the energy-saving factor is:

$$\eta_0 = Bound_{\boldsymbol{\Psi}} / (\boldsymbol{Weight}. * \boldsymbol{U}) \tag{57.15}$$

where $\boldsymbol{Weight}$ denotes the $Weight_i$ vector, $\boldsymbol{U}$ denotes the U_i vector of m-channel task set.

57.3.3 Scheduling Based on Schedulability Condition Approach

As for reliability and real-time performance, receiver design adopts fixed priority scheduling, which is a Non-deterministic Polynomial (NP) problem [8]. Take the Katcher condition as an example, The schedulability condition of task τ_i is [9]:

$$\min_{0<t\le D_i} W_i(t)/t \le 1 \tag{57.16}$$

$$W_i(t) = \sum_{\tau_k \in hp(\tau_i)} \lceil t/T_k \rceil C_k + \sum_{\tau_l \in ip(\tau_i)} C_l$$

where $hp(\tau_i)$ denotes the set of tasks that have priorities higher than that of τ_i and $ip(\tau_i)$ denotes the set of tasks that have the priority the same as that of τ_i.

With (57.7), (57.9), (57.11) and (57.16), the energy-saving factor can be calculated. In order to improve the calculating efficiency of this NP problem, a dichotomy search method is used to search for energy-saving factor between the total utilization interval [$Bound_{RM,}$ 100 %]. The search flowchart is Fig. 57.2:

Solving schedulability condition often takes much time. For on-line application, energy-saving factor η_0 can be pre-calculated off-line corresponding to different weighting rule and different value of $m(0 < m \le M)$. Afterwards, η_0 can be obtained through look-up table as below Table 57.1:

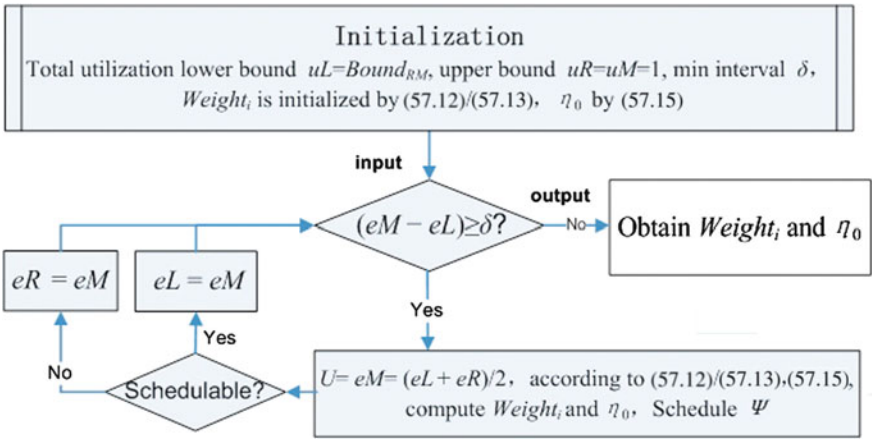

Fig. 57.2 Search flowchart of energy-saving factor

Table 57.1 Energy-saving factor look-up table

m	η_0 (Utilization equilibrium)	η_0 (Utilization reverse-equilibrium)
1	η_{01A}	η_{01B}
2	η_{02A}	η_{02B}
……	……	……
M	η_{0MA}	η_{0MB}

57.3.4 Task Working Frequency

With energy-saving factor calculated, the frequency for each task can be computed by (57.11):

$$f_i = 1/(Weight_i \eta_0) \tag{57.17}$$

Receiver design often chooses a base frequency f_0, the task working frequency can be any multiple of f_0. Assume task working frequency is between $[j_{\min} f_0, j_{\max} f_0]$, with positive integer $j_{\min} < j_{\max}$. The working frequency of each task can be calculated as:

$$f_i = \begin{cases} \lceil f_i/f_0 \rceil f_0 & j_{\min} f_0 \le f_i \le j_{\max} f_0 \\ j_{\min} f_0 & f_i < j_{\min} f_0 \\ j_{\max} f_0 & f_i > j_{\max} f_0 \end{cases} \tag{57.18}$$

57.4 Simulations and Experiments

57.4.1 Monte Carlo Simulation

Use Monte Carlo method simulates task set stochastically. The simulation parameters are:

1. task number N is from 2 to 20, with interval 2.
2. task period is randomly produced between [1, 1000] with uniform distribution.
3. task utilization is randomly produced between [0, 2/N] with uniform distribution.

For each N, produce 1,000 groups of task sets independently. Katcher condition and RM bound are used to obtain the optimal DVFS power consumption. Then, the average power of 1,000 groups of task sets for each N is calculated and plotted below (the normalized power for 100 % utilization is 1):

According to Fig. 57.3, the Katcher condition approach is better than the RM bound approach. Compared to RM bound, Katcher condition can obtain higher total utilization, thus reduce clock frequency more sharply. On the other hand, utilization equilibrium rule is better than its reverse counterpart. This is because

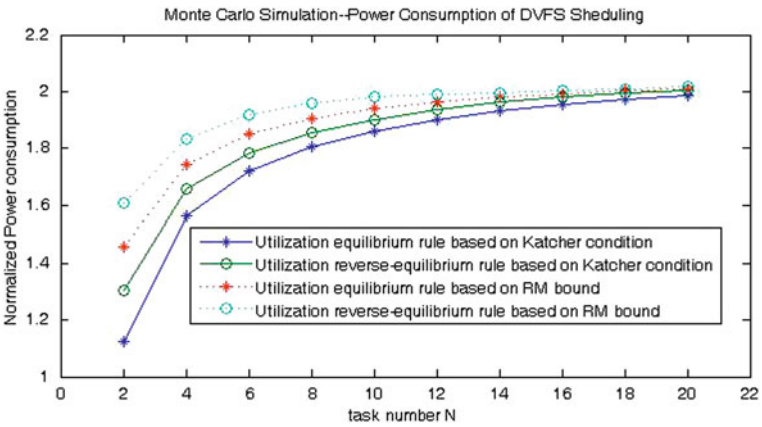

Fig. 57.3 Monte Carlo simulations of DVFS

utilization equilibrium makes frequency reduce proportionally for each task, and the energy-saving factor of each task is uniform. As for utilization reverse-equilibrium rule, the frequency reduction of each task results in disequilibrium. Some tasks may reduce more compared with utilization equilibrium rule, meanwhile some tasks may reduce much less, or even increase contrarily. That is why the utilization reverse-equilibrium rule consumes more power.

57.4.2 Adjust Clock Frequency According to Satellite Number

Certain receiver works at 400 MHz. Its normalized task parameters are as follows: Table 57.2.

With base frequency $f_0 = 10$ MHz, we examine the optimal power consumption corresponding to different channel number m. The Katcher condition is used with utilization equilibrium rule, with the value of m between [5, 12]. The optimal core power consumption with different m is as follows: Table 57.3.

Table 57.2 Task set parameters of a single channel in a receiver

i	Task name	Priority	C_i	$T_i = D_i$
1	Acquisition and tracking	3	51/1000	1
2	Signal decoding	2	57/1000	12
3	Data processing	2	354/1000	60
4	Sporadic server	2	18/1000	60
5	Navigation code processing	1	36/1000	108
6	Peripheral scheduling	1	33/1000	300

Table 57.3 Channel number m versus clock frequency and power

m	Core power	Working frequency (MHz)
5	P_0	200
6	$1.309P_0$	240
7	$1.633P_0$	280
8	$1.969P_0$	320
9	$2.314P_0$	360
10	$2.667P_0$	400
11	$3.025P_0$	440
12	$3.388P_0$	480

Note the power consumption with 5 channels working at 200 MHz is denoted as P_0

57.4.3 Power Consumption Analysis

Use look-up table with Katcher condition approach and utilization equilibrium rule, the energy-saving timing is analyzed below: Fig. 57.4.

In the above plot, figure (a) plots the number of satellites available versus time in 24 h, where the receiver working channel number is equal to the visible satellite number. Figure (b) plots the receiver working frequency versus time, which is proportional to the working channel number. Figure (c) plots the energy-saving factor versus time, which is inversely proportional to the working channel number. Figure (d) plots the instantaneous power consumption of the receiver. Compared with the receiver working at 400 MHz, our method saves about 23.6 % energy, and guarantee receiver schedulable even with 12 channels working.

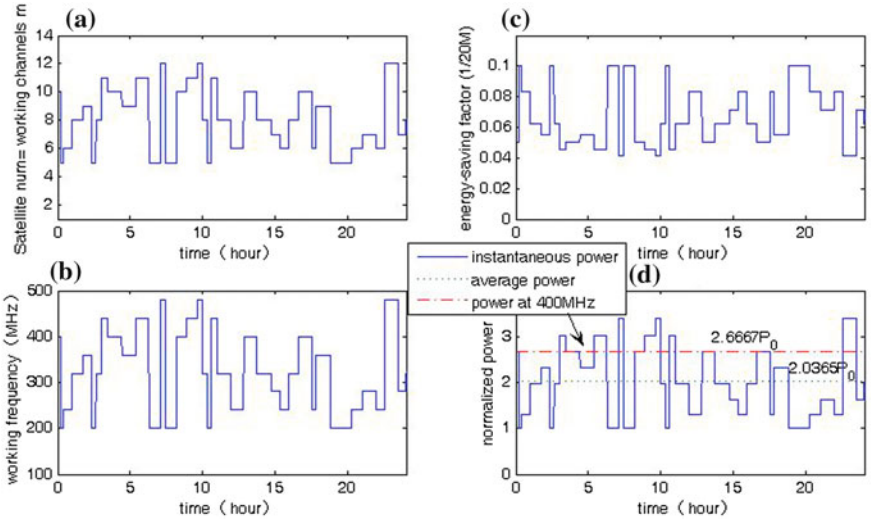

Fig. 57.4 Receiver energy-saving plot: (**a**) number of satellites available in 24 h; (**b**) frequency; (**c**) energy-saving factor; (**d**) core power

57.5 Conclusion

A DVFS energy-saving scheduling method is proposed based on equilibrium optimization. The receiver working channel number is determined according to visible navigation satellite number. Navigation task execution time optimization is achieved by adjusting voltage and frequency. Our method is independent of scheduling algorithm and schedulability condition, thus can extend to multi-channel real-time DVFS energy-saving design. Furthermore, utilization equilibrium optimization can be conveniently applied to both uniprocessor and multiprocessor energy-saving scheduling.

Simulation results show that our method has low time complexity, and can quickly calculate energy-saving factor suitable for receiver timing requirement. Utilization equilibrium rule can obtain more balanced energy-saving factor compared with its reverse counterpart, thus is more suitable for multi-channel receiver DVFS design, and reduces receiver power consumption more effectively.

Acknowledgments The authors acknowledge the many useful insights from Compass Navigation Receiver Design Team.

References

1. X Zuo, Liu Y (2011) Low power performance achievement in embedded system. In: 2nd international conference on artificial intelligence, management science and electronic commerce, 2011, pp 4655–4658
2. Venkatachalam V, Franz M (2005) Power reduction techniques for microprocessor systems. ACM Comput Surv 37(3):195–237
3. Castagnetti A, Belleudy Ć, Bilavarn Ś, Auguin M (2010) Power consumption modeling for DVFS exploitation. In: 13th euromicro conference on digital system design: architectures, methods and tools, 2010, pp 579–586
4. Wang W, Mishra P (2010) PreDVS: preemptive dynamic voltage scaling for real-time systems using approximation scheme. DAC'10, 2010, pp 705–710
5. Kong J, Chung SW, Skadron K (2012) Recent thermal management techniques for microprocessors. ACM Comput Surv 44(3):13:1–13:42
6. Jejurikar R, Gupta R (2004) Dynamic voltage scaling for systemwide energy minimization in real-time embedded systems. In: Proceedings of the 2004 international symposium on low power electronics and design, 2004, pp 78–81
7. Borkar S, Chien AA (2011) The future of microprocessors. Commun ACM 54(5):67–77
8. Laplante P, Ovaska S (2012) Real-time systems design and analysis: tools for the practitioner. Wiley-IEEE Press, New York
9. Wu W, Ni S, Wang F (2011) A method for scheduling receiver tasks based on maximum allowed execution time dichotomy search. J Navig 83–90

Chapter 58
The Modeling and Analysis for the Assessment of GNSS Spoofing Technology

Meng Zhou, Hong Li and Mingquan Lu

Abstract As various application of navigation technology penetrating people's life and national security, spoofing and anti-spoofing techniques have become hot research topics. Since more and more complicated spoofers have emerged, from repeater to creator, then to receiver-spoofer, the research of anti-spoofing is very urgent. Moreover, research and assessment on spoofing are prerequisite and foundation for anti-spoofing research. Considering various aspects of spoofing technology, including spoofing efficiency, blanket factor, influence area, destructiveness, and the risk of being determined, this paper explores the factors needed in comprehensive evaluation of GNSS spoofing technology. Through modeling the spoofing signals, this paper builds up an evaluation computing model for various metrics. And it analyzes the evaluation results of common spoofing technologies by utilizing various models. This paper also builds up a reference score model for these various metrics through expert scoring method. Finally, the paper also introduces the plan for future research work.

Keywords GNSS · Spoofing · Assessment · Modeling

58.1 Introduction

In 2001, the U.S. Department of Transportation released a report, which is about the vulnerability of the U.S. transportation system [1]. It reported that "as GPS further penetrates into the civil infrastructure, it becomes a tempting target that could be exploited by individuals, groups, or countries hostile to the U.S." This report showed that the spoofing has become one of the primary threats to the satellite

M. Zhou (✉) · H. Li · M. Lu
Department of Electronic Engineering, Tsinghua University, Beijing 100084, China
e-mail: maggice-sun@163.com

J. Sun et al. (eds.), *China Satellite Navigation Conference (CSNC) 2013 Proceedings*, Lecture Notes in Electrical Engineering 243,
DOI: 10.1007/978-3-642-37398-5_58,

navigation system as an artificial malicious interference. Spoofing usually makes position/navigation receivers generate wrong positioning or timing information by delaying the real signal or self-generated pseudo-signal. Compared to blanket jamming, spoofing is more concealed. Spoofing threats cannot be ignored in the scenarios like life safety services, financial services, and military confrontation.

Spoofing techniques that have been proposed and implemented can be divided into three categories: (1) Repeater: This approach works through broadcasting the received signal to the interfered region after delaying it and amplifying it. (2) Creator: This approach works through generating the pseudo-signals consistent with the same structure of real signal through the local signal generator [2]. (3) Receiver-spoofer: This kind of spoofer takes the data including Doppler, the pseudo-code delay, the navigation message and the time information which are token from received real signal flow into spoofing signal generator as input, and then generates pseudo-signals flow as output [4].

Therefore, it's extremely necessary to establish GNSS spoofing defense system as soon as possible. However, only a based on the deep research, analysis and evaluation of these spoofing methods, we can effectively the defense systems. The assessments of the spoofing performance and potential threats, can provide reference and guidance for the defense system.

58.2 Assessment Metrics for Spoofing

58.2.1 Valid Probability

A direct result of spoofing has only two states: spoofed and non-spoofed. Valid probability is the probability that the spoofer can successfully deceived GNSS receiver. If a GNSS receiver under deception still receives the normal navigation signal, it will be named as spoofing failure probability.

Spoofing valid probability varies with the GNSS receivers used. In the case with both actual and spoofing signal, we can calculate the probability of the two states of a certain receiver, spoofed or non-spoofed, by analyzing its signal capturing strategy, the receiving process and the anti-spoofing measures. The detailed calculating model and method will be demonstrated and discussed in the Sect. 3.1.

58.2.2 Blanket Factor

Blanket Factor is defined as the power ratio between spoofing signal and normal navigation signal to reach certain spoofing valid probability. Under the same constraint conditions, including receiver, spoofing valid probability and so on, the smaller blanket factor is, the more advanced the spoofing technique is.

58.2.3 Spoofing Region

Spoofing region includes distance and space coverage. With the constraint of spoofing valid probability, the further distance is, or the greater coverage is, the stronger the spoofer is.

58.2.4 Destructiveness

When spoofing successes, the most obvious impact is put on the positioning or timing results. But, the measurement of destructiveness varies indifferent application fields. For example, in the smart grid monitoring system, the GNSS timing function is used to measure the voltage and current phase of grid network. Once the timing is spoofed, that may lead to estimation errors on the grid, which guides the operator to make the wrong operation. In such applications, destructiveness of spoofing should be measured by the economic losses. In the navigation warfare, the use of spoofing to misleading the positioning result to a hostile missiles or other offensive weapons, will reach the purpose of disrupting the enemy's strategy and tactics. Its destructiveness should be measured by the extent of the impact of the war.

58.2.5 Onset Time

The time slot needed between the spoofer launching signals and the target receiver being impacted to a certain extent (for example, the pre-defined positioning results, or deterioration of positioning accuracy to pre-defined threshold) is called onset time. The shorter onset time of the spoofer is, the better performance of the spoofing technology is.

58.2.6 Spoofing Risk

The risk always appears with the benefits. The risk of a spoofer is being detected by the target receiver or even exposing its position to the anti-spoofing technology, which can bring danger to its own. Therefore, if a spoofer cannot disguise itself, although it is highly destructive, we are not able to profit from it. Thus, spoofing risk is an important indicator to assessment one spoofing technology. This assessment should include the reasonableness of signal power, arrival time, arrival azimuth, positioning result, and the similarity between spoofing signal and real navigation signals. The probability that the spoofer will be detected by the target receiver is a

good measurement for spoofing risk. The probability of being discovered is higher, and the risk is greater; the probability of being discovered is lower, and the risk is smaller (higher probability of being discovered means greater risk).

58.2.7 Technology Costs

This indicator is to test the difficulty of the technique to be implemented. If a kind of spoofing technology is too difficult to be achieved, or too costly to be massively produced, it would be more like an armchair strategist than an application, even through it is theoretically feasible, or even with good results. The cost is also one of important evaluation indices.

58.2.8 Comprehensive Assessment

As we mentioned above, it can be found that assessment of spoofing technique includes many factors. Some factors can be calculated by quantifying the specific values, and other factors (such as destructiveness, difficulty of achievement, etc.) are difficult to be quantitatively calculated. Therefore, it is necessary to explore an assessment model, which considers all these factors, to get a more objective assessment of spoofing.

58.3 Computing Model of Evaluation

58.3.1 Valid Probability Calculation

If spoofing signals and GNSS satellite signals at the receiver side co-exist during the capture phase, the receiver may detect the positioning signals through the GNSS satellite signals, or also possibly through spoofing signals. When the GNSS receiver regards a spoofing signal as a normal navigation signal to process, it is a valid spoofing. Capture is the first part of the receiver to receive and process navigation signals. Once the receiver catches spoofing signal, it will probably use the spoofing signal for subsequently tracking, demodulating, ranging, positioning calculating, and etc. Then it will be impacted by the spoofing signal. Therefore, we analyze the valid probability of spoofing from the capturing aspect in this paper. Capture performances are closely related to capture strategies of the receiver. In the same way of spoofing, the receiver adopting different kinds of capture strategies will cause a different probability of spoofing. It is assumed that the receiver uses the decision strategy of maximum threshold value.

58.3.1.1 Computing Model

During the dwell time T, in each cell, the I and Q signals are integrated and dumped and the envelope $\sqrt{I^2 + Q^2}$ is computed or estimated. Each envelope is compared to a threshold to determine the presence or absence of the SV signal. This method called the threshold decision is widely used in GNSS receivers. Figure 58.1 shows the probability distribution functions (pdf) of the envelopes of three signals, including the noise, real signals and spoofing signals. A similar concept was explained in [3].

The pdf for noise with no signal present, p_n, has a zero mean. The pdf for noise with the signal present, p_s, has a nonzero mean. The pdf for noise with the real signal and spoofing signal present, p_j, has a nonzero mean larger than p_s. For the chosen threshold, V_t, any cell envelope that is at or above the threshold is detected as the presence of the signal. Any cell envelope that is below the threshold is detected as noise. The two statistics that are of most interest for us are the probability of detecting real signal, P_{sd}, and the probability of detecting spoofing signal, P_{jd}. These are determined as follows:

$$P_{sd} = \int_{V_t}^{\infty} p_s dz \tag{58.1}$$

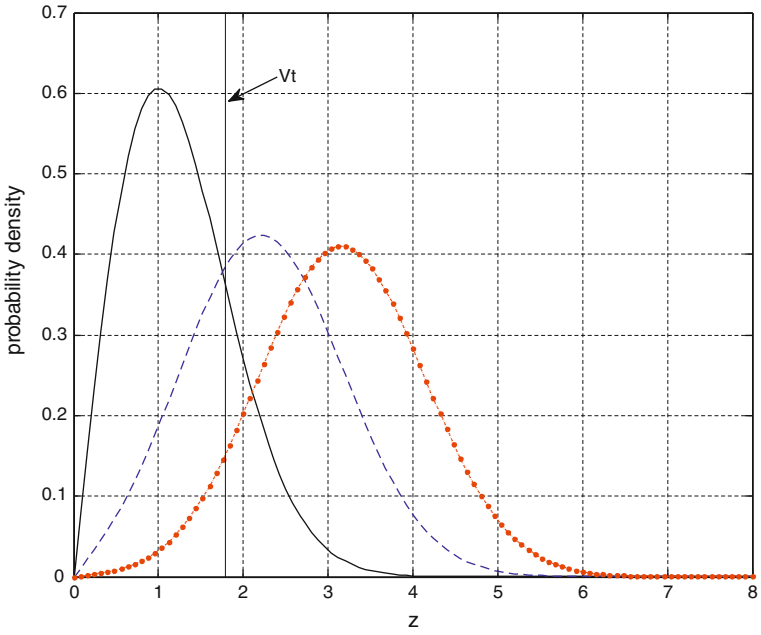

Fig. 58.1 Pdfs of the noise, navigation and spoofing signals

$$P_{jd} = \int_{V_t}^{\infty} p_j dz \tag{58.2}$$

where:
$p_s(z)$ pdf of the real signal's envelope
$p_j(z)$ pdf of the spoofing signal's envelope

We assume that case 1 represents a detection of a real signal, case 2 represents a detection of a spoofing signal, and case 1 and 2 are independent. Thus, we can have the following conclusions:

1. The probability that the real signal and spoofing signal are detected simultaneously is:
$$P_{s\cap j} = P_{sd} \times P_{jd} \tag{58.3}$$

2. The probability of only detecting the spoofing signal is:
$$P_{\bar{s}\cap j} = (1 - P_{sd}) \times P_{jd} \tag{58.4}$$

3. The probability of only detecting the real signal is :
$$P_{s\cap\bar{j}} = P_{sd} \times \left(1 - P_{jd}\right) \tag{58.5}$$

4. The probability that the real signal and spoofing signal are not detected is:
$$P_{\bar{s}\cap\bar{j}} = (1 - P_{sd}) \times \left(1 - P_{jd}\right) \tag{58.6}$$

When situation (2) occurs, the receiver is spoofed, and when situation (3) and (4) occur, the receiver is non-spoofed. Under situation (1), that the real signal and spoofing signal are detected simultaneously, the decision strategy of receiver determines whether the spoofing is successful or not. If the receiver selects signals by timing (first or second appear), the successful spoofing can be ensured by controlling the arrival time of spoofing signal. If the receiver adopts maximum decision, for example, choosing the bigger one between two signals, the probability of valid spoofing equals to the probability that spoofing signal j is higher than real signal s under situation (1), which is determined as follow:

$$\oint_{j>s} p(s,j) = \int_{V_t}^{\infty}\int_{s}^{\infty} p_{s\cap j} djds = \int_{V_t}^{\infty} p_s \int_{s}^{\infty} p_j djds \tag{58.7}$$

We assume that I and Q have a Gaussian distribution. Assuming that the envelope is formed by $\sqrt{I^2 + Q^2}$, then Thus,p_s and p_j are Ricean distributions defined by:

$$p_s(z) = \begin{cases} \frac{z}{\sigma_n^2} e^{-\left(\frac{z^2+A^2}{2\sigma_n^2}\right)} I_0\left(\frac{zA}{\sigma_n^2}\right), & z \geq 0 \\ 0, & z < 0 \end{cases} \tag{58.8}$$

where:

z	value of the random variable
σ_n^2	RMS noise power
A	RMS signal amplitude
$I_0\left(\frac{zA}{\sigma_n^2}\right)$	modified Bessel function of zero order

Equation (58.8) for z ≥ 0 can be expressed in terms of the predetection SNR as presented to the envelope detector, *C/N* (dimensionless), as follows:

$$P_s(z) = \frac{z}{\sigma_n^2} e^{-\left(\frac{z^2}{2\sigma_n^2} + C/N\right)} I_0\left(\frac{z\sqrt{2C/N}}{\sigma_n^2}\right) \tag{58.9}$$

where:

C/N	$C/N = A^2/2\sigma_n^2 = (C/N_0)T$, is predetection of signal to noise ratio
T	search dwell time

Considering formula (58.1), (58.2), (58.3), (58.4), (58.7) and (58.9), let $\sigma_n = 1$ (normalized), spoofing valid probability can be expressed as the function of C/N_0 (real signal to noise ratio), J/N_0 (spoofing signal to noise ratio), and T.

58.3.1.2 Analysis of Computing Results

The proposed method has been tested by the Matlab software in order to observe that how far the parameters like C/N_0, J/N_0, and T can impact the spoofing valid probability. The following parameters setting have been considered for the test:

1. The threshold in terms of the desired single trial probability of false alarm P_{fa} and the measured 1-sigma noise power: $V_t = \sqrt{-2\sigma^2 ln P_{fa}}$. Let $\sigma_n = 1$ (normalized), $P_{fa} = 0.16$, then the threshold $V_t = 1.9144615$.
2. Let C/N = 1 and J/N = 1–10(step intervals is 0.5). Let C/N = 2 and J/N = 2–10(step intervals is 0.5). Let C/N = 3 and J/N = 3–10 (step intervals is 0.5).

Figures 58.2, 58.3, 58.4 show the results with the parameters set above.

As can be seen from Figs. 58.2–58.4: (1) as detecting the two signals simultaneously, the probability that the spoofing signal is greater than the normal

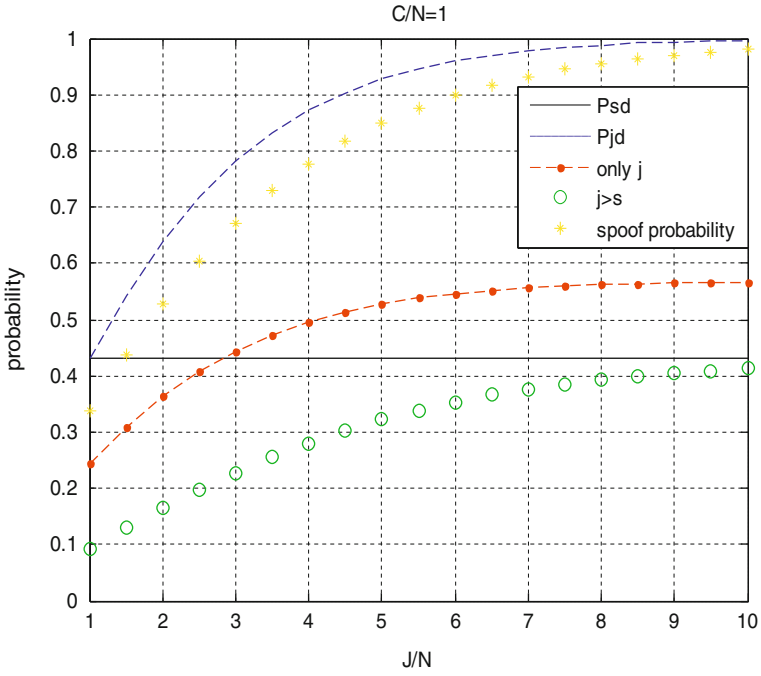

Fig. 58.2 The spoofing probability with C/N = 1

navigation signal increases significantly according to the increasing of J/N, whereas the probability that only the spoofing signal is detected does not change much; (2) spoofing probability is always less than the detection probability of spoofing signals, but with the increasing of J/N, spoofing probability will gradually approaching the detection probability; (3) when the C/N is small (C/N = 1), in the composition of the spoofing probability, the deception caused by situation (2) is greater than the one by situation (1); when C/N is greater (C/N = 2,3), the deception resulted by situation (1) is greater than the one by situation (2).

In addition, we can see from Figs. 58.2–58.4, the changing trend of the spoofing probability are accordant with different setting of C/N. When J/N is greater than 12, the spoofing probability tends to 100 %, and it changes slowly. In order to better observe the change trend of the spoofing probability, the first derivative plates of curve shown above are presented in Fig. 58.5.

As the plates suggest, at J/N∈[1, 6], the change rate of probability is much higher than in other region. When J/N is greater than 12, the change rate is less than 0.01. Therefore, we can get the greatest improvement of spoofing probability by increasing J/N in interval [1, 6]. However, once J/N is over 12, with the increase of J/N, it will raise the risk of being discovered, instead of the improvement of the spoofing valid probability.

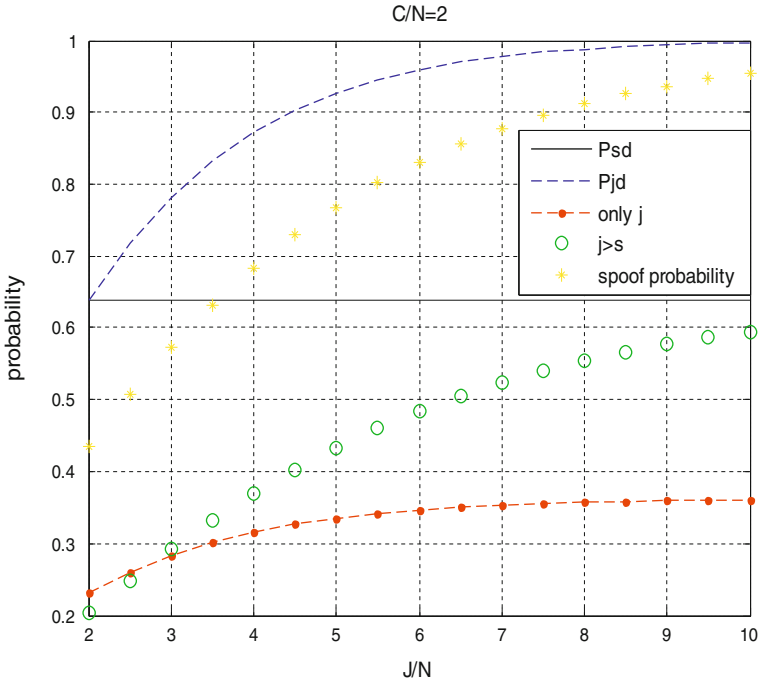

Fig. 58.3 The spoofing probability with C/N = 2

58.3.2 Calculation of Blanket Factor

58.3.2.1 Blanket Factor Lower Limit Computing Model

Blanket factor is the power ratio between spoofing signal and normal navigation signal to reach the certain spoofing valid probability. For $J/N = m \cdot C/N$, the m is named as the blanket factor. Based on the previous analysis, spoofing valid probability can be expressed with C/N and *m*.

Set the minimum blanket factor as the optimization target, and spoofing valid probability as the constraint. The optimization function can be determined as follow:

$$\begin{cases} \min m \\ \text{s.t. } P(m, \frac{C}{N}) \geq P_0 \end{cases} \tag{58.10}$$

According to formula (58.10), we can calculate the lower limit of the blanket factor *m*.

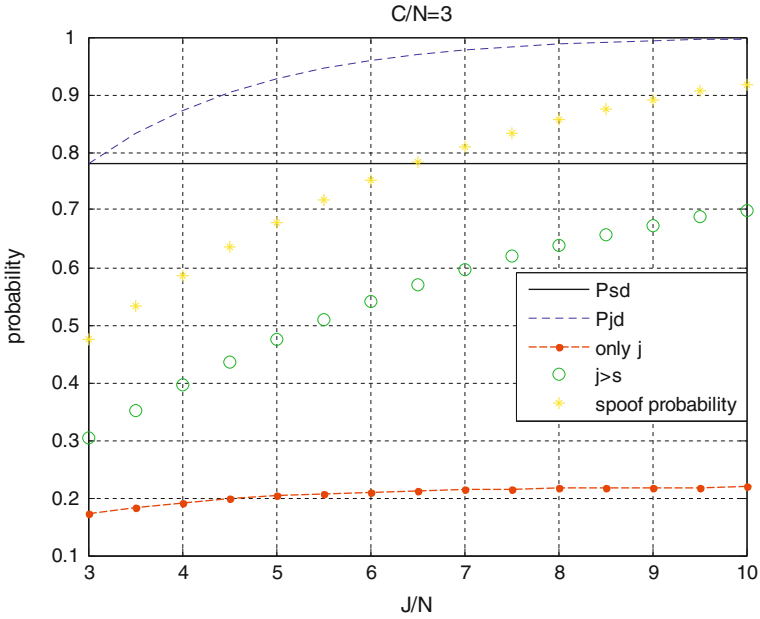

Fig. 58.4 The spoofing probability with C/N = 3

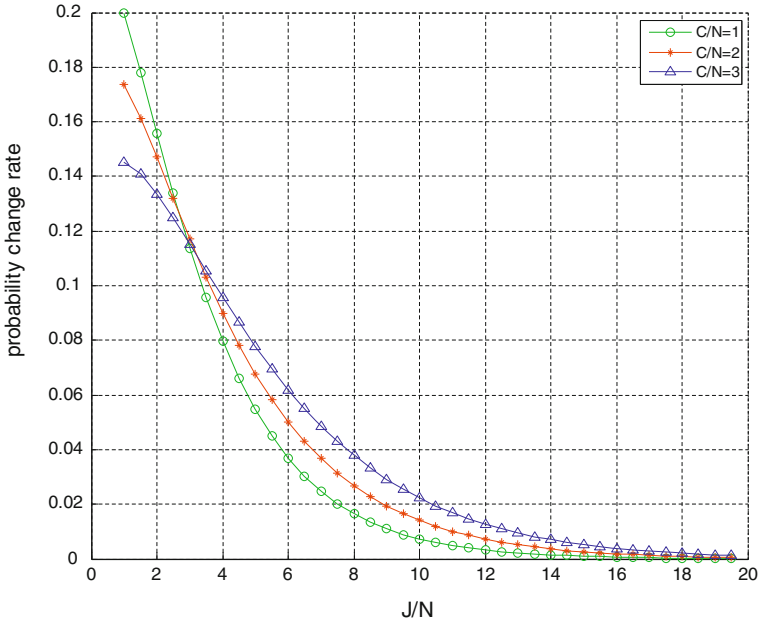

Fig. 58.5 The change rate of spoofing probability

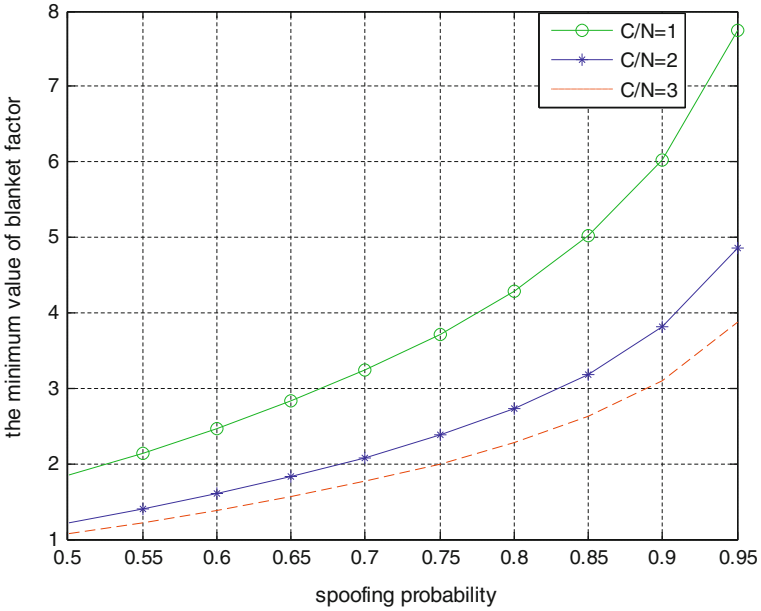

Fig. 58.6 The minimum value of blanket factor

58.3.2.2 Analysis of Computing Results

The proposed method has been tested with a Matlab simulation. The following parameters setting have been considered for the test:

1. Let $\sigma_n = 1$ (normalized), $P_{fa} = 0.16$, then the threshold $V_t = 1.9144615$.
2. Let C/N = 1, 2, and 3, respectively, and spoofing valid probability = 50–95 % (step intervals is 5 %).

Figure 58.6 shows the results with the parameters set above.

As shown in Fig. 58.6, the bigger C/N is, the lower the lower limit of blanket factor is. This is because the blanket factor is equivalent to the amplification factor between J/N and C/N. With the increasing of C/N, the desired blanket factor is smaller to reach the same J/N.

58.3.3 Onset Time

Determination of the Onset Time is divided into two parts. One is the time t_1, represents the time slot from the spoofer emitting the spoofing signal to the receiver capturing that spoofing signal. Another is the time t_2, represents the time slot from the receiver capturing the spoofing signal to its positioning or GPS clock

resulting error to reach the desired value. It is necessary to measure the two time values to assess the performance of spoofer respectively, and gives a comprehensive evaluation result.

58.3.4 Spoofing Risk

The risk of spoofing can be quantitatively evaluated by the probability of being perceived by the target receiver. Means of spoofing detection are usually independent to each other, that is, the detection process can be considered to be a series of several detectors. We assume that P_1 is the detection probability of detector A and P_2 is the detection probability of detector B, then the probability of the two detectors to perceive spoofing signals is given follow:

$$\mathrm{P} = 1 - (1 - P_1) \times (1 - P_2) \tag{58.11}$$

Without loss of generality, we can define the risk function of a specific spoofing technique as follow:

$$\mathrm{P} = 1 - \prod_{i=1}^{n} (1 - P_i) \tag{58.12}$$

where, P_i is the probability that the *i*th detector of the target receiver perceives this spoofing signal.

As can be seen from the definition of the risk function, the more spoofing detection means of a receiver have, the greater risk of the spoofing signal to be detected.

58.3.5 Other Indicator

The other assessment indicators such as destructiveness and technology cost are difficult to be quantified. So we consider to adopt the expert evaluating method for these indicators.

58.3.6 Comprehensive Assessment

Expert scoring method is a qualitative description method. First, it selects several indicators according to the specific requirements. Then it develops the criteria based on the evaluation project. After that, a number of representative experts will be employed. Each of the experts will give a score to the indicators by their experience. Last, the score will be compiled. The characteristics of this method are simple, intuitive, and easy in computing. Furthermore, it is able to calculate

quantitatively and can conduct the evaluation for those indicators, which cannot be calculated. Therefore, this is a good way to do comprehensive assessment. Nowadays, to compile the scores, additive evaluation method, product evaluation method, and multiplying evaluation method, the weighted evaluation method, the efficiency coefficient method are often used.

Because of the multi-attribute of spoofing technical, we usually use the weighted evaluation method for the assessment. The valid probability is the assessment constraints, based on expert experience. And we calculate jamming indicator, destructiveness and onset time, to obtain a comprehensive assessment of the results.

58.4 Conclusions

This paper has mentioned many factors to provide a comprehensive assessment for GNSS spoofing technic, such as: valid probability, blanket factor, spoofing region, destructiveness, spoofing risk. An evaluation model for these indicators is established in this paper. Furthermore, evaluation results based on this model are analyzed. In future research, in order to prove the models and methods which are presented above, a spoof simulation environment will be built to generate spoof signal.

References

1. John A (2001) Vulnerability assessment of the transportation infrastructure relying on the Global Positioning System, Tech. rep. Volpe National Transportation Systems Center, USA
2. Warner J, Johnston R (2003) A simple demonstration that the global positioning system (GPS) is vulnerable to spoofing. J Secur Admin (In Press)
3. Kaplan ED, Hegarty CJ (2006) Understanding GPS: principles and applications [M]. Artech House Publishers, UK
4. Humphreys TE, Ledvina BM, Psiaki ML, O'Hanlon BW, Kintner PM Jr (2008) Assessing the spoofing threat: development of a portable GPS civilian spoofer. In: Proceedings of the ION GNSS meeting. Institute of Navigation, Savannah

Chapter 59
A Code Phase Measurement Method for Snap-Shot GNSS Receiver

Bin Huang, Zheng Yao, Mingquan Lu and Zhenming Feng

Abstract The snap-shot working mode has turned out to be a good choice in location-based services (LBS) applications for it can significantly reduce the calculation and power dissipation in the receiver. However, within a limited snap-shot data, the code loop is difficult to enter into convergence state which leads to a large measurement error. A Kalman filter (KF) based code loop can accelerate convergence but the accuracy is still very poor. In this paper, a novel code phase measurement method is developed and used for snap-shot receivers. A KF based code loop is used to maintaining code tracking, further, a non-causal smoothing estimator is joined to improve measurement accuracy of code phase and obtain more accurate positioning results. Experiment results show that, within a second or less snap-shot data, the method with smoothing can obtain a relatively accurate code phase, and with the same snap-shot length, the proposed method has better estimation accuracy than one without smoothing and the conventional code tracking loop. Finally, the method is applied in a real-time software receiver which working in snap-shot mode.

Keywords Global navigation satellite system · Snap-shot receiver · Kalman filter · Code phase tracking · Non-casual smoother

59.1 Introduction

Usage of global navigation satellite system (GNSS) has become quite common in our society, allowing many applications that are used in our daily life. Conventional GNSS receivers work in a continuous way which at least four satellites are

B. Huang (✉) · Z. Yao · M. Lu · Z. Feng
Tsinghua University, 1109-1110 Wei Qing Building, Beijing 100084, China
e-mail: b-huang09@mails.tsinghua.edu.cn; bing890816@163.com

J. Sun et al. (eds.), *China Satellite Navigation Conference (CSNC) 2013 Proceedings*, Lecture Notes in Electrical Engineering 243,
DOI: 10.1007/978-3-642-37398-5_59,

tracked continuously in order to provide location fixes. In order to provide a fix a conventional GPS C/A code receiver needs at least 30 s for the length of a main frame of navigation message is 30 s. However, for location-based services (LBS) under the demand of these receivers, the computational complexity, resource utilization, power dissipation and the response time of the results are unacceptable.

Under this application background, the receivers with a snap-shot working mode get more and more concerned [1–4]. In snap-shot working mode, the receiver is in a dormant state in most of the time, it turns into the snap-shot operating state only when it receives a user request. Upon each positioning request, the receiver takes a snapshot and performs signal processing to generate a PVT result.

In a snap-shot receiver, the length of the snap-shot data is the key parameter. Considering the application background, the length of the snap-shot data is expected to be as short as possible. However, with a shorter snap-shot length, the conventional Delay-Locked Loop (DLL) is hard to obtain relatively accurate code phase result within less update times. In Driessem [5] and Qian et al. [2], a KF based DLL technique is used to speed up the loop convergence, but the poor accuracy of the code phase is still the most troublesome problem.

In this paper, a non-causal smoother is joined to the KF based DLL to improve the tracking accuracy of the code phase within the limited data. Since the data has been cached, the smoothing result of the code phase can use additional information which contained the future data. The simulation results show that, within a second or less snap-shot data, the method with smoothing can obtain a relatively accurate code phase, and with one hundred milliseconds snap-shot length, the proposed method has better estimation accuracy than one without smoothing and the conventional code tracking loop. In addition, the proposed method has been used on a snap-shot receiver which processes the actual GNSS signals. Actual positioning results show that the snap-shot receiver with smoothing have the smaller RMS error and more focused positioning results. The horizontal RMS error with proposed method is 2.9986 m that has been able to meet most of the LBS applications' demand.

The remainder of this paper is divided into four sections. Section 59.2 gives a brief overview of the snap-shot GNSS receivers. Section 59.3 presents KF base code phase tracking loop models and the proposal loop filter solution. The experiment results and discussions are presented in Sect. 59.4. Finally the conclusions are shown in Sect. 59.5.

59.2 Snap-Shot GNSS Receiver

GNSS positioning has turned out to be an enabler of LBS in recent years. However, the continuous working mode is not suitable for LBS. On the one hand, the positioning information does not actually require a high update rate. On the other hand, in order to ensure the real-time tracking, the receiver must occupy a great many processor resources and have a high priority. In the context of application requirements, a snap-shot working mode is an ideal solution.

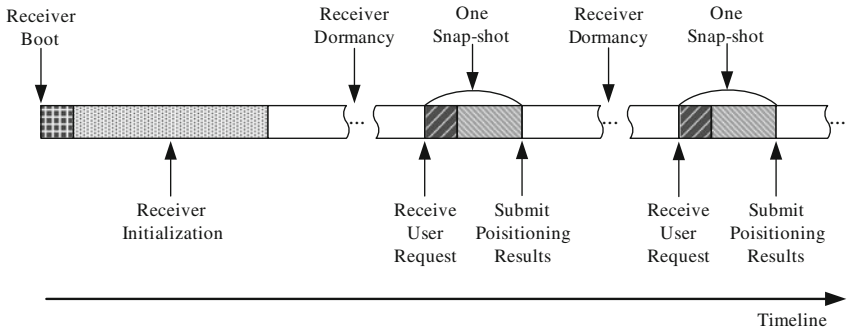

Fig. 59.1 The flow chart of a snap-shot receiver

Figure 59.1 shows the flow chart of the snap-shot receiver architecture [1]. It can be observed that after boot before turning into the snap-shot mode, the receiver need to complete a initialization process, which to get necessary information for the snap-shot positioning such as GNSS time and satellite ephemeris, etc. The initialization process is necessary because the relatively accurate GNSS time is required and it generally difficult to obtain from external auxiliary. For LBS, if receiver can utilize assisted network or internet to obtain the auxiliary information such as current satellite ephemeris and coarse time, both the complexity and the calculation of the initialization process can be greatly reduced.

After the initialization process, the receiver turn into a cycle stage which only in the snap-shot state or dormant state. It turns into the snap-shot working state only when it receives a user request. In the snap-shot working sate, it collects several hundred milliseconds snap-shot data for the latter part of signal analysis. Note that the snap-shot data has been cached, so it is not need real-time signal acquisition and tracking. The receiver can handle these channels serially, which can significantly reduce the occupancy rate of the receiver processor. When code phase estimated values of more than four visible satellites are acquired, a positioning calculating program can be called to obtain positioning results.

Usually, the snap-shot length would be only a few hundred milliseconds for the limited storage of consumer electronics devices. A shorter snap-shot length, however, directly affect the measurement accuracy of code phase thereby affect the positioning results. So, how to solve measurement accuracy of the code phase under the limited snap-shot length is the most critical problem in snap-shot receiver.

59.3 Models of Code Phase Measurements

The conventional GNSS receivers generally use the DLL to track the spreading code and obtain accurate code phase. A wide loop bandwidth make the DLL turn into the locked state faster but it also cause the decline in code phase accuracy.

In Driessem [5] it has been proved that the use of a KF based tracking loop is possible to achieve both rapid full-in and reliable tracking without the tradeoffs associated with conventional fixed loop gain tracking loop. However, the poor accuracy of the code phase is still the most troublesome problem. In snap-shot receiver, the signal data has been cached, which allows a non-causal smoother to be used to further enhance the measurement accuracy of the code phase. In Psiaki [6], a fixed-interval smoother is used which get more accurate than KF, the accuracy increases because the estimate at any given time is based on a larger data set. In Yao et al. [1], it uses a dual update-rate tracking loop with a non-casual smoothing estimator to obtain a relatively accurate estimation. In this section, an equivalent KF based DLL is derived, and the structure of a non-causal fixed-point smoother is presented.

59.3.1 Kalman Filter Model Based Delay-Locked Loop

In order to use the KF theory, the dynamic model of the system must be established. Assuming the signal contains only one order dynamic, the process can be modeled by

$$s_{n+1} = \begin{pmatrix} \phi_{n+1} \\ T \cdot f_{n+1} \end{pmatrix} = \begin{pmatrix} 1 & 1 \\ 0 & 1 \end{pmatrix} \begin{pmatrix} \phi_n \\ T \cdot f_n \end{pmatrix} + \begin{pmatrix} 0 \\ u_n \end{pmatrix} = As_n + U_n \tag{59.1}$$

$$x_n = \begin{pmatrix} 1 & 0 \end{pmatrix} s_n + w_n = hs_n + w_n \tag{59.2}$$

$$u_n \sim N(0, \sigma_u^2), \quad w_n \sim N(0, \sigma_w^2), \quad U_n \sim N(0, Q), \quad \mathrm{Q} = \begin{pmatrix} 0 & 0 \\ 0 & \sigma_u^2 \end{pmatrix} \tag{59.3}$$

where ϕ_n and f_n are the code phase and code Doppler rate at the start of the n-th update interval, T is PIT in seconds, s_n is state vector and x_n is the observation of the n-th code phase, u_n is the additive white Gaussian motivate noise, and w_n is the observation noise of code phase. The observation noise is come from the phase discriminator here, so the noise variance is related to the type of the discriminator. When using the classical early-minus-late power (EMLP) discriminator [7], the variance of the observation noise is

$$\sigma_w^2 = \frac{d}{4(C/N_0)T}\left(1 + \frac{2}{(C/N_0)T(2-d)}\right) \tag{59.4}$$

where d is the early-late chip spacing in chips, and C/N_0 is CNR.

Define $K_n = \begin{pmatrix} K_{n0} & K_{n1} \end{pmatrix}^T$ as the Kalman gain vector, $\hat{\mathbf{s}}_n = \begin{pmatrix} \hat{\phi}_n & T \cdot \hat{f}_n \end{pmatrix}^T$ as the estimated value of the n-th update interval, $s_{n|n-1} = \begin{pmatrix} \hat{\phi}_{n|n-1} & T \cdot f_{n|n-1} \end{pmatrix}^T$ as a prediction value for n-th from sample $n-1$, as $M_{n|n-1}$ the minimum mean square error

(MMSE) matrix of the prediction, and $M_{n|n}$ as the MMSE matrix of the filter. The KF form equations are as follows with the initial conditions $\hat{s}_{-1|-1}$ and $M_{-1|-1}$ [8]:

$$\begin{cases} \hat{s}_{n|n-1} = A\hat{s}_{n-1|n-1} \\ M_{n|n-1} = AM_{n-1|n-1}A^T + Q \\ K_n = \frac{M_{n|n-1}h^T}{hM_{n|n-1}h^T + \sigma_w^2} \\ M_{n|n} = (I - K_n h)M_{n|n-1} \\ \hat{s}_{n|n} = \hat{s}_{n|n-1} + K_n(x_n - h\hat{s}_{n|n-1}) = \hat{s}_{n|n-1} + K_n\varepsilon_n \end{cases} \tag{59.5}$$

where ε_n is equivalent to the output of the phase discriminator.

Figure 59.2 shows estimated value of the code phase which using a conventional DLL and a KF based DLL, it can be clearly seen that, for conventional DLL, the 2 Hz loop bandwidth make the DLL turn into the locked state faster but it also cause the decline in code phase accuracy, and the KF based DLL can achieve fast acquisition time and low tracking jitter when the loop turns into steady-state. However, within a snap-shot length less than one second, the accuracy is still very poor.

59.3.2 Fixed-Point Smoother Model

Since the signal data has been cached, which allows a non-causal filter to be used to further enhance the measurement accuracy of the code phase. The extended RTS for fixed-point smoother is based on the KF, it has the following form Andrew and James [9]:

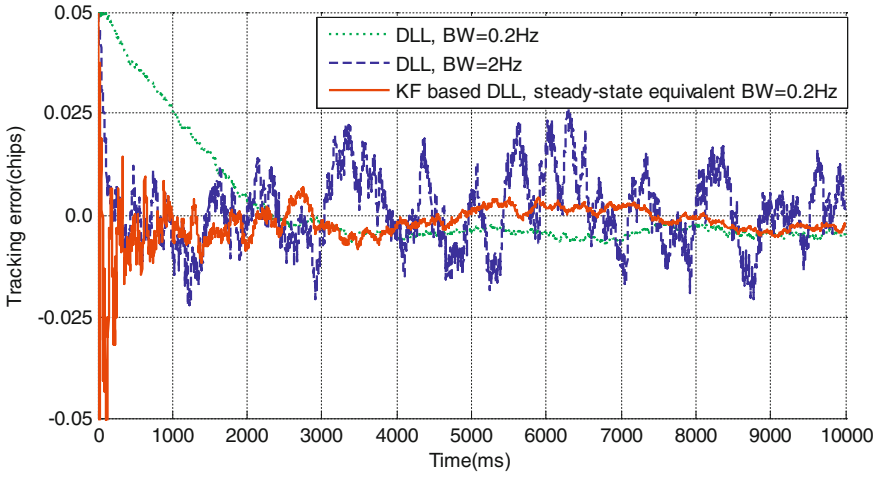

Fig. 59.2 The contrast between a conventional DLL and a KF based DLL

$$\widetilde{s}_{p|n} = \widetilde{s}_{p|n-1} + \Theta_{p,n} K_n \varepsilon_n \,,\ \mathrm{n} > \mathrm{p} \tag{59.6}$$

where t_p is the selected time and p is the fixed-point, and the initial state $\tilde{s}_{p|p}$ is equal $\hat{s}_{p|p}$ which has been estimated at the above KF approach.

$$\begin{cases} \Theta_{p,p} = I \\ \Theta_{p,n+1} = \Theta_{p,n}(I - K_n h) M_{n|n-1} A^T M_{n+1|n}^{-1} \end{cases} \tag{59.7}$$

The error covariance of the smoothing estimator $M_{p,n}$ can be computed by

$$\begin{cases} M_{p,p} = M_{p|p-1} \\ M_{p,n+1} = M_{p,p} - \Theta_{p,n} K_n h M_{n|n-1} \Theta_{p,n}^T \end{cases} \tag{59.8}$$

Assume that N is the total update count of the loop, the smoothing result is $\widetilde{s}_{p|N}$. For fixed-point smoother, there is a problem to be solved is how to select the fixed-point equivalent to how to select p here.

Figure 59.3 shows the typical error variances of KF based DLL. It can be clearly seen that the error covariance after smoothing is smaller than not smoothing. This result is very nature because the smoothing results for fixed-point uses additional information which contained the future data. Besides, it also can be seen that the minimum of the smoothed error covariance can be obtained near the middle time.

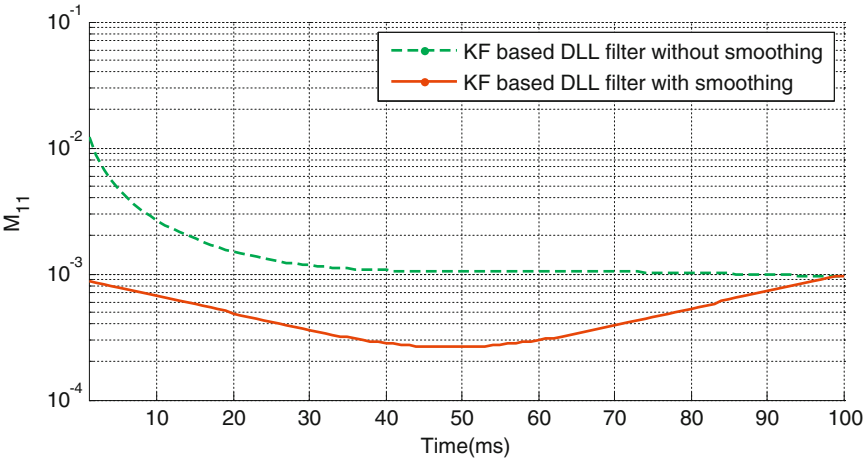

Fig. 59.3 The typical error variances of KF based DLL

59.4 Experiment Results

59.4.1 Code Phase Estimated Accuracy

To illustrate the estimated accuracy of the proposed technique, several simulations will be implemented and the results under different circumstances will be presented. Assuming that the simulation input signal is a GPS C/A signal which is generated by Matlab. The conventional DLL uses a second order loop, and carrier loop is a first order FLL with 10 Hz loop bandwidth.

Figures 59.4 and 59.5 shows the tracking error standard deviations of these loops against CNR. The CNR is from 30 to 50 dB-Hz with 2 dB-Hz increment. The initial code phase deviation is 0.25chips and the initial carrier Doppler deviation is 500 Hz, the accuracy of these values are similar to the capture results of a normal receiver. Each value has been evaluated through a Mote Carlo simulation over 500 tests.

It can be observed that by use of smoothing, the code phase estimate has a higher accuracy. This is primarily because that the smoother uses additional information which contained the future data than the predication. So if the smoothed estimate value of code phase is used to calculate the position, it is possible improve the accuracy of the results. In Fig. 59.4, the KF based DLL has the better tracking performance than the conventional DLL. It is because the KF based DLL has a faster convergence rate. In Fig. 59.5, with a 10,000 ms snap-shot length, it can be seen obviously from the results that the KF based DLL is equivalent with the conventional loop when they are both into the steady-state, and even if they all enter the steady-state, the proposed result still has the highest

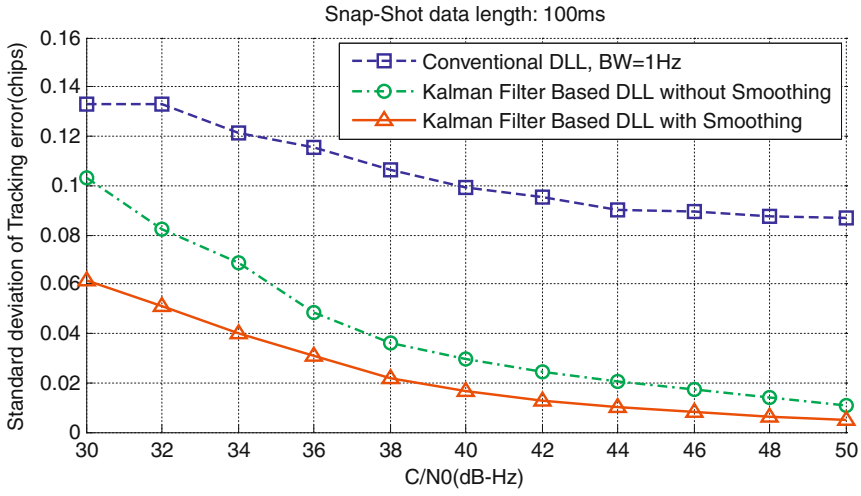

Fig. 59.4 The standard deviation of the tracking error, 100 ms snap-shot

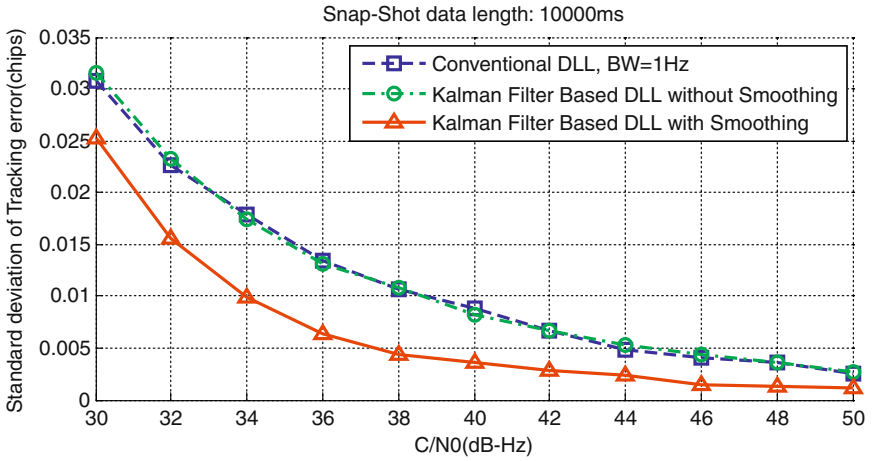

Fig. 59.5 The standard deviation of the tracking error, 10,000 ms snap-shot

accuracy. But 10,000 ms snap-shot is too long, generally for LBS, the length less than 1,000 ms can be accepted.

Figure 59.6 shows the impact of the snap-shot length T_t on the tracking accuracy when C/N_0 is 40 dB-Hz. It can be seen that for all three methods, increasing T_t can improve the tracking accuracy especially when T_t is smaller than 2 s. Ihe loop with smoothing can achieve the better tracking accuracy in the same snap-shot length. The code phase accuracy of proposed method has 3.3 dB larger than the one without smoothing and the conventional loop. It can be clearly seen from Fig. 59.6 that a 500 ms snap-shot for the loop with smoothing can obtain the same accuracy with over 5 s snap-shot for the other two methods. It means in order to achieve the same accuracy, the proposed method required less input data and less memory resource.

59.4.2 Actual Positioning Results

The snap-shot positioning mode is implemented on a GPU based real-time GNSS software receiver which can process all the civil GNSS signals. In snap-shot mode, the receiver complete a initialization process, which to get necessary information for the snap-shot positioning such as GNSS time and satellite ephemeris, etc. The GPS C/A signal is selected as actual measured signal here. The snap-shot data length is 500 ms with the 5 Mchips/s sampling rate, and the steady state bandwidth of KF based DLL is 1 Hz.

To illustrate the accuracy of the positioning results in snap-shot mode, we use the software receiver to receive actual satellites signals and positioning in real-time. A high precision receiver is used to calibrate the position of the antenna in advance. The software results are contrasted with the measurement position to

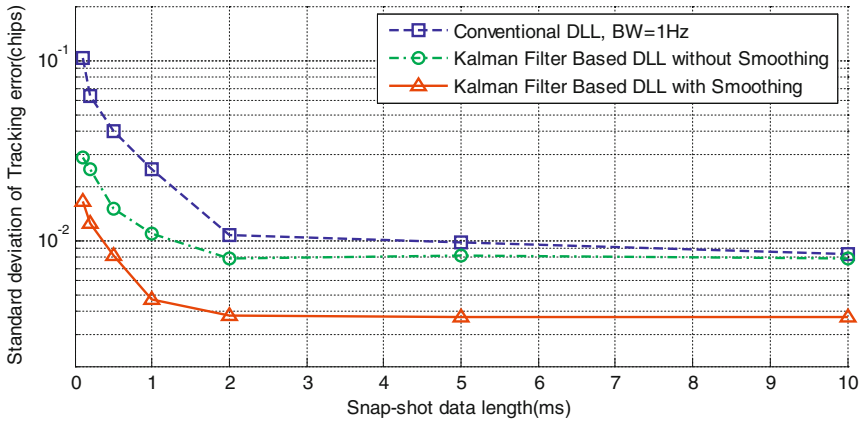

Fig. 59.6 The standard deviation of the tracking error versus the snap-shot length

obtain the positioning error. Meanwhile, in order to illustrate the performance of the receiver, the continuous tracking results are also used to make the contrast.

Figure 59.7 shows the north and east positioning error of the continuous tracking mode and the snap-shot working mode. In snap-shot working mode, due to the limited snap-shot data, so the positioning accuracy would be worse than continuous tracking mode. In the snap-shot receiver, the RMS of the horizontal positioning error is 4.1415 m without smoothing and 2.9986 m with smoothing. If the length of the snap-shot data is increased, then, the equivalent loop width may be further reduced, and thereby it is possible to obtain higher accuracy of the positioning results. However, it also increases the computational complexity and resource utilization. It can be clearly seen from Fig. 59.7 that the snap-shot receiver with smoothing have the smaller RMS error and more focused positioning results. The horizontal RMS error with proposed method, 2.9986 m, has been able to meet most of the LBS applications' demand.

Figure 59.8 shows the cumulative probability distribution of the horizontal positioning error of the continuous tracking mode and the snap-shot working

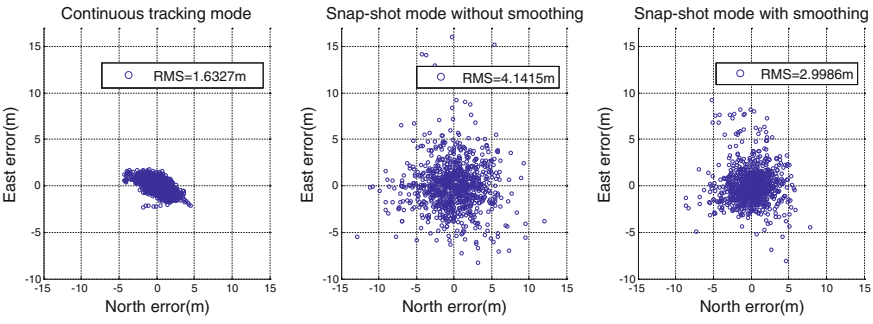

Fig. 59.7 The scatter plot of north and east positioning error

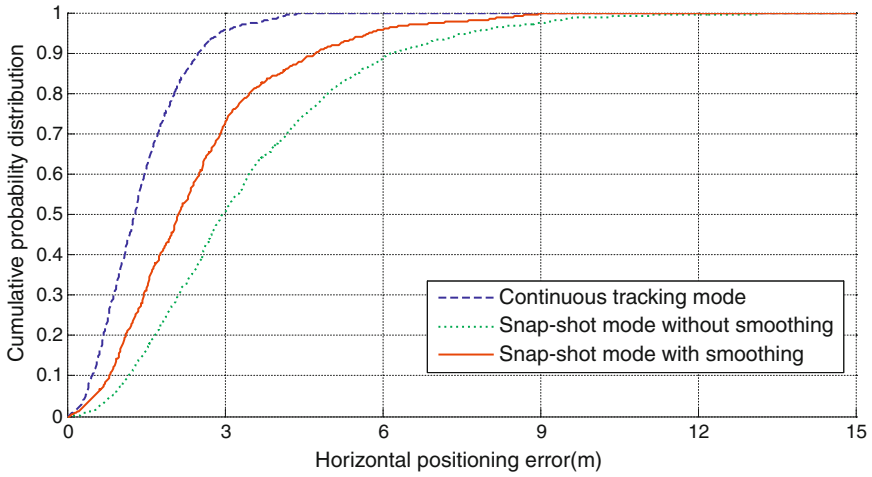

Fig. 59.8 The cumulative probability distribution of horizontal positioning error

mode. It can be observed that by use of smoothing, most of the positioning results are more concentrated near the true value, and more than 90 % of the positioning error is less than 5 m which results cannot be obtained without smoothing. The proposed method achieves the better performance without increasing the snap-shot length. So the required resource and the computational complexity can be reduced.

59.5 Conclusions

In this paper, for the poor accuracy of a snap-shot receiver within a limited snap-shot length, a novel code phase measurement technique has been designed. In this technique, the code phase measurement and extraction is complete in two steps, including a KF based DLL and a non-casual fixed-point smoother. The KF based DLL is used to maintaining code tracking, further, the non-causal smoothing estimator is added to improve measurement accuracy of code phase and obtain more accurate positioning results. This proposed method has been tested using experiment and actual GPS C/A data. The simulation results show that with the same snap-shot length, the proposed method has better estimation accuracy than the loop without smoothing and the conventional loop in common CNR environments. After all loops enter the steady-state, the accuracy of proposed method has 3.3 dB higher than the other two methods. Actual positioning results show that with 500 ms snap-shot length, the snap-shot receiver by use of smoothing has the smaller horizontal RMS error and more focused positioning results. With the proposed method, the horizontal RMS error is 2.9986 m and more than 90 % of the positioning error is less than 5 m. The result is enough for most of the LBS applications.

References

1. Yao Z, Lu M, Feng Z (2010) Spreading code phase measurement technique for snapshot GNSS receiver. IEEE Trans Consum Electron 56(3):1275–1282
2. Qian Y, Cui X, Lu M et al (2008) Snapshot positioning for unaided GPS software receivers. ION GNSS 2008, Savannah, US, pp 2342–2350
3. Knight J, Turetzky G, Norman C et al (1998) SiRF's low power receiver advances. ION GPS 1998, Nashville, US, pp 299–305
4. David JB, Nuria BD, Gustavo LR et al (2006) Innovative techniques for GPS indoor positioning using a snapshot receiver. ION GPS 2006, FortWorth, US, pp 2944–2955
5. Driessem PF (1994) DPLL bit synchronizer with rapid acquisition using adaptive Kalman filtering techniques. IEEE Trans Commun 43(9): 2673–2675
6. Psiaki ML (2001) Smoother-based GPS signal tracking in a software receiver. ION GPS 2001, Institute of Navigation, Alexandria, pp 2900–2913
7. Parkinson BW, Spilker JJ (1996) Global positioning system: theory and applications, vol 1. American Institute of Aeronautics and Astronautice, US
8. Kay SM (1993) Fundamentals of statistical signal processing estimation theory, vol 1: estimation theory. Prentice-Hall, New York
9. Andrew S, James M (1971) Estimation theory with applications to communications and control. McGraw-Hill Book Company, US

Chapter 60
A Novel GPS Cross-Correlation Mitigation Algorithm Based on Code Phase Comparison

Xiaohui Ba, Huahua Duan, Yun Wang and Jie Chen

Abstract The cross-correlation problems occur in any instance in which weak GPS signals need to be acquired and tracked in the presence of other strong GPS signals. The influence of cross-correlation must be considered in the design of high-sensitivity acquisition method. In this paper, a new detection method is presented based on multiple times acquisition and code phase comparison (CPC). One group of code phases is obtained after one acquisition and the code phases of the maximum several peaks are selected and stored in an array. After multiple times acquisition, multiple groups of code phase are obtained. We can find whether the code phase of autocorrelation appears according to the comparison method presented in this paper. The CPC algorithm need not reconfigure the strong PRN signal and has relative higher acquisition sensitivity in the presence of cross-correlation interference. The experimental results show that the CPC method can effectively find autocorrelation peak of weak signal with −147 dBm power level, in presence of one strong signal with −124 dBm power level.

Keywords GPS · Cross-correlation · High-sensitivity · Code phase comparison

60.1 Introduction

The correlation property of GPS C/A code is the relative high autocorrelation peak and the relative low cross-correlation peak. The C/A code cross-correlation functions have peak levels that can be as poor as −24 dB with respect to its maximum autocorrelation for a zero Doppler differences between any two codes. For higher Doppler difference levels at the worst-case intervals of 1 kHz, the

X. Ba (✉) · H. Duan · Y. Wang · J. Chen
The Institute of Microelectronics of Chinese
Academy of Sciences (IMECAS), Beijing, China
e-mail: baxiaohui@ime.ac.cn

J. Sun et al. (eds.), *China Satellite Navigation Conference (CSNC) 2013 Proceedings*, Lecture Notes in Electrical Engineering 243,
DOI: 10.1007/978-3-642-37398-5_60,

cross-correlation levels can be as poor as −21.1 dB [1]. Cross-correlation problems occur in any instance in which weak GPS signals need to be acquired and tracked in the presence of other strong GPS signals. It means that the cross-correlation peak caused by the strong GPS signal may be larger than the auto-correlation peak of weak GPS signal. Thus the influence of cross-correlation must be considered in the design of acquisition method.

There are several cross-correlation mitigation techniques that are currently available for GPS signal processing, such as successive interference cancellation, the near-far detector method, and so on. Successive Interference Cancellation (SIC) is analyzed by Holtzman, in which strong GPS signals are subtracted from the RF input signal prior to correlation of the weak PRN signals [2]. It is the most effective method because the interferences caused by strong signals can be deleted drastically if the strong signals can be perfectly reconfigured. While the method has a large workload, SIC may be unsuitable for inclusion in a GPS chipset in which cost and device complexity are constrained. A near-far detector is presented by Gustavo, which is based on the different statistics of the two largest acquisition peaks [3]. If the different statistic is larger than a threshold, the largest peak is justified as the autocorrelation peak, otherwise, the cross-correlation peak. But its drawback is that the acquisition sensitivity of the method is not enough. Only if the autocorrelation peak is the largest peak, the method may succeed to find the correct code phase of the weak PRN signal. The method is difficult to detect the auto-correlation when the difference of the signal power between strong signal and weak signal is larger than 20 dB. Philip G Mattos presented a new method based on long-time acquisition to solve the cross-correlation [4]. The algorithm adopted shows a smearing response, which means sharp peaks become smooth-topped hills. The signal integrated for 480 ms, is a sharp peak, but after 1.6 s of integration, has a rounded or flat top in the presence of cross-correlation interference. Thus the cross-correlation can be detected. The method needs a relative long GPS IF data (at least one second is required) [4].

In this paper, a new detection method is presented based on multiple times acquisition and code phase comparison (CPC). One group of code phases is obtained after one acquisition and we only select the code phases of the maximum several peaks, and then store the code phases in an array. After multiple times acquisition, we obtain multiple groups of code phases. We can find whether the code phase of autocorrelation appears according to the comparison method presented in this paper.

The CPC algorithm need not reconfigure the strong PRN signal, and has relative higher acquisition sensitivity in the presence of cross-correlation interference. The experimental results show that the CPC method can effectively find autocorrelation peak of weak signal with −147 dBm power level, in presence of one strong signal with −124 dBm power level.

The rest of the paper is organized as follows. The cross-correlation property and how to evaluate the performance of a cross-correlation method are described in Sect. 60.2. The CPC algorithm is presented in Sect. 60.3. Section 60.4 shows simulated and experimental results and Sect. 60.5 draws the conclusions.

60.2 The Analysis of Cross-Correlation and Detection Methods

In this section, we describe the property of cross-correlation and analyze the performance of the cross-correlation mitigation methods.

60.2.1 The Property of Cross-Correlation

The C/A code cross-correlation functions have peak levels that can be as poor as −24 dB with respect to its maximum autocorrelation for a zero Doppler differences between any two codes. For higher Doppler difference levels at the worst-case intervals of 1 kHz, the cross-correlation levels can be as poor as −21.1 dB.

We produce a GPS intermediate frequency (IF) data containing the signal of GPS satellite PRN 1 without adding the Gaussian noise. The Doppler frequency of PRN 1 is zeros. We use PRN 2 to produce the cross-correlation effect with the GPS IF data. The cross-correlation results are shown in Fig. 60.1. The axis of frequency denotes the carrier frequency difference between PRN 1 and PRN 2. It can be seen that multiple peaks appear in the intervals of 1 kHz.

60.2.2 The Evaluation Principle

There are many methods to detect and mitigate the cross-correlation effect. How can we evaluate the performances of these methods? These methods can be divided into two types. The methods of type 1 include Successive Interference Cancellation (SIC) [2], the partitioned subspace projection method [5], Parallel Interference Cancellation [6], Subspace Projection Methods [6], etc. The characteristic of type 1 methods is to delete strong satellite signals from the received digital IF data. If the reconfiguration satellite signals are very close to the real strong satellite signals, the cross-correlation effect can be mitigated effectively. The methods of type 2 include Gustavo's near-far detector [3], the long-time acquisition presented by Philip G Mattos [4], the CPC method presented in this paper, and so on. The characteristic of type 2 methods need not delete strong satellite signals from the received digital IF data. These methods build different rationales to detect the cross-correlation effect.

Here we only evaluate the methods of type 2. The evaluation principles include that the cross-correlation mitigation method should keep relative high detection probability while keeping a low false alarm probability. Further more, the evaluation principles include the acquisition ability of the weak signal in the presence of other strong GPS signals. We use the digital IF data of same length to estimate the performance of the cross-correlation mitigation methods. For example,

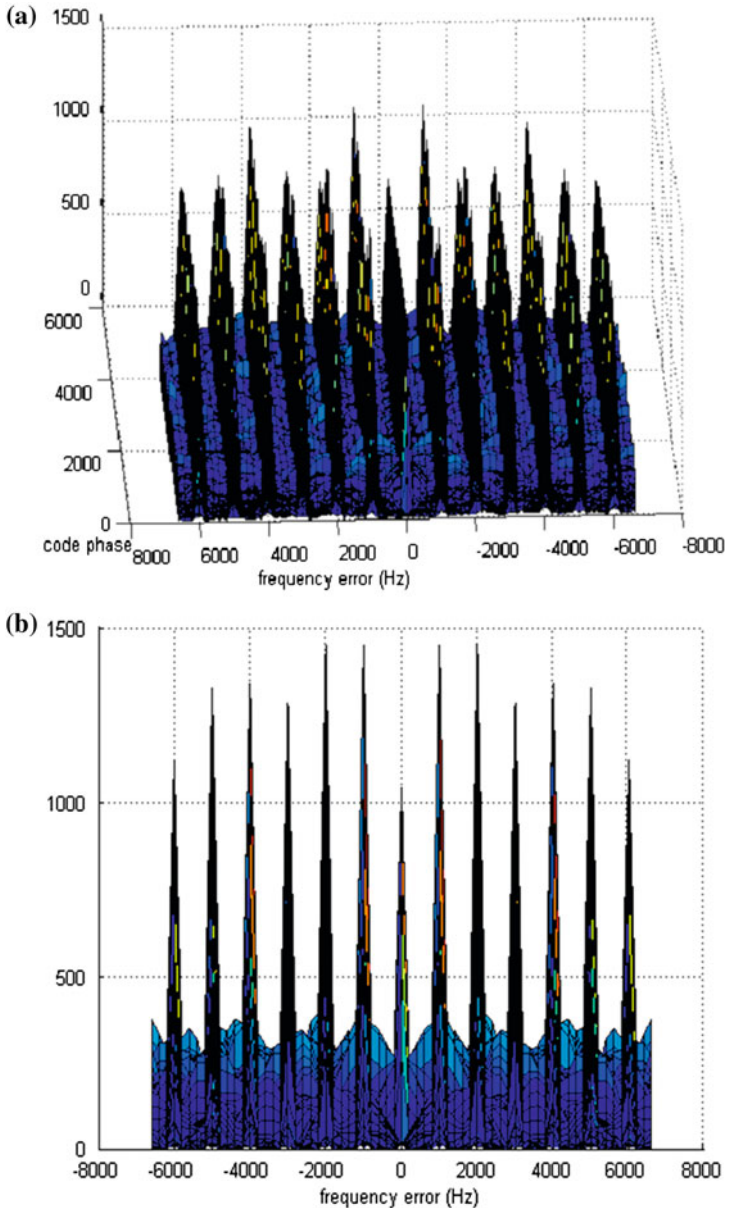

Fig. 60.1 The cross-correlation effect: **a** is the 3D figure, **b** is the 2D figure

we collect a digital GPS IF data of 0.5 s. If there is no strong signal in this IF data, we can only acquire the weak signal as low as −148 dBm (26 dBHz) power level. If there are other strong signals in this IF data, it is very difficult that the acquisition sensitivity is still −148 dBm when we use the methods of type 2. It doesn't

matter if we use the cross-correlation mitigation methods belonging to type 1, because all the strong signals can be deleted before the acquisition for the weak signals. We assume that there is one strong signal of −124 dBm (50 dBHz) power level in the digital IF data of 0.5 s, and we need to acquire other weak GPS signals. We assume that Method A can acquire the weak signal of −144 dBm (30 dBHz) power level in presence of one strong signal of −124 dBm power level. Under the same condition of detection probability and false alarm probability, Method B can acquire the weak signal of −147 dBm (27 dBHz) power level. Thus we can conclude that Method B is better than Method A.

60.3 The CPC Algorithm

This section describes the CPC algorithm in detail. The received GPS IF data can be expressed as below.

$$r(t) = \sum_{i=1}^{M} A_i D_i(t) c_i(t - \tau_i) \cos(2\pi(f_c + f_{di})t) + n(t) \tag{60.1}$$

where A_i is the amplitude of the signal of GPS satellite i, $n(t)$ is the additive Gaussian noise, $D_i(t)$ is the navigation data bit, $c_i(t)$ represents the coarse-acquisition (C/A) code, f_c is the center carrier, f_{di} is the Doppler frequency due to the satellite-receiver relative movement, τ_i is the code delay for each satellite's signal.

The acquisition result can be expressed as below.

$$F(\tau, f_d) = \sum_{r=0}^{N_I - 1} \left| \int_{rN_c}^{(r+1)N_c} r(t) c_L(t - \tau) \exp[j2\pi(f_c + f_d)t] dt \right|^2 \tag{60.2}$$

where N_c and N_I are the coherent correlation time and the number of blocks incoherently integrated, respectively. A higher processing gain can be obtained by coherent correlation, but it is limited by the search interval of Doppler frequency and the message's bits transition losses [7]. The coherent correlation time (N_c) is usually smaller than the bit duration. $c_L(t)$ is the local C/A code replica. τ is the code delay of the local C/A code. f_d is the Dopple frequency need to be searched.

If the Doppler frequency of strong satellite is f_{ds} Hz, the serious cross-correlation effect will appear at $f_{ds} + 1000\ k$ Hz (k = 0, ± 1, ± 2…) according to Sect. 60.2.1. Thus we define a variable as below.

$$X(\tau, f_d') = \begin{cases} F(\tau, f_d') & th_1 < |f_d' - f_{ds}|_L < th_2 \\ 0 & otherwise \end{cases} \tag{60.3}$$

where $|x|_L$ denotes the modulo L operator for the absolute value of x, here L = 1,000. th_1 and th_2 are the thresholds, for example, $th_1 = 100$ and $th_2 = 900$. Thus, $X(\tau, f_d')$ delete the acquisition results which are seriously affected by the cross-correlation.

Let $X_{n,m}$ be a matrix whose entries represent the values of $X(\tau,f_d')$.

$$X_{n,m} = X(\tau_n, f'_{dm}) \tag{60.4}$$

where $n = 0,1\ldots,N_0 - 1$, $m = 0,1,\ldots M - 1$. M denote the number of the frequency segment, and $N_0 = 2{,}046$ for GPS L1 civil signal.

The CPC algorithm is based on multiple times acquisition. We record the corresponding acquisition time as t_k. We define $X_{n,m,tk}$ which denotes $X_{n,m}$ from the acquisition results of t_k. The maximal several peaks will be selected from $X_{n,m,tk}$. For example, N denotes the number of the maximal peaks selected from $X_{n,m,tk}$. The N peaks form a one-dimension array as below.

$$P_{tk} = \{ X_{n_1,m_1,t_k} \quad X_{n_2,m_2,t_k} \quad \ldots \quad X_{n_N,m_N,t_k} \} \tag{60.5}$$

where $X_{n_1,m_1,t_k} > X_{n_2,m_2,t_k} > \ldots > X_{n_N,m_N,t_k}$. $n_1,n_2,..n_N$ denote the phases of PRN code, and form the one-dimension array C_{tk}.

$$C_{t_k} = \{ n_1 \quad n_2 \quad \ldots \quad n_N \} \tag{60.6}$$

$m_1,m_2,..m_N$ denote the search frequency, and form the one-dimension array F_{tk}.

$$F_{t_k} = \{ m_1 \quad m_2 \quad \ldots \quad m_N \} \tag{60.7}$$

After multiply times acquisition, the two 2D arrays are formed and shown in Fig. 60.2. We may find the code phase and carrier frequency of autocorrelation peak according to the CPC method list as follows if they appear in the two arrays C_{tk} and F_{tk}.

At first, we select the $F_{t1}(1)$ and $C_{t1}(1)$ as the objects, and decide whether they are the Doppler frequency and the code phase of the autocorrelation peak. The set (i,j) is as below.

$$(i,j) = \{F_{t_i}(j) = F_{t_1}(1), t_i \in \{t_1,\ldots,t_K\}, j \in \{1,\ldots,N\}\} \tag{60.8}$$

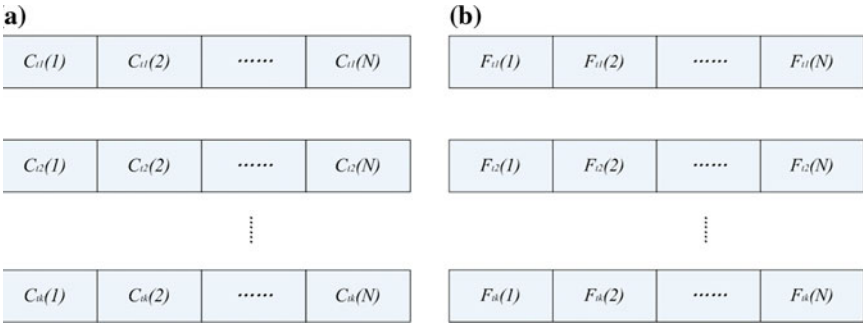

Fig. 60.2 The two 2D arrays formed after multiply times acquisition, **a** the 2D array Ctk, **b** the 2D array Ftk

For GPS L1 civil signal, $C'_{t_i}(j)$ denotes the predicted code phase and can be computed as the Eq. 9 as below.

$$C'_{t_i}(j) = [(2,046,000 + F_{t_1}(1)/770) \times (t_i - t_1) + C_{t_1}(1)]_{2046} \tag{60.9}$$

where 2046000 denote the half chip rate (2.046 Mchips/s), the Doppler on the code is 1540 times less than the carrier, thus the Doppler on the half code chip is 770 times less than the carrier. $[x]_L$ denotes the modulo L operator for the absolute value of x, here L = 2046.

We define the variable *cpc* as the statistical value. When the predicted code phase $C'_{t_i}(j)$ is equal to the real code phase $C_{t_i}(j)$, the statistical value *cpc* increases. If the statistical value *cpc* is larger than the threshold, the autocorrelation peak is found and we obtain the corresponding Doppler frequency and code phase. Otherwise, we select the $F_{t1}(2)$ and $C_{t1}(2)$ as the objects, and repeat the process. After all the elements in two 2D arrays F_{tk} and C_{tk} have been analyzed and compared, these arrays C_{tk} and F_{tk} will be thrown away and the new acquisition results will be supplied if the autocorrelation peak still can not be found.

60.4 Experimental Results

The 2 bit GPS data is sampled at 16.367667 MHz with the intermediate frequency at 4.123 MHz. There are seven satellite signals in the GPS IF data. The PRN numbers include 1, 2, 3, 4, 5, 6 and 7, the corresponding signal power level is −124 dBm, −143 dBm, −144 dBm, −145 dBm, −146 dBm, −147 dBm, −148 dBm. The simulation parameters in the experiments are given, for example, $N_c = 0.005$ s, $N_i = 100$, $N = 20$, $K = 5$. It means that the length of the IF data for one time acquisition is 0.5 s and 5 groups of acquisition results are used. The dimension of the array C_{tk} and F_{tk} are both 5 × 20.

We also test the near-far detector method using this IF data. The experimental results are shown in Table 60.1. The near-far detector method has the approximate false-alarm probability with the CPC algorithm, but the detection probability of the former is much lower than that of the latter. If the Doppler frequency of weak signal doesn't meet $th_1 < |f'_d - f_{ds}|_L < th_2$(see Eq. 3), it is impossible to use CPC algorithm to find the code phase of the correct autocorrelation peak. We exclude this case in the statistical process.

We further performed simulations to acquire weak signals for a wider range of input signal levels. Figure 60.3 shows the weak signal acquisition results for input containing one strong satellite. The strong and weak signal power level ranges −126 ∼ −122 dBm and −150 ∼ −143 dBm, respectively. The acquisition sensitivity is deeply affected by the power level of the strongest satellite signal. The minimum weak signal power levels at which 80 % detection probability can be guaranteed are −147 dBm, −146 dBm and −144 dBm, respectively for a strong signal with −126 dBm, −124 dBm and −122 dBm.

Table 60.1 The comparison between the near–far detector method and CPC algorithm

SV number	Power level (dBm)	The near-far detector method		CPC algorithm	
		The detection Probability (%)	The false-alarm probability (%)	The detection Probability (%)	The false-alarm probability (%)
2	−143	27.6	0	100	0
3	−144	0.8	0.8	100	0
4	−145	1.2	0	98.6	1.4
5	−146	0	1.6	84.7	0
6	−147	0	0.8	29.2	1.4
7	−148	0	0.7	2.8	0

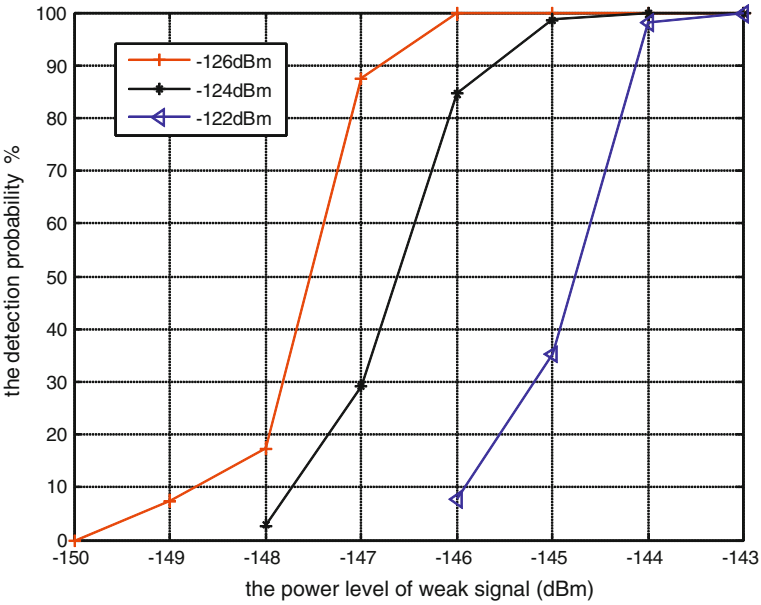

Fig. 60.3 Weak signal acquisition performance

60.5 Conclusions

In this paper, a new cross-correlation mitigation method is presented based on the code phase comparison (CPC). After multiple times acquisition, multiple groups of code phase are obtained. We can find whether the code phase of autocorrelation appears according to the comparison method presented in this paper. The evaluation principle of cross-correlation mitigation methods is also proposed. The CPC algorithm compared with other methods need not reconfigure the strong PRN signal and has relative higher acquisition sensitivity in the presence of cross-correlation interference. The experimental results show that the CPC method can find autocorrelation peak of weak signal at -147dBm power level (the detection

probability is 29.2 %), in presence of one strong signal with -124 dBm power level. The drawback of the CPC algorithm is that its computational cost increases due to multiply times acquisition and comparisons.

Acknowledgments This study is funded by National Natural Science Foundation of China (61221004).

References

1. Kaplan E (2005) Understanding GPS: principles and applications. Artech House, London
2. Holtzman J (1994) DS/CDMA successive interference cancellation. In: IEEE 3rd international symposium on spread spectrum techniques and applications, vol 1, pp 69–78, 4–6 July 1994
3. Lopez-Risueno G, Seco-Granados G (2007) Detection and mitigation of cross-correlation interference in high-sensitivity GNSS receivers. In: IEEE 18th international symposium on personal, indoor and mobile radio communications, (PIMRC 2007), 3–7 Sept 2007
4. Mattos PG(2003) Solutions to the cross-correlation and oscillator stability problems for indoor C/A code GPS. In: Proceedings of the 16th international technical meeting of the satellite division of the institute of navigation (ION GPS/GNSS 2003), Portland, OR, pp 654–659, Sept 2003
5. Morton YT, Miller M, Tsui J, Lin D, Zhou Q (2007) GPS civil signal self-interference mitigation during weak signal acquisition. IEEE Trans Sig Process 55(12):5859–5863
6. Glennon EP, Dempster AG (2004) A review of GPS cross correlation mitigation techniques. In: Proceedings GNSS-2004, Sydney, 6–8 Dec 2004
7. Tsui JB (2005) Fundamentals of global positioning receivers: a software approach, 2nd edn. Wiley, London

Chapter 61
Research on the Effect of Code Doppler on Acquisition Performance and the Compensation Methods

Linfeng Zhang, Tianqiao Zhang, Hong Li, Xiaowei Cui and Minquan Lu

Abstract The relative motion between the navigation satellites and receivers not only brings carrier Doppler (CAD) but also code Doppler (COD). Under a strong signal circumstance, the pre-detection integration time (PIT) is short and only the CAD is needed to be considered, while in the weak signal environments, in order to accumulate more signal energy, the PIT has to be extended. During the extension of PIT, the code autocorrelation function suffers attenuation, displacement and broadening by COD, which should be compensated. This paper studied the impacts of COD on acquisition performance such as sensitivity and availability, and then introduced some existing compensation methods of COD. After investigating the strengths and weaknesses of the existing methods, a new compensation method was proposed, which compensated COD at the stages of down-sampling and non-coherent accumulation (NCA). Different methods were evaluated on a software platform, and testing results proved the superiority of the new method.

Keywords Weak signal · Code doppler · Spread-spectrum code acquisition

61.1 Introduction

With the widespread applications of Global Navigation Satellite System (GNSS) receivers, the newer and more challenging environments, such as indoor, forest and urban, ask for higher acquisition sensitivity [1]. In order to improve the

L. Zhang (✉) · H. Li · X. Cui · M. Lu
Department Electronic Engineering, Tsinghua University,
1110 Wei Qing Building, Beijing, P. R. China
e-mail: zhanglinf04@gmail.com

T. Zhang
Beijing Satellite Navigation Center, Beijing, P. R. China

J. Sun et al. (eds.), *China Satellite Navigation Conference (CSNC) 2013 Proceedings*, Lecture Notes in Electrical Engineering 243,
DOI: 10.1007/978-3-642-37398-5_61,

acquisition sensitivity, it's necessary to extend the PIT to accumulate more signal energy [2]. During this process, by the COD influence, the code autocorrelation function suffers attenuation, displacement and broadening [3], which attenuates the accumulation of signal energy. To solve this problem, a compensation for COD is essential. In literature [4–6], COD is compensated by adjusting the generating rate of local code. This method is simple and intuitive, but the local code sequences has to be updated frequently, which increases the calculation, and the extension of PIT is restricted by the residual code Doppler (RCOD). In literature [7], Code Doppler is compensated in the procedure of NCA by shifting the coherent integration results. This method avoids updating local code frequently, but the shifting operation reduces the autocorrelation peak, and the PIT is also limited by RCOD. In this paper, a novel method is proposed and the compensation is implemented in processes of down-sampling and NCA.

The paper is organized as follows: Sect. 61.2 analyzes the impact of COD on acquisition performance. Section 61.3 introduces the main existing compensation methods and summarizes their strengths and weaknesses. In Sect. 61.4 a novel compensation method is proposed. Section 61.5 presents and analyzes the test results of different methods. Finally, in Sect. 61.6 some conclusions are drawn.

61.2 Effect of Code Doppler on Acquisition Performance

Figure 61.1 shows the pre-detection integration flow of GNSS acquisition module (only code component is considered), in which the input signal is

$$S_1(k) = C[(1+\eta)kT_s - \tau] \tag{61.1}$$

where $C(t)$ is the received PRN code, τ is the code delay, T_s is the sampling interval, $\eta = f_{D,c}/f_c = f_D/f_{RF}$ is the code-phase drift rate and $f_{D,c}$ and f_D are the COD and CAD respectively, f_c and f_{RF} are the nominal code rate and carrier frequency, respectively.

The expression of coherent integration result in Fig. 61.1 is

$$S_2 = \sum_{k=1}^{K} C[(1+\eta)kT_s - \tau]C[kT_s - \hat{\tau}] = R\left(\Delta\tau, T_{coh}, f_{D,c}\right) \tag{61.2}$$

where T_{coh} is the length of coherent integration time,K is the number of samples in T_{coh}, $\hat{\tau}$ is the local code delay and $\Delta\tau = \tau - \hat{\tau}$. Actually, S_2 is the code correlation

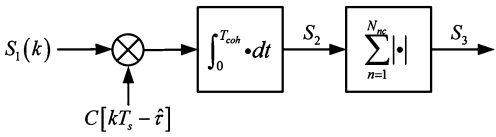

Fig. 61.1 Pre-detection integration flow of acquisition module

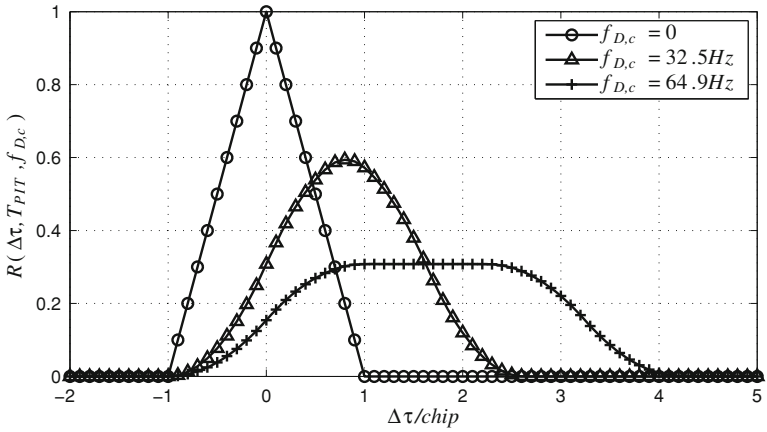

Fig. 61.2 Code Autocorrelation function under different COD

function which considers COD and its formula can be found in literature [3, 8]. The value of S_2 is determined by $\Delta\tau$, T_{coh} and $f_{D,c}$, so we also express it as $R\left(\Delta\tau, T_{coh}, f_{D,c}\right)$.

After the procedure of NCA, we get

$$S_3 = \sum_{n=1}^{N_{nc}} R\left(\Delta\tau_n, T_{coh}, f_{D,c}\right) = R\left(\Delta\tau, T_{PIT}, f_{D,c}\right) \tag{61.3}$$

where N_{nc} is the number of NCA, $\Delta\tau_n = \Delta\tau + (n-1)\eta T_{coh}$, and $T_{PIT} = N_{nc}T_{coh}$.

Figure 61.2 shows the code autocorrelation function under different COD, in which $T_{coh} = 1$ ms, $N_{nc} = 50$ and $f_c = 10.23$ MHz. From Fig. 61.2 we can see that the code autocorrelation peak suffers attenuation, displacement and broadening when $f_{D,c} \neq 0$. The formulas of attenuation ratio, shifting distance and the peak width are as follows [3]:

$$L_p(\Delta p) = \begin{cases} (1 - 0.25|\Delta p|)^{-2}, & |\Delta p| \leq 2 \\ (\Delta p)^2, & |\Delta p| > 2 \end{cases} \tag{61.4}$$

$$S_p(\Delta p) = \Delta p/2 \tag{61.5}$$

$$W_p(\Delta p) = 2 + |\Delta p| \tag{61.6}$$

where $\Delta p = f_{D,c}T_{PIT}$ is the relative sliding code-phase between the received code and the local code during T_{PIT} in number of chips. The attenuation of correlation peak will affect the acquisition sensitivity, while the shifting and broadening of correlation peak will reduce the availability of acquisition results.

61.2.1 Effect on Acquisition Sensitivity

To facilitate the derivation, it is assumed that the object of NCA is power rather than amplitude, then S_3 can be written as

$$S_3' = \sum_{n=1}^{N_{nc}} R^2\left(\Delta\tau_n, T_{coh}, f_{D,c}\right)/\sigma^2 \tag{61.7}$$

where σ^2 is the noise variance of coherent integration result. Then the attenuation ratio in Eq. (61.4) becomes

$$L_p' = N_{nc}R^2(0, T_{coh}, 0)/\sum_{n=1}^{N_{nc}} R^2\left(\Delta\tau_n, T_{coh}, f_{D,c}\right) \tag{61.8}$$

where $\Delta\tau_n = \Delta p/2 + (n-1)\eta T_{coh}$ and $\Delta p/2$ is the position of summit in Fig. 61.2.

When signal is absent, S_3' is distributed according to the Chi square distribution and the probability density function (PDF) is

$$f_A(x;k) = \frac{x^{k/2-1}e^{-x/2}}{2^{k/2}\Gamma(k/2)} \tag{61.9}$$

where $\Gamma(n) = (n-1)!$ is the Gama function and $k = 2N_{nc}$ is the degrees of freedom.

Then the false alarm probability of acquisition is

$$P_{fa} = \int_{x=V_t}^{+\infty} f_A(x;k)dx \tag{61.10}$$

where V_t is the detection threshold.

S_3' is distributed according to the noncentral Chi squared distribution when signal is present and the corresponding PDF is

$$f_D(x;k,\lambda) = \frac{1}{2}e^{-(x+\lambda)/2}(x/\lambda)^{k/4-1/2}I_{k/2-1}(\lambda x) \tag{61.11}$$

where $I_v(z)$ is a modified Bessel function of the first kind, λ is the noncentrality parameter and can be written as

$$\lambda = \sum_{n=1}^{N_{nc}} \left(\frac{a_n}{\sigma}\right)^2 = \sum_{n=1}^{N_{nc}} SNR_n = C/N_0 \times T_{PIT}/L_p' \tag{61.12}$$

where a_n^2 and SNR_n are the signal power and the signal noise ratio of the nth coherent integration result, respectively. C/N_0 is the carrier to noise ratio. Then the final detection probability is

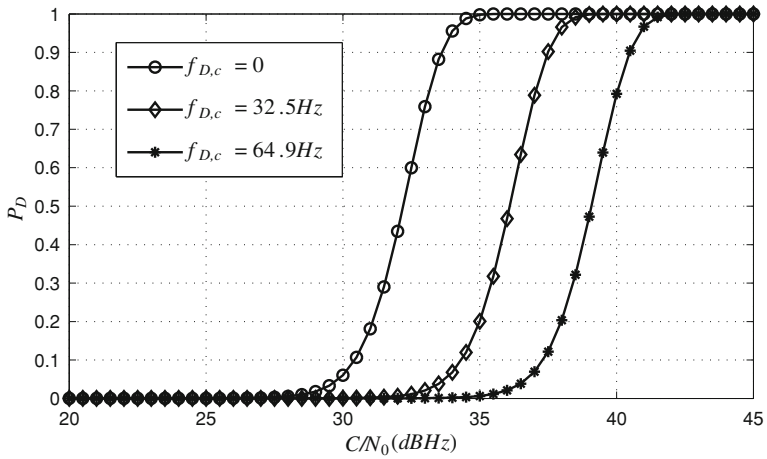

Fig. 61.3 C/N_0 versus P_D under different COD (P_{fa} = 1e-6)

$$P_D = Q_{N_{nc}}\left(\sqrt{\lambda},\ \sqrt{V_t}\right) \tag{61.13}$$

where $Q_n(\cdot,\cdot)$ is the Marcum's Q-function. From the above expressions we can find that when P_{fa} and T_{PIT} are constant, the larger $|f_{D,c}|$ is, the lower P_D is, and the lower acquisition sensitivity is. The curve of C/N_0 versus P_D under different COD is shown in Fig. 61.3 when $P_{fa} = 1e\text{-}6$ and other parameters are the same as Fig. 61.2. In Fig. 61.3, the losses of sensitivity are 3.9 and 6.9 dB, respectively, when $f_{D,c} = 32.5$ Hz and $f_{D,c} = 64.9$ Hz. This part of sensitivity loss is not acceptable in the weak signal conditions and must be compensated.

61.2.2 Effect on Acquisition Results Availability

In this section we define the code-phase error as $\Delta p_0 = p - p_0$, where p is the code-phase reported after a successful acquisition, p_0 is the real code-phase at the beginning of integration. From Eq. (61.5) and (61.6) we know that the distribution of Δp_0 is

$$\Delta p_0 \sim \begin{cases} U[-0.25 + 0.5\Delta p,\ \ 0.25 + 0.5\Delta p], & |\Delta p| \le 2.5 \\ U[1,\ \ \Delta p - 1], & \Delta p > 2.5 \\ U[1 + \Delta p,\ \ -1], & \Delta p < -2.5 \end{cases} \tag{61.14}$$

To ensure the availability of p, Δp_0 should fall within the pull-in scope of discriminator. When the pull-in scope is ± 0.5 chip, by Eq. (61.14) we can deduce that

$$P(-0.5 \le \Delta p_0 \le 0.5) = \begin{cases} 1, & |\Delta p| < 0.5 \\ 1.5 - |\Delta p|, & 0.5 \le |\Delta p| \le 1.5 \\ 0, & |\Delta p| > 1.5 \end{cases} \tag{61.15}$$

It can be drawn from the above formula that the acquisition result is not available at all if $|\Delta p| > 1.5$, which is easily to meet with the extension of T_{PIT}. So the COD needs to be compensated to guarantee the availability of acquisition results.

61.3 The Existing Compensation Methods

There are two main existing COD compensation methods. The first one is to adjust the generation rate of local code according to the CAD hypothesis [4–6] (referred to as method A hereinafter), and the second one is to shift the coherent integration results before NCA [7] (referred to as method B hereinafter). The two methods are briefly described below.

61.3.1 Method A

In method A the expression of local code samplings is $C[(1+\hat{\eta})kT_s - \hat{\tau}]$, where $\hat{\eta} = \hat{f}_D / f_{RF}$ and $\hat{f}_D$ is the hypothetical CAD. Since the value of $\hat{\eta}$ is not constant, the local code samplings need to be updated frequently, which increases the calculations. The results of coherent integration and NCA are

$$\begin{cases} S_{2,A} = R\left(\Delta\tau, T_{coh}, \Delta f_{D,c}\right) \\ S_{3,A} = R\left(\Delta\tau, T_{PIT}, \Delta f_{D,c}\right) \end{cases} \tag{61.16}$$

where $\Delta f_{D,c} = (\eta - \hat{\eta}) f_c$ is the RCOD and its distribution is

$$\Delta f_{D,c} \sim U[-\Delta f_D f_c/(2f_{RF}), \quad \Delta f_D f_c/(2f_{RF})] \tag{61.17}$$

where Δf_D is the search interval of CAD.

The extension of T_{PIT} is limited when $\Delta f_D \neq 0$. By Eq. (61.15) we can infer that the next inequality must be satisfied to ensure the availability of acquisition results.

$$T_{PIT} \le f_{RF}/(\Delta f_D f_c) \tag{61.18}$$

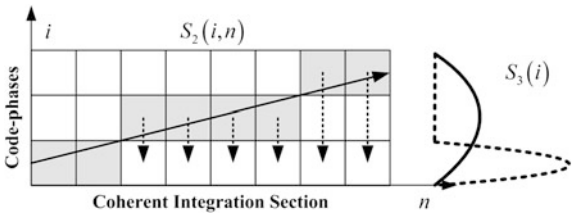

Fig. 61.4 Diagram of shifting NCA of method B

61.3.2 Method B

The principle of NCA in method B is illustrated in Fig. 61.4, in which i and n are the index of code-phases and coherent integration period respectively, the gray grids show the trace of correlation peak. The formula of NCA in Fig. 61.4 is

$$S_{3,B}(i) = \sum_{n=1}^{N_{nc}} S_2\left(i - \left[\left[\hat{f}_{D,c}(n-1)T_{coh}/\tau_s\right]\right],\ n\right) = \sum_{n=1}^{N_{nc}} R\left(\Delta\tau(i,n), T_{coh}, f_{D,c}\right) \tag{61.19}$$

where τ_s is the search step of code-phase, $\hat{f}_{D,c} = \hat{f}_D f_c / f_{RF}$ is the hypothetical COD, $[\![\cdot]\!]$ represents rounding to the nearest integer and

$$\Delta\tau(i,n) = \Delta\tau_i - \tau_s T_c \left[\left[\hat{f}_{D,c}(n-1)T_{coh}/\tau_s\right]\right] + (n-1)f_{D,c}T_{coh}/f_c \tag{61.20}$$

where $\Delta\tau_i = p_i - p_0$ and p_i is the ith code-phase.

The rounding operation in Eq. (61.19) will bring some loss to correlation peak. The average loss of correlation peak is about 0.3 dB when $\hat{f}_{D,c} = f_{D,c}$, $T_{coh} = 1$ ms and $N_{nc} = 500$. From the above formulas we find that the extension of T_{PIT} is also restricted by the RCOD in method B.

61.4 A New Compensation Method

This section presents a novel method (referred to as method C hereinafter), in which COD is compensated at two-stage. The first stage is achieved by adjusting the down-sampling rate according to the hypothetical CAD while keeping the sampling rate of local code unchanged, thus avoids the frequent update of local code samplings. In order to support a longer T_{PIT}, the second stage is carried out during NCA by hypothesis testing the RCOD.

The down-sampling interval of method C is

$$T_s' = T_s(1+\hat{\eta}) = T_s/\left(1+\hat{f}_D/f_{RF}\right) \tag{61.21}$$

By substituting Eq. (61.21) into Eq. (61.2), the coherent integration result is

$$S_{2,C} = R\left(\Delta\tau_0, T_{coh}, \Delta f_{D,c}\right) \tag{61.22}$$

In order to compensate the unknown $\Delta f_{D,c}$, we test a number of hypotheses for $\Delta f_{D,c}$. The mth hypothesis of $\Delta f_{D,c}$ is

$$\Delta f_{D,c,m} = \left(\left[2(m-1) + 1 - M\right]\Delta f_D f_c\right)/(2Mf_{RF}) \tag{61.23}$$

where M is the total number of hypotheses. The expression of shifting NCA in the mth hypothesis is

$$\begin{aligned} S_{3,C}(i,m) &= \sum_{n=1}^{N_{nc}} S_2\left(i - \left[\left[\Delta f_{D,c,m}(n-1)T_{coh}/\tau_s\right]\right],\ n\right) \\ &= \sum_{n=1}^{N_{nc}} R\left(\Delta\tau(i,m,n), T_{coh}, \Delta f_{D,c}\right) \end{aligned} \tag{61.24}$$

where

$$\Delta\tau(i,m,n) = \Delta\tau_i - \tau_s T_c\left[\left[\Delta f_{D,c,m}(n-1)T_{coh}/\tau_s\right]\right] + (n-1)\Delta f_{D,c}T_{coh}/f_c \tag{61.25}$$

After the two-stage of compensation, the distribution of final RCOD $\Delta f'_{D,c}$ is

$$\Delta f'_{D,c} \sim U\left[-\Delta f_D f_c/(2Mf_{RF}),\quad \Delta f_D f_c/(2Mf_{RF})\right] \tag{61.26}$$

By Eqs. (61.18) and (61.26) we know that the longest T_{PIT} supported by method C is M times as long as that supported by method A and B.

If the maximum value of $S_{3,C}(i,m)$ exceeds the detection threshold, which means a successful acquisition, the corresponding $\Delta f_{D,c,m}$ can be used to adjust the CAD. The formula of adjustment is

$$f_D = \hat{f}_D + \Delta f_{D,c,m} f_{RF}/f_c \tag{61.27}$$

After the adjustment, the accuracy of CAD raises M times as before.

The acquisition scheme of method C is presented in Fig. 61.5, in which the CAD is searched in serial while the code-phase is searched in parallel by employing FFT&IFFT implementation [2].

61.5 Simulation Results

This section is devoted to the performance test for the three methods above.

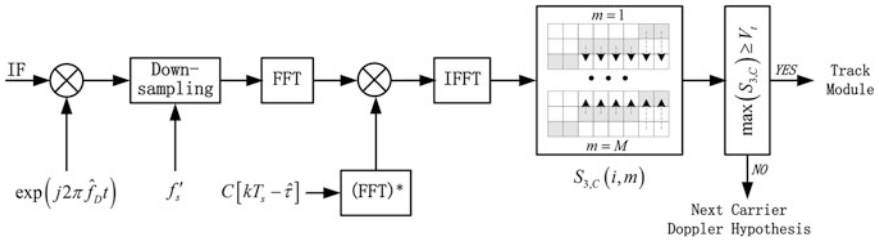

Fig. 61.5 Acquisition scheme of method C

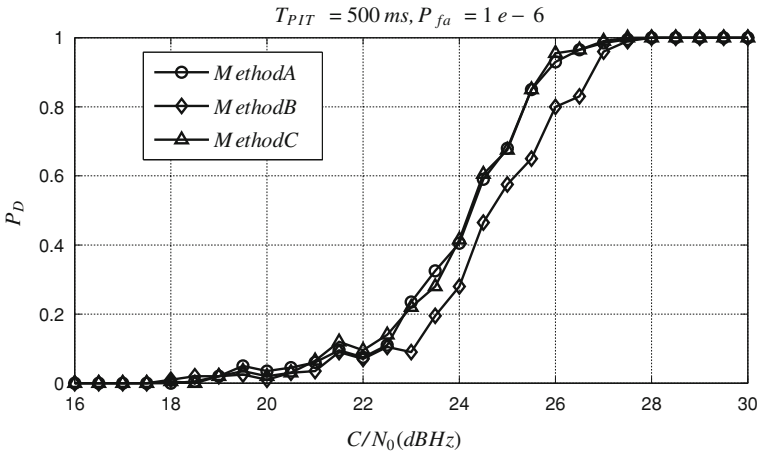

Fig. 61.6 C/N_0 versus P_D for three methods ($T_{PIT} = 500$ ms)

Before the test, an intermediate frequency (IF) signal source is implemented in MATLAB and it can be configured to various parameters. A set of parameters used in this paper are as follows: GPS L1 P-code signal; SV = 5; $f_D = 5.2$ kHz; $p_0 = 9000.5$ chip; $f_{IF} = 46.42$ MHz; $f_s = 62$ MHz; $C/N_0 = 16 \sim 30$ dBHz.

The acquisition parameters used by method A–C are identical and as follows: the search range of code-phase is ± 1 ms with a step of 0.5 chip; the search scope of CAD is ± 6 kHz with a step of 400 Hz; $T_{coh} = 1$ ms; $N_{nc} = 500$ or 1,000; V_t is calculated by Eq. (61.10) when $P_{fa} = 1e-6$. Furthermore, for method C, $M = 5$ in Eq. (61.23).

Every method is tested 200 times under each C/N_0. Figures 61.6 and 61.7 present the curves of C/N_0 versus P_D for method A–C when $T_{PIT} = 500$ ms and $T_{PIT} = 1$ s, respectively.

As we can see from Fig. 61.6, the acquisition sensitivity of method B is about 0.5 dB lower than method A and C. This part of sensitivity loss is caused by the rounding operation in Eq. (61.19). The sensitivities of method A and C are nearly

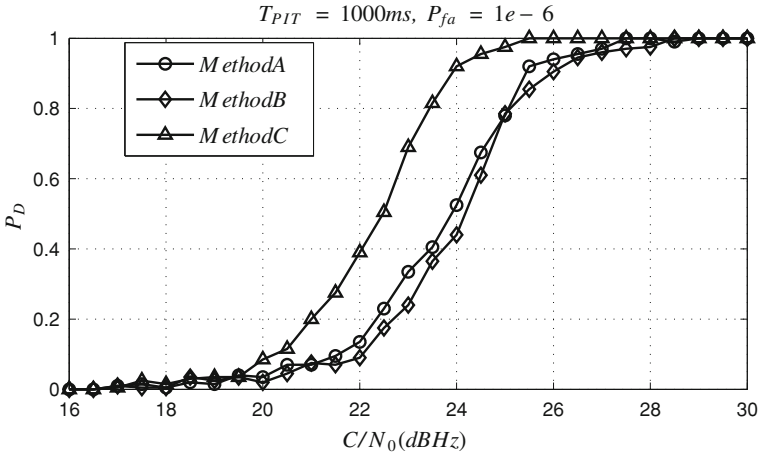

Fig. 61.7 C/N_0 versus P_D for three methods (T_{PIT} = 1,000 ms)

Table 61.1 Maximum amount of FFT and IFFT operations for three methods

Compensation methods	FFT	IFFT
Method A	$(N_{nc} + 2N_{nc}T_{\max}/T_{coh})N_{dl}$	$2N_{nc}T_{\max}/T_{coh}N_{dl}$
Method B	$N_{nc}N_{dl} + 2N_{nc}T_{\max}/T_{coh}$	$2N_{nc}T_{\max}/T_{coh}N_{dl}$
Method C	$N_{nc}N_{dl} + 2N_{nc}T_{\max}/T_{coh}$	$2N_{nc}T_{\max}/T_{coh}N_{dl}$

equal, which means the peak attenuation caused by the RCOD is still relatively small when $T_{PIT} = 500$ ms.

In Fig. 61.7, after the extension of T_{PIT} from 500 ms to 1 s, the acquisition sensitivities of method A and method B both improve only about 0.2 dB, while method C improves about 2 dB. The different improvements of sensitivity illustrate that, as the extension of T_{PIT}, the RCOD becomes the bottleneck of sensitivity improvement. Method C compensates the RCOD, so it achieves a higher sensitivity.

For the search of CAD, results reported by method A and B are 5 kHz, while result from Method C is 5.16 kHz after the adjustment in Eq. (61.27), which is closer to the true value of 5.2 kHz.

Table 61.1 lists the maximum amount of FFT and IFFT operations needed for capturing a satellite. In Table 61.1, N_{dl} is the amount of CAD frequencies being searched, and $T_{\max}$ is the half amount of the searched code-phases. By substituting the acquisition parameters into Table 61.1, it can be drawn that method B and C have the same calculation, which is only 51.27 percent of that needed in method A.

From the above simulation results, a conclusion is made that among the three tested methods, method C obtains the lowest calculation, the highest acquisition sensitivity, and the highest search accuracy of CAD.

61.6 Conclusion

In this paper the effect of COD on acquisition performance is analyzed and a new method of compensating COD is proposed. By adjusting the down-sampling frequency and testing the RCOD under different hypotheses, the new method supports a very long PIT and especially applies to the weak signal acquisition of GNSS. After the comparison test with the existing methods, it can be proved that the new method not only brings about less calculation and higher sensitivity, but also improves the search accuracy of CAD.

Acknowledgments This work was supported by the National Natural Science Foundation of China (Grant No.61101070) and the National Science Foundation for Post-doctoral Scientists of China (Grant No.201104118).

References

1. MacGougan G (2003) High sensitivity GPS performance analysis in degraded signal environments. Master Thesis, Department of Geomatics Engineering, Univerity of Calgary
2. Xie G (2009) Principles of GPS and receiver design. Publishing House of Electronics Industry, Beijing
3. Li C, Wang F, Guo G (2007) Correlation of PN spread spectrum signal under first-order dynamics. Acta Electronica Sinica 35(9):1789–1793
4. Li H, Zhou H, Lu M, Feng Z (2010) Code-doppler-compensation based direct acquisition method for weak GNSS long PN-code. Scientia Sinica Phys, Mech & Astron 40(5):560–567
5. Su SL, Yen NY, Hsieh SC (1995) Code acquisition of direct-sequence spread spectrum communication with Doppler shift. In: Proceedings of IEEE International Conference on Communications, ICC'95 Seattle, 'Gateway to Globalization' vol 3 pp 1663–1667
6. Chen H (2011) Key technologies research on GPS weak signal acquisition. Master Thesis, University of Electronic Science and Technology of China
7. Zhang M, Li G, Zhu Q (2009) Application of doppler frequency compensation algorithm in acquisition of GPS signals. Comput Simul 26(10):69–72
8. Cheng U, Hurd WJ, Statman JI (1990) Spread-spectrum code acquisition in the presence of doppler shift and data modulation. IEEE Trans Commun 38(5):241–250

Chapter 62
Demonstration and Realization of Operating in a Wide Temperature Range for Compass System RDSS Terminal

Bin Tang, Chong Zheng and Zhi Liang

Abstract The RDSS service of Compass system has been applied in many fields. The RDSS service of Compass system is applied in many fields. The old RDSS terminal can not be used for all system coverage area because of its narrow operating temperature range. Based on the RDSS application environment, the new operating temperature range of RDSS terminal is established and demonstrated. In order to meet the new wide temperature range, the new technology for large capacity and strong current discharging in low temperature, and the new method to make RDSS terminal operate in a wide temperature range are put forward. The tests show that the new realization can provide a reference to design a wide temperature RDSS terminal.

Keywords Compass · RDSS terminal · Wide operating temperature range · Discharging in low temperature

62.1 Introduction

Compass satellite navigation system is composed of different satellite constellations. The Compass system can provide the service of active/passive real-time three-dimensional positioning, velocity, high-precision timing and short message communication for China and its surrounding region. In the service area of Compass, there are different temperature region, which include equatorial area, tropical area, subtropical area, warm area and cold area. In the north of 40 degrees north latitude, the temperature of many region is below −20 °C in winter. And the lowest temperature in the some areas of northeast China, Xinjiang, northern

B. Tang (✉) · C. Zheng · Z. Liang
Beijing Satellite Navigation Center, Box 5128 100094 Beijing, China
e-mail: tangbinfriend@yahoo.com.cn

J. Sun et al. (eds.), *China Satellite Navigation Conference (CSNC) 2013 Proceedings*, Lecture Notes in Electrical Engineering 243,
DOI: 10.1007/978-3-642-37398-5_62,

Tibetan Plateau can reach −40 °C in January. In the phase of the Compass test system, the Compass RDSS terminal mainly broke through the key technologies. Because of the key module and chip of the terminal were developed slowly, and the comprehensive study of environment adaptability for the terminal was lacked, the operating temperature range was only from −20 to 55 °C, especially the performance of low temperature was poor. In the course of operating, the receiving sensitivity, transmitting EIRP and the accuracy of transmitting frequency were influenced obviously in large temperature range, which made the RDSS terminal can not use for the full service area of Compass.

With the official opening of the Compass system, the application will be wide. In order to improve the reliability and stability of the terminal in application, it is necessary to consider the design of environment adaptability for the terminal. The high-performance GPS terminal, such as Defense Advanced GPS Receiver (DAGR) [1], Airborne SAASM Receiver [2], TruTrak GPS Receiver [3], which can operate in a wide temperature range from about −40 to 60 °C. The RNSS terminal of Compass can basically operate in this range after the key module chip are used. However, the Compass system RDSS terminal was still unreliable when operating in a wide temperature range. For example, the large capacity and strong current discharging for transmitting signal in low temperature is not realized. The gain will change when receiving and transmitting signal, the frequency of reference crystal will shift because of the change of temperature.

The operating temperature range of RDSS terminal is established and demonstrated in this paper based on the requirements of application environment. Then the performance of RDSS terminal is analyzed because of temperature changing in a wide temperature range. The new technology for large capacity and strong current discharging in low temperature, and the new method to make RDSS terminal operate in a wide temperature range are put forward. At last, the tests for these new technology are done.

62.2 Establishing the Operating Temperature Range

The application area for RDSS terminal is very wide, and mostly these terminal are used in outdoor. It is very important for RDSS terminal to have a wide operating temperature range.

62.2.1 Establishing the Lowest Temperature in China

According to GJB 1172.2-1991, the lowest temperature in China region is shown in Table 62.1 [4].

From Table 62.1, the total probability of less than −41.3 °C is lower than 36 %, so it can be deduced that the lowest temperature will not fall below −40 °C

Table 62.1 The probability of lowest temperature in China region cold

Temperature (°C)	Probability (%)
−41.3	20
−44.1	10
−46.1	5
−48.8	1

in the China region for most of the time. Therefore, the low-temperature operating range for terminal is changed from original −20 to −40 °C.

Similarly, the highest temperature in the China region is also given in the GJB 1172.2-1991, which changes between 30 to 43 °C. Because the terminal may be exposed to the sun in use, and the air temperature condition will be exasperate, the temperature will change from 30 to 63 °C. While the probability of higher than 60 °C is very low. Therefore, the high-temperature operating range for terminal is changed from original 55 to 60 °C.

62.2.2 Demonstrating the Operating Temperature Range

In the phase of Compass test system, the operating temperature range for RDSS terminal is only from −20 to 55 °C. The main limiting factors include: LCD display, low temperature performance of battery, and the stability in wide temperature range are not enough.

For display in low temperature, there is organic light-emitting diode display (OLED) screen in the market, which can operate from −40 to 70 °C [5]. By using of OLED, the problem of display in low temperature can be solved. For discharging in low temperature, there are some factory who can produce Li-ion battery working on −40 °C [6]. But the transmitting signal for RDSS terminal is burst spread spectrum signal, very strong current is need in transmitting. In order to improve standby time for the terminal, discharge capacity is need in low temperature. For the stability in wide temperature range, the pre-terminal has been showing instability when the temperature changes from −20 to 55 °C. The gain will change when receiving and transmitting signal, the frequency of reference crystal will shift because of the change of temperature. So the stability design for the new RDSS terminal operating in a wide temperature range is need.

62.3 Realizing Large Capacity and Strong Current Discharging in Low Temperature

RDSS terminal is needed to work in the condition of −40 °C for a long time, so its battery is needed to work with large discharge capacity in low temperature. The power of the terminal will be up to 30 W when transmitting signal, so its battery is

needed to work with strong current. The low temperature of −40 °C is the biggest obstacle to achieving these power indicators. Therefore, it is necessary to solve the problems of large capacity and strong current discharging in low temperature.

62.3.1 Operating in Low Temperature

The research and development of low-temperature Li-ion battery is a hot topic. U.S. Army Research Laboratory has done a lot of research about low temperature performance of Li-ion battery. Their study show that the low temperature performance of Li-ion battery is mainly dependent on the electrolyte batteries [7, 8]. The electrolyte in the battery is used to convey ion and conduct current between the positive and negative role, it plays a vital role in increasing the capacity of the battery, enlarging temperature range, improving cycle efficiency and safety performance. The electrolyte is mainly composed of Li-ion salt, organic solvent and other additive. Currently, some domestic companies has developed the low-temperature electrolyte by using novel Li-ion salt, confecting multiple organic solvents, and adding functional additives. The key technology for the Li-ion battery operating in −40 °C has been broken through [6].

62.3.2 Discharging with Large Capacity and Strong Current

The core of Li-ion battery is composed of the electrolyte and the electrode. Realizing operating in low temperature mainly depends on the electrolyte, while realizing discharging with large capacity and strong current in low temperature mainly depends on the electrode. It is necessary to design new electrode for low temperature Li-ion battery.

1. The design of large capacity

   The carbon material of negative electrode is an important factor to increase the battery capacity. By trying on a lot of carbon material, a new artificial graphite is selected as the material of negative electrode. The experiments show that the discharge capacity reaches 330 mAh/g or more, the efficiency of first discharge reaches more than 93 %. And the workability of this artificial graphite is good, and it is easy to produce in batch production.

2. The design of strong current

   The material of anode determines the discharging performance of the battery. The important nature of the battery about voltage, working hours and stability is decided by anode material. The anode material of Li-ion battery includes lithium cobalt oxide ($LiCoO_2$), lithium manganese oxide ($LiMnO_2$), lithium iron phosphate ($LiFePO_4$), etc. Many studies and experiments showed that the capacity of

$LiMnO_2$ is unstable in high temperature, and it is easy transition to the spinel structure ($LiMn_2O_4$) in the process of discharging. If $LiFePO_4$ is used as anode material, the resistivity of the battery core will be large, the utilization of the electrode material is low, and strong current discharge is difficult.

$LiCoO_2$ is a good anode material in low temperature. In order to further improve the electrochemical properties of the electrode, increase its stability and reduce cost, some electropositive ions are put into the electrode, such as Ca^{2+}, Mg^{2+}, etc. to improve the conductivity of electrode, and strong current discharging is ensured [9].

62.4 Realizing the Stability in Wide Temperature Range

The new RDSS terminal is needed to work stably in wide temperature range from −40 to 60 °C. Through the components of the terminal can meet the wide temperature range by selecting or developing some individual components. But when these components are made into a whole terminal, the performance of receiving and transmitting will be affected, due to the large temperature range. It is necessary to study some stability technology to make the whole terminal work stably in a wide temperature range.

62.4.1 Gain Control

There are the same character for all amplifiers in the link of receiving and transmitting, their gain and power will increase in low temperature. It is opposite in high temperatures, and their gain power will reduce. In order to ensure that the whole receiving sensitivity and transmitter EIRP are not much affected, it is necessary to make the transceiver link total gain change little in the entire temperature range, and do some gain control in the transceiver link.

The gain in the receiving link of the terminal is about 90 dB, which will change largely between the high and the low temperature. The receiving gain will increase 4–6 dB in the conditions of −40 °C, and will reduce 4–6 dB in the conditions of 60 °C. The changes of the receiving gain are shown in Fig. 62.1. In the receiving link, the quantify amplitude of AD will change corresponding to the receiving gain. In the room temperature, the quantify amplitude of intermediate frequency signal is about 1 V, while it will become about 1.3 V in low temperature, becomes about 0.7 V in high temperature. So the key indicators of the terminal, such as receiving sensitivity will be affected.

In order to control the gain in the receiving link, a new automatic gain control (AGC) is added into the receiving link, which lies near the last amplifier as shown in Fig. 62.2.

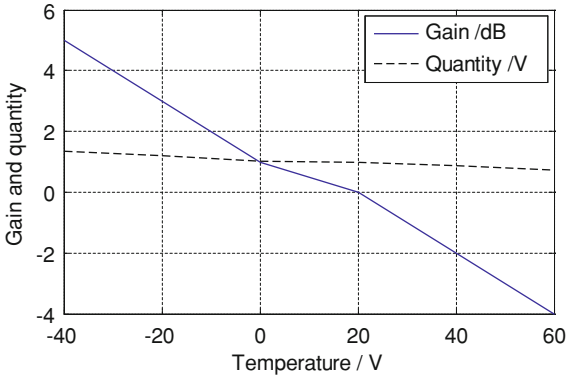

Fig. 62.1 The changing curve of receiving gain and quantity

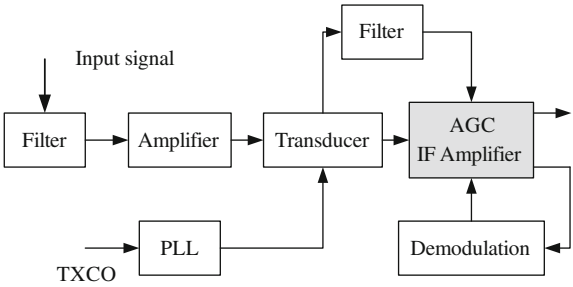

Fig. 62.2 Automatic gain control (AGC) in the receiving link

In low temperature, the gain of preamp will increase. When the final-stage amplifier detects the increase of the previous stage gain, the AGC will be automatically started, and the gain will be reduced. In high temperature, the gain of preamp will decrease, and AGC can automatically increase the gain. Therefore, the up-and-down of the receiving is overcoming, and the power of output noise will be steady. After AGC is put into the receiving link, the change of receiving gain is very small, so as to reduce the impact of A/D sampling in the back end.

There is also the same change in the transmitting link. Temperature compensation can be taken into the transmitting link to compensate the change of amplifier gain reversely. The principle of compensation is shown in Fig. 62.3.

After temperature compensation is taken into the amplifier of the transmitting link, the reverse compensation through the thermostat will make the gain of transmitting link change little in the entire operating temperature range. So the

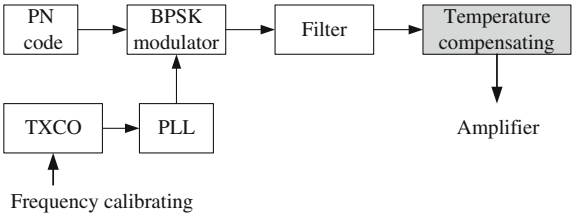

Fig. 62.3 The principle of temperature compensation

output of transmitting amplifier will be effected less, and the value of EIRP in the process of transmitting is insured to meet the requirement.

62.4.2 Frequency Accuracy Control

When working temperature changes, the reference oscillator in the terminal will drift with the change of temperature. The drift of reference oscillator will bring out two problems. First, the dynamic range of receiving frequency. Second, the transmitting frequency accuracy of the terminal will be out of the requirement of the Compass control system. Therefore, it is necessary to compensate the drift of the reference oscillator in the signal processing.

1. Frequency drift control for receiving signal

   When frequency drift of the reference oscillator is larger than 3 ppm, the difference of carrier frequency will be larger than 7.5 kHz, and the difference of code clock frequency will be larger than 12.3 Hz, which is out of DLL bandwidth of the terminal. At the same time, the difference of carrier frequency will bring a great loss of signal-to-noise ratio, and ultimately the satellite signal will lock difficult. The frequency drift control for the received signal is realized by controlling digital frequency synthesizer (DDS) to adjust code NCO and carrier NCO. So the center frequency of the code clock frequency and the carrier clock frequency will be changed to accommodate the frequency drift in a wide temperature range. After the frequency drift is calibrated, the receiving signal will be locked successfully.

2. Frequency accuracy control for transmitting signal

   When compass control system receives the signal from the terminal, the requirements for frequency accuracy is better than 5×10^{-7}. In order to get this accuracy, the signal processing to receive and transmit carrier is designed based on one VCO. So the code clock of the receiving signal can be used to calibrate the frequency error, and the transmitting clock will be controlled. After repeatedly corrected, until the transmitting frequency error reaches a specified range. Through the above process of closed-loop frequency correction, the transmitter frequency of the terminal will meet the requirement of compass control system. The control process of transmitting frequency is shown in Fig. 62.4.

62.5 Experiment and Verification

62.5.1 Discharging Test in Low Temperature

By stirring and wound, the new polymer core is composed of the low temperature electrolyte and the electrode above. Fully charge this polymer core (single-core),

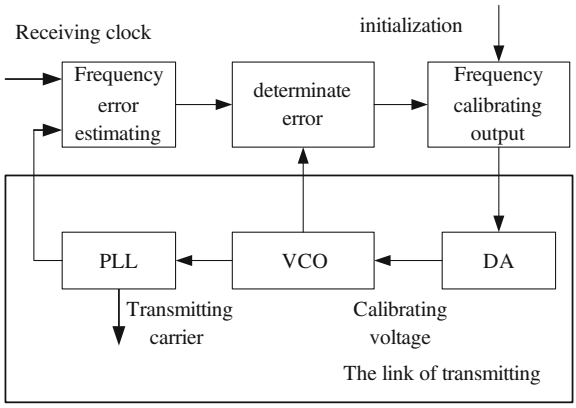

Fig. 62.4 The control process of transmitting frequency

and put in the condition of −40, −20 °C, and room temperature respectively for 4 h. Then discharge the core to 3.1 V as 0.5 °C. In different temperature, the discharge capacity of the core compare with room temperature. The discharge capacity is about 80 and 68 % respectively for −40 and −20 °C. The curve of discharging is shown in Fig. 62.5. The discharge performance of the new polymer core is well to meet the requirement of capacity in low temperature.

Fully charge this polymer core, and discharge it with 0.5, 1 and 2C respectively. The different ratios with 0.5C are calculated. The discharge curve of the core at different current is shown in Fig. 62.6. The discharge capacity of 1C and 2C current is about 94.2 % and 82.4 % compare with 0.5C respectively, which indicates that the new core have good discharge performance and can discharge with strong current. The maximum current is up to 4 A.

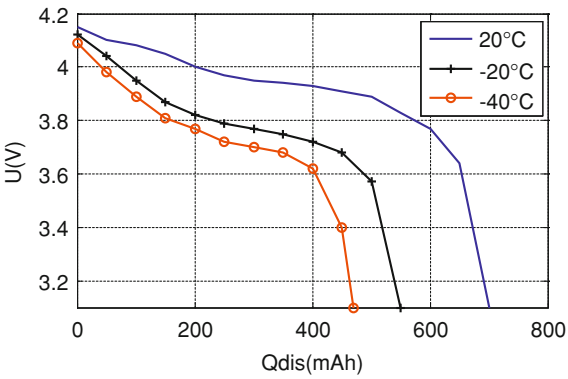

Fig. 62.5 The curve of discharging in different temperature

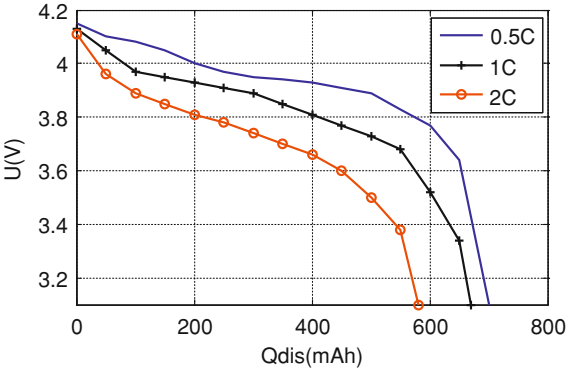

Fig. 62.6 The curve of discharging in different current

62.5.2 Stability Test in Wide Temperature Range

Add automatic gain control to the last amplifier in the receiving link, and adjust the gain reversely based on the temperature change. In the condition of −40, −20, 0, 20, 40 and 60 °C, the gain of receiving link and the quantify voltage are tested, as shown in Table 62.2.

The tests show that the quantify voltage for intermediate frequency signal can be controlled within 0.1 V or less in a wide temperature range. So it will be a very small influence on AD sampling, and the receiving sensitivity of terminal will be eligible.

Add temperature compensation to the link of transmitting, and compensate the gain change based on the temperature change. In the condition of −40, −20, 0, 20, 40 and 60 °C, the gain and output power of the transmitting link are tested, as shown in Table 62.3.

The tests show that the gain fluctuation of the transmitting link is small, and the change of 10 W amplifier output is also small. So the EIRP of the terminal will be eligible after adding temperature compensation.

Table 62.2 The gain and quantity after adding AGC

Temperature (°C)	−40	−20	0	20	40	60
Gain (dB)	90.6	90.3	90.1	90	89.7	89
Quantity (V)	1.07	1.04	1.01	1	0.97	0.95

Table 62.3 The gain and power after adding temperature compensation

Temperature (°C)	−40	−20	0	20	40	60
Gain (dB)	55.5	55.3	54.9	55	55.1	54.7
Power (dBm)	40.5	40.3	39.9	40	40.1	39.7

62.6 Conclusion

In this paper, the operating temperature range of RDSS terminal is established and demonstrated based on the requirements of the Compass system RDSS service. The analysis points out that the low temperature discharge performance of the battery, the gain change in wide temperature range, the reference crystal varies with temperature are main factors for the old RDSS terminals can not operate in a wide temperature range. The new technology for large capacity and strong current discharging in low temperature, and the new method to make RDSS terminal operate in a wide temperature range are put forward. These new design can provide a reference design for wide temperature RDSS terminal.

References

1. Defense advanced GPS receiver. www.rockwellcollins.com
2. Airborne SAASM receiver. www.rockwellcollins.com
3. TruTrak GPS receiver. www.iechome.com
4. GJB 1172.2-1991 Climatic extremes for surface air temperature, Oct 1991:13–22 (Ch)
5. OLED display. www.ideavision.com.cn
6. 14.4 V Li-ion battery. www.xa-hm.com
7. Zhang SS, Xu K, Jow TR (2006) An improved electrolyte for the LiFePO4 cathode working in a wide temperature range. J Power Sources l59:702–707
8. Zhang SS (2006) An unique lithium salt for the improved electrolyte of Li-ion battery. Electrochem Commun 8:l423–1428
9. Rong jun MA (2008) Lithium ion battery and its positive electrode. Mater Nonferrous Met 60(1):1–6 (Ch)

Chapter 63
Analyze of the Pseudorange Noise Error for Compass B1 Open Signal Based on the Receiver

Bin Tang, Haibo He and Chao Xie

Abstract Pseudorange noise error has a strong correlation with the parameters of receiver's antenna and RF, the technology of baseband signal processing. The pseudorange noise error of GNSS system should be analyzed based on the actual parameters of the receiver. In this paper, the relationship between the pseudorange noise error and the code tracking error of the receiver was first analyzed, the linear model of code loop was established, the process of non-coherent code tracking error was derivated, a new analysis method of pseudorange noise error was proposed based on the receiver. Then, the pseudorange noise error of Compass B1 open signal was analyzed based on the Compass universal receiver. The experiment showed that the analysis result for pseudorange noise error was correspond with the actual value, and the analysis method can provide a reference for GNSS system UERE budget.

Keywords Pseudorange noise error · UERE · Universal receiver · Non-coherent code tracking loop

63.1 Introduction

In order to analyze the influence for GNSS system accuracy because of various error, which were usually looked as user equivalent range error (UERE). The UERE error included space segment error (satellite clock error, satellite

B. Tang (✉) · H. He · C. Xie
Beijing Satellite Navigation Center, 5128 Box, Beijing 100094, China
e-mail: tangbinfriend@yahoo.com.cn

H. He
e-mail: zzhhb@126.com

C. Xie
e-mail: xiechao188@sina.com

J. Sun et al. (eds.), *China Satellite Navigation Conference (CSNC) 2013 Proceedings*, Lecture Notes in Electrical Engineering 243,
DOI: 10.1007/978-3-642-37398-5_63,

perturbations etc.), control segment error (ephemeris prediction etc.), environment segment error (ionosphere delay, tropospheric delay etc.), and user segment error (pseudorange noise, multipath etc.). In the process of building GPS, the UERE of GPS were issued by its System Specification since 1980. The error of the space segment, control segment and environment segment were modelled properly and fit for the fact [1]. In recent years, some paper analyzed multipath error by mean multipath envelope or weighted multipath envelope, which solved the problem of multipath error analysis at a certain extent [2, 3]. In the Ref. [1], the pseudorange noise error was analyzed in accordance with the application of ground, air and space, and the relationship was given between the pseudorange noise error and the antenna elevation. But this model is too simple, and it is the result of carrier smoothed, which can not reflect the actual reception performance of the receiver. Galileo signal used BOC or its deformation. In the Ref. [4], the simplified formula for calculating GPS M-code signal in the Ref. [5] was used to analyze the pseudorange noise error of Galileo signal. It was not reasonable apparently. In the Ref. [6], the noise error formula of non-coherent discriminator for the code tracking loop was directly given, but the process of derivation and simplify was not given. In the reference of some performance analysis for GNSS signal, the pseudorange noise error was analyzed based on the RMS bandwidth using Cremer-Rao lower bound as the code tracking error. Cremer-Rao lower bound reflects just the best accuracy for pseudo-code tracking [7, 8]. Moreover, the analysis of the above literature are based on a given carrier to noise ratio (C/N_0), and the parameter of C/N_0 is only a typical value without considering the actual situation of the receiver antenna and the parameters of baseband.

In this paper, the relationship between the pseudorange noise error and the code tracking error of the receiver was first analyzed, then the linear model of code loop was established, the process of non-coherent code tracking error was educed, a new analysis method of pseudorange noise error was proposed based on the receiver. Then, using the parameters of Compass universal navigation receiver, the pseudorange noise error of Compass B1 open signal was analyzed. At last, the experiment verification was done with the actual Compass universal navigation receiver.

63.2 Analyzing Code Tracking Error of the Receiver

In the receiver, the pseudorange was obtained from the code tracking loop after the receiving signal was locked. The pseudorange noise error was also the tracking error of the receiver code tracking loop. The main sources of tracking error included thermal noise, interference, multipath effect, and dynamic stress caused by the relative dynamic between the receiver and the satellite. Interference, multipath and dynamic stress were due to environmental factors. In the process of analyzing the pseudorange noise error, the thermal noise error was primary. Therefore, in the condition of static and no interference, the error of code tracking

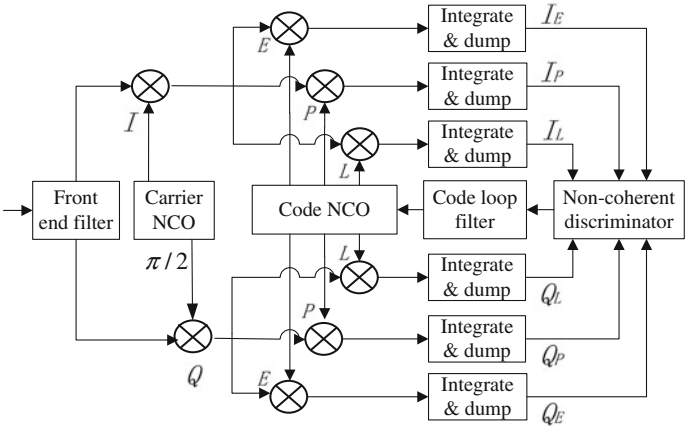

Fig. 63.1 The general structure of the receiver code tracking loop

loop was only caused by thermal noise. The general structure of the receiver code tracking loop was shown below (Fig. 63.1).

The input signal of the receiver code loop was the output signal of the RF front-end. Ignoring various delay, the signal can be expressed as:

$$r(t_j) = A \cdot D(t_j)C(t_j)\cos\left[\omega_m t_j + \theta(t_j)\right] + n_{FE}(t_j) \tag{63.1}$$

where,

j	is the index of sample.
A	is the amplitude of the signal.
$D(\cdot)$	is data bit.
$C(\cdot)$	is the modulation PRN code.
ω_m	is the intermediate frequency of carrier wave.
$\theta(\cdot)$	is the phase of carrier wave including Doppler.
$n_{FE}(\cdot)$	is the narrowband Gaussian white noise output from front-end filter.

The input signal was filtered by the front-end filter, then the carrier and PRN code of the signal were peeled. The I_E, Q_E (Early), I_P, Q_P (Prompt), I_L and Q_L (Late) were formed by integrating and accumulating with local carrier and code.

A non-coherent early minus late power discriminator (EMLP) was often used in the code tracking troop:

$$D_{EMLP} = \left(I_E^2 + Q_E^2\right) - \left(I_L^2 + Q_L^2\right) \tag{63.2}$$

With the condition of ignoring the residual error of Carrier tracking:

$$I_E = R(\Delta\tau_k - d/2 \cdot T_c) + n_{IE}$$
$$I_L = R(\Delta\tau_k + d/2 \cdot T_c) + n_{IL}$$

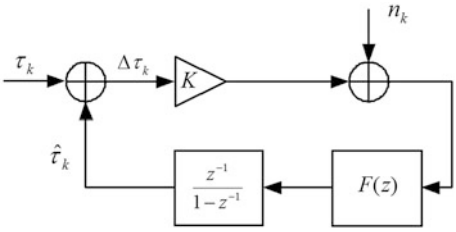

Fig. 63.2 The linear equivalent model of the discriminator

where,

I_E is the output of in-phase early correlator.
I_L is the output of in-phase early correlator.
$R(\cdot)$ is the autocorrelation function of PRN code.
d is the correlator spacing.
$\Delta\tau_k$ is estimation error of code phase.
T_c is width of one chip.

The output of the discriminator was often described as the general linear equivalent model, which was shown in the following figure (Fig. 63.2).

Based on the equivalent model, the output of the discriminator was:

$$V_k = K \cdot \Delta\tau_k + n_k \tag{63.3}$$

where,

K is the slope of the equilibrium point discriminator.
$F(z)$ is loop filter.
$z^{-1}/(1-z^{-1})$ is the Z-domain representation of code NCO.
n_k is the output noise of the discriminator.

Assuming that n_k was zero mean, and the outputs noise was independent of each other between adjacent sampling points. So the variance of the code loop tracking error was [9]:

$$\sigma_f^2 = 2 \cdot B_n \cdot (1 - 0.5 B_n T) \cdot \sigma_n^2 / K^2 \tag{63.4}$$

where,

B_n is the noise bandwidth of code loop.
σ_n^2 is the power of output noise.

Based on the discriminator algorithm and the linear equivalent model for the code loop, the code tracking loop noise error for EMLP discriminator can be calculated [6].

$$\sigma_f = c \times \sqrt{\frac{B_n(1-0.25B_nT)\int_{-B/2}^{B/2} G(f)\sin^2(\pi fd)df}{C/N_0\left(2\pi\int_{-B/2}^{B/2} fG(f)\sin(\pi fd)df\right)^2}} \times \sqrt{1+\frac{\int_{-B/2}^{B/2} G(f)\cos^2(\pi fd)df}{T\cdot C/N_0\left(\int_{-B/2}^{B/2} G(f)\cos(\pi fd)df\right)^2}}(m) \tag{63.5}$$

where,

c is the speed of light.
T is the coherent integration accumulation time.
C/N_0 is the carrier to noise ratio.
B is the bandwidth of front-end filter.
$G(f)$ is normalized power spectral density of GNSS signal.

63.3 Calculating Pseudorange Noise Error Based on the Receiver

Based on the above analysis, the pseudorange noise error can be expressed as code loop tracking error of the receiver, which was correlative with the code loop noise bandwidth, integration accumulation time, carrier to noise ratio, correlator spacing, and power spectral density of the receiving signal. Therefore, the calculation process of the pseudorange noise error was as follows (Fig. 63.3).

(1) Determining the power reached the receiver antenna

According to the link budget of Compass downlink signal, the lowest power of B1 open signal was −163 dBW when it reached the ground, which can be looked as the power to reach the receiver antenna. In the same, this power was used as Compass global System B1C signal, the universal receiver used only the pilot channel to track B1C signal, and the signal power was assumed as −158.5 dBW.

(2) Calculating C/N_0 based on the parameters of receiver antenna and RF end

The C/N_0 output from the RF end of receiver is:

$$C/N_0 = P_{in} - k + G_a - (T_a + T_e) \tag{63.6}$$

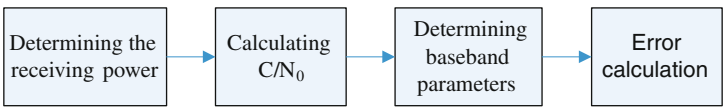

Fig. 63.3 The calculation process of the pseudorange noise error

Table 63.1 The antenna gain of compass universal receiver

Frequency	Size/mm	Elevation/degree	Gain/dBic
B1	Handhold 45 × 45 × 10	50	0
	Vehicle Φ146 × 40	30	−2

where,

P_{in} is the power reached the receiver antenna.
k is Boltzmann's constant, about −228.6 dB.
G_a is the gain of the receiver antenna.
T_a is the noise temperature of the receiver antenna, about 100 K.
T_e is the overall equivalent noise temperature from the export of antenna to the section of RF chip.

The antenna gain of Compass universal receiver was shown on Table 63.1. The calculation process of T_e was:

$$T_e = (F - 1)T_0 \tag{63.7}$$

where,

T_0 is room temperature, about 290 K.
F is the noise figure of the whole section from the export of antenna to the section of RF chip.

According to the expression of the noise figure in the cascade network:

$$F = L\left(F_{LNA} + \frac{F_{RF} - 1}{G_{LNA}}\right) = 1.35 \tag{63.8}$$

where,

L is the loss of transmission line between the antenna and low-noise amplifier (LNA), about 0.5 dB.
G_{LNA} is the gain of LNA, about 30 dB.
F_{LNA} is the noise figure of LNA, about 0.8 dB.
F_{RF} is the noise figure of the RF chip, about 5 dB.
So $T_e = (1.35 - 1) \times 290 = 101.5\,K$

Thus, C/N_0 can be calculated with Eq. 63.6. At room temperature, C/N_0 was about 42.6 dBHz (50° elevation) for a handhold antenna, about 40.6 dBHz (30° elevation) for a vehicle antenna. In addition, the quantization loss of RF chip can be ignored because the quantization bits were 4 bit. For the Compass global system, there is no mature antenna and RF for reference, this C/N_0 was also used temporarily.

Table 63.2 The pseudorange noise error of compass system B1 open signal

Signal	Modulation	Elevation/degree	Error/m
B1I	BPSK(2)	Handhold 50	0.60
		Vehicle 30	0.78
B1C	TMBOC (6, 1, 4/33)	Handhold 50	0.54
		Vehicle 30	0.72

(3) Determining the parameters of baseband signal processing

The front-end filter bandwidth of universal navigation receiver was usually the main lobe of the receiving signal power spectrum. For BPSK modulation, the code rate was f_c, and the corresponding main lobe was $2f_c$. For BOC modulation signal, the corresponding main lobe was $4f_c$. Correlator spacing multiplied with the parameter of front-end filter bandwidth (BPSK modulation was 2, BOC modulation was 4) generally equal to 2. Therefore, for Compass regional system B1I signal, the front-end bandwidth was 4 MHz, and the correlator spacing was 1 chip. For Compass global system B1C signal (TMBOC (6, 1, 4/33) modulation), the front-end bandwidth was 4 MHz, and the correlator spacing was 0.5 chip.

The other parameters of baseband signal processing for calculating pseudorange noise error included: the coherent integration cumulative time was 1 ms, the loop noise bandwidth was 1 Hz. For BPSK modulation, the normalized power spectral density of the received signal was:

$$G_{BPSK}(f) = \frac{1}{f_c}\left(\sin c\left(\pi\frac{f}{f_c}\right)\right)^2 \tag{63.9}$$

For TMBOC (6, 1, 4/33) modulation, the normalized power spectral density of the received signal was [6]:

$$G_{TMBOC}(f) = \frac{29}{33}G_{BOC(1,1)}(f) + \frac{4}{33}G_{BOC(6,1)}(f) \tag{63.10}$$

(4) Error calculation

Based on the above parameters of the receiver, the pseudorange noise error of Compass system B1 Open signal can be calculated with the Eq. 63.5. The result was shown in the follow table (Table 63.2).

63.4 Actual Receiver Test Verification

In order to verify the above analysis, the test verification was done with Compass universal vehicle receiver in the area of Beijing. The test was divided into two steps. First, the relationship between elevation and C/N_0 was verified by receiving

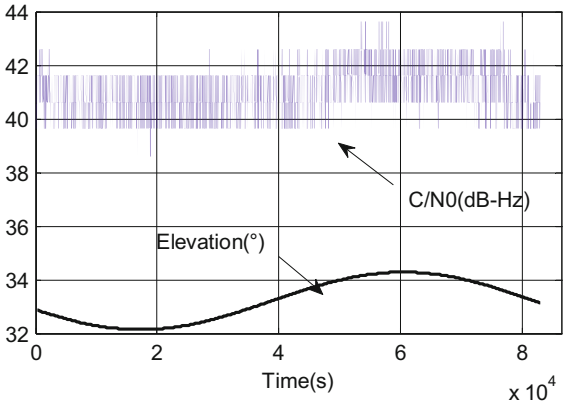

Fig. 63.4 The monitoring results of elevation and C/N_0 in one day

actual signal. Second, the pseudorange noise error was verified using the method of zero baseline.

(1) Elevation and C/N_0 verification

To facilitate the analysis, the GEO satellite of Compass system was selected to monitor. Monitoring point lay on the open roof of Beijing suburb, and multipath can be ignored. In the area of Beijing, the elevation of 3rd satellite was near 30°. B1 open signal was received and processed with Compass universal vehicle receiver. The monitoring results of elevation and C/N_0 in one day were shown in the following figure (Fig. 63.4).

The statistical result showed that the mean of elevation was 33.2°, the mean of C/N_0 was 42.1 dBHz in one day for 3rd satellite in the Beijing area. The results were equivalent with above analysis, C/N_0 was 40.6 dBHz when elevation was 30°.

(2) Pseudorange noise error verification

The same type of universal vehicle receivers were used to monitor pseudorange noise error with the method of zero baseline pseudorange double difference

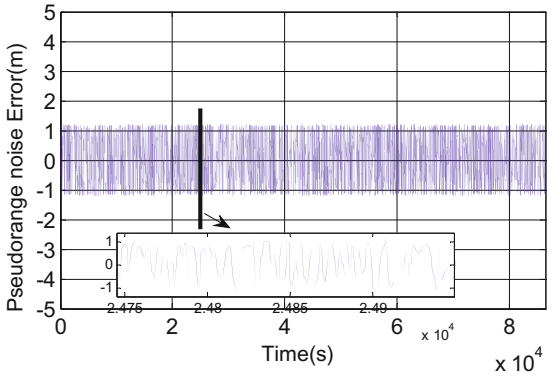

Fig. 63.5 The monitoring results of pseudorange noise error in one day

observation. The observed values can eliminate the error of space segment, control segment, environmental segments and multipath, the residual was basically pseudorange noise error. The monitoring results of pseudorange noise error in one day were shown in the following figure (Fig. 63.5).

The statistical result showed that pseudorange noise error was 0.69 m (1σ), which was equivalent with above analysis.

63.5 Conclusion

In this paper, a new analysis method of pseudorange noise error was proposed. According to the characteristics of Compass universal navigation receiver, the antenna and baseband processing parameters were selected, the pseudorange noise error of Compass system B1 open signal was analyzed. The analysis method and result can provide a reference for the application of Compass system at this stage and UERE budget for the global system.

References

1. Kovach K (2000) New user equivalent range error (UERE) budget for the modernized Navstar global positioning system (GPS). ION NTM 2000, Anaheim, CA, pp 550–573
2. Markus I, Rodriguez J, Hein GW (2005) Criteria for GNSS multipath performance assessment. ION GNSS 2005, Long Beach, pp 2166–2177
3. Bin T, Haibo H (2012) Study on the analysis method of GNSS system UERE error for environment segment and user segment. In: China satellite navigation conference 2012 proceedings, Guangzhou
4. VEGA Group PLC (2005) Galileo system simulation facility GSSF models and algorithms [EB/OL]. www.vega.de, pp 73–75
5. Betz JW (2000) Design and performance of code tracking for the GPS M code signal. ION GNSS 2000, Salt Lake City, pp 2140–2150
6. Betz JW (2001) Binary offset carrier modulations for radio navigation. J Inst Navig 48(4):227–246
7. Zhang B, Liu F (2011) Research on compass B1 open service signal modulation. Scientia Sinica 1(5):568–574
8. Zuping T, Hongwei Z (2012) Research on performance evaluation of compass signal. In: China satellite navigation conference 2010 proceedings, Beijing
9. Holmes JK (2000) Code tracking loop performance including the effect of channel filtering and Gaussian interference. ION AM 2000, San Diego, pp 382–398

Chapter 64
Doppler-Aided Algorithm for BeiDou Position

Dengyun Lei, Weijun Lu and DunShan Yu

Abstract Real-time GNSS positioning rely mainly on pseudorange and carrier-phase. The pseudorange is not accurate because of a lot of noise and interference in environment. High-precision carrier-phase used to smooth pseudorange. While, when cycle slip occurs, the carrier-phase measurement is bias. Unlike Carrier observations, the Doppler observations tend to have higher continuity. In Beidou system, GEO satellites local in geostationary orbit with lower dynamic. So, we can use the small noise bandwidth to improve the accuracy of measurement. This paper analyzes the characteristics and methods of Doppler-assisted positioning the the settlement equation using the weighted least squares method. The simulation and test results show that the positioning of the reliability of the results has been improved.

Keywords Doppler-aided · BeiDou System · Position Algorithm · Least square

64.1 Introduction

Due to satellite signal need to go through the long distance transmission, the transmission proceeds is interference. The interference is including thermal noise, ionospheric scintillation, tropospheric delay and multipath. Those interferences

D. Lei · D. Yu
Institute of Microelectronics, Peking University, Beijing, China
e-mail: dengyun.lei@pku.edu.cn

D. Yu
e-mail: yuds@pku.edu.cn

W. Lu (✉)
School of Electronics Engineering, Beijing University of Posts and Telecommunication, Beijing, China
e-mail: luwj526@gmail.com

J. Sun et al. (eds.), *China Satellite Navigation Conference (CSNC) 2013 Proceedings*, Lecture Notes in Electrical Engineering 243,
DOI: 10.1007/978-3-642-37398-5_64,

make the pseudorange measurement inaccurate. While the precision of code measurement is lower by 2–3 magnitudes than that of carrier, the use of carrier phase smoothing pseudorange is a frequently method. Hatch filter [1] using carrier phase difference as an accurate measurement to smooth pseudorange, is widely used. However, in some circumstances, such as the trees obscured or low signal-to-noise ratio, the phase-locked loop (PLL) may loss of lock, which causes resulting in a discontinuity of the carrier phase measurements. If the loss of PLL lock cannot be detected, the positioning results are biased. Hatch filter need to set a period, to prevent the errors from accumulating. Cycle slips occurring frequently, results the Hatch filter performance is not prominent in urban environments.

Doppler measurement is good at continuity and anti-jamming. Doppler measurements to assist pseudorange smoothing become a new choice [2]. In the following sections, firstly brief overview of BeiDou signal structure and satellite constellation is described. Then Doppler aided algorithm is introduced and PLL noise bandwidth is analysis. Finally numerical test results are shown and conclusion is given.

64.2 BeiDou Signal Model and Satellite Constellation

64.2.1 BeiDou Broadcast Signal

The B1 signal radio (channel I) from BeiDou satellite [3] can be given as:

$$S_{B1i}(t) = \sqrt{2P_c}D_i(t-t_i)C_i(t-t_i)\cos[2\pi f_i(t-t_i)+\theta_i]+n_i(t) \tag{64.1}$$

where: i is the satellite number, S_{B1i} is the B1 signal received from satellite i, P_c is the ranging code power, $D_i(t)$ is the navigation data, f_i is carrier frequency, $C_i(t)$ is the pseudorandom noise spreading sequence ranging code, t_i is the propagation delay, θ_i is unknown phase, and $n_i(t)$ is noise.

From formula (64.1), the signal transmitting delay can be got from the difference of code or carrier measurements. When the code delay measurements are used to determine pseudorange, the pseudorange is expressed as:

$$\rho_i(t) = r_i + c\delta t(t) + I_i(t) + T_i(t) + \varepsilon_{p,i}(t) \tag{64.2}$$

where $\rho_i(t)$ is the pseudorange of satellite i, c is velocity of light, $\delta t(t)$ is the clock error, $I_i(t)$ is ionosphere delay, $T_i(t)$ is troposphere delay, and $\varepsilon_{p,i}(t)$ is the measurement noise. r_i is the geometric distance between satellite i and receiver (x_i, y_i, z_i is satellites position, x, y, z is receiver position):

$$r_i = \sqrt{(x_i-x)^2+(y_i-y)^2+(z_i-z)^2} \tag{64.3}$$

The formula (64.3) is substituted into (64.2), and rearrange, we can get the position formula:

$$(\rho_i - I_i - T_i) = \sqrt{(x_i - x)^2 + (y_i - y)^2 + (z_i - z)^2} + c\delta t + \varepsilon_{p,i} \quad (64.4)$$

The satellite position is solved from satellite broadcast message. The ionospheric and tropospheric delay is modeled.

64.2.2 BeiDou Satellite Constellations

Beidou Navigation Satellite System is an independent system offering regional position and timing service now. Comparing with GPS satellite, BeiDou navigation system consists of three kinds of orbit satellites, include Geostationary Earth Orbit (GEO) satellites, Medium Earth Orbit (MEO) satellites and Inclined Geosynchronous Satellite Orbit (IGSO) satellites.

The GEO satellites are local in orbit with low dynamic. The elevation change of visible satellites shown in Fig. 64.1 in 24 h (cut-off angle 10°). The elevations of GEO satellites only have minor changes. Unlike GPS satellite, BeiDou receiver can decrease the PLL noise bandwidth for low dynamic in order to reduce noise.

64.3 Doppler-Aided Position Algorithm

64.3.1 Doppler Model

Doppler is generated by the relative movement of the satellite and user. According to General relativity, the doppler is expressed as:

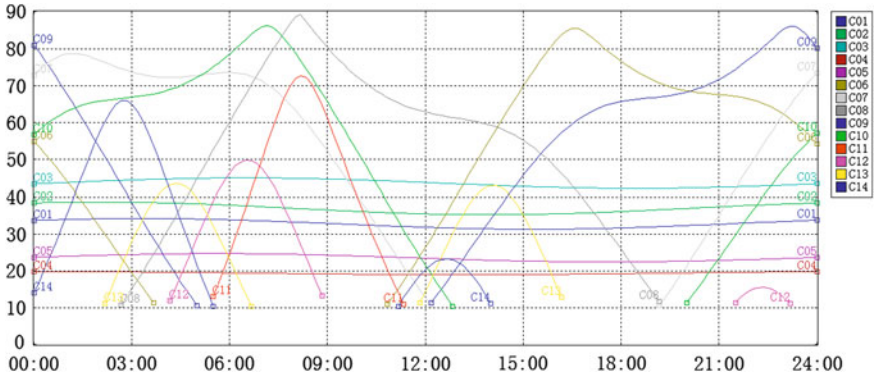

Fig. 64.1 Elevation change of visible satellites of Beijing (24 h)

$$\frac{f_r}{f_0} = \frac{1 - \frac{(\vec{v}_i - \vec{v})(\vec{p}_i - \vec{p})}{c\|\vec{p}_i - \vec{p}\|}}{\sqrt{1 - \frac{\|\vec{v}_i - \vec{v}\|^2}{c^2}}} \tag{64.5}$$

where f_r is carrier frequency at the receiver, f_0 is the transmitted carrier frequency (1561.098 MHz), $\vec{p}_i, \vec{v}_i$ is the vector of satellite position and velocity. $\vec{p}, \vec{v}$ is the vector of user position and velocity.

The relative movement between satellites and user is lower than the velocity of light. The denominator of formula (64.5) is close to 1, then the equation simplifies as:

$$f_{di} = \frac{f_0}{c} * \frac{(\vec{p}_i - \vec{p})}{\|\vec{p}_i - \vec{p}\|} * (\vec{v}_i - \vec{v}) \tag{64.6}$$

Equation (64.6) consists of three parts: the first part is constant, and the second part represents the unit vector from satellite to user, and the last part is relative velocity vector.

64.3.2 Position Algorithm Using Pseudorange

The least square (LS) method is used to calculate the location. The equation include four unknowns $(x, y, z, \delta t)$ is settled with four satellites.

The least squares method can only solving the linear equation. The nonlinear Eq. (64.4) are linearized with Talyor series [4].

$$\rho_i^0 - (\rho_i - I_i - T_i) + \varepsilon_{p,i} = \frac{(x_i - x^0)}{\rho_i^0}\delta x_i + \frac{(y_i - y^0)}{\rho_i^0}\delta y_i + \frac{(z_i - z^0)}{\rho_i^0}\delta z_i - c\delta(\delta t_i) \tag{64.7}$$

where ρ_i^0 is the pseudorange of predict position.

Define the following arguments:

$$\begin{aligned} \delta\rho_i &= \rho_i^0 - (\rho_i - I_i - T_i) \\ a_{xi} &= \frac{x_i - x^0}{\rho_i^0} \quad a_{yi} = \frac{y_i - y^0}{\rho_i^0} \quad a_{zi} = \frac{z_i - z^0}{\rho_i^0} \end{aligned} \tag{64.8}$$

Ignoring the measurement noise, the formula (64.7) simplifies:

$$\delta\rho_i = a_{xi}\delta x_i + a_{yi}\delta y_i + a_{zi}\delta z_i - c\delta(\delta t_i) \tag{64.9}$$

When the available satellites (N) are more than four satellites, the equations list as:

$$\delta\vec{\rho}_i = H_{pp}\delta\vec{x}_i \tag{64.10}$$

where:

$$\delta\vec{\rho}_i = \begin{bmatrix} \delta\rho_1 \\ \delta\rho_2 \\ \delta\rho_3 \\ \vdots \\ \delta\rho_N \end{bmatrix} \quad \delta\vec{x} = \begin{bmatrix} \delta x \\ \delta y \\ \delta z \\ -c\delta(\delta t) \end{bmatrix} \quad H_{pp} = \begin{bmatrix} a_{x1} & a_{y1} & a_{z1} & 1 \\ a_{x2} & a_{y2} & a_{z2} & 1 \\ a_{x3} & a_{y3} & a_{z3} & 1 \\ \vdots & \vdots & \vdots & \vdots \\ a_{xN} & a_{yN} & a_{zN} & 1 \end{bmatrix} (N \geq 4) \tag{64.11}$$

When $H^T H$ is symmetric, positive definiteness and reversible, the solution of the problem is given by:

$$\delta\vec{x} = (H_{pp}^T H_{pp})^{-1} H_{pp}^T \delta\vec{\rho}_i \tag{64.12}$$

From the Eq. (64.12), the offset of user position $(x, y, z, \delta t)$ and predict position $(x^0, y^0, z^0, \delta t^0)$ is given. If the offset is small, the user position is get. If the offset is large, the iteration is used to lessen the offset.

64.3.3 Doppler-Aided Position Algorithm

In signal transmission process, the doppler measurement is not sensitive to environment noise. So, the doppler measurement is more accuracy than that of pseudorange and thus can be used to assist smooth positioning.

Similar with formula (64.4), linear Eq. (64.6) at the predicted position and velocity $(x^0, y^0, z^0, \delta t^0, v_x^0, v_y^0, v_z^0)$ [5]:

$$\begin{aligned} f_{di} = \frac{f^0}{c}\Bigg\{ & \left(\frac{(v_{xi} - v_x^0)}{\rho_i^0} + \frac{(x_i - x^0)}{(\rho_i^0)^3}\right)\delta x + \left(\frac{(v_{yi} - v_y^0)}{\rho_i^0} + \frac{(y_i - y^0)}{(\rho_i^0)^3}\right)\delta y \\ & + \left(\frac{(v_{zi} - v_z^0)}{\rho_i^0} + \frac{(z_i - z^0)}{(\rho_i^0)^3}\right)\delta z + \frac{(x_i - x^0)}{\rho_i^0}\delta v_x \\ & + \frac{(y_i - y^0)}{\rho_i^0}\delta v_y + \frac{(z_i - z^0)}{\rho_i^0}\delta v_z \Bigg\} + \delta f \end{aligned} \tag{64.13}$$

where δf is frequency deviation

Define the following argument:

$$b_{xi} = \frac{f^0}{c}\left(\frac{(v_{xi} - v_x^0)}{\rho_i^0} + \frac{(x_i - x^0)}{(\rho_i^0)^3}\right) \qquad c_{vxi} = \frac{f^0}{c}\left(\frac{(x_i - x^0)}{\rho_i^0}\right)$$

$$b_{yi} = \frac{f^0}{c}\left(\frac{(v_{yi} - v_y^0)}{\rho_i^0} + \frac{(y_i - y^0)}{(\rho_i^0)^3}\right) \qquad c_{vyi} = \frac{f^0}{c}\left(\frac{(y_i - y^0)}{\rho_i^0}\right)$$

$$b_{zi} = \frac{f^0}{c}\left(\frac{(v_{zi} - v_z^0)}{\rho_i^0} + \frac{(z_i - z^0)}{(\rho_i^0)^3}\right) \qquad c_{vzi} = \frac{f^0}{c}\left(\frac{(z_i - z^0)}{\rho_i^0}\right) \tag{64.14}$$

The formula (64.13) simplifies:

$$f_{di} = b_{xi}\delta x + b_{yi}\delta y + b_{zi}\delta z + c_{vxi}\delta v_x + c_{vyi}\delta v_y + c_{vzi}\delta v_z + \delta f \tag{64.15}$$

In (64.15), there are seven unknowns which mean that seven satellites measurements are used. However, in urban, it is not common to get seven satellites. Combing (64.10) and (64.15), the position and velocity are solved with four satellites.

$$\begin{bmatrix} \delta\vec{\rho} \\ f_d \end{bmatrix} = \begin{bmatrix} H_{pp} & 0 \\ H_{pf} & H_{ff} \end{bmatrix} \begin{bmatrix} \delta\vec{x} \\ \delta\vec{v} \end{bmatrix} \tag{64.16}$$

where:

$$\begin{aligned} f_d &= \begin{bmatrix} f_{d1} \\ f_{d2} \\ f_{d3} \\ \vdots \\ f_{dN} \end{bmatrix} H_{ff} = \begin{bmatrix} c_{vx1} & c_{vy1} & c_{vz1} & 1 \\ c_{vx2} & c_{vy2} & c_{vz2} & 1 \\ c_{vx3} & c_{vy3} & c_{vz3} & 1 \\ \vdots & \vdots & \vdots & \vdots \\ c_{vxN} & c_{vyN} & c_{vzN} & 1 \end{bmatrix} \\ \delta\vec{v} &= \begin{bmatrix} \delta v_x \\ \delta v_y \\ \delta v_z \\ \delta f \end{bmatrix} H_{pf} = \begin{bmatrix} b_{x1} & b_{y1} & b_{z1} & 0 \\ b_{x2} & b_{y2} & b_{z2} & 0 \\ b_{x3} & b_{y3} & b_{z3} & 0 \\ \vdots & \vdots & \vdots & \vdots \\ b_{xN} & b_{yN} & b_{zN} & 0 \end{bmatrix} \end{aligned} \tag{64.17}$$

Similar, the unbiased estimate of $\delta x, \delta y, \delta z, \delta t, \delta v_x, \delta v_y, \delta v_z, \delta f$ is given:

$$\begin{bmatrix} \delta\vec{x} \\ \delta\vec{v} \end{bmatrix} = (H^T H)^{-1} H^T \begin{bmatrix} \delta\vec{\rho} \\ f_d \end{bmatrix} \tag{64.18}$$

where:

$$H = \begin{bmatrix} H_{pp} & 0 \\ H_{pf} & H_{ff} \end{bmatrix} \tag{64.19}$$

The result of the Eq. (64.18) is

$$\begin{bmatrix} \delta\vec{x} \\ \delta\vec{v} \end{bmatrix} = (H^T W H)^{-1} H^T W \begin{bmatrix} \delta\vec{\rho} \\ f_d \end{bmatrix} \tag{64.20}$$

where the weight is defined as:

$$W = \begin{bmatrix} \left[\sigma_{\rho_i}^{-2}\right] & 0 \\ 0 & \left[\sigma_{f_i}^{-2}\right] \end{bmatrix} \tag{64.21}$$

σ is the variance of measurement

64.3.4 Optimize Loop Parameter

In order to improve the accuracy of the Doppler measurement, the noise bandwidth is reduced which reduce the noise for the carrier loop. The noise bandwidth of the control into the loop filter the noise energy, the effect can be improved by reducing the noise bandwidth of the loop filter, to improve tracking accuracy.

The width of the noise bandwidth depends on the tracking dynamic and SNR. Small noise bandwidth may reduce the noise in the band, but not be able to track a large dynamic, it is easy to cause the frequency and phase tracking error; large noise bandwidth will introduce a large noise energy, affecting the the signal tracking stability [6].

Users generally smaller dynamic system dynamics is mainly caused by the satellite movement. Beidou system system uses a three-orbit satellites, the dynamic of the GEO satellites is very low. For this reason, we can reduce the noise bandwidth of the GEO satellite tracking filter to make it match with MEO and IGSO, the same dynamic, improved the GEO carrier ring accuracy so without reducing the dynamic case.

Considering the essential requirement PLL loop parameter:

$$\sqrt{\sigma_{tPLL}^2 + \sigma_v^2 + \sigma_A^2} + \frac{\theta_e}{3} \leq 15^\circ \tag{64.22}$$

where σ_{tPLL} is 1σ thermal noise, σ_v is 1σ vibration, σ_A is Allan deviation, θ_e is PLL dynamic stress.

Consider thermal noise errors and dynamic stress error, the state of motion of the vehicle terminal user as example [7], we can set the PLL noise bandwidth is 15 Hz for GEO and 30 Hz for others respectively. The accuracy of position result is improved by improving the GEO doppler measurement accuracy and weight.

64.4 Testing and Analysis

To demonstrate the performance, the proposed algorithm has been investigated using Beidou date under static real-time condition. In this section, the detail of experiments is introduced.

The platform (Fig. 64.2) is built with GPS/BD2 chip named BD-ZS3121 which is designed by lab of SoC, Peking University.

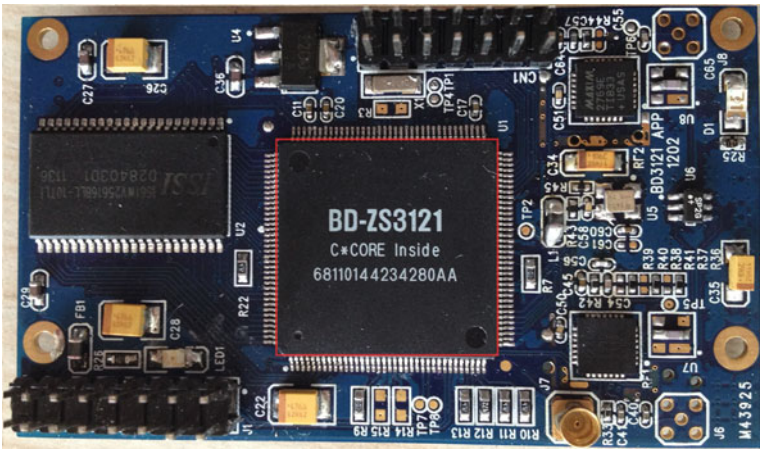

Fig.. 64.2 BD-ZS3121 Platform

In order to compare different algorithms, the pseudorange algorithm, Hatch filter and dopper-aided position algorithm. During the entire measurement campaign, six Beidou satellites (four GEO satellites and two MEO satellites) were captured with a cut-off elevation angel of 10̊. Time interval of an epoch is 1 s, and 1,000 continuous points are collected for each method. The signal power is −130 dBm. The means and variances are shown in Tables 64.1 and 64.2.

From Tables 64.1 and 64.2, the carrier phase smoothed or doppler smoothed pseudorange reduce the variances and mean. When the probability of cycle slip is in low level, the Hatch filter provide more accuracy than doppler-aided method but the different is not evident.

In order to further verify the cycle slip effect on smoothing progress, additional tests are included in which the signal power is attenuated extra 10 dB (Tables 64.3, 64.4).

Table 64.1 Test result of user position (−130dBm)

Method	Mean	Variance	Maximum
Pseudorange	4.27	4.50	10.42
Hatch filter	3.17	3.09	4.38
Doppler-aided	3.20	3.22	4.16

Table 64.2 Test result of user velocity (−130dBm)

Method	Mean	Variance	Maximum
Pseudorange	0.028	0.029	0.075
Hatch filter	0.028	0.020	0.079
Doppler-aided	0.027	0.021	0.060

Table 64.3 Test result of user position (−140dBm)

Method	Mean	Variance	Maximum
Pseudorange	9.38	10.4385	28.33
Hatch filter	7.91	5.0442	15.58
Doppler-aided	5.91	4.0709	7.47

Table 64.4 Test result of user velocity(−140dBm)

Method	Mean	Variance	Maximum
Pseudorange	0.065	0.0838	0.127
Hatch filter	0.038	0.0658	0.104
Doppler-aided	0.040	0.0417	0.095

In Tables 64.3 and 64.4, the variance of Hatch filter immensely increases with the increasing cycle slip times. In each time of cycle slip, the Hatch filter accumulates error. While, the doppler-aided algorithm is not sensitive to cycle slip and the accuracy is high than Hatch filter.

From the test result, in low signal-to-noise ratio environment, due to the probable of the loss of lock, the position accuracy of Hatch filter is fall. Doppler-aided position algorithm provides a good robustness, and low noise bandwidth improves the accuracy of the measurement data, and achieves a good position results.

64.5 Conclusions

The Doppler-assisted positioning algorithm is introduced. This algorithm combines both pseudorange and doppler measurement. Taking advantage of the low dynamic satellites, the PLL noise bandwidth is lesson to improve the measurement accuracy. Under low signal-to-noise ratio, comparing with Hatch filter, doppler measurement is not suffer from cycle slips and improve the performance and stability.

References

1. Hatch R (1983) The synergism of GPS code and carrier measurements. In: Proceedings of the 3rd international geodetic symposium on satellite doppler positioning, 1983, pp 1213–1231
2. Cheng P (1999) Remarks on Doppler-aided smoothing of code ranges. J Geodesy 73:P23–P28
3. China Satellite Navigation Office (2011) BeiDou navigation satellite system signal in space interface control document, p 3.www.beidou.gov.cn
4. Tsui JBY (2001) Fundamentals of global positioning system receivers: a software approach. Wiely, New York

5. Simsky A, Boon F (2003) Carrier phase & Doppler-based algorithms for real-time standalone positioning. Proceedings of GNSS, Austria
6. Rinder P, Bertelsen N (2004) Design of a single frequency GPS software receiver, Master thesis. Aalborg University, Denmark
7. Lian P (2004) Improving tracking performance of PLL in high dynamic applications, Master thesis. The University of Calgary, Alberta

Chapter 65
Analysis of the Anti-Spoofing Performance of Acquisition with Threshold Method

Jian Wang, Hong Li, Xiaowei Cui and Mingquan Lu

Abstract With the rapid development of navigation technologies, spoofing has become a significant threat to navigation system. As a key step in receiver signal processing, acquisition is an important barrier to anti-spoofing. Nowadays, researching on anti-spoofing performance of acquisition is in a blank stage, threshold method in acquisition is the most commonly used detection strategy. In this article, we add a single spoofing signal on GPS P code and through the construction of mathematical model, we define successful probability of anti-spoofing as the assessment standard, then we analyze the relationship between factors influencing acquisition threshold and the successful probability of anti-spoofing, finally we give the theoretical calculate method of upper bound of threshold method's anti-spoofing performance, which all have a guiding significance for the design of receiver.

Keywords Threshold · Acquisition · Amplification factor of spoofing signal · Successful probability of anti-spoofing

65.1 Introduction

With the rapid development of navigation technologies, safety of navigation signal has gradually become a topic of concern by the user, and research on spoofing and anti-spoofing of GPS signal has also become a hot spot.

Currently, there are some anti-spoofing methods existed, for example: an internal memorandum [1] from the MITRE recommended six techniques to counter spoofing and Wen proposed ten countermeasures for civil GPS signal

J. Wang (✉) · H. Li · X. Cui · M. Lu
Department of Electronic Engineering, Tsinghua University,
Beijing 100084, China
e-mail: tswangjian05@gmail.com

J. Sun et al. (eds.), *China Satellite Navigation Conference (CSNC) 2013 Proceedings*, Lecture Notes in Electrical Engineering 243,
DOI: 10.1007/978-3-642-37398-5_65,

spoofing [2], both of which introduced kinds of methods comprehensively, but simply enough to put forward ideas, no further studies or results. Humphreys et al. [3] proposed two technique based on baseband processing technology; Cavaleri et al. [4] further elaborated how to achieve anti-spoofing on monitor phase-locked loop and delay locked loop, both of which focused on the technical aspects of baseband, mainly on the loop design. The Novariant Corporation detailed their research results on anti-spoofing platform with dual-antennas [5] and Daneshmand et al. [6] published their research results and the experimental data on GNSS12 meeting, both of which introduced multi-antenna technology to detect and eliminate spoofing. Huang et al. [7] presented a series of countermeasures and steps for spoofing in the point of signal designing and processing, which do some research on anti-spoofing methods and evaluation means. Generally speaking, the anti-spoofing technology is still in the groping stage. Though some countermeasures have been introduced, they have not been achieved yet. What is more, there is not effective assess tools to evaluate the merits of the anti-spoofing methods.

Acquisition determines whether the receiver can find the true signal, so it is an important barrier to anti-spoofing. However, researching on anti-spoofing performance of acquisition is in a blank stage. In this paper, we deal with GPS P-code, define successful probability of anti-spoofing as the assessment standard and analyze the anti-spoofing performance of acquisition with threshold method, then we give the theoretical calculate method of upper bound of threshold method's anti-spoofing performance, which all have a guiding significance for the design of receiver.

65.2 Assessment Standard of Anti-Spoofing

65.2.1 The Basic Principle of Acquisition with Threshold Method [8]

Acquisition of GNSS signal is a two-dimensional search process. In each search grid, since the thermal noise is a Gaussian distribution, when the local signal is not aligned with the received true signal and spoofing signal, envelope $\sqrt{I^2 + Q^2}$ is formed, thus the noise is Rayleigh distribution and otherwise Rician distribution. The corresponding probability density function can be unified as formula 65.1:

$$p(z) = \begin{cases} \frac{z}{\sigma_n^2} \exp\left(-\frac{z^2+A^2}{2\sigma_n^2}\right) I_0\left(\frac{zA}{\sigma_n^2}\right), & z \geq 0 \\ 0, & z < 0 \end{cases} \tag{65.1}$$

Where σ_n^2 is RMS noise power, A is RMS signal amplitude and $I_0\left({}^{zA}/_{\sigma_n^2}\right)$ is zero order modified Bessel function. When it indicates noise, $A = 0$, and true signal, $A = A_s$, and spoofing signal, $A = A_j$.

In order to distinguish between signal and noise, we utilize NP criteria that calculate threshold after determining the probability of false alarm p_{fa}, showed as formula 65.2:

$$V_t = \sigma_n \sqrt{-2\ln p_{fa}} \tag{65.2}$$

Where V_t is the threshold. When the envelop detected is lower than V_t, we regard it as noise and when higher, it is signal, therefore, detection probability of true signal and spoofing signal is as follows:

$$p_d^s = \int_{V_t}^{\infty} p_s(z)dz \tag{65.3}$$

$$p_d^j = \int_{V_t}^{\infty} p_j(z)dz \tag{65.4}$$

65.2.2 Successful Probability of Anti-Spoofing

The purpose of spoofing is to enable the receiver to lock spoofing signal. The first correlation value higher than threshold is the result when using threshold method. In this case, whether the receiver detect the true signal or it doesn't detect both the true and the spoofing, we can consider it as successful anti-spoofing, and define its probability as successful probability of anti-spoofing. Assume that detecting the true signal and spoofing signal be relatively independent, successful probability of anti-spoofing can be expressed as formula 65.5:

$$p_d = p_d^s + \left(1 - p_d^s\right)\left(1 - p_d^j\right) = \int_{V_t}^{\infty} p_s(z)dz + \int_0^{V_t} p_s(z)dz \int_0^{V_t} p_s(z)dz \tag{65.5}$$

Integrated formula 65.1, 65.2 and 65.5, we can get the calculate method of successful probability of anti-spoofing: First, we determine the threshold according to the probability of false alarm p_{fa} and noise power σ_n^2, then the probability density function based on the input signal to noise ratio and coherent integration time, finally the successful probability of anti-spoofing through integration. Describe amplitude relation between true signal and spoofing signal as formula 65.6, we can make sure that the factors influencing ting successful probability of anti-spoofing p_d are the input signal-to-noise ratio (SNR) without spoofing signal, spoofing signal amplification factor (k), probability of false alarm (p_{fa}) and coherent integration time (c_h).

$$A_j/A_s = k \tag{65.6}$$

65.3 Analysis of Factors that Influence Anti-Spoofing Performance

According to Sect. 65.2.2, there are many factors influencing successful probability of anti-spoofing, and the followings are the influence of each factor.

65.3.1 Input SNR and Spoofing Signal Amplification Factor k

S/N and k are both factors which influence and noise power of signal received, and therefore influence the threshold and the probability density function. Figure 65.1 shows the influence to the success probability of anti-spoofing p_d, where the probability of false alarm $p_{fa} = 0.001$ and coherent integration time $c_h = 1$ ms.

Following points can be seen from Fig. 65.1: (1) When the input SNR is too low to detect the true signal, the successful probability of anti-spoofing is the probability that spoofing signal can't be detected; (2) The success probability of anti-spoofing increases as the input SNR increases, and increases as the spoofing signal amplification factor decreases, for the reason that it actually increases the SNR received, which increases the detection probability of true signal; (3) When the spoofing signal amplification factor is less than 1,the successful probability of anti-spoofing is approximately equal to 1, which indicates that when spoofing signal is weaker than true signal, it can't achieve spoofing. Overall, input SNR

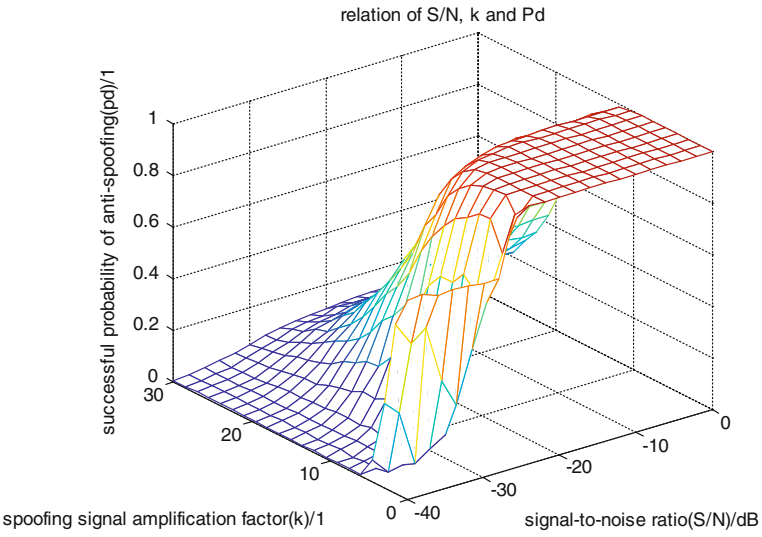

Fig. 65.1 Influence of S/N and amplification factor of spoofing signal to the probability

plays a positive role to the successful probability of anti-spoofing, while spoofing signal amplification factor is negative. However, for the received signal, input SNR and spoofing signal amplification factor is immutable (unless changing the signal gain by using a directional antenna or by means of beam-forming), though they can affect the success probability of anti-spoofing, but do little use of anti-spoofing.

65.3.2 Coherent Integration Time c_h

The coherent integration time can bring the coherent integration gain, which can influence SNR and noise power of signal received, and therefore influence the threshold and the probability density function. Figure 65.2 shows the influence to the success probability of anti-spoofing p_d, where the probability of false alarm $p_{fa} = 0.001$ and input SNR $= -19$ dB.

Following points can be seen from Fig. 65.2: (1) The successful probability of anti-spoofing increases as the coherent integration time increases, for the reason that more coherent integration gain will be acquired when the coherent integration time increases, which actually increases the SNR received and increases the detection probability of true signal; (2) When the coherent integration time is determined, it can tolerable limited spoofing signal amplification factor, which means if the power rate between the spoofing signal and the true signal exceeds a certain threshold, it needs to increase the coherent integration time. Therefore, the coherent integration time plays a positive role to the successful probability of anti-

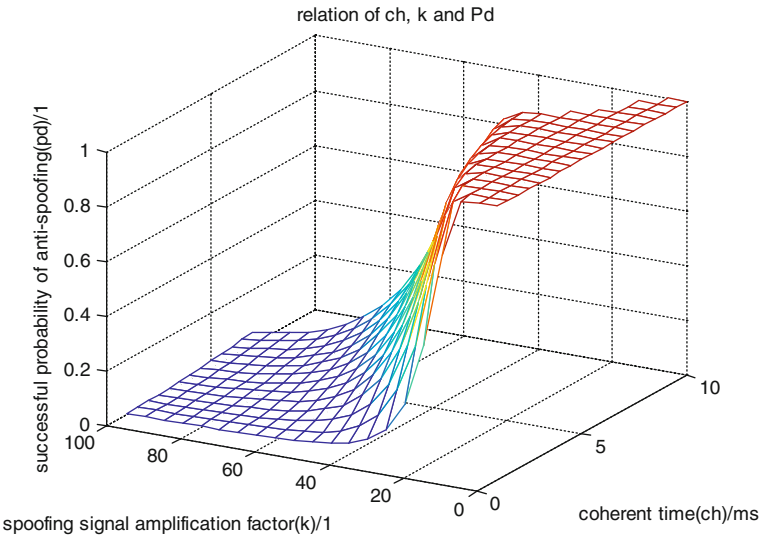

Fig. 65.2 Influence of coherent integration time to the probability

spoofing, and the receiver can increase the successful probability of anti-spoofing by increasing the coherent integration time. However, the coherent integration time is influenced by the bit flip, and the frequency grid for searching will also increase as its increases, so the coherent integration time can't be increased unlimited.

65.3.3 Probability of False Alarm p_{fa}

According to formula 65.2, the probability of false alarm can have a direct influence on the threshold, which can influence the successful probability of anti-spoofing. Figure 65.3 shows the influence to the success probability of anti-spoofing p_d, where the input SNR $= -19$ dB and the coherent integration time $c_h = 1$ ms.

Following points can be seen from Fig. 65.3: (1) The successful probability of anti-spoofing increases as the probability of false alarm increases, for the reason that the threshold will be decreased when the probability of false alarm increases, which actually increases the detection probability of true signal; (2) When the probability of false alarm is determined, it can tolerable limited spoofing signal amplification factor, which means if the power rate between the spoofing signal and the true signal exceeds a certain threshold, in order to ensure a certain successful probability of anti-spoofing, it needs to increase the probability of false alarm. Therefore, the probability of false alarm plays a positive role to the successful probability of anti-spoofing, and the receiver can increase the successful probability of anti-spoofing by increasing the probability of false alarm. However, higher

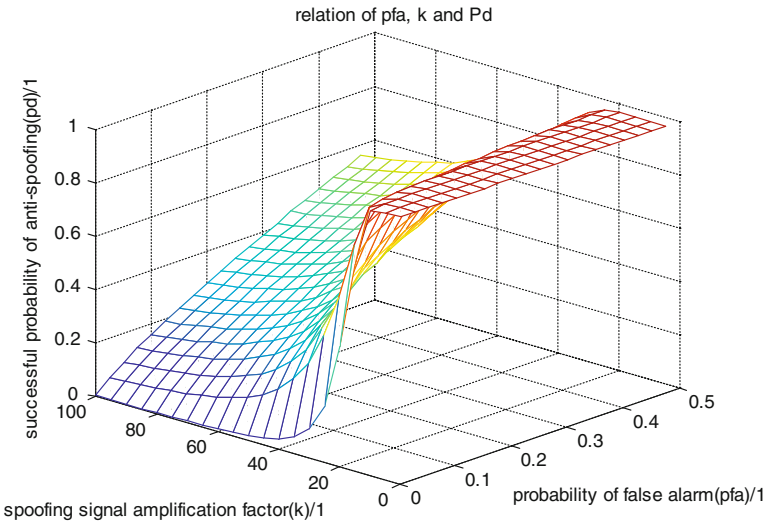

Fig. 65.3 Influence of probability of false alarm to the probability

probability of false alarm means higher risk of error acquisition, for example: if the probability of false alarm is sixteen percent, it means that error acquisition may be occurred 16 per 100 times, which is a serious burden to receiver.

65.3.4 Summary of Factors that Impact Anti-Spoofing Performance

There are many factors influencing anti-spoofing performance of threshold method. The input SNR and spoofing signal amplification factor influence the SNR of signal received by the receiver, which belong to the input of the receiver and can't be a mean of anti-spoofing (unless changing the signal gain by using a directional antenna or by means of beam-forming), but the revelation is that higher input SNR (such as the open environment) does favor to anti-spoofing performance; The coherent integration time and the probability of false alarm can also improve receiver's anti-spoofing performance, which both have their own limitations.

65.4 Analysis of the Upper Bound of Anti-Spoofing Performance

According to the above, it is not easy to absolutely quantize the anti-spoofing performance of the threshold method, however, we can quantitative assessment its anti-spoofing performance by deducing its bounds.

65.4.1 Determining the Upper Bound of Anti-Spoofing Performance

The spoofing signal can cause interference and decrease the input SNR of the true signal. Considering carrier-to-noise ratio as standard of signal's quality available, we can describe influence of the spoofing signal as formula 65.7 [8] and 65.8:

$$(C_s/N_0)_{\text{eff,dB}} = -10\lg\left[10^{-\frac{(C_s/N_0)_{\text{dB}}}{10}} + \frac{k^2}{QR_c}\right] \tag{65.7}$$

$$(C_s/N_0)_{\text{dB}} = S/N + 10\lg(B) \tag{65.8}$$

Where $(C_s/N_0)_{\text{eff,dB}}$ is the carrier-to-noise ratio of the true signal with the spoofing signal added; $(C_s/N_0)_{\text{dB}}$ is the carrier-to-noise ratio of the true signal without the spoofing signal added; B is the bandwidth of the signal received; Q is

the quality factor of anti-jamming and for GPS P code, Q is approximately equal to 1.5; R_c is the code rate.

To enable to detect the true signal, it is required that the signal-to-noise rate after the coherent integration is equal to which introduced by the threshold. In this case, the successful probability of anti-spoofing is approximately equal to 0, which is the upper bound of anti-spoofing performance of the threshold method. We can get formula 65.9:

$$(C_s/N_0)_{\text{eff,dB}} - 30 + 10\lg(c_h) - L(c_h) + \varepsilon = 10\lg(-2\ln p_{fa}) \tag{65.9}$$

Where $L(c_h)$ is the incoherent loss and ε is losses of baseband signal processing.

In formula 65.9, in order to ensure that the threshold method can detect the true signal, it is needed that threshold is higher than the noise, so the right term is required to be larger than 0. Therefore, we can obtain the constraint condition as formula 65.10:

$$p_{fa} < 1/\sqrt{e} \tag{65.10}$$

Integrated formula 65.7, 65.8, 65.9 and 65.10, the upper bound of spoofing signal amplification factor tolerated can be calculated by the parameters given.

65.4.2 *Examples of the Upper Bound of Anti-Spoofing Performance*

The essence of anti-spoofing with threshold method is that the receiver competes with spoofing signal amplification factor by acquisition algorithm. According to the above, the algorithm is related to the coherent integration time and the probability of false alarm, and the input SNR also influences the anti-spoofing performance. As is given in formula 65.7 and 65.8, Fig. 65.4 shows the upper bound of the spoofing signal amplification factor tolerated when the probability of false alarm is fixed. In the figure, each curve represents a set of upper bound.

65.5 Conclusion

Threshold method is the most common algorithm used by the receiver, and research on its anti-spoofing performance is of great significance. In this paper, we define successful probability of anti-spoofing as the assessment standard and propose four factors that influence the successful probability of anti-spoofing: input SNR without spoofing signal, the spoofing signal amplification factor, the coherent integration time and the probability of false alarm. The results show that the input SNR without spoofing signal, the coherent integration time and the probability of false alarm can increase the anti-spoofing performance of the

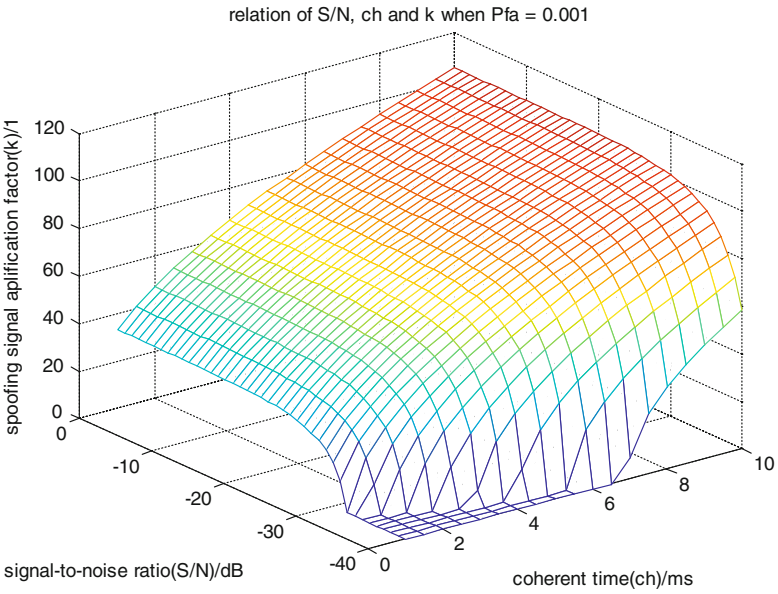

Fig. 65.4 Influence of coherent integration time to the upper bound

receiver, but all have some limitations, the receiver need to balance each other in order to get the best anti-spoofing performance. Finally, we present the theoretical upper bound of the anti-spoofing performance of threshold method and give some examples, unify anti-spoofing performance with various factors, which has a guiding significance for the design of the receiver.

References

1. Key EL (1995) Techniques to counter GPS spoofing, internal memorandum. MITRE Corporation, USA, Feb 1995
2. Wen H et al. (2005) Countermeasures for GPS signal spoofing. ION GPS, Long Beach. 13–16 Sept 2005
3. Humphreys TE et al (2008) Assessing the spoofing threat: development of a portable GPS civilian spoofer. In: Proceedings of ION GNSS2008. Savannah, Institute of Navigation, GA, 2008
4. Cavaleri A et al. (2010) Detection of spoofed GPS signals at code and carrier tracking level. In: Satellite navigation technologies and European workshop on GNSS signals and signal processing, 2010
5. Montgomery PY, Humphreys TE, Ledvina BM (2009) Experimental results of a multi-antenna receiver defense against a portable civil GPS spoofer. In: Proceedings of the 2009 international technical meeting of the institute of navigation, Anaheim, 26–28 Jan, 2009
6. Daneshmand S, Jafarnia-Jahromi A, Broumandan A, Lachapelle G (2012) A low-complexity GPS anti-spoofing method using a multi-antenna array. In: Proceedings of ION GNSS 2012, 8–21 Sept, 2012

7. Huang L, Tang X, Wang F (2011) Anti-spoofing techniques for GNSS receiver. Geomatics Inf Sci Wuhan Univ 36(11): 1344–1347
8. Elliott D. Kaplan etc. (2008) Understanding GPS-principles and applications, 2nd edn. Publishing House of Electronics Industry

Chapter 66
Dual-Update Rate INS Aided Carrier Phase Lock Loop for New Generation Global Navigation Satellite Signals

Peng Lv, Mingquan Lu and Zheng Yao

Abstract Most of the new generation of satellite navigation signals using a pilot channel to improve the tracking capability of the receiver. Without constraints of navigation data bit length, the carrier phase-locked loop (PLL) can prolong easily the Pre-detection integration time (PIT) to improve the anti-jamming ability of the receiver, but the prolongation of the PIT is still subject to the restrictions of the carrier dynamic conditions. In this paper, an algorithm of dual-update rate inertial navigation system (INS) aided carrier PLL was proposed. First, the mathematic model of INS aided carrier PLL was developed with the Kalman filter. Taking into account the high INS update rate and high short-term accuracy, the INS observation information was used to control the frequency of the carrier numerically controlled oscillator (NCO) during the PLL integral period. At the end of one integral period, the output of phase discriminator was used to correct the reproduced carrier phase. The algorithm proposed by this paper can effectively prolong the PLL PIT in high dynamic conditions and improve the anti-jamming ability of the receiver in high dynamic conditions. Finally, the effectiveness of the proposed algorithm was verified by simulation.

Keywords Pilot channel · INS aiding · PLL · High dynamic · Anti-jamming

P. Lv (✉) · M. Lu · Z. Yao
Department of Electronic Engineering, Tsinghua University, Beijing 100084, China
e-mail: yuanao100@126.com

P. Lv
Institute of Communication, Equipment Academy of Air Force, Beijing 100085, China

J. Sun et al. (eds.), *China Satellite Navigation Conference (CSNC) 2013 Proceedings*, Lecture Notes in Electrical Engineering 243,
DOI: 10.1007/978-3-642-37398-5_66,

66.1 Introduction

Carrier PLL is used to track the Doppler frequency of the received satellite carrier signal, and is the key technology of the global navigation satellite system (GNSS) receiver. Narrower noise bandwidth of the carrier tracking loop and longer PIT is required in order to improve the anti-jamming ability of the receiver, but prolongation of the PIT is limited by the bit length of the navigation data and the carrier dynamic. Most of the new generation of navigation satellite signals, such as the GPS L2, L5 signals, the Galileo E1, E5, E6 signals and the Compass B1, B2, B3 signals, use or plan to use a pilot channel in addition to the traditional data channel [1, 2]. The pilot channel can use a pure PLL which avoids squaring loss and has a larger linearity region than a Costas loop [3]. What is more, when tracking pilot signal the PIT can be prolonged without considering bit boundaries.

In some applications, the receiver is required working in the high dynamic and heavy jamming conditions. If there is a large accelerated motion between the receiver and the satellite, long PIT will cause for a large dynamic stress error of the PLL, even cause for the PLL loss of lock. To solve this problem, the literatures Yao et al. [4] and Jin et al. [5] proposed respectively dual-update rate PLL algorithm and dual-update rate frequency assisted phase lock algorithm. But the tracking ability of these methods depend largely on the tracking loop which has the higher update rate. In the weak signal and high dynamic conditions, once the high update rate loop loses lock, it will be difficult to re-capture the signal.

INS and GNSS are different types of navigation systems. The former has higher update rate and higher short-term accuracy. Once the GNSS PLL loses lock temporarily for some reasons, the output information of INS can be used to re-capture the GNSS signal quickly. The literatures Alban et al. [6] and Babu and Wang [7] have researched the algorithms of INS aiding PLL and made detailed performance analysis. However, these algorithms fuse the INS observational data and the PLL phase discriminator in the same update rate. When the long PIT is used, if the acceleration between the receiver and the satellite is large, the phase error between the received carrier and the recovered carrier may exceed the linear range of the phase discriminator, thereby causing for the PLL phase gliding or even loss of lock [8]. In this paper, take into account of the high update rate and high short-term accuracy of INS [9], a new algorithm was proposed. Assuming that the update rate of INS is higher than the update rate of PLL discriminator, the INS observation information was used to control the frequency of the carrier NCO during the coherent integral period. At the end of one integral period, the output of phase discriminator was used to correct the recovered carrier phase. Finally, the effectiveness of the proposed algorithm was verified by simulation.

66.2 Basic Model of INS Aided PLL

66.2.1 Signal Mathematic Model

The received signals in the present of thermal noise used in this process can be modelled as [4]:

$$s(t) = \sqrt{2C/N_0 T}x(t-\tau)\cos((\omega_{IF}+\omega_D)t+\theta)+n(t) \tag{66.1}$$

where C is the received power, N_0 is the thermal noise power spectral density, T is the coherent integral period, $x(t)$ is the pseudo-random noise (PRN) codes modulated on the pilot channels, τ is the code group delay due to travel time, ω_{IF} is the intermediate carrier frequency of the sending signal, ω_{D} is the Doppler shift frequency, θ is the carrier phase of the signal and $n(t)$ is the normalized thermal noise. In the baseband process, $s(t)$ is multiplied by an in-phase replica and a quadrature-phase replica of the estimated carrier, respectively, and then the signals are correlated with a replica of PRN code over a period T referred to as the coherent integral time. The correlator outputs can be modeled as:

$$I_{\mathrm{k}} = A_k \cos(\Delta\omega_{\mathrm{k}} T/2 + \Delta\theta_{\mathrm{k}}) + n_{I\mathrm{k}} \tag{66.2a}$$

$$Q_{\mathrm{k}} = A_k \sin(\Delta\omega_{\mathrm{k}} T/2 + \Delta\theta_{\mathrm{k}}) + n_{Q\mathrm{k}} \tag{66.2b}$$

where $A_k = \sqrt{2C/N_0 T}R(\Delta\tau)\sin c(\Delta\omega_k T/2)$, $\mathrm{sinc}(x) = \sin x/x$, $\mathrm{R(x)}$ is the autocorrelation function of PRN code, $\hat{\tau}$ is the estimated code delay time, $\Delta\tau = \tau - \hat{\tau}$, $\omega_{k|k-1}$ and $\theta_{k|k-1}$ are predicted carrier Doppler and phase at the $(k-1)$th interval, respectively, $\Delta\omega_k = \omega_k - \omega_{k|k-1}$, $\Delta\theta_k = \theta_k - \theta_{k|k-1}$, n_{Ik} and n_{Qk} are I and Q baseband noises in the pilot channel respectively. It is assumed the tracking loop is locked. At this condition, $\Delta\tau$ and $\Delta\omega_k$ is approach to 0. Thus, $R(\Delta\tau)\sin c(\Delta\omega_k T/2)$ is approach to 1 and Eqs. (66.2a, b) can be rewritten as:

$$I_{\mathrm{k}} = \sqrt{2C/N_0 T}\cos(\Delta\omega_{\mathrm{k}} T/2 + \Delta\theta_{\mathrm{k}}) + n_{I\mathrm{k}} \tag{66.3a}$$

$$Q_{\mathrm{k}} = \sqrt{2C/N_0 T}\sin(\Delta\omega_k T/2 + \Delta\theta_k) + n_{Qk} \tag{66.3b}$$

Since there is no message data bit modulated on pilot channel carrier, one can use a so-called coherent discriminator [4], the expression of which is:

$$r_{\theta,k} = \frac{Q_k}{\sqrt{2C/N_0 T}} \tag{66.4}$$

Assuming $\Delta\tau$ and $\Delta\omega_k$ is approach to 0, substituting Eq. (66.3b) into Eq. (66.4), we have

$$r_{\theta,k} = \Delta\theta_{\mathrm{k}} + \Delta\omega_k T/2 + \delta\theta_k \tag{66.5}$$

where

$$\delta\theta_k = \frac{n_{Q,k}}{\sqrt{2C/N_0 T}} \approx \frac{n_{Q,k}}{\sqrt{\frac{1}{N}\sum_{i=1}^{N-1}(I_{k-i}^2 + Q_{k-i}^2)}} \tag{66.6}$$

N is the smoothing times

66.2.2 Kalman Filter Model of INS Aided PLL

Take the received carrier phase $(\theta(t))$, Doppler frequency $(\omega(t))$ and the Doppler frequency variation rate $(a(t))$ as state variables. It is assumed that the three order derivative of the carrier phase is random white noise witch main dues to carrier's dynamic and the clock oscillator. The dynamic equation is:

$$\begin{bmatrix} \dot{\theta}(t) \\ \dot{\omega}(t) \\ \dot{a}(t) \end{bmatrix} = \begin{bmatrix} 0 & 1 & 0 \\ 0 & 0 & 1 \\ 0 & 0 & 0 \end{bmatrix} \begin{bmatrix} \theta(t) \\ \omega(t) \\ a(t) \end{bmatrix} + \begin{bmatrix} 0 \\ 0 \\ 1 \end{bmatrix} j(t) \tag{66.7}$$

Discretizing Eq. (66.7), we have:

$$\mathbf{x}_{k+1} = \mathbf{\Phi}\mathbf{x}_k + \mathbf{w}_k \tag{66.8}$$

where $\mathbf{x}_k = [\theta_k, \omega_k, a_k]^T$,

$$\mathbf{\Phi} = \begin{bmatrix} 1 & T & T^2/2 \\ 0 & 1 & T \\ 0 & 0 & 1 \end{bmatrix} \tag{66.9}$$

$\mathbf{w}_k$ is Gaussian white noise which covariance matrix is $\mathbf{Q}_k = E[\mathbf{w}_k \mathbf{w}_k^T]$.

There are two observables for the INS-aiding PLL. One is the output of coherent correlator, and the other comes from the velocity of INS. Thus, the observation equation can be written as

$$\mathbf{z}_{k+1} = \begin{bmatrix} \theta_{k+1} + \omega_{k+1}T/2 + \delta\theta_{k+1} \\ \omega_{k+1} + \frac{2\pi f_c}{c}\delta v_{k+1} \end{bmatrix} = \mathbf{H}\mathbf{x}_{k+1} + \mathbf{w}_{k+1} \tag{66.10}$$

where δv_{k+1} is INS speed error projected in the sight of receiver and satellite, c is light velocity, f_c is radio carrier frequency. The observation matrix is:

$$\mathbf{H} = \begin{bmatrix} 1 & \mathrm{T}/2 & 0 \\ 0 & 1 & 0 \end{bmatrix} \tag{66.11}$$

The observation covariance matrix is:

$$\mathbf{R}_{k+1} = \begin{bmatrix} \sigma_{r,k+1}^2 & 0 \\ 0 & \sigma_{INS,k+1}^2 \end{bmatrix} \tag{66.12}$$

where $\sigma_{r,k+1}^2 = \frac{1}{2C/N_0 T}$, $\sigma_{INS,k+1}^2 = \frac{4\pi^2 f_c^2}{c^2}\sigma_{v,k+1}^2$, $\sigma_{v,k+1}^2$ is the variance of δv_{k+1}. The Kalman state update equation of carrier is:

$$\mathbf{x}_{k+1|k+1} = \mathbf{x}_{k+1|k} + \mathbf{K}_k\left(\mathbf{z}_{k+1} - \mathbf{H}\mathbf{x}_{k+1|k}\right) \tag{66.13}$$

where $\mathbf{K}_k$ is the gain matrix of Kalman filter. As can be seen from the Eq. (66.13), the first part of the innovation is:

$$\begin{aligned} y_1 &= (\theta_{k+1} + \omega_{k+1}T/2 + \delta\theta_{k+1}) - \left(\theta_{k+1|k} + \omega_{k+1|k}T/2\right) \\ &= \Delta\theta_k + \Delta\omega_k T/2 + \delta\theta_k \end{aligned} \tag{66.14}$$

Comparing Eq. (66.14) with Eq. (66.5), it shows that y_1 is the output of the phase discriminator [10].

66.3 Proposed Dual Update-Rate INS Aided PLL

The base Kalman filter model described in Sect. 66.2 requires both observables have the same update rate. Under weak signal conditions, the PIT is often prolonged to improve the anti-jamming ability of PLL. In the above model, the carrier NCO control frequency is a fixed constant. If the acceleration between the receiver and the satellite is too large, the phase error between the received signal and the numerically controlled oscillator (NCO) may exceed the linear range of the phase discriminator, thereby causing for the PLL phase gliding or even loss of lock.

Taking into account the INS's high update rate and high short-term accuracy, the output of INS can be used to update the NCO control frequency in the PLL PIT. Figure 66.1 is the schematic diagram. In the diagram, t1 ~ t6 is assumed the update time of INS, t1 and t6 is the update time of PLL discriminator. $\Delta\theta$ is the difference between received carrier phase and local generated carrier phase without INS aiding. $\Delta\theta'$ is the difference when there is INS aiding during PLL coherent integral period. It's obvious that $\Delta\theta'$ is smaller than $\Delta\theta$. Therefore, the PLL loop can withstand larger carrier dynamic. Based on this, we propose a dual update rate INS aided PLL algorithm.

Assuming the carrier PIT is M times of the INS update time. The observation matrix with INS separately providing observations is $\mathbf{H}' = [0 \quad 1 \quad 0]$. The Eq. (66.9) can be rewritten

$$\mathbf{\Phi}' = \begin{bmatrix} 1 & T/M & T^2/2M^2 \\ 0 & 1 & T/M \\ 0 & 0 & 1 \end{bmatrix} \tag{66.15}$$

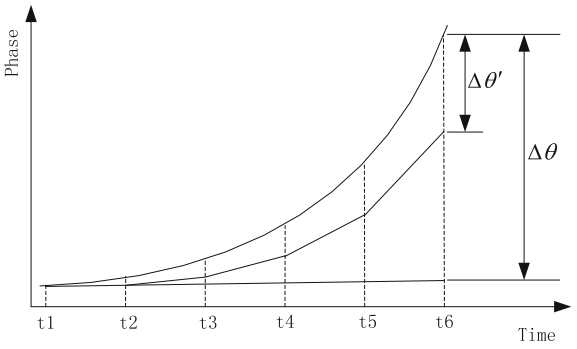

Fig. 66.1 Schematic diagram of carrier loop phase with INS-aiding

The rank of the observability matrix can be calculated as [11]:

$$Rank\left(\begin{bmatrix} H' \\ H'\Phi' \\ H'\Phi'^2 \end{bmatrix}\right) = 2 < 3 \tag{66.16}$$

Equation (66.16) shows that the state vector $\mathbf{x}_k$ is not completely observable. Further analysis shows that the phase is not observable. During PLL coherent integral period, INS output is the only observations. Selecting $\mathbf{x}_k^{INS} = [\omega_k^{INS}, a_k^{INS}]^T$ as the state vector, state equation and observation equation are:

$$\mathbf{x}_{k+1}^{INS} = \mathbf{\Phi}^{INS}\mathbf{x}_k^{INS} + \mathbf{w}_k^{INS} \tag{66.17}$$

$$\mathbf{z}_{k+1}^{INS} = \mathbf{H}^{INS}\mathbf{x}_{k+1}^{INS} + \mathbf{v}_{k+1}^{INS} \tag{66.18}$$

where

$$\mathbf{\Phi}^{INS} = \begin{bmatrix} 1 & T/M \\ 0 & 1 \end{bmatrix} \tag{66.19}$$

$\mathbf{w}_k^{INS}$ and $\mathbf{v}_{k+1}^{INS}$ are the state noise and observation noise respectively, and the covariance matrices are respectively:

$$\mathbf{Q}_k^{INS} = E[\mathbf{w}_k^{INS}(\mathbf{w}_k^{INS})^T] \tag{66.20}$$

$$\mathbf{R}_{k+1}^{INS} = E[\mathbf{v}_{k+1}^{INS}(\mathbf{v}_{k+1}^{INS})^T] = \sigma_{INS,\,k+1}^2 \tag{66.21}$$

Owned to INS aiding, the NCO control frequency control frequency is no longer kept constant within a PLL coherent integral period. Therefore Eq. (66.8) can be re-expressed as:

$$\begin{bmatrix} \theta_{k+M}^{PLL} \\ \omega_{k+M}^{PLL} \\ a_{k+M}^{PLL} \end{bmatrix} = \mathbf{\Phi}\begin{bmatrix} \theta_k^{PLL} \\ \omega_k^{PLL} \\ a_k^{PLL} \end{bmatrix} + \begin{bmatrix} \frac{T}{M}\sum_{i=0}^{M-1}\omega_{k+i}^{INS} \\ 0 \\ 0 \end{bmatrix} + \mathbf{u}_k^{PLL} + \begin{bmatrix} \frac{T}{M}\sum_{i=0}^{M-1}n_{\omega,k+i}^{INS} \\ 0 \\ 0 \end{bmatrix} \tag{66.22}$$

where θ_k^{PLL} is the carrier phase, ω_k^{PLL} and a_k^{PLL} are residual carrier frequency and acceleration, $n_{\omega,k}^{INS}$ is error noise of INS which variance can be calculated by high update rate Kalman filter.

With INS aiding during coherent integral period, the PLL's discriminator is:

$$r_{\theta,\,k+M} = \frac{\sum_{i=0}^{M-1} Q_{k+i}}{\sqrt{2(C/N_0)TM}} \tag{66.23}$$

Neglecting INS's error, Eq. (66.23) can be rewritten:

$$r_{\theta,\,k+M} \approx \Delta\theta_k^{PLL} + \frac{T\omega_k^{PLL}}{2} + \frac{\sum_{i=0}^{M-1} n_{Q,\,k+i}}{\sqrt{2(C/N_0)TM}} \tag{66.24}$$

PLL observation noise matrix is:

$$R_k^{PLL} = \frac{M}{2(C/N_0)T} \tag{66.25}$$

66.4 Simulation Results

Assuming the GNSS pilot channel frequency is 1575.42 MHz, the INS update rate is 200 Hz (5 ms), the speed accuracy of INS after Integrating with GNSS is 0.2 m/s. The input pilot channel signal is generated by Matlab. Figure 66.2 shows the pilot channel Doppler frequency shift. In the first second, the velocity between the satellite and receiver is assumed to be 200 m/s. From 1 to 3 s the acceleration between them is assumed to be 50 g. Then the acceleration is assumed to be 0. And now the velocity between the satellite and receiver keeps 1,180 m/s. Other dynamic (including the oscillator's error) is assumed to noise, and the standard deviation is assumed to be 0.5 g/s. A phase locked indicator is used to indicator the tracking accuracy degree of the carrier phase. The phase locked indicator is:

$$\mathrm{PLI} = \frac{I^2 - Q^2}{I^2 + Q^2} \approx \cos(2\Delta\theta) \tag{66.26}$$

When the PLL is locked, the PLI is approach to 1.

First, we simulate the tracking capability of new algorithm under high dynamic condition. Figure 66.3 shows the tracked Doppler frequency when the carrier-to-noise ratio is 43 dB $*$ Hz. When the PLL PIT is 5 ms, PLL can correctly track the Doppler frequency. When the PIT is prolonged to 10 ms, PLL loses lock. However, the new dual-update INS aided PLL algorithm can track the Doppler frequency even the PIT is prolonged to 20 ms.

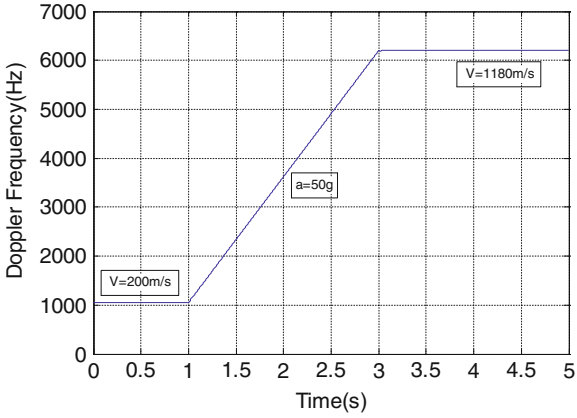

Fig. 66.2 Doppler frequency caused by vehicle dynamic

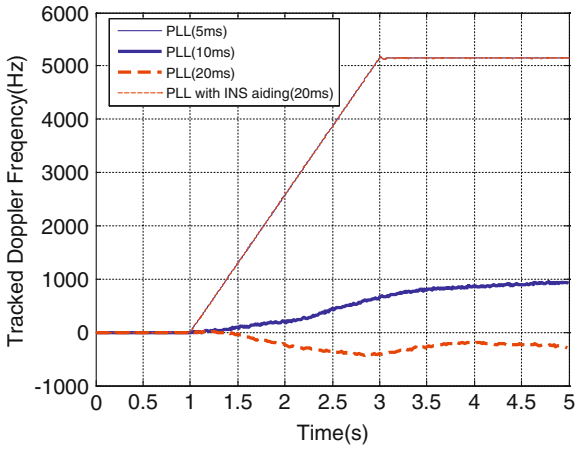

Fig. 66.3 Tracked doppler frequency

Followed, we simulate the tracking capability of new algorithm in the low carrier-to-noise ratio and high dynamic conditions. Figure 66.4 shows the output of the phase locked indicator when the carrier-to-noise ratio is 26 dB $*$ Hz. When the PIT is 5 ms, the alone PLL can generally track the carrier, but there is phase glide at 1 and 3 s when large acceleration between the receiver and satellite appears and disappears. The new dual-update INS aided PLL algorithm can track the carrier without any phase glide even when the PIT is prolonged to 20 ms. And it is obvious that the accuracy degree of phase tracked when the PIT is 20 ms is higher than when PIT is 10 and 5 ms.

Figure 66.5 is the curve of phase jitter using proposed algorithm to track the carrier dynamic process of Fig. 66.2 in different carrier-to-noise ratio conditions. For each carrier-to-noise ratio, 50 Monte Carlo simulations was made. In the low carrier-to-noise ratio and high dynamic conditions, the PLL coherent integral time can be significantly prolonged using the proposed algorithm, and a greater spreading gain can be obtained to improve the anti-jamming ability of the receiver.

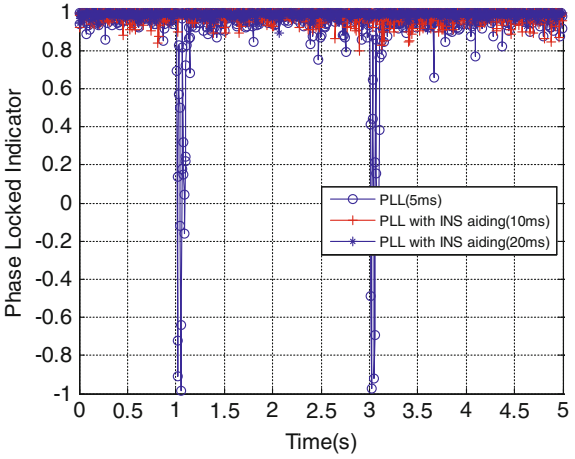

Fig. 66.4 Phase locked indicator output

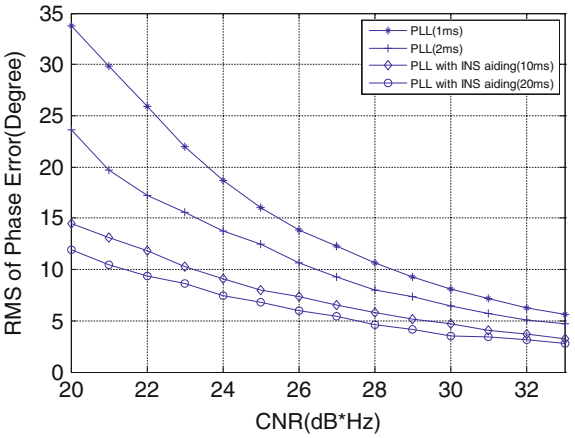

Fig. 66.5 Phase jitter of phase lock loop

66.5 Conclusion

New generation navigation signals have pilot channels which improve the anti-jamming ability of the receiver, but when in the high dynamic condition this advantage has been very limited. In this paper, the dual-update rate INS aided GNSS PLL algorithm was proposed. When the PLL loop coherent integral time is longer than INS update time, the INS observation information was used to control the frequency of the carrier NCO during the coherent integral period. At the end of the coherent integral period, the phase discriminator output was used to correct the carrier phase. The new algorithm can reduce the limitation of high dynamic on the PLL coherent integral time. In the low carrier-to-noise ratio and high dynamic conditions, the PLL coherent integral time can be significantly prolonged using the proposed algorithm, and a greater spreading gain can be obtained to improve the anti-jamming ability of the receiver.

References

1. Fontana RD, Cheung W, Novak PM, Stansell TA (2011) The new L2 civil signal. Proceedings of Institute of Navigation, Salt Lake City, Sep 2011, pp 617–631
2. Spilker JJ, Van Dierenddnck AJ (2011) Proposed new L5 civil GPS codes. Navig J Inst Navig 48(3):135–144
3. Kaplan ED, Hegarty CJ (2006) Understanding GPS principles and applications, 2nd edn. Artech House, Boston
4. Yao Z, Cui X, Lu M, Feng Z (2009) Dual update-rate carrier tracking technique for new generation global navigation satellite system signals in dynamic environments. IET Radar Sonar Navig 3(3):203–213
5. Jin L, Yao Z, Cui X et al (2011) Dual updata-rate FLL-assisted phase lock loop of novel robust receivers for new generation global navigation satellite signals ION GNSS 2011. In: Proceedings of the ION GNSS 2011, Portland, pp 3652–3659
6. Alban S, Akos D, Rock S et al (2003) Performance analysis and architectures for INS-aided GPS tracking loops. NTM, Institute of Navigation, Anaheim, pp 611–622
7. Babu R, Wang J (2005) Dynamics performance of carrier and code tracking loops in ultra-tight GPS/INS/PL Integration IEEE Indicon 2005 conference, Chennai, 11–12 Dec 2005. USA: IEEE, pp 233–236
8. Gardner FM (2005) Phaselock techniques, 3rd edn. Wiley, Hoboken
9. Titterton DH, Weston JL (2004) Strapdown inertial navigation technology, 2nd edn. Institution of Electrical Engineers, UK
10. Patapoutian A (1999) On phase-locks and Kalman filters. IEEE Trans Commun 47(5):670–672
11. Grewal MS, Andrews AP (2008) Kalman filtering-theory and practice using matlab, 3rd edn. Wiley, Hoboken

Chapter 67
Algorithm Weights Optimization Method for Inter-Satellite Communication Array Antennas Based on Differential Evolution Algorithm

Qiwei Han, Junwei Nie, Pengpeng Li and Feixue Wang

Abstract The inter-satellite communication network is an important part of the communications satellite system and relay satellite system. Interference faced by inter-satellite communication networks comes mainly from ground. Therefore, the inter-satellite communication networks need to be able to avoid intentional or unintentional interference from the ground, to be able to ensure the sound operation of the whole system. Optimum design of antennas is an important means to satisfy the special needs for inter-satellite communication networks to stand against ground interference. Array antennas are preferred for inter-satellite payload design due to its excellent characteristics of enhancing useful signals while suppressing interference. This article analyzed the features of the working environment of inter-satellite communication array antennas, established a spatial filter model, optimized the array weights by differential evolution algorithm, and designed array patterns which satisfy the special need of inter-satellite communication. Experimental results show that the proposed method achieved very good results, the designed array pattern provides interference rejection capability of 46 dB to the ground direction, which well meet the requirement of inter-satellite communication anti-jamming antenna designing.

Keywords Inter-satellite links · Differential evolution · Array antennas · Weights optimization

Q. Han (✉) · J. Nie · P. Li · F. Wang
Satellite Navigation R&D Center, National University of Defense Technology, Changsha 410073, China
e-mail: hanqiweialex@163.com

J. Sun et al. (eds.), *China Satellite Navigation Conference (CSNC) 2013 Proceedings*, Lecture Notes in Electrical Engineering 243,
DOI: 10.1007/978-3-642-37398-5_67,

67.1 Introduction

Inter-satellite communication network applications are mainly concentrated in the communications satellite system and relay satellite system. The most successful example of the former is the Iridium system [1], while the most successful examples of the later are TDRSS [2] and Milstar system [3]. In addition, inter-satellite communication and ranging network are applied in the main satellite navigation systems [4–7], and its main function is inter-satellite time synchronization, spatial location solving, and spatial data transfer. When the inter-satellite communication networks are affected by interference, the entire service performance of the satellite system will be affected. Therefore, to improve the anti-jamming capability of inter-satellite communication system is particularly important.

Interference faced by inter-satellite communication network mainly from the direction of the ground, such as high-power radar signals. Optimize the design of the inter-satellite communication antennas, form the ground direction null, thereby suppress the interference from the direction of the ground, can effectively improve the viability of inter-satellite links in the case of interference.

Differential evolution algorithm was proposed in 1995 by Storn and Price [8], is a real-coded optimization algorithm suitable to problems with parameters that can be continuously changed. It has increasingly wide applications because advantages such as fewer parameters, simple, easy programming [9–11], etc. The greatest feature of differential evolution algorithm is that a linear combination of more than one individual of parent generation is used in the process of generating a new individual.

This paper analyzed the characteristics of the application environment of the inter-satellite communication array antennas, and via spatial filter modeling, inter-satellite communication antenna array weights optimization problem is modeled as function maximum value finding problem, thus DE algorithm can be used to optimize the design of the inter-satellite communication planar array antenna pattern. Simulation experiments with planar arrays are implemented, which are divided into two cases according to whether constraining the gain in signal directions. In each case, perform the optimization processing, find the optimal array weights satisfying the design requirements, and simulate the antenna patterns.

67.2 Theoretical Analysis of the Algorithm

67.2.1 Differential Evolution Algorithm

Differential evolution algorithm firstly generates a random initial population, and then updates the evolutionary population through operation consists of selection,

mutation and crossover. Assume variable of the objective function $f(\vec{x})$ is a vector in the D-dimensional continuous space R^D, $\vec{x} = (x_1, x_2, \ldots, x_D)$. Optimization goal is to make the function $f(\vec{x})$ reach its maximum value, i.e. to find $\vec{x}^*$ that satisfy $f(\vec{x}^*) = \min(f(\vec{x}))$.

In the evolutionary process, a test vector must be produced corresponding to each individual (vector) of every DE population.

Label the ith individual of the Gth generation is $\vec{x}_i^G$, whose jth dimension is $x_{i,j}^G$; label the test vector corresponding to the ith individual is $\vec{u}_i^G$, whose jth dimension is $u_{i,j}^G$.

The operation used to generate test vectors is mutation and crossover. So far, there are some more improved versions of DE mutation operation, and the following five kinds are commonly used [8, 12].

1. DE/rand/1: $\vec{v}_i^G = \vec{x}_{r_1}^G + F \cdot \left(\vec{x}_{r_2}^G - \vec{x}_{r_3}^G\right)$
2. DE/best/1: $\vec{v}_i^G = \vec{x}_{best}^G + F \cdot \left(\vec{x}_{r_1}^G - \vec{x}_{r_2}^G\right)$
3. DE/current to best/1: $\vec{v}_i^G = \vec{x}_i^G + F \cdot \left(\vec{x}_{best}^G - \vec{x}_i^G\right) + F \cdot \left(\vec{x}_{r_1}^G - \vec{x}_{r_2}^G\right)$
4. DE/best/2: $\vec{v}_i^G = \vec{x}_{best}^G + F \cdot \left(\vec{x}_{r_1}^G - \vec{x}_{r_2}^G\right) + F \cdot \left(\vec{x}_{r_3}^G - \vec{x}_{r_4}^G\right)$
5. DE/rand/2: $\vec{v}_i^G = \vec{x}_{r_1}^G + F \cdot \left(\vec{x}_{r_2}^G - \vec{x}_{r_3}^G\right) + F \cdot \left(\vec{x}_{r_4}^G - \vec{x}_{r_5}^G\right)$

where r_1, r_2, r_3, r_4, r_5 are distinct indicators randomly selected from the population, and are different from the ith individual (if the mutation operation relates to the ith individual). $\vec{x}_{best}$ is the individual with highest fitness value in contemporary population. F is variation factor that takes value on (0,1].

After mutation operation, take crossover operation on each $v_{i,j}^G$ in $\vec{v}_i^G$: where the number randomly uniformly generated in [0, 1] is less than constant CR which takes value in [0, 1], or j exactly equals to a randomly selected number from [1, D], adopt the jth element of mutated individual $\vec{v}_i^G$; otherwise adopt the jth element of $\vec{x}_i^G$, then ultimately obtaine the test vector $\vec{u}_i$ corresponding to $\vec{x}_i$. That is

$$u_{i,j}^G = \begin{cases} v_{i,j}^G & \text{if } rand(0,1) \le CR \text{ or } j = j_{rand} \\ x_{i,j}^G & \text{otherwise} \end{cases} \tag{67.1}$$

where $i = 1, 2, \ldots, NP$; $j = 1, 2, \ldots, D$; NP is the number of individuals in each generation of populations, namely the population size, D is the dimension of single individual. Crossover probability CR $\in$ [0, 1]. j_{rand} is vector index randomly selected from $\{1, 2, \ldots, NP\}$, which is in order to ensure there is at least one dimension of $\vec{u}_i^G$ is different from $\vec{x}_i^G$.

Next, choose between the test vector $\vec{u}_i^G$ and $\vec{x}_i^G$, select the one with higher fitness value to go into the next generation of population. Function value is generally selected as fitness value in function optimization problems. For example, if

the problem is seeking the maximum value of a function, the individual with higher function values goes into the next generation of population.

The most unique characteristic of DE algorithm is its adaptive mutation operation. In the early stages of evolution, individual differences in the population is big, so the differential vector used for mutation is big, individual variability is big (significant), which is conducive for global search of the algorithm. With the process of evolution, when the algorithm tends to converge, individual differences in the population become smaller, and then the differential vector used for mutation become smaller adaptively, which is conducive for local contraction of the algorithm. This simple and unique mutation operation make DE algorithm has good global and local search capabilities.

67.2.2 Inter-Satellite Communication Antenna Array Weights Optimization Modelling

67.2.2.1 Definition of Inter-Satellite Observation Elevation and Azimuth

This section defines the elevation and azimuth angles in inter-satellite observations. As shown below, take satellite A observe satellite B for example. The self coordinate system of satellite A is defined as: the origin of coordinates is the satellite centroid, Z-axis points to geocentric from the satellite centroid. X-axis is in the orbital plane and perpendicular to the Z-axis, points to the direction of satellite motion. XYZ constitute a right-handed coordinate system. Satellite B is on another orbit. Projection of satellite B on XOY plane of satellite A is labeled as B'. Make perpendicular line from B' to X-axis, foot point is B_x. Make perpendicular line from B' to Y-axis, foot point is B_y. As geometrical relationship showed in the Fig. 67.1, $\angle BOB' = \theta$ is the elevation angle for satellite A observe satellite B, OB' is 0° elevation direction. $\angle B_xOB' = \varphi$ is the azimuth angle for satellite A observing satellite B, X axis is 0° azimuth direction. Elevation and Azimuth increase in counterclockwise direction. Range of azimuth and elevation is 0–360°.

67.2.2.2 Objective Function Modelling

Weights optimization target of inter-satellite communication antenna array is to find the optimal weights $\vec{w}^*$ that meet:

1. Gain of planar array in inter-satellite direction is positive.
2. Maximize the difference between the maximum gain in interference direction and minimum gain in signal direction, that is, maximize null depth in direction of the interference.

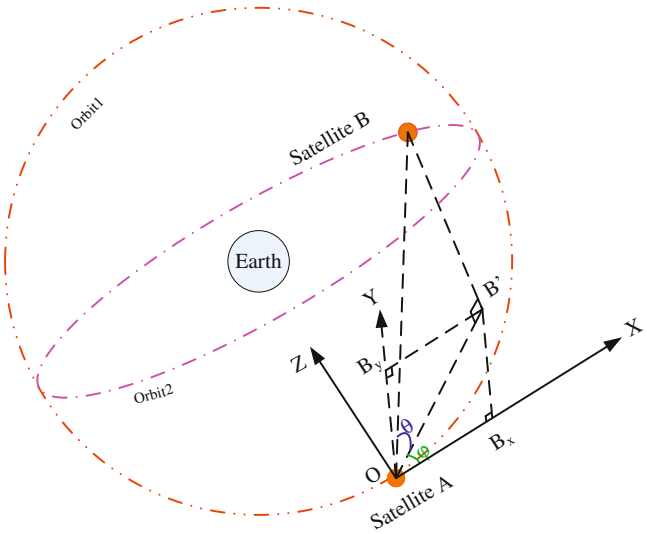

Fig. 67.1 Definition of inter-satellite observation elevation and azimuth

Null depth in direction of interference can be expressed as:

$$f\left(\overrightarrow{w}\right) = \min\left(f\left(\overrightarrow{w}, \theta_1, \varphi_1\right)\right) - \max\left(f\left(\overrightarrow{w}, \theta_2, \varphi_2\right)\right) \tag{67.2}$$

where (θ_1, φ_1) is the interference direction, i.e. the ground direction. (θ_2, φ_2) is the signal direction, i.e. the inter-satellite direction.

Restrict gain in inter-satellite direction be positive can be expressed as:

$$\min\left(f\left(\overrightarrow{w}, \theta_1, \varphi_1\right)\right) > 0 \tag{67.3}$$

Equation (67.2) focuses on making the interference direction null the deeper the better, Eq. (67.3) focuses on making the gain in signal direction the larger the better. Above both need to be weighted, so as to establish the objective function suitable for DE algorithm processing.

Define η is weighting factor, then the objective function suitable for DE algorithm processing can be expressed as:

$$C\left(\overrightarrow{w}^*\right) = \eta f\left(\overrightarrow{w}^*\right) + (1-\eta)\min\left(f\left(\overrightarrow{w}^*, \theta_1, \varphi_1\right)\right) \tag{67.4}$$

where $\overrightarrow{w}^*$ is the optimum weights meet the requirements of the antenna array beamforming.

If $\eta = 0$, indicates that only requires null the deeper the better, constraints are not imposed on gain in inter-satellite direction. At this time, the objective function can be simplified as:

$$C(\overrightarrow{w}^*) = (f(\overrightarrow{w}^*, \theta_1, \varphi_1)) = \max[\min(f(\overrightarrow{w}^*, \theta_1, \varphi_1)) - \max(f(\overrightarrow{w}^*, \theta_2, \varphi_2))] \tag{67.5}$$

At this point, the array weights optimization problem has been transformed to problems of finding optimal function value. Optimal weight $\overrightarrow{w}^*$ that satisfies Eqs. (67.4) or (67.5) can be found through the selection, mutation and crossover processing of DE algorithm.

67.3 Simulation Experiments

In this section, the inter-satellite communication plane array weights optimization is simulated. Set incidence angle range of inter-satellite communication signals is 30–55°. Interference comes from ground. Incidence angle of interference from edge of the Earth is 80°, therefore incidence angle range of interference is 80–90°. The above-mentioned angles are all defined in the coordinate system of the satellite. Concentric circle array with 19 elements was selected (as shown in Fig. 67.2), while radius of the inner and outer circle is half wavelength and a wavelength of the carrier respectively.

Firstly, calculate plane array weights with DE algorithm iteratively. Then simulate the plane array antenna pattern with CST software. The experiment is

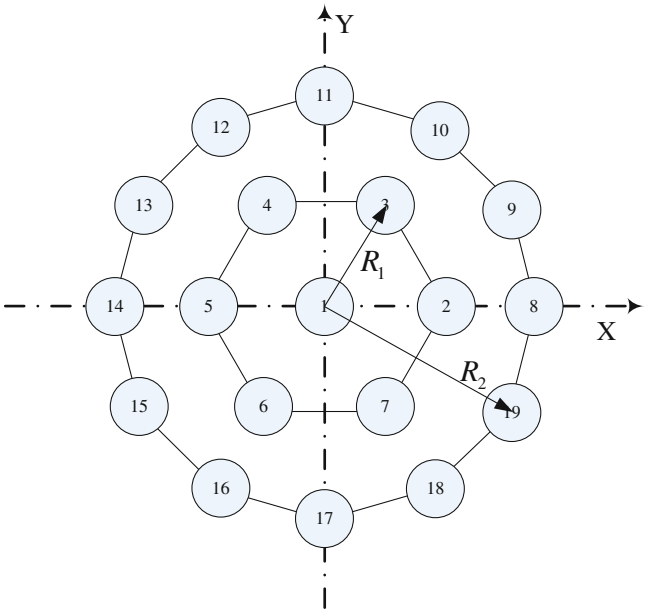

Fig. 67.2 Plane array schematic diagram

divided into two cases according to whether constraining the gain in signal directions. In each case, array weights were calculated.

67.3.1 No Constraints on Minimum Gain in Signal Direction

Do not restrict the minimum gain in signal directions, i.e. $\eta = 0$, then the objective function can be expressed as Eq. (67.5).

Calculate optimal array weights with DE algorithm, and simulate the array pattern according to the optimal weights. Array pattern of elevation angle range 0–360° is shown in Fig. 67.3.

The simulation results show that: the maximum gain and minimum gain in inter-satellite directions are 1.9 and −6.0 dBi respectively, the maximum gain and minimum gain in ground directions are −52.1 and −86.0 dBi respectively. The difference between minimum gain in signal directions and maximum gain in ground directions is 46.1 dBi, which indicates that the ground interference rejection capability of inter-satellite communication plane array antennas is better than 46.1 dBi.

Use optimal weights as input parameters for CST software, simulate the array antennas pattern as shown in Fig. 67.4.

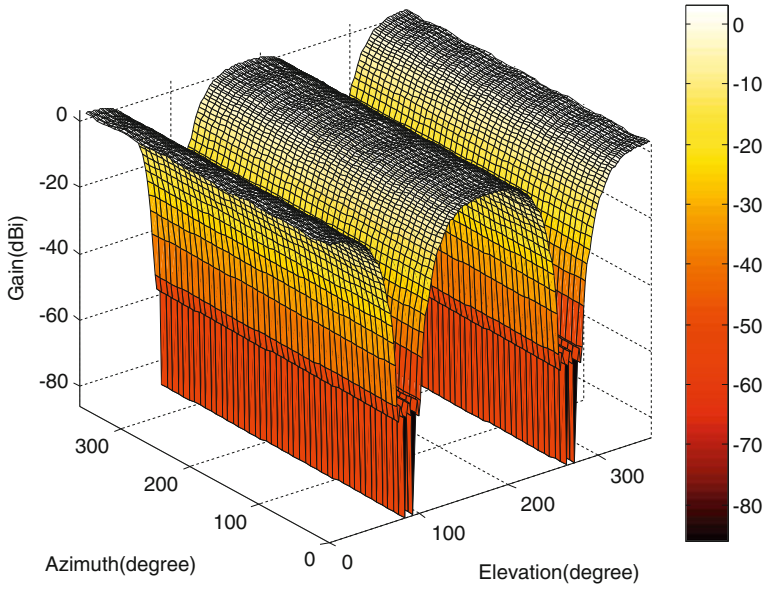

Fig. 67.3 Plane array pattern optimization results (no constraints for minimum gain in signal directions)

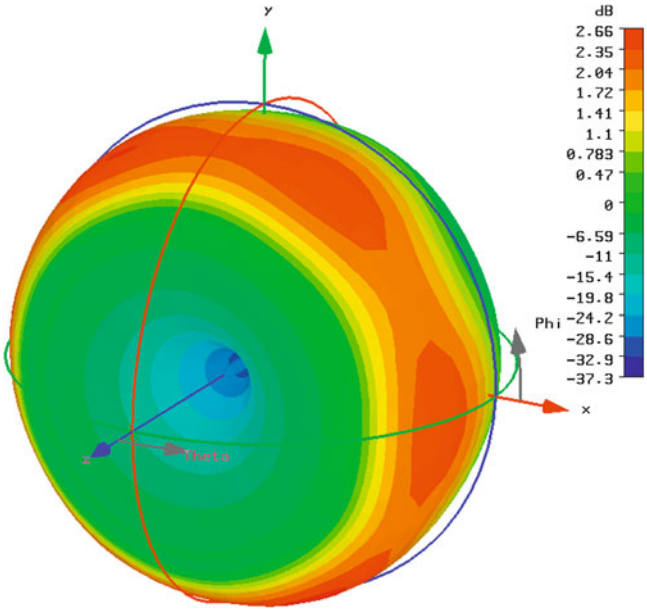

Fig. 67.4 Three-dimensional plane array pattern with CST software (no constraints for minimum gain in signal directions)

As can be seen from Fig. 67.4, the simulated three-dimensional pattern of inter-satellite communication array antennas is tire-shaped; gain of its surrounding part is relatively much higher, which corresponds to inter-satellite directions; gain of its middle part is relatively much lower, which corresponds to ground interference directions.

Figure 67.5 shows the plane array weights calculating procedure with DE algorithm, can be seen, a total of about 150 generations of evolution were experienced.

In the simulation procedure, if results of continuous 50 times of evolution are the same, it can be believed that the expected results have been reached through the iterated calculations, and then terminate algorithm.

67.3.2 Restrict the Minimum Gain in Signal Directions be Positive

Restrict the minimum gain in signal directions be positive, and then the objective function can be expressed as Eq. (67.4).

In the previous section condition, there are no constraints on the minimum gain in signal directions, then the minimum gain in inter-satellite directions of the optimal array pattern is −6.0 dBi, i.e. there is approximate 6 dBi attenuation to the

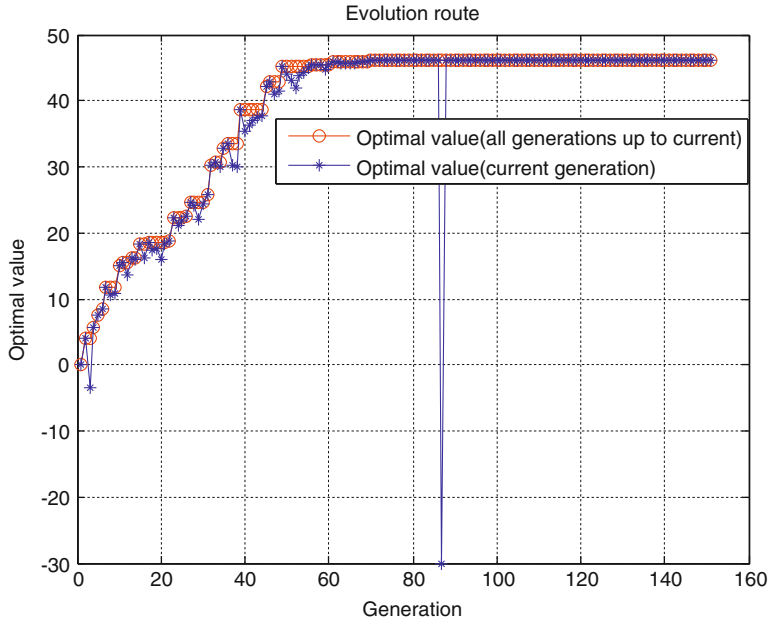

Fig. 67.5 Iterative calculation procedure of DE algorithm (no constraints for minimum gain in signal directions)

inter-satellite communication signals. In order to reduce the attenuation to useful signals, this section restrict that the minimum gain in signal directions must be greater than 0, i.e. ensure that the array antennas gain is positive for inter-satellite communication signals in any case.

In this case, calculate optimal array weights with DE algorithm, and simulate the array pattern according to the optimal weights. Array pattern of elevation angle range 0–360° is shown in Fig. 67.6.

The simulation results show that: the maximum gain and minimum gain in inter-satellite directions are 0.7 and 0.2 dBi respectively, the maximum gain and minimum gain in ground directions are −15.3 and −48.1 dBi respectively. The difference between minimum gain in signal directions and maximum gain in ground directions is 15.6 dBi, which indicates that the ground interference rejection capability of inter-satellite communication plane array antennas is better than 15.6 dBi.

In contrast to the simulation results in Sect. 67.3.2, it can be found that by adding constraints on minimum gain in signal directions, the minimum gain in signal direction increased for 6 dBi while the ground direction null depth decreased for 30.5 dBi. The cost of reducing the ground interference rejection capability was paid at the same time of improving minimum gain in signal directions. Maximization of minimum gain in signal direction and maximization of

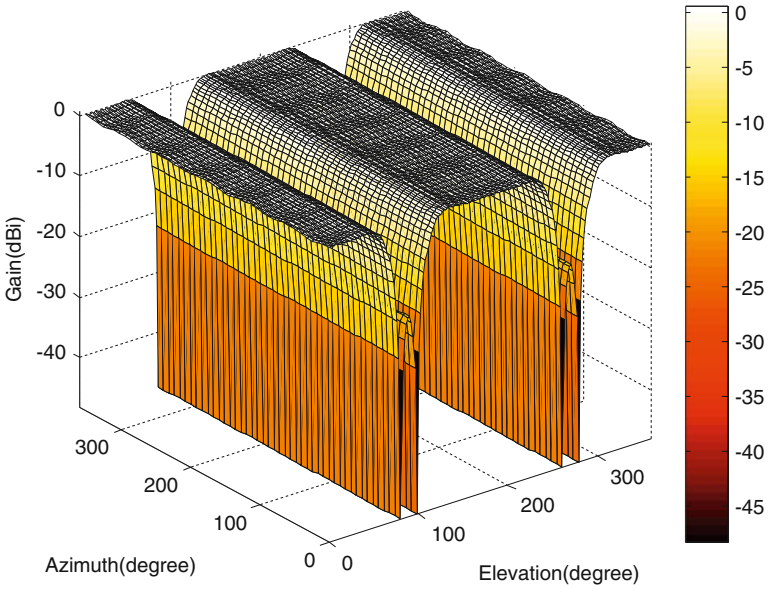

Fig. 67.6 Plane array pattern optimization results (restrict the minimum gain in signal directions)

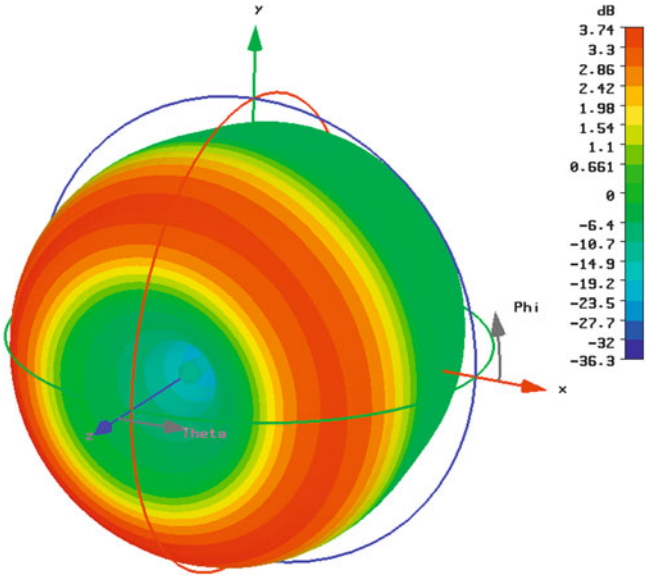

Fig. 67.7 Three-dimensional plane array pattern with CST software (restrict the minimum gain in signal directions)

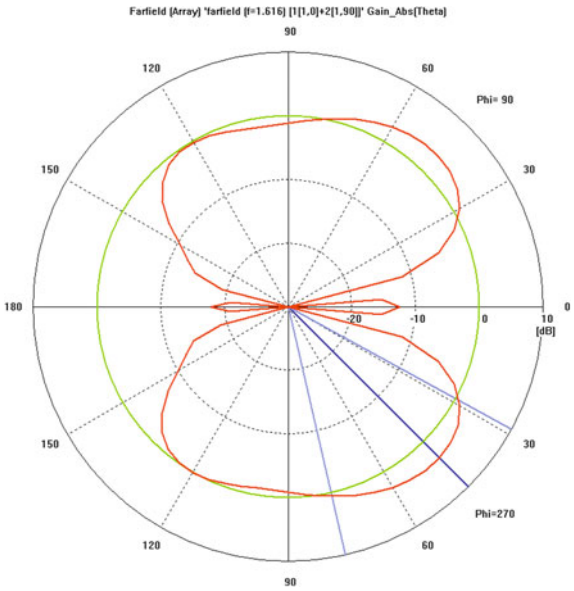

Fig. 67.8 Polar coordinate plane array pattern with CST software (restrict the minimum gain in signal directions)

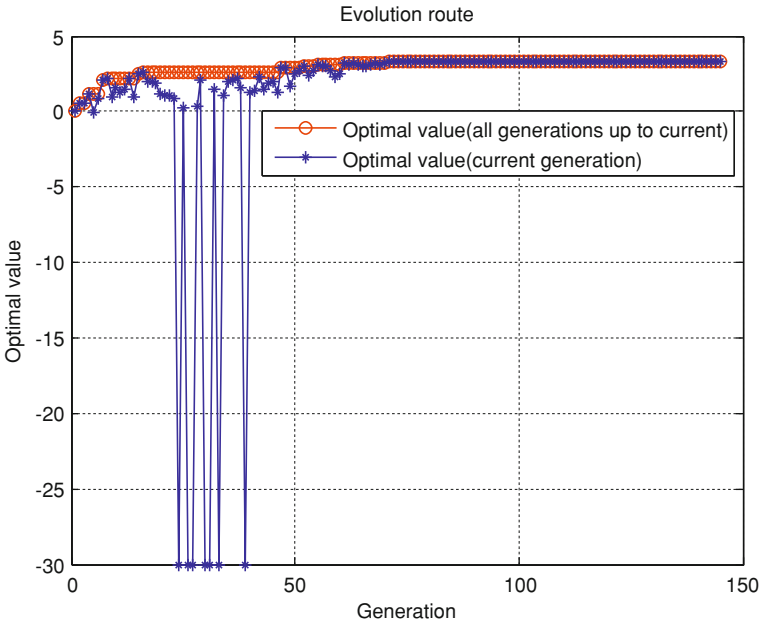

Fig. 67.9 Iterative calculation procedure of DE algorithm (restrict the minimum gain in signal directions)

ground interference rejection capability can not be achieved together, a compromise between them should be considered.

Use optimal weights as input parameters for CST software, and then simulate the array antennas pattern as shown in Figs. 67.7 and 67.8.

As can be seen from Fig. 67.7, the simulated three-dimensional pattern of inter-satellite communication array antennas is tire-shaped; gain of its surrounding part is relatively much higher, which corresponds to inter-satellite directions; gain of its middle part is much lower, which corresponds to ground interference directions. Figure 67.8 shows that there is a narrower band side lobe in the ground direction.

Figure 67.9 shows the plane array weights calculating procedure with DE algorithm, can be seen, a total of about 170 generations of evolution were experienced.

67.4 Conclusion

In this paper, inter-satellite communication antenna array weights optimization problem is modeled as function extremum finding problem, thus DE algorithm can be adopted to find the optimal weights of planar array antennas. Simulation results show that, through the spatial filter modelling, the array pattern designed by using differential evolution algorithm well meets the requirements of inter-satellite communication network. Null was created in the ground direction, thereby suppressing the interference from the ground. The design of the objective function has a great impact on the final optimization results of the DE algorithm. In the case does not restrict the minimum gain in signal direction, null depth for more than 46 dBi can be got. If restrict the minimum gain in signal directions be greater than 0 dBi, null depth decreased to approximately 15.6 dBi, as an exchange, the gain in signal direction increased for approximately 30.5 dBi.

References

1. Pratt SR, Raines RA, Fossa CE et al (1999) An operational and performance overview of the IRIDIUM low earth orbit satellite system. Commun Surv Tutorials IEEE 2(2):2–10
2. Israel DJ (1993) Low-cost TDRSS communications for NASA's long duration balloon project. Aerosp Electron Syst Mag IEEE 8(2):43–47
3. Leonard WA (2000) Milstar and DoD teleport. MILCOM 2000. In: Proceedings of the 21st century military communications conference, pp 1181–1186
4. John AR (2002) Highlights of GPS II-R autonomous navigation. In: The 58th annual meeting of the institute of navigation and CIGTF 21st guidance test symposium, Albuquerque, NM, pp 354–363
5. Francisco AF (2011) Inter-satellite ranging and inter-satellite communication links for enhancing GNSS satellite broadcast navigation data. Adv Space Res 47(5):786–801
6. Sanchez M, Pulido JA, Amarillo F et al (2008) The ESA GNSS+ project inter-satellite ranging and communication links in the frame of the GNSS infrastructure evolutions. In: The

21st international technical meeting of the satellite division of the institute of navigation (ION GNSS 2008) Savannah, GA, pp 2538–2546
7. Yu Y, Chang Q, Yu Z (2012) One new measurement and communication techniques of GNSS inter-satellite links. Sci China Technol Sci 55(1):285–294
8. Storn R, Price K (1997) Differential evolution: a simple and efficient heuristic for global optimization over continuous space. J Global Optim 11(4):341–359
9. Himdi M, Kurup DG, Rydberg A (2003) Synthesis of uniform amplitude unequally spaced antenna arrays using the differential evolution algorithm. IEEE Trans Antennas Propag 51(9):2210–2217
10. Storn R (1996) Differential evolution design of an IIR-filter. IEEE Conf Evolutionary Comput, Nagoya, pp 268–273
11. Storn R (1999) Systemdesign by constraint adaptation and differential evolution. IEEE Trans Evolutionary Comput 3(1):22–34
12. ZHANG J, SANDERSON A. JADE (2007) Self-adaptive differential evolution with fast and reliable convergence performance. IEEE Cong Evol Comput pp 2251–2258

Chapter 68
Navigation Technology Research on GNSS Loop Structure Aided by Acoustic MEMS IMU

Cheng Jiang, Hailing Wu, Wenhai Jiao, Wang Wen and Xiaowei Cui

Abstract In order to improve the reliability of MEMS IMU application and the accuracy of integration navigation in high jerk environment, an acoustic MEMS Gyro was researched, the result show that the planar IC structure can transform the angle velocity to frequency output, and has better jerk tolerance compare with the three-dimensional structure silicon micro gyroscope in theory. The GNSS loop structure aided by acoustic MEMS gyro and accelerometer was designed and principally simulated. The results show that GNSS Loop Structure Aided by Acoustic MEMS IMU has great practicability potential.

Keywords Ultra-tight integration · Acoustic MEMS gyro · SAW gyro · Loop aided

68.1 Introduction

Ultra-tight Integration of Micro Electronic Mechanical System (MEMS) Inertial Measurement Unit (IMU) and Global Navigation Satellite System (GNSS) is a hot topic in recent years. MEMS IMU's advantages are small volume, low cost and

C. Jiang (✉) · H. Wu · W. Jiao
Beijing Institute of Tracking and Telecommunications Technology, Beijing, China
e-mail: jiangchengjc@gmail.com

H. Wu
e-mail: wuhl@beidou.gov.cn

W. Jiao
e-mail: jiaowh@beidou.gov.cn

W. Wen
The Chinese Academy of Sciences Institute of Acoustics, Beijing, China

X. Cui
Department of Electronic Engineering, Tsinghua University, Beijing, China

J. Sun et al. (eds.), *China Satellite Navigation Conference (CSNC) 2013 Proceedings*, Lecture Notes in Electrical Engineering 243,
DOI: 10.1007/978-3-642-37398-5_68,

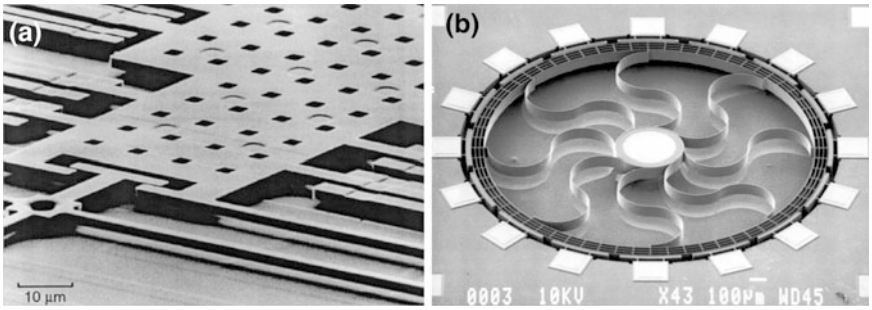

Fig. 68.1 ADXRS150 gyro capacitance measure unit (**a**) and MEMS four ring gyro (**b**)

high reliability, which can improve navigation survival ability and capacity of resisting disturbance when integrated with GNSS [1].

Traditional MEMS gyroscope use quartz or silicon material, the processing technology is Lithography and three-dimensional orientation of anisotropic etching, as a result, the sensors are in semi-suspended state, which are driven in resonant vibration by electro-circuit to sense Coriolis force. Two typical structures of silicon MEMS gyroscope are showed in Fig. 68.1.

Due to three dimensional structure and friableness of silicon-material, silicon MEMS gyroscope faces a challenge when using in cannonball which suffers from 20,000 g striking and strong oscillation. Even successful applications are reported in foreign publications, there is no application case in China. Meanwhile, output of silicon MEMS gyroscope is voltage or electric current, but not frequency, when integrated with code frequency and carrier frequency, additional errors and heavy calculation tasks are introduced.

A novel assistant GNSS tracking loop structure based on acoustic MEMS gyroscope is proposed in this article which can be applied to capturing and tracking GNSS signals. This structure is easier to realize and more efficiency.

68.2 The Principle and Experimental Results of SAW MEMS-IDT Gyroscope

The surface acoustic wave (SAW) based gyroscope provides a new way for angular rate detection with excellent inherent shock robustness, very larger dynamic testing range, small size, low cost, simplicity and long working life over currently available gyroscopes such as rotating wheel, fiber optic, laser, and micro machined gyroscopes [2]. It is very promising in real application of sports braking, electronic products and the guidance system for military.

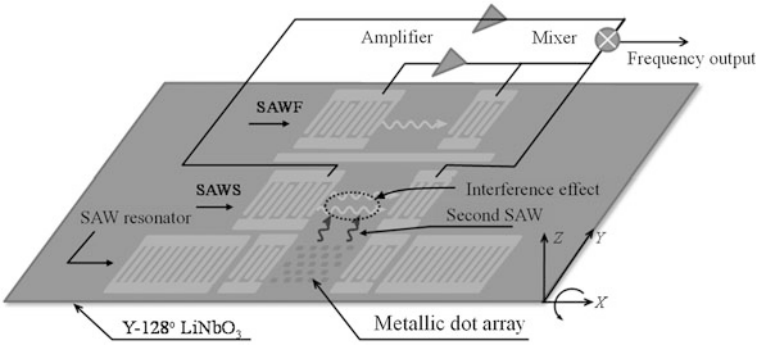

Fig. 68.2 The schematic of SAW gyroscope

68.2.1 Principle and Structure of SAW MEMS-IDT Gyroscope

In this paper, we propose a new design of SAW MEMS gyroscope with operation frequency of 80 MHz. Figure 68.2 shows the schematic diagram and working principle. It consists of a two-port SAW resonator with metallic dot array within the cavity, and two SAW oscillators structured by two delay lines in which one is used for a sensor element (SAWS) and the other is used for a reference element (SAWF). The details of the principle in our gyroscope system are as the following: A standing wave is generated on the two port resonator. Metallic dots at an antinode of the standing wave are vibrating in the normal direction (±z axis). When the gyroscope is subjected to an angular rotation, the induced Coriolis force acts on vibrating metallic dots, and it is proportional to the mass of the metallic dot (m), the vibrating velocity of the dot (v), and the rotational velocity of the substrate (Ω) ($F_{Coriolis} \sim 2\ mv \times \Omega$). Then, the Coriolis force generates a secondary SAW in the orthogonal direction of the primary standing wave (±y axis). The generated secondary SAW interferes with the Rayleigh SAW propagating in SAWS, causing a change in the acoustic velocity, and it induces a shift in the oscillator frequency. By measuring the mixed frequency difference between the sensor oscillator and the reference oscillator, the input rotation can be evaluated.

68.2.2 Sensitivity Evaluation of SAW MEMS-IDT Gyroscope

A new SAW gyroscope with 80 MHz based on standing wave mode was developed, and it consists of a two-port SAW resonator and two delay lines parelling to the resonator fabricated on a same 112°YX $LiTaO_3$ piezoelectric wafer. To improve the frequency stability of the oscillator, the single phase unidirectional transducers (SPUDTs) and combed transducers are utilized to structure the SAW

delay lines [3]. The fabrication procedure of the new SAW gyroscope is as fellows. Aluminum with thickness of 300 nm was deposited on the substrate by using thermal evaporator. Then, 1 μm thick photoresist (PR) was spin-coated, exposed, and developed for the resonator and two delay lines. Aluminum was wet-etched and PR was dissolved in acetone. Then, 10 μm thick PR was spin-coated, exposed, and developed for lift-off processing. The 300 nm thick gold dot array was deposited to obtain sufficient metallic mass. Finally, the PR was dissolved in acetone. The optical microscope and scanning electron microscopy (SEM) images of the fabricated SAW gyroscope are shown in Fig. 68.3. Individual components (resonator and SAW delay lines) were tested using the HP 8510 network analyzer without connecting to printed circuit board (PCB). RF power was applied, and the frequency response of each component was observed. First, the amplitude and phase response of S_{21} for SAW delay line were measured in the frequency domain under matched condition. As shown in Fig. 68.4a, low insertion loss of $\sim$7 dB was observed. Next, the frequency response of the two-port SAW resonator was characterized by the HP 8510 network analyzer. As shown in Fig. 68.4b, low insertion loss ($<$7 dB) was observed. A single steep resonant peak was observed in frequency bandwidth of the resonator due to the optimal spacing between the IDT and adjacent reflector.

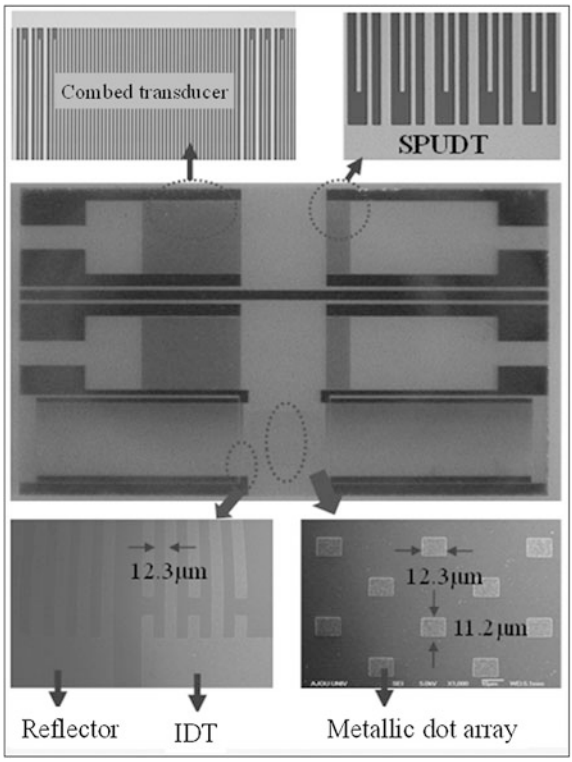

Fig. 68.3 SEM picture of the fabricated SAW gyroscope

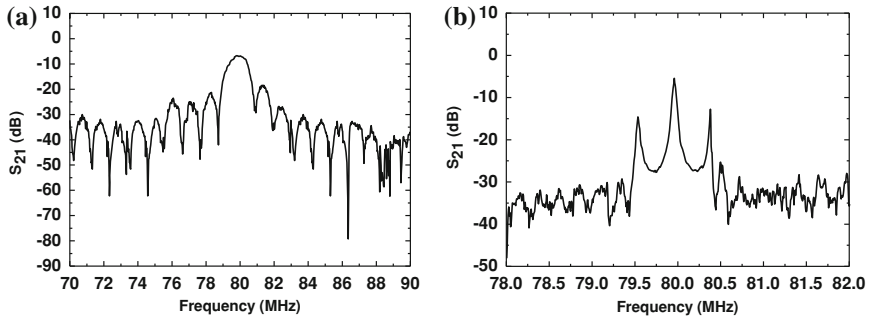

Fig. 68.4 Measured frequency response of **a** delay line and **b** resonator

Then, a voltage controller oscillator (VCO, KSV-5M075A, K.S.E Ltd.) was connected to the fabricated 80 MHz resonator to keep maintaining an 80 MHz resonant frequency in resonator by tuning the DC bias. The input and output transducers of the SAW delay line were connected by oscillator circuit, which is composed of amplifier with low gain, phase shifter, mixer, LC filter, and low pass filter (LPF). The output of two oscillators was mixed to reduce the influence of the thermal effect and provides low frequency signals in the KHz range. The output of the oscillator was monitored by a programmable frequency counter and the digital oscilloscope (GDS-2102).

The fabricated SAW gyroscope was mounted onto the PCB, and then the PCB was placed on the precision rate table (920CT) in vacuum chamber. The device was tested in vacuum. Constant temperature and humidity levels were maintained in the testing chamber during all the testing period to prevent any unwanted performance variations due to temperature and humidity changes. The input voltage of ±5 V was applied to the PCB when the rate table was not rotated. The output of the oscillator was monitored by the digital oscilloscope and programmable frequency counter.

As the rotation speed increases, the mixed oscillator frequency difference was increased as shown in Fig. 68.5 due to larger secondary wave interference to the SAWS induced by Coriolis force. The sensitivity of the SAW gyroscope with rotation in x-axis were measured in rate range of 0–200°/s as 119 Hz deg^{-1} s.

68.3 GNSS Loop Structure Based on Acoustic MEMS IMU

68.3.1 Physical Structure of Aided loop

Due to frequency outputs of acoustic MEMS IMU, frequency outputs can be applied to remove Doppler effect in carrier tracking loop directly, as shown in Fig. 68.6.

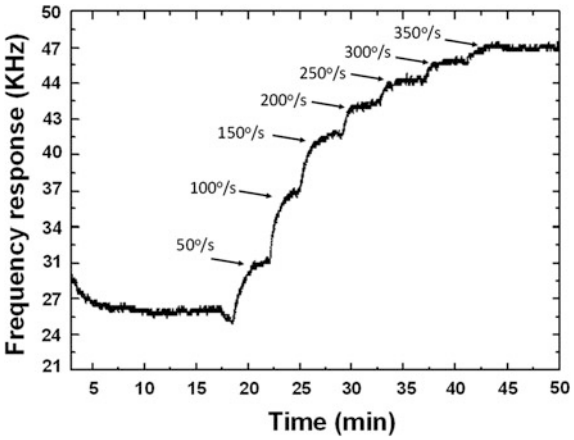

Fig. 68.5 Measured response of the fabricated SAW gyroscope

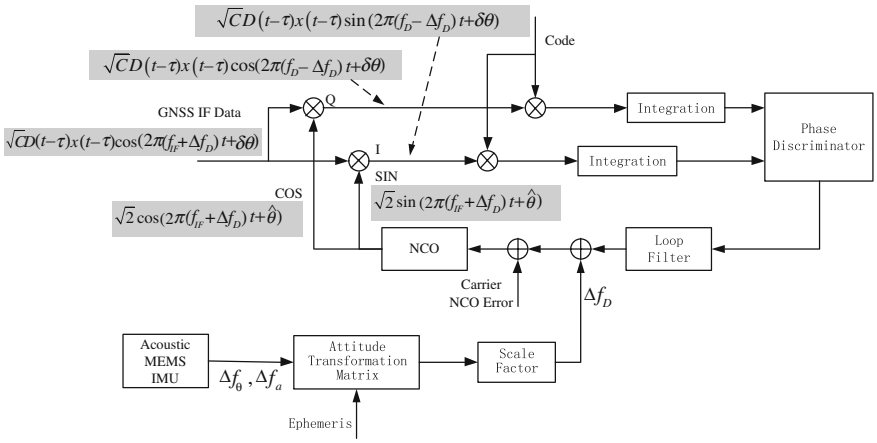

Fig. 68.6 Block diagram of Acoustic MEMS IMU aided GNSS integration

In Fig. 68.6, frequency outputs of acoustic MEMS IMU represent angular rate and acceleration of the GNSS receiver, multiplied by attitude transformation matrix and scale factor, Doppler frequency is made which represent relative velocity between satellites and the GNSS receiver.

After down-conversion, GNSS signal which sent to carrier tracking loop can expressed as:

$$\sqrt{C}D(t-\tau)x(t-\tau)\cos(2\pi(f_{IF}+f_D)t+\delta\theta) \tag{68.1}$$

where C stands for amplitude of signal, D is the navigation data, f_D is the true Doppler frequency, f_{IF} is intermediate frequency, τ is time-delay of the satellite signal, $\delta\theta$ is carrier phase.

Based on Doppler frequency measured by acoustic MEMS IMU, replica signal of SIN carrier and COS carrier can be expressed as:

$$\sqrt{2}\cos\left(2\pi(f_{IF}+\Delta f_D)t+\widehat{\theta}\right) \tag{68.2}$$

$$\sqrt{2}\sin\left(2\pi(f_{IF}+\Delta f_D)t+\widehat{\theta}\right) \tag{68.3}$$

Where Δf_D stands for Doppler frequency which produced by outputs of acoustic MEMS IMU and navigation data.

After mixing, time sample sequence of I path and Q path can be expressed as:

$$\sqrt{C}D(t-\tau)x(t-\tau)\cos(2\pi(f_D-\Delta f_D)t+\delta\theta) \tag{68.4}$$

$$\sqrt{C}D(t-\tau)x(t-\tau)\sin(2\pi(f_D-\Delta f_D)t+\delta\theta) \tag{68.5}$$

Even true Doppler can't be removed completely by Δf_D, but with Doppler aided from acoustic MEMS IMU, bandwidth of carrier tracking loop can be compressed effectively to improve navigation accuracy.

68.3.2 Calculation of Doppler Aided Frequency

Doppler frequency represents relative velocity between IMU and satellite. The Doppler frequency between the Kth satellite and IMU is:

$$\Delta f_D = e_k^T \cdot \frac{\Delta\left(V_{INS}-V_{SV,k}\right)}{\lambda_{L1}} \tag{68.6}$$

Which can be spread as [4]:

$$\Delta f_D = \frac{1}{\lambda_{B1}}\begin{bmatrix} e_{kx}\cdot\Delta(v_{INS,x}-v_{SV,xk})+e_{ky}\cdot\Delta(v_{INS,y}-v_{SV,yk}) \\ +e_{kz}\cdot\Delta(v_{INS,z}-v_{SV,zk}) \end{bmatrix} \tag{68.7}$$

Where λ_{B1} stands for wavelength of B, $e_k = [\,e_{kx} \quad e_{ky} \quad e_{kz}\,]^T$ is the line-of sight unit vectors from the MEMS IMU to the Kth satellite which can be calculated as:

$$e_k = \begin{bmatrix} e_{kx} \\ e_{ky} \\ e_{kz} \end{bmatrix} = \begin{bmatrix} \frac{\partial r_k}{\partial x} \\ \frac{\partial r_k}{\partial y} \\ \frac{\partial r_k}{\partial z} \end{bmatrix} = \begin{bmatrix} \frac{x-x_{s,k}}{r_k} \\ \frac{y-y_{s,k}}{r_k} \\ \frac{z-z_{s,k}}{r_k} \end{bmatrix} \tag{68.8}$$

In Eq. (68.8), (x, y, z) represent receiver position in ECEF, $\left(x_{s,k}, y_{s,k}, z_{s,k}\right)$ is the Kth satellite's position in ECEF, r_k is distance between the Kth satellite and receiver which can be expressed as:

$$r_k = \sqrt{(x - x_{s,k})^2 + (y - y_{s,k})^2 + (z - z_{s,k})^2} \tag{68.9}$$

In Eqs. (68.6) and (68.7), $V_{INS} = [\, v_{INS,x} \quad v_{INS,y} \quad v_{INS,z} \,]^T$ is velocity of IMU in ECEF which can be transformed from ENU Topocentric coordinate system to ECEF by multiplying transfer matrix R_l^e, $V_{INS} = R_l^e V^l$, R_l^e is [1]:

$$R_l^e = \begin{bmatrix} -\sin\lambda & -\sin\varphi\cos\lambda & \cos\varphi\cos\lambda \\ \cos\lambda & -\sin\varphi\sin\lambda & \cos\varphi\sin\lambda \\ 0 & \cos\varphi & \sin\varphi \end{bmatrix} \tag{68.10}$$

$V_{SV,k} = [\, v_{SV,xk} \quad v_{SV,yk} \quad v_{SV,zk} \,]^T$ is velocity of the Kth satellite in ECEF which can be calculated from ephemeris. Meanwhile, scale factor is defined by experiment fitting.

68.4 Simulation Verification

68.4.1 Simulation Trajectory Design

Design a coordinated turn trajectory of airplane, velocity of the airplane is 200 m/s, the trajectory is shown in Fig. 68.7. Suppose the bias stability of acoustic MEMS gyroscope is 150°/h, bias stability of acoustic MEMS accelerometer is 5 mg. Set 7 visual satellites, use intermediate frequency simulator to generate GNSS signal, pre-detection integration time is 20 ms, and use 2-order-FLL assisted 3-order-PLL carrier tracking loop structure, also code tracking loop is assisted by carrier tracking loop.

Without IMU aided, set FLL bandwidth to 20 Hz, set PLL bandwidth to 18 Hz, set DLL bandwidth to 2 Hz, with which generate the best performance [5, 6].

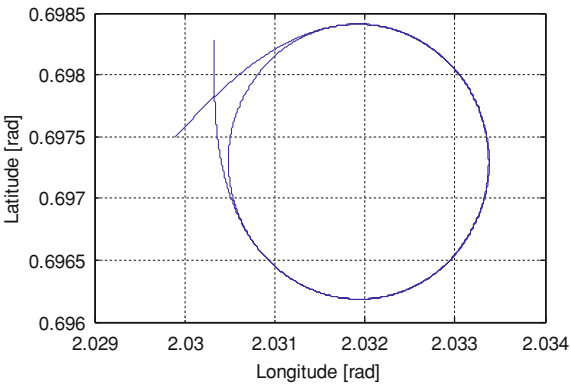

Fig. 68.7 Trajectory of the aircraft

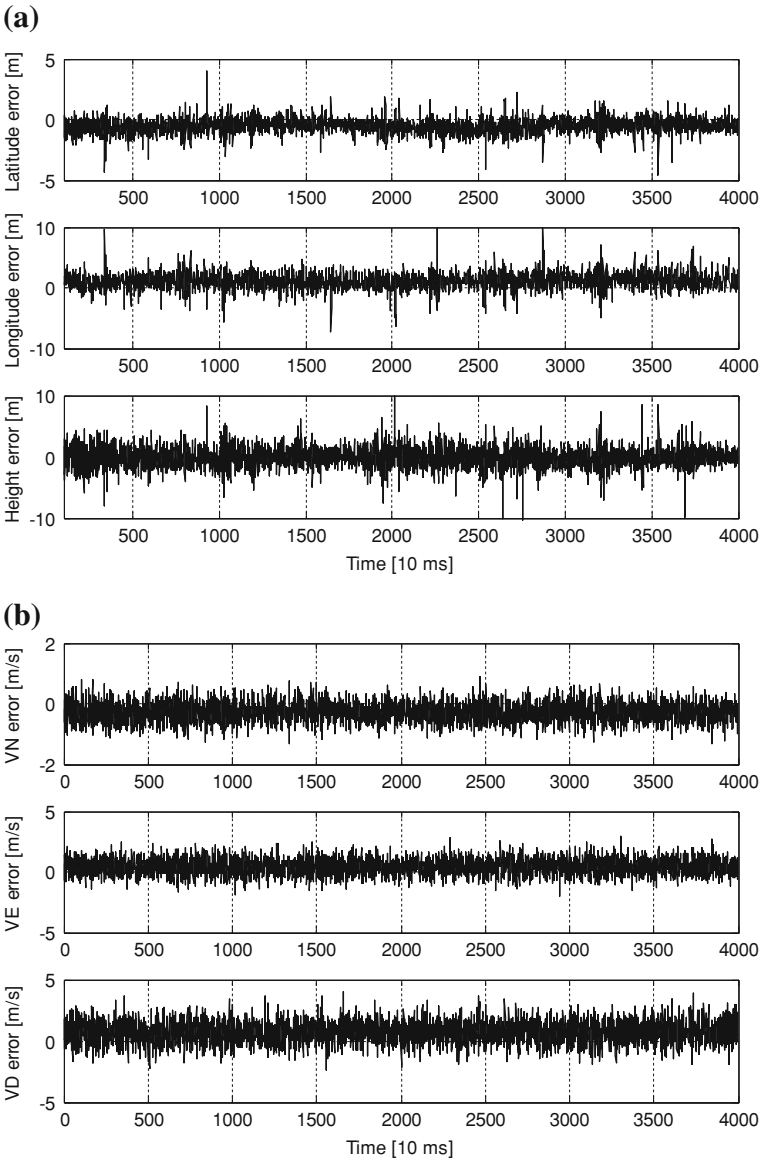

Fig. 68.8 Position errors (**a**) and Velocity errors (**b**) without IMU aided

With IMU aided, set FLL bandwidth to 10 Hz, set PLL bandwidth to 5 Hz, set DLL bandwidth to 1 Hz, under which the tracking loop can work stably.

During simulation, bandwidth of PLL could be adjusted below 5 Hz, tracking loop works steadily but tracking performance decreases.

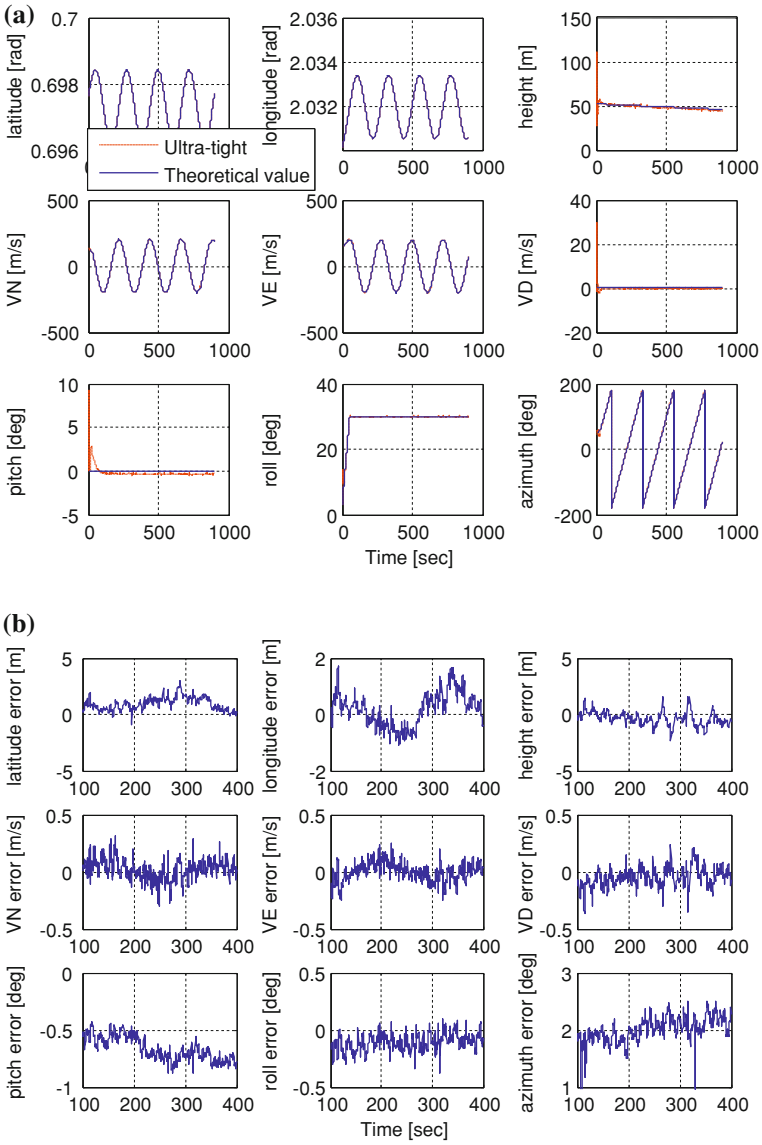

Fig. 68.9 Navigation results (**a**) and errors (**b**) with IMU aided

68.4.2 Simulation Result

Apply serial search capture method to re-capture GNSS signal. Simulation result shows that re-capture time is 10 s without IMU aided, 1 s with IMU aided.

Navigation performance is defined by comparing navigation result with ideal trajectory. As shown in Fig. 68.8, without IMU aided, position error is larger than 5 m, velocity error is larger than 1 m/s.

Figure 68.9 gives navigation performance with IMU aided, position error is less than 3 m, velocity error is less than 0.5 m/s, attitude error is less than 0.5°.

68.5 Conclusions

Firstly, principle and characteristic of a novel acoustic MEMS gyroscope are introduced. Then aided GNSS tracking loop structure is designed according to feature of acoustic MEMS IMU. Finally, simulation of ultra-tight integration method of acoustic MEMS IMU and GNSS is carried out. Simulation results show that compared with unaided method, PLL bandwidth can be compressed to 5 Hz, re-capture time change from 10 to 1 s, position error changes from 5 to 3 m, velocity error changes from 1 to 0.5 m/s, which indicate significant improvement.

References

1. Guo M, Lin S, Zhou B, Lv S, Liu G (2011) GPS/MINS tightly-coupled integrated navigation system. J Chin Inertial Technol
2. Lee SW et al (2007) A micro rate gyroscope based on the SAW gyroscopic effect, Micromech Microeng 17:2272
3. Wen SW (2011) Development of a new surface acoustic wave based gyroscope on a X-112o Y LiTaO3 substrate. Sensors 11(11):10894
4. Zhao S (2011) GNSS/INS integrated navigation: research on key technologies and working performance. PhD thesis, Tsinghua
5. Kaplan ED, Hegarty CJ (2006) Understanding GP—principles and applications, 2nd edn. Artech House, London
6. Parkinson BW, Spilker JJ (1996) Global positioning system: theory and applications. AIAA, Washington, DC

Chapter 69
Design Paradigms for Multi-Constellation Multi-Frequency Software GNSS Receivers

James T. Curran, Mark Petovello and Gérard Lachapelle

Abstract This study addresses the challenges of designing a tracking architecture for a multi-constellation, multi-frequency GNSS receiver. Using a C++ software defined receiver platform, the design of a receiver which operates on the BeiDou, Galileo, GLONASS and GPS civil signals is explored and a modular, reconfigurable GNSS tracking architecture is presented. The component parts of this architecture are tested in a pedestrian navigation scenario examining a range of different code and carrier tracking algorithms. The challenges of developing of a flexible, universal design is addressed while also highlighting some of the benefits of signal and application specific designs. In particular, the improvements in both performance and reliability that can be leveraged by the use of dedicated multi-signal tracking strategies when operating under certain challenging conditions, is shown. Results illustrate the various trade-offs that can be made between performance and receiver flexibility when applied to a diverse set of GNSS signals.

Keywords BeiDou · DLL · FLL · Galileo · GLONASS · GNSS · GPS · Kalman Filter · PLL · SDR

69.1 Introduction

Modern GNSS receivers are becoming increasingly complex devices. In the near future these receivers will have four GNSS constellations at their disposal, each transmitting on a minimum of two frequencies with at least as many signals and modulation schemes. Furthermore, depending on the receiver application, be it survey, outdoor/indoor pedestrian, vehicular, aviation or timing, a receiver may

J. T. Curran (✉) · M. Petovello · G. Lachapelle
Location and Navigation Group, University of Calgary,
Calgary, Canada
e-mail: James.T.Curran@ucalgary.ca

J. Sun et al. (eds.), *China Satellite Navigation Conference (CSNC) 2013 Proceedings*, Lecture Notes in Electrical Engineering 243,
DOI: 10.1007/978-3-642-37398-5_69,

comprise of many different acquisition and tracking strategies, each fulfilling a different functionality. Key benefits of a software receiver platform are its flexibility and reconfigurability and, so, it is naturally suited to the multi-signal, multi-application problem. The design of a receiver to suit all needs, however, is not without its challenges.

As the number of combinations of ranging signals and processing strategies has become immense, it is perhaps desirable to strive for some signal independence in the receiver design. Doing so promotes code reuse and results in a receiver which is more readily adaptable to new signals. Of course, basic receiver operation requires, at the very least, knowledge of the signal modulation scheme, the navigation message structure and the satellite orbit and, so, a receiver cannot be completely signal independent. Nonetheless, the majority of the receiver modules can, through appropriate design, be rendered independent of the particular signal they process. Key modules amongst these are the acquisition and tracking strategies.

Tempting as a one-size-fits-all receiver may be, given the diverseness of the available signals, conventional wisdom holds that there is some merit in tuning acquisition and tracking strategies and some receiver operations to the specific strengths and weaknesses of each individual signal structure. Such a receiver architecture, while rigid and possibly more labour intensive to develop, has potential to elicit more accurate signal observations and, thus, yield enhanced navigation performance.

Against the backdrop of an ever-growing set of broadcast ranging signals, this paper presents an investigation into the merits of these two opposing design principles via implementation in GSNRx^{TM}, a GNSS software receiver developed and maintained by the PLAN Group of The University of Calgary. The study explores challenges of developing a flexible, universal design and identifies and quantifies the performance benefits that can be gained by sacrificing some flexibility through tailoring strategies to specific signals. A novel receiver architecture is presented, which facilitates significant code reuse without sacrificing receiver performance. The design is based on decomposing the receiver processing strategies in such a way as to maximize the commonality of its constituent elements. With this structure, receiver modification for new signals or different applications is reduced to simple build-time configuration.

Utilizing a C++ software receiver platform, Sect. 69.2 presents a signal- and system-independent tracking architecture, capable of hosting an arbitrary collection correlator-based tracking algorithms. An illustrative example, exhibiting the basic functionality and design of a specific tracking strategy is presented in Sect. 69.3. A number of receiver implementations are tested using simulated signals from the GPS, Galileo, GLONASS and BeiDou constellations, discussed in Sect. 69.4, revealing the relative performance of different signals using different architectures. Results of this experiment, discussed in Sect. 69.5, illustrate how some signals can benefit significantly from customized receiver design.

69.2 Tracking Architecture

The general hierarchy of the GSNRx^{TM} software receiver is depicted in Fig. 69.1. The receiver is primarily composed of a list of satellites, a list of sample sources, a Doppler removal and correlation (DRC) object, and a navigation solution. As can be seen, each satellite contains one or more channels, each of which operates on one or more signals. A channel can contain a selection of processing strategies which may include, for example, cold- and warm-acquisition strategies and a variety of tracking strategies. Which to use at any given time is at the discretion of the channel. This paper will focus on the tracking strategies and their implementation and will consider the design of a flexible, modular multi-signal tracking architecture. Depicted in Fig. 69.2 is the proposed architecture, which implements a compartmentalized design, allowing for effective code reuse and flexibility in algorithm design.

A key feature of this design is the separation of the housekeeping of maintaining a tracking strategy; the strategy implementation; and the fundamental tracking operations. Specifically, the design of a practical strategy has been partitioned into a three layers, referred to herein as a 'Tracker' layer, a 'Composite Strategy' layer and an 'Strategy-Interface' layer.

A 'Tracker' is a simple tool which dictates the correlator request, directly observes correlator values and predicts signal parameters. Trackers conform to a standard interface, depicted in Fig. 69.3, and estimate carrier phase, carrier frequency, code phase and code rate. The interface includes a facility for the tracker to report its internal estimates of lock or loss-of-lock. Example implementations include an FLL-DLL pair, a PLL-DLL pair, a code-frequency fine-search or a Kalman filter, although a tracker could implement any correlator-based tracking

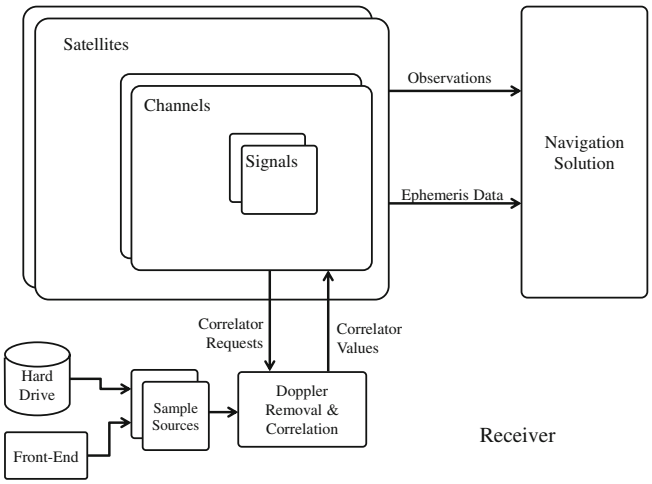

Fig. 69.1 A simplified view of the GSNRx^{TM}receiver architecture

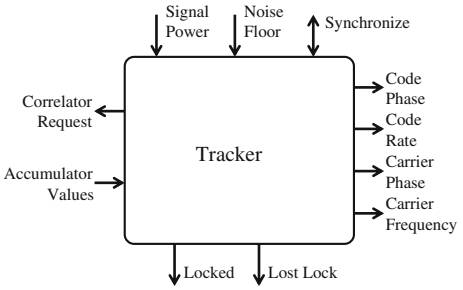

Fig. 69.2 Block diagram the standardized 'Tracker' interface

algorithm. Compliance with a standard interface allows the strategy to operate without requiring any knowledge of the particular tracking algorithm. Users can, therefore, freely design tracking algorithms (trackers) and readily incorporate them into a fully receiver implementation.

A 'Composite Strategy' is defined by a set of trackers and a scheduling state-machine. Within GSNRx^{TM}, a unique strategy can be defined at the 'composite strategy' layer by, firstly, instantiating a specific set of trackers to be used by the strategy and, secondly, implementing a state-machine which schedules the use of each tracker. This schedule may be based on time, signal-strength, bit-synchronization status or by observing a variety of lock indicators, at the discretion of the designer. At any given time, only one tracker is declared active by the state-machine, while all other trackers operate passively. To avoid transients when the state-machine switches from one tracker to another, signal parameter estimates within all passive trackers are continuously updated from those of the active one. When tracking multiple signals, it is likely that a different coherent integration period will be used on different signals and that the desired tracking loop update period may be longer than the shortest coherent integration period. To handle this eventuality, the 'Composite Strategy' layer maintains a buffer of accumulator values for use by the active tracker at each loop update epoch.

The 'Strategy-Interface' layer co-ordinates the interface between the tracking strategy and the receiver. Its tasks include driving the DRC engine to produce correlator values for all tracked signals; building signal observations; operating a set of signal monitoring utilities. Notably, these utilities, which include a C/N_0 estimator, phase and frequency lock monitors, a secondary-modulation syncher and a navigation decoder [1, 2], are maintained in this interfacing layer, as they are utilized by both the state-machine within the 'Composite Strategy' layer and are also (optionally) logged to the hard-drive by the interface layer for post-processing. In general, functionality that is deemed universal to all tracking strategies, is contained within the strategy interface layer, as it serves as the foundation for all strategy implementations.

In the implementation of a multi-signal architecture, synchronization is an important consideration as, if observations of two or more signals are to be combined, a common epoch should be defined at which to update the tracking loops. To do so, the concept of a master- and slave-signals is employed. The

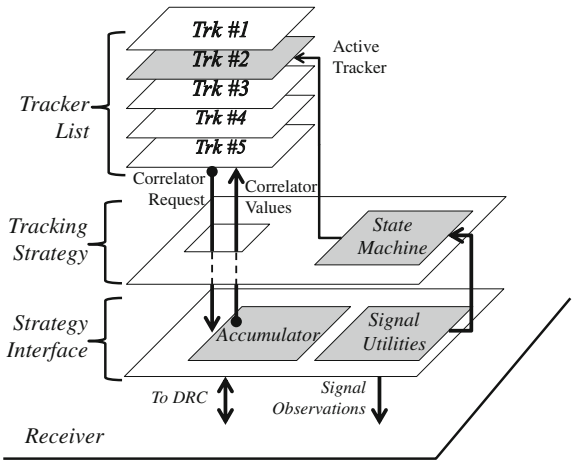

Fig. 69.3 A block diagram of the three-layer architecture of the composite tracking strategy illustrating containment of trackers (*Trk #1–5*) within tracking strategy definition and use of strategy interface with the receiver

choice of which of the tracked signals is the master signal is at the discretion of the composite strategy implementation but, typically, it will base the decision on the signal type and the status of the signal utilities. For example, the strategy may opt for a pilot-only signal, or one for which its secondary code has been synchronized, also, preference may be given to a signal which can provide the longer coherent integration period. Updates of the current active tracker are then aligned with epochs of the master signal, at which point the buffer of all accumulator values (corresponding to both master and slave signals) accrued since the last loop update is passed to the active tracker for processing. An example of this, for the Galileo E1 BC signals, is depicted in Fig. 69.4.

Another important feature of this tracking architecture is its focus on a multi-signal support. The design leverages resources such as the *vector*, *list* and *map* features of the C++ ISO standard library to effect an architecture which operates on an ensemble of quasi-synchronous[1] signals broadcast from a single transmitter. This multi-signal architecture can then be tailored to manifest any single- or multi-signal strategy (for example, data-pilot or dual-frequency), by specifying at the 'Composite Strategy' layer, the signals on which the active tracker operates. This approach confers many distinct advantages over architectures which augment, extend, or dither a single-signal strategy to achieve data-pilot operation, prominent among which being ease of use and re-usability.

[1] Although signals may have different centre frequencies and symbol (chipping) rates, they are synchronous in the sense that they experience the same time dilation induced by line-of-sight dynamics.

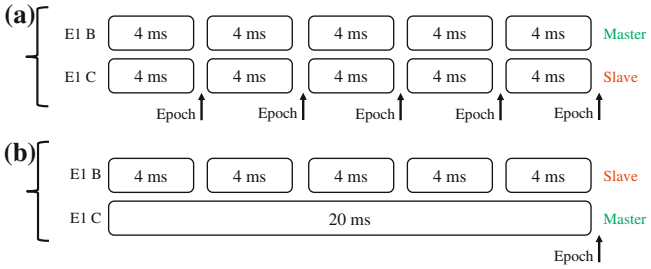

Fig. 69.4 Scheduling of tracking loop updates for a multi-signal tracking strategy operating on the Galileo E1 BC data-pilot pair before (**a**), and after (**b**), synchronization with the secondary code on E1 C

69.3 Tracking Strategies

The principle of the tracking strategy presented here is that the tracking strategy is only responsible for activating or de-activating its member tracking algorithms while each tracking algorithm (tracker) is be self-contained and build-time configurable only. By enforcing this principle, the tracking strategy need not be aware of any of the internal workings of the tracker, thus promoting simplified code and re-usability. Rather than re-tune the tracker as the prevailing conditions change, the strategy can simply select a more appropriately tuned tracker. This approach preserves the benefits of adaptive tracking algorithms without incurring the increased complexity.

The design of tracking strategies within GSNRx^{TM} involves two steps: first a list of available trackers must be populated with suitable tracker instances and, secondly, a state machine, defining when each tracker is to be used, must be defined. When populating a list of trackers, a designer may avail of a library of predefined tracker objects, or opt to design a custom algorithm. For example, the tracker objects used within this work include a selection of standard tracking algorithms [1, 3–5]:

- Fine Search: a continuous re-acquisition scheme involving a refined search in the code and frequency domains.
- pull-in FLL+DLL: a standard FLL and DLL incorporating a false-frequency lock detection algorithm.
- FLL+DLL: a standard FLL and DLL with configurable loop filters, code-aiding, and integration periods.
- PLL+DLL: a standard PLL and DLL with configurable loop filters, code-aiding, and integration periods.
- Kalman Filter: an iterated extended Kalman filter approach.

All implementations, excluding the Kalman filter,[2] support both single-signal and data-pilot operation. A given tracking strategy may contain many instances of the same tracker but each configured with differently, for example, stipulating various filter bandwidths or integration periods.

As mentioned previously, within the 'Composite Strategy' one tracker is active at any given time. This active tracker performs signal parameter estimation (code and carrier tracking) while the remainder are continuously synchronized with it. The active tracker is chosen by a synchronous, finite Mealy state machine containing a unique state corresponding to each of the available trackers and two further states, representing the 'Initialized' state at which the strategy begins and the 'Lost-Lock' state which indicates to the receiver that a re-acquisition may be necessary. The input to the state machine are a set of Boolean values given by conditional operations applied to the signal utilities and the trackers internal indicators. The inputs include: C/N_0, a phase-lock indicator (PLI), a frequency-lock indicator (FLI), bit and secondary code-synch status, navigation synch status, tracking time and, tracker internal lock and loss-of-lock indicators.

An example of such a state machine is depicted in Fig. 69.5, representing that of the GSNRx^{TM} weak-signal tracking strategy. The two fine-search trackers differ only in cell size, the second having both a smaller search space and smaller cells. The second of the two FLL+DLL trackers has the narrower filter bandwidths and, unlike the first, employs carrier aiding of the code loop. The variables ζ_i represent the various conditions which dictate changes of state and are defined in Table 69.1, note, however, the subtle difference between the tracker 'Lost Lock' status and the strategy 'Lost Lock' state. The flow rational is as follows: the Kalman filter tracker provides excellent steady-state tracking performance but is unreliable during the initial transient or pull-in stage. To reach this steady state, and to hand-over to the Kalman filter tracker, either a series of fine-search trackers, or a series of FLL and DLL trackers can be used. The fine search trackers are reliable under weak-signal conditions, but are relatively slow. In contrast, the FLL and DLL trackers are relatively fast, but are only suitable when the received C/N_0 is moderate or high. This system, therefore defaults to the fine-search trackers and, should it detect a sufficiently high C/N_0, will transition to the FLL and DLL branch of the state-machine.

Of course, the use of this architecture is not restricted to the above design and can be utilized to implement any multi-algorithm strategy. For example, one tracking algorithm (tracker) may be employed to absorb the initial transient, before a transition to another tracking algorithm more suited to steady state operation. Likewise, strategies which implement phase tracking with a PLL may first apply an FLL to the received signal, transitioning to the PLL only when the frequency uncertainty had reduced sufficiently. Indeed, context-aware strategies, which are becoming increasingly popular, can be readily implemented within this proposed

[2] This is not due to a fundamental incompatibility between the Kalman filter and data-pilot signals, but rather lack of development time.

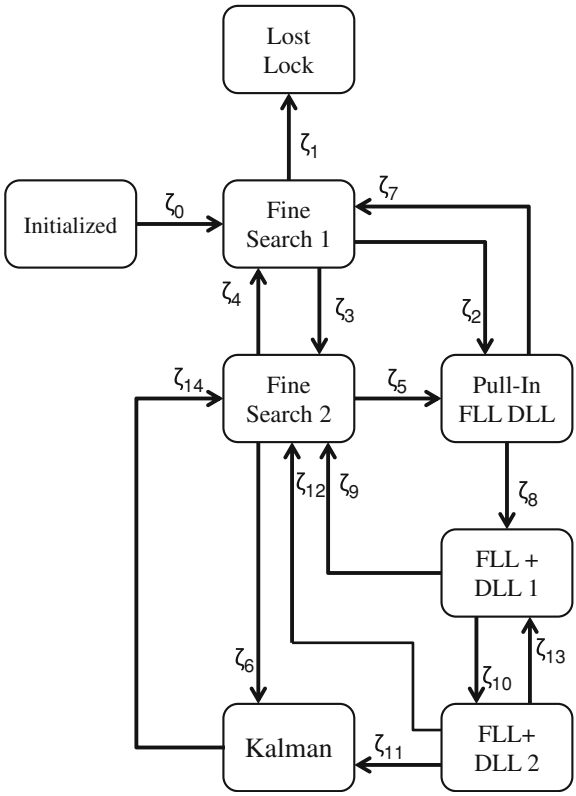

Fig. 69.5 An example of a state machine for a weak-signal tracking strategy

Table 69.1 Weak-signal tracking strategy conditional statements

ζ_0	–
ζ_1	$C/N_0 < 15.0$
ζ_2	$C/N_0 > 35.0$
ζ_3	Locked
ζ_4	$C/N_0 < 15.0$
ζ_5	$C/N_0 > 35.0$
ζ_6	Locked
ζ_7	(Lost lock) OR ($C/N_0 < 15.0$)
ζ_8	Locked
ζ_9	(Lost lock) OR ($C/N_0 < 15.0$)
ζ_{10}	FLI > 0.6
ζ_{11}	FLI > 0.85
ζ_{12}	$C/N_0 < 15.0$
ζ_{13}	FLI < 0.2
ζ_{14}	$C/N_0 < 15.0$

architecture. In all of these cases, the desired strategy can be effected by populating a list of suitably configured trackers and defining a protocol, via the state machine, to transition from one to the next.

As discussed in Sect. 69.2, the scheduling of correlator values from the DRC is handled by the 'Composite Strategy' layer. At any given tracking epoch, the buffer of available correlator values is presented to the active tracker. The tracker itself is responsible for both dictating the correlator request and processing these resultant correlator values and, so, the decision to perform a multi-signal algorithm (for example, a data-pilot, or dual-frequency tracking scheme) is at the discretion of the current active tracker. This architecture, therefore, not only supports these multi-signal algorithms, but can provide a blend of single- and multi-signal algorithms, by appropriately populating 'Composite Strategy' with the appropriate trackers.

69.4 Test Scenario

While the previous sections have detailed the design of a flexible tracking strategy architecture, and the means by which it can be configured, the question of which tracking algorithms to use, when they should be used, and to which signals they should be applied, remains. To explore this question, this section presents a simple pedestrian navigation scenario within which the performance of a selection of trackers can be examined.

Tracking performance was examined by processing a set of simulated IF data, representing a pedestrian navigation scenario. The data contained three front-end channels, the first was configured with a centre frequency of 1569.0 MHz to receive BeiDou B1I signals [6], the second was configured with a centre frequency of 1575.0 MHz to receive GPS L1 C/A and Galileo E1bc signals [7, 8], and the third was configured with a centre frequency of 1602.0 MHz to receive the GLONASS L1 OF signals [9]. A complex sample rate of 8.0 MHz was used on each front-end channel. The simulation was designed to provide one satellite from each of the four systems at the same elevation and azimuth, of 52°and 90°, respectively, relative to the receiver. Although not necessarily realistic from a constellation perspective, this ensured that the receiver observed the same line-of-sight (LOS) dynamics on each signal, facilitating a more fair comparative analysis, from a signal processing perspective.

In total, eleven minutes of data were generated, during which time the user traversed a rectangular trajectory measuring 50 m east-west and 100 m north-south with a cornering radius of 5 m. The received signal strength on all satellites was set to an initial value of 48 dBHz, at which it was held constant for a period of one minute and, subsequently, reduced at a rate of 0.05 dB/s reaching a final value of 18 dBHz at the end of the eleventh minute. A second set of data was collected as a reference, using the same simulation configuration but without applying attenuation to the received signal. This data-set served as a reference against which

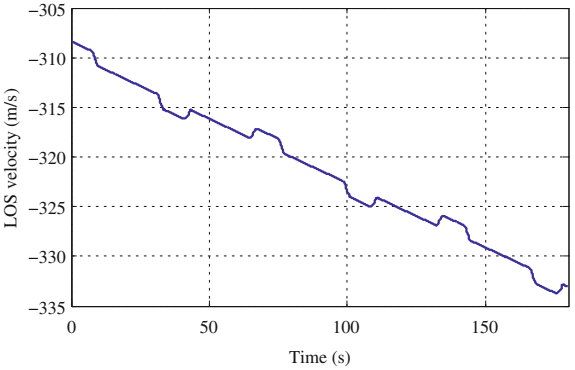

Fig. 69.6 Line of sight velocity between the satellites and the receiver fore the first three minutes of the simulated dataset

tracking performance was measured. The LOS velocity observed on these received signals is depicted in Fig. 69.6.

Rather than testing full tracking strategies, the focus of this experiment was to assess the relative tracking performance and efficiency of some key tracker objects. In particular, the FLL-DLL, the PLL-DLL and the Kalman filter trackers were examined. To observe the tracking performance, the receiver was executed and, following successful acquisition, the strategy was stalled in the tracking state of interest for the duration of the data-set. For the GPS, GLONASS and BeiDou signals, a single-signal strategy was employed, while for the Galileo signals a single-signal strategy was applied to the E1b signal, another single-signal strategy was applied to E1c and a data-pilot strategy was applied to the E1bc pair. In this way, the benefits of employing a signal specific custom tracking strategy can be directly measured. In this case, a the difference between employing a single-signal, pilot-only or data-pilot strategy on the Galileo E1bc pair is examined.

Table 69.2 details some of the characteristics of the received signals, notable amongst which are the slope and the coherent integration period. The absolute slope of the ranging code correlation function (denoted Abs. Slope), evaluated at a code offset of one half of the corresponding code spacing (denoted E-L Spacing), is a key contributor to discriminator-based code tracking performance. The maximum attainable coherent integration period (denoted Coh. Int. Period),

Table 69.2 Signal details

	GPS L1 C/A	GLONASS L1 OF	BeiDou E1BI	Galileo E1 B	Galileo E1 C
Chip rate (Mcps)	1.023	0.511	2.046	1.023	1.023
Code period (ms)	1	1	1	4	4
Data modulated	y	y	y	y	n
Coherent integration period (ms)	20	20	20	4	∞
Wavelength (cm)	19.0	18.7	19.1	19.0	19.0
E-L spacing (chip)	0.4	0.4	0.4	0.4	0.4
Absolute slope (m^{-1})	3.4e-3	1.7e-3	6.8e3	13.2e-3	50e-3

restricted here by the presence of data modulation, has implications for tracking accuracy and sensitivity. In all receiver configurations, the coherent integration period adjusted to 20 ms where possible (but, of course, was limited to 4 ms on the Galileo E1b signal). For data-modulated signals, Costas-style carrier phase and frequency discriminators were employed where appropriate and coherent discriminators applied otherwise. Similarly, when the carrier phase was tracked, where appropriate, an early-minus-late in-phase discriminator was used while an early-minus-late envelope discriminator was used when only the carrier frequency was tracked.

The reference data-set was tracked using the weak-signal tracking strategy described in Sect. 69.3. The test data-set was tracked with each of the tracking algorithms under examination. In each case a log of the estimated signal parameters was recorded, at a rate of 1.0 kHz. Estimates of tracking errors were made by analyzing the difference between the log corresponding to the reference data and that of the attenuated data. The results are discussed in Sect. 69.5.

69.5 Tracking Performance

The results of the experiment described in Sect. 69.4 are discussed here. Results are presented for FLL+DLL, PLL+DLL, and Kalman filter tracking algorithms, using single-signal implementations for all signals and, also, using a data-pilot combining algorithm for the Galileo E1bc pair. One important point to consider here is that the different tracking algorithms have not been tuned to provide compatible tracking results and, so, a direct comparison between, for example, the FLL+DLL tracking error and that of the PLL+DLL, is not valid. Rather, these results are intended to provide insight into the relative performance of different signals for a given tracking algorithm. For example, a comparison of the frequency tracking error observed when using either the PLL+DLL or FLL+DLL trackers on the GPS L1 C/A signal is not meaningful whereas a comparison of the frequency tracking error observed when using the FLL+DLL tracker on either the GPS L1 C/A or BeiDou B1I is quite useful.

Figure 69.7a, b and c show the root-mean square (rms) code phase tracking error versus received signal C/N_0 for each of the three tracking algorithms. In both Fig. 69.7a, b, the code tracking is implemented using a standard DLL algorithm, the difference being that the former employs an early–minus-late envelope discriminator as it tracks only carrier phase, while the latter can avail of an early-minus-late in-phase discriminator as the phase is tracked by a PLL. The results clearly confirm the well known result that the tracking error is inversely proportional to the slope of the ranging code auto correlation function, whereby GLONASS exhibits the poorest tracking precision and strategies which include the Galileo E1c signal exhibit the best. Evident also are the effects of integration period for both the PLL and FLL algorithms, whereby the Galileo E1b signal looses lock at a higher C/N_0 in all cases, due to the 4 ms limit imposed by data-

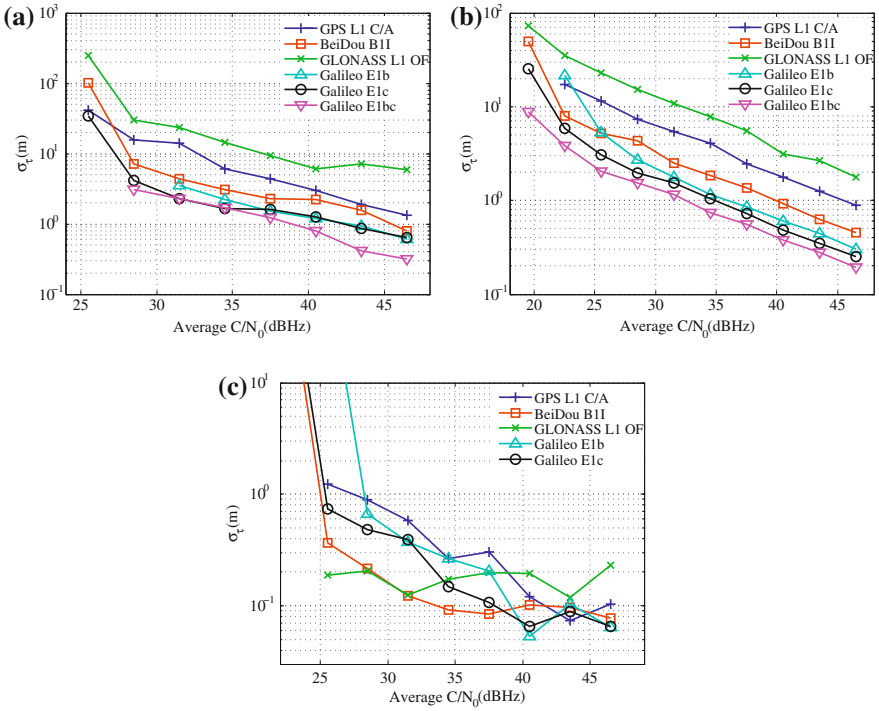

Fig. 69.7 Code phase tracking error, in metres, for the FLL+DLL, PLL+DLL and Kalman filter tracking architectures. **a**, **b** The PLL+DLL tracking architecture. **c** The Kalman filter tracking architecture

modulation. Interestingly, for the PLL+DLL algorithm, the Galileo E1bc data-pilot algorithm provides the best performance, owing to the lack of data modulation on the pilot channel and the sharpness of the ranging code correlation function, while for the FLL+DLL algorithm, the Galileo E1c algorithm performs best. This is perhaps the result of the carrier aiding applied to the code loop which, for the data-pilot combining FLL, as illustrated in Fig. 69.8a, performs more poorly than the pilot-only implementation.

In contrast to the differences in code tracking performance between the various signals when using FLL+DLL or PLL+DLL algorithms, Fig. 69.7c suggests that the Kalman filter can provide a similar level of code tracking accuracy for all signals, irrespective of the modulation scheme. The only exception being the tracking of Galileo E1b which, due to a reduced coherent integration period of 4 ms, loses lock at a higher C/N_0 than the other signals.

Figure 69.8a and b show the root-mean square (rms) carrier frequency tracking error versus received signal C/N_0 for FLL+DLL and the Kalman filter tracking algorithms. Examining Fig. 69.8a, it is clear that the signals which can offer a coherent integration period of 20 ms perform the best, with the 4 ms integration period of the Galileo E1b signal resulting in significantly poorer tracking

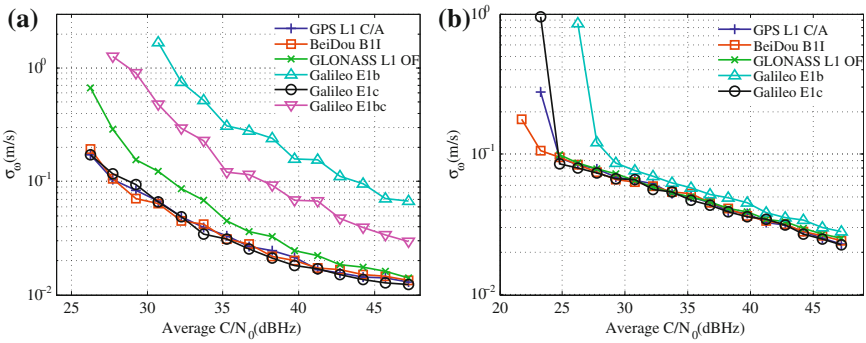

Fig. 69.8 Carrier frequency tracking error, in metres per second, for the FLL+DLL and Kalman filter tracking architectures. **a** The FLL+DLL tracking architecture. **b** The Kalman filter tracking architecture

performance. Surprisingly, the algorithm which combines the Galileo E1bc data-pilot pair, performs by almost as poorly. This observation betrays a sub-optimal data-pilot combining, indicating that, perhaps, data-pilot combining is not as straightforward for carrier frequency tracking as it is for carrier phase or code phase. Similar to the FLL+DLL algorithm, the carrier frequency tracking performance of the Kalman filter, presented in Fig. 69.8b, is similar for all signals which can support a 20 ms coherent integration period, the Galileo E1b signal, once again, suffering from the effects of a 250 bps data modulation. Another curious feature of these results is the relationship between received signal strength and carrier frequency tracking error. For the Kalman filter algorithm, the rms tracking error exhibits a linear inversely proportional relationship with the received C/N_0. The FLL, in contrast, incurs a much more rapid degradation in tracking performance with reducing C/N_0.

Finally, the carrier phase tracking performance of the PLL+DLL and Kalman filter tracking algorithms is presented in Fig. 69.9a and b. Here the benefits of the

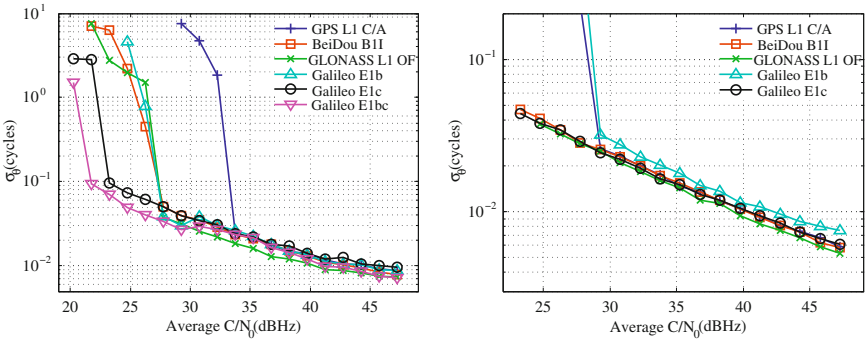

Fig. 69.9 Carrier phase tracking error, in cycles, for the PLL+DLL and Kalman filter tracking architectures. **a** The PLL+DLL tracking architecture. **b** The Kalman filter tracking architecture

pilot signal become pronounced as the Galileo E1c and Galileo E1bc data-pilot pair significantly outperform the other signals when tracked by a PLL+DLL algorithm. For the Kalman filter tracking algorithm, the limited coherent integration period afforded by the Galileo E1b signal, once again results in a reduced tracking precision, relative to the other signals.

It is worth commenting on the tracking error incurred while tracking the GPS L1 C/A signal, as shown in Fig. 69.9a. The eleven minute data-set was tracked from beginning to end and the rms tracking error calculated over successive 30 s windows. Should the tracking algorithm begin to loose lock early in the data-set, the accumulated phase error will continue to contribute to the rms error for later time-points. Examining Fig. 69.9a, it appears that the receiver lost lock on the carrier phase at approximately five minutes (corresponding to a C/N_0 of 34 dBHz) thus rendering tracking error estimates for later time-points (lower C/N_0 values) invalid.

69.6 Conclusions

A novel GNSS tracking architecture has been presented in this work which address receiver design challenges which arise when implementing a multi-constellation receiver. The design features a highly modular design that facilitates fast and efficient tracking algorithm design and definition by promoting a high degree of module and code re-use. Moreover, this design lends itself to simple and rapid adaptation to new signals as the become available. The effectiveness of this architecture was demonstrated and tested in the context of a pedestrian navigation scenario using the BeiDou, Galileo, GLONASS and GPS constellations.

While the tracking performance results presented here cannot be interpreted as a commentary on the relative performance of the various tracking algorithms, they do serve to indicate the suitability and efficiency of each strategy when applied to signals from each of the constellations. That is, for a given tracking algorithm, be it the PLL-DLL, the FLL-DLL, or the Kalman filter, the relative suitability of each signal to that algorithm can be examined, in particular, the cost-benefit tradeoff of implementing a data-pilot tracking algorithm can be assessed.

In terms of ranging code tracking, results show that the Kalman filter based tracking algorithm provides the best overall performance, exhibiting the least sensitivity to modulation scheme or coherent integrations period. For the DLL-based tracking algorithms, however, the attainable performance is sensitive to the absolute slope of the ranging code auto-correlation function.

In contrast, the carrier frequency tracking performance of both the FLL-based and Kalman filter based tracking algorithms, exhibit a similar trend across the various signals. The tracking performance is most heavily influenced by the attainable coherent integration period and the only notable difference being the relationship to the prevailing C/N_0, it being linear for the Kalman filter and not so for the FLL.

The carrier phase tracking performance of both the PLL-based algorithms and the Kalman filter algorithm, also exhibits some interesting features. It is apparent that the PLL-based algorithm is relatively insensitive to the coherent integration period afforded by the tracked signal and, at least for moderate to high C/N_0 values, achieves comparable tracking performance for all of the signals. In contrast, the Kalman filter clearly achieves a poorer precision for the Galileo E1b signal, which can only support coherent integration period of 4 ms. Collectively, these observations suggest that, for a given target application, environment and set of constellations, there are some clear advantages to employing one tracking a algorithm over another. There does not, therefore, appear to be an individual algorithm which has a distinctly universal appeal.

References

1. Kaplan ED (ed) (2006) Understanding GPS: principles and applications, vol 1, chap 5, pp 179–194. Artech House Inc. ISBN 1-58053-894-0
2. VanDierendonck AJ (1996) Global positioning system: theory & applications (Volume One) (Progress in Astronautics and Aeronautics), chap 8, pp 329–408. AIAA (American Institute of Aeronautics & Ast, 1996). ISBN 1-56347-106-X
3. Misra P, Enge P (1996) Global positioning system, signals, measurements and performance, vol 2. Ganga-Jamuna Press. ISBN 0-9709544-1-7
4. Curran J, Lachapelle G, Murphy C (2012) Improving the design of frequency lock loops for gnss receivers. Aerosp Electron Syst, IEEE Trans 48:850–868
5. Gleb A (1974) Applied optimal estimation. MIT Press, Cambridge, Mass. ISBN 9780262570480
6. BeiDou Navigation Satellite System (2013) Signal in space interface control document. http://www.beidou.gov.cn/attach/2012/12/27/201212273da29c5eb8274deb8cd2b178228ba2bd.pdf. (Accessed: 01 Jan 2013)
7. GPS Navstar JPO (2013) Navstar GPS Space Segment / Navigation User Interfaces. http://www.navcen.uscg.gov/pubs/gps/icd200/default.htm. (Accessed: 01 Jan 2013)
8. Galileo Project Office (2013) Galileo OS SIS ICD http://ec.europa.eu/enterprise/policies/satnav/galileo/files/galileo_os_sis_icd_revised_3_en.pdf. (Accessed: 01 Jan 2013)
9. GLONASS Navigation Satellite System (2013) Interface Control Document. http://gauss.gge.unb.ca/GLONASS.ICD.pdf. (Accessed: 01 Jan 2013)

Chapter 70
Erratum to: An Initial Evaluation About BDS Navigation Message Accuracy

Zhihang Hu, Guo Chen, Qiang Zhang , Jing Guo, Xing Su, Xiaotao Li, Qile Zhao and Jingnan Liu

Erratum to:
Chapter 70 in J. Sun et al. (eds.), *China Satellite Navigation Conference (CSNC) 2013 Proceedings*,
DOI 10.1007/978-3-642-37398-5_44

Page	Item or line	Correction
483	Chapter 44	Equations (44.2–44.4) are replaced by new equations.
483	Chapter 44	The sentence "Supposing that the Earth's radius is 6,371 km, the height of MEO orbit is 21,500 km, the GEO orbit height of 21,500 km..." should read as "Supposing that the Earth's radius is 6,371 km, the attitude of each MEO Satellite orbit is 21,528 km, and 35,786 km for GEO Satellite [9]"

Old Eq. (44.2)

$$SISRE = \sqrt{(\alpha R - T)^2 + \beta(A^2 + C^2)} \tag{44.2}$$

$$\alpha = \frac{1}{D}\int_0^{\theta_{\max}}\int_0^{2\pi}\frac{D_s - D_e\cos\theta}{\sqrt{D_e^2 + D_s^2 - 2D_eD_s\cos\theta}}\sin\theta d\phi d\theta$$

The online version of the original chapters can be found under DOI 10.1007/978-3-642-37398-5_44

Z. Hu (✉)
School of Geodesy and Geomatics, Wuhan University, Wuhan 430079, China
e-mail: zhigang.hu@whu.edu.cn

Z. Hu · G. Chen · Q. Zhang · J. Guo · X. Su · X. Li · Q. Zhao · J. Liu
GNSS Research Center of Wuhan University, Wuhan 430079, China

J. Sun et al. (eds.), *China Satellite Navigation Conference (CSNC) 2013 Proceedings*, Lecture Notes in Electrical Engineering 243,
DOI: 10.1007/978-3-642-37398-5_70,

$$\beta = \frac{1}{D}\int_0^{\theta_{\max}}\int_0^{2\pi}\frac{D_e^2\sin^2\theta\cos^2\phi}{\sqrt{D_e^2+D_s^2-2D_eD_s\cos\theta}}\sin\theta d\phi d\theta$$

where, D = $2\pi(1-\cos(\theta_{\max}))$ is the coverage area of the satellite footprint

New Eq. (44.2)

$$SISRE = \sqrt{(\alpha R - T)^2 + \beta(A^2 + C^2)} \tag{44.2}$$

$$\alpha = \frac{1}{D}\int_0^{\theta_{\max}}\int_0^{2\pi}\frac{D_s - D_e\cos\theta}{\sqrt{D_e^2+D_s^2-2D_eD_s\cos\theta}}\sin\theta d\phi d\theta$$

$$\beta = \frac{1}{D}\int_0^{\theta_{\max}}\int_0^{2\pi}\frac{D_e^2\sin^2\theta\cos^2\phi}{D_e^2+D_s^2-2D_eD_s\cos\theta}\sin\theta d\phi d\theta$$

where, D = $2\pi(1-\cos(\theta_{\max}))$ is the coverage area of the satellite footprint.

Old Eq. in (44.3)

$$SISRE_{BDS(GEO,IGSO)} = \sqrt{(0.99R - T)^2 + \frac{1}{128}(A^2 + C^2)} \tag{44.3}$$

Replaced by new Eq. in (44.3)

$$SISRE_{BDS(GEO,IGSO)} = \sqrt{(0.99R - T)^2 + \frac{1}{127}(A^2 + C^2)} \tag{44.3}$$

Old Eq. in (44.4)

$$SISRE^{Orbit\ only}_{BDS(GEO,IGSO)} = \sqrt{(0.99R)^2 + \frac{1}{128}(A^2 + C^2)} \tag{44.4}$$

Replaced by new Eq. in (44.4)

$$SISRE^{Orbit\ only}_{BDS(GEO,IGSO)} = \sqrt{(0.99R)^2 + \frac{1}{127}(A^2 + C^2)} \tag{44.4}$$